Geosynthetics Conference

A VIRTUAL EVENT

CO-LOCATING WITH

IECA ANNUAL CONFERENCE and Expo

Proceedings

CO-LOCATING WITH
IECA ANNUAL CONFERENCE and Expo

SUPPORTED BY
IFAI Geosynthetic Material Association
Geosynthetics Magazine
IGS NORTH AMERICA
IGS

SPONSORED BY

Geosynthetics Conference 2021 Proceedings

Edited by:

Melissa Beauregard, Ph.D., P.E.

Jennifer E Nicks, Ph.D., P.E.

ISBN: 978-0-935803-23-5

Table of Contents

Environmental 2

Erosion Solutions 1

Erosion Solutions 2

Geosynthetic Barriers

Geosynthetic Clay Liners

Geosynthetic Testing and Properties

Foreword to Technical Paper Sessions

The Geosynthetics 2021 Conference was held virtually for the first time on February 22-25, 2021. Co-located with the IECA Annual Conference and Expo, the Geosynthetics 2021 conference was hosted by the Geosynthetic Materials Association (GMA), a division of Industrial Fabrics Association International (IFAI), and supported by the North American chapter of the International Geosynthetics Society under the auspices of the International Geosynthetics Society.

The conference proceedings consist of 70 technical papers presented in 18 technical sessions during the 4-day conference. These papers represent the forefront of geosynthetics in research, engineering applications, and testing to advance the resilience, durability, and protection of our infrastructure. Paper topics include a variety of aspects: advancements in sediment control, environmental applications, erosion solutions, geosynthetic barriers, geosynthetic clay liners, geosynthetic testing and properties, geosynthetics in pavements and roadways, ground improvement, geosynthetic reinforced soil abutments, lightweight backfill, walls, embankments and slopes, and case histories. Each paper was peer-reviewed by a minimum of two independent reviewers.

The Technical Co-Chairs sincerely appreciate and thank the Conference Organizing committee, led by Committee Chair Prof. Jie Han, the Technical Program committee, authors, session chairs, and reviewers who contributed their valuable time and effort, resulting in the production of these proceedings.

In addition to the technical sessions, the conference program included a welcome plenary session, 6 panel discussions, 10 special sessions, 6 short courses, 2 engineering business sessions, and the Koerner Award Lecture, all of which focused on a variety of leading topics on geosynthetics engineering and education.

The Technical Co-Chairs also thank the efforts of these other contributors, the Koerner Lecturer, plenary speakers, panel and round-table discussion chairs, and IFAI members for organizing and contributing to the outreach and interaction on important topics within the geosynthetics community.

Lastly, Technical Co-Chairs thank Ms. Barbara J. Connett and Ms. Megan M. Firl of IFAI for their experience and commitment in planning and organizing a successful conference. This conference would not have been possible without their dedication and guidance.

Melissa Beauregard, Ph.D., P.E.
Jennifer E. Nicks, Ph.D., P.E.
Co-Chairs, Technical Program Committee

Geosynthetics Conference

GEOSYNTHETIC ADVANCEMENTS IN SEDIMENT CONTROL TECHNOLOGIES – Socks and Wattles: An Evolving Technology

Dr. Britt Faucette, PhD, CPESC, LEED AP[1]

[1]Filtrexx International, Decatur, GA; email: brittf@filtrexx.com

Introduction

Erosion and sediment control technologies have evolved significantly over the last two decades. While erosion control is commonly considered prevention and sediment control considered treatment, in reality sediment control technologies have been developed and designed to be used in a wide variety of applications - and the sock and wattle technologies have become the most versatile. Leading applications include perimeter control, inlet protection, check dam, slope interruption, sediment trap, and various on-site treatment practices. Unique to the sock and wattle family of technologies is they typically use a variety of fill materials, some designed for filtration, some for deposition, but are typically based on material availability, quality, and cost. Typical fill materials include coarse compost, wood mulch, straw, excelsior wood fiber, and coir. Each of these fill materials utilize a knitted or extruded mesh containment system to hold the fill material and allow for easy product manufacture, transport, job-site delivery, and installation. The most common mesh materials are polypropylene and HDPE, with a variety of denier, tensile strength, and mesh opening sizes based on the use and application. More recently, new mesh materials developed from bioplastics and biodegradable materials have entered into the market, mostly due to demand from state and federal agencies. Most performance testing and research has focused on the whole product rather than exclusively on the mesh or fill media, and in particular on compost filter socks, straw wattles, and silt fence as the three industry leading sediment control technologies. Research also suggests these mesh containment systems not only make transport, handling, and installation easier and more cost-effective, it also reduces overall material cost and improves performance.

Methods, Results & Discussion

Several studies have compared the performance of these technologies. The first study was conducted at San Diego State University in San Diego, CA (Table 1). The second study was conducted by the USDA Agricultural Research Service in Beltsville, MD (Table 2). The third study was conducted by the University of Georgia in Athens, GA (Figure 1). The final study was conducted by TRI Environmental in Anderson, SC (Table 3).

The first study, conducted at San Diego State University, utilized a modified ASTM D6459 test method. The sediment control barriers were installed on a loamy sand soil at the base of a 3:1 slope with an exposed soil and drainage of area of 2 meters wide by 8 meters long. The design storm used a Norton Ladder Rainfall Simulator developed by the USDA ARS National Soil Erosion Research Laboratory and was programmed for an intensity and duration of 2 in (5 cm)/20 minutes followed by 4 in (10 cm)/30 minutes. Average peak runoff rate exposed to the

sediment control barriers was 28.4 liters/ min, average runoff volume was 986 liters, average sediment concentration was 460,000 mg/L, and average sediment load was 385 kg. Experimental runs were conducted in triplicate to obtain statistical means.

Table 1: Compost filter sock and straw wattle sediment removal efficiency performance.

	Total Sediment Removal Rate
Compost Filter Sock	77%
Straw Wattle	59%

The second study was conducted at the USDA ARS, Environmental Quality Lab in Beltsville, MD. Sediment control barriers were installed at the base of soil plots with sandy loam soil, utilizing three replicates per treatment on a 5:1 slope. Rainfall intensity was 3.1 in/hr of simulated rainfall intensity for a duration of 30 min. Average runoff sediment concentrations on the bare soil test plots were 100,000 mg/L.

Table 2: Compost filter sock and silt fence sediment removal efficiency performance.

	TSS Removal	Turbidity Reduction
Compost Filter Sock	78%	63%
Silt Fence	67%	52%

The third study was conducted at the University of Georgia, in Athens, GA. For this study sediment control barriers were installed at the base of field test plots, 1 meter wide by 5 meters long. Rainfall simulation (Norton Rainfall Simulator with 4 variable speed V-jet oscillating nozzles obtained from the USDA ARS National Soil Erosion Research Lab) was used to produce a standard storm intensity of 12.5 cm (5.0 in)/hr for a duration of 3 hrs and total rainfall of 37.5 cm (15.0 in). This is greater than the 1-hour storm event for a 100-year return and similar to a 24-hr 10-yr return for North Georgia. Site soil was classified as an eroded Pacolet Clay Loam to Sandy Clay Loam and has a soil erodibility factor (K value) of approximately 0.36. The testing area was cleared of vegetation and graded to a 10% slope exposing the subsoil (B horizon) to simulate construction site conditions. Each sediment control barrier was tested in triplicate.

Figure 1: Compost filter sock and uncontained materials sediment removal efficiency performance.

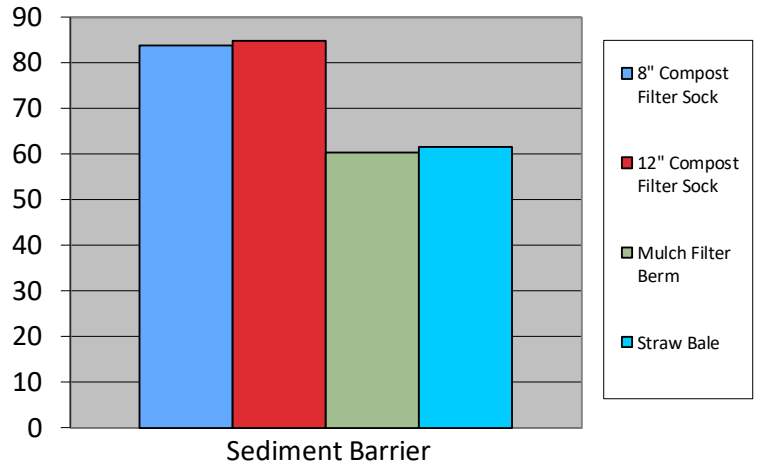

The final study was conducted by TRI Environmental in Anderson, SC. Similarly, each sediment control barrier was installed at the base of the slope, and each was tested in triplicate. This method utilized a modified ASTM D6459, which included 3:1 slopes, a sandy clay soil, and test plots measuring 27 ft long x 8 ft wide. Simulated rainfall was produced by simulators arranged around the perimeter of each test slope. Each simulator had four sprinkler heads atop a 15-ft riser pipe. The target rainfall intensities were 2, 4, and 6 in/hr and were applied in sequence, each for 20 minutes duration.

Table 3: Sediment control technology sediment removal efficiency performance comparison.

Sediment Control Barrier	Design Dia (in)	Weight (lbs/linear ft)	Undermined‡/ Overtopped (min)	Sediment Loss (tons/acre)	P Factor	Removal Efficiency (%)
Compost Sock	8	10.4	28	2.6	0.18	82
Compost Sock	12	25	NA	0.4	0.03	97
Straw Wattle	9	2.2	43‡	2.8	0.21	79
Straw wattle	20	2.7	33‡	4.1	0.30	70

Off-Spec compost sock	12	14.7	26	4.6	0.34	66

While most research has centered on the performance of these technologies anecdotal field evidence shows that by containing the material in a cylindrical sock or wattle performance is increased (Figure 1) and fill material volume is significantly reduced compared to installation of the same material in a berm design configuration. Fill material is typically the most expensive and heaviest fraction of the product, therefore even small reductions can lead to significant savings in raw material cost and transportation. Additionally, the mesh containment system allows these technologies to be pre-manufactured at central locations and sold through distribution hubs or direct shipped, taking advantage of existing distribution channels.

While HDPE and polypropylene materials have historically been the geotextile mesh containment systems of choice for these technologies, recent trends toward stronger and more flexible materials have found transportation and regulatory agencies specifying a knitted polypropylene with mesh opening sizes between 1/16 and 3/8 in. This mesh combines high tensile strength, durability on soil and pavement, and effective filler material containment without blinding from sediment. Opening sizes greater than 3/8 in are ineffective at containing the filler material, while opening sizes less than 1/16 in will restrict water flow and blind with sediment, thereby not allowing the organic filler material to filter the storm water and drastically decreasing the performance and design capacity of the technology as a whole. Note in Table 3 the significant reduction in performance when a mesh with opening sizes less than 1/16 in is utilized (12 in Off Spec Compost Sock) relative to a compost sock that utilizes the correct geotextile mesh (12 in Compost Sock).

Finally, in response to state and federal agency requests and trends in green building and infrastructure a new generation of biodegradable bioplastics and natural fiber mesh materials have entered the industry and are also utilized by these technologies. Common materials include jute, cotton, and wood fiber, with wood fiber providing the most tensile strength and field functional longevity among the group. It is anticipated that the specification and use of these materials will grown drastically in next several years.

Conclusions

Studies show compost filter socks and wattles can be very effective erosion and sediment control best management practices. While straw wattles are generally less expensive, compost filter socks are typically more versatile, higher performance, more environmentally sustainable, and have a lower total cost of ownership. Performance values very greatly between these technologies, however, the geotextile and natural mesh materials utilized to contain their respective filler materials has allowed them to be easily manufactured, shipped, and installed – making these technologies some of the most widely use in the erosion and sediment control industry today.

Objective Performance Assessment of Toe-of-Slope Sediment Retention Devices (SRDs)

James E. Sprague, CPESC,[1] and C. Joel Sprague, P.E.[2]

[1]TRI Environmental, 112 Martin Road, Greenville, SC 29607; jesprague@tri-env.com
[2]TRI Environmental, 112 Martin Road, Greenville, SC 29607; jsprague@tri-env.com

ABSTRACT

To be effective, sediment retention devices (SRDs) must provide the desired balance between flow rate and filtration efficiency. A sizable database of both bench-scale (ASTM D5141) and large-scale (ASTM D7351) test results related to toe-of-slope applications is presented on a variety of SRDs. This data is analyzed to determine product category-specific performance, and guidance is provided on SRD selection based on the desired balance between flow rate and sediment retention during construction operations.

INTRODUCTION

Sediment retention devices (SRDs) include silt fence, wattles, filter logs, compost socks, and various types of storm water inlet protectors, and are a widely used BMP to provide sediment filtration in stormwater runoff while allowing water passage. SRDs are frequently selected without knowing if the device can be expected to be sufficiently effective in providing the desired balance between flow rate and filtration efficiency. A sizable database of objective performance data has been developed based on recognized standard ASTM test procedures. The database includes data determined using both the bench-scale standard test method, ASTM D 5141, "*Standard Test Method for Determining Filtering Efficiency and Flow Rate of the Filtration Component of a Sediment Retention Device Using Site-Specific Soil*", and the large-scale standard test method ASTM D 7351, "*Standard Test Method for Determination of Sediment Retention Device Effectiveness in Sheet Flow Applications*." These test methods quantify both the sediment removal efficiency and the associated flow rate of an SRD, so that the potential for either excessive sediment loss or the back-up of runoff can be assessed.

STANDARDIZED TESTING OF SEDIMENT RETENTION DEVICES (SRD)

While sediment ponds have been widely studied and have generally accepted quantitative design procedures, this is not the case for most other BMPs, including sediment retention devices (SRDs). SRDs include silt fence, wattles, filter logs, compost socks, compost and earth berms, as well as various types of storm water inlet protectors. SRDs offer the potential to prevent water pollution without the large area requirement and safety concerns of a sediment pond. Unfortunately, SRDs are frequently selected without a quantitative means of knowing if the device can be expected to perform sufficiently. Without standardized test procedures there is no generally recognized way for specifiers/designers to verify marketing claims or one-time field trials, or for innovators to reliably test new products. Standardized testing procedures also assist the users of SRDs in establishing improved construction specifications. Owners and contractors can save money by installing the correct SRD for the expected site conditions. And, product manufacturers have a clear, generally recognized methodology for establishing product capabilities.

Testing SRD Performance in Sheet Flow Applications: ASTM D5141 & D7351. SRD material components can be accurately evaluated in a laboratory for hydraulic properties using the bench-scale standard test method, ASTM D5141, "*Standard Test Method for Determining Filtering Efficiency and Flow Rate of the Filtration Component of a Sediment Retention Device Using Site-Specific Soil*". Yet, the effectiveness of many SRDs systems is installation dependent. Therefore, a large-scale test that can incorporate the full-scale "as installed" condition is the ideal evaluation procedure. These needs are addressed by the large-scale standard test method ASTM D7351, "*Standard Test Method for Determination of Sediment Retention Device Effectiveness in Sheet Flow Applications*." These test methods both are able to quantify sediment removal and associated flow rate through an SRD, so that the potential for either excessive sediment loss or the back-up of runoff can be assessed.

Summary of Test Method ASTM D5141. Test method ASTM D5141 quantifies the ability of an SRD to retain eroded sediments carried by flowing water under bench-scale conditions. In the test method, sediment-laden water of a known concentration and sediment type is allowed to flow up to and through the filtration component of an SRD. The filtration component of an SRD is often the geotextile or fabric portion of the SRD. However, some SRDs, such as composts socks, utilize both a geotextile mesh and a compost filtration component encased within the geotextile component. The filtration component of an SRD should not be confused with the structural component(s) of an SRD. Examples of structural SRD components include; T-Posts in a silt fence system, metal grate insert of an inlet filter system, and wooden stakes used in a compost sock installation.

At a minimum, the effluent water and associated sediment passing through the SRD is measured and compared to the influent, or delivered, water and associated sediment to quantify the effectiveness of the SRD in retaining sediments while allowing water seepage. This test method may also assist in identifying physical attributes of SRDs, such as apparent opening size, permeability, or tensile strength that contribute to an SRD's ability to capture sediment while allowing water seepage, and it is useful for comparison of products. As discussed above, since the effectiveness of SRDs can also be installation dependent, this test method may not be completely indicative of product performance.

D5141 Apparatus and Procedures. **T**he test apparatus used in ASTM D5141 can accommodate a vertical SRD, such as a silt fence or wattle, or a horizontal SRD, such as an inlet filter. The full test apparatus is shown in Figure 1. The typical setup for silt fence testing is shown.

After positioning the SRD and ensuring that it is sealed around the edges, sediment-laden runoff is created by combining water and soil in the upstream mixing tank and agitating for one minute prior to initiation of the test. In the test method it is prescribed that 50 L (13.3 Gal) of water and 0.15 kg (0.33 Lb) of the prescribed soil should be mixed and introduced to the upstream face of the SRD. The soil can be either site-specific, or a default silty clay. The silty clay soil prescribed in the standard test method shall conform to the target gradation shown in Table 1, and shall have a PI $\leq$ 15. During the test, the sediment-laden flow passing thru the installed SRD is collected, and the total time required for the entire influent volume to pass through the SRD is recorded. After the completion of the test, vacuum-assisted filtration of the collected effluent seepage is used to obtain the mass of the sediment that was able to pass

through the SRD. Vacuum filtered sediments are dried and weighed, and the weight of collected sediment is compared to the initial influent amount of sediment put into suspension to determine the filtering efficiency. In addition, the total time required for the entire influent volume to pass through the SRD is used to calculate a flow rate, represented in $m^3/m^2/min$ (gal/min/ft^2).

Figure 1. ASTM D 5141 Test Setup

Figure 2. ASTM D 7351 Test Setup

Table 1. ASTM D 5141 and D7351 Prescribed Target Soil Gradations

Sieve Size	Percent Passing	
	D5141	D7351
No. 10 (2.0 mm)	100	92 – 100
No. 40 (0.420 mm)	80 – 100	80 – 100
No. 100 (0.149 mm)	70 – 90	50 – 93
No. 200 (0.075 mm)	50 - 70	35 - 84
Plasticity Index	NP	2 < PI < 8

Summary of Test Method ASTM D7351. ASTM D7351 is a standard full-scale performance test commonly used to characterize *installed* SRD system performance, including sediment and flow retention, and structural behavior under hydraulic loading. Sediment-laden water is allowed to flow up to and through an installed SRD. At a minimum, the amount of sediment-laden flow and associated sediment passing thru the SRD is measured. The measurement of flow (seepage) and sediment that passes through the SRD subtracted from the amount in the upstream flow, and then divided by the amount in the upstream flow, is used to quantify the water retention percentage and filtration effectiveness percentage of the SRD under full-scale conditions.

This test method may also assist in identifying physical attributes of the SRD system that contribute to their sediment control performance, and it is useful for comparison of different SRDs and their unique installation requirements. In contrast to ASTM D5141, D7351 evaluates the “as installed” SRD system performance. This is an important difference in the test methods. As an example, a silt fence system with a low flow, high sediment retention filtration component would require robust post size and frequent post spacing as the filtration component will retain a high volume, and consequently, high weight of water that may break posts of weaker construction or less frequent spacing. In another example, a compost filter sock installed with a 3” installation trench may provide better soil retention than a compost filter sock with no installation trench. Since the effectiveness of SRDs is installation dependent, this test method is indicative of actual field performance when installed with the appropriate techniques.

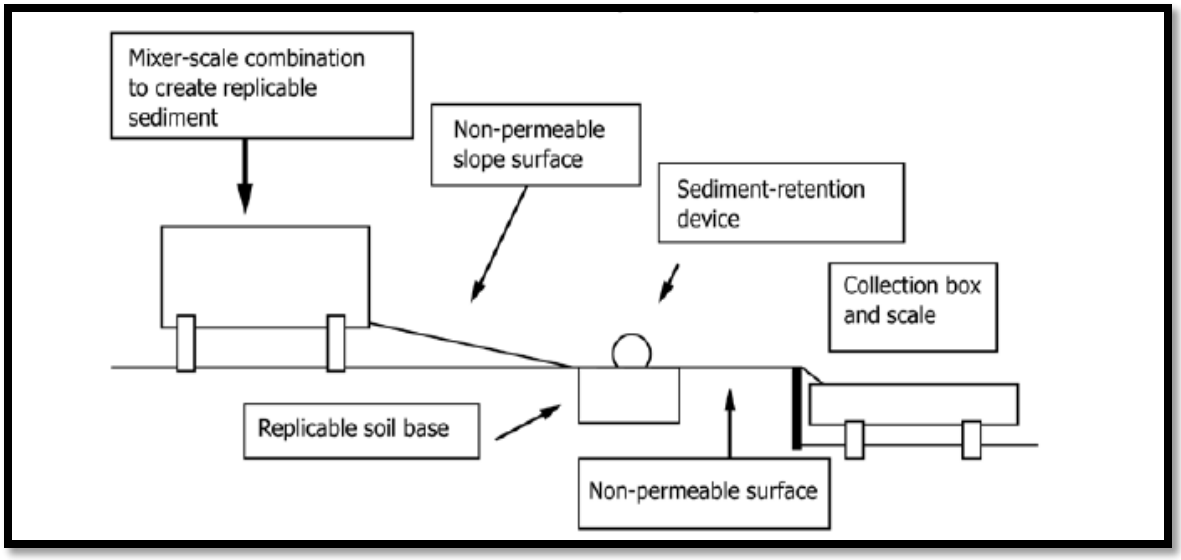

Figure 3. ASTM D 7351 Apparatus Schematic

D7351 Apparatus and Procedures. The test method is commonly executed using the following equipment:

- A mixing tank with an internal paddle mixer device mounted on scales ;
- A sufficient source of water and associated pumping equipment to fill the mixing tank in a timely manner; and
- A tank of sufficient volume to collect all runoff passing the SRD, mounted on scales.

The mixing and collection tanks are separated by areas, or zones, as shown in Figure 3. A non-permeable slope surface immediately below the mixer discharge spreads the initial discharge and provides a retention zone above the installation zone. The installation zone is comprised of prepared soil subgrade to allow full-scale installation of the SRD to be tested. The area below the installation zone is non-permeable to facilitate efficient transmission of runoff passing the SRD to the collection tank.

A representative sample of the SRD to be tested is installed in the installation zone in accordance with the manufacture's recommendations. A sediment-laden runoff is then created by combining water and soil in the mixing tank and maintaining agitation during the test. A typical "construction phase" sediment concentration for testing is 6%. The rationale for the "construction phase" sediment concentration used in the test method is described in the standard as follows: *"An important variable in any testing procedure is the establishment of test "conditions." For a sediment control performance test this means selecting an appropriate design storm event and associated runoff along with an expected amount of sediment to be transported by the runoff. For this testing, a standard 10-y, 6-h storm event (mid-Atlantic region of US) was selected. This return frequency is commonly used for sizing sediment control ponds and, thus, was deemed appropriate for the testing of other SRDs. Using this criterion, a 100 mm (4 in.) rainfall was selected. It was also assumed that approximately 25% of the storm would occur during the peak 30 minutes, and that 50 % of the rainfall would infiltrate into the ground (Goldman, et al., 1986). A theoretical contributory area of 30 m (100 ft) slope length by 6 m (20 ft) wide was selected to limit runoff to sheet flow conditions (Richardson, 1990). Runoff and associated sediment were calculated using the Modified Universal SoilLoss Equation (MUSLE)*"

As described above, the Modified Universal Soil Loss Equation was used in the standard test method to produce test quantities of runoff of 2250 kg (approx. 5000 lb) and sediment load of 136 kg (approx. 300 lb) for a 20' linear SRD installation, or a sediment concentration of approximately 6%. A constant valved discharge is released evenly across the slope for thirty minutes to replicate the peak thirty minutes of the prescribed storm event.

Periodic grab samples are taken as influent discharge flows through, over, or under the installed SRD and into the collection tank. Depth and weight of the collected seepage inside the collection tank is measured and recorded at the same intervals. Observations such as height of ponding, undermining, overtopping and the associated times are recorded. The grab samples are evaluated in a lab to determine percent solids content of the filtrate, and to determine the percent filtering efficiency of the installed SRD. Turbidity is also measured on the samples.

ASTM D5141 & ASTM D7351 SRD TESTING RESULTS

D5141 and D7351 testing are most commonly used by various state Departments of Transportation (DOTs) to confirm that SRDs conform to state specifications for sediment removal and sustained seepage. DOT projects are typically linear, requiring the extensive use of toe-of-slope SRDs, such as silt fence, wattles, and compost socks. As a result, DOTs must often be mindful of excessive ponding behind SRDs caused by sediment build-up on SRDs that might cause a safety hazard on adjacent roadways. As noted earlier, D5141 effectively quantifies the sediment removal effectiveness and the associated sustained seepage of the filtration component of an SRD, while D7351 quantifies the balance of sediment removal and sustained seepage for the installed SRD system.

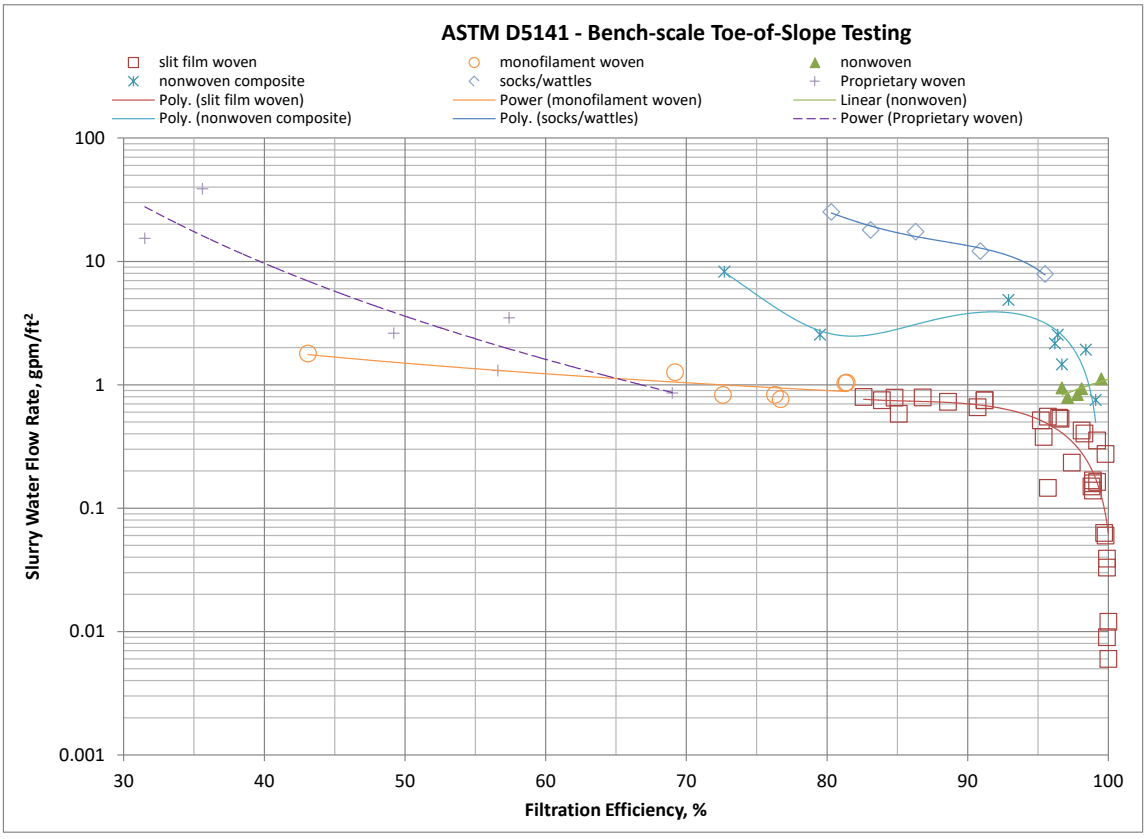

Figure 4. D5141 Testing of Various SRD Types

ASTM D5141 Test Data. Figure 4 presents results of ASTM D5141 testing of a wide range of SRD types commonly used in linear, toe-of-slope applications. SRDs tested include both woven and nonwoven geotextile-based silt fence as well as various proprietary composite and woven fences and socks/wattles.

Discussion of D5141 Data. Figure 4 shows a clear delineation between product types and their relative performance in both filtration efficiency and flow rate. This data is comprised of six nominal categories of products tested using ASTM D5141. The nominal categories, as identified by the authors, and the number of tested products are as follows:

- 32 Woven Slit Film Geotextile Silt Fence
- 6 Woven Monofilament Geotextile Silt Fence
- 5 Nonwoven Geotextile Silt Fence
- 8 Nonwoven Composite Geotextile Silt Fence
- 5 Three Dimensional Filter Socks and Fibrous Wattles
- 6 Proprietary Woven Geotextile Silt Fence

Sprague and Sprague (2020) discussed the data from all this testing for each category of products. Their primary findings included:

Woven Slit Film Geotextile Silt Fence: This category of filtration component provides excellent filtration efficiency across all tested products. All of the 32 tested products provided greater than 80% filtration efficiency, and the majority of the tested products providing greater than 90% filtration efficiency. However, this category of product is also the category with the lowest flow rate, in general. These results point to a critical issue: excessive ponding. Excessive ponding may be an acceptable risk when slit film fabric is used to protect sensitive water bodies, but may be an unnecessary risk along roadways when excessive ponding could lead to road way flooding and potential risk to motorists. It must be noted as well, that slit film fabrics when deployed as two dimensional silt fences, must be adequately supported by robust posts with frequent post spacing to reduce the risk of fence failure due to the load associated with high volume ponding.

Woven Monofilament Geotextile Silt Fence: This product category provides moderate filtration efficiency, providing between 65% and 85% filtration efficiency and moderately high, yet relatively uniform, flow rate.
This product category may be exceptionally valuable to designers in areas where the risk of excessive ponding and road way flooding would lead to unnecessary motorist risk, but where downstream impairment is of relatively low risk.

Nonwoven Geotextile Silt Fence: This product category, in general, provides excellent filtration efficiency, with all tested products providing greater than 95% filtration efficiency and moderately high, yet uniform, flow rate. Nonwoven fabrics are commonly utilized for filtration, because they are able to retain very fine soil particles while maintaining higher flow characteristics than a comparable woven product.

Nonwoven Composite Geotextile Silt Fence: Aside from the two noticeable outliers, this product category provides excellent filtration efficiency with all products providing greater than 90% filtration efficiency and high flow rate. In contrast to the nonwoven geotextile silt fence

category, products in the nonwoven composite geotextile product category are composed of a multi-layer nonwoven geotextile component impregnated, or filled, with natural fibers. The combination of multi-layer nonwoven fabric and fiber impregnation leads to a high strength, relatively thick, filtration component that provides a structurally three dimensional profile allowing high water flow and soil capture.

Three Dimensional Filter Socks and Fibrous Wattles: This product category provides moderately high filtration efficiency with all tested products providing greater than 80% filtration efficiency and excellent flow rate. Three dimensional filter socks and fibrous wattles are generally composed of either a geosynthetic fabric or mesh filled with compost, rock, straw, or other agricultural or synthetic media. This product type typically provides a much lower vertical profile. This lower vertical profile will lead to more frequent maintenance/clean-out requirements to avoid over-topping and lack of product efficacy.

Proprietary Woven Geotextile Silt Fence: This product category provides poor filtration efficiency, but high flow rate – by design. The target use is for special conditions such as a prefilter or as a filter to prevent trash migration without runoff impoundment.

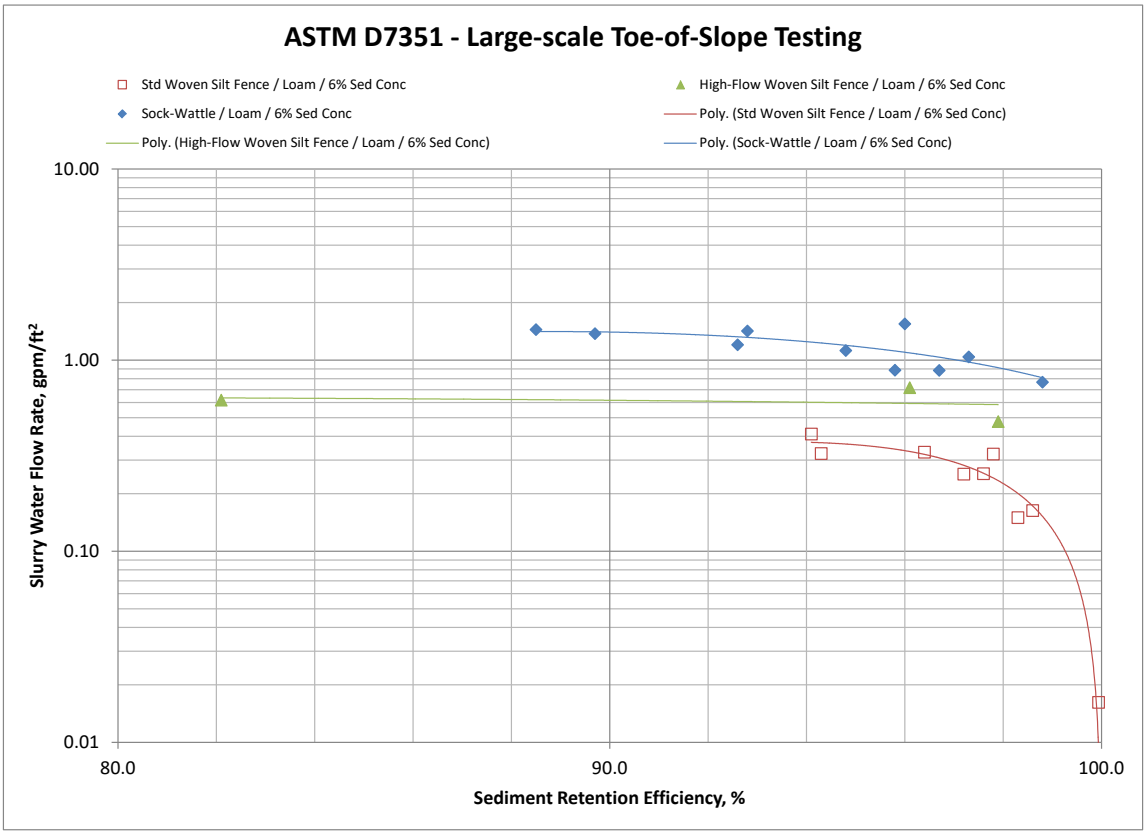

Figure 5. D7351 Testing of Various SRD Types – In Terms of Flow Rate

ASTM D7351 Test Data. Figure 5 presents results of D7351 testing of a range of SRD types commonly used in linear, toe-of-slope applications. SRDs tested include both woven slit film and specialty high-flow woven silt fence, along with various socks/wattles. Typically, the results from D7351 testing are presented as efficiencies: Water Retention Efficiency vs. Sediment Retention Efficiency. But, the data has been recalculated and presented in Figure 5 in the same

terms as the data from D5141: Slurry Water Flow Rate vs. Sediment Retention Efficiency. This allows the results of both tests to be more easily compared, as will be done in section 7.6.

Discussion of D7351 Data. ASTM D7351 was used for the evaluation of twelve unique two dimensional silt fence SRD products and ten unique three dimensional sock/wattle SRD products in this research. All of the products were subjected to the theoretical thirty minute peak discharge of a design storm event as prescribed in the standard calculated using the Modified Universal Soil Loss Equation (MUSLE). The resulting influent sediment concentration is prescribed at approximately 6%, and the soil type used in this research was Loam with a PI $\leq$ 8. Sprague and Sprague (2020) discussed the data from this testing. While observing that there was a clear delineation in performance between the two dimensional and three dimensional SRD products, their primary findings included:

Two dimensional SRD products: These products provide consistently high sediment retention efficiency. However, performance in terms or water retention efficiency, ranges greatly, from 7% water retention effectiveness to 98% water retention effectiveness over the course of the design storm. This is most likely a result of the material characteristics of the tested product similarly to the product categories tested in the ASTM D5141 testing program described above.

Three dimensional SRD products: All three dimensional products provided high sediment retention efficiency, with performance ranging from 88%-98% efficiency. However, as a product category, and as opposed to two dimensional SRDs, three dimensional SRDs as a product category have a consistently high flow capacity. But caution is in order, in contrast to two dimensional SRDs which are typically installed with a six inch burial trench sealing the fabric to the soil surface, three dimensional SRDs are often installed in a shallow installation trench or laid directly on the soil surface. This lack of a sealing burial trench allows water to more freely seep under the installed three dimensional SRD, further relying on the unit weight per length of the product to seal against the soil surface and slow seepage. A light- weight three dimensional SRD of a given nominal height/diameter may not provide the performance of a heavy weight three dimensional SRD of a similar nominal height/diameter owing to the lighter-weight SRD's buoyancy when ponding runoff.

D5141 vs. D7351. Figure 6 presents combines Figures 4 and 5 into a single chart in order to better see the relationship between bench-scale and large-scale test results. Although the exact same products were rarely used in both tests, similar products were included in both and can provide a reasonable comparison between the test results. The solid data points (filled square, circle, and diamond) are from large-scale (D7351) testing and relate most closely to the same open data points (unfilled square, circle, and diamond) which are from bench-scale (D5141) testing of similar products. It is quite clear when comparing data from D5141 to D7351 for similar product categories (slit film woven vs. std woven silt fence; monofilament woven vs. high-flow woven silt fence; and socks/wattles vs. sock-wattle) that in all cases large-scale testing produced lower slurry water flow rates and higher filtration efficiency. This makes sense when it is considered that the D7351 testing is done with a higher sediment concentration (6% vs. 0.3%) providing much more sediment to deposit on and in front of the device, enhancing removal but reducing seepage. Additionally, in large-scale "as installed" testing of silt fence, the ponding on the fence leads to the fence stretching between support posts. This creates a "belly" in the fabric which causes the silt fence weave to tighten like a "Chinese finger trap" which also reduces seepage.

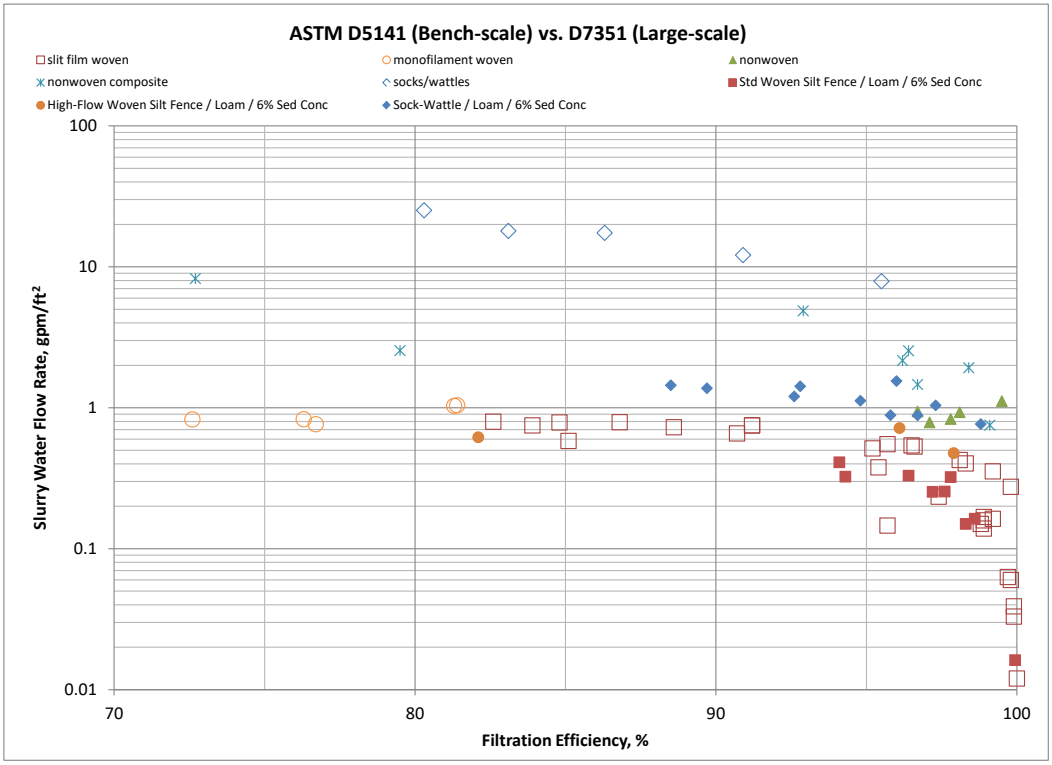

Figure 6. D7351 Testing of Various SRD Types – In Terms of Flow Rate

CONCLUSIONS

This paper has presented substantial data, via two standardized test methods, on the performance of both SRD filtration components and "as installed" SRD systems. Yet to be invented is the SRD that has 100% seepage and 100% sediment retention. Typically, when sediment retention, a.k.a. filtration efficiency, is increased, loss of seepage, or retention efficiency, also increases. Test results show that both ASTM D5141 and D7351 are able to differentiate between SRD types used in toe-of-slope applications. There are clear performance differences, using both methods, when evaluating filtration components and installed systems. Additionally, test results show that when full-scale, construction-phase conditions are simulated, the more accurate performance characteristics are the higher filtration efficiencies and lower flow rates resulting from large-scale (D7351) testing.

REFERENCES

ASTM D5141, "Standard Test Method for Determining Filtering Efficiency and Flow Rate of the Filtration Component of a Sediment Retention Device". ASTM, Conshohocken, PA.

ASTM D7351, "Standard Test Method for Determination of Sediment Retention Device Effectiveness in Sheet Flow Applications". ASTM, Conshohocken, PA.

Sprague, J.E., and Sprague, C.J. (2020), "Comparative Analysis of the Flow and Filtration Capabilities of Sediment Retention Devices (SRDs)", Conf. L, International Erosion Control Assoc., Raleigh, NC.

Geosynthetics Conference

Technologies used for Sediment Control: How are they Tested and How do they Perform

J. Blake Whitman, Ph.D., P.E., CPESC[1]

[1]School of Concrete & Construction Management, Middle Tennessee State University, 1301 East Main Street, Murfreesboro, TN 37127; e-mail: blake.whitman@mtsu.edu

ABSTRACT

Construction sites around the world rely on sediment barrier technologies to intercept, treat, and effectively discharge stormwater emanating from land disturbing activities. Silt fence systems are often selected as the perimeter control of choice due to their economics, ease of installation, and published performance capabilities. Silt fence systems are temporary sediment barrier practices constructed by attaching a geotextile fabric (non-woven or woven) to support posts (wood or steel) and the ground surface via trenching or mechanical slicing. Historically, silt fence performance capabilities have been identified using standardized ASTM testing methodologies. While these testing strategies provide data for performance analyses, research efforts have identified several short comings associated with these standardized testing practices. The aim of this study was to address these short comings and develop improved testing methodologies to facilitate comprehensive sediment barrier performance analyses and comparisons. This study introduces two state-of-the-art testing methodologies (i.e., small-scale and large-scale) for determining performance capabilities of silt fence systems, as well as other innovative sediment barrier practices used within the construction industry. Testing apparatus designs and performance results are summarized to illustrate how these testing innovations advance the overall body of knowledge within the field of erosion and sediment control.

INTRODUCTION

Sediment barriers (SBs) are sediment control practices typically installed along the perimeter of construction sites that are intended to intercept, capture, and temporarily contain sheet to shallow concentrated flows prior to site discharge. SBs are categorized as sediment retention devices (SRDs) due to the removal of sediment primarily through sedimentation and, to a lesser degree, filtration (*ASTM Standard D7351 2013, Barrett et al. 1998*). SB practices primarily reduce eroded soil transport through impounding stormwater runoff upstream of the practice and allowing for suspended particles to settle. Sediment capture is also achieved when flow passes through the SB and particles become lodged within the porous medium; however, this method of sediment removal is commonly less effective. The filtration efficiency of SB material is based upon, and is limited by, the size of the pore passages often resulting in small soil particles passing through void spaces within the material medium (*Barrett et al. 1998*). In addition, the flow-through capacity of materials degrade over time as pores become clogged with sediment, thereby increasing impoundment potential (*Haan et al. 1994*).

Silt fence SBs essentially consist of a geotextile supported vertically by wooden or steel posts. Geotextiles used in silt fence applications generally fall into one of two categories, woven and nonwoven. Silt fences are available as pre-assembled systems ready for jobsite installation

or kits that require assembly during the installation process. In order for a silt fence to contain runoff, the geotextile must be secured into the soil by trenching or mechanical slicing and compacting. In areas of high runoff flows or velocities, geotextile reinforcement in the form of woven-wire or polypropylene netting may be required to enhance the silt fence's resistance to hydrostatic loading.

OBJECTIVES

The objectives of this paper are to: (1) provided a brief overview of ASTM testing methods used to quantify SB performance; (2) present innovative advancements in small- and large-scale SB testing methodologies that yield results based on geographical location; and (3) summarize major findings from small- and large-scale performance evaluations of SB practices. The overall aim of this paper is to introduce readers to new and innovative SB testing strategies that have been shown to produce performance results linked to sediment and hydrological loading conditions for a specific geographical climate zone.

STANDARDIZED SB TESTING METHODOLOGIES

Currently, ASTM recognizes two standards for testing SB performance: (1) ASTM D5141, *Standard Test Method for Determining Filtering Efficiency and Flow Rate of the Filtration Component for a Sediment Retention Device (SRD)* [aka: small scale] and (2) ASTM D7351, *Standard Test Method for Determination of Sediment Retention Device (SRD) Effectiveness in Sheet Flow Applications* [aka: large scale]. Performance results emanating from these tests have been widely accepted within industry and are often used by Departments of Transportation when evaluating SBs for inclusion on their approved products list.

ASTM D5141 Test Method

ASTM D5141 (*2011*) describes the procedures for conducting small-scale flume experiments to determine sediment removal efficiency and flow through rates of geotextile fabrics. The development of this test method was a direct result of the work done by Wyant (*1981*), where he evaluated multiple nonwoven geotextile fabrics within a laboratory setting. The test apparatus developed consists of a 49.2 in. (125 cm) long by 33.5 in. (85 cm) wide flume with an 8% slope. Sediment-laden flow is introduced using a 19.8 gallon (75 L) container equipped with a mechanical stirrer to facilitate soil suspension. Wyant (*1981*) observed average sediment removal efficiencies of 92% for silty soil and 97% for sandy soil and flow rates ranging from 0.0004 to 3.5 $m^3/m^2/min$ (0.0013 to 11.5 $ft^3/ft^2/min$). Henry and Hunnewell (*1995*) also used this standard test method to evaluate nonwoven polyester and polypropylene geotextiles using dredged sediment that mainly consisted of silt and clay. Results indicated sediment removal efficiencies of 45.5% and 72.8%, respectively, and flow rates ranging from 0.063 to 0.026 $m^3/m^2/min$ (0.206 to 0.085 $ft^3/ft^2/min$). Risse et al. (*2008*) performed sediment removal tests on two silt fence geotextiles using the standard test method, as well as a modified version. The modified version increased the slope of the flume from 8% to 58% to produce increased hydraulic head on the geotextile. This testing method allows for the evaluation of geotextile performance properties under sediment-laden flows. Nonetheless, it does not provide a means

for evaluating installation improvement strategies, structural integrity, or full-scale performance capabilities.

ASTM D7351 Test Method

ASTM D7351 (*2019*) describes the procedure for conducting a full-scale experiment and quantifying a SRB's ability to retain soil eroded by sheet flow conditions. Sediment-laden flow is generated by mixing 5,005 lb. (2,270 kg) of water and 300 lb. (136 kg) of sediment within a tank equipped with an internal agitator. The tank is positioned on a scale and the weight of the tank is monitored at regular intervals while discharging sediment-laden water at a constant flow rate of 176.8 lb./min (80 kg/min) during a 30-minute test. Test conditions are designed to simulate the peak 30 minutes of a 10-yr, 6-hr storm event in the mid-Atlantic region that produces 4 in. (10.1 cm) of rainfall. The flow and sediment load were determined by assuming 25% of the rainfall from the 10-yr, 6-hr storm occurs in the peak 30 minutes of the storm event and that 50% of the precipitation infiltrates into the ground. The associated sediment load resulting from erosion was calculated using the Modified Universal Soil Loss Equation (MUSLE) (*Williams and Berndt 1977*), which allows the calculation of a storm specific quantity of sediment yield. The sediment-laden flow is directed down an impervious 3*H*:1*V* slope to the 20 ft (6 m) wide impervious test area where the SRD is installed. The flow passing through the SRD is collected and directed toward a collection tank where effluent weight is measured using a scale. Bottle grab samples are also taken, typically every 5 minutes. Though the tanks provide a measurement of the amount of sediment-laden runoff discharged and collected, the flow rate for the 30-minute test is limited by the capacity of the tank. In addition, the scales only provide the total weight of sediment-laden water and do not have the ability to differentiate between the composition of sediment and water.

MODIFIED SB TESTING METHODOLOGIES

Through research efforts at the Auburn University – Erosion and Sediment Control Testing Facility (AU-ESCTF), two (small and large scale) innovative SB testing apparatuses and methodologies have been developed.

Small-Scale Testing

The small-scale SB testing apparatus was designed to evaluate geotextiles installed as perimeter control practices. The apparatus was constructed out of lumber and plywood with overall dimensions of 4 ft (1.2 m) wide, 16 ft (4.9 m) long, and height of 3 ft (0.9). The profile of the apparatus consists of a 3*H*:1*V* slope that transitions to a 1% slope, which mimics typical slopes associated with highway construction projects. When evaluating geotextiles using ASTM D5141, geotextiles are installed at the toe of an 8% slope, which limits the installations stormwater storage capacity due to the close proximity to the slope. To increase storage capabilities, geotextiles were installed 6 ft (1.8 m) from the toe of the 3*H*:1*V* slope within the small-scale testing apparatus. Flow is directed into the apparatus via an 8 ft (2.4 m) plywood sheet with 2 by 6 in. (5 by 15 cm) lumber borders that transition inflow form shallow concentrated to sheet flow.

To prevent flow from passing through joints of the small-scale apparatus during testing, a 0.006 in. (0.15 mm) thick polypropylene liner was placed inside the apparatus. Geotextiles were held in place using 2 by 4 in. (5 by 10 cm) lumber and wood screws. Flow bypass between the geotextile and polypropylene liner was prevented by sealing each installation with heavy-duty construction caulk during the installation process. After each evaluation was completed, the geotextile and dried caulk sealant were carefully removed to prevent damage to the liner. This process allowed a single liner to be used for multiple installations. However, if liner damage occurred during post-test geotextile or sediment removal, a new liner was installed. This method proved effective at preventing seepage, while also providing a means for collecting retained sediment.

Water introduction into the apparatus was designed to facilitate accurate flow rate monitoring throughout testing while also providing a means for easy flow rate adjustments. To achieve the desired flow control necessary during testing, a four-stage process was implemented. The setup consisted of a submersible 2 in. (5 cm) pump, a 300-gallon (1,135 L) equalizing tank, a 90° v-notch discharge weir plate for controlling apparatus inflow, and two 4 in. (10 cm) discharge valves for controlling flow exiting the bottom of the tank. The submersible pump transported water from the onsite supply pond into the equalizing tank located upstream of the test apparatus. As water filled the tank and began to flow across the weir plate, discharge gate valves were adjusted until the desired water level within the tank was achieved. A custom scale and pressure head tube apparatus were installed adjacent to the tank to monitor water levels. The scale provided a correlation between water depth flowing across the weir plate and flow rate entering the apparatus. This method of water introduction and monitoring allows for a wide range of flow rates, which may vary based on regional rainfall events.

Sediment metering was achieved by manually feeding soil into the soil/water mixing trough built on the plywood flow introduction sheet. To maintain a consistent rate throughout testing, 5-gallon (3.79 L) buckets were pre-filled with the exact amount of soil to be introduced over a 2 minutes duration. Workers would monitor a stopwatch while feeding soil from the buckets into the system so that one bucket of soil would be emptied every 2 minutes. Workers would position themselves beside the flow introduction sheet so that at the end of every 2-minute cycle, a new bucket of soil could be easily place over the mixing trough and soil feeding could continue without interruption. A mechanical means of soil introduction was available; however, soil texture caused particles to bridge together preventing soil from flowing from the hopper into the mechanical auger at a consistent rate. Figure 1 illustrates the newly developed small-scale testing apparatus.

Figure 1. Small-Scale Testing Apparatus

The developed small-scale testing methodology sought to improve the standard ASTM testing methodology by incorporating realistic runoff conditions intercepted by silt fence practices installed in the field as opposed to a one-size-fits-all approach. While ASTM D5141 indicates that soil used during testing should be representative of the site location in which the geotextile will be implemented, it fails to address changes in hydraulic and sediment loads based upon site location. One unique element that distinguishes the newly developed methodology from that of ASTM D5141 is that it incorporates regionally specific hydraulic and sediment loads resulting from the peak 30 minutes of a 2-yr, 24-hr design storm. An additional enhancement of the presented methodology is the incorporation of time variable reporting of effluent flow rates and filtering efficiencies over the course of an experiment. The nominal filtering efficiency and flow rate determined using ASTM D5141 does not indicate geotextile performance variations over time. These shortcomings can be attributed to the rapid introduction of sediment-laden flow into the testing apparatus and the limited duration of time in which data can be collected. The presented methodology addresses these limitations by introducing flow for 30 minutes and continually collecting data during the 90-minute dewatering period. This allows variations in performance to be identified, as well as the times in which these changes occur. Results obtained using the developed methodology allow for enhanced data analyses and improved characterization of in-field geotextile performance.

Small-scale performance evaluations were based on observations and data collected throughout experiments. Hydraulic performance, sediment retention, and water quality data were collected for each experiment. These parameters were used to compare the performance of each geotextile tested. Whitman et al. 2019(a) provides a more detailed description, with images, of the small-scale testing apparatus.

Large-Scale Testing

The large-scale SB testing apparatus was designed to evaluate various SB practices (e.g., silt fence, wattles, erosion tubes, etc.) when subjected to sheet flow runoff. The apparatus was constructed out of concrete, masonry block, and steel. The apparatus consisted of an impervious 3*H*:1*V* slope 20 ft (6.1 m) wide by 20 ft (6.1 m) long that transitioned to an earthen area (compacted bare soil) 20 ft (6.1 m) wide by 12 ft (3.7 m) long. SB practices were installed 6 ft (1.8 m) downstream of the slope transition, in the earthen test area, as they would be installed on a construction site. A concrete catch basin was installed downstream of the earthen test area to collection sediment-laden flow passing through SB practices during testing.

Simulated flow was introduced to the system with a 3 in. (7.62 cm) trash pump that draws water from an on-site supply pond. Water was pumped into a 300-gallon (1,135 L) water equilibrium tank that uses a series of valves and orifices to control flow over a calibrated weir prior to entering a mixing trough. The calibrated weir is monitored with a pressure tube that indicates flow rate across the weir. Adjustments to weir flow rates are accomplished via water tank discharge lines fitted with gate valves. The weir discharges into a mixing trough where sediment is introduced at a controlled rate and mixed with highly turbulent flowing water.

Sediment introduction is accomplished using a steel hopper equipped with a hydraulic driven conveyor chain that allows sediment to be metered at a constant rate of 37.6 lb./min (16.9 kg/min) into the mixing trough. The conveyor chain is calibrated to assure the desired sediment introduction rate is achieved. After mixing has occurred, the sediment-laden water enters the top of the 3*H*:1*V* impervious slope of the test apparatus. The concentrated flow exiting the bottom of the mixing trough is converted to sheet flow using slotted diversion vanes mounted to the impervious slope. Figure 2 illustrates the newly developed large scale-testing apparatus.

Figure 2. Large Scale Testing Apparatus

Similar to the small-scale testing methodology, the large-scale testing methodology also sought to improve the standard ASTM test by incorporating realistic runoff conditions intercepted by sediment barrier practices installed in the field. One unique element that distinguishes the newly developed methodology from that of ASTM D7351 is that it incorporates regionally specific hydraulic loading resulting from a drainage area of 0.5 acres as opposed to only 0.05 acres per 100 LF of sediment barrier. This relationship was established based on design guidelines outlined in stormwater design manuals that specify no more than 0.5 acres drain to 100 LF of installed sediment barrier. Additionally, sediment loading was calculated based on the Modified Universal Soil Loss Equation (MUSLE) for a 0.5-acre plot of land in the region of sediment barrier implementation as opposed to being set at 300 lb. per ASTM performance test.

Large-scale performance evaluation of SBs was based on structural integrity, sediment retention capabilities, hydrodynamic flow characteristics, and water quality impacts. These parameters were used to compare the performance of various SB perimeter controls used in highway construction. Bugg et al. 2017 provides a more detailed description, with images, of the large-scale testing apparatus.

RESULTS SUMMARY

Small-Scale Results

Under the developed small-scale testing regime, performance evaluations were conducted on two nonwoven geotextiles, three woven geotextiles, and a stacked sandbag installation. Data collection included: impoundment depth, sediment retention weights, and grab samples for water quality analyses. Each of these parameters were subsequently used to evaluate the performance capabilities of each material evaluated. Effluent flow rates observed during the test period for nonwoven geotextiles were on average 43% lower than woven materials, which resulted in extensive retention times for nonwoven materials. Sediment retention results indicated that on average nonwoven geotextiles (e.g., 97%) outperform woven geotextiles (e.g., 91%). Water quality analyses suggest that the primary means for turbidity reduction is sedimentation during the test period (e.g., 46%) and filtration during dewatering (e.g., 19%). This suggests that having adequate stormwater storage upstream of an installation is important to dissipate inflow energy, promote sedimentation, and minimize resuspension of particles. Finally, an evaluation of stacked sandbags established that performance capabilities of three-dimensional SB products can be determined using the small-scale SB testing apparatus. Detailed analyses associated with these results is presented in Whitman et al. 2019(a). Table 1 provides a summary of results.

Table 1. Small-Scale Geotextile Performance

Material		Avg. Sediment Retention
Nonwoven Geotextiles	Needle Punched	97%
	Spunbond	98%
Woven Monofilament Geotextiles	Blue Stripe	87%
	Red Stripe	94%
	Green Stripe	93%

Large-Scale Results

Using the large-scale testing apparatus, performance evaluations were conducted on multiple silt fence installation modifications, as well as several manufactured sediment barrier practices. Silt fence results suggest that T-post size, T-post spacing, fence height, and geotextile entrenchment method play a significant roll in silt fence performance. Evaluations of manufactured sediment barrier practices suggest that practices which achieve impoundment depths between 1 and 1.5 ft (0.3 and 0.46 m) achieve sediment capture rates of at least 90% and reduce impoundment surface turbidity up to 60% when compared to turbidity along the bottom of the impoundment. Detailed analyses associated with these SB practices are presented in Whitman et al. 2018 and Whitman et al. 2019(b). Table 2 provides a summary of sediment retention results.

Table 2. Large-Scale Installation Performance

Material		Avg. Sediment Retention
Nonwoven Silt Fence	Standard Installation	83%
	Modified Installation	93%
Manufactured Silt Fence Systems	Red Stripe System	90%
	Green Stripe System	85%
Manufactured Sediment Barriers	Excelsior Wattle	82%
	Compost Tube	80%
	Excelsior Block	84%

CONCLUSION

The objectives of this paper were to (1) describe standardized testing methodologies used to evaluate SB practices, (2) discuss research efforts that have focused on improving standardized testing methodologies, and (3) present a brief summary of results obtained through these research efforts. Collectively, each of the research efforts discussed will provide improved SB practices that are designed, implemented, and installed correctly on construction sites. Ultimately, this study will provide engineers, stormwater professionals, and researchers with a comprehensive view of the efforts undertaken over the past few years to improve construction site stormwater management practices.

REFERENCES

ASTM International. (2011). “Standard test method for determining filtering efficiency and flow rate of the filtration component for a sediment retention device.” *ASTM D5141 - 11*, West Conshohocken, PA, USA.

ASTM International. (2019). “Standard test method for determination of sediment retention device effectiveness in sheet flow applications.” *ASTM D7351 - 13*. West Conshohocken, PA, USA.

Barrett, M. E., Malina, J. F., Jr., and Charbeneau, R. J. (1998). “An Evaluation of Geotextiles for Temporary Sediment Control.” *Water Environment Research*, Vol. 70, No. 3, 283-290.

Bugg, R. A., Donald, W. N., Zech, W. C., and Perez, M. A. (2017). "Improvements in Standardized Testing for Evaluating Sediment Barrier Performance: Design of a Full-Scale Testing Apparatus." *J. Irrig. Drain Eng.*, Vol. 143, No. 8.

Haan, C. T., Barfield, B. J., and Hayes, J. C. (1994)."*Design Hydrology and Sedimentology for Small Catchments.*" *Academic Press, San Diego, CA.*

Henry, K. S., and Hunnewell, S. T. (1995). "Silt Fence Testing for Eagle River Flats Dredging." Special Report 95-27 U.S. Army Corps of Engineers Cold Regions Research & Engineering Laboratory. NTIS, Springfiled, Virginia 22161.

Risse, L. M., Thompson, S. A., Governo, J. and Harris, K. (2008). "Testing of new silt fence materials: a case study of a belted strand retention fence." *Journal of Soil and Water Conservation*, Vol. 63, No. 5, 265-273.

Williams, J. R., and Berndt, H. D. (1977). "Sediment yield prediction based on watershed hydrology." *Trans. ASAE*, Vol. 20, No. 6, 1100-1104.

Whitman, J.B., Zech, W.C., and Donald, W.N. (2019) (a). "Improvements in Small-Scale Standardized Testing of Geotextiles used in Silt Fence Applications", Geotextiles and Geomembranes, Vol. 47, No. 5, pp. 598-609. doi: 10.1016/j.geotexmem.2019.04.002

Whitman, J.B., Zech, W.C., and Donald, W.N. (2019) (b). "Full-Scale Performance Evaluation of Innovative and Manufactured Sediment Barrier Practices", Transportation Research Record: Journal of the Transportation Research Board, Vol. 2673, No. 8, 284-297. doi: 10.1177/0361198119827905

Whitman, J.B., Zech, W.C., Donald, W.N., and LaMondia, J. (2018). "Full-Scale Performance Evaluation of Various Wire-Backed Nonwoven Silt Fence Installation Configurations", Transportation Research Record: Journal of the Transportation Research Board, Vol. 2672, No. 39, 68-78. doi: 10.1177/0361198118758029

Wyant, D. C. (1981). "Evaluation of Filter Fabrics for use as Silt Fence." Transportation Research Record: Journal of the Transportation Research Board, No. 832, 6-12.

Use of Geotextile Filtration Fabrics with Skimmers for Stormwater Quality

James D. McCutchen, Jr., P.E[1]

[1]Rymar Waterworks Innovations, 3620 Pelham Rd, Greenville, SC 29615;
jamie@rymarwaterworks.com

ABSTRACT

Skimmers have become common for use in sediment basins during construction but rarely remain in the basin once construction is complete. This paper will focus on research underway to use geotextiles as filtration media in conjunction with skimmers in order to meet post construction water quality requirements for stormwater basins.

Stormwater basins are typically designed to detain water and use settling of pollutants as the primary means of providing water quality. However, this has several flaws. The settling only occurs when there is a large enough rain event to partially fill the basin, therefore, smaller storm events receive little, if any, treatment. Holding the water quality volume for an extended time requires the pond volume to be increased. In addition, each rain event has potential to cause pollutants to be re-suspended and possibly discharged from the basin.

The use of skimmers with filtration media may solve many of these issues and provide treatment of 100% of the runoff for any storm event up to the water quality storm, as well as treating a substantial amount of runoff from larger storms. This paper includes the results of recent testing of several different filtration media materials and configurations, combined with a skimmer.

BACKGROUND

Stormwater Management has evolved significantly over the past 50 years and has seen a much greater emphasis on stormwater quality in the past few decades. Most stormwater programs began as part of the 1972 Federal Clean Water Act that created the National Pollutant Discharge Elimination System (NPDES) Permit program. The NPDES program authorizes to state governments by EPA to regulate and address point sources that discharge pollutants to waters of the United States and has taken a phased approach.

Table 1. Phase I (1990)

Construction Activities	Required all construction sites disturbing 5 or more acres to obtain coverage to discharge stormwater under the NPDES Program.
Industrial Activities	Defined 11 categories of industrial activity (including construction) if disturbance of activity is equal to 5 acres or more than NPDES approval was required.
MS4s	Required all municipalities with populations equal to 100,000 or more to acquire coverage for NPS discharge under the NPDES Program.

Table 2. Phase II (March 2003)

Construction Activities	Required all construction sites disturbing 1-5 acres to acquire coverage under NPDES program.
Industrial Activities	Added 1-5 acres in Industrial activities and expanded upon the no exposure limitation from 1 group of activity to all 11 groups.
MS4s	Required municipalities with populations between 10,000 and 100,000 to obtain NPDES Coverage.

The EPA typically issues a Construction General Permit (CGP) to the state, which expires after five years and must be renewed. As stormwater management has continued to evolve, so have the permit requirements. Since passing of the Clean Water Act and implementation of the Phase 1 and Phase 2 NPDES Programs (Tables 1 and 2), stormwater management requirements have seen many changes. In most areas the initial focus was on sediment control during construction and stormwater quantity management for new developments, typically including requirements to manage the 2-year and 10-year storm events. There were little to no requirements for post-construction water quality. This resulted in construction of many stormwater ponds and other facilities that aid in flood control but provide minimal water quality benefit.

In the past 10 to 15 years, we have seen a much greater focus on stormwater quality. For example, South Carolina passed the SC Water Pollution Control Permits Regulation in 2008, which significantly increased the requirements for post-construction stormwater quality. Many other states have passed similar regulations. It is interesting to note that the specific regulations vary widely from state to state and even among MS4s within the same state, and just as important is the actual enforcement of these regulations, which has even greater variation. This is reflective of the differences in climate, rainfall and soil types across the United States.

Another example of evolution in stormwater management is that in 2013 when South Carolina renewed their CGP, it added a requirement for Water Surface Dewatering that states: "When discharging from sediment basins and similar impoundments, utilize outlet structures that only withdraw water from near the surface of the basin or impoundment, unless infeasible. This outlet structure should be capable of conveying the flow for the 10-year, 24 storm event."

Over 30 other states have added similar language to their CGPs over the past 10 years. The most common way to meet this requirement is through the use of a floating pond skimmer. There are many variations of skimmers that include several by manufacturers that are designed to meet this requirement. These include the Faircloth skimmer, the ESC skimmer, the IAS skimmer and the Marlee Float skimmer. As the use of skimmers becomes more accepted across the country there are sure to be more types become available.

The primary purpose of the skimmer is to be used during construction when the sediment pollution loads are the highest. By withdrawing from the surface of the basin, it releases cleaner water (not necessarily clean water) from the highest portion of the water column and allows time for sediment to settle to the bottom of the basin. This method of dewatering the sediment basins has been widely recognized to greatly increase sediment trapping efficiency over the old methods of draining the basin from the bottom, which releases the muddiest water. Research suggests that a

properly designed sediment basin utilizing a floating skimmer has the potential to remove over 90% of suspended sediment.

USE OF GEOTEXTILES WITH SKIMMERS FOR POST CONSTRUCTION WATER QUALITY

The Concept. With the increased use and acceptance of floating skimmers to increase sediment trapping efficiency during construction, it would seem natural to apply the same logic for post construction. Afterall, one of the primary means of meeting water quality requirements through the use of dry, wet or extended detention basins is to detain the water quality volume for a period of time, which in theory, will allow pollutants that are typically attached to sediment particles to settle to the bottom of the basin before being discharged. Therefore, discharging from the bottom of the basin would naturally release more of these pollutants compared to use of a surface withdrawal system. Use of a floating skimmer to aid in meeting post-construction requirements would seem to be a natural progression in the evolution of stormwater management.

There are many flaws with using extended detention time as a means of water quality. Designs are based on a water quality storm event or specified runoff volume. This is typically assumed to be 1 in. of runoff from the area draining to the pond. Designs typically assume this volume arrives instantly and an orifice is sized to release this volume over 24 to 48 hours. This design has several flaws, including:

- The actual runoff volume will often arrive over an extended period of time. This will result in much less to no ponding and, therefore, little to no settling time.
- Smaller storm events magnify this issue and often flow straight through the pond with very little ponding or detention time.
- The volume-based design requires pond sizes to increase and take up more area on the site or require larger underground detention volume. This reduces developable area or significantly increases the cost for underground systems.

A filtration-based method offers many benefits that may include:

- The peak rate of the discharge from the basin can often be increased vs. the extended detention model, without causing erosion downstream. Depending on local requirements, this could be as high as the 2-year pre-development peak rate if the filtration system is capable of treating at this rate. This can significantly reduce the required pond volume.
- The pond outlet design is based upon the filtration capacity of the treatment system. The pond volume is used to reduce peak flows to rates that the filtration system can manage.
- All runoff from storm events at or below the water quality storm are fully treated by the filtration system, including very small storms that often contain high levels of pollutants.
- The filtration media can be customized to target specific pollutants of concern in the watershed or at the specific site. This may include filtration media to target metals at industrial sites, hydrocarbons at gasoline stations or large parking areas, or bacteria or nutrients in other areas.
- There is better potential to retrofit older basins that do not currently provide water quality benefit without having to significantly redesign the outlet control system or provide additional pond volume.
- The pond provides a large containment volume to reduce the maintenance frequency requirements, especially compared to filtration systems that are contained within vaults or

have limited containment areas. This also allows the system to handle a much larger drainage area.

The Challenges. Sediment and pollutant loads are very different during construction versus post-construction. During construction, the typical standard is to retain 80% to 85% of the anticipated sediment load, which can be more than 100 times greater than post-construction. Sediment yield during construction can range from 40 to 400 tons per acre per year, compared to a sediment load of 600 pounds per acre per year, which is a recognized standard for post-construction conditions assuming the site is reasonably stabilized. In addition, there are many other pollutants of concern that may need to be considered in the post-construction conditions, such as hydrocarbons, metals, bacteria and/or nutrients (phosphorous & nitrogen). Meeting an 80% or more trapping efficiency for the post-construction sediment loads can be much more difficult and expensive to achieve than during construction. In addition, removal of other pollutants, especially those that are in a dissolved state, often require additional treatment methods.

The primary challenge is meeting the filtration requirements needed to meet the post-construction trapping efficiency requirements. To be acceptable for post-construction use, MS4s typically require that the device function for at least one year. This is also part of the NJCAT Certification protocols. If the filtration media is going to clog or blind off too quickly, then it will not be a good choice for post-construction use. It is critical to select a filtration media system that has the proper balance of staged filtration to insure adequate life of the device for the specific site. It must also be understood there will be a need to periodically change the filtration media, typically annually, and to monitor the pond to confirm it is functioning properly, which should be part of every pond maintenance plan. This can be burdensome if the pond has above average debris, trash or pollutant load, however, the intent is to catch as much of this as possible to prevent it from being released downstream.

Another consideration is durability and maintenance of the post-construction system. Although routine maintenance must be part of any stormwater management facility, systems that require excessive maintenance are likely to fail or not be properly maintained. A concern is that many floating skimmers are made of primarily PVC materials. PVC is typically not considered a durable or UV-resistant material and is likely to need to be replaced every few years if left in the outdoor elements. Because most floating skimmers are made of PVC, it is likely that this has led to concern over their use as part of the permanent outlet system. In fact, some MS4s have specifically stated that skimmers are not allowed for post-construction use due to this issue. For this reason only skimmers made of more durable materials, such as HDPE, should be used in permanent applications.

Testing Protocol. Over the past two plus years, Rymar has been conducting research to develop a combination of filtration media and skimmer system to meet NJCAT protocols for filtration for post-construction requirements. The research is focused on development of a system to meet the "New Jersey Department of Environmental Protection Laboratory Protocol to Assess Total Suspended Solids Removal by a Filtration Manufactured Treatment Device" (January 25, 2013). This protocol defines the pollutant loading requirements, testing procedures, scaling of Filtration Manufactured Treatment Devices (MTDs), and establishment of Maximum Allowable Inflow Drainage Area.

NJCAT is one of two widely accepted testing and certification options for MTDs. The other is the Washington TAPE program. The key difference between the two programs is that NJCAT is done in a more controlled laboratory setting and Washington TAPE is done in a true field condition. Because of this, the Washington TAPE program can be more expensive and take longer to complete than the NJCAT option. There are ongoing efforts within the stormwater management community, including within ASTM, to develop more widely accepted national standards for stormwater management testing, however, at this time those are still under development.

Testing Results. Rymar has completed several iterations of both controlled testing and field testing, often with surprising outcomes. The initial concept was to use a woven geotextile material (Belton PD-1198) with an AOS of 45 and flow rate of 22 gpm/sf to create a skirt around the skimmer (Figures 1, 2 & 3). The skirt was drawn together below the skimmer to minimize flow that could reach the skimmer without going through the fabric. There was also a slight opening for the skimmer barrel. We quickly realized that the flow rate through this type of fabric was not sufficient and the material would blind much too quickly.

Figure 1. Skimmer with Geotextile Skirt

Figure 2. Skimmer with Geotextile Skirt

Figure 3. Skimmer with Geotextile Skirt

The next prototype had a different type of woven geotextile (Trace Linq GTF-400EO) with a larger opening size of 40 AOS and flow rate of 145gpm/sf (Figures 4 & 5) The total surface area of the fabric was designed to provide a total flow rate of nearly 10 times that of the skimmer. Initial testing was better, with an improved flow rate, but after limited testing it was determined this material would also blind too quickly**.**

Figure 5.
Skimmer with Geotextile Skirt

Figure 4. Skimmer with Geotextile Skirt

The next prototype tested used several different non-woven geotextile fabrics. These included ADSORB-it filter fabric by Stormwater BMP Products, Ultra-X-Tex fabric by Ultratech International and Siltron by MKB.

We first performed some field tests with the Siltron fabric (Figure 6). However, the flow rate through the fabric was not sufficient to keep up with the skimmer flow and resulted in the skimmer tending to float and have a very slow flow rate (Figure 7).

Figure 6. Skimmer with Siltron

Figure 7. Skimmer in Basin with Siltron

To improve flow, the bottom of the fabric was opened and slits were cut in the side walls of the fabric to provide improved flow rates (Figure 8). This helped improve flow significantly. However, after being in the basin for about 3 months significant vegetation started to grow in and on the filter fabric (Figure 9).

Figure 8. Skimmer with Siltron with Open Bottom

Figure 9. Skimmer with Vegetation Growing

The fabric was removed, and it was noted that the roots of the grasses were growing in and

through the fabric material (Figure 10). It should be noted that this was in a typically wet pond with a large amount of trash and debris.

Figure 10. Siltron Fabric with Vegetation Growing

Testing revealed that although the flow rates of many of fabrics had been tested per ASTM D-4491 to have water flow rates of over 100 gpm/sf, this was not applicable to using the skimmer to pull water through the fabric and the actual flow rates were substantially less. Based upon initial results, it was determined that larger surface area of fabric was needed in order to provide sufficient flow to the skimmer. A "basket" was constructed that would surround the skimmer and provide a larger diameter and therefore greater surface area of the geotextile fabric (Figure 11). This also allowed a two-stage system to be used. Initial trials used the non-woven Ultra-X-Tex on the outside of the filter (which included slits to allow for higher flow) and a lighter weight Mirafi 140NL on the inside of the filter (Figure 12).

Figure 11. Skimmer Basket with Outer Layer X-Tex & Inner Layer Mirafi

Figure 12. Skimmer Basket with Outer Layer X-Tex & Inner Layer Mirafi

When tested, the performance was noticeably better than previous trials. After several runs the suction of the skimmer began to pull the Mirafi fabric into the middle and flow rate began to diminished. When the outer fabric was removed, there was obvious build up on the inner layer (Figure 13). The latest prototype includes a staged filtration system with higher flow materials. The outer layer was constructed of strips of a combination of the ADSORB-it fabric and Ultra-X-

TEX. Strips were approximately 4” wide and overlap approximately 2” (Figure 14). Water can flow through the material or through the openings between the strips.

Figure 13. Inner Layer of Mirafi

Figure 14. Outer Layer X-Tex/ADSORB-IT Strips and Inner Layer Blocksom Inlet Filter

Two layers of Blocksom Inlet Filter material were installed in an offset manner to allow flow through and around them. An outer layer was positioned with a 2” opening at the bottom and an inner layer was positioned with a 2” opening at the top. The inner layer also covered the bottom of the basket wall (Figure 15). Water could flow through the material or enter at bottom and flow up to the top of the second layer to enter the skimmer area.

The bottom of the basket was a solid section of the Ultra-X-Tex material. There is a 6” wide opening to allow the skimmer barrel to pivot as the skimmer floats up and down. This area was closed with a filter sock material (Figure 16).

Figure 15. Blocksom Inlet Filter Configuration

Figure 16. Opening for Skimmer Barrel

Testing of this version was significantly better than previous prototypes. Flow was maintained relatively well. A 4" Marlee Float skimmer with 4" orifice (max flow rate of +/- 0.4 cfs) was used in testing (Figures 17 & 18). A flow meter is attached to a weir tank just outside of the test tank and the flow rates were very similar to the skimmer without the filtration basket configuration

Figure 17. Skimmer Testing in Test Tank

Figure 18. Skimmer Testing in Test Tank

The water in the weir tank was noticeably clearer than in the test tank (Figure 19). The test tank contained a significant amount of algae and none was noticed in the weir tank. (Note the dark areas in the weir tank photo are paint chips and not debris)

During testing food coloring was added to the water to gauge flow through the fabric and suction levels. Drops of food coloring were placed around the entire basket (Figure 20). Flow was not

significantly noticeably higher at the filter sock at the pipe inlet compared to other parts of the basket.

Figure 19. Effluent in Weir Tank

Figure 20. Flow Testing with Food Coloring

During the end of the first run, as the water level was approximately 2' in the tank, it was noticeable that the basket was floating slightly. More research is required to determine the reason; however, the prototype basket was made of HDPE and the final version is most likely to be stainless steel. The additional weight should easily overcome the minimal buoyancy of the fabric and frame.

Upon completion of two runs, the filter basket was removed from the tank and the outer layer of fabric was removed. There was some algae and debris on the inner Blocksom fabric, but it was minimal and had not caused any significant blinding (Figures 21 & 22).

Figure 21. Blocksom Inlet Filter Material After Testing

Figure 22. Blocksom Inlet Filter Material After Testing

CONCLUSIONS

Additional research and development are needed to complete development of a commercially viable product. However, the concept of using filtration to aid in meeting post-construction stormwater quality requirements appears to be a viable option.

Further research is required to confirm the proper materials to achieve a balanced staged filtration system. This will likely include research on additional stages of filtration, as well as additional material combinations to achieve the desired TSS removal efficiency and obtain a minimum of one-year life cycle for the filtration media under “average” conditions.

The difference in flow rate achieved through the fabrics created by the suction of the skimmer versus what was achieved per ASTM D-4491 is a significant challenge. A target flow rate provided by the fabric was initially ten times that of the skimmer, to allow for substantial blinding before there would be a noticeable flow rate decrease. This has proved to be a flawed assumption that will have to be addressed during further testing.

Although the research conducted by Rymar to date has not included testing for other pollutants, several of the materials utilized in the prototypes have been tested for removal of hydrocarbons, metals and bacteria and this will be the logical next step in the evolution of this system.

IFAI Geosynthetics Conference

Reinforcement Over Soft Soils with High Strength Geogrids, Case Studies

Marianna Ferrara, M.S.[1]

[1]Maccaferri Inc., Rockville, MD; e-mail: m.ferrara@maccaferri.com

ABSTRACT

Construction of embankments or any kind of structure over soft foundation soils can be very challenging for engineers. Soft soils present very low shear strength, excessive differential settlements, poor bearing capacity, surface instability associated with sinkhole development and require special construction practices. Traditional construction methods used in fine grained saturated soils such as removal and replacement of soft soil, pre-loading the site to reduce settlements and achieve higher strength or stabilize the soil by injecting additives, can be expensive and time-consuming. An alternative, more cost-effective solution is the use of high strength geogrids placed directly onto soft soils at the base of the embankment. Such application of a geogrid is often called Basal Reinforcement. The combination of high strength geogrids and granular fill material is also called Reinforced Granular Mattress (RGM), it creates an adhesive interface with the soft soil, and a stiff platform ensuring a uniform distribution of loads onto soft soil. The RGM promotes the distribution of loads and minimize differential settlements. In some cases, when primary and secondary settlements need to be controlled, rigid intrusions are commonly installed to provide support and settlement control by transferring the load to a stiffer foundation. In these cases, a load transfer platform designed with one or multiple layers of high strength geogrids can be considered to redistribute uniformly the loads to the piles and optimize the design. This paper presents recent case studies of basal reinforcement over piles, and weak foundations.

INTRODUCTION

Construction over soft foundation soils is usually associated with poor bearing capacity, excessive differential settlements, and lateral sliding instability. Furthermore, the presence of poor ground conditions in a construction site is historically the most frequent cause of long construction durations.

There are several alternatives that can be employed to achieve project objectives in these conditions. Common primary functions of these alternatives are to increase shear strength and bearing resistance, increase density and drainage, and provide lateral stability. (Schaefer et al., 2017). These alternatives include: (1) bypassing the poor ground through relocation of the project to a more suitable site or through the use of a deep foundation; (2) removing and replacing the unsuitable soils; (3) designing the planned structure to accommodate the poor/marginal ground; or (4) modifying (improving) the existing soils, either in-place or by removal, treatment and replacement of the existing soils; (ASCE 1978; Mitchell 1981).

Typical ground improvement techniques include: prefabricated vertical drains and accelerated consolidation, lightweight fills, deep compaction, aggregate columns, column supported embankments, soil mixing, grouting, pavement support stabilization and reinforced soil structures (FHWA – Ground Modification Methods – Reference Manual). Each ground improvement technique has inherent limitations on their applicability as related to the type of soil,

depth or treatment and performed function. Long duration ground improvement projects are too costly and, in many instances, unacceptable for the current financial and political approach to highway jobs.

In addition, many new highway projects are widening of existing roads or they cross special soil deposits where traditional methods are not technically viable.

An alternate solution is to use a high strength geosynthetic reinforcement placed directly on top of the soft soil and build the structure on top of it. This type of geosynthetic application is often referred to as "Basal Reinforcement". The use of a geosynthetic reinforcement under embankments or other type of structures constructed over soft soils or localized weak areas (i.e. sinkholes) can be categorized in two different applications based on the design target:

- Basal reinforcement alone or combined with vertical drains to control the stability of the structure without controlling overall settlement.
- Basal reinforcement combined with foundation stabilization system such as rigid intrusions: control the stability of the structure but also to prevent or limit the settlements.

This paper summarizes herein the two cases where a Basal Reinforcement may be included underneath and embankment.

BASAL REINFOCEMENT OVER SOFT SOILS

The stability of an embankment built over soft soil is primarily governed by the shearing resistance of the foundation, and the construction of the embankment itself is influenced by the bearing capacity of the soft foundation soil. A geosynthetic reinforcement may be placed at foundation level to prevent shear failure both in the embankment fill and in the foundation soil. It is crucial to highlight that the stability of an embankment on soft soil is most critical during construction, because the relatively low permeability of the soft foundation does not allow full consolidation in the normal time scale of construction. At the end of construction, even if the embankment loading has been applied the gain in shearing resistance of the foundation due to consolidation might be insufficient for stability. Once consolidation has occurred due to the weight of the embankment, the improvement in shearing resistance and the increased bearing capacity in the foundation soil should usually remove the need for the reinforcement to improve stability. Therefore, during the period between the end of construction and complete consolidation of the soft foundation, the main strength requirement of the reinforcement should be that at any instant in time the factored reinforcement design strength equals or exceeds the design load.

The design approach for basal reinforcement over soft soils is to verify the potential mode of failure for the following ultimate limit states: local stability of embankment fill, rotational stability of the embankment, lateral sliding of the embankment, foundation extrusion stability, overall stability (see Figure 1). Although a geosynthetic reinforcement may change the stress distribution leading to a possible reduction in differential settlements, total foundation settlement is not directly affected by a geosynthetic reinforcement layer. Nevertheless, the embankment settlements need to be checked since it may lead to excessive geosynthetic strain levels resulting in an increase in tensile strain and load.

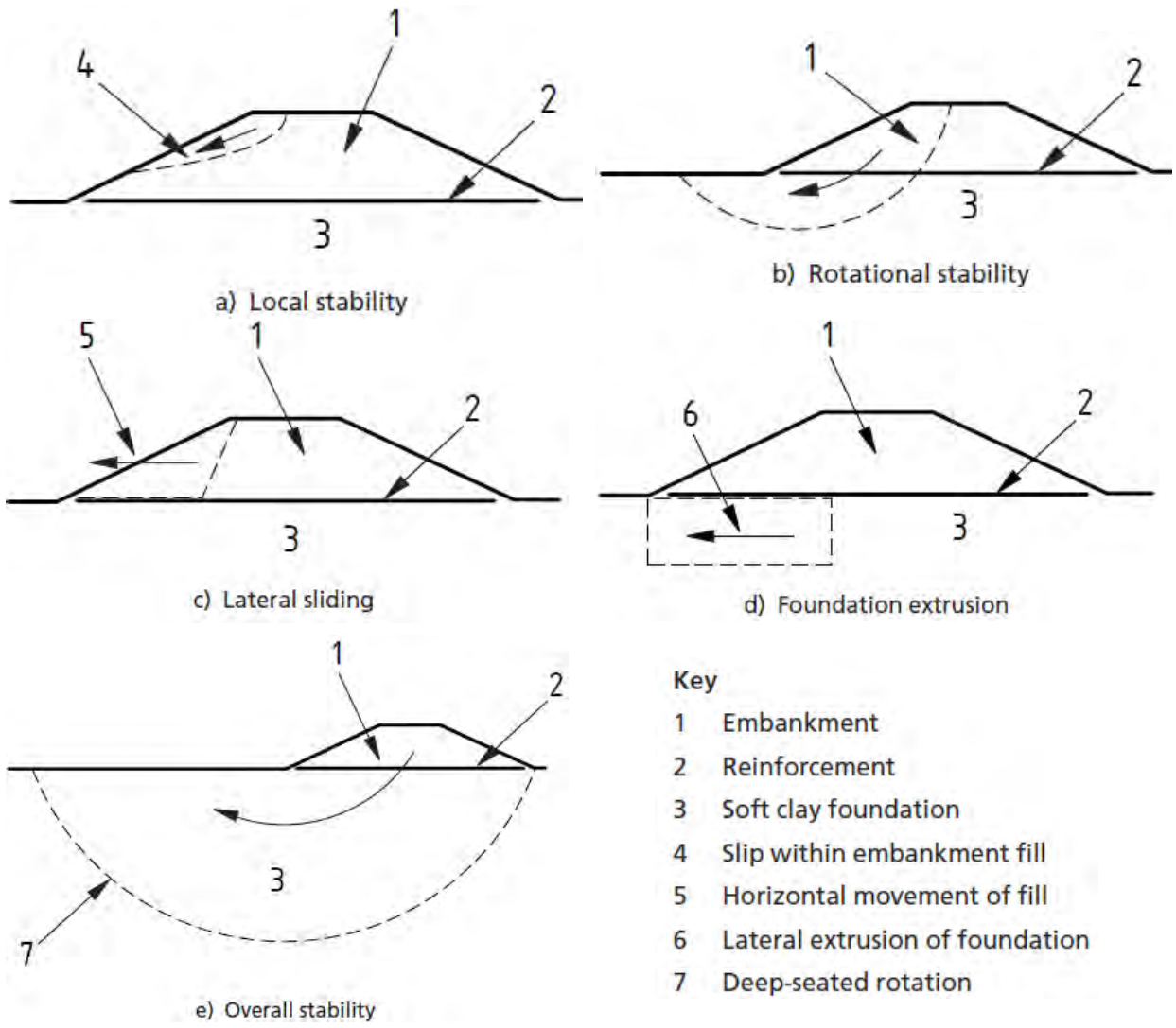

Figure 1. Potential modes of failure considered in the design process (British Standard BS 8006:2010).

One form of Basal Reinforcement that may be used in embankments is a Reinforced Granular Mattress (RGM), which is a three dimensional structure formed from a series of interlocking units fabricated directly on the soft foundation soil from geogrid reinforcement and filled with granular material. The RGM structure is usually 3.28 ft (1 m) deep structure. A basal mattress reinforcement may be incorporated to interact with the embankment and produce:

- a good adhesive interface between the soft foundation and the contained granular fill of the mattress.
- a relatively stiff platform to ensure both an even distribution of load onto the foundation and a more uniform stress field within the soft foundation.

These properties enable the basal mattress to influence the deformation of the soft foundation and hence may be used to mobilize its maximum shear strength and bearing capacity. A Reinforced Granular Mattress was used in a project in Mexico for a basal reinforcement within a port area.

CASE STUDY: PORT OF GUAYMAS BASAL REINFORCEMENT

The Port of Guaymas, located on the northwest coast of Mexico in the Gulf of California, is one of the most important ports in Mexico from both commercial and touristic point of view. It manages the shipment of agricultural and mineral bulk, fluids, and general cargo. It is an important hub for commercial relations between Mexico and the southern part of US, moving up to 3 million tons of minerals like copper, steel, bauxite, etc. In recent years, the port storage area has been experiencing significant settlements due to the increase of loads managed in this area and the poor conditions of the foundation soil.

The Port Authority (API Guaymas) decided on a major renovation of the area to build new concrete pavement over the whole storage area using a Reinforced Granular Mattress (RGM) with high strength geogrids as a basal reinforcement solution. High strength geogrids are spaced out within layers of granular material to create an adhesive interface between the soft soil and the granular fill, and a stiff platform ensuring a uniform distribution of loads onto soft soil. The Port Authority chose this solution because of its advantages compared to traditional solutions: easy and fast installation, more cost-effective application, and excellent performance.

The development of the port took place through subsequent stages of land reclamation from the sea, causing the foundation soil to be saturated and very soft. In fact, the geotechnical investigation carried out over the project area of 7,654 yd^2 (6400 m^2) showed a 46 ft (14 m) deep layer of soft soil characterized by grey-green silty sands and dark brown sandy clays with high plasticity. The total tensile strength of geogrids required to support the load of the RGM self-weight and the overload of the minerals dumped in the area for a total uniform load of 9,398psf (450 kPa) was calculated using the design method for embankments on soft soils included in the British Standard BS 8006:2010. This method considers both short and long-term tensile strength of the geogrid: hence the resulting ultimate tensile strength already considers all the reduction factors for tensile creep, installation damage, and environmental degradation.

The detailed design of geogrid reinforcement was carried out using the Geogrid Design method (Rimoldi and Scotto, 2012; Rimoldi and Simons, 2013). This method, based on elastic multi-layer analysis, allows to introduce different geogrid layers at different elevations, and to set the design strain for each geogrid. Given the RGM thickness and considering separately the effect of the static loads and the instant effect of dynamic loads, it is possible to calculate the distribution of the horizontal tensile forces in the whole RGM structure and select the appropriate geogrid for each layer based on a limit state criterion. In this case, restriction of the deformation was chosen as limit state criterion, so the geogrid strain was limited to a maximum of 5%, as suggested by practical experience as well as by the British Standard BS 8006:2010.

The geogrids used in the RGM were high strength uniaxial geogrids characterized by a high tenacity polyester core covered in polyethylene resistant to physical, chemical and biological conditions found in reinforced soil structures. The RGM layout consisted of a 3.28 ft (1 m) thick aggregate layer with two sets of transversally installed high strength uniaxial geogrids (see Figure 2).

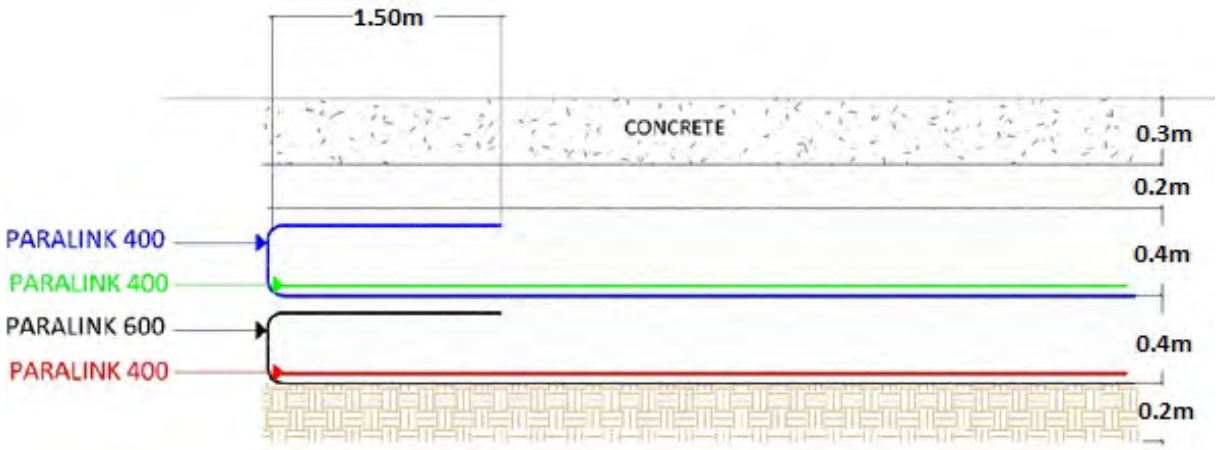

Figure 2. Reinforcement layout in the RGM.

The construction of the RGM included the following steps:

1. Preparation of the site by excavating to 3.94 ft (1.2 m) depth the entire area and cleaning it from sharp objects that could possibly damage the geogrids (Figure 3a);
2. Placement of 8 in (0.2 m) thick layer of good quality soil (well graded sand and gravel mixture, with friction angle $\varphi = 36°$) to get a perfect flat surface;
3. Installation of the first layer of high strength geogrid. The rolls have been placed on the West side of the storage area with the use of a lifting beam, and unrolled carefully towards the East side, ensuring that no slack or undulations occurred. At both the edges 6.56 ft (2 m) anchorage length has been left out for eventually wrapping around the geogrids;
4. Installation of the second layer of high strength geogrids by placing the rolls, with the help of a lifting beam, on the South side of the area and unrolling them towards the North side, which is perpendicular to the first geogrid. As in step 3, care has been taken, while unrolling the geogrids, to lay the adjacent rolls flat and untwisted; 6.56 ft (2 m) anchorage length has been left out at the two edges by wrapping around the geogrids (Figure 3b);
5. Placement of 16 in (0.4 m) of fill material in two lifts paying attention to spread and compact it in the longitudinal direction of the top high strength geogrid (Figure 4a);
6. Wrapping of the high strength geogrids to provide the required anchorage lengths, at the end of the compaction of the second lift of fill material;
7. Steps from 3 to 6 have been repeated to install the other 2 layers of high strength geogrids. Finally, another 8 in (0.2m) lift of fill material has been placed and compacted to provide a perfectly flat surface for the construction of the concrete pavement slab.

(a) **(b)**

Figure 3. Preparation of the site (a) and geogrid installation (b).

(a) **(b)**

Figure 4. Laying down of fill material (a) and view of completed storage area (b).

PILED EMBANKMENTS WITH BASAL REINFORCEMENT

When time constraint is a critical aspect of the project, and primary and secondary settlements need to be controlled, rigid intrusions (i.e. piles, columns) are commonly installed to provide support and settlement control by transferring the load through the soft compressible soil layer to a stiffer foundation. Many different types of columns can be used, including stone columns, vibro-concrete columns, deep-mixing method columns, driven piles, and auger piles (Collin, 2004, Collin et al., 2005). Probably the most critical aspect when designing column supported structures is that the load must be transferred effectively to the columns to prevent punching of the columns into the soil structure, this would lead to severe differential settlements in the surface of the structure. The spacing between piles is therefore a crucial design aspect to develop an efficient soil arching.

A load transfer platform (LTP) or a bridging layer is commonly installed immediately above the columns to help transfer the load from the soil structure to the columns. The goal of the geosynthetic reinforcement is to span across pile caps carrying all or a portion of the load and transferring it to the columns. By doing so, spacing between piles can be significantly increased and piles caps size can be decreased. In addition, the reinforcement can be used to counteract the horizontal thrust of the embankment fill, eliminating the need of raking piles along the extremities of the foundation.

The design of column supported soil structures usually need to consider both limit state and serviceability state failure criteria. Most of these design steps are followed using engineering practices covered either by Schaefer et al. 2017 or the British Standard BS 8006:2010. However, the design of geosynthetic reinforced pile supported embankments involves the calculation of the vertical stresses on the geosynthetic reinforcement. From which, strain and tension developed in the geosynthetic can be calculated.

Two design models are currently in use in the US: the *Beam Method* and the *Catenary Method*. The *Beam Method* (Collin, 2004, Collin et al., 2005, Schaefer et al. 2017) considers multiple layers (minimum 3) of low strength geosynthetic reinforcement equally spaced within a select granular structural fill (i.e. load transfer platform) that act as a single rigid beam. The *Catenary Method* (British Standard BS 8006:2010) considers one single high strength geosynthetic that acts as a catenary single layer at the interface between the columns and the soil structure.

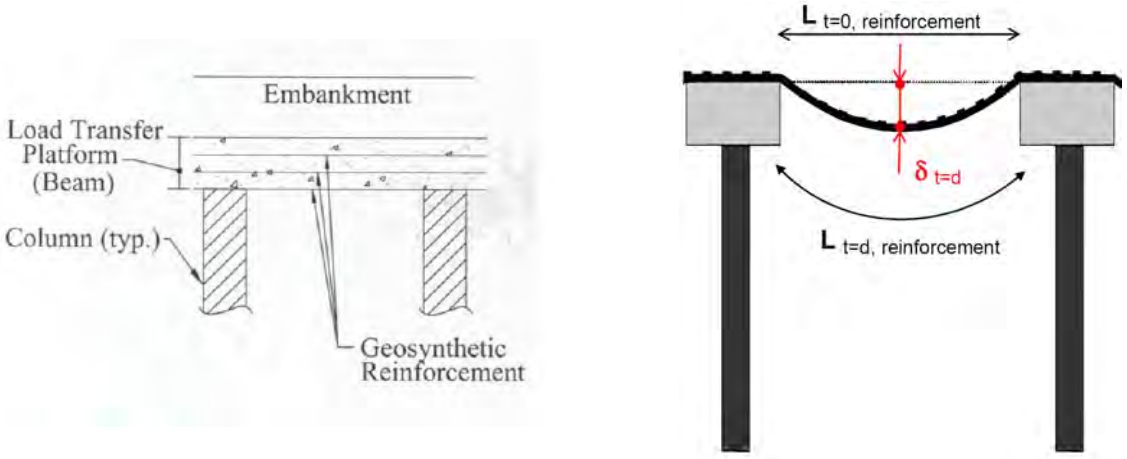

(a) **(b)**

Figure 5. Basic layout of (a) the rigid beam design approach and (b) catenary design approach.

The design of the geosynthetic reinforcement over piles includes calculating the vertical stresses on the geosynthetic reinforcement and its strain and tension. Several models have been developed to calculate the vertical stresses and several others to calculate the strain and required strength in the geosynthetics. Sloan, 2011 summarizes twelve different arching theories to directly calculate the vertical stress and three analysis methods to calculate the strain and tension in the geosynthetic. Each column supported embankment analyses procedure is categorized based on preliminary ratings for the appropriate use of performance criteria/indicators, subsurface conditions, loading conditions, material characteristics, construction techniques and geometry. Given the extent of the analysis's methods available, their complexity and the scope of this paper, design methods will not be discussed in detail herein.

CASE HISTORY: I-95 TELEGRAPH ROAD INTERCHANGE PILED EMBANKMENT

Each day close to 50,000 motorists pass through the Telegraph Road Interchange along the integral I-95/495 Capital Beltway in between Virginia and Maryland. In early 2008, extensive upgrades to the interchange began as part of a multi-year project tied to the final phase of the Woodrow Wilson Bridge project. Roughly $235 million was dedicated to the interchange's improvement.

Construction of a grade separated interchange, new ramps, and the construction of a bike and pedestrian trail. A joint venture company was contracted for the work, which focused on 2.5 miles stretch of Capital Beltway, with 321,000 yards of paving, 11 bridges, drainage improvements, retaining and noise walls, and environmental mitigation. The goal of the new interchange was to improve vehicle capacity and provide safer and more efficient travel through a series of bridges and ramps. The project was the single largest design-bid-build construction contract ever awarded by the Virginia Department of Transportation (VDOT) and was awarded an Engineering Excellence Award by the American Council of Engineering Companies of metropolitan Washington (ACEC/MW EEA) and a transportation engineering award from the VDOT.

The design included column supported embankment with aggregate piers and a load transfer platform. The VDOT specifically requested high strength geosynthetic reinforcement (defined as an "HGSG" by VDOT) with an ultimate tensile strength of 38,000 lb/ft (555 kN/m). A uniaxial geogrid manufactured with high molecular weight and high tenacity polyester multifilament yarns was used in the project. Roughly 14,500 yd^2 (12,123 m^2) of geogrid were used for basal reinforcement over aggregate piers and under mechanically stabilized earth (MSE) walls and slopes. The project requested oversized geogrid panels, which varied in length from 350 ft to 450 ft (106 m to 137 m), were overlapped 2 ft (0.6 m) and tied together to prevent movement during backfilling. Additionally, all overlaps of geosynthetic panels were "shingled" in the direction of the fill placement. This ensured that the pushing of fill material did not alter the careful overlap alignment.

(a) **(b)**

Figure 6. Geogrid installation (a) and laying down of fill material (b).

CONCLUSIONS

Basal reinforcement over soft soils has been used for several years as a practical and economical alternative to traditional ground improvement techniques. One or multiple layers of geosynthetic reinforcement can be installed directly between the embankment fill and the soft foundation soils to increase the design safety factor, bridge sinkholes or span between piles to redistribute the loads and increase pile spacing. Design methods are available nationally and internationally to properly identify the required tension and subsequently the design strain. Two case studies have been presented that showcase the successful use of geosynthetic reinforcement over soft soil, and rigid intrusions. In order to guarantee the required design life, installation of the geosynthetic reinforcement should be carefully carried out, preparing a flat surface clear of sharp objects,

ensuring an accurate alignment of the rolls with proper overlap between end of one roll and beginning of next one and providing enough continuous bond length or edge anchoring.

REFERENCES

BS8006-1:2010. Code of practice for strengthened/reinforced soils and other fills.

Collin, J.G. 2004. Column supported embankment design considerations. Proceedings 52nd Annual Geotechnical Conference, University of Minnesota, Minneapolis, MN.

Collin, J.G., Watson, C.H., and Han, J. 2005. Column supported embankment solves time constraint for new road construction. ASCE Geo-Frontiers Conference, Austin TX.

Fowler, J., Koerner, R.M., 1987. Stabilization of very soft soils using geosynthetics. Proceedings of the Geosynthetics ’87, New Orleans, Louisiana, IFAI, ST. Paul, MN, pp. 289-300.

Rimoldi, P. and Scotto, M. 2012. Design method for geogrid reinforcement of road bases. Proceedings EuroGeo 5, 5th European Conference of Geosynthtics, Valencia, Spain

Rimoldi, P. and Simons, M.J., 2013. Geosynthetic reinforced granular soil mattress used as a foundation support for mechanically stabilized earth walls. Proceedings GeoMontreal 2013 conference, Montreal, Ontario, Canada.

Schaefer, V. R., Berg, R. R., Collin, J. G., Christopher, B. R., DiMaggio, J.A., Filz, G. M., Bruce, D. A. and Ayala, D. 2017. Ground modification methods reference manual – Volume I and II. Federal Highway Administration (FHWA), U.S. Department of Transportation, Publication No. FHWA-NHI-16-028, National Highway Institute, Washington D.C., USA

Sloan, J.A. 2011. Column-Supported Embankments: Full-Scale Tests and Design Recommendations. Doctor of Philosophy Dissertation, Virginia Polytechnic Institute and State University, Blacksburg, VA

USACE. (1999). Guidelines on ground improvement for structures and facilities. Technical Letter No. 1110-1-185, Department of the Army. U.S. Army Corps of Engineers, Washington, D.C., 42p.

Geosynthetics Conference

The Economics of Open Top Reservoirs and Floating Covers

Brian Fraser,[1] and Daniel Lotufo[2]

[1]Layfield USA Corp. 10038 Marathon Parkway, Lakeside, CA 92040, USA;
brian.fraser@layfieldgroup.com
[2]Layfield USA Corp. 10038 Marathon Parkway, Lakeside, CA 92040, USA;
daniel.lotufo@layfieldgroup.com

ABSTRACT

Open top reservoirs have been used for thousands of years for the storage of water for municipal, natural resource and agriculture applications. While these reservoirs are still presently utilized, restrictions have been instituted over time to regulate protection of these water storages. As a result, geosynthetic floating covers have been developed as a method of providing protection to meet these regulations. Floating covers are designed to eliminate water loss from evaporation and to protect the water source from dirt, debris and other contamination sources. Floating covers have consistently demonstrated their ability to be a long-term solution and are increasing being used as an economical method to protect water supplies. This paper will cover the history and performance of geosynthetic floating covers over time, as well as their economic advantage compared to other common below and above ground structural alternatives. Lastly, this paper will highlight the long history of chlorosulfonated polyethylene (CSPE) as the primary material for floating covers in potable water storage resulting from its outstanding UV performance and chemical resistance to chlorine and other disinfectants used in water treatment. With over forty years of documented use, CSPE has proven to be one of the best performing materials for floating covers and geomembranes in long term potable water storage applications.

.

Figure 1. Ramona Water District. CSPE Tension Cable Systems installed in 2020

Figure 2. MWDS Skinner Reservoir. CSPE Defined Sump 2013

INTRODUCTION

Open top reservoirs have been used for thousands of years for various water storage applications, with the oldest known reservoir in the world being the Jawa Dam in present-day Jordan. It was built in about 3000 BCE to store water for irrigation (National Encyclopedia 2011). Today, open top reservoirs are still frequently used worldwide for many applications including potable, reclaimed, recycled and wastewater storage. These reservoirs are often lined with a geomembrane water proofing barrier to prevent seepage. A geomembrane is a low permeability synthetic membrane liner or barrier used to control fluid migration in an earthen containment project, structure or system. Uncovered water reservoirs are often impacted by evaporation, which can be substantial in hotter, arid climates. Geosynthetic floating covers are an excellent method of protecting large volumes of water from evaporation. Additionally, floating covers can help to reduce odors while preventing dirt and debris from contaminating the water being stored. An example of a floating cover is shown in Figure 1 and 2 above.

ECONOMICS OF FLOATING COVERS

Reservoirs with geomembrane floating covers are an economical method of storing larger volumes of water. For example, in 2009 an 18-acre, 244 million-gallon, (923 ML) water reservoir designed with a geomembrane liner and floating cover was completed for the Upper Chiquita Reservoir (Figure 3) owned by the Santa Margarita Water District in Southern California, USA (Mills and Falk, 2013). The overall cost of the Upper Chiquita project including the construction of the earthen dam, installation of the liner and floating cover was approximately $53 million US dollars and took 1.5 years to complete. Based on the cost to construct the reservoir, the average price per gallon of water was $0.22 USD.

In comparison, the Kelly Butte reservoir in East Portland, Oregon, USA (Figure 4) was completed around the same time period. The Kelly Butte project involved the replacement of two older 10 million-gallon covered storage reservoirs. The original reservoirs, covered by a steel enclosure, were replaced with two 12.5 million-gallon (47.3 ML) storage reservoirs covered by a

rectangular concrete structure. The surface area of these reservoirs is about 2.5 acres. The overall investment in the Kelly Butte project was an estimated $90 million taking about 4 years to complete and working out to a cost of $3.60 USD per gallon. The comparison between the Upper Chiquita and Kelly Butte projects shows how a floating cover on an open top reservoir can be substantially more economical.

Figure 3. Upper Chiquita Reservoir

Figure 4. Kelly Butte Clearwell Reservoir

Another economical advantage of floating covers is evaporation control. In many hot arid regions of the Southern United States evaporation rates can reach 90" annually. The cost of water in these regions can also be very high, making water losses expensive. This has applications in particular in West Texas where upstream oil and gas producers require large volumes of water for hydraulic fracturing. In the Permian Basin region producers have reported water costs ranging from $0.50 to $1.00 USD per barrel ($42 USD per gallon) (Fraser and Killian 2015). For the hydraulic fracturing process, this water is stored in frac water pits or structural above ground storage tanks. These frac pits or tanks can incorporate the use of floating covers to eliminate all evaporation loss. Figure 5 shows a 250,000 ft^2 (23,200 m^2) frac pond reservoir with a floating cover installed in West Texas in 2014. The producer was losing the equivalent of 13 million gallons annually at an estimated cost of $310,000. The floating cover in this project was supplied and installed for $325,000 and eliminated all evaporation, providing a return on investment period of approximately 13 months. A total of 8 of these floating covers were installed for the operator in this region.

Figure 5. Evaporation Control Cover, Permian Basin, Texas in 2014

CSPE HISTORY & PROPERTIES

Chlorosulfonated polyethylene (CSPE) was first introduced in the United States in the 1970's as a geomembrane material for water and wastewater containment applications. Initial applications included potable water and wastewater storage for municipalities and tailings ponds for the mining sector. The first floating covers on record using CSPE were installed in the late 1970's in Southern California for municipal potable water storage (Fraser, et al, 2017). The covers were designed and used for evaporation control as well as to prevent dirt and debris from contaminating the water storage supply.

CSPE has many advantages over other commonly specified materials. CSPE is manufactured as a thermoplastic material that will vulcanize over time, becoming a thermoset material capable of surviving thermally stressful, high-temperature environments and UV exposure. When formulated and calendared into a lining grade material, it provides outstanding UV resistance and weathering properties allowing it to be used for long term exposed containment applications. It also demonstrates slow reduction of its mechanical and endurance properties over time. The material's unique cross-linking properties provide exceptional resistance to several chemicals used as disinfectants in municipal water treatment including chlorine, sodium hypochlorite and chloramines, which act as accelerators in breaking down the antioxidant packages of many geomembranes, resulting in environmental stress cracking that causes premature material failure in other geomembrane materials (Mills 2011). CSPE also has a low coefficient of thermal expansion and contraction, providing excellent dimensional stability and lay-flat characteristics in the field. Expansion and contraction problems caused by temperature changes are virtually nonexistent.

CSPE's synthetic rubber properties also provide it with a unique combination of flexibility and durability. In floating cover applications, CSPE is flexible enough to be factory fabricated in large prefabricated panels that can be folded, rolled, and transported efficiently to a containment project site. These larger prefabricated panels are unrolled into position and field welded on site significantly reducing installation time and construction costs. It also provides consistent seam integrity and liner quality by using shop seams. CSPE is produced in accordance to the Geosynthetic Research Institute GM 28 standards (GRI GM 28).

PROJECT PROFILES

The following section highlights two projects where CSPE floating covers have been installed in hotter, dryer climates for potable water storage and protection. These profiles demonstrate the unique ability of CSPE to withstand weathering and UV exposure as well as common water treatment chemicals.

PROJECT PROFILE 1: HINKLE RESERVOIR - San Juan Water District

- Granite Bay, California
- Hinkle Reservoir
- 62 million Gallon (238 Million Liters) Capacity
- Potable Water Storage
- CSPE Liner & Cover installed in 1980

Figure 6. Hinkle Reservoir. 40-year-old cover installed in 1980

San Juan Water District's Hinkle Reservoir (Figure 6) had a 45 mil (1.14 mm) CSPE liner and floating cover installed in 1980. The water district chose a floating cover based on the substantial cost savings versus other storage options. When the reservoir was initially constructed, alternatives such as steel and concrete tanks were considered. After evaluating the costs of each option, the CSPE liner and floating cover system was approximately 60% to 80% less than alternative storage systems considered. This also factored in lifecycle cost for maintenance and servicing. As a result, a CSPE floating cover was selected and installed as one of the first-generation larger scale floating covers at the time. The is located north east of Sacramento, CA, spanning 5.7 hectares (14 acres) in a region is known for hot, arid summers and high UV exposure. The winters are typically a bit cooler, wet, and partly cloudy. Over the course of the year, average temperature can vary from 4°C to 40°C (35°F to 104°F).

The reservoir is currently scheduled to have a new liner and cover installed over the next couple of years. At that time the original installed liner and cover materials will have been in

service for over 42 years. The Hinkle Reservoir is believed to be one of the longest reported CSPE floating cover systems still operating.

PROJECT PROFILE 2: Upper Stone Canyon LADWP

Los Angeles Department of Water & Power (LADWP) Upper Stone Canyon

- Beverly Hills, CA
- Upper Stone Canyon Reservoir
- 139 Million Gallon (526 ML) Capacity
- Potable Water Storage

Figure 7. 45 mil CSPE Defined Sump Cover installed in 2019

The Upper Stone Canyon reservoir is owned and operated by Los Angeles Department of Water & Power (LADWP). In 2019 a new 700,000 ft^2 (65,000 m^2) floating cover was installed as part of an initiative to protect and preserve the city's drinking water supplies. This 139 million-gallon-reservoir was first constructed in 1954 for water storage in the Bel Air, CA region. The reservoir provides water to approximately 450,000 residents in the areas of West Los Angeles, Pacific Palisades, Marina Del Rey, and the UCLA campus. The large reservoir was covered to comply with State and Federal laws. The cover material installed was 45 mil CSPE manufactured with a distinctive green color to better match the surrounding environment. Beverly Hills, CA is a warm Mediterranean climate known for its dry, arid summers and high UV exposure. Prior to construction, LADWP conducted an environmental impact assessment to investigate the impact of different methods to cover the Upper Stone Canyon Reservoir (Los Angeles Department of Water & Power, 2011). The two main options considered were a concrete roof and a geomembrane floating cover. Looking at the overall cost of the concrete roof option, the LADWP estimated a $140 million expenditure over a 60-year life cycle. Also noted in this study was that most of that cost would be the up-front capital for construction. The construction timeline was estimated to be 4-5 years. The floating cover option was estimated to be $35 million in overall costs and would only take an estimate 1.5 years to complete installation. The estimated lifespan of a floating cover is in excess of 30 years (Fraser 2019) and even with scheduled cover replacements would still be

significantly less expensive than the overall cost of the concrete roof structure. This highlights the cost advantage of using a floating cover, with savings being observed in both the initial purchase and installation and over the lifespan of the cover.

The floating cover replaced the use of plastic HDPE balls which were used temporarily until a more permanent floating cover system could be installed. The main project challenges were primarily the large scale of the cover system and tight access in the conjected Beverly Hills region. To address the tight space constraints, the floating cover system had to be prefabricated and installed on site in sections. Upon completion, the installed floating cover eliminated all evaporation losses and prevented dirt and debris from entering the potable water storage to comply with state and federal regulations.

CONCLUSION

This paper points out the several cost advantages of using open top reservoirs combined with a geosynthetic floating covers compared to structural above ground steel tanks or underground concrete clearwells water storage systems. Floating covers are able to provide the same coverage of traditional water storage methods at a fraction of the costs. Floating covers have consistently demonstrated their ability to perform as long-term exposed covers and are increasing being used as an economical method to protect valuable water supplies

REFERENCES

National Geographic contributors. (January 21, 2011) Reservoirs, In National Geographic Encyclopedia, https://www.nationalgeographic.org/encyclopedia/reservoir/

Mills A., and Falk S (2013). Upper Chiquita Reservoir Floating Cover and Liner, Geosynthetics 2013, IFAI, Long Beach CA, USA.

Fraser, B, and Killian B (2015). Emerging Applications for Evaporation Control Covers, Geosynthetics 2015, Portland, OR, USA.

Fraser, B., Roades, S, Neal, M., and Gersch, Alex (2019). CSPE Performance & History in long term Potable Water Storage Applications, *Geosynthetics 2019*, IFAI Houston, Texas, USA

Mills, A. (2011) The effects of chlorine on very low-density thermoplastic olefins, Geofrontiers 2011, IFAI, Dallas TX, USA.

GRI-GM 28. Standard Specification for Test Methods, Test Properties, and Testing Frequencies for Reinforced Chlorosulfonated Polyethylene (CSPE-R) Geomembranes, Geosynthetics Research Institute, Geosynthetic Institute, Folsom, PA, USA

Upper Stone Canyon Reservoir Water Quality Improvement Project. Los Angeles Department of Water and Power, 2011, *Upper Stone Canyon Reservoir Water Quality Improvement Project*, www.ladwp.com/cs/idcplg?IdcService=GET_FILE&dDocName=QOELLADWP006808&RevisionSelectionMethod=LatestReleased.

Water-filled Barrier Walls for Stormwater and Sediment Control on Steep Slopes

Chase Hemming, P.E.[1] and Josef Tootle, P.E.[2]

[1]ENGEO Incorporated; e-mail: chemming@engeo.com
[2]ENGEO Incorporated; e-mail: jtootle@engeo.com

ABSTRACT

The use of water-filled barrier walls for stormwater and sediment control was evaluated for a hillside construction project in Northern California. Water-filled barrier walls were configured along one of the project's exposed hillsides to create a series of nine temporary detention basins. The water-filled barrier walls were evaluated for ease of deployment, construction practicability, and stability for varying slope conditions, surface placement types, and configurations. When properly anchored, the water-filled barrier wall basins detained large volumes of sediment and stormwater along the steep hillside.

INTRODUCTION

A low density polyethylene (LDPE) barrier wall product called "Muscle Wall" was evaluated for its use in stormwater and sediment control on steep slopes. The barrier walls are approximately 4 feet in height, 6 feet in length, 2.5 feet in base width, 0.7 feet in top width, and 120 pounds in weight. The barrier walls are interlocked, secured to each other using ratchet tie down straps, filled with water, and wrapped with a plastic or geotextile liner to produce a linear barrier system. An image of two interlocked barrier walls without ratchet tie down straps or liner is shown in Figure 1.

Figure 1. Two interlocked barrier walls.

The barrier wall product was evaluated for ease of deployment, construction practicability, and stability for varying slope conditions, surface placement types, and configurations during the 2018-19 winter season at a construction project site in Northern California. Northern California has a climate characterized by moist mild winters and dry summers, with a majority of rainfall

occurring between November and March. The site's topsoil consisted predominantly of silty sand with a fines content ranging between 13 and 32 percent (percent passing the number 200 sieve). The site's slope grades ranged between 15 and 60 percent.

Prior to the 2018-19 winter season, approximately 10 acres of hillside terrain within the project site was grubbed; the contractor needed to complete mass grading of the hillside during the winter season to meet construction schedule demands. Because of this, traditional erosion control measures such as hydroseed, hydromulch, straw wattle, and woven netting/blanket were not practical to install prior to each storm, since they would need to be immediately removed so that grading could continue following the storm. The steep unvegetated slopes posed a high risk for sediment erosion, which could lead to turbid stormwater discharges if no containment measures were installed. California's Construction General Permit (CGP) requires Best Management Practices (BMPs) be implemented onsite, with the intent of reducing stormwater discharge leaving certain construction sites to a turbidity value less than 250 Nephelometric Turbidity Units (NTU). In order to comply with CGP requirements, the barrier wall product was used to create temporary stormwater and sediment detention basins along the hillside, with the intent of reducing stormwater velocity and detaining turbid stormwater.

METHODS

Shipping and Storage. Approximately 4,000 linear feet (LF) of the barrier wall product was ordered for the project site. The barrier walls, plastic liner, ratchet tie-down straps, and liner clips were shipped to the project site on seven truck trailers (approximately 95 barrier walls per truck trailer). Each pallet of the barrier wall product was observed to take up an approximately 8 feet by 6 feet footprint, and contained 12 barrier wall segments as shown in Figure 2. The barrier wall product pallets were removed from the truck trailer using a forklift and stored on the project site prior to deployment.

Figure 2. Stacked barrier walls.

Placement Strategy. Based on experience from previous winters on the construction site, turbid stormwater that collected in holding ponds often took more than two weeks of settling time before meeting the CGP turbidity threshold of 250 NTU. Because of this, it was assumed that no stormwater runoff from the hillside would be clear enough to discharge offsite during a storm event; the strategy was to install a series of basins to detain and control the hillside's stormwater, which would limit the possibility of discharges exceeding 250 NTU. It was expected that turbid stormwater would seep under the barrier wall basins at the bottom of the hillside, but at a low enough flowrate to be controlled and rerouted as needed to avoid offsite discharge. Polymer flocculant to reduce turbidity in the basins was not considered because it was not approved for use by the Regional Water Quality Control Board. The basins would also act as check dams to slow stormwater velocity along the hillside to reduce erosion and sediment transport. Based on an average watershed slope of 20 percent, shallow concentrated flow velocities were expected to reach 4.5 feet per second (fps) over bare soil, and 9 fps over pavement (USDA, 2010).

The basins were designed to detain the runoff volume produced by a rainfall depth of 2 inches (approximately equal to that of a 10-year-recurrence-interval, 6-hour-duration storm). For storms forecasted to produce greater than 2 inches of rainfall, water trucks were staged at one of the downslope basins so that collected stormwater could be pumped and transported to a high capacity infiltration-evaporation basin in a flat region of the site. While expensive, the cost of the pumping and trucking operation was deemed cheaper than the cost of not completing the mass grading work on time. A series of nine temporary barrier wall basins with an average spacing of 150 feet were placed along the hillside, as shown in Figure 3.

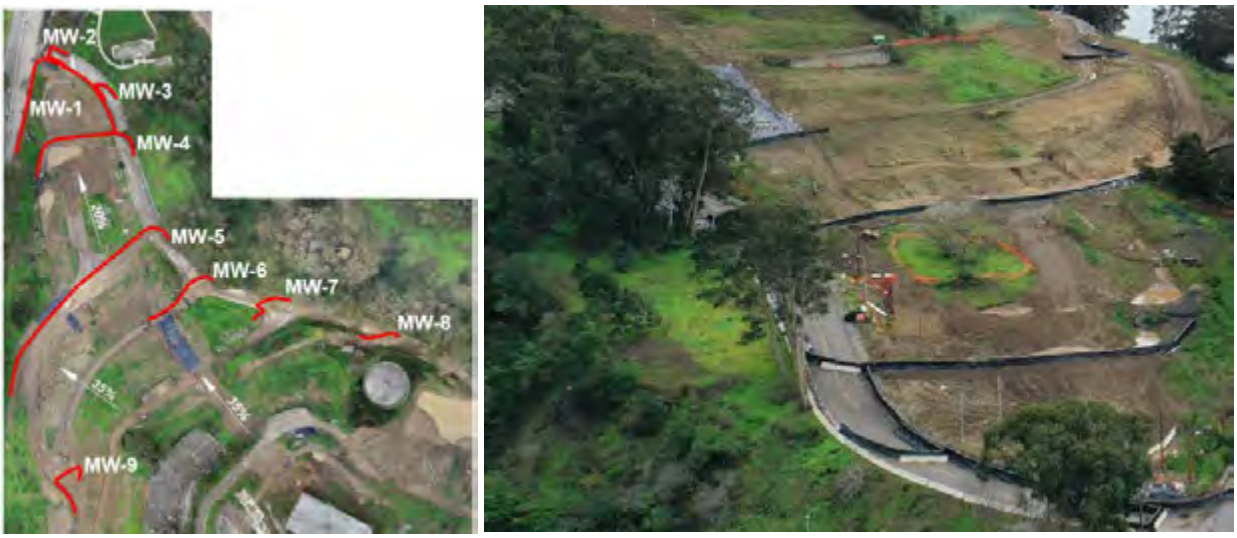

Figure 3. Aerial view (left) and side view (right) of the barrier wall basin locations.

Table 1 summarizes each barrier wall basin's length, cross slope (defined as the average slope perpendicular to the basin length), and surface placement type. Barrier walls that crossed active haul roads were not filled with water to allow for rapid removal during non-storm conditions. All barrier walls that were not located across an active haul road were filled completely with water to increase stability. In addition, all barrier walls were wrapped with plastic to limit seepage beneath the base and connection points of the barrier wall basins. The bottom area of the basins was left unlined to promote infiltration and reduce the need for pumping.

Table 1. Summary of barrier wall basin properties.

Basin number	Length (feet)	Cross slope (%)	Surface type
MW-1	450	~10	Concrete Sidewalk
MW-2	100	~10	Asphalt Concrete
MW-3	100	~18	Asphalt Concrete
MW-4	260	flat	Compacted Soil
MW-5	500	flat	Compacted Soil
MW-6	170	~15	Asphalt Concrete
MW-7	105	~13	Asphalt Concrete
MW-8	80	~5	Compacted Soil
MW-9	160	~10	Compacted Soil

Deployment. The nine barrier wall basins were deployed intermittently from the end of November 2018 through mid-December 2018, based on the project schedule and contractor's availability. In locations where the barrier wall basins were to be placed on soil, grading was performed to provide a level surface for the barrier walls. A level surface was preferred in order to limit seepage under the barrier walls and to increase stability. According to the contractor, it took approximately 9 hours to install 500 LF of the barrier wall product, which included the time to grade a level surface, place the barrier walls, connect the barriers with straps, fill the barriers with water, wrap the barriers with plastic lining, and secure the plastic lining with clips. When the barrier walls were placed on a paved surface where grading a level surface was not necessary, the installation process took about 5 hours for 500 LF.

FINDINGS

During the study period between December 2018 and March 2019, the site received approximately 19 inches of rain. The largest storm occurred between February 13 and February 15, and produced approximately 4 inches of rain over the course of three days. Other storms during the study period generally produced between 1 and 3 inches of rain over the course of 2 to 4 days. Even though the design rainfall depth was exceeded during multiple storms, the downslope basin (MW-4) that collected a majority of the site's stormwater did not overtop due to the pumping and trucking operation.

When each barrier wall basin was properly anchored, the series of basins successfully detained and controlled the hillside's turbid stormwater. The velocity of stormwater was not measured during storm events, but it is assumed that the average velocity along the hillside was reduced, as stormwater was brought to a halt approximately every 150 feet. Turbidity of stormwater entering and exiting the barrier wall basins was not measured, but as expected due to site sediment's high fines content, turbidity did not visually appear to decrease upon exiting the basins. An individual breakdown of each barrier wall basin's performance is discussed below.

MW-1. Basin MW-1 was located at the toe of the hillside along a concrete sidewalk with a cross slope of approximately 10 percent. All barrier walls were filled with water. Basin MW-1 held back large volumes of sediment during the study period, with the contractor removing built-up sediment with an excavator following storms as needed. Turbid water was observed seeping from the bottom of the basin at a low flowrate during storms. This water was routed using sand bags into a traditional excavated sediment basin further downstream to prevent discharge from the site.

MW-2. Basin MW-2 was located at the bottom of an asphalt concrete haul road with a cross slope of approximately 10 percent. The initial configuration (Figure 4, left) was composed of four unfilled barrier walls (red) anchored by three water-filled barrier walls (blue) on each end. Two 90-degree corner walls were used to assist in forming the basin. After the first storm, the entire basin slid (but did not overturn) due to sediment impact and buildup (Figure 4, right). After this storm, two additional water-filled barrier walls were added on each end of the basin (Figure 5, left). Following this addition, Basin MW-2 did not slide during subsequent storm events (Figure 5, right).

Figure 4. MW-2 initial configuration (left) and performance after first storm (right).

Figure 5. MW-2 revised configuration (left) and performance after subsequent storms (right).

MW-3. Basin MW-3 was located across an asphalt concrete haul road with a cross slope of approximately 18 percent. The initial configuration (Figure 6, left) was composed of four unfilled barrier walls (red) anchored by three water-filled barrier walls (blue) on each end. One 90-degree corner wall was used to assist in forming the basin. After the first storm, the basin slid and multiple barrier walls disconnected from each other due to sediment impact and buildup (Figure 6, right). After this storm, three additional water-filled barrier walls were added on each end of the basin (Figure 7, left). Following this addition, Basin MW-3 remained stable during subsequent storm events (Figure 7, right).

Figure 6. MW-3 initial configuration (left) and performance after first storm (right).

Figure 7. MW-3 revised configuration (left) and performance after subsequent storms (right).

MW-4. Basin MW-4 was placed on fairly level compacted soil with all barrier walls filled with water. In addition, an approximately 4-feet-deep sediment basin was excavated on the interior of the barrier wall basin. The barrier wall product and excavated sediment basin combination increased the storage depth to approximately 7.5 feet. Figure 8 shows a conceptual detail of the combined basin system. With the plastic liner overlapping the barrier walls and extending down the 2:1 sediment basin side slopes, water was unable to seep under the barrier walls. Water discharging from Basin MW-5 (upslope) through seepage or overtopping would make its way to Basin MW-4, where it would then be pumped into water trucks after filling up during storm events.

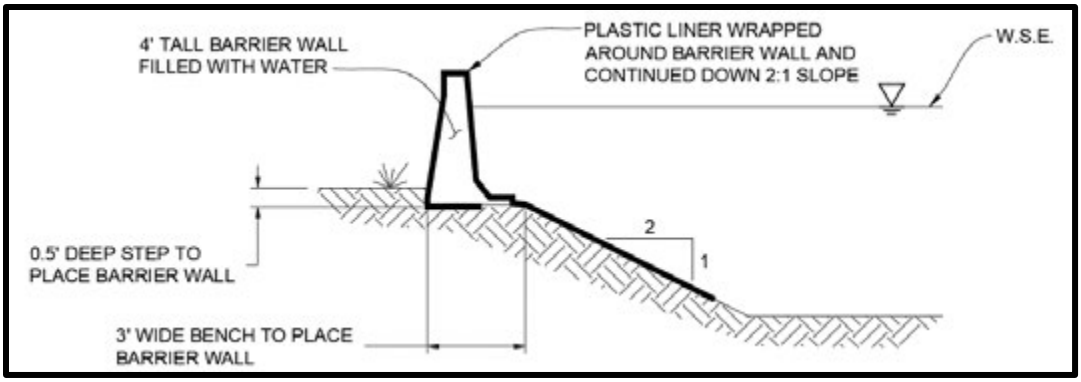

Figure 8. Detail of combined barrier wall and excavated sediment basin.

MW-5. Basin MW-5 was placed on fairly level compacted soil with all barrier walls filled with water. Basin MW-5 was effective at slowing stormwater runoff and trapping entrained sediment; once volumetric capacity was reached during a rain event, stormwater would both overtop and seep under the barrier walls down gradient to Basin MW-4 (Figure 9). Stormwater was able to seep under the barrier walls of MW-5 since the plastic liner did not continue along the interior of the basin like Basin MW-4. In addition, irregularities in the ground surface created small gaps for water to flow through. The turbidity of water leaving the basin appeared similar to that of water entering the basin. Basin MW-5 did not experience any lapses in stability, even when overtopped by stormwater and impacted by sediment buildup.

Figure 9. Seepage under the barrier wall.

MW-6. Basin MW-6 was located across an asphalt concrete haul road with a cross slope of approximately 15 percent. Unlike Basins MW-2 and MW-3, which made use of corner walls, Basin MW-6 had enough width across the haul road to form a semi-circular basin without using corner walls; the connection joints between barrier walls allowed for a deflection of approximately 11 degrees between each wall. Five barrier walls located across the haul road were not filled with water. Like Basin MW-5, Basin MW-6 did not experience any lapses in stability while at capacity with stormwater and entrained sediment (Figure 10). Stormwater was observed to seep under the barrier walls during storm events; the turbidity of water leaving the basin appeared similar to that of water entering the basin.

Figure 10. Basin MW-6 retaining 4 feet of sediment following a storm.

MW-7. Basin MW-7 was located across an asphalt concrete haul road with a cross slope of approximately 13 percent. The initial configuration was composed of five unfilled barrier walls anchored by six water-filled barrier walls on one end and four water-filled barrier walls on the other end. Two 90-degree corner walls were used to assist in forming the basin. After the first storm, the basin did not slide (like Basins MW-2 and MW-3), but the empty barrier walls rotated outward. After this storm, the five previously empty barrier walls were filled with water. Following this reconfiguration, Basin MW-7 remained stable during subsequent storm events.

MW-8. Basin MW-8 was located across a compacted soil haul road with a cross slope of approximately five percent. Like the other basins located across haul roads, five middle barrier walls were not filled with water. Figure 11 below depicts the empty barrier walls set aside during dry weather so that the haul road could be used. Because Basin MW-8 was the furthest upslope basin, it collected the least amount of stormwater runoff and never filled to capacity. However, it succeeded as a check dam for slowing water flow and detaining entrained sediment.

Figure 11: Empty barrier walls set aside for haul road use.

MW-9. Basin MW-9 was located across a compacted soil haul road with a cross slope of approximately 10 percent. Five barrier walls in the middle of the basin were not filled with water, and the basin utilized two corner walls to assist in forming the basin. Basin MW-9 often filled to capacity with water during storms, and accumulated sediment throughout the study period (Figure 12). Over the duration of the study period, Basin MW-9 did not experience any lapses in stability while at capacity with water and sediment. The turbidity of water leaving the basin through overtopping and seepage appeared similar to that of water entering the basin.

Table 2 summarizes each barrier wall basin's stability results in relation to its configuration characteristics.

Figure 12: Basin MW-9 overtopping during a storm event.

Table 2. Summary of basin performance results.

Basin number	Cross slope (%)	Surface type	Empty barrier walls?	Corner walls utilized?	Stability issues?
MW-1	~10	Concrete Sidewalk			
MW-2	~10	Asphalt Concrete	✓	✓	✓
MW-3	~18	Asphalt Concrete	✓	✓	✓
MW-4	flat	Compacted Soil			
MW-5	flat	Compacted Soil			
MW-6	~15	Asphalt Concrete	✓		
MW-7	~13	Asphalt Concrete	✓	✓	✓
MW-8	~5	Compacted Soil	✓	✓	
MW-9	~10	Compacted Soil	✓	✓	

DISCUSSION

The barrier wall basins that had initial stability issues (Basins MW-2, MW-3, and MW-7) were each installed on slopes greater than or equal to 10 percent, placed on asphalt concrete, contained empty barrier walls, and utilized corner walls. While Basin MW-6 was on a slope greater than 10 percent, placed on asphalt concrete, and contained empty barrier walls, it did not experience stability issues. It appears the lack of corner walls in the configuration may have increased the basin's stability. In general, stress tends to concentrate over sharp changes in geometry (Dundurs and Lee, 1972). It was observed that for basins where barrier walls came apart or rotated out of place (Basins MW-2, MW-3, and MW-7), a corner wall was the weak point.

While Basin MW-9 was located on a slope of approximately 10 percent, contained empty barrier walls, and utilized corner walls, it did not experience stability issues. The compacted soil on which it was placed may have been the reason for its increased stability compared to other similar basin configurations that were installed on asphalt concrete; the coefficient of friction between plastic and soil is generally higher than that of plastic and asphalt concrete. In addition,

the barrier walls of Basin MW-9 may have been more secure since they were able to "settle" into the soil, as opposed to sitting on top of relatively rigid asphalt concrete.

While Basin MW-8 was placed on asphalt concrete, contained empty barrier walls, and utilized corner walls, it did not experience stability issues. This is likely because the basin was located on a 5 percent slope (compared to 10 percent or greater) and never filled to capacity due to its upslope location on the hillside.

Based on pull-out sliding tests performed by the barrier wall product manufacturer on a flat grade under static water loading conditions, the sliding factor of safety for the barrier wall was 1.37 when placed on asphalt, and 1.44 when placed on soil. These sliding factor of safety values were used to calibrate a static water load retaining wall sliding analysis for a 0 percent slope. The retaining wall analysis was then repeated for slopes of 5, 10, 15, and 20 percent. Table 3 presents the results from the sliding factor of safety analysis for varying slope grades and surface placement types.

Table 3. Sliding factor of safety (FS) results.

Slope (%)	FS on Asphalt	FS on Soil
0	1.37*	1.44*
5	1.18	1.25
10	1.04	1.10
15	0.93	0.98
20	0.84	0.88

*Per barrier wall product manufacturer pull-out sliding tests.

As expected, sliding factor of safety decreases with increasing slope grade, and is slightly greater for a soil surface. The results generally align with field observations, where some barrier walls showed signs of instability on slope grades exceeding 10 percent. To increase barrier wall stability on slope grades exceeding 10 percent, water-filled barrier walls or k-rail can be placed behind and perpendicular to the barrier wall basin. For horseshoe shaped basins, additional water-filled anchor walls can be placed on each end. If enough water-filled anchor walls are used, some barrier walls in the center of the basin can even be left unfilled, as exemplified by Basins MW-2 and MW-3. Basin MW-2 was on a slope of approximately 10 percent, and was initially unstable with a ratio of water-filled to unfilled barrier walls of 1.5:1; however, Basin MW-2 remained stable with a ratio of water-filled to unfilled barrier walls of 2.5:1. Basin MW-3 was on a slope of approximately 18 percent, and was initially unstable with a ratio of water-filled to unfilled barrier walls of 1.5:1; however, Basin MW-3 remained stable with a ratio of water-filled to unfilled barrier walls of 3:1. Table 4 provides recommended "rule of thumb" ratios of water-filled to unfilled barrier walls to improve basin stability for various slope grades.

Table 4. Ratios of water-filled to unfilled barrier walls for various slope grades.

Slope (%)	Ratio of water-filled to unfilled barrier walls
0-5	2:1
5-10	2.5:1
10-15	3:1
15+	Fill all barrier walls

Leaving some barrier walls unfilled when located across an active haul road was convenient for the contractor's site access; during non-storm conditions, the contractor would disconnect the unfilled barrier walls from the basin and set them aside to allow haul road use. If a storm event was forecasted, the contractor was able to quickly reconnect the unfilled barrier walls across the haul road.

To reduce seepage under the barrier walls, the plastic or geotextile liner could be trenched into the ground on the water side of the barrier wall (if placed on soil). For barrier walls placed on pavement, seepage under the barrier walls could be mitigated by placing sand bags tightly along the toe of the barrier walls. To reduce uncontrolled overtopping, the barrier wall product manufacturer developed a double-orifice discharge port during the end of the study period. A hose could be connected to the discharge port to route stormwater to an active treatment system or other water quality BMP to help reduce stormwater turbidity before offsite discharge. A rendering of the discharge port (left) and photo of the manufactured discharge port at the project site (right) are shown in Figure 13. The discharge port was not tested during the study period.

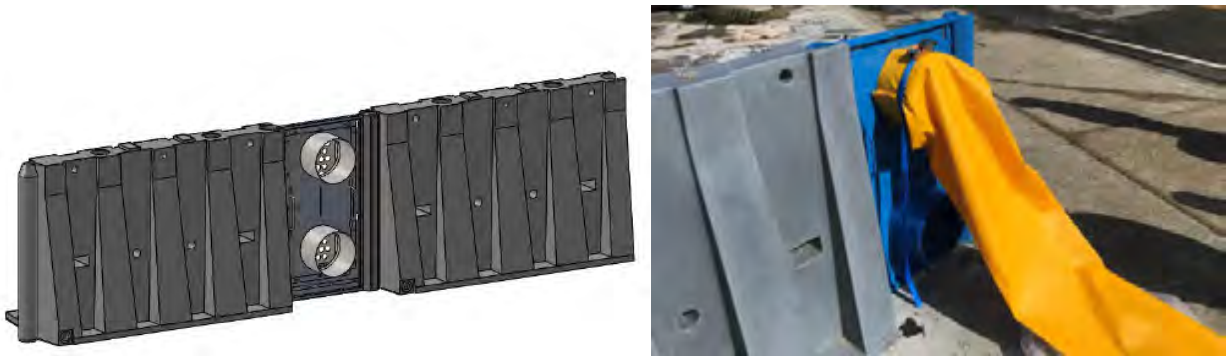

Figure 13. Rendering of the discharge port (left) and photograph of the discharge port (right).

The barrier wall product provides an alternative to traditional barrier BMPs such as sandbags and k-rail. Compared to a sandbag barrier of the same height, the United States Army Corps of Engineers (USACE) concluded the barrier wall product was over 25 times quicker to construct, had four times less seepage, and remained undamaged by waves, overtopping, debris impact, and riverine current (Ramos-Santiago, Blades, and Gutshall, 2020). One 4-foot-tall barrier wall is equivalent to approximately 470 sand bags. Compared to a typical 10-feet-long, 2.7-feet-tall, 4,000-pound section of k-rail, a 6-feet-long, 4-feet-tall, 120-pound barrier wall (when unfilled) is easier and greener to deploy because it does not require heavy machinery. Once filled with water, the barrier wall weighs approximately 1,400 pounds.

CONCLUSION

The use of water-filled barrier walls for stormwater and sediment control was largely effective for the hillside construction project in Northern California. The series of nine temporary detention basins created by the barrier walls held back large volumes of turbid stormwater and transported sediment, and reduced the velocity of stormwater as it made its way down the hillside. Given enough water-filled "anchor" walls, the basins remained stable for various configurations and on slopes of varying steepness and surface type.

Since the end of the study period in March 2019, the barrier wall product has continued to be used at the project site. In addition to being used to create temporary detention basins on steep slopes, the barrier wall product was used as a sediment perimeter control BMP, a secondary containment BMP for liquid construction materials, and a temporary retaining wall for soil. Due to the barrier wall product's LDPE material, it is expected the barrier walls will continue to be reused on the project site for multiple additional years. ENGEO Incorporated is currently evaluating the average effective lifespan of the barrier wall product based on data from its use at the subject project site in Northern California, and two additional project sites in Southern California.

REFERENCES

Dundurs, J. and Lee, M.S. (1972). Stress concentration at a sharp edge in contact problems, *Journal of Elasticity*, 2: 109–112.

Ramos-Santiago, E., Blades, C., and Gutshall, J.D. (2020). Evaluation of 4-Foot Muscle Wall Flood Fighting Barrier, *Engineer Research and Development Center*, United State Army Corps of Engineers: 1 –53.

United States Department of Agriculture (2010). Time of Concentration, *Part 630 Hydrology National Engineering Handbook*, 210-VI-NEH: 15-8.

70 Ranch Case Study: Interpreting the Data

Matthew P. Kemnitz

Leak Location Services, Inc; e-mail: mattk@llsi.com

ABSTRACT

This technical paper will discuss the results from two different types of leak location surveys on a large project near Greeley, Colorado. A bare liner survey as well as a soil survey were completed on the primary fabricated geomembrane of a cell over seven million square feet in size. These surveys began in August of 2018 and were completed in May 2019 over five separate mobilizations. In particular, the paper will discuss what type of damage was found during each type of leak location survey and where specifically it was found, for example seam welds, extrusion welds or on the panels. On this project a majority of the seams were factory fabricated under ideal conditions and therefore resulted in fewer defects. What can we learn from this project and how many other leaks could be avoided? With the ideal outcome of zero leaks let us learn from this project to know what can be done not only to avoid making leaks in the field during construction, but also to ensure the potential for leaks is diminished before the liner ever arrives at the site. This coupled with a thorough leak location survey will result in an exceptional liner system that will hold water and deliver on its intended purpose.

INTRODUCTION

The 70 Ranch Reservoir located in Colorado was lined with 7,350,000 square feet of 45-mil reinforced polyethylene. The 4H:1V slopes are lined from the bottom up with a prepared subgrade, an 8-oz nonwoven geotextile with the 45-mil RPE on top. The floor of the reservoir was lined from the bottom up with a prepared subgrade, an 8-oz nonwoven geotextile and a 30-mil RPE with approximately 1.5 feet of soil cover placed on top. The project specifications for this project required the reservoir to be leak tested using both the bare liner survey (ASTM D7002) method as well as the soil survey (ASTM D7007) method. The bare liner survey was to be used on the slopes of the reservoir while the soil survey was to be performed on the floor areas as well as the benches on the slopes.

The first mobilization took place on August 23rd through 29th of 2018. The slopes were tested prior to the deployment of the geotextile. Twenty-four leaks were found during this mobilization in a total of eleven separate areas. Figure 1 shows the area that was leak tested on this initial mobilization. The size of leaks found ranged from a 16-foot tear to a 1/32-inch pinhole. Table 1 lists the leaks that were found, their location as well as a description. Twenty-three of the leaks were found using the soil survey method and one leak was found using the bare liner survey method. All of these leaks were found on the panels and none of them were found on seams or welds.

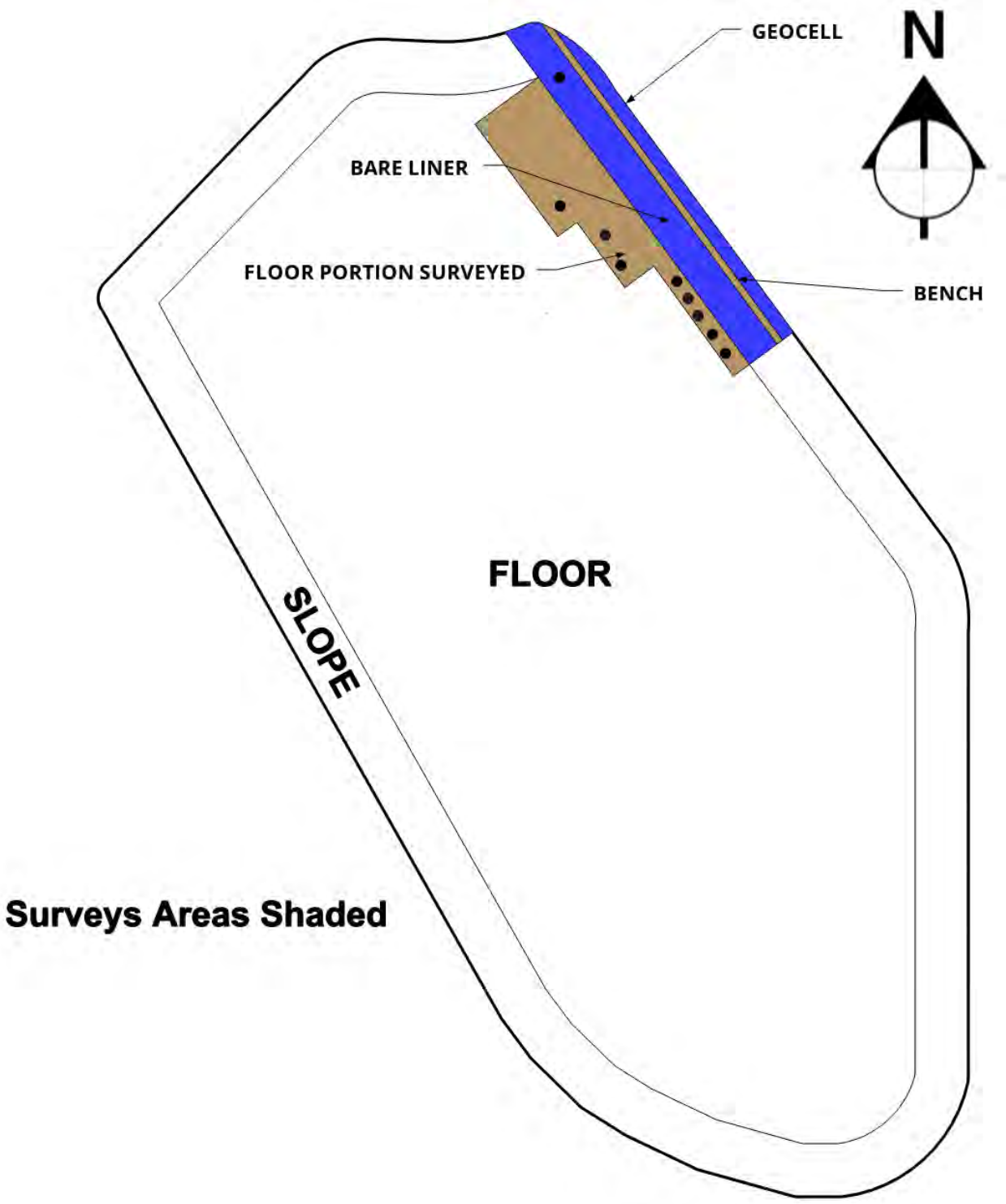

Figure 1. Area Surveyed on the 1st Trip

Table 1. List of Leaks Located on the 1st Trip

LEAK	LOCATION	DESCRIPTION
1	Floor of area – soil survey – exposed	16-foot machine tear
2	Floor of area – soil survey – exposed	Two 1/16-inch holes
3	Floor of area – soil survey - exposed	1/8-inch hole
4	Floor of area – soil survey – exposed	1/16-inchhole
5	Floor of area – soil survey – exposed	1/8-inch hole
6	Floor of area – soil survey – exposed	Group of six small holes
7	Floor of area – soil survey – exposed	Two 1-inchholes
8	Floor of area – soil survey – exposed	Two holes
9	Floor of area – soil survey – exposed	½-inch hole on panel
10	Floor of area – soil survey - exposed	Group of six small holes
11	9 feet south of seam S1 and S2 and 57 feet east of tie in at tow. Found during bare liner survey of slope	1/32-inch pinhole on panel

The second mobilization took place on September 24th through 27th of 2018. Twenty leaks were found during this mobilization. Figure 1 shows the area that was leak tested on the second mobilization. The floor area of the soil survey from the first area was retaken on this trip due to a condition of compromised isolation on the first mobilization. Leak number 16 was the only leak that was found in the previously surveyed area from the first mobilization, it was a 1/16-inch hole on a panel. It is from this example that we see how isolation of the perimeter affects the sensitivity of the leak location survey. It is also just as important to expose any leaks as they are found so they do not mask smaller leaks in the area. The size of leaks found ranged from a 6-foot tear to a 1/16-inch hole. Table 2 lists the leaks that were found, their location as well as a description. All of these leaks were found using the soil survey method. All of these leaks were found on the panels and none of them were found on seams or welds. From this mobilization moving forward electrical isolation of the reservoir was exceptional and allowed the leak location survey to be performed with great sensitivity and accuracy.

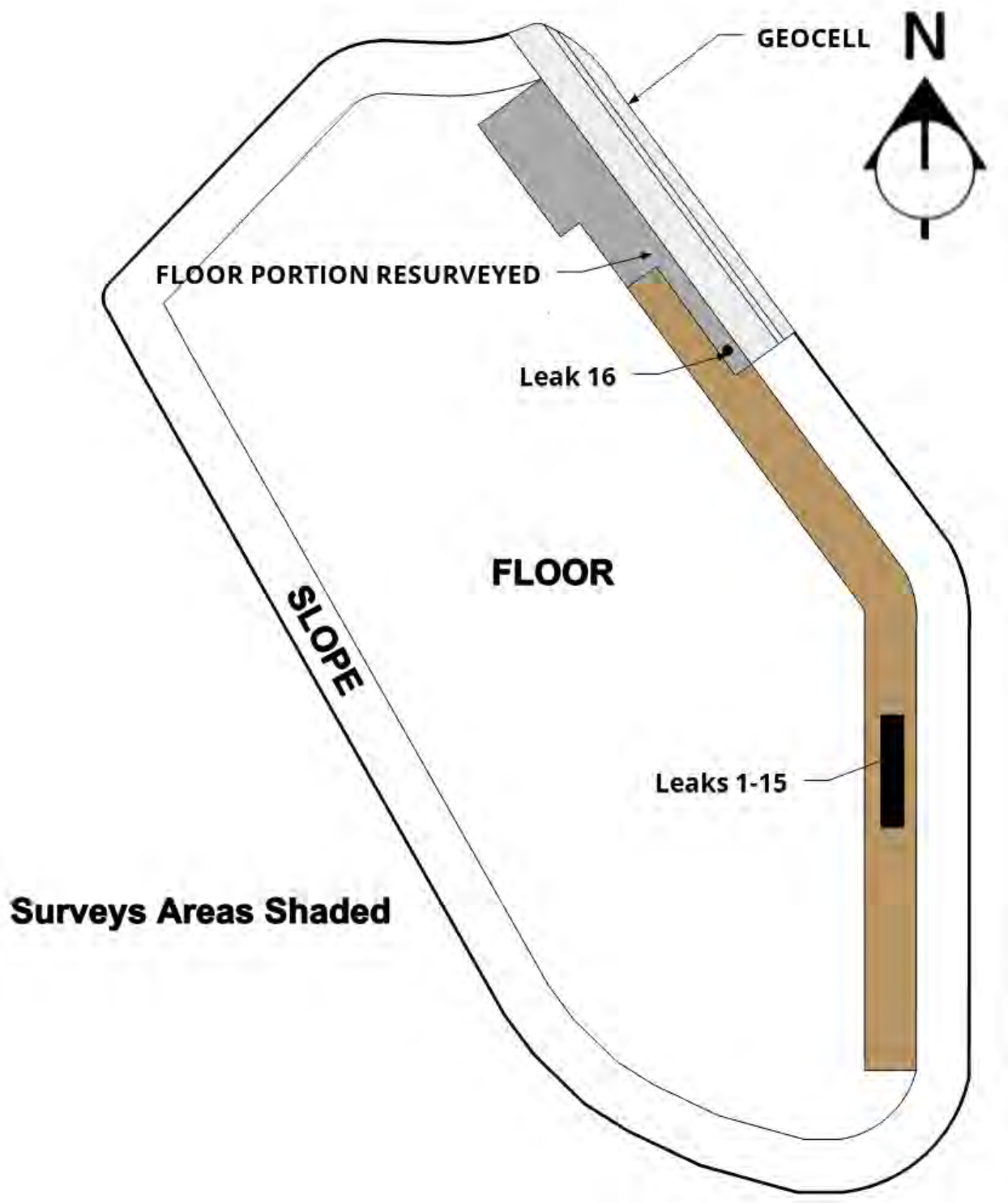

Figure 2. Area Surveyed on the 2nd Trip

Table 2. List of Leaks Located on the 2nd Trip

LEAK	LOCATION – SOIL SURVEY	DESCRIPTION
1	Floor of area – 80 feet from east tow – exposed	3-foot by 5-inch tear on panel
2	Floor of area – 80 feet from east tow – exposed	8-inch by 12-inch tear on panel
3	Floor of area – 80 feet from east tow – exposed	5-inch by 4-inch tear on panel
4	Floor of area – 80 feet from east tow – exposed	Three 2-inch tears on panel
5	Floor of area – 80 feet from east tow – exposed	1/2-inch hole on panel
6	Floor of area – 80 feet from east tow – exposed	3-foot by 4-foot tear on panel
7	Floor of area – 80 feet from east tow – exposed	Group of multiple-machine damage on panel
8	Floor of area – 80 feet from east tow – exposed	6-inch tear on panel
9	Floor of area – 70 feet from east tow – exposed	2-foot by 3-foot tear on panel
10	Floor of area – 70 feet from east tow – exposed	3-foot by 4-inch tear on panel
11	Floor of area – 70 feet from east tow – exposed	Multiple ½-inch tears on panel
12	Floor of area – 70 feet from east tow – exposed	2-foot by 3-foot tear on panel
13	Floor of area – 70 feet from east tow – exposed	2-foot by 6-inch tear on panel
14	Floor of area – 70 feet from east tow – exposed	6-foot by 4-inch tear on panel
15	Floor of area – 70 feet from east tow – exposed	5-inch linear cut on panel
16	Floor of area – 65 feet from east tow – in resurvey area - exposed	1/16-inch hole on panel

The third mobilization took place on November 13th through 19th of 2018. Eleven leaks were found during this mobilization. Figure 1 shows the area that was leak tested on the third mobilization. The size of leaks found ranged from a 3-inch tear to a 1/16-inch hole. All of these leaks were found using the soil survey method with one of them being on the side slope bench and the remainder on the floor of the reservoir. All of these leaks were found on the panels and none of them were found on seams or welds.

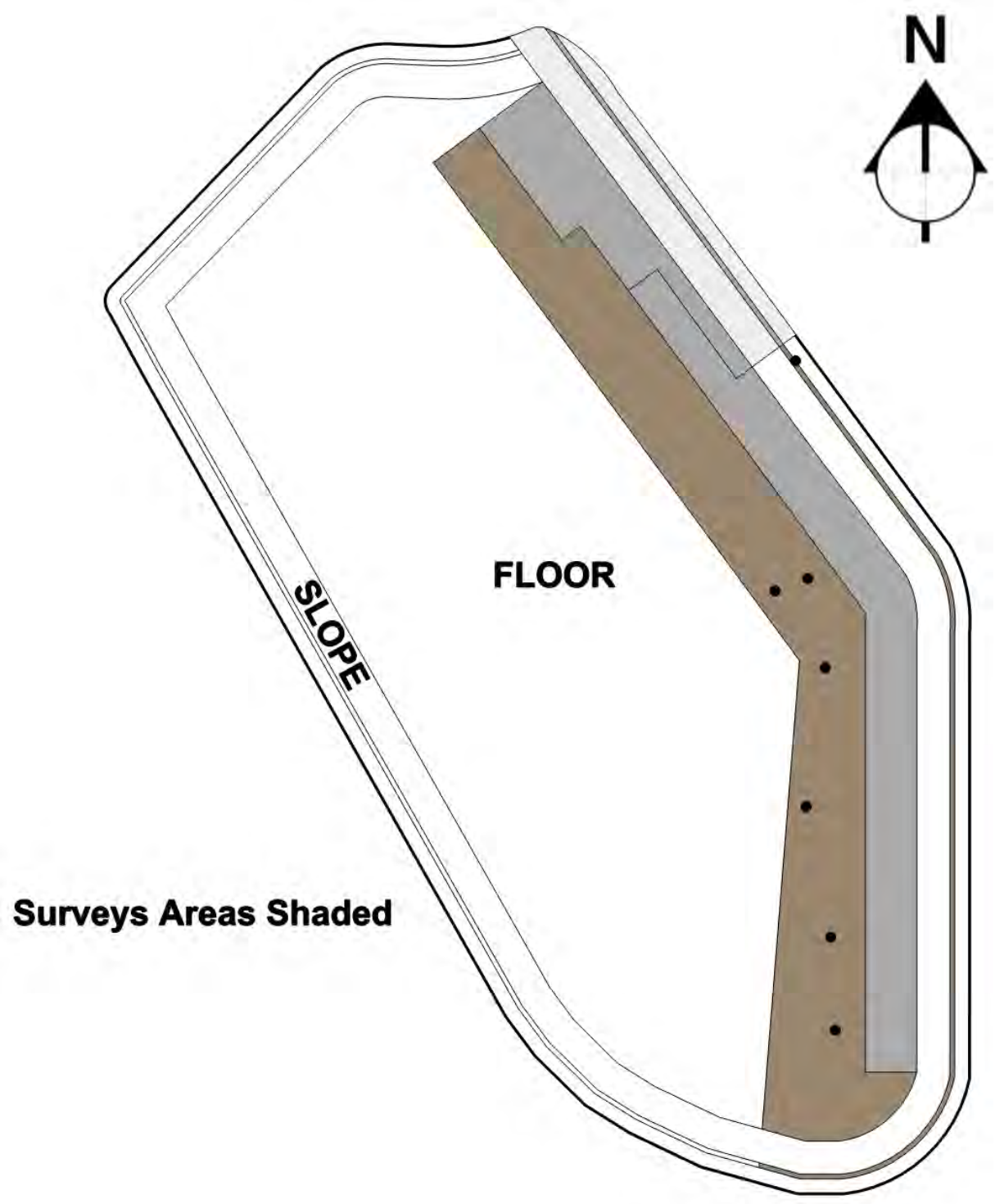

Figure 3. Area Surveyed on the 3rd Trip

Table 3. List of Leaks Located on the 3rd Trip

LEAK	LOCATION – SOIL SURVEY	DESCRIPTION
1	Approximately 500 feet from the toe of the east side slope	0.50-inch hole
2	Approximately 440 feet from the toe of the east side slope	3.00-inch tear
3	Approximately 360 feet from the toe of the east side slope	0.75-inch hole
4	Approximately 200 feet from the toe of the east side slope	Two 0.13-inch holes
5	Approximately 45 feet from the toe of the east side slope	1.00-inch hole
6	Approximately 370 feet from the toe of the east side slope	0.06-inch hole
7	Approximately 80 feet from the toe of the east side slope	Four 0.06-inch holes

The fourth mobilization took place on April 1st through 16th of 2019. Approximately 4,020,000 square feet were surveyed on this trip. Sixteen leaks were found in the soil-covered area during this mobilization and six leaks were found in the bare geomembrane of the slopes. Figure 4 shows the area that was leak tested on the fourth mobilization. The size of leaks found ranged from a 3-foot tear to a 1/16-inch hole. All of these leaks were found on the panels and none of them were found on seams or welds. The leaks from this mobilization are spread out in all area of the floor as well as opposite side slopes. This helps to know that isolation is good and the flow of current throughout the entire cell is consistent.

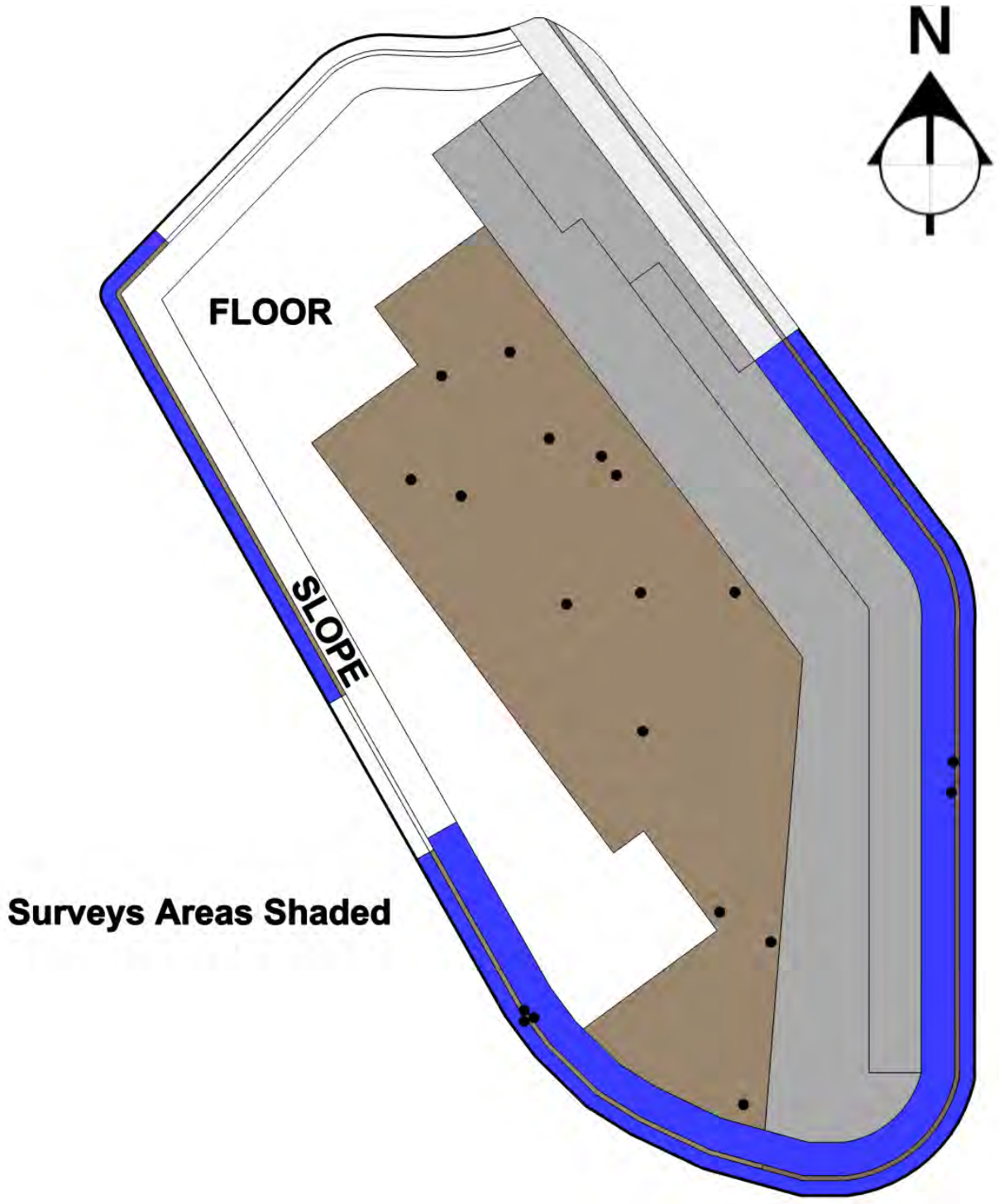

Figure 4. Area Surveyed on the 4th Trip

Table 4. List of Leaks Located on the 4th Trip

LEAK	LOCATION – SOIL SURVEY	DESCRIPTION
1	Approximately 843 feet from the toe of the east side slope and 24 feet from the toe of the south side slope	5-inch tear
2	Approximately 615 feet from the toe of the east side slope and 922 feet from the toe of the south side slope	0.75-inch hole
3	Approximately 1300 feet from the toe of the east side slope and 1000 feet from the toe of the south side slope	0.50-inch tear
4	Approximately 1325 feet from the toe of the east side slope and 880 feet from the toe of the south side slope	3-foot by 2-foot tear
5	Approximately 945 feet from the toe of the east side slope and 1745 feet from the toe of the south side slope	5-foot tear
6	Approximately 1292 feet from the toe of the east side slope and 640 feet from the toe of the south side slope	4-foot by 2-foot tear
7	Approximately 1215 feet from the toe of the east side slope and 2210 feet from the toe of the south side slope	10-inch tear
8	Approximately 730 feet from the toe of the east side slope and 2915 feet from the toe of the south side slope	Three 1-inch holes
9	Approximately 770 feet from the toe of the east side slope and 2920 feet from the toe of the south side slope	1-inch tear
10	Approximately 770 feet from the toe of the east side slope and 3173 feet from the toe of the south side slope	5-inch tear
11	Approximately 1100 feet from the toe of the east side slope and 2905 feet from the toe of the south side slope	13-inch tear
12	Approximately 1290 feet from the toe of the east side slope and 3180 feet from the toe of the south side slope	0.13-inch tear
13	Approximately 1050 feet from the toe of the east side slope and 3333 feet from the toe of the south side slope	1-inch tear
14	Approximately 970 feet from the toe of the east side slope and 3330 feet from the toe of the south side slope	6-inch tear

LEAK	LOCATION – BARE LINER SURVEY	DESCRIPTION
1	On Panel 34, approximately 15 feet from the toe of the east side slope	1.50-inch tear
2	On Panel 38, approximately 20 feet from the toe of the east side slope	3-inch cut
3	On Panel 74, approximately 50 feet from the toe of the west side slope	0.06-inch hole
4	On Panel 74, approximately 70 feet from the toe of the west side slope	Two 0.13-inch holes
5	On Panel 74, approximately 100 feet from the toe of the west side slope	0.06-inch hole

The fifth and final mobilization took place on May 1st through 10th of 2019. Approximately 1,710,000 square feet were surveyed on this trip. Thirteen leaks were found in the soil-covered area during this mobilization and one leak was found in the bare geomembrane of the slopes. Figure 5 shows the area that was leak tested on the fifth mobilization. The size of leaks found ranged from a 4-foot tear to a pin hole. All of these leaks were found on the panels and none of them were found on seams or welds. Once again notice how the leaks are spread out all over the floor area showing how consistent the data is all over the survey area.

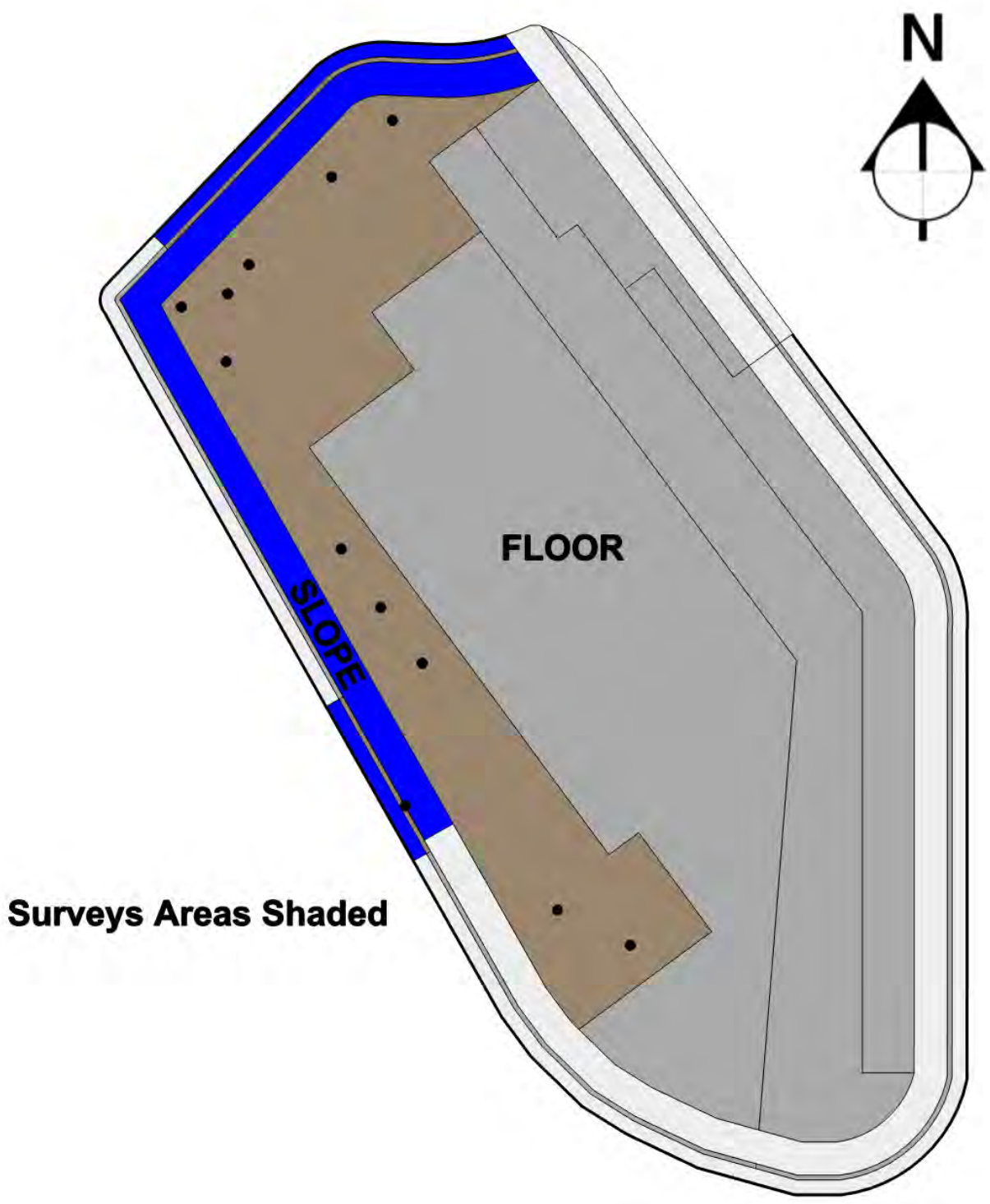

Figure 5. Area Surveyed on the 5th Trip

Table 5. List of Leaks Located on the 5th Trip

LEAK	LOCATION – SOIL SURVEY	DESCRIPTION
1	Approximately 260 feet from the toe of the west side slope	2.75-inch hole
2	Approximately 185 feet from the toe of the west side slope	2-foot tear
3	Approximately 95 feet from the toe of the west side slope	4-foot tear
4	Approximately 90 feet from the toe of the west side slope	8-inch tear
5	Approximately 91 feet from the toe of the west side slope	6-inch tear
6	Approximately 35 feet from the toe of the north side slope	0.13-inch holes
7	Approximately 65 feet from the toe of the north side slope	1-inch tear
8	Approximately 30 feet from the toe of the north side slope	Three pin holes
9	Approximately 45 feet from the toe of the north side slope	2-inch tear
10	Approximately 75 feet from the toe of the north side slope	2.75-inch tear
11	Approximately 40 feet from the toe of the north side slope	1-inch tear
LEAK	**LOCATION – BARE LINER SURVEY**	**DESCRIPTION**
1	On panel 84 approximately 75 feet from the west bench.	1-inch tear

CONCLUSION

In conclusion a total of 91 leaks were located and repaired at the 70 Ranch Dam & Reservoir in Colorado. Figure 6 shows the entire area and the locations of the leaks found. Table 6 shows the breakdown of each mobilization and how many leaks were found for each different type of survey and the area covered.

The bare liner survey covers every square inch of liner that is exposed resulting in 100% of the liner being surveyed and tested for leaks. For the soil survey it was taken with a data density of 1,540 data points or readings per acre. We removed about 75 percent of our data to represent what type of leaks and size of leaks would have been found if we had not taken the data at the higher density, but instead interpreted the data at a much lower 400 data point per acre. This would have resulted in ten of the leaks being missed. Taking data is easy and fast, but taking good data takes a little more time, but if the ultimate goal is a zero-leak installation than the answer is in the details of the data. This coupled with isolation and site preparation is key.

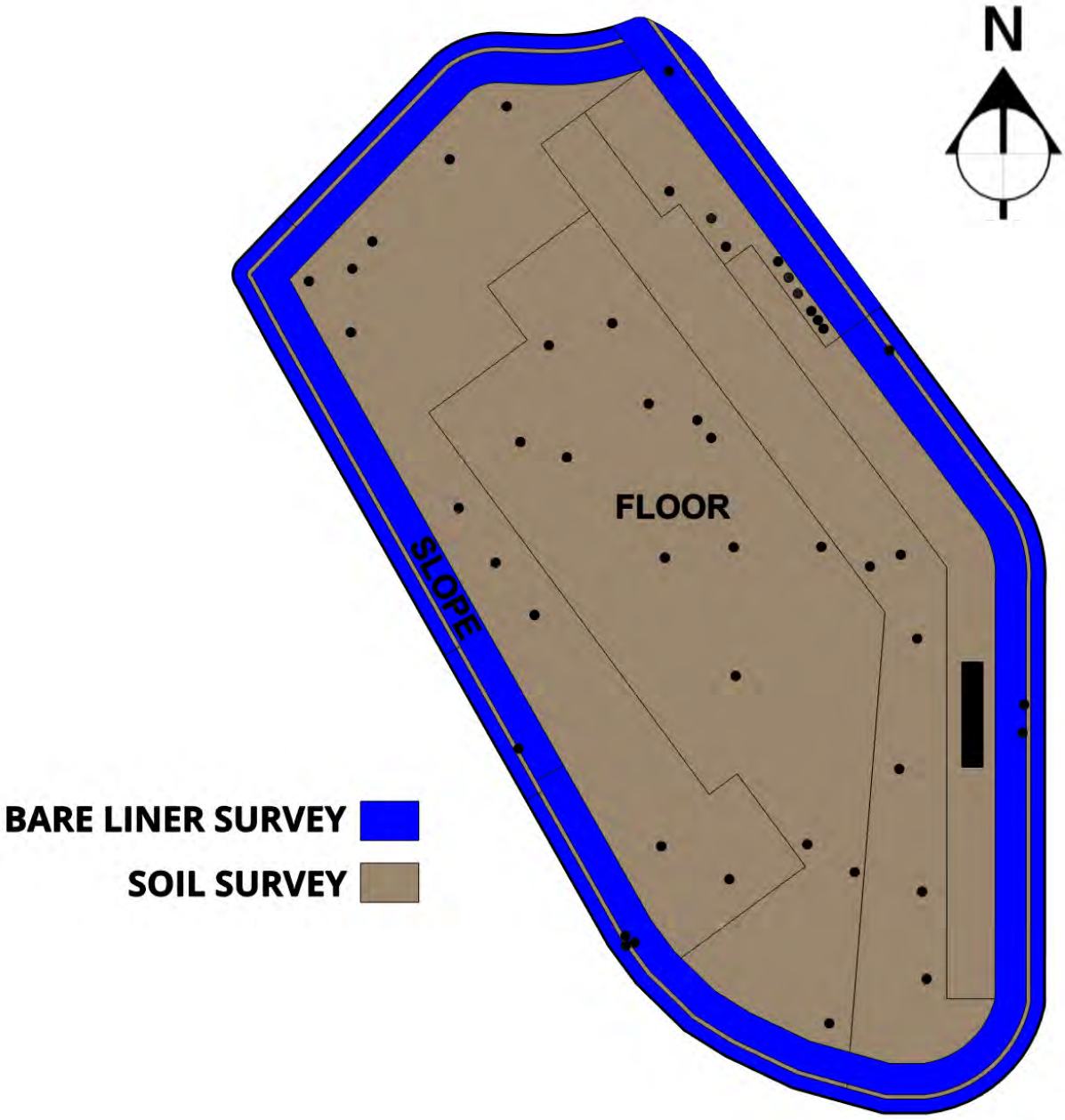

Figure 6. Final Leak Map Covering all Areas Surveyed

Table 6. Breakdown of Leaks found on each mobilization.

Mobilization	Soil Survey Leaks	Bare Liner Leaks	Area Surveyed (square feet)
1	23	1	270,000
2	20	0	350,000
3	11	0	1,000,000
4	16	6	4,020,000
5	13	1	1,710,000
Totals	83	8	7,350,000

It is important to mention once more that none of the leaks found were on any of the seams that were factory fabricated. The damage that occurred on this site was not due to the fabrication of the seams. Most of the larger leaks found are due to machine damage and the remainder of the leaks located are from some other type of damage that is typical to the installation process. The number of defects per acre for this installation are at 0.54leaks/acre or 1.33 leaks/hectare which is much less than reported by Giroud (2016) of about 5 to 6 leaks per hectare. This is another example of the quality of all parties involved on this installation. It is pleasing to know that not only were leaks located but leaks of all sizes were found in a consistent manner to help ensure the best possible outcome for this site. Since filing, the reservoir has served its purpose without any evidence of leakage: this is a testament to a ton of focus and cooperation by the Owner, Engineers, Contractors, and many technical evaluators to achieve this exceptional outcome.

REFERENCES

Giroud, J.P., (2016), Leakage Control Using Geomembrane Liners, *Geosynthetics International*, 5th Victor de Mello Lecture, J. Soils and Rocks, Brazilian Society for Soil Mechanics and Geotechnical Engineering, 39(3): 213-235.

Stark, T.D., Hernandez, M.A., and Rohe, D.S., Geomembrane Factory and Field Thermally Welded Geomembrane Seams Comparison, *Geotextiles and Geomembranes Journal*, 48(4), August, 2020, 454-467.

70 Ranch Raw Water Reservoir: A Geosynthetic Lining System Solution for a Difficult Site

Ronald K. Frobel, P.E.,[1] and Ray Peebles[2]

[1] R K Frobel & Associates, Evergreen, CO, email: geosynthetics@msn.com
[2] Cooley Containment Solutions, Pawtucket, RI, email: peeblessr@cooleygroup.com

ABSTRACT

The largest prefabricated scrim reinforced polypropylene (fPP-R) geomembrane lined raw water reservoir in North America was recently completed east of Greely, Colorado. At over 170 acres (7.5 mm sq. ft.), 45 ft depth with an embankment dam and designed to impound over 5500 acre ft of water, the primary seepage barrier was designed with large prefabricated fPP-R panels consisting of 30 mil bottom liner and 45 mil side slope liner. Geotechnically, the site was located in highly porous sands and bedrock and required a cost-effective seepage barrier. The slopes were designed at 4:1 with a 20 ft wide soil covered bench positioned at mid slope. Upper slope section was protected with rock filled geocell and protection geotextiles to resist wave and ice damage and the lower slope below the soil covered bench and operating water level was left exposed. The bottom was fully lined with large prefabricated 30 mil fPP-R panels and then overlaid with 12-inch minimum sandy soils carefully placed with LGP equipment. This paper will provide design and construction details associated with using cost effective large area prefabricated fPP-R panels, reduction in wrinkling for soil cover operations, efficient construction sequencing, reduction in site install time, QC testing and the implementation of ELLS for final CQA acceptance.

INTRODUCTION

Irrigation water in the Western United States has always been a major concern for farming and ranching, especially in drought years. Water can be both scarce and expensive and planning for future water storage and accessibility based on projected use is of paramount importance for irrigation districts. These considerations were of particular interest to the United Water Conservation District (UWCD) when planning for storage and future use of water in Weld County, Colorado. To this end and as part of the overall water use plan, investigation, and selection of a site for a storage reservoir was initiated in 2012. Based on feasibility studies and access to off season stream water, a site was selected east of Kersey, Colorado at a location known as 70 Ranch.

The 70 Ranch Reservoir property site encompasses approximately 250 acres and is located in the northwest corner of the intersection of SH 34 and Weld County Road (WCR) 69 just east of Kersey, Colorado. The site is located just south of the South Platte River and off stream surface water access to the reservoir site was available and sufficient for storage.

Site investigations as well as the preliminary design for the reservoir was begun in 2013. Site geology and geotechnical investigation was completed in 2014 and design alternatives for the reservoir were provided by the design enineer (ref 1)

GEOTECHNICAL CONSIDERATIONS AND ALTERNATIVES

Many pond and reservoir sites can be excavated into native soils that are sufficient to retain water or located in an area where clay deposits allow for a compacted clay liner (CCL) with acceptable and economical water loss. Seepage rates can also determine whether or not the cost of water collected vs loss is economical. However, the 70 ranch reservoir site was a challenge due to geotechnical investigation and results based on limited available cohesive site soils and strata that could hold water. Additionally, the quality and porosity of bedrock was considered highly variable.

The extensive site investigation included numerous borings and test pits throughout the proposed reservoir site as well as a proposed embankment dam centerline alignment and slurry wall alignment. The investigation encountered native soils consisting of sand, silty sand, clay and gravel at depths ranging from ground surface to 100 feet below ground surface. Bedrock was encountered at depths ranging from 40 to 100 ft. Small clay lenses were encountered, and the bedrock varied from sandstone to siltstone but no significant clay strata. The geologic mapping and exploratory drilling on site identified five major geologic strata:

Overburden. Clayey sand occurring at the surface across the entire site

Sandy Clay. The deposit was considered sparse and varies from clay to clayey sand with classifications of CL and SC.

Silty Sand. The silty sand deposit was extensive and eolian (wind deposited) and varied in thickness of 20 to 70 ft across the entire site

Sand. Fine to course sand deposits were also extensive and varied in thickness from near surface to over 70 ft depth

Bedrock. The bedrock consisted of Siltstone, Sandstone and Claystone as three distinct subunits and varied between 40 and 100 ft below existing grade.

Based on seepage analysis performed on typical cross sections as well as composite samples, the loss of water due to seepage was considered excessive when considering use of existing site soils and the cost of water lost per acre-ft. Thus, alternative methods of seepage control were investigated and proposed in the preliminary design report. To summarize, four alternative liner options to evaluate water storage cost and performance for the 70 Ranch Reservoir were evaluated. The four alternatives were as follows:

Alternative 1: Below Grade slurry Wall and Upper Synthetic Liner.

This alternative would have all slopes at 4H:1V with a 40 ft wide bench at mid slope elevation 4552. A slurry wall would be constructed on the bench down to bedrock. An upper synthetic liner would tie into the slurry wall and extend to the top of the dam embankment at elevation 4575 ft and tie into an anchor trench.

Alternative 2. Full Synthetic Liner.

This alternative would have all slopes constructed at 4H:1V with a bench at elevation 4552 ft. The bench effectively shortens slope length, provides greater stability, and allows for the potential for cover materials.

Alternative 3. Full Depth Slurry Wall

This alternative also allows for slopes constructed at 4H:1V with a bench at elevation 4552. A lower slurry wall would be constructed from the bench to bedrock and a second offset slurry wall would be constructed from elevation 4575 to 4552 with tie in at the bench elevation.

Alternative 4. Slurry Wall and Compacted Clay Liner.

This alternative allows for slopes constructed at 4H:1V with a bench at elevation 4552 and a lower slurry wall to bedrock as in previous alternatives. The upper slopes in this case would be a compacted clay liner to crest elevation 4575. The clay liner would be installed using on site clayey soils and imported clay or bentonite.

All of the above alternatives were evaluated with pros and cons for each as well as estimated cost to the owner per acre-ft of storage. Due in part to the highly variable and in most cases unknown porosity of the bedrock areas, the slurry wall concept was questionable as far as efficient seepage control and costly to construct. Depth to bedrock for a slurry wall would be at maximum depth for trencher methods. Additionally, native materials and bedrock were both considered at the low end for use as seepage barriers. The full liner alternative was originally based on an exposed liner and estimated 20 year life. However, a covered lining system would extend any liner life and protect the lining system from environmental and external mechanical damage while reducing long term cost per acre-ft of storage volume.

GEOSYNTHETIC LINING SYSTEM SOLUTION

The 70 Ranch Reservoir site location and geotechnical investigation into site soils, soil/bedrock strata and possible alternatives resulted in a decision to ultimately look at lining the entire reservoir impoundment with a cost-effective geomembrane, protection geotextiles, cover soils and upper slope wave/ice impact and environmental protection**.** The goal was to provide a final lining system design that would be cost effective to the owner and provide an extended design life over that of a fully exposed liner. Additionally, on site sandy soils could be utilized to provide a protective bottom cover and mid slope bench cover/ballast layer.

Reservoir Design Using Geosynthetics and Site Soils

Although most of the reservoir footprint was excavated to grade, the North and Northwest section was predominately a filled embankment and required design as an embankment dam with spillway which also required approval by the Colorado State Division of Dam Safety. The embankment was constructed in lifts with site soils and the primary upstream seepage barrier was the geomembrane on the upstream face. The embankment upstream slope was 4H:1V with a mid level bench 20 ft in width.

The reservoir surface area is approximately 170 acres and irregular in shape. The top of berm elevation is 4575.0 ft and the bottom elevation was constructed at 4530.0 ft. A mid slope bench 20.0 ft in width was designed at elevation 4552.0 ft. Maximum water surface elevation was designed at 4572.0 resulting in a 3.0 ft freeboard. Based on site soils type and characteristics, the interior slopes of the reservoir were set at 4H:1V. This slope inclination provides stability of the underlying site soils and allows for placement and stability of upper slope mechanical protection using rock filled geocell.

The entire bottom of the reservoir is constructed with a roller compacted site soils base, protection and 30 mil scrim reinforced geomembrane. The bottom liner is then protected with a

12 inch thick layer of sandy soil excavated from the site and carefully placed by LGP equipment. Approximate bid item area of the bottom was 5,392,397 sf

The side slopes were designed at 4H:1V with roller compacted site soils, protection geotextile, 45 mil scrim reinforced geomembrane. The upper slope section above the bench is protected with a 10 oz/sy nonwoven geotextile, 8-200-8 geonet composite and covered with 6 inch deep geocell infilled with 2 inch angular rock. The bench is protected with a 3.0 ft depth of site soils over 10 oz/sy nonwoven geotextile and the bottom slope area below elevation 4552 is fully exposed but designed to be covered by water 90% of the time. Approximate bid item area for the reservoir slopes was 1,881, 239 sf.

Geomembrane Selection

Once the decision was made to fully line the 170 acre reservoir, the primary seepage barrier type, thickness and polymer was investigated for a cost effective solution. In reviewing the types of geomembranes, a number of design and construction considerations were looked at and included the following:

Site geotechnical considerations

- Sandy soils and silty sands – difficult to roller compact and maintain smooth surfaces under equipment and personnel loading.
- Volume of Available site soils for embankments and cover soils was limited and borrow material from off site was cost prohibitive.
- Sandy soils on slopes tend to erode rapidly and displace under loading
- Sands tend to blow in high winds and will affect installation/seaming
- Fine grain subgrade with little or no aggregate. Sandy soils for cover material.
- Minor settlement potential of base sandy soils

Site Weather Considerations

- Eastern Colorado plains experience high winds/wind events
- Installation in Summer and Winter conditions
- High rainfall or snow events cause subgrade damage and slope erosion
- High surface temperatures on black liner affect wrinkling/distortion material.
- High UV exposure for polymer materials above the waterline
- Winter operation at low water surface elevation will result in ice/impact on liner

Construction Considerations

- Maintenance of smooth/dry subgrade just prior to placement of geomembrane
- Preparation of subgrade in sequence with liner placement
- Cover soils placement over liner with LGP equipment requires no wrinkles/waves

- Cover soils staging and placement must be sequenced with liner panel placement
- Cover soils placed on liner immediately after panel placement/tie-in seams
- Large areas on the bottom must be completed on daily basis to include cover soils
- Rapid large area panel tie in seaming and NDT QC
- Use of LGP equipment in placement of a 12 inch sandy soil cover
- Final QC by Electrical Leak Location Survey (ELLS)

Operation Considerations

- Large surface area producing wave and ice action on upper slopes above elevation 4552 ft
- Deep reservoir at over 42 ft with 3 ft of freeboard
- Filling and Drawdown rate of water surface
- Minimum operating level to be maintained at or above Elevation 4552 bench
- Potential ice accumulation at low water surface levels in winter

Based on evaluation of the above design and construction considerations, the geomembrane material options were narrowed to the following characteristics:

- Base polymer longevity exposed > 20 years life with warranty
- Scrim reinforced for high puncture, tear resistance, tensile strength as well as stability in temperature extremes
- Factory fabrication into large custom panels using thermal fusion welds
- Minimization of field seaming by using efficient and high quality factory fabrication and thermal fusion seams QC tested and accepted in the factory.
- Minimum thickness of 45 mil on slopes
- Minimum thickness of 30 mil on bottom in consideration of a fully protected liner system, little or no subsidence and large flat surface area.
- Efficient thermal fusion welding and NDT testing for field seams
- High resistance to creasing and wrinkling for panel factory fabrication and shipping/storage
- Little or no wrinkling during installation to provide efficient soil cover operation
- Testing by ELLS for final installation QC

Geomembrane material options selected for lining system design included the following:

- 45 and 30 mil scrim reinforced Polyethylene (RPE)

- 45 and 30 mil scrim reinforced Polypropylene (fPP-R)

Construction and Installation of the Geosynthetics

A final bid package was sent out to prospective earthworks contractors in March 2016. The bid package included contract documents and geosynthetics specifications prepared by Civil Resources LLC, Frederick, CO. and R.K. Frobel & Associates, Evergreen, CO. The contract was awarded to Fiori and Sons General Contractors, Denver, CO. Geosynthetics Supply and Installation was by subcontract to Consolidated Divisions Inc. (CDI), Sedalia, CO. Final Electrical Leak Location Survey was awarded to Leak Location Survey, Inc. (LLSI), San Antonio, TX. The geosynthetics materials selected for the project with approximate installed quantities were as follows:

Primary Geomembrane 45 and 30 mil fPP-R manufactured by Cooley Containment Solutions, Pawtucket, RI – 7,696,000 sf

45 mil fPP-R – 2,080,000 sf

30 mil fPP-R – 5,616,000 sf

Panel Factory Fabrication for the 45 and 30 mil fPP-R was provided by Environmental Protection, Inc.(EPI), Michigan

45 mil Slope Panels – 104 ft x 190 ft / Total Panels 132

30 mil Bottom Panels – 104 ft x 300 ft / Total panels 180

Protection 10 oz/sy Geotextile manufactured by Skaps Industries – 150,400 sy

Protection 8-200-8 Geonet Composite by Skaps Industries – 150,400 sy

6 inch Geocell manufactured and supplied by Presto GeoSystems – 1,080,700 sf

In addition to the geosynthetics materials, the following approximate quantities were required:

20,000 cy 2 inch angular stone (6 inch geocell infill)

3,000,000 cy earthwork (excavation, hauling, moisture conditioning, placement)

3800 lf 24 inch pressure pipe

3000 lf 36 inch pressure pipe

450 lf 48 inch concrete pipe

Miscellaneous concrete inlet/outlet structures and spillway

Installation

Geomembrane Panels were installed beginning at the North end of the Reservoir with slope panels first placed down the NE side of the reservoir. This was followed by placement of large bottom panels with tie-in to the slope panels again down the NE side of the reservoir. Once sufficient bottom panels were placed, staging of cover soils and cover soil placement by LGP was started. Figures 1 - 5 illustrate side slope panels transition to bottom panels, panel layout, typical slope section as well as sequential soil cover operations that required close coordination

between lining install and earthworks. It should be noted that there were 7 construction operations on the side slopes that were carried out simultaneously and that were staged to provide completion and cover protection of the geomembrane as it was installed. The reservoir bottom operation required 4 distinct operations that were carried out sequentially. The construction/installation operations were as follows:

Reservoir Side Slopes

1. Soil Subgrade and Anchor Trench Preparation and Acceptance
2. Placement and Welding of Protection Geotextile
3. Placement, Seaming of Geonet Composite – Upper Slope Section
4. Placement, Joining and Tensioning 6 inch Geocell – Upper Slope Section
5. Placement and Compaction of 3.0 ft of sand on the 20 ft wide bench
6. Placement of 2 inch angular stone in Geocell
7. Placement, Seam Welding and QC of 45 mil fPP-R slope Panels

Reservoir Bottom

1. Soil Subgrade Preparation and Acceptance
2. Placement, Tie-in Seam Welding, QC of 30 mil fPP-R Bottom Panels
3. Staging of Cover Soils Material in Stockpiled Rows
4. Spreading of Cover Soils over 30 mil fPP-R with LGP equipment

Electrical Leak Location Survey (ELLS)

In addition to routine QC testing of geomembrane seams by trial welds, NDT air lance and destructive sampling, it was decided early in the project to test the completed sections using ELLS to primarily detect damage due to soil and rock cover operations. Leak Location Services, Inc. (LLSI) of San Antonio, Texas was contracted to test the entire 170 acre site as final CQA acceptance. LLSI performed the ELLS in general accordance with ASTM D 7007 using a dipole survey. A water puddle survey was conducted on the lower slope bare liner. The survey was performed as the lining system was completed and required return trips or mobilizations to complete. The ELLS survey found mostly damage caused by installation equipment during the bottom liner soil cover operation. Minimal damage was found in the upper geocell/rock covered section of the slope. Once damage was detected, the area was carefully excavated and the liner repaired and re-covered. A total of 37 leak sites with minor to significant mechanical damage were detected and repaired. Figure 5 illustrates a typical damaged area that required repair.

Figure 1. North End of reservoir showing slope panels transitioned into bottom panels and staged cover soils placement on bottom panels

Figure 2. North End of reservoir showing from top to bottom – Geocell, 2 inch stone infill, soil covered bench, lower exposed section and finished bottom soil cover

Figure 3. Photo showing large fPP-R panel unfolding and positioning on bottom. Note soil cover material staged for immediate placement after tie-in seaming

Figure 4. Photo showing cover soil placement by GPS guided LGP dozer and tracked skidsteer. Note minimal wrinkling or waves during placement

Figure 5. ELLS photo showing significant damage due to contractor equipment during cover soil placement on bottom lining system.

SUMMARY

The 70 Ranch Raw Water Reservoir was located in a difficult area for water retention with little cohesive soils, sandy soils and bedrock that was susceptible to potentially high seepage rates. The entire 170 acre reservoir was successfully lined with a geosynthetic lining system that will hold valuable irrigation water for distribution in an otherwise dry region of the eastern Colorado plains for many years.

The lining system was designed and constructed with large factory fabricated fPP-R panels to reduce construction time in both summer and winter, reduce wrinkles for soil cover placement, allow rapid earth cover scheduling in large areas and reduce on site QC and CQA. Large 45 mil fPP-R factory fabricated panels on the slopes were sized for full length slope placement and tie-in to the bottom 30 mil fPP-R. In addition to reduction in installation time and soil placement, onsite QC and NDT, the entire reservoir was tested by Electrical Leak Location Survey (ELLS) as a final acceptance of the lining system.

The 70 Ranch Reservoir is arguably the largest flexible reinforced polypropylene (fPP-R) prefabricated geomembrane lined impoundment in North America and will serve the irrigation districts in eastern Colorado for many years to come.

REFERENCES

Civil Resources LLC, 70 Ranch Reservoir – Preliminary Geotechnical Investigation and Design Alternatives, March 2014

Civil Resources LLC, 70 Ranch Dam and Reservoir – Contract Documents & Technical Specifications C 2041, February 2016

Geosynthetics Conference

Advantages of using International Specs in PVC geomembranes for mining

Myriam Astrid Acevedo Soriano, [1] and
Juan Manuel Cortés [2]

[1]Filmtex S.A.S.; Universidad Nacional de Colombia; e-mail: macevedo@filmtex.com
[2]Filmtex S.A.S; Universidad de Los Andes; e-mail: jcortes@filmtex.com

ABSTRACT

As part of FGI´s Technical Track, this document analyzes the advantages of using international specifications in PVC fabricated geomembrane for Latinamerica´s mining industry. The most significant Lithium natural resource in Latinamerica is called the Lithium triangle. It is located in three countries, Chile, Bolivia and Argentina. The natural resource, the brines, are located in extreme climates classified as desertic areas. The technique to extract the lithium salt is called open sky mining. Huge areas are covered by geomembranes and filled with brine, which, thanks to the climate environment, promotes the salt crystallization process. This paper shows the typical situations the project owners face to decide the geomembrane´s technical properties to reach the best performance from the technical and financial view. The article analyzes climate condition influence and how it affects the PVC geomembrane performance since the storage until the covered pond is in service. Finally, the paper examines two relevant properties which come from two international specifications for PVC geomembrane. Both of them are used in buried applications. Density and average molecular weight are the additional properties connected with one of the requirements to avoid wrinkles and possible fractures under the “Salar's” arid climate.

INTRODUCTION

In the last ten years, electronic devices came into our lives and will remain for many years. It is the case with cell phones, cameras, laptops, tablets, and electric vehicles' launch. The last one to join as a real option for a clean energy type. Behind this technological change is lithium, one of the raw materials present in the different batteries. However, batteries' applications are just one of numerous uses lithium has: it is used in aircraft aluminum alloys due to its low density; lithium soaps are used as a grease lubricant additive to improve thermal resistance (Stwertka, A., 1998). Lithium carbonate is used in pharmaceutical drugs for neurologic treatments. (Gray, T., 2009). The review "Litio en Argentina" (Lopez, A., et al., 2019) regarding the state of lithium in this country points out that prices have changed dramatically from the last ten years, reaching almost USD 10/kg in 2017, and expected world demand can be around 425000 ton in 2025.

This element is found in some ores, including spodumene and amblygonite, and in nature in underground brines (Stwertka, A., 1998, De la Hoz, M., et al., 2013). The formation of those brines comes to a place when some geographic variables are joined along time (Bradley, D., et al., 2013). One of those variables, the arid climate, is useful for extracting the Lithium Carbonate, based on brine's evaporation in big pools covered by a PVC geomembrane, which has shown an excellent performance along time. Photo 1 shows a typical view of this kind of pond. These are built in the “Salares”, where the brines are located underground. Once the infrastructure is finished

and the ponds are filled, it can take 12 to 24 months to obtain the first lot of lithium carbonate (Lopez, A., et al., 2019). Photo 2 shows a pond already in service. So, any delay in the design and pool building steps can alter the sales schedule dramatically. The possible failures should be analyzed carefully because of the arid climate. The ASTM organization launched the specification for non- reinforced PVC Geomembranes, ASTM D7176, has used this in buried applications since 2006, reviewed in 2018. Also, the Fabricated Geomembrane Institute, FGI -before PGI, PVC Geomembrane Institute-, has been analyzing the performance of different PVC geosynthetics for more than 15 years. FGI 1115 specification introduced a change in the specs for arid climates, which is the final focus for this review. Both standards list the density as an index property, representing indirect information regarding the membrane composition, field performance in desertic climates, and an idea of the geomembrane cost. Although PVC geomembranes have shown good performance following these standards in the “Salares”, particularly FGI 1115 specification, not all the project owners chose them for different reasons analyzed herein. The governments involved had built politics to protect the mining environment, regulate lithium extraction, research to add value to the relevant lithium salts, etc., but there are no technical regulations for the geosynthetic system used in the waterproof systems to use in this kind of projects.

Photo 1. Open sky mining: typical view for a covered pond with PVC geomembrane

Photo 2: Pond is already in service to obtain salt crystals by evaporation

ECONOMIC REVIEW- LITHIUM INDUSTRY

Batteries, electric cars, and energy storage systems have made lithium a critical and essential element in our daily lives. Lithium is one of the most important metals of the 21st century, generating massive interest in the world´s population, and creates excellent expectations regarding its future. Every time consumers want faster, lighter, and long-lasting products, the tech industry hears what the market is asking for and is giving the customers just what they need. Lithium mines in Latin America are located in Chile, Bolivia, and Argentina,, countries with more than half of the world´s lithium reserves (De la Hoz, M, et al., 2013).

With a global demand that far exceeds current production, the lithium business expansion is assured in the short and medium run. A tendency reports by one of the most relevant digital newspapers in Chile, -"El Mostrador, August 27th, 2020" -, says: "T*he international demand of the mineral can be close to 300,000 tons of lithium in 2019, so the expected growth of the demand before the pandemic was to get 1,793,000 Tons to 2030"*

The constant technological advances and the concern for new kinds of energies to replace oil are pushing the industries into the lithium batteries option. As a sustainable solution, with the lowest CO2 emissions and the most prolonged performance, this is something to massify electric cars in the future. Another technologic industry focusing on personal items is consolidated: watches, cellphones, laptops, cordless tools, even for medical purposes, where the lithium batteries offer the customers the most extended performance with lighter products.

After exploration studies from different underground lithium´s deposits have been made, the infrastructure of evaporation ponds covered by the PVC geomembrane is built. The brine is pumped to the pools to promote fractioned crystallization by the wind and sun action (Berube, D., et al., 2007). This evaporation process can take several months to obtain a concentrated brine in lithium salts, purified and dried in another chemical plant.

The impact of the PVC geomembrane technical specification is enormous, considering the projects' investment and narrow schedules. Brine leakages in any crystallization step or, in the

worst case, material failures can be avoided if the owner selects an optimal quality PVC geomembrane.

SELECTING THE PVC GEOMEMBRANE FOR PONDS

Part of the process where engineers, project owners, manufacturers, and constructors need to face is selecting the proper material to do the job of containing the brine along the evaporation cycle. But this part is not easy, and every actor in the project will confront some of the above challenges:

Cost reduction for the waterproofing system:
Most of the projects need to save and reduce costs in most details of a mining waterproofing system. In this rush to save money, they start evaluating different suppliers and materials to save time, initial investment, and labor.

The PVC geomembrane performance will be one of the concerns because if it fails, it can cause an enormous loss of money in the global project expectations. At this point, the project owner should balance the available resources and the price of the defined geosynthetic system. PVC geomembrane cost depends strongly on its composition. The density gives an idea of it, and allows to predict a relationship with the possible performance in field, located in an arid area. This topic will be analyzed later.

In response to money saving, PVC geomembrane manufacturers developed technologies to manufacture seamed large panels (around 3600 m^2), which diminishes the area of seams in field. It represents less time to cover the same total area, less labor work, and confidence in the seam quality in all panel area (https://e2techtextiles.com, 2020, Berube, D., 2007).

High turnover of technical personnel at the mining company*:*
This is one of the most current mining industry problems. Usually, part of the technical inspectors, and personnel on the field, work only for specific projects, not for the companies. So, when they finish the project, they jump into another mining industry. So, the technical knowledge and experience they have acquired just goes away. Climate conditions where the mines are located are not the same, so the considerations to stablish the technical specifications for the water-proof system are different.

Lack of geographic stations:
It allows the acquisition data of historical and environmental conditions at mining exploration sites: UV radiation, rainfall, hailstorms, and wind speed, are some of the most important factors to consider by owner projects, membrane manufacturers, and installers. The ideal situation is to have meteorological stations in site where the extraction process will be carried out. (Lopez, A., et al., 2019).

THE BRINE AND THE CLIMATE

Groundwater brine deposits are a result of a group of geographic events, across time, sharing the same area: the presence of closed basins, where water could not flow to the ocean or rivers, rocks

and other sources of lithium, which with enough time had been erosional and then dissolved in water (Bradley, D., et al., 2013, Christopherson, R., 1994, Coentraads, R., et al., 2008). Apparently, it occurred more than 120.000 years ago. The surface salts dried and formed a thick surface layer, leaving the brine in some salts underground, with important concentrations of lithium salts. Another variable to form the brine is the tectonic basin movements, which influenced the internal space to promote brine's storage in long periods (Food and Agriculture Organization of the United Nations, FAO, 1989, Garcés, I., 2000, https://sciencing.com/characteristics-arid-climates-8441465.html, 2020). The geographic position of "Salares" in South America, -Bolivia, Argentina and Chile-, China, and some parts of Australia met the conditions to promote huge water evaporation quantities.

The studies carried out in the United States by USGS (Bradley, D., et al, 2013), showed that climate is between semi-arid and hyper-arid type, being the typical the arid one. In terms of geography classification, the climate is based on temperatures, wind speed, elevation, which gives an idea for the UV-Index and precipitation, among others (Christopherson, R., 1994). Based on Weather Atlas (https://www.weather-atlas.com/en/bolivia/uyuni-climate#temperature, https://www.weather-atlas.com/de/argentinien/san-salvador-de-jujuy-, https://www.weather-atlas.com/en/chile/san-pedro-de-atacama-climate#temperature, 2020), and Meteoblue (https://www.meteoblue.com/es/tiempo/historyclimate/weatherarchive/san-pedro-de-atacama_chile, https://www.meteoblue.com/es/tiempo/historyclimate/weatherarchive/uyuni_bolivia, https://www.meteoblue.com/es/tiempo/historyclimate/weatherarchive/san_salvador_de_jujuy-uy-argentina, 2020), Table 1 summarizes some characteristics for locations close to the Atacama "Salares" in Chile, Uyuni in Bolivia, and Jujuy in Argentina:

Table 1. Some climate characteristics for places near three Southamerican "Salares"

Point near to every Salar	Property	Jan - Feb	Jun-Jul	Nov-Dec
Atacama-Chile (2300 m.a.s.l.)	Temperature max to min, °C	24 to 10	16 to 0	24 to 9
	Wind speed max, km/h	42 to 44	45 to 41	41 to 42
	Index UV	12	6	12
	Precipitation, mm, max	22-5	0	1-3
Uyuni -Bolivia (3804 m.a.s.l.))	Temperature max-min, °C	18 to 1	13 to -13	20 to -1
	Wind speed max, km/h	42 to 40	52 to 55	42 to 45
	Index UV	12	8	12
	Precipitation, mm, max	70 to 40	0	0 to 30
San Salvador de Jujuy-Argentina (1411 m.a.s.l.))	Temperature max-min, °C	30 to 17	20 to 6	30 to 17
	Wind speed max, km/h	18 to 15	24 to 40	20 to 18
	Index UV	12	5	12
	Precipitation, mm, max	199 to 141	2 to 6	58 to 139

Temperature is not too high:

This is the reason to call this climate "cold arid" (Christopherson, R., 1994, Food and Agriculture Organization of the United Nations, FAO, 1989, Garcés, I, 2000). There is a big contrast between high and low temperatures. It suggests the PVC geomembrane should support dimensional changes once it is installed. Even the environmental temperature is not too high, compared with other deserts in other places, the PVC geomembrane takes infra-red energy from the sun. Because of the

black color, the film increases its temperature at noon up to 70 °C. At night temperature goes down. In winter, the temperature can decrease even at -10 °C or less.

Precipitation:
It is very low, especially in the middle of the year. This kind of places normally show higher evaporation rates than precipitation level. Because of the low level of precipitation in Atacama Salar, there are no expected failures in the geomembrane. In contrast, situation can be different por Uyuni and Jujuy Salares.

Wind velocities:
It is quite important to promote water evaporation, but unfortunately, also promotes plasticizer loss, which represents a risk for the geomembrane's performance. If the plasticizer level decreases extremely fast because of the high wind speed, the elongation will do the same, and the geomembrane will fracture easily.

***High UV-index*:**
Depending on the area, it can range from 6 to 12, quite high, which should be relevant to the PVC geomembrane design to avoid a lack of properties once the geomembrane has been installed and previous to the filled.

POSSIBLE FAILURES IN PVC GEOMEMBRANES UNDER ARID CLIMATE

Once the environmental conditions are exposed, it is important to analyze the different behaviors the PVC geomembrane can show because of the cold arid climate's relevant variables. For better understanding, it is exposed in three scenarios: when the geomembrane is still in storage -probably near to the ponds-, then when it is already installed, and finally, when it is ready in service:

In storage:
In order to save installation time and have seams with optimal control of variables -seaming temperature and pressure, time of contact-, the rolls are normally delivered in big rolls, which can weigh around 2.5 ton depending on dimensions, being 3000 kg the typical weight. The packaging of the rolls should protect the external winding turns of UV degradation.

The roll has numerous folds and, therefore, a lot of wrinkles. So, the pressure onto the film is high, especially in the external inferior winding turns. When the temperature goes up, the film turns softer and tries to dilate in the transverse direction and contract in the machine direction.

After cooling, the geomembrane should accommodate again, but with minimum internal tensions in the best condition. At this point the dimensional stability of the geomembrane is quite important . If the film shrinks a lot, internal tension can occur.

If the temperature decreases at night, the geomembrane's flexibility should allow the folding and wrinkled areas to keep the film intact without promoting any fracture or any weakness, particularly in wrinkles (Rowe, K., 2018). The lowest the temperature at night, the highest performance requirement of the geomembrane. In this first situation, dimensional stability,

elongation, and impact resistance at low temperatures play a relevant role in the performance of the PVC geomembrane.

Installed:
Once the pool has been covered but is not yet filled, the changes in temperature, the UV energy, and the winds start to influence the performance of the geomembrane.

A wrinkle-free surface is desirable and even more, after day/night cycles. If all the original wrinkles present in the big-roll disappear, it is a good starting for the geomembrane (Berube, D., et al. 2007). The geomembrane must adapt to the surface in the ideal situation. It is quite important to obtain good contact with the soil, which helps with the slope's stability (Stark, T., 2018). This behavior depends on the quality process and its composition. It is optimum for the geomembrane to act as an elastic rubber: when the film is heated up-with sun light-, it elongates, but when the tension disappears -at night-, the film recovers the initial length. If the geomembrane can accommodate its service life will be longer of. Density, elongation, tensile strength, tear strength, impact resistance at low temperature, and volatile loss are important properties to analyze at this second stage (FGI 9119, 2019, ASTM D7176, 2018).

Some wrinkles come not only from the folding but from some deviations in the initial profile in the calendering process. Wrinkles from strong camber are not easy to disappear once the geomembrane´s temperature increases (https://e2techtextiles.com/performance-benefits-of-factory-fabricated-geomembrane-liners/R&D, 2020). This is one of the reasons FGI technical committee decided to enclose the camber as a control property in the last version (FGI Specification 9119).

Degradation of the PVC membrane is nowadays successfully controlled under the right composition and process, but it affects the product's cost. If the PVC is not protected enough, the geomembrane will lose its mechanical properties faster under arid climate, especially mechanical properties critical at anchorage points and slopes (Stark, T., 2018). The owner of the project understands this risk very well. So, as soon as possible, the pool is covered with different materials to protect the membrane surface (Berube, D., et al., 2007). Nevertheless, the PVC geomembrane manufacturer should warranty a minimum time without relevant changes in the mechanical properties, so the protection against UV light degradation of the geomembrane is one of the relevant design parameters. The highest the uncovered time the pool, the highest the protection against UV degradation.

Another characteristic of the arid climate is wind speed. Table 1 shows that all the three “Salares” have high wind speeds in common, being a minimum value of 20 km/h. Once the geomembrane is deployed on to the soil, it reaches the maximum exposed area. The volume of air delivered by strong air currents promotes a significant risk in the geomembrane: loss of plasticizer. The quality calender process is relevant to delay this loss, but composition plays a big important role in keeping the geomembrane's initial properties. So, the formulator should be sure that at the levels of speed that winds at the “Salares” have, the composition will not change in the time the geomembrane has not been covered yet. When the PVC geomembrane loses some part of plasticizer, mechanical properties such as tensile strength, tear, and puncture resistance increase, but flexibility goes down. This situation can be a big risk when the geomembranes' temperature goes down because the impact resistance can be reduced, and depending on the temperature,

fractures may occur . The FGI introduced a little remark but quite important: the plasticizer average molecular weight for arid areas should be more than 410 g/mol (FGI 1115 Specification).

In service:

After the pool is checked under different methods for leaks detection, -being air channel method very useful for the efficiency and simple to qualify the seams-, the pool is covered with different materials and then is filled with the selected brine. The UV degradation is not now a risk, neither the wind speed. Mechanical properties as tear, tensil, puncture, and hydrostatic resistance, particularly in seams or near them, will permanently work to have the PVC geomembrane's optimal performance. The pressure the brine acts onto the watertight system is tremendous because of the brine density, being a typical value of 1220 kg/m^3 (Garcés, I., 2000, estimated).

The geomembrane's chemical resistance is also another issue, but depending on the pond design, contact is not always direct. Nevertheless, the PVC geomembrane should offer very good chemical resistance for water, and of course, salt solutions. A low water extraction loss value can complement a quality index for this stage.

If the geomembrane could successfully pass the previous steps: storage and installing, its properties will offer a long expectance life superior to 20 years.

RELEVANT PROPERTIES AT INTERNATIONAL STANDARDS

As it has been exposed, some properties in the PVC geomembrane have a strong influence on its performance in arid climates. One of the most relevant is perhaps, the capacity the PVC geomembrane has to disappear wrinkles from folding and also, to accommodate without tensions once the cycle warm-cool is presented (Rowe, K., 2018). In a certain way, this capacity can be a resilience of the geomembrane like an elastomer has. Also, the importance of having flexibility at low temperatures was exposed to both storage and installation. The plasticized PVC resin gives this performance, but unfortunately, one of the typical components in the formulation can negatively influence reaching the behavior mentioned above.

A basic property gives a previous idea of the cost and quality the project owner expects to receive from the PVC geomembrane: it is the density. FGI Spec, 9119 (effective since September 2019), gives the density a typical value of 1200 kg/m^3.

This value comes from the density of components in the PVC film. The PVC resin has a density of 1400 kg/m^3, and plasticizers have densities from 960 to 980 kg/m^3. It is known to obtain flexibility at low temperatures, elongations -with a minimum decrease in tensile and tear forces-, is necessary to add between 30 to 35 % w/w of plasticizers. Due to the low density of plasticizers, the compound's density decreases to values around 1220 kg/m^3. But density can be superior to this value, even more than 1300 kg/m^3 depending on other raw materials. Some minerals -with densities higher than PVC resin-, could be present in the film for different reasons. One of them is to occupy more volume in the final film. Then, the cost of PVC formulation decreases. Unfortunately, minerals cannot act as an elastic material inside of the PVC resin. The result is that the geomembrane can partially lose resilience. Some properties can be altered and represent severe risks for leaks, mainly in the storage and uncovered installation steps in arid climates. PVC

geomembrane with densities close to 1300 kg/m3 can be cheaper but will have serious risks in its performance, as was explained above.

Using a plasticizer average molecular weight of 410 g/mol, minimum in the formulation, helps to maintain the mechanical properties being the resilience, and impact resistance at low temperature, perhaps the most relevant to achieve the expected performance in the field. The highest the molecular weight of the plasticizer, the lowest its volatility, the highest probability to keep flexibility at typical environmental temperatures in "Salares", in the day/night cycle.

Another interesting spec introduced in the last version is the control of the lay-flat of the calender rolls, camber mentioned before. To have a good lay flat is important to avoid wrinkles along the seams, so suppliers who can comply with this spec will also contribute to having very flat covered pools for the sky-mining process, wrinkles free.

The general mechanical properties specified in both international specs, ASTM D7176 and FGI Spec 9119, give reliability for projects owners, installers, and PVC fabricated geomembrane manufacturers on the historical data that Universities and industries have collected for more than 20 years.

CONCLUSIONS

Using international standards to specify the mining projects is the first step to reducing the human staff's weaknesses in the mining companies, who extract the lithium from brines and transform it into lithium carbonate in arid climates.

The FGI Spec 9119 joins a group of relevant properties for the PVC geomembrane, which values are proven to be enough to comply with the performance lithium project owners need to have for a good startup of the crystallization mining process for lithium extraction in brines.

Even the geomembrane cost can be high complying FGI Spec 9119; it can be lower than the cost of any delay at the starting of the evaporation process.

REFERENCES

ASTM D7176-06(2018), *Standard Specification for Non-Reinforced Polyvinyl chloride (PVC) Geomembranes Used in Buried Applications*, *ASTM International*, West Conshohocken, Pennsylvania, USA.

Berube, D., Diebel, P., Rollin, A., Stark, D., (2007), Massiv mining evaporation ponds constructed in Chilean desert, *Geosynthetics*, 25(1), 26:31

Bradley, D., Munk, L, Jochens, H., Hynek, S., Labay, Keith, (2013), *A Preliminary Deposit Model for Lithium Brines*, U.S. Department of the Interior, U.S. Geological Survey, Reston, Virginia, USA.

Christopherson, R.W., T, (1994), *Geosystems. An Introduction to Physical Geography*, Macmillan College Publishing Company, Englewood Cliffs, NJ, USA

Coentraads, R.R., Koivula, J.I., (2008), *Geológica, Las fuerzas dinámicas de la Tierra*, Tandem Verlag GmbH, H.F. Ullman, Millenium House Pty Ltd, Elanora Hights, Australia.

Fabricated Geomembrane Institute, FGI, (2015), *Material Specification for New PVC Geomembranes 1115.*

Fabricated Geomembrane Institute, FGI, (2019), *Material Specification for New PVC Geomembranes 9119.*

Food and Agriculture Organization of the United Nations, FAO, (1989), *Arid zone forestry: A guide for field technicians*, FAO Publications Division, Rome, Italy.

Garcés, I., (2000, estimated), *La Industria del Litio en Chile*, Universidad de Antofagasta, Departamento de Ingeniería Química, Chile.

Gray, T, (2012), *The Elements, A visual Exploration of Every Know Atom in the Universe*, Black Dog & Leventhal Publishers, Inc, New York, NY, USA

De la Hoz, M., Martínez, V.R., Vedia, J.L., (2013), *El Litio: desde los Salares de la Puna a nuestros celulares*, Temas BGNoa, 3(3), 58:67

https://e2techtextiles.com/performance-benefits-of-factory-fabricated-geomembrane-liners/R&D Feb 10, 2020, August 17th, 2020

https://www.elmostrador.cl/dia/2020/08/27/chile-doblara-produccion-de-litio-a-2030-pero-disminuira-su-cuota-de-mercado/, September 9th, 2020

https://www.meteoblue.com/es/tiempo/historyclimate/weatherarchive/san-pedro-de-atacama_chile, September 8th, 2020

https://www.meteoblue.com/es/tiempo/historyclimate/weatherarchive/uyuni_bolivia, September 9th, 2020

https://www.meteoblue.com/es/tiempo/historyclimate/weatherarchive/san_salvador_de_jujuy-uy-argentina, September 8th, 2020

https://sciencing.com/characteristics-arid-climates-8441465.html, September 9th, 2020

https://www.weather-atlas.com/en/bolivia/uyuni-climate#temperature, September 8th, 2020

https://www.weather-atlas.com/de/argentinien/san-salvador-de-jujuy-Klima, September 8th, 2020

https://www.weather-atlas.com/en/chile/san-pedro-de-atacama-climate#temperature, September 8th, 2020

Lopez, A, Obaya, M, Pascuini, P, Ramos, A., (2019), *Litio en la Argentina: Oportunidades y desafíos para el desarrollo de la Cadena de Valor*, BID, Ministerio de Educación, Cultura, Ciencia y Tecnología, Presidencia de la Nación, Argentina.

Rowe, K., (2018), Webinar Part 3 of 6: *The Effects of Wrinkles on Geomembranes*, Queens University,

Stark, T., (2018), GMA Webinar *Stability of Geosynthetics Lined Slopes Part 1*, FGI, Illinois, USA

Stwertka, A., (1998), *A Guide to Elements*, Oxford University Press, New York, NY, USA

Geosynthetics Conference

Factory versus Field Fabrication Cost Comparison

Timothy D. Stark, Ph.D., P.E.[1] and G. Farid Saud Medina[2]

[1] University of Illinois at Urbana-Champaign, 205 N. Mathews Ave., Urbana, IL 61801; e-mail: tstark@illinois.edu
[2] University of Illinois at Urbana-Champaign, 205 N. Mathews Ave., Urbana, IL 61801; e-mail: gfs@illinois.edu.

ABSTRACT

Because the cost of installation and third-party construction quality assurance (CQA) of a geomembrane for a containment system can be comparable to the cost of the geomembrane itself, field installation and CQA must be understood and optimized to obtain the most benefit for the owner and not to slow overall construction. This paper describes a cost comparison calculator/spreadsheet that can be used to estimate the installation and CQA cost difference between factory and field fabricated geomembranes. The cost comparison includes the shorter site time, less field CQA, seaming, sampling, and testing, reduced installation crew expenses, such as, lodging and per diem, and quicker installation using factory fabricated geomembranes. The cost comparison for a 0.9 hectare (2.3 acre) pond is presented to illustrate the 65% lower costs associated with a factory fabricated geomembrane, which also results in a higher quality installation because most of the seams are completed in the climate controlled and clean factory setting.

INTRODUCTION

Factory welded seams have been long presumed to be of higher quality, less variability, and higher predictability than field welded seams due to the controlled and consistent indoor conditions, e.g., little dirt and moisture in the seam, no wind or significant ambient temperature changes in the factory, more rested technicians, and no changes in cloud cover. These factory constants result in a larger and more constant "welding window" than in the field. For thermally welded seams, higher quality means factory welded seams exhibit higher and more consistent seam strengths than field welded seams and less variability.

Stark et al. (2020) show a unique comparison of geomembrane factory and field welded thermal seams for a large off-stream water reservoir project. The results of this comparison show that factory welded seams are about 10% stronger than field seams in shear and about 9% stronger in peel strength at yield. More importantly, these higher strengths resulted in 100% of the factory welded seams passing the project seam strength requirements (Stark et al., 2020). Conversely, about 25% of the field welded seams did not pass the specified field seam shear strength requirement, which caused significant delays, patching, scheduling, and other construction issues. The use of a factory fabricated geomembrane resulted in improved quality of the completed geomembrane and protection of the prepared subgrade because a larger area could be covered quicker to minimize environmental degradation.

The use of factory fabricated geomembranes can reduce the amount of field seams by as much as 85% over a geomembrane that is completely field fabricated, which reduces installation

time, field destructive sampling and testing, and CQA costs. This reduction in field seams is due to individual geomembrane rolls being welded into large panels in the factory and then the panels are shipped to the project site. Conversely, field fabricated geomembranes utilize individual geomembrane (GM) rolls for projects and 100% of the thermal seam welding occurs in the field. As a result, the amount of field installation and CQA time and testing is greater than for factory fabricated geomembranes. This also results in significant destructive sampling and testing of completed seams, which requires lower quality patches of the completed geomembrane. However, to date there was no convenient means for estimating the installation cost savings related to factory versus field seaming and the subsequent installation.

The quality of the weld in the short-term (Scheirs, 2009) and long-term (Shoaib and Rowe, 2013; Rowe and Shoaib, 2014) is significantly influenced by welding temperature, speed, applied pressure, damage to the geomembrane, e.g., scoring, reduced thickness, notches, etc., and environmental conditions, such as, ambient temperature, moisture, cleanliness, adhered soil, wind, and personnel fatigue (Zhang et al., 2017). As a result, minimizing the length of field seaming is desirable. More importantly, Rollin et al. (1999) report that 55% of the damage recorded in GMs installed in basins, ponds, and landfills occurred at seams. Gassner and Fairhead (2014) report a leakage rate survey on sixty-seven (67) liquid holding ponds and report that 32% of the leaks/defects occurred at defective seams with most of them occurring on the floor of the ponds where the hydraulic head is the greatest. They also report that all of the defects identified on the slopes occurred at faulty seams (Zhang et al., 2017). In summary, GM seams are a weak point and source of leakage so efforts should be made to create the highest quality welds to reduce one of the largest sources of leakage.

This paper describes a cost comparison calculator/spreadsheet that can be used to estimate the installation and CQA cost difference between factory and field fabricated geomembranes. The cost comparison calculator/spreadsheet can be downloaded free using the following link: https://www.fabricatedgeomembrane.com/protected/pond-liner-calculator. The cost comparison does not include the cost of the geomembrane or other required materials. This calculator is "For estimating purposes only" and a formal cost estimate should be conducted for each project

COST COMPARISON CALCULATOR

The cost comparison includes the shorter site time, less field seaming and testing, reduced installation crew expenses, such as, lodging and per diem, and quicker installation using factory fabricated geomembranes. The cost comparison for a 9.3 hectare (23 acre) pond is presented to illustrate the significantly reduced costs with a factory fabricated geomembrane, which also results in a higher quality installation because most of the seams are completed in the factory.

Figure 1 presents the opening screen of the cost comparison calculator/spreadsheet, which estimates the installation costs for a factory fabricated geomembrane. **Figure 2** presents the second worksheet of the cost comparison calculator/spreadsheet, which estimates the installation costs for a field fabricated geomembrane. **Figure 3** presents the third worksheet of the cost comparison calculator/spreadsheet, which provides a direct comparison of the total installation costs, e.g., labor, equipment lodging, per diem, mobilization, etc., for the factory (**Figure 1**) and field (**Figure 2**) fabrications and the time required for installation.

In each page of the factory (**Figure 1**) and field (**Figure 2**) cost calculations, the blue cells are items that the user inputs, e.g., area to be lined with a geomembrane, geomembrane panel width and length which is usually controlled by allowable shipping weight. The units for each input parameter are provided next to each input cell but English and SI units can be used but all of the input parameters must be in a consistent system. Each geomembrane has a weight per area and the allowable shipping weight is divided by this unit weight to develop an initial estimate of the panel size. The green cells in each page are the items that are calculated using the user inputs, e.g., number of panels required, length of basic and cross seams, and costs. The following list provides some additional information for the various input parameters:

- Deployment/shape factor" depends on the geometry of the area to be lined and ranges from 0.75 for a site with only slopes, e.g., a side hill fill, to 1.25 for a site that is all flat with only a small berm around the perimeter.
- "Panel width" and "Panel length" are specified by the geomembrane fabricator, depending on the geomembrane type to be used and allowable shipping weight,
- "Length of Tie-in Seam" is the welded connection to the existing geomembrane panel or geomembrane,
- "Average seam welding speed" is the speed of the primary seam wedge welder in feet per minute or meters per minute is SI units are used, which can be estimated or assumed based on prior projects,
- "Hours per day" is the time of work that crews will be on site per day, e.g., 8 hours,
- "Set up time" is the number of days required to set up all of the installation equipment and crews depending on the length of the project,
- "Extra hours per day" is the time corresponding to the hours worked out of the "Hours per day" time,
- "Number of details" is the number of pipe penetrations through the geomembrane needed in the project, which require additional time besides geomembrane installation,
- "Time per detail" is the time needed for each detail in the project,
- "Travel time to site" is determined and entered by the user depending on the crew being mobilized,
- "Training days pre-start" is the site specific safety training days needed before geomembrane installation can begin,
- For labor, the number of "Supervisors", "Quality Control (QC) technicians", "Welding technicians", and "Laborers" are specified, and can be varied for a sensitivity analysis by the user,
- For tools and equipment, the number of "Trucks", "Generators", "Wedge Welders", "Large loader", "Small loader", and "Other tools & Equipment" are specified, and can be varied for a sensitivity analysis, by the user, and
- "Hotel rooms/lodging", "Per diems", and "Mobilization" depend on the labor specified above and can be varied for a sensitivity analysis.

Factory Fabrication Installation Cost Calculator - August 2020
By: Timothy D. Stark, Ph.D., P.E., D.GE, F.ASCE
Fabricated Geomembrane Institute
University of Illinois at Urbana-Champaign

Input Parameters
Calculated

Factory Fabrication Installation Cost Estimating - Large Panels

Area	1,000,000	square feet, net lined area					
Deployment/shape factor	1.00	e.g., range 0.75 (all slope) to 1.25 (all flat)					
Panel Width	125.0	feet, e.g., for 40 mil reinforced FML					
Panel Length	400.0	feet, e.g., for 40 mil reinforced FML					
Number of Panels	20	e.g., for 40 mil reinforced FML					
Feet of Basic Seam	8,000.0	feet, net lined area divided by panel width					
Feet of Cross Seam	2,500.0	feet, basic seam length divided by panel length					
Total Seam length	10,500.0	feet, total seam length (need to check panel layout)					
Length of Tie-in Seam	1,000.0	feet, e.g., welded connection to exisiting liner					
Ave Seam Speed	20.0	feet/minute, assumed speed of primary seam wedge welder per minute					
Hours per Day	8.0	hours per work day on site					
Extra Hours per Day	2.0	extra hours per work day on site					
Set Up Time	1.0	i.e., basic no. days for factory production set up, ranging from 1 to 2 days depending on the length of the proj					
Seaming Time	2.4	i.e. basic no. days for factory production seaming assuming standard QC & 50% actual welding time					
Deployment Time	0.6	i.e., days to deploy & ballast geomembrane panels (assumes 0.25 hour per panel)					
Number of Details	8	pipe pentrations					
Time per Detail	1.0	hours					
Details Time	1.0	i.e., added days for detail work					
Total Days on Site	4	i.e., assumes QC included				i.e. 2,490	sq-ft / man-hour
Travel Time to Site	0.0	i.e., mobilization charge				i.e. 5.7	acres per day
Training Days Pre-Start	0.0	e.g., site specific safety training				i.e. 4	days on site
Days Total	5	i.e., assumes QC included					
Non-Work Days	2.0	Sundays and rain/weather delays. Depending on duration of project and location, this ranges from 2-5					
Days Required		Unit Cost	Cost		Man-hours		
Supervisor	1.0	$ 60.00	$ 2,410.00	non-union	40		
QC Tech	1.0	$ 50.00	$ 2,008.33	non-union	40		
Welding Techs	2.0	$ 40.00	$ 3,213.33	non-union	80		
Laborers	4.0	$ 20.00	$ 3,213.33	non-union	161		
Extra Hours		Unit Cost	Cost				
Supervisor	1.00	$ 90.00	$ 903.75	non-union	10		
QC Tech	1.00	$ 75.00	$ 753.13	non-union	10		
Welding Techs	2.00	$ 60.00	$ 1,205.00	non-union	20		
Laborers	4.0	$ 30.00	$ 1,205.00	non-union	40		
			Cost		Cost		
Labor Total (Crew Size)	8.0		$ 10,845.00	non-union	402	i.e. $ 27.00	ave. cost of labor per man hour
Trucks	3.0	$ 30.00	$ 3,615.00	i.e. charge out rate			
Generators	2.0	$ 20.00	$ 1,606.67	i.e. charge out rate			
Fuel	0.0	$ 20.00	$ -	i.e. charge out rate			
Wedge Welders	2.0	$ 20.00	$ 1,606.67	i.e. charge out rate			
Other Tools & Equipment	4.0	$ 20.00	$ 3,213.33	i.e. charge out rate			
Large loader	1.0	$ 30.00	$ 1,205.00	i.e. charge out rate			
Small loader	1.0	$ 20.00	$ 803.33	i.e. charge out rate			
Equipment Total	13.0		$ 12,050.00	i.e. charge out rate		i.e. $ 2,400.00	per day for equipment
Hotel rooms	5.0	$ 120.00	$ 3,012.50				
Per diems	8.0	$ 40.00	$ 1,606.67				
Mobilization	8.0	$ 750.00	$ 6,000.00				
Non-Work Day Expenses	2.0	$ 100.00	$ 200.00				
Factory Project Total Cost	→		**$ 33,514.17**			i.e. $ 0.034	per sq. ft.

Does not include costs for materials.

Legal disclaimer regarding liability from cost and schedule related damages. This calculator is "For estimating purposes only" and a formal cost estimate should be conducted for each project

Figure 1. Cost spreadsheet for factory fabricated geomembranes.

Field Fabrication Installation Cost Calculator - May 2020
By: Timothy D. Stark, Ph.D., P.E., D.GE, F.ASCE
Fabricated Geomembrane Institute
University of Illinios at Urbana-Champaign

FGI Fabricated Geomembrane Institute

Input Parameters
Calculated

Field Fabrication Installation Cost Estimating - Rolled Goods

Area	1,000,000.0	square feet, net lined area							
Deployment/shape factor	1.0	e.g. range 0.75 (all slope) to 1.25 (all flat)							
Roll Width	22.5	feet, e.g. for 60 mil HDPE geomembrane							
Roll Length	560.0	feet, e.g. for 60 mil HDPE geomembrane							
Number of Rolls	79	e.g. for 60 mil HDPE geomembrane							
Feet of Basic Seam	44,444.4	net lined area divided by roll width							
Feet of Cross Seam	1,785.7	basic seam length divided by roll length							
Total Seam length	46,230.2	feet, total seam length (need to check panel layout)							
Length of Tie-in Seam	1,000.0	feet, e.g. welded connection to exisiting liner							
Ave Seam Speed	22.0	feet assumed speed of primary seam wedge welder per minute							
Hours per Day	8.0	hours per work day on site							
Extra Hours per Day	2.0	extra hours per work day on site							
Set Up Time	2.0	i.e. basic no. days for field production set up, ranging from 2 to 3 days depending on the length of the project							
Seaming Time	8.9	i.e. basic no. days for field production seaming assuming standard QC & 50% actual welding time							
Deployment Time	2.5	i.e. days to deploy & ballast geomembrane rolls (assumes 0.25 hour per roll)							
Number of Details	8.0	pipe pentrations							
Time per Detail	1.0	hours							
Details Time	1.0	i.e. added days for detail work							
Total Days on Site	14	i.e. assumes QC included					i.e.	867	sq-ft / man-hour
Travel Time to Site	0.0	i.e. mobilization charge					i.e.	1.6	acres per day
Training Days Pre-Start	0.0	e.g. site specific safety training					i.e.	14	days on site
Days Total	14	i.e. assumes QC included							
Non-Work Days	3.0	Sundays and rain/weather delays. Depending on duration of project and location, this ranges from 2-5							
Days Required		Unit Cost		Cost		Man-hours			
Supervisor	1.0	$ 60.00	$	6,924.13	non-union	115			
QC Tech	1.0	$ 50.00	$	5,770.11	non-union	115			
Welding Techs	2.0	$ 40.00	$	9,232.17	non-union	231			
Laborers	4.0	$ 20.00	$	9,232.17	non-union	462			
Extra Hours		Unit Cost		Cost		Extra man-hours			
Supervisor	1.0	$ 90.00	$	2,596.55	non-union	29			
QC Tech	1.0	$ 75.00	$	2,163.79	non-union	29			
Welding Techs	2.0	$ 60.00	$	3,462.06	non-union	58			
Laborers	4.0	$ 30.00	$	3,462.06	non-union	115			
				Cost		Cost			
Labor Total (Crew Size)	8.0		$	42,843.04	non-union	1154	i.e.	$ 37.13	av. cost of labor per man hour
Trucks	3.0	$ 30.00	$	10,386.19	i.e. charge out rate				
Generators	2.0	$ 20.00	$	4,616.08	i.e. charge out rate				
Fuel	0.0	$ 20.00	$	-	i.e. charge out rate				
Wedge Welders	2.0	$ 20.00	$	4,616.08	i.e. charge out rate				
Other Tools & Equipment	4.0	$ 20.00	$	9,232.17	i.e. charge out rate				
Large loader	1.0	$ 30.00	$	3,462.06	i.e. charge out rate				
Small loader	1.0	$ 20.00	$	2,308.04	i.e. charge out rate				
Equipment Total	13.0		$	34,620.63	i.e. charge out rate		i.e.	$ 2,400.00	per day for equipment
Hotel rooms	5.0	$ 120.00	$	8,655.16					
Per diems	8.0	$ 40.00	$	4,616.08					
Mobilization	8.0	$ 750.00	$	6,000.00					
Non-Work Day Expenses	3.0	$ 100.00	$	300.00					
Field Project Total Cost			**$**	**97,034.91**			i.e.	$ 0.097	per sq. ft.

Figure 2. Cost spreadsheet for field fabricated geomembranes.

The following list provides information on the various output parameters:

- The number of factory fabricated panels and field fabricated rolls is calculated by dividing the area of the project by the area of the panels and rolls, i.e., roll width multiplied by the roll length,
- “Feet of basic seam” is obtained by dividing the area of the project by panel and roll width for factory and field fabricated geomembranes, respectively,
- “Feet of cross seam” is calculated by dividing the “Feet of Basic Seam” by the panel and roll length for factory and field fabricated geomembranes, respectively,
- The “Total Seam Length” is the sum of the “Feet of Basic Seam” and “Feet of Cross Seam”,
- “Seaming time” represents the number of days required for seaming assuming standard Construction Quality Control (CQC) and using two (2) times the actual welding time, i.e., dividing by the actual time by 50%, to reflect delays caused by the CQC process for both factory and field fabricated geomembranes,
- “Deployment time” is the days required to deploy and ballast the geomembrane panels and rolls for factory and field fabricated geomembranes, respectively,
- “Detail time” is the number of days added to complete the details or pipe penetrations in the project. This value is obtained by multiplying the number of details by the time that it takes to complete one (1) detail divided by the hours worked per day,
- “Total days on site” is the summation of the “Set up time”, “Seaming time”, “Deployment time”, and “Details time”,
- “Days total” for the project is the total number of days on site mentioned above and travel time to and from the site and number or training days required prior to starting the project,
- “Non-Work days” represent Sundays, holidays, and delays caused by rain or inclement weather in which work cannot be performed but the installation personnel are still mobilized,
- Costs for laborers are obtained by the following multiplication of factors:
  unit cost per hour * hours per day worked * number of laborers required * total time needed for the project. This is usually a big cost difference between factory and field fabricated geomembranes because in the factory setting non-union labor can be used while in the field union labor is usually required, which results in a higher unit cost per hour. Of course, if the factory workers are unionized the costs will be similar unless there are different hourly rates.
- Extra hours cost for laborers consists of the same calculation as shown above but for extra hour above the normal day for the “cost of laborers” and the unit cost per hour is 50% higher than normal because it is considered to be overtime.
- Number of hours for each laborer type, i.e., man-hours, is obtained by multiplying:
  hours worked per day * total days worked * number of laborers in question.

- Extra man hours result from a similar calculation for man-hours but is focused on the extra hours worked per total days needed for the project.
- “Labor total (crew size)” is the number of all laborers needed for the project.
- For tools and equipment, the costs are calculated the same as for the costs of laborers but using different a unit cost for the equipment.
- “Equipment total” is the number of all equipment described in the calculator.
- “Hotel rooms” is calculated per the labor total or “crew size” and is the number of hotel rooms required to accommodate the crew so the longer the field installation the greater the lodging and per diem costs.
- “Per diem” and “mobilization” items are related to the number of laborers involved in the project and the project duration. Costs for both items are calculated by multiplying the unit cost of the item times how many “Days Total” to complete the project.
- “Non-work Day Expenses” are calculated by multiplying the estimated unit cost for this matter times the number of non-work days.
- “Project Total Cost” is calculated by adding up all of the calculated costs for the factory and field fabricated scenarios to develop a total cost estimate for each fabrication scenario.

Figure 3 presents the third worksheet of the cost comparison calculator/spreadsheet that provides a direct comparison of the total installation costs, e.g., labor, equipment lodging, per diem, mobilization, etc., for the factory (**Figure 1**) and field (**Figure 2**) fabrications. The cost comparison for a 9.3 hectare (23 acre) pond in **Figure 3** shows that geomembrane fabrication and installation will be 65% less for the factory fabricated geomembrane than the field fabricated geomembrane, i.e., $97,034 v. $33,513. More importantly, the use factory fabricated geomembrane panels will result in a 10.4 days fewer days on site, which will accelerate the overall construction schedule. This will also make the geomembrane installation more modular and more predictable so the other contractors can better plan and complete their work. It is easy to use this calculator to quickly conduct parametric cost comparisons by varying different parameters, such as, number of penetrations/details, installation rate, and different unit costs, for factory and field geomembrane fabrication.

Figure 4 presents a graphical comparison of the installation costs and time between factory and field fabricated geomembranes. The bar chart in **Figure 4** clearly shows the largest cost is the Labor Total or the total labor cost. This is due to the longer site time and higher rate usually required by field personnel versus factory personnel because field personnel are usually unionized. More importantly, the comparison of the histograms clearly shows the difference in time required for deployment between factory fabricated geomembrane panels (7 days) and field fabricated rolls (17.4 days).

Cost comparison

	Field	Factory
	Cost	
Labor Total (Crew Size)	$ 42,843	$ 10,845
Equipment Total	$ 34,621	$ 12,050
Hotel rooms	$ 8,655	$ 3,013
Per diem	$ 4,616	$ 1,607
Mobilization	$ 6,000	$ 6,000
Non-Work Day Expense	$ 300	$ 200
Project Total Cost	$ 97,035	$ 33,514

If choosing factory fabricated pannels for deployment, total savings will be: $ 63,520.7

Time comparison

	Field	Factory	
	Time (days)		
Days total	14.4	5.0	
Non work days	3.0	2.0	
If choosing factory fabricated pannels for deployment, the time saved is:		10.4	days

Figure 3. Comparison of cost and installation time between factory and field fabricated geomembranes.

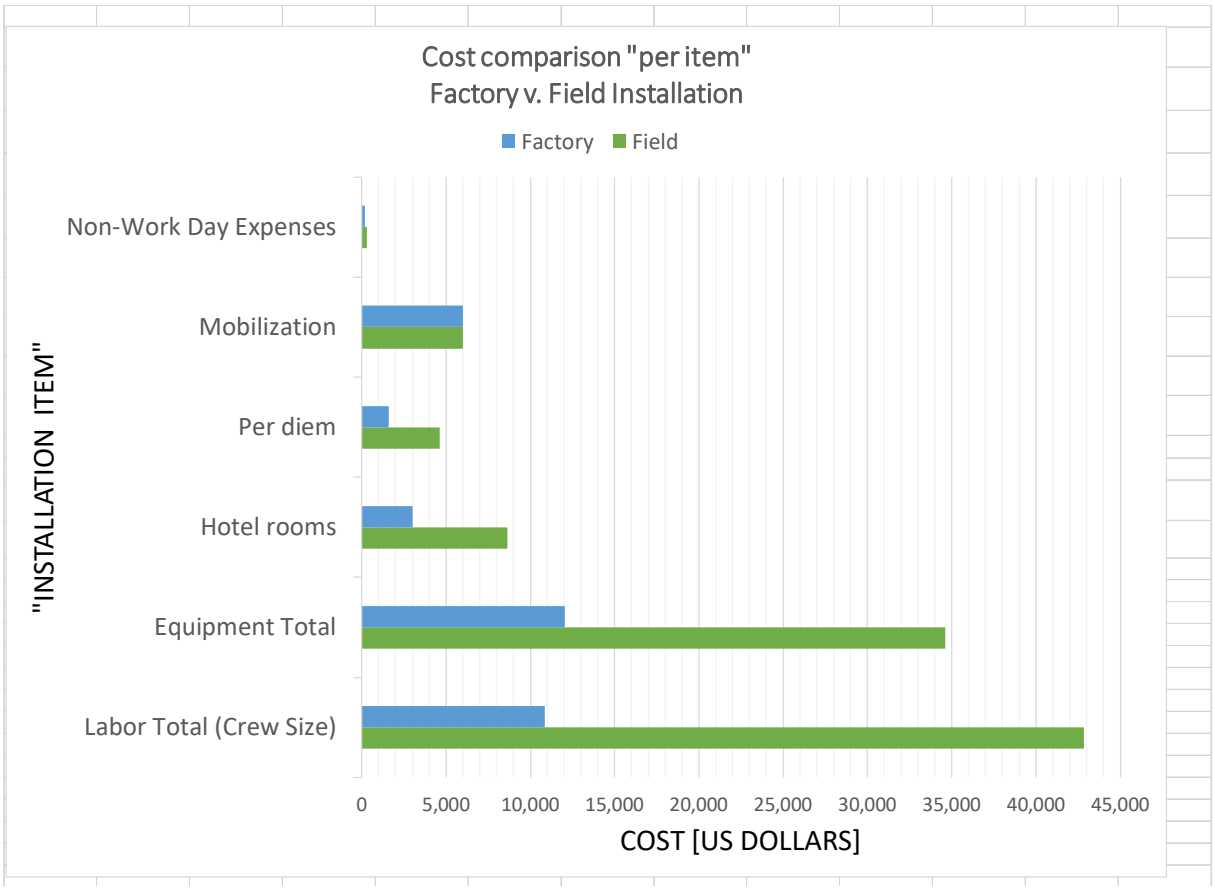

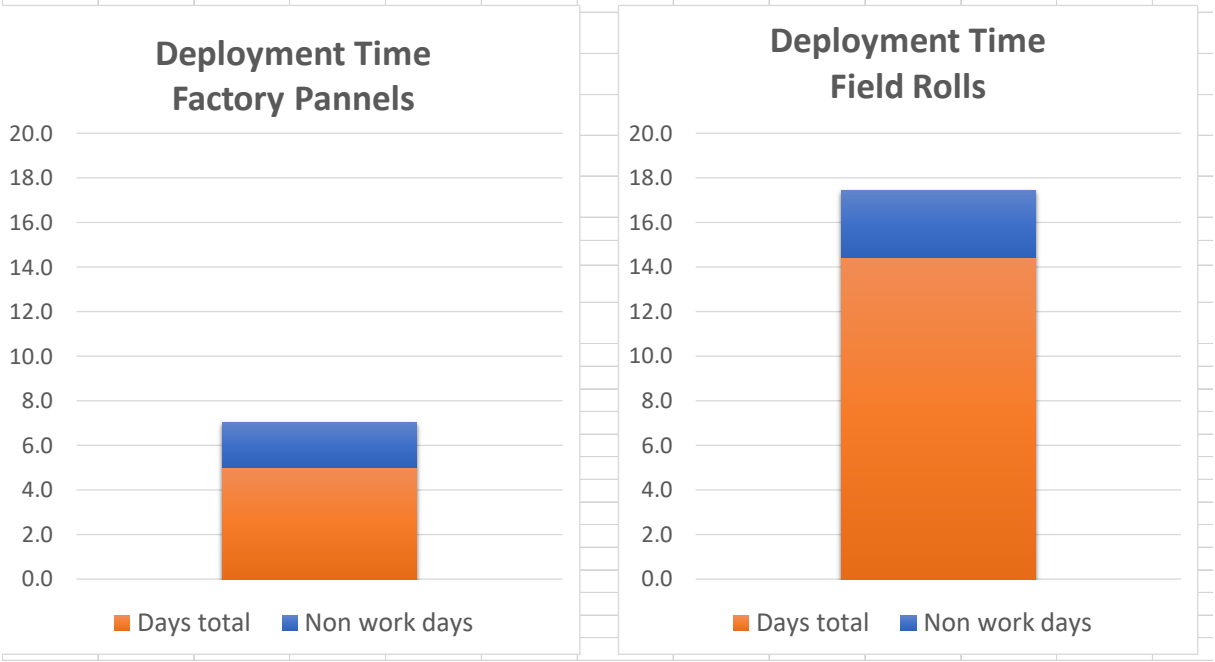

Figure 4. Comparison of costs and installation time between factory and field fabricated geomembranes.

SUMMARY

A cost comparison calculator is described herein that can be used to quickly assess the significant cost savings created by factory fabricating geomembrane panels and installing them compared to field cutting, sizing, and seaming all of the required geomembrane rolls. The calculator is easy to use so parametric studies using different field installation costs can be quickly performed to assess the benefit of different labor rates, number of days on site, and equipment. For the hypothetical 9.3 hectare (23 acre) pond used herein, a factory fabricated geomembrane is 65% less than a field fabricated geomembrane, i.e., $97,034 v. $33,513. More importantly, the use of factory welded seams are of higher quality, less variability, and higher predictability than field welded seams due to the controlled and consistent indoor conditions, e.g., little dirt and moisture in the seam, no wind or significant ambient temperature changes in the factory, more rested technicians, and no changes in cloud cover. Stark et al. (2020) show that factory welded seams are about 10% stronger than field seams in shear and about 9% stronger in peel strength at yield.

REFERENCES

Stark, T.D., Hernandez, M.A., and Rohe, D.S. (2020). "Geomembrane Factory and Field Thermally Welded Seams Comparison," *J. Geotextiles and Geomembranes,* Elsevier, **48**, 454-467.

Above Ground Storage Tank: Bucket versus Flat liners

Ron MacKenzie[1]

[1]Inland Tarp & Liner, LLC –1600 N Main St, Fostoria, OH 44830; e-mail: ronm@inlandtarp.com

ABSTRACT

Over the past 20 years as hydraulic fracking rules and regulations have become more stringent and Oil and Gas (O&G) producers more concerned with environmental stewardship. The need for quality factory-fabricated liners for the above ground storage tank (AST) market has become a critical part of the fracking infrastructure. As most O&G service companies and producers prefer not to field-fabricate tank liners, liner design and appropriate materials consideration ensure safe and compliant installation as well as performance of the products. This technical paper addresses the historical differences between a "bucket liner" and a flat or "tapered" liner as well as the considerations of the appropriate liner material and the associated density, and chemical compatibility issues associated with the AST and fracking (Frac) tanks in general as evolved over years of collaborative efforts across the industry.

BACKGROUND

For hundreds of years, man has been storing water in tanks, with most early tanks made from clays, cement, and soils. Around 1850, wood and varying metals such as copper, as seen in Figure 1, began to be used in oil and gas.

Figure 1. Wooden oil tank near Odessa, Texas. Source Ron MacKenzie

Around the late 1800's in the United States, and in response to the need for a growing O&G industry, more modern tanks were made with steel and concrete. Outside of the manufacturing and construction process, very little has changed with these tanks since. They contain walls, a floor, and sometimes a cover. While tanks may vary in size, composition and requirements for chemical compatibility, they are time-consuming installations for often permanent storage needs. To create temporary storage and minimize the footprint associated with permanent tanks, the O&G industry came up with Frac tanks and AST's in the early 2000's.

Unique to AST tanks is they only have a wall designed into the structure. AST tanks, as pertaining to the O&G drilling portion of the industry are merely a steel wall, typically around 12'

tall, between 60-260’ in diameter and built in sections of varying lengths that either bolt or pin together creating the walled diameter of a tank (as seen in Figure 2). They require no floor and rely solely on the subgrade or soil as a bottom, so a compliant lining system is the only way to hold the desired product (water or flowback chemicals) that vary in the drilling processes.

Figure 2. Typical wall section for AST, photo courtesy Western Tank and Lining

Bucket Liners and Tapered Liners:
A traditional bucket liner is two components of liner (a wall/skirts and a floor), connected with a radial weld. Bucket liners work well in permanent applications when AST walls and a floor are fixed and provide support to the liner in all dimensions. Typical installation requires hanging the wall sections or skirts, installing a floor piece built to the diameter of the tank and welding the two sections together via radial weld around the perimeter of the floor attaching the two pieces to create a solid liner or bucket. (Figure 3).

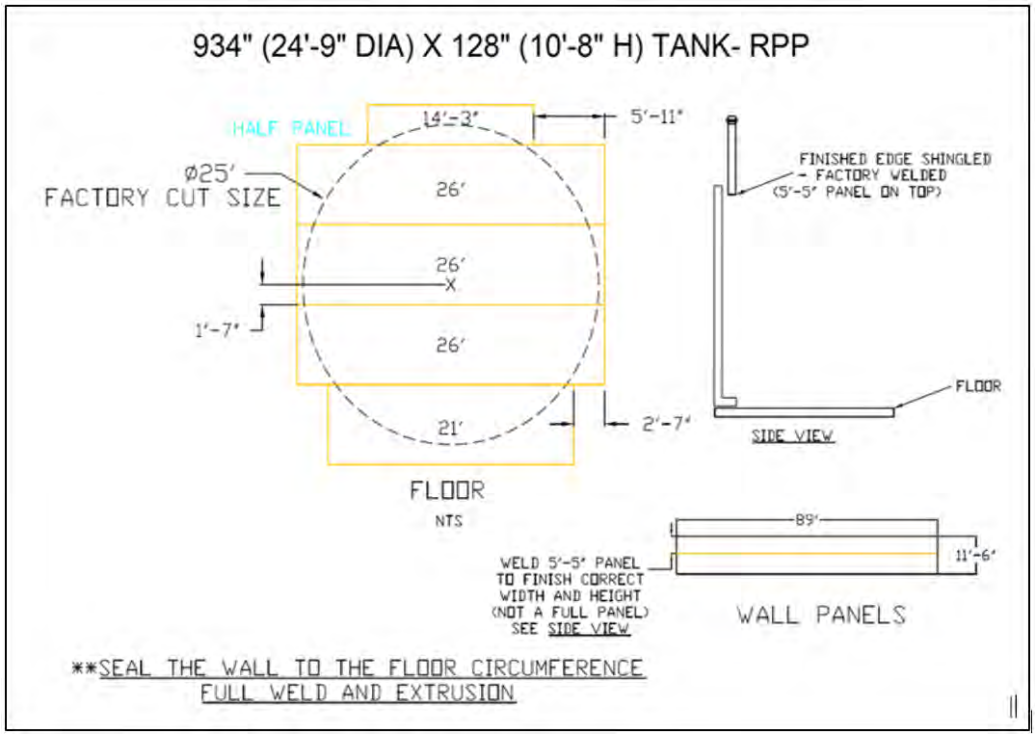

Figure 3. Typical bucket liner manufacturer drawing for field/factory assembly

Based on the permanent nature of the tank and liner in this configuration, settling and/or movement of the liner is not as concerning. However, the most significant risk associated with this configuration and radial weld is no bridging or voids away from the interior wall and floor transition thus creating a load point or possible failure issue.

While these liners provide a uniform and clean fit to the tank, the liners must be installed by qualified technicians as the radial weld, extrusion and subsequent capping patching and testing are crucial to a quality and compliant installation. This brings us to tapered liners.

A tapered liner is a flat sheet made with staggered liner panels to create a diameter large enough to fit an AST floor, wall and overlap (Figure 4).

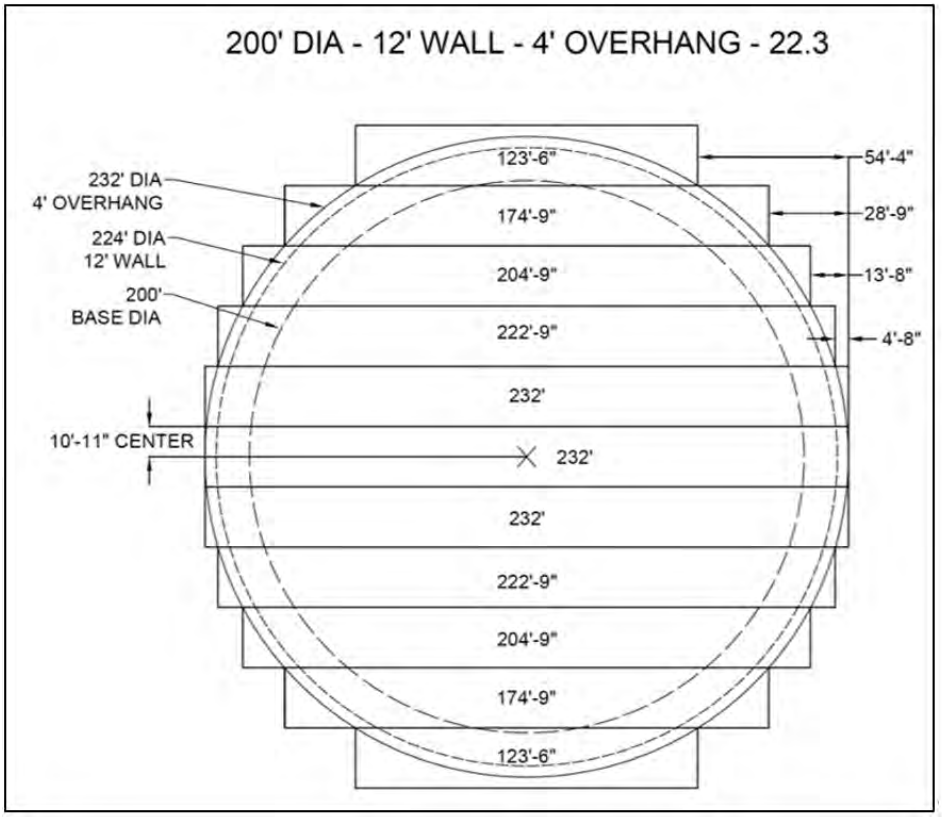

Figure 4. Typical tapered liner fabrication drawing

In the above example, a 12’ tall, 200’ diameter tank requires a tapered liner of 232’. This is 200‘for the floor, 24’ total for the 2 walls and 8‘excess to allow 4’ over the back of the tank all around.

A typical installation requires the liner to be stretched out on the ground folded back in on the AST perimeter as the AST walls are installed and secured around it. The liner is then unfolded back up and over the AST walls allowing the excess material to be draped along the walls vertically and evenly around the inside of the tank. In most applications clamps are put on the top ring of the tank to secure the liner and/or the excess material over the tank and secured below the top edge with straps or a large cable. The most significant advantage of these liners is there is no one single radial field weld, a potential point of failure, as the liners are factory-welded and folded into one single piece, significantly reducing risks associated with field fabrication. However, challenges and careful considerations remain.

During installation of the tapered liner, it is imperative that the wrinkles along the walls are installed uniformly around the interior of the tank. Also, with a typical AST containing no hard tank bottom, the tapered tank liner’s integrity is contingent on a properly prepared and compacted subgrade. With the tapered liner being anchored at the top, any movement of the liner or settling of the subgrade can lead to failures of the liner at the point of the wall transition to the ground, or “failure load point” as pictured in Figure 5.

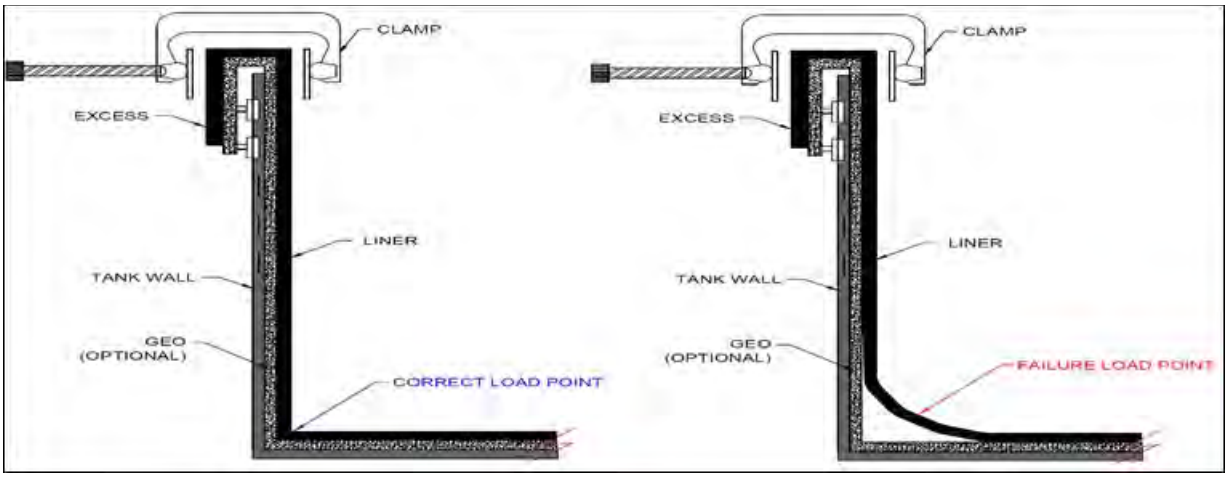

Figure 5. AST Load Point

To minimize risk of a failure load point, after the tapered liner is unfolded inside the AST, 1-2' of water is added to achieve the correct load point before clamping at the top of the tank. Lessons learned also include the necessity for doing the AST, tapered liner installation, and filling with intended liquid within a short time span. Empty tanks are susceptible to shifting of the liner due to wind, thermal expansion and contraction and are rarely ever realigned prior to introduction of product or fluids, lending to increased risk of liner and project integrity. Fortunately, years of trial and error have led most producers and installers to enact procedures that have product put in the tank prior to any clamping or locking of the liner and failures from tension to the liner have become almost nonexistent.

Material choices and chemical compatibility

Strength of the products, chemical compatibility, potability, color, lifespan desired and in some cases even disposal concerns or recyclability are considered when designing a liner for an AST. Modern liners have evolved over the past 50 years to be made in both reinforced and non-reinforced variants, and polymers can range from polyvinyl chloride (PVCs), polyethylene (PEs) to bitumen materials and a variety of polymers in-between including Tripolymer for specialty applications.

Dating back 35 years, the most commonly used product in the liner industry is high density polyethylene (HDPE). Available as a non-reinforced polyolefin sheet it is typically found in the range of 20 -120 mil thickness and is used extensively today in the landfill market and many other industrial applications. HDPE has great chemical resistance, UV stabilization and considerable strength characteristics for a non-reinforced material. While cost-effective, the most concerning aspect of HDPE product is its limited flexibility, stress crack resistance and workability in colder climates. As a result, most HDPE products are strictly field-fabricated and lend themselves best to large scale flat square footage projects. While many cost effective reinforced hybrid materials such as reinforced polyethylenes (RPE) have overcome these challenges, and can be factory-welded, many lack the long-term chemical and or UV resistance required of largescale projects based partially on the coating thicknesses that can range anywhere from 1- 6 mils thick.

Availability on the higher end of reinforced materials, such as reinforced PVC or Tripolymer blends, have excellent chemical resistance, strength and UV characteristics also allowing for the factory welding. While suitable for primary containment of crude oil during the recent storage crisis in the oil and gas industry, for short-term solutions use in AST's the materials

are cost prohibitive. This is where linear low-density polyethylene (LLDPE) presents the most compliant, workable, and cost-effective material for these temporary AST industrial applications. In the 1980s a need arose for more flexible material for industrial applications. Growing on the benefits of the HDPE successes, resin and sheet manufacturers worked to improve the compounds involved in the manufacturing of polyolefin sheets. In short, the idea was to retain the high chemical resistance characteristics of the HDPE and create a cost effective non reinforced material that could be factory welded and fabricated. By adjusting the polymers and additives involved and decreasing the density, LLDPE showed not only high stress crack resistance, but also excellent elongation, flexibility and extreme cold weather durability and workability, all characteristics ideal for the AST liner application. While clean water poses no concerns for chemical compatibility flow back water from drilling operations contains chemicals, hydrocarbons and additives that can be harmful to the liner. Coupled with the proprietary nature of many drilling fluids, obtaining data and safety data sheets on the liquids for purposes of continued study remain challenging. While many states have mandated chemical disclosures, many have not, leaving the need for a liner that is compatible with a broad spectrum of chemical and hydrocarbon tolerances that is found in the LLDPE. With the high chemical resistance of the LLDPE, its ability for factory welding/fabrication and testing it will continue to be the most compliant and cost-effective solution now and in the immediate future of these applications.

CONCLUSION

While the AST market has significantly evolved over the last 20 years, it is partnerships between the O & G producers, tank installers, factory liner fabricators and liner manufacturers working together that has made the “Frac” containment a safe and environmentally sound market it is today. By eliminating the need for field fabrication, solving field and weather issues, to simplifying the design to allow for factory fabricated and tested tapered liners to go in round tanks. Significant vetting of the chemical compatibility liner needs for the short-term containment and advent of better LLDPE resins, as well as training installers on proper procedures, the industry has done an excellent job of providing a safe and sound solution.

Geosynthetics Conference

Creating Operational Flexibility with Limited Storage Options

Alex Gersch[1] and Kieron Jeffries[2]

[1]Layfield Australia Ltd, 11120 Silversmith Place, Richmond, BC V7A 5E4 Canada; e-mail: alex.gersch@layfieldgroup.com
[2]Concept Environmental Services Pty. Ltd, 509 Zillmere Rd, Zillmere QLD 4034 Australia; e-mail: kjeffries@conceptservices.com.au

ABSTRACT

During planning for a quadrennial plant shut down, a global mining and mineral processing client was grappling with the significant challenge of managing 15ML (4 million gallons) of process liquor containing around 1,500 tonnes (1,655 tons) of Nickel at an Australian refinery. The client recognized unless the process liquor could be stored on site, the mineral laden liquor would need to be pumped along 7.5km (4.7 miles) of pipework through the community to existing evaporation ponds. Once co-mingled with the liquor in the evaporation ponds, the liquor would be too contaminated to process. The client required a storage solution with minimal land usage and no excavation to meet the state EPA requirements for protection of groundwater, flora and fauna. This made a very difficult project. This paper discusses the various storage options considered and the innovative solution adopted using large precast above ground open top tanks incorporating double lined geomembrane containment systems with integral leak detection.

INTRODUCTION

During planning for a quadrennial plant shut down, a global mining and mineral processing client was grappling with the significant challenge of managing 15ML (4 million gallons) of process liquor containing around 1,500 tonnes (1,655 tons) of Nickel at an Australian refinery. The client recognized unless the process liquor could be stored on site, the mineral laden liquor would need to be pumped along 7.5km (4.7 miles) of pipework through the community to existing evaporation ponds. Once co-mingled with the liquor in the evaporation ponds, the liquor would be too contaminated to process, and the nickel would be lost representing a significant cost to the business of approximately AUD $3 Million. Additionally, the site had ongoing issues with regard to water balancing and managing liquor inventories, particularly when principal pipelines and storage vessels were offline for inspection, maintenance and repairs.

The client's facility was located in an industrial area with very limited land available for construction of a suitable storage. Furthermore, groundwater was only 2.1m (7') below natural ground level and the area adjoined the local catchment area. The state EPA regulations required a minimum 2.0m (6'6") clear zone to minimise potential ground water contamination and the site was built on a sandy substrate. In addition to these challenges, the area was also home to endangered bird and rare vegetation species eliminating any possibility of land clearing.

The project timetable was very restricted with feasibility assessment, design, construction and commissioning all required to be completed within six months to meet the client's shutdown commencement date.

With this design brief, all possible storage options were assessed. Any containment option had to demonstrate failsafe containment and required a high level of chemical resistance to the liquor and capability to withstand very high levels of UV exposure.

POTENTIAL STORAGE OPTIONS

Alternative storage options considered included structural steel tank/s, cut and fill earth bank storage, off site storage, bladders etc. Multiple orthodox structural steel storage tanks would be necessary to provide sufficient capacity and due to the sandy substrate conditions on site would require extensive site works to provide adequate foundational requirements. The option would require significant capital expenditure with considerable engineering and procurement lead times. It was immediately apparent that a compacted clay lined storage solution was not acceptable as no suitable clay material was available creating an unacceptable contamination risk and would create a significant legacy issue at the site. Geosynthetic lined solutions were the only options considered acceptable. Geomembrane lined earth bank storages have wide acceptance in the industry, however in this particular application, it was recognised there were a number of notable issues. As ground water was only 2.1m (7') below natural ground level and the state EPA regulations required a minimum 2.0m (6'6") clear zone, a cut and fill construction method was not an option, requiring importation of suitable fill material resulting in significant logistical challenges and potential disruption and vehicle congestion in the local area. It was further noted that to achieve acceptable bank stability the internal and external batter slopes would take up significant area on a site and would require land clearing of an area of site that had already been revegetated to restore valuable habitat that had already been lost. Self supporting geosynthetic storage bladders also had similar challenges. The number of bladders required to achieve the storage volume was high and the corresponding lay down area required was substantial.

OPERATING CONDITIONS

The weather for the region can be categorised as Mediterranean hot summer climate with maximum temperatures exceeding 46^{o}C being recorded and very high solar exposure of up to 29MJ/m^2 and associated UV radiation typical of this latitude in Australia (refer Table 1. Regional Climate Statistics).

Table 1. Regional Climate Statistics													
Statistic Element	**Jan**	**Feb**	**Mar**	**Apr**	**May**	**June**	**July**	**Aug**	**Sept**	**Oct**	**Nov**	**Dec**	**Annual**
Mean max. temp. (°C)	31.8	32	29.7	25.6	21.8	19	18	18.6	20.2	22.8	26.1	29.1	24.6
Highest temp. (°C)	46	46.7	43.8	39.6	35.3	27.8	25.7	29.9	34.5	37.7	41.1	44.5	46.7
Lowest max. temp. (°C)	19.7	17.1	15.8	13.9	11.7	9.4	10.7	9.9	12.7	12.3	14.2	15.2	9.4
Mean min. temp. (°C)	17	17.5	16	13	10.4	9	8	8.1	8.9	10.3	12.8	15	12.2
Lowest temp. (°C)	6	5.7	3.1	1.2	-0.4	-1.3	-1	0.1	-0.2	1.2	3.2	4.8	-1.3
Highest min. temp. (°C)	28.5	28.7	28.6	23.9	20.8	17.7	16.2	16.7	19.2	21.3	26.3	27.5	28.7
Mean daily ground min. temp.(°C)	14.9	15.6	13.7	10.8	8.3	6.8	6.2	6.3	7.1	8.4	10.7	12.7	10.1
Lowest ground temp. (°C)	1.7	2.5	-1	-0.1	-1.1	-3.6	-2.4	-2.1	-0.5	-1.6	0.2	1.3	-3.6
Mean rainfall (mm)	10.9	15	16.2	39.7	97.6	155.1	154.2	118.7	72.2	43	25.4	11.2	762.1
Highest rainfall (mm)	102.4	150.4	61.9	135	229	424.1	446.7	340.3	172.4	124.8	84.8	67.4	1164.7
Lowest rainfall (mm)	0	0	0	0	12.4	23	30.6	19	11.5	1.3	1.3	0	479.6
Highest daily rainfall (mm)	90.2	132	43.2	61	57.4	78.2	99	66.4	59.6	60.2	41.1	36	132
Mean number of days of rain	2.5	2.8	3.9	7.3	12.1	16.1	17.5	15.7	13.2	9.3	6.4	3.9	110.7
Mean daily wind run (km)	483	473	443	370	324	325	329	335	368	410	456	479	399
Max. wind gust speed (km/h)	113	100	113	115	122	106	124	109	113	98	113	108	124
Mean daily sunshine (hours)	11.5	11	9.5	8.1	6.9	6	6.1	7.1	7.8	9.6	10.8	11.5	8.8
Mean daily solar exposure (MJ/m^2)	29	25.6	20.7	15.1	11.2	9.2	9.8	12.7	16.5	22.1	26.5	29.6	19
Mean number of clear days	18	16	15.5	10.7	8.3	6.9	6.7	8.1	9.2	11	11.8	16.5	138.7
Mean number of cloudy days	4.6	4.8	6	10	12	12.7	12.8	11.3	10.2	9.3	7.8	5.4	106.9
Mean daily evaporation (mm)	10.2	9.6	7.7	5	3	2.2	2.1	2.6	3.7	5.4	7.6	9.1	5.7

The process liquor was considered harmful to the environment with strict regulatory guidelines on permissible background levels detailed on the clients operating licence for the site. The typical *average* process liquor chemistry was relatively moderate, however peak concentrations of ammonium sulphate and peak influent temperature were of concern for material selection (refer Table 2. Liquor Chemistry).

Table 2. Liquor Chemistry

Property	UOM	Average	Peak
Chloride Content	g/L	0.3	15
Ammonium Sulphate Content	g/L	65	5003
Nickel Content	g/L	10	50
Cobalt Content	g/L	0.25	2
Copper Content	g/L	0.05	1
Ammonia Content	g/L	7.5	45
Total Suspended Solids	ppm	125	750
Specific Gravity		1.052	1.251
pH		7.1	2.5 – 10
Temperature	^{o}C	Ambient	50-60

TECHNICAL STORAGE SOLUTION

After reviewing the design brief, the tank contractor and geomembrane manufacturer developed a suitable solution using innovative large precast above ground open top tanks incorporating double lined geomembrane (GMB) containment systems with integral leak detection. The tank construction uses an engineered modular concrete vertical wall panel, restrained by use of a series of post tensioned steel cables.

The tank lining system comprises a proprietary polyethylene primary and secondary liners with a leak detection system. Further risk mitigation was achieved by using a geosynthetic clay liner (GCL) as a tertiary containment.

The modular tank system chosen has proven very successful in the Australian coal seam gas industry. One of the key features of this tank design is the significant reduction in earthworks compared to a construction of a traditional storage pond. The modular storage tanks are installed on compacted ground unlike in traditional tanks, which require a concrete ring beam. Key benefits of the design include:

- An engineered wall structure - Reduced risk of failure vs traditional earthen embankment structures, i.e. No vegetation damage, no animal damage (to embankments and liner), no rat holing, no risk of embankment fill liquefaction (during seismic events) and no erosion by rain or wind.
- Modular tank structure can accommodate some level of localised settlement and ground movement unlike traditional tank designs.
- Triple geosynthetic liner system with leak detection – any breach in the primary GMB liner would be contained by the secondary GMB liner and any breach of the full GMB lining system will be contained by the GCL and clearly visible with flow from under the walls, as opposed to embankment where leaks are undetectable until contaminated groundwater is detected in a monitoring bore

- Demolition of earthen bund ponds will generate very large volumes of contaminated fill. Under this design the tank walls can be re-used and hence hugely reduces the legacy impact and closure costs.
- The modular tank system is able to be readily dismantled and is fully relocatable reducing waste and environmental impacts of disposal of large volumes of fill materials as would be used in earth embankments. A high degree of flexibility is available to the client if future plans for land use conflict with the location of the tanks.

The design saved a volume of 19,000m^3 (24,900yd^3) of fill that was required to form the embankments and reduced the required land area by half. Cost analysis also determined the geosynthetic cost was for the modular tank system was half that of the earth bank storage option.

Figure 1. Traditional Storage pond onsite with above ground embankment.

Figure 2. Two Modular Storage Tanks.

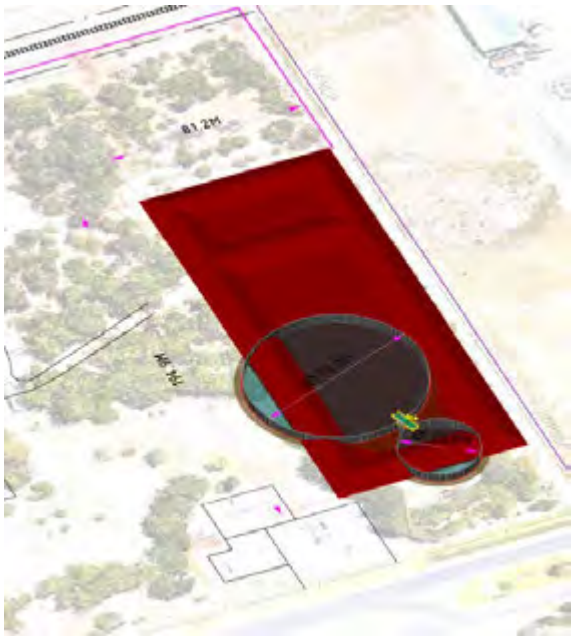

Figure 3. Comparative footprint of tanks vs embankment pond.

The ground water table at the site is shallow at 2.1m (7') depth. A loss of containment would prove disastrous and likely contaminate the groundwater. The tank design incorporated a leak detection system, consisting of a primary geomembrane liner, a non-woven geotextile separation layer and a secondary geomembrane liner incorporating a drainage sump. Any liquid detected in the secondary liner sump activates a return pump and triggers an alarm in the plant control room to alert the operator in the event of a leak. The return pump maintains a zero head pressure on the secondary liner. For additional redundancy a tertiary geosynthetic clay liner (GCL) was included in the design under the tank liner system. A water filled ballast system was incorporated into the design to retain geomembrane liner system in position until the tank entered into service.

GEOSYNTHETIC MATERIAL SELECTION

While a number of alternate geomembrane material options demonstrate the required resistance to the process liquor, a combination of factors made geomembrane material selection critically important. In addition to the required chemical resistance, the primary geomembrane liner material needed to have excellent resistance to UV radiation, be flexible for ease of installation in a tank structure, have high puncture resistance, tolerant to folding and wrinkles, and ability to tolerate elevated ambient and operating temperatures.

A selection process using a decision making and risk assessment matrix was used to determine suitable materials. The material evaluation included analysis of test results for UV weathering, oxidation induction time (OIT and HP-OIT), tensile strength and elongation, notched constant tensile load stress crack resistance, truncated cone testing and axi-symmetric break resistance strain (multiaxial tensile) tests. It was evident a highly fortified polyolefin was required. The geomembrane manufacturer's 1.00mm thick Enviro Liner 6000 geomembrane, a proprietary polyethylene material was selected as having the best combination of properties to achieve the required performance. During the development of the geomembrane, considerable long-term

testing was undertaken. The material exhibited 90% retention of original strength after exposure to 30,000hours of UV exposure to ASTM D 4329, and achieves a high-pressure oxidative induction time (HPOIT) greater than 2000 minutes.

In addition, a white surface was specified to minimise thermal impacts associated with the high levels of solar exposure. Testing revealed geomembrane surface temperatures can be reduced by up to 46% using a white surface in comparison to the traditional black surface.

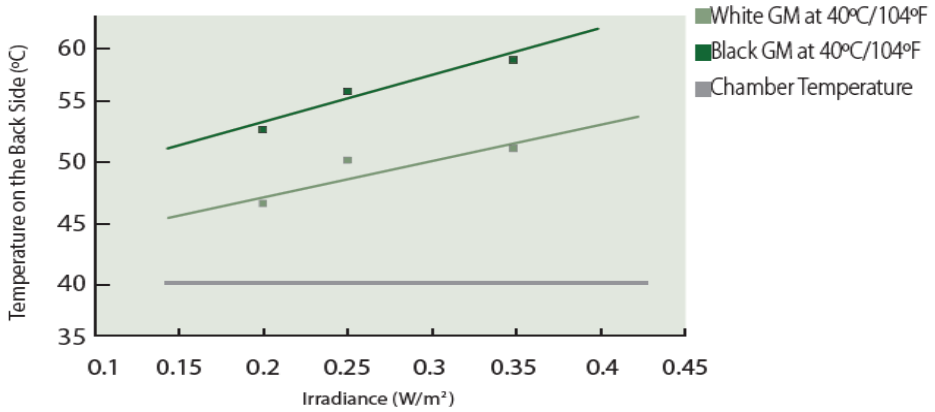

Figure 4. Effect of geomembrane colour on surface temperature.

It was decided to use the same geomembrane material for both the primary and secondary liners to provide installation flexibility, reduce logistical and material handling requirements and to maximise material utilisation (minimal wastage).

The leak detection system incorporated a geotextile separation layer to provide rapid transmissivity of any leakage in the primary liner to the leak detection sump. A non-woven conductive geotextile was selected with appropriate chemical resistance to the process liquor. By using a conductive geotextile, the primary liner could be spark tested after installation providing additional quality assurance capability prior to commissioning and hand-over to the client.

The design of the containment system included water filled ballast system to keep the liner system in position after installation prior to the tank being placed into service. The material selected for the ballasting system was a thin film polyethylene blown tubing utilising a similar stabilisation package as used in the primary liner.

OPERATONAL FLEXIBILITY

With a storage solution determined it became apparent to the client that additional operational flexibility could be realised. While the focus had been on achieving a 15ML storage solution for the planned shut down it was recognised the tanks would be capable of alleviating other operational issues at the plant. While the region is classified as Mediterranean hot summer climate, during winter storms the site has experienced incidents of stormwater flooding. The state regulatory authority had previously identified storm water management as an issue due to the lack of a facility to receive stormwater that needed to be addressed. Of particular concern was the risk surface contamination could escape the site boundary during wet weather events. During normal plant operation when not required to store process liquor the storage tanks can be converted to storm water storage, which can be used internally in the plant for refinery water balancing, potentially saving up the 15ML of municipal supplied water.

The tanks also eliminate the necessity to use the evaporation cells for temporary storage where process liquor become heavily contaminated with chlorides. When returned to the processing plant the contaminated liquor causes severe corrosion effects on vessels, pumps and pipework.

PROJECT EXECUTION and RESULTS

During the evaluation stage the client inspected several sites interstate to review similar installations and undertook detailed structural, integrity and environmental analysis, prior to making the required submissions to the state environmental and regulatory authorities for approval. The authorities were sufficiently impressed with the innovative solution that a contingent of 8 regulators made an extraordinary site visit to witness the site during construction to educate themselves in the understanding of the design and the high level of quality assurance and quality control measures being adopted on the geomembrane liners. The project also demonstrated to the authorities the client was making pro-active improvements to their operations with a high degree of focus on minimising their environmental impact.

Due to the tight timeline and desire to minimise construction time on site, both the primary and secondary liners were prefabricated into large panels in a factory environment before being deployed on site in a number of hours. The entire construction period for both tanks, including civil earthworks, was completed in less than 3 weeks with the tanks tested and commissioned before the required date and have been in incident free operation since.

Figure 5. Tanks at handover.

Figure 6. Tank in use.

ACKNOWLEDGEMENTS

Barry, S.; Avey, P.; Tunney, P.; Ormsby, J.; Jeffries, N.; Concept Environmental Services Pty. Ltd.

REFERENCES

Bhartu, V.G. (2015): *Degradation of Mechanical Properties of Geotextiles and Geomembranes Exposed to Outdoor Solar Radiation under Various Exposure Conditions—Part I: Results of UV-Degradation.*

Dolez, P. I.; Beaumier, D.; Taghizadeh, A.; Blond, E. (2017): *Effect of White and Black Colors on Heat Generation in Polyethylene Geomembranes Exposed to Solar Radiation.*

Geiger, R. (1954): Landolt-Börnstein – *Zahlenwerte und Funktionen aus Physik, Chemie, Astronomie, Geophysik und Technik,* alte Serie Vol. 3, Ch. Klassifikation der Klimate nach W. Köppen. – Springer, Berlin. 603–607. [Landolt-Börnstein - *Numerical Values and Functions from Physics, Chemistry, Astronomy, Geophysics and Technology,* old series Vol. 3, Ch. Classification of Climates According to W. Köppen. – Springer, Berlin. 603–607].

Geiger, R. (1961): Überarbeitete Neuausgabe von Geiger, R.: KöppenGeiger / Klima der Erde. (Wandkarte 1:16 Mill.). – KlettPerthes, Gotha. [Revised new edition by Geiger, R .: KöppenGeiger / Klima der Erde. (Wall map 1:16 Mill). - KlettPerthes, Gotha].

Masuo, T. (1996): *Effects of Solar Radiation Intensity on the Surface Temperature of Colored HDPE Geomembrane.*

Mills, A. (2009): *Long-Term Weathering Stability and Warranty Implications for Thin Film Geomembranes*.

Department of Meteorology, Australian Government (2020): *Monthly Climate Statistics for 'PERTH AIRPORT' [009021] – 1944-2020.*

Geosynthetics Conference

Geomembrane Defect and Wrinkle Leakage Calculator

Timothy D. Stark, Ph.D., P.E.[1] and G. Farid Saud Medina[2]

[1] Professor of Civil Engineering, University of Illinois at Urbana-Champaign, 205 N. Mathews Ave., Urbana, IL 61801; e-mail: tstark@illinois.edu
[2] Research Assistant of Civil Engineering, University of Illinois at Urbana-Champaign, 205 N. Mathews Ave., Urbana, IL 61801; e-mail: gfs3@illinois.edu.

ABSTRACT

This paper describes a leakage rate calculator/spreadsheet that can be used to estimate and contrast the leakage for different containment facilities or ponds when using a compacted soil liner, geomembrane, or composite liner system and the money lost for each scenario given a particular water cost per volume. This calculator also estimates the leakage if wrinkles are present in the overlying geomembrane. These wrinkles increase the area over which leakage can occur because the leakage area is no longer the area of the geomembrane defect. The leakage area is increased even further if the wrinkles are interconnected across the containment area. The leakage rate with and without wrinkles is estimated using poor and good intimate contact (Giroud, 2016) and different types of geomembranes. It is anticipated that this calculator/spreadsheet can be used to facilitate selection of the containment system and geomembrane type to minimize leakage to the environment.

INTRODUCTION

Initially containment systems could consist of only a compacted soil liner (CSL) without a geomembrane. However, early studies by Kirk Brown and his colleagues (Brown and Anderson, 1980; Brown et al., 1983 and 1984) showed that some contaminants caused micro and macro changes in the CSL that could lead to an increase in hydraulic conductivity and additional contaminant transport or leakage. This resulted in the U.S. Environmental Protection Agency (USEPA) requiring a geomembrane to be placed over a CSL so the CSL would only be subjected to the contaminants at the location of geomembrane defects, if any. The resulting containment system is termed a composite liner system (CLS) and consists of a geomembrane in intimate contact with the underlying CSL (RCRA, 1988) so leakage only occurs over the area of the geomembrane defects. More recently, the required thickness of the CSL can be reduced or the CSL can be replaced with a geosynthetics clay liner (GCL).

Without a geomembrane the seepage or leakage through a CSL is estimated using Darcy's law:

$$Q = k_{CSL} * i * A_{Leakage} \quad (1)$$

where Q is the seepage or leakage through the CSL in Length $(L)^3$/second, e.g., m^3/sec, $A_{Leakage}$ is the area of leakage, e.g., m^2, which is the entire containment area without a geomembrane, k_{CSL} is the hydraulic conductivity of the CSL in L/second, e.g., m/sec, and i is the hydraulic gradient

which is the decrease in hydraulic head from the top to the bottom of the CSL divided by the thickness of the CSL. Darcy's law is used in the leakage rate calculator to estimate the leakage through just a CSL. Equation (1) shows that without a geomembrane the leakage area is the area exposed to the contained liquid, which will be large and thus and a large amount of leakage will be calculated. If the geomembrane (GM) is in intimate contact with the CSL, the area of leakage is just the area of the GM defects, which is significantly smaller than the entire containment area.

GEOMEMBRANE DEFECTS

The requirement of intimate contact is important because Giroud and Bonaparte (1989a) state that: "All liners leak" so reducing the area of leakage is important. Giroud (2016) revisits the frequency of GM holes per unit area after providing some guidelines in Giroud and Bonaparte (1989a and b). For example, Giroud and Touze-Foltz (2003) conclude that: (i) with construction quality assurance (CQA), the number of holes after installation is 1 to 5 holes per hectare but they are generally small and (ii) after soil placement above the geomembrane, the number of holes varies from 1 to 20 per hectare but these holes can be large. The area of the defects with good CQA range from 1 to 10 mm^2 and is important because the area of defects is used to calculate the leakage rate in Equation (2). If the defect occurs during soil placement, the area of the GM defects is much greater than 1 to 10 mm^2.

Giroud (2016) concludes that even with good CQA, 5 to 6 holes per hectare are typical after GM installation with good CQA. With limited CQA, i.e., limited to an engineer spot-checking the work performed by the geomembrane installer, a frequency of 25 holes per hectare or more is possible. Giroud (2016) presents the following equation for calculating the rate of leakage through a GM hole with an area (a_{defect}) in a composite liner system:

$$Q = 0.21 * \left[1 + 0.1 \left(\frac{h_{w-GM}}{t_{CSL}} \right)^{0.95} \right] * a_{defect}^{0.1} * (h_{w-GM})^{0.9} * k_{CSL}^{0.74} \qquad (2)$$

where:

Q = seepage or leakage through one (1) geomembrane defect with an area a, e.g., m^3/sec,
a_{defect} = area of GM defect, e.g., m^2,
t_{CSL} = thickness of the CSL, e.g., m,
h_{w-GM} = hydraulic head on GM, e.g., m, and Subpart D regulation limit is 0.3 m, and
k_{CSL} = hydraulic conductivity of CSL, e.g., m/sec.

Equation (2) is used in the calculator to estimate the leakage through a composite liner system with a GM defect. The area of the GM defect can refer to one defect or the total number of defects times the typical area of the defects. For example, if there are ten (10) GM defects with an area of 10 mm^2 each, the total defect area is 100 mm^2 (10*10 mm^2) or 0.1 m^2. Just a GM can be simulated in the calculator by assigning a high value of hydraulic conductivity to the underlying CSL, e.g., $k_{CSL} = 1x10^{-1}$ m/second, so flow can occur quickly through the GM defect.

WRINKLES

Field observations (see Figure 1) and prior studies (e.g., Giroud and Peggs 1990; Koerner et al. 1999) show that unreinforced high density polyethylene (HDPE) GMs are prone to significant thermally-induced wrinkles due to the high coefficient of thermal expansion and bending modulus of the GM.

Figure 1. Aerial photo showing connected wrinkles at Queens University Test Site (photo from Rowe, 2012).

Rowe (2012) presents the following equation to predict the amount of leakage through a hole in a GM coincident with (or adjacent to) a wrinkle using the variables shown in Figure 2:

$$Q_{Wrinkle} = L_{Wrinkle}\left[2*b*k_{CSL} + 2*\left(k_{CSL}*t_{CSL}*\theta\right)^{0.5}\right]*\left(\frac{h_d}{t_{CSL}}\right) \quad (3)$$

where:

$Q_{Wrinkle}$ = seepage or leakage through one (1) GM defect coincident with a wrinkle, e.g., m^3/sec,
$L_{Wrinkle}$ = length of the connected wrinkle, e.g., m,
$b_{Wrinkle}$ = one-half (1/2) the wrinkle width (see Fig. 2), e.g., m,
□ = transmissivity or flow between GM and CSL/GCL, e.g., m^2/sec,
t_{CSL} = thickness of the CSL, e.g., m,
h_d = head loss across composite liner system (see Fig. 2 where $h_d = (hw + H_L + H_A - h_a)$), e.g., m, and
k_{CSL} = hydraulic conductivity of CSL, e.g., m/sec.

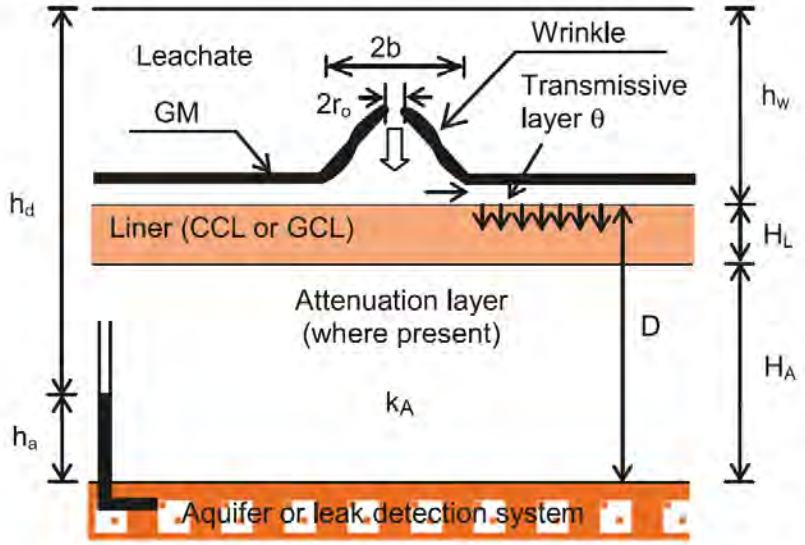

Figure 2. Schematic showing wrinkle dimensions and transmissivity below the wrinkle along the top of the GCL (figure from Rowe, 2012).

In Equation (3), the quantity 2 x $b_{Wrinkle}$ is the width of the wrinkle (see Figure 2), which is the dimension that is typically measured in the field. The other important parameter for estimating the leakage with a GM wrinkle is the transmissivity or flow between the GM and underlying CSL or GCL (□). Rowe (1998) provides the following guidelines for selecting the value of transmissivity when GM wrinkles are present:

- Good intimate contact between the GM and CSL with as few wrinkles as possible and a smooth subgrade surface, □ = 1.6×10^{-8} m^2/second and
- Poor intimate contact between the GM and CSL with a number of wrinkles and a rough subgrade surface, □ = 1.0×10^{-7} m^2/second.

Equation (3) is used in the calculator to estimate the leakage through a composite liner system with a wrinkle coincident or adjacent to the GM defect. A typical wrinkle width and length is included in the calculator for four different unreinforced GMs, which are defined below. The calculator is being expanded to include reinforced GMs that exhibit much greater dimensional stability and smaller winkles than unreinforced GMs. The calculator can be used to show that the presence of a wrinkle results in 100 to 1,000 times more leakage than for just a GM defect with the GM being in intimate contact with a CSL or GCL. The greater leakage rates calculated with a coincident wrinkle are in better agreement with field measured leakage through composite liner systems (Rowe, 2012), which confirms the importance of reducing wrinkles and complying with RCRA (1988) requirement of the geomembrane being in intimate contact with the CSL or GCL.

LEAKAGE CALCULATOR

This section describes the calculator/spreadsheet that can be used to estimate the leakage rate and money loss by leakage from a pond when it is lined with a CSL, GM, and/or a single composite

liner system with and without wrinkles. The leakage rate calculator/spreadsheet can be downloaded for free using the following link and distributed to colleagues: https://www.fabricatedgeomembrane.com/protected/pond-liner-calculator.

A hypothetical pond is used to illustrate use of the calculator and the range of leakage rate for different unreinforced GMs. The hypothetical pond is 122 m (400 ft) wide, 183 m (600 ft) long, and 7.6 m (25 ft) deep pond and illustrates a significant reduction in leakage and money lost is possible when using a GM or single composite liner system is used instead of just a CSL. Even with accounting for GM defects and wrinkles, the use of a GM significantly reduces the leakage mainly because the entire containment area is not being used to calculate in the leakage (see Equation (1)).

The GM leakage calculator is divided into four (4) main steps: (1) Input Project Information and General Calculations, (2) Detailed information on CSL and GM engineering properties, (3) calculation of Typical Leakage Rates for CSL, GM, and composite liner system, and (4) Plotting the results for comparison purposes.

Figure 3 presents a screen-shot of Step One (1) of the GM leakage calculator, which summarizes the general information of the pond or containment facility that is being considered. In each step of the calculator, the blue cells are items that the user inputs, e.g., pond top width, top length, and depth of the pond being considered. The units for each input parameter are provided next to each input cell but English and SI units can be used. However, all of the input parameters must be in a consistent system. The green cells are the items that are calculated using the user inputs, e.g., total volume of the pond, leakage through the CSL and GM and money lost due to the leakage based on the cost of the water supplied by the user. Some other calculated parameters are presented in the worksheet in a different format given that these are used simply for further calculations, but at the same time, it may be valuable for the user to view these items, e.g., area of the bottom of the pond, side slopes, and total leakage area, hydraulic gradient through the CSL and GM defect (obtained from the landfill requirements and specifications of the different geomembranes).

STEP ONE (General Calculations & Summary)

For a pond with the following dimensions: Top Width	400	meters
Pond Top Length	600	meters
Pond Depth,	25	meters
Total/overall volume of the pond is:	31,852,428.2	m3
with a compacted soil hydraulic conductivity of *	1.00E-07	cm/sec
and a geomembrane hydraulic conductivity of **	1.00E-12	cm/sec
Leakage through the compacted soil liner is:	1,078.2	cm3/sec
Leakage through a geomembrane is ONLY:	2.1	cm3/sec
Cost of water is:	US$25,000.00	/acre-foot
Lost Money due to Compacted Soil Leakage:	30,500.65	$/year
Lost Money due to Geomembrane Leakage:	60.04	$/year

NOTES:

*Compacted soil hydraulic conductivty is 1x10-7 cm/sec based on Subtitles D and C landfill requirements

**Geomembrane hydraulic conductivty ranges from 1x10-10 to 1x10-14 cm/sec for typical products based on vapor transmission testing

Figure 3. Step One input parameters for the GM leakage calculator for a CSL, GM, and a composite liner system.

In particular, Step One (1) requires the following user input **(**see Figure 3):

- "Pond Top Width" for the pond to be analyzed in meters or feet,
- "Pond Top Length" in m or feet,
- "Pond Depth" in m or feet,
- "…with a compacted soil hydraulic conductivity of *", refers to the hydraulic conductivity of the CSL and a typical value of $1x10^{-7}$ cm/second is shown below Step One*.
- "…with a geomembrane hydraulic conductivity of **", refers to the hydraulic conductivity of the GM geomembrane and a typical value of $1x10^{-10}$ to $1x10^{-14}$ cm/second is shown below Step One**.
- "Cost of Water is:" the cost in USD of an acre-foot of water for a determined site, e.g. $25,000.00. An additional cell right next to this parameter provides a typical range of $200 to $3,400,000.

Figure 4 presents Step Two (2) of the GM leakage calculator, which involves entering the hydraulic conductivity and thickness of the CSL and GM. In addition, the number of GM defects and level of intimate contact with the CSL anticipated for the GM are entered depending on the level of CQA. In this section, typical wrinkle dimensions are included for unreinforced High Density Polyethylene (HDPE), Linear Low Density Polyethylene (LLDPE), Polyvinyl Chloride (PVC), and flexible polypropylene (fPP) but these values can be changed by the user. In this section the head loss anticipated across the CSL is entered along with the transmissivity between the GM and the underlying CSL or GCL (□). Using this information, the calculator estimates the leakage for a CSL, GM without defects, GM with defects, the four (4) unreinforced GMs with defects and wrinkles, and a composite liner system.

Figure 4. Step Two input parameters and the calculated values of leakage for a CSL, GM, and a composite liner system.

In particular, Step Two (2) has three major subdivisions that group the parameters to characterize pond geometry and various properties of the CSL and GM **(**see Figure 4):

- "Pond freeboard", represents the distance to the top of the water or liquid below surface of the pond,
- "H" is the horizontal component of the slope ratio of pond to be analyzed,
- "V" is the vertical component of the slope ratio.
- "Thickness" of the CSL and GM in m or feet,
- "Hydraulic Conductivity, k" of the CSL and GM, and
- "# of holes per hectare" measured for a geomembrane when measured with "high inspection" as specified by …

Figure 5 presents Step Three (3) of the GM leakage calculator, which involves calculating the values of leakage rates for a CSL and GM in cm^3/second and gallons/day (not pictured) for different pond depths with a sideslope of 3H:1V. Figure 6 presents the final step of the calculator, Step Four (4), in which the leakage rate and the money lost for both CSL and GM based liner systems are tabulated for an easy comparison and plotting.

Typical Leakage Rates (cm^3/sec) For Slope 3H:1V					
Hydraulic Conductivity (cm/sec)	1.5 m depth	3 m depth	4.5 m depth	6 m depth	7.5 m depth
1 x 10-4-Compacted Soil	3,920.55	10,617.61	17,459.41	24,378.10	31,305.83
1 x 10-5-Compacted Soil	392.05	1,061.76	1,745.94	2,437.81	3,130.58
1 x 10-6-Compacted Soil	39.21	106.18	174.59	243.78	313.06
1 x 10-7-Compacted Soil	3.92	10.62	17.46	24.38	31.31
1 x 10-8-Compacted Soil	0.39	1.06	1.75	2.44	3.13
1 x 10-14 Geomembrane	0.000009	0.000025	0.000042	0.000059	0.000075

Figure 5. Step Three calculated values of leakage rates for a CSL and GM in cm^3/second.

STEP FOUR (Plot and Comparison)					
Compacted Soil Liner Hydraulic Conductivity	1.00E-07	cm/sec			
Geomembrane Hydraulic Conductivity	1.00E-12	cm/sec			
Depth (m)	Volume of Pond (m^3)	Leakage for Soil Liner (cm^3/sec)	Leakage for Geomembrane (cm^3/sec)	Money Loss for Compacted Soil (US Dollar/Day)	Money Loss for Geomembrane (US Dollar/Day)
5	8,210,693.6	137.45	0.270560	US$240.69	US$0.47
10	15,400,296.1	368.89	0.726150	US$645.97	US$1.27
15	21,669,794.8	603.03	1.187060	US$1,055.98	US$2.08
20	27,120,176.4	839.57	1.652700	US$1,470.21	US$2.89
25	31,852,428.2	1078.24	2.122515	US$1,888.14	US$3.72

Figure 6. Step Four calculated values of pond volume, leakage rates, and money lost for a CSL and GM in cubic meters (m^3), cm^3/sec, and dollars/day, respectively.

Figure 7 presents a graph of pond volume in cubic meters versus total leakage in cm^3/sec for a CSL and GM. This plot shows that even with considering defects in the GM, the leakage is significantly less than that of just a CSL because of the large seepage area. In fact, the leakage with just a GM is so low that the trend line plots at essentially zero (0).

Figure 8 presents a graph of pond volume versus total leakage for the four unreinforced GMs considered, i.e., HDPE, LLDPE, PVC, and fPP. All of the leakage rates are significantly less than that for just a CSL, i.e., Figure 8 uses an expanded scale to show the difference in the leakage rates for the four unreinforced GMs all of which are much less than just a CSL. Figure 8 shows the highest leakage rate for an HDPE geomembrane because of the larger wrinkle size and fPP and PVC geomembranes yield essentially the same leakage rate so their separate curves are not visible.

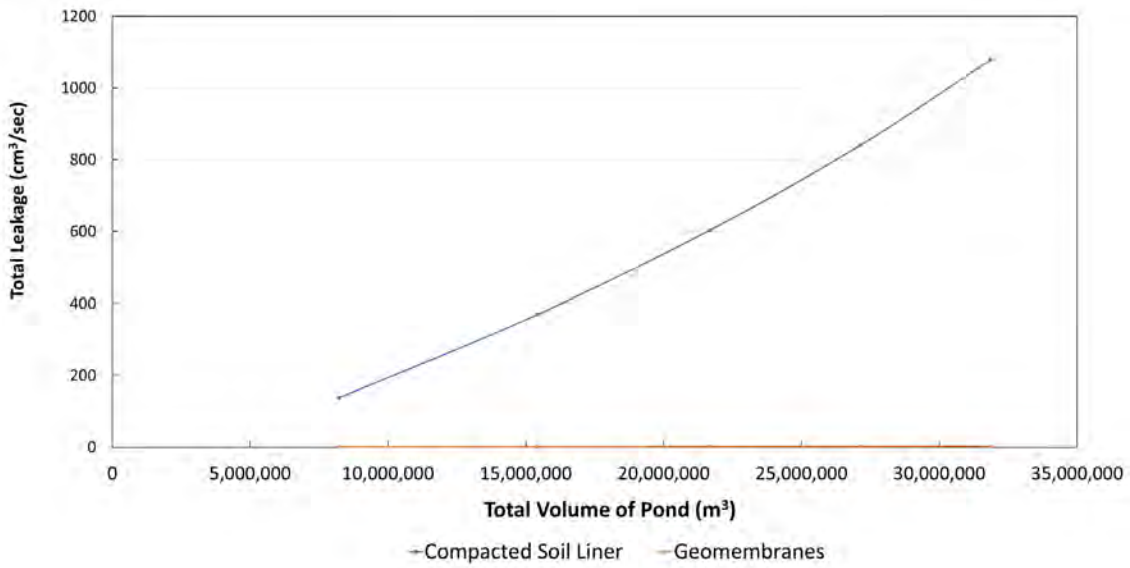

Figure 7. Plot of pond volume versus total leakage with 3H:1V sideslopes for a CSL and GM.

SUMMARY

A leakage calculator is described herein that can be used to quickly estimate the leakage rates for a CSL, GM, and composite liner system. The calculator uses Darcy's Law to calculate the leakage rate for a CSL, which results in the highest leakage because the entire area of the containment facility that is exposed to liquid is used in the calculation. The leakage equation from Giroud (2018) is used to estimate leakage through a geomembrane with defects and good and poor contact with the underlying subgrade. Geomembrane wrinkles are considered in the leakage rate calculation via the equation by Rowe (2012) and typical wrinkle dimensions for unreinforced geomembranes that are included in the calculator based on field observations. The results for a hypothetical pond show that even with defects and wrinkles, the geomembrane lined pond still yields significantly lower leakage than a CSL lined pond.

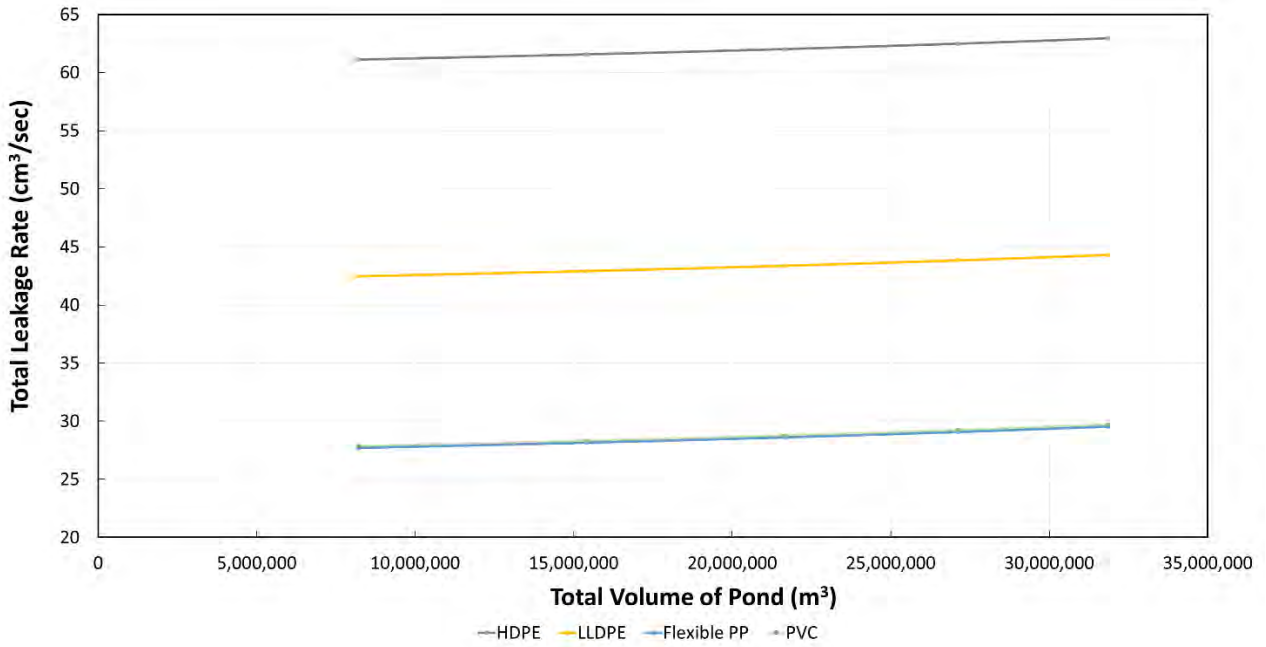

Figure 8. Step Four calculated values of pond volume and leakage rates for the unreinforced HDPE, LLDPE, fPP, and PVC geomembranes with fPP and PVC plotting together.

REFERENCES

Brown, K.W. and Anderson, D.C. (1980). "Effect of Organic Chemicals on Clay Liner Permeability: A Review of Literature. In Disposal of Hazardous Waste," Proceedings of Sixth Annual Research Symposium, EPA - 60019 -80 -010, Chicago, Illinois, March 17 - 20.

Brown, K.W., Green, J., and Thomas, J. (1983). "The Influence of Selected Organic Liquids on the Permeability of Clay Liners. Land Disposal of Hazardous Waste," Proceedings of Ninth Annual Research Symposium, EPA - 60019 - 83 - 018, Ft. Mitchell, Kentucky, May 2 - 4.

Brown, K.W., Thomas, J.C., and Green, J.W. (1984). "Permeability of Compacted Soils to Solvents Mixtures and Petroleum Products In Land Disposal of Hazardous Waste," Proceedings of the Tenth Annual Research Symposium, EPA - 60019 - 84 - 007, Ft. Mitchell, Kentucky, April 3 - 5.

Giroud, J.P. (2016) Leakage Control Using Geomembrane Liners. Geosynthetics International, 5th Victor de Mello Lecture, *J. Soils and Rocks*, Brazilian Society for Soil Mechanics and Geotechnical Engineering, 39(3): 213-235.
http://victorfbdemello.com.br/arquivos/Lectures/Giroud-de-Mello-Lecture-Paper.pdf

Giroud, J.P. and Bonaparte, R. (1989a) Leakage through liners constructed with geomembranes, Part I: Geomembrane liners. Geotextiles and Geomembranes Journal, 8(1):27-67.

Giroud, J.P. and Bonaparte, R. (1989b) Leakage through liners constructed with geomembranes, Part II: Composite liners. Geotextiles and Geomembranes Journal, 8(2):71-111.

Giroud, J.P. and Peggs, I.D. (1990). Geomembrane construction quality assurance. In Waste containment systems: construction, regulation and performance. Geotechnical Special Publication No. 26. Edited by R. Bonaparte. American Society of Civil Engineers, New York. pp. 190–225.

Koerner, G.R., Eith, A.W., and Tanese, M. (1999). Properties of exhumed HDPE fieldwaves. Geotextiles and Geomembranes, 17(4): 247–261. doi:10.1016/S0266-1144(98)00024-7.

Resource Conservation and Recovery Act (RCRA), (1988). Code of Federal Regulations (CFR) parts 239 through 282, CHAPTER 4 SUBPART D DESIGN CRITERIA https://archive.epa.gov/epawaste/nonhaz/municipal/web/pdf/subpartd.pdf

Rowe, R.K. (1998). Geosynthetics and the minimization of contaminant migration through barrier systems beneath solid waste. In Proceedings of the 6th International Conference on Geosynthetics, Atlanta, Ga., 25–29 March 1998. Edited by R.K. Rowe. Industrial Fabrics Association International, St. Paul, Minn. Vol. 1, pp. 27–103.

Rowe, R.K. (2012) Short- and long-term leakage through composite liners. The 7th Arthur Casagrande Lecture. Canadian Geotechnical Journal, 49:141-169.

Geosynthetics Conference

Renewing the Maerkle Reservoir for the City of Carlsbad with Advanced Floating Cover Technology

Douglas Hilts P.E.,[1] and Patrick Elliott[2]

[1]Hilts Consulting Group, Yorba Linda, CA; e-mail: doug.hcg@hiltsconsulting.com
[2] Director of Installation Services, Raven Engineered Films, P.O. Box 5107, Sioux Falls, SD; e-mail: pat.elliott@ravenind.com

ABSTRACT

Maerkle Reservoir is the primary potable water storage reservoir for the City of Carlsbad and provides 10-day operational storage. Carlsbad Municipal Water District (CMWD) is a subsidiary of the City of Carlsbad. Maerkle reservoir was originally constructed in the early 1960s as an earthen, open-air reservoir. In 2019, CMWD decided to replace the existing floating cover and incorporate industry advancements. The 20-year old floating cover was at the end of its useful material life.

CMWD retained Hilts Consulting Group to provide engineering design services, and Raven Engineered Films / Raven CLI Construction for installation services of the Maerkle geomembrane floating cover. Jobsite challenges included an expedited installation schedule while still providing a high-quality, cost-effective solution. The short installation schedule was addressed through the effective use of large factory fabricated panels to increase quality and save time and costs. The unique reservoir geometry with varying slopes provided some design challenges. The design work had to be completed while the reservoir was in-service without the benefit of knowing the reservoir geometry below water level. The reservoir geometry was later verified during construction and the initial design adjusted to actual site conditions.

This project was highly challenging to bring in on time and within budget. Still, through massive teamwork and creative thinking, the collective team overcame obstacles to successful completion. Ultimately CMWD received a high-quality advanced floating cover system to meet their budget and effectively protect one of our most precious resources; clean drinking water.

INTRODUCTION

Carlsbad Municipal Water District (CMWD) is a subsidiary to the City of Carlsbad, California. CMWD purchases potable water through the San Diego County Water Authority (SDCWA) via four metered connections. Water is imported from the Colorado River via the Metropolitan Water District of Southern California. Maerkle Reservoir is the primary water storage reservoir for the City of Carlsbad and provides 10-day operational storage. The capacity is approximately 741 million liters (196 million gallons), with a 69,000 square meters (17-acre) horizontal surface and 18.3-meter (60-foot) maximum water depth. Additional onsite storage is available from an adjacent 38 million liter (10 million gallon) buried concrete tank.

Maerkle Reservoir was originally constructed in the early 1960s as a potable water open-air reservoir with earthen side slopes and floor and meandering shorelines. The reservoir was

created with the construction of an earthen dam with a maximum height of 50.3 meter (165 feet) and 243.8 meter (800 feet) long.

In 1996 the reservoir interior was reformed into a defined shape with straight tangents and geometric curves, floor and side slopes were regraded, and a porous asphalt liner was placed on the reservoir slopes and floor. Additionally, a perimeter concrete ringwall was constructed at the top of the slope, and a reinforced polypropylene geomembrane floating cover was installed. The polypropylene floating cover was then anchored to the perimeter cast-in-place concrete ringwall at the top of the slope. The polypropylene floating cover was weight tensioned with defined sumps, included multiple small submersible pumps to serve as the rainwater removal system, and multiple aluminum access hatches. The rainwater removal system included discharge hoses on the floating cover to pump rainwater up to the top of the slope and then discharged onto the existing asphalt perimeter road, sloped down to V-ditches, and buried storm drainpipes.

After approximately 20 years in service, the existing polypropylene floating cover geomembrane had reached the end of its useful material life. CMWD sought to replace the existing floating cover. The principle project objective was to replace the existing floating cover system with a new floating cover that would incorporate the latest industry advancements since the original polypropylene floating cover was installed. All reservoir modifications and improvements were to be performed in compliance with and approved by the California Division of Drinking Water (CA-DDW) and California Division Safety of Dams (CA-DSOD). The objective for the replacement geomembrane floating cover project was to provide a cost-effective solution that would protect and preserve the potable water quality and meet regulatory requirements.

PROJECT DESCRIPTION

The Maerkle Reservoir is formed by an earthen dam on the south end and graded earthen side slopes on the other reservoir sides. Maerkle Reservoir has a potable water storage capacity of approximately 741 million liters (196 million gallons) with a horizontal surface area defined by the top of slope across 69,000 square meters (17 acres). The reservoir shape is unique, with eight straight tangent sections and eight curves. The interior earthen side slopes vary throughout the reservoir ranging from 2½: 1 to 4½: 1. The reservoir interior is over 19.2 meter (63 feet) high with a maximum water depth of 18.3 meter (60 feet), the reservoir floor slopes with a 3 meter (10-foot) height differential. The top of the slope is defined with a cast-in-place concrete ringwall and an asphalt paved perimeter road. Site drainage is provided by catch basins and storm drainpipes located on the reservoir east and west sides.

The reservoir has a single 107 centimeter (42 inch) buried inlet pipe, which terminates in the reservoir floor with an upturned pipe located in a cast-in-place concrete inlet structure covered with a stainless steel grillage cage. The reservoir outlet consists of a single 76 centimeter (30 inch) buried pipeline with three cast-in-place concrete outlet structures covered with stainless steel grillage cages and located along the reservoir interior slope. Within each concrete outlet structure, there is a 76 centimeter (30-inch) valve to control outlet flows and regulate the depth of water introduced into the water distribution system. A cast-in-place concrete overflow structure is located near the top of the slope discharges into a concrete channel. The overflow structure opening is covered with a stainless steel grillage cage.

The reservoir normal operating ranges vary between 7.3 meter to 11.3 meter (24 feet to 37 feet) in water depth. During winter outages for water system maintenance periods, the reservoir will operate at a maximum water depth of 17.7 meter to 18.3 meter (58 feet to 60 feet).

With the prior polypropylene floating cover, CMWD personnel would work on the floating cover several times a week to obtain water quality samples at the cover access hatch locations. The replacement floating cover project consisted of the following major project elements:

- A geomembrane chafer located on reservoir side slopes anchored at the top of the slope ringwall and extending downslope to the below the reservoir low water operating level.
- Weight tensioned geomembrane floating cover system with rainwater removal sumps and pumps, access hatches, vacuum vents, and walkways.
- A remote water quality sample retrieval system.
- Three outlet butterfly valves with hydraulic actuators, hydraulic lines, and a hydraulic power unit located at the top of the slope.
- New buried rainwater removal pipe laterals in perimeter roadway.
- Electrical system upgrades to accommodate larger rainwater removal pump capacity and provisions for possible future mixer equipment.
- Reconditioning of existing stainless steel pipe grillage cages.
- Recoating exposed portions of the existing inlet pipe and outlet pipes within the reservoir.

The project consisted of the following phases:

1. Preliminary Design Report: includes defining project scope, establishing design parameters, selection of critical materials and systems, initial regulatory agency coordination, development of overall project schedule, and construction cost estimates.
2. Final design: includes the performance of detailed design resulting in comprehensive design drawings, engineering calculations, contract documents, technical specifications, engineer's opinion of construction cost, and regulatory agency approvals.
3. Public Bidding and Award: includes project documents issued for public bidding by experienced, knowledgeable, and qualified contractors, submission of sealed bids, Owner's evaluation of bids, and award of construction contract by City council.
4. Construction: includes material procurement, preparation of construction submittals/shop drawings, shop fabrication of geomembrane panels, early procurement of long-lead items, site construction, floating cover inflation, inspection, and implementation of quality assurance provisions.
5. Start-up and Commission: includes equipment testing, reservoir filling and disinfection, water quality testing, and Owner Operations and Maintenance (O&M) training.

DESIGN

Floating covers are generally classified as non-tensioned or tensioned. Non-tensioned floating covers are less efficient in removing rainwater and are less accommodating for personnel access on top of the floating cover. A non-tensioned floating cover for potable water reservoirs is not considered current state-of-the-art practice and, therefore, was not recommended. Tensioned floating covers are either weight-tensioned or mechanically tensioned. Tensioning the floating

cover material enhances rainwater removal and permits personnel access on top of the floating cover. Therefore, the preferred method for potable water reservoir applications is tensioned floating covers.

The floating cover type recommended was a weight-tensioned floating cover constructed with minimum 45-mil thick reinforced geomembrane material. Weight-tensioned floating covers consist of rainwater collection troughs located on the reservoir floor near the toe of the slope, reservoir curves, and other key locations where slack floating cover material will develop. Rainwater collection troughs contain a series of weights and floats strategically located throughout the floating cover. The depth of the rainwater collection troughs varies to accommodate slack floating cover material as it develops during reservoir water surface fluctuations. A tensioned floating cover allows personnel to walk on the floating cover while in service to conduct as-needed water quality tests and to perform necessary inspections and maintenance activities. A tensioned floating cover also reduces the amount of wrinkles (see figure 7), ponding of surface water on the top side, and provides more efficient removal of rainwater. The floating cover is tensioned by a series of strategically placed weights and floats, which will also serve as the rainwater removal troughs (see figure 9).

A 45-mil geomembrane chafer was installed between the floating cover and existing asphalt concrete lining. The chafer serves as a sacrificial material to protect the floating cover from incidental punctures and rough subgrade abrasions. The chafer was attached to the perimeter ringwall and extended from the top of the slope downslope to an elevation below the reservoir low water operating range. The chafer enables the floating cover to rest on a similar sacrificial geomembrane material when those portions of the cover are not floating on the water surface.

Total floating cover appurtenances included (18) stainless steel access hatches. A portion of the access hatches have special provisions to accommodate pressure sensors that monitor reservoir water depth, water temperature, and possible future submersible mixers. Five stainless steel vacuum vents were provided at hydraulic structures (inlet, outlets, and overflow). Textured geomembrane material was incorporated in the floating cover to provide personnel access onto the floating cover, especially on the reservoir side slopes.

Geomembrane Material Selection. During preliminary design, several geomembrane material options were investigated for the geomembrane chafer and floating cover components. The initial evaluation considered unreinforced and reinforced geomembranes. Unreinforced geomembranes were eliminated based on required long-term strength, flexibility requirements, and floating cover regulatory requirements. Reinforced geomembrane material options were evaluated based on historical performance, required physical properties, environmental properties, material warranty, material cost, installation, seaming, aged repairs, color options, and NSF 61 approval for contact with potable water. Material advantages and disadvantages were then compared and reviewed with CMWD. Reinforced Chlorosulfonated Polyethylene (CSPE) was ultimately selected as the geomembrane providing the best value for the floating cover and chafer.

Rainwater Removal. The floating cover rainwater removal system was scoped and sized based on two storm-level designs. The first design was based on pumping capacity to remove a 10-year storm, a 24-hour duration 48 hours after the start of the storm. The second design was based on a 25-year storm, a 24-hour duration 72 hours after the start of the storm. Pump redundancy was provided by assuming that one pump may be out of service at any given time. A total of four 5-horsepower submersible pumps were provided. The submersible pumps are located in perforated

PVC pipe sump wells located within the rainwater removal troughs, as part of the floating cover tensioning mechanism (see figure 8).

Remote Water Quality Sampling. Previous practice for CMWD personnel to obtain water quality samples involved walking on the floating cover and manually obtaining water samples through floating cover access hatches. The new floating cover system provides updated remote water quality sampling directly through sampling pumps incorporated at identified hatch locations with flexible tubing installed from the sampling pump to a sample station port located at the top of the slope. Water quality samples can now be conveniently obtained by site personnel at the reservoir perimeter road without entering onto the floating cover.

Outlet Valves & HPU replacement. The older existing pneumatic actuated outlet valves were replaced with new hydraulic operated butterfly valves with submersible actuators. The hydraulic system utilizes food-grade oil to operate the valve actuators. The valve actuators are controlled by a hydraulic power unit located at the top of slope. Stainless steel hydraulic tubing was installed, and the system is pressurized.

Electrical Modifications. The electrical modifications included upgrading the reservoir area electrical system capacity and infrastructure to power the new advanced floating cover rainwater removal pumps. The new pump size was significantly increased in scale, horsepower, and pump capacity from the previous floating cover pumps. The older 120/240 volt transformer/panel was replaced with a new 480 volt, 3-phase electrical distribution system.

Storm Drain Laterals. Four new buried PVC pipe laterals were installed in the reservoir perimeter road to accommodate the rainwater removal pump discharge at the top of the slope perimeter ringwall, and rainwater was conveyed to existing storm drainpipes.

Future Mixer Provisions. Updated provisions were incorporated in the floating cover access hatches, and electrical modifications were made to accommodate up to six submersible electrical mixers. This update was done to allow for future water quality enhancements by reducing stagnant zones and creating a more uniform distribution of disinfectant throughout the water.

CONSTRUCTION

Material Procurement. With a project of this magnitude, procuring the critical path items in a timely manner was crucial to the construction project's success. The CSPE floating cover material and outlet valve components were the largest obstacles to overcome for the Maerkle floating cover construction — it took a highly-collaborative effort to ensure items were submitted, approved, and ordered within the milestone dates of the project. The complex floating cover design required the use of advanced accessories and hardware with extended delivery dates, Hilts Consulting Group worked closely with Raven to ensure the team maintained on top of the procurement process and that items were reviewed weekly with the Maerkle team and tracked closely through completion to align with the delivery and installation dates of the cover material.

Fabrication. Fabrication played a vital role in this project for several reasons. The CSPE material chosen for this project is manufactured in rolls that are 155 centimeters (61 inches) wide. By

custom fabricating the panels for this project, the fabricator could maximize their production in a controlled factory environment and significantly reduce the number of field welded seams. The large fabricated panels utilized roll stock that combined seven panels to create one large custom panel. The chafer layer consisted of 101 fabricated panels total (see figure 1) and an additional 117 custom panels for the floating cover (see figure 2). The fabricator was also able to prefabricate all the appurtenances for this project, including sand tubes, float skins, repair floats, sand tube tabs, hatch floats, vent floats, etc., this considerably reduced the field time required for installation.

Installation. As the General Contractor of this project, the installation contractor regularly coordinated with all of the project subcontractors to ensure a smooth installation of work to be done. Starting with the interior fence removal for better site access to allow for demo of the existing floating cover. The installation contractor then coordinated with their subcontractors to remove existing asphalt for new storm drain connections and new electrical trenches for the upgraded electrical system (see figure 4). The installation contractor began deploying the chafer (see figure 3) after the electrical trenches were backfilled and followed the electricians around the reservoir, working together to keep production levels high. Upon completion of the chafer, deployment of the actual floating cover prefabricated panels began (see figure 5). Both the chafer and the floating cover panel deployments went very smoothly due to the cost-effective use of the large prefabricated factory panels provided by the fabrication team (see figure 6). Finally, the floating cover system was closed up; however, it needed to be cut open again to reinstall the valves and actuators due to delays of the advanced valves and actuators. Upon the final closing of the floating cover, the interior fence was reinstalled around the reservoir, and the electrical and storm drain trenches were all tested for compaction, and new asphalt was placed as applicable (see figure 10).

Outlet Valves & HPU. Although the outlet valves and hydraulic power unit (HPU) were fabricated and managed domestically, the actuators needed for the project were manufactured in Italy, posing some coordination and timing issues for the project completion. Due to the timing, being faced with seemingly unreachable goals for overseas shipments, the installation contractor and the Maerkle construction team had to perform many workarounds to accommodate the timing issues and keep the project moving forward. However, with the assistance of subcontractors Rotork and Henry Pratt, the General Contractor was able to get all the valves, actuators, and HPU to site and installed meeting a firm Division Safety of Dams (DSOD) inspection date. With only a few minor issues during the installation process, the system worked flawlessly during the initial start-up and was an excellent addition to the upgraded Maerkle Reservoir project.

Construction Start-up. The reservoir disinfection and fill phase started in late January 2020. The reservoir was disinfected following American Water Works Association (AWWA) Standard C652, Method 3, which consisted of filling the reservoir to 5% of reservoir volume with potable water and an available chlorine concentration of not less than 50 ppm. A target 60 ppm chlorine residual was established for the initial fill. A licensed specialty contractor was used to perform reservoir start-up disinfection by injecting a liquid chlorine solution into the reservoir inlet pipe at a rate dependent on the solution chlorine concentration, reservoir water inflow rate, and desired target chlorine residual. The reservoir water chlorine concentration was monitored every couple of hours at various access hatches located in the floating cover. The water/chorine fill proceeded continuously at a reduced flow rate for approximately 30 hours until it obtained the 5% reservoir

volume mark. At this point, the reservoir fill and chlorine injection were temporarily stopped for a 6 hour hold period. At the end of the hold period, the reservoir water chlorine residual was tested to verify that the reservoir water chlorine residual was acceptable to meet standards. At this point, the reservoir fill with potable water resumed at a higher flow rate. The increased flow rate varied based on available potable water due to customer demands, water transmission system hydraulic limits, and operator preferences. Chlorine residual was tested several times per day to monitor the dilution of the initial higher chlorine dose. Chlorine was periodically injected into the inlet pipe to boost chlorine residual as needed to achieve the end target residual of +/- 2-3 ppm. Reservoir fill continued for another 14 days until the reservoir water reached overflow level. The reservoir fill was stopped, and the reservoir was isolated for a minimum of 24 hours. After this hold period, water samples were obtained for water quality testing consisting of chlorine residual, bacteriological, trihalomethanes, volatile organic compounds, and other constituents required by the California Division of Drinking Water. After receiving passing water-quality test results, CMWD was allowed to return the reservoir to service.

Start-up also included O&M training to CMWD personnel for critical components. Contractor provided O&M manuals and followed up with providing onsite training sessions for outlet valves, actuators, and HPU; floating cover rainwater removal pumps; water quality sampling pumps; and overall floating cover maintenance, inspections, cleaning, and repairs.

LESSONS LEARNED

Floating cover designs are typically performed while a reservoir is in service. Accurate as-built drawings and underwater dive inspection photos and videos are essential to document and verify actual existing conditions. Best practices show, and not unique to this project, the information shown on as-built drawings may not always be accurate as a single resource. Existing conditions should always be documented and reviewed by the design engineer once the reservoir is dewatered and existing floating cover is removed. Any unforeseen conditions revealed should be addressed early in the construction phase to avoid potential project delays.

Long-lead components must be identified early and adequately addressed as soon as possible. On this project specifically, the CSPE geomembrane stock material for the chafer and floating cover, along with the outlet valves, actuators, and hydraulic power unit, were all identified as long-lead items. The CSPE manufacturing supply chain for large quantities of geomembrane roll stock materials, which are then used by the fabricator to produce large custom shaped factory panels, require highly coordinated schedules and upfront time to facilitate. This process guarantees the project-specific sized panels deliver to the job site within the project timeline to be installed. The valve actuators were manufactured in Italy, the valves manufactured in Chicago, Illinois, and HPU manufactured in Rochester, New York. All three components were assembled, and shop tested in Chicago before being sent to the reservoir site in Carlsbad, California.

During this project, lessons learned included the sheer-importance of preparation through the coordination of shop drawing submittals, fabrication schedules, different contracting entities, and subcontractors, which all proved to be essential components of success. All of these components should be aggressively pursued right at the project onset.

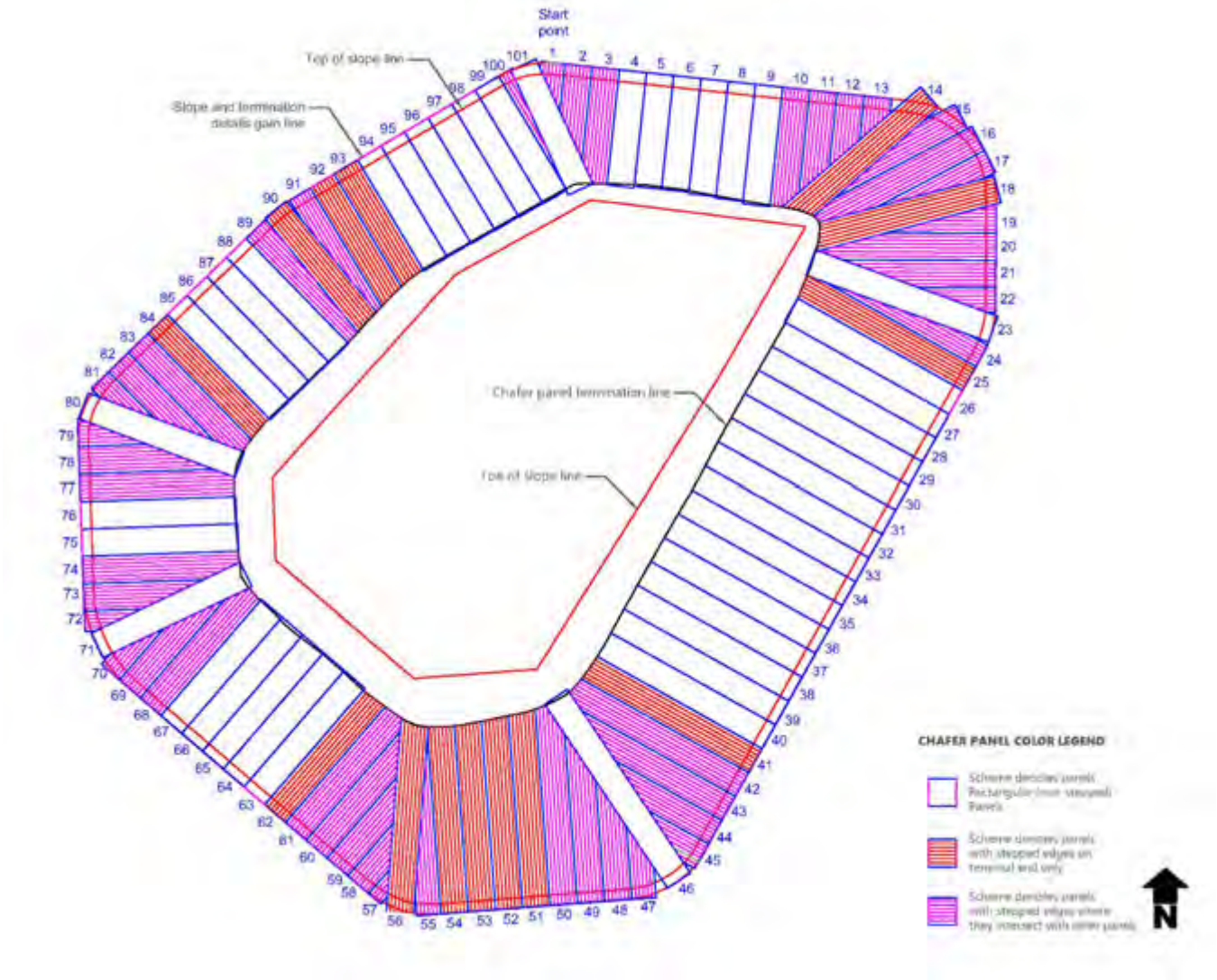

Figure 1. Chafer panel design illustration.

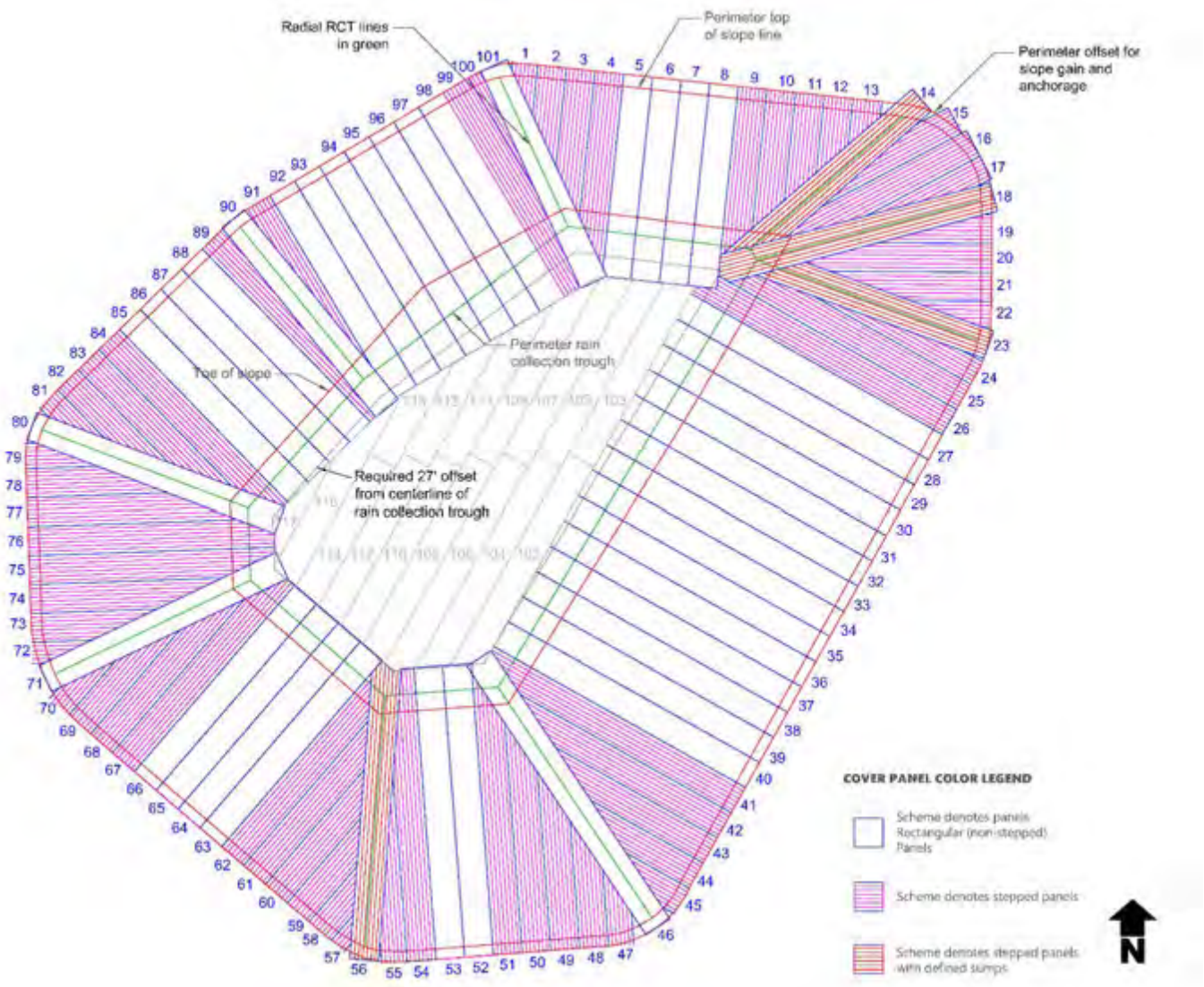

Figure 2. CSPE cover panel design illustration.

Figure 3. Chafer panel installation progress.

Figure 4. Cleaning existing AC subgrade prior to floating cover.

Figure 5. Floating cover panel seaming progress.

Figure 6. Floating cover fabricated panel deployment progress.

Figure 7. Positioning of the floating cover and wrinkle removal.

Figure 8. Floating cover and rainwater collection trough progress.

Figure 9. Floating cover system view with prefabricated appurtenances for the project.

Figure 10. Aerial view of completed floating cover system with high aesthetic value.

Geosynthetics Conference

Dipole Measurement Density and Dipole Spacing for Electrical Leak Location

Abigail Gilson-Beck, M.S., P.E.,[1]

[1]TRI Environmental, Inc. Austin, TX; e-mail: abeck@tri-env.com

ABSTRACT

Electrical leak Location (ELL) methods are the most technologically advanced way to control leakage from containment facilities. The method used for locating the most significant damage, caused during cover material placement, is the dipole method. Measurement density and dipole spacing both have an effect on the sensitivity of the dipole method, with a higher measurement density and a larger dipole resulting in a more sensitive ELL survey. In order to quantify the benefit of an increase in measurement density and a larger dipole, field trials were conducted by the Author. A three-meter (ten-foot) dipole and a one-meter (three-foot) dipole, both commonly used instruments for dipole testing, were used to measure electrical signal strength at two different offsets from a simulated leak as outlined by both ASTM D7007-16 and ASTM D8265-20. The results of the measurements are presented in order to quantify the benefit of using a measurement density of 1.5 m (5') by 1.5 m (5') rather than 3 m (10') by 3m (10') and by using a 3-meter (10-foot) dipole rather than a one-meter (three-foot) dipole. The results also reveal a fundamental flaw in the standard D7007-16 in specifying measurement density without addressing dipole spacing and in using signal strength to define a leak detection distance. The testing details investigated herein can be used to improve existing standard methodologies and to craft project specifications that maximize both the sensitivity and efficiency of ELL surveys with the end result of locating more leaks more efficiently.

INTRODUCTION

Many variations of the dipole method are practiced, so engineers lean on standardized methodologies in order to ensure a properly applied test. However, there is much room for variability within the standardized methodologies. Significant factors in method sensitivity such as measurement density and dipole spacing are not adequately addressed in either of the standardized practices where the dipole method is used (ASTM D7007-16 and ASTM D8265-20). For that reason, the goal of this paper is to quantify the benefit of an increase in measurement density, reported to be beneficial by ASTM D7007-16 and an increase in dipole spacing, reported to be beneficial by Gilson and Ferreira (2020) and Lugli and Mahler (2016).

ASTM D7007-16 was the first standardized practice for the dipole method. The procedures require the application of measurements in a grid pattern at some spacing, referred to as the measurement density. The determination of the measurement density is controlled by the "leak detection distance". To determine the "leak detection distance", data are acquired along a transect at some offset from an actual or artificial leak. The magnitude of the signal generated by the leak is divided by the "background noise" of the survey area to obtain an "R" value. "Background noise" was defined as the magnitude of voltage oscillations without a leak nearby. The offset distance from the actual or artificial leak when the R value is equal to 3.0 is considered to be the "leak detection distance". The "R" value has previously been questioned for its scientific validity (Gilson-Beck and Ferreira, 2017). At the time ASTM D7007-16 was

written, data analysis was performed by viewing graphs of the data along a transect, so presumably the goal was to require a signal that was significant enough to be viewed along said transect and a value of 3.0 times any sporadic background noise seemed reasonable to the original authors of the standard.

The evolution of data acquisition has led to GPS-based voltage maps, where leak signals generate three dimensional patterns on the mapping and a leak signal is easily visible with a very low magnitude signal simply by the characteristic pattern that a leak generates on the voltage map. Additionally, the Author has tested many sites where an artificial leak is barely visible or not visible at all and cannot generate a signal magnitude three times the background noise, but actual leaks are easily detectable. This could be due to the fact that the artificial leak is raised above the geomembrane surface where it is wettest when a site is properly prepared, but mainly because a voltage map can display the characteristic shape of a leak signal regardless of signal magnitude. Also, the signal to noise ratio can be manipulated by taking "noise" readings where they are lowest within the survey area. In some survey areas, there is a high level of background noise but leaks are still easily detectable due to their characteristic signal pattern (Gilson-Beck and Ferreira, 2017).

ASTM D8265-20, which was recently published to enhance covered geomembrane surveys and address the shortcomings of ASTM D7007-16, does not specify a measurement density. This standard simply requires that the artificial or actual leak be "detectable" using the chosen electrical method at the chosen measurement density and the practitioner must demonstrate the detectability on the requisite voltage map. ASTM D8265-20 does require the reporting of the dipole spacing and measurement density used for voltage mapping. This information is useful if, for example, a survey is done with a one meter dipole and a problematic leak is not found. The survey can subsequently be performed with enhanced leak detection sensitivity using a three meter dipole.

The Author commonly utilizes either a one-meter or a three-meter dipole, depending on the application. The one-meter dipole is typically only used when the survey area is too small for a three-meter dipole. When the Author uses a one-meter dipole, a measurement density of one meter by one meter is always used, since the leak detection distance is noticeably smaller with a one-meter dipole. At some sites, both dipole sizes were present and the Author noted that very small leaks were detectable with the three-meter dipole but not with the one-meter dipole. Dipoles larger than three meters are physically unwieldy, since it must be carried by the operator throughout the survey area and picked up and set down for each data point acquired. ASTM D7007-16 states that dipole spacing is typically 0.2 to 1 m for water-covered surveys and 0.5 to 3 m for soil-covered surveys.

It was Lugli and Mahler (2016) who first reported that the leak signal along a transect, from peak to peak, is directly proportional to the dipole spacing. The physical size of the leak signal, rather than the magnitude of the signal, was indicated by Lugli and Mahler as a criterion for determining measurement density. A 30% increase in signal strength and a 300% increase in peak-to-peak signal length was demonstrated by Lugli and Mahler when the dipole spacing was increased from one meter to three meters along a transect directly over a simulated leak.

The measurements produced by Lugli and Mahler were from a computer simulation model. This paper is the first publication known to the Author to obtain field measurements of a leak signal at several commonly used measurement density offsets for dipole method surveys. Both one and three meter dipoles are used for direct comparison of two different dipole measurement densities along transects of the same leak signal.

BACKGROUND

The physics of a leak signal propagating through soil material, how that signal is measured by a dipole method testing apparatus, and how dipole method voltage mapping is used in leak location surveys are described here in order to provide the fundamental background for understanding the results obtained by this study.

Applied Voltage. A DC voltage is applied across an installed geomembrane by inserting a current injector electrode into the cover material and inserting a current return electrode into the underlying conductive layer. Geomembranes are sufficiently electrically isolative that an intact geomembrane will restrict current flow, while current will readily flow through holes in the geomembrane, as long as those holes are electrically conductive (i.e. filled with water and/or soil). The current flowing through a leak will create a bull's eye pattern in the voltage field, with the eye centered on the leak. This is due to the series of voltage drops leading to the hole from all directions, similar to what the surface of water does when a drain is pulled, creating a funnel shape in the water surface, as shown in Figure 1.

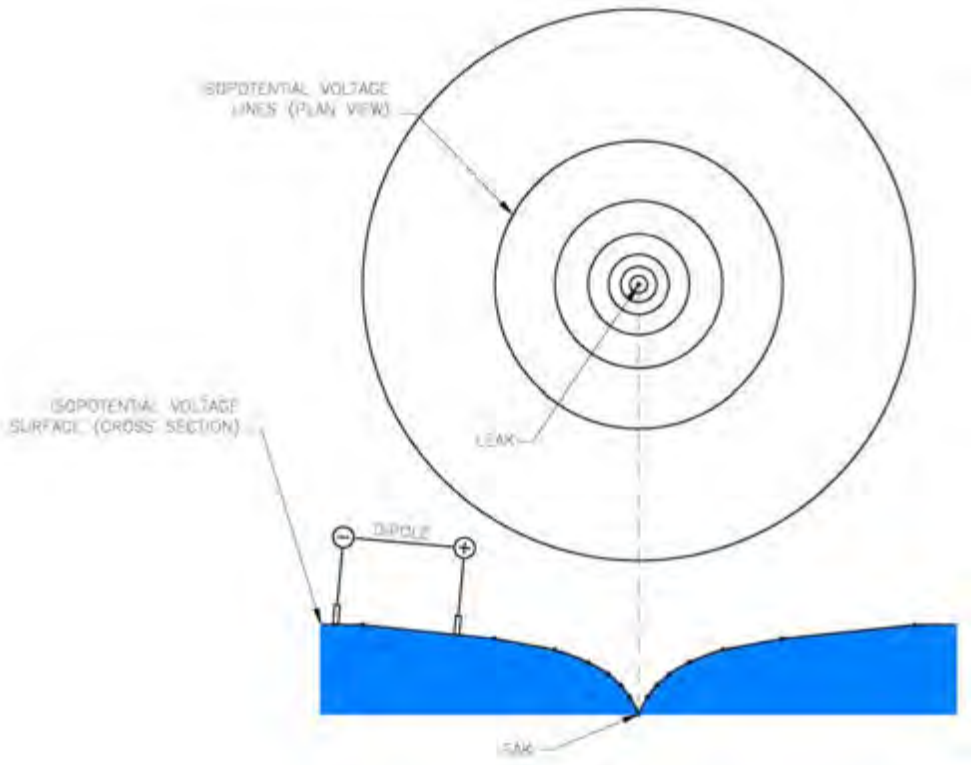

Figure 1. Water surface analogy of voltage field at leak location.

Dipole Method. The definition of the dipole method is the measurement of voltage across a surface using two closely spaced electrodes. The spacing of the electrodes is kept constant as the dipole travels across the surface. Therefore, the dipole is actually measuring the voltage gradient as opposed to absolute voltage potential. When approaching this bull's eye-shaped dip in the voltage field, and when measuring from front electrode to rear electrode, a drop in the voltage value will be measured, with the peak occurring when the front electrode is nearest the leak. The

voltage value will then go to near zero when the dipole is straddling the leak, and then the voltage value will spike when the rear electrode is directly over the leak, as shown in Figure 2.

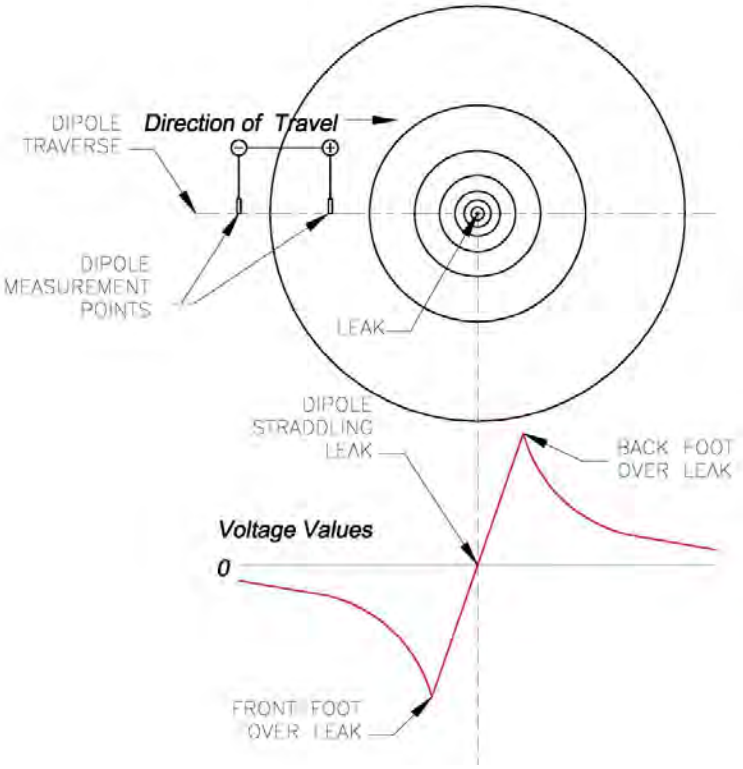

Figure 2. Leak signal traveling directly over a leak, as measured by a dipole.

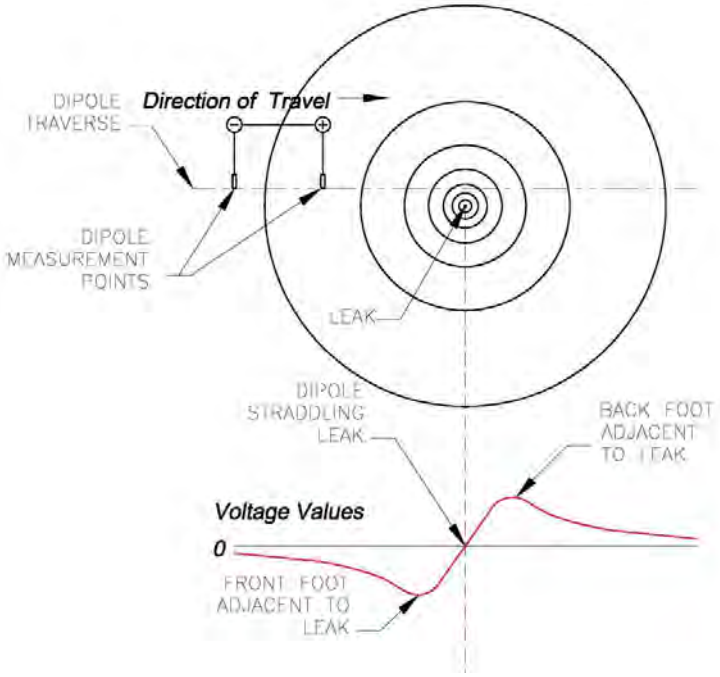

Figure 3. Leak signal at an offset from a leak, as measured by a dipole.

Leak Signal. The leak signal itself drops off logarithmically with distance from the leak as approximated by Figures 2 and 3. The magnitude of the signal as measured by the dipole will therefore also attenuate with increasing offset distance from the leak, as shown by Figure 3. A dipole with a larger spacing between measurement electrodes will result in a larger voltage differential measurement, since a larger dipole crosses more voltage contour lines. The voltage differential is what determines the detectability of a leak.

Dipole Method Voltage Mapping. A voltage map generated by the dipole method will look different than an isopotential voltage map (used to portray plan view leak signals in Figures 1-3). On a dipole method voltage map, the dip followed by a peak can be seen in two dimensions by a butterfly-like signature, as shown in Figure 4. Leak signatures feature a positive circular peak stacked directly on top of a negative peak, with closely spaced contour lines between the two peaks. The colors on the map represent voltage values in order to easily recognize a shift from positive to negative values. Negative values are represented by red changing to blue with increasing magnitude and positive values are represented by green changing to yellow with increasing magnitude. The negative/positive polarity of the entire survey area is created by the current injector electrode. The characteristic leak signal voltage pattern is opposite that of the current injector electrode, since current is exiting the survey area at current leakage locations and entering the survey area at the current injector location.

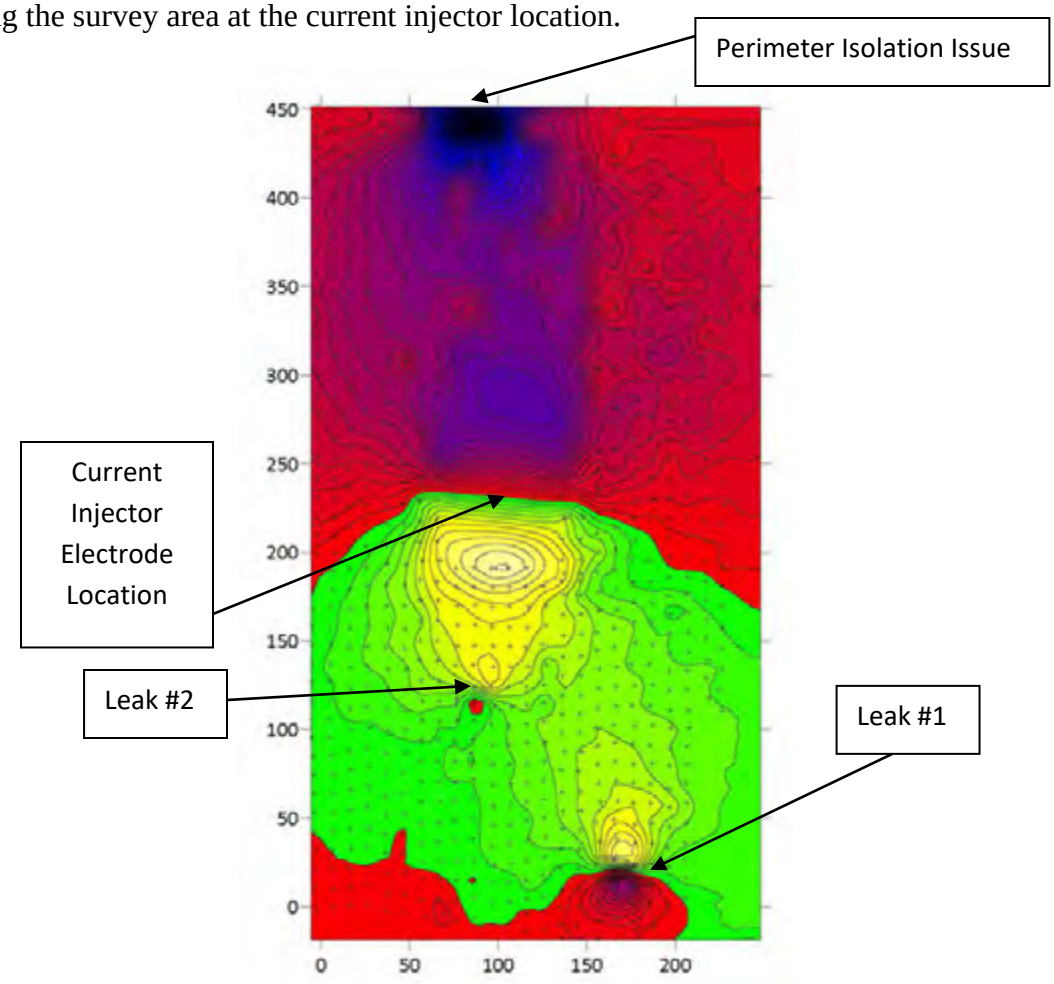

Figure 4. Voltage map created by dipole measurements.

TESTING SET UP

A DC voltage was introduced between two electrodes. The applied voltage value was adjusted in order to keep the dipole voltage meter from maxing out when the dipole was placed directly on the electrode used to simulate the leak signal. The same applied voltage was used for all trials.

Materials and Methods. A circular stainless steel electrode was inserted into a soil layer to simulate the signal generated by a leak. A stationary physical grid was laid out up to a distance of 7.6 meters from the electrode. Each dipole apparatus was spaced along the measurement lines so that each dipole would straddle the electrode at the closest measurement point to the electrode at the specified offset. A three meter dipole and a one meter dipole were used, each one using the same copper sulfate reference electrodes and voltage meter for measurements. For each dipole and offset, multiple readings were taken along the transect and the values were averaged to produce the values published here. For each dipole spacing, measurement densities of 1.5 x 1.5 meters and 3 x 3 meters were simulated using a 0.75 meter and 1.5 meter offset, respectively. One additional trial was done simulating a 1 x 1 meter measurement density using a one meter dipole.

RESULTS

Results are displayed both graphically and along transects that would be displayed as part of a dipole method voltage map with the same color coding method of voltage values used for Figure 4. The scales of the graphs for each measurement density are kept the same for comparison. The zero voltage line is shown in bold to show when the voltage values change from negative to positive, a key indicator of detectability. Values under the zero line correspond with the red/blue/black regions of the adjacent map and values above the zero line correspond with the green/yellow/white regions of the adjacent map. The contour interval for all of the color coded voltage maps is 0.005. The graphs more readily depict the signal strength (vertical distance between peaks in the voltage values), while the voltage maps more readily depict the leak detection distance. For the voltage maps, the leak is detectable as soon as a negative value is measured as the dipole approaches the leak (initially shown by red). The distance from the simulated leak to this color shift on the map is defined here as the “leak detection distance”. The dipole direction of travel is from bottom to top. The Y-axis of the voltage maps represent meters, with increasing Y-values representing distance from beginning of transect. The leak is located approximately at a Y-value of 7.6. The location of the leak is not exactly shown by the mapping, because when the dipole is straddling the leak it can be either slightly positive or slightly negative, since it is highly improbable to land exactly on a value of zero.

It is common for leak signals in the field to be lopsided, usually caused by the location of the current injector relative to the leak, since a stronger current density will be present on the side of the leak closest to the current injector. The data presented here shows that the leak is slightly more detectable in the “fore” rather than the “aft” side of the simulated leak. This tendency should not be viewed as testing error, but as a typical feature of field measurements.

The testing results presented in Figures 5 through 9 are also summarized in Table 1. A leak detection distance of greater than 7.6 meters means that the distance exceeded the limit of the testing area. The signal magnitude is the voltage differential, from peak to peak.

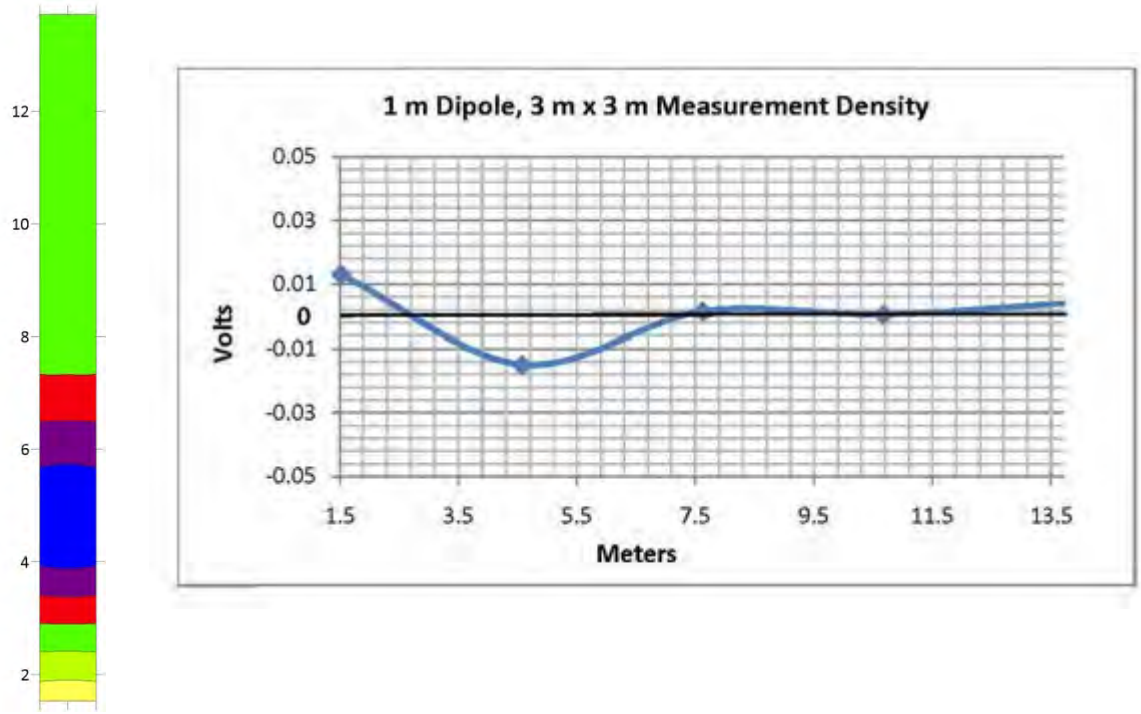

Figure 5. Signal detected by one meter dipole at 1.5 meter offset.

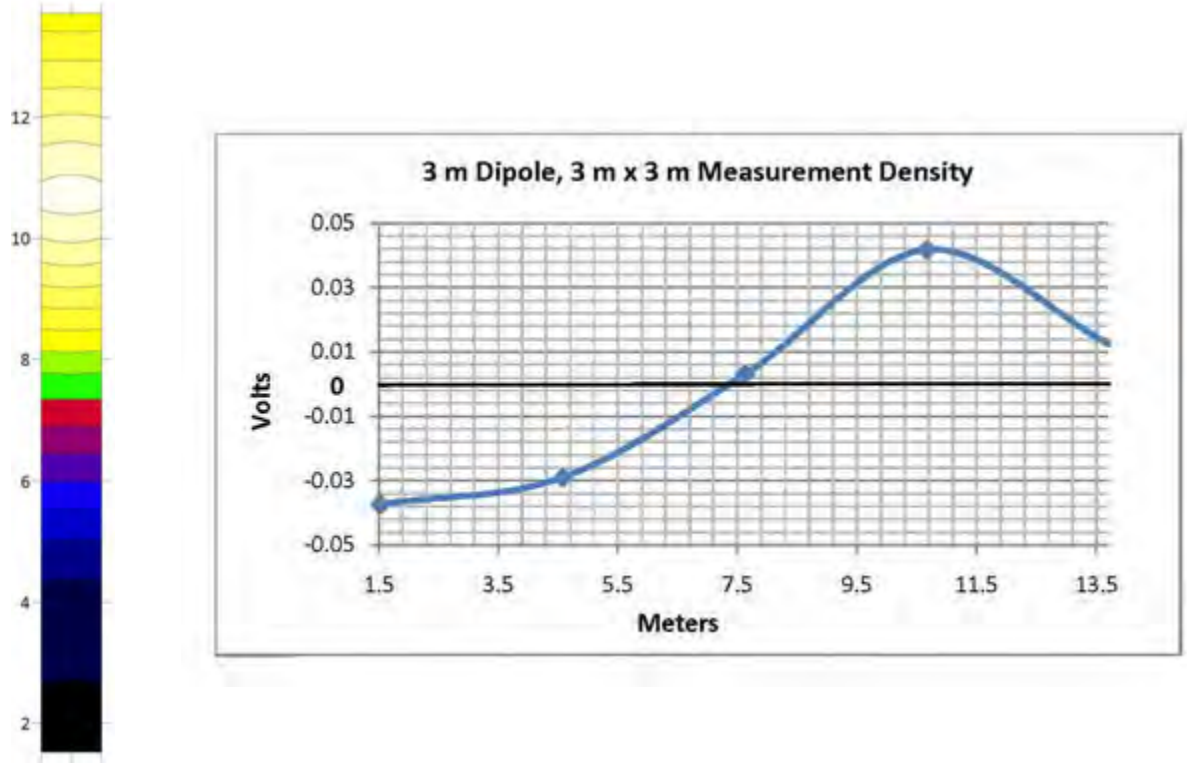

Figure 6. Signal detected by three meter dipole at 1.5 meter offset.

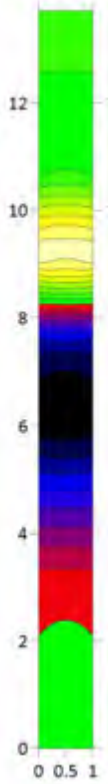

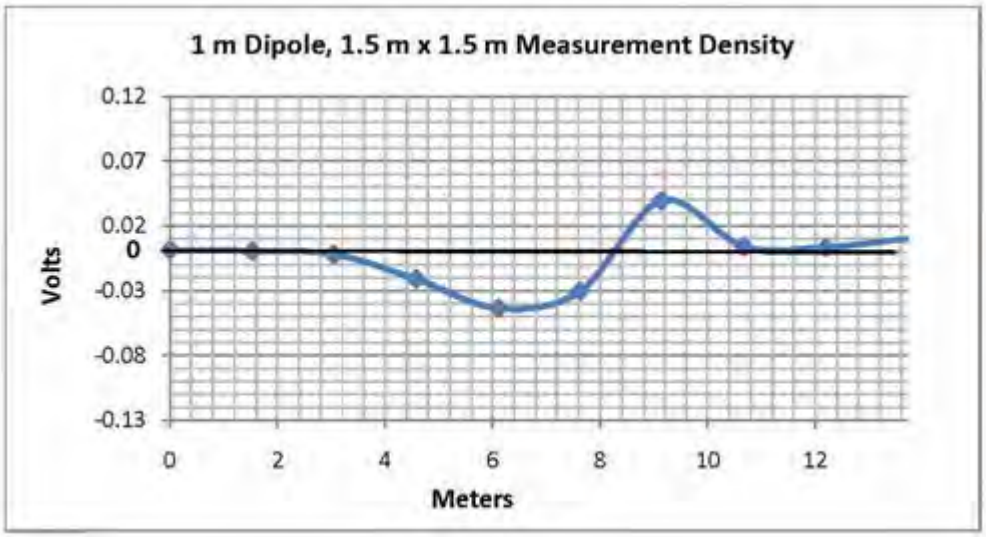

Figure 7. Signal detected by one meter dipole at 0.75 meter offset.

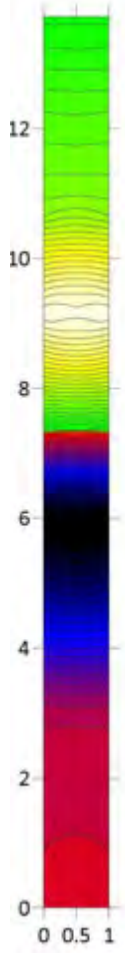

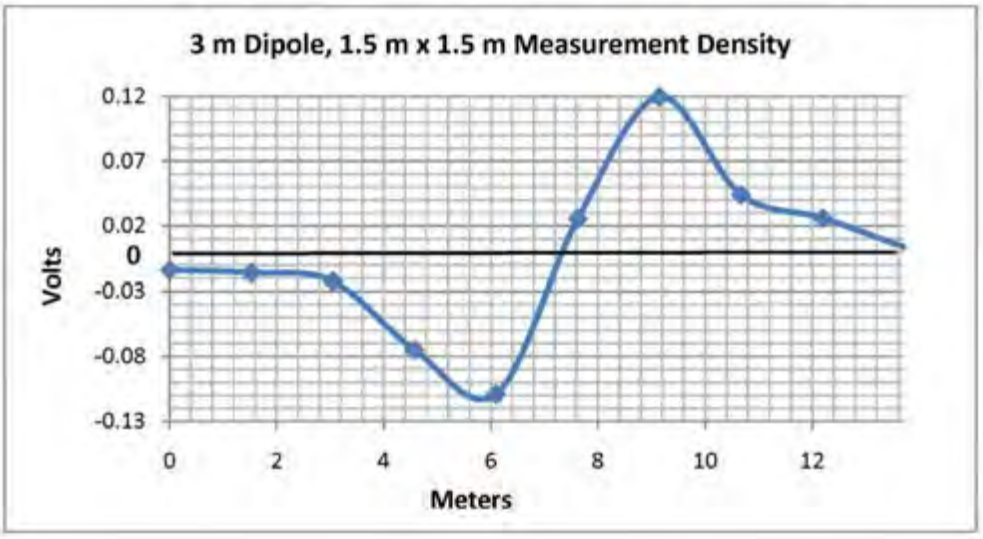

Figure 8. Signal detected by three meter dipole at 0.75 meter offset.

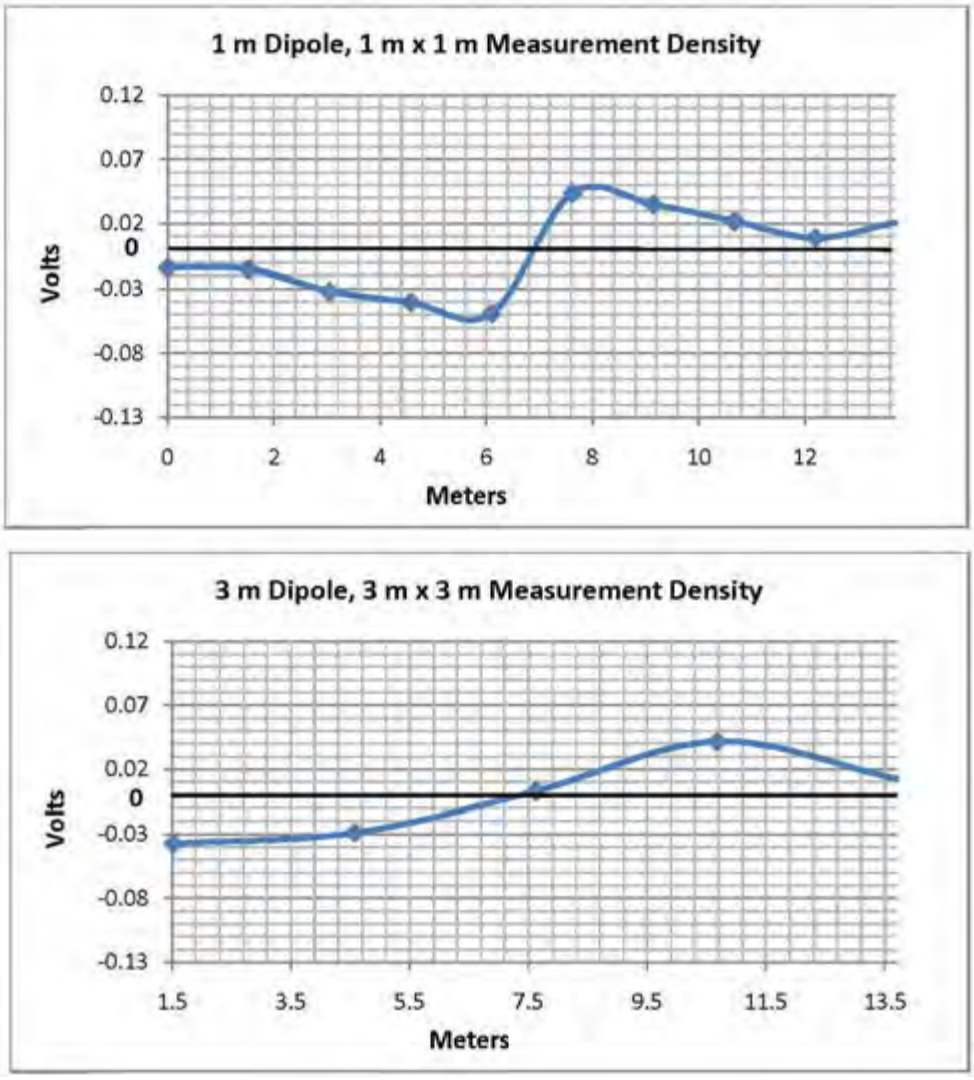

Figure 9. Comparison of signal detected by one meter dipole at 0.5 meter offset and signal detected by three meter dipole at 1.5 meter offset.

Trial	Description	Signal Magnitude	Leak Detection Distance
1	1 meter dipole, 1.5 meter offset	0.019 V	4.7 meters
2	3 meter dipole, 1.5 meter offset	0.079 V	>7.6 meters
3	1 meter dipole, 0.75 meter offset	0.083 V	5.2 meters
4	3 meter dipole, 0.75 meter offset	0.229 V	>7.6 meters
5	1 meter dipole, 0.5 meter offset	0.093 V	>7.6 meters

Table 1. Numerical Summary of Testing Results.

DISCUSSION

In order to quantify the benefit of a larger dipole spacing, trials 1-4 were analyzed. For a three meter by three meter measurement density, the three meter dipole increased the signal strength by 315% when compared to the signal measured by the one meter dipole. For a 1.5 meter by 1.5 meter measurement density, the three meter dipole increased the signal strength by 176% when compared to the signal measured by the one meter dipole. However, this does not capture the most important aspect of the testing, which is the leak detection distance. The only trial of the one meter dipole that approached the leak detection distance of the three meter dipole was the one meter by one meter measurement density (Trial 5). It is interesting to compare the one meter dipole at a one by one meter measurement density to the three meter dipole at a 3 meter by 3 meter density (Figure 9). The signal strengths are about the same, but the leak detection distance of the three meter dipole is larger, as determined by the Y-axis value on the far left side of the graphs.

Since the leak detection distance of the 3 meter dipole exceeded the testing area in every case, the benefit of increasing the measurement density can best be quantified by analyzing the one meter dipole trials. Increasing the measurement density of a one meter dipole from 3 meters by 3 meters to 1.5 meters by 1.5 meters, which quadruples the number of data points required, only increased the leak detection distance by 11%, even though the signal strength increased by 337%. In fact, with the larger offset, the peak to peak signal distance is larger. Lugli and Mahler argue that the peak to peak distance should determine the maximum offset between survey transects (i.e. measurement density). Even though an exact measurement for leak detection distance for the three meter dipole trials was not obtained, a comparison can be made by looking at the voltage value on the left side of the 3 meter dipole graphs at the same location along the transect. The increase in measurement density with the three meter dipole actually resulted in a faster attenuation of the signal, from a value of approximately -0.03 to -0.02 at the same location along the transect. This shows that there is no significant increase of leak detection distance with an increase in measurement density. In addition, these results show that it is inappropriate to determine a measurement density by using the signal strength along an offset distance, as prescribed by ASTM D7007-16.

Measurement density has been argued as a method of increasing sensitivity by practitioners of D7007-16, however those practitioners generally use one meter dipoles. There is certainly an increase in sensitivity when a one meter dipole changes from any measurement density other than one meter by one meter, which is the maximum prescribed by ASTM D7007-16. Practitioners using a three meter dipole have long been resistant to this claim, since excellent sensitivity is always achieved with a three meter dipole as long as site conditions are good. In fact, the Author has tested many problematic sites with a three meter dipole where the measurement density was increased in order to increase sensitivity and this method has only ended up costing owners more time and resources while not solving the problem (i.e. locating the hole(s)). It is also telling that ASTM D7007-16 prescribes a measurement density for water-covered areas of 0.4 meters by 0.4 meters when the artificial leak is not detectable (using 0.2-1 m dipole) and for soil-covered areas a measurement density of 1.0 meters by 1.0 meters when the artificial leak is not detectable (using a 0.5 – 3 m dipole). The tighter measurement density was likely prescribed for water-covered areas because the typical dipole testing apparatus was smaller, resulting in a smaller leak detection distance.

CONCLUSION

It is clear from the results that a larger dipole spacing enhances the leak signal and increases the leak detection distance. A one meter dipole, even when applying the maximum measurement density prescribed by ASTM D7007-16, cannot achieve the level of sensitivity of a three meter dipole at a three meter by three meter density. On a practical level, this means that surveying with a one meter dipole at this measurement density will take nine times as many measurements as the three meter dipole to get close to the same level of leak detection sensitivity. Nine times as many measurements results in a survey that takes nine times longer.

Part of the dysfunctionality of ASTM D7007-16 is that an ELL practitioner assumes a specific measurement density as part of the bidding and proposal stage of a project. A lump sum cost is given for that measurement density. If the measurement density must increase after the project is awarded, then a change order would have to be issued, which is not always allowed. In addition to the additional cost, the survey would take additional time. Construction schedules are very tight and every day is accounted for. A one day survey turning into nine days of surveying would be problematic for most projects. From a practical perspective, project specifications should therefore specify a three-meter dipole to get the best price for the least amount of survey time.

It may not be within the purview of a standardized methodology to specify dipole spacing, since there are some physical and technical constraints for this larger structure. For example, the dipole method is sometimes used in physically restrictive areas where a larger dipole would not physically fit. However, the methodologies can certainly specify that the measurement density should be determined by the dipole spacing, since this is the technically correct approach for maximizing the leak detection distance for a given dipole instrument.

Specifying a measurement density with a grid spacing less than the dipole spacing will not likely result in a higher quality survey, but will result in a more costly survey. Therefore, project specifications will get the biggest benefit, both from a technical perspective and economic perspective, by simply specifying a minimum dipole spacing of three meters wherever appropriate.

REFERENCES

ASTM D 7007-16. Standard Practices for Electrical Methods for Locating Leaks in Geomembranes Covered with Water or Earthen Materials, *ASTM International*, West Conshohocken, Pennsylvania, USA.

ASTM D 8265-20. Standard Practices for Electrical Methods for Mapping Leaks in Installed Geomembranes, *ASTM International*, West Conshohocken, Pennsylvania, USA.

Gilson, A. and Ferreira, J. (2020). New Standard Practice for Electrical Leak Location of Covered Geomembranes. *GeoAmericas 2020,* 4th Pan American Conference on Geosynthetics, Virtual Conference, October 26, 2020.

Gilson-Beck, A. and Ferreira, J. (2017). Maximizing the effectiveness of electrical leak location for covered geomembranes, *Geosynthetics 2017*, First International Conference on Technology and Applications of Geosynthetics, 18-20 October, 2017.

Lugli, F. and Mahler, C.F. (2016). Analytical study of the performance of a geomembrane leak detection system, *Waste Management & Research,* Vol 34(5) 482-486.

Geosynthetics Conference

Evolution in Geosynthetics Starts with Utilizing Technology

Gregory Pignataro[1], David Scherbaty[2], and Evan Bao[3]

[1] COMANCO, Plant City, FL; e-mail: gpignataro@comanco.com
[2] COMANCO, Plant City, FL; e-mail: dscherbaty@comanco.com
[3] COMANCO, Plant City, FL; e-mail: ebao@comanco.com

ABSTRACT

Technology is an essential advancement towards more efficient and effective geosynthetic installations. In its most basic form, technology is a means of gathering, storing, and utilizing information more easily than its predecessor(s). If implemented appropriately, technology improves process efficiency. Users and downstream stakeholders of process improvements can then capitalize by delivering quicker, better-quality, more economical products. The geosynthetics industry is lagging in this area. From a feasibility perspective and assessing practical implementation opportunities, many means, and methods widely used for geosynthetic installations are antiquated and, furthermore, lack reliable authenticity verification. Fortunately, however, the current landscape does require a robust catalog of information reporting to substantiate this important environmental construction practice. The combination of room to evolve in practice and existing data requirements make it an ideal suitor for technology integration. While advancements in materials manufacturing, welding equipment, and post-installation leak surveys already contribute to progression, there is a lack of universally accepted information infrastructure to bring all facets of an installation together. Therefore, this paper focuses on automating the QA/QC process by way of software integration in the field and office setting. Software automation will catalyze resultant cyclical benefits to the geosynthetics industry as a whole.

INTRODUCTION

The QA/QC process is the logical starting point for this proposition as it performs three key functions when autonomized and then accepted as an industry norm. First, it improves physical field quality assurance (QA), which produces superior containment systems. Second, automation expedites the review and reporting quality control (QC) by built-in analysis algorithms usually performed by multiple parties. And third, it creates a centralized database that leverages future installs and supplementary parts of geosynthetics projects throughout the industry (Ramsey 2019). These general principles will be examined more in-depth and evolve in the following paragraphs, but the cyclical nature of improved QA/QC through automation is illustrated versus the current process in Figures 1 and 2.

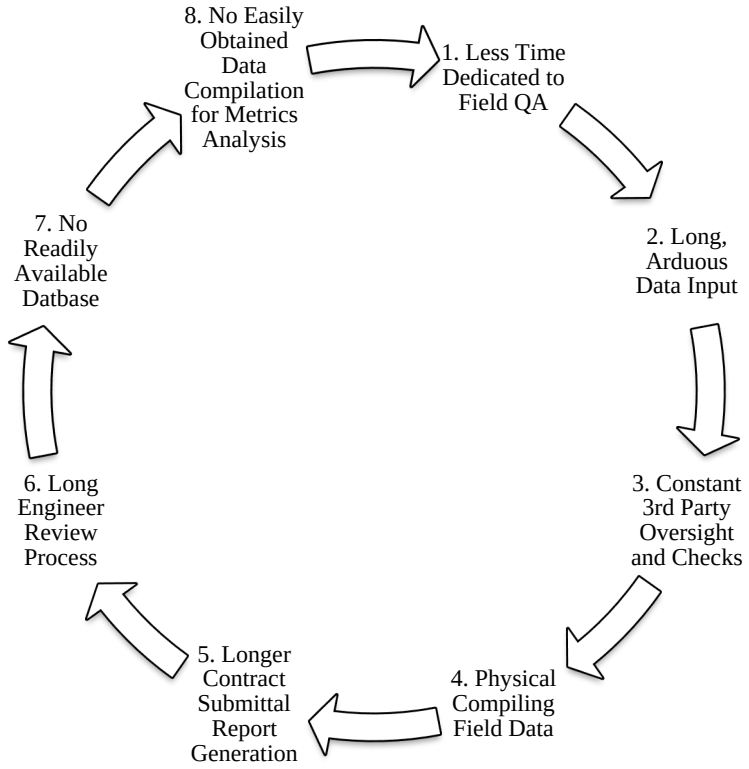

Figure 1. Manual QA/QC Process

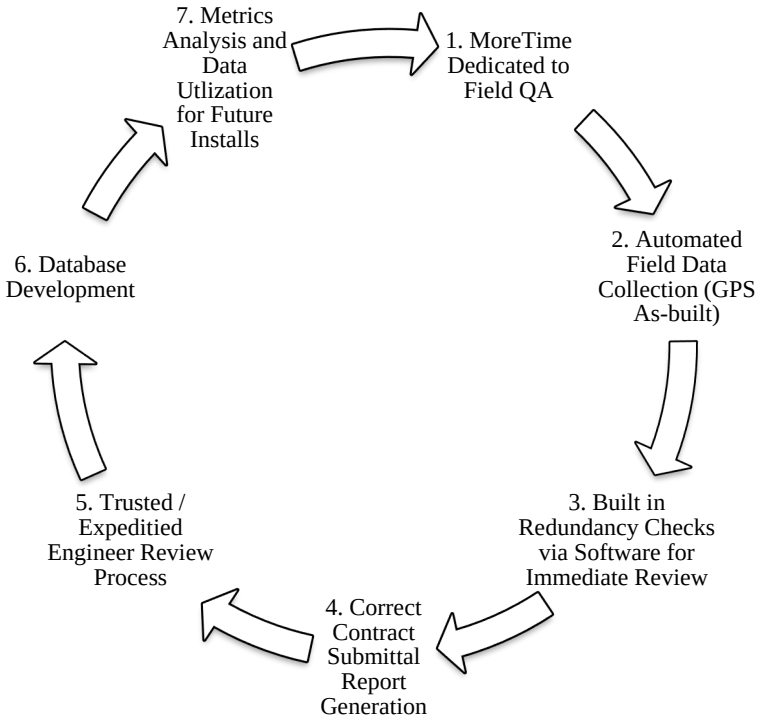

Figure 2. Automated QA/QC Software Process

AUTOMATED FIELD DATA COLLECTION

Geosynthetics by nature (i.e., typical industry specifications derived from GSI and ASTM Standards) require a large amount of redundancy when it comes to proper deployment and seaming. These practices must be performed meticulously (QA) and then documented (QC) as such as well. Typically, these duties are completed by an installer's individual QA/QC technician and verified by an on-site 3rd party owner representative (CQA). There are more specifications within a geosynthetic system having to do with subgrade conditions, cover soil placements, and more, but for this paper, we will specifically examine data associated with deployment and seaming. However, there are boundless opportunities to integrate these ancillary components of a system when a software infrastructure has been established.

Currently, the industry handwrites QA/QC documentation. This is hard to comprehend in 2020 considering the magnitude of legitimate QA needed for this craft and associated documentation required on a per-acre basis by installer QA/QC technician and 3rd Party CQA (Koerner 2012). There are two main identifiable liabilities with this current practice. The first is that it takes a great deal of time throughout the day to keep up with documentation alone, such as As-built drawings with all associated panel, roll number, seam and repair info, roll deployment, trial welds, destructive sample testing, seam information, and repair information. The real value from a QA/QC Technician and 3rd party CQA is within the QA portion. Their roles should lean heavily on making sure physical performance is of good quality, not necessarily just the documentation (Toepfer 2016). The documentation can be perfect, but if the systems fail due to improper workmanship that went unaddressed during construction because QA efforts were limited due to the QC effort, project stakeholders are still at risk. The second is that handwriting allows for more chance of human error and information fabrication/manipulation. Concisely, improvements to speed and reliability for the day-to-day field documentation will directly enhance the quality of geosynthetic installations.

Based on these observed areas of improvement to means and methods, automation must be applied to each section of required QC to address speed and reliability. This automation begins with as-built generation. Hand sketched, scaled drawings that include all pertinent panel information are extremely labor-intensive to complete, and information can easily be missed. If information is missed during the as-built phase, ripple effects on seam and repair info will also go unnoticed, leaving the door open for future loss. An existing step in the right direction is the seldom-seen "GPS As-built" specification requirement. Anyone with GPS equipment can shoot points at each panel intersection and grade break. Once that is completed in the field, the points file can eventually become a GPS coordinated as-built once they are connected by a program such as AutoCAD or similar. However, to populate this "GPS As-built," a reference hand drawing is likely needed to refer back to in order to know which information goes where. This includes panel numbering, roll assignment, repair and destruct locations, and terminations. Therefore, simple "GPS As-built" within these limited parameters does not address speed but addresses reliable future use. With no speed improvement, QA/QC technicians cannot shift that time allocation to physical QA, which is the more valuable time commitment.

A more encompassing improvement to the As-built portion of QA/QC, and in turn, other downstream information collection practices, would be universal use of "*automated* GPS As-built" generation. Computer software can automatically generate the linework, panel, repair, and destruct numbering and termination call-outs without handwriting or using another software to connect the dots and annotate manually. By merely assigning attributes to the GPS points, the

software algorithm creates physical lines and other panel information. This allows field techs to quickly see the as-built evolve in the field to address any missing information or shots in real-time. This approach now allows for more time looking at seams, assessing changing in-situ conditions, examining proper heat seal and grinding techniques, all of which are direct to the system's sustainability. Finally, with a software platform, these field documents can also be uploaded via cloud technology, so office personnel or clients may see this information in real-time. This functionality can be used as another set of eyes for checking information, specification adherence, real installed quantity verification, material

BUILT IN RECORD KEEPING AND REAL-TIME CQA

Remembering automated GPS as-built is the foundation for an improved system; we can now use the abundance of metadata within the as-built to populate the other QC specification requirements. Because the software knows every panel intersection, the locations of every repair and destruct, terminations, panel placement square footage reports, seam and repair information are automatically generated as a result. This automation makes sure that every piece of info on the repair and seam reports is in line with what is on the as-built and, most importantly, within project specification. Currently, the typical process is to walk the liner physically, hand draw the as-built, then once again walk the liner to populate every line of seam control and repair reporting on their separate respective report sheets. Using a field tablet or similar technology, automated GPS as-built offers the opportunity to shoot points and attribute those points once. Welding and testing information can then be filled in on the already generated lines. Automation eliminates the need to collect the same information multiple times and eliminates paper recordkeeping.

To further improve efficiency, it is essential to acknowledge that some information does need to be “filled in,” requiring the tech to read the information on the liner itself. These parameters are set up prior to the job so that he/she is not repeatedly writing the same information, once again saving time. These “fill in” areas on the seam and repair reports are replaced with dropdowns accompanied by other pre-set conditions. One example of those pre-set conditions is air test information input. With software, the technician will utilize a pre-set drop down for the initial start time only, and the end time will automatically populate based on job specification previously set up, typically five minutes later. See the example screenshot below in Figures 3.

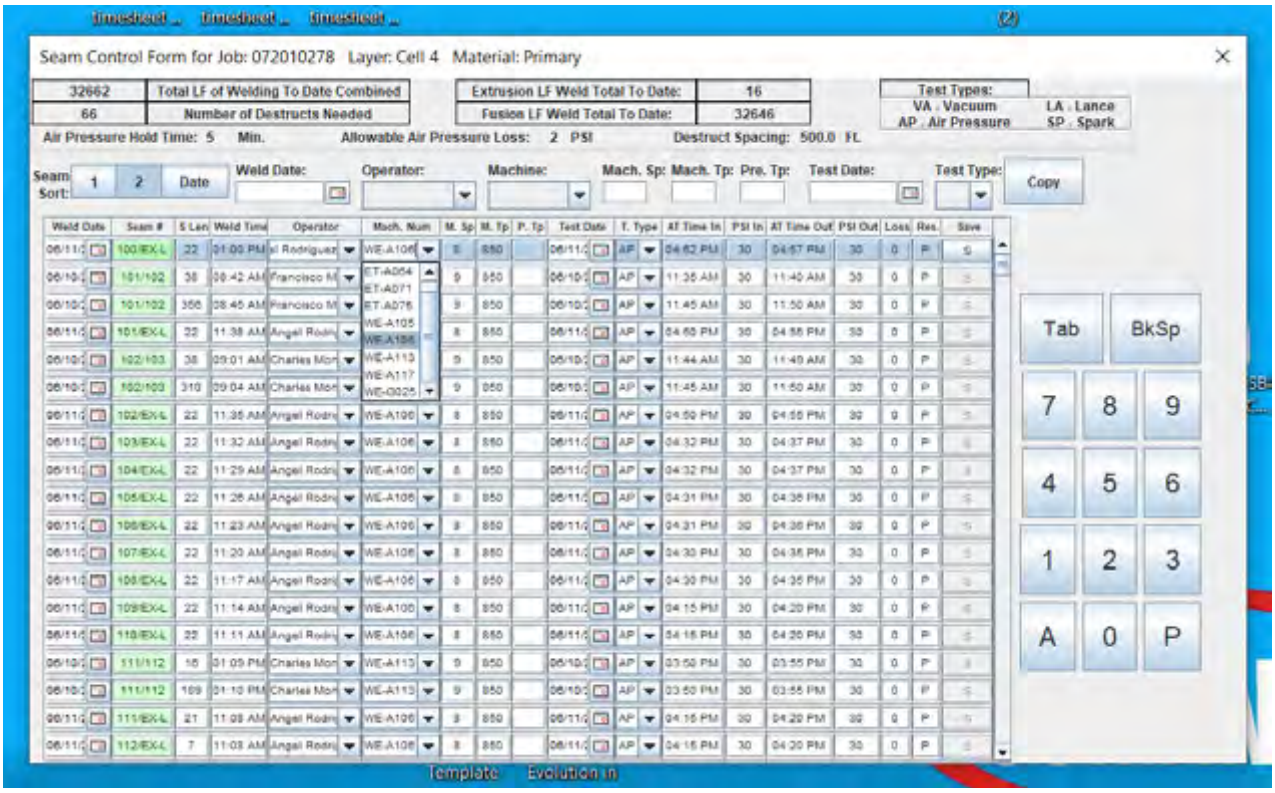

Figure 3. Populated Seam Control Example
Hundreds of lines auto populated from automated GPS as-built

Currently, the industry relies on thorough contractor QA/QC technicians, persistent site CQA's, and post-project data review by engineers to catch all of this information. But do we really know the QC data submittals are correct per project specification during and at the completion of the project? Initiating redundant software assistance benefits owner representative CQA as well. To some extent, the software can do the job of a CQA from a documentation standpoint by cross-referencing all of this data with the appropriate previously defined specification. For example, when a line of seam control or repair reporting is completed, a check function automatically makes sure the information is in line with the appropriate pre-weld information. This real-time inspection principle provides unique advantages in terms of speed of work and reassurances to the CQA team that everything is completed and documented prior to being covered by a subsequent layer in the lining system. If incorrect or missing data is identified, it may be too late to confirm or verify the information because another layer may cover the materials in question.

REPORT GENERATION

Thus far, foundational improvements to QA/QC field means and methods have helped make the physical data collection quicker, less strenuous, and more authentic for field personnel. It has also been recognized that automated QA/QC software integration provides real-time project updates via a cloud platform for other stakeholders in geosynthetic installation projects to monitor progress.

Because all parties within the field setting are working more effectively, the final phase of an install relating to submittals is now more easily developed. Again, comparing to the current state of practices, multiple sheets of paper or, at best, excel documents typically need to be compiled, put into a clean format, and printed in a legible manner for professional submission. This process requires an additional meticulous individual (usually a corporate QA/QC Engineer or similar) by the installation contractor to make sure every piece of info is accounted for. Once submitted, this process must be essentially repeated by the project's engineer of record. QA/QC software provides solutions to this sequence of events.

By having a centralized program, users may "print" submittals upon completion. Furthermore, as examined previously, the process of checking accuracy is an on-going effort within the software. Therefore, once the final panel, seam, repair, or other is documented with automated GPS as-built and ran through QA/QC software, the reports can be trusted for accuracy. This process substantially decreases the time allocation needed for report review and submission post-installation. On a per 20-acre basis, this type of systematic field approach results in an 80%-time reduction requirement by the installation QA/QC engineer compiling the final submittal. Conservatively, a 20-acre installation's final package, including as-built drawing, can be completed in an 8-hour workday.

DATA BASE DEVELOPMENT AND LEVERAGING

At the completion of a geosynthetics installation, contractors and engineers are left with a vast amount of data and information. Previously, this info would not be used post project completion. At most, installers keep track of their destructive test failure rate as a general industry parameter to track a company's quality. But there is much more in-depth analysis that can be made with a metrics analysis tool. Some parameters which are valuable for installers, engineers, and owners include:

- Field Pre-weld Pass/Fail Rate
- Field Destruct Pass/Fail Rate
- Laboratory Destruct Pass/Fail Rate
- LF Welded – Extrusion
- LF Welded – Fusion
- SF Deployed
- Repairs by Type (are we burning out, losing laps, etc.)
- Waste Percentages (how well a company utilizes material)

All of which can then be filtered by:

- Date Range (time of year)
- Material
- Welding Technician
- Welding Equipment Used
- Superintendent
- Job Site
- Client

- Design Engineer

A combination of these metrics paints a far more comprehensive picture of a project's success above any beyond simple Pass/Fail percentages.

The climate of our generation is data-driven. Every industry in the world is optimizing data collection to be able to leverage its operating efficiency. Accurate, centralized data management software benefits installers, engineers, owners, manufacturers, and other stakeholders in the geosynthetics industry. Up until now, tangible improvements to field and reporting under the QA/QC umbrella have been addressed. But in addition to these baseline improvements, there are more widespread advantages downstream that can recirculate to an improved next project.

Some examples include targeted internal training by installers if trends are seen with specific employees not performing well or a specific material is continually underperforming. Legitimate resume generation during pre-con submittals for owners and engineer's that they can trust they do have the experience that is being submitted. Other miscellaneous data optimization examples include reductions in billing conflicts (Geo-X 2020) and advantages going into prospect cell or cover construction projects. Tie-in points are known for the existing cell or covered area; cut and fill plans are easily and accurately adopted from a known boundary previously established from the as-built GPS locations.

While advancements in materials manufacturing (better additives, taped seams, conductive backed materials), welding equipment (data acquisition fusion welders), post-install leak detection (leak integrity testing), and existing "justified quality management systems" (Koerner 2012) are already contributing greatly to advance the geosynthetics business, a QA/QC software platform is needed to substantiate and document the effectiveness of these tangential advances. Show how these other stewards of the industry improved failure rates. Record the data that tells us which material in which the application performs the best. Right now, these metrics are stored within the heads of those who performed on these specific projects.

CONCLUSION

It is important to recognize that other solutions are on the market; specifically, Glen Toepfer's Supertek and Geo-X's 'Geo-Q' platforms, with similar principles and have paved the way for better installations and improved containment. The roadblock for universal acceptance of QA/QC software use seems to be that existing systems only address field CQA and lack authentication grounds. No approach begins with automated GPS as-built generation and subsequent automatic deployment and seaming redundancies. Furthermore, the database storage and filtering for unique metrics analysis is novel. For software to catch on, it must benefit all stakeholders in a geosynthetics installation. All of these advantages outlined above, and there are many more, lead to a cost savings that can be related back to the project owner.

REFERENCES

ASTM D 638. Standard Test Method for Tensile Properties of Plastics, *ASTM International*, West Conshohocken, Pennsylvania, USA.

Koerner, K.M. & Koerner, G., (2012), *Need for and Justification of Quality Management Systems for Successful Geosynthetic Performance* [White Paper]. Geosynthetic Institute. https://geosynthetic-institute.org/papers/paper26.pdf

Ltd, Geo-X (Pty). "QA/QC Management System." *GeoX*, 2020, geo-x.co.za/qaqc-management system/.

Toepfer, Glen. Interview by Chris Kelsey. *An Insurance Policy for Geosynthetic Installations*, 21 Jan. 2016, https://www.geosynthetica.com/cqas-insurance-policy-geosynthetic-installations/. Accessed 11 Sept. 2020.

Ramsey, B. (2019). Improvements and Advances in Construction Quality Assurance for Geosynthetics, *17th African Regional Conference on Soil Mechanics and Geotechnical*, Boyd Ramsey Consulting LLC, Houston, Texas, USA: 1-9.

IFAI Geosynthetics Conference

High Density Polyethylene (HDPE) Lined Produced/Flow-back Water Evaporation and Recycling Ponds

Neil C. Nowak, P.E.[1]

[1]SCS Engineers, Denver, Colorado, USA, email: nnowak@scsengineers.com

ABSTRACT

The problem to be solved is the disposal and recycling of millions of liters of production water (brine water) and flow-back water generated annually from the oil and gas industry in an environmentally safe, low cost, and efficient manner. A technology that is effective and safe is the evaporation of the water in lined containment ponds after separation and removal of the hydrocarbon component from the water. Three projects are the case studies for this paper, located near Wright, Wyoming, Cisco, Utah and Midland, Texas in the Permian Basin. They were designed to evaporate or recycle water in geomembrane lined ponds. Purpose of this paper is to demonstrate that the black HDPE increases evaporation over the use of clay or unlined ponds, and the use of white liner reduces evaporation relative to black color liner.

INTRODUCTION

The aforementioned projects are complete and have been operational for a number of years, and continue to be expanded per their permit. The production and flow back water from oil and gas wells in the area local to each site is trucked to the sites for disposal. The water is evaporated in ponds lined with high density polyethylene (HDPE) as the top layer by using a combination of factors that are favorable to the evaporative process, including the following:

- Natural characteristics of the site, including the arid climate, windy conditions, and numerous sunny days,
- The top liner in the ponds is black HDPE, which creates a hot surface,
- HDPE liner was chosen to protect the surface and ground waters of the area and to assist with the evaporation of the water (evaporation is enhanced due to the black color of the liner).
- Liner was white for the storage and to reduce the evaporation relative to the black liner.

The projects are interesting in that each facility provides oil and gas production companies in the area with a large commercial alternative to production water and flow-back disposal versus numerous small ponds that may service only one well pad, or expensive re-injection wells, or even more expensive water recycle treatment facilities. The regulatory agencies like it for centralization and protection of the state's waters.

CASE STUDIES

Project Location – Wright, WY

Bluegrass Water, Wright, Wyoming. The project is located in a semi-arid region of northeastern Wyoming in Campbell County, which is situated at approximately 1,490 meters above mean sea

level (amsl). The site is located approximately 20 southeast of Wright, Wyoming.

Background and Site Conditions - The ground surface is privately owned land primarily used for arid farming and stock grazing. No residences are located within 10 kilometers of the site. Access to the site is over unpaved roads used primarily for agriculture, oil and gas vehicles. The topography at the site slopes gradually from elevation 1,500 meters amsl to 1,400 meters amsl to the southeast. There are no major watercourses on the site.

Climatological Data - According to the U.S. Department of Agriculture (USDA) Natural Resources Conservation Service (NRCS) map, the average annual precipitation is 43.5 centimeters.

Design Evaporation Data - The National Weather Service developed an isopleths map of the Free Water Surface Evaporation (shallow lake evaporation) based on 24 years of data. The free water surface evaporation rate is the amount expected to evaporate from the disposal ponds, which is 114.3 centimeters per year. Approximately 88.9 centimeters of that rate occurs from May to October. The remaining 25.4 centimeters would evaporate from November to April. This evaporation data is based on a water containment that is not lined with white or black HDPE.

Project Location – Cisco, UT

Danish Flats, Utah. The project is located in an arid region of eastern Utah in the area known as Danish Flat, which is situated at approximately 1,405 meters above mean sea level (amsl). The site is located in Grand County approximately 5.6 kilometers north of Interstate 70 interchange exit number 214, and approximately 69.2 kilometers west of the Utah-Colorado state line.

Background and Site Conditions - The ground surface is privately owned land primarily used for stock grazing and oil and gas transmission piping. No residences are located within 16.1 kilometers of the site. Access to the site is over unpaved roads used primarily for oil and gas vehicles. The topography at the site slopes gradually from elevation 1,407 meters amsl to 1,402 meters amsl to the southeast. There are no major watercourses on the site. The site is located in the Mancos Shale lowland area including the Greater Cisco area. The Mancos Shale Formation is the predominant outcrop in this area (Hunt et al. 1996).

Climatological Data - According to the U.S. Department of Agriculture (USDA) Natural Resources Conservation Service (NRCS) map, the average annual precipitation is six inches.

Design Evaporation Data - The National Weather Service developed an isopleths map of the Free Water Surface Evaporation (shallow lake evaporation) based on 24 years of data. The free water surface evaporation rate is the amount expected to evaporate from the disposal ponds, which is 127 centimeters per year. Approximately 88.9 centimeters of that rate occurs from May to October. The remaining 38.1 centimeters would evaporate from November to April. This evaporation data is based on a water containment that is not lined with white or black HDPE.

Project Location – Midland, TX

XRI Blue Buchanan Pond, Texas. The project is located in an arid region of west Texas in the area known as the Permian Basin, which is situated at approximately 820 meters above mean sea level (amsl). The site is located in Midland County approximately 16 kilometers south of Wyoming.

Background and Site Conditions - The ground surface is privately owned land primarily used for stock grazing and oil and gas transmission piping. No residences are located within 16 kilometers of the site. Access to the site is over paved county roads. The topography at the site

slopes gradually from elevation 820 meters amsl to 815 meters amsl to the southeast. There are no major watercourses on the site.

Climatological Data - According to the U.S. Department of Agriculture (USDA) Natural Resources Conservation Service (NRCS) map, the average annual precipitation ranges between 30.5 and 38.1 centimeters.

Design Evaporation Data - The National Weather Service developed an isopleths map of the Free Water Surface Evaporation (shallow lake evaporation) based on 24 years of data. The free water surface evaporation rate is the amount expected to evaporate from the disposal ponds, which is 147 centimeters per year. This evaporation data is based on a water containment that is not lined with white or black HDPE.

PROJECT DETAILS

Purpose

The main purpose of the projects is to evaporate the production water and flow back water as quickly as possible or store and recycle the water while maintaining environmental controls and containment. The projects were planned and built in order to service the oil and gas industry for the disposal and recycling of production water and flow back water from oil and gas production in the service areas local to each facility location.

Several water disposal options exist, including reinjection wells, frac injection, treatment for surface discharge, recycling for reuse in the development of oil/gas, and evaporation. The evaporation technology was chosen for some of these projects due to the ideal site conditions for evaporation, including low precipitation, windy conditions, high ambient temperatures and sun. Other projects are designed to store the water for reuse, and therefore, use white color liner. Other factors that made the project sites ideal include the following; little or no residences within several kilometers of the site (other than consenting adjacent land owners), easy access to/from a major highway, long distance to open water at several kilometers, deep groundwater, and low permeable geologic formations below the sites.

Selection of Technology

To adequately contain the brine water, the top layer of the pond lining needs to be a durable long-lasting product that is cost-effective and helps to enhance evaporation (black liner) or reduce evaporation (white liner) while being acceptable to the regulatory agencies involved. Some of the liner technologies considered include compacted clay, geosynthetic clay liner (GCL), polyvinyl chloride (PVC), polypropylene (PPE), and high density polyethylene (HDPE). While several lining technologies exist and are allowed by the regulatory agencies, the HDPE liner was chosen for the top layer for several reasons, including, durability, resistance to ultraviolet (UV) degradation, chemical resistance, black color, and ease of construction.

HDPE is designed to be the top layer of ponds and be exposed to the elements (sun, freeze/thaw, and physical impact), therefore, the material needs to be resistant to UV degradation and be durable. The addition of the proper amount of high quality carbon black to the geomembrane during manufacturing is universally accepted as being resistant to significant deterioration caused by weathering. In addition to high quality carbon black, highly effective chemical UV stabilizers further extend the life of the liner. These additives absorb incident radiation and/or terminate free radical production, thus protecting the HDPE against thermal degradation and possible chemical reactions with surrounding materials. Other factors that affect

the potential UV resistance of a material include average density, density range or dispersion, chemical stabilizer system, catalyst type and amount of residue, copolymer type, combined chemical exposures, and failure criteria (GSE 2003). HDPE was chosen for this application due to these characteristics.

Implementation

To enhance the evaporative quality of each facility, and to adequately contain the brine water, high density polyethylene (HDPE) was chosen as the top layer. The top or primary liner was designed and constructed with 60-mil thick textured HDPE to help ensure a durable long-lasting containment. The liner was textured to increase the safety factor for personnel using the facility (i.e. the textured surface increases traction and gripping to enable easier egress in case of someone falling into the pond. White color liner was used for the reuse facilities with the intent to reduce evaporation for storage relative to black liner.

The facilities have been or are currently being constructed. The facilities consist of the following components (refer to Figures 1 and 2 for details):

- Access road and truck off-loading pad
- Piping and valves
- Acceptance Pits (vaults) or advanced oil/water separation equipment
- Sludge Pond covered with bird control netting or no sludge pond if oil/water separation equipment used
- Evaporation and storage ponds (constructed or planned):
    - Bluegrass Wright, WY has 8 ponds at approx. 3.2 hectares each and 7.62 meters deep (GCL, double lined HDPE with leak detection in between the liners)
    - Danish Flats, UT has 14 ponds built at approx. 2.1 hectares each and are 3.66 or 6.71 meters deep (single HDPE liner underlain by compacted clay layer)
    - XRI Buchanan, TX has one pond built at approx. 2.1 hectares each and are 3.66 meters deep (GCL, double lined HDPE with leak detection in between the liners)

General: Production water and flow back water is delivered to the sites via tanker trucks and via pipeline from well sites located within the geographic area local to each site, and depends on transportation costs and disposal fees when compared to other alternatives for water disposal in the area. The tanker trucks are off-loaded and the water is sent through a treatment process, including separation equipment, gun-barrel tanks, or state-of-the art equipment.

The Danish Flats facility's plan view is shown on the following Figure 2. The operation units include gun barrel tanks, a sludge pond, and a series of 2.1 hectare evaporation ponds. All of the structures are connected via gravity or force-main fed via an underground piping system. The Bluegrass Water facility process is similar to the Danish Flats layout.

Pond Inlet: Various methods exist for the separation of the oil and water prior to placement in the ponds for evaporation, and the proper removal of the oil from the water will dictate whether or not the ponds should be covered with bird control netting.

The incoming water at the Danish Flats and Bluegrass Water sites flows through the gunbarrel tank systems and the sludge pond before entering the evaporation ponds. The pre-treatment facilities and the evaporation ponds have been designed to follow the topography, allowing for gravity flow throughout the system, and the Bluegrass Water and Danish Flats sites are equipped with force-mains to allow pumping of the water from the lower Phase 1 ponds to

the upper Phase 2 ponds.

Volatile organic compound (VOC) emissions from the separation equipment and ancillary tankage are controlled to maintain air quality.

Shut-off valves have been installed on the header piping to allow for proper flow management. If necessary, portable gasoline powered pumps will be used to transfer liquid to ponds that are not in the gravity flow line or to empty a pond for maintenance or liner repair.

Slope Design: The sludge ponds and evaporation ponds have an interior slope of 3 horizontal to 1 vertical, and a maximum exterior slope of 2 to 1 at Danish Flats. At Bluegrass Water and XRI Buchanan, the pond interior and exterior slopes were designed with 4 to 1 slopes. The HDPE chosen has a textured surface, which will increase the safety characteristics of the facility by making it easier to walk on, especially on the interior slopes.

Berm Design: Surface water will not be allowed to enter the ponds because the constructed berms are several meters higher than the surrounding ground surface and also diversion and control ditches are used to direct the run-on and run-off for minimizing impact of storm water. The interior berm walls are covered with a protective layer of 60-mil high density polyethylene (HDPE). The HDPE will provide erosion control. The area between the evaporation ponds has been covered with HDPE or compacted clay to prevent erosion, control dust and enhance evaporation. The exterior sides of the berm have been seeded as necessary.

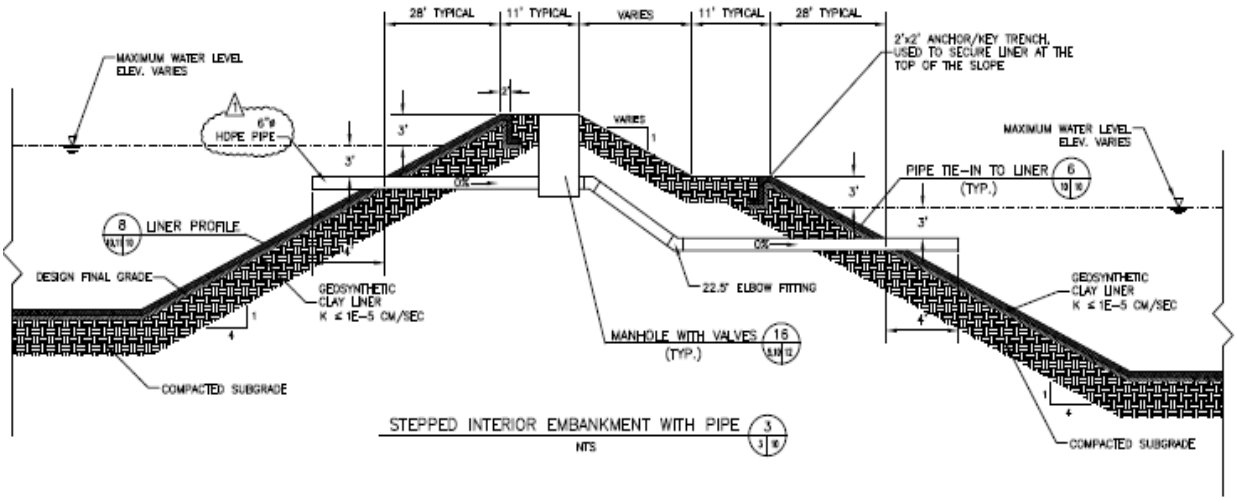

Figure 1. Pond Liner Details

Leak Detection System: As described in the geology/hydrology section of this paper, each site is underlain by low permeability layers of shale or clay, including at Danish Flats approximately 365.8 meters thick of Mancos Shale. The first usable aquifers for human use are below these formations for these sites. The geological investigations did not detect perched groundwater. The first usable aquifer will be protected by the three layers of liner in the pond, as well as natural clay aquitards below the pond bottoms at approximately 9.1 and 18.2 meters below the ground surface, which also includes the leak detection under the primary liner.

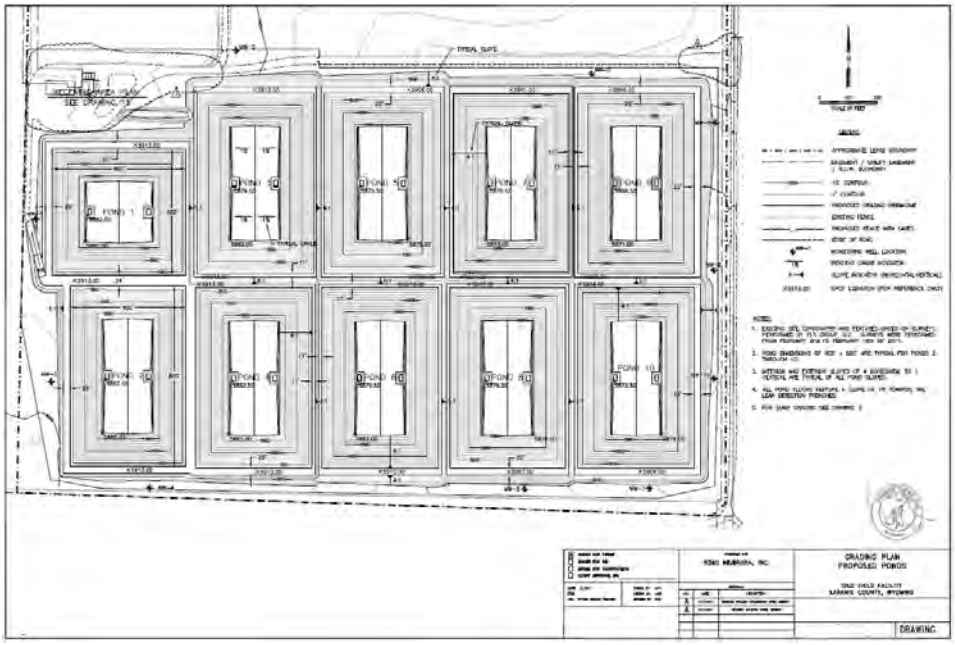

Figure 2. Facility Design Plan View – Permit Approved Layout

In addition to the ideal natural conditions at each site, a 60-mil HDPE liner has been installed as the top layer in all of the ponds. The pond floors slope toward sumps that are fitted with a riser monitoring pipe and leak detection equipment.

The leak detection system is inspected and data recorded as required. A summary of the inspections are reported to the regulatory agencies as needed. Liquid from the sump can be pumped back into the pond, if excessive amounts accumulate then specific protocols for repairing the liner are required if the volume of the leak exceeds certain thresholds.

Livestock/Wildlife Protection Measures: The entire facility area at each site has been fenced and gated to help prevent cattle or other animals from entering. Since the sludge ponds could have oily material on the surface, netting has been used to deter the entry of birds or other wildlife at the Danish Flats and Bluegrass Water sites.

Capacity: The volume of water able to be stored for evaporation or storage in the ponds is as follows:

- Bluegrass Water Wright – Ponds 1-8 are 7.62 meters deep of water holding capacity and nearly 1,000,000 barrels (at 159 liters per barrel) each for a total water holding capacity of approximately 8,000,000 barrels.
- Danish Flats - Ponds 1 through 8 are 3.65 meters of water holding depth and nearly 240,000 barrels each for a total capacity of approximately 2,000,000 barrels. Ponds 9 through 13 are 6.7 meters of water holding depth at Danish Flats and nearly 632,000 barrels each for a total capacity of 3,160,000 barrels.
- XRI Buchanan - Pond 1 is 3.65 meters of water holding depth and nearly 500,000 barrels.

Figure 3. Aerial Photo of Project at Danish Flats, UT

The partially completed and partially operational project at Danish Flats was photographed from the air on June 29, 2009 and is shown above. The water was distributed from the sludge pond to the Ponds 1 through 12, which appear as "black". The Ponds 13 appears to have "brownish" water, which includes some construction water is shown in the background and was not yet approved for water disposal at the time of the photography, but has since been put into operation. Currently, 14 evaporation ponds are operational at Danish Flats.

Operational Data

At Danish Flats they have experienced various quantities of water deliveries ranging from 10,000 barrels to 35,000 barrels per day. Each barrel is equal to 159 liters. The water is moved from the off-loading area through the sludge pond and to the evaporation ponds by gravity or via force main for distribution to Phase 2. Each pond at Danish Flats, Utah has a free board requirement of 0.61 meters, and each pond the Bluegrass Water has a free board requirement of 0.91 meters.

When an individual evaporation pond was brought on-line, such as Ponds 5 through 8 at Danish Flats, and the water was allowed to flow into the empty pond lined with HDPE, the water was observed as "disappearing" due to the evaporative nature of the HDPE when in combination with the hot sun and arid climate in Utah in July and August.

In Cisco, UT in July and August the ambient air temperatures often exceeds 37.8 degrees Celsius and the wind normally blows to some extent. The actual evaporation encountered during the months of July and August 2008 at the site was measured to be approximately 38.1 and 45.7 centimeters per day, respectively. The facility operators observed very favorable evaporation of the water and measured the total evaporation for the year 2008 above the estimate of 127 centimeters for approximately six months of operation.

In year 2009, the Danish Flats facility was measured to have 152.4 centimeters of evaporation, which took place mostly in the months from April 1 to October 31, and again in year 2010 the evaporation total has exceeded 152.4 centimeters over the entire water surface of

the ponds. The deeper ponds at Danish Flats experienced an approximately 30 percent lower evaporation rate due to the deeper water depth, therefore, the entire depth of water was not able to be achieve warmer temperatures as did the shallower ponds.

Each site is equipped or designed with leak detection systems that are monitored on a monthly basis or continuously, depending on the equipment chosen. Two ponds at Danish Flats were adversely affected by shifting ice at the HDPE pipe boots when the liquid level in the ponds were adjusted, which resulted in leaks at the pipe boots. The liner was easily repaired.

Figure 4. Weep system to enhance evaporation on black liner

In an effort to increase evaporation with low costs in mind, a "weep" system was added to the allow water to flow and fan out over the surface of the HDPE liner that is above the water line. This system utilizes the exposed HDPE liner to increase evaporation by using the heat generated from the exposed HDPE liner in combination with the increased surface area of the water fanning out over the liner. Please refer to the photograph of the "weep" system.

At XRI Buchanan, the top liner used was a white color 60-mil thick HDPE to reduce the evaporation relative to the black liner, due to the facility wanting to retain the water for reuse in the fracking operations.

CONCLUSIONS

The use of HDPE as the primary liner in the ponds appears to be favorably enhancing the evaporation of the water. At Danish Flats, the estimate of 127 centimeters of evaporation per year was far exceeded given the 83.8 centimeters of evaporation experienced in only July and August 2008, which totaled 177.8 centimeters for 2008. In years 2009 and 2010, the evaporation rate was over 152.4 centimeters. In 2012, the evaporation rate was 106.7 centimeters from May through August. The "weep" system was an enhancement to increase evaporation, which was not quantitatively measurable, but may have been a factor in the total evaporation. The deeper ponds at Danish Flats experienced approximately a 30 percent lower evaporation rate due to cooler water at depth. Similarly, the actual evaporation experienced at the Bluegrass Water

project was also more than the pan evaporation estimate based on ponds without the HDPE liner effects, including the increase in evaporation from the estimate of 114.3 centimeters per year to nearly 139.7 centimeters.

The evaporation rates at Bluegrass Water Wright has been enhanced with the use of the sprayers that assisted with the evaporation.

The durability and resistance to UV degradation due to the proper amount of carbon black in the geomembrane and other factors as discussed above are the major reasons for the use of the HDPE geomembrane liner as the top layer. The increase with the rate of evaporation due to the black color of the HDPE has been a great benefit and in combination with the "weep" system has realized an increase with the total evaporation at each facility.

The white liner at XRI Buchanan was used to reduce evaporation relative to the black liner. The surface temperature of the white liner as compared to black liner can be 104 degrees Fahrenheit cooler (Solmax) due to reflecting the sunlight, thus, reducing the ability of the water to heat and hence reducing the water evaporation. The quantitative reduction in the amount of evaporation is not known.

Some of the liner was installed during the summer months and due to the expansion and contraction of the liner with ambient air temperature gradients, the anchor trenches were only filled during the coolest part of the day to reduce bridging.

The leak detection system is used to capture leaks through the primary liner, which worked as designed at the Danish Flats site when a leak was propagated due to ice on the water and the level in the ponds changing which resulted in the ice grabbing onto the pipe and pulling on the pipe boot. The liner was repaired and the leak did not appear again.

An existing study was conducted on an HDPE liner installed at a site in Colorado after 20 years of service where the liner was not buried and exposed to weathering, UV light and cooling tower blow-down water. The material was tested for various properties and was found to have no significant reduction in the primary physical properties of the HDPE (Ivy 2002).

ACKNOWLEDGEMENTS

Thank you to Bluegrass Water and XRI Buchanon, and to Mustang Extreme and Raven/Colorado Lining, Inc. who provided installation expertise and also performed the construction of the HDPE liners at the ponds in field, which all are performing exceptionally well and without leaks due to construction.

REFERENCES

Gundle/SLT Environmental, Inc. (GSE). (2003). "Technical Note – HDPE, UV Resistance for GSE Geomembranes." http://www.truslate.com/grid/techspec.pdf .

Hunt, G. L. (1996). Environmental Handbook, Environmental Regulations for the Oil & Gas Exploration and Production Industry.

Solmax (2020). White Prime Finish brochure.

Ivy, N (2002). HDPE geomembrane after 20 years of service, GFR Magazine June/July 2002.

Geosynthetics Conference

Hydraulic Conductivity of Bentonite-Polymer Geosynthetic Clay Liners to Coal Combustion Product Leachates

Dong Li[1] and Kuo Tian, Ph.D.[2]

[1]PhD student, Department of Civil and Environmental Engineering, George Mason University, Fairfax, VA 22030, USA; e-mail: dli8@gmu.edu
[2]Assistant Professor, Department of Civil, Environmental, and Infrastructure Engineering, George Mason University, Fairfax, VA 22030, USA; e-mail: ktian@gmu.edu

ABSTRACT

Experiments were conducted to evaluate the hydraulic conductivity of bentonite-polymer (B-P) GCLs to coal combustion product leachates. Two commercially available B-P GCLs with polymer loading of 0.5% (B-P-0.5) and 5.5% (B-P-5.5) and one sodium-bentonite (Na-B) GCL were tested in this study. Hydraulic conductivity tests were conducted with one synthetic CCP leachate that was chemically representative to the leachate from typical flue gas desulfurization solid disposal facilities ((TFGDS, ionic strength = 473 mM). The hydraulic conductivity of Na-B GCL and B-P GCLs permeated with TFGDS leachate ranged from 1.4 x 10^{-11} m/s to 3.1 x 10^{-7} m/s at 20 kPa, which were much more permeable than those permeated with DI water (9.4x10^{-12} m/s to 2.2x10^{-11} m/s). Increasing in effective confining stress resulted in decreasing in hydraulic conductivity. The hydraulic conductivity of Na-B GCL decreased from 3.1 x 10^{-7} m/s to 2.1 x 10^{-9} m/s as effective confining stress increased from 20 to 500 kPa, whereas B-P-0.5 and B-P-5.5 GCLs had hydraulic conductivity lower than 10^{-10} m/s at 20 kPa and 250 kPa, respectively. The test results illustrate that B-P GCLs can be used to manage TFGDS leachate.

INTRODUCTION

Geosynthetic clay liners (GCLs) consist of a thin layer of sodium bentonite (Na-B) sandwiched between two geotextiles (Shackelford et al. 2000; Jo et al. 2001, 2005; Scalia et al. 2014; R. Kerry Rowe, 2020). The Na-B in GCLs primarily consists of Na-montmorillonite (65 to 90%), which has large surface area, high cation exchange capacity, and high swelling potential (Shackelford et al. 2000; Jo et al. 2001, 2005; Bradshaw and Benson 2014). Osmotic swelling of montmorillonite yields narrow and tortuous flow channels, resulting in low hydraulic conductivity of GCL (Edil et al. 2011; Tian et al. 2019). However, several researchers have reported that leachates with high ionic strength (e.g., I > 300 mM), predominantly polyvalent cations, and/or extreme pH condition can inhibit the swelling of Na-B, resulting in large intergranular pore space and high hydraulic conductivity of GCL (>10^{-10} m/s) (Shackelford et al. 2000; Jo et al. 2001, 2005; Di Emidio et al. 2015; Tian et al. 2016, 2019; Chen et al. 2019).

Recognize these deficiencies, the Na-B have been modified using organic compounds or polymer to improve the chemical compatibility of GCLs (Kolstad et al. 2004; Katsumi et al. 2008; Scalia et al. 2014; Özhan, 2018; Chai et al. 2020). These polymer-modified GCLs, also known as bentonite-polymer (B-P) GCLs, comprise of bentonite-polymer composites (BPC) or dry-blended polymer and bentonite (Scalia et al. 2014; Di Emidio et al. 2015; Tian et al. 2016, 2019; Chen et al. 2019). B-P CCLs have been found to have high resistance to chemicals and lower hydraulic conductivity to leachates from coal combustion product (CCP) (Chen et al. 2019; Binte and Tian

2020). Chen et al. (2019) reported that the B-P GCLs with high polymer loading (>1.9%) can maintain low conductivity ($<10^{-10}$ m/s) to CCP leachates with ionic strength ranging from 39.5 mM to 755 mM). Binte and Tian (2020) also reported the hydraulic conductivity of B-P GCL with sufficient polymer loading (>5%) was lower than $<10^{-10}$ m/s when permeated synthetic leachate with an ionic strength = 2577 mM.

The objective of this study was to evaluate the hydraulic conductivity of B-P GCLs to leachate from CCP disposal facilities. Two commercially available B-P GCLs with polymer loading of 0.5% (B-P-0.5) and 5.5% (B-P-5.5) and one sodium-bentonite (Na-B) GCL were tested in this study. Hydraulic conductivity tests were conducted in the flexible wall permeameter following falling head method according to ASTM D6766. Tests were conducted with one synthetic CCP leachate that was chemically representative to the leachate from typical flue gas desulfurization (FGD) solid disposal facilities (I = 473 mM). Tests were initially conducted at 20 kPa effective confining stress until reaching hydraulic and chemical equilibrium, and then the effective confining stress was increased incrementally from 20 kPa to 100, 250, and 500 kPa to mimic the stress induced by the waste body. Tests were also conducted with DI water as controls.

MATERIALS AND METHODS

Geosynthetic Clay Liners. Three GCLs were used in this study, including one conventional Na-B and two B-P GCLs. B-P GCLs are manufactured by mixing granular polymer with granular Na-B. The granule size distribution of the GCLs was determined by mechanical sieve analysis following ASTM D6913. All the GCLs had similar grain size distribution (medium to fine sand), as shown in Figure 1. Mass per unit area, thickness and polymer loading of the GCLs is given in Table 1.

Polymer loading in B-P GCLs were determined following the loss on ignition (LOI) method adopted by Scalia et al. (2014) and Tian et al. (2016). Polymer loading was determined based on the assumption that polymer burns completely during LOI test and by discounting the LOI of the conventional Na-B. One B-P GCL has 0.5% polymer loading and the other one has 5.5% polymer loading.

Table 1. Mass per unit area, initial thickness and polymer loading of sodium bentonite (Na-B) and bentonite-polymer (B-P) GCLs used in this study.

GCL	Mass per unit area (kg/m^2)	Thickness (mm)	Polymer loading (%)
Na-B	4.5	5.0	-
B-P-0.5	5.7	7.0	0.5
B-P-5.5	6.0	8.1	5.5

Note: Polymer loading is calculated based on loss on ignition as per ASTM D7348. Mass per unit area is measured as per ASTM D5993. "-" indicates not applicable. The numeric digits with B-P GCLs represent their polymer loading.

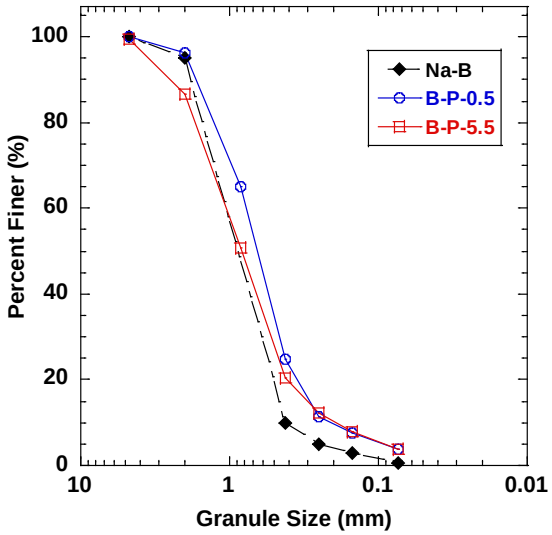

Figure 1. Grain size distribution of sodium bentonite (Na-B) and bentonite polymer (B-P) GCLs used in this study.

Permeant Solutions. CCP leachate data collected from more than 130 CCP disposal units (landfills and impoundments) located within United States was chemically characterized based on dominant CCP type i.e., bottom ash, fly ash, flue gas desulfurization (FGD) materials (e.g., FGD gypsum, FGD solids, fixated FGD), mixed coal ash. The master variables that affect the hydraulic conductivity of GCL were I, pH, relative abundance of monovalent and divalent cations (RMD). Synthetic FGD solids (TFGDS) leachate (I = 473 mM, RMD = 0.65 $M^{1/2}$) was created by taking the geometric mean of all the leachates collected from FGD solids disposal facilities shown in figure 2. The concentration of major cations, anions and the bulk properties (I, RMD, pH) of the TFGDS leachates selected for this study are given in Table 2.

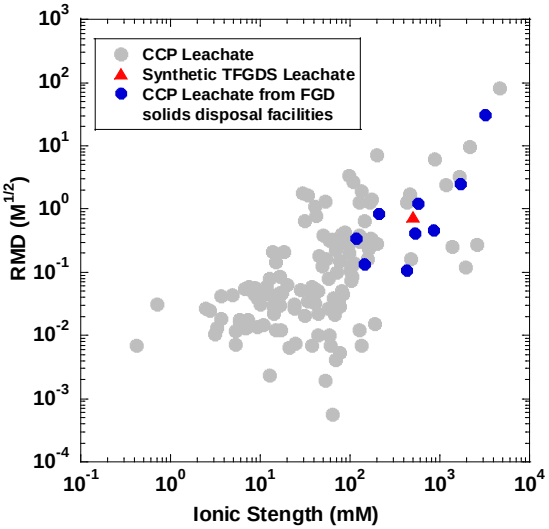

Figure 2. Ionic strength and RMD of CCP leachates collected from more than 130 CCP disposal units across U.S.

Table 1. Properties of selected synthetic TFGDS leachates.

Leachate	Major cations			Major anions		Bulk properties		
	Na^+ (M)	K^+ (M)	Mg^{2+} (M)	Cl^- (M)	SO_4^{2-} (M)	I (mM)	RMD ($M^{1/2}$)	pH
TFGDS	0.17	0.00	0.06	0.06	0.11	473	0.65	6.5

Note: I = Ionic strength, RMD = Relative abundance of monovalent and divalent cations, TFGDS = Typical FGD solids.

The synthetic TFGDS leachate was prepared by dissolving reagent-grade NaCl, $MgSO_4$ and Na_2SO_4 in Type II DI water as per ASTM D1193. The synthetic leachate was stored in sealed carboy to prevent interaction with atmosphere (CO_2). The electrical conductivity (EC) and pH of the synthetic leachate was checked periodically to assure no changes in the leachate chemistry.

Hydraulic Conductivity. The hydraulic conductivity of GCLs were measured with falling-head test using flexible-wall permeameters according to ASTM D6766. GCL specimens were hydrated with permeant solution at an effective stress of 20 kPa for 48 hours, and then conducted hydraulic conductivity test. Fifty mL burettes were used to gather the influent liquid and the effluent were collected using 60 mL HDPE bottles.

Tests were conducted until reaching hydraulic and chemical equilibrium (Jo et al. 2005). Hydraulic equilibrium criteria require the measurements of hydraulic conductivity are steady, and the last three consecutive measurements of ratio between the outflow (Q_{out}) and influent volumes (Q_{in}) are between 25% variation. The chemical equilibrium criteria require that the electric conductivity (EC) of the effluent (EC_{out}) are falling within 1.0 ± 10% of influent value (EC_{in}) , and the ratio of the pH of effluent (pH_{out}) and influent (pH_{in}) are within 1.0 ± 10. Tests were initially conducted at 20 kPa confining effective stress. Once the hydraulic conductivity and chemical equilibrium reached, the confining effective stress was increased to 100, 250, and 500 kPa to mimic the stresses induced by the mass of the waste placed in the landfill.

RESULTS AND DISCUSSION

Temporal behavior of the B-P-0.5 permeated with TFGDS leachate is shown in Figure 3. The hydraulic equilibrium achieved at the early stage of the test, where the Q_{out}/Q_{in} was within 1 ± 25% (Fig. 3a). The chemical equilibrium reached around 13 PVF, i.e., both EC and pH of the effluent leveled off and fell within the 1 ± 10% of the EC and pH in the influent (Fig. 4b). The confining stress of the hydraulic conductivity test was then increased from 20 kPa to 100, 250, and 500 kPa. The hydraulic conductivity of B-P-0.5 GCL decreased from 1.4 x 10^{-7} to 1.5 x 10^{-9} when the confining stress increased from 20 kPa to 100 kPa. At 250 kPa, the hydraulic conductivity of B-P-0.5 GCL decreased approximately two orders of magnitude (6.9 x 10^{-11} m/s). The hydraulic conductivity of B-P-0.5 to TFGDS decreased drastically at a PVF of 17.6 to 18.0 because polymer that eluted from GCL clogged the effluent tubes, resulting in decreasing of hydraulic conductivity. After removing polymer clogging by flushing tubes, the hydraulic conductivity of B-P-0.5 GCL increased from 3.0 x 10^{-12} m/s to 7.2 x 10^{-11} m/s and remained constant. The hydraulic conductivity of B-P-0.5 further decreased to 1.3 x 10^{-11} m/s at 500 kPa.

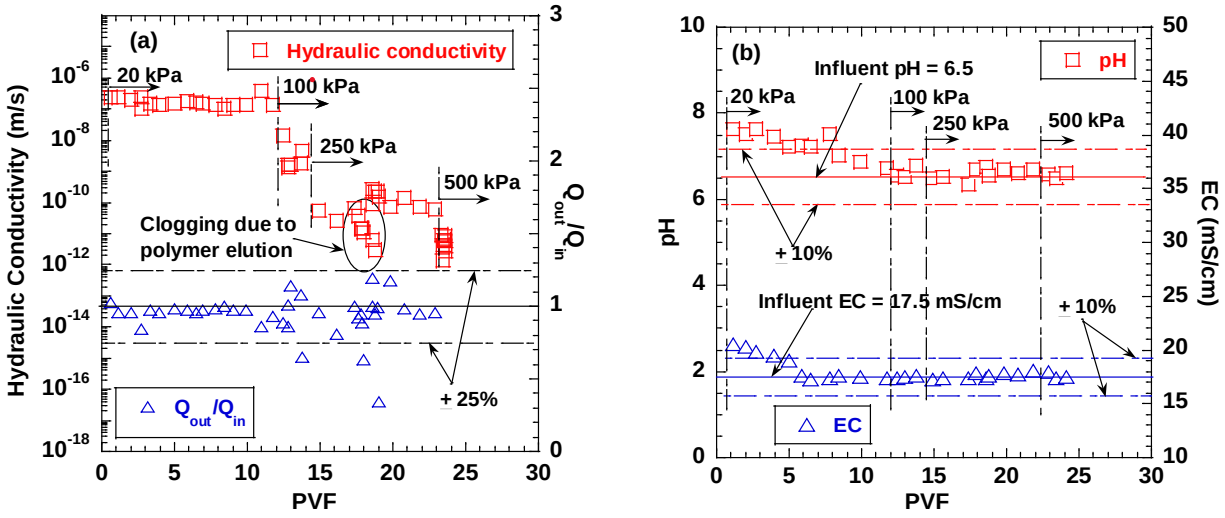

Figure 3. Hydraulic conductivity, ratio of inflow to outflow (Q_{out}/Q_{in}), pH, and EC from test on B-P-0.5 permeated to TFGDS leachate.

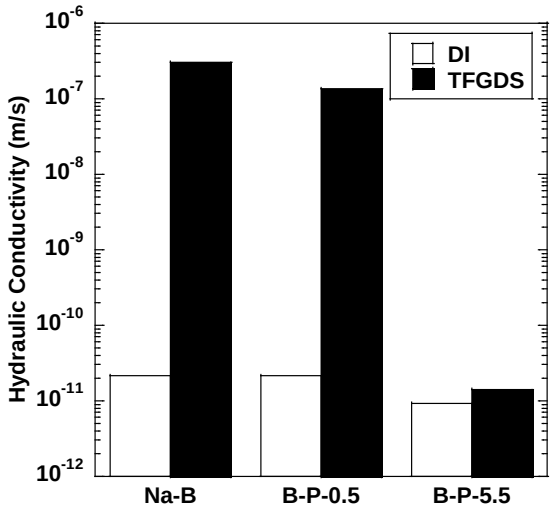

Figure 4. Hydraulic conductivity of GCLs permeated with TFGDS leachate at 20 kPa.

Hydraulic conductivity of Na-B and B-P GCLs to TFGDS leachate and DI water are shown in Figure 4. Hydraulic conductivity of all the GCLs (Na-B, B-P-0.5 and B-P-5.5) to DI water were less than 10^{-10} m/s. Both Na-B and B-P-0.5 GCLs showed hydraulic conductivity > 10^{-10} m/s when permeated with TFGDS-473 leachate at 20 kPa effective confining stress, which were much faster than that of Na-B and B-P-0.5 GCLs to DI water. B-P-5.5 GCL had similar hydraulic conductivity when permeated with TFGDS-473 leachate and DI water.

Hydraulic conductivity of the Na-B and B-P GCLs permeated with TFGDS leachate decreased as the confining stress increased (Figure 5). The hydraulic conductivity of Na-B GCL decreased from 3.1 x10^{-7} m/s to 2.1 x 10^{-9} m/s when the effective confining stress increased from 20 kPa to 500 kPa. Chen et al. (2018) also reported that increasing the effective stress from 20 to 450 kPa caused the hydraulic conductivity of Na-B GCLs decreased up to three orders of magnitude.

The B-P-0.5 GCL showed a faster decreasing trend of hydraulic conductivity than that of Na-B GCL as the confining stress increased from 20 to 500 kPa. The hydraulic conductivity of B-P-0.5 GCL to TFGDS-473 leachate was similar to that of Na-B GCL at 20 kPa (1.4×10^{-7} vs. 3.1×10^{-7} m/s). As the effective stress increased, the hydraulic conductivity of B-P-0.5 GCL was approximately two orders of magnitude lower than that of Na-B GCL.

The B-P GCLs with higher polymer loading (>5%) can maintain the low hydraulic conductivity (< 10^{-10} m/s) to TFGDS-473 leachate at 20 kPa, whereas the hydraulic conductivity of B-P-0.5 GCL decreased to lower than 10^{-10} m/s as the effective stress increased to 250 kPa. It indicates that B-P GCL with higher polymer loading can effectively block intergranular pore space to leachates at lower effective stress.

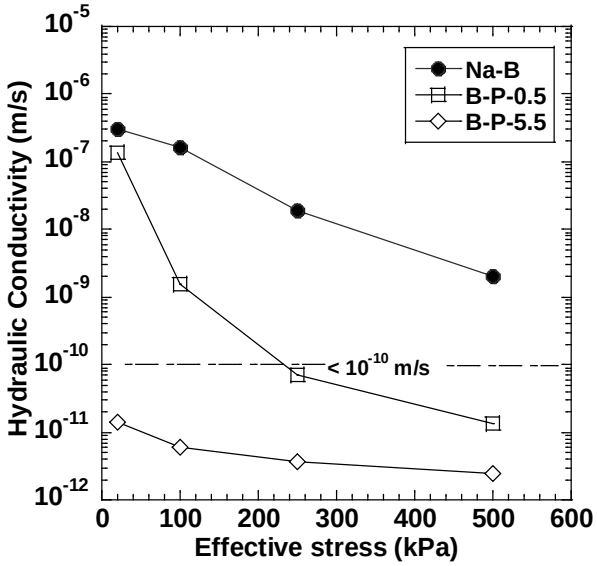

Figure 5. Hydraulic conductivity of GCLs to TFGDS leachate as a function of effective stress.

CONCLUSIONS

Hydraulic conductivity of Na-B and two B-P GCLs were evaluated using TFGDS leachate and DI water. The following conclusions can be made based on the findings of the study:

1. The hydraulic conductivity of B-P GCLs were lower than Na-B GCL when permeated with TFGDS leachate.
2. Increase of the effective confining stress lead to the decrease in the hydraulic conductivity of the GCLs permeated with TFGDS leachate. B-P GCLs showed a fast decreasing trend of hydraulic conductivity than that of Na-B GCL.
3. Additionally, B-P GCLs with higher polymer loading have better chemical compatibility than B-P GCLs with low polymer loading, and can be used to manage CCP leachates.

ACKNOWLEDGEMENTS

This material is based upon work supported by the Environmental Research & Education Foundation (EREF) and CETCO Inc. Any opinions, findings and conclusions in this material are those of the authors and do not necessarily reflect the views of EREF and CETCO Inc.

REFFERENCES

ASTM D 1193. Standard Specification for Reagent Water, *ASTM International*, West Conshohocken, Pennsylvania, USA.

ASTM D 5993. Standard Test Method for Measuring Mass per Unit of Geosynthetic Clay Liners, *ASTM International*, West Conshohocken, Pennsylvania, USA.

ASTM D 6766. Standard Test Method for Evaluation of Hydraulic Properties of Geosynthetic Clay Liners Permeated with Potentially Incompatible Aqueous Solutions, *ASTM International*, West Conshohocken, Pennsylvania, USA.

ASTM D 6913. Standard Test Methods for Particle-Size Distribution (Gradation) of Soils Using Sieve Analysis, *ASTM International*, West Conshohocken, Pennsylvania, USA.

ASTM D 7348. Standard Test Methods for Loss on Ignition (LOI) of Solid Combustion Residues, *ASTM International*, West Conshohocken, Pennsylvania, USA.

Bradshaw, S. L. and Benson, C. H. (2014). Effect of municipal solid waste leachate on hydraulic conductivity and exchange complex of geosynthetic clay liners, *Journal of Geotechnical and Geoenvironmental Engineering*, 140(4): 04013038.

Chai, J. and Prongmanee, N. (2020). Barrier properties of a geosynthetic clay liner using polymerized sodium bentonite, *Geotextiles and Geomembranes*, 48(3): 392–399.

Chen, J. N., Benson, C. H. and Edil, T. B. (2018). Hydraulic conductivity of geosynthetic clay liners with sodium bentonite to coal combustion product leachates, *Journal of Geotechnical and Geoenvironmental Engineering*, 144(3): 04018008.

Chen, J. N., Salihoglu, H., Benson, C., Likos, W., and Edil, T. (2019). Hydraulic Conductivity of Bentonite-Polymer Composite Geosynthetic Clay Liners Permeated with Coal Combustion Product Leachates, *Journal of Geotechnical and Geoenvironmental Engineering*, 145 (9):04019038.

Di Emidio, G., Mazzieri, F., Verastegui-Flores, R. D., Van Impe, W., and Bezuijen, A. (2015). Polymer-treated bentonite clay for chemical-resistant geosynthetic clay liners, *Geosynthetics International*, 22(1):125-137.

Edil, T., Shackelford, C., Scalia, J., Benson, C., & Bohnhoff, G. (2011). Geosynthetic clay liners containing bentonite polymer nanocomposite, *Geo-Frontiers 2011*, ASCE, Dallas, TX, USA: 2001-2009.

Jo, H. Y., Katsumi, T., Benson, C. H., and Edil, T. B. (2001). Hydraulic conductivity and swelling of nonprehydrated GCLs permeated with single-species salt solutions, *Journal of Geotechnical and Geoenvironmental Engineering*, 127(7): 557-567.

Jo, H. Y., Benson, C. H., Shackelford, C. D., Lee, J. M., and Edil, T. B. (2005). Long-term hydraulic conductivity of a geosynthetic clay liner permeated with inorganic salt solutions, *Journal of Geotechnical and Geoenvironmental Engineering*, 131(4): 405-417.

Katsumi, T., Ishimori, H., Onikata, M., and Fukagawa, R. (2008). Long-term barrier performance of modified bentonite materials against sodium and calcium permeant solutions, *Geotextiles and Geomembranes*, 26(1): 14-30.

Kolstad, D.C., Benson, C.H. and Edil, T.B. (2004). Hydraulic conductivity and swell of nonprehydrated geosynthetic clay liners permeated with multispecies inorganic solutions, *Journal of Geotechnical and Geoenvironmental Engineering*, 130(12): 1236-1249.

Özhan, H.O., (2018). Hydraulic capability of polymer-treated GCLs in saline solutions at elevated

temperatures, *Apply Clay Science*, 161(Sep): 364-373.

Rowe, R. K (2020). Geosynthetic clay liners: Perceptions and misconception, *Geotextiles and Geomembranes*, 48(2): 137-156

Shackelford, C. D., Benson, C. H., Katsumi, T., Edil, T. B., and Lin, L. (2000). Evaluating the hydraulic conductivity of GCLs permeated with non-standard liquids, *Geotextiles and Geomembranes*, 18(2): 133-161.

Scalia IV, J., Benson, C. H., Bohnhoff, G. L., Edil, T. B., and Shackelford, C. D. (2014). Long-term hydraulic conductivity of a bentonite-polymer composite permeated with aggressive inorganic solutions, *Journal of Geotechnical and Geoenvironmental Engineering*, 140(3), 04013025.

Tian, K., Benson, C. H., and Likos, W. J. (2016). Hydraulic conductivity of geosynthetic clay liners to low-level radioactive waste leachate, *Journal of Geotechnical and Geoenvironmental Engineering*, 142(8), 04016037.

Tian, K., Likos, W. J., and Benson, C. H. (2019). Polymer Elution and Hydraulic Conductivity of Bentonite–Polymer Composite Geosynthetic Clay Liners, *Journal of Geotechnical and Geoenvironmental Engineering*, 145(10), 04019071.

Zainab, B. and Tian, K. (2020). Hydraulic Conductivity of Bentonite-Polymer Geosynthetic Clay Liners to Coal Combustion Product Leachates *Geo-Congress 2020*, ASCE, Minneapolis, MN, USA: 579-586.

Geosynthetics Conference

New Geomembranes for Challenging Containment Applications - Formulations for Site Specific Chemistry and Environmental Conditions.

Javier Páez , MEng[1]; Gabriel Martín, MSc[2];
Jorge Fernández, MEng[3] and Marc Amtsberg, B.Eng[4]

[1]Atarfil Group; jpaez@atarfil.com
[2]Atarfil Group; gmartin@atarfil.com
[3]Atarfil Group; jfernandez@atarfil.com
[4]Atarfil Group; mamtsberg@atarfil.com

INTRODUCTION

High density polyethylene (HDPE) geomembranes have been used as containment application barriers in geoenvironmental applications for more than 40 years. The first general specification available to support geomembrane engineering design was published in 1983 in USA by the National Sanitation Foundation - Standard No. 54. After several revisions, in 1997 the standard was withdrawn for several interrelated issues. One of the most important issue was that this standard did not address the long-term performance of the material. The geomembrane industry at the prompting of the U.S. Environmental Protection Agency in 1997 started working on a new HDPE specification. This was provided by the Geosynthetic Research Institute (GRI) with the standard GRI GM13.

The GRI GM13 standard covers Manufacturing Quality Control (MQC) considerations for both smooth and textured HDPE geomembranes. It sets forth a minimum physical and mechanical properties of geomembranes, as well as key long-term performance properties that should be tested. This requirement for long-term performance testing was a unique aspect in comparison to previous HDPE specifications.

Since 1997 and now, in its fifteenth revision, the GRI GM13 standard for HDPE is used and adopted throughout the industry by specifiers and government regulatory bodies. However, the fundamental GRI-GM13 aim was directed towards product MQC, it was not intended to consider site-specific design conditions. Even GRI GM13 states that "*1.3 In the context of quality systems and management, this specification represents manufacturing quality control (MQC)"* and "*1.4. This standard specification is intended to ensure good quality and performance of HDPE geomembranes in general applications, but is possibly not adequate for the complete specification in a specific situation. Additional tests, or more restrictive values for test indicated, may be necessary under conditions of a particular application."*

The conclusion is that the GRI GM13 requirements are appropriate for projects where the leachate in contact and exposure condition is relatively inert, but now geomembranes are being used in applications where the site chemistry and conditions will challenge traditional HDPE formulations. Therefore, further research is needed to ensure that diffusion properties of the barrier are understood and evaluated long term for the specific critical site.

GRI GM 13 STANDARD CONSTRAINTS

The GRI GM13 standard's main function as a quality control document, is to identify the properties, test methods and intervals of the HDPE Geomembrane to be evaluated. The standard does not reference hydraulic performance because it assumes HDPE compatibility with the site leachate and therefore does not consider the chemical degradation potential of high-risk sites.

The initial performance evaluation testing proscribed by GRI GM13, considers Oxidative Induction Time (OIT) - Standard S-OIT (ASTM D 3895) and high-pressure HP-OIT (ASTM D 5885) tests as an either/or requirement. The purpose of including the two tests by GRI GM13 was to provide the manufacturer an option to choose the appropriate test method to evaluate their specific antioxidant packages, and the recommended values (Std OIT >100min or HP OIT > 400min) based on different geomembranes historically, but not correlated directly to site needs.

To evaluate the performance of the antioxidant packages over the long-term, the standard incorporates incubation tests for Oven Aging and UV. The purpose of these tests was to challenge the long-term thermal oxidation behavior of the HDPE geomembrane over an extended period, although antioxidant retention as per the intentions of the document, is an MQC benchmark and not considered directly to project exposure conditions.

The final key longevity measure in GRI GM13 is resistance to stress crack failure, with the GRI GM13 recommending Stress Crack Resistance (SCR) values that have adjusted periodically with better manufacturing capability to today's specified value (>500hrs). It is the high crystallinity of HDPE that gives it chemical resistance in challenging applications, but also makes it susceptible to stress crack failure. Challenging projects may result in a material that has high chemical resistance but possibly lower longevity to stresses onsite. Studies would suggest that material to be used in crucial facilities should contain a SCR exceeding 1000hr, preferably 2000 hr. As such GRI GM-13 specification values for SCR >500 h may be again considered a minimum benchmark with the resins now available, and not recommendations based on project specific conditions.

In view of this summary, GRI GM13 may be viewed as a minimum benchmark measure to evaluate Geomembrane performance in low risk containment applications. It is an ideal quality control and suitable test method specification as intended, to provide the tool kit that allows the designer to implement site specific testing regimes linked to site performance.

The challenge for the designer is to understand both the required test methods and specification values suitable for long term performance, but also whether these can be manufactured with sufficient quality control that other properties remain unaffected. This can only be achieved by long term performance testing of custom-made formulations proscribed by the manufacturer.

CHEMICAL RESITANCE OF HDPE GEOMEMBRANES

The chemical resistance of a geomembrane is usually the initial aspect of the design process and HDPE geomembranes are generally chosen because of it. In a project where the chemicals will interface directly with the liner, the geomembrane's resistance must be assured for the life of the facility. This situation has long been evaluated by manufactures and has resulted in various chemical resistance charts which lists generic chemicals against HDPE geomembranes on a relative basis. The principal primary effects of chemical interaction with HDPE geomembrane resin is mass gain / swelling, changes in their elongation at break and reductions in their tensile strength. Also, the chemicals can interact with the antioxidant package, inactivating them.

Chemical resistance charts are based in these effects just mentioned. These tables would be generally reliable but there are many circumstances where specific testing is required, and further assessment is needed. Chemical situations where the charts may not be appropriate:

- site which includes chemical that is not a single component, therefore chemical effects are not identified or even composition of the resulting chemical is not known until the project is not constructed;
- chemical composition changes over the course of geomembrane service lifetime;
- non-tested site circumstances, such as chemical exposure with extreme heat or cold conditions and liners under high stress that can greatly accelerate chemical attacks;
- long-term properties not evaluated with extensive exposure to the chemicals directly in contact with the geomembrane.

Moreover, it is very important to mention that these chemical charts only evaluate how the pure resin (PE) resist to the chemicals, but it does not assess how the antioxidant package of the geomembrane will interact with this chemical environment. There are many circumstances that the antioxidant will interact with the chemicals therefore leaving the geomembrane rapidly without any protection, inactivating them.

Consequently, one of the most important analysis that should be considered in a critical site with aggressive chemicals is the effects in the changes in SCR and OIT tests. These are both important parameters that should be tested in addition to simple mechanical properties. The decrease of oxidative stability and stress cracking are very relevant in assessing the chemical resistance of the material. OIT testing is of particular significance in identifying the susceptibility of the lining material to oxidation under process, service conditions or their loss due to unwanted migration reactions. SCR is also extremely important, although HDPE polymer is recognized and accepted for its broad resistance to chemicals in term of chemical charts, exposure to some of this ‘accepted’ chemicals can increase highly the environmental stress crack failure of a geomembrane and hence reducing its lifetime considerately.

HDPE liners in mining applications will experience extreme chemical degradation which will lead, as mentioned above, to a reduction on its lifetime. The service life of HDPE geomembranes is normally evaluated using a three-stage degradation model: Stages A, B and C. GSI GRI considers this to be the most appropriate determinant of end of life when the data is available. The Stage A represents the period during which depletion of antioxidants and stabilizers occurs. In the Stage B the antioxidant and stabilizers are effectively depleted but then follows the induction time to the onset of polymer degradation. Finally, The Stage C degradation of various properties begin to gradually develop. The point of 50% retention of mechanical properties is taken as the failure point. Stage A is the only stage that is well delimited by the Std-OIT and HP-OIT tests. Stages B and C may vary depending on the parameters being considered, e.g., tensile break strength, tensile break strain, and stress crack resistance. Therefore, any testing program to assess the performance of HDPE geomembranes in contact with chemical liquors as present in mining process solutions should evaluate changes to the OIT testing parameters. Since once the antioxidant package is spent, Stage A, then oxidation degradation begins, and properties of the geomembrane will consequently decrease.

GRI GM13 HDPE GEOMEMBRANE LIFETIME BEHAVIOR IN DIFFERENT LIQUORS

In order to evaluate how a HDPE Geomembrane behaves with different chemicals, it has been incubated two samples of a regular HD Geomembrane that meets GRI GM13 requirements with two different liquor environments taken directly from two landfills. One acid leachate with a pH 5.67 and the other one an alkaline leachate with a pH 8.10. By setting at the same time three immersions in those liquors with different temperature (20°C, 60°C and 85°C), then the results have been used to conduct lifetime extrapolations via the Arrhenius equation and by monitoring the incubated geomembranes coupons.

The various coupons were monitoring by periodically removed and evaluated. With the results obtained, it is being reproduced their Stage A prediction lifetime in these environments. Table 1 below shows the stage A prediction lifetime of this standard GRI GM13- HD Geomembrane incubated in these two liquors.

HDPE geomembrane with GM13 GRI minimum specs - Stage A prediction lifetime		
Temp (ºC)	**Immersion in Alkaline Liquor (pH 8.10)**	**Immersion in Acidic Liquor (pH 5.67)**
	Time(yrs)	**Time(yrs)**
10	87	19
20	53	15
30	34	12
40	22	10
50	15	9
60	10	7
70	7	6
80	5	5
90	4	5
100	3	4

Table 1 GRI GM13 - HD Geomembrane lifetime immersion in Alkaline & Acidic liquors prediction.

Analyzing the results, it can be observed that in both immersions at ambient temperatures (20ºC) the lifetime prediction is considerably lower than the estimation predicted by GSI (GRI White Paper 6) for non-exposed geomembranes in landfills (Stage A - lifetime of 208 years at 20ºC). Approximately four times reduction in alkaline liquors and fourteen times in acidic liquors.

In addition, it can be seen how the liner behaves differently in each liquor. It shows a significant impact of the acid liquors on the geomembrane lifetime in comparison with the alkaline one. Moreover, it can be observed how the influence of temperature affects significantly above 70 degrees, equaling the lifetime prediction at this temperature. From this temperature onward, this becomes the main factor in the loss of antioxidants.

Given these results, a deeper research has been done to understand the behavior of a standard GRI GM13 geomembrane in acidic solutions. It has been incubated two samples of a regular HDPE that meets GRI GM13 requirements with a highly aggressive acid liquors – high concentration of sulphuric acid (10% of concentration of H_2SO_4) with pH close to 1 at two high temperatures 85°C and 100°C. The two coupons were monitoring by periodically removed and evaluating their antioxidant package by S-OIT and HP-OIT tests. Figure 1 and 2 shows the results obtained.

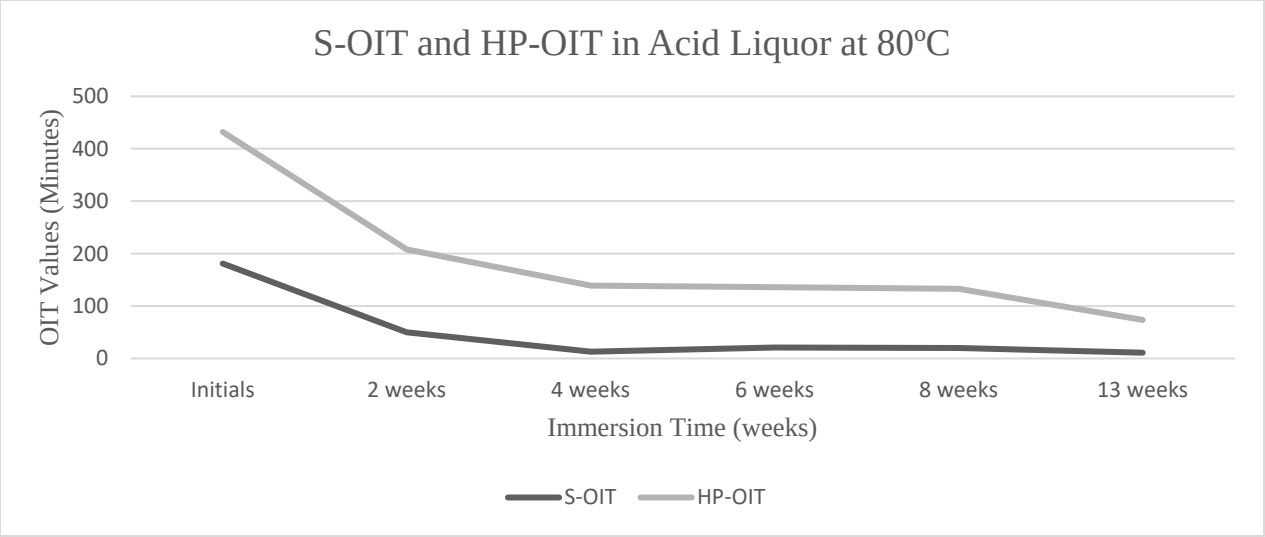

Figure 1 GRI GM13-HDPE geomembrane OIT depletion in highly acidic liquor immersion at 80ºC

Analyzing Figure 1, it can be observed that, after 13 weeks of immersion the GRI GM13 geomembrane in a highly aggressive acid liquor at 85 ºC, the antioxidant package is already consumed, starting the induction period to onset of degradation. The results show how in the first two weeks both OIT tests steep dropped. In four weeks, the S-OIT is not detecting any antioxidant package and the HP-OIT remain from that point with a low level of antioxidants up to three months (13 weeks), in where any antioxidant is detected in the liner.

It should be noted that a correct reading of OIT test values should be done, understanding test value outputs. It is considered in these test standards that when S-OIT reach 1 minute and the HP-OIT reach 50 minutes, there would be no remaining antioxidants.

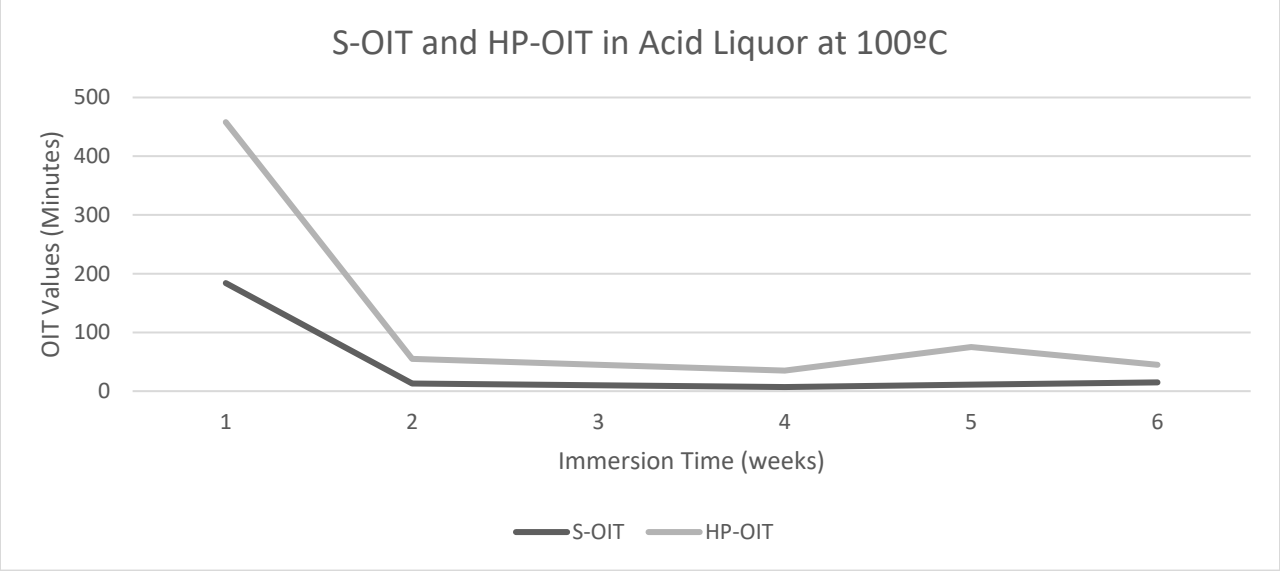

Figure 2 GRI GM13-HDPE geomembrane - OIT depletion in highly acidic liquor immersion at 100ºC

Figure 2 shows after two weeks of immersion in a highly aggressive acid liquor at 100 ºC the antioxidants/stabilizers of the geomembrane are already consumed, starting the induction period to onset of degradation.

The comparison between Figure 1 and 2 clearly show the effect of increasing the temperatures. Higher temperatures increase the reaction velocity and accelerate any physical degradation as volatize and migration of the antioxidant package, so both S-OIT and HP-OIT should decrease as can be observed.

In based of this research and the consequently risk involve, a new approach to geomembrane formulation is felt to be necessary, in order to evaluate correctly the service life of a geomembrane in this critical condition.

UNDERSTANDING HDPE GEOMEMBRANES FORMULATION

As a prelude to assess in detail how aggressive liquors impact on HDPE geomembrane formulations and how it could be manufacture liners to resist to them, a brief explanation on HDPE formulation is felt to be necessary.

HDPE geomembranes formulation normally includes PE resin (~97%), carbon black/pigment and an additive package (antioxidants and stabilizers). Carbon black/pigment acts as a UV screen, absorbing most of the UV radiation that strikes the geomembrane and converting it to heat. Antioxidants and stabilizers are added to the resin to inhibit oxidation and extend the induction period to onset of degradation. Since HDPE geomembranes are manufactured at high temperatures (200 to 220 ◦C), antioxidants are needed that function at the high temperatures associated with manufacturing as well as the lower temperatures associated with in-service applications. Consequently, most of the HDPE geomembrane recipes, to provide complete stability, includes a combination of two or more types of antioxidants and stabilizers. These are all key and important elements in the HDPE geomembrane formula. All of them are fundamentally important used for a specific function. The different between all the HDPE geomembranes in the industry will be the specific amount, relative percentage and types of these additives as well as the specific resin and carbon black/pigment chosen. For long-term performance of the geomembrane it is very important how they will interact with each other (synergistic mixtures) and with the environment will be in contact with. It will be necessary to select the right combination of additives to protect the geomembrane to ensure their long life.

The most broadly used test for assessing the resistance of polyolefin geomembranes to oxidative degradation and evaluates the quality of the antioxidant additive package is the oxidative induction time (OIT) test (ASTM D 3895). This test is conducted at 200 ºC and since this temperature is above some antioxidant’s effective temperature, they can be volatilized or degraded when testing by this standard OIT test. Consequently, it was created a modified test of OIT to be performed at a lower temperature in a pressurized oxygen atmosphere, the high-pressure HP-OIT (ASTM D 5886). Hence the Std-OIT and the HP-OIT are the two necessary tests to assess the complete antioxidant additive package in a HDPE geomembrane.

IDENTIFICATION OF HOW CHEMICAL SOLUTIONS INTERACT WITH HDPE GEOMEMBRANE FORMULATIONS

In the following section it is analyzed how the chemical solutions affect to the HD geomembrane recipes.

- Alkaline Solutions. Solutions with pH more than 8. These solutions can impact significantly on some necessary types of antioxidants. Other types of antioxidants will not be affected in excess in alkaline liquors due to their resistant nature to basics solutions. As such geomembranes in contact with alkaline solutions will show a drop in their S-OIT. The HP-OIT values will not be reduced rapidly as those specific antioxidants that this test identified will not be too affected chemically in this environment.
- Acid Solutions. Solutions with pH lower than 6. HD geomembrane additive packages would be adversely affected by the acids. Some antioxidants would be rapidly consumed, deactivated and decomposed under acidic environments. HDPE geomembrane in contact permanently with acid solutions most likely would show a reduction in their S-OIT values and a steep drop in their HP-OIT values.
- Liquors that contains transition metals, such as gold, copper or titanium, accelerates the oxidation process by a catalytic reaction. Hence, the durability of the geomembrane will be affected, reducing both values of HP-OIT and S-OIT after their exposure to them. Special recipes can be made to reduce the effect of these transition metals.
- Solution which includes extremely reactive and strong oxidizing agent elements such as Chlorine. The geomembrane in direct contact with them will show reductions on the S-OIT and HP-OIT. In order to minimize this effect, a high antioxidant package should be present in the geomembranes to ensure their life service.
- Solutions with high in-service temperatures in addition to aggressive chemicals. The high temperatures will increase the reaction velocity and accelerate any physical degradation as volatize and migration of the antioxidant package. Both S-OIT and HP-OIT would show a decrease. Specially the HP-OIT will be the one more compromise by thermal in project sites stabilizer. The solution for this effect will be the use of specific types of antioxidants for in service high temperatures as antioxidants with higher molecular weight. Also, to improves their behavior, it can be used specific HDPE resins that will help up better to permanent exposure to high temperatures.

HDPE GEOMEMBRANES - MINING APPLICATION

Mining industry is the pillar of many economies around the world, providing in many countries more than 50% of the export earnings. This impact is not only economic, the industry is also found to be the largest producer of waste worldwide. Whereas, in order to obtain a gram of gold, one tonne of mineral bearing rock should be crushed and processed, and approximately another tonne of waste rock is produced, it can give a general picture of the immensity of the waste containment problem faced by the mining sector. Environmental impacts made by the chemicals emitted from mining processes is a major concern within the industry and that is the reason behind why this industry calls for the best standards in lining systems to reduce any possible risk of contamination.

As a result, the need for high performance lining systems have become a critical issue to face in the mining sector. HDPE geomembranes has emerged as a key component to address this demand as barrier containment of process solutions, after being proven of its relatively well behavior. However, as these geomembranes should face extreme conditions not present in any other containment application, a complete and deep analysis should be taken by designer to understand and specify the most suitable geomembranes.

In a mine the geomembrane is used to retain chemical solution, utilized to dissolve minerals from ore, and to allow the leachate to be collected and refined. Heap leaching presents a combination of extreme base pressures and highly acidic/alkaline conditions on the geomembrane not present in any other containment application. These extreme conditions push standard known geomembrane performance beyond the recommended general design limits. As such, the biggest challenge will be the chemical exposure conditions that the liners would be exposed to. More specifically, the geomembranes are in contact with liquors incorporating solvent solutions in heap leach mining like sodium cyanide (alkaline solution) for gold/silver and sulphuric acid (acidic solution) for copper/nickel ones. Likewise, tailing storage facilities, although will not have ultra-high loading common to the heap leach application, will also have to face issues with chemical resistance with extreme pH solutions. Consequently, appropriate site chemical assessment is essential to understand how the geomembrane will behave under these extreme circumstances.

Several studies have been conducted to assess the performance of HDPE liners exposed to landfill solutions, but only a few have been completed for geomembrane exposure to leachate associated with the mining process. In this paper, not only, is analyzed this impact directly on HD typical formulations, but also it is proposed how to adapt the geomembrane formulation to create bespoken geomembranes after a complete site-specific assessment. To accomplish this, it has been selected and assessed two types of mines, Aluminum and Gold mines. Providing some mining specific scenarios where the HD geomembrane is in contact directly with aggressive environments. It has been done a completed breakdown of the full assessment that, in the authors opinion, should be considered in any design of a high-risk mining project, where a failure of a geomembrane could cause a huge damage on the environment, the public health and the economy.

ALUMINIUM (BAUXITE) MINE, BAUXITE RESIDUE (RED MUD)

Bauxite is the naturally way form of aluminium ore, being the world's main source of aluminium. It is often strip mined/open-pits and normally processed into alumina. Approximately four or five tonnes of bauxite are needed to produce one tonne of aluminium. Over 95% of the alumina produced globally is through the Bayer process. Bauxite residue, also called red mud, is an inevitable secondary product that is generated in the extraction of alumina from bauxite by the Bayer process. The bauxite refining alumina production generates liquors with highly alkaline pH leachate (pH > 10), high sodium (NaOH) concentrations as well as elevated temperature of cooling water (>60ºC). The effects that these liquors might have on HDPE geomembrane are as follows:

- Highly alkaline pH leachate (pH > 10) – Some antioxidants may be affected. Possible changes in HD geomembrane formulation could be increasing the amount of the antioxidants and the selection of specific ones to be more resistant to alkalis environments.
- High sodium (NaOH) concentrations. The present of sodium (Na) will not impact in excess in the durability of the geomembrane.
- Elevated temperature (>60ºC). This will increase the risk of oxidation rising the reaction velocity and accelerating any physical degradation. The geomembrane could include specific type of antioxidant for in service high temperatures as antioxidants with higher molecular weight and HDPE resins that behaves better in high temperatures.

Consequently, the formulated HD geomembrane for this specific environment would include high amount of antioxidants, specific ones resistant to alkalis environments and with high molecular weight. Also, may include resins that behaves well in high temperatures. In terms of geomembrane

HD parameters should include high SCR, high initial S-OIT and HP-OIT values and Oven Aging at 85 ºC with retained percentage of both HP-OIT and S-OIT.

GOLD MINES, GOLD ORE WASTE

Gold is often strip mined/open-pits or using underground hard rock mining techniques. Once the ore is mined the gold is normally extracted by means of cyanide leaching. Gold ore waste rock pile, heap leach process liquors and tailings dam leachates generate liquors with acid drainage (pH down to 2) and acid and metalliferous water (pH < 1). The effects that these liquors from gold ore waste processing might have on HDPE geomembrane can now be identified.

- Acid drainage (pH down to 2) / Acid and metalliferous water (pH < 1). HD geomembrane additive packages with this highly acidic liquor would be adversely affected. HDPE geomembrane would show a steep drop in HP-OIT and S-OIT parameters. Possible changes in HD geomembrane formulation could be the use of specific antioxidants to acid solutions.

Liner formulation for this site will include high amount of antioxidants, with specific ones resistant to acid environments. In terms of geomembrane HD parameters should include high SCR, high initial HP-OIT and S-OIT values, Oven Aging at 85 ºC with retained percentage of both HP-OIT and S-OIT.

Gold mines can also generate another type of leachate by gold processing. Liquors with elevated chloride and sulfate salinity, and moderate to strongly alkaline solutions (pH 9–11) containing highly elevated CN- and possibly NH_4OH. The effects that this might have on geomembrane are present as follows:

- Liquors with elevated chloride and sulfate salinity. Chlorine (Cl2) is an extremely reactive and strong oxidizing agent element, therefore a high antioxidant package should be present in the geomembranes to ensure their life service.
- Moderate to strongly alkaline solutions (pH 9–11) containing highly elevated CN- and possibly NH_4OH. Some antioxidants may be affected. Possible changes in HD geomembrane formulation could be increasing the amount of the antioxidants and the selection of specific ones to be more resistant to alkalis environments.

Geomembrane formulation for this site would be similar to the one formulated for the bauxite residue which would include specific antioxidants that resist to alkalis environments.

EXAMPLE OF GEOMEMBRANE FORMULATIONS IN MINING SITE CONDITIONS. RESULTS OF FORMULATED GEOMEMBRANES WITH EXTREME PH SOLUTIONS

A formulated HDPE geomembrane has been created for a site that the liner will be in contact directly and permanently with high acid liquor. Similar conditions to the one presented in a Gold mine (liquors generated by Gold ore waste rock pile, heap leach process liquors and/or tailings dam leachates). It has been formulated a geomembrane with high quality resin, high amount of Antioxidants, specific ones resistant to acid environments and with high molecular weight. In terms of geomembrane HD parameters includes high SCR (>3000h), high initial HP-OIT(>1000min) and S-OIT (>200min), Oven Aging retention at 85 ºC (HPOIT retention > 80% AND S-OIT retention > 55%).

In contact with Acid a regular geomembrane would show a steep drop in their antioxidant package. The result of this formulated geomembrane incubated in high concentration of sulphuric

acid (10% of concentration of H_2SO_4) with pH close to 1 at 20 ºC, 60 ºC and 85ºC are shown below in the Figures 3 and 4.

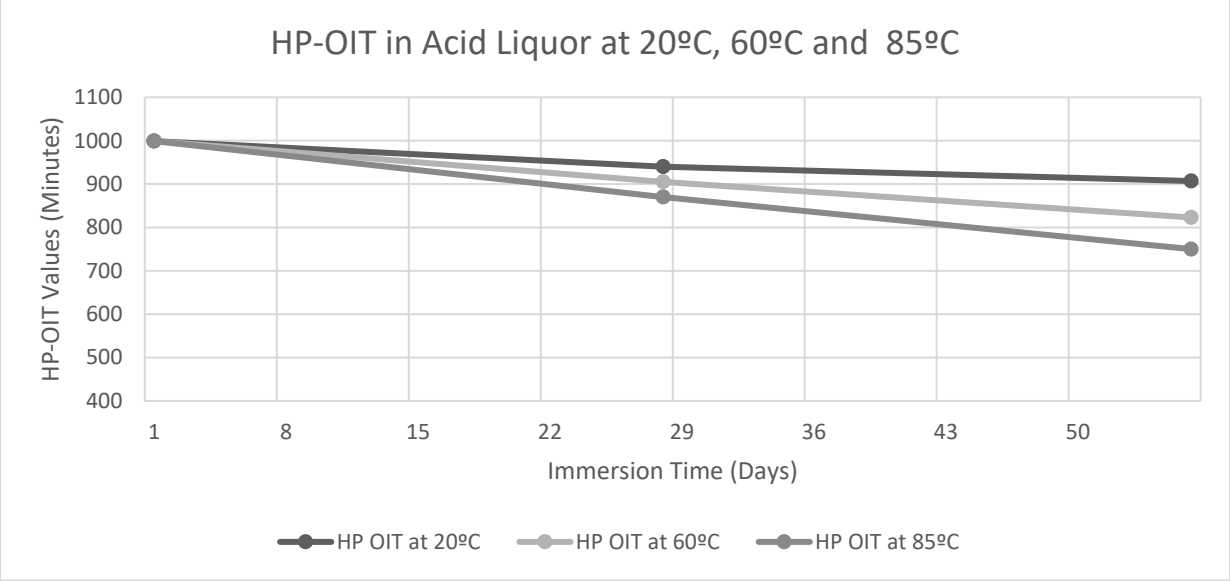

Figure 3 Formulated HDPE - HP-OIT depletion in highly Acidic Liquor immersion at 20ºC , 60ºC and 85ºC

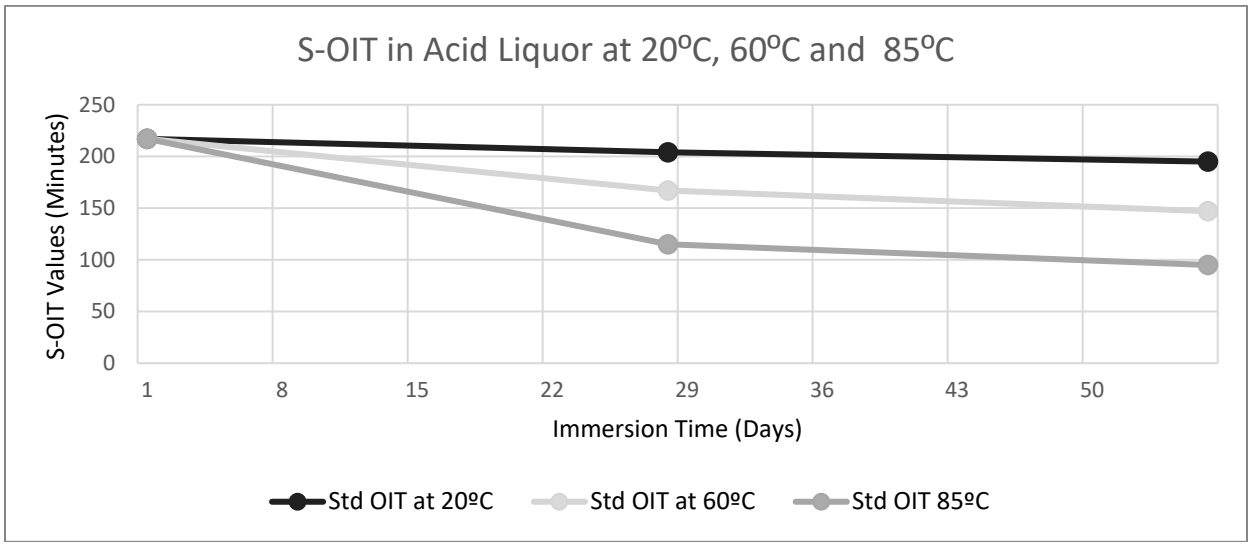

Figure 4 Formulated HDPE - S-OIT depletion in highly Acidic Liquor immersion at 20ºC , 60ºC and 85ºC

Figure 3 shows that after almost 60 days of immersion in acid liquors at 20ºC , 60ºC and 85ºC the site-specific formulated HD geomembrane has retained more than 80% of their HP-OIT not showing any steep drop. Figure 4 shows that after almost 60 days of immersion in acid liquors at 20ºC , 60ºC and 85ºC the site-specific formulated HD geomembrane has retained more than 90%, 65% and 40% of their S-OIT respectively. It shows a drop in the first 30 days essentially at 85ºC and then it remains. These results show the impressive behavior this formulated

geomembranes will have in direct contact with this highly acid environment at even high temperatures. After almost two months in this immersion the formulated geomembrane antioxidant package is not consumed yet, not starting the induction period to onset of degradation. The results do not show the typical steep drop in their antioxidant package that a regular geomembrane will present in this environment, proving that a geomembrane well formulated for a specific site extreme conditions can be ensuring for long-term performance. Minimizing the site risk by creating and customizing the most suitable geomembrane for the project needs.

PROJECT REQUIREMENTS – WARRANTIES IN CRITICAL SITES

In 1995 GSI (GRI at the time), all geomembrane specifications contained a requirement for warranty of 5 years duration. In 2006, GSI removed all warranty clauses with the following comment: *"They were added appendages from the outset and they never provided any realistic added security for the user"*. As it has been evaluated and presented in this document, the aim should be to understand the geomembrane design life by defining it, identifying the potential degradation mechanisms against the product properties, and ensuring a high-quality installation. Rising the product properties in order to ensure geomembrane expected lifetime.

Currently in the industry, rather than specified a geomembrane parameter that technically can be linked to specific site conditions, it sometimes specifies in critical projects GM13 geomembranes parameters along with requesting warranties of 10, 20 or even 30 years. Clearly. if well specified and linked the material properties with the site conditions, the geomembrane will be within the materials capability to meet this requirement, and technically can be proved. However, these warranties represent a questionably relevant and useful document for the final user, more related with paperwork than a real parachute in case of a degradation before the end of the warranty period. Specially, as any Geomembrane manufacturing warranty offered will disclaim against clauses that include "normal" conditions/weathering, which are conditions that actually exist on only very few sites, and certainly not a critical site. Not providing any realistic added security to the client. As such, the aim should be identifying site conditions to technically ensure geomembrane expected lifetime.

Therefore, a detailed risk analysis in terms of exposure to chemicals and the related studies about which formulation fits better for those specific ones, including a lifetime estimation, seems to be more logical to add security to the end user.

NEW APPROACH FOR HDPE GEOMEMBRANES IN CHALLENGING CONTAINMENT APPLICATIONS – MINING

In mining applications as a challenging site where the risk should be reduced at minimum, a new approach in term of specifying HDPE geomembrane is felt to be necessary being site specific formulated. It would benefit all parts involves in a project as well as the risk would be minimized by creating and customizing the most suitable HD geomembrane for the site needs. Asset owners and designers could prescreen and test a set of liners under site-specific environmental conditions that include short and long-term immersion testing. When assessed by index tests and performance tests at different concentrations and temperatures, longevity prediction can be linked to ambient exposure to provide reliable lifetime prediction.

A preevaluation model for geomembrane products in critical applications also allows an assessment of long-term durability risk onsite. If sufficient project specific testing is carried out

during the design phase, the opportunity is to sample the product installed onsite over time (using fully immersed coupons in the actual service environment), creating a direct measure of degradation performance against the design expectation. Degradation and premature service life issues can be forecasted rather than simply acting upon after a problem manifest. This would be predictive monitoring rather than reactive monitoring. A direct measure of degradation onsite, not risk assessment in design alone.

Geomembranes in critical applications could also be linked to deformulation testing of the additive package. If the best environmental choice is to create a specific tailored geomembrane formulation for the project, then the capacity to measure constituent loss by analyzing the geomembrane post testing is at the heart of identifying the recipe changes that establishes longevity.

The final piece of the challenging contaminant puzzle defines the need to be able to measure long-term testing outcomes by utilizing short term testing measures. Inevitably with increasing contaminant exposure risk, geomembranes that have enhanced durability properties will take much longer for traditional testing models to evaluate. The expectation would be HDPE Geomembrane specifications will increasingly demand much higher longevity measures in the form of S-OIT and HPOIT values, and Stress Crack Resistance values than those presently required by GRI-GM13. A key issue in this critical site would be managing testing risk through short and long-term test correlations. The new approach for challenging project would be to be able to correlate this key longevity measures with new accelerated methods. This new approach in testing can be summaries as follows;

- Accelerated immersion test. Traditional long-term pot immersion testing (up to 12 months) for a range of site conditions are now be tested in less than a month through accelerated new immersions techniques.
- Oxidation degradation QC/QA testing HP-OIT and Oven Aging Curves established over 30 / 60 and 90 days to establish failure risk after just 30 days.
- Stress Crack Resistance. Measuring the SCR by the Strain Hardening Modulus (SHM) testing to provide a direct correlation to long-term Stress Crack Resistance ASTM D5397 as an alternative to the traditional way of measuring the SCR, to simplify and accelerate the data collection.

CONCLUSION

Currently geomembranes are being used in applications where the site chemistry and conditions challenge traditional HDPE formulations. GRI GM13 standard, whilst being an excellent general-purpose specification, would be inadequate in projects where the leachate in contact is very aggressive as mining processing sites. To ensure long-term performance of this site’s geomembrane, it is very important to understand geomembrane formulation, how resin and antioxidant package interact with each other and with the environment that are in contact with. In this document has been presented a complete preliminary assessment, identifying site conditions and their impact on HD formulations. As well as being proposed formulated HD geomembranes that has been proved to behave better in this environment, minimizing the site risk by creating and customizing the most suitable HD geomembrane for the site needs. For challenging containment applications where the risk should be reduced at minimum, the HD geomembrane designed should be site specific. Using most up-to-date geomembrane technology to reduce any environmental, public health and economy impact.

REFERENCES

Abdelaal, F.B. Rowe, R.K., and Islam, M. Z. 2014. Effect of leachate composition on the long term performance of a HDPE geomembrane. Geotextiles and Geomembranes, 42(4):348-362.

ASTM D 5747. Standard Practice for Tests to Evaluate the Chemical Resistance of Geomembranes to Liquids, *ASTM International*, West Conshohocken, Pennsylvania, USA

ASTM D 5885. Standard Test Method for Oxidative Induction Time of Polyolefin Geosynthetics by High-Pressure Differential Scanning Calorimetry, *ASTM International*, West Conshohocken, Pennsylvania, USA

ASTM D 3895. Standard Test Method for Oxidative-induction Time of Polyolefins by Differential Scanning Calorimetry. *ASTM International*, West Conshohocken, Pennsylvania, USA.

Bouazza, A., Gates, W.P, Scheirs, J., Geosynthetics in Mining Applications, *GhIGS GeoAfrica 2013 Conference*, International Geosynthetics Society, Accra, Ghana.

GRI GM13 Standard Specification, revision 15th - 2019. *Geosynthetic Institute*. Folsom, Pennsylvania, USA.

GRI Guide GM10, revision 4th - 2015. The Stress Crack Resistance of HDPE Geomembrane Sheet**.** *Geosynthetic Institute*. Folsom, Pennsylvania, USA.

GRI Guide GS12 - 2012. Lifetime Prediction of Geosynthetics Using Time-Temperature-Superposition (TTS) and Arrhenius Modeling. *Geosynthetic Institute*. Folsom, Pennsylvania, USA.

GSI White Paper 32 – 2015. Rationale and Background for the GRI-GM13 Specification for HDPE Geomembranes. *Geosynthetic Institute*. Folsom, Pennsylvania, USA.

Hornsey, W.P., Scheirs, J., Gates, W.P., Bouazza, A. (2010) Impacts of Mining Solutions/liquors on Geosynthetics, *Geotextiles and Geomembranes* 28 (2010):191–198.

Hsuan, Y. G., Schroeder, H. F., Rowe, R.K., Müller, W., Greenwood J., Cazzuffi, D., R.M. Koerner, Long-Term Performance and Lifetime Prediction of Geosynthetics, *EuroGeo4 - European Geosynthetics Conference 2008,* International Geosynthetics Society, Edinburgh, United Kingdom, UK Chapter.

Koerner, R.M (2012) *Designing with Geosynthetics - 6th Edition*, Xlibris, USA.

Peggs, I., Gassner, F., Scheirs, J., Tan, D., Noval Arango, A., Burkard, B. Is there a Resurgence of Stress Cracking in HDPE geomembranes?, *10th International Conference on Geosynthetics, September 2014*, International Geosynthetics Society, Berlin, Germany.

Rowe, R. K., Abdelaal, F. B. (2016). Antioxidant depletion in high-density polyethylene (HDPE) geomembrane with hindered amine light stabilizers (HALS) in low-pH heap leach environment. *Canadian Geotechnical Journal*. 53(10): 1612-1627

Rowe, R.K., Islam, M.Z., Brachman, R.W.I., Arnepalli, D.N., Ragab Ewais, A. (2009), Antixidant Depletion from a High Density Polyethylene Geomembrane under Simulated Landfill Conditions, *Journal of Geotechnical and Geoenvironmental Engineering,* ASCE,136:930-939.

Rowe, R.K., Rimal, S, (2008), Depletion of Antioxidants from n HDPE Geomembrane in a Composite Liner, *Journal of Geotechnical and Geoenvironmental Engineering,* ASCE, 134:1(68): 68-78.

Scheirs, J. (2009) *A Guide to Polymeric Geomembranes*, John Wiley and Sons Ltd, West Sussex, United Kingdom.

World Aluminium Publications, Opportunities for use of bauxite residue in Supplementary Cementitious Materials – March 2020, *International Aluminium Institute.,* London, United Kingdom.

Geosynthetics Conference

Stress-Cracking Resistance of a Bi-modal PE-RT HDPE Geomembrane

Rohit Sati, M.Sc[1] and David Beaumier, Eng., M.Sc.A.[2]

[1]Layfield Group, 17720 - 129 Avenue NW, Edmonton, Alberta, Canada; e-mail: rsati@layfieldgroup.com
[2]CTT Group Sageos, 3000, avenue Boullé, St-Hyacinthe, Quebec, Canada; e-mail: dbeaumier@gcttg.com

ABSTRACT

Stress crack resistance (SCR) of high-density polyethylene (HDPE) geomembranes, with densities higher than 0.94 g/cc, has been widely researched and documented. Over the years, PE resin technology has evolved and has helped to improve many long-term performance properties including SCR. In this study, resistance to stress-cracking of bi-modal polyethylene raised temperature (PE-RT) HDPE was assessed and compared to HDPE and LLDPE geomembranes over a load range from 28 to 60% of yield stress. The higher tensile resistance of this specific bi-modal resin resulted in higher resistance in the ductile failure mode than standard HDPE, but moreover, its stress-cracking resistance behavior was found without any clear transition of the failure envelope from a ductile to a brittle behavior. This observation suggests a longer projected lifespan of this unique bi-modal PE compared to existing geomembranes developed using uni-modal resins. Previous studies on this material have analyzed tensile, antioxidant depletion, and resistance to brine and chlorine at elevated temperatures. In all cases, an improvement in durability was demonstrated. This study on stress cracking provides a comprehensive understanding of all known key mechanisms contributing to bi-modal PE geomembrane durability.

INTRODUCTION

This paper describes the stress crack testing that was performed on a geomembrane made with a bi-modal HDPE resin. It is well documented that stress cracking in geomembrane is caused by tensile stresses lower than its short-term mechanical strength. Stress cracking is essentially a brittle cracking phenomenon that occurs at a constant stress lower than the short-term yield strength of the material (Peggs, 2003). Most stress crack resistance testing on bi-modal resins have been performed on pipe grade resins that are reported to have high resistance to the primary exposures that lead to failure in polyethylene gas piping systems. Notable material properties that are used as performance indicator of pipe robustness are 1. slow crack growth (SCG) resistance and 2. rapid crack growth (RCG) resistance. Resistance to defects and external damage is another property tested by pipe manufacturers to evaluate robustness of bi-modal resins for high performance pipe applications. These tests “as is” can’t be extended to geomembranes primarily due to product type and the end use applications. In 2014, the authors started a research project to see if any of these new bi-modal pipe resins had the potential to be used as a geomembrane. While the pipe industry testing looked very good there was no correlation that would show how a geomembrane would work with the same resin. This is the fifth research paper on the development of bi-modal resins for geomembrane applications.

NCTL TESTING

Notched Constant Tensile Load test is a standard test to evaluate stress cracking under a constant tensile load condition in an accelerated environmental condition . In this test, dumbbell shaped specimens are notched to 20% of their thickness and are subjected to stress between 20-50% of the geomembranes tensile yield strength as measured using ASTM D6693. The specimens are then placed in a solution containing surface-active agent and tested at 50°C. These accelerated test conditions cause the material to develop crack growth and fail. A plot of the percent yield stress versus average failure time of the three tests at each load is shown in figure 1 below (GRI GM10). The test requires at least 3 points to be in the ductile region of the curve and at least 3 points shall be in the brittle region of the curve. The transition between ductile and brittle failure indicates the stress crack resistance of the material.

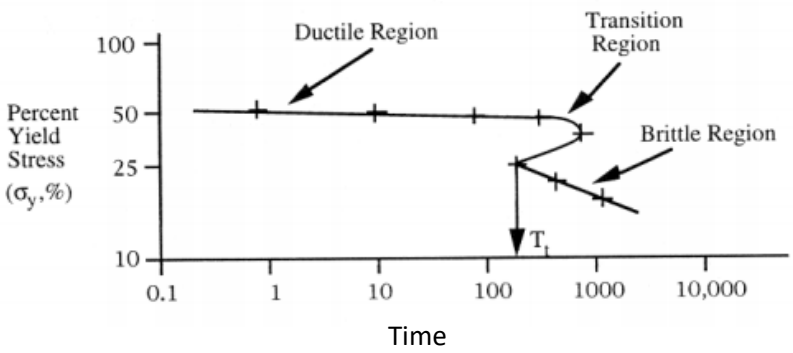

Figure 1. Transition from ductile to brittle failure, adapted from Hsuan, 1995.

BI-MODAL POLYETHYLENE TECHNOLOGY

In general, the molecular weight distribution of the polymer determines the polymer properties (plasticpipe.org). The bottom axis shows the molecular weight (the length of each chain). The vertical axis shows the weight fraction. These graphs usually create a classic bell curve (normal distribution in statistics). A uni-modal distribution, on the left of Figure 2, shows a single peak distribution.

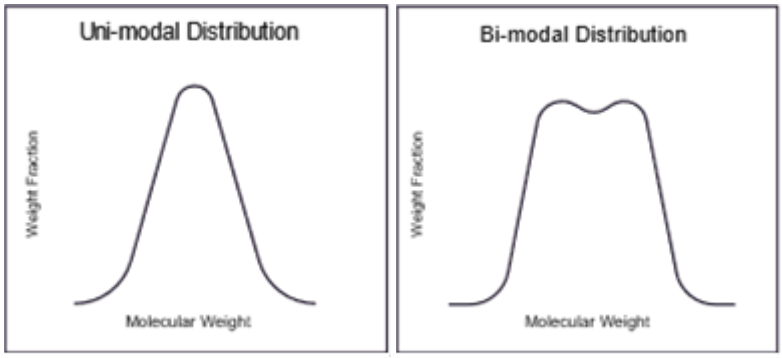

Figure 2. Uni-modal and bi-modal distribution.

The resin manufacturer can control the reactor conditions and change the catalysts to control the kind of polymer that is made. A very narrow distribution will be strong, stiff, and difficult to push through plastic processing equipment (all other properties being equal). A very wide distribution (graph is shorter and wider at the base) will normally be softer and more pliable, and easier to process. Current HDPE geomembrane resins are made with unimodal resins. Over the years stress cracking issues have led resin manufacturers to reduce the density of their resins and to widen the molecular weight distribution. The result is that current HDPE geomembranes are made with medium density (MDPE) resins. While this has reduced the risk of stress cracking, it has resulted in the reduction of chemical resistance. When considering ESCR as a failure mechanism, in the traditional unimodal sense, the lower the density generally led to better performance (less stress cracking risk). This is a result of a higher amount of comonomer incorporation into the polymer backbone. Unfortunately, the higher the amount of comonomer, the lower the density; thus, lower chemical resistance.

Newer resins have been developed using a technique that creates a bi-modal molecular weight distribution. In Figure 2, a bi-modal distribution that shows two distinct peaks on the graph. Bi-modal resins are generally made utilizing dual reactors. The first reactor has the feedstock, catalyst and comonomer injected into it where a polymer is formed with a tremendous amount of comonomer. That material is then transferred to a second reactor operating in a comonomer-starved condition where the polymer continues to build the homopolymer backbone. The result is a more robust product with very low risk of stress cracking.

The research into bi-modal PERT HDPE geomembrane has included high temperature tensile strength testing (Beaumier et al, 2016), high service temperature testing (Mills and Beaumier 2017), chlorine resistance testing (Rangel et al 2017), and brine resistance testing (Mills et al, 2019).

MATERIALS AND METHODS

The main material investigated in this evaluation was a bi-modal PERT geomembrane. Since this was the first time a bi-modal PERT geomembrane resin was evaluated for stress cracking performance, the authors felt it was necessary to compare its performance with other polyethylene types commonly used for the manufacturing of geomembranes. The following geomembranes were part of this study:

- GM13 complaint HDPE
- GRI GM 17 complaint LLDPE
- Bi-modal PERT HDPE

Table 1 provides summary of physical properties of the material tested in this study.

Table 1. Material properties of geomembranes tested.

Material	Density[1], g/cm^3 (nominal range)	Thickness, mm (mils)	Tensile strength[2], psi (yield)
HDPE	0.940 – 0.955	1.5 (60)	1754 / 1753
LLDPE	0.910 – 0.939	1.5 (60)	2676 / 2667
PE-RT HDPE (bi-modal)	0.940 – 0.955	1.5 (60)	3378 / 3564

Notes to Table 1:

(1) GRI-GM13 and GRI-GM17 does not establish density range but a cut-off value for LLDPE, 0.939 g/cm^3 and under, or HDPE, 0.940 g/cm^3 and over.

(2) Tensile strength is reported respectively in machine and cross machine directions.

TEST METHODOLOGY

The resistance to stress cracking was determined in accordance to ASTM D5397, including a complete evaluation of test loads, test loads were selected between 28-68% of the measured stress at yield which was determined as per ASTM D6693. Table 2 summarizes the test loads used for this study. Samples were retrieved at different intervals and evaluated for stress crack resistance. The last sample tested was exposed to 10,000 hours before being tested for SCR. Images by scanning electron microscopy (SEM) on the surface was carried out to determine brittle or ductile failure.

Table 2. Test loads for NCTL testing.

Load	LLDPE (tested in CMD)		HDPE (tested in CMD)		PE-RT HDPE (tested in CMD)		PE-RT HDPE (tested in MD)	
	psi	% y.s	Psi	% y.s	psi	% y.s	psi	% y.s
#1	526	30	747	28	1069	30	1013	30
#2	614	35	800	30	1247	35	1182	35
#3	701	40	853	32	1426	40	1351	40
#4	789	45	933	35	1604	45	1520	45
#5	877	50	1067	40	1782	50	1689	50
#6	964	55	1200	45	1960	55	1858	55
#7	1052	60	1334	50	2138	60	2027	60
#8	1139	65	1467	55	2317	65	2196	65

RESULTS AND DISCUSSION

NCTL Tests. Figure 3 describes the relation between the load in percent of the measured yield stress to failure time.

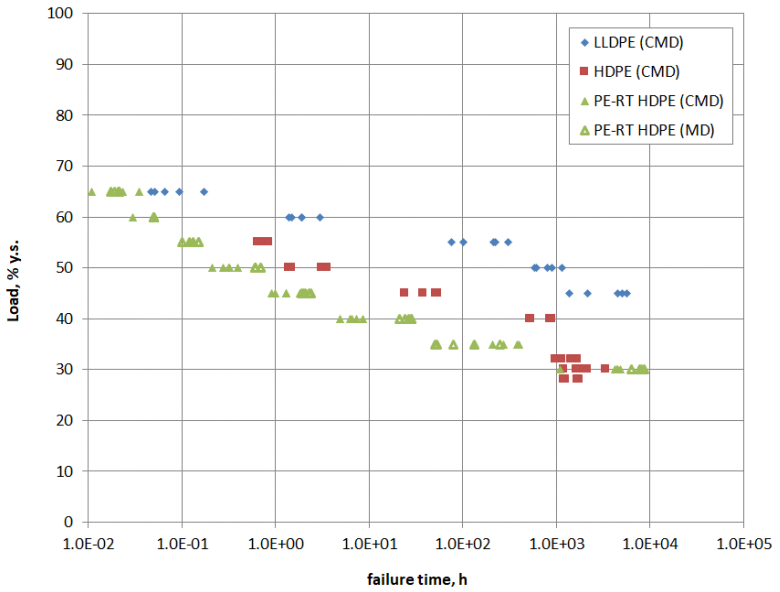

Figure 3. Comparison of geomembrane types to stress crack propagation, in terms of percent yield stress.

This type of analysis induces a bias from the initial resistance to tensile stress. On an absolute basis, Figure 4 presents the resistance to stress crack propagation in terms of tensile stress, in psi.

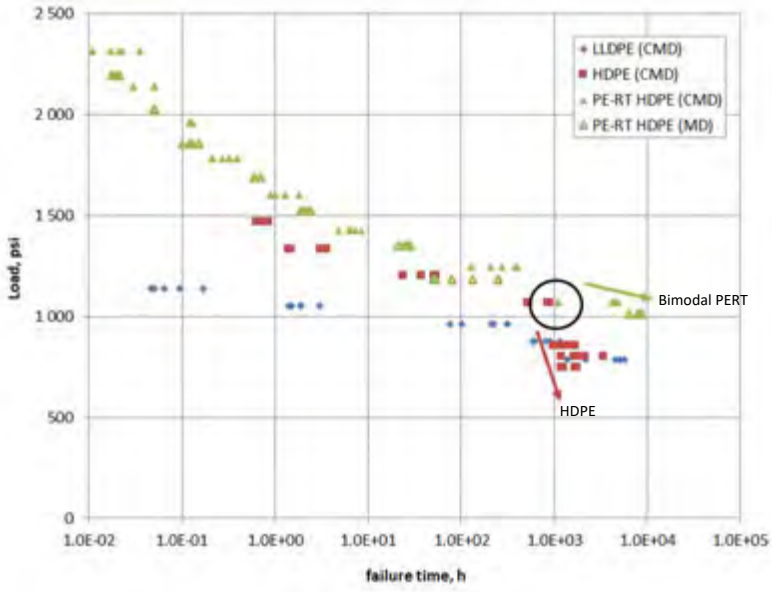

Figure 4. Comparison of stress crack propagation of geomembranes under tensile load.

This graph shows a more realistic picture of the resistance of long-term tensile stress and stress-crack propagation. The LLDPE shows lower stress resistance because its resistance to a ductile failure mode remains lower than the stress crack propagation of HDPE.

In addition to its greatest resistance to failure in the ductile region, bi-modal PE-RT HDPE shows a completely different trend of its failure time to tensile load after reaching its ductile-brittle transition when compared to standard grade HDPE, shown in circle on Figure 4.

The mode of failure was confirmed from images under electronic microscopy. An apparent textured surface is observed when brittle failure occurs by stress-crack propagation. A wavy surface likely correlates to ductile failures. In this study, no failure by stress-cracking was observed with LLDPE. The ductile to brittle transition was evaluated at 35% of HDPE yield stress. For PE-RT HDPE it was evaluated at 30% of its yield stress. Figure 5 presents the surface indicating failure at the ductile-brittle transition for each material.

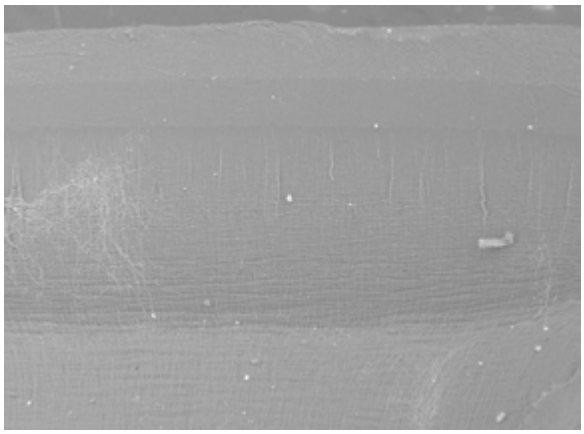

LLDPE 45% y.s./ 789 psi

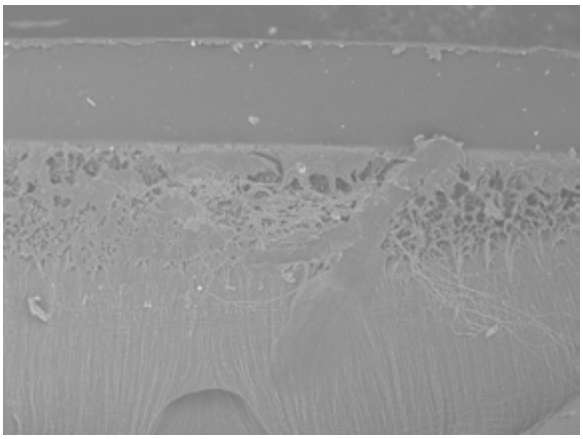

HDPE 35% y.s. / 933 psi

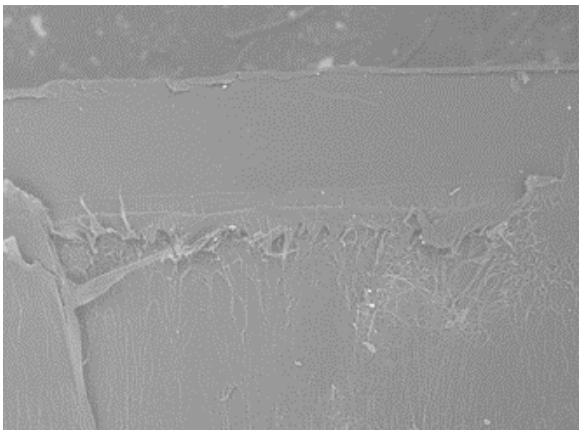

PE-RT 30% y.s. /1069 psi (tested in CMD)

Figure 5. Images of rupture faces by scanning electron microscopy.

DISCUSSION

The behavior of PE-RT HDPE to ASTM D5397 describes three possible NCTL response curves as shown in Figure 6. These are the bi-linear or knee curve, the overshoot or nose curve, and the tri-linear or step curve.

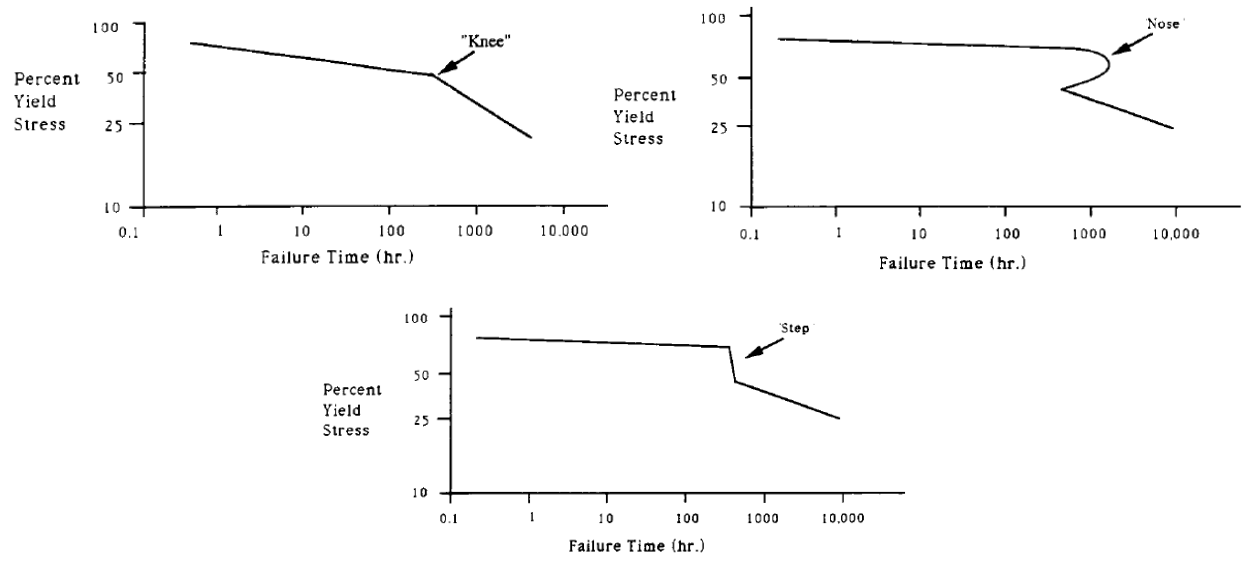

Figure 6. Evaluation of ductile-brittle failure adapted from ASTM D5397.

While variability in testing data makes it difficult to determine which of these curves may apply, the more important goal is to identify the transition point between a brittle failure and a ductile failure. In all the curves shown it is the transition in the slope of the line in which we are most interested.

Identifying the transition point in our data (highlighted in Figure 1) is complicated by the variability of the data. Fitting curves to the data it is still not immediately clear enough to draw conclusion from trends on the location of the ductile-brittle transition. However, the transition point may be assessed from microscopic view of the specimen rupture faces, which may provide evidence of ductile or brittle failures, shown on Figure 3. The use of microscopy allowed us to find the transition times for each material, this transition can then be looked upon on the graph to see if the data on the graph are close to that transition time. For bi-modal PE-RT HDPE, this transition was showing an inflection opposite to the ones proposed by ASTM D5397.

CONCLUSION

The assessment of stress-crack resistance of PE-RT bi-modal HDPE was done using ASTM D5397, and compared to reference materials commonly used for geomembranes. Whereas no stress-cracking failures were observed with LLDPE, both HDPE grades have shown a transition from ductile to brittle behavior under accelerated long-term tensile stresses. The bi-modal PE-RT HDPE grade has shown longer time to ductile-brittle transition, and failure by stress-cracking than the reference HDPE. The findings of this study are in accordance with previous studies on the aging of bi-modal polyethylene grades for its usage in the geomembrane applications, including

high temperature tensile resistance, antioxidant depletion, and resistance to brine and chlorine at elevated temperatures. In all cases, an improvement in durability was demonstrated with bi-modal HDPE.

ACKNOWLEDGEMENT

This project has been funded under a grant from NSERC. The study on the resistance of this novel bi-modal PE-RT HDPE was initiated by Andrew Mills, formerly from Layfield. Andrew has now retired, the authors would like to acknowledge the great contribution of Andrew to this paper, and well as previous ones on the subject.

REFERENCES

Peggs, I.D. 2003. Geomembrane liner durability: contributing factors and the status quo. Proceedings from the First United Kingdom Geosynthetics Symposium, UK Chapter of IGS. June 2003.

Hsuan, Y.G., Koerner, R.M. (1995). The Single Point-Notched Constant Tension Load Test: A Quality Control Test for Assessing Stress Crack Resistance, Geosynthetics International, 1995, Vol. 2, No. 5.

Beaumier D., Mills A., Dolez P., Blond E. (2016). Tensile Resistance of Geomembranes for High Temperature Applications, *GeoVancouver 2016*, Canadian Geosynthetics Society, Vancouver, BC, Canada.

Mills A., Beaumier D. (2017). Long-term Performance of HDPE Geomembranes Exposed to a High Temperature Brine Solution, *GeoFrontier 2017*, IFAI, Orlando, FL, USA.

Rangel E., Mills A., Beaumier D., Fraser B. (2017), A new geomembrane for chlorinated water containment, *Geosynthetics 2017*, Santiago, Chile.

Mills A., Fraser B., Beaumier D., Long-term Performance of HDPE Geomembranes Exposed to a High Temperature Brine Solution, *Geosynthetics 2019*, IFAI, Houston, TX, USA.

ASTM D 5397. Standard Test Method for Evaluation of Stress Crack Resistance of Polyolefin Geomembranes Using Notched Constant Tensile Load Test, *ASTM International*, West Conshohocken, Pennsylvania, USA.

ASTM D 6693. Standard Test Method for Determining Tensile Properties of Nonreinforced Polyethylene and Nonreinforced Flexible Polypropylene Geomembranes, *ASTM International*, West Conshohocken, Pennsylvania, USA.

GRI - GM13. Standard Specification for “Test Methods, Test Properties and Testing Frequency for High Density Polyethylene (HDPE) Smooth and Textured Geomembranes” , *Geosynthetic Institute*, Folsom, Pennsylvania, USA.

GRI - GM17. Standard Specification for “Test Methods, Test Properties and Testing Frequency for Linear Low Density Polyethylene (LLDPE) Smooth and Textured Geomembranes”, *Geosynthetic Institute*, Folsom, Pennsylvania, USA.

Plasticpipes.org. Extracted from https://plasticpipe.org/pdf/chapter03.pdf, Plastics Pipe Institute. Material Properties, Chapter 3, pg. 53.

Geosynthetics Conference

Creating a Soft, Green, Living Shoreline Using Sand Filled Composite Geotextile Tubes and Native Species of Vegetation

Tom Stephens,[1] Joe Little[2]

[1] TenCate Geosynthetics, 813 Oak Street Bedford, Va. 24523; e-mail: t.stephens@tencategeo.com

[2] Joe Little, Raleigh, 5016 North Hills Drive, NC 27612; e-mail: joseph.little@littleenvironments.com

ABSTRACT

A Living Shorelines as defined by the National Oceanographic Atmospheric Association (NOAA) are green infrastructure techniques to stabilize the shoreline by providing alternatives to "hard" shoreline stabilization methods like rip rap or bulkheads. These Living Shorelines also provide an environment for native vegetation plus other benefits such as buffering from waves and storms. This paper will present the detail of the Currioman Bay project where a spit of land in the environmentally sensitive James River where it opens into the Chesapeake Bay had experienced sever erosion over the years to the point of being breached and required restoration. Details will include the investigation, design, construction, and performance of a green, soft shoreline protection using sand filled tubes constructed of composite geotextiles to provide the green, soft shoreline protection alternative.

INTRODUCTION

Shoreline and inland estuary erosion protection has been and will continue to be a major concern for inhabitants, businesses, and tourist living near or visiting these areas. Traditional methods of protection, in too many cases, have exacerbated versus mitigating the erosion problems causing engineers and regulators to rethink adaption living shoreline designs for new projects or rehabilitation of old projects. Given these conditions, Living Shorelines, once only a dream of environmentalist and government regulators, are becoming a reality. Marine engineers practicing erosion control, for shoreline protection design and construction now have an expanding verity of engineered materials to select from that have proven track records of performance. This is the case of the Currioman Bay project in Westmorland County, Virginia.

CHALLENGE:

The James River and the adjacent Currioman Bay located in the Northern Neck of Virginia is a very popular body of water enjoyed by local sports fishermen and water enthusiast. See Figure 1. Because of this location's popularity and access to the Chesapeake Bay, Westmorland County built a boat launch and has provided the Currioman boat launch facility free of charge for those enjoying the river and bay to launch and trailer their sports crafts since the early 1950's. However, over the

year the Currioman Bay barrier island protecting this area has been split in two by the annual tropical storms and the occasional hurricane. See Figure 2. Due to the barrier island cut opening becoming wider over the years, the spit of land protecting the boat launch experience severe erosion to the point of being cut in two in 2017. With this opening in the spit of land, sand and sediment transported by storms were deposited around the boat launch to the point that it became unusable to launch or trailer the any boat. See Figure 3.

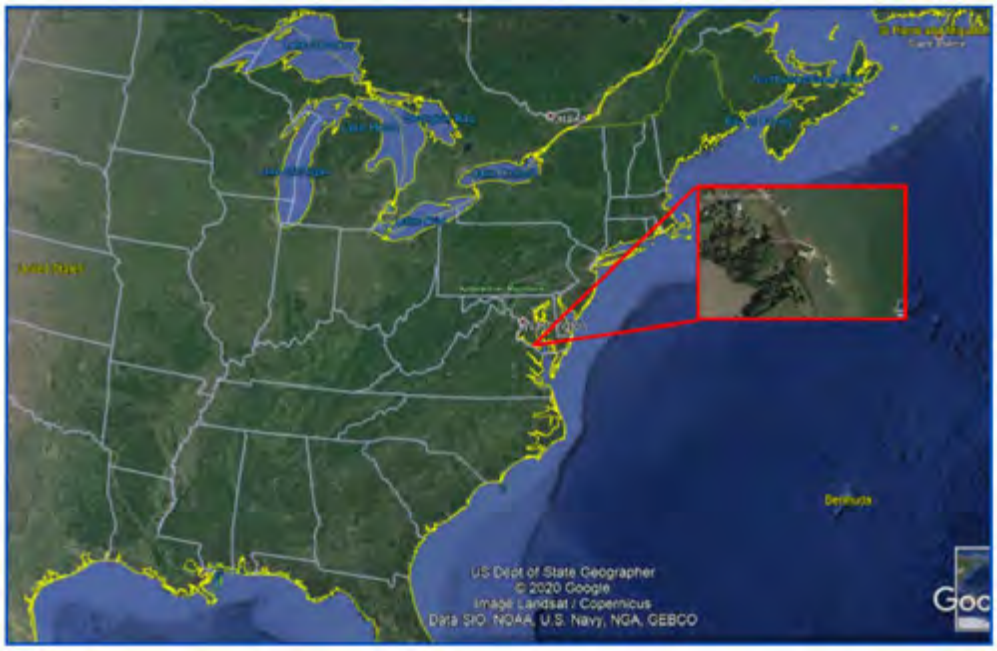

Figure 1 Google Earth Project Location

Figure 2 Currioman Bay Barrier Island 1984 and 2015

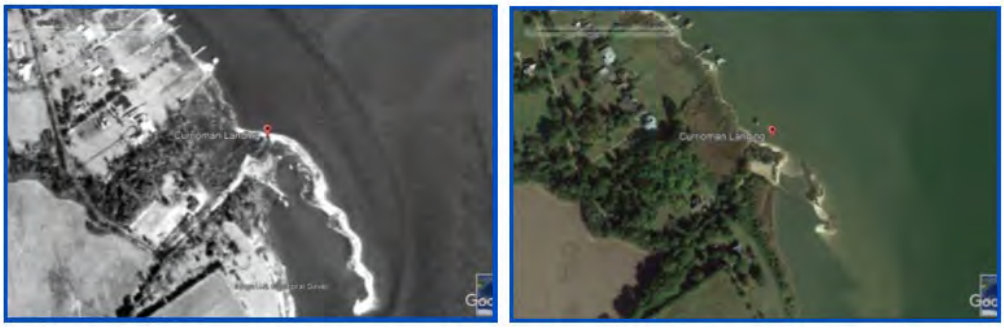

Figure 3 Currioman Landing 1994 and 2017

SOLUTION

In 2018 Westmorland hired a local marine engineering firm to develop a master plan for the redevelopment and protection and reestablishment of the spit of land to its' pre 1994 condition, dredging the entry channel, upgrading the surrounding property, and reopening the Currioman Boat Launch for public use.

The priority was the development of an erosion protection design for spit that would incorporate a soft armor system that would blend with the natural setting yet provide a Living Shoreline environment. The option chosen by the engineering firm was to install a geotextile tube with a scour apron around the entire perimeter or the original spit. The top elevation of the geotextile tube would be the +0.9m (+3.0 ft.) MLW elevation. See Figure 4. The engineer specified a composite geotextile for the geotextile tube. The composite geotextile consisting of three layers. The outer layer was 1,050 grm/m3 (30 oz/yd2) of UV stabilized high denier polypropylene fiber needled into a high strength woven polypropylene geotextile with a non-woven geotextile backing. See Figure 5 for an image of the composite geotextile used to fabricate the geotextile tubes and Table 1 for the physical and hydraulic properties of this composite geotextile tube material. The outer layer is designed to entrap the sand and sediment taking on a natural appearance that blends in with the surrounding environment. This composite geotextile was chosen based on the ability of a data reported by Little et al in their 2016 published paper geotextile that concludes Soft Substrate Geotextiles support soft marine growth when deposited in an estuarine condition. The thick soft fiber structure of the composite geotextiles provides this type of substrate for an environmentally sustainable structure. The engineer specified that sediments deposited around the boat launch and within the channel leading from the boat launch would be used as fill material for the geotextile tubes.

The second level of the design requires that once the geotextile tube perimeter has been installed, the remaining sediments of silt and sand within the boat launch and channel will to dredged and deposited within the geotextile tube perimeter to a level of +1.25m (4.0 ft.). See Figure 4 for the final design. This will create a channel for the boats to enter the bay and return to the boat launch with a channel depth of -1.25m (4.0 ft.).

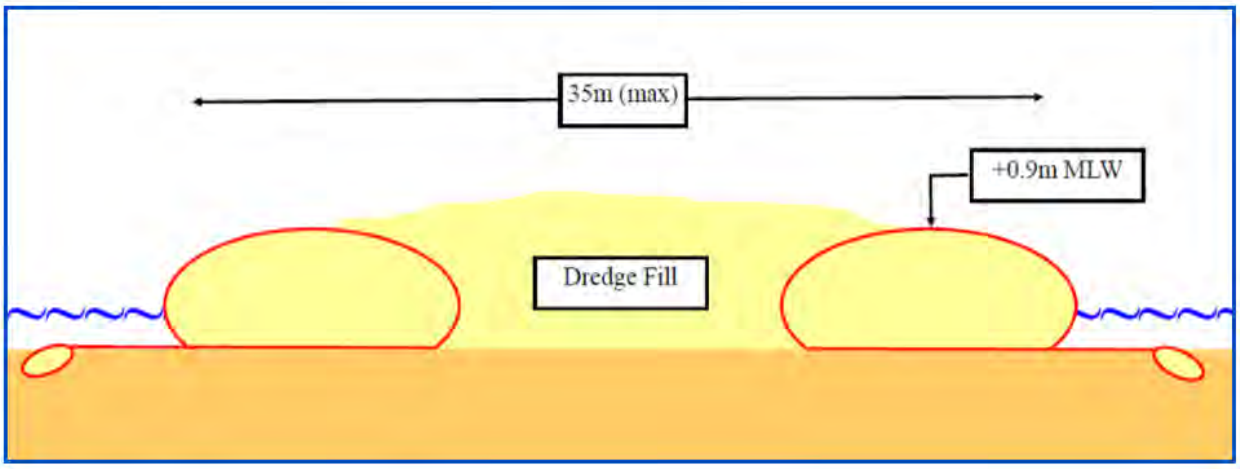

Figure 4 Cross Section Design of Perimeter Erosion Protection

Figure 5 Composite Geotextile Tube Material

Table 1 Composite Geotextile Physical and Hydraulic Properties

Mechanical Properties	Test Method	Unit	Minimum Test Value	
			MD	CD
Wide Width Tensile Strength	ISO 10319	lbs/in (kN/m)	360 (63)	310 (54)
Factory Seam Strength	ISO 10321	lbs/in (kN/m)	286 (50)	
CBR Puncture Strength	ISO 12236	lbs (N)	1821 (8100)	
Rigid Port Strength[1]	ASTM D6241	lbs/in (kN/m)	1356 (53.4)	
Hydraulic Properties			**Minimum Test Value**	
Pore Size O_{90}	ISO 12956	(mm)	(0.14)	
Water Permeability	ISO 11058	gpm/ft^2 (l/min/m^2)	(9.8)	
Durability Properties			**Test Value**	
Impact Energy[2]	ASTM E1886	ft-lbs (N-m)	1233 (1671)	
Abrasion Resistance[3]	BAW RPG 3.11	%	93	
UV Resistance	ASTM D4355	%	90	

Physical Properties	Test Method	Unit	TC120MB Typical Value	TC120MG Typical Value
Mass/Unit Area	ASTM D5261	oz/yd^2 (g/m^2)	35 (1186)	35 (1186)
Color			Tan	Green

The final design consideration was to be able to reestablish the native vegetation that grew on the spit of land before it was destroyed by erosion. To provide additional stabilization and restore the spit to its' original function and appearance. Three types of native species will be planted on the east side of the spit facing the bay and three different native species will be planted on the west side facing the land. See Table 2 for the types of marsh grass. In total more than 22,000 plugs grown in a local nursery will be planted. In addition, any remaining grass on the spit after the installation of the geotextile tube perimeter and before the dredging operation will be removed with the root mat and preserved for replanting like sod on the spit.

Table 2 Native Species to be planted

Dune Planting Species

Scientific Name	Common Name	Location planted*	No. planted	Notes
Spartina patens	saltmeadow cordgrass	E	3,702	
Panicum amarum var. amarum	bitter seabeach grass	E	3,702	
Schizachyrium littorale	seaside little bluestem	E	3,702	
Panicum amarum var. amarum	bitter seabeach grass	W	3,702	
Solidago sempervirens var. sempervirens	seaside goldenrod	W	3,702	
Ammophila breviligulata	Am. Beach Grass	W	3,702	

*E=Eastern side of spit W=Western side of Spit

CONSTRUCTION

The construction phase of the project began in July 2020 with the installation of the outer row of scour aprons and geotextile tubes. The inside row installation was completed September 2020 and the dredging completed in the same month with the grass planting finishing the project in mid-October 2020. All dredging was performed mechanically using a long stick excavator. The geotextile tubes were filled using a hopper and water pump. See Figures 6, 7, 8, 9, and 10.

Figure 6 Installation of Geotextile Tube Perimeter Structure

Figure 7 Dredging Fill In-between Geotextile Structure

Figure 8 Dredging Backfill

Figure 9 Planting Native Species Marsh Grass

During the installation of the geotextile tubes forming the perimeter of Currioman Bay Spit Restoration, a variation of local materials was accessed to fill the containers. When the project was bid in 2019 the area at the base of the spit peninsula had already washed out good quality sand was evenly spread over this area in a thickness of about 1' depth. However, by the time geotextile tube installation commenced in June 2020, this area had experienced additional overwash for about six months resulting in a concentration of preferred sediments more toward the south of the site. An on-site investigation identified there were acceptable sediments remaining below where the previous sand strata previously existed. The combination of mini suction dredges along with a double port fill hopper allowed for filling the geotextile tubes with both types of material and variations in between. As a result, additional double handing of material was implemented. The flexibility of having two type of fill devices on site allowed the construction team to vary fill methods based on the proximate sediment types. Layers of saturated bark were encountered on the site. Therefore, the use of the mini suction dredge allowed these deposits to be easily identified and avoided.

ENVIRONMENTAL ASSYMILATION OF GEOTEXTILE TUBES:

Each geotextile tube section was installed either with a suction dredge or a combination of fill hopper and an excavator on a floating barge. Each type of method had minimal impact on the environment. The floating barge made it possible for access to occur without significantly impacting benthic area designated for protection from work area. Also, the mini suction dredges were deployed atop a Carolina skiff in a similar manner preventing further impact. Throughout the

project, continuous positive interaction with natural flora and fauna was observed. In less than two days after initial geotextile tube was install, marine growth was observed establishing on the surface of the composite geotextile. During the entire installation process, blue herons were observed fishing from the tube spit immediately after installation and prior to placement of backfill. Pelagic fish were observed feeding on the newly established marine growth including black drum. Shrimp were observed congregating in between the scour apron tube and the primary geotextile tube. Blue crabs were observed mating and hunting from the side of the geotextile tubes. The composite geotextile material allowed the crabs to dig in their back legs for grip while mating and hunting. See Figure 11. After the installation of the first four tubes on the other perimeter in the north of the spit, congregations of jelly fish formed in the temporary embayment where there was shelter from the wind driven waves and primary littoral current. From a geotechnical interest, the bottom drift in sediments was observed atop the scour apron tube. Sedimentation atop the scour tubes occurred in a similar manner as it would on a bottom without any deployed geosynthetics. This demonstrates that while the tubes are there to provide erosion and scour protection in extreme events that might mobilize these sediments, in regular weather the geotextile tubes and scour aprons have little or no environmental impact on natural sedimentation in and around the recreated spit of land.

Figure 10 Completed Project

Figure 11 Jelly Fish and Crab

CONCLUSION

- Traditional hard armor erosion control material like stone rip rap are expensive and not conducive to environmentally friendly Living Shoreline solutions.
- Geotextile Tube structures with soft armor surfaces have the capability of providing a sustainable Living Shoreline environment that supports and encourages marine growth.
- The Geotextile Tube Living Shoreline design and installation created a lower cost than traditional construction technique that allowed the project to be completed within the owner's budget without impacting the sensitive surrounding environment.
- The Geotextile Tube Living Shoreline had no environmental impact on the natural site sedimentation or literal drift.

ACKNOWLEDGEMENT

This paper could not have been completed without the information provided by John Brooks at Apex Engineering in Richmond, Virginia and Shannon Wilkins of Docks of the Bay Construction Company in Irvington, Virginia.

REFERENCES

Little, J, et al, 2016, Quantitative Evaluation of Marine Growth on Geosynthetic Reef Trials in Beaufort, North Carolina, Geosynthetics 2016, Miami, Florida, USA.

Geosynthetics Conference

Engineered Geotextile Solutions for Inland Waterway Erosion Protection

Bryan Hamilton,[1] Jun Yuen Tan,[2] Tack Weng Yee[3]

[1] TenCate Environmental Infrastructure Group, Americas; b.hamilton@tencategeo.com
[2] TenCate Water & Environment, Asia; jy.tan@tencategeo.com
[3] TenCate Geosynthetics, Asia; tw.yee@tencategeo.com

ABSTRACT

This paper explores Geocontainment Systems used in erosion control works for inland waterways. Over time, rivers and canals are subject to natural erosion processes. If left unattended, the continued erosion can cause major destruction of the basin and/or watercourse resulting in increased flooding, reduced vegetation growth and destroyed habitat. A variety of erosion control systems are available, with rock-based or concrete based systems being adopted traditionally. However, a soft and environmentally friendly solution, or Geocontainment solution, is often preferable. Examples of Geocontainment Systems include geotextile bags and sand filled mattresses. There is a wide range of engineered geotextiles and composites used for the fabrication of Geocontainment Systems. These engineered fabrics are designed for strength, robustness, abrasion resistance, UV resistance, etc. for the most demanding of site conditions. Our goal is to show how the versatility of these materials as Geocontainment Systems together with their low cost, and simple design makes a compelling case for their adoption as commonly used methods for erosion control.

INTRODUCTION

Inland waterways are continually subjected to natural erosion resulting in flow meandering, flooding and damage to infrastructure. Erosion is the action of surface processes, such as water flow or wind, that removes soil, rock or dissolved material from one location on the Earth's crust, and then transports it to another location. In order for erosion to occur three processes must take place; detachment, entrainment and transport (Yee, 2012). Detachment occurs when soil particles are removed from the earth's surface through the impact of raindrops, running water, scouring action, flowing debris abrasion or wave breaking action. Entrainment refers to the loss of frictional resistance of the soil to its surrounding environment due to the forces of fluid drag. Once a particle is entrained it tends to move as long as the velocity of the current is high enough to transport the particle horizontally. The transport of entrained soils continues until the flow velocity is lower than the settling velocity. Figure 1 shows the erosion and settling velocities for different soil particles sizes.

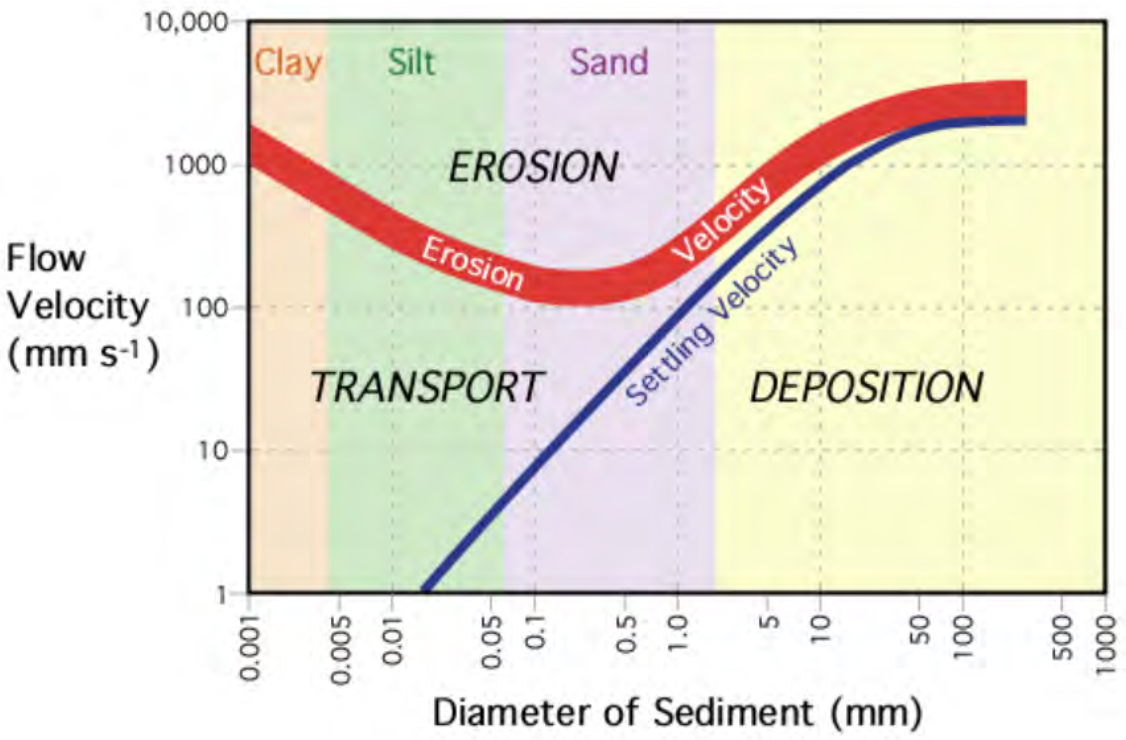

Figure 1. Erosion and settling velocities for different soil particles sizes (Pidwirny, 1999).

Traditionally, hard armor erosion control materials, such as rock and/or concrete based systems, have been used to mitigate bank erosion. But, as those materials become increasingly scarce, and more expensive, the use of Geocontainment Systems is being adopted as a viable alternative. The earliest recorded use of Geocontainment Systems is sand filled geotextile bags in The Netherlands and Northern Germany in the 1950s (Koerner, 2016). The geotextile bags were used to encapsulate sand fill to form erosion resistant gravity structures. Since that time Geocontainment Systems have been widely developed and can be categorized in three main categories; geotextile bags, geotextile mattresses and geotextile tubes. The information provided in this circular focuses only on geotextile bags and sand filled mattresses.

TRADITIONAL METHODS OF PROTECTION

Traditional methods used to prevent soil erosion on channel banks include rock-based systems, such as gabions, rubble and riprap, or concrete based systems, such as filter point or fabric formed mats, block and poured concrete. While these systems offer some advantages, such as stability and endurance, they also present disadvantages, such as higher cost and limited availability. The cost disadvantage exceeds that of just the materials. Transportation, site preparation, site access, heavy machinery, and installation all contribute to the higher cost of these type cover layers. Also, in many regions, materials for rock-based systems are unavailable, and thus are not an option. Apart from the cost and availability of traditional materials, they are often unattractive and alter the natural appearance of the waterway.

Traditional cover layers often require a secondary, or tertiary sublayer to prevent particle erosion. Particle erosion is a hydraulic phenomenon which results when the tractive force exerted by flowing water exceeds the cover layers ability to resist motion. Quality standards in hydraulic engineering include the use of geotextile filter fabrics as a component in revetment structures to replace multiple granular filter layers (Pilarczyk, 2000). So, it is common to see engineered geotextiles in traditional cover layer systems.

GEOCONTAINMENT SYSTEMS

Geotextile Bags

Geotextile bags come in different shapes and sizes, with fill volume ranging between 0.3 to 10m3 (Bezuijen and Vastenburg, 2013). Most geotextile bags found in the market today are either pillow shape or box shaped. A pillow shaped geotextile bag is comprised of a folded piece of specially engineered fabric that is seamed along three sides. A box shaped geotextile bag is comprised of several pieces of geotextile seamed along the edges to form a box like unit.

Designs for geotextile bag structures include stacked arrangements that greatly increase stability under hydraulic actions. Geotextile bags are usually installed using two types of geometry. Figure 2(a) depicts geotextile bags stacked horizontally in an offset fashion. Figure 2(b) depicts geotextile bags placed length wise following the profile of the slope surface. The two geometries have a different effective thickness that impacts the hydraulic stability of the structure. As with traditional protection methods, these designs also include a secondary layer of filter fabric to prevent particle erosion on the slope face.

(a) (b)

Figure 2. Geotextile bags arrangement (a) geometry I (b) geometry II (Yee, 2012)

Geotextile bags, as shown in Figure 3, can be filled with various materials such as soil, gravel and concrete. However, the preferred fill material is sand. Sand is a common resource along many waterways. And, because it is mechanically and volumetrically stable, it has predictable engineering properties. Selecting the right fill material to maximize the fill density of geotextile bags is critical to ensure they maintain their shape over the life of the structure. It is a common practice to hydraulically fill geotextile bags to fully compact and maximize the volume of the sand fill.

Geotextile bags used for erosion protection include many advantages when compared to traditional hard cover layers. The size and shape of geotextile bags can be customized to meet design requirements for hydraulic loading. Localized soils can be used to fill geotextile bags which reduces both material and material transportation cost. Since a geotextile bag structure is

modular, it is easier to repair if a section of the structure is damaged. Finally, geotextile bags offer more flexibility for armoring steep slopes.

Figure 3. Examples of geotextile bags

SAND FILLED MATTRESS

Sand filled mattress, as shown in Figure 4, is a double fabric layer product. The two layers of fabric are systematically linked with uniformly spaced parallel stitches in the machine direction to create tubular filling spaces that are filled with sand. The parallel stitches are meant to prevent the movement of the sand and to create a definite circumference for the tubular compartment. The filled thickness of a sand filled mattress is controlled by the circumference of each tubular compartment which is restrained by the spacing of the parallel stitches. The effective thickness of a sand filled mattresses is a crucial parameter in determining how it will withstand hydraulic action as determined by a ratio of 0.6 to 0.8 of the whole diameter.

The top layer is an engineered composite fabric with durability features such as abrasion resistance, impact resistance and UV resistance. The composite fabric is also capable of trapping settling soils and particles.

Sand filled mattresses are normally supplied by the roll. Cutting the mattress may be required to achieve a specified length. Field sewing is required to close the bottom of a field cut mattress. Stitching, lacing, or pneumatic staplers are used to join sections of sand filled mattresses and create a continuous structure. Sand filled mattresses are securely anchored to the crest of the slope by using an anchor trench to prevent slippage after installation. Sand slurry is pumped, or gravity fed, to install sand filled mattresses. This provides maximum density and weight to the structure for stability under hydraulic actions.

Figure 4. Examples of sand filled mattress

Green Geotextile Bags and Sand Filled Mattresses

Conventional geotextile bags are fabricated using high strength woven geotextiles, nonwoven geotextiles, or a combination of both. The woven and nonwoven geotextiles are made from either polyamide (nylon), polyester (PET) or polypropylene (PP). And, like sand filled mattresses, geotextile bags can also be fabricated from an engineered composite fabric. The combination of these materials creates a high strength geotextile bag that has the same durability features of a sand filled mattress.

The geotextile bags and sand filled mattresses made from the composite geotextile are considered to be "green" in two ways:

1. The composite fabric is available in green color. This provides the option for Geocontainment Systems installed in vegetated areas to immediately blend in with the environment.
2. The crimped composite fabric captures entrained sediments . This allows topsoil to accumulate on the structure and rapidly establish vegetation that covers the Geocontainment System as shown in Figure 5.

Figure 5. Vegetated Geocontainment Systems

DISCUSSIONS AND CONCLUSION

Bank erosion is a naturally occurring process. But, the rate at which it occurs is often increased by human activities such as urbanization and agriculture. Changes in land use can cause banks to erode at rates much faster than those seen in natural, undisturbed systems. Increases in storm frequency and intensity are also causing increased erosion along inland waterways requiring them to withstand higher water flow velocity and water levels.

Hard armoring is the traditional response to controlling and minimizing erosion in waterways. But, as technologies and techniques advance in finding ways to secure land from the ravages of erosion, alternative solutions like Geocontainment Systems are being included with the traditional engineering approaches.

Geocontainment Systems replace hard armoring in the form of geotextile bags and sand filled mattresses. These systems are manufactured from engineered fabrics that are designed for strength, robustness, abrasion resistance, UV resistance, etc. Different design configurations are possible with geotextile bags. For example, they can be stacked parallel to the bank, or they can be installed length wise (perpendicular) on an embankment. Geotextile bags are used in waterways subject to high flow velocity while sand filled mattresses are generally used in waterways with low turbulence and lower flow velocity.

Geocontainment Systems can be designed as a “Green” solution by selecting green colored composite fabric and by being installed in natural environments where vegetation is part of the engineered approach. Green colored composite fabric blends with the natural environment and aids in plant growth by holding seeds and topsoil in place. As the vegetation grows, it covers the geocontainment system returning the waterway to its natural state.

REFERENCES

Bezuijen, A. & Vastenburg, E.W. 2013.Geosystems: design rules and applications, CRC/Balkema, Leiden, The Netherlands.

Koerner, R.M. 2016. Geotextiles: From Design to Applications, Woodhead Publishing Co., Cambridge, UK. Pidwirny, M. 1999. Fundamentals of Physical Geography. Chapter 10: Introduction to the Lithosphere, (w) Erosion and Deposition, PhysicalGeography.Net.

Pidwirny, M. 1999. Fundamentals of Physical Geography. Chapter 10: Introduction to the Lithosphere, (w) Erosion and Deposition, PhysicalGeography.Net.

Pilarczyk, K.W. 2000. Geosynthetics and Geosystems in Hydraulic and Coastal Engineering, A.A. Balkema, Rotterdam, The Netherlands.

Yee, T.W. 2012. Geosynthetics for erosion control in hydraulic environment. Fifth Asian Regional Conference on Geosynthetics, Bangkok, Thailand, pp. 119-134.

Geosynthetics Conference

The Use of Geotextile Tubes to Protect a Historic Lighthouse located on the Delaware Bay

Nathalia P. B de Castro, MSc.,[1] Thomas Stephens[2]

[1]TenCate Geosynthetics, e-mail: n.castro@tencategeo.com
[2]TenCate Geosynthetics, e-mail: t.stephens@tencategeo.com

ABSTRACT

Built in 1849 and originally known as the Maurice River Lighthouse, the two-story brick structure, now known as the East Point Lighthouse, is the second oldest lighthouse in the state of New Jersey. Over the last decades, the historic building has become vulnerable to storms and flooding due to years of shoreline erosion and today at mean high tide, it sits just 90 feet from the shoreline. The geotextile tube technology was invented in the early 60's in the Netherlands and for more than 25 years it has been successfully used in the United States. The first shoreline application was installed in Atlantic City, New Jersey in 1993. Throughout the years, thousands of tubes have been being installed for marine application around the country, which helped to restore many miles of natural protective coastal dunes. As the geosynthetics evolved over time, new composites and high strength geotextiles have been engineered to provide better aesthetics, higher UV resistance, higher performance and consequently more durability to geosystems as marine structures. It's also important to highlight that these new materials provide a more susceptible media for marine life growth. This paper presents the case study of the use of the geotextile tube technology to protect an American symbol, the East Point Lighthouse, and shows how this innovative solution draw a line in the sand in order to stop the erosion to progress.

INTRODUCTION

Over the last decades, storm surge and flooding have washed the sediments away from the beaches on the Delaware Bay. The advanced erosive process has been causing serious environmental and historical impact on the region. This paper presents the case study of the use of the geotextile tube technology to protect an American symbol, the East Point Lighthouse, and shows how this innovative solution draw a line in the sand in order to stop the erosion to progress. Figure 1 details how erosion in this region over the past 73 years has impacted the sensitive coastal wetlands environment and is threatening the historic lighthouse structure.

HISTORIC BACKGROUND

This two-story structure built in 1849 and originally known as the Maurice River Lighthouse, now known as the East Point Lighthouse, is the second oldest lighthouse in the state of New Jersey, surpassed in age only by the Sandy Hook Lighthouse, built in 1764.

The Cape Cod-style Lighthouse provided hundreds of Delaware Bay oyster schooners with a guiding light to the ports of Port Norris and Port Elizabeth, operating until the time of the Second

World War. It was added to the National Register of Historic Places on August 25, 1995 because of its significance in engineering, maritime history, and transportation.

Deterioration set in following its decommissioning. A combination of public funding sources has provided much-needed restoration work, including installation of a new roof and lantern, repointing of brickwork and installation of flood pumps. Over the last decades, the historic building has become vulnerable to storms and flooding due to years of shoreline erosion and today sits just 90 feet from mean high water. (http://www.njlhs.org/njlight/eastpoint.html)

Figure 1: Google Earth images showing the erosive process from 1940 to 2013.

ENVIRONMENTAL IMPACT

The East Point Lighthouse is surrounded by wetlands, a preserved ecosystem that provide habitat for thousands of species of aquatic and terrestrial plants and animals. They also are valuable for flood protection, water quality improvement, shoreline erosion control, recreation, and aesthetics.

The geotextile tube structure was installed all around the wetlands as a reinforced sand dune core.

GEOTEXTILE TUBE TECHNOLOGY

The geotextile tube technology was invented in the early 60's in the Netherlands and for more than 20 years it has been successfully used in the United States, which had its first application in Atlantic City, New Jersey (Pilarczyk, 2000, Lawson, 2006, Bezuijen, 2013). Throughout the years, thousands of tubes have been being installed for marine application around the country, which helped to restore many miles of natural protective coastal dunes. As the geosynthetics evolved over time, new composites and high strength geotextiles have been engineered to provide better aesthetics, higher UV resistance, higher performance and consequently more durability to geosystems as marine structures. It's also important to highlight that these new materials provide a more susceptible media for marine life growth. Figure 2 shows the first job using the geotextile tube technology in 1962 and Figure 3 shows the geotextile tubes in Atlantic City, New Jersey in 1993.

Figure 2: First job using the geotextile tube technology in 1962 (TenCate Geosynthetics)

Figure 3: First geotextile tubes installed in the United States (Atlantic City, New Jersey in 1993).

PROJECT DESIGN

Solution. The solution was to use the geotextile tube technology to protect the 600ft (183m) of shoreline right in front of the lighthouse, reinforcing the sand dune core that had been eroded over

the past 40 years. The technology consists installing high tenacity woven geotextile containers, which is filled with slurry sand, local or imported. These containers are aligned and or stacked to create a structure to protect the shore against erosion. In order to prevent the base of the geotextile container from being scoured during waves and currents attacks, a geotextile scour apron with anchor tubes are installed to have the function of anchoring the system to the ground.

The 600ft structure was designed to have eight sections and each section to have three elements: the scour apron with two anchor tubes, a Sand Filled Mattress (SFM) on top of the scour apron, and geotextile tube elements on top of the SFM. The SFM is made by a durable composite and was used in this project to provide extra weight to the scour apron. Figure 4 shows the eight sections on a plan view and the relative position of the Lighthouse and the wetlands to the structure. Different lengths of tubes were used to allow the system to follow the designed alignment.

Geotextile Specifications. The geotextile used to fabricate the Scour Apron was a woven geotextile with a tensile strength of 79 x 110 kN/m (450 x 635 lb/in) and seam strengths of 70 kN/m (400 lb/in). The SFM tri-composite top layer geotextile has a thickness of 6.35mm (0.25 in.), a mass of 1,200 grm/m2 (35 oz/yd2). See Figure 5 for an example of the Tri-Composite geotextile. In addition, the SFM has a hurricane impact resistance according to ASTM E1886 of 1,665 N/m (1,233 lbf) and a high UV resistance. When tested according EN12224 the estimated half life of +35 years when exposed to sunlight at the latitude of New Jersey. Also, the SFM has a tensile strength of 63 kN/m (360 lb/in). The geotextile tube was fabricated from a woven textile with a tensile strength of 200 x 200 kN/m (1,250 x 1,250 lb/in) and the same hurricane impact resistance as the SFM. These unique high strength – high impact resistant geotextile materials were selected for this project because the anticipated exposure to annual hurricane and nor'easter storm events and for their proven track record on other projects with similar weather patterns.

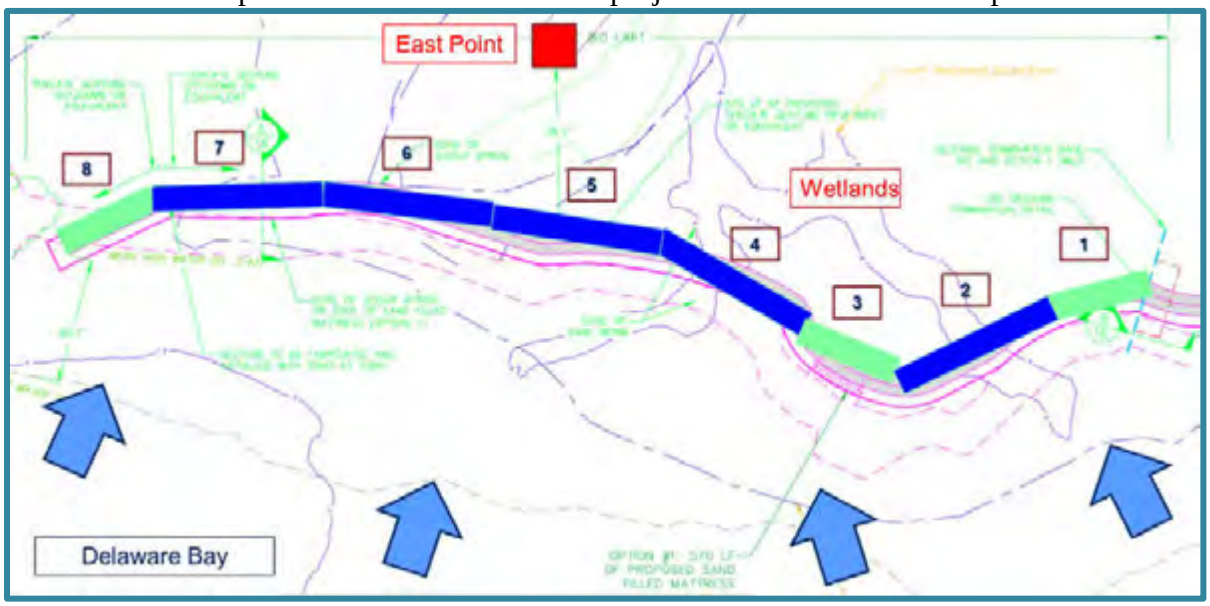

Figure 4: The eight sections on a plan view and the relative position of the Lighthouse and the wetlands to the structure.

Figure 5: Sand Filled Mattress Tri-Composite Geotextile

.

Conceptual Design. The geotextile tube was designed using the Geotube® Simulator, which is a proprietary TenCate software that has been developed to create the cross sectional geotextile tube image with dimensions and volume and to calculate the forces exerted against the container in the circumference and axial direction, and against the fill ports when the container is filled with a fluid of any given density (Plaut, 2018). Input variables to the Geotube® Simulator are the circumference and fill height of the tube, the relative density of the fill material, the type of geotextile to be used, the type of filling port, and the tube fabrication method. The output data are the tensile forces exerted on the container in the circumferential and the axial directions, the tube fill width, the cross section area and the volume per unit length, and the FoS (Factors of Safety) against rupture for the given input parameters. Figure 6 shows the Geotube® Simulator graphic output for the East Point Lighthouse project.

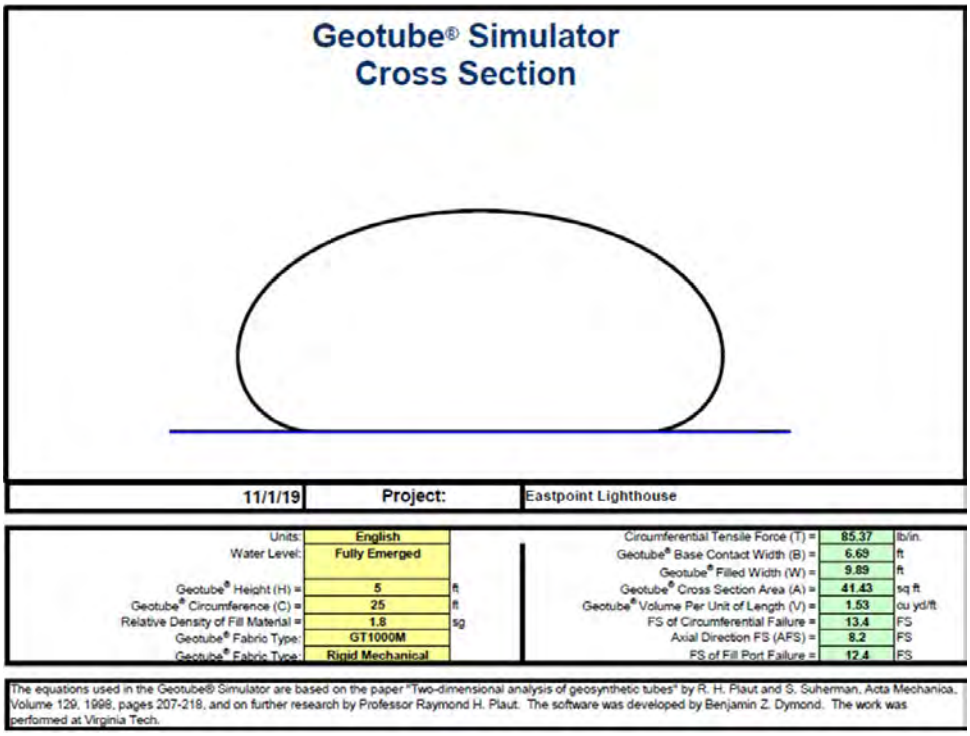

Figure 6: Geotube® Simulator graphic output.

PROJECT EXECUTION

The first step was to excavate the terrain and level it up in order to keep the designed elevation of the crest of the structure. Next, the scour apron was installed having the two anchor tubes filled with slurry sand from a fix sand box. The next element was the SFM, which was filled separately and positioned by using an excavator, and finally the geotextile tube was placed and filled up to 5ft. It was used geotextile tubes with flat ends to assure that the structure would not have lower zones where the tubes overlap.

The project was implemented in December of 2019 and it took about 30 days to be concluded. It was the contractor's first job installing geotextile tubes, although they learned fast and did a great job. The method they developed to install the SFM helped to speed up the installation process. Figure 7 shows geotextile tube with its flat end.

Figure 7: Geotextile tube flat end.

As the sections were being finalized, they were covered with sand that from time to time, specially after big storms, it is recommended to be replaced. Figure 8 shows the Sand Filled Mattress being installed. Figure 9 shows the structure completed after six months.

Figure 8: Sand Filled Mattress installation.

Figure 9: Project after six months. Recreation and marine life in the beach.

CONCLUSIONS

The main objective of the project was achieved, which was to stop the advancement of the erosion that was threatening the historic lighthouse building.

The use of geotextile tubes with flat ends provided cost savings because it was not necessary to overlap the units and lose a portion of the structure longitudinally.

The use of geotextile tubes provides a clean and safe environment for the beachgoers, since there are no rocks spread all over the beach.

It's important to address that the geosynthetics that were used are chemically inert, allow vegetation growth and interact very well with marine life. For instance, the horseshoe crabs spawn on the beach of Delaware Bay every year and 2020 was not different.

REFERENCES

Bezuijen, A., Vastenburg, E. W., Geosystems: design rules and applications, 1st edition, ISBN 978-0-415-62148-9, TA455.G44B49 2013.

Lawson, C.R. Geotextile containment for hydraulic and environmental engineering. In. INTERNATIONAL CONFERENCE ON GEOSYNTHETICS ,8th, Yokohama, 2006. Proceedings…, [S.l.: s.n]. 2006. p. 9-48, 2006

New Jersey Lighthouse Society, http://www.njlhs.org/njlight/eastpoint.html, October, 9th of 2020.

Pilarczyk, K. W. Geosynthetics and geosystems in hydraulic and coastal engineering. ISBN-9058093026. 2000, Balkema. 2000

Plaut, R. H., Suherman, S., “Two-Dimensional Analysis of Geosynthetic Tubes”, Acta Mechanica, Volme 129, 1998, pages 207 – 218

25m^3 Geotextile Bags and Geotextile Tubes used to protect a 42" pipeline against scouring, 30m deep on the seabed, Covenas, Colombia, S.A

Eng. Nicolas Ruiz R.[1], Eng. Mauricio Rendón G.[2]

[1]TenCate Geosynthetics Americas, Bogota, Colombia; e-mail: n.ruiz@tencategeo.com
[2]Geosoluciones de Ingenieria SAS, Bogota, Colombia; e-mail: gerencia@geomembranas.com.co

ABSTRACT

The buoy that is part of the offshore terminal for tanker ships loading oil off the Colombian coastline is anchored to a submerged pipeline 42" in diameter that sits 30m deep over the seabed.

Underwater currents have caused localized scouring along the pipeline, creating voids underneath it and additional strain on the pipe. To provide a definitive solution, it is key to understand that loading of the ships is the number one priority of the facility, therefore very specific windows of operation are open to install or build any solution.

With this restriction in mind, the project opted to fill onshore large Geotextile bags, 25m^3 in capacity each, that would be loaded onto a barge using a lifting harness made of polyester geogrid and a PVC coating. The geotextile bags would be lowered into position using a large crawler crane which would be fixed on to the barge and set into position with the help of deep-sea divers. With the bags in place, resting on each side of the pipeline, a geotextile tube would be installed in between the bags and under the pipeline and filled from the surface with a sand and water slurry.

The geotextile bags are 5.0m long x 2.5m wide x 2.0m high and each has a filled capacity of 25m^3 and weighs in approximately 40 tons. Once the Geotextile bag and Geotextile tube are in position, a final Geotextile tube type-of -mattress would be placed overlapping the bags and the geotextile tube and filled with a sand slurry to fill in voids so that it can provide the support required to keep the submerged pipeline stable and in place. This geosynthetic system will provide a long-lasting solution for this scouring problem for good.

1. INTRODUCTION

1.1 Project Background

The crude oil pipeline stretches from the south eastern plains in Colombia, in Cusiana and runs northwest to Covenas, on the Caribbean coast of Colombia, covering a total length of 850km on land and 12km underwater, lying on the bottom of the sea bed, 30m deep, where it connects to a manifold and valve system known as "TLU buoy" where super tanker ships are loaded, and the crude oil is exported or sent to the refinery in near-by Cartagena. Figure 1 – Project Location.

Figure 1 – Project Location

The submerged pipeline is 42” (1.06m) in diameter, it seats on the seabed and undergoes constant electronic monitoring and scuba diving supervision. Localized scouring along the pipeline has been detected in the past, mainly caused by underwater currents and several attempts to stop it have been made, with partial success.

An inquiry was brought to our attention on finding a way to solve this scouring problem for good and a solution utilizing a combination of geosynthetics was chose: large Geotextile bags units would be placed along each side of the pipeline; then, Geotextile Tubes and a Geotextile tube type-of-mattress would be installed. Figure 2 – Condition Prior to Geotextile Tube Solution

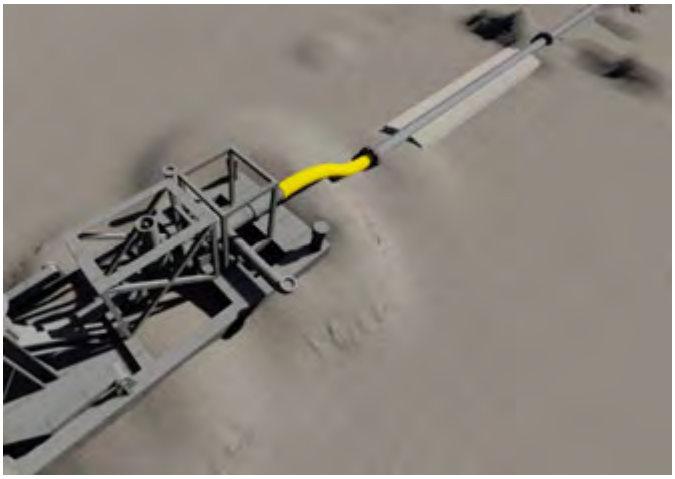

Figure 2 – Condition Prior to Geotextile Tube Solution

1.2 The Challenge

One of the constraints to carry out the installation of the Geotextile Bags and Tubes, was the time frame allowed to move near the buoy and carry out field maneuvers, as the priority of operation of the buoy consists in exporting crude oil, therefore any attempt to work around the site, would have to

be done in between tankers approaching the buoy. Any schedule overrun, could mean thousands of dollars in liabilities.

To reduce such risk, it was decided to split the construction process into two phases: the first phase would be carried out onshore, with the deployment of the Geogrid Lifting Harness and the Geotextile bag units. Initially, these bags were designed with a capacity of $35m^3$, but it was later decided to bring them down to $25m^3$. The bags would be deployed over the geogrid lifting harness, filled and then loaded on to a barge. A total of 21 Geotextile bag units would be required for this project, containing over $525m^3$ of coarse grain material.

Once the Geotextile bag units were lowered into position, all crane and additional vessels would no longer be required, thus reducing construction risks to manual deployment of the Geotextile tubes and mattresses.

2. LABORATORY TESTS

2.1 Geogrid Pullout Testing

To determine the Geogrid Lifting Harness Factors of Safety, we carried out Pullout tests, as per ASTM D 6706, using a 400kN/m geogrid as pullout specimen overlying by a 200kN/m x 200kN/m geotextile sample, so as to simulate the behavior of the geogrid – geotextile bag system interaction.

Geogrid Setup | Geotextile Setup | Complete Test Setup

Image 1 – Pullout Tests

2.2 Test Results

2.2.1 Apparent Friction Coefficient

Pullout tests allowed us to determine the apparent coefficient of friction of Geogrid – Geotextile system, which would be used to calculate the geogrid's lifting harness factors of safety against rupture and pullout resistance, based on the geotextile bag's geometry and weight.

3. GEOBAG AND GEOTEXTILE TUBE DIMENSIONING

Several factors were taken into consideration for the design of the geotextile bag and Geotextile Tubes used on this project. Although geotechnical information was not made available, a recent survey and

bathymetric report were used to determine the fill height and capacity of all units, as shown on Figure 3 – Localized Scouring.

Sector 1 Sector 2 Sector 3

Figure 3 – Localized Scouring

Three sectors were identified that would require stabilization. As there was no geotechnical data, information provided by the diving team was used to determine the size of geotextile bags. A layer of fine grain material, approximately 1.2 to 1.5m in thickness was present. Therefore, geotextile bag units that would be placed along the side of each sector should be as heavy as possible so that they would sink through this layer and become stable reducing future settlements. Initially, geotextile bag units were designed to contain $35m^3$ but were later reduced to $25m^3$ each. Fabrication and lifting would have been possible; however, this decision was made in stake of risk management on behalf of the client. Final geotextile bag design was a unit made of a woven geotextile, 200kN/m x 200kN/m and 5.0m long, 2.5m wide and 2.0m high. Finally, each geotextile was 30m lowered into position with the use of a crawler crane and the Geogrid lifting harness. Figure 4 – Geotextile bag Lifting Harness and Installation.

Figure 4 – Geotextile Bag Lifting Harness and Installation

Geotextile Tubes were designed with a fill height of 2.0m also, having Flat-Ends on each end so that they would snug fit between Geobag units. These Geotextile tubes were lowered and secured into

position by divers and pumped from the surface using electric submersible pumps from a sand box located on board of the service tug. Figure 5 – Sand Box

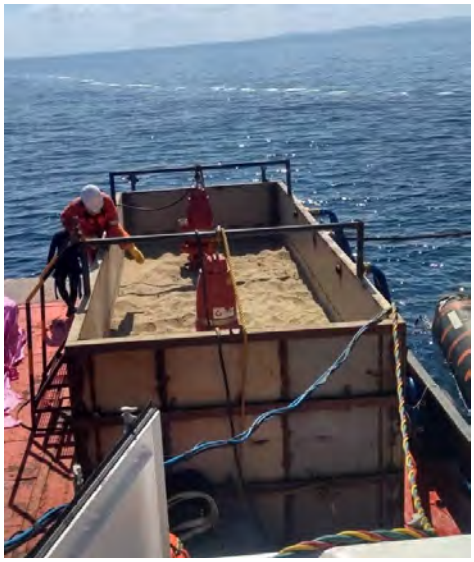

Figure 5 – Sand Box

4. RESULTS AND CONCLUSIONS

All Geobag units and Geotextile tubes were installed successfully and have provided support to all scoured sections. Installing the Geotextile tubes on the seabed by divers proved difficult as time was limited during each dive, yet it was achieved. Also, pumping the sand slurry 30m to the bottom was accomplished successfully.

Project was completed in 2019 and first monitoring will be made during the first quarter of 2020.

4.1 REFERENCES

Ruiz, N., Geobags para la protección de la socavación en las esclusas de Gatún, Canal de Panamá, Geosynthetics 2017, Santiago, Chile, 2017

Anmoba Solutions SAS, Análisis de cargas durante el bombeo de estabilización de lecho en oleoducto submarino, Bogota, 2019

SGI Testing Services, LLC, TenCate Geosynthetics Geogrid Pullout Testing (ASTM D 6706), Georgia, 201166

Geosynthetics Conference

Natural Sand Accumulation with Submersible Geotextile Geometries

Alice Jia Li Song,*[1] Jeremy Bilotti,*[2] Sarah Dole,[3] Hassan Maniku,[4] Tom Stephens,[5] Schendy Kernizan,[6] Jared Laucks,[7] Skylar Tibbits[8]

* Authors contributed equally.
[1] Self-Assembly Lab, MIT; e-mail: jlsong@mit.edu
[2] Self-Assembly Lab, MIT; e-mail: jcb432@mit.edu
[3] Invena; e-mail: sarahd@hima.asia
[4] Invena; e-mail: hassan@hima.asia
[5] Tencate, e-mail: t.stephens@tencategeo.com
[6] Self-Assembly Lab, MIT; e-mail: schendyk@mit.edu
[7] Self-Assembly Lab, MIT; e-mail: jlaucks@mit.edu
[8] Self-Assembly Lab, MIT; e-mail: sjet@mit.edu

ABSTRACT

This paper presents a new approach for promoting sand accumulation through strategically placed submersible geotextile geometries. This technique is being tested both in a laboratory environment and full-scale field experiments in the Maldives. Typical attempts to reduce wave forces or fight erosion rely on static physical barriers or continual beach replenishment, which resist the constantly changing natural forces of the ocean. Our approach instead, attempts to work with waves and currents to harness their energy in promoting sand accumulation. With large scale triangular prismatic geometries (20m × 4m × 2m) fabricated from geotextile membranes, the interaction of the water and sediment flowing over the geometries has shown to promote targeted accumulation. This paper will compare our approach to existing strategies for erosion control, discuss the material fabrication techniques, existing laboratory experiments as well as our latest results from the field experiments showing substantial sand accumulation within a targeted area.

INTRODUCTION

As climate change progresses, island nations and coastal regions face a growing risk of flooding. Sea level rise due to increasing global temperatures and ice melt will likely cause inundation of coastal regions. As storms grow in frequency and severity, coastlines will be further battered and eroded. Increasing ocean temperatures could also contribute to the loss of the remaining coral reefs, which serve to protect coastal and island integrity. With more than 40% of the world's population living near coastlines, it is imperative that we find novel approaches to address this mounting threat.

The Maldives has faced continued environmental challenges throughout its 2500 year history. The development of the Maldives is very much based on the ecosystem that surrounds it. Studies indicate that 89% of GDP depends on biodiversity (Das, 2010), mainly the marine ecosystems (coral reefs) which are at their thresholds due to the impacts of climate change. Out of the 200 inhabited islands around 85% are directly impacted by erosion. Some islands have even lost large percentages of their land due to erosion. On the other hand, there has been an increase of human-induced dredging and expanding of islands which applies further strain on the already

weak coral reef ecosystems. These factors are creating an extremely fragile situation for the human, economic and environmental sustainability of the Maldives.

Our research explores the relationship between the natural forces of the ocean and the formation of sand morphologies, aiming to promote the accumulation of sand in targeted locations. Our hypothesis is that strategically placed submersible objects with specific geometries sitting on the ocean floor, much like a moveable artificial reef or other geomorphic feature, can influence and guide sediment transport to help grow beaches or islands. We have conducted a series of lab experiments and full-scale field experiments to test this hypothesis and understand the most successful geometries and specific parameters for guiding sand accumulation. Our field experiments aim to test the effectiveness of our submersible geosynthetic bladders in accumulating sand with real world conditions. The lab experiments attempt to understand the dynamics of the sediment transport in a controlled environment by simulating the forces and material characteristics.

Our aim for this research is to develop a scientific understanding of sediment transport in the Maldives with our underwater geotextile structures and test our hypothesis for sand accumulation. Additionally, we are aiming to develop a working model through lab and field experiments which can eventually be scaled to provide an environmentally sustainable approach to mitigate erosion and sinking islands. Our latest field experiment is showing early promising results with hundreds of cubic meters of sand accumulation in a targeted area over the course of several months. We hope to eventually expand this research to other island nations and coastal regions to understand the dependent regional dynamics and independent scalable parameters of our system.

BACKGROUND

It has long been understood by the Maldivian communities that their islands shift, grow and move over the course of the year. An island can grow by many meters on one side during one monsoon season, and then shift to the other side of the island in the opposite season. Leading researchers, such as Paul Kench, have documented this phenomenon in a number of noteworthy publications, showing that many Maldivian islands have actually grown in size even while sea levels have increased dramatically in the past decades (Kench, et al., 2014, 2015, 2018). This unique finding argues that these coral-based islands can be extremely active and may continue to shift with the increasing dynamics of climate change. It does not guarantee their survival, however, because the islands are built from coral; with ocean temperatures rising, the coral is bleaching and dying, thereby decreasing the production of sand and limiting the size of the island. Thus, it is imperative that we understand how to utilize the potentially scarce resource of sand by helping to transport and guide its accumulation in strategic areas.

Historically, Maldivians have been attempting to mitigate erosion through a variety of techniques (Shakir, 2015). One approach includes growing vegetation in coastal regions of the island with large palm trees or native plants. This is a practice that provides a longer term solution and is very effective as the root system stabilizes the sand to prevent displacement. However, as we are now faced with the impacts of unpredictable and increasing frequency of severe weather, the long time frame for plant growth is likely not viable as a single solution. Another approach is

to build groins with locally sourced material such as dead coral or rocks from the ocean which are placed in long strips perpendicular to the beach. The goal is to reduce longshore drift and trap sand that shifts around the islands, preventing the eroding sand from dispersing. Since this is a static approach, with the dynamic forces of the environment, the groins often deteriorate and need to be replaced over time. This sometimes can be an effective method to mitigate existing sand erosion, however, is not a solution to help increase sand accumulation. An alternative traditional approach was to identify shallow areas of the lagoon which can be easily reclaimed to artificially create more land mass. Prior to modern engineering solutions, locals would collect boulders and coral and create a perimeter extending from the original land mass, surrounding the shallow lagoon region. Afterwards, they would fill in this perimeter with a mix of debris, garbage and sand. Then the locals would collect beach sand from the lagoon in coconut fiber bags or buckets and cover the reclaimed region to make it look like a seamless extension of the existing island. However, this could only be done in shallow regions of the lagoon because it relies on the manual forming of sand with debris. The scalability of this approach is limited.

There has been a wide range of engineered solutions attempted more recently to fight beach erosion, longshore drift and flooding (the results of storm surges and sea level rise). The most typical engineered approaches include fixed infrastructural systems like dykes, jetties, sea walls, tetrapod walls and geotextile breakwaters. Soft approaches include sand dunes, beach nourishment and dredging (Pilkey et al., 2012). Technologically innovative solutions have been proposed like artificial seaweed networks, tidal power generators or chemical sand additives (Linham et al., 2012). Similarly, a recent approach developed in the Netherlands, the Sand Engine, is attempting to guide the accumulation of sand by first dredging and placing sand in one location then letting the natural currents of the water to redistribute it (Speybroeck, 2006). However, this method still relies on dredging and does not promote the accumulation of new sand. Rather, it moves artificially placed volumes of sand.

Simultaneously, material developments over the past several decades have led to new approaches for erosion mitigation technologies that go beyond hard rock walls and concrete barriers. Synthetic geotextiles, for example, were first developed in the early 1950s but did not come into widespread use until the late 1970s and early 1980s. The most common products during this time were non-woven geotextiles with tensile strength in the 20 to 40 kN/m range. By the 1980s industrial textile weaving and fiber extrusion equipment was developed that had the capability to produce high strength woven polypropylene geotextile products that could reach uniaxial strengths of 100 kN/m. By the mid 1990s textile innovations made possible the production of geotextiles that could achieve biaxial strengths upwards of 200 kN/m. Accompanying these critical advances, geotextile fabrication using seaming reached a level of refinement such that seam strengths exceeded 50% of the textile strength.

Recent geotextiles advances have focused on survivability from UV exposure, impact, and abrasion resistance (Stephens, 2019, Timpson, 2018). The most recent geotextiles are composites, combining the woven geotextile substrates and cover layers of course fibers that entrap sand and sediments, and help establish vegetation for installations above the water level while encouraging marine organism attachment for underwater bladders. Also, fabrication techniques, materials, and equipment have improved such that seaming can reach 80% of the geotextile’s tensile strength.

Given these recent advances in material capabilities as well as new approaches to soft engineered solutions for coastal erosion, it is increasingly clear that we need an adaptable solution that works with the dynamic forces of the environment rather than one which fights or harms marine ecosystems. In the Maldives, this is increasingly important due to their two predominant monsoon seasons oriented from northeast and southwest, creating forces that cycle in opposite directions at different times of year. Using an adaptable approach, we aim to minimize the impact on the environment surrounding our solution without placing permanent engineered structures that degrade or damage the ecosystem. Nor does our solution rely on continually dredging material to artificially build beaches. Our approach combines the benefits of soft engineered systems and natural geomorphology like sand dunes with innovations in geotextile structures. Taking the form of a submerged geotextile bladder, our solution allows for movement, adjustment and continual system monitoring.

Together with our collaborators in the Maldives, we have analyzed, designed, tested and deployed a series of submersible geotextile bladders that have been shown to promote sand accumulation in targeted areas simply as a result of their geometry, orientation and material resilience over time. By harnessing wave forces to guide the accumulation of sand in strategic locations, and adapting the placement of the devices to seasonal changes or storm direction, our approach aims to naturally and sustainably reshape sand bathymetry using the forces of nature. In the long-term, we aim to better understand sediment transport dynamics to be able to scale our approach to other regions, helping to rebuild and stabilize heavily-populated coastlines and other vulnerable island nations.

METHODS

Two types of experiments were performed to inform geotextile design decisions and assess the effectiveness of submersible geotextile bladders: Tank Experiments in a laboratory setting and Field Experiments in the Maldives. The laboratory tank experiments were performed before the field experiments and informed the setup of subsequent field experiments. A controlled laboratory setting allowed testing to be accelerated compared to slower and more complex field experiments. A laboratory environment also allowed for the isolation of conditions for the purpose of studying sediment transport behavior with fewer environmental variables.

The full-scale field experiments allowed our research to move from idealized lab conditions into the real world. The field experiments also informed transportation and deployment strategies, material properties, as well as data and environmental observations affecting the bladders. In the latest field experiment, the geotextile bladders were left on site for a prolonged period of time allowing for long term recording of data and observations of sand accumulation over a number of seasons.

LABORATORY TANK EXPERIMENT

As a first step, a scaled sample beach was recreated and contained in a 1.82 m table top wave tank. In this series of tests, the goal was to rapidly generate iterations of geotextile bladder geometries in order to glean patterns and visual results while building an intuition for sediment transport behavior. A ramp-like geometry was selected as the most effective form for producing sand

accumulation after hundreds of wave tank experiments exploring a wide range of shapes and strategies. The selected tests described in this paper focus on the ramp geometry series which directly informed the next phase of testing on site in February 2019. This series of tests focused on the ramp angle as its major variable while the test results were compared based on the sand movement and the height of accumulation.

This phase of lab testing focused on producing rapid and accelerated conditions compared to those found on-site while undergoing condensed experiment run times of 20 minutes. A Universal Robot arm with a sculpted foam paddle was used to produce patterned wave movement. The paddle was accelerated toward the ramp, and then decelerated and stopped after travelling 15cm. The paddle then returns to its starting position. This process represents one period, lasting 1.5 seconds, and is repeated throughout the duration of the test. Using this method, we were able to produce desired wavelengths and wave height with pre-programmed repetitive movements. Height ratios from 1:3 to 2:3 were used as the volume of sand to water within the tank. The height of water within the tank was always fixed at 7.62 cm, measured from the bottom of the tank, in order to submerge the tested geometry. The sediment bed gradually sloped upwards towards the far side of the tank to simulate a beach condition.

In this experiment, the tested geometry is placed at the center of the glass tank. The lower end of the ramp geometry faces towards the wave paddle to receive the movement of water and sediment while the higher end of the ramp geometry faces towards the beach. A consistent wavelength and wave height are produced for the duration of the testing period of 20 minutes while results are observed from side and top views and analyzed via video documentation. Sediment retention observations, accumulated sediment depth, and associated times are recorded. Figure 1 shows the typical test setup.

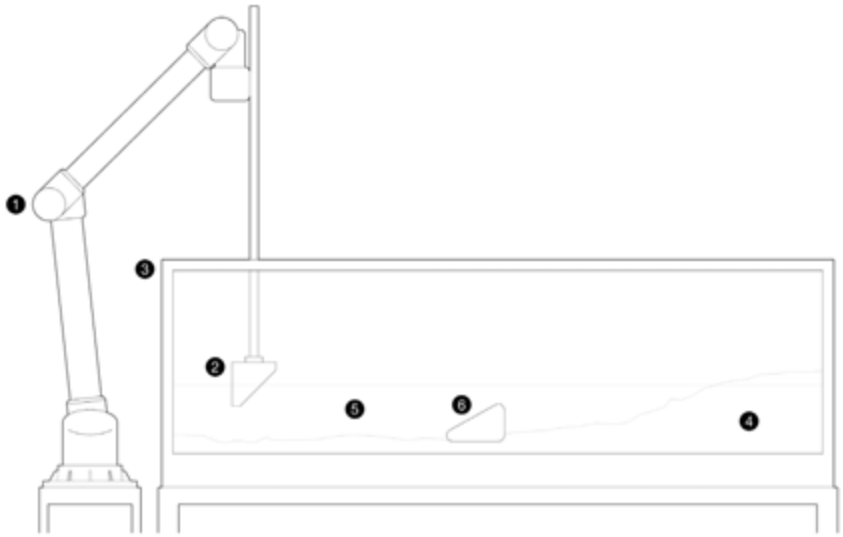

Fig 1. Typical test setup including a UR arm (1) to the left with paddle attachment (2). The wave tank (3) is shown with sand (4) and water (5). Wedge geometry (6) located in center of tank.

Tank Experiment: Results. Table 1 summarizes the results of the ramp geometry experiments. The wedge with a ramp angle of 20° produced sand accumulation of 5.91 cm. The wedge with angle 50° produced an accumulation of 2.29 cm, and the double wedge of the same angle produced an accumulation of 2.54 cm. The two halves of the double wedge, when placed next to one another, were equal in width to the single 50° wedge.

The wedge shape with an angle close to 20° produced the most substantial accumulation of sand in the given timeframe. However, the double wedge demonstrated a potentially effective method of increasing deployability in the field by splitting the wedge into two pieces. There was no observed disadvantage to this design decision; in fact, a slightly larger amount of accumulated sand was observed when the wedge was split in two.

Refer	Ramp Angle	Sand Accumulation Height
Fig 2.	20°	5.91 cm
Fig 3.	50°	2.29 cm
Fig 4.	50° (double wedge)	2.54 cm

Table 1. Tested Geometry and Produced Results

Fig 2. Profile view of 20° bladder geometry with change of 5.91 cm over 20 mins.

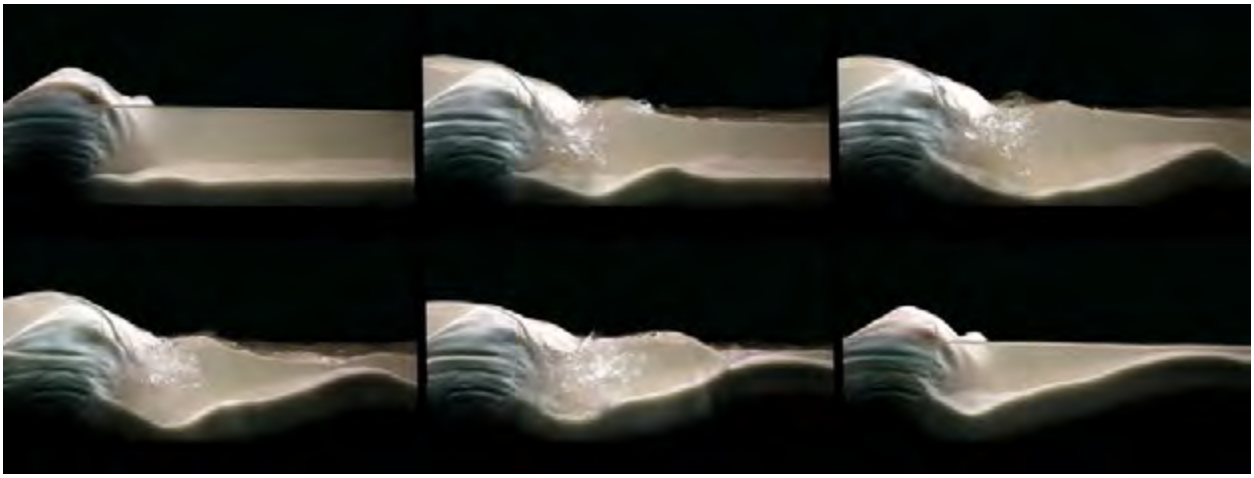

Fig 3. Profile view of 50° bladder geometry with change of 2.29 cm over 20 mins.

Fig 4. Profile view of 50° double wedge bladder geometry, change of 2.54 cm over 20 mins.

FIELD EXPERIMENTS

Field Experiment 1. The first field experiment was conducted in February 2019. Two bladders were fabricated at MIT and installed in the Maldives. A shallow reef flat lagoon in the Maldives was selected as the site due to its ease of accessibility. The specific location within the lagoon was selected due to the consistent water depth of 1-2m which could accommodate the fabricated bladder height of 2m. The MIT team fabricated two bladders with dimensions of 3m × 2m × 2m from heavy canvas material. The angle of the ramp was fabricated at 33.69 degrees. This angle was selected to fall between the two laboratory tests and could accommodate the amount of available material to produce a 2m tall bladder. The bladders were flat-packed and transported to the site. Figure 5 depicts the procedures for producing, packing and deploying the bladder in the field.

The first field test required an excavator to fill the geotextile bladders with sand, forming two 3m × 2m × 2m ramp geometries which were then placed side by side in the water. They were oriented such that the lower end of the ramp geometry was facing east and the higher end was facing west. This orientation was selected due to the predominant wave and current forces moving from east to west in this particular location during the targeted monsoon season.

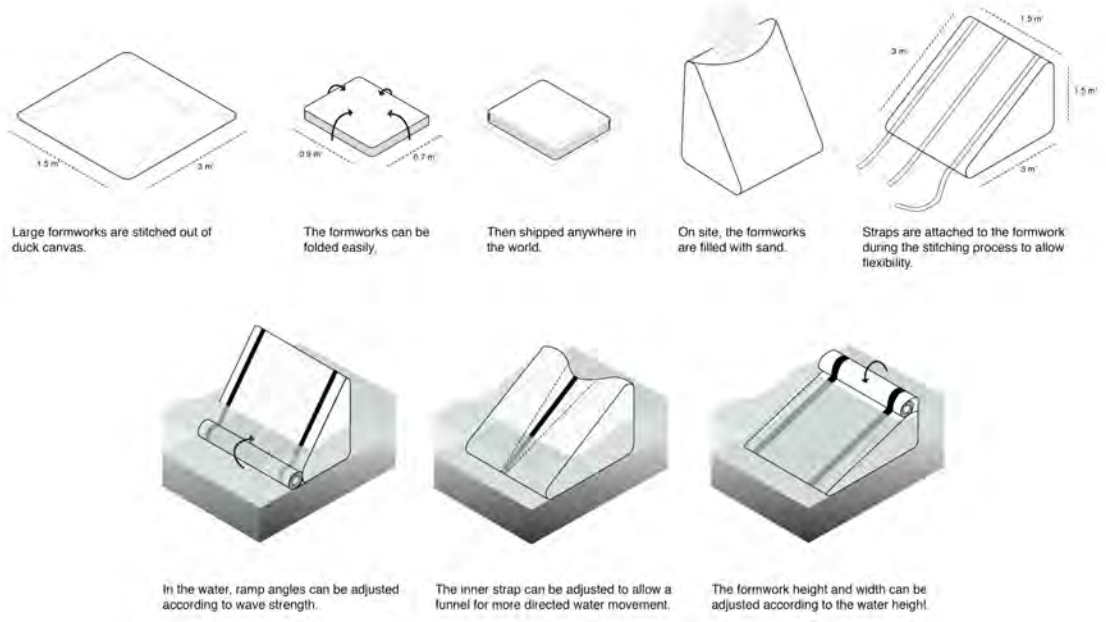

Fig 5. Diagram illustrating deployment of the 1st field experiment from a flat-pack geotextile bladder.

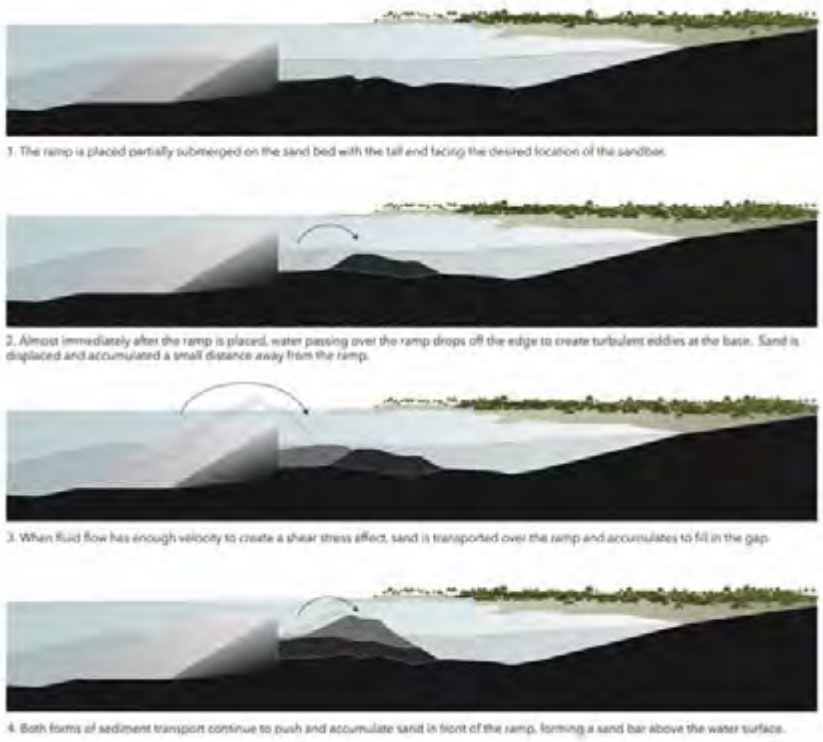

Fig 6. Resultant sand accumulation after placement of a wedge-shaped body.

Field Experiment 1: Results. This initial field installation was installed in February and lasted roughly one-month due to degradation of the bladder's biodegradable canvas material. We had intended for the material to be biodegradable yet it dissolved much more quickly than anticipated. In addition to the material degradation, the monsoon season shifted in March/April switching the predominant wave and current directions from northeast to southwest. Initially the results from this field experiment looked promising after only a few days, however, we did not record any accumulation data given the short timeframe of the experiment. Even though this field experiment did not lead to clear results in terms of sand accumulation, the learnings from this test led to substantial changes in the next field experiment, focusing our development on the geotextile bladder material and a longer deployment that could be studied over many months or years.

Fig 7. Field Experiment 1: aerial photo of installed bladders on site with a change over 3 days.

Field Experiment 2. The second field experiment was conducted in October 2019. It was focused on the geotextile material and two large-scale bladders (10m × 4m × 2m each) with longer deployment on-site. The triangular prismatic bladders were fabricated by Tencate and maintained a similar geometry to the previous field experiments and lab experiments. The field experiment was installed in the Maldives in a similar location as the second field experiment within the shallow reef flat lagoon with water depths measuring 1-2m.

For this field experiment, we used a sand pump on the end of an excavator to fill the geotextile bladders. Given the large bladder sizes, the previous method of filling the bladders was not possible and therefore the sand pump was selected as the most efficient method. First, the geotextile bladders were delivered to site and unrolled, then placed in the water. Vertical poles were placed within the sand and the unfilled geotextile bladder was placed in the water and secured to the poles. The sand pump was then inserted into openings in the bladder and a sand/water mix was pumped into the bladders. The water is able to move through the geotextile membrane while the sand is tramped within the geometry, thus, filling the bladder completely. The bladders were oriented such that the lower end of the ramp geometry was facing east and the higher end was facing west. This orientation was selected due to the predominant wave and current forces moving from east to west in this particular location during the targeted monsoon season.

Satellite images were collected periodically and analyzed to glean a 2-dimensional indication of the patterns of accumulation in relation to time.

Fig 8. Field Experiment 2: aerial photo of one installed bladder.

Field Experiment 2: Results. Over the subsequent 4 months from installation, there were approximately 0.5m of new sediment accumulation over an area of approximately 20m × 30m. This is ~ 300m^3 of new sand over an area of 600m^2. By inspecting satellite images in between this period, a "v-shape" formation can be found with significant sediment accumulation occurring at the tall edge of the bladder and trailing in the direction of sediment movement. A shallow sediment trough can be found in between the horns of sand accumulation. On the two sides of the sediment area there is a fairly steep incline from the ocean floor to the top of the accumulation zone. Two areas of scouring were observed behind the two short ends of the bladder. The physical measurements of sand accumulation were taken using GPS coordinates and a measuring stick recording the height of the sand while factoring in the changes in the water level due to the tides. These early results show a substantial amount of sand accumulation within a short time frame within our targeted zone. Following the 4 month timeframe of the measurements we have continued to monitor this area with satellite images and are seeing what appears to be a continual growth of the sand accumulation zone in the x and y directions. However, further physical dimensions have not yet been recorded due to travel restrictions during the COVID-19 pandemic.

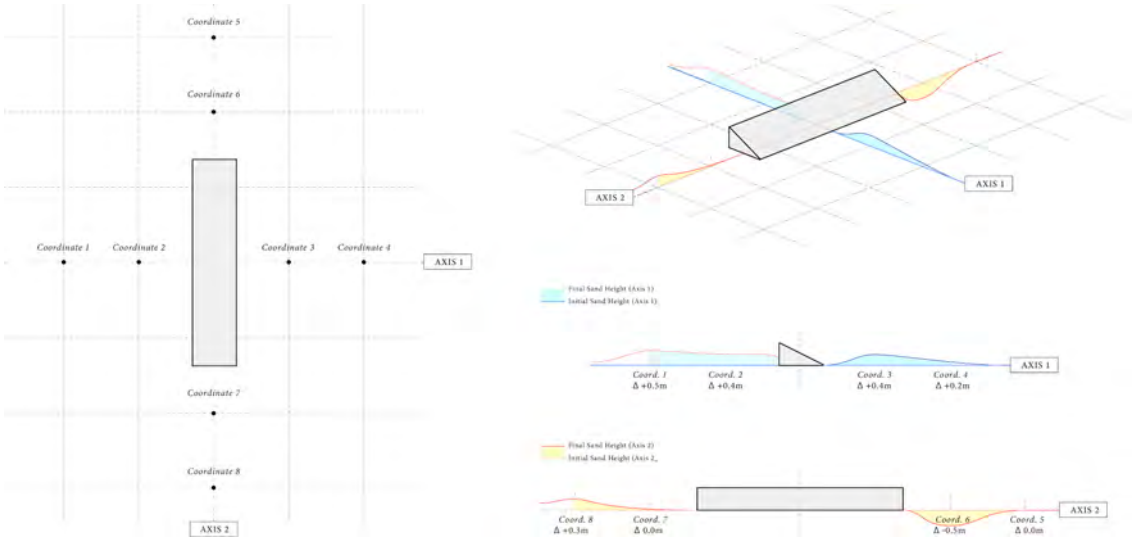

Fig 9. Pole Coordinates and Sediment Accumulation Change. Top to bottom: Plan view of bladder, long side view of bladder, profile view of bladder.

Fig 10. Aerial photos of the bladder over 4 months showing accumulated sediment change.

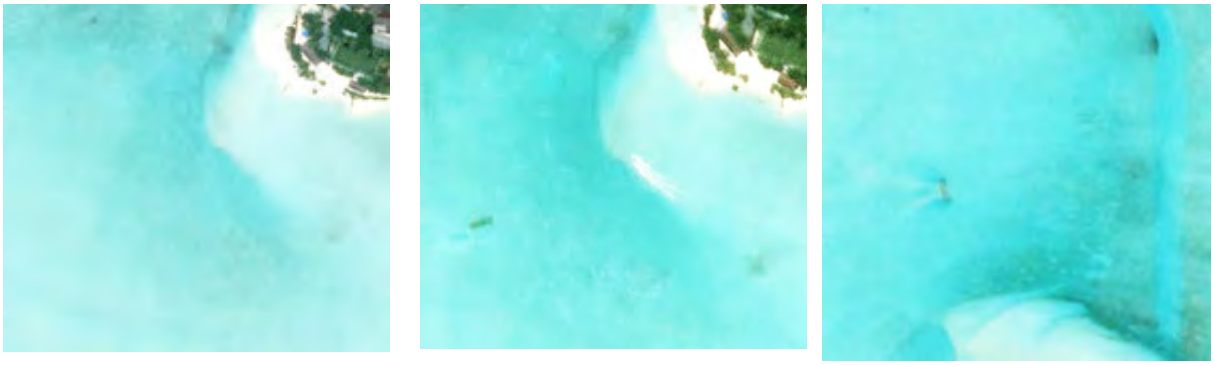

September 19, 2019 (before) October 23, 2019 (install) March 11, 2020

Fig 11. SkySat satellite imagery.

DISCUSSION

We are seeing early signs of success in our field studies and tank experiments, however, we acknowledge there is a substantial amount of work to be done and challenges to overcome in the future. The specific location that we are studying is only one small area within the larger atoll and the even larger Maldives context. It is not yet clear how our results and our approach would translate to other locations within the Maldives or other island nations.

To further understand the dominant forces and important variables in promoting sand accumulation, we have begun to build simple computational models that bridge the lab and field experimental results. Our initial models are built using Computational Fluid Dynamics simulation frameworks (Weymoth, 2015), and begin to model our empirical observations from the tank and field experiments. This work points towards a simple, yet effective method for using natural ocean forces to promote sand accumulation based on geotextile bladders. As we develop these simulations in tandem with continued testing in the field, we aim to be able to finely tune the design of the geotextile bladders' shape and material composition.

Further research aspires to explore other field locations to provide a quantitative understanding of the accumulation results in differing environmental contexts. Although our research aims at a sustainable approach that reduces the environmental impact, energy usage and harmful effects to the local environment, further studies need to be conducted to understand the longer term impact of our work on the local and regional ecosystem. We are hopeful that our mindful, adaptive and soft-engineering approach to this problem will reduce or eliminate any negative impacts on the marine environment.

The research that we have conducted to date uses geotextile bladders that are relatively easy to fill and place underwater. However, in our next field experiments we are looking to further advance our light footprint and adaptability goals by exploring movable and buoyancy-controlled systems that can be reoriented or completely removed in order to adjust to varying seasons and ocean dynamics. We also acknowledge that substantial development needs to be conducted to ensure scalability. To do this, we are aiming to reduce the material usage, manufacturing time and installation complexity to ensure that larger field experiments can be scaled and easily deployed.

CONCLUSIONS

The research presented in this paper proposes a new approach for promoting sand accumulation in targeted locations through simple and adaptable geotextile geometries submerged in a shallow lagoon. We have tested this approach through laboratory experiments and full-scale field experiments in the Maldives. Through our lab experiments we have tested idealized conditions of wave dynamics with various bladder geometries to maximize the morphological change through sand accumulation. These studies lead to two different field experiments with meter-scale geotextile bladders manufactured and installed in a shallow reef flat lagoon in the Maldives. Through physical measurements, drone footage and high-resolution satellite imagery we have monitored the accumulation of sand over the course of several months. We have seen hundreds of cubic meters of sand accumulation in an area cover 20m $\times$ 30m offering early, yet promising results.

Our research attempts to translate natural destruction into natural construction. Our approach is looking to the forces of nature to help guide and accumulate sand rather than try to resist or block the ocean. If our research is successful in the long-term, we believe this method could provide one step towards a sustainable outlook for island nations and coastal regions through this adaptable method of targeted sand accumulation.

REFERENCES

Andrew, J. & Cooper, Andrew & Pilkey, Orrin. 2012. Pitfalls of Shoreline Stabilization: Selected Case Studies. Pitfalls of Shoreline Stabilization: Selected Case Studies, by J. Andrew, G. Cooper, and Orrin H. Pilkey. Coastal Research Library, Vol. 3. Berlin: Springer Verlag, 2012.

Das, P. K.. 2010. "Climate Change and Education: Maldives". UKaid, Department for International Development. https://www.unisdr.org/files/16354_climatechangeedmaldives.pdf

Erftemeijer, Paul & Riegl, Bernhard & Hoeksema, Bert & Todd, Peter. 2012. Environmental impacts of dredging and other sediment disturbances on corals: A review. Marine pollution bulletin. 64. 1737-65. 10.1016/j.marpolbul.2012.05.008.

Kench, P. S., Ford, M. R., & Owen, S. D. 2018. Patterns of island change and persistence offer alternate adaptation pathways for atoll nations. Nature communications, 9(1)10.1038/s41467-018-02954-1

Kench, P. S., Thompson, D., Ford, M. R., Ogawa, H., & McLean, R. F. 2015. Coral islands defy sea-level rise over the past century: Records from a central Pacific atoll. Geology, 43 (6), 515-518. 10.1130/G36555.1

Kench, P. S., Owen, S. D., & Ford, M. R. 2014. Evidence for Coral Island Formation During Rising Sea Level in the Central Pacific Ocean. Geophysical Research Letters 10.1002/2013GL059000

Kench, P.S., R.F. McLean, S.D. Owen, M. Tuck, and M.R. Ford. 2018. "Storm-Deposited Coral Blocks: A Mechanism of Island Genesis, Tutaga Island, Funafuti Atoll, Tuvalu." *Geology* 46 (10): 915–18. https://doi.org/10.1130/G45045.1.

Linham, Matthew M., and Robert J. Nicholls. 2012. "Adaptation Technologies for Coastal Erosion and Flooding: A Review." *Proceedings of the Institution of Civil Engineers - Maritime Engineering* 165 (3): 95–112. https://doi.org/10.1680/maen.2011.29.

Pilkey, Orrin H., and J. Andrew G. Cooper. 2012. "'Alternative' Shoreline Erosion Control Devices: A Review." In *Pitfalls of Shoreline Stabilization*, edited by J. Andrew G. Cooper and Orrin H. Pilkey, 3:187–214. Coastal Research Library. Dordrecht: Springer Netherlands. https://doi.org/10.1007/978-94-007-4123-2_12.

Rankey, Eugene C., Bernhard Riegl, and Kelley Steffen. 2006. “Form, Function and Feedbacks in a Tidally Dominated Ooid Shoal, Bahamas.” *Sedimentology* 53 (6): 1191–1210. https://doi.org/10.1111/j.1365-3091.2006.00807.x.

Shakir, Kashima Ahmed. 2015. “Memories of Umar Zahir’s Services”. Umar Zahir.

Shin, E. C., and Y. I. Oh. 2007. “Coastal Erosion Prevention by Geotextile Tube Technology.” *Geotextiles and Geomembranes*, Special Issue on Tsunami Reconstruction with Geosynthetic Containment Systems, 25 (4): 264–77. https://doi.org/10.1016/j.geotexmem.2007.02.003.

Speybroeck, J., Bonte, D., Courtens, W., Gheskiere, T., Grootaert, P., Maelfait, J.-P., Mathys, M., Provoost, S., Sabbe, K., Stienen, E.W., Lancker, V.V., Vincx, M. and Degraer, S. (2006), Beach nourishment: an ecologically sound coastal defence alternative? A review. Aquatic Conserv: Mar. Freshw. Ecosyst., 16: 419-435. doi:10.1002/aqc.733

Stephens, T. (2019), Sand Filled Geotextile Mattress Installed to Recover and Protect a Critical Section of Waikiki Beach. Geosynthetics 2019 Conference Proceedings, vol. 1. ISBN: 978-1-5108-9352-8

Stephens, T., Ruiz, N. (2019), Innovative Technology Saves 100-Year-Old Panama Canal Locks. Smart Rivers 2019 Conference Proceedings.

Timpson, C., Stephens, T. (2018), Beach Development and Protection of Resort Coastline using Geotextile Tubes. Dredging Summit 2018 Conference Proceedings.

Trower, Elizabeth J., Marjorie D. Cantine, Maya L. Gomes, John P. Grotzinger, Andrew H. Knoll, Michael P. Lamb, Usha Lingappa, et al. 2018. “Active Ooid Growth Driven By Sediment Transport in a High-Energy Shoal, Little Ambergris Cay, Turks and Caicos Islands.” *Journal of Sedimentary Research* 88 (9): 1132–51. https://doi.org/10.2110/jsr.2018.59.

Weymouth, Gabriel D. 2015. “Lily Pad: Towards Real-Time Interactive Computational Fluid Dynamics.” *ArXiv:1510.06886 [Physics]*, October. http://arxiv.org/abs/1510.06886.

Geosynthetics Conference

Performance of Fiber-Reinforced Bio-Bricks against Water Erosion

Shihui Liu,[1] Ph.D., and Lin Li, Ph.D., P.E., F.ASCE[2]

[1]Department of Civil and Architectural Engineering, Tennessee State University, Nashville, TN 37209, e-mail: sliu1@tnstate.edu
[2]Department of Civil and Architectural Engineering, Tennessee State University, Nashville, TN 37209, e-mail: lli1@tnstate.edu

ABSTRACT

Microbial induced calcium carbonate precipitation (MICP) is one of promising technology to improve engineering properties of sandy soil. Bio-bricks through the MICP technique have been developed as one of innovative building materials. There is very limit study of bio-bricks again water erosion during their long-term durability study. This paper is to investigate the resistance of fiber-reinforced bio-bricks again water erosion. The reinforcing effects of synthetic fibers on properties of MICP-treated bio-bricks were investigated. Experimental results showed a significant improvement in the performance of bio-bricks could be achieved through fiber reinforcement. The flexure strength of bio-bricks reinforced by 0.3% synthetic fibers increased from 1185 kPa to 1210 kPa. The inclusion of 0.3% of synthetic fibers in the bio-bricks would increase the resistance of bio-bricks against accelerated erosion.

INTRODUCTION

Microbial induced calcite precipitation (MICP) is a promising technology to improve soil engineering properties. Calcite precipitation act as an agent of cohesion which can bond sand grains together and improve the engineering properties of sand (DeJong et al. 2006). As new building materials, bio-bricks through the MICP technique using the immersing method were developed by Bu et al. (2018). They found that the flexure strength of MICP-treated bio-bricks was similar to that of 20-25% cement-treated sand bricks. The brick compressive strength of bio-bricks was similar to that of 30% lime-treated bricks. They also reported that the precipitated $CaCO_3$ was distributed uniformly in the brick samples prepared by the immersing MICP method. However, study of bio-bricks against water erosion is limited.

Reinforced soils with synthetic polypropylene fiber can help to enhance the soil properties. Li et al. (2015) investigated the effect of randomly distributed synthetic polypropylene fiber on the mechanical properties of MICP-treated soil. They found that the shear strength, ductility, and failure strain were improved remarkably with fiber addition, and the optimum fiber content was 0.2-0.3% by weight of dry sand. The goal of this paper is to use synthetic fiber reinforcement to enhance the erosion resistance of bio-bricks. To demonstrate the erosion resistance of MICP-treated bio-bricks and investigate the enhancement with fiber reinforcement, flexure behavior and resistance against accelerated erosion were studied.

MATERIALS AND METHODS

Materials

Ottawa sand (99.7% quartz) was used in the experiments. The sand is uniformly with a median particle size of 0.46 mm. It was classified as poorly graded sand based on the Unified Soil Classified System.

Fibermesh 150 synthetic fiber (see Figure 1) was used as reinforcement additions in the soil, and the same fiber was used by Li et al. (2015). This fiber is 100% homo-polymer polypropylene multifilament fiber and it is a very light material with a specific gravity (G_s) of 0.91. It is chemically inert and has uniform characteristics. The length of the fibers was 12 mm.

Figure 1. Fibermesh 150 synthetic fiber

Sporosarcina pasteurii (ATCC 11859) was used in this study. The growth media (ATCC 1376) is constituted by following per liter of deionized water: (1) 0.13 M tris buffer (pH = 9.0), (2) 10 g $(NH_4)_2SO_4$, and (3) 20 g yeast extract. The bacteria and growth media were centrifuged at 4,000 g for 20 min after incubating aerobically at 30^0C in a shaker at 200 revolutions /min overnight. Then supernatant was removed and replaced with fresh growth media before the bacteria was resuspended every time. The bacteria were grown for 24–28 h to an optical density (OD) of 600 nm (OD_{600}) of 0.3–1.5 (Al Qabany et al. 2011). The bacteria concentration was controlled by measuring absorbance (optical density) of the suspension using a spectrophotometer (Genesys 20, Thermo Scientific) at 600-nm wavelength. Higher OD_{600} value means higher bacteria growth and more calcite precipitation and properties improvement may be resulted. The OD_{600} of bacteria solution in this study was kept as 0.6, and the urease activity of bacteria solution was 3.31 mM hydrolyzed urea/min.

Cementation medium provided chemical compositions for ureolysis in the MICP process, including urea, $CaCl_2 \cdot 2H_2O$, NH_4Cl, $NaHCO_3$, and nutrient broth (Mortensen et al. 2011). The chemical concentration of cementation media in this paper was kept constant as 0.5M Ca. The chemical compositions were 10.0 g/L NH_4Cl, 3 g/L nutrient broth, 2.12 g/L $NaHCO_3$, 30 g/L urea, and 73.5 g/L $CaCl_2 \cdot 2H_2O$ with urea-Ca^{2+} molar ratio of 1:1.

MICP Samples Preparation Method

MICP process was conducted in a batch tank reactor using the immersing method. The reactor shown in Figure 2a included a plastic box to contain samples, cementation media, sample supported shelf, and air pumps to provide oxygen for bacteria. For non-reinforced bio-bricks, the uniform mixture of 900 g sand and 250 mL bacteria solution was compacted into the rigid full contact mold. The rigid full contact mold (see Figure 2b) used in this study was consist of a flexible layer and rigid holder. The flexible layer was made of geotextile which is fully permeable. The geotextile was a polypropylene, staple-fiber, needle-punched nonwoven material

with grab tensile strength of 1700 kN, a thickness of 1.5 mm and opening size of 0.15 mm; water flow rate of 34 mm/s; and unit mass of 200 g/m^2. The rigid holder was made by polypropylene perforated sheet with 6.35 mm thickness. The sheet had 6.35 mm diameter staggered holes and the clearance distance between hole and hole was 9.53 mm. The rigid holder was assembled with different pieces of polypropylene perforated sheet with different sizes by plastic screw rods and nuts. The holder size can be varied to prepare different sample sizes, and it is 177.8 mm in length, 76.2 mm in width, and 38.1 mm in height in this study. The flexible layer was laid on the bottom and inside the wall of the rigid holder. The open holes in the rigid mold allowed cementation media flowing through the geotextile. Once the sand was added into the rigid full contact mold, a geotextile layer was covered on the top of the sand sample.

(a) (b)

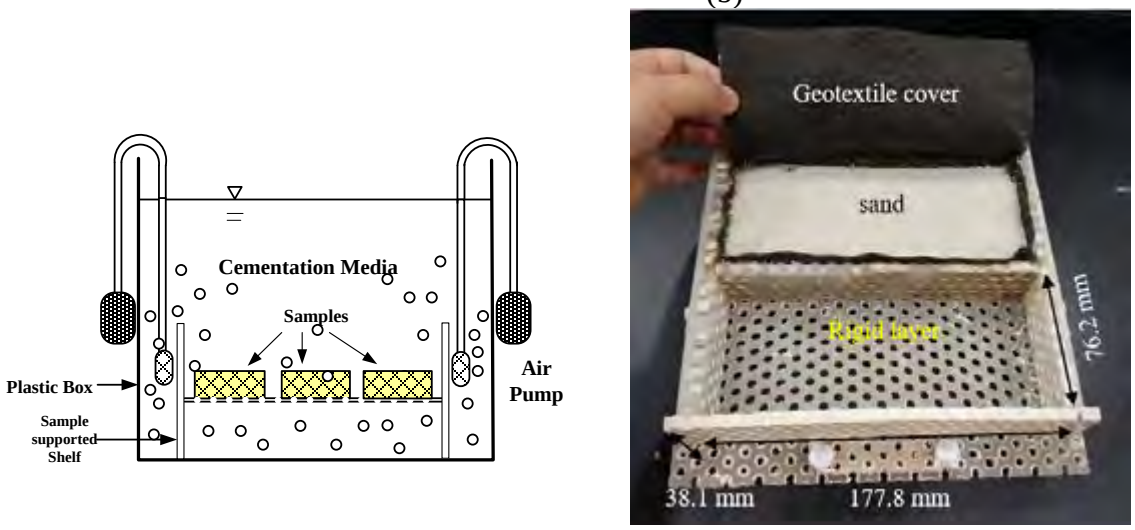

Figure 2. (a) sketch drawing of batch reactor for immersing treatment method, (b) Sample preparation of bio-brick in rigid full contact mold.

For synthetic fiber-reinforced bio-bricks, the proportion of fiber was 0.3% by weight. The synthetic fiber was uniformly mixed with sand then placed in the rigid full contact mold, and 250 mL bacteria solution was added in the sand through geotextile cover. At least four samples were prepared for each case to produce a representative condition. In the single MICP process, the soil samples within the bacteria solution were submerged in the 0.5 M Ca cementation media for 7 days of reaction. All treatments were carried out at the ambient temperature of the laboratory.

Four-Point Bending Testing and Water Erosion Test

The four-point bending tests as shown in Figure 3a were conducted on the bio-bricks to study their flexure behavior. The samples were located on two adjusted supports that were 152.4 mm apart from each other, and the vertical load was applied on top two supports in the middle of the specimen with a 50.8 mm distance. Following the testing method of ASTM D6272, the vertical load was conducted under strain control conditions at a uniform loading rate of 1.5%/min until the beam failed.

The accelerated erosion testing carried out on the bio-bricks was similar to the testing method outlined by Walker (2002). The erosion set up of this study is shown in Figure 3b. A jet of water was sprayed onto the surface of brick at a constant pressure of 200 kPa and a constant distance of 470 mm. The erosion depth was recorded in Fig. 4b at frequent intervals in a 60 min period. The maximum erosion rate of the sample was determined by the following:

$$\text{Maximum erosion rate} = \frac{maximum\ erosion\ depth}{height\ of\ brick} \times 100\% \quad (1)$$

(a) (b)

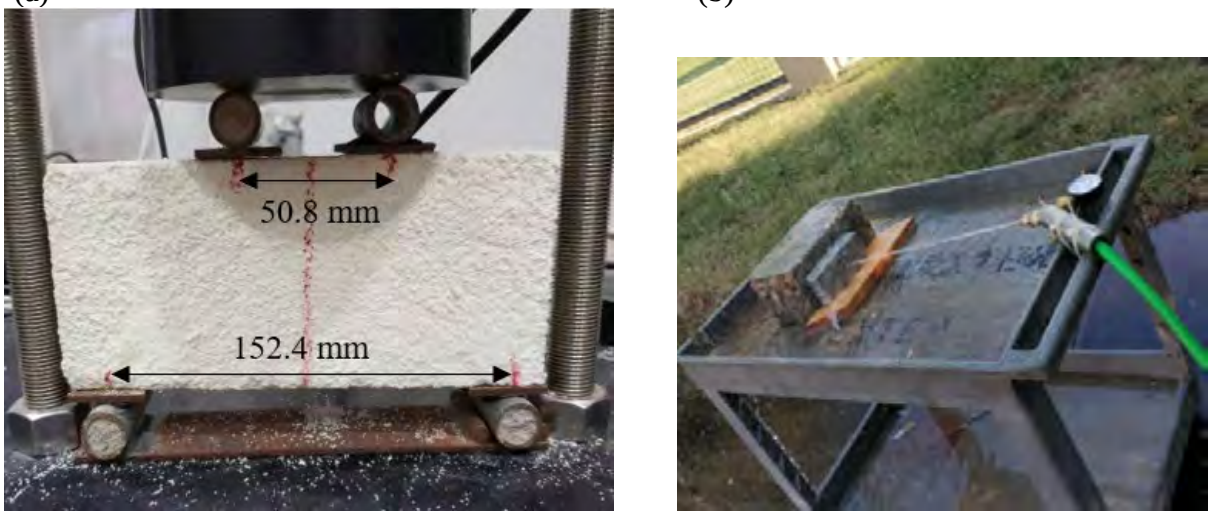

Figure 3 (a) Four point bending testing system; (b) Accelerated erosion set up.

RESULTS AND DISCUSSION

Results of Fibers Addition on Bio-Bricks

The stress-strain curves obtained from four-point bending tests on MICP-treated bio-bricks without fiber, with 0.3% synthetic fiber is shown in Figure 4. Li et al. (2015) and Wen et al. (2018) found that the optimum synthetic fiber content in the reinforcement of bio-specimens was 0.3%. The improvement of the ductility of bio-specimens was significant when 0.3% fiber was added to reinforce the bio-beam. The flexure stress and strain of the MICP-treated samples increased by 105% and 210%, respectively, through 0.3% synthetic fiber addition in bio-bricks. These results indicated that the ductility of bio-bricks was improved significantly by 0.3% synthetic fiber content.

Figure 5 shows the maximum erosion rate of non-reinforced and 0.3% synthetic fiber reinforced bio-bricks under accelerated erosion test. The maximum erosion rate of 0.3% synthetic fiber reinforced bio-bricks was 0.08 mm/min, which was around 51.6% reduction from erosion rate of 0.165 mm/min of non-reinforced bio-bricks. This implied that the inclusion of 0.3% synthetic fibers in the bio-bricks would increase the resistance of bio-bricks against accelerated erosion. Liu et al. (2019) studied the effect of 0.3% synthetic fiber addition on wet-dry cycles of MICP-treated samples. They found that the failure strain of fiber-reinforced samples reached 1.6% compared with non-reinforced samples of 0.4% after 5 wet-dry cycles.

The synthetic fibers prevented the sand particles and calcite crystals from being washed away by water in these erosion set-ups.

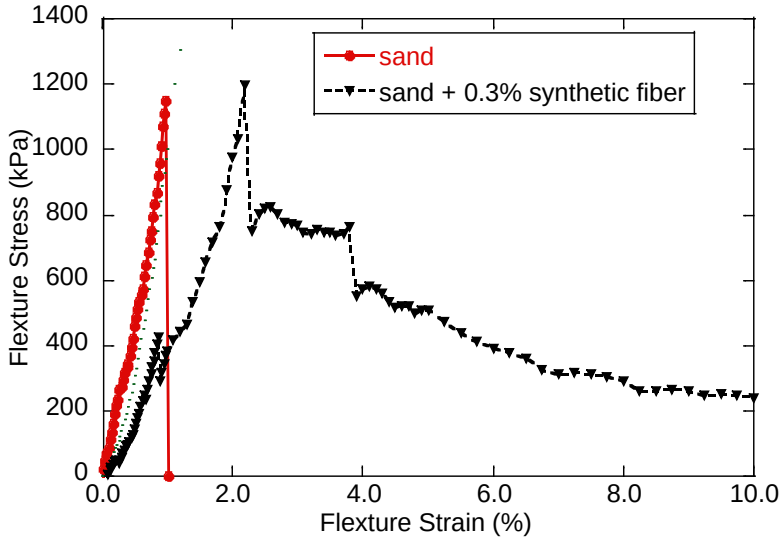

Figure 4 Flexure stress-strain curves for MICP-treated samples

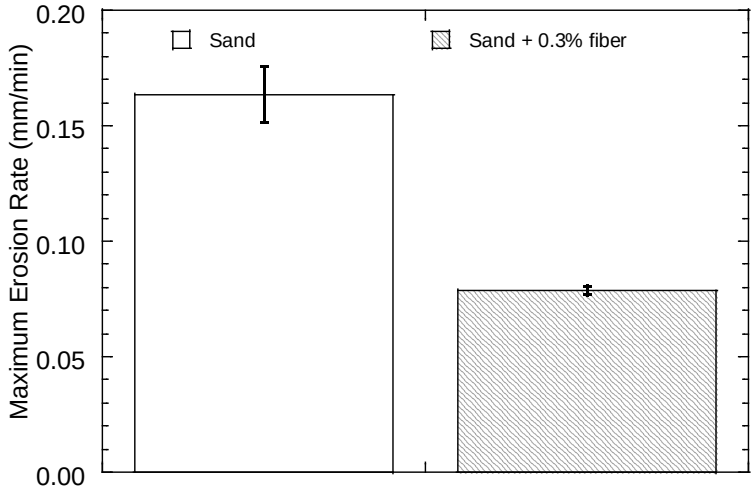

Figure 5 Maximum erosion rate for MICP-treated sample with fibers reinforcement.

CONCLUSION

This paper presents the properties of MICP-treated bio-bricks enhanced with synthetic fibers. The flexure strength of bio-bricks reinforced by 0.3% synthetic fibers increased from 1185 kPa to 1210 kPa. The MICP-treated samples were subjected to erosion with a maximum erosion rate of around 0.165 mm/min during the test of 60 min period. The maximum erosion rate of 0.3% synthetic fiber reinforced bio-bricks was 0.08 mm/min, which was around 51.6% reduction from

erosion rate of 0.165 mm/min of non-reinforced bio-bricks. This implied that the inclusion of 0.3% synthetic fibers in the bio-bricks would increase the resistance of bio-bricks against accelerated erosion.

REFERENCES

Al Qabany, A., Soga, K., Santamarina, C., 2011. Factors affecting efficiency of microbially induced calcite precipitation. J. Geotech. Geoenviron. Eng. 138, 992-1001.

ASTM D6272-17, Standard Test Method for Flexural Properties of Unreinforced and Reinforced Plastics and Electrical Insulating Materials by Four-Point Bending, ASTM International, West Conshohocken, PA, 2017. 10.1520/D6272-17.

DeJong, J. T., Fritzges, M. B., Nüsslein, K., 2006. Microbially induced cementation to control sand response to undrained shear. J. Geotech. Geoenviron. Eng. 132, 1381-1392.

Li, M., Li, L., Ogbonnaya, U., Wen, K., Tian, A., Amini, F., 2015. Influence of fiber addition on mechanical properties of MICP-treated sand. J. Mater. Civ. Eng. 28, 04015166.

Liu S, Wen K, Armwood C, Bu C, Li C, Amini F, Li L. 2019, Enhancement of MICP-Treated Sandy Soils against Environmental Deterioration, Journal of Materials in Civil Engineering. 10.1061/(ASCE)MT.1943-5533.0002959.

Mortensen, B. M., Haber, M. J., DeJong, J. T., Caslake, L. F., & Nelson, D. C. 2011. Effects of environmental factors on microbial induced calcium carbonate precipitation. Journal of applied microbiology, 111(2), 338-349.

Walker, P. 2002. The Australian Earth Building Handbook: HB 195, Standards Australia International Ltd, New South Wales, https://doi.org/10.1016/j.cemconcomp.2018.04.013.

Wen, K., Bu, C., Liu, S., Li, Y., & Li, L. 2018. Experimental investigation of flexure resistance performance of bio-beams reinforced with discrete randomly distributed fiber and bamboo. Construction and Building Materials, 176, 241-249. https://doi.org/10.1016/j.conbuildmat.2018.05.032.

Geosynthetics Conference

Hydraulic Conductivity of Bentonite-Polymer Composite Geosynthetic Clay Liners Permeated with Bauxite Liquor

Jiannan Chen, Ph.D., EIT,[1] Sarah A. Gustitus, Ph.D. Candidate, EIT,[2] and Craig H. Benson, Ph.D., P.E, NAE[3]

[1]Department of Civil, Environmental, and Construction Engineering, University of Central Florida, Orlando, FL 32816; e-mail: jiannan.chen@ucf.edu

[2]School of Engineering, University of Virginia, Charlottesville, VA 22903; e-mail: sgustitus@virginia.edu

[3]School of Engineering, University of Virginia, Charlottesville, VA 22903; e-mail: chbenson@virginia.edu

ABSTRACT

Hydraulic conductivity tests were conducted on bentonite-polymer composite (BPC) geosynthetic clay liners (GCLs) using bauxite liquors obtained from alumina refineries in the US, Australia, Brazil, Saudi Arabia, United Arab Emirates, and China. Bauxite liquors are hyperalkaline (pH > 12), with ionic strength up to 1.5 M. Hydraulic conductivity of the BPC-GCLs to bauxite liquor ranged from 10^{-13} to 10^{-8} m/s, and was often 1 to 5 orders of magnitude lower than the hydraulic conductivity of NaB-GCLs permeated with the same solutions (10^{-9}-10^{-7} m/s). The hydraulic conductivity of BPC-GCLs is affected by the ionic strength of the liquor and the polymer loading in the BPC-GCL. Higher hydraulic conductivity was obtained for bauxite liquors having higher ionic strength. BPC-GCLs with a polymer loading greater than 7.5% as measured by loss on ignition was more likely to have low hydraulic conductivity (< 10^{-10} m/s) to bauxite liquor.

INTRODUCTION

Approximately 275 Tg of bauxite ore is mined each year globally for alumina production, with Australia (33%), China (20%), and Brazil (16%) the leading bauxite producers (Xue et al. 2016, Kishida et al., 2017). Approximately 60 Tg/yr of red mud, a highly alkaline residue from refining bauxite ore to produce aluminum, is generated as a byproduct of alumina refining annually. Most red mud (85%) is stored in impoundments on-site or adjacent to alumina refineries.

Red mud consists primarily of fines (particles < 0.075 mm) and has high alkalinity (Sun et al. 2019). The porewater in red mud is “bauxite liquor,” having high pH (>14 in some cases) and high ionic strength (I >1 M in some cases) due to the NaOH used for the dissolution of alumina. Geosynthetic clay liners (GCLs) are used as liners in red mud disposal facilities (Benson et al. 2010, Athanassopoulos et al. 2015, Tian and Benson 2019), generally in conjunction with a geomembrane in a composite liner (geomembrane directly over a GCL). Hydraulic conductivity (K) of the GCL component in a composite liner has a controlling influence on the effectiveness of the barrier.

The sodium bentonite (NaB) in conventional GCLs is composed primarily of the clay mineral montmorillonite, which swells when hydrated in water to form a gel with very low hydraulic conductivity (Jo et al. 2001, Kolstad et al. 2004, Benson et al. 2010). However, the high pH and ionic strength of bauxite liquor can suppress swelling of the montmorillonite, resulting in

GCLs with much higher hydraulic conductivity (Benson et al. 2010, Chen et al. 2018, Tian and Benson 2019).

Bentonite-polymer composite GCLs (BPC-GCLs) have been developed as alternatives to traditional sodium bentonite GCLs for use with aggressive leachates (Scalia et al. 2011, Tian et al. 2016, Ozhan 2018, Chen et al. 2019, Hosney and Rowe 2019). Some BPC-GCLs have very low hydraulic conductivity to liquids that have extreme pH and/or ionic strength, like bauxite liquors. (Athanassopoulos et al. 2015, Tian and Benson 2019, Sun et al. 2019, Li et al. 2020). Athanassopoulos et al. (2015) evaluated the hydraulic conductivity of NaB and BPC-GCLs to two leachates with high pH: trona ash leachate (pH = 11, I = 1.05 M) and bauxite liquor (pH = 13, I = 2.35 M). The hydraulic conductivity of the BPC-GCL was up to 4 orders of magnitude lower than the hydraulic conductivity of a NaB GCL to the same liquids. Tian and Benson (2019) measured the hydraulic conductivity of a NaB GCL and a BPC-GCL (polymer content = 6.8%) to a bauxite liquor (pH = 13, I = 700 mM) and found that the BPC-GCL had much lower hydraulic conductivity (4.3×10^{-12} m/s) than the NaB GCL (~10^{-7} m/s). The low hydraulic conductivity of the BPC-GCL was attributed to polymer clogging intergranular pores rather than swelling of bentonite. Chen et al. (2019) report similar findings for BPC-GCLs and NaB GCLs permeated with coal combustion product leachates. The BPC-GCLs were much less permeable to the CCP leachates than the NaB GCLs, provided the BPC-GCLs had sufficient polymer loading.

This paper reports on hydraulic conductivity tests conducted with BPC-GCLs on bauxite liquors collected from alumina refineries in the US, Brazil, China, Saudi Arabia, and United Arab Emirates (UAE). Hydration behavior of the NaB and BPC with bauxite liquor was investigated using swell index tests, and the influence of polymer loading on the hydraulic conductivity of BPC-GCLs permeated with bauxite liquor was evaluated.

MATERIALS AND METHODS

Bauxite liquors. Samples of bauxite liquor were obtained from red mud management facilities in the aforementioned countries. These bauxite liquors are labeled: USBL1 and USBL2 (US), BRABL (Brazil), SAUBL (Saudi Arabia), UAEBL (UAE), and CHNBL1 and CHNBL2 (China). The pH, electrical conductivity (EC), and ionic strength of the liquors are summarized in Table 1. The bauxite liquors are hyperalkaline, with pH ranging from 12.0 to 14.2. The ionic strength ranges from 239 to 1546 mM. EC of the bauxite liquor ranges from 1.8 to 16.4 S/m at 25 ^{o}C.

Table 1. Bulk chemical parameters of bauxite liquors.

Bauxite Liquor	USBL1	USBL2	BRABL	SAUBL	UAEBL	CHNBL1	CHNBL2
pH	12.0	12.4	12.9	12.8	14.2	12.4	12.6
EC@25 ^{o}C (S/m)	6.7	8.9	1.8	3.2	16.4	2.63	5.1
Ionic Strength (mM)*	941	1081	129	288	1546	239	620

*Calculated using Visual MINTEQ, charge differences <5%.

Geosynthetic clay liners. One conventional NaB GCL and sixteen BPC-GCLs were evaluated in this study, all of which are commercially available. The BPC-GCLs are manufactured by dry mixing granular proprietary polymers (one or more polymers) with granular sodium bentonite. These BPC-GCLs are labeled as C6.3, C6.4, C6.5, C7.3, C7.5, C7.6, C10.1, C10.8, C12.1, G4.3, G8.1, N3.8, N5.4, N7.3, GE3.0, and O6.5 with the letter designating the supplier and the numerical suffix representing the polymer loading in % dry mass determined based on loss on ignition (LOI) of the BPC and NaB using the procedure in Scalia et al. (2014).

Hydraulic conductivity of GCLs. Hydraulic conductivity of each of the GCLs was measured in flexible-wall permeameters using the falling headwater - constant tailwater method in ASTM D5084 (ASTM 2016) and ASTM D6766 (ASTM 2012). GCL specimens with a diameter of 150 mm were prepared and assembled in flexible-wall permeameters following the procedure in Jo et al. (2001). Bauxite liquor or DI water was used as the permeant solution. The GCLs were hydrated with the permeant solution in the permeameter for 48 h prior to permeation with the cell pressure and headwater applied and the effluent valve closed (no hydraulic gradient). The effective stress was set at 20 kPa. No backpressure was used to prevent geochemical alterations of the permeant liquid.

Permeation continued until the hydraulic conductivity was stable, the flow ratio (ratio of incremental outflow to inflow, Q_{out}/Q_{in}) was within 1.00±0.25, and the pH ratio (pH_{out}/pH_{in}) and EC ratio (EC_{out}/EC_{in}) were 1.00±0.10. Influent of specimens with high hydraulic conductivity ($K > 10^{-8}$ m/s) was spiked with rhodamine WT dye at the end of the test to mark flow paths and to identify if sidewall leakage occurred. If sidewall leakage was identified, the test result was rejected, and a new test was conducted.

Swell Index. The Swell index of bentonite or BPC from each GCL was measured in accordance with ASTM D5890 (ASTM 2011) using bauxite liquors or ASTM Type II DI water as the hydrating liquid. The bentonite (or BPC) was ground with a mortar and pestle to pass the No. 200 US standard sieve (0.075 mm) and oven-dried for 24 hours at 105 ^{o}C. A 100-mL graduated cylinder was filled with 90 mL of the test liquid, and 2 g of ground bentonite was added to the cylinder in 0.1 g increments. The graduated cylinder was then filled to 100 mL and let sit for 24 h prior to recording the swell index.

RESULTS

Effect of Ionic Strength. Hydraulic conductivity of the NaB and BPC-GCLs as a function of ionic strength of the bauxite liquors is shown in Fig. 1. The hydraulic conductivity to DI water is shown in Fig. 1 for comparison (plotted at ionic strength = 10^{-3} mM).

Hydraulic conductivity of the NaB GCL is closely related to the ionic strength of the bauxite liquor (Fig. 1 – closed symbols). The NaB GCL has low hydraulic conductivity (2.4×10^{-11} m/s) to DI water, but much higher hydraulic conductivity to bauxite liquor ($>3.6 \times 10^{-9}$ m/s). Hydraulic conductivity of the BPC-GCLs is lower than for the NaB bentonite when permeated with DI water and with bauxite liquors (Fig. 1 – zone enclosed by dashed lines).

The effect of the ionic strength on the hydraulic conductivity of the BPC-GCLs is evident. When permeated with DI water or bauxite liquor with ionic strength lower than 288 mM, the hydraulic conductivity of BPC-GCLs is less than 1×10^{-10} m/s. However, when permeated with bauxite liquor with ionic strength higher than 620 mM, the BPC-GCLs exhibit a wide range of

hydraulic conductivity (10^{-13} to 10^{-7} m/s), with the some BPC-GCLs (e.g., G2) very permeable (K $\approx 10^{-7}$ m/s) and others having very low hydraulic conductivity.

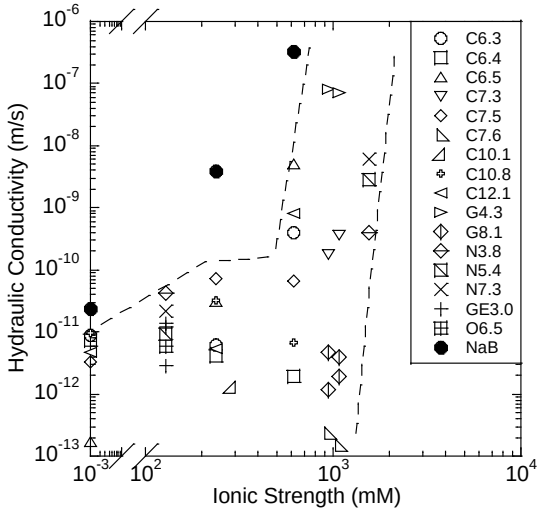

Figure 1. Hydraulic conductivity as a function of ionic strength of \bauxite liquors. The zone enclosed by dashed lines bounds hydraulic conductivity of BPC-GCLs to bauxite liquors.

Effect of Swell Index. Hydraulic conductivity of the NaB GCL and BPC-GCLs versus swell index of the bauxite liquors is shown in Fig. 2. Hydraulic conductivity of the NaB GCL is closely related to swell index, indicating that bentonite swelling controls the hydraulic conductivity of the NaB GCL (Fig. 2 closed symbols). However, a different mechanism controls the hydraulic conductivity for the BPC-GCLs. When swell index of BPCs is higher than 15 mL/ 2g, all GCLs have low hydraulic conductivity (< 10^{-10} m/s) to bauxite liquor. However, when the swell index is less than 15 mL/2 g, some BPC-GCLs have low hydraulic conductivities (<10^{-10} m/s) and others are much higher. For example, the hydraulic conductivity of the R6.4 BPC-GCL is less than 10^{-11} m/s when permeated with bauxite liquor or DI water, even though the swell index of R6.4 is only 7 mL/2 g in bauxite liquor.

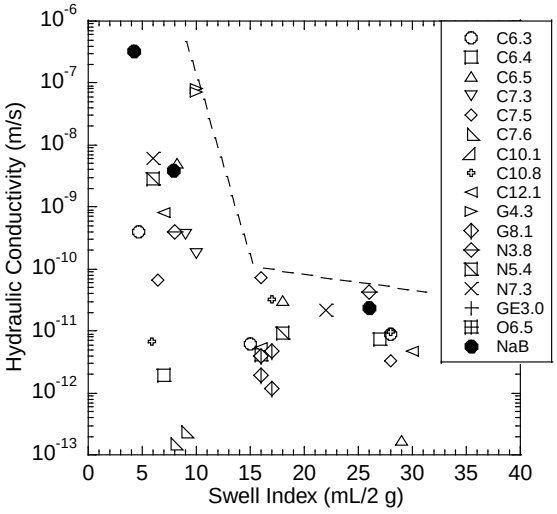

Figure 2. Hydraulic conductivity as a function of swell index in bauxite liquors.

Effect of Polymer Loading. Tian et al. (2019) and Chen et al. (2019) indicate that the hydraulic conductivity of BPC-GCLs permeated with aggressive solutions is controlled by polymer hydrogel clogging intergranular pores between the granules of bentonite. Intergranular pores in BPC-GCLs with higher polymer loading have a greater likelihood of being filled by hydrogel, and low hydraulic conductivity (Tian et al. 2019). For example, Tian et al. (2016) found that a polymer loading exceeding 5% is required for BPC-GCLs to have low hydraulic conductivity to low-level radioactive waste leachate.

The hydraulic conductivity of the BPC-GCLs to the bauxite liquors is shown in Fig. 3 as a function of polymer loading. The hydraulic conductivity of the BPC-GCL reported by Tian et al. (2019) is also shown in Fig. 3 (polymer loading = 6.8%, bauxite liquor with pH 13.0, I = 700 mM). As the polymer loading increases, the maximum hydraulic conductivity of the BPC-GCLs decreases, and the hydraulic conductivities become increasingly consistent. For example, when the polymer loading is less than 7.5%, the hydraulic conductivity of the BPC-GCLs ranges from 10^{-13} to 10^{-8} m/s. In contrast, when the polymer loading exceeds 7.5%, the BPC-GCLs generally have hydraulic conductivity less than 1 x 10^{-10} m/s (BPC-GCL C12.1 is an exception). These hydraulic conductivities represent the equilibrium condition obtained with the aforementioned methods. In the long-term, polymer elution may alter the hydraulic conductivity of the BPC-GCLs (Tian et al. 2019).

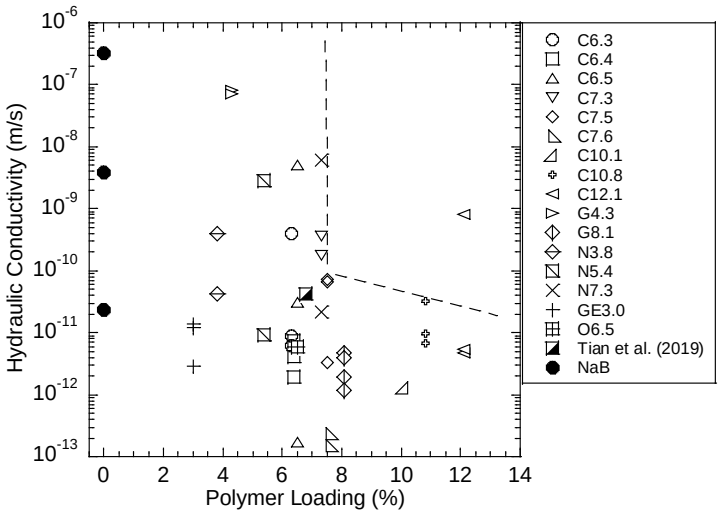

Figure 3. Hydraulic conductivity of BPC-GCLs to bauxite liquor as a function of polymer loading.

SUMMARY AND CONCLUSIONS

Hydraulic conductivity tests were conducted on BPC-GCLs and a NaB GCL using DI water and bauxite liquors as permeant liquids. The bauxite liquors were obtained from red mud management facilities at alumina refineries around the world. The bauxite liquors were hyperalkaline (pH>12) and had ionic strengths ranging from 239 to 1546 mM.

Based on the findings of this study, the following conclusions and recommendations are drawn.

- Hydraulic conductivity of the BPC-GCLs to bauxite liquor ranged from 10^{-13}-10^{-8} m/s. This range of hydraulic conductivities is higher than the hydraulic conductivities of the same BPC-GCLs permeated with DI water (10^{-13}-10^{-12} m/s), but lower than the hydraulic conductivity of a sodium bentonite (NaB) GCL permeated with the same liquors (10^{-9}-10^{-7} m/s).

- BPC-GCLs tend to have higher hydraulic conductivities when permeated with bauxite liquors having higher ionic strength and more alkaline pH. However, they are less permeable than NaB GCLs permeated with the same liquors.

- Sufficient polymer loading is needed to ensure a BPC-GCL has low hydraulic conductivity. For the bauxite liquors in this study, a polymer loading greater than 7.5% was necessary to ensure the hydraulic conductivity was less than 1 x 10^{-10} m/s.

REFERENCES

ASTM D5890. Standard test method for swell index of clay mineral component of geosynthetic clay liners, *ASTM International*, West Conshohocken, Pennsylvania, USA.

ASTM D6766. Standard test method for evaluation of hydraulic properties of geosynthetic clay liners permeated with potentially incompatible aqueous solutions, *ASTM International*, West Conshohocken, Pennsylvania, USA.

ASTM D5084. Standard test methods for measurement of hydraulic conductivity of saturated porous materials using a flexible wall permeameter, *ASTM International*, West Conshohocken, Pennsylvania, USA.

Athanassopoulos, C., Benson, C., Chen, J., Donovan, M. (2015). Hydraulic Conductivity of a Polymer-Modified GCL Permeated with High-pH Solutions, *Geosynthetics '15*, IFAI, St. Paul, MN, 181-186.

Benson, C., Oren, A., Gates, W. (2010). Hydraulic conductivity of two geosynthetic clay liners permeated with a hyperalkaline solution, *Geotext. Geomembr.* 28(2):206–218

Chen, J., Benson, C., Edil, T., and Likos, W. (2018), Hydraulic Conductivity of Geosynthetic Clay Liners with Sodium Bentonite to Coal Combustion Product Leachates, *J. Geotech. Geoenvironmental Eng.*, 144(3), 0401800.

Chen, J., Salihoglu, H., Benson, C. H., and Likos, W. J. (2019). Hydraulic Conductivity of Bentonite-Polymer Geosynthetic Clay Liners to Coal Combustion Product Leachates, *J. Geotech. Geoenviron. Eng.*, 145(9), 04019038.

Li, Q., Chen, J., Benson, C., and Peng, D. (2020). Hydraulic Conductivity of Bentonite-Polymer Composite Geosynthetic Clay Liners Permeated with Bauxite Liquor, *Geotextiles and Geomembranes*, doi: 10.1016/j.geotexmem.2020.10.015 .

Hosney, M., and Rowe, K. (2019). Polymer-enhanced Bentonite–Sand to Cover Calcium-Rich Soil, *Environmental Geotechnics*, 6(3), 155–161.

Jo, H., Katsumi, T., Benson, C., and Edil, T. (2001). Hydraulic conductivity and swelling of non-prehydrated GCLs permeated with single species salt solutions, *J. Geotech. Geoenviron. Eng.*, 127(7), 557-567.

Kishida, M., Harato, T., Tokoro, C., Owada, S. (2017). In situ remediation of bauxite residue by sulfuric acid leaching and bipolar-membrane electrodialysis, *Hydrometallurgy*, 170, 58–67.

Kolstad, D., Benson, C., and Edil, T. (2004). Hydraulic conductivity and swell of nonprehydrated GCLs permeated with multi-species inorganic solutions, *J. Geotech. Geoenviron. Eng.*, 130(12), 1236-1249.

Ozhan, H. (2018). Hydraulic Capability of Polymer-Treated GCLs in Saline Solutions at Elevated Temperatures, *Applied Clay Science*, 161, 364-373.

Scalia, J., and Benson, C. (2011). Hydraulic conductivity of geosynthetic clay liners exhumed from landfill final covers with composite barriers, *J. Geotech. Geoenviron. Eng.*, 10.1061/(ASCE)GT.1943-5606.0000407.

Scalia, J., Benson, C., Bohnhoff, G., Edil, T., and Shackelford, C. (2014). Long-term hydraulic conductivity of a bentonite-polymer composite permeated with aggressive inorganic solutions, *J. Geotech. Geoenviron. Engr.*, 04013025.

Sun, C.; Chen, J., Tian, K., Peng, D., Liao, X., Wu, X. (2019). Geochemical Characteristics and Toxic Elements in Alumina Refining Wastes and Leachates from Management Facilities, *Int. J. Environ. Res. Public Health,* 16, 1297.

Tian, K., Benson, C., and Likos, W. (2016). Hydraulic conductivity of geosynthetic clay liners to low-level radioactive waste leachate, *J. Geotech. Geoenviron. Eng.*, 04016037.

Tian, K., and Benson, C. H. (2019). Containing Bauxite Liquor Using Bentonite-Polymer Composite Geosynthetic Clay Liners. *Proceedings of the 8th International Congress on Environmental Geotechnics* Volume 2, Springer Singapore, Singapore, 672–678.

Tian, K., Likos, W., and Benson, C. (2019). Polymer Elution and Hydraulic Conductivity of Bentonite–Polymer Composite Geosynthetic Clay Liners. *J. Geotech. Geoenviron. Eng.*, 145(10), 04019071.

Xue, S., Kong, X., Zhu, F., Hartley, W., Li, X., Li, Y. (2016). Proposal for management and alkalinity transformation of bauxite residue in China, *Environ. Sci. Pollut. Res.* 23, 12822–12834.

Geosynthetics Conference

The Fundamentals of Geomembrane Seaming and Weld Quality

Glen W. Toepfer, C.E.T.[1]

[1]CQA Solutions, Ltd., 723A Phillips Avenue, Suite 201, Toledo, Ohio 43612;
gwtoepfer@cqasolutions.co

ABSTRACT

There are three primary components required to produce a quality geomembrane seam using thermal welding techniques: heat, speed, and pressure. Each of these components can be impacted by a multitude of variables – from design through the actual field installation. This paper will look at factors influencing each of the three primary components from design through field installation and identify key visual clues that indicate one or more components of the welding process are compromising weld integrity. The reader will come away with a better understanding of the thermal welding process, things that impact weld quality, ways to mitigate poor weld quality, and proper ways to remedy poor welds should they occur in the field.

INTRODUCTION

Thermal welding is the use of heat as the primary agent for joining or repairing geomembrane panels and consists of three different methods: hot air, fusion, and extrusion. One or more methods of thermal welding is used for the joining of many different geomembrane formulations including polyethylene (PE), polypropylene (PP), polyvinylchloride (PVC) and Ethylene Interpolymer Alloy (EIA) resin-based materials. These geomembrane materials are further defined at the molecular or polymer level, chemical compositions, and the presence of a reinforcement scrim. Chlorosulfinated Polyethylene (CSPE), Linear Low Density Polyethylene (LLDPE), Low Density Polyethylene (LDPE), and High Density Polyethylene (HDPE) are some of the PE resin based materials. LLDPE and flexible polypropylene (fPP) are both manufactured with or without reinforcement scrims (with scrims the designation is LLDPE-R and fPP-R respectively) whereas CSPE and EIA are manufactured exclusively with reinforcement scrims (CSPE-R and EIA-R respectively).

There are also woven coated polyethylene (WCPE) geomembranes and reinforced composite geomembranes (RCG) for which thermal welding methods are used. Additionally, each of these materials can have different characteristics which impact the weld settings used by the installer; for instance: extra carbon black content on the bottom of an HDPE liner to facilitate electric leak location surveys, thickness (HDPE and LLDPE range from 0.5 mm (20 mils) to 3.0 mm (120 mils)), the presence or absence of a surface texturing, the presence or absence of reinforcement scrim, and so forth. In the case of extra carbon black, the machine speed may need to be reduced while the temperature is increased from that of a geomembrane of the same thickness without the carbon black. Similarly, materials that have a reinforcement scrim may need a reduction in temperature and/or an increase in speed so that the reinforcement scrim is not compromised during.

On the other side of the spectrum, textured geomembrane sometimes requires additional heat and a slower speed than a non-textured geomembrane. A liner installation welding technician may be exposed to any or all of these materials in a single construction season. Understanding and remembering the difference in the parameters required to get a good weld when dealing with so many variances is critical. While the material type, thickness, and surface

texturing all must be accounted for in producing a sound weld, this is only the starting point for determining the specific welding criteria.

The range of material possibilities and specific welding criteria (temperature, speed, and pressure) are too extensive to cover comprehensively in one paper. However, these basics do apply to each individual material and will be covered broadly within this paper where they can be applied to any material being welded. Specific examples by certain materials will also be presented in this paper.

Creating a sound weld begins with the material being used. The temperature must be controlled such that it uniformly melts the surfaces being joined together creating a homogenous bond between the two surfaces – overheating or underheating will result in seam (or even parent material) failure through degradation (overheating) or lack of a bond (underheating). The amount of heat applied is not only controlled by a setting on the machine, but by the duration for which the heat is applied (speed). A third component, pressure, is required. In the case of a weld between the surfaces such as hot air or fusion welding, the pressure is applied immediately following the heating process to force the two molten surfaces together whereas in the case of extrusion welding, force is required to ensure the weld adheres to the prepared surface.

THERMAL WELDING METHODS

The three most common types of thermal welding are hot air, fusion, and extrusion welding. While each of these is a unique method, they all require a correct blend of heat, speed, and pressure to produce a quality weld. With the exception of temperature, which is universally controlled by adjustable settings on each of the thermal methods, speed and pressure could either be completely operator dependent (manual), or controlled by adjustable settings on the machine.

Hot Air. Hot air welding consists of air preheated to a certain temperature being applied to the geomembrane to melt the surfaces being joined. Hot air can either be directed manually through a hand-held hot air gun or mechanically through a motor driven machine. Both hot air welding methods utilize settings to control the output temperature of the air. With the manual application, speed is controlled by the rate at which the user pulls the apparatus through the seam. The speed of the mechanical device is controlled by settings which control the drive motor. In the case of manual application with a heat gun, pressure is usually applied either by force from the foot of the welding technician or by a roller whereas the mechanical machine will have rollers (called nip rollers) which apply pressure. The pressure applied in manual application will be a downward force as oriented towards the top sheet of the geomembrane while the mechanical method allows both upward and downward pressures.

Fusion. Fusion welding consists of heat application through a preheated element most commonly shaped as a wedge which is applied to the surfaces to be joined as the machine moves through the area. Both the temperature and the speed are controlled independent of each other by machine settings. Pressure in some machines is controlled directly by a mechanical setting whereas in other machines the pressure is predetermined by settings corresponding to different material thicknesses, which do not allow for much variance or control over the pressure. Again, as with mechanically propelled hot air welding devices, fusion welding devices use nip rollers to apply the pressure that creates the weld.

Extrusion Fillet. Extrusion fillet welding is perhaps the most laborious of the three welding methods as a bead of molten extrudate is placed over the prepared seam joint to compose the weld. The extrusion fillet welding apparatus typically has a preheat nozzle just forward of the extrudate discharge barrel – both the preheat temperature and the temperature of

the molten extrudate are adjustable and set by the user. The speed is determined by how fast the operator applies the extrudate. Pressure is determined by the force the operator is applying to the welding apparatus, the angle of the welding apparatus, and the resistance of the subgrade upon which the operator is pushing. Because the extrusion fillet weld is heavily dependent upon the skill of the welding technician, it is recognized to be an inferior weld when compared to the fusion weld.

Additionally, the extrusion fillet weld quality is highly dependent on the quality of the labor-intensive preparatory activities, which include beveling the material (when necessary), heat tacking the top sheet to the bottom sheet, abrading the surface (when necessary), all before applying the extrudate weld in a timely manner. Although these preparatory activities impact weld quality just as much or perhaps even more than the three primary welding components, they generally do not impact the weld temperature, speed, or pressure which are the focus of this paper and therefore are excluded from further discussion within this paper.

Table 1 below is a quick reference summation to how heat, speed, and pressure are adjusted for each method.

Thermal Method	Temperature	Speed	Pressure
Hot Air: Handheld device	Adjustable Setting	Manual	Manual
Hot Air: Mechanically Propelled	Adjustable Setting	Setting	Setting -no adjustment Setting - adjustment capable
Fusion: Mechanically Propelled	Adjustable Setting	Setting	Setting -no adjustment Setting - adjustment capable
Extrusion Fillet	Preheat - Adjustable Setting Barrel - Adjustable Setting	Manual	Manual

Table 1. Thermal welding heat, speed, and pressure control methods.

No matter the method used, geomembrane welding is an imperfect science in that at the time of the writing of this paper, there are no guarantees that every inch of every seam will be uniform even when temperature, speed, and pressure remain constant.

DESIGN

Design must take field construction into consideration in order to be a valid design. Reality is millions of dollars can be spent on design and materials but if a project is not constructed correctly, then it is all wasted. If a designer is not taking field construction into account in every aspect of their design, then they are failing. The ability to obtain good quality welding starts with the design process.

Field constructability. Issues with in project designs is a consistent problem throughout the industry. Designers must be aware of and account for the limitations of welding personnel and welding equipment within their designs. Welds fall in places they simply cannot be welded properly and maneuverability of the equipment is one of the main limitations. When equipment

cannot be properly operated, one (or more) of the three requirements for quality welds is going to be missing and result in a poor-quality weld. In this regard, the designer needs to account for every type of welding to be performed on the jobsite. As an example, a seam running the length of a vertical wall may easily be welded with a mechanical device that controls its own speed and pressure. However, while performing a repair it will be challenging to obtain sufficient pressure using a more labor-intensive method. To assume repairs will not be needed is short-sighted and potentially erroneous.

Best welding methods. The designer should take time to investigate the options available to ensure the best quality welds can be obtained for all aspects of the project. For instance, the use of prefabricated corner and angle pieces when lining sharp angles will yield a higher quality containment system. Prefabricated corners are a small increase in material cost but the will move the weld joint away from the confines of the corner/angle where equipment/personnel can maneuver and perform a higher quality weld. A constructability review and peer review of the design and specifications will go a long way towards avoiding areas that limit welding capabilities.

Reduction of inferior weld types. Given that some welds are inferior to other types of welds, the design should attempt to minimize these inferior types of welds to the best extent possible. For instance, while primary seaming of the materials listed in the introduction can usually be performed with a mechanically propelled device, repairs and penetration boots are typically performed with an inferior welding method; PVC will require chemical or adhesive welds, PE's will require extrusion fillet for some repairs, and reinforced products may require a hand-held hot air weld and/or an extrusion fillet weld. Table 2 illustrates the different methods used for seaming the primary weld versus the methods used for repairs and appurtenances. Note the primary weld method listed is the industry standard/preferred method at the time of writing and is so because it is proven to yield a higher quality. Additional discussion on ways to reduce inferior weld types will occur throughout the remainder of the document.

	HDPE	LLDPE	LLDPE-R	EIA-R	fPP	fPP-R	PVC	WCPE
Primary Seam (preferred method)	Thermal Fusion	Thermal Fusion	Thermal Fusion	Thermal Fusion	Thermal Fusion	Thermal Fusion	Thermal Fusion	Thermal Fusion
Repairs	Thermal Extrusion Only	Thermal Extrusion Only	Thermal Extrusion Only - No Grinding	Chemical	Handheld Hot Air, Tape w/ Primer, Extrusion	Handheld Hot Air, Tape w/ Primer	Chemical Adhesive	Handheld Hot Air, Tape, Extrusion - No grind w/ LLDPE Rod

Table 2. Primary and repair seaming methods by geomembrane type.

Testing Protocols. Another often overlooked design consideration is allowing for the proper non-destructive testing and/or destructive testing of the weld. If neither can be performed, there is often no other way to verify the continuity and/or integrity of the weld. There is this concept that certain types of welds such as fusion welds have become so sophisticated that

they are no longer failing in the field. This could not be more incorrect and recent field studies show a different reality.

The designer should also account for proper construction as they develop the technical specifications that go along with their design. Engineers should keep the following phrase in mind as they go through the design and specifications of their project: “If it is not in the specs, it doesn’t get done”.

TECHNICAL SPECIFICATIONS

The technical specifications should not only ensure the proper materials and equipment are used for the design, but they should also empower Quality Assurance/Quality Control personnel to enforce quality concerns. Some of most overlooked areas include those mentioned below.

Power supply. For thermal welding of any type to be consistent, the power supply to the welding apparatus must be sufficient and consistent (no fluctuations). Power supply variations will predominantly impact speed and temperature and these variations will then show-up in the quality of the welds. The power supply not only consists of using a power source meeting the manufacturer’s recommendations, but also requires the proper gauge of cord with associated maximum run lengths of cords as well as a maximum number of connections between lengths of cord. The power source also needs to remain consistent from trial welds through the welding process.

As an example, Revision E of Demtech’s VM-20 Operators Manual recommends in-field generators be rated for 3,500 watts minimum with a preferred rating of 5,000 watts or more “in order to obtain the best welder performance and temperature control.” The manual further states that extension cords between the generator and welding device be at least 12 gauge with 3 plug end connections. At table is provided for maximum recommended cord lengths, based on 3 wire cords by gauge; the maximums listed are: 10 gauge, 500 feet; 12 gauge, 250 feet; and 14 gauge, 100 feet.

Interface. Interface refers to the layers being bonded together – namely the top surface of the bottom sheet and the bottom surface of the top sheet where the weld will occur (or in the instance of extrusion fillet welding, the top surface of both sheets). Interface of the weld plays an important role in weld quality, at least among textured and smooth variations of HDPE geomembranes. A textured geomembrane typically has the same core thickness (nominal) as it’s smooth counterpart but the asperity height increases that thickness, even more significantly in double-sided textured products. As a result, fixed pressure devices allow for little accommodation in this area so the most common adjustment is to slow down the machine speed while sometimes leaving the temperature constant. Without the ability to accurately adjust for varying thicknesses that textured liners present, the pressure setting can be too much or too little.

Based on prior research, there can be significant variations in failure rates within the overall failure rate on a project. Toepfer and Duganiero state that on a study of 7 projects (two LLDPE and 5 HDPE, the combined average destructive failure rate was 5.4% (range 3.7% - 9.4%). However, when looking at interfaces within these projects, the smooth/smooth interface averaged 4.3% (range 0% - 6.9%). However, the textured/textured interface failure rate averaged 10.8% (range 4.2% to 20.0%) and the smooth/textured interface averaged a failure rate of 11.4% (range 0% to 25.0%). The failure rates of the smooth/textured interface is 271% higher and the textured/textured is 257% higher than the smooth/smooth interface on these same projects.

Specifications should address the seam destructive testing of different material interfaces encountered on any project to ensure each interface is adequately represented.

Weather. Changes in weather conditions will vary on a project throughout the day and duration of the project. These changes can impact the temperature and speed variables required to produce a quality weld and should be monitored by quality personnel throughout the welding shift. Thermal welding is extremely sensitive to cold weather and as such, proper precautions should be taken. Such precautions may include things like incorporating GRI GM-9 or a site-specific cold weather seaming plan into the specifications, mandating the use of wind shields when wind speeds exceed a certain velocity, preheating the geomembrane prior to welding, and so forth.

Destructive seam testing protocols. Often the only requirement for destructive testing of trial welds and field screening of destructive samples is that the coupons meet similar requirements to those for which laboratory testing is going to be performed. However, both the trial weld sample and the destructive sample offer a glimpse into the quality of the weld that goes beyond the normal peel and shear testing. Key indicators observed in trial welds, such as an off-center extrusion fillet weld or a fusion weld showing uneven pressure characteristics should be cause to sound the alarm, especially if the sample somehow passes (and they do). Some issues of weld quality such as crystallization of the weld, off-center welds, lack of homogenization in the weld, etc. will only be visible by looking at a cross-section cut of the seam.

If the trial weld is poorly prepared and barely passes, any welding performed after that trial weld is likely to be welded under the same conditions which can result in excessive failures, which in turn means excessive repairs, most likely performed by an inferior welding method. The destructive sample obtained for laboratory testing means the welding has already been performed, so adjustments can only be made from that point forward – that point could be several thousand feet or more of welding beyond that sample. In that regard, obtaining destructive sample feedback as quickly as possible after welding is critical to keeping issues with a seaming device or devices from propagating. The benefit of identifying a poor-quality weld during the field screening of the laboratory destructive sample is that bounding can commence immediately and failing samples are not shipped to the laboratory. Designers should ask themselves how can they address trial weld quality in their Technical Specifications beyond peel and sheer? Are they empowering the quality to staff to make judgement calls to ensure site-owners get the best end result possible?

End coupons are another valuable destructive test that allow for examination of the quality of the weld at starting and ending points of a mechanically propelled welding device (hot air or wedge). These coupons are cut by the installer and evaluated in a peel test – the evaluation method should be specified otherwise it becomes a meaningless exercise. For the most accurate assessment of the seam, the end coupon should be tested in a tensiometer according to the material specific testing requirements for trial seams and destructive sample screening as this assures both strength and incursion requirements are met. It is recommended that third party quality assurance (QA) personnel observe these tests.

It is imperative that destructive sampling programs evaluate inferior welding methods, particularly repairs. The author has successfully witnessed the use of seam destructive sampling of repairs on numerous projects and the results speak for themselves. On a standard HDPE cell liner installation, extrusion welding of repairs accounts for between 91.4m and 182.8m per 0.4 hectares (300 and 600 feet per acre) installed. This number adds up quickly and should not be forsaken. The failure rates in these same studies ranged from 0% to 60.0% for these welds.

Establishing maximum failure rates. Regardless of the type of welding, maximum failure rates should be clearly defined and the consequences for exceeding these rates should also be defined. Maximum failure rates are a somewhat tangible measurement of quality when competent QA is used. There are varying opinions on what current failure rates actually are in the industry and it is a topic the author has discussed and continues to discuss elsewhere in great depth. That being said, the author feels a reasonable target maximum failure rate for any project should be 5% or lower for any type of thermal welding method. If these values are exceeded, then the installer should be directed to stop the welding process until they have proven a successful remedy.

Minimize inferior weld type length. The amount of inferior welding can be minimized, through design, materials (wider panels), and proper planning. Massive amounts of inferior welding do not need to take place on a project.

For instance, the author was involved in the highly discussed 493-acre zero-leak geomembrane installation at the Palo Verde Nuclear Generating Station. The owner set the precedent that the maximum allowable length of any inferior (or non-preferred) weld type (i.e. extrusion on HDPE, chemical on PVC) would be 10 feet. The installer also implemented having no single repair exceed 10 feet in length (perimeter could exceed 10 feet – for instance, a 2 x 5 foot patch has a perimeter of 14 lineal feet) – any repairs over this length were performed with the primary seaming method (fusion) with appropriate inferior repairs at the starting and ending point which greatly reduced the amount of inferior weld type on the project. In fact, as far as primary seaming goes, many of the ponds had less than 10 lineal feet total of primary seaming performed using the extrusion welding methods.

Project specifications such as minimizing the amount of inferior welding performed are definitely adventitious to the owner when it comes to long-term quality.

GEOMEMBRANE INSTALLER

The geomembrane installer is critical to producing quality seams. Not all geomembrane installers are created equally nor are the crews for any given company created equally. It is important to find a reputable installer who has a crew having significant installation and welding experience with the material being used on each project. This crew should be designated to the project and should not be exchanged.

Panel layout. One requirement of an installer that is often required (and should always be required) is the submittal of a proposed panel layout drawing to the owner or the owner's representative (often the construction certifying engineer). The panel layout drawing is an opportunity to not only verify the seams fall in accordance with the design and specifications, but it is also an opportunity to gauge the installer. A sloppy panel layout drawing missing butt seams and other details can be an indicator of the quality to expect during the installation. The panel layout drawing should then be approved by the engineer and the approved layout should then be followed during the field installation with any modifications approved solely by the engineer. A sample proposed panel layout drawing is shown below in Figure 1 which illustrates the presence of butt seams.

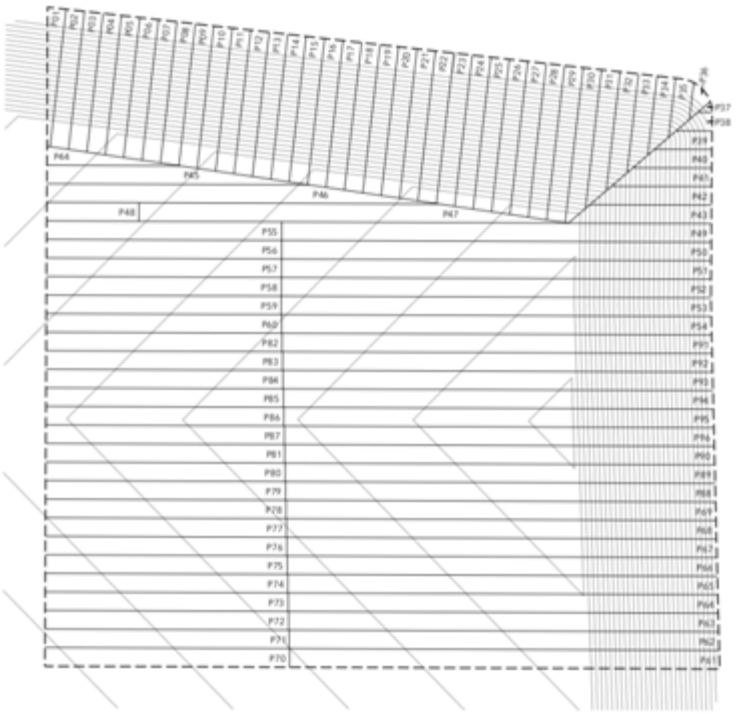

Figure 1. Proposed panel layout drawing provided by installer.

Experience and qualifications. It is important to ensure that the installation crew, particularly those welding the materials, have significant experience with the material being installed. Experience should be well vetted – just because someone has 30 years or millions of square feet of experience does not mean they were taught how to properly weld. Vetting installer references is one way to find out the quality of a company – it is sometimes a bit more difficult to find out the qualifications of an individual welding technician. Another qualification that can help is certification through the International Association of Geosynthetic Installers (IAGI), particularly individual certification as a Certified Welding Technician (CWT) in the particular material being installed. It should be noted that the CWT program is not available for all materials so a check with IAGI should be performed in the planning stages of the project to see if there is a program to meet the needs of the materials used on a specific project. Two examples of poor quality work illustrate the value of trained technicians. Photo 1 shows were a technician improperly performed an extrusion repair by creating what the industry refers to as a "Gorilla bead" where multiple passes are made with the extrusion gun to repair a large area. This results in severe overheating of the geomembrane, which can lead to stress cracking in the future. Photo 2 shows an untrained installation technician attempting to fix HDPE geomembrane with caulk.

Photo 1. Untrained installation technician created "Gorilla bead".

Photo 2. Untrained installation performing improper HDPE repair using caulk.

WELDING EQUIPMENT

Normally it is the responsibility of the installation contractor to provide the proper welding equipment for the material being installed. Having the proper equipment is equally as critical as using the proper procedures. Many personnel involved in the project outside of the installation firm have little knowledge of some of the equipment that may be customized by the installer for a specific material or application. The following is a short list of these items:

Wedge. The wedge-shaped heating element used in mechanically propelled hot air and fusion welders comes in a variety of materials – copper, stainless steel, and porcelain to name a few. While copper provides some of the most uniform heat transfer, it also reacts with PVC. Most installers will switch out the wedge component without anyone even knowing. Some hot air devices also utilize an interchangeable short wedge/long wedge which also impacts the amount of heat transfer to the material.

Nip rollers. Like the wedge, nip rollers come in a variety of materials including stainless steel (with fine or coarse knurls), HDPE, silicone, and rubber. A thin material and reinforced materials are often better suited with HDPE or rubber nip rollers that are softer and do not have

the knurls. Nip rollers are another item that the installer will switch out to match the material being welded with few people outside the installation crew the wiser (and sometimes the welding technicians do not know either because the crews master seamer sets up the machines.

Porcelain welding shoe. The tip of the extrusion welder, the shape of the shoe determines the shape and thickness of the extrusion weld. The tips sometimes degrade or break over time. Installers will switch to a thicker contour shoe for cold weather seaming applications. Generally, installers should not be modifying the contour as doing so can impact the amount of extrudate in the seam area which impacts the temperature, speed, and pressure.

While welding equipment is the responsibility of the installer, the quality control/quality assurance team understanding of these aspects is key to monitoring weld quality. Field personnel should be on the lookout for any indicators that something may have changed, such as knurl marks on the geomembrane where the welding machine ran, different shapes to extrusion welds, and so forth.

CONSTRUCTION QUALITY ASSURANCE

At first glance it seems that construction quality assurance has nothing to do with weld quality – or does it? It would seem that weld quality would fall solely on the hands of the installer. That being said, industry leader Boyd Ramsey (Boyd Ramsey Consulting) has been quoted saying numerous times "the first dollar I would spend on a project would be on construction quality assurance". There are numerous studies that show the importance of construction quality assurance (CQA) as it pertains to installation quality, suggesting the mere presence of CQA can increase quality. Abigail Beck references the Forget et. al. 2005 in her December 2012 article "*How Much Does My Landfill Leak?"* then rightfully clarifies, "This concept can be expanded to an improvement in construction quality with rigorous CQA as opposed to poor or inattentive CQA." This is a strong statement. Rightfully so. CQA personnel are the eyes and ears of the project and need to have their finger on the pulse of the project at all times, which cannot happen if their head is constantly buried in paperwork. While documentation is a key deliverable from CQA, the greater focus must be on the quality of the work actually being performed. Documentation should always come second place to observation.

Quality CQA will not only identify problems, but will help in identifying them before they propagate, such as during the inspection of trial seams. It is the visual clues that help identify issues in the quality of welds. Photo 3 shows a crease and cut through the geomembrane resulting from improper pressure settings on the welding device. The operator should have immediately stopped when they noticed this and corrected the issue – instead, there were about ½ dozen such instances on a 125' slope seam.

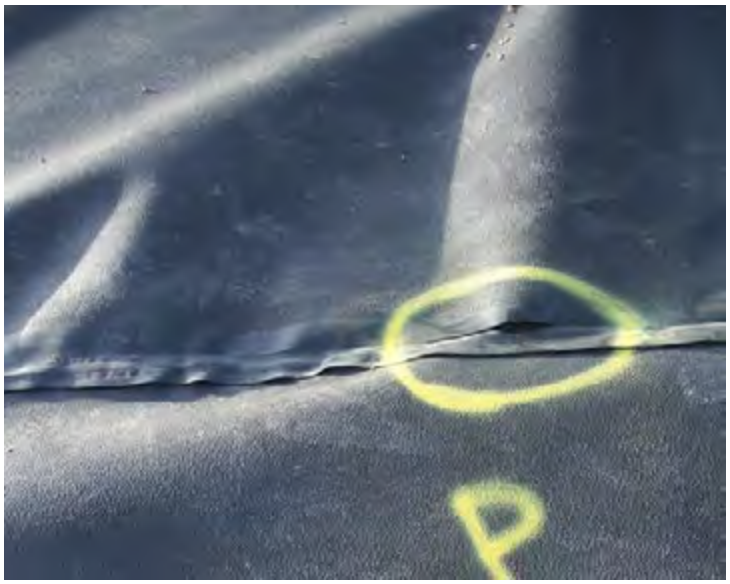

Photo 3. Improper pressure should have been observed by operator.

VISUAL ASSESSMENT

Visual assessment consists not only of looking at trial seams, the weld itself, and destructive seam results, but in looking at the wholistic picture being told at any moment in time during the preparation and welding of a seam. There are many challenges in the field that impact one or more of the fundamental requirements for a quality weld: geomembrane surface temperature, wind speed, and moisture to name a few. Likewise, welding technicians that are careless or tired may drip sweat into the weld area, fail to adjust machine settings from one weld interface to another, or gradually decrease the angle of an extrusion welder from nearly perpendicular to a 45-degree angle or less. Each of these play a role in the overall quality of the weld and often lead to failures because minor changes like these can have a huge impact on heat, speed, and pressure. An example of work performed by a tired crew shown in Photo 4 is the failure to abraid the HDPE geomembrane prior to an extrusion weld, resulting in weld failure as it separates from the geomembrane.

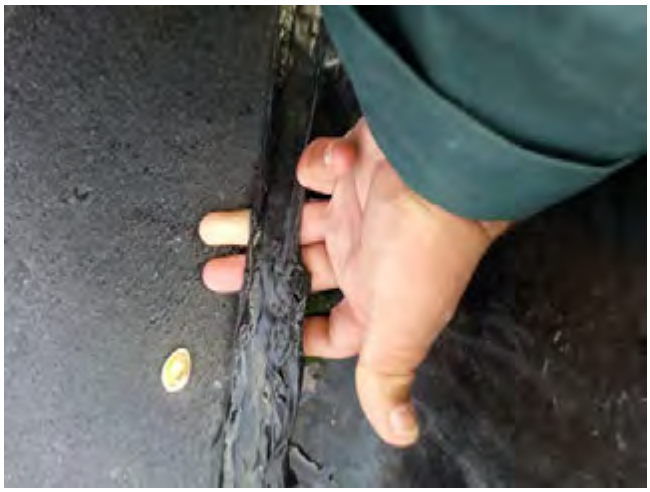

Photo 4. Tired crew did not abraid HDPE geomembrane prior to extrusion weld.

MITIGATION

Ideally, mitigation occurs along each step of the process preceding the actual field welding itself – constructability and peer reviews alter the design and specifications to remove all previously existing roadblocks to a quality weld, qualified and experienced installation and quality assurance teams are hired, and the fieldwork team thoroughly evaluates trial welds and prevents failing welds from occurring. Even when all the stars align, there will usually be some issues with seam quality that just crop up as part of the normal cycle of installation. As mentioned herein, the key is quickly identifying those and keeping them from propagating when they do happen.

Issues happen for a multitude of reasons and it cannot be forgotten that mitigation may require the removal of equipment and/or personnel from welding, or even more drastic, the removal of the entire crew or installation firm. When mitigating isolated instances of poor weld quality, it is important return to the roots of minimizing the amount of inferior welding. Equally important is limiting the amount of intersections in thermal welds (reheat, pressure) as illustrated in the following photo of multiple overlapping extrusion weld repairs. Rather than having a bunch of intersections, the whole cluster can be cut out, removed, and replaced with a larger patch without the overlaps.

CONCLUSION

Thermal welding is highly adventitious and can yield good, long-term results when heat, speed, and pressure are properly controlled. There are many extraneous variables present on projects beyond heat, speed, and pressure that were not discussed, such as dust/dirt in welds, because they negatively impact weld quality even when the operator has the primary three components of a good weld properly established.

In order to give the installation team the best chance of success welding, the variables discussed within this paper need to be considered and monitored on every project, from conception through the installation. There are frequent case studies at conferences illustrating these successes but they often leave out the most integral part of the equation that is understanding the principles of seaming and addressing them before the field crew ever hits the site.

REFERENCES

Beck, Abigail. (2016, April). *How much does my landfill leak.* Plastatech https://plastatech.com/media/literature/geomembrane_product_comparison.pdf

D. Daniel & R Koerner, *Waste Containment Facilities, 2nd edition*, Reston, VA, USA, American Society of Civil Engineers, 2007

Demtech. (2015). *Operators Manual – Model 500—1—XL.* Demtech https://www.demtech.com/wp-content/uploads/2012/10/Pro-Wedge-XL-Manual.pdf

B.J. Duganiero & G.W. Toepfer, Material Interface Types: Impact on Destruct Sample Failure Rates, Presented at Geosynthetics 2019, Houston, TX, USA February 10-13, 2019, 1129

Geosynthetic Research Institute. 2013. "GRI GM-9" Accessed October 1st, 2020 https://geosynthetic-institute.org/grispecs/gm9.pdf

G.W. Toepfer, Weld Integrity – Moving Beyond Peel and Sheer, Presented at Geosynthetics 2019, Houston, TX, USA February 10-13, 2019, 1129

G.W. Toepfer, Extrusion Welds – The Good, The Bad, and The Ugly, Presented at Geosynthetics 2015, Portland, OR, USA February 15-18, 2015, 246

G.W. Toepfer, "*The Complete Field Guide to Ensuring Quality Geosynthetics Installations:*

Volume 1: Fundamentals & Geomembrane", 1st Edition, Toledo, OH, USA, Integrity, 2015, Various

IAGI. 2020. "Certified Welding Technician Program" Accessed October 1st, 2020 https://www.iagi.org/certified-welding-technician-cwt-

Geosynthetics Conference

Using Bentonite-Polymer Composite Geosynthetic Clay Liners to Contain Coal Combustion Product Leachates

Jiannan Chen, PhD, EIT,[1] Sarah A. Gustitus, PhD Candidate, EIT,[2] and Craig H. Benson, PhD, PE, NAE[3]

[1]Department of Civil, Environmental, and Construction Engineering, University of Central Florida, Orlando, FL 32816; e-mail: jiannan.chen@ucf.edu
[2]School of Engineering, University of Virginia, Charlottesville, VA 22903; e-mail: sgustitus@virginia.edu
[3]School of Engineering, University of Virginia, Charlottesville, VA 22903; e-mail: chbenson@virginia.edu

ABSTRACT

Hydraulic conductivity tests were conducted to evaluate the hydraulic conductivity of bentonite-polymer composite (BPC) geosynthetic clay liners (GCLs) to coal combustion product (CCP) leachates from coal-fired power plants in the United States. The CCP leachates ranged from acidic to highly alkaline (pH = 4.3 to 12.0), with ionic strengths up to 681 mM. All tests were conducted in flexible-wall permeameters with direct permeation and without prehydration. Hydraulic conductivity of BPC-GCLs to the CCP leachates ranged from 10^{-12}-10^{-10} m/s and was often several orders of magnitude lower than the hydraulic conductivity of NaB-GCLs permeated with the same leachate (10^{-8}-10^{-7} m/s). Hydraulic conductivity of BPC-GCLs depends on the chemical properties of the CCP leachate and the polymer loading.

INTRODUCTION

Coal combustion products (CCPs) are residuals from coal-fired boilers that are disposed in lined landfills when they cannot be used beneficially in other applications (EPRI 2009). Land disposal of CCPs is regulated under the "coal ash rule" incorporated into Subtitle D of the Resource Conservation and Recovery Act (RCRA) (Federal Register 2015). The coal ash rule requires that coal ash disposal facilities be lined with a composite liner consisting of a geomembrane underlain by a compacted clay liner at least 0.6 m thick having a hydraulic conductivity no greater than $1x10^{-9}$ m/s (Bittner et al. 2019). Geosynthetic clay liners (GCLs) can be used in lieu of compacted clay liners provided that the GCL meets the equivalency criteria in the coal ash rule. This generally requires that the hydraulic conductivity of the GCL be less than $3x10^{-11}$ m/s when tested with the CCP leachate to be contained (Bittner et al. 2019).

CCPs leachates contain a variety of cations and anions that can affect the hydraulic conductivity of GCLs (Chen et al. 2018). Jo et al. (2001) and Xu et al. (2009) evaluated how ionic strength, cation valence, and pH of permeant solutions affect the swelling and hydraulic conductivity of sodium bentonite (NaB) GCLs. They show that the hydraulic conductivity of NaB GCLs increases as the ionic strength of the leachate increases, and that GCLs are more permeable to solutions with polyvalent cations (e.g. calcium, magnesium, aluminum) than those with monovalent cations (e.g., sodium, potassium, lithium), all other factors being equal. Extreme pH (pH>13 or pH<2) also alters the hydraulic conductivity of NaB GCLs. Kolstad et al. (2004) evaluated how multi-species solutions affect swelling and hydraulic conductivity of NaB GCLs.

They report that the ionic strength and the relative abundance of monovalent and polyvalent cations of a solution are master variables affecting swelling and hydraulic conductivity of NaB GCLs. Chen et al. (2018) evaluated the hydraulic conductivity of NaB GCLs permeated with CCP leachates representing a broad range of conditions in the US. They found that the hydraulic conductivity of NaB GCLs increased from 10^{-10} to 10^{-6} m/s as the ionic strength of the CCP leachate increased from 40 to 755 mM. Thus, for many CCPs, a conventional NaB GCL may not satisfy the criteria in the coal ash rule as an alternative to a compacted clay liner. In contrast to NaB GCLs, the hydraulic conductivity of most compacted clay liners is relatively insensitive to CCP leachates (Benson et al. 2018).

The chemical compatibility of GCLs has been enhanced in some applications by adding polymers to the bentonite (Di Emedio et al. 2011, Mazzieri et al. 2010, Scalia et al. 2014, Katsumi et al. 2008). These polymeric additions may be interlayer substitution or polymer surface treatment of the montmorillonite fraction (e.g., a polymer-modified bentonite or PMB) or consist of a dry mixture of bentonite and polymer granules to form a bentonite-polymer composite (BPC) material. Some polymer additions are effective, whereas others are not. For example, Shackelford et al. (2010) report that the hydraulic conductivity of a PMB GCL was 9 to 21 times higher than that of NaB GCL when permeated with the same solution. In contrast, Scalia et al. (2014) report that the hydraulic conductivity of a BPC-GCL permeated to $CaCl_2$ solutions was up to four orders of magnitude less permeable than a NaB GCL prepared with the same bentonite and the same $CaCl_2$ solutions.

The hydraulic conductivity of several BPC-GCLs to actual CCP leachates was evaluated in this study as part of chemical compatibility testing conducted to identify suitable GCL products for CCP disposal facilities. Polymer loading was also measured to understand mechanisms affecting hydraulic conductivity of the BPC-GCLs.

MATERIALS

CCP Leachates. Seven CCP leachates were obtained from coal ash diposal facilities in Virginia (CCP-VA1, CCP-VA2, CCP-VA3, and CCP-VA4), Wyoming (CCP-WY), and Minnesota (CCP-MN1, CCP-MN2). Two of the synthetic CCP leachates (i.e., FGD and HS) from Chen et al. (2018) were also used. Bulk chemical parameters, including pH, electrical conductivity (EC), ionic strength (I), relative abundance of monovalent and polyvalent cations (RMD), and anion ratio (molar ratio of chloride to sulfate, Cl^-/SO_4^{2-}) are summarized in Table 1. The pH of the CCP leachates ranges from 4.3 to 9.9, the ionic strength ranges from 33 to 681 mM, and the EC ranges from 0.3 to 4.4 S/m at 25 ^oC. The leachates range from chloride rich (CCP-VA2) to sulfate rich (CCP-VA1).

Table 1. Bulk chemical parameters of CCP Leachates.

CCP Leachates	CCP-VA1	CCP-VA2	CCP-VA3	CCP-VA4	CCP-WY	CCP-MN1	CCP-MN2	FGD	HS
pH	4.3	8.3	9.9	8.4	8.5	7.2	9.0	8.0	8.0
EC@25 ^oC (S/m)	0.4	0.3	1.5	0.07	4.4	0.3	0.8	0.8	1.4
Ionic Strength (mM)*	46.4	34.8	233.1	13.7	680.6	32.8	85.1	94	174
RMD ($M^{1/2}$)	0.2	0.4	2.4	0.07	1.2	0.3	0.07	0.4	1.0
Cl^-/SO_4^{2-}	0.09	154.8	2.4	2.0	1.1	0.4	0.2	0.8	1.0

*Calculated using Visual MINTEQ, charge differences <5%.

Kolstad et al. (2004) defined the parameter RMD to quantify the relative abundance of monovalent and polyvalent cations in a permeant liquid:

$$RMD = \frac{M_M}{\sqrt{M_D}} \quad [1]$$

where M_M is the total molarity of the monovalent cations and M_D is the total molarity of polyvalent cations in the permeant solution. RMD of the CCP leachates ranges from 0.07 to 2.4 $M^{1/2}$, or predominantly polyvalent (low RMD) to predominantly monovalent (high RMD).

The relationship between RMD and ionic strength for the CCP leachates is shown in Fig. 1 along with leachates in the Electric Power Research Institute (EPRI) leachate database reported by Chen et al (2018, 2019). The CCP leachates in this study (closed symbols in Fig. 1) predominantly have ionic strengths in the upper portion of the ionic strengths in the EPRI leachate database (open symbols in Fig. 1), and tend to have lower RMD (more polyvalent).

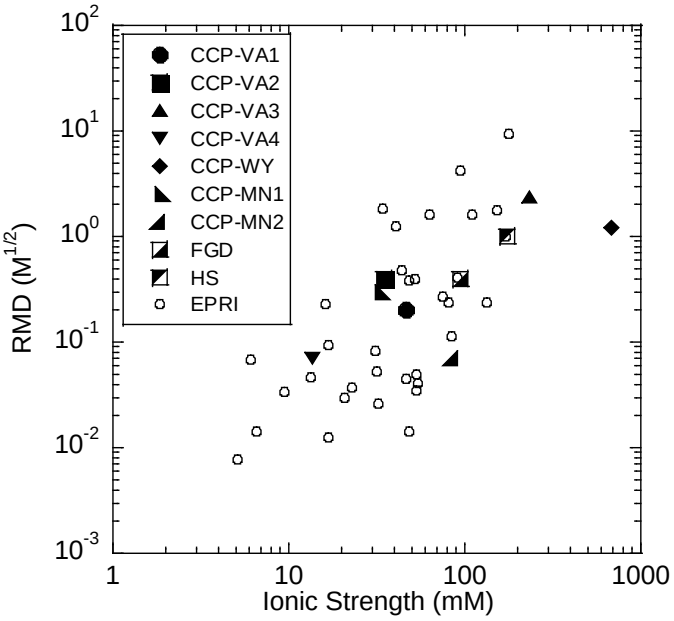

Figure 1. RMD versus ionic strength for CCP leachates in this study. Leachates from EPRI database shown with open symbols.

Geosynthetic clay liners. Seven commercially available BPC-GCLs were evaluated in this study. All of the BPC-GCLs are manufactured by dry mixing one or more granular proprietary polymers (cross-linked or linear polymers) with granular sodium bentonite. The BPC-GCLs are labeled as BP4.0, BP5.8, BP6.3, BP8.6, BP8.9, BP9.0, and BP9.7, with the numerical suffix representing the polymer loading in percent by dry mass as measured based on loss on ignition (LOI) of the BPC and NaB using the procedure in Scalia et al. (2014).

Hydraulic conductivity of GCLs. Hydraulic conductivity tests were conducted on 150-mm-diameter GCL specimens using flexible-wall permeameters in accordance with ASTM D5084 and ASTM D6766. The falling headwater-constant tailwater method was used. GCL specimens were

trimmed from the rolls following the method described in Jo et al. (2001). Excess geotextile fibers were carefully removed from the edge of GCL specimens, and bentonite paste prepared with the permeant liquid was applied to the edge of specimens to prevent bentonite loss that could potentially induce sidewall leakage. The GCL specimens were placed between two nonwoven geotextiles (mass per area = 240 g/m^2) to evenly distribute flow and to prevent fouling with polymer eluted from the GCLs. The effective stress was set at 20 kPa and the average hydraulic gradient was 190.

GCL specimens were hydrated with CCP leachate for 48 h prior to permeation. Hydration was conducted in the permeameters with the cell pressure applied, the headwater applied, and the effluent valve closed. Permeation followed immediately afterward and was conducted until the hydraulic conductivity was steady, the ratio of incremental outflow to outflow (Q_{out}/Q_{in}) was within 1.00 ± 0.25, and the pH and EC of the effluent were within 10% of those of the influent. Duplicate tests were conducted to ensure the results were reproducible. When relatively high hydraulic conductivities (10^{-8} m/s) were obtained, the influent was spiked with rhodamine WT dye to stain flow paths through the GCL.

RESULTS

Hydraulic Conductivity. Typical graphs of hydraulic conductivity, Q_{in}/Q_{out}, pH_{out}/pH_{in}, and EC_{out}/EC_{in} vs. cumulative inflow are shown in Fig. 2, which shows data from the test on GCL BP6.3 permeated with the CCP-VA2 leachate. The final hydraulic conductivity was $4.2x10^{-12}$ m/s. Hydraulic conductivity of the GCL gradually decreased and then leveled out after about 100 mL of inflow. The ratio of Q_{in}/Q_{out} was near 1.0 after 50 mL cumulative inflow, indicating the GCL was hydrated. The EC ratio diminished as salts were flushed from the pore space, with EC_{out}/EC_{in} within 1± 0.1 after 240 mL. The ratio pH_{out}/pH_{in} was always within 1± 0.1, indicating pH equilibrium.

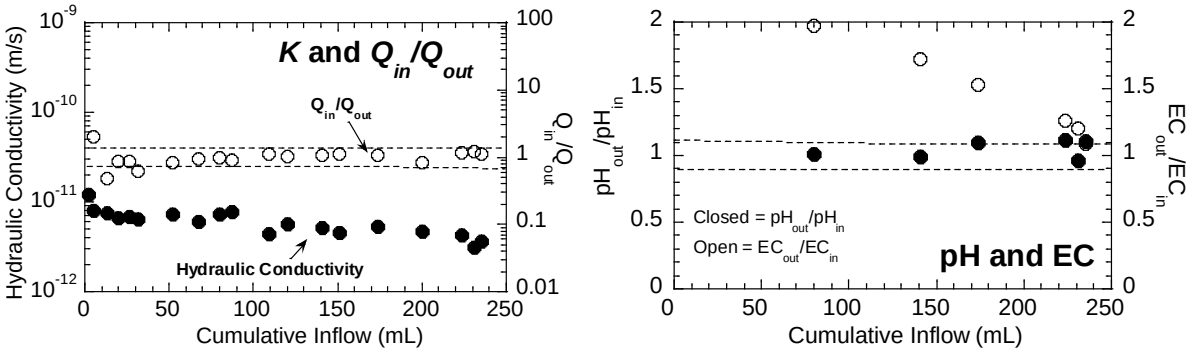

Figure 2. Hydraulic conductivity, Q_{in}/Q_{out}, pH_{out}/pH_{in}, and EC_{out}/EC_{in} from test on BPC6.3 GCL permeated with CCP-VA2 leachate.

Effect of Ionic Strength. Hydraulic conductivity of the BPC-GCLs as function of ionic strength of the CCP leachates is shown in Fig. 3. Hydraulic conductivities of the NaB GCLs to CCP leachates from Chen et al. (2019) are also shown in Fig. 3. Hydraulic conductivities of the BPC-GCLs are one to four orders of magnitude lower than hydraulic conductivities of the NaB GCLs (zone enclosed by dashed lines in Fig. 3) for similar ionic strength. Hydraulic conductivity of the NaB GCLs is strongly affected by ionic strength, whereas hydraulic conductivity of the BPC-GCLs is nearly independent of ionic strength. All of the BPC-GCLs had hydraulic conductivity

less than 10^{-10} m/s, even permeated with leachate of high ionic strength (i.e., CCP-WY with I = 681 mM), and most were less than $1x10^{-11}$ m/s.

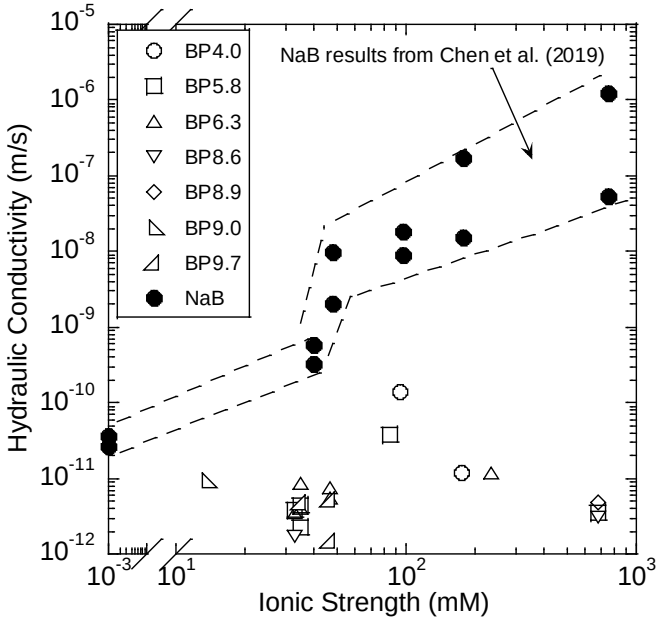

Figure 3. Hydraulic conductivity versus ionic strength of the CCP leachates. Zone enclosed by dashed lines corresponds to hydraulic conductivities of NaB GCLs to CCP leachates.

Effect of RMD and Anion Ratio. Hydraulic conductivity of the BPC-GCLs is shown as a function of RMD and anion ratio of the CCP leachates in Fig. 4. No trends are evident with RMD or anion ratio, except the highest hydraulic conductivities were obtained for leachates with lower RMD and lower anion ratio, and the lowest polymer loading. The low RMD may have suppressed swelling of the bentonite, rendering the polymer loading insufficient to achieve low hydraulic conductivity for these more permeable BPC-GCLs.

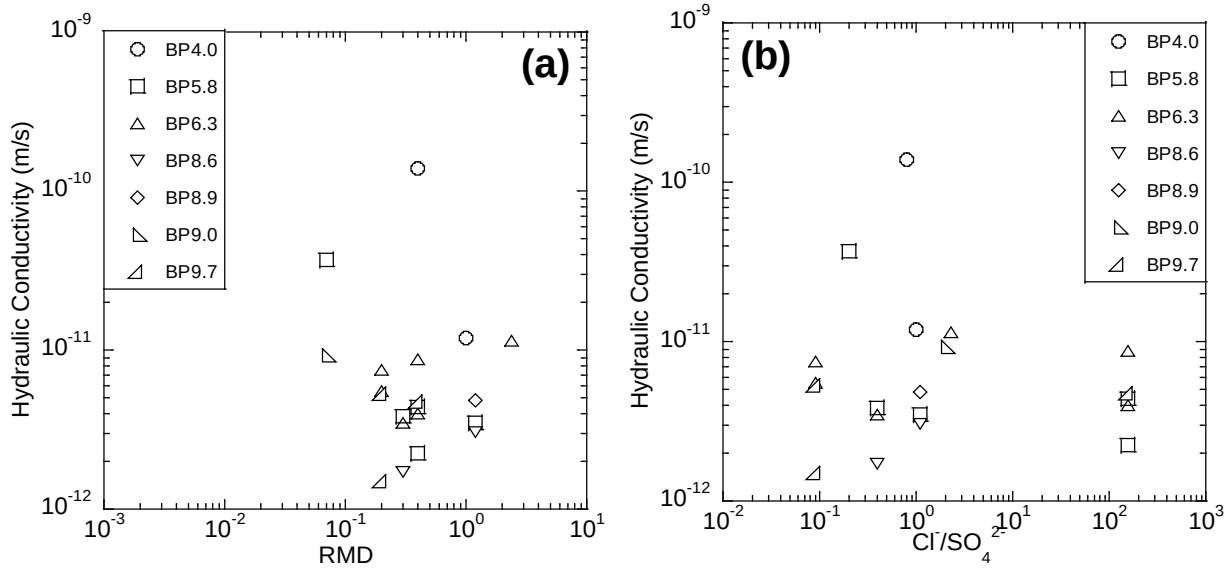

Figure 4. Hydraulic conductivity vs. (a) RMD and (b) anion ratio of CCP leachates.

Mechanisms Controlling Hydraulic Conductivity of BPC-GCLs to CCP. Tian et al. (2019) and Chen et al. (2019) indicate that the hydraulic conductivity of BPC-GCLs is controlled by polymer hydrogel clogging intergranular pores. Higher polymer loading in the BPC-GCL provides greater likelihood that flow paths are clogged and the hydraulic conductivity is low. Hydraulic conductivity to the CCP leachates is shown in Fig. 5 as a function of polymer loading of the BPC-GCLs (open symbols). Hydraulic conductivities of the NaB GCLs are shown in Fig. 4 as zero polymer loading (closed symbols). As the polymer loading increases, the maximum hydraulic conductivity of the BPC-GCLs decreases, and the hydraulic conductivities become increasingly consistent. The hydraulic conductivity is consistently less than 10^{-10} m/s when the polymer loading is greater than 4%, and less than 10^{-11} m/s when the polymer loading is greater than 6%. The type of polymer used in the BPC probably influences the threshold as well, but was not provided by the GCL manufacturers. These hydraulic conductivities represent the equilibrium condition obtained with the aforementioned methods. In the long-term, polymer elution may alter the hydraulic conductivity of the BPC-GCLs (Tian et al. 2019).

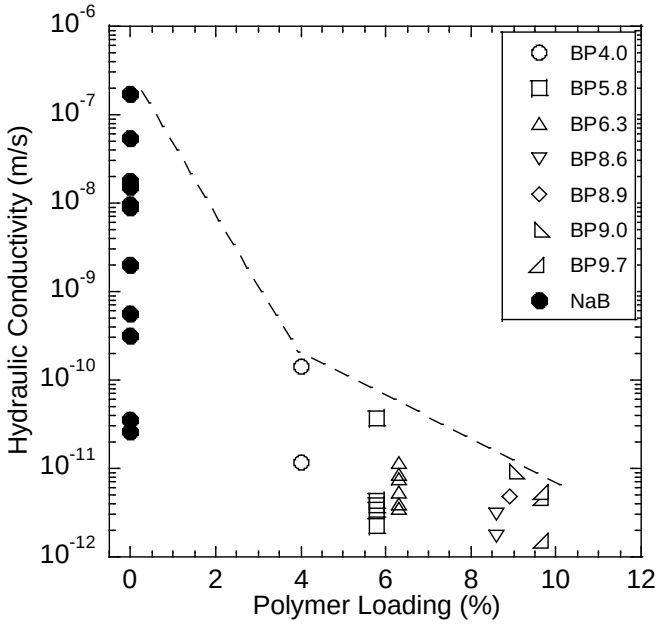

Figure 5. Hydraulic conductivity of BPC-GCLs to CCP leachates as a function of polymer loading. Data for NaB GCLs (closed symbols) from Chen et al. (2019).

CONCLUSION

Hydraulic conductivity tests were conducted on seven BPC-GCLs using seven coal combustion product (CCP) leachates. The GCLs were permeated directly with leachate (no prehydration) at an effective stress of 20 kPa. The following conclusions are drawn:

- BPC-GCLs have appreciably lower hydraulic conductivity than NaB GCLs when permeated with CCP leachates. The BPC-GCLs had hydraulic conductivities to CCP leachates ranging from 10^{-12} to 10^{-10} m/s, whereas the NaB GCLs had hydraulic conductivities to the CCP leachates ranging from 10^{-10} to 10^{-6} m/s.

- Hydraulic conductivity of BPC-GCLs with higher polymer loading tend to have lower hydraulic conductivity to CCP leachates. BPC-GCLs consistently had hydraulic conductivity less than 10^{-10} m/s when the polymer loading was greater than 4%, and less than 10^{-11} m/s when the polymer loading was greater than 6%. Polymer type likely affects these thresholds, but was not explored in this study.

REFERENCES

ASTM D6766. Standard test method for evaluation of hydraulic properties of geosynthetic clay liners permeated with potentially incompatible aqueous solutions, *ASTM International*, West Conshohocken, Pennsylvania, USA.

ASTM D5084. Standard test methods for measurement of hydraulic conductivity of saturated porous materials using a flexible wall permeameter, *ASTM International*, West Conshohocken, Pennsylvania, USA.

Benson, C., Chen, J., Likos, W., and Edil, T. (2018). Hydraulic Conductivity of Compacted Soil Liners Permeated with Coal Combustion Product Leachates, *J. Geotech. Geoenvironmental Eng.*, 144(4), 04018011.

Bittner, A., Kondziolka, and J., Benson, C. (2019) Relative Liner Performance for Coal Combustion Product Management Sites: Conceptual Review and Model Evaluation for Surface Impoundments. EPRI, Palo Alto, CA, 3002016498.

Chen, J., Benson, C. H., and Edil, T. B. (2018). Hydraulic Conductivity of Geosynthetic Clay Liners with Sodium Bentonite to Coal Combustion Product Leachates. *J. Geotech. Geoenviron. Eng.*, 2018, 144(3): 04018008.

Chen, J., Salihoglu, H., Benson, C. H., and Likos, W. J. (2019). Hydraulic Conductivity of Bentonite-Polymer Geosynthetic Clay Liners to Coal Combustion Product Leachates, *J. Geotech. Geoenviron. Eng.*, 145(9), 04019038.

Di Emedio, G., Van Impe, W., Flores, V. (2011). Advances in geosynthetic clay liners: polymer enhanced clays. GeoFrontiers 2011. *Advances in Geotechnical Engineering*, American Society of Civil Engineers, Reston, 1931-1940.

EPRI (2009). Coal ash: characteristics, management, and environmental is-sues. *Electric Power Research Institute*, Palo Alto, CA.1019022.

Federal Register (2015), 80 FR 21301, Federal Register, *the Daily Journal of the US Government*, 21301-21501.

Jo, H., Katsumi, T., Benson, C., and Edil, T. Hydraulic conductivity and swell of non-prehydrated GCLs permeated with single species salt solutions. *J. Geotech. Geoenviron. Eng.*, 2001, 127(7), 557-567.

Katsumi, T., Ishimori, H., Onikata, M., and Fukagawa, R. (2008). Long-term barrier performance of modified bentonite materials against sodium and calcium permeant solutions. *Geotext. Geomembr.*, 26(1), 14−30.

Kolstad, D., Benson, C., and Edil, T (2004). Hydraulic conductivity and swell of non-prehydrated GCLs permeated with multi-species inorganic solutions. *J. Geotech. Geoenviron. Eng.*, 130(12), 1236-1249.

Mazzieri, F., Emidio, G., Van Impe, P. (2010). Diffusion of calcium chloride in a modified bentonite: Impact on osmotic efficiency and hydraulic conductivity. *Clays Clay Miner.*, 58(3), 351-363.

Scalia, J., Benson, C., Bohnhoff, G., Edil, T., and Shackelford, C. (2014). Long-term hydraulic conductivity of a bentonite-polymer composite permeated with aggressive inorganic solutions. *J. Geotech. Geoenviron. Eng.*, 04013025-1-13.

Shackelford, C., Benson, C., Katsumi, T., Edil, T., and Lin, L (2000). Evaluating the hydraulic conductivity of GCLs permeated with non-standard liquids. *Geotext. Geomembr.*, 18(2-4), 133-162.

Shackelford, C.D., Sevick, G.W., and Eykholt, G.R. (2010). Hydraulic conductivity of geosynthetic clay liners to tailings impoundment solutions. *Geotext. Geomembr*, 28 (2), 149-162.

Tian, K., Likos, W., and Benson, C. (2019). Polymer Elution and Hydraulic Conductivity of Bentonite–Polymer Composite Geosynthetic Clay Liners. *J. Geotech. Geoenviron. Eng.*, 145(10), 04019071.

Xu, C., Li, Z., and Gao, Y. (2009). Influence of Solution Characteristics on Swelling and Hydration Performance of Geosynthetic Clay Liners. *Journal of Tonji University (Nature Science)*, 37(1), 36-40.

Geosynthetics Conference

Flow-Swell Index as an Indicator of Chemical Compatibility of Bentonite-Polymer Composite Geosynthetic Clay Liners

Sarah A. Gustitus[1] and Craig H. Benson[2]

[1]EREF Scholar and Jefferson Fellow Doctoral Candidate, Dept. of Engineering Systems and Environment, University of Virginia, Charlottesville, VA 22903; e-mail: sgustitus@virginia.edu
[2]Dean and Hamilton Endowed Chair, School of Engineering, University of Virginia, Charlottesville, VA 22903 USA; e-mail: chbenson@virginia.edu

ABSTRACT

Flow stress of polymer gel and swell index of bentonite in bentonite-polymer composite (BPC) geosynthetic clay liners (GCLs) were assessed as indices of hydraulic conductivity. Three commercially available BPC-GCLs were permeated with aggressive solutions, yielding hydraulic conductivities ranging from $1.3x10^{-12}$ m/s to $4.2x10^{-8}$ m/s. Hydraulic conductivity of the BPC-GCLs was not strongly related to flow stress of the polymer gel or swell index of the BPC. However, high ($> 10^{-9}$ m/s) and low ($< 10^{-11}$ m/s) hydraulic conductivities were differentiated by the product of flow stress of the polymer gel and swell index of the NaB component of the BPC, herein referred to as the flow-swell index. The flow-swell index accounts directly for the two mechanisms controlling hydraulic conductivity in BPC-GCLs – swelling of the NaB component and propensity for elution of the polymer component. A narrow transition zone between high and low hydraulic conductivities was identified corresponding to a small change in flow-swell index. Flow-swell index greater than 14 kPa - mL/ 2g corresponded to long-term hydraulic conductivities $< 7x10^{-12}$ m/s.

INTRODUCTION

Bentonite-polymer composite (BPC) geosynthetic clay liners (GCLs) are employed in containment facilities for wastes that generate aggressive leachates that can adversely affect the hydraulic conductivity of GCLs containing sodium bentonite (NaB). Aggressive leachates that may necessitate the use of BPC-GCLs are derived from wastes including red mud from alumina refining, coal combustion products, or low-level radioactive wastes (Athanassopoulos et al. 2015; Tian et al. 2016a; Donovan et al. 2017; Tian and Benson 2018; Chen et al. 2019).

Mechanisms controlling the hydraulic conductivity of NaB- and BPC-GCLs are illustrated in Fig. 1. For NaB-GCLs, the hydraulic conductivity is controlled by swelling of the NaB. As NaB granules swell, the intergranular pore spaces become smaller and more tortuous, resulting in low hydraulic conductivity ($<10^{-9}$ m/s, Fig. 1A). However, if swelling is suppressed by the hydrating or permeant liquid, the intergranular pores are much larger and the hydraulic conductivity of a NaB-GCL will be much higher (Fig. 1B; Kolstad et al. 2004, Jo et al. 2006, Scalia and Benson 2011). In a BPC-GCL, the size and tortuousity of the pore spaces is affected by swelling of the bentonite as well as clogging of intergranular pores by hydrated polymer gel. If the NaB component of a BPC swells minimally, the hydraulic conductivity of the BPC-GCL is primarily controlled by polymer gel filling the pores (Scalia et al. 2014; Tian et al. 2016a; b; Özhan 2018). For this reason, BPC-GCLs can maintain low hydraulic conductivity when hydrated or permeated with aggressive solutions for which NaB-GCLs are much more permeable (i.e., solutions with high

ionic strength, abundance of polyvalent cations, extreme acidity, or extreme alkalinity) (Jo et al. 2001; Hornsey et al. 2010; Shackelford et al. 2010; Chen et al. 2019; Prongmanee and Chai 2019; Wang et al. 2019).

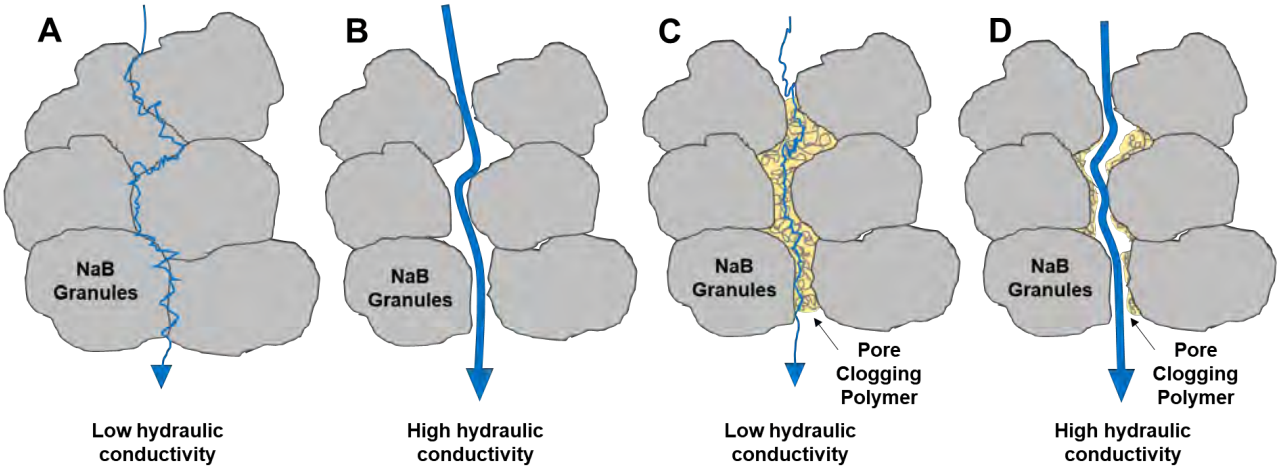

Figure 1: (A) Swollen bentonite with narrow tortuous pores and low hydraulic conductivity; (B) bentonite with swell suppressed, large intergranular pores, and high hydraulic conductivity; (C) bentonite-polymer composite with polymer gel filling intergranular pores and low hydraulic conductivity; (D) bentonite-polymer composite after elution of polymer gel, with large pores, and high hydraulic conductivity.

BPC-GCLs maintain low hydraulic conductivity provided the polymer gel remains within the pores, creating narrow and tortuous flow paths similar to those found in highly swollen NaB (Scalia et al. 2014; Tian et al. 2016a; b; Özhan 2018). However, the polymer in BPC-GCLs is prone to elution during permeation, which can result in preferential flow paths and higher hydraulic conductivity (Tian et al. 2019; Gustitus and Benson 2020). Identifying conditions under which NaB swelling and polymer retention yield high or low hydraulic conductivity is critical to evaluate whether a BPC-GCL can be an effective barrier for an aggressive solution.

Currently there are no standardized or widely used index tests to screen BPC-GCLs for compatibility with aggressive leachates. An effective index test to evaluate compatibility between BPC-GCLs and aggressive solutions should represent the mechanisms controlling the hydraulic conductivity (i.e., retention of the polymer and/or swelling of the NaB), similar to how swell index represents the dominant mechanism controlling hydraulic conductivity of NaB-GCLs. Swell index measured in accordance with ASTM D5890 is routinely used to screen NaB-GCLs, but is not suitable for BPC-GCLs because swelling is only one mechanism contributing to low hydraulic conductivity (McRory and Ashmawy 2005; Scalia et al. 2011, 2018; Salihoglu et al. 2016; Chen et al. 2019). Water vapor sorption has been suggested as an index of compatibility, but the relationship between hydraulic conductivity and water vapor sorption depends on the chemistry of the permeating solution (Akin et al. 2017), precluding an assement of hydraulic conductivity *a priori*. Correspondence between hydraulic conductivity and the fluid indicator test (FIT) has been reported for one type of BPC permeated with $CaCl_2$ solutions of various concentrations, but the generality of this correpondence has not been demonstrated for other BPCs or permeant solutions (Norris et al. 2019). Viscosity of the BPC hydrated with leachate has been suggested as an index

of compatibility (Geng et al. 2016); however, a general relationship between hydraulic conductivity and viscosity has not been established.

Propensity for a hydrated polymer gel to move in the pores of a BPC can be described using viscoelastic properties such as flow stress - the shear stress above which a gel flows like a liquid rather than rebounding elastically like a solid (Mezger 2015). In this study, flow stress of polymer gels was evaluated as an index of compatibility between BPC-GCLs and aggressive solutions, both alone and in conjuction with swell index of the NaB component.

MATERIALS AND METHODS

Materials. Three commercially available BPC-GCLs were used in this study. All of the GCLs consisted of BPC constrained by upper and lower non-woven geotextiles bound by needlepunching. BPC-GCL-PL also contained a woven slit-film between the BPC and the lower non-woven geotextile. BPC-GCL-PC contains 6.5 g polymer/kg BPC of polymer PC, a cross-linked polymer. BPC-GCL-PL contains 4.0 g polymer/kg BPC of polymer PL, a linear polymer. BPC-GCL-PM contains 4.5 g polymer/kg BPC of polymer blend PM, a mixture of linear and cross-linked polymers. All of the polymers were synthetic and water-soluble or water-swellable. They are proprietary to the GCL manufacturers and therefore their chemical formulations are not available.

The same NaB was used as the base clay for each of the BPC-GCLs. Quantitative X-ray diffraction (XRD) conducted using the methods in Moore and Reynolds (1989) and Scalia et al. (2014) indicate that the montmorillonite content of the bentonite is 75%. Other minerals in the bentonite include cristobalite content (16%), tridymite (3%), oligoclase (3%), quartz (1%), calcite (1%), and gypsum (1%). Grain size distribution measured following ASTM D6913 indicates that 99.6% of the NaB was finer than a US No. 10 (2 mm) sieve, 38.7% was finer than a US No. 20 (0.841 mm) sieve, and 0.9% was finer than a US No. 200 (0.074 mm) sieve.

Three solutions with varying chemical compositions were used as permeants: 50 mM $CaCl_2$ (electrical conductivity, EC = 1.0 S/m; pH 5.8), a synthetic bauxite liquor (EC = 6.6 S/m; pH 13.5), and the CEN alkaline standard solution (EC = 1.4 S/m; pH 12.4) as described in EN 14030:2001. The synthetic bauxite liquor contained 287.2 mM NaOH, 0.06. mM $CaCl_2$, 3.0 mM KCl, 0.3 mM Na_3PO_4, 0.4 mM $NaNO_3$, 54.2 mM Na_2O-Al_2O_3, 19.1 mM NaCl, and 5.0 mM Na_2SO_4.

Methods.

Hydraulic conductivity. Hydraulic conductivity was determined using the falling headwater, constant tailwater method using flexible-wall permeameters in accordance with ASTM D6766. The average effective stress was 29 kPa and the average hydraulic gradient was 115. Prior to permeation, GCLs were hydrated with the permeant solution in the permeameter for 48 h with the cell pressure and headwater applied and the outflow line closed. No backpressure was used to preclude geochemical alterations that would not occur at natural porewater pressures.

In-situ gel moisture content. The flow stress of hydrated polymer gels varies with the moisture content of the gel. Therefore, the in-situ moisture content of the polymer gel in a BPC-GCL is needed to assess the flow stress corresponding to conditions in the pore space. Moisture content of polymer gels within BPCs cannot be measured directly because the polymer component cannot be effectively separated from the bentonite component after BPC hydrates. In addition, within a BPC, the bentonite and polymer gel have different moisture contents because each component has different affinity for water.

The bentonite-polymer moisture affinity test was developed to simulate these competing hydration processes and estimate the in-situ moisture content of the polymer and NaB components. The test is conducted in a hydration tray, as illustrated in Fig. 2. The polymer and bentonite are placed in the cell in the same mass proportions that exist in a BPC, and are separated by a 5-µm polyester filter. The filter delivers the hydrating solution and ensures that the bentonite and gel remain separated. The polymer and NaB compete for solution in the hydration tray in a manner that approximates what occurs during hydration within a well-mixed BPC. Moisture contents determined by the bentonite-polymer moisture affinity test are intended to represent conditions within the BPC-GCL prior to polymer elution. Moisture content of the polymer remaining within the pore space is expected to change as gel elutes during permeation.

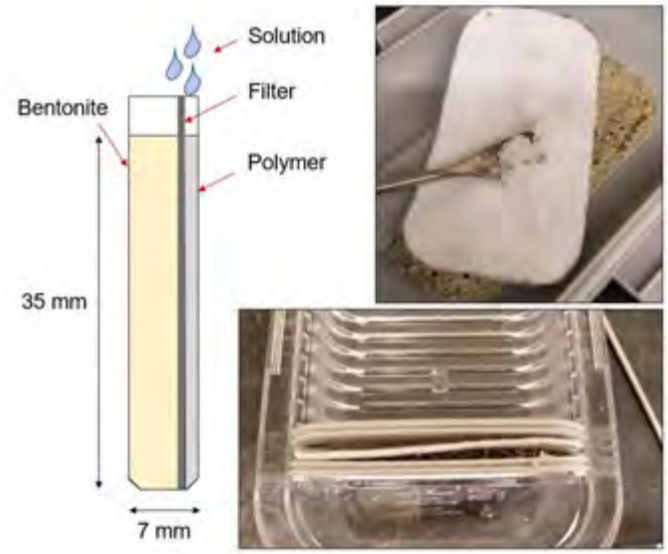

Figure 2: Shematic illustration of bentonite-polymer moisture affinity test (left), hydrated polymer and bentonite components at end of test period (top right), and top view of filled test cell in hydration tray (bottom right).

The hydration tray used in these experiments had 7 mm wide compartments. Within each compartment, oven-dry granular NaB was placed on one side the polyester filter and oven-dry polymer was placed on the other. A combined total of 12 g of NaB and polymer was used for each test, of which the masses were distributed to replicate the polymer to NaB ratio in the BPC-GCL. The NaB and polymer were carefully spread across the opposite faces of the filter using a small spatula. Solution (10 g) was directly applied to the filter using a small bulb dropper. The container was sealed for 30 min, after which an additional 2 g of solution was added to the filter. Two steps were used because preliminary testing demonstrated that the filter could only imbibe 10 g of fluid. The container was then resealed and the contents allowed to equilibrate for at least 48 hr. Following

this equilibration period, each component was carefully removed from the filter using a spatula, and the moisture content of each was measured in accordance with ASTM D2216.

Triplicate tests were performed for each BPC. To avoid cross-contamination from polymer migrating past the edge of the filter, bentonite within 1 mm of the the edge of the filter was removed and discarded. Cross-contamination of the polymer with bentonite was visually identifiable, and was avoided during sampling. Even hydration of the gel and betonite was confirmed via visual inspection on completion of the test. The hydrated polymer gels also appeared visually similar to gels observed in hydrated BPC-GCLs.

Viscoelastic properties. Storage and loss moduli of polymer gels were measured using shear-strain-amplitude sweeps with controlled-shear deformation with an Anton Paar MCR 302 rheometer (Anton Paar, Austria). Amplitude sweeps were completed over a range of 0.01 to 10,000% shear strain using a 25-mm-diameter sandblasted parallel plate. Flow stress of the hydrated polymer gels was determined as the shear stress corresponding to equality of the storage and loss moduli. Tests were conducted on polymer gels hydrated with permeant solution to moisture contents of 200, 500, 1000, and 2000%. This range of moisture content encompasses the range of moisture contents determined using the bentonite-polymer moisture affinity test.

Swell index. Swell index was measured on the NaB alone and each BPC in general accordance with ASTM D5890, except the BPC was ground to 100% passing the US No. 40 sieve and 65% passing the US No. 60 sieve. A coarser grind then stipulated in D5890 was used to reduce the effect of grinding on the polymer structure, and to ensure that there was no segregation of polymer that would alter the results (Christian et al. 2020). Scalia et al. (2019) demonstrate that swell indices of bentonite ground to pass a No. 40 sieve are similar to those for bentonite ground to pass a No. 200 sieve.

Polymer loading. Polymer loading of the BPC-GCLs was determined by total carbon analysis following the methods in Gustitus et al. (2020) using a Shimadzu TOC-L analyzer (Kyoto, Japan) paired with a solid sample module (SSM).

RESULTS

Hydraulic conductivity. Hydraulic conductivities of the BPC-GCLs are summarized in Table 1. The hydraulic conductivities range from 1.3×10^{-12} m/s for BPC-GCL-PL with the CEN alkaline standard solution, to 4.2×10^{-8} m/s for BPC-GCL-PC with the 50 mM $CaCl_2$ solution. With the exception of BPC-GCL-PL with the CEN alkaline standard solution, all tests were conducted until the termination criteria described in ASTM D6766 were satisfied. The test on BPC-GCL-PL permeated with CEN alkaline standard solution met all of the termination criteria, but had only transmitted 1.0 pore volumes of flow (PVF) at the time this was prepared.

Table 1. Hydraulic conductivity, pore volume of flow (PVF), and elapsed time of permeation; moisture content and flow stress of in-situ polymer gel from bentonite-polymer moisture affinity test; and swell indices of NaB and BPC for each GCL.

GCL	Permeating Solution	Hydraulic Conductivity (m/s)	PVF	Elapsed Time (days)	Polymer Gel Moisture Content	Polymer Gel Flow Stress (kPa)	NaB Swell Index (mL/2g)	BPC Swell Index (mL/2g)
BPC-GCL-PC	50 mM $CaCl_2$	$4.2x10^{-8}$	2.9	62	613%	1.23	11	11
	CEN Alkaline Standard	$6.7x10^{-12}$	6.6	579	685%	1.07	31	29
	Synthetic Bauxite	$2.5x10^{-12}$	5.1	576	405%	1.21	11	13
BPC-GCL-PL	50 mM $CaCl_2$	$6.0x10^{-9}$	3.9	0.3	667%	1.07	11	11
	CEN Alkaline Standard	$1.3x10^{-12}$	1.0	164	573%	1.36	31	41
	Synthetic Bauxite	$6.7x10^{-12}$	10.6	458	563%	2.24	11	13
BPC-GCL-PM	50 mM CaCl2	$3.4x10^{-9}$	4.6	0.6	983%	0.45	11	17

Component in-situ moisture contents. Moisture contents of the polymer gels determined using the bentonite-polymer moisture affinity test are summarized in Table 1. The gel moisture content ranged from 405% for BPC-GCL-PC with synthetic bauxite liquor to 983% for BPC-GCL-PM with 50 mM $CaCl_2$. Moisture content of the hydrated NaB was consistently much lower than that of the polymer, and ranged from 51% for BPC-GCL-PC with CEN alkaline solution to 77% for BPC-GCL-PL with 50 mM $CaCl_2$. For a given BPC, the polymer gel and NaB moisture contents varied between hydrating solutions.

Total BPC moisture content from the competitive hydration test was between 90-110%, which is comparable to the total moisture content of 100% used to define the volume of hydrating solution added to the filter. The total moisture content (~100%), compartment width (7 mm), and BPC loading (~3 kg/m^2) in the bentonite-polymer moisture affinity test were representative of typical conditions in the BPC-GCLs evaluated in this study.

Flow stress of hydrated polymer gels. Flow stress (τ_f) of each gel decreased with increasing moisture content. Examples of flow stress relationships are shown for each polymer hydrated with 50 mM $CaCl_2$ in Fig. 3A. The relationship between flow stress and moisture content was unique for each polymer-solution pair, but followed the power function:

$$\tau_f = \alpha w^{\beta}$$

where w is the moisture content and α and β are empirically derived parameters. The relationship between flow stress and moisture content varies with the chemistry of the hydrating solution for a given polymer, as illustrated in Fig. 3B for polymer PC hydrated with the 50 mM $CaCl_2$, synthetic bauxite, and CEN alkaline standard solutions.

Flow stresses of the gels at moisture contents anticipated in the GCLs ranged from 0.45 kPa for BPC-GCL-PM with 50 mM $CaCl_2$ to 2.24 kPa for BPC-GCL-PL with synthetic bauxite solution (Table 1). These flow stresses may be higher than shear stresses within the pores at the low velocities seen in BPC-GCLs. Nevertheless, flow stress is a useful quantifiable characteristic for understanding the viscoelastic character of a polymer gel.

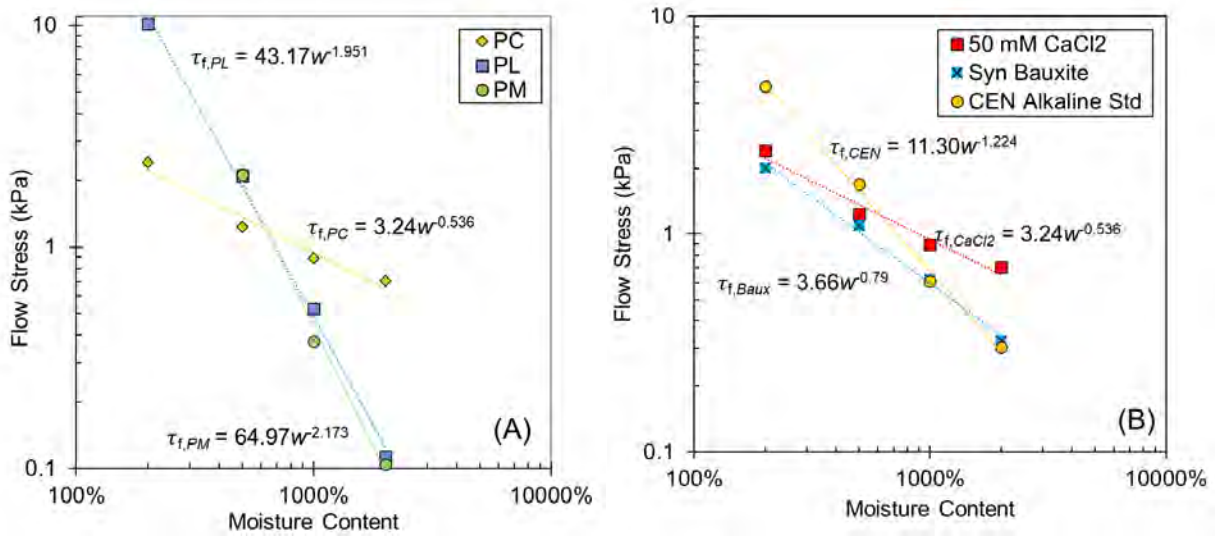

Figure 3. Relationships between flow stress and moisture content (A) for polymer gels hydrated with 50 mM $CaCl_2$ and (B) for polymer PC hydrated with each permeant solution.

Swell Index. Swell indices of the BPCs and the NaB from each BPC are summarized in Table 1 for each solution. Swell index of the NaB ranged from 11 mL/2g with 50 mM $CaCl_2$ and synthetic bauxite liquor to 31 mL/2g with the CEN alkaline standard solution. Swell index of the BPCs ranged from 11 mL/2g for BPC-GCL-PC and -PL with the 50 mM $CaCl_2$ solution to 41 mL/2g for BPC-GCL-PL with the CEN alkaline standard solution. Swell index of the BPCs was similar to or higher than swell index of the NaB alone when hydrated in the same solution.

DISCUSSION

Hydraulic conductivity is shown versus flow stress in Figure 4A and versus BPC swell index in Figure 4B. There is no distinct correspondence between hydraulic conductivity and flow stress or swell index, but both data sets indicate thresholds that segregate low and high hydraulic conductivities. For example, BPC-GCLs with a gel flow stress > 1.2 kPa have hydraulic conductivity < 10^{-11} m/s. Similarly, BPC-GCLs with a BPC swell index greater than 17 mL/2g have hydraulic conductivity < $7x10^{-12}$ m/s. The lack of strong correspondence for either index is not suprising, as neither index accounts for both mechanisms affecting the hydraulic conductivity for BPCs. That is, low hydraulic conductivity corresponding to narrow and tortuous pore spaces can be achieved by swelling of bentonite granules, polymer clogging pore spaces between unswollen bentonite granules, or a combination of both mechanisms.

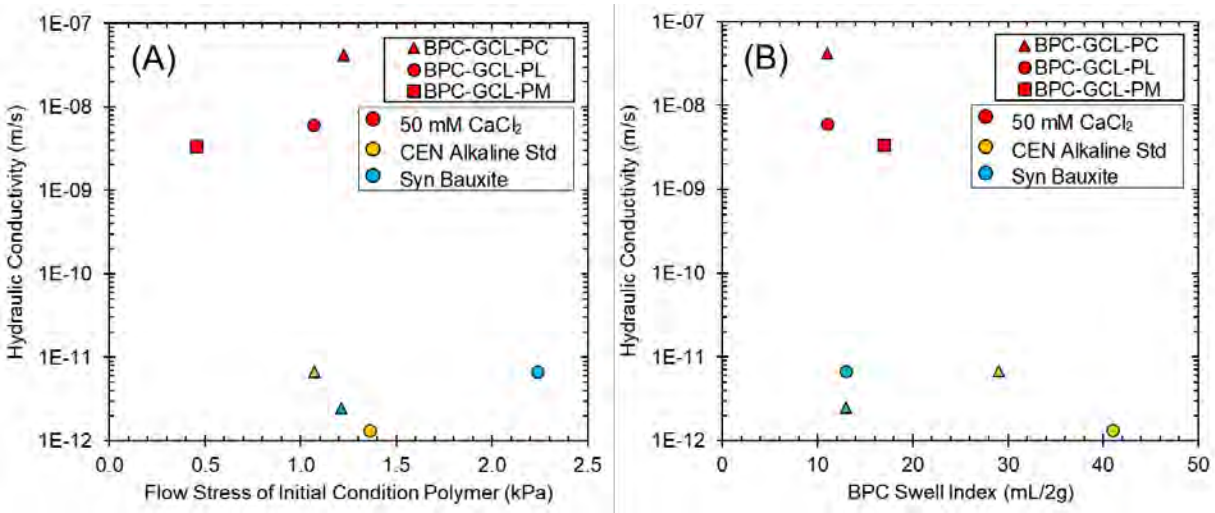

Figure 4. Hydraulic conductivity of BPC-GCLs as a function of (A) flow stress of the initial condition in-situ polymer and (B) BPC swell index.

To account for both mechanisms, hydraulic conductivity was graphed vs. the product of NaB swell index and flow stress of the gel in the BPC as shown in Fig. 5, where the flow stress corresponds to the moisture content of the gel obtained from the competitive moisture content test. Swell index of the NaB is used in lieu of swell index of the BPC to account for the NaB swelling mechanism independent of the gel. This product is referred to herein as the flow-swell index and has units of kPa-mL/2 g.

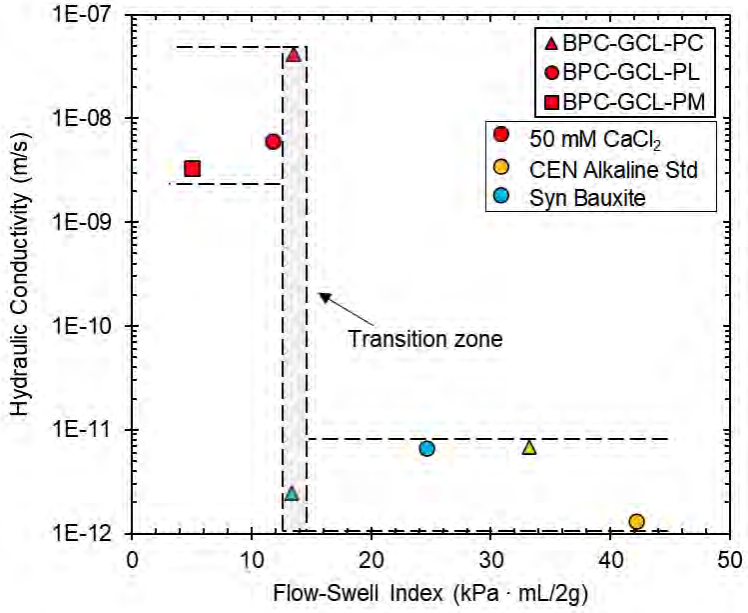

Figure 5. Hydraulic conductivity as a function of flow-swell index, the product of flow stress of polymer gel corresponding to moisture content from bentonite-polymer moisture affinity test and the swell index of NaB in permeant solution.

As illustrated in Fig. 5, a sharp demarcation exists between BPC-GCLs with high and low hydraulic conductivity depending on the flow-swell index. BPC-GCLs with a flow-swell index < 13 kPa-mL/2 g have hydraulic conductivity > $3x10^{-9}$ m/s, whereas BPC-GCLs with a flow-swell index > 14 kPa-mL/2 g have hydraulic conductivity < $7x10^{-12}$ m/s. There is a narrow transition zone where high or low hydraulic conductivties coincide. In this transition zone, BPC-GCL-PC has a similar BPC-GCL flow-swell index when permeated with 50 mM $CaCl_2$ (13.5 kPa-mL/2 g) and synthetic bauxite liquor (13.3 kPa-mL/2 g), but has a much higher hydraulic conductivity ($4.2x10^{-8}$ m/s) when permeated with 50 mM $CaCl_2$.

BPC-GCL-PC permeated with 50 mM $CaCl_2$ initially satisfied the termination criteria described in ASTM D6766 with a hydraulic conductivity of $5.6x10^{-12}$ m/s after transmitting 0.8 PVF, which was similar to the hydraulic conductivity when permeated with the synthetic bauxite liquour ($2.5x10^{-12}$ m/s). However, after after 0.9 PVF the hydraulic conductivity of BPC-GCL-PC to 50 mM $CaCl_2$ increased rapidly, whereas the hydraulic conductivity of BPC-GCL-PC permeated with synthetic bauxite liquor remained relatively constant through 5.1 PVF. Permeation with rhodamine dye revealed a preferential flow path opened in BPC-GCL-PC permeated with 50 mM $CaCl_2$, which was likely a result of polymer elution (Gustitus and Benson 2020). Due to the potential impact of polymer elution, hydraulic conductivities reported early in permeation should be used with caution, even if measurements have met the termination criteria described in ASTM D6766.

CONCLUSIONS

Hydraulic conductivity tests were conducted on three commercially available BPC-GCLs with three permeant solutions ranging in ionic composition, ionic strength, and pH. Flow stress of the polymer gel and swell index of the BPC and the NaB alone were also measured using the same solutions to evaluate whether an index could be identified as an indicator of chemical compatibility.

A clear correspondence between hydraulic conductivity of the BPC-GCLs could not be identified between swell index of the BPC or flow stress of the polymer gel, although thresholds for both indices exist that correspond to low hydraulic conductivity. The lack of correspondence is not suprising, as neither index completely represents the mechanisms controlling the hydraulic conductiviy of BPC-GCLs. The product of polymer gel flow stress and swell index of the NaB component, referred to as the flow-swell index, provides a clear demarcation between conditions corresponding to low and high hydraulic conductivity and a very narrow transition zone where low and high hydraulic conductivities both reside. The flow-swell index is a more effective indicator of chemical compatibility because both of the primary mechanisms (swelling of NaB granules and retention of polymer gel in pore spaces) affecting the size and tortuousity of the pore space are represented. Additional testing using a broader range of BPC-GCLs and chemical solutions is needed to confirm the generality of flow-swell index as an indicator of chemical compatibility.

ACKNOWLEDGMENTS

Financial support for this study was provided by CETCO of Minerals Technology Inc., the US Department of Energy's Consortium for Risk Evaluation with Stakeholder Participation (CRESP) III through Cooperative Agreement No. DE-FC01-06EW07053, the Environmental Research and

Education Foundation through a fellowship to the first author, and the Jefferson Scholars Foundation at University of Virginia. Materials for the study were provided by CETCO.

REFERENCES

ASTM D2216-19. Standard Test Methods for Laboratory Determination of Water (Moisture) Content of Soil and Rock by Mass. *ASTM International*, West Conshohocken, PA.

ASTM D6766-20a. Standard Test Method for Evaluation of Hydraulic Properties of Geosynthetic Clay Liners Permeated with Potentially Incompatible Aqueous Solutions. *ASTM International*, West Conshohocken, PA.

Akin, I. D., Chen, J., Likos, W. J., and Benson, C. H. (2017). Water Vapor Sorption of Bentonite-Polymer Mixtures Contacted with Aggressive Leachates. *Geotechnical Frontiers 2017*, 209–218.

Athanassopoulos, C., Benson, C., Donovan, M., and Chen, J. (2015). Hydraulic Conductivity of a Polymer - Modified GCL Permeated with High - pH Solutions. *Geosynthetics 2015*, Industrial Fabrics Association International, St. Paul, MN, 181–186.

Chen, J., Salihoglu, H., Benson, C. H., and Likos, W. J. (2019). Hydraulic Conductivity of Bentonite-Polymer Geosynthetic Clay Liners to Coal Combustion Product Leachates. *Journal of Geotechnical and Geoenvironmental Engineering*, 145(9), 04019038.

Donovan, M. S., Valorio, R., and Gebka, B. (2017). Polymer Enhanced Geosynthetic Clay Liners for Bauxite Storage. *Proceedings of 35th International ICSOBA Conference, Hamburg, Germany, 2-5 October, 2017*, 469–478.

Geng, W., Likos, W. J., and Benson, C. H. (2016). Viscosity of Polymer-Modified Bentonite as a Hydraulic Performance Index. *Geo-Chicago 2016*, 498–507.

Gustitus, S. A., and Benson, C. H. (2020). Assessing polymer elution and hydraulic conductivity of bentonite-polymer composite geosynthetic clay liners permeated with aggressive solutions. *4th Pan American Conference on Geosynthetics*.

Gustitus, S.A., Nguyen, D., Chen, J. & Benson, C.H. (2020). Quantifying Polymer Loading in Bentonite-Polymer Composites Using Loss on Ignition and Total Carbon Analyses. *Geotechnical Testing Journal*. In Press.

Hornsey, W. P., Scheirs, J., Gates, W. P., and Bouazza, A. (2010). The impact of mining solutions/liquors on geosynthetics. *Geotextiles and Geomembranes*, Elsevier Ltd, 28(2), 191–198.

Jo, H. Y., Katsumi, T., Benson, C. H., and Edil, T. B. (2001). Hydraulic Conductivity and Swelling of Nonprehydrated GCLs Permeated with Single-Species Salt Solutions. *Journal of Geotechnical and Geoenvironmental Engineering*, 127(7), 557–567.

Kolstad, D. C., Benson, C. H., and Edil, T. B. (2004). Hydraulic Conductivity and Swell of Nonprehydrated Geosynthetic Clay Liners Permeated with Multispecies Inorganic Solutions. *Journal of Geotechnical and Geoenvironmental Engineering*, 130(12), 1236–1249.

McRory, J. A., and Ashmawy, A. K. (2005). Polymer Treatment of Bentonite Clay for Contaminant Resistent Barriers. *Geo-Frontiers Congress 2005*, Austin, TX.

Mezger, T. G. (2015). *Applied Rheology*. Anton Paar GmbH, Austria.

Moore, D. M., and Reynolds, R. C. (1989). *X-Ray Diffraction and the Identification and Analysis of Clay Minerals*. Oxford University Press, Oxford.

Norris, A., Scalia, J., and Shackelford, C. (2019). Fluid indicator test (FIT) for screening the hydraulic conductivity of enhanced bentonites to inorganic aqueous solutions. *Proceedings*

of the 8th International Congress on Environmental Geotechnics, 2, 446–453.

Özhan, H. O. (2018). Hydraulic capability of polymer-treated GCLs in saline solutions at elevated temperatures. *Applied Clay Science*, 161, 364–373.

Prongmanee, N., and Chai, J. C. (2019). Performance of Geosynthetic Clay Liner with Polymerized Bentonite in Highly Acidic or Alkaline Solutions. *International Journal of Geosynthetics and Ground Engineering*, Springer International Publishing, 5, 1–11.

Salihoglu, H., Chen, J. N., Likos, W. J., and Benson, C. H. (2016). Hydraulic Conductivity of Bentonite-Polymer Geosynthetic Clay Liners in Coal Combustion Product Leachates. *Geo-Chicago 2016*, 438–447.

Scalia, J., Bareither, C., and Shackelford, C. D. (2018). Advancing the use of geosynthetic clay liners as barriers. *Geotechnical Engineering Journal of the SEAGS & AGSSEA*, 49(4), 100–114.

Scalia, J., Benson, C. H., Bohnhoff, G. L., Edil, T. B., and Shackelford, C. D. (2014). Long-Term Hydraulic Conductivity of a Bentonite-Polymer Composite Permeated with Aggressive Inorganic Solutions. *Journal of Geotechnical and Geoenvironmental Engineering*, 140(3), 04013025.

Scalia, J., Benson, C. H., Edil, T. B., Bonhoff, G. L., and Shackelford, C. D. (2011). Geosynthetic Clay Liners Containing Bentonite Polymer Nanocomposite. *Geo-Frontiers 2011*, 2001–2009.

Scalia, J., Benson, C. H., and Finnegan, M. (2019). Alternate Procedures for Swell Index Testing of Granular Bentonite from GCLs. *Geotechnical Testing Journal*, 42(5), 1169–1184.

Shackelford, C. D., Sevick, G. W., and Eykholt, G. R. (2010). Hydraulic conductivity of geosynthetic clay liners to tailings impoundment solutions. *Geotextiles and Geomembranes*, Elsevier Ltd, 28(2), 149–162.

Tian, K., and Benson, C. H. (2018). Containing Bauxite Liquor Using Bentonite-Polymer Composite Geosynthetic Clay Liners. *Proc. 8th Intl. Conference on Environmental Geotechnics*, L. Zhan, ed., Springer Nature, Singapore, 672–678.

Tian, K., Benson, C. H., and Likos, W. J. (2016a). Hydraulic Conductivity of Geosynthetic Clay Liners to Low-Level Radioactive Waste Leachate. *Journal of Geotechnical and Geoenvironmental Engineering*, 142(8), 04013037.

Tian, K., Likos, W., and Benson, C. (2019). Polymer Elution and Hydraulic Conductivity of Bentonite – Polymer Composite Geosynthetic Clay Liners. *Journal of Geotechnical and Geoenvironmental Engineering*, 145(10), 04019071.

Tian, K., Likos, W. J., and Benson, C. H. (2016b). Pore-Scale Imaging of Polymer-Modified Bentonite in Saline Solutions. *Proc. Geo-Chicago 2016*, American Society of Civil Engineers, ed., Reston, VA, 468–477.

Wang, B., Dong, X., Chen, B., and Dou, T. (2019). Hydraulic Conductivity of Geosynthetic Clay Liners Permeated with Acid Mine Drainage. *Mine Water and the Environment*, Springer Berlin Heidelberg, 38, 658–666.

Geosynthetics Conference

Implications of the Effect of Freeze-Thaw Cycles on a GCL Performance and Potential Leakage through Covers over Arctic Mine Waste

Farah B. Barakat,[1] R. Kerry Rowe,[1] Farhana Jabin,[1] and Richard Brachman[1]

[1]Queen's University; e-mail: 19fb4@queensu.ca

ABSTRACT

Based on the results of composite liners exposed to freeze-thaw conditions where ice lenses were formed due to cryogenic sections, the effect of these conditions on the interface transmissivity and subsequent potential leakage through composite liners used in mine waste covers is examined. This paper briefly discusses the testing conducted to establish the interface transmissivity parameters followed by the modelling conducted to assess the potential leakage for three scenarios, three cover thicknesses giving applied stresses of 10 kPa, 15 kPa, and 20 kPa. The significance of the difference in the thickness of the cover is discussed in the context of both its impact on the number of freeze-thaw cycles and on the ultimate leakage.

INTRODUCTION

There is extensive use of geosynthetics for hydraulic containment applications. Composite liners which are typically comprised of a geomembrane (GMB) laid over a geosynthetic clay liner (GCL) are widely used in applications such as lining the base of landfills or acting as a cover in mine waste facilities to prevent the contamination of the environment surrounding these areas. The GMB and GCL will each typically contain several different types of imperfections such as variations in the thickness of the bentonite along the GCL which results in the lack of perfect direct contact between them. As a result, a parameter called the interface transmissivity, denoted by θ and with dimension of $[L^2T^{-1}]$, is used to represent the resistance to fluid flow between the geomembrane and GCL layers.

Uncovered and exposed to sunlight, polyethylene geomembranes expand when heated and develop wrinkles due to the high coefficient of thermal expansion of polyethylene (Take et. al 2012). The different construction operations performed on top of the liner result in the development of holes in the geomembrane, especially in wrinkles once the cover soil is placed. This occurs even when good quality assurance is present (Gilson-Beck 2019, Rowe 2020). When holes are present in wrinkles, the wrinkles act as a conduit for distributing fluid over a much larger area than would occur if the hole were in direct contact with the GCL. This results in the development of downward flow directly beneath the wrinkle. Due to the lack of perfect contact between the geomembrane and GCL, lateral flow will also develop between the two layers beyond the edges of the wrinkle along a distance called the wetted distance measured from the center of the wrinkle outwards. The presence of this wetted distance leads to the development of additional downward flow beyond the edges of the wrinkle and along the width of the wetted distance. The interface transmissivity, hydraulic conductivity of the GCL, and the pressure head along the GMB-GCL interface are the three main parameters that influence the extent of the wetted distance.

Once the wrinkles form, the GCL section beneath the holed wrinkle is no longer confined since the applied stress on the geomembrane would arc over the wrinkle. The hydraulic conductivity of the GCL, k_{GCL}, is dependent on the stress applied on it. Thus, the hydraulic conductivity along the area beneath the wrinkle will generally be higher than the remaining GCL where the confining stress on the GMB and GCL causes consolidation of the GCL corresponding to a decrease in its bulk void ratio and hydraulic conductivity (Petrov et. al 1997). To differentiate between these two magnitudes of the hydraulic conductivity of the GCL, the value corresponding to the confined section where the GMB and GCL are in direct contact will be denoted by k_a and that of the unconfined section beneath the wrinkle by k_b.

The pressure head on the GCL, h, beneath the wrinkle, decreases as we move away from the wrinkle outwards until it reaches a constant value at a location of zero pressure head difference. The top of the GCL is typically taken as the datum for h. The minimum wetted distance occurs when the subgrade beneath the GCL is fully saturated and the head, h, is zero. This wetted distance is typically denoted by a_o. If the subgrade is not fully saturated and the water table is below the GCL, suctions will develop at the subgrade – GCL interface and the head will continuously decrease until it reaches the point of zero pressure at a depth of C, $h = -C$, and a wetted distance denoted by a. If the soil beneath the GCL is not saturated, the hydraulic conductivity of this soil will be unsaturated; thus, it will vary until it reaches a value that is nearly equal to the saturated conductivity once it reaches the point of zero suction (head). The flow that will pass along the subgrade is highly dependent on this hydraulic conductivity of the soil. As a result, to avoid complication, and to focus on the main scope and objective of this paper, the pressure head on the GCL, h, is assumed to be acting along the GCL-GMB interface ($h = 0$) resulting in leakage under saturated conditions where the wetted distance extends from the center of the wrinkle outwards for a distance of a_o. If a drainage layer is present beneath the GCL then under the applied stress, C is equal to the thickness of the GCL, H_{GCL}.

The flow or leakage that develops beneath the wrinkle, Q (m^3/s), is highly dependent on the wetted distance and the two different hydraulic conductivities of the GCL, and it is calculated using Equation 1 (Rowe 1998).

$$Q = 2L\left[k_{sb}b + \frac{k_{sa}}{\propto}\left(1 - e^{-\propto(a_0 - b)}\right)\right]\frac{h_d}{D} \quad [1]$$

where L is the length of the wrinkle, b is half of the width of the wrinkle, k_{sa} and k_{sb} are the harmonic mean of the hydraulic conductivities of the GCL and the foundation layer beneath it, i.e.,

$$k_{sa} = D / (H_{GCL} / k_a + H_{AL} / k_{AL}), \quad [2]$$

$$\propto = \left[\frac{k_{sa}}{D\theta}\right]^{0.5}, \quad [3]$$

$$D = H_{GCL} + H_{AL}, \quad [4]$$

h_d is the difference in heads between the top of the GCL and the point where there exists zero pressure head, $h_d = h_w + C$, and h_w is the applied water head on the composite liner.

The wetted distance, a_o, can be directly calculated using (Rowe 1998):

$$a_o = b - [ln(C/(h_w+C)]/\alpha, \quad [5]$$

Composite liners have been increasingly used in mine waste applications as covers to prevent contaminant transport. Mine waste covers are typically subjected to low applied stresses that can range between 10 and 25 kPa. The use of composite liners for mine waste covers under arctic conditions results in the formation of ice lenses along the GMB-GCL interface or between the geotextile and sodium bentonite layers of the GCL (Jabin et. al 2020). Depending on the weather conditions and thermal gradient between the top and bottom of the composite liner and the moisture content of the GCL, these lenses experience different number of freeze and thaw cycles over time. Jabin et al. (2020) and Jabin (2020) tested the impact of the number of freeze and thaw cycles on the interface transmissivity of the GMB-GCL interface by performing transmissivity tests on composite liners that have been subjected to five and sixteen freeze and thaw cycles in closed system conditions permeated with GS (Godfrey silty) solution. In addition, to observe the impact of applied stress, Jabin performed these tests under 10 and 15 kPa applied stress (Table 1). Once the specimens experienced the number of freeze and thaw cycles required, they were transferred into a transmissivity cell for testing at the desired applied stress.

Table 1: Interface Transmissivity Results for Composite Liners Subjected to Five and Sixteen Freeze-Thaw Cycles in a Closed System.

Interface Transmissivity, θ (m^2/s)	**Applied Overburden Stress**	
Number of Freeze- Thaw Cycles	10 kPa	15 kPa
5	$4.5x10^{-8}$	$9.2x10^{-10}$
16	$8.3x10^{-7}$	$2.0x10^{-9}$

Additional tests were performed to compare the transmissivity values that can be obtained under low applied loads (10, 15, and 20 kPa) using composite liners subjected to five freeze and thaw cycles under both open and closed system conditions. A solution with the chemical composition to simulate rainwater that has percolated through the cover soil above the GCL was also used as the permeant for these tests. Open system conditions are setup to represent field conditions; thus, the transmissivity results obtained from the composite liners used in this system are meant to be more representative of field conditions than traditional methods of freeze-thaw sample preparation (Jabin et. al 2020). In this setup, the GCL and composite liner was directly placed on the subgrade and was allowed to hydrate from the soil beneath it and, the GCL remained sandwiched between the geomembrane and subgrade throughout its initial hydration and while being subjected to freeze and thaw cycles.

Table 2. Interface Transmissivity Results for Open and Closed System Tests Subjected to Five Freeze-Thaw Cycles.

Interface Transmissivity, θ (m^2/s)	**Applied Overburden Stress**		
System	10 kPa	15 kPa	20 kPa
Closed	$6.0x10^{-9}$	$2.9x10^{-10}$	$1.5x10^{-10}$
Open	$1.1x10^{-6}$	$1.3x10^{-9}$	$6.9x10^{-10}$

The differences in the obtained results listed in Table 2 show that the number of freeze and thaw cycles and the applied overburden stress on the composite liner has an impact on the interface transmissivity of the GMB-GCL interface. In addition, under low loads, there was a large difference in the interface transmissivity results obtained from open and closed system tests. Since the interface transmissivity is a function of the wetted distance and thus, leakage, the main

objectives of this paper is to show how the number of freeze and thaw cycles and their impact on transmissivity can influence leakage and contamination, and discuss the accuracy of the transmissivities obtained from tests subjected to closed system conditions compared to those under open system conditions. These two points will be targeted for cases where the composite liners are subjected to low pressures. In addition, their impact on wetted distance and leakage beneath holed wrinkles will be discussed. Lastly, the paper will identify the impacts of changing the hydraulic conductivity of GCL's on the wetted distance and leakage using open test transmissivity results under different applied stresses, and show how the head on the liner affects leakage beneath the holed wrinkles for different combinations of k_a, k_b, and applied stresses.

METHODOLOGY

Three base cases representing one hectare (ha) of mine waste facility (100 m x 100 m) are assessed in this paper. All three cases consist of 0.3 m thick foundation layer covered with a composite liner consisting of a 1.5 mm thick HDPE geomembrane followed by a 0.01 m thick GCL. The foundation layer was taken to be a sandy material and given a hydraulic conductivity, k_{AL}, of $1x10^{-5}$ m/s. The geosynthetic clay liner was given a k_a value of $6x10^{-11}$ m/s and a k_b value of $6x10^{-10}$ m/s. The applied water head on the composite liner, h_w, was assumed to be 0.15 m. It was assumed that there is one 100 m long holed wrinkle per hectare with a wrinkle width, $2b$, of 0.1 m. The pressure head was assumed to be zero beneath the GCL. For all the calculations that were performed, these parameters remained constant unless otherwise stated. The only difference between the three base cases are the overburden stresses applied on the composite liner for each case shown in Figure 1.

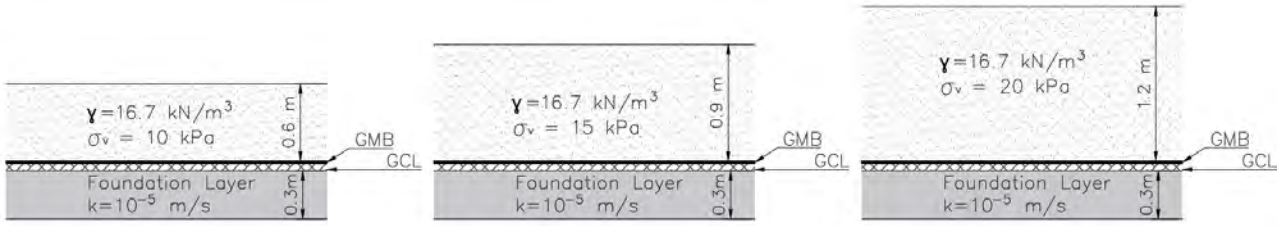

Figure 1: Schematic Drawing of the Three Base Cases

For each case considered and depending on the transmissivity test result taken into consideration from Tables 1 and 2, the wetted distance and leakage flow were calculated using Equations 1 and 5 to identify the degree of leakage flow and contamination that occurs due to the presence of holed wrinkles under the different cases, systems, and parameters considered.

ANALYSIS AND RESULTS

Impact of Number of Freeze and Thaw Cycles under Different Applied Loads.

The wetted distances and leakage were calculated for two of the base cases developed, the cases subjected to 10 and 15 kPa overburden stress, using the different transmissivities obtained where the composite liners were subjected to 5 and 16 freeze-thaw cycles under closed system conditions listed in Table 1.

Table 3: Wetted Distance and Leakage Results under Different Number of Freeze-Thaw Cycles and Applied Overburden Stresses.

Applied Overburden Stress (kPa)	Number of Freeze-Thaw Cycles	a_o (m)	Q (lphd)*
10	5	7.6	50.9
10	16	32.7	191.2
15	5	1.1	14.4
15	16	1.7	17.3

*lphd: liters per hectare per day

The results are listed in Table 3 and show that under a constant overburden stress of 10 kPa, the wetted distance and leakage obtained using the transmissivities of the composite liners subjected to 16 freeze-thaw cycles are more than 4-fold and 3-fold higher than the results obtained using the composite liners subjected to five freeze-thaw cycles respectively. Under an overburden stress of 15 kPa, the wetted distance and leakage calculated using the composite liners that were subjected to 16 freeze-thaw cycles were 50% and 20% higher in magnitude compared to those obtained from the composite liners subjected to five freeze-thaw cycles respectively. This shows that under low overburden stresses, the more the composite liner is subjected to freeze and thaw cycles, the higher the leakage and contamination that is expected to develop beneath the holed wrinkle. As the overburden applied stress on the composite liner increases, the less the degree of impact of the number of freeze-thaw cycles the composite liner is subjected to is on the wetted distance and leakage.

Impact of Using Interface Transmissivity Test Results Obtained from Open and Closed System Setups on Wetted Distance and Leakage.

The transmissivity results tabulated in Table 2 that were obtained for composite liners subjected to five freeze-thaw cycles from two different lab setup systems, an open and closed system, have been used to calculate the wetted distance and flow that will develop beneath the three base cases considered in this paper.

Table 4: Wetted Distance and Leakage Results for Open and Closed System Setup Transmissivities.

Applied Overburden Stress (kPa)	System Type	a_o (m)	Q (lphd)
10	Closed	2.8	23.8
10	Open	37.6	218.8
15	Closed	0.7	11.7
15	Open	1.3	15.5
20	Closed	0.5	10.7
20	Open	1.0	13.6

Under a constant overburden stress of 10 kPa, the wetted distance and leakage obtained from the interface transmissivity listed for the composite liner that was subjected to open system conditions were more than 13-fold and 9-fold higher than those obtained using the transmissivity listed for the test that used a composite liner that was subjected to closed system test conditions for the same number of freeze-thaw cycles. The wetted distance and flow calculation results for

the composite liner subjected to open system conditions under 15 kPa overburden stress were approximately 85% and 30% higher than those obtained under closed system conditions while those under a 20 kPa overburden stress were 2-fold and nearly 25% higher than those obtained under closed system conditions respectively.

The calculated leakage results show that using the parameters obtained from the tests performed for the composite liners subjected to open system conditions were higher than for a closed system. Thus, performing freeze-thaw in an open system gives the more realistic, but higher, calculated flows. Of the cases considered, the difference in the leakage results obtained under the two system setups was maximum for 10 kPa overburden stresses and decreased significantly as the overburden stress increased to 15 and 20 kPa. Therefore, the thickness of cover soil above the liner, and hence overburden stress, becomes an important parameter affecting leakage.

Thus, from this point onwards in this paper, the interface transmissivities obtained from the transmissivity tests using the composite liners subjected to open system lab conditions will be used.

Impact of Using GCL's with Different Hydraulic Conductivities on Leakage.

The hydraulic conductivities of the GCL, k_a and k_b, represent the resistance to the flow of water through the GCL. Thus, the magnitude of the leakage flowing beneath the wetted distance of a holed wrinkle is highly dependent on this parameter. The higher the hydraulic conductivity of the GCL, the higher the leakage expected to be flowing beneath a holed wrinkle. To identify the degree of impact of the hydraulic conductivity of the GCL on the leakage through a holed wrinkle present in a composite liner used for cover applications in the arctic, the same calculations for wetted distance and leakage as those performed in the previous section were made using different combinations of k_a and k_b while keeping all other parameters constant for the three different base cases developed (applied overburden stress on composite liner: 10, 15, and 20 kPa).

The results show that for all three cases, as the hydraulic conductivity of the stressed portion of the GCL, k_a, increases, the flow further increases (Figures 2 to 4). As k_b was increased for all three cases, the flow increased, and this can be seen through the upward shift of the curves in Figures 2 to 4.

Although the same trends are seen along the curves of all three figures, under an applied stress of 10 kPa, the extent of the increase in leakage beneath the wrinkle as k_a is increased was much larger. Under an applied overburden pressure of 15 and 20 kPa, the curves (Figures 3 and 4) show very similar results in terms of magnitude of flow (along the vertical axis) compared to those shown under a 10 kPa overburden stress which indicates that the effect of k_a and k_b is much less as the applied overburden pressures increase and is more applicable when low loads are applied on the composite liner.

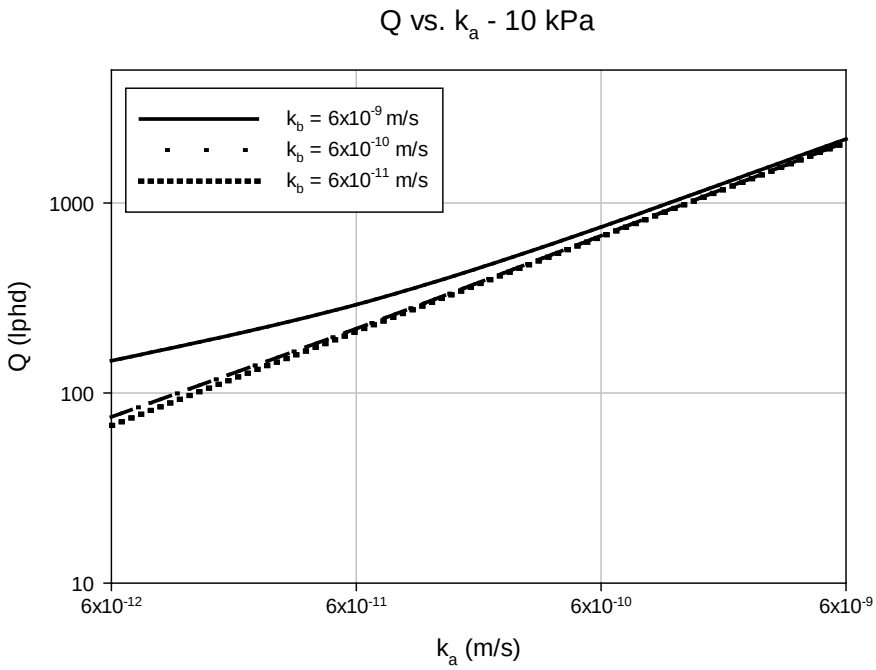

Figure 2: *Q* vs. k_a at Different k_b values under 10 kPa of Applied Stress

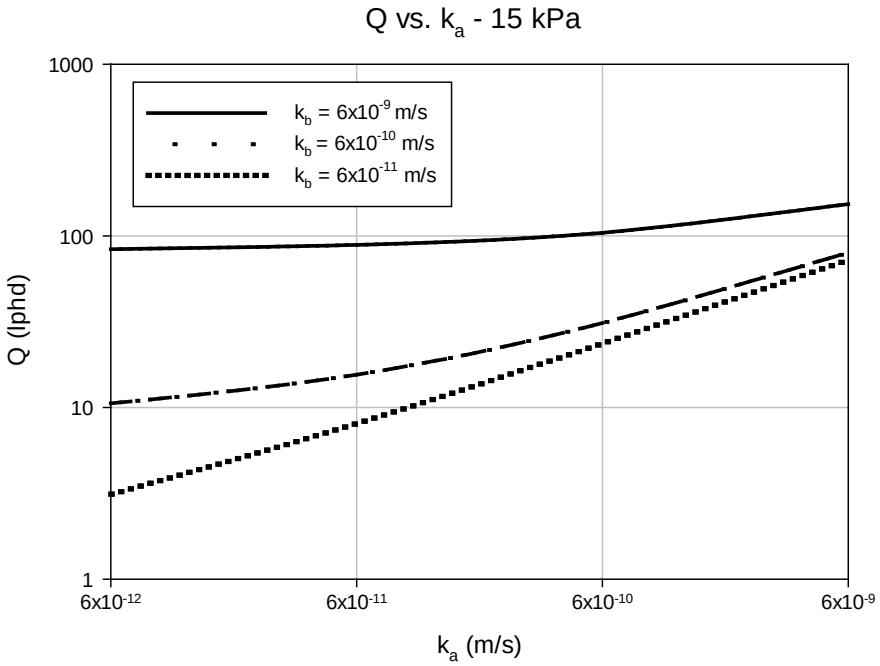

Figure 3: *Q* vs. k_a at Different k_b values under 15 kPa of Applied Stress.

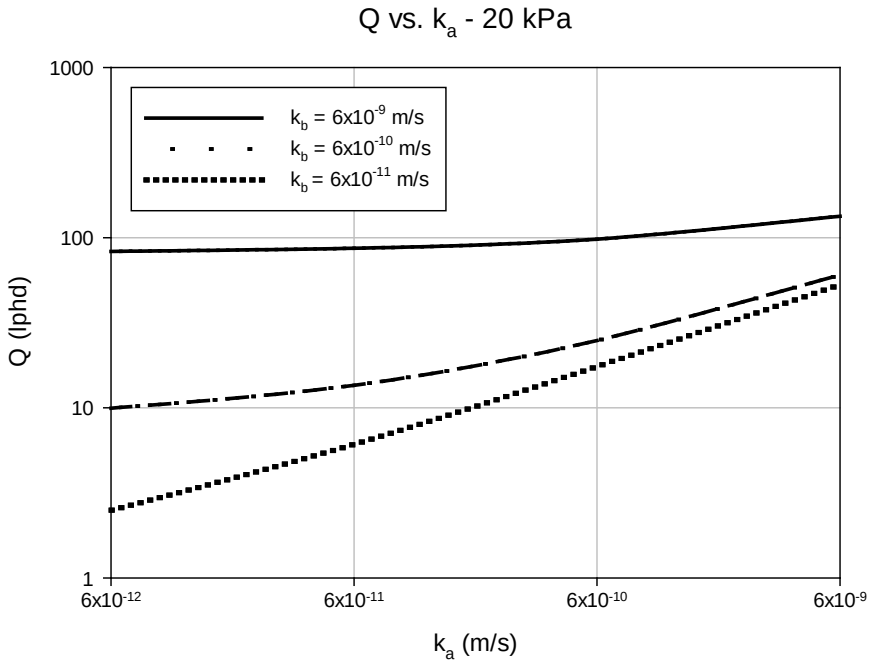

Figure 4: *Q* vs. k_a at Different k_b values under 20 kPa of Applied Stress.

Impact of Changes in the Applied Leachate Head on Flow under Different k_a Values.
The impact of changing the applied water head of the three base cases considered under different k_a values on leakage was tested, and the calculated results were graphed (Figures 5 to 7).

All three figures show that as h_w increases, the curves shift upwards and the calculated leakage increases. In addition, for all applied water heads, as k_a increases, the flow increases especially once k_a exceeds $6x10^{-11}$ m/s where the slopes of the curves increase significantly. In addition, the graphs show that the higher the applied water head on the composite liner, the steeper and more significant is the slope increase of the curves as k_a increases. Comparing Figures 5, 6 and 7 shows that the impact of increasing k_a on leakage is much more significant for a 10 kPa overburden stress compared to 15 and 20 kPa. The effect on leakage of a 5 kPa increase in overburden stress from 15 to 20 kPa was very small compared to the decrease that was observed when the overburden stress is increased from 10 to 15 kPa. This stresses the importance of considering the dependence of the degree of contamination on the applied overburden stresses and obtained interface transmissivity when a composite liner is being used in low load applications such as mining covers.

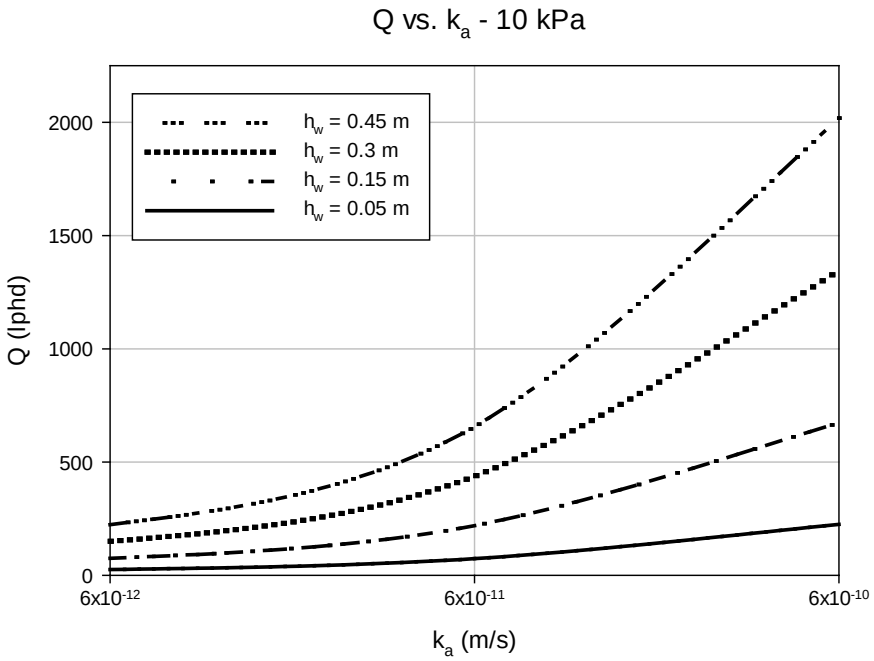

Figure 5: *Q* vs. k_a at Different h_w values under 10 kPa of Applied Stress (k_b = 6x10^{-10} m/s)

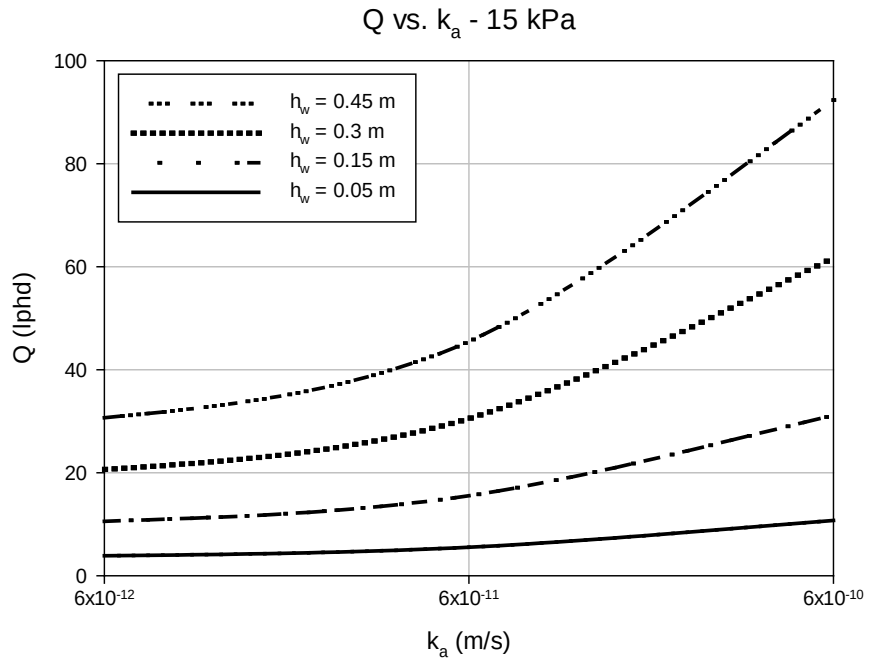

Figure 6: *Q* vs. k_a at Different h_w values under 15 kPa of Applied Stress (k_b = 6x10^{-10} m/s)

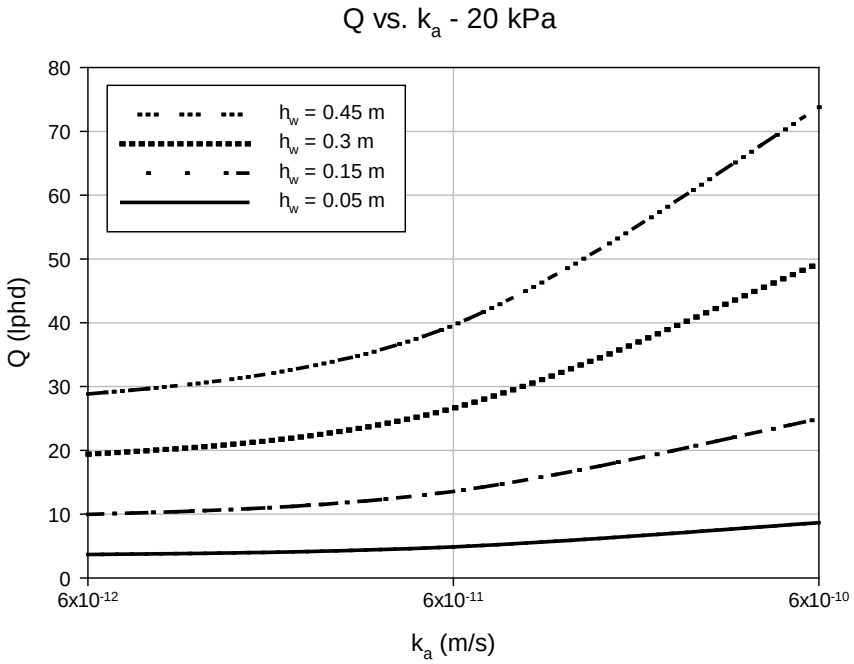

Figure 7: *Q* vs. k_a at Different h_w values under 20 kPa of Applied Stress (k_b = 6x10^{-10} m/s)

CONCLUSION

Recent data published by Jabin et. al listing interface transmissivity values detected under low loads for different conditions subjected to arctic conditions in two different lab setups, closed and open system setups, were used to evaluate the impact of the number of freeze and thaw conditions, type of GCL used in the composite liner, and the applied water head on the leakage that occurs beneath a holed wrinkle in a composite liner used for cover applications. This was done by performing wetted distance and leakage calculations for a hectare of a mine waste facility that uses a composite liner for cover applications having a 100 m long holed wrinkle. Calculations were performed for a range of different parameters under conditions where the cover soil placed on the composite liner applied an overburden pressure of 10, 15 and 20 kPa. Based on these results and for the conditions considered, the following conclusions were reached:

- For composite liners subjected to 5 and 16 freeze-thaw cycles, there was a substantial difference in the interface transmissivity at an applied load of 10 kPa. This resulted in higher calculated leakage for the composite liners subjected to 16 freeze-thaw cycles compared to those subjected to 5 freeze-thaw cycles under the same load. The difference between the leakage calculated under an applied stress of 15 kPa was small compared to that detected under a 10 kPa applied stress.
- Using the interface transmissivities obtained from the composite liners subjected to open system freeze-thaw gave higher calculated leakage than those obtained from the composite liners subjected to closed system freeze-thaw. The difference was most substantial for the case where 10 kPa stress was applied on the composite liner. This shows the importance of selecting the type of lab test setup especially when low loads are applied on the composite liner.
- The hydraulic conductivity of the GCL beneath the GMB is stress dependent causing leakage to be impacted by it. Thus, under the same conditions and parameters, the

calculated leakages for the cases with an overburden stress of 10 kPa were much larger than those calculated under a stress of 15 and 20 kPa. The impact of the applied stress was shown to be much higher on the case with 10 kPa overburden stress.

ACKNOWLEDGEMENTS

Funding for the development of the research infrastructure was provided by Grant CFI 36663 of the Canada Foundation for Innovation and Project 36663 of the Ontario Innovation Trust and the Ontario Research Fund Award. The research was funded by Strategic Grant STPGP 521237 from the Natural Sciences and Engineering Research Council of Canada The support of all those listed above is much appreciated; however, the opinions expressed in the paper are solely those of the authors.

REFERENCES

Gilson-Beck, A. (2019). Controlling Leakage through Installed Geomembranes using Electrical Leak Location. *Geotextiles and Geomembranes*, 47(5):697-710.

Jabin, F. (2020). *Effect of Coating Defect, Desiccation, and Freeze-Thaw Cycles on Geosynthetic Clay Liner (GCLS) – Geomembrane Interface Transmissivity.* Queen's University, Kingston, Ontario, Canada.

Jabin, F., Brachman, R.W.I., and Rowe, R.K. (2020). Preliminary Study of the Effect of Pre-hydration and Freeze-Thaw Cycles on GCL/Geomembrane Interface Transmissivity, *GeoVirtual 2020*, Calgary, AB, Canada.

Petrov, R.J., Rowe, R.K., and Quigley, R.M. (1997). Selected Factors Influencing GCL Hydraulic Conductivity. *Journal of Geotechnical and Geoenvironmental Engineering*, 123(8): 683–695. https://doi.org/10.1061/(ASCE)1090-0241(1997)123:8(683)

Rowe, R.K. (1998). Geosynthetics and the minimization of contaminant migration through barrier systems beneath solid waste. *The 6th International Conference on Geosynthetics*, Industrial Fabrics Association International, St. Paul 25–29 Minn, Atlanta, Ga, USA. 1: 27–103.

Rowe, R.K. (2020). Protecting the Environment with Geosynthetics - The 53rd Karl Terzaghi Lecture. *ASCE Journal of Geotechnical and Geoenvironmental Engineering*, 146(9): 04020081, 10.1061/(ASCE)GT.1943-5606.0002239.

Take, W. A.; Watson, E.; Brachman, R. W. I.; Rowe, R. K. (2012). Thermal Expansion and Contraction of Geomembrane Liners Subjected to Solar Exposure and Backfilling. *Journal of Geotechnical and Geoenvironmental Engineering*, 138 (11):1387–1397. https://doi.org/10.1061/(ASCE)GT.1943-5606.0000694.

Geosynthetics Conference

Premature Hydration of Geosynthetic Clay Liners

Bruno Herlin, P.Eng.,[1] Ryan Ackerman,[2] and Bill Kennedy P.Eng.[3]

[1]Terrafix Geosynthetics Inc., Toronto, ON, Canada; bherlin@terrafixgeo.com
[2]TAG Environmental Inc., Barrie, ON, Canada; ryan_ackerman@tagenv.com
[3]TAG Environmental Inc., Barrie, ON, Canada; bill_kennedy@tagenv.com

ABSTRACT

In general, a Geosynthetic Clay Liner (GCL) deployment should not be carried out in the presence of excessive moisture, nor shall they be left exposed overnight. If the GCL is prematurely hydrated, the project technician and/or engineer shall determine whether the material is acceptable or if alternative measures must be taken to ensure the quality of the design – dependent upon the degree of damage. However, most project sites do not have the luxury of being moisture free. Subgrades might contain the presence of a constant stubborn groundwater and/or a weather event occurs during the deployment of a GCL. What are the effects of "Premature Hydration" on a GCL and what to do in these instances are commonly asked questions. While there are no definitive procedures to quantify a product's usefulness after this type of occurrence, or for determining whether or not the material should be removed and replaced, there are a few rules of thumb that can be followed to aid project personnel in formulating the proper plan of action. The aim of this paper is to offer project site technicians and/or engineers with some guidance that certain needle punched GCLs can withstand weather events and/or be left exposed to the elements for a certain period of time without cause for concern – application dependent. Some basic peel strength laboratory testing was done on fully saturated GCL samples, to provide some insight on how certain GCLs retain their initial needle-punched strengths.

INTRODUCTION

Geosynthetic Clay Liners (GCLs) are typically needle punched reinforced composites which combine two or more durable geotextiles outer layers with a uniform core of natural sodium bentonite clay to form a hydraulic barrier. The wide range of GCL uses include landfill caps and base liner applications, dams, canals, ponds, rivers and lakes, and even waterproofing of buildings and similar structures. Numerous laboratory studies have shown the excellent performance capable with natural sodium bentonite GCLs. In general, GCL deployment should not be carried out in the presence of excessive moisture. In addition, in the usual instance when these materials are to be covered by geomembranes or soil materials, only a certain amount should be deployed in a given working shift as can be covered by geomembrane or soil in that given work shift. This will minimize the potential exposure of material to poor weather conditions. These deployment guidelines on GCLs were made and written prior to the development of needle punched GCLs when GCLs were unreinforced. Unreinforced GCLs such as glued bentonite to a geomembrane are prone to the loss of bentonite in hydrated soil/site conditions rendering them to have no hydraulic barrier capabilities whatsoever, not to mention the fact they should not be used in slope conditions due to the low midplane friction angle of bentonite. A key parameter of needle punched GCLs is their peel strength, the ability of the two or more geotextiles to hold together when shear

stresses are applied, such as when installed on a slope. Needle punching is the process of taking fibers from the "cap" (top) nonwoven geotextile and driving the fibers thru the bentonite (interlocking the bentonite) and driving these fibers into the "backing" (bottom) geotextile. The amount of fibers introduced thru the bentonite and introduced to the backing geotextile determines the peel strength of the product. Some manufacturers will thermally lock these needle-punched fibers to further increase the peel value of the finished GCL. Needle punched GCLs with their interlocking peel strength characteristics offer a mechanical bonding not found with unreinforced GCLs.

PREMATURE HYDRATION

What are the effects of "Premature Hydration" on needle punched GCLs and what to do in these instances are commonly asked questions. While there no definitive procedures to quantify a product's usefulness after this type of occurrence, or for determining whether or not the material should be removed and replaced, there are a few rules of thumb that can be followed to aid project personnel in formulating the proper plan of action. However, it should first be understood from where the remove and replace strategy originated in order to put it into proper context.

BACKGROUND

Prior to the invention of mechanically bound or "reinforced" composite products, or GCLs, bentonite clay was used as an *in-situ* waterproofing barrier system, i.e. constructed in the field. Later, others employed bentonite in a prefabricated product held together with glue. Both the in-situ system and the prefabricated product were delicate in nature due to their non-reinforced construction. Moreover, a small amount of moisture could hydrate the bentonite and essentially render the system or product useless if it were not properly confined. The bentonite was able to swell relatively freely and unconfined, delaminating the geotextiles and rendering it unable to perform as a hydraulic barrier. Even where the geotextiles did not entirely separate, the bentonite could absorb so much water and become so swollen that the bentonite would become very plastic, prone to displacement when subjected to light foot traffic or other localized construction stresses. This phenomenon was easily prevented by adding a modest amount of cover material (6 to 12 inches). However, when this cover material requirement was not achieved, these GCL product manufacturers suggested *"remove and replace GCL that is significantly hydrated before placement of overlying geomembrane or minimum of 12 inches of approved cover soil"*. By the time the reinforced GCLs entered the market, the practice of removal and replacement was commonplace and accepted as the only recourse when premature hydration occurred.

NEEDLE PUNCHED GCLs

Reinforced needle punched GCLs are significantly different from the unreinforced GCLs and other systems (stich bonded or glued GCLs), as there are thousands of fibers extending from one geotextile (nonwoven) through the layer of bentonite into the other carrier geotextile ('scrim' woven or nonwoven) and/or geotextiles (scrim-nonwoven – 2 textiles). This mechanical bonding provides an inherent confining stress not found with unreinforced GCLs. When exposed to water, the swelling bentonite is unable to break this bond. Some GCLs are thermally locked following the needle punching bond, providing an added strength to this bond, leaving the quality of the GCL

essentially undiminished. Therefore, the typical *removal and replacement* practice is typically not necessary.

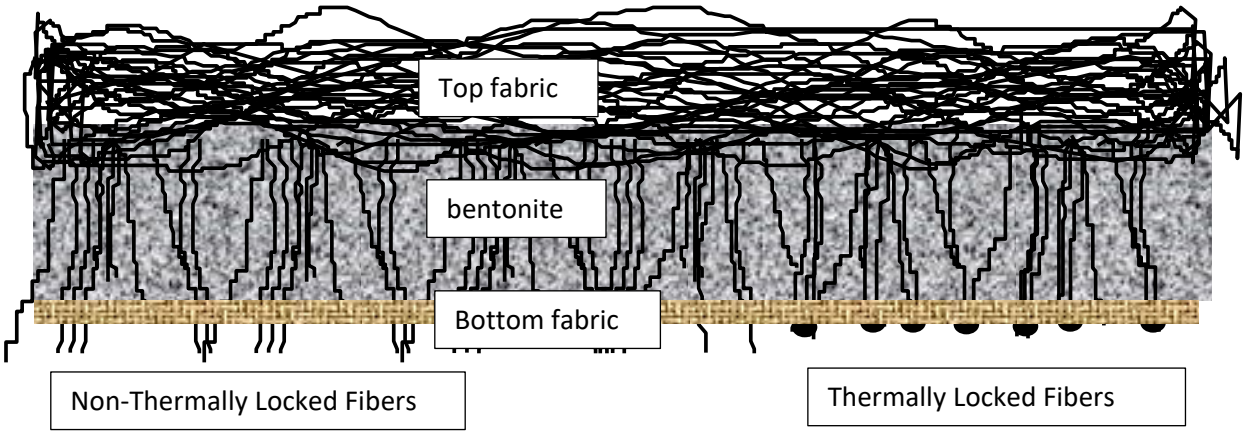

Figure 1: Cross-section of needle punched Geosynthetic Clay Liner. Top fabric being a nonwoven geotextile. Bottom fabric being either a woven or nonwoven or scrim-nonwoven geotextile. Bentonite sandwiched between the top fabric and bottom fabric. Fibers from the top fabric nonwoven are introduced into the bentonite with needle punching boards (needles) and released into the bottom fabric. Some needle punched GCLs are thermally locked to increase the peel strength, i.e. interlock the bottom fabric.

As precipitation can fall in many ways, such a heavy rainfall or a prolonged mist, and as the degree of GCL saturation will be dependent on this factor, the focus of the issue is most appropriately placed on subsequent installation procedures rather than hydration qualifications. With a reinforced needle punched GCL, it is more often the activity that takes place over the hydrated material which causes the damage, not the hydration itself.

Premature hydration or partial hydration in and of itself is not necessarily a damaging event; it merely changes the installation conditions. The needle punching and thermally locked GCLs differentiates these types of GCLs versus other types of GCLs, as they are not prone to delaminating, a phenomenon that can occur with unreinforced GCL products.

That is not to say there aren't circumstances when the removal and replacement of the prematurely hydrated GCL product is necessary. Many site-specific factors influences the "to leave or not to leave" decision including the degree of UV exposure, the degree of hydration, the location of the hydrated material, the liner system profile, the differential loading that the affected area will be subjected to during the completion of the installation as well as by the construction techniques being utilized. All of these factors must be weighted for a 'site-specific' decision to be made.

It should be noted that "removal and replacement" should never be done on a flat-no slope section of a particular project. Leaving a fully hydrated GCL in place will not harm the project design. If the decision is made that the fully hydrated GCL will not achieve the required

permeability during coversoil placement and/or other Geosynthetic material over the fully hydrated GCL, then a new GCL should be applied over the existing fully hydrated GCL, resulting in a double lined GCL system. More harm can be done to the whole project, for example damaging the compacted subgrade during removal of a fully hydrated GCL. For steep slope applications, one might seriously consider removal of a fully hydrated GCL due to slope stability concerns that might arise. The subject of Peel vs Shear for slope stability is not covered in this paper. This paper only looks at the peel strength of fully hydrated GCL located in flat conditions, i.e. at the bottom of a landfill cell or bottom of a pond.

Figure 2. Scrim-Reinforced GCL left exposed for 3 days in a SWM Pond application.

ACCEPTANCE CRITERIA

At a minimum, the GCL should not be torn, separated or otherwise physically damaged. Substantial indentations should not remain where walked upon nor should bentonite extrude through the fabrics when subjected to any other stress. Overlapped seams should be intact, including any accessory bentonite used in the laps. If the surface of the affected area has been subjected to direct flow it should be checked for mass per unit area as prolonged turbulent flow may have the effect of "eroding" away some of the bentonite. Finally, the affected area should not be on a slope greater than 4H:1V.

If these basic conditions are met, the product will likely not require replacement. Once subjected to the design normal loads, the excess absorbed water will consolidate out of the

compressed bentonite and be re-absorbed into the subgrade or drain into the lower drainage media. In some instances where the above conditions are not met, it may be possible to allow the hydrated material to air-dry to the extent where it would not require removal. Again, this is a site-specific determination.

Another factor to consider is the type of GCL being used on a particular project. A standard needle punched GCL with a top fabric nonwoven and a bottom fabric woven will behave and perform differently than a GCL with a top fabric nonwoven and a scrim-nonwoven GCL (3 textile GCL). As shown later in this paper, with testing done on fully hydrated GCLs over an exposed elapsed time.

MATERIALS AND METHODS

Specimens are cut from across the entire width of a Geosynthetic Clay Liner creating a representative sample, which are then submerged in deionized water for various lengths of time. The bottom and top layers of these hydrated samples are gripped individually in tensile grips and pulled at a specified constant rate of extension by a tensile testing machine until the top and bottom layers separate. The average bonding peel strength is then calculated by the Instron Merlin IX interface software as per ASTM Method D6496/D6496M – Standard Test Method for Determining Average Bonding Peel Strength Between Top and Bottom Layers of Needle-Punched Geosynthetic Clay Liners. These values are then compared against the peel bonding strength of the original dry specimen in order to calculate the percentage of peel strength lost over time.

It should be noted that the testing done herein did not review permeability performance. Testing done herein only reviewed the interlocking peel strength of samples after a fully hydrated duration (time) length.

EQUIPMENT

Tensile testing machine - Instron 3365 Universal Testing Machine Utilizing Merlin IX software.
Clamps – 1 by 4 in Instron Screw Action Side Grips, 5kN capacity.
Die – One 13 by 13 in, and one 4 by 8 in.
Container – Appropriately sized waterproof container for submerging samples.
Miscellaneous – Utility Knife.

SAMPLING PROCEDURE

Using a dye as a template, five 13 by 13 in specimens are carefully cut from across the width of the sample. This is repeated four times in total, with an individual 4 by 8 in sample cut from the interior. All samples are cut parallel to machine direction. The 13 by 13 in specimens are then marked with unique identifiers to differentiate soaking times.

Figure 3. Sectioned GCL.

Figure 4. Cut Submerged GCL.

Specimens are completely submerged in a waterproof container for various lengths of time, at which point they are removed from the container, and five 4 x 8 in specimens are carefully cut from the interior of the 13 by 13 in samples.

Using a sharp knife, the bottom and top layer of the GCL are separated for the first 2 in. Specimens are then mounted centrally in the clamps. The Instron 3365 Universal testing machine is set to 12in./min. While running, readings of force and time are collected from 2 in. to 10 in. of grip separation, where an average peeling force is calculated.

Figure 5. GCL in Instron.

RESULTS AND DISCUSSIONS

The results of the tests are summarized in Tables 1 and 2. The percentage loss results are calculated from a dry specimen taken from the same sample to show the loss in strength as a percentage.

Table 1. Nonwoven (top fabric) & Woven (bottom fabric) / Heat Treated GCL.

Time Submerged	ASTM 6496 - Percent loss of peel strength (lbs/in)
8 Hours	38.1%
16 Hours	41.0%
1 Day	42.1%
2 Day	39.0%
5 Day	42.6%
7 Day	46.0%
14 Day	51.0%

Table 2. Nonwoven (top fabric) & Scrim-Nonwoven (bottom fabric) / Heat Treated GCL.

Time Submerged	ASTM 6496 – Percent loss of peel strength (lbs/in)
8 Hours	28.7%
16 Hours	33.1%
1 Day	36.5%
2 Day	35.7%
5 Day	33.6%
7 Day	36.5%
14 Day	40.4%

*All GCLs tested had 3.66 kg/sqm of dry bentonite (@ 0% moisture content) prior to testing.

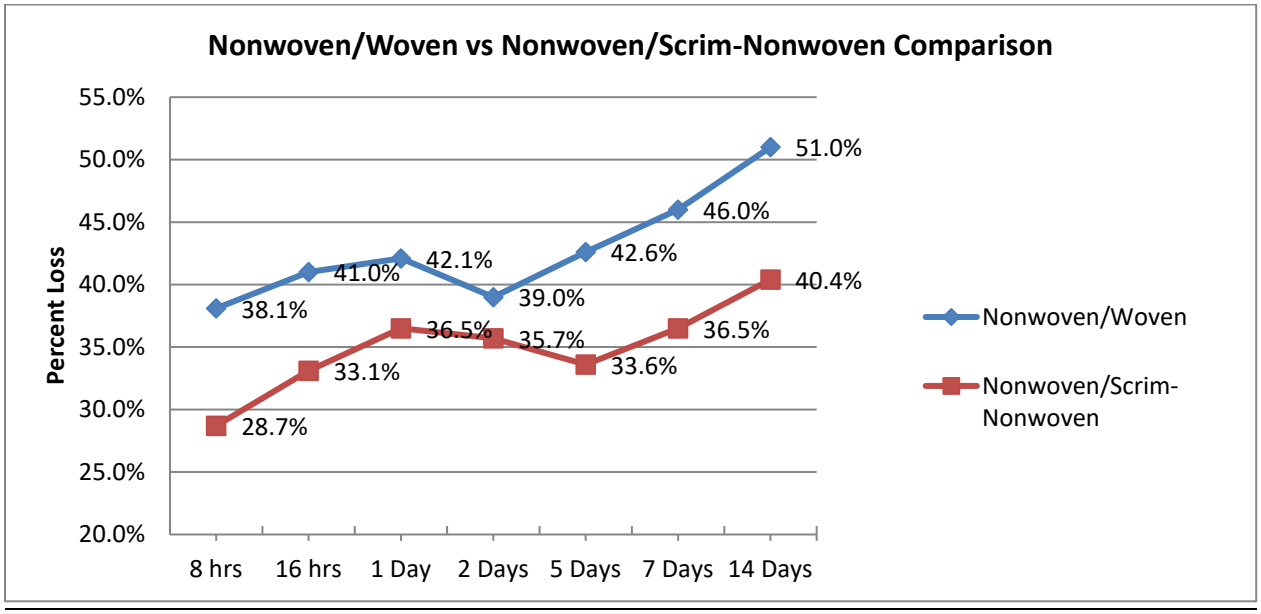

Chart 1. Comparison of Nonwoven/Woven GCL vs Nonwoven/Scrim-Nonwoven Percent Loss of Peel Strength

From the results listed above, one can say that a Scrim-Reinforced Geosynthetic Clay Liner which contains three textiles (Nonwoven top fabric & a Scrim-Nonwoven bottom fabric) can withstand a hydrated event more than a standard two textile GCL. An overnight storm event is no cause for concern for a Scrim-Reinforced GCL but leaving a GCL exposed without any coversoil deployment for more than 2 days might be a cause for concern for a standard two textile GCL (Nonwoven top fabric and woven bottom fabric). A Scrim-Reinforced GCL that contains three textiles can withstand a longer period of hydrated exposure without coversoil based on the results provided herein (up to a week). It should be noted that the testing completed herein was done on fully hydrated samples and we would expect lower percentage loss of peel values if the samples only had a passing rain event, i.e. overnight rain event if the liner was left exposed overnight (the GCL would not be fully hydrated for example on slopes).

Further testing will be done on GCLs which are not thermally treated as well as testing double nonwoven GCLs which are not scrim-reinforced.

CONCLUSIONS

Rejecting and removing a partially hydrated GCL can compromise an installation schedule even if only a small area is affected, without increasing liner quality or performance. While the removal or repair of *damaged* material is recommended to ensure a quality liner is construction, removing partially hydrated GCL is not logical if it is not physically damaged or will not be damaged by a quantified and predetermined installation and/or covering procedure.

Attempting to quantify the degree of hydration is very difficult. A sample with a modest moisture content may not “appear” to be in satisfactory condition whereas a sample with what could be considered an unacceptable moisture content (100% under a confining stress of only 5 psi is possible), may be deemed entirely acceptable. Each case of premature hydration tends to be unique and site specific. The subsequent remedy should be based on the conditions that exist at the location where the hydration occurs.

In the absence of an all-encompassing and industry accepted, quantifiable test procedure, a commonsense approach must be applied when evaluating these relatively common situations.

As this is an installation-related phenomenon, the use of reinforced GCLs should be maximized to ensure the potentially damaging affects of premature hydration are minimized.

REFERENCES

ASTM. (2009). *Standard test method for determining average bonding peel strength between the top and bottom layers of needle-punched geosynthetic clay liners.* ASTM International

Geosynthetics Conference

Comparison of Post-Peak Strengths and Shear Displacements for Multi-Layer and Single Interface Tests for Composite Liner Systems

Thevachandran Shenthan, Ph.D., P.E., G.E., [1] Kris Khilnani, P.E., G.E.,[2] and Timothy D. Stark, Ph.D., P.E., D.GE[3]

[1] Advanced Earth Sciences, Inc., Irvine, California 92618; shenthan@aesciences.com
[2] Advanced Earth Sciences, Inc., Irvine, California 92618; kkhilnani@aesciences.com
[3] Department of Civil and Environmental Engineering, University of Illinois at Urbana-Champaign, Urbana, IL 61801; tstark@illinois.edu

ABSTRACT

Multi-layer interface tests using site-specific composite liner components, typically involving 4-5 layers, provide a direct measure of the lowest peak and large displacement strength of the entire liner system. If performed properly using site-specific and well-developed test procedures, the multi-layer interface test provides reliable, consistent, and repeatable test results that compare well with the results of single interface tests on the weakest interface. This paper presents multi-layer interface shear test results for composite liner systems from eighteen landfill projects in California. Peak strengths, shear displacements at peak strengths, and post-peak strength reduction at the end of shearing were analyzed for multi-layer and single interface tests for four of the eighteen projects. The correlations between the results of multi-layer and single interface tests are found to be excellent. Shear displacements at peak strength for multi-layer tests tend to be slightly higher than for single interface tests, but these have no impact on the mobilized peak and large displacement (LD) strengths, which show excellent agreement between the two test types.

INTRODUCTION

Municipal solid waste and hazardous waste landfills in California are typically lined with a composite liner system involving multiple layers of geosynthetics and earthen materials including low-hydraulic conductivity compacted soil liner, high-density polyethylene (HDPE) geomembrane (GM), geosynthetic clay liner (GCL), drainage geocomposite, geotextile, leachate collection and removal system (LCRS) gravel, and protective cover soil. The composite liner system configurations are designed based on the waste characteristics, level of groundwater protection needed, landfill geometry (slope stability considerations), and regulatory requirements. Interface and internal shear strengths of the composite liner components govern the stability of refuse slopes and are critical for optimizing landfill capacity (Stark and Choi 2004; Stark et al. 2015). Two methods to determine the interface shear strength are: (a) single interface shear tests (using two materials in contact) for each of the interfaces involved and determining the combination peak shear strength envelope for the weakest interface, and (b) multi-layer interface shear test using all of the relevant liner components in a sandwich configuration (Stark et al. 2015, Khilnani et al. 2017, Shenthan et al. 2019). Use of multi-layer method has received considerable recent attention and is now included in the ASTM D5321, 2020 edition.

Although single interface tests provide a better understanding of each interface behavior, it requires multiple tests for each interface and typically 5 to 6 interfaces depending upon the number of liner material components to determine the weakest interface. The multi-layer tests, on

the other hand, directly measure the shear strength of the weakest interface that can be readily used in slope stability analyses (ASTM D7702), reducing costs, and saving time. However, some of the concerns for reliability of multi-layer test results are: (a) shear strength parameters are only obtained for the failure surface and not for other materials or interfaces, some of which may have moved or may have been close to failure, (b) the critical failure surface may be different at different normal loads and the discernment of this may be difficult to interpret from multi-layer interface tests, and (c) shear displacement to reach peak strength in multi-layer tests could be much larger than in single interface tests possibly resulting in an overestimate of LD shear strengths at defined post-peak displacement (typically 75 mm for a 300 mm x 300 mm shear box). Some of these issues were addressed in Shenthan et al. (2019) paper. Also, achieving reliable test results from multi-layer tests requires carefully designed test setup. For example, for tests involving compressible subgrade soil, the test sample is prepared approximately 2 mm above top of the lower shear box to compensate (offset) the potential compression of subgrade soil in the lower shear box for high pressure tests. Additionally, to eliminate the potential for in-plane elongation of the geosynthetics, which is another area of concern, the geosynthetic layer is not clamped or fixed at either end, so no tension is mobilized.

This paper expands on the data presented in Shenthan et al. (2019) for a total of 18 composite liner projects for 11 landfill sites in California and addresses, in particular, comparison of shear displacements at peak strengths for single and multi-layer tests at four of the landfill projects. The paper also discusses the post-peak strength reduction (ratio of peak to LD strength difference to peak strength) for the full data base of 18 landfill projects involving 377 test points.

COMPOSITE LINER SYSTEMS

Figure 1 shows typical details for floor (base/bottom) and side slope composite liner systems discussed. They include (Shenthan et al. 2019):

Floor Composite Liner System (from Top to Bottom)

- Protective cover soil: typically, minimum 0.6 m of minus 25 mm material
- Geotextile filter: typically, 271 g/sm non-woven (NW)
- Granular drainage media: typically, LCRS gravel or coarse sand; sometimes replaced with geocomposite, in which case geotextile filter and cushion layers may be eliminated
- Geotextile cushion: typically, 407 g/sm NW
- Double-side textured (DST) HDPE GM: typically, 1.5 mm or 2.0 mm thick
- GCL: typically, granular bentonite encapsulated between two layers of NW geotextile or between NW and woven geotextile layers, and needle punched (reinforced)
- DST HDPE GM (in case of encapsulated GCL): typically, 1.0 mm or 1.5 mm thick
- Prepared subgrade, foundation soil layer, or compacted soil liner: typically, a 0.3 to 0.6 m engineered fill material with typical hydraulic conductivity of $1.0x10^{-5}$ to $1.0x10^{-6}$ cm/sec

Side Slope Composite Liner System (from Top to Bottom)

- Protective cover soil: typically, minimum 0.6 m of minus 25 mm material
- Geotextile cushion or geocomposite: typically, 542 g/sm NW geotextile or 7.5 mm geocomposite

- Single-side textured (SST) HDPE GM: typically, 1.5 mm or 2.0 mm thick and installed textured side down to create a slip layer on the smooth side; in a few cases, DST HDPE GM is used on the side slope, where higher interface strength is desired for slope stability
- GCL
- Prepared subgrade soil that may be native soil or engineered fill

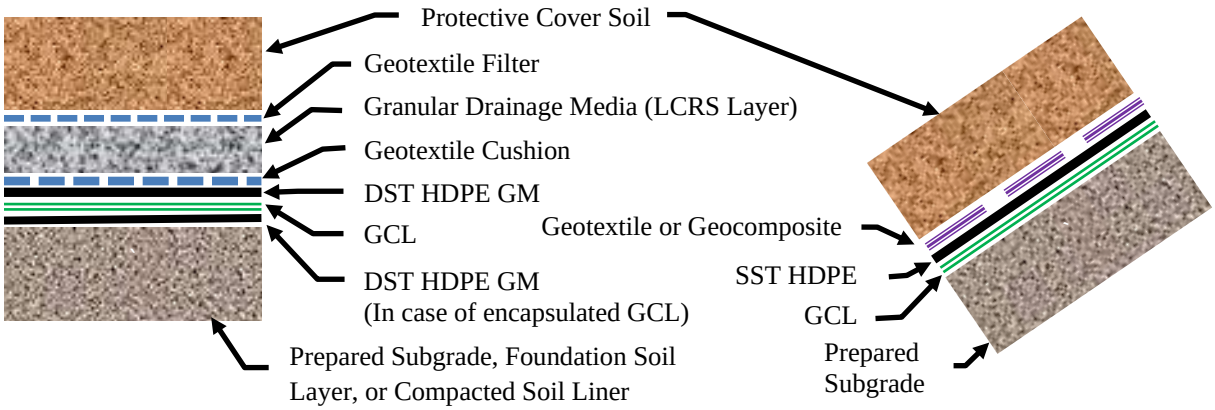

(a) Floor Liner (b) Side Slope Liner

Figure 1. Typical Composite Liner System

The key parameter that controls the critical interface and the corresponding interface shear strength is texturing of the GM. When SST GM is used, the critical interface will almost always be the smooth side of the GM against geotextile or geocomposite, as applicable. On the other hand, when DST GM is used, the weakest interface could be on Geotextile/GM, GM/GCL, or GM/Subgrade depending on the peak strength of the respective interfaces. The weakest interface would be the one with the lowest peak strength. For an unencapsulated GCL, i.e., GCL installed directly on subgrade (or compacted soil liner), the critical interface could even be the GCL/subgrade (or compacted soil liner), although that is uncommon. The composite liner systems discussed in this paper include four different configurations, including (a) DST GM/GCL/DST GM (encapsulated GCL), (b) DST GM/GCL/subgrade (unencapsulated GCL), (c) DST GM/Compacted Soil Liner (no GCL) – Subtitle D liner (Code of Federal Regulations 2012), and (d) SST GM on GCL and overlain by Geotextile or Geocomposite (for side slope liner).

COMPARISON OF SINGLE AND MULTI-LAYER INTERFACE TESTS

Data from four projects, where both single interface and multi-layer interface shear tests were performed are presented in this section. Peak strengths, shear displacements at peak strengths, and post-peak strength reduction at large displacement were analyzed.

Site 1 (Encapsulated GCL). The composite liner for this site consists of (top to bottom) LCRS gravel, geotextile, DST HDPE GM, GCL, DST HDPE GM, and prepared subgrade. Single and multi-layer interface tests were conducted using hydrated and as-received (unhydrated) GCL. In the multi-layer interface tests, concrete sand was used in place of the LCRS gravel. Results from these tests were subjected to detail studies by Stark et al. (2015). A comparison of LD strengths between single and multi-layer interface tests were also made by Shenthan et al. (2019). Figure 2

presents a comparison of displacements at peak strengths for both multi-layer and single interface tests. For tests with unhydrated GCL, the failure occurred on either the GM/Geotextile or GCL/GM interface depending on the applied normal stress. For hydrated GCL, the failure always occurred on GCL/GM interface.

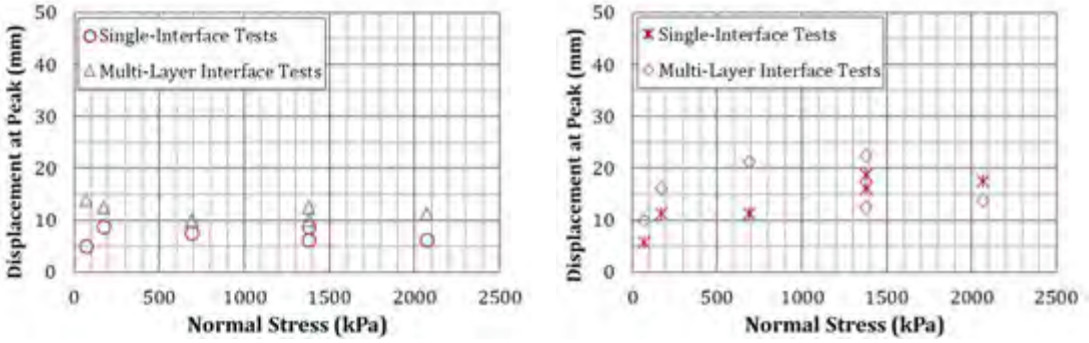

(a) Unhydrated GCL (b) Hydrated GCL

Figure 2. Comparison of Shear Displacements at Peak Strength for Site 1

For the unhydrated GCL, the shear displacements at peak strength for single interface tests and multi-layer tests are relatively close at about 10 mm. For the hydrated GCL tests, the displacements at peak strengths for multi-layer tests are larger than single interface, but both appear to increase with increasing applied normal stress. However, the LD strengths for both single and multi-layer interface tests with the hydrated GCL are nearly identical, as discussed below.

Figure 3 compares peak and LD shear strength results for the above tests. Combination strength envelopes for single interface tests were developed using Stark et al. (2015) methodology. For unhydrated GCL tests, both peak and LD shear strengths from multi-layer tests compare well with those from single interface tests, except at the highest normal stress (1,500 kPa), at which the LD strength from single interface test is slightly lower than the multi-layer test. In Figure 3(b), the peak hydrated GCL shear strengths from multi-layer tests are higher than those from single interface tests with the difference increasing with normal stress. LD results from single interface tests using hydrated GCL are about 30% lower for a normal stress of 700 kPa and up to 15% lower for larger normal stresses. The average LD strengths of hydrated and unhydrated GCL tests, which is adopted as the design strength for an encapsulated GCL liner system in California, are typically 10% lower for single interface tests as compared to multi-layer tests.

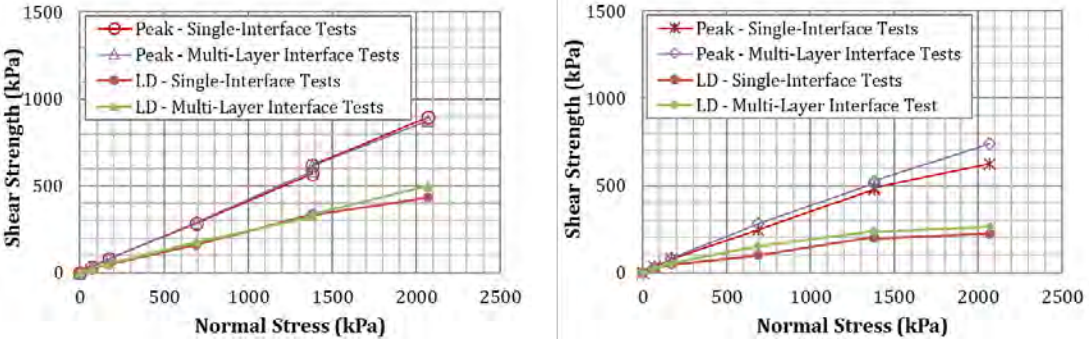

(a) Unhydrated GCL (b) Hydrated GCL

Figure 3. Comparison of Peak and LD Shear Strength Envelopes for Site 1

Based on the information provided by the testing laboratory, the differences may be due to the type of substrate. For the single interface tests, the GM was affixed to steel with mini spikes,

while for multi-layer tests, the actual soil material was used (Stark et al. 2015), which allows some compression and extra shear resistance as the upper shear box translates.

Another criterion, although qualitative in nature, that could be used to compare single interface vs. multi-layer interface strengths, is the post-peak strength drop. The peak to LD strength drop is dependent on the material types and applied normal stress. Figure 4 compares the post-peak strength drop for single and multi-layer interface tests for Site 1. The strength drops are relatively close for the unhydrated and hydrated GCLs.

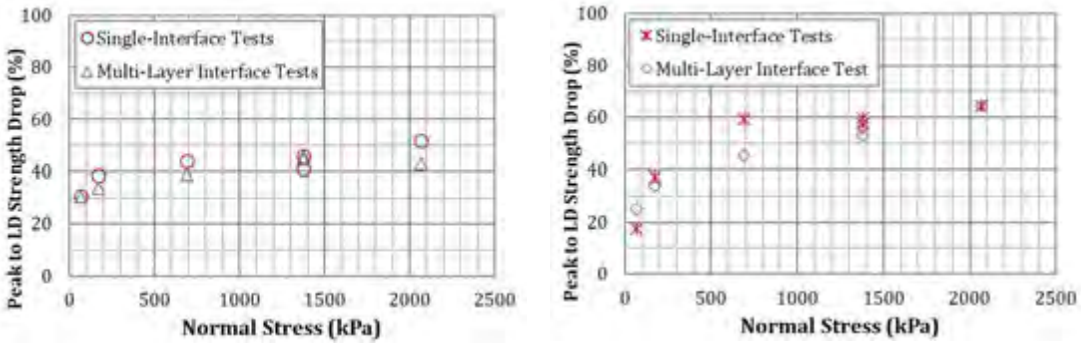

(a) Unhydrated GCL (b) Hydrated GCL

Figure 4. Comparison of Post-Peak Shear Strength Reduction for Site 1

Site 2 (Unencapsulated GCL). There were two types of composite liner used: (a) LCRS Gravel/ DST GM/GCL/Foundation Soil Layer and (b) Protective Soil Cover/Geocomposite/DST GM/GCL/Subgrade soil. For both liner systems the GCL was tested in a hydrated condition. A comparison of shear strength vs. shear displacement plots for single and multi-layer tests are presented in Figure 5. For liner system (a), the weakest interface is the hydrated GCL/DST GM. At the highest normal stress, internal failure of the GCL occurred for both the single and multi-layer tests. Although the stress-displacement plots vary slightly (see Figure 5), the LD strengths for single and multi-layer tests are nearly identical.

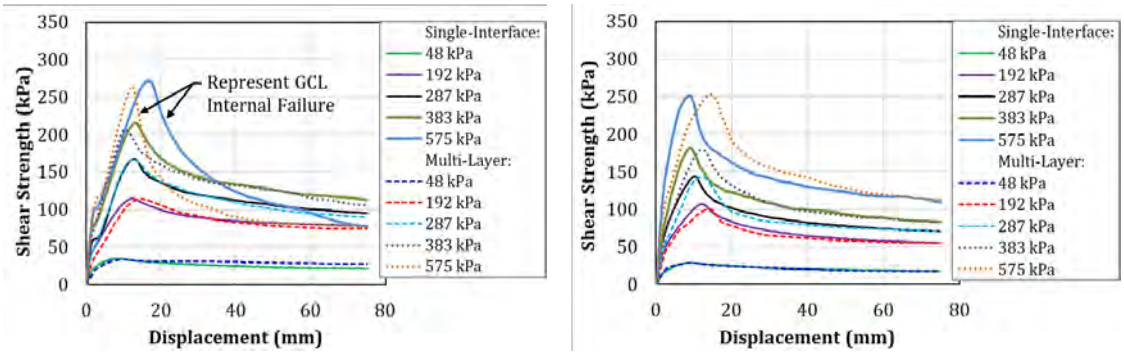

(a) Failure on GCL/DST GM (b) Failure on DST GM/Geocomposite

Figure 5. Shear Strength vs. Shear Displacement Plots for Site 2

Figure 6 presents shear strength vs. displacement relationships for all of the single interface tests performed for liner system (b) at a normal load of 383 kPa. Figure 6 also presents the result from the corresponding multi-layer test. During the Foundation Soil Layer/GCL single interface test, the GCL failed internally. However, the GM/Geocomposite interface is the critical interface because it exhibited the lowest peak strength. In summary, the multi-layer test correctly identified the critical interface identified by the single interface tests.

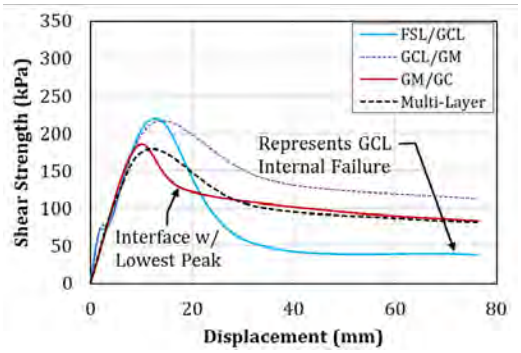

Figure 6. Shear Strength vs. Displacement Plots at Normal Load of 383 kPa for Site 2

A comparison of shear displacements at the peak strength condition for Site 2 is presented in Figure 7. Displacements are similar for both types of liner systems, i.e., (a) and (b), under both types of tests. These displacements, typically 10 to 15 mm, are low compared to the LD (75 mm), and have no impact on the LD strengths from single and multi-layer tests.

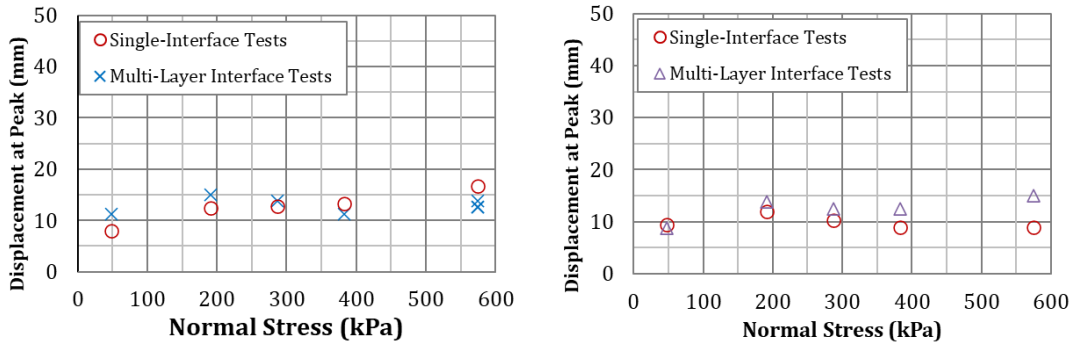

(a) Failure on GCL/DST GM (b) Failure on DST GM/Geocomposite

Figure 7. Comparison of Shear Displacements at Peak Strength for Site 2

Figure 8 presents peak and LD shear strength envelopes from the single and multi-layer tests for Site 2. The multi-layer test strength envelopes compare well with the single interface test envelopes for the weakest interface. A comparison was also made of the post-peak strength drop, and the results are presented in Figure 9. Once again, the strength drop, although only a qualitative indicator as previously discussed, is similar for single interface and multi-layer interface tests, which is important because the LD strength controls the static and seismic slope design using the scenarios proposed by Stark and Poeppel (1994).

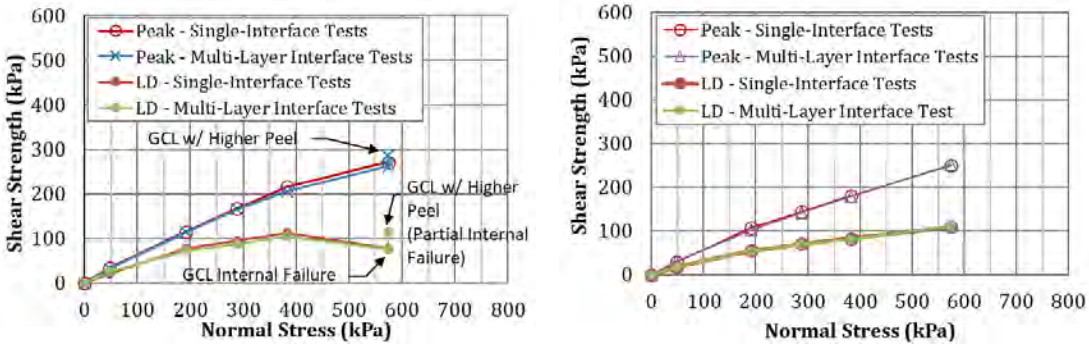

(a) Failure on GCL/DST GM (b) Failure on DST GM/Geocomposite

Figure 8. Comparison of Peak and LD Shear Strength Envelopes for Site 2

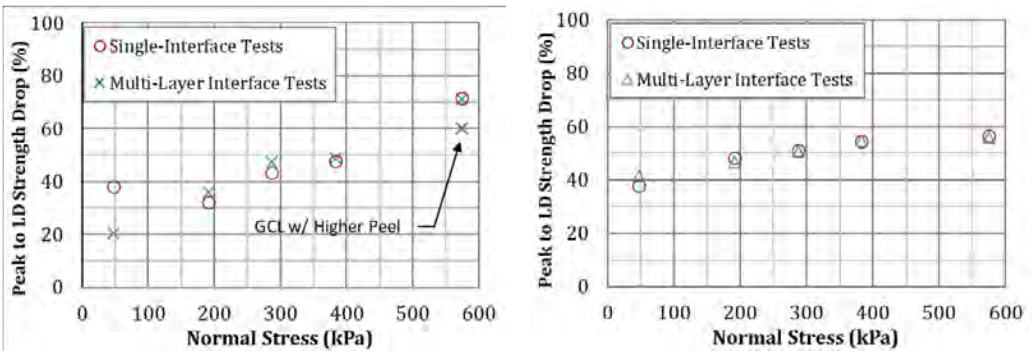

(a) Failure on GCL/DST GM (b) Failure on DST GM/Geocomposite

Figure 9. Comparison of Post-Peak Shear Strength Reduction for Site 2

Site 3 (Unencapsulated GCL). The composite liner system for this site consists of (top to bottom) Protective Cover Soil/Geocomposite/DST GM/GCL/Foundation Soil Layer. Single interface tests were only performed on the weakest interface, i.e., GM/Geocomposite. Shear strength vs. displacement plots and displacements at peak strength are presented in Figure 10. The multi-layer tests show larger displacements at the peak strength compared to single interface tests. However, the displacements are relatively small (10 to 20 mm) compared to the LD value of shear displacement (75 mm) and the interfaces underwent similar post-peak displacements to reach almost the same LD strength values as single interface tests. The large difference in displacements at peak strength between multi-layer and single interface tests may be attributable to the type of GCL (needle punched vs. threads locked by heat burnishing), type of bentonite (powdered vs. granular), test conditions, etc. More data on different types of GCL material are needed to confirm this. Figure 11(a) presents peak and LD shear strength envelopes for the single and multi-layer tests for Site 3. The multi-layer test peak and LD strength envelopes are in excellent agreement with the single interface test envelopes for the weakest interface. A comparison was also made of the post-peak strength drop, and the results are presented in Figure 11(b). The strength drop is again similar for single interface and multi-layer interface tests, which is important for slope design.

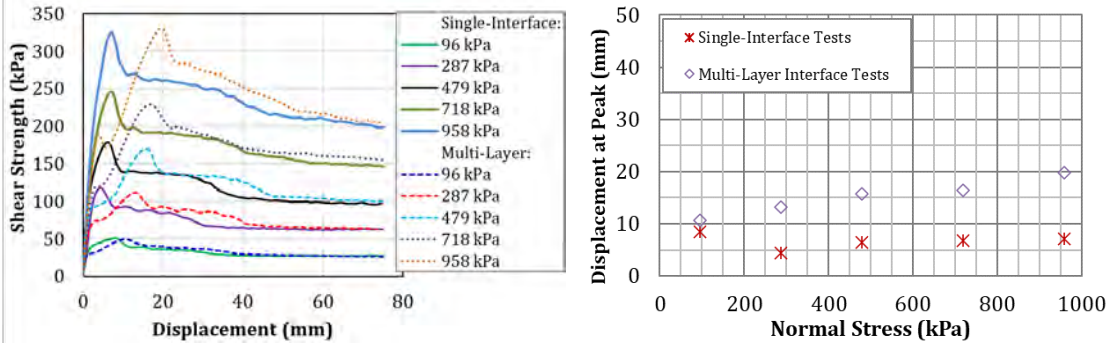

(a) Shear Strength vs. Displacement (b) Shear Displacements at Peak

Figure 10. Comparison of Shear Displacement Relationships and Displacements at Peak Strength for Site 3 (Failure on DST GM/Geocomposite)

Site 4 (Subtitle D Liner – GM/Compacted Soil Liner, No GCL). The composite liner system for this site consists of (top to bottom) LCRS Gravel/Geotextile/DST GM/Compacted Soil Liner. Single interface tests were only performed for the critical interface, i.e., GM/Geotextile. Shear strength vs. displacement plots and displacements at peak strength are presented in Figure 12.

Displacements at peak strength, and peak and LD strength values are almost identical for the single and multi-layer interface tests. Figure 13(a) presents peak and LD shear strength envelopes for the single and multi-layer tests for Site 4. The multi-layer test peak and LD strength envelopes are again in excellent agreement with the single interface test envelopes for the weakest interface. A comparison was also made of the post-peak strength drop, and the results are presented in Figure 13(b). The strength drop is again similar for single interface and multi-layer interface tests, which is important for slope design.

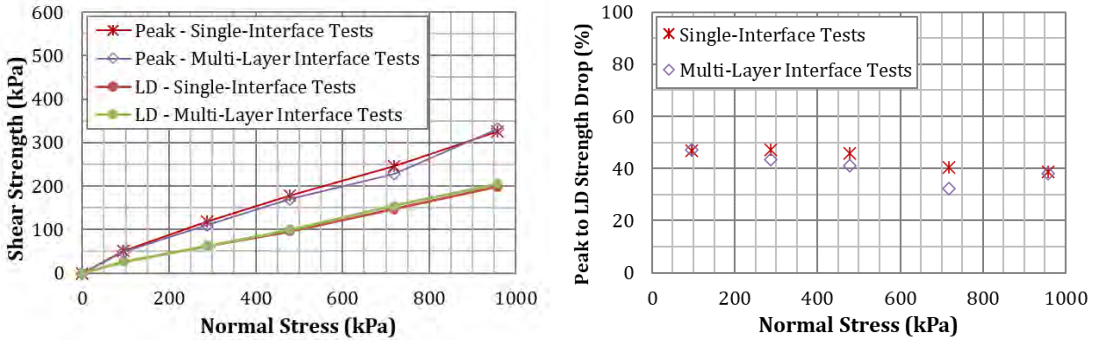

(a) Shear Strength Envelopes (b) Post-Peak Shear Strength Reduction

Figure 11. Comparison of Peak and LD Shear Strength Envelopes for Site 3

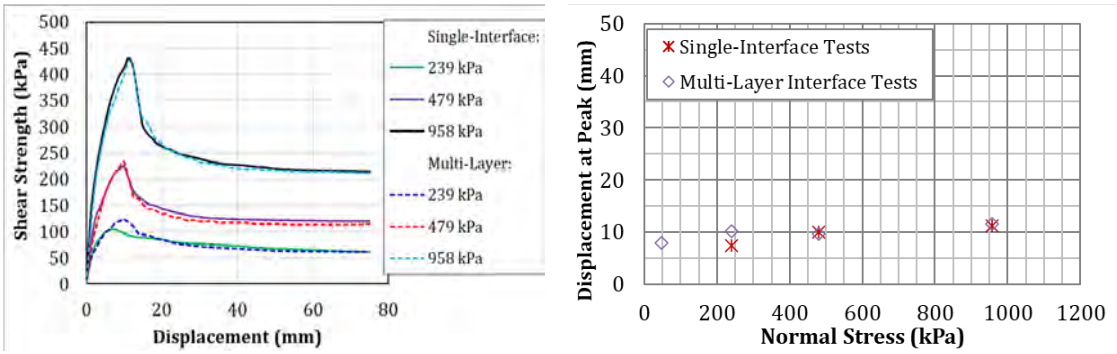

(a) Shear Strength vs. Displacement (b) Shear Displacements at Peak

Figure 12. Comparison of Shear Displacements for Site 4 (Failure on DST GM/Geotextile)

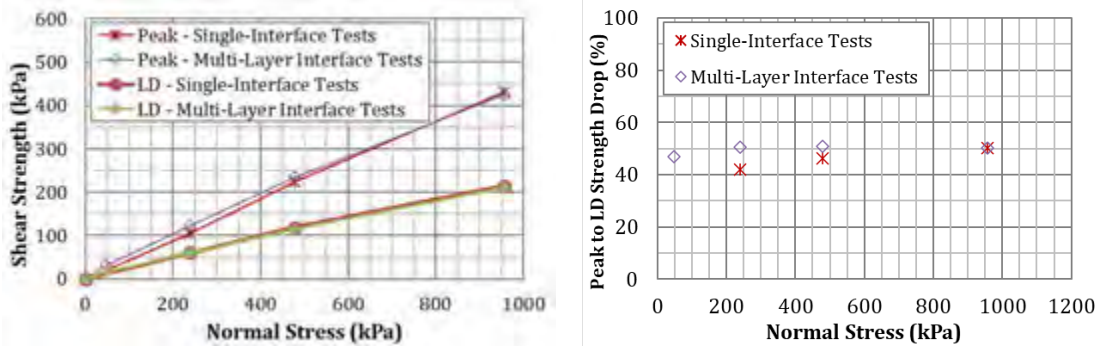

(a) Shear Strength Envelopes (b) Post-Peak Shear Strength Reduction

Figure 13. Comparison of Peak and LD Shear Strength Envelopes for Site 4

Summary of Data from All Four Sites. Figure 14 presents a comparison of displacements at peak strength and shear strength results for 30 single and multi-layer tests performed for the four sites discussed above. The results show strong agreement for peak and LD strengths from single and

multi-layer interface tests. The scatter in the displacements at peak strengths between the two types of tests (see Figure 14(a)) is from the data for Site 3 (Figure 10(a)) discussed above.

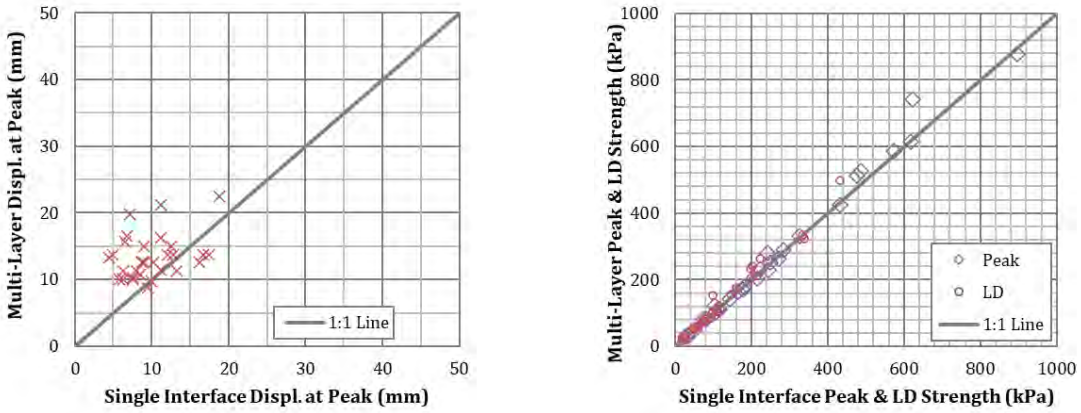

(a) Shear Displacements at Peak (b) Peak & LD Shear Strength

Figure 14. Comparison of Peak Shear Displacements and Shear Strengths for All Four Sites

PEAK STRENGTH DATA SUMMARY

A large database of multi-layer interface tests (ASTM D5321/D6243) has been developed from interface tests for 18 landfill projects. The results are divided into the four composite liner configurations described above. The LD strengths are reported in Shenthan et al. (2019). Peak strengths and shear displacements at peak strengths are reported herein.

Category (a) - DST GM and Encapsulated GCL. Figure 15 shows peak shear strength results from six projects, with a total of 74 test points for hydrated GCL and 62 tests points for unhydrated GCL. The results indicate the following:

- For the tests with hydrated GCL, the critical interface is the GM/GCL interface for 70 of the 74 points. For four (4) points, the failure occurred on the GM/Compacted Soil Liner interface.
- For the tests with unhydrated GCL, the critical interface is generally the upper or lower GM/GCL (37 out of 62); for 19 out of 62 tests, the critical interface is the GM/Geotextile or Geocomposite interface, and for 6 out of the 62 tests, failure occurred on the GM/Compacted Soil Liner interface.
- The data shows good repeatability between multi-layer interface tests for normal stresses up to about 1,350 kPa. Significant scatter is observed at normal stresses greater than 1,350 kPa. Best strength envelopes and the corresponding equations are shown in Figure 15. The average of the LD strengths for the hydrated and unhydrated GCL tests in Figure 15 can be used for preliminary design of an encapsulated GCL but must be verified for final design.
- The results show stress-dependent shear strength behavior with adhesion trending to zero.
- There is considerable scatter in the shear displacements at peak strength (typically 10 to 30 mm) with much greater scatter for the hydrated GCL condition.

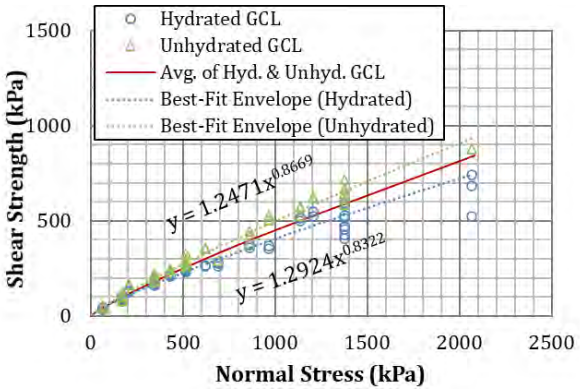

Figure 15. Peak Shear Strength Data - DST GM and Encapsulated GCL

Category (b) - DST GM and Unencapsulated GCL. Figure 16 shows the results from 110 tests performed using unencapsulated GCL for eight projects. Tests were performed with a fully hydrated GCL. The results indicate:

- Similar to an encapsulated GCL, the unencapsulated GCL liner system also exhibits stress-dependent shear strength behavior.
- The weakest interface is either GM/hydrated GCL or GM/Geotextile or Geocomposite, when geocomposite was used. GM/Geotextile provides the benefit that it typically exhibits a lower peak strength than the GM/hydrated GCL interface at low normal stresses, but a higher LD strength.
- Displacements at the peak strength typically range from 10 mm to 30 mm.

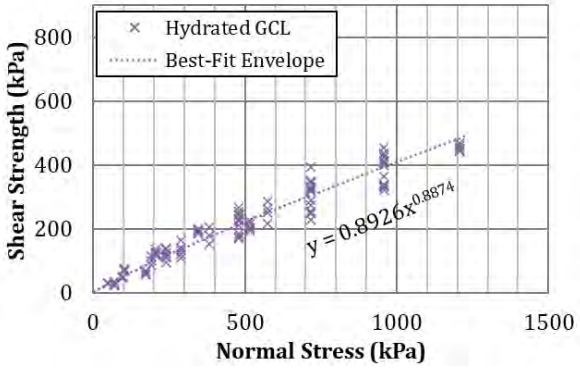

Figure 16. Peak Shear Strength Data - DST GM and Unencapsulated GCL

Category (c) - DST GM on Compacted Soil Liner. Figure 17 shows results from 39 tests performed for six projects, where a Subtitle D composite liner system with a GM underlain by 600 mm thick low hydraulic conductivity compacted soil liner was used as the composite liner. The results indicate:

- Critical failure surface is either the GM/Compacted Soil Liner (15 out of 39) or GM/Geotextile or Geocomposite interface, when geocomposite was used.
- The best-fit strength envelope also shows stress dependent shear strength behavior.
- Displacement at the peak strength typically ranges from less than 10 mm to 20 mm.

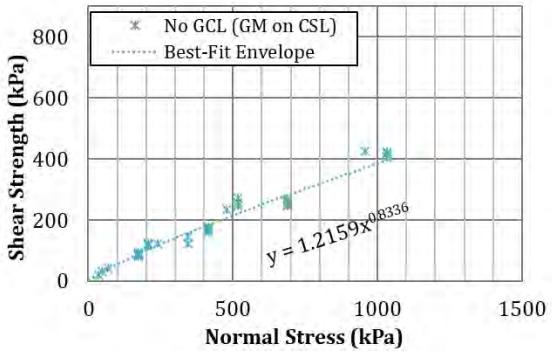

Figure 17. Peak Shear Strength Data – DST GM on Compacted Soil Liner and No GCL

Category (d) - Composite Liner with SST GM (Side Slope Liner). Figure 18 shows the results from 92 tests performed for eight projects, where SST GM was used on side slopes. The multi-layer test configuration included a GM with the textured side down against a hydrated GCL and overlain by cushion geotextile or geocomposite. The results indicate:

- The critical failure surface is always the smooth GM/Geotextile or Geocomposite interface as expected.
- The peak shear strengths are consistent and repeatable because the smooth geomembrane surface creates little variability.
- The best-fit strength envelope is relatively linear and not stress dependent because there is little change in behavior with increasing normal stress.
- Because the tests results show limited variability and the critical interface is always the smooth GM side and geotextile or geocomposite, single interface tests may generally suffice in lieu of multi-layer tests.
- The shear displacements at the peak strength are typically less than 10 mm.

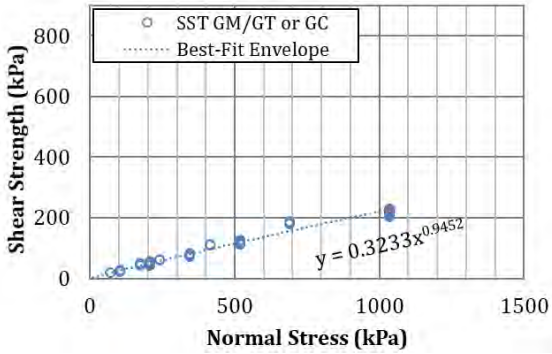

Figure 18. Peak Shear Strength Data - Composite Liner System with SST GM (Side Slope Liner)

SUMMARY

Multi-layer interface data from 18 projects involving 377 interface tests are presented in this paper. Comparisons are made between multi-layer and single interface tests for four sites where both types of interface tests were performed. The following observations can be made:

- Multi-layer interface tests, if performed using careful test setup and well-developed site-specific test procedures, provide reliable, consistent, and repeatable results for direct use of measured LD strengths for slope stability analyses.

- Failure interfaces from the multi-layer tests are the same as those interpreted from single interface tests for the four projects discussed in this paper.
- Peak and LD strength envelopes from multi-layer tests compare extremely well with those from single interface tests for 3 out of the 4 projects and liner systems compared.
- Using boundary conditions (clamping of geosynthetics, substrate material, drainage, etc.) that do not represent the actual field conditions may affect the test results. Particularly, the slight difference in strength envelopes discussed in the paper may be attributed to the different substrates used in the single and multi-layer interface tests.
- For multi-layer tests, displacements at the peak strength tend to be slightly higher compared to single interface tests. However, the displacements are typically less than 30 mm, allowing adequate post-peak displacements. The LD strengths are nearly identical for single and multi-layer interface tests despite the variability in the shear displacements at peak strength.
- Another qualitative tool that may be used as an indicator of reliability of multi-layer tests vs. single interface tests is strength reduction from peak to LD strengths. This reduction or the ratio of LD strengths to peak strengths is typically consistent for single and multi-layer tests based on the 18 projects considered herein.
- When tests involve hydrated GCL, the displacements at peak strength for multi-layer tests are higher than for single interface tests. The composition/type of GCL and bentonite type are likely causes for the difference. More data needs to be developed to confirm this.

REFERENCES

ASTM D5321/D5321M. Standard test method for determining the shear strength of soil-geosynthetic and geosynthetic-geosynthetic interfaces by direct shear, *ASTM International*, West Conshohocken, Pennsylvania, USA.

ASTM D6243/D6243M. Standard test method for determining the internal and interface shear resistance of geosynthetic clay liner by the direct shear method, *ASTM International*, West Conshohocken, Pennsylvania, USA.

ASTM D7702/D7702M. Standard Guide for Considerations When Evaluating Direct Shear Results Involving Geosynthetics, *ASTM International*, West Conshohocken, Pennsylvania, USA.

Code of Federal Regulations (2012). Criteria for Municipal Solid Landfills, *Title 40, Part 258*.

Khilnani, K., Stark, T.D. and Bahadori, T.M. (2017). Comparison of Single and Multi-Layer Interface Strengths for Geosynthetic/Geosynthetic and Soil/Geosynthetic Interfaces, *Geotechnical Frontiers 2017: Waste Containment, Barriers, Remediation, and Sustainable Geoengineering*, GSP 276: 42-51.

Shenthan, T., Khilnani, K. and Stark, T.D. (2019). Case Histories of Multi-Layer Interface Tests for Composite Liners and Comparison to Single Interface Tests, *Geo-Congress 2019: Earth Retaining Structures and Geosynthetics*, GSP 306, ASCE: 331-343

Stark, T.D. and Choi, H. (2004). Peak vs. Residual Interface Strengths for Landfill Liner and Cover Design, *Geosynthetics Intl. J*, 11(6), December 2004: 491-498.

Stark, T.D., Niazi, F., and Keuscher, T. (2015). Comparison of Single and Multiple Geosynthetic Interface Tests, *Intl. J. Geotech. and Geol. Eng.*, Springer Publishing, April 2015: 1-17.

Stark, T.D. and Poeppel, A.R. (1994). Landfill Liner Interface Strengths from Torsional Ring Shear Tests, *Journal of Geotechnical Engineering*, ASCE, 120(3), March 1994: 597-615.

Geosynthetics Conference

Designing Geotextiles for Filtration: A Review of the State of the Practice, Development of Design Standard ISO 18228-3

Eric Blond, P.Eng., M.Sc.A.[1]

[1]Eric Blond Consultant, Montreal, Canada; e-mail: eric@ericblond.com

ABSTRACT

This paper presents the results of the survey on geotextile filtration conducted in 2012-2013 by the International Geosynthetics Society (IGS). This survey received more than 200 responses from practitioners from over 5 continents. It was focusing on identification of design practices around the world; occurrence of failures or perceived failures; confidence in the technology; as well as regulatory aspects. The results of this survey were used to define the structure of Standard ISO 18228-3 on the design of geotextiles for filtration, developed by ISO TC221 on Geosynthetics, in press at the time this publication is written. This structure is presented in this paper as well. This document is not intended to provide an exhaustive description of all relevant publications and practices currently available on filtration. It presents a state of the practice based on a survey conducted among IGS members, as well as a design strategy which has reached consensus among all the nations member of ISO TC221.

INTRODUCTION

In geosynthetics, the filtration function is to stabilize a soil by maintaining in place the skeleton in contact with the geotextile, while allowing the passage of water or other fluids across the filter. The filtration function has historically been provided by soils slightly coarser than the soils being retained. However, the simplicity of use of geotextiles has made them a replacement of choice of granular filters. A geotextile filter also avoids the need for multiple, staged soil filters by offering a continuous structure capable to retain the soil, and openings which must be selected to retain the skeleton of the soil.

The most frequent uses of geotextiles for their filtration capability include:

- Filter envelope for drainage systems. A drain work thanks to the difference of permeability between the material being drained and the material acting as a drain, such as coarse gravel, drainage pipe, edge drain, drainboard, geonet, or prefabricated vertical drains (PVDs). To maintain the efficiency of the drain, it is essential to avoid its contamination by particles of the soil being drained, therefore to install a filter selected to avoid contamination of the drainage core by fine particles, while not restraining the flow of water.
- Filter used between a soil and a rip-rap, gabions or similar products, e.g. for coastal protection, banks protections, in canals or in dams. The geotextile filter is then intended to let the water flow freely between the soil and the environment, while avoiding erosion.
- Separators for roadway applications, where they are intended to avoid interpenetration of the road base and the infrastructure, while avoiding the development of pore pressure.

In geosynthetics, the filtration function is to stabilize the soil by maintaining in place the soil skeleton in contact with the geotextile surface and restrain uncontrolled passage of soil, while

allowing the passage of water or other fluids and some of the finest particles transported in suspension across the filter. The geotextile filter can be thought of as a catalyst to create a natural granular filter in the thin soil layer in contact.

Given their physical properties, i.e. a very thin layer of material concentrating a critical function for the project, time was needed for the geotechnical community to accept their use in embankment, dams, roadways and other major infrastructures. Several studies were made throughout the years to develop a good understanding of their behavior. Comprehensive review of the mechanisms governing the performance of geotextile and granular filters were eventually published (Giroud, 1996, 2010).

Geotextile filters are now more broadly accepted in engineering practice, although they are not systematically used in all applications where they would offer a more economical and sustainable option than granular filters.

To assess the actual acceptance, perception and regulatory framework prevailing regarding the use of geotextiles worldwide as filters, the Filtration Committee of the IGS (International Geosynthetics Society) has made a survey in 2012 among its membership, worldwide. This document presents the key findings from this survey, which is believed to reflect the state of the practice as of 2012.

As a separate initiative, ISO committee TC221 on Geosynthetics initiated an effort to generate design guidance in 2013. This document introduces as well key elements of the standard, and in particular its structure, which was strongly influenced by the findings of the IGS Survey.

KEY FINDINGS OF THE SURVEY ON CURRENT PRACTICES WITH THE USE AND DESIGN OF GEOTEXTILE FILTERS

In order to gather information on current practice, the following groups were consulted:

- Membership of ISO TC221-WG6-PG3
- Membership of the IGS TC-H (Technical Committee on Hydraulics) and TC-F (Technical Committee on Filtration)

Overall, about 1000 survey were distributed, and more than 200 were returned. Qualifications of the respondent is summarized below:

- 97 % were holding an engineering or higher degree;
- More than 65 % had at least 10 years of experience with the use of geosynthetics, and less than 15 % had only three years of experience with geosynthetics or less.
- Respondents were well distributed over five continents, with 25 from Africa, 39 from Asia, 7 from Oceania, 57 from Europe, 48 from North America and 29 from South America.
- They were involved in different fields of practice (research, design, manufacturing, installation).
- Their practice included coastal protection, road drainage, foundation drainage, slope drainage, mine waste applications, municipal solid waste applications.

Overall, these numbers suggest that the results of the survey reflect the opinion of a group of individuals familiar with the industry, with a high education, without emphasizing too much on a particular region, profession, or field of practice. The response to the survey were analyzed, and eventually led to the definition of a few observations which are presented below.

1- Unawareness of the existence of National Guideline for the Design of Geotextile Filters. It was found that even where there are national guidelines focusing on the design of geotextiles for filtration, the majority of respondents were not aware of them, despite being specialized in geosynthetics. It is important to highlight that the question was focusing solely on guidelines for the design for filtration and not mechanical design or other application-related specifications.

2- Variety of standards used to qualify geotextile properties. It was found that there are two main standardization bodies used to qualify geotextile properties: ASTM and ISO, but there is also more than 25% of respondents who are using methods other than ASTM or ISO. Responses can be summarized as follow:

- ISO (i.e. ISO 12956, ISO 11058, etc) : 77
- ASTM (i.e. ASTM D4751, ASTM D4491, etc): 119
- Other national standard (often based on ISO): 67
- Other standards, i.e. from institutes or private agencies: 59

Overall, ISO standards were found to be used by ± 50 % of respondents, considering that several of the 'National Standards' were in fact ISO Standards adopted nationally, i.e. in European countries. ASTM standards appeared to be used as well by about 60 % of respondents. It was also found that in some regions, geotextiles are qualified by either one or the other system (ISO or ASTM) depending on the specifications.

3- Are geotextiles filters performing well? A section of the survey was dedicated to the observation of failures, with the question focused arbitrarily on witnessing the failure within the last three years. The intention of this question was to assess qualitatively whether geotextile filters actually fail in the field on a regular basis, or not. Three options were offered for the answer, to distinguish failures actually witnessed, first-hand, from failures that could have been promoted for various reasons, e.g. for commercial reasons, by a party representing a competitive technology. Results were classified depending on the primary activity of the respondent. They are summarized in table 1.

Table 1. Observation of failures in practice.

	Yes, I have observed it myself, and I know what the causes of the failure are	I have heard of a failure and can identify one person who was involved or witnessed it	I have not directly or indirectly witnessed any failure
Design / Owner	20	19	45
Installation / Inspection	4	1	5
Manufacturer / Distrib.	18	11	19
Research / Education	18	12	33
Total	**60**	**43**	**102**

It was interesting to observe that for each professional practice, less than 30 % of all respondents have directly witnessed a failure, disregarding the type and magnitude of the failure.

This percentage was found to be a little bit higher for manufacturers, despite the manufacturer is the most likely to be contacted, i.e. for a claim. These numbers did not allow to distinguish situations where two or three different respondents could have witnessed the same failure. Finally, the vast majority of respondent had more than 10 years of experience in geosynthetics.

Overall, it was considered that the answers provided to this question suggest that failures primarily caused by a filtration problem do not appear to be extremely frequent.

4- Level of confidence (of the respondents) in geotextile filters. The question asked was: "*Would you specify a geotextile filter (based on available current filter criteria) to a large geotechnical or geoenvironmental project (for instance: a medium to high risk project such as an embankment dam over 30 m high, or a project with a total value > 50 M$ where the geotextile plays a significant role)?*" The answers provided are reported in Table 2.

Table 2. Confidence.

Yes	34	166 (73.5 %)
Yes, depending on the project characteristics	132	
No, because of lack of long-term performance of geotextile filters in such applications.	20	47 (20.1 %)
No, because of lack of confidence on the success of the filter.	9	
No, because of concerns regarding durability, damages during installation, etc.	12	
No, because it is not in the codes and there is no local experience for this application.	6	
Other (please specify)	13	13 (5.7 %)

Based on these answers it seems that about three quarter of respondents have a good level of confidence in geotextile filters. The concerns raised for a quarter of the respondents include:

- Lack of confidence in long term durability.
- Lack of confidence in the ability of the filter to perform as intended.
- Regulatory / building code-related issues.

5- Most important issue restraining the use of geotextile filters. For this question, 65% of respondents highlighted the need to have a better control and understanding of the products functions and behavior; 27% pointed toward the lack of confidence of owners of the projects, while about 10 % mentioned regulatory issues.

Observations based on the Survey. The most important observations made in this survey were as follow:

- There are, in fact, a relatively limited number of failures related to filtration performance of geotextiles.
- There are sometimes regulatory issues restraining the use of geotextile filters.
- The lack of confidence of some owner and some design engineer in long-term performances of geotextile filters needs to be addressed.

Further analysis suggests that a limitation to the use of geotextiles for their filtration function is not supported by evidence of problems, but more by the lack of information, and/or

regulatory issues. A path to broader adoption of this technology includes more education and the development of evidence supporting their long-term performance in the field.

Concurrently, but independently from this IGS initiative, ISO TC221 initiated an effort to develop harmonized design guidance for various functions of geosynthetics, such as ISO 18228-3 for geotextile filtration. It was therefore decided to bring the results of the survey to the ISO TC221 WG6 Technical Committee for further valorization.

When 'translated' into standardization goals, the most important need identified by the survey were defined as the need to increase the confidence or early users in the reliability of the technology, and to provide them with simple design tools – i.e. avoid complexity when not necessary. It was therefore decided to propose simple design approaches, along with boundaries beyond which expert(s) should be involved, and performance testing conducted.

ISO TC221 STANDARDIZATION

ISO TC 221 is the Technical Committee on Geosynthetics of the International Standardization Organization.Membership and attendance to the meetings is decided by National Mirror Committee, usually the National Standardization Body for a given country. This national committee proposes delegates and experts who will be working on projects, such as ISO 18228-3 on the design of geotextiles for filtration. The approval process includes the subcommittee review, a committee review, and then various administrative reviews. The approval strategy is designed to favor consensus but does not require unanimity.

ISO TC221 includes five 'Work Groups' focusing on five different topics:

- WG2 on Terminology, Identification and Sampling
- WG3 on Mechanical Properties
- WG4 on Hydraulic Properties
- WG5 on Durability
- WG6 on Design with Geosynthetics

10 projects were set up within WG6 on Design with Geosynthetics. Each of them will lead to a standard that will help users not familiar with a product identify relevant concerns and design practice:

- PG1 – General
- PG2 – Separation
- PG3 – Filtration
- PG4 – Drainage
- PG5 - Stabilization
- PG6 – Protection
- PG7 – Reinforcement
- PG8 – Surface Erosion
- PG9 – Barriers
- PG10 – Asphalt Overlays

ISO TC221-WG6-PG3 on Designing for Filtration was initiated in 2014. Canada coordinated this project. The development of the standard started with the analysis of the IGS survey, as reported above. Based on the survey it was decided that the design standard should stay relatively simple in its format and give confidence to users in the high performance of geotextile

filters When adequately designed. About five years were needed to finalize the design guidance, which was finally in press at the end of 2020.

CONTENT OF ISO 18228-3

ISO TC 221 Working Group 6, Project Group 3 (WG6-PG3) worked on the development of this standard, including the recommendations arising from the survey, and gathering the various design recommendations available from the committee members. Although this document is protected by copyrights, the key, important sections are described herein:

- Chapters 1 to 3: Scope, Normative references, Terms and Definitions
- Chapter 4: Concepts and fundamental principles
- Chapter 5: Typical applications
- Chapter 6: Materials
- Chapter 7: Functional properties relevant to design
- Chapter 8: Principles of design
- Chapter 9: Testing the soil/geotextile filtration compatibility
- Chapter 10: Examples of material specifications and design guidance

Chapter 4: Concepts and fundamental principles. In this section, key concepts defining filtration performance are proposed. Basic performance goals are formulated, i.e. the geotextile must retain the soil skeleton and let water pass perpendicularly to its plane. Additional propositions are also formulated, such as the need to properly understand the application: type of soil, type of fluid (liquid or gas). A distinction is proposed between slurry and soil filtration.

The need for the geotextile to meet minimum mechanical properties is defined, considering survivability requirements as well as the capacity of the product to resist mechanical stresses during service, if any. Finally, durability and long-term degradation are discussed.

No minimum values are proposed in this section for mechanical properties or durability requirements as these are typically project- or application-specific.

Chapter 5: Typical applications. In this section, a short review of typical applications of geotextile filters is presented. Distinction is made between soil filtration, where an intimate contact with the soil is expected throughout the life of the geotextile, and slurry filtration, where the geotextile is expected to be exposed to a slurry instead of a soil. Understanding the difference between soil and slurry filtration is essential as failure mechanisms are very different from one application to the other.

Examples of soil filtration include drainage systems (perimeter drains around buildings, tile drainage in agriculture, etc.), dams, prefabricated vertical drains, roadways, rail track bed, waterways/canals, coastal protection, landfills – leachate collection systems. For geotextile filters exposed to the flow of gases, soil filtration also includes protection systems against the intrusion of radon and other subsurface gases into buildings, or gases collection layers in landfills.

Examples of slurry filtration include filtration of slurries and dewatering applications, geocontainers and silt fences.

Understanding which mechanism prevails for the design is essential for the success of the application. In example, a geotextile designed for soil filtration may not perform well if it is exposed to a slurry before backfilling is completed, i.e. should heavy rain transport fine particles from the adjacent soil onto the geotextile, in a slurry.

Chapter 6: Materials. In this section, the structures commonly found for geotextiles are described: different types of woven, non-woven, or knitted materials. Typical ranges of properties are also indicated for opening size, velocity index (permeability), or Percent Open Area when applicable.

Chapter 7: Functional properties relevant to design. The relevant ISO, ASTM and other standards which should be used to qualify the various properties of geotextiles are identified in this section:

- Opening size, which can be a characteristic opening size, or a value selected from the pore size distribution.
- Velocity index and permittivity – or permeability.
- Resistance to water penetration.
- Number of constrictions, although there is no consensus on criteria that can be used for design.
- Percent open area.

It is important to highlight that this ISO guidance is intended to be international and useable in any country or jurisdiction. For that reason, Chapter 7 (and the rest of the document) does not point toward single test methods as the unique solutions for evaluating given properties. As identified in the survey, there are as many experts using ISO as there are using ASTM standards. The primary focus of this section is therefore to list properties and standards available to measure them, instead of limiting options, therefore limiting the applicability of the guidance.

Chapter 8: Principles of design. This chapter is basically the core of the standard, and among the most important for potential new users of geotextiles as it defines the environmental conditions that need to be controlled to ensure long-term performance of the structures utilizing a geotextile filter. Considerations are given to:

- Installation conditions, and the need to ensure an intimate contact between the soil and the geotextile before the filtration process is initiated, i.e. before liquid flows through from the soil to the geotextile.
- Risk of premature degradation caused by solar exposure, excessive heat or chemical exposure.
- Risk of premature degradation caused by abrasion, puncture, tearing or other mechanical damage.
- Control of the risk of biological or chemical clogging, i.e. iron ochre, or mineral precipitation, as well as specific environmental conditions such as leachate filtration.
- Risk associated to high suspended particle content in the water, in particular with filters used for shore protection, on riverbanks, etc.

Guidance provided for the design of geotextiles for soil filtration are then provided. These are essentially based on the Canadian Geotechnical Manual as modified by Heibaum (2014). A step by step approach is offered as follow:

Step 1: Define environmental conditions

Should a critical condition be identified, the design is immediately set to be outside of the scope of the design guidance. Such condition includes high presence of ferrous iron (Fe2+) or manganese oxide (MnO2), presence of high organic matter, or suspended solids in the water.

It is then proposed to confirm that installation conditions are adequate, with respect to water runoff, intimate contact of the soil and the geotextile, that all measures are taken to avoid abrasion, tear, cuts or other physical degradations of the geotextile.

Finally, this step requires to collect relevant soil properties, essential for further steps.

Step 2: Designing the geotextile

In Step 2 three criteria are defined:

- Retention criteria of the soil skeleton, where the characteristic opening size (COS) of the geotextile must be smaller than an indicative diameter of the soil (d_I) multiplied by a constant, to avoid excessive piping of soil through the geotextile: $COS \leq B \times d_I$
- Non-retention criteria of fines in suspension, where the characteristic opening size of the geotextile (COS) must be larger than another indicative diameter of the soil (d_J) multiplied by a constant, to avoid clogging or blinding of the geotextile: $COS \geq C \times d_J$
- Permeability criteria, where the geotextile must exhibit a Velocity Index (V_F) larger than the permeability of the soil (k_S) multiplied by a constant (E) and the anticipated hydraulic gradient prevailing in the soil (i_s), to avoid pressure buildup upstream of the geotextile: $V_F \geq E \times k_S \times i_s$

The various factors (B, C, E) as well as the selection of the indicative diameters of the soil d_I and d_J are defined in the standard and depend on soil properties and operating conditions:

- For the retention criteria, B and d_I depend on the coefficient of uniformity of the soil and flow conditions.
- For the non-retention criteria of fines in suspension, C and d_J depend on the coefficient of uniformity of the soil and flow conditions. In the case of woven geotextile filtration, a minimum value of Percent Open Area (POA) is also specified.
- For the permeability criteria, E depends on the risk and associated consequence of the pressure build up on the upstream side of the geotextile and varies from 10 to1000.

Chapter 8 also introduces the design of geotextile for slurry and suspended solids filtration as in geocontainers, silt fences, sludges and tailing filtration. However, a criterion is not provided per se, as slurry filtration is far more complex and efficiency may be defined in several different ways depending on the application. The design of a geotextile to interact with a given slurry is usually performed using laboratory tests.

Chapter 9: Testing the soil/geotextile filtration compatibility. This chapter describes laboratory tests commonly used to assess the performance of a soil / geotextile systems, including:

- Soil/geotextile compatibility (ASTM D5101, ASTM D5567 and ISO 10772)
- Evaluation of slurry/geotextile behavior (ASTM D7701 and D7880)
- Biological or chemical clogging potential (ASTM D1987)
- Impact of abrasion on the filtration properties of geotextiles (ASTM D4886 and ISO 13427)

Chapter 10: Examples of material specifications and design guidance. Standard ISO 18228-3 ends with a (non-exhaustive) list of material specifications and design guidance, which may prevail over ISO 18228-3 or be used as a complement in some regions, and in particular in France, USA, Canada, Germany and Japan.

CONCLUSION

The results of a survey on the use of geotextiles for filtration was introduced. The results of this survey were used to define the structure of Standard ISO 18228-3 on the design of geotextiles for filtration, developed by ISO TC221 on Geosynthetics, which reflects an international consensus from experts from all around the world on this matter.

The most important finding arising from the survey was the relatively small number of failures encountered by experts with typically more than 10 years of experience with the use of geotextiles for filtration. This observation suggests that the reliability of geotextiles for filtration is, in general, very high.

A secondary finding from this survey was that education and availability of simple guidance is needed to increase the confidence of potential users of geotextiles. The development of ISO 18228-3 was made with this goal in mind. Such simple design guidance and good practices are provided. These reflect a consensus from international experts involved in ISO TC221.

REFERENCES

Giroud, J.P., 1996, “Granular Filters and Geo1987textile Filters”, Proceedings of GeoFilters ’96, Lafleur, J. & Rollin, A.L., Editors, Montréal, Canada, May 1996, pp. 565 – 680.

Giroud, J.P., 2010, “Development of criteria for geotextiles and granular filters”, Prestigious Lecture, Proceedings of the 9th International Conference on Geosynthetics, Guarujá, Brazil, May 2010, Vol. 1, pp. 45-64.

Heibaum M., 2014, “Rethinking geotextile filter design”, Proceedings of the 10th International Conference on Geosynthetics, 21 to 24 Septembre 2014, Berlin

ASTM D4751 - Standard Test Methods for Determining Apparent Opening Size of a Geotextile

ASTM D4491 - Standard Test Methods for Water Permeability of Geotextiles by Permittivity

ASTM D5101 - Standard Test Method for Measuring the Filtration Compatibility of Soil-Geotextile Systems

ASTM D5567 - Standard Test Method for Hydraulic Conductivity Ratio (HCR) Testing of Soil/Geotextile Systems

ASTM D7701 - Standard Test Method for Determining the Flow Rate of Water and Suspended Solids from a Geotextile Bag

ASTM D7880 - Standard Test Method for Determining Flow Rate of Water and Suspended Solids Retention from a Closed Geosynthetic Bag

ASTM D1987 - Standard Test Method for Biological Clogging of Geotextile or Soil/Geotextile Filters

ASTM D4886 - Standard Test Method for Abrasion Resistance of Geotextiles (Sandpaper/Sliding Block Method)

ISO 18228-3 (in press) - Design using geosynthetics – Part 3: Filtration

ISO 12958:2010 - Geotextiles and geotextile-related products – Determination of water flow capacity in their plane

ISO 11058:2010 - Geotextiles and geotextile-related products – Determination of water permeability characteristics normal to the plane, without load
ISO 10772 - Geotextiles - Test method for the determination of the filtration behaviour of geotextiles under turbulent water flow conditions
ISO 13427 - Geosynthetics — Abrasion damage simulation (sliding block test)

SPONSORED BY

Geosynthetics Conference

Interface Shear Testing: Specifying, Review and Available ASTM References

J. P. Kline, P.E.[1]

[1] Geotechnics, Inc., East Pittsburgh, PA; Email: jpkline@geotechnics.net

ABSTRACT

Geosynthetic products used to construct waste containment systems may be tested during the design or to pre-qualify the product, but most often by the manufacturer after production as quality control and by construction quality assurance to confirm the product meets project specified requirements. These tests consist of index tests that confirm that the product is the same product approved for construction, and performance tests which verify that the product will meet the specified design requirements. For performance testing, project specific test parameters are required to produce results that are relevant to each project.

The direct shear test is one of the most critical performance tests used for construction materials used in containment structures. Through this testing, it can be demonstrated that the materials being used will provide a stable structure throughout the containment system design life. There are a number of factors that go into producing a successful and relevant interface or internal shear test. How the test specimens are prepared, the test is set up and performed can have a significant influence on the results.

In the United States, shear testing is performed using the ASTM D5321 test standard for interfaces incorporating geosynthetic products excluding geosynthetic clay liners (GCL) and ASTM D6243 test standard for GCL interfaces and internal shear. After test results are provided by the testing laboratory, the interpretation of the test data can influence whether a product's shear results are acceptable. ASTM has provided a standard guide, ASTM D7702, for considerations when evaluating geosynthetic shear results. This paper will discuss the necessary test parameters to establish applicable project test results, considerations when evaluating the tests results and the available ASTM referenced standards.

INTRODUCTION

There are three ASTM standards concerning direct shear testing with geosynthetics. These ASTM standards are living documents that are periodically updated to improve the standards. It should be noted that any update or change is discussed within its task group and must be approved by the committee through a ballot process before being incorporated into the standard.

The first standard, ASTM D5321 "Standard Test Method for Determining the Shear Strength of Soil-Geosynthetic Interfaces by Direct Shear," was originally approved in 1992 with the current revised version being approved and published in 2020. The second standard, ASTM D6243 "Standard Test Method for Determining the Internal and Interface Shear Strength of Geosynthetic Clay Liner by Direct Shear Method," was originally approved in 1998 with the current revised version also being approved and published in 2020. The D5321 and D6243 test standards basically mirror each other in content except for considerations specific to GCLs in the D6243 test standard. These test standards are performance based tests intended to model field conditions as closely as possible to provide project relevant shear data. Both standards provide

requirements for the test equipment used and instruction on how to perform shear tests with geosynthetics.

Lastly, to aid the reviewer of geosynthetic and GCL shear results, ASTM D7702 "Standard Guide for Considerations When Evaluating Direct Shear Results Involving Geosynthetics" was developed. Originally approved in 2011, this standard guide is a summary of available literature regarding the interpretation of shear test data provided when performing the D5321 and D6243 test standards. The current version was approved in 2014.

SPECIFYING DIRECT SHEAR TESTS INVOLVING GEOSYNTHETICS

Regarding the actual test parameters that a specific test is performed, ASTM D5321 & D6243 test standards are not prescriptive to allow the requester the freedom to specify the test conditions most appropriate to their construction situation. Both test standards provide a checklist in its appendix to aid the test requester in specifying the shear test. It is worthwhile to note that some of the test labs performing these tests have their own test request forms similar to these checklists that can be used to specify the shear tests. The following test parameters should be specified to obtain the intended representative shear results.

Products

To model field conditions for interface shear testing, the actual products or materials to be installed or representative samples of the same material should be used. In many cases, it is also important to identify the side of the product to be tested at the interface and possibly the orientation of the product.

Product Side @ Interface

In most waste containment installations, the geosynthetic materials are rolled out so the product's inner roll is up and the outer roll is down. It is recommended to confirm how the products are to be deployed prior to specifying the shear test to make sure the appropriate product surfaces that will be in contact with each other in the field will be tested in the shear test. Many of the products currently available differ from one side to the other which could affect the interface shear results and thus which side of the product to be tested for a particular interface should be identified. Some of these differences may be:

- Geomembrane – texturing, color
- GCL – carrier geotextile (woven, nonwoven, or scrim-nonwoven) or geomembrane, color
- Geocomposite – geonet structure, geotextile if different weight or type
- Geotextile - heat treated (burnished).

Product Orientation

Because products are mostly installed in the slope direction, it is generally assumed that shearing will also occur in the same direction; thus, specimen are usually placed in the shear box oriented in the machine direction. If the shear direction is not in the product machine direction, this should be clearly identified.

Sample Conditioning

Soil Specimens

If there is a soil layer as part of the interface test, how the soil is to be placed or compacted in the shear box must be specified to replicate how it would be in the field. Many times, the soil will be placed relative to soil Proctor test results; either standard effort (ASTM D698) or modified effort (ASTM D1557). If placement is based on soil Proctor test results, the test specifier must communicate the percent of maximum dry density and percent relative to optimum moisture content the soil is to be placed. It is important to note that rock corrected Proctor values are not applicable as the maximum soil particle size used for shear test is similar to that of the Proctor test; thus, only uncorrected Proctor values should be used. Alternatively, not being based on a single Proctor test result of the sample, the test specifier can provide the actual dry density and moisture content values they would like the soil to be placed.

The soil may simply be placed in the field by tracking it in without any specified compaction density. To achieve this for the shear test, the soil is lightly compacted or tamped in the box at either a specified moisture content or most often just at the sample as-received moisture content. The weight of the soil is measured during placement of the first normal load so the same placement density and moisture content can be replicated for the remaining normal loads to be tested.

GCL Specimens

If the shear test contains a GCL, the GCL specimen can be placed in the shear box as-received or conditioned by wetting the specimen. Wetting of the GCL specimen can be accomplished by pouring water over entire specimen, spray wetting the surface of the specimen, partially hydrating the specimen to a specified bentonite water content, or hydrating entire specimen submerged in water. The GCL may be hydrated at the test normal load for a specified duration prior to shearing or at a much lower normal load for a specified duration before increasing the applied pressure to test normal load prior to shearing. Hydrating at the lower normal load is usually done to model the GCL hydration shortly after installation that may happen in the field.

Geosynthetic (Non-GCL) Specimens

Geosynthetic specimens can be placed in the shear box as-received or wetted prior to placement in the shear box. Wetting of the geosynthetic specimens can be accomplished by pouring water over entire specimen or spray wetting the surface of the specimen.

Shear Testing Parameters

Applied Test Normal Loads

A minimum of 3 normal loads is required to determine the Mohr-Coulomb shear strength envelop. These normal loads should bracket the range of project normal loads of interest for slope stability. Shear strength envelop plots provided in the Shear Stress vs Normal Load graphs are curvi-linear. Thus, extrapolation of shear data beyond the range of normal loads tested would be unconservative.

Interface Saturation Condition

The interface saturation condition refers to the wetting condition within the shear box during seat time under test load and shearing. Interface saturation conditions can be dry, interface surfaces spray wetted during placement in shear box, or inundated with water. For inundated with water saturation condition where interface is submerged in water, the water is added to the shear box after applying test normal load. Most often, shear tests are requested to be inundated with water as this is the worst case, most conservative scenario.

Seating/Consolidation Time

The seating or also referred to as consolidation time for shear tests with soil or hydrated GCLs is the duration of time that the test normal load is applied to the interface prior to shearing. For geosynthetic materials and drainable soils, such as sands and gravels, a seating time of 1 hour may suffice for allowing the test normal load to act upon the interface prior to shearing. For less drainable soils or GCLs, the seating or consolidation time prior to shear is usually a time period of 16 hours (overnight) to 24 hours to allow for dissipation of any potential pore pressures created while applying the test normal load.

Shear Displacement Rate

The rate of applied shear force should be slow enough to dissipate any excess pore pressures during shearing that may decrease the measured shear resistance. For interfaces where excess pore pressures are not expected, the test standards offer default maximum shear displacement rates of 5 mm/min (0.2 in/min) for geosynthetic interfaces and 1 mm/min (0.04 in./min) for interface with GCLs or soils. For interfaces in which excess pore pressures may be expected, such as with higher plasticity clay soils, the shear displacement rate may need to be slowed down considerably.

Complimentary Information

Although not required by either shear test standard, certain properties for each interface material can be measured to provide better insight into the shear characteristics of that material. Shear results with textured geomembranes are directly influenced by the texturing of that geomembrane; thus, asperity height measurements (per ASTM D7466) of each shear specimen prior to placement in shear box are typically included with the interface shear results.

Although usually not directly influencing the measured interface shear results, a shear test requester may want a peel test (per ASTM D6496) for GCLs or ply adhesion test (ASTM D7005) for geocomposites performed on the same sample the shear is being performed. These index tests can offer an understanding of the product's bond strengths needed to prevent the shear failure plane happening in the internal reinforcement of the GCL or the bond between the geocomposite's geonet and geotextile instead of at the intended interface. For GCL peel strength and Geocomposite ply adhesion, it is recommended that the test specimens be taken adjacent and in-line in the machine direction to the shear specimen. Soil gradation and classification is also beneficial information to have for the soil samples used for interface shear testing.

REVIEW

After the shear test had been completed, per the test standards, the test lab is to report the peak and post-peak shear stress values at each applied normal load tested, plots of the shear force versus shear displacement and shear stress versus normal stress with the adhesion intercept, coefficient of friction and/or the friction angle identified as well as the test parameters for which the shear test

was performed. The Mohr-Coulomb friction angle can be calculated from the test results using the following equation:

$$t = C_a + s_n * \tan(d) \quad (1)$$

where:

t = peak shear strength
C_a = adhesion intercept
s_n = normal stress
d = friction angle (degrees)

This equation is derived for each shear test from the best fit line drawn through the data points on the Shear Stress vs. Normal Stress graph for the shear test. The below graphs 1a & 1b provide an example of the Shear Force vs Shear Displacement and Shear Stress vs Normal Stress graphs that are included in the shear results.

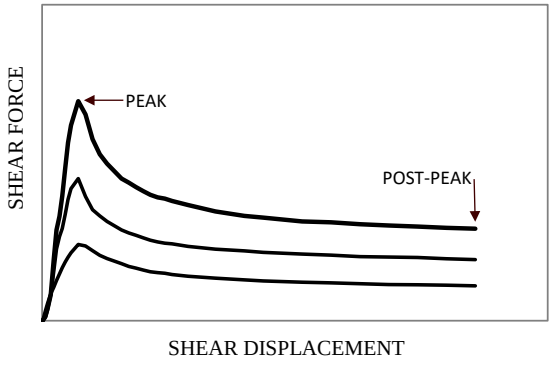

1a. Shear Force vs Shear Displacement

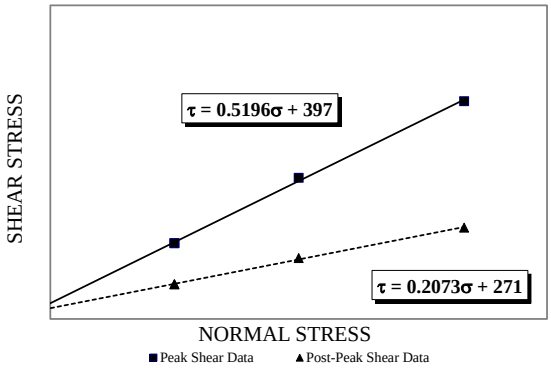

1b. Shear Stress vs Normal Stress

The peak and post-peak shear values can be viewed for each normal load tested on the Shear Force vs Shear Displacement graph. The post-peak shear values are taken at the end of the shear displacement distance. This displacement distance is typically 75 mm (3 in.) as that is the limit of most commercially available large scale shear machines. Note that the post-peak shear value is often referred to as the "residual" shear value, although it may not be the true residual value as the shear displacement may need to exceed the 75 mm displacement to attain the residual value.

The identified peak and post-peak shear values for each normal load from the Shear – Displacement curves are plotted on the Shear Stress vs Normal Stress graph and the best fit lines are drawn to provide the Mohr-Coulomb shear strength envelops. From the example above, the peak friction angle is calculated taking the inverse tangent of coefficient of friction (0.5196) in the first term of the peak shear equation which equals 27.5 degrees. The second term provided in the peak shear equation (397) is the adhesion intercept. Caution should be given to simply evaluating shear data based on the calculated Mohr-Coulomb friction angle without consideration of the adhesion value. Doing so may greatly underestimate the actual shear strength of the interface being tested.

Another value that may be included in the reported shear test results is the secant friction angle which is the friction angle specific to the normal load tested. It is the angle of the line drawn

from a data point on the Shear Stress vs Normal Stress graph to the origin and can be calculated as follows:

$$d_{sec} = \tan^{-1}(t / s_n) \quad (2)$$

where:

d_{sec} = secant friction angle (degrees)
t = peak shear stress
s_n = normal stress

When evaluating test shear data with respect to a specified required Mohr-Coulomb friction angle, the secant friction angles at each tested normal load can be an indication of whether the Mohr-Coulomb shear strength envelop of the tested interface may meet the intent of the specified Mohr-Coulomb friction angle. If the secant friction angles for all the normal loads tested exceed the specified Mohr-Coulomb friction angle, then the shear failure envelop of the tested interface exceeds the shear strength envelop defined by the specified required Mohr-Coulomb friction angle.

For an in-depth discussion of shear strength fundamentals, interpretation of adhesion, evaluation of shear displacement curves, comparison of shear results to historic data and post-test sample inspection, see the standard guide ASTM D7702. Although this standard is an excellent refence, it is not intended to replace education or experience and should only be used in conjunction with professional judgement; as noted in this standard guide.

CONCLUSION

Interface shear testing with geosynthetics and GCLs are performed using ASTM D5321 and D6243 test standards. These standards provide instruction of the equipment requirements, instruction of how to perform tests and guidance of the information needed from the test requestor to achieve project relevant test results. When reviewing the test results, standard guide ASTM D7702 is a helpful tool in understanding the test results provided by the geosynthetic and GCL shear tests.

REFERENCES

ASTM D 5321. Standard Test Method for Determining the Shear Strength of Soil-Geosynthetic Interfaces by Direct Shear, *American Society for Testing and Materials*, West Conshohocken, Pennsylvania, USA.

ASTM D 6243. Standard Test Method for Determining the Internal and Interface Shear Strength of Geosynthetic Clay Liner by Direct Shear Method, *American Society for Testing and Materials*, West Conshohocken, Pennsylvania, USA.

ASTM D 7702. Standard Guide for Considerations When Evaluating Direct Shear Results Involving Geosynthetics, *American Society for Testing and Materials*, West Conshohocken, Pennsylvania, USA.

Geosynthetics Conference

Laboratory Mechanical Property Testing for Turf Reinforcement Mats

Yue Xu,[1] J. David Frost, Ph.D., P.E.[2], Susan E. Burns, Ph.D., P.E.[3]

[1]School of Civil and Environmental Engineering, Georgia Institute of Technology, 790 Atlantic Dr. NW, Atlanta, GA, 30332; email: yuexu24@gatech.edu
[2]School of Civil and Environmental Engineering, Georgia Institute of Technology, 790 Atlantic Dr. NW, Atlanta, GA, 30332; email: david.frost@ce.gatech.edu
[3]School of Civil and Environmental Engineering, Georgia Institute of Technology, 790 Atlantic Dr. NW, Atlanta, GA, 30332; email: susan.burns@ce.gatech.edu

ABSTRACT

Turf reinforcement mats differ from other rolled erosion control products by providing long-term erosion protection under higher expected flow conditions. Different turf reinforcement mats can vary significantly in terms of basic laboratory index properties and field performance. Physical and mechanical property testing approaches are designed for product quality control. Generally, manufacturers and the National Transportation Product Evaluation Program report physical properties for turf reinforcement mats. However, turf reinforcement mats can be damaged during installation and operation by heavy or sharp stones. One approach to model the potential damage due to heavy loading is to perform standard tests such as static puncture and dynamic perforation tests. These tests are necessary because they indicate the endurance of turf reinforcement mats under potential mechanical damage. This experimental study investigated index properties and mechanical performance in the laboratory for several turf reinforcement mat products. This study adopted ASTM D6241 and ISO13433 to measure the puncture resistance under static and dynamic puncture processes, respectively. The experimental results show that the static puncture resistance and extension of tested woven turf reinforcement mats increases as mass per unit area increases. Maximum hole diameter, puncture strength, and extension at failure of turf reinforcement mats should be tested and routinely included in product reports together with basic index properties as indicators in rolled erosion control material selection.

INTRODUCTION

The development of rolled erosion control products (RECP) by industry is attributed to the higher demand for various turf reinforcement mats (TRMs), which are applicable for long-term slope or channel erosion control. As a class of geosynthetics, TRMs have not received as much attention as geogrids and geotextiles. There have not been sufficient studies to evaluate the performance of TRMs. Available index property values of widely used TRMs are provided by manufacturers' brochures and the National Transportation Product Evaluation Program (NTPEP) reports, which is summarized in Table 1. Basic index properties such as thickness and mass per unit area are used for product quality control. However, TRMs lose strength primarily during installation as a result of penetrations by heavy or sharp stones since the literature shows that many geosynthetics are damaged during construction (Bolt and Duszynska, 2010; Collins and Holtz, 2005). ASTM and ISO standards provide instructions on impact and puncture resistance tests for turf reinforcement mat, the results of which are not normally provided in manufacturer's brochures. These tests are

important because they indicate the endurance of turf reinforcement mats under potential mechanical damage.

Table 1. Index properties of TRMs (data from NTPEP).

TRM	Mass per unit area (g/m^2)	Thickness (mm)	Tensile Strength MD×TD (kN/m)
TM1	436.0	8.4	6.1 × 4.3
TM2	508.2	12.3	13.2 × 12.6
TM3	783.6	13.9	6.1 × 4.3
TM4	353.6	5.9	4.4 × 2.5
TM5	465.2	11.8	6.3 × 4.1
TM6	683.9	12.4	12.9 × 12.5
TM7	312.3	7.0	6.8 × 3.5
TM8	436.4	8.3	11.2 × 10.4
TM9	454.7	7.2	13.7 × 13.5
TM10	331.6	6.7	5.2 × 3.1
TM11	389.9	7.1	6.8 × 3.6

Termonia (2006) summarized the four steps of puncture failure under a needle projectile as: (1) the initial steady increase in force with penetration of tip due to contact pressure between the tip and fiber strand; (2) a sudden drop of force due to slippage of cylinder behind the tip into inter-fiber space; (3) another increase in force due to friction of cylinder against fabric; (4) a steady decrease in force due to further penetration of cylinder behind the tip. Atmatzidis and Chrysikos (2002) investigated correlations between static puncture strength and tensile strength of nonwoven PP (polypropylene) geotextiles and indicated a linear relationship between puncture resistance and tensile strength as well as mass per unit area. Koerner and Koerner (2011) compared three standard puncture tests on PP and PET (polyester) needle punched nonwoven geotextiles and indicated that puncture resistance of geotextiles is linearly related to fabric mass per unit area. In contrast, Jones et al. (2000) conducted static puncture testing and concluded that static puncture resistance was a nonlinear function of mass per unit area for needle punched nonwoven geotextiles but linearly related with tensile strength in the cross-machine direction. They also stated that static puncture resistance provided "a better indication of protection performance" compared with other tests such as the tensile strength test and the drop cone test. These experimental studies were performed on geotextiles, while no related studies were conducted on turf reinforcement mats.

The main objective of this study was to investigate mechanical performances among several turf reinforcement mat products in the laboratory. Laboratory testing results of basic index properties were compared with manufacturer's data as well as other data collected from NTPEP reports. The correlation between physical properties and the mechanical performance of these TRMs is discussed in the manuscript.

EXPERIMENTAL METHODS

Materials

The six three-dimensional, woven TRM materials used in the tests were provided by different manufacturers and they were made of non-degradable, UV-stabilized polypropylene filament. Five materials are categorized as high-performance turf reinforcement mats (HPTRM) by the manufacturers because of their higher tensile strength. Only TRM C is classified as a TRM. HPTRM A, B, C and E have a similar matrix of a pyramid structure. HPTRM F is the only multi-layered woven HPTRM with a unique corrugated structure. The physical properties obtained from manufacturers' brochures are listed in Table 2.

Table 2. Index properties of tested TRMs (manufacturers' data).

TRMs (Manufacturer)	Mass/Area (g/m^2) ASTM D6566	Thickness (mm) ASTM D6525	Tensile elongation MD×TD (%) ASTM D6818	Tensile Strength MD×TD (kN/m) ASTM D6818
HPTRM A	457.7	10.2	40 × 35%	58.4 × 43.8
HPTRM B	457.7	10.2	40 × 35%	58.4 × 43.8
TRM C	254.3	7.6	50 × 50%	35.0 × 29.2
HPTRM D	288.2	11.4	17 × 17%	44× 44
HPTRM E	312	8	25 × 20%	59 × 44
HPTRM F	495	10.2	35 × 20%	52.6 × 55.5

The mass per unit area of all TRMs including those in Table 1, ranges from 254.3 to 783.6 g/m^2.The range 288.2~457.7 g/m^2 for high-performance HPTRMs. The range of tensile strength of HPTRMs is between 43.8 and 59 kN/m, while the range of tensile strength of general TRMs is between 2.5 and 35 kN/m.

Static puncture testing

This test simulates the resistance of geosynthetics to penetration by a long-term heavy mass. The test was conducted using a CBR (California Bearing Ratio) load apparatus, according to ASTM D 6241-14. All (HP)TRM materials were prepared as 30 cm × 30 cm specimens whose border dimensions were longer than the outer diameter of the clamping ring. The test specimen was clamped without tension between circular plates (Figure 1) and fixed on a CBR testing machine. The force was applied at the center of the unsupported portion of the test specimen by a steel probe (diameter of 50 mm) attached to a load cell. The clamping platform was uplifted to apply penetration force on the specimen during the test. An LVDT was placed on the surface of the clamping platform to measure the displacement. The specimen was loaded at a speed of 50 mm/min until failure occurred. Load-displacement data were recorded every two seconds by a data acquisition system (Keysight 34972A), and the puncture strength was read directly from the load-displacement curve. Three specimens of each (HP)TRM material were tested to ensure repeatability.

Dynamic perforation test

This test measures the resistance of geosynthetics to penetration by a steel cone, of 45° tip angle, dropped from a fixed height (50 cm). The test was conducted within a cone drop frame following ISO 13433 (2006). The degree of penetration simulates the behavior of the geosynthetic when

penetrated by sharp stones. All TRM materials were prepared with a specimen size suitable for the standard apparatus used in this study. The diameter of the punctured hole in combination with the drop height gives a measure of impact resistance (strength). The smaller the diameter of the hole, the greater the impact resistance of the geosynthetic to damage. The maximum hole diameters for tested specimens were calculated from the average value of five tests for each specimen. A configuration of the test locations is displayed in Figure 2. These locations were selected to reflect the variability of the material at possible impact locations.

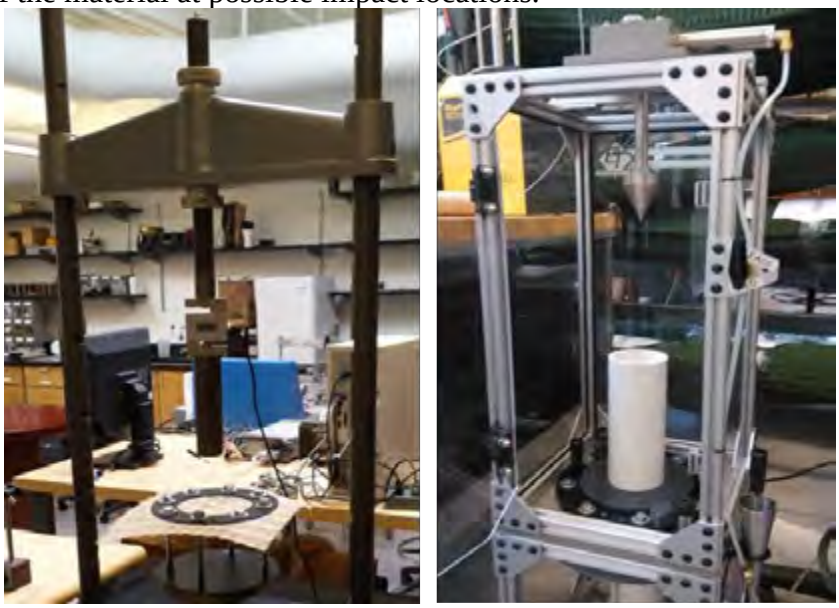

Figure 1. Test configuration for ASTM D6241 standard test of static puncture strength(left) and ISO13433 geosynthetics dynamic perforation test(right).

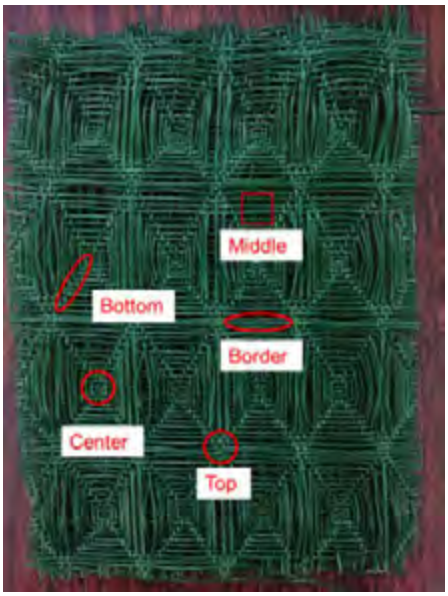

Figure 2. Test locations for HPTRM A: same test locations can also be applied to HPTRM B, TRM C, and HPTRM E.

TEST RESULTS AND ANALYSIS

Static puncture test results

The load-displacement curves of static puncture test results are presented in Figure 3. The loading process for woven (HP)TRMs experienced fiber rearrangement, fiber extension, and monofilament failure, which is similar to the description by Termonia (2006). The static puncture strength of each specimen is obtained from the maximum value of load in the load-displacement curve. Among the six (HP)TRMs tested, HPTRM A has the largest puncture strength to failure. Figure 4 is a photo of a specimen after failure. HPTRM F has the longest extension, while HPTRM D has the shortest extension.

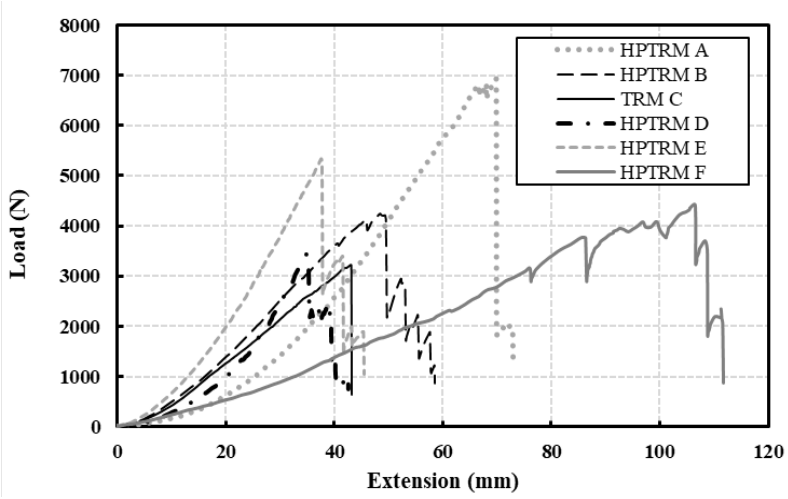

Figure 3. Load versus displacement for seven TRMs.

Figure 4. HPTRM A specimen after static puncture test.

Dynamic perforation test results

Figure 5(a) is a comparison of the maximum hole size obtained from testing. TRM C has the largest hole diameter, which means it is the weakest material to cone penetration among the six (HP)TRMs. Figure 5(b) summarized the hole diameter for four TRMs with similar weave structure after perforation at different locations. The center and bottom areas are the weakest part for both HPTRM B and TRM C, while the top area is the strongest part for them. It can be explained as a vaulted structure has a better bearing capacity than a flat or concave structure. Figure 6 shows specimens after cone penetration. There is no fiber breakage during dynamic perforation. The cone easily penetrated through the yarn gap by separating apart the (HP)TRM fibers.

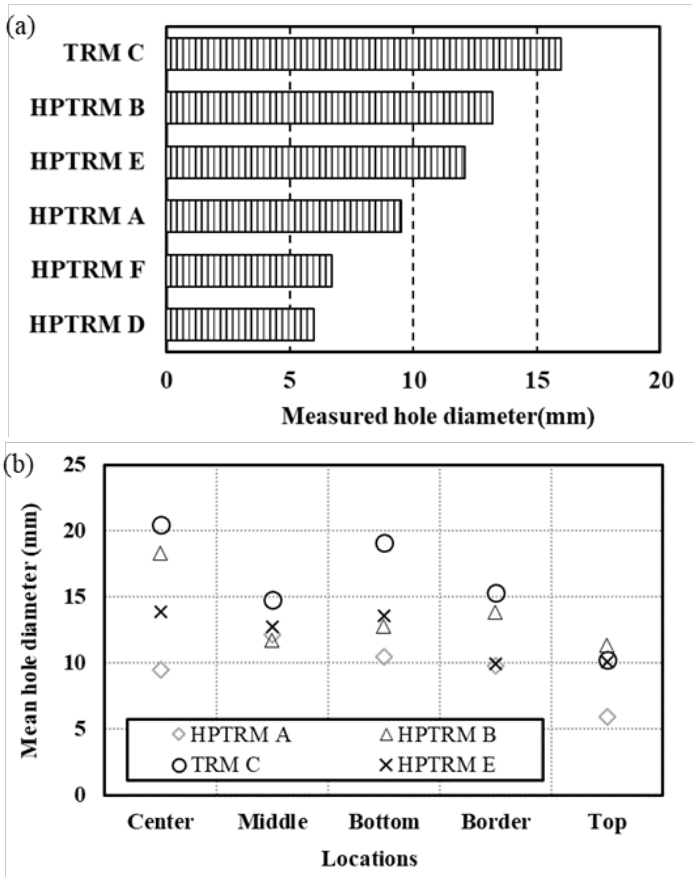

Figure 5. (a) Maximum hole diameters for tested specimens and (b) hole size for (HP)TRMs with the same lattice structure at different locations.

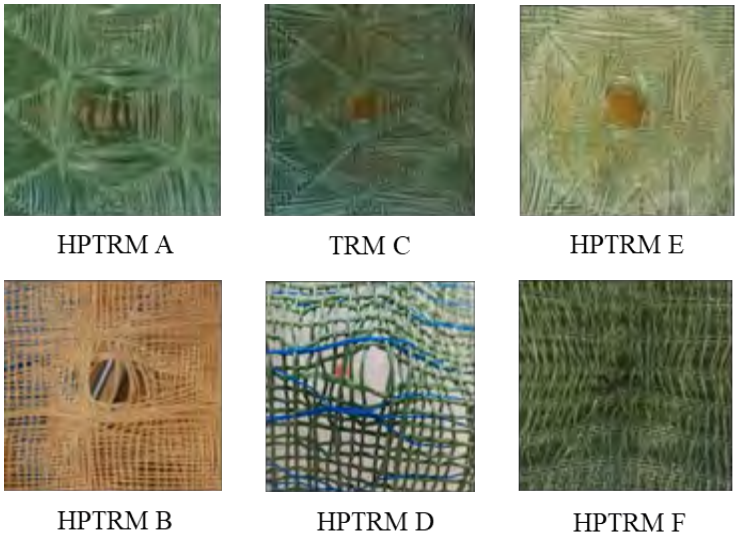

Figure 6. Photos of specimens after dynamic perforation test.

Figure 7 illustrates that mass per unit area influences the static puncture strength in woven and nonwoven geotextiles. This figure indicates that static puncture strength increases with increased mass per unit area. The results for (HP)TRM from the current study are also included

and generally follow the same trend. Figure 8 plots the correlation between various index properties and puncture test results for the six (HP)TRMs tested. The results indicate that both static puncture resistance and static puncture displacement increase while hole diameter decreases as mass per unit area increases. Similarly, puncture resistance and static puncture displacement both increase as tensile strength in the machine direction increases. The maximum hole diameter appears to be largely independent of the tensile strength in the machine direction.

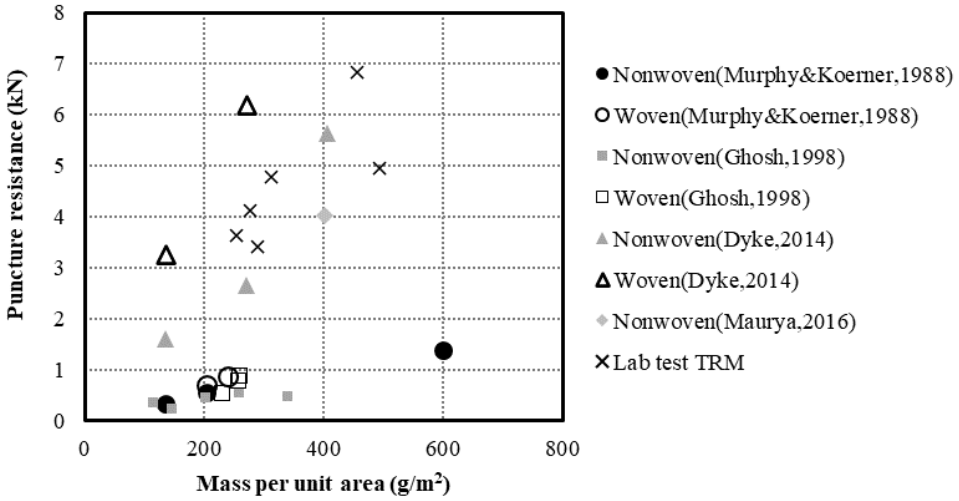

Figure 7. Correlation between static puncture resistance and mass per unit area of woven and nonwoven materials

CONCLUSIONS AND RECOMMENDATIONS

Turf reinforcement mats provide protection for exposed soil slopes or high flow channels during vegetation development. Any potential damage on the turf reinforcement mat can lead to failure of its function in erosion protection. Standard tests such as static puncture test and dynamic perforation test can simulate the damage caused by heavy or sharp stones during installation or construction. From this study, the following conclusions can be drawn:

(1) Static puncture test simulates the resistance of geosynthetics to penetration by long-term heavy loading. The loading process of woven (HP)TRMs experienced fiber rearrangement, fiber extension, and monofilament failure. Measured puncture strengths range from 3415 to 6825 N for the tested (HP)TRM specimens. Both puncture strength and extension at failure should be considered as indicators to describe the puncture behavior of (HP)TRMs.

(2) Static puncture test can be viewed as a modified tensile test, and higher tensile strength indicates higher static puncture. Higher mass per unit area shows greater static puncture strength and extension for woven turf reinforcement mats.

(3) The diameter of the punctured hole under the fixed drop cone energy indicates the impact resistance. Among the six tested TRM specimens, HPTRM D and F show better impact resistance to the dropped cone because of smaller hole diameter. The fiber compactness of a woven (HP)TRM affects dynamic puncture resistance.

(4) The measured maximum hole diameter values of punctured (HP)TRMs range from 6.7 to 20.5 mm. There is no strong relationship between tensile strength and maximum hole diameter.

It is suggested that maximum hole diameter, puncture strength, and extension at failure should be tested and routinely included in the (HP)TRM product report together with basic index properties to help designers better select appropriate (HP)TRM products in practice.

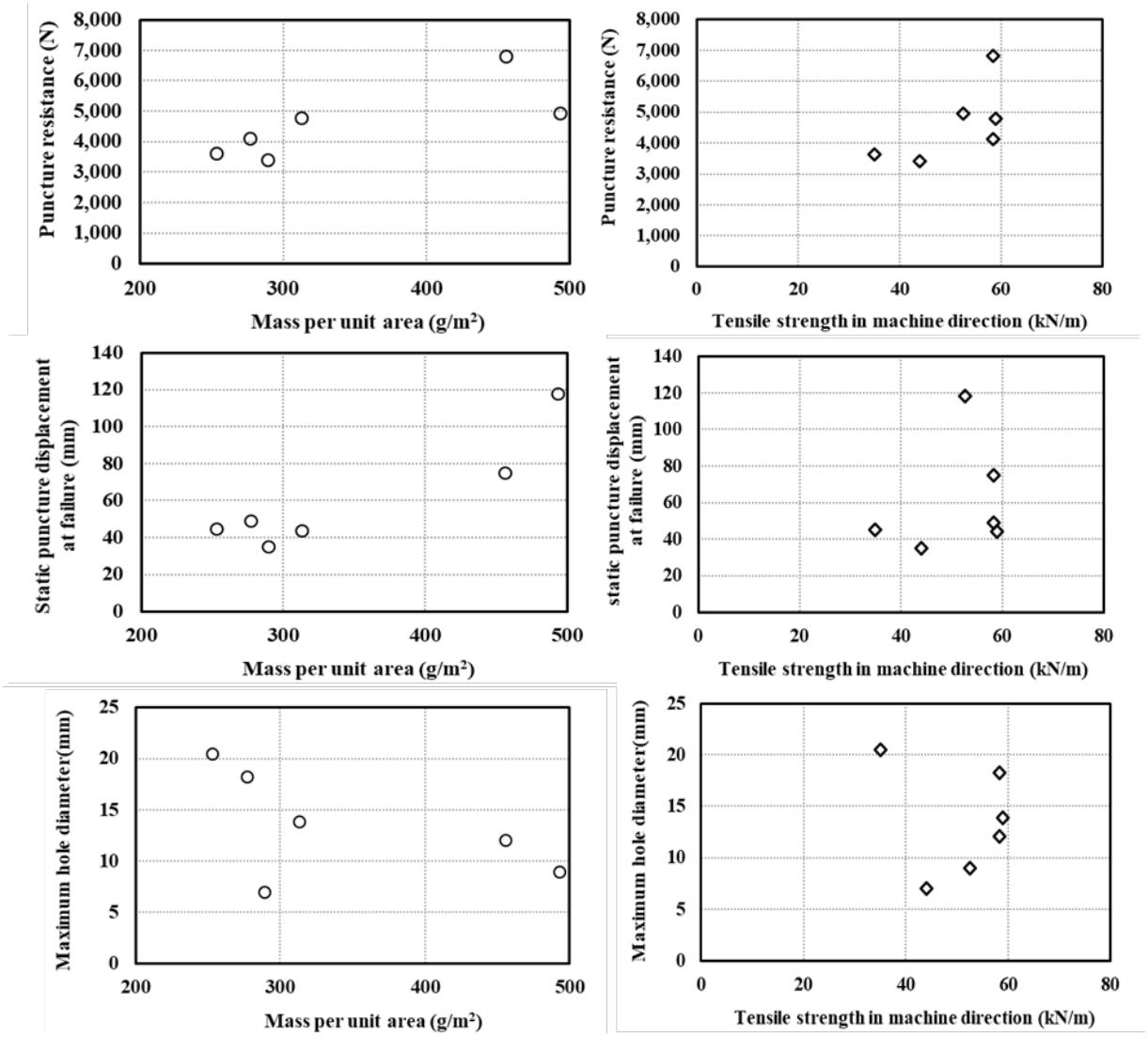

Figure 8. Correlation of static puncture resistance, average extension at failure, maximum hole diameter, and index properties of woven turf reinforcement mats.

ACKNOWLEDGEMENTS

The (HP)TRM manufacturers are thanked for providing samples for this study. The assistance of a former graduate student, Zhi Ge, who helped with static puncture strength tests in this study, is acknowledged. Partial support for the first author was provided through the Gene Boyd-Vulcan Materials Company Endowed Fellowship.

REFERENCES

ASTM D6566-18. Standard Test Method for Measuring Mass Per Unit Area of Turf Reinforcement Mats, *ASTM International*, West Conshohocken, Pennsylvania, USA.

ASTM D6525/D6525M-18. Standard Test Method for Measuring Nominal Thickness of Rolled Erosion Control Products, *ASTM International*, West Conshohocken, Pennsylvania, USA.

ASTM D6241-14. Standard Test Method for Static Puncture Strength of Geotextiles and Geotextile-Related Products Using a 50-mm Probe, *ASTM International*, West Conshohocken, Pennsylvania, USA.

ASTM D6818-18a. Standard Test Method for Ultimate Tensile Properties of Rolled Erosion Control Products, *ASTM International*, West Conshohocken, Pennsylvania, USA.

Atmatzidis, D.K., and Chrysikos, D.A. (2002). On the Static Puncture Strength of Non-woven Geotextiles. *7th International Conference on Geosynthetics*. Nice (pp. 1363-1366).

Bolt, A., and Duszynska, A. (2010). Static puncture resistance of nonwoven geotextiles. In Modern Building Materials, Structures and Techniques. *Proceedings of the International Conference*, Vol. 10, p. 1083

Collins, B. M., Holtz, R. D., and Allen, T. (2005). Long-term Performance of Geotextile Separators, Bucoda Test Site--Phase III (No. WA-RD 595.1). *Washington State Department of Transportation*.

EN ISO13433 (2006) Geosynthetics–Dynamic perforation test (cone drop test)

Ghosh, T.K. (1998). Puncture resistance of pre-strained geotextiles and its relation to uniaxial tensile strain at failure. *Geotextiles and Geomembranes*, 16(5): 293-302.

Jones, D.R.V., Shercliff, D.A., and Dixon, N. (2000). Difficulties associated with the specification of protection geotextiles using only unit weight. *Proceedings of the Second European Geosynthetics Conference*, Bologna, Italy (pp. 551-555).

Koerner, G.R., and Koerner, R.M. (2011). Puncture resistance of polyester (PET) and polypropylene (PP) needle-punched nonwoven geotextiles. *Geotextiles and Geomembranes*, 29(3): 360-362.

Maurya, S., Gupta, M., and Chitra, R. (2016). Engineered Anti-erosion Works Along the Right Bank of Jiabharali River in Assam. In *Ground Improvement Techniques and Geosynthetics* (pp. 381-389). Springer, Singapore.

Murphy, V. P., and Koerner, R. M. (1988). CBR strength (puncture) of geosynthetics. *Geotechnical Testing Journal*, 11(3): 167-172.

Termonia, Y. (2006). Puncture resistance of fibrous structures. *International Journal of Impact Engineering*, 32(9), 1512-1520.

Van Dyke, S. (2014). Comparison of CBR and Pin Puncture Strength Testing Used in the Evaluation of Geotextiles. *Theses and Dissertations*, University of Wisconsin-Milwaukee

Geosynthetics Conference

Asphalt Strain Response of Geosynthetic-Reinforced Asphalt Overlays under Static Plate Loads

V. Vinay Kumar, Ph.D.,[1] Gholam H. Roodi, Ph.D.,[2] and Jorge G. Zornberg, Ph.D., P.E.[3]

[1]Department of Civil, Architectural and Environmental Engineering, University of Texas at Austin, Austin, Texas-78712; e-mail: vinay.vasanth@utexas.edu
[2]Department of Civil, Architectural and Environmental Engineering, University of Texas at Austin, Austin, Texas-78712; e-mail: hroodi@utexas.edu
[3]Department of Civil, Architectural and Environmental Engineering, University of Texas at Austin, Austin, Texas-78712; e-mail: zornberg@mail.utexas.edu

ABSTRACT

Geosynthetic interlayers have proven successful in retarding the rate of reflective crack development in asphalt overlays. In addition, geosynthetic interlayers are also expected to enhance the structural capacity of pavements (e.g., by retarding the development of permanent deflections and tensile strains within the asphalt layers). However, the relevant mechanisms leading to an enhanced performance of geosynthetic-reinforced asphalt layers are not clearly understood and the structural benefits from geosynthetics are yet to be quantified. In this study, the asphalt strain response in full-scale field test sections comprising both unreinforced (control) and geosynthetic-reinforced asphalt overlay test sections was evaluated using static plate load tests. The road sections included an oxidized old asphalt layer and rehabilitation involved placing tack coat, installing geosynthetic interlayer (only in the geosynthetic-reinforced section), and finally constructing a 3-inch-thick asphalt overlay. The asphalt strains were recorded by the asphalt strain gauges installed at a depth of 3 inches within the old asphalt layer, under a static plate load application. Comparison of settlement and asphalt strain response of geosynthetic-reinforced overlay section with that of control section indicates that the geosynthetic reinforcements significantly reduced tensile strains in the asphalt layers. Specifically, under the same plate loads, the tensile strains in the geosynthetic-reinforced section was at least 90% less than the tensile strains in the unreinforced (control) section.

INTRODUCTION

A wide range of pavement interlayers have been used to enhance the performance of the asphalt overlays. The main functions that have been expected from using pavement interlayers include waterproofing, stress relieving and reinforcement (Lytton 1989). Engineering fabrics (such as geotextiles) and geocomposites have been typically used to provide waterproofing and stress relieving while grid-structure interlayers (such as geogrids and glass grid materials) have been mostly used to provide reinforcement function. However, specific conditions in which the benefits from each type of interlayers are realized are still unclear and need further investigation.

A wide range of experimental procedures have been used to evaluate performance of pavement interlayers. Examples include bond strength tests (e.g., Canestrari et al. 2005; Kumar et al. 2017; Leutner 1979; Roodi et al. 2017; West et al. 2005), flexural beam tests (e.g., Khodaii et al. 2009; Kumar and Saride 2017; Montestruque et al. 2004; Pasquini et al. 2014), and physical

pavement model tests (e.g., Correia and Zornberg 2016; Saride and Kumar 2019). Pavement models have been loaded using plate load setup, wheel loads, or accelerated pavement loading facilities. However, comparatively limited field trials have been conducted to explore the reinforced asphalt performance (e.g., Zou et al. 2007).

This study presents the results of static plate load tests conducted on a highway section in Texas. The roadway was tested before and after construction of an asphalt overlay. The tests were conducted at two locations including a location where a geocomposite interlayer was placed between the old and new asphalt and a location where no interlayer was placed. The settlement under the plate load test as well as tensile strain in the old asphalt were evaluated between the two sections.

PAVEMENT SECTIONS AND INSTRUMENTATION

As part of a rehabilitation plan along a long section of State Highway 21 in Texas, a 3-inch-thick asphalt overlay was constructed over the existing pavement. As part of this research study, a short section of the construction was used to investigate effectiveness of using pavement interlayers. Specifically, two different pavement interlayer systems were tested at two sections under static plate load test. In Section 1, referred to as the control section (CS), no pavement interlayer was used while in Section 2, referred to as the GG section, a geocomposite interlayer was used.

The road profile at the two tested locations were investigated by drilling from the pavement surface through the subgrade. Figures 1a and b show the road profile in Sections 1 and 2, respectively. The thickness of the old asphalt was 6 and 5 inches in Sections 1 and 2, respectively. The thickness of the base and subbase courses were 6 and 10 inches in Section 1, respectively, and 7 and 9 inches in Section 2, respectively. The old asphalt, base course and subbase course had similar characteristics in the two sections. The new asphalt included a 2-inch-thick Type D mix overlain by a 1-inch-thick thin overlay mix (TOM), classified according to Texas Department of Transportation (TxDOT) Standard Specifications for Construction and Maintenance of Highways, Streets, and Bridges (TxDOT 2014).

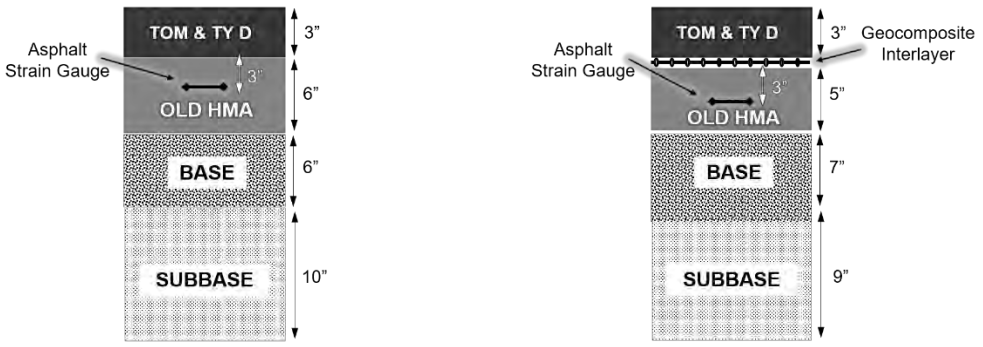

Figure 1. Roadway profile at test sections: a) Section 1 (control section); b) Section 2 (reinforced section).

The interlayer material that was used in Section 2 was a geocomposite consisting of a glass-fiber grid backed by a thin layer of fabric. The geocomposite (GG) had a coating with 60% bitumen content and an ultimate tensile strength of 100 kN/m at 3% strain in both machine and cross-machine directions.

Before construction of the new overlay, H-shaped asphalt strain gauge (Figure 2) was installed at a depth of 3 inch in the old asphalt. To install the asphalt strain gauges, cores were drilled to reach the desired depth in the old asphalt; then, a thin bed of sand-bitumen mix was placed in the bottom of the core, and the core was filled with Type D asphalt mix following placement of the asphalt strain gauges. The asphalt strain gauges were made of high temperature resistance material and included a full-bridge configuration of strain gauges in the web of the H-shaped sensor. The sensors were coated with bitumen to improve contact with surrounding asphalt mix.

Figure 2. Typical asphalt strain gauge installed in the old asphalt.

EXPERIMENTAL PROGRAM

The test sections were loaded using a static plate device before and after construction of the overlay. The plate load tester device, provided by Humboldt, conformed to specifications required by DIN 18134:2012-04 standard (DIN18134, 2012). The testing plate had a diameter of 300 mm and a thickness of 25 mm.

The loading system consisted of a hydraulic pump connected to a hydraulic jack via a high-pressure hose. One end of the hydraulic jack was placed on the loading plate and the other end was secured against a heavy truck for reaction. Both ends had a hinged connection and a load cell was placed between the hydraulic jack and the settlement plate to measure the applied load. The system was capable of applying, maintaining, and releasing the load in controlled stages. The load capacity of the system was 50 kN, equivalent of an applied stress of 0.7 MPa.

The settlement measurement system included a support frame resting on a three-point bearing support. A rotatable rigid contact arm was mounted onto the support frame and could be extended for 1.5 m to reach the loading plate. The end of the contact arm could be adjusted at the center of the plate through a measuring tunnel designed on the plate. A displacement transducer was mounted onto the support frame and attached to the free end of the contact arm to record the settlement. The above system could measure the settlement with a resolution of 0.01 mm. Figure 3 shows a picture of static plate load setup used in this study.

The static plate load tests were conducted in two phases exactly on the same locations, including before (Phase 1) and after (Phase 2) construction of the overlay. In both phases, a seating load of 0.01 MPa were applied to the pavement surface in the beginning of the test. In the first phase (before overlay construction), consistent with DIN 18134:2012-04, the test sections were loaded in six approximately equal increments of 0.08 MPa to reach the maximum stress of 0.5 MPa. Each loading stage was completed within one minute and after a waiting period of 120 seconds, the plate settlement was recorded. Asphalt strain gauges had not yet been installed in this phase; thus, the plate settlement was the only measurement made.

Figure 3. Static Plate Load setup used in the study.

The loading in the second phase of the test (after overlay construction) was identical to the first phase except for the maximum stress. The maximum stress in the second phase was limited to 0.24 MPa, which was applied in three approximately equal increments of 0.08 MPa. In addition, asphalt strain gauges had been installed in this phase; hence, the tensile strain in the old asphalt layer was measured for each loading stage in addition to the plate settlement.

RESULTS AND DISCUSSION

The pavement response under a static plate load test (PLT) is generally presented in a typical load-settlement plot. In addition, the time corresponding to each load and unload stage was carefully recorded in this study. The settlement response corresponding to each load and unload stages were then correlated with the corresponding response recorded from the asphalt strain gauges, as a function of time. Figures 4 and 5 present the 'Time-settlement' and 'Time-strain' recorded under a typical static PLT adopted, for the control and geosynthetic reinforced pavement test sections, respectively. It can be observed that the time corresponding to a settlement is almost the same as that of strain, suggesting a good correlation between the settlement and strains recorded. In addition, both, settlement and tensile strain increased with an increase in the applied load and vice-versa. However, the settlement in the control section (Fig. 4a) is consistently lower than that of geosynthetic reinforced section (Fig. 5a), while the tensile strains in the control section (Fig. 4b) is consistently higher than that of the geosynthetic-reinforced section (Fig. 5b), under the same loading and unloading stages. This condition could be attributed to the influence of ambient and surface temperature during the test and the pre-existing pavement conditions in the control and geosynthetic-reinforced test sections, which will be discussed in next sections of this paper. The average asphalt surface temperature during the static PLT conducted on the control and geosynthetic-reinforced sections were 15 °C (59 °F) and 22 °C (72 °F), respectively.

Besides, another important observation from 'Time-strain' plots (Figs. 4b & 5b) suggest that the strains recorded under a typical load/unload stage did not completely stabilize, before proceeding to the next load stage.

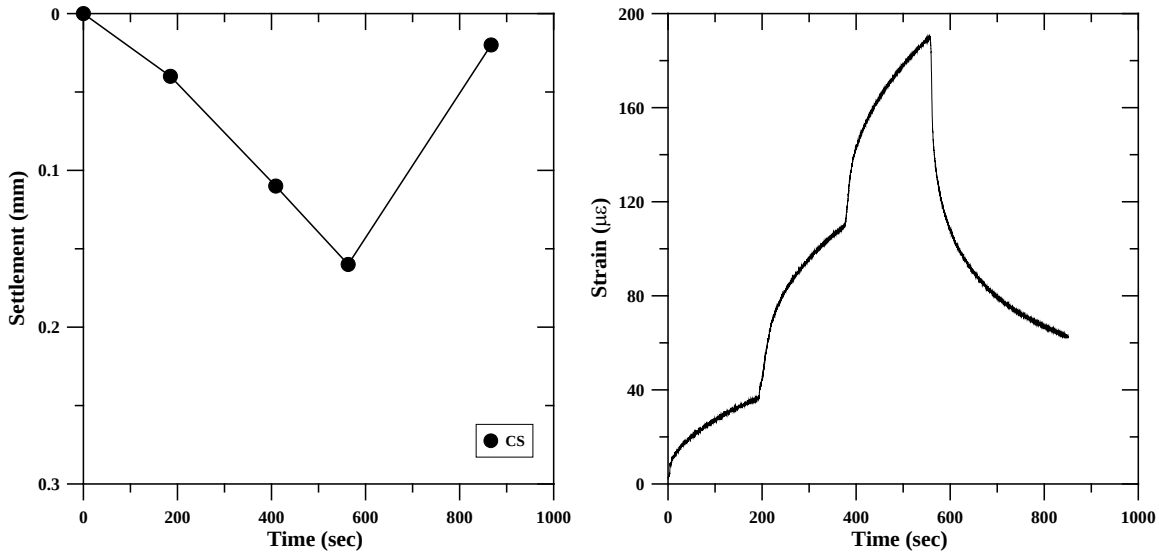

Figure 4. Settlement and strain response in control section.

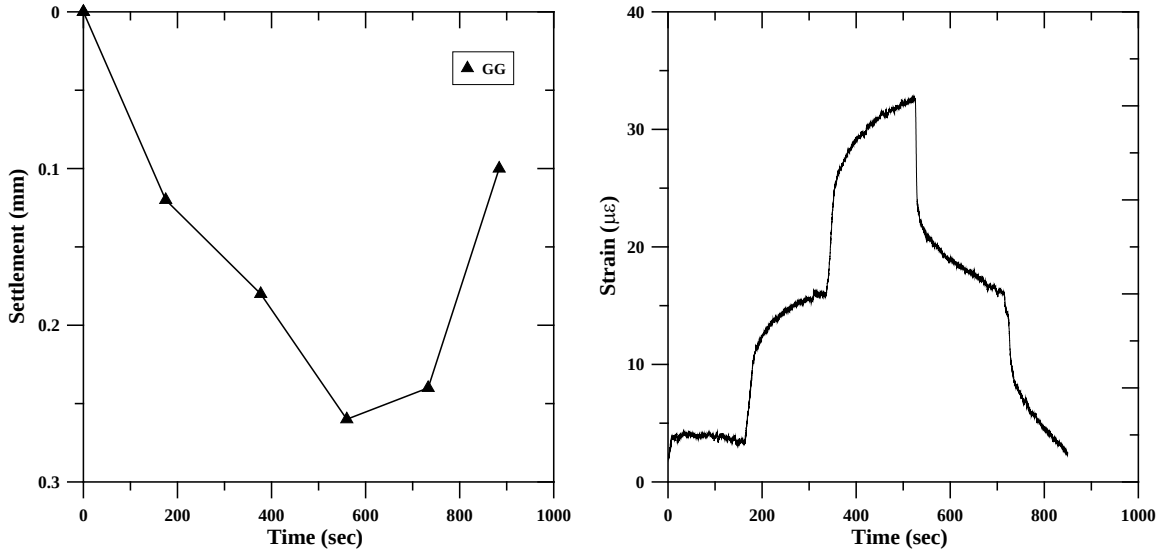

Figure 5. Settlement and strain response in geosynthetic-reinforced section.

Hence, to understand this condition, a typical load and unload stage was considered for the control and geosynthetic-reinforced sections, as shown in Fig. 6. It can be seen that the slope of the strain-time curve for both load and unload stages are steep indicating the settlement and strains recorded under an applied load after 120 seconds of wait period was not completely stabilized. The displacement transducers adopted with the PLT device to record the settlements were not able to record continuous displacements at micro-level and only the ultimate settlement at the end of each loading and unloading stage was recorded. On the other hand, the strain gauges adopted in the study were capable of recording the strain values on the order of micro-strains, suggesting to adopt waiting periods longer than that prescribed in DIN 18134:2012-04. It should also be noted

that the slope of 'Time-strain' curve for geosynthetic-reinforced section looks flat in comparison to the control section, due to the high strains recorded in the latter case.

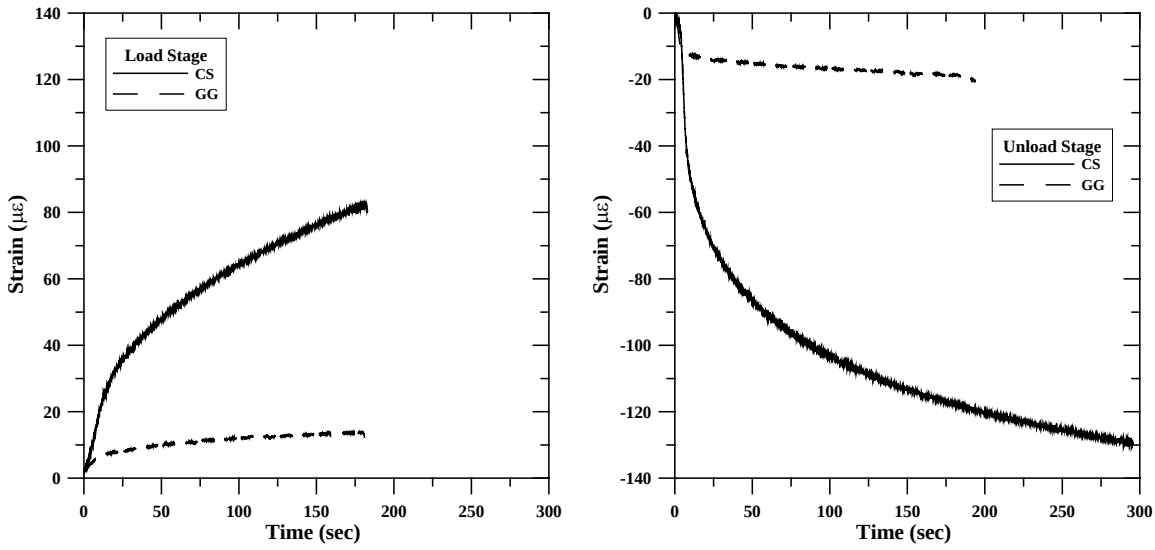

Figure 6. Typical loading and unloading stages of static PLT.

Figure 7 shows the settlement and strain responses for three loading stages adopted in the second phase (i.e., after overlay construction) of testing in this study and it can be observed that the settlement and strains increased with an increase in the applied load. The settlement in the control section is consistently lower than that of the geosynthetic-reinforced section, while the strains in the control section are consistently higher than that of the geosynthetic-reinforced section. As previously discussed, this may be due to the influence of asphalt surface temperature and the pre-existing pavement conditions. The influence of asphalt surface temperature and the pre-existing conditions on the surface settlement and asphalt strains are discussed in the sections below.

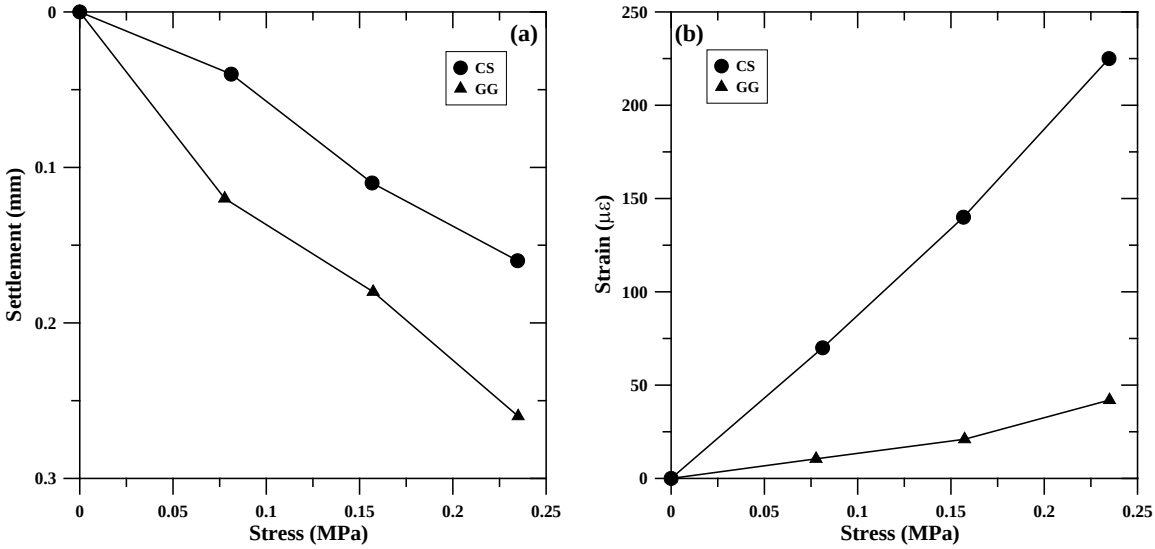

Figure 7. Settlement and strain responses under different loading stages (as recorded).

Influence of Temperature.

It is well known that the asphalt mixes are viscoelastic under small strain conditions, which is a function of time and temperature (Witczak and Solti 2004; Hu et al. 2019). The ambient and asphalt surface temperatures greatly influence the resilient modulus of asphalt layer and changes in the modulus influence the surface settlement and the tensile strains within the asphalt layer. Hence, to completely characterize the asphalt mixture adopted in the study, dynamic modulus tests were conducted at different temperatures of 14 °F, 40 °F, 70 °F, 100 °F, and 130 °F, and different frequencies of 0.1 Hz, 0.5 Hz, 1 Hz, 5 Hz, 10 Hz, and 25 Hz. Subsequently, a dynamic modulus master curve was developed, as shown in Fig. 8. The dynamic modulus master curve is often described by a sigmoidal function as follows (Witczak and Solti 2004; Hu et al. 2019):

$$log|E^*| = \delta + \frac{\alpha}{1+e^{\beta+\gamma log t_r}} \quad (1)$$

where, δ is the minimum value of $log|E^*|$ in the sigmoid function; α is the vertical span of the function; β and γ are shape parameters for the sigmoid curve; and t_r is the reduced loading time.

Based on the time-temperature superposition principle, $log\ t_r$ in Eq. 1 can be expressed as:

$$log t_r = log\ t - log a_T \quad (2)$$

where, t is the actual loading time at a given temperature (T); a_T is the temperature shift factor. The time-temperature shift factor can be fitted by a second order polynomial as shown in Fig. 8b.

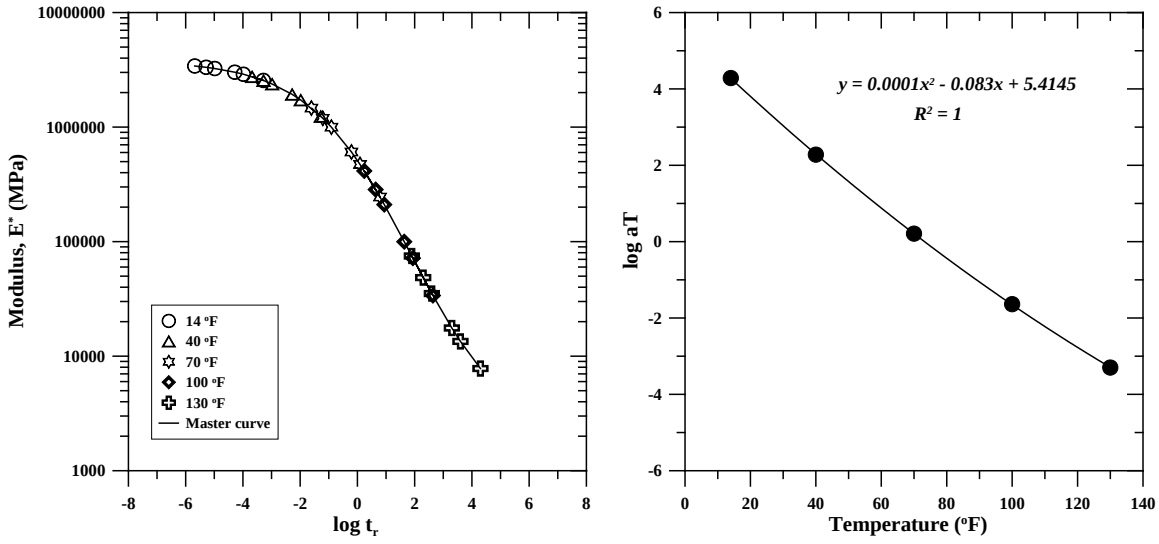

Figure 8. Dynamic Modulus Master Curve of the asphalt mixture used in the study.

From Fig. 8 and Eq. 1, the dynamic modulus of the asphalt mixture adopted in the study could be estimated for different temperatures between 14 °F and 130 °F and different frequencies (load time) between 0.01 Hz (10 secs) and 25 Hz (0.04 secs). However, to understand the influence of dynamic modulus of asphalt concrete on the surface settlement and asphalt strains at a depth of 6 inches, multi-layer linear elastic analysis (MLEA) was performed. The MLEA was performed

considering a pavement model with an overall asphalt layer of 8.5 inch thickness (3 inch overlay and 5.5 inch old asphalt), base and subbase layer of 16 inch thickness and infinite thickness for subgrade soil. The modulus input values for all the pavement layers was adopted based on the back-calculated modulus values predicted from the falling-weight deflectometer (FWD) test results. The MLEA was repeated for different modulus values of asphalt layer ranging from 70 MPa to 68,950 MPa and the corresponding surface settlements and tensile strains at a depth of 6 inch were estimated and plotted as shown in Fig. 9. A power function was separately fitted to 'Modulus-Settlement' (Fig. 9a) and 'Modulus-Tensile strain' (Fig. 9b) values, as shown in Equations 3 and 4. These equations can fairly estimate the surface settlement and tensile strain values for any asphalt modulus values ranging from 70 MPa to 68950 MPa.

$$\Delta = 3.9849(E')^{-0.349} \quad (3)$$

$$\varepsilon_{xx} = 0.0531(E')^{-0.924} \quad (4)$$

where, Δ is the surface settlement in mm; E' is the modulus of asphalt layer in MPa; and ε_{xx} is the tensile strain at a depth of 6 inch in the asphalt layer.

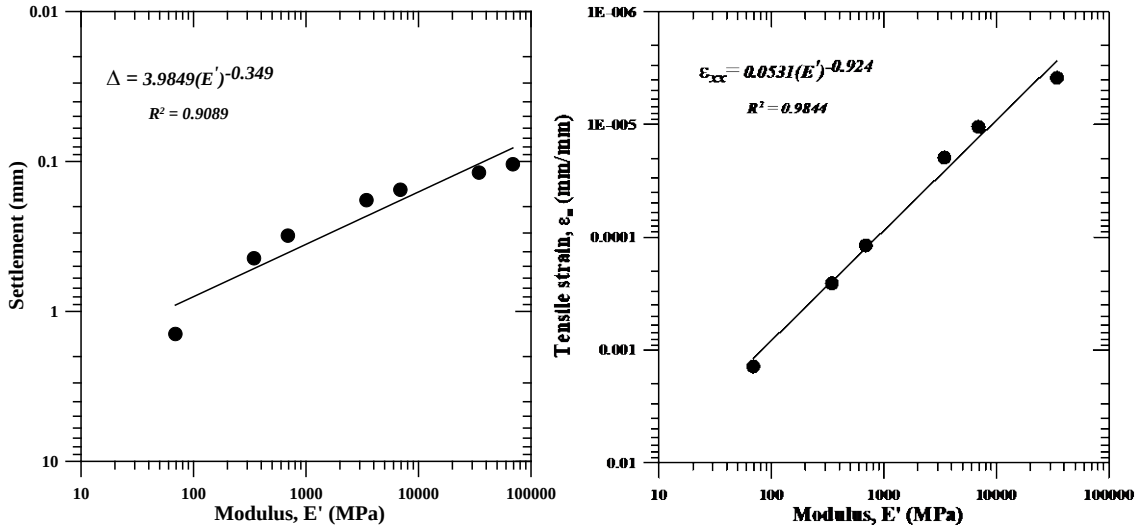

Figure 9. Multi-layer linear elastic analysis: (a) Variation of surface settlement with modulus of asphalt layer; (b) Variation of tensile strain (depth of 6 inch) with modulus of asphalt layer.

Since the asphalt surface temperature was different for the static PLT performed on the control and geosynthetic-reinforced pavement sections, a reference temperature of 77 °F was chosen. The modulus value corresponding to reference temperature of 77 °F was estimated to be 217,170 MPa, using Eq. 1 and Fig. 8. The estimated modulus value was then adopted in Equations 3 and 4 and the corresponding settlement and tensile strains were estimated to be 0.054 mm and 6.22×10^{-7} mm/mm, respectively. Similarly, the modulus values corresponding to test temperatures of 59 °F and 72 °F were estimated to be 575,610 MPa and 282,648 MPa, respectively. Subsequently, the settlement and strains corresponding to the modulus values at 59 °F and 72 °F were estimated to be 0.0389 mm and 2.53×10^{-7} mm/mm, and 0.0498 mm and 4.88×10^{-7} mm/mm, respectively, in the control and geosynthetic-reinforced sections. Eventually, temperature

correction factors for the surface settlements and tensile strains were determined separately for the control and geosynthetic-reinforced sections, based on the ratio of estimated settlement and tensile strain values at the reference temperature to that of the test temperature. The correction factors were then multiplied to the corresponding settlement and tensile strain values in the control and geosynthetic-reinforced sections. Fig. 10 presents the settlement and tensile strain response for different loading stages adopted in the study, normalized to a reference temperature of 77 °F. It can be observed that the tensile strains in both control and geosynthetic-reinforced sections are now increased to 560 με and 55 με from 225 με and 45 με, respectively. Similarly, an increase in the settlement of the control and geosynthetic-reinforced sections was observed from 0.16 mm and 0.26 mm to 0.24 mm and 0.29 mm, respectively. However, it should also be noted that the settlements in the control section are consistently lower than that of the geosynthetic-reinforced section, while the tensile strain trends suggest otherwise. This condition could be due to the pre-existing condition of the pavement sections, which is discussed below.

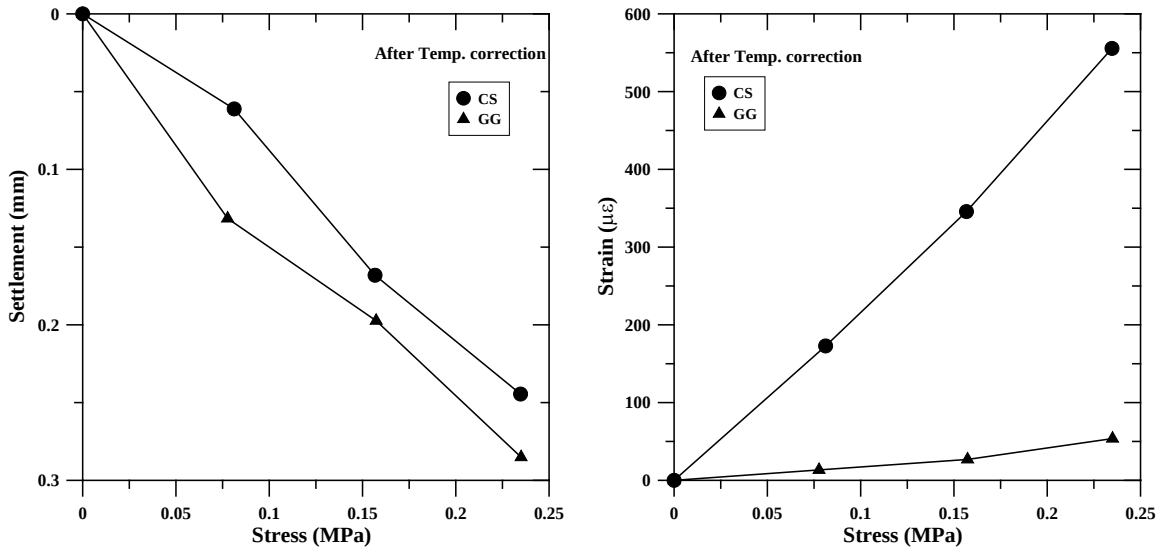

Figure 10. Settlement and strain response under different loading stages (after temperature correction).

Influence of pre-existing conditions.

The influence of pre-existing conditions of the pavement sections before the overlay construction is an important parameter to understand and fairly evaluate the performance of geosynthetic-reinforced section against the control section. Hence, to address the influence of pre-existing pavement conditions, static PLT performed on the old pavement prior to the installation of asphalt strain gauge and overlay construction, as discussed under 'Experimental Program,' has been considered. It should also be noted that only settlement response was recorded from the PLTs performed on the old pavement, but not strain response.

A maximum static plate load corresponding to a stress of 0.24 MPa was considered in the study, even though a maximum stress of 0.50 MPa was applied on the old pavement, to have a fair comparison between the PLTs performed on the old pavement and overlay. Fig. 11 presents the settlement response of the old pavement on which the control and geosynthetic-reinforced overlay sections were constructed. The PLTs were performed at different temperatures during this phase of testing as well, hence, a temperature correction corresponding to a reference temperature of 77

°F was applied to Fig. 11a and resulted in Fig. 11b. It can be observed that the settlements in old pavement below the control section are consistently lower than that of old pavement below the geosynthetic-reinforced section, suggesting a better settlement response in the control section.

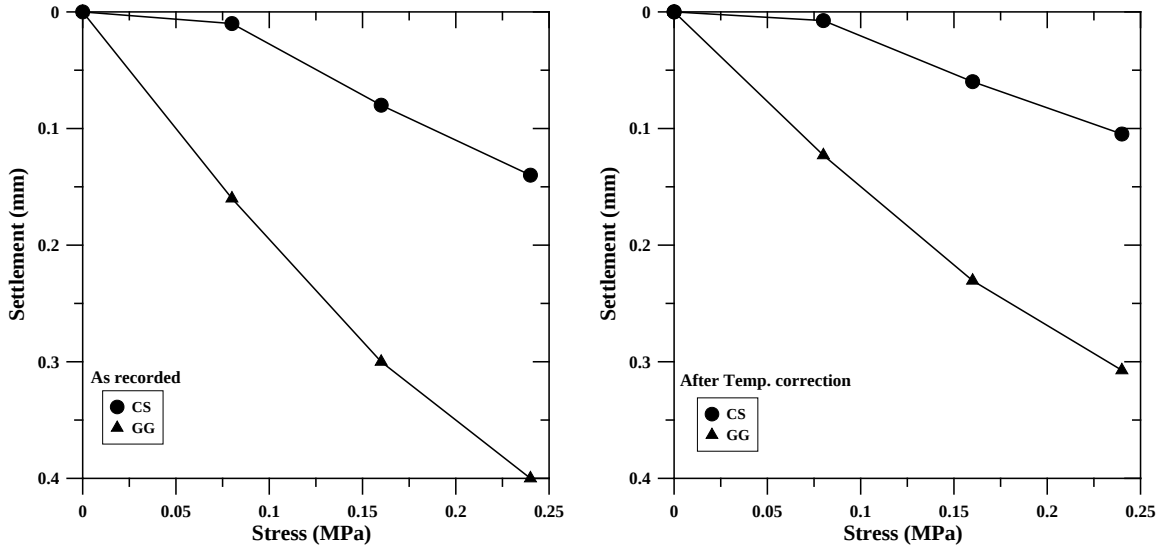

Figure 11. Settlement response of pavement section before overlay construction: (a) as recorded; (b) after temperature correction.

Besides, to understand the influence of pre-existing pavement conditions on the settlement response of the control and geosynthetic-reinforced sections, the settlements from Fig. 11b and Fig. 10a were compared and the percentage reduction were determined, as plotted in Fig. 12a. Similarly, from Fig. 10b, the reduction in tensile strains in the geosynthetic-reinforced section with respect to the control section was determined, irrespective of pre-existing pavement condition and plotted, as shown in Fig. 12b.

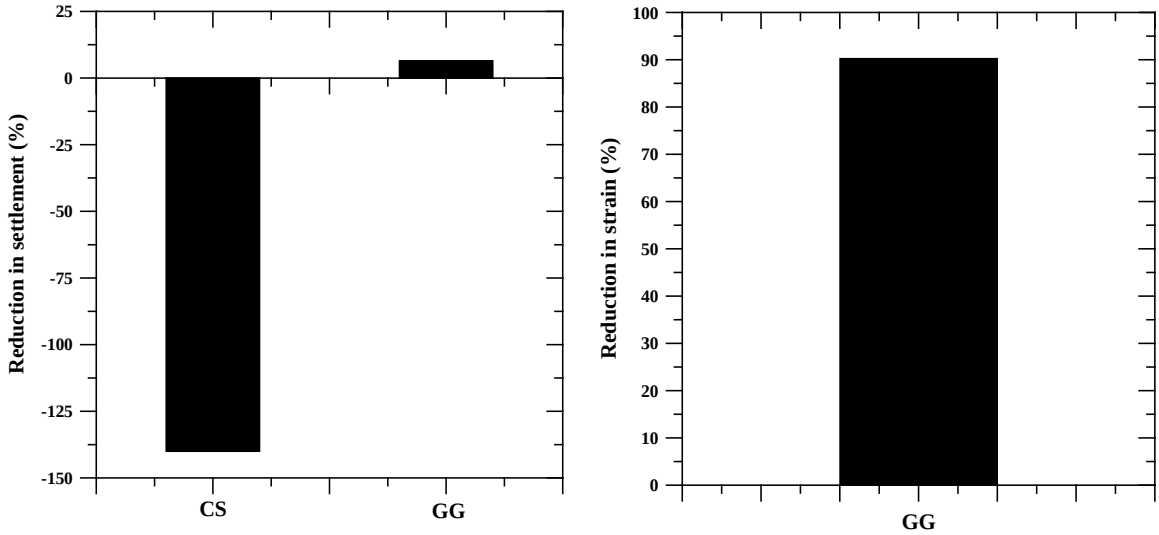

Figure 12. (a) Percentage reduction in settlement; (b) Percentage reduction in tensile strain.

It can be observed that the plate settlement on asphalt overlay increased by 140% compared to the plate settlement on the old pavement in the control section. While, the plate settlements on the asphalt overlay reduced by 6.5% compared to that on the old pavement in the geosynthetic-reinforced section. The important observation in the control section suggests that the oxidation of old pavement resulted in a stiffer and brittle asphalt layer compared to the fresh resilient asphalt overlay, hence higher settlements in the latter case. However, the geosynthetic reinforcement provides enough stiffness and resilience to the asphalt layers and effectively resist the settlements under the plate loads. In addition, a reduction in tensile strain by 90% was witnessed in the geosynthetic-reinforced section, irrespective of pre-existing pavement condition.

Overall, it can be summarized that the geosynthetic reinforcement adopted in the study was effective in resisting the plate settlements and minimizing the critical tensile strains responsible for asphalt cracking.

CONCLUSION

In this study, the plate settlement and asphalt strain responses in full-scale field test sections comprising both unreinforced (control) and geosynthetic-reinforced asphalt overlay test sections was evaluated using static plate load tests. The following conclusions can be drawn from the study:

The asphalt strain gauges adopted in the study were capable of measuring the influence of plate loads on the order of micro strains, suggesting a waiting period greater than 120 seconds between successive load/unload stages during a static plate load test.

The plate settlements and asphalt strains recorded under the static plate loads suggest a significant influence of the asphalt surface temperature and the pre-existing condition of the pavement sections on their responses.

The plate settlements on the overlay was found to be 140% higher than that on the old pavement in the control section, owing to the oxidation of the old asphalt resulting in a stiffer and brittle asphalt layer.

The geosynthetic reinforcement provided additional flexural stiffness and resilience to the asphalt layers and the geosynthetic-reinforced section effectively resisted the settlement under the plate loads.

A reduction of 90% in the tensile strain was quantified in the geosynthetic-reinforced section against the control section, irrespective of the pre-existing pavement conditions.

Overall, it can be summarized that the geosynthetic-reinforcement adopted in the study was effective in resisting the plate settlements and minimizing the critical tensile strains responsible for asphalt cracking.

ACKNOWLEDGEMENTS

The authors wish to thank the Texas Department of Transportation (TxDOT) for financial support of this study.

REFERENCES

Canestrari, F., Ferrotti, G., Partl, M.N. and Santagata, E. (2005). Advanced testing and characterization of interlayer shear resistance, *Transportation Research Record*, 1929:69-78.

Correia, N. S. and J. G. Zornberg (2016). Mechanical response of flexible pavements enhanced with geogrid-reinforced asphalt overlays. *Geosynthetics International,* 23 (3):183–193.

DIN 18134:2012-04 (2012). Soil Testing procedures and testing equipment- Plate load test. *Deutscnes Institut fur Norrnung e. V.*, Berlin, Beuth Verlag Gmbh, Berlin, Germany.

Hu, S., Rahman, A., Zhang, J., Zhou, F. and Scullion, T. (2019). *Implementation of Texas Mechanistic-Empirical Flexible Pavement Design System (TxME),* Project Report, FHWA Project TX-18/5-6622-01-R1: Texas A&M Transport Institute, College Station, Texas.

Khodaii, A., Fallah, S. and Nejad, F.M. (2009). Effects of geosynthetics on reduction of reflection cracking in asphalt overlays, *Geotextiles and Geomembranes*, Elsevier Science Publishers Ltd, England, 27(1):1-8.

Kumar, V.V. and Saride, S. (2017). Use of Digital Image Correlation for the Evaluation of Flexural Fatigue Behavior of Asphalt Beams with Geosynthetic Interlayers, *Transportation Research Record*, 2631:55-64.

Kumar, V.V., Saride, S. and Peddinti, P.R.T. (2017). Interfacial Shear Properties of Geosynthetic Interlayered Asphalt Overlays, *Geotechnical Frontiers-2017,* Orlando, Florida, ASCE, GSP-277, 442-451.

Leutner, R. (1979). Untersuchung des Schichtverbundes beim bituminösen Oberbau, (In German) *Bitumen,* Hamburg, Germany, 3.

Lytton, R.L. (1989). Use of Geotextiles for Reinforcement and Strain Relief in Asphalt Concrete, *Geotextiles and Geomembranes*, Elsevier Science Publishers Ltd, England, 8:217-237.

Montestruque, G., Rodrigues, R., Nods, M. and Elsing, A. (2004). Stop of reflective crack propagation with the use of PET geogrid as asphalt overlay reinforcement, *5th RILEM Conference on Cracking in Pavements*, Limoges, France, RILEM Publications S.A.R.L., 231-238

Roodi, G.H., Morsy, A.M. and Zornberg, J.G. (2017). Experimental Evaluation of the Interaction between Geosynthetic Reinforcements and Hot Mix Asphalt, *International Conference on Airfield and Highway Pavements,* ASCE, Philadelphia, Pennsylvania, USA, 428-439.

Saride, S. and Kumar, V.V. (2019). Estimation of Service life of Geosynthetic-Reinforced Asphalt Overlays from Beam and Large-Scale Fatigue Tests, *Journal of Testing and Evaluation*, 47(4): 2693-2716.

TxDOT. 2014. Standard Specifications for Construction and Maintenance of Highways, Streets, and Bridges. *Texas Department of Transportation,* Austin, Texas, USA.

West, R.C., Zhang, J. and Moore, J. (2005). Evaluation of bond strength between pavement layers, *NCAT Report 05-08, National Center for Asphalt Technology*, Auburn, AL.

Witczak, M.W. and A. Solti. (2004). *A Recommended Methodology for Developing Dynamic Modulus E* Master Curves from Non-Linear Optimization,* Project Report, NCHRP Project 9-19: Arizona State University, Tempe, Arizona.

Zou, W., Wang, Z. and Zhang, H. (2007). Field Trial for Asphalt Pavements Reinforced with Geosynthetics and Behavior of Glass-Fiber Grids, *Journal of Performance of Constructed Facilities*, ASCE, 21(5):361-367.

Geosynthetics Conference

Evaluation of Bond Strength, Permeability, and Recyclability of Geosynthetic Products

Fan Gu, Ph.D., P.E.,[1] David Andrews, P.E.,[2] and Mark Marienfeld, P.E.[3]

[1]National Center for Asphalt Technology, 277 Technology Parkway, Auburn, AL 36830; e-mail: fan.gu@auburn.edu
[2]Propex Operating Company, 4019 Industry Drive, Chattanooga, TN 37416; e-mail: David.Andrews@propexglobal.com
[3]TreadMark Inc., 4821 Thornhill Drive NW, Acworth, GA 30101; e-mail: mark.marienfeld@gmail.com

ABSTRACT

In this study, the influences of geosynthetic interlayers on permeability and interface bond strength of asphalt pavements were evaluated using Florida permeability and NCAT bond strength tests, respectively. The permeability test results indicated that the inclusion of geosynthetic interlayers effectively reduced the permeability of asphalt pavement. The bond strength results demonstrated that the asphalt specimens containing geosynthetic had lower bond strength values than the control specimens, but asphalt samples containing polyester and polypropylene-based geosynthetic products still had bond strength greater than 100 psi, indicating satisfactory interface bonding. In addition, this study evaluated the performance of a new hot mix asphalt with 30% RAP containing a new polypropylene paving fabric. The moisture susceptibility test results demonstrated that this geosynthetic RAP asphalt mixture had much higher dry and wet tensile strength values than those minimum values specified by Caltrans Specification Section 39. The Hamburg wheel tracking test results showed that this geosynthetic RAP asphalt mixture only had a rut depth of 2.65-mm after 15,000 wheel passes, which was significantly better than the maximum rut depth specified by Caltrans (i.e., 12.5-mm). The Illinois flexibility index test results showed that this geosynthetic RAP and Control RAP asphalt mixtures had comparable flexibility index values.

INTRODUCTION

Geosynthetic interlayers have been widely used in pavement rehabilitation to mitigate the reflective cracking distresses of asphalt overlays. Lytton (1989) described the three benefits of geosynthetic interlayers, which included stress relief, waterproofing barrier, and reinforcement. The geosynthetic reinforcement in asphalt layers provides additional tensile strength to the resulting composite by increasing the amount of energy that can be absorbed during the repeated loading (Correia et al. 2014). The geosynthetic also absorbs and retains the asphalt tack coat to form a moisture barrier with low permeability. Ridgeway (1982) evaluated the relationship between permeability of paving fabric and application rate of tack coat. He found that the permeability of paving fabric reduces to 1×10^{-6} - 1×10^{-7} cm/sec when the application rate reaches 1.13 liter/sq. meter (0.25 gallon/sq. yard). For conventional dense-graded asphalt pavement, the permeability usually ranges from 1×10^{-5} to 1×10^{-3} cm/sec, which is considered impermeable

according to Florida Department of Transportation (FDOT) Specification Section 334. However, when any cracking occurs in asphalt pavement, the permeability can increase to 1×10^{-1} cm/sec, which results in a significant amount of rain water infiltrated into a pavement system. It is believed that the geosynthetic interlayer can effectively serve as a moisture barrier. Due to the waterproofing function, the bearing capacity of the underlying layers is increased to provide stronger support to the pavement; and underlying asphalt layers will suffer less moisture damage.

Although geosynthetic interlayers show promising benefits for pavement structures, they also bring concern for interface bonding. Poor interface bonding may result in delamination, pavement slippage, and fatigue cracking, which can cause significant reduction in pavement life. Therefore, the use of a geosynthetic interlayer shall provide satisfactory bonding strength between existing pavement and asphalt overlay.

If a geosynthetic is used as an asphalt interlayer, it will be milled and recycled with asphalt material at the end of service life. Accordingly, the geosynthetic manufacturers bring two concerns: (1) Can a geosynthetic product be easily torn into small pieces by the milling machine? (2) Will the milled geosynthetic product adversely affect the engineering performance of new asphalt concrete pavement using a percentage of reclaimed asphalt pavement (RAP) containing paving fabric? Traditional paving fabrics are usually difficult to tear apart by a milling machine and difficult to process through asphalt plant screening. Recently Propex developed a new generation of polypropylene paving fabric product that is easy to be milled and recycled. If this new recyclable paving fabric is proven to have no adverse effect on milling operations or the engineering performance of new hot mix asphalt containing RAP with milled pieces of the fabric, the reclamation issue of asphalt pavements containing paving fabric interlayer will be thoroughly solved.

The objective of this paper was two-fold: one was to evaluate the influences of geosynthetic interlayers on permeability and bond strength of asphalt pavements; and the other was to evaluate the performance of a new hot mix asphalt with a percentage of RAP containing a new millable and recyclable paving fabric and to determine whether the presence of the fabric has an adverse impact on the quality of a new asphalt mixture.

MATERIALS AND TEST METHODS

Six commercially available geosynthetic interlayer products were selected for permeability and bond strength tests. Table 1 presents the properties of these geosynthetic products.

Table 1. Properties of Geosynthetic Products

Product Code	Product Description	ASTM D5035 Tensile Strength (kN/m)	Asphalt Retention Rate (liter/sq. meter)
PFR[a]	Polypropylene	4	0.91
PF	Polypropylene and polyester	11	0.91
PMH	Fiberglass and polyester	14	0.81
PMC1	Fiberglass and polyester	25	0.45
PMC2	Fiberglass and polyester	50	0.45
PGM	Polyester	35	0.54

Note: [a] New millable and recyclable paving fabric.

Permeability Test

To simulate the actual field construction, the specimens for permeability test were prepared according to the following procedures:

- Place an old asphalt slab of dense-graded asphalt mixture at the bottom of slab compactor, which aimed to simulate the existing pavement;
- Place an aluminum sheet on top of bottom slab;
- Place tack coat of PG 64-22 asphalt binder at the recommended application rate shown in Table 1;
- Place geosynthetic products over tack coat;
- Pour the open-graded friction course (OGFC) mix with 135°C on top of geosynthetic and compact the slab using the kneading method;
- Remove the bottom slab of dense-graded asphalt mixture;
- Cool down the compacted slab for two days;
- Remove aluminum sheet, core cylindrical asphalt specimens with geosynthetic, and seal the side of specimens using the candle wax, as shown in Figure 1a.

The Florida permeability test apparatus was used to determine the flow rate of water through the specimen, as shown in Figure 1b. The side of specimen was sealed by latex membrane. An air pump capable of applying 103.4 kPa (15 psi) pressure and capable of applying vacuum was used to evacuate the air from the sealing membrane cavity. Water in graduated cylinder flowed through the saturated specimen and the interval time taken to reach a known change in head was recorded. The permeability of specimen was determined using Equation 1, which is based on Darcy's Law.

$$k = \frac{aL}{At} \ln\left(\frac{h_1}{h_2}\right) t_c \quad (1)$$

where: k is the coefficient of permeability, a is the cross-sectional area of the burette, L is the thickness of specimen, A is the cross-sectional area of specimen, t is the elapsed time between h_1 and h_2, and t_c is the temperature correction factor for viscosity of water.

(a) Side-Sealed Sample

(b) Florida Permeability Test Apparatus

Figure 1. Florida Permeability Test

Bond Strength Test

Similar to the permeability test, the laboratory samples for bond strength were also drilled from the compacted slabs. The laboratory sample preparation procedures were described as follows.

- Compact a 2-inch thick dense-graded asphalt slab;
- Place tack coat of PG 64-22 at the recommended application rate shown in Table 1;
- Place geosynthetic products over tack coat;
- Pour hot dense-graded asphalt mix on top of geosynthetic products, and compact it to a 50-mm (2-inch) thick slab;
- Cool down the compacted slabs for two days;
- Core asphalt samples for bond strength test.

The interlayer bond strength of an asphalt specimen containing a geosynthetic interlayer was evaluated using the National Center for Asphalt Technology (NCAT) bond strength device. The test was performed on 150-mm (6-inch) diameter specimens at 25°C. The loading machine produced a uniform vertical movement of 50 mm/min (2 inch/min). The loading head was aligned adjacent to the bonded interface, and rested parallel to the bonded interface. During the test, the shear load and vertical displacement were recorded. The interlayer bond strength was calculated based on the maximum shear load and specimen geometry using Equation 2.

$$S_B = \frac{4P_{\max}}{\pi D^2} \quad (2)$$

where: S_B is the interlayer bond strength, P_{max} is the maximum shear load applied to test specimen, and D is the specimen diameter (i.e., 150 mm).

Recyclability Tests

A new millable and recyclable paving fabric was installed on an existing pavement per manufacturer recommendations under a 50-mm (2-inch) Caltrans surface mix and subsequently milled using standard procedures to produce RAP containing the paving fabric (labeled as “Enviro RAP”). Meanwhile, a similar RAP material without geosynthetic was labeled “Control

RAP". Figure 2 shows the photos of the two types of RAP. As presented, the Enviro RAP only contained small pieces of milled paving fabric.

According to ASTM D2172, the binders from Control and Enviro RAP were extracted with trichloroethylene. The binder contents of Control and Enviro RAP were 4.5% and 5.0%, respectively. It is reasonable that the RAP with the paving fabric had a slightly higher binder content since the paving fabric absorbed a considerable amount of tack coat in the field. The new 12.5-mm nominal maximum aggregate size (NMAS) mixes were designed in accordance with Caltrans Specification Section 39. The designed mixes contained 30% of each type of RAP. The mixes used the same virgin granite aggregate and PG 67-22 asphalt binder. A liquid antistrip agent was added in the mixes with a dosage rate of 0.5%. The mixes were designed with an N_{des} of 85 gyrations. Table 2 summarizes the volumetric properties of the Enviro RAP mix and the same ratios of aggregate blends were used for the Control RAP mix. The only difference between these two mixes is that the Control RAP mix had 3.9% virgin binder, while the Enviro RAP mix only contained 3.7% virgin binder. This implied that the Enviro RAP mix might have a lower material cost than the Control RAP mix.

a. Control RAP

b. Enviro RAP

Figure 2. Photos of Control and Enviro RAP

Table 2. Summary of Volumetric Properties of Enviro RAP Mix

Mixture Property	Enviro RAP	Caltrans Criteria
NMAS (mm)	12.5	--
Virgin binder PG	67-22	--
N_{des}	85	85
Optimum total asphalt content (%)	5.2	--
Asphalt content from virgin binder (%)	3.7	--
Asphalt content from RAP (%)	1.5	--
Design air voids (%)	4.0	4.0
Voids in mineral aggregate (%)	15.5	14.5-17.5

Voids filled with asphalt (%)	74.4	--
Effective asphalt content - P_{be} (%)	4.9	--
Dust/Asphalt ratio	0.9	0.6-1.3
Absorbed asphalt content – P_{ba} (%)	0.3	--

In this study, the performance tests included tensile strength ratio (TSR) test, Hamburg wheel tracking test (HWTT), and Illinois Flexibility Index (I-FIT) test to evaluate the moisture susceptibility, rutting resistance, and cracking resistance of asphalt mixtures, respectively.

RESULTS AND DISCUSSION

Results of Permeability Test

Figure 3 shows the results of the permeability test. As can be seen, the OGFC specimen had a coefficient of permeability greater than 20,000 $\times 10^{-5}$ cm/sec, which was a highly permeable material. The inclusion of a geosynthetic interlayer significantly reduced the permeability of OGFC specimen. According to FDOT Specification Section 334, the asphalt mixture is considered impermeable if its coefficient of permeability is less than 125×10^{-5} cm/sec. Thus, the use of geosynthetic products PFR, PF, PMC1, and PMC2 as interlayers made OGFC specimens impermeable, and the use of product PMH made them marginally impermeable. But the OGFC specimens were still permeable when using product PGM. In general, the geosynthetic products combined fiberglass and polyester with low asphalt retention rate provided the best moisture barrier function, while the polyester-based product did not show any significant reduction in permeability. One potential reason was that the polyester-based product was damaged during kneading compaction of surface mix, thus water flow easily penetrated the interlayer through cracks.

The Tukey's honestly significant difference test was conducted to compare the permeability of OGFC specimens with geosynthetic interlayers. The confidence interval was assigned as 95%. As presented, these specimens were classified into four groups. Group A represented the specimen had the highest permeability, while Group D indicated the specimen had the lowest permeability. As can be seen from Figure 3, the specimens with product PMC2 showed the statistically lowest permeability. There was no significant difference between products PFR and PMC1 in terms of permeability reduction. In general, the OGFC specimens with PFR, PF, PMC1 and PMC2 only had slightly statistical differences in permeability.

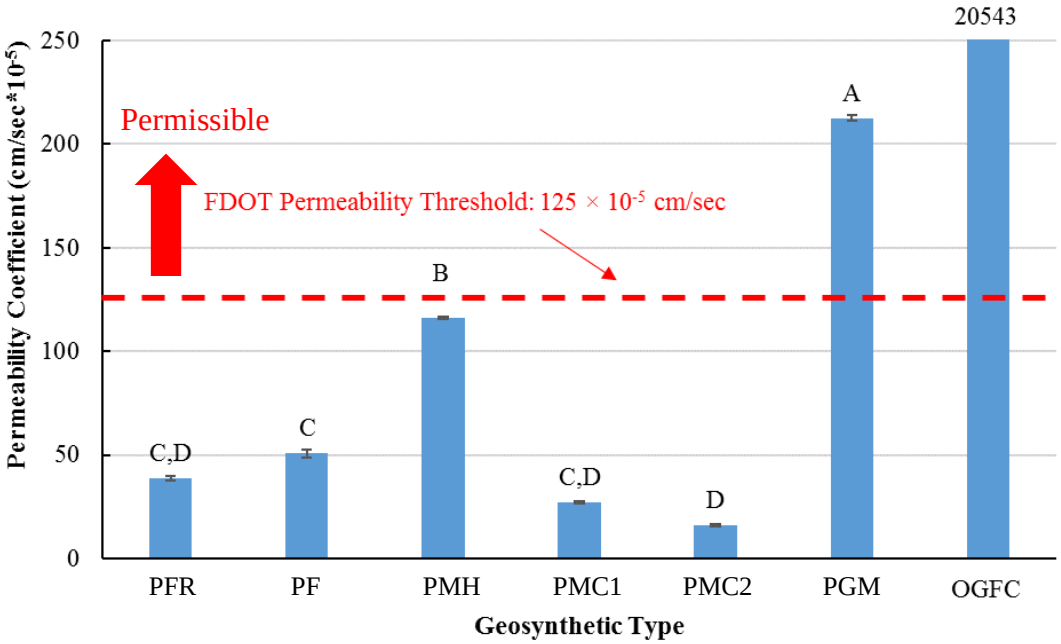

Figure 3. Permeability of OGFC Specimens with Geosynthetic Interlayer

Results of Bond Strength Test

A proper bond between pavement layers is crucial to provide a well-bonded pavement structure. The lack of interface bonding usually results in the premature distresses of slippage, shoving, and top-down cracking, thereby dramatically reducing pavement service life. Figure 4 presents the bond strength of laboratory specimens containing different types of geosynthetic interlayers. Compared to the control specimens, the specimens with a geosynthetic had lower bond strength values at the interface between geosynthetic and asphalt mixture. This was reasonable because the geosynthetic needs flexibility to deform, which can absorb the energy of reflection cracking. West et al. (2005) recommended the minimum bond strength as 689 kPa (100 psi) to ensure satisfactory interlayer bonding for asphalt pavement. Accordingly, the use of geosynthetic products PFR, PF, and PGM fully met the bond strength criterion, the use of PMC1 marginally satisfied the criterion, while the use of PMH and PMC2 did not meet the criterion. In general, the specimens with fiberglass-based geosynthetic interlayer showed less bond strength than those with polyester and polypropylene-based geosynthetic interlayer. The Tukey comparison of bond strength test results for laboratory samples. As presented, the specimens with PFR, PF, and PGM products showed the statistically highest level of bond strength, while those with products PMH and PMC2 had the statistically lowest level of bond strength.

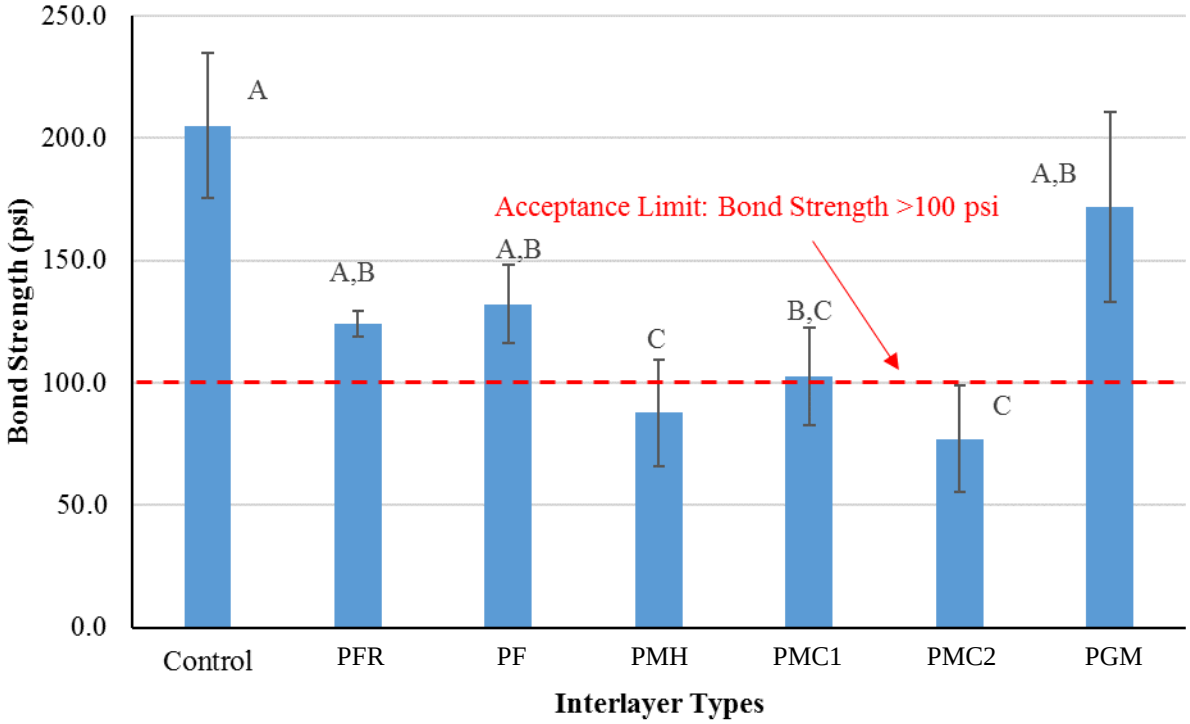

Figure 4. Bond Strength of Asphalt Specimens Containing Geosynthetic Interlayer

Results of Tensile Strength Ratio Test

The moisture susceptibility of the asphalt mix was tested according to AASHTO T283. This test determines the TSR between dry and moisture-saturated specimens of the same mix. Six specimens were compacted to 95 mm with a target air void level of 7% ± 0.5%. Three of the specimens were vacuum-saturated until 70-80% of the internal air voids were filled with water and underwent one freeze-thaw cycle. The conditioned and unconditioned specimens were then tested in a Marshall Stability Press, and the load and displacement data were recorded. The maximum load was then used to calculate the indirect tensile strength of each specimen, and the TSR for the mix was then calculated as a ratio of the indirect tensile strength of conditioned specimens to the indirect tensile strength of unconditioned specimens. According to Caltrans Specification Section 39, the minimum allowable dry strength and wet strength are 689 kPa (100 psi) and 483 kPa (70 psi), respectively. Figure 5 presents the moisture susceptibility test results. As can be seen, the dry and wet strength of Enviro RAP were significantly higher than the minimum values specified by Caltrans Specification Section 39. The TSR of asphalt mixture containing Enviro RAP mix was 0.93, which was also much greater than the industry acceptable limit (i.e., TSR ≥ 0.80). This demonstrated that the Enviro RAP mix had excellent moisture susceptibility.

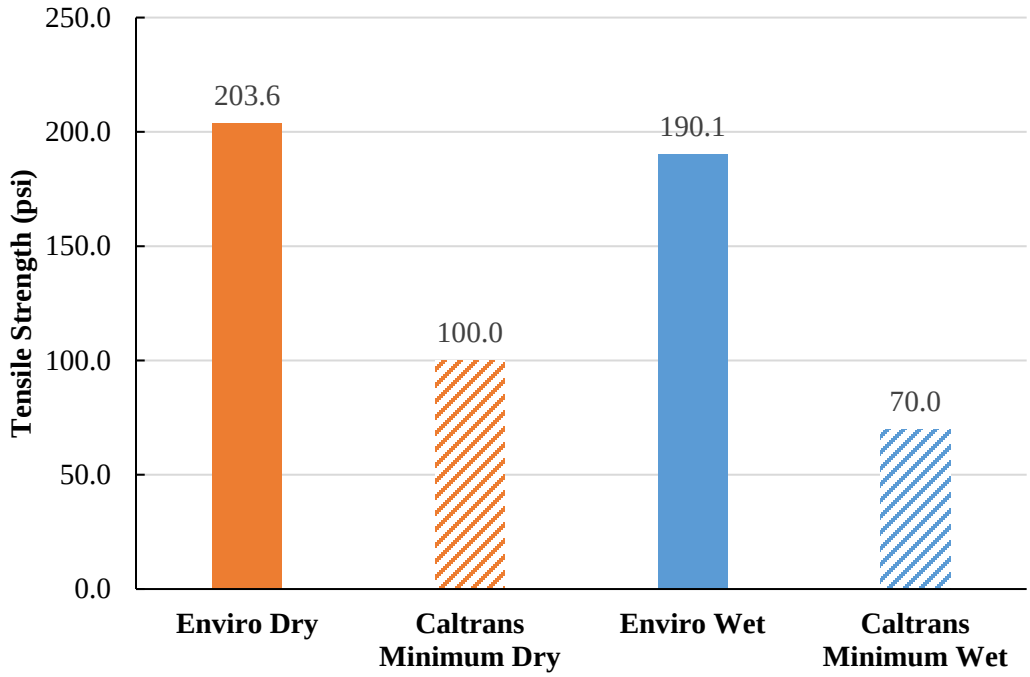

Figure 5. Moisture Susceptibility of Asphalt Mixture Containing Enviro RAP

Results of Hamburg Wheel Tracking Test

The HWTT was used to determine the resistances of asphalt mixtures to rutting and moisture damage. All specimens were fabricated and tested according to AASHTO T 324. The specimens were subjected to a load of 0.7 ± 0.005 kN. The specimens were submerged and conditioned in a 50°C water bath for 30 minutes prior to testing. The water bath maintained the 50°C temperature for the duration of the testing. All data output of the linear variable differential transformer attached to each arm was recorded by a computer and analyzed to determine the rut depth and stripping inflection point (SIP) of each mix. Figure 6 presented the HWTT results of the two replicated asphalt mixtures containing Enviro RAP. The average rut depth of asphalt mixtures at 10,000 wheel passes was 2.42 mm, the average rut depth at 15,000 wheel passes was 2.65 mm, and the average rut depth at 20,000 wheel passes was 2.89 mm. According to Caltrans Specification Section 39, an asphalt mixture with PG 67-22 binder should have less than 12.5 mm (0.5-inch) rut depth after 15,000 wheel passes, and no stripping problem after 10,000 wheel passes. It was shown that the accumulated rut depths of the mixture at 15,000 wheel passes was far less than the threshold value. In addition, the asphalt mixture did not show any stripping problem after 20,000 wheel passes, which also met the Caltrans Specification. This demonstrated the asphalt mixture containing Enviro RAP had excellent resistance to rutting and moisture damage.

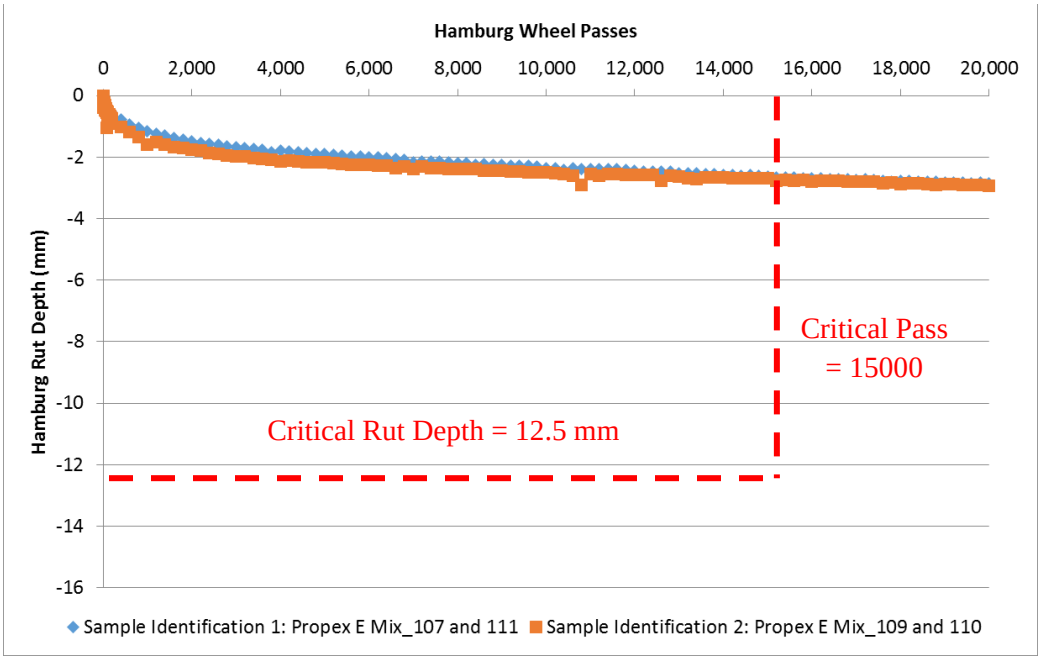

Figure 6. HWTT Results of Asphalt Mixture Containing Enviro RAP

Results of Illinois Flexibility Index Test

I-FIT test was employed in this study to discriminate asphalt mixtures with different cracking potentials at intermediate test temperature (Al-Qadi, 2015). The specimens with the dimensions of 150 mm in diameter and 61 mm thick were first cut in half to create a semi-circular specimen, and a notch was then introduced along the axis of symmetry with 15 mm in depth and 1.5 mm in width. A monotonic load was applied along the vertical radius of the specimen with a constant displacement rate of 50 mm/min, and the test temperature was 25°C. The flexibility index (FI) that was defined as the fracture energy divided by the slope at the inflection point of the post peak load versus displacement curve was used to evaluate the load-related cracking resistance of asphalt mixes. Figure 7 shows the I-FIT test configuration and typical test results. Compared against other cracking indicators, the FI was better to discriminate the cracking performance of asphalt mixes containing RAP material (Al-Qadi, 2015).

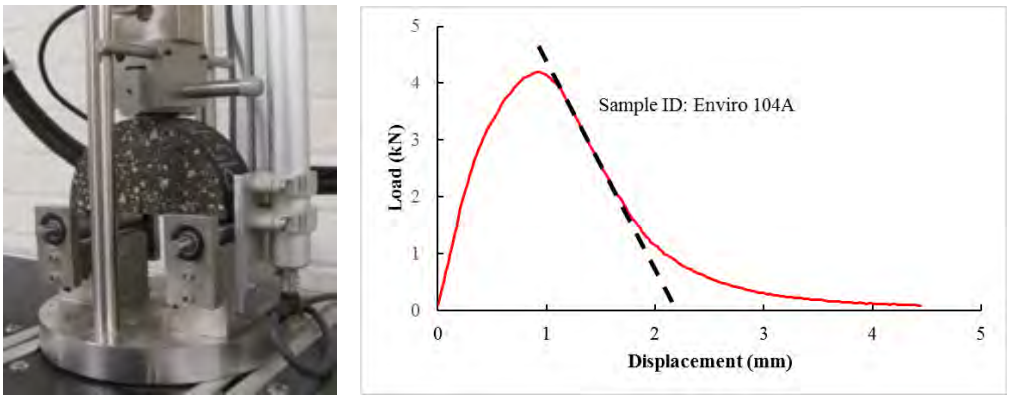

(a) (b)

Figure 7. I-FIT Test; (a) Specimen Setup, (b) Typical Results.

Figure 8 shows the I-FIT results of the Enviro RAP and Control RAP mixes with a comparison to that of the material from NCAT Test Track Section N1 (West et al. 2018). As illustrated, asphalt mixtures with Enviro RAP and Control RAP showed comparable FI value. This demonstrated that the milled fabric was not detrimental to the cracking resistance of asphalt mixture. It is also shown that the mixture containing the recyclable paving fabric RAP had a higher FI value than the asphalt mixture at Test Track Section N1. The field observation at NCAT Test Track indicated that the Section N1 only showed slight top-down cracking after 10 million equivalent single axle loads (ESALs). This implied that the asphalt mixtures containing Enviro RAP should surpass crack resist performance at the same traffic level.

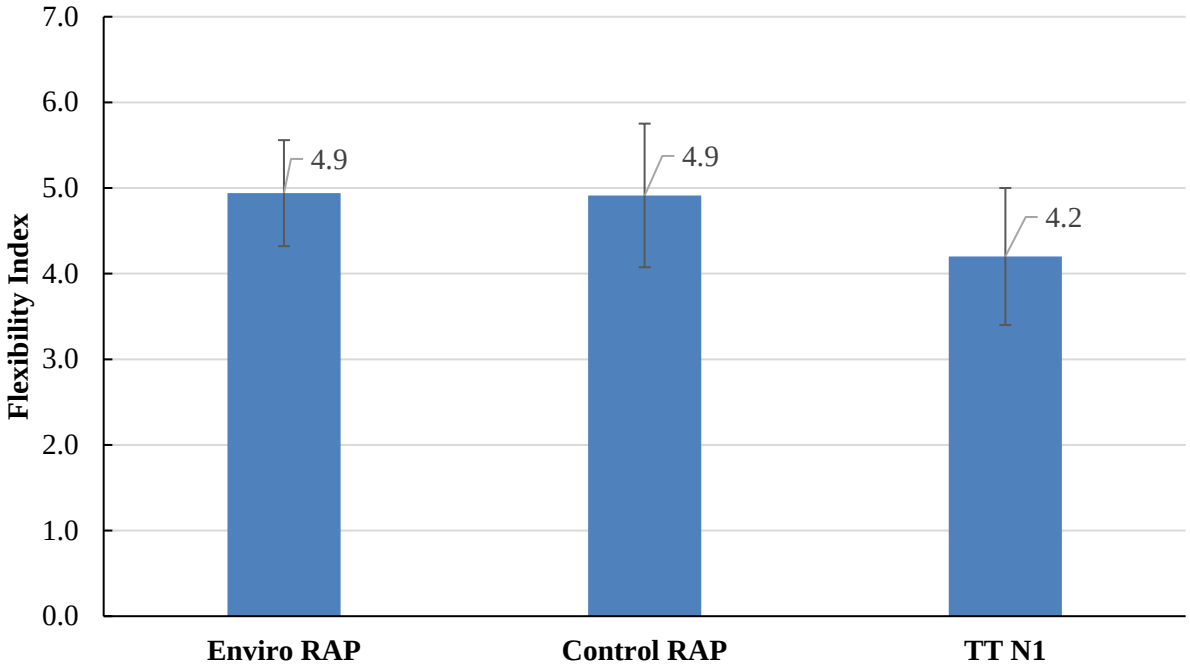

Figure 8. I-FIT Test Results of Asphalt Mixtures

SUMMARY AND CONCLUSIONS

In this study, the influences of geosynthetic interlayers on permeability and interface bond strength of asphalt pavements were evaluated using Florida permeability test and NCAT bond strength test, respectively. To simulate the actual field construction, the specimens were cored from the laboratory slabs prepared using the kneading compaction method. The permeability test results indicated that the inclusion of geosynthetic interlayer systems effectively reduced the permeability of asphalt pavement. The use of the geosynthetic products containing polypropylene-only, polyester-polypropylene, or polyester-fiberglass as interlayers turned highly permeable OGFC specimens to be impermeable. The bond strength test results demonstrated the asphalt specimens containing geosynthetic interlayers had lower bond strength values than the control specimens. Only the asphalt samples with the paving fabrics and the all polyester paving mat had bond strength greater than 689 kPa (100 psi), indicating asphalt mixture and those geosynthetic interlayers had satisfactory bonding.

To evaluate the recyclability of geosynthetic product, 30% RAP containing milled polypropylene fabric was utilized to produce a new asphalt mixture. The RAP containing the paving fabric had a slightly higher binder content than the Control RAP, which might result in a lower production cost for asphalt mixture. The volumetric mix design was performed in accordance with Caltrans Specification Section 39. The designed asphalt mixture had an NMAS of 12.5-mm. The moisture susceptibility test results demonstrated that the Enviro RAP asphalt mixture had much higher dry and wet tensile strength values than those minimum values specified by Caltrans Specification Section 39. The Hamburg wheel tracking test results showed that the Enviro RAP asphalt mixture only had a rut depth of 2.65-mm after 15,000 wheel passes, which was significantly better than the maximum rut depth specified by Caltrans (i.e., 12.5 mm). The Illinois flexibility index test results showed that the Enviro RAP and Control RAP asphalt mixtures had comparable flexibility index values, which were higher than one asphalt mixture showing good crack resisting performance at the National Center for Asphalt Technology (NCAT) Test Track. Overall, these performance testing results demonstrated that the asphalt mixture containing 30% Enviro RAP had excellent resistances to moisture damage, rutting, and cracking. This indicated that the presence of new fabric in RAP added back into new hot mix asphalt did not adversely impact the performance of RAP.

REFERENCES

Al-Qadi, I., Ozer, H., and Lambros, J. et al. (2015). Testing protocols to ensure performance of high asphalt binder replacement mixes using RAP and RAS. Illinois Center for Transportation Report No. FHWA-ICT-15-017, Urbana-Champaign, Illinois.

American Association of State Highway and Transportation Officials (AASHTO). (2014). Standard method of test for resistance of compacted asphalt mixtures to moisture-induced damage. AASHTO T 283, Washington, D.C.

AASHTO. (2019). Standard method of test for Hamburg wheel-track testing of compacted asphalt mixtures. AASHTO T 324, Washington, D.C.

ASTM International. (2017). Standard test method for quantitative extraction of asphalt binder from asphalt mixtures. ASTM D2172, West Conshohocken, PA.

ASTM International. (2019). Standard test method for breaking force and elongation of textile fabrics (Strip method). ASTM D5035-11, West Conshohocken, PA.

Correia, N., Zornberg, J., and Bueno, B. (2014). Behavior of impregnated paving geotextiles: study of optimum tack coat rate. Journal of Materials in Civil Engineering, 26(11): 04014077.

Lytton, R. (1989). Use of geotextiles for reinforcement and strain relief in asphalt concrete. Geotextiles and Geomembranes, 8(3): 217-237.

Ridgeway, H. (1982). Pavement subsurface drainage systems. NCHRP Synthesis of Highway Practice 96, Washington, D.C.

West, R., Zhang, J., and Moore, J. (2005). Evaluation of Bond Strength between Pavement Layers. NCAT Report 05-08, Auburn, AL.

West, R., Timm, D., Powell, B., et al. (2018). Phase VI NCAT Test Track Findings. NCAT Draft Report 18-04, Auburn, AL.

Geosynthetics Conference

Feasibility of Measuring the Performance of Pavement Interlayers Using Full-Scale Rolling Wheel Load Testing Device

Eli Cuelho, P.E.,[1] and David Andrews, P.E.[2]

[1] TRI Environmental, Inc.; Austin, TX; ecuelho@tri-env.com
[2] Propex; Chattanooga, TN; david.andrews@propexglobal.com

ABSTRACT

A study was undertaken to determine the feasibility of assessing the performance of pavement interlayer products using a full-scale, rolling wheel load, testing device. The test was conducted on paved test sections carefully constructed in an indoor roadway systems laboratory. Four pavement interlayer materials were evaluated along with a control (i.e., no interlayer). Paved test sections were built within a concrete-lined trench. Transverse cracks were sawed into the initial asphalt layer, which subsequently received various pavement interlayer treatments prior to resurfacing with an asphalt overlay. Performance was evaluated by trafficking the test sections using an accelerated pavement tester (APT) and measuring crack progression on the pavement surface over time. Reflective cracks did not extend through the entire thickness of the overlay in any of the test sections; however, after removal of samples from the test area, side profiles revealed the beginning of reflective crack in the control test section. A full description of the test effort is outlined, and based on the lessons learned, two main recommendations are proposed to improve the outcome of this type of testing in the future.

BACKGROUND

Geosynthetic interlayers have been used for decades to prevent water infiltration, impede reflective crack propagation through overlays, or reinforce asphalt pavements. Some interlayer products are used to provide mechanical reinforcement through tensile stresses borne in the material. These products improve the crack area through the use of a stiff structural geogrids or stiff composite matrix. Another common approach is to use a thicker non-woven geotextile interlayer designed to absorb the stresses by de-coupling the two layers from one another. Field studies have be undertaken to evaluate the performance of these products with respect to the suppression of reflective cracks (e.g., Button and Lytton, 2003, Makowski et al., 2005); however, field studies take a long time to conduct. Laboratory tests on bench top sized sample have also been used to estimate the performance (e.g., Germann and Lytton, 1987; Lytton, 1989; Mukhtar and Dempsey, 1996; Prieto et al., 2007; Khodaii et al., 2009; Yu et al., 2013). The use of large-scale pavement simulation, however, is rarer (Correia and Zornberg, 2016). The study covered in this paper undertook to determine the feasibility of testing relative performance of several interlayer products using full-scale pavement test sections trafficked by an accelerated pavement tester (APT). The setup and design of experiments was created to resemble an asphalt beam fatigue test that includes an interlayer (Wargo et al., 2016).

INTRODUCTION

TRI Environmental, Inc. (TRI) conducted a study to determine feasibility of assessing the performance of various pavement interlayer products using a full-scale rolling wheel load tester. The test was conducted at TRI's indoor roadway systems laboratory located in Greenville, SC. Paved test sections were built within a concrete-lined trench. The test area was comprised of

subgrade topped with compacted gravel and surfaced with asphalt pavement. Transverse cracks were sawed into the initial asphalt layer, which subsequently received various pavement interlayer treatments and resurfacing with an asphalt overlay. Performance was evaluated by trafficking the test sections using an APT and measuring crack progression on the pavement surface over time.

MATERIALS

Construction of the test area was designed to quantify differences in performance of various pavement interlayer materials under the same conditions (i.e., same subgrade, base course thickness and asphalt thickness). Four pavement interlayer materials were used along with a control (i.e., no interlayer) are described in Table 1. A description of the subgrade, base course and asphalt is described below.

Table 1: General Description of the Interlayer Products

Interlayer Material	Composition	Tensile Strength	Mass per Unit Area (g/m^2)	Asphalt Retention (l/m^2)
A	Fiberglass mesh in polyester mat	25 kN/m†	136	0.471
B	Fiberglass mesh in polyester mat	50 kN/m†	237	0.471
C	Non-woven polypropylene mat	450 N‡	140	0.91
D	Non-woven polypropylene and polyester mat	534 N‡	156	1.13

† ASTM D5035
‡ ASTM D4632

The subgrade soil was obtained from a large nearby stockpile. It was classified as sandy silt (ML) according to the USCS classification system, and had the properties listed in Table 2.

Table 2: Material Properties of Subgrade

Property	
Liquid Limit	47
Plastic Limit	33
Plasticity Index	14
% passing #200 sieve	52.4%
Maximum dry unit weight†	14.9 kN/m^3
Optimum moisture content†	24.2%

† determined using Standard Proctor method (ASTM D698)

The base course consisted of 50 mm minus crushed granite obtained from a local gravel pit. It classified as poorly-graded gravel (GP) according to the USCS classification system. The maximum dry unit weight was 22.2 kN/m^3 and the optimum moisture content was 5.3%, according to the Standard Proctor test protocol (ASTM D698, Method C).

The asphalt used to pave the test area consisted of a Surface C mix, based on a South Carolina Department of Transportation mix design. The maximum nominal aggregate size of the asphalt mix was 12.5 mm.

CONSTRUCTION

Construction began by mixing and placing the subgrade in the concrete trench using a skid-steer tractor. Larger clumps of subgrade were broken down and mixed in to ensure the subgrade was uniform when placed. The subgrade was placed in the trench at its natural moisture content and graded smooth to form lifts approximately 150 mm thick. Compaction of the subgrade was accomplished using a smooth drum vibrating compactor. The sixth and final layer of the subgrade was leveled by hand to a tolerance of ±6 mm. In-place density of the final layer of subgrade was measured using a sand cone. The four sand cone tests resulted in an average dry unit weight of 17.3 kN/m^3. DCP tests run on the compacted subgrade resulted in an average CBR strength of approximately 5.4%.

The base course was constructed in two layers. The aggregate was moisture conditioned and screeded to form a uniform thickness across the entire test area. The smooth drum vibrating roller used to compact the subgrade was also used to compact the gravel. The final total thickness of the gravel layer was 275 mm. The in-place density of the base course was measured using a nuclear densometer gauge, resulting in an average dry unit weight of 21.3 kN/m^3.

Hot-mix asphalt was placed in a single lift that had an average thickness of 81 mm over an area approximately 2.9 m wide by 11 m long. The final surface of the test area is shown in Figure 1.

Figure 1: Final surface of test area.

EXPERIMENTAL DESIGN

Pavement interlayer fabrics are designed to mitigate reflective cracking in pavement overlays. To simulate an aged, cracked pavement upon which to deploy the interlayer materials, transverse pavement cracks were cut through the depth of the asphalt using a walk-behind wet saw. Finished crack widths were approximately 6 mm wide (see Figure 2). A sawcut was also made in the longitudinal direction to separate the test area having the transverse cuts from the remaining adjacent pavement, forming blocks approximately 0.8 m wide by 1.2 m long that could move independently from one another. A layout of the sawcuts made in the pavement surface is shown in Figure 3.

Figure 2: View of typical section with sawcut.

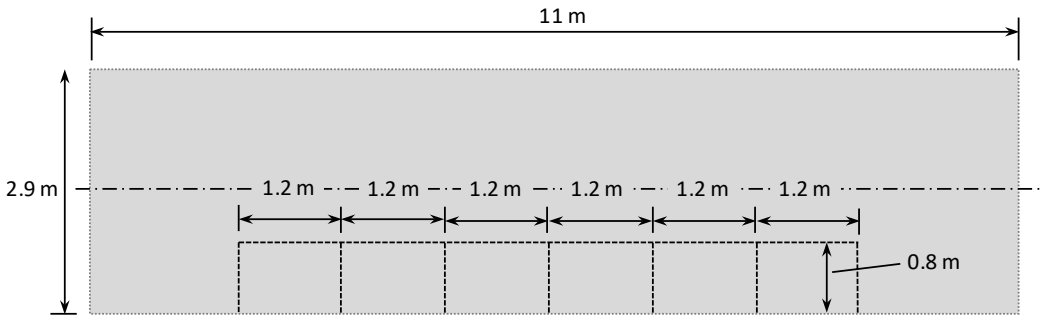

Figure 3: Plan view of paved test area showing sawcuts (dashed lines).

Installation of the four interlayer products began by applying hot asphalt emulsion to the pavement surface. The asphalt emulsion was provided by a local paving contractor and was heated to 66° C using a portable heating kettle. The average residue fraction of the emulsion was determined to be 56.8%. Using this value, target and in-place residual emulsion rates for each interlayer product were determined (summarized in Table 3). The hot emulsion was placed using a portable hand sprayer to carefully control and distribute the amount applied in each test section (Figure 4), and masking paper was used to protect areas outside of each test section from overspray. A minimal amount of emulsion was used in the control areas.

Table 3: Residual Emulsion Rates

Interlayer Material	**Target Emulsion Rate** (l/m^2)	**In-Place Emulsion Rate** (l/m^2)
A	0.68	0.72
B	0.68	0.68
C	1.27	1.45
D	1.13	1.13

Figure 4: Application of asphalt emulsion onto pavement surface.

Individual interlayer test strips were approximately 0.9 m wide by 1.2 m long and positioned so that they straddled a transverse sawcut midway along their length. An illustrated plan view is provided in Figure 5 to illustrate how the interlayer fabrics were oriented with respect to the position of the sawcuts. Note that the interlayer fabrics also overlapped the longitudinal sawcuts. The interlayer fabrics were carefully placed onto the surface and pressed into place using a push broom to ensure full contact (Figure 6). It was determined that it was not necessary to wait for the emulsion to "break" (i.e., allow the water component to evaporate) prior to placing the interlayers because placement of the overlay would not take place for several days, leaving time for full evaporation. The installed interlayer materials are shown in Figure 7 prior to the asphalt overlay.

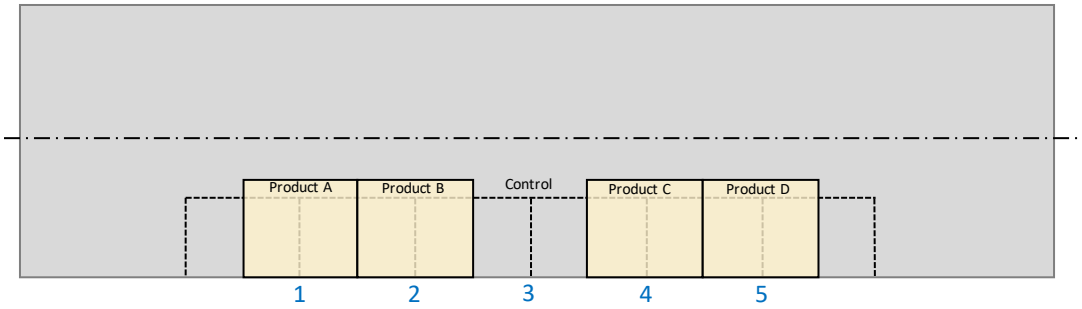

Figure 5: Plan view illustration of the installed interlayers with respect to sawcuts.

Figure 6: Installation of interlayer fabrics.

Figure 7: Installed interlayer materials prior to asphalt overlay.

The asphalt overlay consisted of the same material (South Carolina, Surface C mix) that was used for the base pavement. Placement of the asphalt overlay was done using a paving machine (Figure 8), and compaction was done using a pneumatic roller and steel drum roller. The finished thickness of the overlay was 57 mm on average.

Figure 8: Asphalt overlay paving.

Performance of the interlayers and controls was evaluated by trafficking the test sections using a full-scale accelerated pavement tester (Figure 9), and recording the number of traffic passes needed for a crack to propagate through the overlay. The surface of the pavement was painted white in the areas of the sawcuts to help perceive cracks as they propagated to the surface. Wheel loads on the APT were applied through a dual-wheel assembly equipped with 315/80 R 22.5 HSU2 tires rated for high load carrying capacity. The downward force applied to the

pavement was 40 kN, and the tire pressure was 590 kPa. The total width of the two wheels is approximately 560 mm, and the tires were centered on the interlayer fabrics from east to west. Bi-directional trafficking was continuously applied (24 hours/day) on the east set of test sections only. Time lapse cameras were set up at each of the transverse cracks to record the development of cracks during trafficking (Figure 9).

No reflective cracks were observed in the surface of the pavement in any of the test sections after the first 80,000 traffic passes were applied. A longitudinal cut was made in the pavement (new cut lined up with the original longitudinal cut in the bottom layer of pavement) to decouple the test blocks from the adjacent pavement and promote crack progression. Trafficking was resumed until a total of 195,000 traffic passes had been applied. Transverse cracking had not reflected through to the surface of the overlay in any of the test sections by the end of trafficking.

Figure 9: Accelerated pavement testing device.

Samples were cut from the test sections after trafficking and the side profiles were examined to evaluate their performance. A photo of the side profile was taken of each sample. A summary of pertinent observations made in reference to these photos is listed below.

- All of the sawcut gaps had closed during trafficking, significantly limiting reflective crack propagation into the overlay (Figure 10 through Figure 14).
- In Test Section 1 (Product A) no reflective crack was evident in the overlay above the interlayer (Figure 10).
- Test Section 2 (Product B) performed similarly to the Test Section 1, where no reflective crack was evident in the overlay above the interlayer (Figure 11).
- In the Control test section, a reflective crack initiated directly above the sawcut, but did not extend through the entire thickness of the overlay (Figure 12).
- In Test Section 4 (Product C), a crack had formed in the overlay approximately 50 mm to the left of the sawcut (Figure 13). The crack was wider at the top indicating that it likely extended from the top down (possibly during removal of the slab from the test area).
- In Test Section 5 (Product D), a hairline crack could be noticed on the surface of the overlay, but it was difficult to determine whether that crack extended through the entire

thickness of the overlay (Figure 14). This distress may also have been caused during the slab removal process.

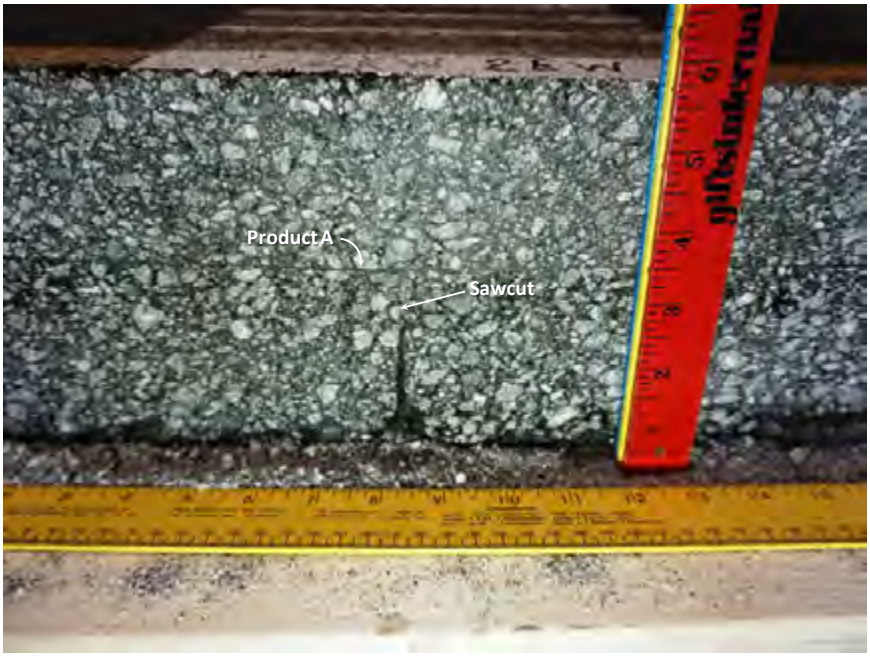

Figure 10: Profile view of Test Section 1, Product A.

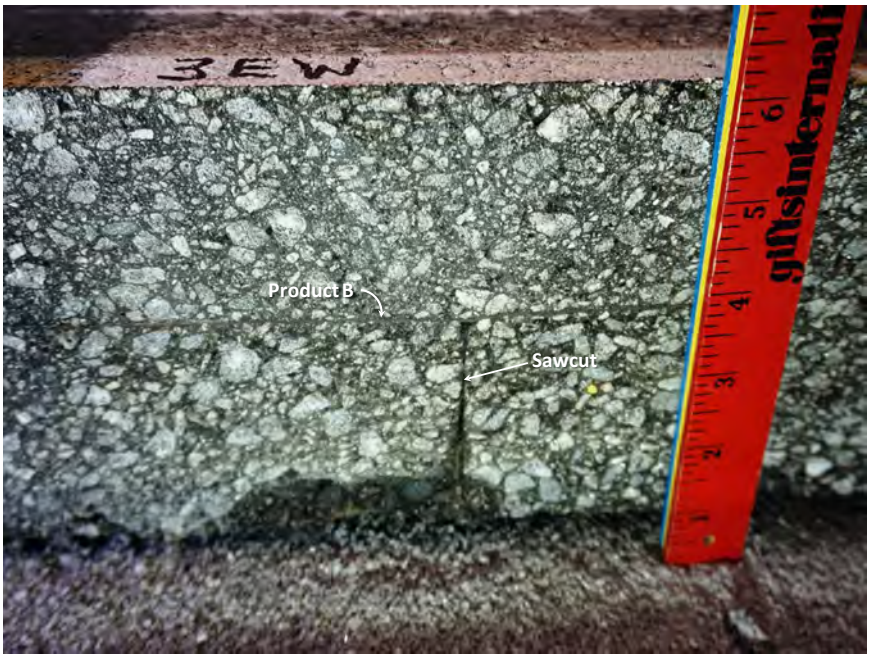

Figure 11: Profile view of Test Section 2, Product B.

Figure 12: Profile view of Test Section 3, Control.

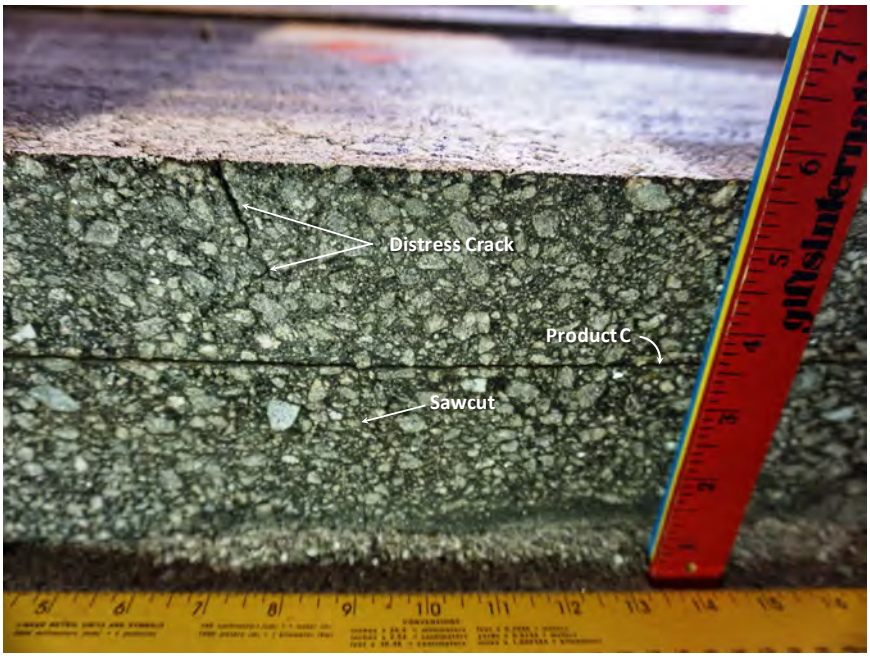

Figure 13: Profile view of Test Section 4, Product C.

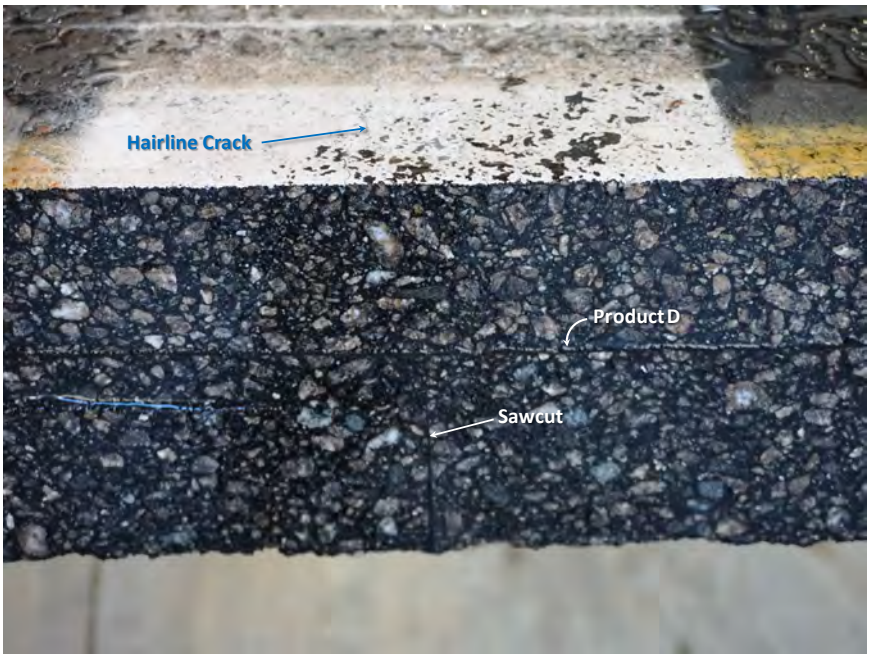

Figure 14: Profile view of Test Section 5, Product D.

CLOSING REMARKS

A full-scale test was designed and constructed to evaluate the relative performance of four interlayer fabrics and a control. The test area consisted of subgrade topped with compacted gravel, and paved with 81 mm of asphalt. Transverse cuts were made in the initial pavement surface to simulate existing cracks. Interlayer fabrics were installed and a 57 mm overlay was constructed on top of the existing pavement. Simulated traffic from an APT was used to load the test sections, and the progression of reflective cracking was monitored over time as the main measure of performance. Reflective cracks did not extend through the entire thickness of the overlay in any of the test sections. After removal of samples from the test area, side profiles revealed the beginning of reflective crack in the control test section; however, the crack did not extend through the entire thickness of the overlay.

Two recommendations are proposed to improve the outcome of this type of testing in the future. First, it is recommended that sand or other filler be used to keep the sawcut gaps from closing during trafficking. The filler will help maintain the gap without bonding the two pieces together. This will allow the two slabs being bridged by the interlayer to move independently, and thereby promote reflective cracking of the overlay. Second, it is recommended that the asphalt on the outside of the test sections be cut away and removed to expose the side profile of the test samples. This will significantly improve the ability to monitor the progression of reflective cracks from the side rather than from the top where it is more difficult to see cracks due to the rougher surface texture.

ACKNOWLEDGEMENTS

The research described in this paper was made possible through the generous support provided by Propex. Special thanks are extended to Mark Marienfeld of TreadMark, Inc. and Joel Sprague of TRI Environmental, who helped with the installation of the interlayer fabrics.

REFERENCES

Button, J. and Lytton, R.L. (2003) Field Synthesis of Geotextiles in Flexible and Rigid Pavement Overlay Strategies Including Cost Considerations, Project 0-1777-P2, Texas Department of Transportation.

Correia, N.S. and Zornberg, J.G. (2016) Mechanical Response of Flexible Pavement Enhanced with Geogrid-Reinforced Asphalt Overlays, *Geosynthetics International*, Vol 23, Issue 3, 183-193.

Germann, F.P. and Lytton, R.L. (1979) Methodology for Predicting the Reflection Cracking Life of Asphalt Concrete Overlays, Research Report FHWA/TX-79/09+207-5, Texas State Department of Highways and Public Transportation.

Khodaii, A.; Fallah, S. and Moghadas Nejad, F. (2009) Effects of Geosynthetics on Reduction of Reflection Cracking in Asphalt Overlays, *Geotextiles and Geomembranes*, Vol. 27, Issue 1, 1-8.

Lytton, R.L. (1989) Use of Geotextiles for Reinforcement and Strain Relief in Asphalt Concrete, *Geotextiles and Geomembranes*, Vol. 8, Issue 3, 217-237.

Makowski, L., Bischoff, D.L., Blankenship, P., Sobczak, D. and Haulter, F. (2005) Wisconsin Experiences with Reflective Crack Relief Projects, *Transportation Research Record, Journal of the Transportation Research Board*, No. 1905, 44-55.

Mukhtar, M.T. and Dempsey, B.J. (1996) Interlayer Stress Absorbing Composite (ISAC) for Mitigating Reflection Cracking in Asphalt Concrete Overlays, UILU-ENG-96-2009. Illinois Cooperative Highway Research Program, Project IHR-533.

Prieto, J.N. Gallego, J. and Perez, I. (2007) Application of the Wheel Reflective Cracking Test for Assessing Geosynthetics in Anti-Reflection Pavement Cracking Systems, *Geosynthetics International*, Vol. 14, Issue 5, 287-297.

Wargo, A.D., Safavizadeh, S., and Kim, R.Y (2016) The Use of Four-Point Bending Notched Beam Fatigue Tests to Rank Crack-Mitigating Layers, 8th RILEM International Symposium on Testing and Characterization of Sustainable and Innovative Bituminous Materials, 359-370.

Yu, B. Lu, Q. and Yang, J. (2013) Evaluation of Anti-Reflective Cracking Measures by Laboratory Test, *International Journal of Pavement Engineering*, Vol. 14, Issue 6, 553-560.

Geosynthetics Conference

Large-Scale Laboratory Box Testing as a Performance Test for Geosynthetic Base Reinforcement in Pavement Applications

Jeb S. Tingle, P.E.,[1] William J. Robinson, Ph.D.,[2] Eli Cuelho, P.E.[3], and Erol Tutumluer, Ph.D.[4]

[1]U.S. Army Engineer Research and Development Center, 3909 Halls Ferry Road, Vicksburg, MS; e-mail: Jeb.S.Tingle@usace.army.mil
[2]U.S. Army Engineer Research and Development Center, 3909 Halls Ferry Road, Vicksburg, MS; e-mail: Jeremy.Robinson@usace.army.mil
[3]TRI-Environmental, 9063 Bee Caves Rd, Austin, TX; e-mail: ecuelho@tri-env.com
[4]University of Illinois at Urbana-Champaign, Department of Civil and Environmental Engineering, 205 N. Mathews, Urbana, IL 61801; e-mail: tutumlue@illinois.edu

ABSTRACT

The objective of this paper is to present large-scale laboratory box testing as a performance test for evaluating the benefits of including commercial geogrid products in pavement applications. A literature of relevant large-scale laboratory box experiments was conducted, and the results from pertinent studies summarized. Results from the literature review are used to propose the standardization of large-scale laboratory box test equipment and methods including minimum box dimensions, box features, loading mechanisms, load frequency, minimum instrumentation requirements, model pavement construction specifications, and recommendations for data analyses and reporting of results.

INTRODUCTION

There is general widespread agreement among pavement engineering professionals that the inclusion of geosynthetics within the pavement foundation can provide significant performance benefits in terms of extended pavement service life and/or a reduction in the thickness of the engineered pavement layers. The primary function of geotextiles within the pavement foundation is typically separation of the engineered material from the natural subgrade with some secondary benefits in terms of reinforcement resulting from the tensioned membrane effect in pavement working platforms which may involve large surface deformations. In contrast, the primary function of geogrids within a pavement foundation is reinforcement and stiffening due to aggregate interlock with some minor secondary benefits of separation depending upon the soil properties of the two layers and the effectiveness of the interlocking mechanism at the layer interface.

While the separation of dissimilar materials within a pavement foundation can be reasonably accomplished with a variety of different geosynthetic types, it is desirable that the geosynthetics allow the transmission of water to alleviate the accumulation of pore pressure while retaining the fine particles of the subgrade to prevent contamination of the engineered granular layer. Fortunately, filtration criteria and the filtration properties of the geosynthetics are reasonably well understood and characterized; thus, providing practitioners with reasonable design criteria and specifications for geosynthetic selection. Alternatively, the reinforcement of aggregate base and subbase layers is less defined. The potential reinforcement mechanisms of tensioned membrane effect, general bearing capacity improvement, and lateral restraint have been reasonably

proposed and explained in a qualitative manner, yet definitive quantification of the reinforcement benefits associated with these mechanisms requires additional research. Full-scale experiments by Cuelho et al. (2014) and Cuelho and Perkins (2016) provided some quantification of reinforcement benefits, but additional experimentation is needed to expand their findings to other test conditions. Practical estimates of the vertical resistance force associated with the tensioned membrane effect have been developed, and the rational but empirical modification of bearing capacity factors has been proposed. As for the quantification of lateral restraint, multiple approaches have been proposed including the direct measurement of interface friction properties and the laboratory measurement of aperture stability and junction stiffness for geogrid products (Cuelho and Perkins, 2017). Unfortunately, the direct measurement of interface friction properties is not as applicable to the small-strain cyclic loads associated with pavement applications as it is to traditional plane-strain geotechnical applications. While the concept of aperture stability seemed reasonable and appropriate for capturing the aggregate interlock potential for the large variety of geogrid products, the use of the test method in design criteria and specifications has been largely unsuccessful to date in providing a definitive quantifiable engineering solution for assessing the performance of geogrids in pavement foundations. Essentially, there are a large variety of commercially-available geogrid products, and product selection based upon aperture stability alone is not widely accepted. Since the majority of the reinforcement and stiffening benefits of geogrids appear to be derived from the mobilization of lateral restraint due to aggregate interlock, this lack of an established link between the geogrid properties and performance within a pavement foundation has limited the use of geogrids. Therefore, pavement design and construction practitioners have been reticent to routinely include geogrid reinforcement products in new pavement designs due to the uncertainty of the performance benefits compared to the cost of inclusion as well as the lack of universally accepted specifications for product selection stemming from an inadequate understanding of the critical performance characteristics of the geogrids.

OBJECTIVE AND SCOPE

The objective of this paper is to present large-scale laboratory box testing as a performance test for evaluating the benefits of including commercial geogrid products in pavement foundations. This paper summarizes several large-scale laboratory box testing efforts and demonstrates the utility of the test method for differentiating the performance benefits of different commercial geogrid products in pavement foundation applications. This paper also discusses the need for standardization of large-scale laboratory box testing methods for this application, as well as the advantages and disadvantages of implementing this method as a means of product specification.

LARGE-SCALE LABORATORY BOX TESTING EXPERIMENTS

Large-scale laboratory box tests have been used by researchers for decades to evaluate the behavior of pavement materials in a laboratory environment, particularly where smaller-scale laboratory apparatus cannot reasonably capture the behavior of the pavement materials or where the cost of full-scale testing is prohibitive. Performance evaluation of geosynthetic reinforced pavement materials lends itself to large-scale laboratory box testing due to the characteristics of the geosynthetics (i.e. geogrid aperture sizes, etc.) and the proposed reinforcement mechanisms (i.e. tensioned membrane effect and lateral restraint). Small-scale laboratory test methods have difficulty in capturing the realistic global behavior of reinforced pavement materials. A literature

review was completed to summarize large-scale laboratory box testing experiments for geosynthetic reinforced pavement sections. Table 1 summarizes the laboratory test devices used by selected researchers to evaluate different pavement sections. Table 1 shows that the use of cyclic plate load testing of geosynthetic reinforced pavement sections constructed in laboratory containment vessels or "box testing" has been used for some time. The dimensions of the apparatus and loading characteristics vary significantly between experiments, yet the use of circular plates to apply a 40-kN load with a 550-kPa contact pressure has become increasingly common as researchers seek to simulate the Equivalent Single Axle Load (ESAL).

Table 1. Laboratory "Box" Tests on Geosynthetic Reinforced Pavement Sections

Experiment	Box Description	Loading	Applied Load kN	Contact Area cm^2	Contact Pressure kPa	Load Frequency
Bauer and Abdelhalim (1987)	Reinforced Plywood: 1.8m X 4.6m X 1.0m	Circular Plate	40.0	730	550	3.0 Hz
Haas et al. (1988)	Reinforced Plywood: 4.6m X 1.8m X 0.9m	Circular Plate	40.0	730	550	0.125 Hz
Barksdale et al. (1989)	Reinforced Concrete Box: 4.9m X 2.4m X ?	Wheel	6.6	183	365	0.14 Hz
Douglas and Valsangkar (1992)	PCC Pit: 3.0m X 4.0m X 2.0m	Circular Plate	4.5	730	63.7	0.5 Hz
Gregory and Bang (1994)	Steel CBR Mold: 0.15-m diameter X 0.30m	Circular Plate	Varied	19.4	Varied	Static
Al-Qadi et al. (1994)	Reinforced Concrete Box: 3.1m X 1.8m X 2.1m	Circular Plate	40.0	730	550	0.5 Hz
Kelly et al. (1995)	Rigid Box: 1.2m X 1.2m X 0.8m	Circular Plate	15.0	490.8	305.6	2.0 kN/min
Douglas (1997)	Reinforced Plexiglass: 1.2m X 0.3m X 0.6m	Beam	Varied	Varied	Varied	0.4 Hz
Montanelli et al. (1997)	Reinforced Steel Box: 0.9m X 0.9m X 0.9m	Circular Plate	40.0	730	570	5 or 10 Hz
Perkins et al. (1999)	Reinforced Concrete Box: 2.0m X 2.0m x 1.5m	Circular Plate	40.0	730	550	0.77 Hz
Leng et al. (2002)	Reinforced Concrete Box: 1.5m X 1.5m X 1.4m	Circular Plate	36.5	730	550	0.67 Hz
Tingle and Jersey (2005)	Reinforced Steel Box 1.8m X 1.8m X 1.4m	Circular Plate	40.0	730	550	1.0 Hz
Chen et al. (2009)	Reinforced Steel Box: 2.0m X 2.0m X 1.7m	Circular Plate	40.0	730	550	0.77 Hz
Abu-Farsakh and Chen (2011)	Reinforced Steel Box: 2.0m X 2.0m X 1.7m	Circular Plate	40.0	730	550	0.77 Hz
Qian et al. (2011)	Reinforced Steel Box: 2.0m X 2.2m X 2.0m	Circular Plate	40.0	730	550	0.77 Hz
Sarici et al. (2016)	Reinforced Steel Box: 2.0m X 2.0m X 2.0m	Circular Plate	40.0	730	550	0.77 Hz
Tingle (2019)	Reinforced Steel Box: 1.8m X 1.8m X 1.4m	Circular Plate	40.0	730	550	0.83 Hz
Robinson et al. (2019)	Reinforced Steel Box: 1.8m X 1.8m X 1.4m	Circular Plate	128.0	730	1750	0.77 Hz

Table 2 provides generalizations of the materials used and profiles of the pavement sections evaluated by each researcher. Table 2 shows that a variety of materials have been used in previous experiments and that material thicknesses and engineering properties vary significantly between

experiments. The table shows that large-scale laboratory box tests have been used to evaluate the performance of a wide variety of pavement materials including pavement sections surfaced with hot mix asphalt as well as those surfaced with aggregate base materials simulating aggregate roads. In addition, the data show that the use of large-scale laboratory box testing mitigates the need for scaling of materials by allowing realistic pavement layer thicknesses to be used. However, the data provided in these tables suggest that the results of individual experiments are not easily compared due to different material properties and test conditions. Thus, while similarities between experiments exist, there is no standardized test method for large-scale laboratory box testing.

Table 2. Materials and Pavement Profiles Used in Large-Scale Laboratory Box Experiments

Experiment	Asphalt Surface	Thickness mm	Relative Strength	Base Type	Thickness mm	Relative Strength	Subgrade Type	Thickness mm	Relative Strength	Geosynthetic Type[1]	Location
Bauer and Abdelhalim (1987)	None	None	None	Crushed Limestone	75-3000	High	SP	900	Medium	GT	Varied
Haas et al. (1988)	Hot Mix	50-100	Medium	Crushed Stone	100-300	High	SP	175-375	Very Low to Medium	GT or GG	Varied
Barksdale et al. (1989)	Hot Mix	25-38	Medium	Varied	150-200	Low-High	ML-CL	450	Very Low	GT or GG	Varied
Douglas and Valsangkar (1992)	None	None	None	Varied	150	Low-High	Peat	1200	Very Low	GT and GG	Varied
Al-Qadi et al. (1994)	Hot Mix	70	Medium	Granite	150	High	SM	1220	Medium	GT or GG	Interface
Gregory and Bang (1994)	None	None	None	Crushed Limestone	0-50	High	CL & CH	175	Low	GT and/or GG	Interface
Kelly et al. (1995)	None	None	None	Sandy Gravel	200	High	CL	500	Low	GT or GG	Interface
Douglas (1997)	None	None	None	Clean Sand	25-75	Low	Peat	NR	Very Low	GT	Interface
Montanelli et al. (1997)	Hot Mix	75	Medium	Crushed Limestone	300	High	SP	400	Low-High	GG	Interface
Perkins et al. (1999)	Hot Mix	75	Medium	Crushed Stone	300-375	High	CH or SM	970-1045	Very Low to Medium	GT or GG	Varied
	Cold Mix	75	Low		200-210			1128-1145			
Leng et al. (2002)	None	None	None	Granite	150 or 250	High	SC	750-900	Low	GG	Interface
Tingle and Jersey (2005)	None	None	None	Crushed Limestone	360-510	High	CH	710-810	Very Low	GT and/or GG	Interface
Qian et al. (2011)	None	None	None	Clayey Gravel	300	Low	SC	1000	Very Low	GG	Interface
Sarici et al. (2016)	None	None	None	Granite	300-450	High	ML-CL	1400	Low	GG	Varied
Tingle (2019)	None	None	None	Varied	150	Low-High	CH	610	Low	GT and/or GG	Interface
Robinson et al. (2019)	Hot Mix	127	High	Crushed Limestone	483	High	CH	711	Low	GT or GG	Interface

[1]GT indicates the inclusion of a geotexttile, and GG indicates the inclusion of a geogrid.

The literature demonstrates the ability to effectively identify improved pavement performance of geosynthetic-reinforced unbound road sections compared to similar unreinforced sections using large-scale laboratory box testing. The performance improvement was shown in terms of reduced permanent surface deformation and extended service life.

STANDARDIZATION OF LARGE-SCALE LABORATORY BOX TESTING

The literature clearly demonstrates that large-scale laboratory box testing can be effectively used to evaluate the potential of geosynthetics for performance improvement of pavement sections. There are numerous caveats regarding the direct use of absolute values such as the number of load-cycles-to-failure for design, but the preponderance of the experimental evidence shows that the test method can verify that performance improvements are likely and aid in the relative ranking of products. Thus, several researchers, the authors included, have proposed the use of large-scale laboratory box testing as a performance test for base reinforcement applications. To accomplish this, the test method would require standardization so that different test agencies could generate

the same results for the same materials and pavement structures. As shown in the tables, historically the large-scale laboratory box testing has not been standardized. This section of this paper describes an initial proposal for a standardized large-scale laboratory box test method for the performance evaluation of geosynthetics for base reinforcement applications.

Laboratory Box Test Equipment

This section describes recommendations for standardization of the laboratory equipment to conduct large-scale laboratory box testing for the purpose of evaluating the performance of geosynthetic reinforcement of aggregate bases. It would be impractical to expect every testing laboratory to have the exact same test vessel or box as significant investments have already been made by a number of laboratories. Thus, the configuration and composition of the containment vessel or box should be based upon its intended purpose, and minimum requirements based upon satisfying that purpose. Consideration of the minimum requirements for an appropriate containment vessel yielded three primary requirements. First, the containment vessel or box must be large enough to capture the global response behavior of the pavement section, essentially the boundaries must be far enough away from the load to not influence the material response. Second, the boundaries must be rigid enough not to yield under loading, even relatively small deflections could alter the measured stress, strain and deflection responses that are typically captured by instrumentation. Third, the containment vessel must allow for construction of the model pavement sections while still providing rigid boundary conditions.

Tingle and Jersey (2005) conducted a finite element analysis to minimize the influence of the rigid boundary conditions on the interior response of the pavement section while maintaining an acceptable scale for laboratory construction. They recommend minimum box dimensions of 1.8 meters by 1.8 meters in plan and a depth of 1.3 meters. To minimize the potential for wall deflection during loading, the sides of the box were constructed of 25-mm steel plate reinforced with 155-mm square steel tubing to minimize the potential for wall deflection during loading. However, suitable designs could be fabricated from reinforced concrete as evidenced by Perkins (1999) or other materials provided that the deflections at the boundaries are minimized. In order to facilitate construction, Tingle and Jersey as well as Perkins designed their boxes such that one side of the box was removable. The predominant concern is that the method of closure of the box must minimize deflections. Rigidly enclosed box designs such as concrete tanks could provide a suitable containment vessel provided that their dimensions are large enough to allow reasonable construction of the pavement section. Containment vessels constructed at or near the minimum recommended dimensions would provide a very confined construction space that would likely affect the ability to achieve quality construction results representative of normal construction processes. Figure 1 shows the reinforced steel box designed and used by Tingle and Jersey (2005), Tingle (2019), and Robinson et al. (2019).

Figure 1. Reinforced steel box used by Tingle and Jersey (2005), Tingle (2019), and Robinson et al. (2019)

In addition, to the containment vessel or box design, standardization of the loading mechanism would aid in establishing repeatability between laboratories as well as allow meaningful comparisons between experiments. A review of the testing methods summarized in Table 1 shows that the vast majority of researchers have elected to simulate the ESAL, consisting of a 40 kN load on a 305-mm diameter circular steel plate (25.4 mm thick) that generates a contact pressure of approximately 550 kPa. Most researchers also used a 6- to 12.5-mm thick neoprene rubber pad attached to the bottom of the steel plate to provide a better distribution of load from the plate to the pavement surface, minimizing stress concentrations at the edge of the plate. The dynamic load can be generated using a variety of equipment; however, the use of hydraulic actuators is most common. Pneumatic actuators have been reported to have difficulty maintaining a consistent and repeatable load pulse. It is recommended that the loading system be standardized to a hydraulic system for improved and consistent control of the applied load. The applied loading sequence is also very important, as the frequency and shape of the load pulse can affect the mechanistic response and performance of the pavement sections. Most researchers reported using a sinusoidal wave pulse as more representative of the load pulse produced by wheel loads. Tingle and Jersey (2005) reported difficulty in achieving the measured loading over very soft subgrades for a 1 Hz frequency (0.1 second of loading with a 0.9 second rest period). A review of the load frequencies reported in literature shows that a load frequency of 0.77 Hz is the most common, typically consisting of a 0.4-second loading and 0.9-second rest period. The load frequency of 0.77 Hz allows the pavement section to completely deflect during loading, even for very weak subgrades, which provides adequate time for resistance of the load and ensures that the measured loads are consistent with the target applied load of 40 kN. In addition, it is recommended that a seating load of 0.45 kN be maintained on the plate to ensure constant contact with the pavement surface. Thus, standardization of the loading mechanism should consist of a hydraulically controlled load of 40 kN on a 305-mm diameter circular steel plate (25.4 mm thick) with a relatively thin rubber pad applied in a sinusoidal wave at a frequency of 0.77 Hz (0.4-second loading and 0.9-second rest period). Figure 2 shows the recommended sinusoidal load pulse as reported by Sarici et al. (2016).

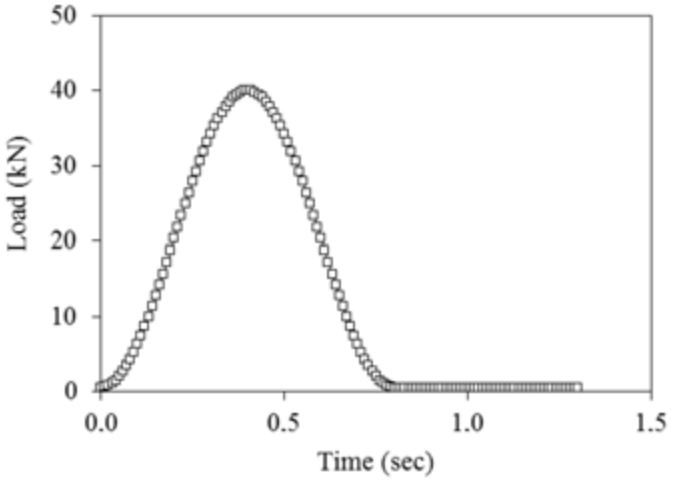

Figure 2. Sinusoidal load pulse at 0.77 Hz used by Sarici et al. (2016)

Laboratory Instrumentation

Instrumentation is typically included in large-scale laboratory box testing of model pavement sections to measure the pavement response to loading. This section describes recommendations for a basic instrumentation array; however, the inclusion of instrumentation should be specifically designed to accomplish the test objectives. The most basic instrumentation consists of an in-line load cell on the actuator that is capable of measuring the maximum applied loading with an accuracy of at least 0.05 kN, an internal Linear Variable Differential Transducer (LVDT) for measuring the plate deformation, and at least 1 externally mounted LVDT to measure the deformation of the load plate near the edge as a check on the internal LVDT measurement and to monitor plate bending. Optional but recommended sensors include a minimum of three LVDTs spaced at set distances from the center of the load plate to measure pavement surface deformation, earth pressure cells (EPC) for measuring the load-induced stress at different locations within the pavement, at least one pore pressure transducer to monitor the accumulation of pore pressure near the top of subgrade soils, a temperature transducer, and a moisture transducer. The surface LVDTs can be used in conjunction with the internal actuator LVDT to create a deflection basin for backcalculation of the pavement layer moduli using layered elastic analysis software. In addition, the shape of the deflection basin provides insight as to the failure behavior of the model pavement section. The inclusion of earth pressure cells at critical locations within the pavement structure can be used to compare the stress distribution profiles of unreinforced and reinforced pavement sections as well the calibration of mechanistic models. The pore pressure transducers, moisture sensor, and temperature probe are used to monitor the environment for the model subgrade. Additional instrumentation can be included as necessary to accomplish specific test objectives. An example instrumentation array used by Tingle and Jersey (2005) is shown in Figure 3. Figure 4 shows an example of the test setup including the LVDT arrangement from Tingle and Jersey (2005).

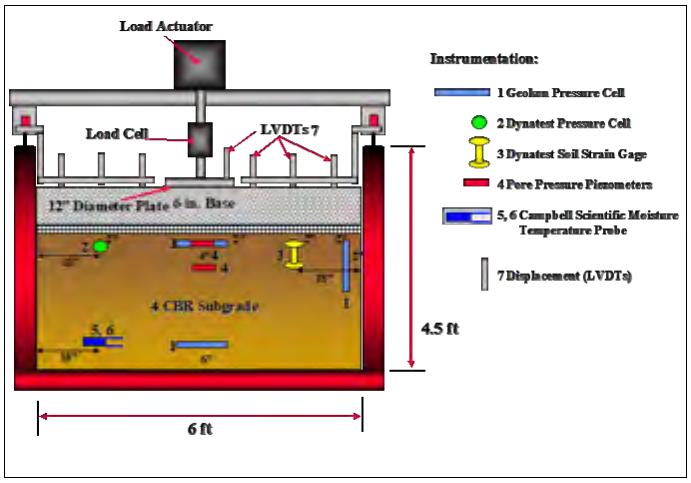

Figure 3. Example instrumentation layout from Tingle and Jersey (2005) [note: 1 in. = 25.4 mm and 1 ft = 304.8 mm].

Figure 4. Completed test set up prior to load testing from Tingle and Jersey (2005).

Construction of Model Pavement Sections

The construction of the model pavement sections should be performed as similar to standard field construction techniques as reasonably possible given the practical restrictions related to large-scale laboratory box testing. First, each model pavement section should be constructed and tested separately including complete reconstruction of subgrade materials to ensure that there are no residual effects from previous load sequences. Prior to subgrade placement, the test box should be lined with plastic membrane to retard moisture loss. Subgrade soil should be mechanically processed to achieve the target moisture content necessary to produce the desired strength when compacted within target density limits. It is recommended that layer thicknesses be limited to less than or equal to 125-mm due to the reduced size of the compaction equipment used in box testing versus standard compaction equipment. For fine-grained materials, it is recommended that the material be compacted using a pneumatic compactor to ensure kneading of the material. For coarse-grained materials, compaction can be achieved by a combination of vibratory plate compactors and a pneumatic compactor at the very edge where the curvature of the bottom plate of the vibratory compactor doesn't permit proper contact. When appropriate,

the subgrade and/or base material should be carefully excavated by hand for sensor placement. Geosynthetics should be cut to dimensions slightly less than the plan area of the box and held in place with base material. Generally, the geosynthetics are not anchored, nor are they extended up the sides of the box to induce restraint. The minimum dimensions of the box were selected such that the area is sufficient to ensure mobilization of the reinforcement mechanisms for pavement applications. The aggregate base material should be processed to its optimum moisture content for placement, with no free draining moisture that could collect at the interface. The aggregate base is typically placed in 150-mm or smaller lifts depending upon the design thickness of the layer. Due to the thixotropic nature of many granular materials, the initial compacted strength may be less than expected while the moisture content is still close to optimum. Thus, a critical step for consistency between model pavement sections is to leave the compacted base uncovered for exactly 48 hours to simulate in situ “curing” and strength improvement prior to testing or placement of a hot mix asphalt (HMA) surface. The authors have attempted several different methods of placement of an HMA surface layer. The most common method is to procure HMA from a local plant, and place the mix directly on the surface of the compacted base. However, the authors’ experience is that inconsistencies in the compaction process using small laboratory compaction equipment to compact viscous HMA leads to excessive variability in the compacted HMA layer. The authors developed an alternative method that includes paving a lane of HMA on a layer of 25-mm-thick plywood using normal asphalt paving and compaction equipment. Once the asphalt has cooled, the paved section can be saw cut into HMA slabs for placement on the compacted base layer in the box using a forklift (Figure 5). Additionally, should the HMA thickness exceed design tolerances, the field construction section could be diamond-ground to ensure design thickness are near target values. This method produces HMA that is much closer to standard HMA than the results achieved by compacting within the test box, and the HMA slabs used on different model pavement sections are very similar which reduces potential variability in test results. It is noted, however, that placement of the HMA layer in this manner does not induce construction stresses in the underlying soils nor are in interface bonding conditions similar to that that would be attained in full-scale construction. However, it is the authors’ opinion that consistency in HMA construction and material properties outweigh the differences in box testing and full-scale construction techniques. It is imperative that detailed quality control data be collected for the as-constructed pavement layers to verify that minimum compaction standards have been achieved and that target strengths are within acceptable limits for reasonable comparisons between model pavement sections to be drawn. As a minimum, the following construction data should include oven dried moisture content, dry density of compacted unbound materials, in situ strength results for unbound materials (individual test results not averages), void in mineral aggregates for the HMA, density data from cores for the HMA, and accurate thickness values for each layer. Additional construction data should include relative elevation data, nondestructive testing for layer modulus, and other information specific to test objectives.

a) Paving HMA on a plywood base. b) Saw cut HMA slabs transported to box.

Figure 5. Installation of HMA layer on compacted base (Robinson et al. 2019)

Load Testing

As noted, a seating load of 0.45 kN is recommended to maintain contact between the load plate and the pavement surface. Static and dynamic response data should be collected prior to load testing each model pavement section. This "conditioning" sequence should include 10 cycles at 4.4-kN increments up to a maximum of 40 kN. This "conditioning" sequence provides preliminary response data and is considered representative of typical construction traffic during the construction of new pavement sections. Once the conditioning sequence is complete, baseline static data should be collected and then cyclic loading of the test item commenced. While continuous data collection and storage are desired, dynamic data in 10-cycle increments can be collected at selected intervals in the test sequence to minimize data storage requirements. Dynamic testing of the model pavement sections should continue beyond the typical failure criteria for flexible pavements (25 mm) for standard tests and may extend to greater levels of deformation to meet specific test objectives. It should be noted that the temperature of the test environment should be relatively constant between model pavement sections. A target temperature of 25^{o}C is recommended, and the actual temperature should be recorded during testing. This is particularly important for model pavement sections including HMA.

Minimum Data Analysis and Reporting Requirements

In order to standardize test results, the analysis and reporting of results for large-scale laboratory box testing should include the as-constructed pavement properties for both pre-test and post-test (forensic) conditions. In addition, the results of the measured load at different test intervals should be reported to demonstrate that the applied loading was consistent. Finally, a plot of the permanent deformation versus the number of load cycles should be created and reported. Additional material and a pavement properties can be reported as well as analytical results to satisfy test objectives. However, these minimum analyses and reporting standards will ensure that the basic information between tests is communicated for long-term use.

CONCLUSION

This paper summarizes relevant experiments utilizing large-scale laboratory box testing to evaluate the benefits of including geosynthetic products in flexible pavement foundations. The results of this review demonstrate the utility of the test method for differentiating the performance benefits of different commercial geotextile and geogrid products in pavement foundation applications. The

authors provide preliminary recommendations for the standardization of large-scale laboratory box testing for use as a performance test for evaluating the effectiveness of geosynthetics for base reinforcement in flexible pavements. Key recommendations include the following.

1. Minimum containment vessel or box dimensions based upon finite element analyses are 1.8m by 1.8m in plan and 1.3m in depth.
2. The boundaries of the containment vessel or box should be rigid to minimize deflections in support of modeling efforts.
3. The recommended loading consists of a hydraulically controlled load of 40 kN on a 305-mm diameter circular steel plate (25.4 mm thick) with a thin rubber pad applied in a sinusoidal wave at a frequency of 0.77 Hz (0.4-second loading and 0.9-second rest period).
4. The minimum recommended instrumentation consists of an in-line load cell on the actuator capable of measuring the maximum applied loading with an accuracy of at least 0.05 kN, an internal Linear Variable Differential Transducer (LVDT) for measuring the plate deformation, and at least one externally mounted LVDT to measure the deformation of the load plate edge to monitor plate bending.
5. Construction of the model pavement sections should be as close to standard field methods as reasonably possible. Fine-grained materials should be compacted to minimum acceptable density standards using pneumatic compaction equipment. Unbound granular materials should be compacted to minimum acceptable density standards in relatively thin lifts using vibratory compaction equipment. Compacted base course materials should be "cured" for 48 hours to allow for thixotropic strength gain prior to testing or placement of an HMA layer. HMA layers should be constructed using full-scale paving equipment, cut into slabs and placed in the box apparatus to ensure that materials are representative of standard compacted HMA.
6. Static and dynamic response data should be collected and reported including an abbreviated "conditioning" sequence prior to load testing of the model pavement sections.
7. Pavement response data should be collected during dynamic load testing, and testing conducted until the pavement section exceeds at least 25 mm of permanent deformation.
8. Minimum data analyses and reporting requirements should include as-constructed pavement properties including both pre-test and post-test (forensic) conditions, measured load data at different test intervals, and a plot of permanent surface deformation versus applied load cycles.

REFERENCES

Abu-Farsakh, M. Y., and Chen, Q. (2011). Evaluation of geogrid base reinforcement in flexible pavement using cyclic plate load testing. *International Journal of Pavement Engineering*, 12(03), 275- 288.

Al-Qadi, I. L., Brandon, T. L., and Bhutta, A. (1997). Geosynthetic stabilized flexible pavements, Proceedings of *Geosynthetics '97*, IFAI, Vol. 2, Long Beach, California, pp. 647-662.

Barksdale, R. D., Brown, S. F., and Chan, F. (1989). Potential benefits of geosynthetics in flexible pavement systems, National Cooperative Highway Research Program Report No. 315, Transportation Research Board, National Research Council, Washington, D.C.

Bauer, G.E. and Abdelhalim, A.O.A. (1987). The performance of geogrid reinforced road bases, In *Construction & Building Materials*, Vol. 1, No. 2, pp. 71-75.

Chen, Q., Abu-Farsakh, M., and Tao, M. (2009). Laboratory evaluation of geogrid base reinforcement and corresponding instrumentation program. *Geotechnical Testing Journal*, 32(6).

Cuelho, E., Perkins, S. and Morris, Z. (2014). Relative operational performance of geosynthetics used as subgrade stabilization, Final report to the Montana Department of Transportation, FHWA/MT-14-002/7712-251, 328 pp.

Cuelho E. and Perkins, S. (2016). Mechanisms of reinforcement benefit from geosynthetics used as subgrade stabilization, Proceedings of *EuroGeo 6*, Istanbul, Turkey.

Cuelho, E. and Perkins, S. (2017). Geosynthetics subgrade stabilization – field testing and design method calibration, *Transportation Geotechnics*, Vol. 10, p. 22-34.

Douglas, R.A. (1997). Repeated-load behavior of geosynthetic-built unbound roads, *Canadian Geotechnical Journal*, Vol. 34, pp. 197-203.

Douglas, R.A. and Valsangkar, A.J. (1992). Unpaved geosynthetic-built resource access roads: stiffness rather than rut depth as the key design criterion, In *Geotextiles and Geomembranes*, Vol. 11, pp. 45-59.

Berg, R.R., Christopher, B.R., and Perkins, S. (2000). Geosynthetic reinforcement of the aggregate base/subbase courses of pavement structures: GMA white paper II. Published by the Geosynthetics Material Association, pp. 176.

Gregory, G.H. and Bang, S. (1994). Design of flexible pavement subgrades with geosynthetics, In Proceedings of the *30th Symposium on Engineering Geology and Geotechnical Engineering*, Boise, Idaho, pp. 569-582.

Haas, R., Walls, J., and Carroll, R. G. (1988). Geogrid reinforcement of granular bases in flexible pavements, *Transportation Research Record 1188*, pp. 19-27.

Kelly, D., Fairfield, C., and Sibbald, A. (1995). Geosynthetics for the improvement of unpaved roads, In *Highways & Transportation*, Vol. 42, No. 07/08, pp. 13-15.

Leng, J., Ju, T., and Gabr, M. (2002). Characteristics of geogrid-reinforced aggregate under cyclic load. *Transportation Research Record 1786*, pp. 29-35.

Montanelli, F., Zhao.A., and Rimoldi, P. (1997). Geosynthetic-reinforced pavement system: testing & design. *Proceedings of Geosynthetics '97*, IFAI, Vol. 2, Long Beach, California, pp. 619-632.

Perkins, S. (1999). Geosynthetic reinforcement of flexible pavements: laboratory based pavement test sections. Report No. FHWA/MT-99-001/8138, U.S. Department of Transportation, Federal Highway Administration, Washington D.C.

Qian, Y., Han, J., Pokharel, S., and Parsons, R. (2011). Stress analysis on triangular-aperture geogrid-reinforced bases over weak subgrade under cyclic loading. *Transportation Research Record 2204*, 83-91.

Robinson, W.J., Mahaffey, B.J., Howard, I.L., and Norwood, G.J. (2019). Cyclic plate testing of geosynthetic-reinforced airfield pavements. *Ground Improvement*, 172(4), pp. 229-243.

Sarici, T., Demir, A., Tutumluer, E., Demir, B., Gungor, A.G., Epsileli, E., Comez, S. and Ok, B. (2016). Evaluation of geogrid reinforced unpaved roads using large scale tests. *Proceedings of EuroGeo 6*, Istanbul, Turkey, pp. 1185-1193.

Tingle, J.S. (2019). Mechanistic analyses of geosynthetic reinforced aggregate road test sections, *Transportation Research Record 2673*, pp. 783-797.

Tingle, J.S. and Jersey, S.R. (2005). Cyclic plate load testing of geosynthetic reinforced unbound aggregate roads. *Transportation Research Record 1936*, pp 60-69.

IFAI Geosynthetics Conference

Design of Reinforcement Geosynthetics in Landfill Piggyback Expansion

Jean-Baptiste Duquet[1], Cédric Sarbach[2] and Stephan Fourmont[3]

[1]Antea Group, Bvd Duhamel du Monceau, Olivet, France; jean-baptiste.duquet@anteagroup.com
[2]Afitexinov, Rue Louis Blériot, Champhol, France; cedric.sarbach@afitex.com
[3]Afitex-Texel, Parc Industriel, Sainte-Marie, Quebec, Canada; sfourmont@afitextexel.com

ABSTRACT

The construction of a vertical expansion of existing waste disposal facilities (piggyback landfills) involves the use of reinforcement geosynthetics to address differential settlements and stability issues that will be reactivated under the load of the new cell. The challenge is to guarantee the integrity of the new liner system. This paper presents the extension project of an old landfill and the design method used to evaluate the tensile strength of the required reinforcement geosynthetic. The methodology used in this project is a calculation method for the design of geosynthetics in the case of soil subsidence and sinkholes. This reference method, usually used with granular backfill, has been adapted and optimized to consider waste material-specific properties.

PROJECT OVERVIEW

To extend the life of its Non-hazardous Waste Storage Facility (NWSF), an operator proposed to continue operating its site, within the perimeter already authorized, by a vertical expansion of the cells already in operation to a maximum thickness of waste of about 16 m (52 ft). This project is based on non-hazardous waste storage cells about 15 m (50 ft) thick, some of which are more than 20 years old and, therefore, at different degradation stages.

The vertical expansion requires the new cell to be hydraulically independent of those already in place underneath. The overall leachate barrier system must comply with the current regulation and must remain functional in the long term. The design included the installation of a soil layer rein-forced with geosynthetics over the old final cover system. This layer is becoming the subgrade soil for the new leachate barrier system. A typical section is shown in Figure 1. As the site also operates as a valorization and disposal site for incinerator bottom ash, it has been decided to use this material to construct the soil-reinforced layer.

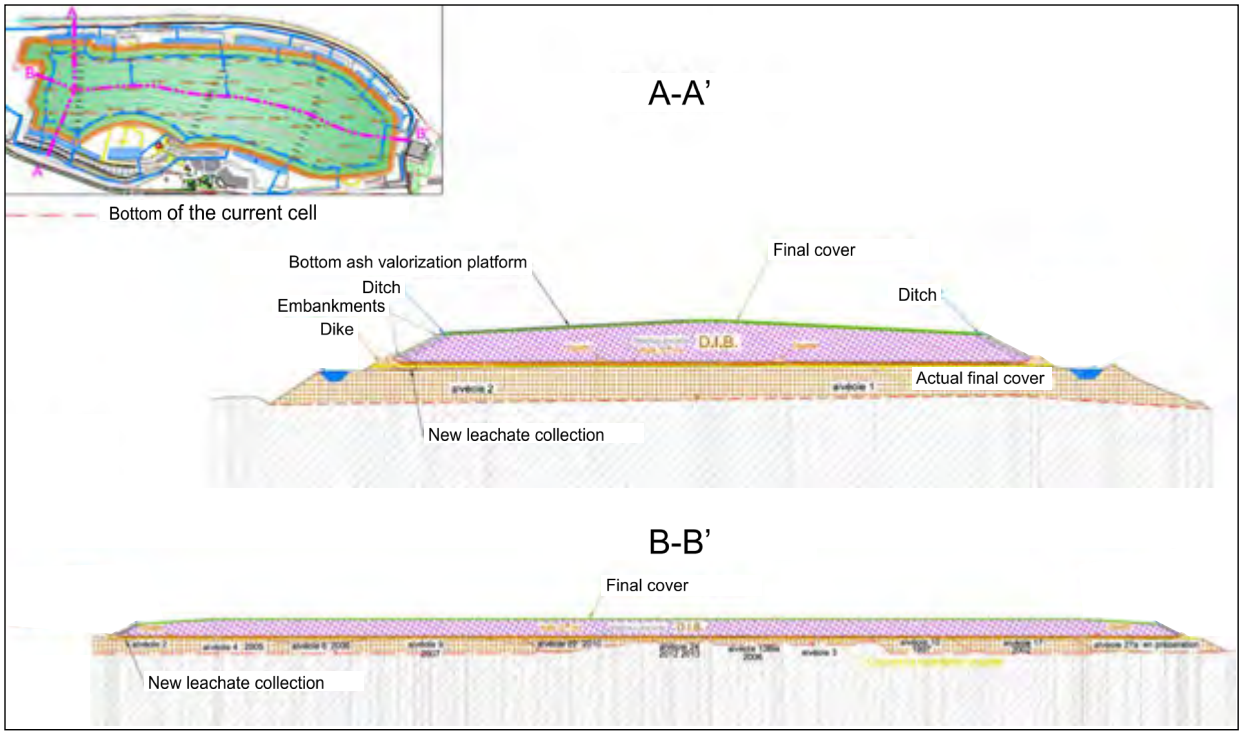

Figure 1. Typical cross-sections

GEOTECHNICAL DESIGN

In addition to the slope stability considerations and design, the vertical expansion of the cell requires a specific analysis to estimate the overall settlements that will occur.

Global settlements. Global settlements in waste result from complex phenomena that occur over time. They can be determined by adding up:

- Primary settlements caused by the weight of the new waste (short term);
- Residual secondary settlements due to the non-homogeneous degradation of the old waste (long term).

The guide "Recommandations pour la conception des extensions d'ISDND en appui sur des casiers anciens" (BRGM, 2020) recommends the application of the "Modèle Incrémental de Prédiction des Tassements" (Olivier, 2003 and ADEME, 2005), also called ISPM model. This model, developed from field experience in France and abroad, allows the prediction of the evolution of the primary (short-term) and secondary (long-term) settlements of a waste mass in the case of a vertical expansion over it. It is recommended to apply this model by retro-analysis (or calibration) to improve accuracy, which has been done on that project.

The estimation of the primary settlements was carried out from the field data by applying the pressiometric method from modulus values measured on-site (average Pressuremeter Modulus E_{PMT} = 9.2 MPa) and the ISPM method from data collected in the literature. The estimation of the secondary settlements was achieved by applying the ISPM method with data resulting from a retro-analysis carried out using the topographic survey on the post-operation settlements of the site. In

the worst-case scenario, the global settlements were estimated at 1.20 m (4 ft): 0.90 m (3 ft) of primary settlements and 0.30 m (1 ft) of secondary settlements.

Structural differential settlements. Structural differential settlements develop in areas where there are significant variations in the geometric parameters and the nature of the support, such as:

- Variations in the thickness and nature (age, composition) of the compressible support or even the presence of geotechnics structures (dikes, etc.);
- Variations of the load on the compressible support (thickness and unit weight of the material).

The consideration of the structural differential settlements led to specific constructive measures:

- Modification of the landfill gas collection network, including the vertical wells, to avoid the development of localized hardpoints;
- Specific layout with the installation of two monodirectional reinforcement geosynthetic layers orthogonally crossed to have a homogeneous reinforced soil structure at any point under the new cell.

Localized differential settlements. Localized differential settlements are difficult to anticipate. The BRGM guide suggests taking them into account by considering a cavity with a diameter of about 1.0 to 2.0 m (3 to 6 ft) within the waste mass, as explained in Figure 2. It illustrates the main geometric definitions and notations that will be used. The value n = 3 is to be considered for household waste.

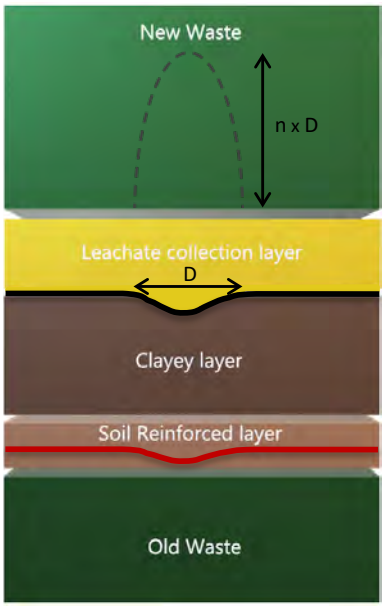

Figure 2. Illustration of the behavior of a homogeneous waste mass under loading

The following limit state designs are to be considered:

- Serviceability limit state (SLS) to address the failure of the reinforced soil layer, either by insufficient geosynthetic tensile strength or low interaction properties between the geosynthetic and the soil;

- Ultimate Limit State (ELU), to verify that the maximum allowable deformation in the leachate barrier system is not exceeded. It ensures that the system will continue to perform appropriately even after localized and global settlements.

It must be verified that none of these limit states are to be reached either during construction or during the expected service life of the cell.

Serviceability limit state (SLS). The maximum admissible deflection for the lining system is first determined. A value of 3% is used in the literature for a 2 mm (80 mil) HDPE geomembrane used as a primary lining system (Seeger et al., 1996). The other components of the leachate barrier system may influence this value.

The stress distribution on the reinforcement geosynthetic is considered uniform and vertical without considering any contribution from the circumference of the soil cylinder:

$$\sigma = FS_{Gsup} \times \left(\gamma_{waste} \times n \times D + \gamma_{pb} \times H_{pb} + \gamma_{sb} \times H_{sb} + \gamma_{ll} \times H_{ll} + P\right) + FS_{Qsup} \times Q \quad (1)$$

where:
σ: Stress on the reinforcement geosynthetic
FS_{Gsup}, FS_{Qsup}: Factors of safety
γ_{waste}: Unit weight of the waste
n: arching effect factor (n=3 for municipal solid waste)
D: diameter of the cavity
γ_{pb}: Unit weight of the primary leachate barrier system
H_{pb}: Thickness of the primary leachate barrier system
γ_{sb}: Unit weight of the secondary leachate barrier system
H_{sb}: Thickness of the secondary leachate barrier system
γ_{ll}: Unit weight of the leveling layer (above the reinforcement geosynthetic layer)
H_{ll}: Thickness of the leveling layer (above the geosynthetic layer)
P: Permanent loads
Q: Temporary loads

The residual stiffness of the reinforcement geosynthetic during the service life of the structure must be greater than:

$$J_{min} = \frac{\sigma \times D}{2 \times \varepsilon_{max}} \times \sqrt{1 + \frac{1}{6 \times \varepsilon_{max}}} \quad (2)$$

where:
ε_{max}: maximum allowable elongation in the reinforcement geosynthetic to ensure that the barrier system remains fully functional.

The strength increase in the reinforcement geosynthetic will cause the geosynthetic deformation in the anchoring zones and increase the deflection in the cavity. The stiffness of the reinforcement geosynthetic must then be overdesigned to take it into account and remain within the allowed deformations.

Ultimate Limit State (ULS). The ultimate limit state design regarding the minimum required strength of the reinforcement geosynthetic shall consider the long-term behavior of the product and its installation. This will be covered in the "Geosynthetic Design" paragraph. The ULS verification is then:

$$T_{ELU} \leq \frac{T_{ult}}{RFs} \quad (3)$$

where:
T_{ult}: Ultimate tensile resistance of the reinforced geosynthetics
RFs: Reduction factors specific to the product, the environment, and the installation

GEOSYNTHETIC DESIGN

Product description. The selected reinforcement geosynthetic is a high-modulus woven geotextile made with high tenacity yarns, manufactured by a warp knitting process (Figure 3). The woven geotextile provides the separation function, whereas the high-tenacity yarns give the high strength capacity to the overall product. It allows tensile strength up to 2,000 kN/m.

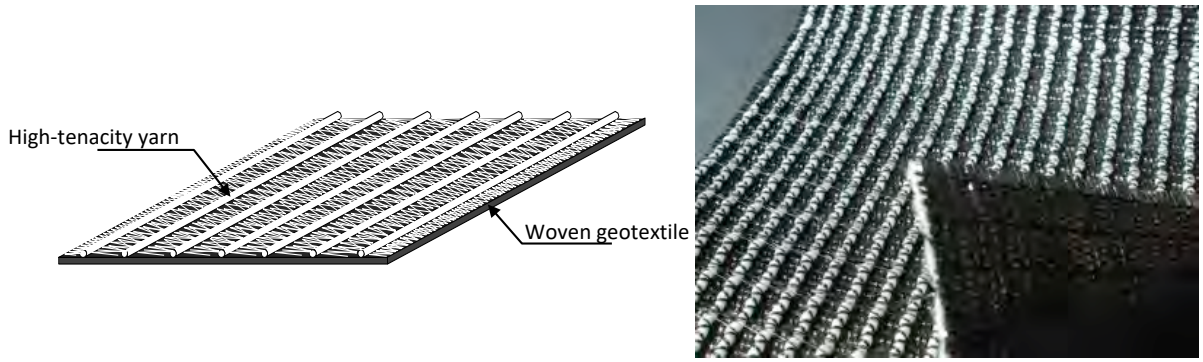

Figure 3. Description of the reinforcement geosynthetic

The process guarantees a high level of reinforcement with reduced elongation as the cables are inserted without undulation during the knitting process. It also allows dissociating the separation and reinforcement functions. Indeed, because the high-tenacity polymer yarns provide the reinforcement capability of the product, the woven geotextile keeps its filtration opening size constant regardless of the tensile strength of the geosynthetic. The composition of the high-tenacity yarns (PET, PVA, etc.) is selected according to the type of structure and the nature of the surrounding soils.

The reinforcement geosynthetic selected for this project is GEOTER F PVA 450. It is made with PVA high-tenacity yarns and has an ultimate tensile strength of 450 kN/m. The sizing of the geosynthetic is described in the following paragraphs.

Product sizing. The minimum required long term tensile strength and elongation for the reinforcement geosynthetic has been calculated by the project engineer with a geotechnical design. Then, a study has been performed by the geosynthetic manufacturer to select the appropriate product. As for any project using geosynthetics, this study took into account:

- Tensile creep of the high-tenacity cables,
- Damages on the geosynthetic during the installation,
- Chemical resistance of the geosynthetic.

The ultimate tensile resistance T_{ult} of the reinforced geosynthetics is then given using the following formula:

$$T_{design} = \frac{T_{ult}}{RF_{CR} \times RF_{ID} \times RF_{D} \times RF_{global}} \quad (4)$$

where
T_{design}: allowable tensile strength (kN/m)
RF_{CR}: reduction factor for creep to account for long term behavior,
RF_{ID}: reduction factor for installation Damage, determined form construction damage tests,
RF_{D}: reduction factor for durability, chemical resistance of the polymer in the specific environment under consideration
RF_{global}: safety coefficient on the geosynthetic material, equal to 1,25 for every application.

Creep behavior. The creep behavior was determined by an independent expert laboratory using ASTM D6992 standard. The isochronous curves were obtained according to this test, which was performed during several months at several strains on a creep bench.

The reduction factor for creep is obtained from the isochronous curves, getting the remaining fraction of the initial ultimate strength (Load UTS) at the allowed elongation (determined by the geotechnical design), as written in the following formula:

$$RF_{CR} = \frac{100}{Load\ UTS\ (maximum\ elongation\ (\%))} \quad (5)$$

Installation Damage. The installation damage reduction factor has been determined by doing in-situ tests (as described in NF G38-064 and ISO/TR 20432 standards). Strips of the product have been backfilled with several soil types, from fine soils to gravel 0-12in (Figure 4).

Figure 4. In-situ tests with several types of soil over the geosynthetic

After exhuming the product, a visual inspection was carried out (Figures 5 and 6). The woven geotextile on one side of the GEOTER F reinforcement geosynthetic protects the high-tenacity yarns. Therefore, the product presents less degradation than most uncoated geosynthetics on the market.

Figures 5 and 6. Visual inspection on the geosynthetic after exhumation

Tensile strength tests have been carried out on the exhumed product by an independent laboratory to determine the installation damage reduction factor function of the tested soils (Table 1).

Table 1. RF_{ID} for several types of soil in contact with the reinforcement geosynthetic

	Fine material	Sand < 2mm	Gravel 0/100mm	Gravel 0/300mm
RF_{ID}	1.05	1.19	1.15	1.26

Durability. The high-tenacity yarns of the selected reinforcement geosynthetic are made in Polyvinyl Alcohol (PVA). Oxidation has been identified to be the significant degradation mechanism of PVA. Tests on PVA yarns in wet and dry cycles for the use in reinforced earth structures (Nait-Ali et al., 2009) results in a reduction factor for durability of 1.20.

Applying the reduction factors to the allowable tensile strength determined by the geotechnical design led to the selection of the reinforcement geosynthetic with PVA high-tenacity yarns and ultimate tensile strength of 450 kN/m: GEOTER F PVA 450.

FINAL CROSS-SECTION AND LAYOUTS

The final cross-section for the vertical expansion of the cell is presented in Figure 7.

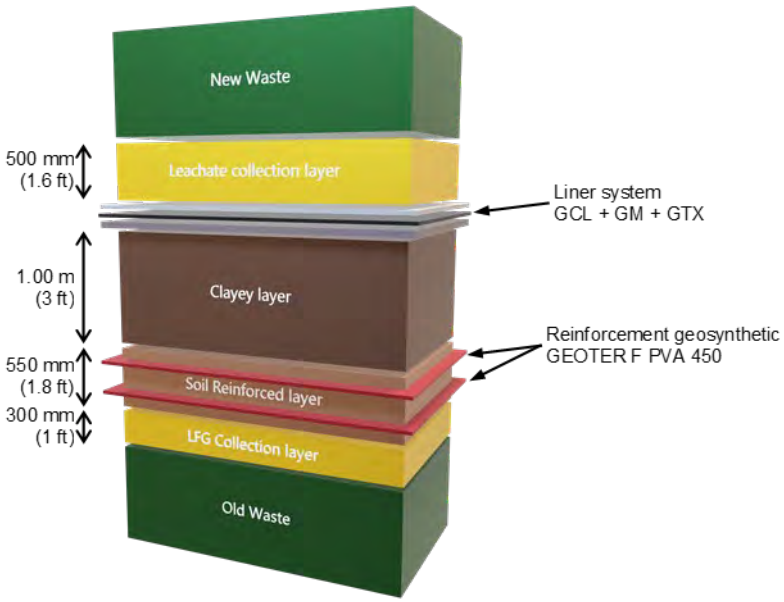

Figure 7. Final cross-section of the new cell

Landfill gas management. To ensure the collection of landfill gas from the existing waste and to avoid the development of hardpoints under the embankment, the following improvements have been proposed:

- Old wells are modified to ensure a safe distance from the soil-reinforced layer. This distance is equivalent to the estimated maximum settlement under the future cell;
- Old wells are not connected to the horizontal collector pipes; the gas flows through a 300 mm (1 foot) gravel drainage layer between the old waste and the soil-reinforced layer.

Soil-reinforced layer. A 550 mm (1.8 ft) thick soil-reinforced layer is required to have a uniform load distribution over the old waste mass and limit the differential settlements. It is composed of:

- Two layers of PVA reinforcement geosynthetic with an ultimate tensile strength of 450 kN/m and a maximum elongation of 6% installed perpendicularly at two different levels to fully mobilize the interface friction angles; the overlaps are calculated to ensure continuity of the reinforcement;
- Incinerator bottom ash material available on site.

Numerous analyses have been carried out on the bottom ash material to characterize its physical, mechanical, and chemical properties (Table 2). It has been found suitable as a backfill material. The pH, which may exceed 10, has been considered when selecting the reinforcement geosynthetic. PVA material has been proven to be more adapted for that range of pH.

Table 2. Bottom ash material characterization

Bottom ash material				
Test	Symbol	Unit	Value	Comment
Natural water content	W_n	%	12.1	0.8 W_{opn} < W < 1.1 W_{opn}
Dry unit weight	ρd	T/m^3	1.28	
Particule size distribution	D_{max}	mm	23	PSD 0/20mm
	<50mm	%	100	
	<2mm	%	39.7	
	<80µm	%	4.7	
Methylene blue	MBV	%	0.04	
Sand equivalent	SE	-	67.8	
Organic content by loss on ignition	LOI	%	7	
GTR class			F_{61}	Similar to D_2
Proctor test	$ρd_{OPN}$	%	14	
		T/m^3	1.75	
Immediate bearing capacity factor	IPI		40.3 46.2 34.3 7.1 2.2	IBC > 20 (average and for 3 values over 5)
Fragmentability	FR		1.9	High fragmentability
Consolidated drained triaxial	c'	kPa	42	
	ϕ'	°	37	

Leachate barrier system. The leachate barrier system required by the French regulation is implemented on top of the soil-reinforced layer. It is composed of (from bottom to top):

- A clayey layer 1 meter (3 feet) thick with a hydraulic conductivity inferior to 1x10^{-9} m/s, and a geosynthetic clay liner (GCL);
- A 2 mm (80 mil) HDPE geomembrane protected by a non-woven geotextile;
- A gravel drainage layer 0.50 m (1.6 ft) thick.

The barrier system allows the leachate generated in the new cell to be collected separately with dedicated collection wells. The slope of the bottom cell has been increased to 3% in the drainage direction to ensure a remaining long-term slope of 1% after the maximum expected settlements.

GEOSYNTHETIC INSTALLATION

To limit overlaps, simplify the installation, and ensure the continuity of the reinforcement, rolls with specific lengths have been produced. The length of the product was 120 m (395 ft). Handling was achieved using mechanical shovels.

Roll placement. GEOTER F PVA is unrolled on a base that has been graded and compacted (Figures 8 and 9).

Figure 8. Installation of reinforcement geosynthetic

Figure 9. Continued installation of reinforcement geosynthetic

The product is placed with the woven geotextile on top to protect the high-tenacity yarns during the backfilling. Two layers of geosynthetics were installed, perpendicular to each other, with a soil layer in between.

Overlaps. Side by side (longitudinal) connections are achieved with a minimum overlap of 300 mm (12 in.) following the direction of the backfill placement (Figure 10).

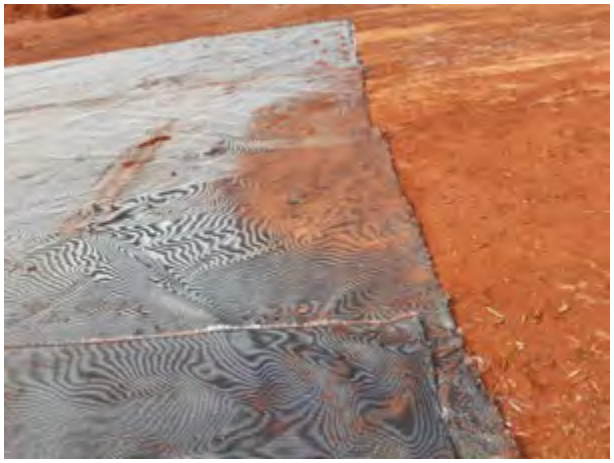

Figure 10. Longitudinal overlap of the reinforcement geosynthetic

Bottom ash material placement. The incinerator bottom ash material is free of foreign matter that could damage the geosynthetic. A 300 mm (1 ft) thick layer has been placed between the two geosynthetic layers to improve the interface friction properties (Figures 11 and 12).

Figure 11. Placement of bottom ash soil over geosynthetic

Figure 12. Continued placement of bottom ash soil over geosynthetic

MONITORING

The implementation of a monitoring system to record the settlements of the reinforcement geosynthetic aims to validate and refine the calculation and assumptions taken into account in the geotechnical model, and to better understand the reality and dynamics of the settlements.

The settlement monitoring system includes hydraulic settlement gauges connected to a reference tank. They are arranged as required, in line every 30 m (100 ft). Each gauge has been placed on the reinforcement geosynthetic on a rectangular plate and protected with sand to limit unexpected settlements (Figures 13 and 14).

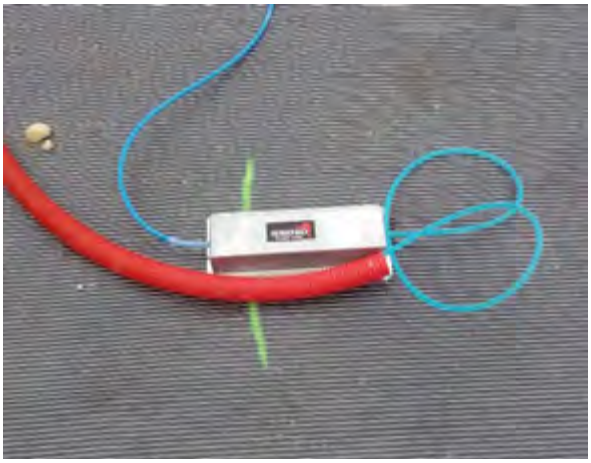

Figure 13. Hydraulic settlement gauge

Figure 14. Backfilling of the gauges

The gauges are connected to a reference tank, and a data logger is mounted on a concrete base outside the cell (Figures 15 and 16). The concrete base must not settle and is under a topographical survey. The data acquisition is made manually by connecting a reading device to the datalogger.

Figure 15. Reference tank

Figure 16. Datalogger

CONCLUSION

The use of a soil-reinforced layer as a subgrade for a piggyback landfill ensures that the leachate barrier system of the new cell will remain functional over the long-term. The designed and selected GEOTER F PVA reinforcement geosynthetic is a high-modulus woven geotextile made with high tenacity yarns that exhibits a tensile strength of 450 kN/m at 6% strain. It creates a uniform repartition of the load on the old waste and controls the differential settlements.

The high tenacity yarns made in PVA permit to re-use the bottom ash material (available on site) as backfill material on the product.

The methodology followed for the design of the reinforcement is already in use and described in several guides; however, the implementation of a monitoring system permits to refine the calculation and assumptions taken into account in the geotechnical model and confirm the expected behavior of the structure.

REFERENCES

BRGM (2020). Guide de recommandations pour la conception des extensions d'ISDND en appui sur des casiers anciens, France, 81 p.

Olivier, F. (2003). Tassement des déchets en CSD de classe II : du site au modèle, *PhD Thesis*, Grenoble University, France, 325 p.

ADEME (2005). Guide méthodologique pour le suivi des tassements des Centres de Stockage de Classe II, France.

Seeger, S. and Müller, W. (1996). Limits of Stress and Strain: Design Criteria for Protective Layers for Geomembranes in Landfill Liner Systems, *Proceedings Geosynthetics: Applications, Design and Construction*, Rotterdam, The Netherlands, pp 153-157.

ASTM D6992, Standard Test Method for Accelerated Tensile Creep and Creep-Rupture of Geosynthetic Materials Based on Time-Temperature Superposition Using the Stepped Isothermal Method, *ASTM International*, West Conshohocken, Pennsylvania, USA

NF G38-064, Utilisation des géotextiles et produits apparentés - Murs inclinés et talus raidis en sols renforcés par nappes géosynthétiques - Justification du dimensionnement et éléments de conception, *AFNOR*, La Plaine Saint-Denis, France

ISO/TR 20432, Guidelines for the determination of the long-term strength of geosynthetics for soil reinforcement, *ISO*, Geneva, Switzerland

Nait-Ali, K.L. and Freitag, N. (2009). Reinforcement made of Polyvinyl Alcohol yarns: Effect of wet/dry cycles and consequences on the design in the framework of the French standards, *Rencontres Géosynthétiques*, CFG, Nantes, France: 181-188.

Geosynthetics Conference

Geosynthetics for Solar Farm Development

Ashley MacMillan, P.E.,[1]

[1]TenCate Geosynthetics, Austin, TX; e-mail: a.macmillan@tencategeo.com

ABSTRACT

Contractors and owners are interested in innovative and cost-effective solutions for solar farm development over weak soils. One efficient solution is to use high strength geosynthetics to provide constructability and long-term reinforcement to the access roads, staging areas, and other site features. Soil-geosynthetic interaction provides an improved soil stress distribution from the surface loads to the underlying soft soils, which can reduce the required aggregate thickness for the site construction. This paper will explore soil-geosynthetic considerations, including suggested measures during site assessment, design and installation sequencing which will increase the performance of geosynthetic-soil stabilization. The economical savings and reduced environmental impact of two recent solar development projects in Chicot County, AR and Lamar County, TX using geosynthetics for soft soil stabilization will be explored.

INTRODUCTION

Solar power is more affordable in the United States than ever before, leading to its widespread development. If solar photovoltaic (PV) panels were to be installed on 0.6% of the nation's total land area, the United Stated could have enough solar potential to provide electricity to power the entire country (Office of Energy Efficiency & Renewable Energy , n.d.). Although these systems have become more cost-effective, there is a need to reduce the costs associated with development and maintenance of solar energy to be more practical up against traditional energy sources. Typically, rural, and often undesirable land is selected for solar site development due to affordable land cost. Following contractor selection, construction activities over unsuitable soil such as saturated soils, marshlands, high fines, or expansive subgrades present challenges. Many times, the selected project site requires soil stabilization to improve the bearing capacity of the section. Stabilization with aggregate alone leads excessive import material quantities and associated transportation and placement of that material.

High strength geotextiles have been used in the heavy civil and energy sector to bridge soft spots, provide separation and filtration and provide long term reinforcement to site features including component storage yards, access roads, and construction entrances. This is a highly efficient and economical solution which does not require specialized equipment or labor and can handle high stress installations and ultimately reduced the amount of money and time spent on importing materials to strengthen weak subgrades on large project areas.

OVERVIEW OF GEOSYNTHETICS FOR SUBGRADE STABILIZATION

Although the apparent desired function when discussing soil stabilization with geosynthetics is reinforcement, it is important to understand other functions that affect the overall performance of a geosynthetic reinforced subgrade system. Geosynthetics in subgrade stabilization applications are typically used to provide one or more of the following functions:

- *Separation* – to prevent intermixing of two dissimilar materials
- *Filtration* – to allow movement of water through the geosynthetic while retaining soil on upstream side (product selection should consider long term resistance to clogging)
- *Confinement* – to prevent lateral movement (spread) of the aggregate fill
- *Reinforcement* – introduction of a tensile element to improve bearing capacity
- *Durability* – selection of product designed to resist damage during moderate to severe stress installations

In selecting a product to optimize performance, consider the two main categories of stabilization geosynthetics (geogrids and geotextiles) and how they function.
Geogrids are formed from plastics sheets and strips or woven from high tenacity yarns into a very open, grid like configuration, i.e., they have large apertures (see Figure 1). They may be coated with polymers to provide additional protection. Geogrids function almost exclusively as materials that provide confinement and reinforcement.

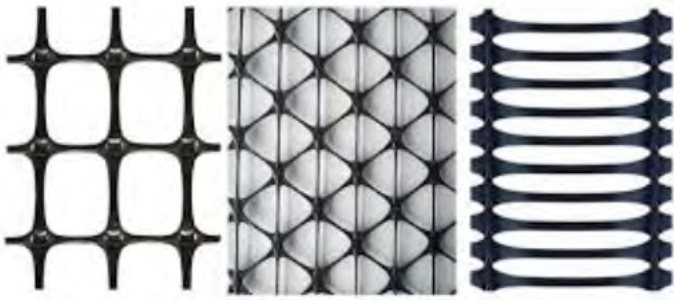

Figure 1. Common geogrid shapes

The geogrid will provide reinforcement and confinement when properly sized aggregate is placed above the geogrid to provide interlock to develop tensile strength. Typically, the graded aggregate needs to be ½" to 1.5" to work in accordance with most standard subgrade reinforcement geogrids. Regardless of aggregate size, a geogrid will not provide separation or filtration. To address these functions, a non-woven geotextile should be placed below the geogrid.

Geotextiles are permeable planar materials that can provide reinforcement, confinement, separation, filtration, and drainage. Geotextiles are either woven or nonwoven as highlighted in Figure 2. For non-woven geotextiles, yarns or fibers are mechanically or chemically entangled, or bonded to produce textile material. For woven geotextiles, the yarns are mechanically interlaced. Geotextiles are sometimes considered to be weaker products; however engineered geotextiles can provide the same or even higher tensile strengths than geogrids.

Figure 2. Common geotextiles (left – nonwoven; right – woven)

There are many different types of both woven and nonwoven geotextiles which will vary in their performance based on their physical properties. Properties such as apparent opening size, pore size distribution, and coefficient of interaction are important to consider when selecting a geotextile to serve the project requirements.

Proper selection of the product related to the unique site conditions as well as the intended functions is the first step in included geosynthetics as a solution for subgrade stabilization.

PROJECT CONSIDERATIONS: SOIL STRENGTH ANALYSIS, EXTENT OF GEOSYNTHETIC COVERAGE

Similar to all geotechnical systems, the collection and evaluation method to determine the subgrade strength which will be used in a geosynthetic reinforced design will influence the recommended solution and the confidence in the final design. Geosynthetic systems are installation sensitive so the constructability of the section is equally as important as the required long-term capacity. For solar farms specifically, loads during geosynthetic installation and aggregate compaction (and possible paving activities) are commonly the heaviest loads the section will experience during its design life. Successful installation is inherently dependent on the soil conditions present at the time of site stabilization activities. The design of geosynthetic reinforced sections should always consider constructability for the possible site conditions that could be encountered, including weather events which could cause increase in moisture content of soils and decrease of soil strength.

The strength of the subgrade input to the design is an influential parameter directly related to the required aggregate thickness. Consider an analysis using the subgrade strength in terms of California Bearing Ratio (or CBR). The designer must address the difference between a CBR and a soaked CBR in their design. For example, if the subgrade strength was quantified by a dynamic cone penetrometer, or DCP, during a dry condition, the soils could be weaker when saturated (especially true for fine grained soils). When available, a soaked CBR following ASTM D1883 (D18.05, 2018) will provide the designer with a high level of confidence that the design subgrade strength accounts for strength related to the soil in a saturated state. However, a CBR value (by other methods) can decrease rapidly during the first 24 hours of wetting and will continue to decrease at a reduced rate following the initial wetting period as shown in Figure 3 (Chandravali Pandey, 2019).

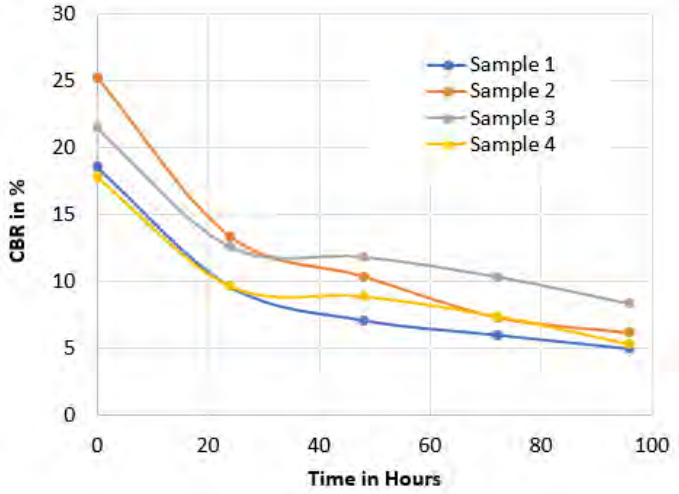

Figure 3. Variation of CBR values of different samples with their respective soaking time

As designers are constantly pushed to develop the most economical solutions from a cost perspective, a geosynthetic reinforced section could be under-designed based on values presented in a geotechnical report or through field analysis. If test methods were used that do not capture the weakest soil state, the designer needs consider further soil testing or an added factor of safety. One possible solution to balance out a conservative or non-conservative analysis based on soils which could lose strength due to added moisture is to provide a "wet-weather" and "dry-weather" section to optimize the required sections which would address constructability concerns for each case. Similarly, other components which are not always known as the time of design can influence the required thickness such as the quality of the fill material placed above the geosynthetic and the compactive efforts that will be used.

In the same effort to produce economical site stabilization designs, contamination of the stabilized sections is commonly overlooked. For most sites, it is quickly identified that stabilization of the access roads is required. While access roads, parking areas or construction entrances receive this attention and are considered for stabilization efforts, it is common that other areas are left untreated. On solar farms, segmented rows of adjacent solar panels are typically called "cells" and it is uncommon that there would be any geosynthetic installed in these areas. However, consider development of a 50-acre solar farm, where several crews are simultaneously working. It is common that the in-situ soils could have one or more of the following characteristics: high plasticity clays or fine-grained soils, poor strength, moisture sensitive (swell/shrink, freeze/thaw potential), high water table. These types of problematic soil are present over the entire project area, and due to the ongoing efforts of multiple crews operating construction equipment to install solar panel piles, solar panels, build roads, and construct facilities, contamination of the treated access road sections is inevitable.

If the crew driving piles is working in an untreated area of the project (for example in a high plasticity clay subgrade) it will track that material onto the stabilized access roads. Contamination of fines into the aggregate sections of roadway pose several issues: (1) Aggregate thickness loss due to equipment removing the upper layer of aggregate (2) Strength loss due to contamination of fines into the aggregate section. Even with as little as eight percent (8%) fines contamination, the effective strength of this aggregate layer can be decreased by up to fifty percent (50%) as shown in Figure 4 (Hicks, 1986).

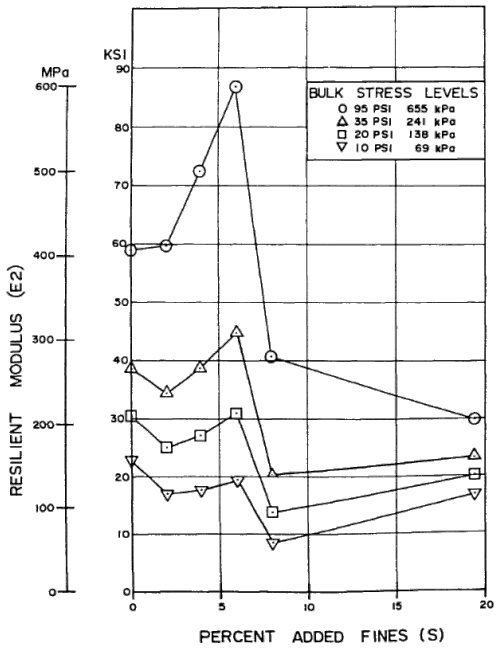

Figure 4. Resilient Modulus versus Percentage of Added Fines (Hicks, 1986)

Depending on the in-situ soil types, treatment with a geosynthetic over the entire site area should be considered to reduce potential contamination and degradation of the structural thickness of the road sections. For the areas of the project where only separation is required (not reinforcement) consider use of a lower tensile strength geosynthetic. This will provide an affordable option to minimize contamination of the site infrastructure. This will provide an economical treatment for the non-load bearing areas.

ECONOMIC BENEFIT

During the evaluation of subgrade stabilization options, the focus is on designing a long-lasting structure which can withstand environmental effects and dynamic loading. Selection considerations commonly include cost, ease of installation, successful history with achieving compaction requirements, and permanency of strength. There are three primary stabilization solutions to treat unsuitable soil: (1) remove the unsuitable material and replace with higher shear strength aggregate, (2) Geosynthetic Reinforcement and, (3) Chemical Stabilization (lime, Portland cement or fly ash).

Typically, option 1, the remove and replace method, involves undercutting and removing soft, weak, possibly wet or otherwise undesirable soils and replacing with an engineered fill. This method is costly and may not address the problem at hand. Sometimes, excavation through the weak surface soil exposes even lower strength soil and has the potential to interfere with ground water. Additionally, depending on the project's cut/fill requirements, removal of excavated material and importing select materials "engineered/granular fill" can prove to be costly and time consuming. For solar farm projects, it is common that the haul distance for import and export of materials is substantial adding to the construction schedule and cost of this method.

Option 3, chemical stabilization, improves short term strength, bearing capacity and shrink/swell behavior, however durability issues are a top concern, as well as potential health issues. These methods are time and weather dependent and begin to experience a break down in structure very soon after hardening. For certain soil types (for example, sulfates present with lime stabilization), reactions between natural occurring ground elements and the chemical additives are detrimental to the durability of the stabilized platform. Additionally, chemical stabilization requires a unique mix design, cure time, and still the results are highly variable.

Geosynthetic stabilization enhances the performance of the section, enabling the contractor to use less stone and provides a reduction in thickness or complete elimination of undercutting of in-situ soils. Unlike chemical stabilization, no special equipment is required to place and install geosynthetics. There is no cure time, and following compaction, the geosynthetic stabilized roadway can be immediately trafficked. This solution becomes a permanent structural component of the system.

The following case histories explore successful solar farm projects using high strength geosynthetics to stabilize unsuitable soils. Cost benefits and environmental impacts are discussed.

Chicot Energy Center – Chicot County Arkansas, USA

Located in Southeast Arkansas, the Chicot Solar Energy Center will be the largest universal, utility-scale solar energy project in Arkansas (Segrave, 2019). The 825-acre site will include 350,000 solar panels capable of generating enough power for more than 18,000 homes. This site was constructed over former rice fields, presenting significant soil support challenges for site access and development. Cultivated rice is extremely sensitive to water shortages; to ensure sufficient water supply, most rice farmers aim to maintain flooded conditions in their fields. With the area's historical agricultural purpose, as well as the wet 2019-2020 construction season, saturated soils drove the need for site stabilization. The subgrade soils were classified as CH soils (fat clay) under the unified soil classification system. The soil has a soaked California Bearing Ratio, CBR, of 1.5%. Moisture induced volume changes and strength loss due to high water content were of concern for load support. Figure 5 shows site conditions prior to stabilization measures.

Figure 5. Site at Chicot Energy Center (pre-construction) (Segrave, 2019)

Once it was determined that stabilization efforts were required, Giroud-Han unpaved design methodology (Giroud-Han, 2004) was utilized to determine the required unreinforced and reinforced thickness of aggregate. The Giroud-Han method employs stress distribution theory to

estimate vertical pressure on the subgrade resulting from a wheel load at the road surface. The aggregate base thickness required, h, to reduce the vertical pressure imparted on the subgrade to a value equal to its estimated bearing capacity is computed.

$$h \geq \frac{r}{\tan\alpha}\left(\sqrt{\frac{P}{\pi r^2 m N_c c_u}} - 1\right)$$

Where: h = required base thickness (m) ; α = load distribution angle; *r* = radius of load (equivalent to wheel or dual wheel) (m); *P* = wheel load (kN); N_c = bearing capacity factor; c_u = undrained cohesion of subgrade soil (kPa) and *m* = bearing capacity mobilization coefficient

Geosynthetics are incorporated into this equation with the bearing capacity factor N_c, which is based on the presence of geotextile or geogrid reinforcement.

$N_c = \pi$	no reinforcement
$N_c = \pi + 2$	geotextile reinforcement
$N_c = 3"\pi" /2 + 1$	geogrid reinforcement (with geotextile separator)

It was determined that the required unreinforced thickness was sixteen inches (16”) of an aggregate with a CBR of 20%, or seven inches (7”) of aggregate over the high strength geotextile with properties displayed in Table 1.

The geotextile and aggregate section increased the bearing capacity of the soft, saturated soils, providing a surface capable of supporting the intended loads as shown in Figure 6.

Figure 6. Stabilized Access Road with High-Strength Geotextile

Table 1. Performance and Index Properties of Geotextile used for Chicot Energy Center

Roadway Design and Performance Properties	Guidance Document / Test Method	Unit	Design / Calibration Value	
Base Course M_R Improvement Factor[1]	AASHTO R50-09	---	1.30	
Traffic Benefit Ratio: TBR[2,3,4]	AASHTO R50-09	---	3.9 / 5.2 / 21.75	
Interaction Coefficient: C_i[5]	ASTM D6706	---	0.89	
Pore Pressure Dissipation Ratio[6]	Measured	---	1.6	
Typical Dynamic Filtration Pore Size O_{95} / O_{50} [7]	ASTM D6767	microns	365 / 185	
Tensile Strength @ 2% Strain (MD/CD) (MARV)	ASTM D4595	lb/ft (kN/m)	MD	CD
			600 (8.8)	1,020 (14.9)
Tensile Strength @ 5% Strain (MD/CD) (MARV)	ASTM D4595	lb/ft (kN/m)	1,800 (26.3)	2,256 (32.9)

Index Properties	Test Method	Unit	Roll Value
Apparent Opening Size, AOS (Maximum Roll Value)	ASTM D4751	U.S Sieve (mm)	40 (0.425)
Hydraulic Flow Rate (MARV)	ASTM D4491	gal/min/ft^2 (l/min/m^2)	75 (3,056)
Permittivity (MARV)	ASTM D4491	sec^{-1}	0.9
UV Resistance (at 500 hours exposure)	ASTM D4355	% strength retained	90

The equipment during construction was the governing load case since long-term use of the facility intended to have lighter, less frequent vehicle traffic. As road construction activities advanced ahead of pile driving activities, the use of the geosynthetic roads by tracked pile driving equipment caused some section loss of the aggregate-geosynthetic road sections. This section loss was not due to heavier loads or more axle passes than considered in the design, but rather by constant tracking of the pile driving equipment between the untreated native high plasticity clay areas and the geosynthetic-aggregate roads causing contamination of the aggregate road sections as well as section loss. Due to the adhesive properties of the clay, the tracked equipment would pull aggregate away from the road section. The reduction of aggregate was severe in some spots exposing the geotextile (Figure 7). For this reason, sacrificial thickness of aggregate was added to preserve the integrity of the seven-inch structural section. Alternatively, the project team could have elected to provide a geotextile separator over the entire site to minimize contamination of the roadway sections.

Figure 7. Exposed Geotextile Caused by Unanticipated Use of Access Road

In evaluating costs, assuming $7.00 per ton for excavation and removal, $20 per ton for import aggregate and $3.25 per square yard for the geotextile, this project solution saved 40% or $560,000 for the 70,000 square yards of stabilized roadways.

In addition to providing a monetary cost savings, this solution reduced the environmental footprint by preserving natural resources and reducing CO_2 emissions from hauled materials, material transportation and material placement. Assuming 15 miles (one way) to a rock quarry, Figure 8 displays the environmental advantages this solution provided including a reduction of the number of estimated trucks for hauled materials from 382 trucks to 167 trucks, with a corresponding reduction in CO_2 emissions from 20,000 kg to 8,800 kg.

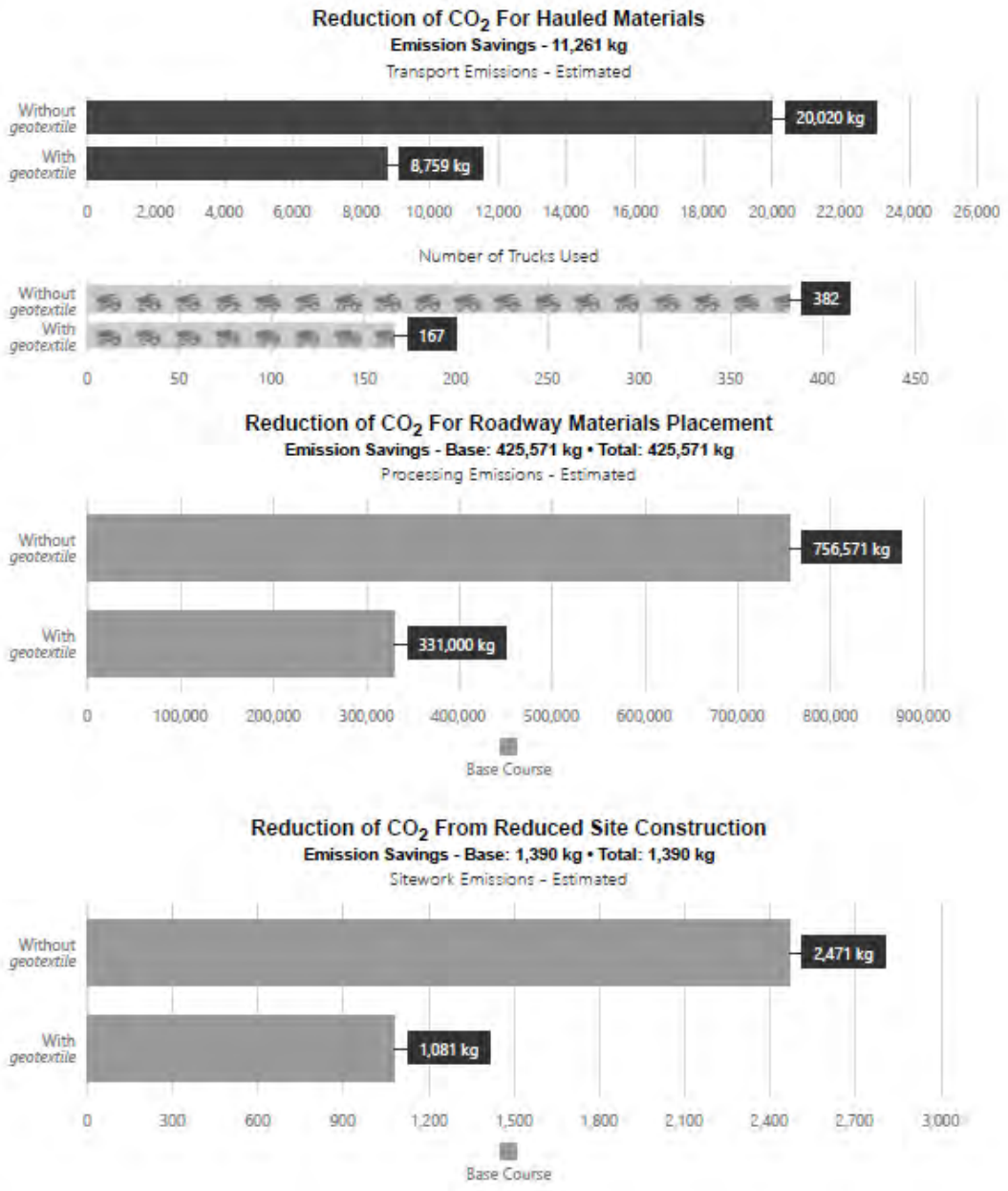

Figure 8. Environmental Savings with Geotextile

Impact Solar – Lamar County Texas, USA

Located 120 miles northeast of Dallas, the Impact Solar project is a 260 MW solar facility. The geotechnical report indicated soils generally consisting of medium to hard clays, including expansive soils which can experience large volume changes. Figure 9 displays the soft soil conditions that the project team was faced with stabilizing. Initially the project team executed lime stabilization over the soft areas. However, the stabilized layer began to degrade almost immediately, and the contractor sought other methods to provide long term stabilization of the road sections. In some areas, minimal aggregate cover (6 inches) was anticipated, where other fill areas required several feet of boulders to bring the road up to grade. Based on the design criteria in the geotechnical report, and subgrade strength verified independently on-site using DCP (On site DCP reported CBR values between 1.5% to 3%), several stabilization options with high strength geosynthetics were considered.

Figure 9. In-Situ Soils for Impact Solar Project

The recommended option included six to eight inches (6”-8”) of Texas Department of Transportation flexible base over a high strength woven geotextile. The product selected had the following performance and index properties shown in Table 2.

Figure 10 exhibits a stabilized roadway with the high strength geotextile and six inches (6”) of aggregate on this project. Note the excessive rutting on the adjacent unreinforced section. Each road sections constructed with this option experienced exceptional performance, minimal surface rutting and provided a significant cost savings for this project.

Figure 10. Reinforced Access Road vs. Unreinforced Conditions

Table 2. Performance and Index Properties of Geotextile used for Impact Solar Project

Roadway Design and Performance Properties	Guidance Document / Test Method	Unit	Design / Calibration Value	
Base Course M_R Improvement Factor[1]	AASHTO R50-09	---	1.40	
Subgrade M_R Improvement / Increase[2]	AASHTO R50-09	lb/in² (MPa)	9,000 (62.0)	
Cyclic Tensile Modulus: J_{cyclic}[3]	ASTM D7556	kip/ft (kN/m)	MD	CD
			60 (876)	160 (2,336)
Resilient Interface Shear Stiffness: G_i[3]	ASTM D7499	kip/in² (MPa)	329 (2,268)	
Traffic Benefit Ratio: TBR[4,5,6]	AASHTO R50-09	---	9.0 / 13.1 / 39.0	
Interaction Coefficient: C_i[7]	ASTM D6706	---	0.90	
Pore Pressure Dissipation Ratio[4]	Measured	---	2.0	
Typical Dynamic Filtration Pore Size O_{95} / O_{50} [8]	ASTM D6767	microns	337 / 192	
Maximum Percent Open Area: MPOA[9]	ASTM D6767	Percent	7.3	
Tensile Strength @ 2% Strain (MARV)	ASTM D4595	lb/ft (kN/m)	480 (7.0)	1,800 (26.3)
Tensile Strength @ 5% Strain (MARV)	ASTM D4595	lb/ft (kN/m)	1,440 (21.0)	4,380 (63.9)

Index Properties	Test Method	Unit	Roll Value
Apparent Opening Size, AOS (Maximum Roll Value)	ASTM D4751	U.S Sieve (mm)	40 (0.425)
Hydraulic Flow Rate (MARV)	ASTM D4491	gal/min/ft² (l/min/m²)	75 (3,056)
Permittivity (MARV)	ASTM D4491	sec^{-1}	1.0
UV Resistance (at 500 hours exposure)	ASTM D4355	% strength retained	90

Initially the subgrade stabilization plan included twelve inches (12”) of worked subgrade with six inches (6”) of lime stabilization, and six inches (6”) of flexbase. The lime stabilization was budgeted at $32 per square yard. Using the high strength geotextile above with up to 8 inches (8”) of aggregate was budgeted at $7.00 per square yard (including installation). For the thirteen (13) miles of road on the project, seventeen (17) foot wide roads, this provided a savings of over $3.2M in subgrade material reinforcement alone. The solution was quick to install and provided the required stabilization both during constructability and for facility use. The

roadways treated with this section will be handed over to TXDOT after the solar farm construction is complete.

CONCLUSION

Since the main purpose of solar energy is to preserve natural resources, doing so during the construction of the solar facilities should be an apparent consideration in the selection of treatment to strengthen unsuitable soils. Geosynthetics provide an economical option for mechanical stabilization of subgrades with unsuitable soils both during construction and to adhere to long-term performance requirements of the solar facilities. Evaluation of the soil properties in the geotechnical report or by other provided information (in-situ field testing or by visual inspection) could potentially underestimate soil strength for the saturated condition. Since geosynthetic-soil performance for subgrade stabilization is dependent on the soil strength during at the time of installation, consider soil strength parameters that capture the saturated case as well. Two case studies were presented where high strength geotextiles provided effective solutions for solar farm development providing the project with significant cost savings and long-term advantages over other methods of stabilization such as remove and replace or chemical stabilization.

REFERENCES

Christopher, B. R., Perkins, S. W., Lacina, B. A., Marr, W. A., “Pore Water Pressure Influence on Geosynthetic Stabilized Subgrade Performance” Proceedings, *2009 Geosynthetics Conference*, Salt Lake City, Utah, February 2009

Pandey, C., Agarwal, S. (2019). "Comparitive Study Between Soaked & Unsoaked Value of Soil Samples" *International Research Journal of Engineering and Technology*, Volume 6, Issue 6. pg 3263

Jornbey, B. Hicks, R.G. (1986). *Base Course Contamination Limits.*

Giroud, J.P., Han, J. (2004). “Design method for geogrid-reinforced unpaved roadsPart I: theoretical development. *ASCE Journal of Geotechnical and Geoenvironmental*, 776-778.

Giroud, J.P. and Noiray, L. (1981), “Geotextile-reinforced unpaved road design” *ASCE Journal of Geotechnical and Geoenvironmental Engineering*, 107(9), pp 1233-1253.

Office of Energy Efficiency & Renewable Energy . Retrieved from Energy.gov: energy.gov/eere/solarpoweringamerica/solar-energy-united-states#:~:text=Solar's%20abundance%20and%20potential%20throughout,power%20the%20entire%20United%20States.&text=PV%20can%20also%20be%20installed,essentially%20no%20land%20use%20impacts.

Segrave, K. E. (2019, December 05). Steps taken toward solar farm. *Chicot Newspaper*.

ASTM D 1883-16. Standard Test Method for California Bearing Ratio (CBR) of Laboratory-Compacted Soils, *ASTM International*, West Conshohocken, Pennsylvania, USA.

Geosynthetics Conference

High Vertical Loads on Soft Foundation Soils Supported by Rigid Inclusions and High Strength/Modulus Geosynthetic Reinforced Load Transfer Platforms

Lilma R Schimmel, M.Sc.Eng., P.E.[1] and Alex Potter-Weight, P.E.[2]

[1]HUESKER Inc, 3701 Arco Corporate Drive, Suite 525, Charlotte, NC, 28273; e-mail: lschimmel@huesker.com
[2]Menard Group USA, 20 W Kinzie St, 17th Floor, Chicago, IL 60654; e-mail: apotter-weight@menardgroupusa.com

ABSTRACT

This paper discusses the construction of high embankments on challenging, weak foundation soils using Controlled Modulus Columns (CMC)™ combined with Load Transfer Platforms (LTPs) reinforced with high modulus, high strength geosynthetic reinforcements. It describes relevant characteristics of each of the main elements comprising the ground improvement system. It discusses the benefits of the solution when compared to traditional and typically less cost-effective alternatives. Two short case studies are included to discuss the design approach and local geotechnical conditions. On both of the presented cases, CMCs combined with high strength reinforced LTPs were successfully utilized. The inclusion of high strength polyvinyl alcohol (PVA) geosynthetic reinforcements in the platform made it possible to minimize horizontal deformation on the CMC foundation systems.

INTRODUCTION

Construction of embankments and stockpiles on soft soils presents significant challenges. The lack of soil bearing capacity needs to be remediated to avoid impacts such as lateral squeeze, excessive deformation, and global failures.

Different techniques employed to address these issues vary widely in cost, constructability, and performance. The focus of this paper will be the use of a grid of vertical rigid inclusions, namely Controlled Modulus Columns (CMC)™, topped with a granular Load Transfer Platform (LTP), which is reinforced with very high strength and tensile modulus woven polyvinyl alcohol (PVA) textiles. The combination offers highly improved factors of safety against global stability failures, significantly reduced total and differential settlements, and stabilized column tops to minimize lateral displacement.

This paper will provide an introductory explanation regarding the use of CMCs as bearing elements combined with PVA reinforcement as part of the LTP for heavy vertical surcharges on soft foundation soils. It will provide two case studies illustrating the solution used on recent projects.

CONSTRUCTION ON SOFT SOILS

Many different solutions are available to prevent failure of the foundation soil due to its low bearing capacity. Local conditions, loads, performance criteria and cost are among the main

considerations when selecting the type of foundation system to be applied. Soil excavation and replacement, staged construction, and deep foundations using piles are among the traditional techniques for such conditions.

Ground improvement solutions such as rigid inclusions and aggregate columns (either geotextile- encased or not encased) are becoming more popular due to their simplicity, flexibility and competitive costs. Typically, these systems are composed of a rigid or non-rigid inclusion/column, and an LTP, often reinforced with horizontal geosynthetic reinforcement. This paper will focus on a system combining CMCs and PVA textile reinforced LTPs.

CMC Rigid Inclusions. CMCs, or CMC Rigid Inclusions, are displacement-drilled grouted elements which reinforce soft ground by attracting a significant portion of the overlying load and transferring it to more competent strata at depth. This lower stress level in compressible soil layers can reduce typical ground settlement by factors of 2 to 10. In addition, CMCs can provide substantial improvements in global stability by keeping shear stresses in weak soil layers well below ultimate strengths, while also providing moderate lateral capacity in the inclusions themselves. Finally, CMCs increase allowable bearing capacity by adding the frictional and end-bearing capacity of the inclusion to the existing capacity of the ground.

One of the most common applications for CMCs is supporting embankment fills, often generically known as a “Column Support Embankment” (CSE). For embankment projects, the settlement reduction and improved stability offered by CMCs can allow for rapid construction or paving without extensive waiting periods or staged construction. In the US, CMCs have been designed for post-paving settlement tolerances as strict as 12 mm (0.5 inch), although more typical post-paving tolerances are between 25 mm and 76 mm (1 and 3 inches).

The CMC design must be performed in concert with the Load Transfer Platform design. The LTP consists of a compacted, granular soil layer directly above, and often surrounding, the tops of the CMCs. The high shear capacity of this layer allows for efficient distribution of loads into the tops of the inclusions. This stress transfer, often described as “arching”, is based on a variety of factors, such as LTP material, compaction level, stress level, and properties of the underlying soils. The incorporation of geosynthetics within the LTP will enhance this stress distribution, while aiding in overall stability and bearing capacity. Various design methods and considerations for geosynthetics are discussed later in this paper.

For shorter embankments, especially those topped with flexible pavements, proper design of the LTP and CMCs is critical to the surficial performance. If excessive stress is transferred to the soft soil between the CMCs, this will result in consolidation or compression of this material. While limited settlement between inclusions is often expected as part of the CMC design, in a short embankment there is less vertical distance for the LTP to smooth out this differential settlement. If this differential deflection were to be transmitted at the surface, in a phenomenon known as “dimpling”, pavement sections could become bumpy and unusable.

For taller embankments, dimpling is not typically a concern, but different considerations are required. In taller embankments, even when CMCs permit only a small percentage of the total bearing pressure to be transmitted to compressible soil layers, it can result in significant deformations due to the higher overall stress levels. A portion of this vertical deflection also manifests as lateral displacement. In retaining wall scenarios or where adjacent structures are present, this lateral displacement must be considered. Furthermore, the lateral displacement can potentially damage perimeter CMCs by causing excessive bending and shear forces. To address this issue, steel reinforcement can be installed within the CMCs. Alternatively, the LTP layer can

be modified to incorporate either a rebar mesh or a high-strength/high-stiffness geosynthetic to limit lateral deformation. The two case studies presented in this paper will discuss the incorporation of geosynthetics for tall embankments constructed over soft soil.

LTP Geosynthetic Reinforcement Design. The function and design method used will define the requirements for the reinforcement integrated into the platform. Some methods can underestimate the required resistance of reinforcement, which can lead to excessive vertical and lateral deformations, punctures, etc. Naturally, the poorer the soil resistance, the larger the risk and consequences. Good understanding of each method is important, especially its assumptions, limitations and indicated function for the reinforcement.

The study by Ariyarathne and Liyanapathirana (2015), identified that methods based on a simplified approach, for example those where triangles or pyramids with fixed angles are used to determine the surcharge carried by the reinforcement, greatly underestimate the tension to be transferred to the geosynthetic. The results obtained from such methods cannot be relied upon because material parameters are not considered. There are many cases of excessive deformation, settlement and failure of even low surcharge fills where the LTP was designed using these simplified methods. As explained ahead, the LTP should contain as few layers of reinforcement as possible, whereas the simplified methods recommend a minimum of three reinforcement layers.

Codes that better model soil arching and consider multiple sources of stresses to be developed on the reinforcement are more reliable. Examples are the British Code of practice for strengthened/reinforced soils and other fills (2010) and the New German Method as presented on Recommendations for Design and Analysis of Earth Structures Using Geosynthetic Reinforcements – EBGEO (2010).

The latter two methods referenced above consider arching as semi-spheres or as multi-shells. The stress on the reinforcement is estimated using the membrane theory, and support from the soft soil between the CMCs can either be considered or ignored. The German method also considers the tensile modulus of the reinforcement as part of the design procedure. Both guidelines recommend the designer to minimize the number of reinforcement layers to be placed within the LTP. That is due to concerns of uneven distribution of stresses among the layers, since force distribution is not fully understood and failure of the system becomes possible. Therefore, the tensile resistance should, where possible, be provided in one reinforcement layer (in each direction of main stresses).

The more sophisticated approaches, BS 8006-1:2010 and EBGEO, verify the tensile stress condition of the reinforcement under different requirements: load redistribution due to arching, and lateral spreading and extrusion. The reinforcement also increases the overall stability of the embankment and allows for greater spacing of the CMCs.

In addition to these verifications, it is also important to assess the deformation and stresses that could be experienced by the CMC Rigid Inclusions. The behavior mechanisms of a CMC system consist of a sequence of complex interactions: between the embankment and the LTP, between the LTP and the soft soil, between the CMC and the soft soil, and between the CMC and the end-bearing soil. For this complicated analysis, the Finite Element Method is recommended. A first-level analysis typically consists of a unit cell study, modeling one CMC and its tributary area to assess typical settlements and load transfer efficiency in the middle of an embankment. To assess global effects such as lateral displacement, more complex models are required. A plane-strain finite element model, typically cut across an embankment, allows the designer to model multiple rows of CMCs and study the bending and shear stresses on each row. From there, a

structural design can be performed to determine whether steel reinforcement or modification of the LTP is required.

LTP Geosynthetic Reinforcement Material Properties. Geosynthetic reinforcements are manufactured with different raw materials (polymers). Different polymers result in different mechanical properties, including stress-strain behaviors. The tensile modulus of the reinforcement is very important since failure can occur not only due to lack of tensile resistance but also due to excessive deformation of the structure. Therefore, the strength as well as the allowable deformation should be specified for reinforcement applications.

Many polymers are available for the manufacturing of geosynthetics: polypropylene (PP), polyethylene (PE), polyester (PET), polyvinyl alcohol (PVA) and Aramid (AR). Various short-term load-extension curves for a few geosynthetic products are shown in Figure 1. At low strains the materials show similar tensile modulus, but it can be noted that the AR and PVA materials exhibit the smallest strain at failure (100 % utilization factor) while PP and PE can break at very large strains.

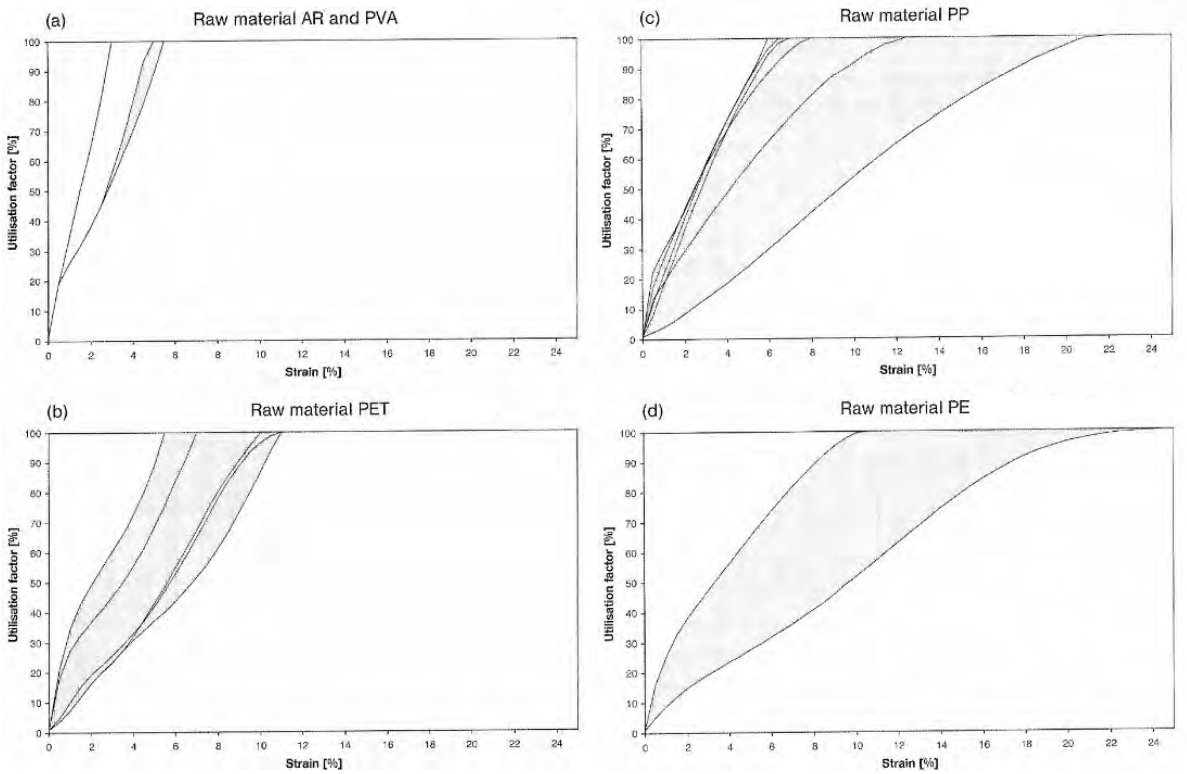

Figure 1. Typical geosynthetic load-extension zones.
(*source: EBGEO 2010)*

Besides tensile modulus, creep (elongation over time under constant load) of the material also has a strong influence on the performance of the reinforced structure. Creep is especially important over the long term and unless considered, the structure may fail shortly or years after construction is completed. Strain over time must be considered during design to account for this phenomenon. Isochronous curves are used to evaluate the creep behavior of geosynthetic materials. Figure 2 illustrates typical load-extension curves for a few polymers. Clearly, there is a remarkable difference in strain accumulation with time between the two materials represented. The

polyethylene material (HDPE) suffers much larger creep than the PET product. Also represented by the graphs is the amount of deformation to occur between short term and long term (i.e. the horizontal distance between curves at any given utilization factor). Again, the PET outperforms HDPE. This must be considered during design, and a maximum allowed strain through the service life of the embankment should be specified. PVA and AR, although not illustrated in Figure 2, have the highest tensile modulus and improved creep performance among the materials herein discussed.

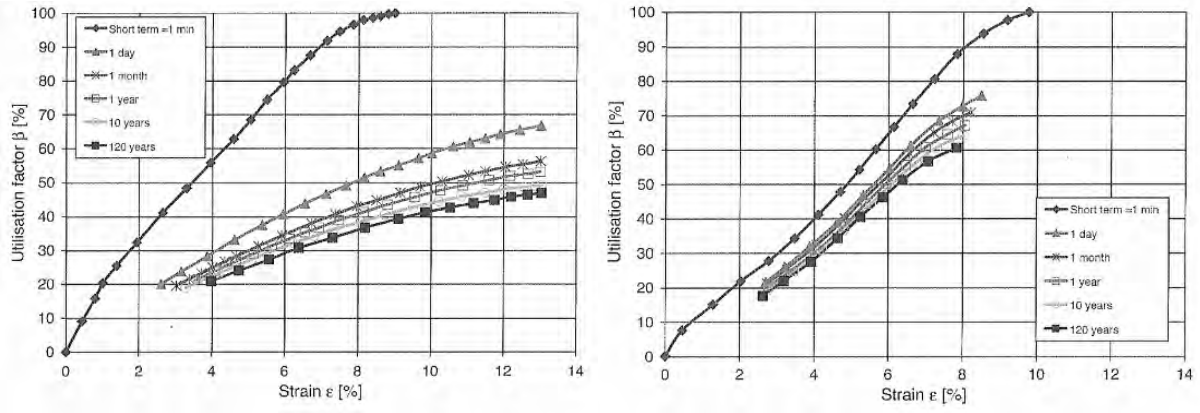

Figure 2. Example isochrones for: (left) a HDPE extruded geogrid, (right) a PET product.
(source: EBGEO 2010)

Besides the parameters discussed above, durability and installation damage are also considered during selection of the reinforcement. When the pH of the soil in contact with the material is too low, or too high, PET is not suitable. In applications in direct contact with CMCs, PVA or AR should be used instead of PET due to the alkalinity of cement.

From the discussion above, the materials with the best combined performance, considering durability, low strain tensile modulus and creep are PET, PVA and AR. HDPE and PP exhibit very large creep and are not recommended for medium/high load requirement structures with more than a few weeks of service life like embankments, slopes and walls.

CASE STUDIES

Ground improvement utilizing a system comprised of CMCs and geosynthetic reinforced LTP can address multiple geotechnical issues: lack of bearing capacity, low factor of safety against rotational and translational failures, excessive deformation, sliding, soil extrusion, lateral deformations and need of distribution of stresses to the supporting columns.

For the two case studies presented, significant fills were planned over top of soft soils which necessitated a Column Supported Embankment system using CMCs. In both cases, the initial CMC design was performed first without utilizing reinforcements. The predicted horizontal deformations using the Finite Element Method were excessive, resulting in high estimated bending moments and shear stresses in the CMCs. To limit the lateral displacement, aid load transfer into the CMCs, and improve overall stability, the LTPs for these two embankment systems were reinforced with high strength PVA geogrids and woven fabrics. The high-tensile-modulus, creep-

resistant PVA increased the factor of safety of the design while greatly reducing horizontal displacement at the top of the columns.

Iron Stockpiles. In 2018, construction commenced on a new production plant for hot-briquetted iron in Toledo, OH. The selected location was a brownfield site which was redeveloped for this project. The new facility requires significantly less energy for steel production, and generates lower greenhouse gas emissions than traditional methods. Furthermore, no hazardous or toxic by-products are generated, and water use and discharges are minimized. Commissioning and startup of the facility are expected to take place in late 2020.

The iron oxide storage areas had to be designed for stockpiles with heights up to 16 m (approximately 54 ft), with a material unit weight of approximately 23 kN/m^3 (144 lb/ft^3). The underlying soil profile consisted of a small amount of shallow, variable fill over top of a cohesive glacial till layer. Within the top 9 m (30 ft), the till stratum exhibited only moderate over-consolidation and fairly low shear strengths. Therefore, high vertical loads combined with the existing subgrade's geotechnical parameters posed significant challenges. To mitigate potential issues, a CSE system with CMC Rigid Inclusions drilled into the deeper, harder till zone was proposed.

During the design process, the surcharge loads caused excessive predicted lateral forces on the top portions of the CMCs, especially towards the perimeter of the CMC support grid. Under the estimated lateral strain, unreinforced CMCs would have been compromised, resulting in loss of global stability and bearing capacity. Rebar cages within the CMCs to handle these strains were too costly to the project and would have slowed down the overall schedule. Therefore, the final design called for a ground improvement system combining CMCs with an LTP reinforced with transversal layers of woven PVA reinforcement. Figure 3 shows a detail of the typical, PVA, high strength, high modulus reinforcement material used.

Figure 3. Detail of a high strength, high modulus, PVA reinforcement used on LTPs.
(source: HUESKER Inc.)

The family of materials used, Stabilenka Xtreme, is among the highest strength geosynthetics produced in the world. On this project, the strongest reinforcement used, had an

ultimate tensile resistance of 1800 kN/m (123,000 lb/ft). The purpose of the reinforcement was to control deformation, minimizing lateral movement of the system.

The cross-section of the final design of the reinforced LTP is shown in Figure 4. The bottom layer of geosynthetic (strength direction across the stockpile) was installed 0.15 (6 inches) above the CMC tops, and the upper layer (strength direction into the page) was installed 0.30 m (12 inches) above the CMC tops. The 0.46 m (18-inch) diameter CMCs were installed on center-to-center spacings varying from 2.1 m to 3.0 m (7 ft to 10 ft).

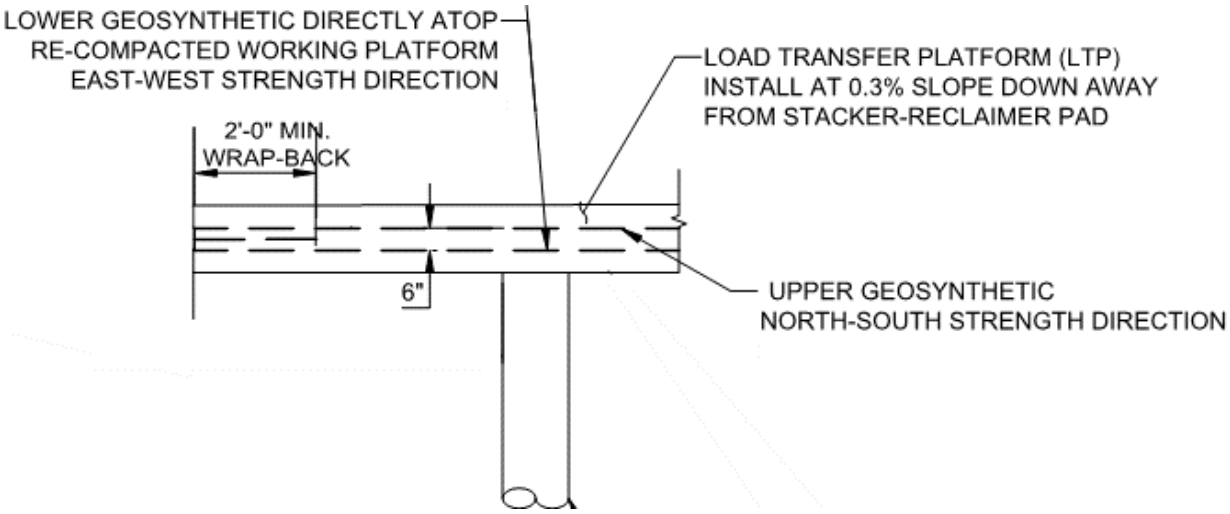

Figure 4. Cross-section of CMC and geosynthetic-reinforced LTP.
(source: Menard Group USA)

Figure 5 illustrates the final predicted lateral movement plot, after incorporation of the high-stiffness (high tensile modulus) geosynthetic into the model. The reduction in lateral movement allowed all CMCs to be installed without steel reinforcement, resulting in a rapid and economical installation process. The CMCs and LTP were completed in 2019, with the stockpiles reaching full height in 2020 in preparation for startup of the processing facility.

I-75 DiSalle Bridge Replacement Project. This major project by the Ohio Department of Transportation encompasses the widening and reconstruction of Interstate 75, interchange reconfigurations, and the replacement of the DiSalle Bridge over the Maumee River in Toledo, OH.

At the south bridge approach, a historical man-made fill resulting from byproducts from the glass-making industry formed a variable composite layer known locally as “Rouge”. Most comparable to an over-saturated silt, this material generally exhibited high moisture contents but seemingly high undisturbed “strengths” due to chemical cementation. When sheared, however, the high-water content caused the material to become semi-liquid. Underlying the rouge was a soft, native silt layer above the dense glacial till bearing layer.

To support significant Mechanically Stabilized Earth (MSE) wall fills in this area up to 9 m (30 ft) high, the DOT proposed a Deep Soil Mixing approach with permitted alternatives. The selected alternative was comprised of a combination of CMC Rigid Inclusions to support the MSE walls and retained embankment fills, with Prefabricated Vertical Drains (PVDs, or wick drains) to accelerate settlement. By draining excess water, the PVDs also served as a contingency to quickly return the Rouge layer to near its original state if it became disturbed during installation of the

CMCs. Compared to Deep Mixing, the CMC + PVD system did not rely on using the highly variable Rouge layer to form soil mixed columns. Instead, the CMCs would transfer load away from the Rouge, down into the deeper, dense till.

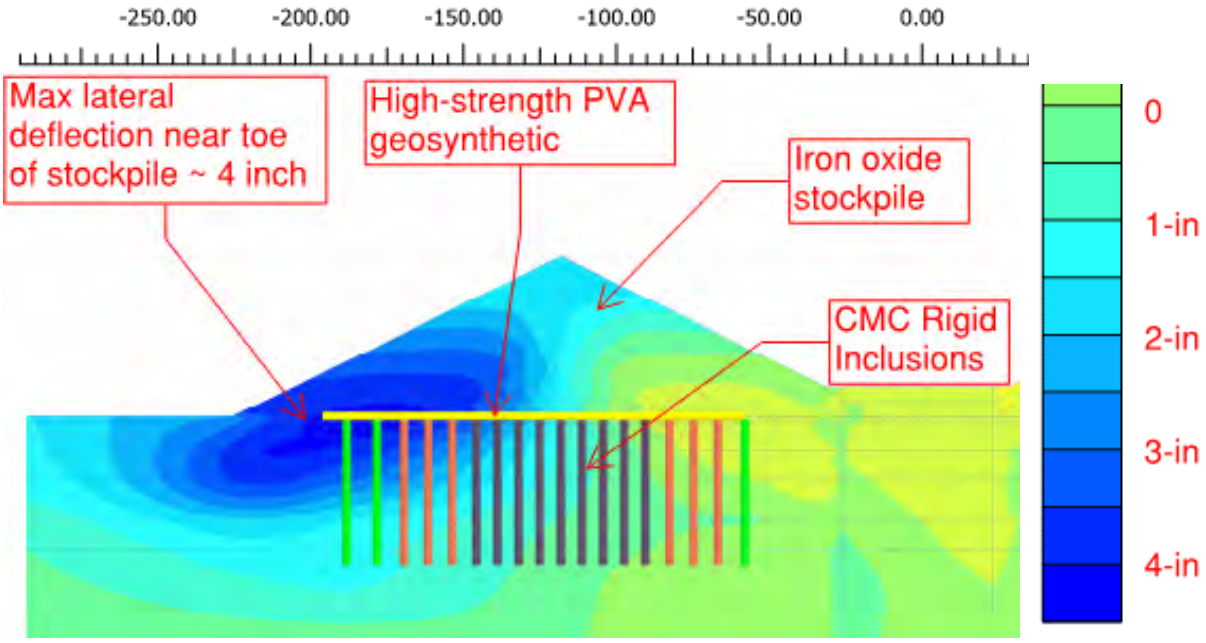

Figure 5. PLAXIS output – lateral deflection – CMCs and geosynthetic supporting iron stockpile.
(source: Menard Group USA)

In a portion of the south approach, a retention basin in front of the MSE wall posed considerable design challenges. For the typical MSE wall areas without the basin, the fill in front of the wall acted as a lateral restraint and the CMCs were designed with only light steel reinforcement to handle moderate lateral strains. However, in the basin area, the proposed geometry would potentially cause the wall to slide down into the lower elevation zone in front of it.

Based on FEM results, this phenomenon resulted in significant predicted lateral deformations and high bending moments and shear stresses on the majority of the supporting CMCs. To counteract this effect, the LTP layer between the CMC grid and the MSE wall was reinforced with a layer of woven PVA reinforcement.

Figure 6 illustrates the FEM lateral movement output plot from the final design, after incorporating the high-strength geosynthetic, as well as the typical soil profile. The strong direction of the geosynthetic was oriented perpendicular to the wall to resist the tendency for the wall to move outward and limit overall deformation. This resulted in reduced lateral stresses on the CMC elements, limited the amount steel reinforcement in the inclusions, and allowed the design to meet a strict 13 mm (0.5-inch) post-paving settlement criterion. The CMCs, PVDs, and LTP for the first phase of the bridge re-construction were installed in 2019 and 2020 (Figure 7), with the final phase of ground improvement planned for 2021.

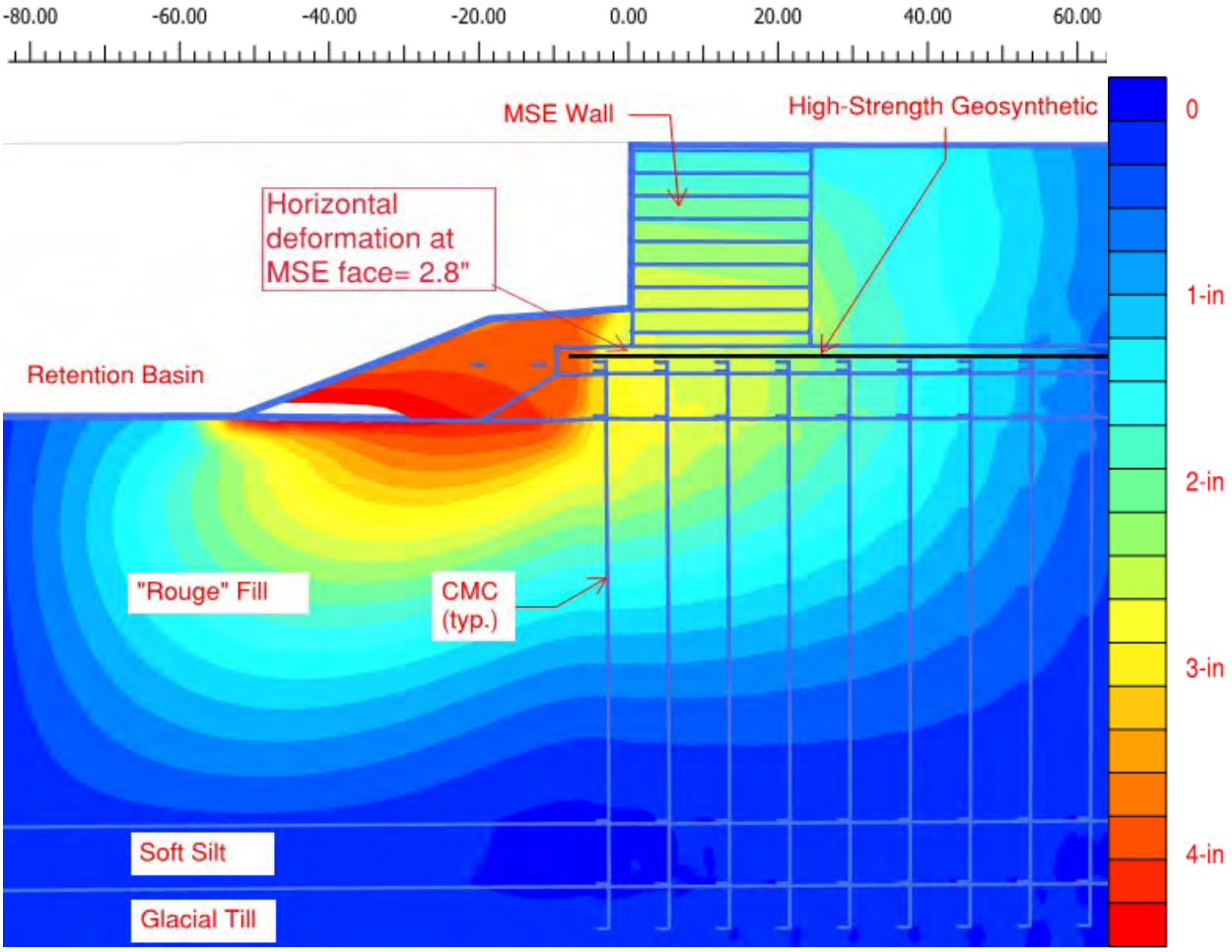

Figure 6. PLAXIS output – lateral deflection – CMCs and geosynthetic supporting MSE wall. ***(source: Menard Group USA)***

Figure 7. CMC rigid inclusion installation at the DiSalle Bridge Replacement Project. ***(source: Menard Group USA)***

CONCLUSION

Different methods are available to allow for the construction of embankments on weak soils. The ground improvement technique comprised of CMCs and high strength, high modulus reinforced LTPs offers an efficient, simple and cost-effective solution for this type of construction.

The geosynthetic reinforcement can have multiple functions when utilized as part of an LTP. The foundation system, including the platform, shall be designed considering multiple loading conditions, and through the use of safe, non-simplified design methods which take into account soil parameters and material stress-strain behaviors.

This paper discussed the utilization of high strength, high modulus PVA geogrids and woven fabrics for the primary purpose of minimizing horizontal stresses on CMCs, so that the need for rebar reinforcement can be eliminated or greatly reduced.

Two successful, high profile projects where high surcharge embankments were to be built on challenging soil conditions were presented. The foundation solution for both cases was the combination of CMC grids overlaid by high strength, high modulus reinforced LTPs.

REFERENCES

Ariyarathne, P. and Liyanapathirana, D.S. (2015), Review of existing design methods for geosynthetic-reinforced pile-supported embankments, *Soils and Foundations,* The Japanese Geotechnical Society, 55(1):17-34.

German Geotechnical Society (2010), *Recommendations for Design and Analysis of Earth Structures Using Geosynthetic Reinforcements – EBGEO*, Ernst & Sohn, Munich, Germany.

BS 8006-1:2010. Code of Practice for Strengthened/Reinforced Soils and other Fills, British Standards Publication.

Geosynthetics Conference

Performance of Prefabricated Thermal Drains in Soft Clays

Radhavi Samarakoon, M.S.,[1] John McCartney, Ph.D., P.E.[2]

[1]University of California San Diego, Department of Structural Engineering, 9500 Gilman Drive, La Jolla, CA 92093-0085, USA; e-mail: rabeysir@ucsd.edu
[2]University of California San Diego, Department of Structural Engineering, 9500 Gilman Drive, La Jolla, CA 92093-0085, USA; e-mail: mccartney@ucsd.edu

ABSTRACT

This paper focuses on the use of prefabricated thermal drains to improve saturated clay layers using heating. A prefabricated thermal drain can be formed by integrating a closed-loop geothermal heat exchanger within a conventional prefabricated vertical drain (PVD). Prefabricated thermal drains can be installed in a similar way to a PVD but operate by circulating a heated fluid through the heat exchanger tubing to induce an increase in temperature of the soft clay. This increase in temperature will lead to thermal consolidation, which can be accelerated by drainage through the PVD. Although thermal drains have been tested in proof of concept field experiments, there are still several variables that need to be better understood. This paper presents numerical simulations of the coupled heat transfer, water flow, and volume change in layers of kaolinite, illite and smectite clays where a prefabricated thermal drain was embedded. Thermally induced excess pore water pressures and a slight initial expansion was observed for clay layers with low hydraulic conductivity. However, the overall volume change resulted in contraction where the rate as well as the magnitude of settlement was greater for a thermal PVD compared to a conventional PVD. A further analysis on kaolinite layers at different initial porosities indicated that the increase in the magnitude of settlement observed when using a thermal PVD was independent of the hydraulic conductivity of the clay whereas the increase in the rate of settlement was more pronounced for clays with lower hydraulic conductivity.

INTRODUCTION

Soft soil deposits often cause issues for structural stability due to their undesirable properties such as high compressibility and low shear strength. Prefabricated vertical drains (PVD) are widely used for ground improvement prior to construction. A PVD is a type of geosynthetic consisting of a perforated plastic core with high transmissivity wrapped with a nonwoven geotextile that provides filtration. PVDs help accelerate drainage processes in soft soils by shortening the drainage path for excess pore water pressures and shortening the time required for consolidation. PVDs are typically used in combination with a surcharge to induce an excess pore water pressure.

Although the use of PVDs helps expedite consolidation of soft clay layers, there still exist challenges when they are being used in ground improvement applications. Installing and maintaining a stable embankment above the clay layer may be expensive and time consuming, especially for very soft soils. Furthermore, in some instances the time required for primary consolidation can still be significant. PVDs are installed in the field using a mandrel and the installation process causes disturbance of the soil adjacent to the drain. This region of disturbance is referred to as the smear zone and several researchers have investigated its effects on the performance of PVDs (e.g., Hansbo 1981, Indraratna and Redana 1998). The hydraulic

conductivity of the soil in the smear zone has been found to be significantly lower than the hydraulic conductivity of the intact soil, which would decrease the rate of the consolidation process. To address some of these challenges, the use of thermal prefabricated vertical drains (thermal PVDs) has been investigated in recent studies (Abuel-Naga et al. 2006, Pothiraksanon et al. 2010). This technique combines a geothermal heat exchanger with a vertical drain where it can also conduct heat to the surrounding soil. The studies in literature have observed an increase in the rate as well as the magnitude of settlement when using a thermal PVD, in comparison to a conventional PVD. Furthermore, thermal PVDs can be used for geothermal heat exchange or underground heat storage for overlying structures after the ground improvement process is complete.

This paper focuses on the performance of a thermal PVD in different clay types using a numerical model developed by the authors in a previous study (Samarakoon and McCartney 2020). Operation of thermal PVDs in saturated normally consolidated layers of kaolinite, illite and smectite were considered in this analysis. Specifically, the coupled processes of heat transfer, fluid flow and volume change in the soil surrounding a thermal PVD were modeled using a finite difference formulation. A further analysis on the effect of hydraulic conductivity on the performance of a thermal PVD is presented using a kaolinite clay layer.

BACKGROUND

A thermal PVD is a prefabricated vertical drain which can also behave as a geothermal heat exchanger. This can be achieved by placing closed-loop plastic tubing within or around the core of a conventional PVD through which heated fluid will be circulated. A limited number of studies found in literature observed an increase in the magnitude as well as the rate of settlement when using thermal PVDs in lieu of conventional PVDs (Abuel-Naga et al. 2006, Pothiraksanon et al. 2010, Artidteang et al. 2011, Salager et al. 2012).

In these studies, thermally induced excess pore water pressures, increases in hydraulic conductivity and thermo-plastic volumetric strains in normally consolidated clays due to elevated temperatures were found to be factors influencing the settlements observed in soil surrounding a thermal PVD. Excess pore water pressure generation at elevated temperatures in undrained or partially drained soils has been observed by several researchers (Campanella and Mitchell 1968, Hueckel and Pellegrini 1992, Abuel-Naga et al. 2006). The generation of thermally induced excess pore water pressure is attributed to the differences in the coefficients of thermal expansion of soil particles and the pore fluid. The soil will undergo volumetric contraction as the excess pore water pressures are dissipated.

An increase in temperature will also decrease the density and viscosity of the pore fluid which will result in an increase in hydraulic conductivity. The relationship between hydraulic conductivity (k) with fluid and soil properties can be understood using the definition of the intrinsic permeability K in Equation 1.

$$K = \frac{k\eta_w}{\rho_w g} \quad [1]$$

where K is the intrinsic permeability, η_w is the dynamic viscosity of the fluid, ρ_w is the fluid density and g is the coefficient of gravity. An increase in hydraulic conductivity was observed with an increase in temperature by Abuel-Naga et al. (2006) for Bangkok clay. However, the intrinsic permeability was found to be independent of temperature. The density of water will vary with

temperature (T) according to the relationship in Equation 2 where α_w is the volumetric coefficient of thermal expansion of water. The fluid viscosity will vary with temperature following the empirical relationship given by Hillel (1980) in Equation 3.

$$\frac{\partial \rho_w}{\partial t} = -\rho_w \alpha_w \frac{\partial T}{\partial t} \quad [2]$$

$$\eta_w(T) = -0.00046575 \ln(T) + 0.00239138 \quad [3]$$

Many studies have investigated the changes in volume of soils with changes in temperature under different stress states and drainage conditions (e.g., Campanella and Mitchell 1968, Baldi et al. 1980, Abuel-Naga et al. 2006). Most relevant to the application of thermal PVDs in ground improvement is that normally consolidated clays experience permanent, plastic volumetric contraction during drained heating (Abuel-Naga et al. 2006). On the other hand, overconsolidated soils typically show recoverable, elastic volumetric expansion during drained heating. These thermally induced volume changes are attributed to a thermal yielding mechanism that has been integrated into thermo-elasto-plastic models (Hueckel and Borsetto 1990, Cui et al. 2000, Laloui and Cekerevac 2003, Abuel-Naga et al. 2006). A thermal yield limit is defined for the soil where thermo-elastic strains occur at stress levels or temperatures below the thermal yield limit whereas thermo-plastic strains occur at stress levels on or above the thermal yield limit. Using a thermo-elasto-plastic model, Laloui and Cekerevac (2003) proposed the following relationship to obtain the thermo-plastic volume changes for normally consolidated soils during drained heating.

$$\partial e_T = \frac{(1+e_0)\gamma \partial T}{2.303 \beta T (1-\gamma log\left[\frac{T}{T_0}\right])} \quad [4]$$

where γ is a material parameter, e_0 is the initial void ratio, β is the inverse of the plastic compressibility and T_0 is the room temperature.

When a thermal PVD is being used, the temperature of the surrounding soil will increase. Heat transfer through the soil medium can be considered using Fourier's law and energy conservation principles. This increase in temperature will impact the fluid flow through the porous media by thermally induced excess pore water pressures and increased hydraulic conductivity. Fluid flow through the porous media can be expressed using principles of mass conservation and Darcy's law where Equations 2 and 3 can be incorporated to account for the effects of temperature. The volume change in a thermal PVD application will consist of mechanical and thermal components. The mechanical volume change due to a surcharge can be obtained using compressibility relationships for a normally consolidated clay. The thermo-plastic volume changes are obtained using a constitutive relationship as shown in Equation 4. For a simultaneous application of a surcharge and heat, the total stress will remain constant. The change in effective stress resulting from a change in the pore water pressure can be obtained by subtracting the pore water pressure from the total stress. Furthermore, the volume change will also lead to a change in the thermal conductivity of the bulk soil. As the void space reduces, more heat conduction can occur through the soil particles. The theoretical framework and the numerical formulation simulating the coupled phenomena of heat transfer, fluid flow and volume change in soft clay surrounding a thermal PVD are described in detail in previous work by the authors (Samarakoon and McCartney 2020). The numerical model was validated using experimental data available in literature. A parametric analysis conducted on the performance of a thermal PVD showed that the

amount of surcharge required when using a thermal PVD was significantly less compared to that used in combination with a conventional PVD. In addition, higher magnitudes of settlement and faster rates of consolidation were observed as the magnitude of the temperature at the drain increased.

NUMERICAL STUDY

Soil domain geometry. To simulate the soil behavior around a thermal PVD, a finite soil domain was considered with a single thermal PVD located at the center. A clay layer with a diameter of 0.45 m and a height of 0.7 m was considered in this analysis, where radial drainage was only permitted at the location of the thermal PVD (i.e., no vertical drainage or drainage from the outer boundary). The dimensions of the clay layer are similar to those of the large-scale consolidometer experiment performed by Artidteang et al. (2011) A 50 kPa surcharge was applied to the saturated clay layer simultaneously with an increase in temperature along the length of the thermal PVD from 25 °C to 90 °C. The clay layer was assumed to be normally consolidated under the surcharge. A schematic of the arrangement of the thermal PVD in the clay layer is shown in Figure 1. Heat transfer and fluid flow were considered to be axisymmetric about the axis of the drain for the numerical simulation presented in this study. The variation of temperature in the vertical direction was assumed to be uniform thereby simplifying the geometry to a radial drainage problem. The outer edge of the cylinder acts as an oedometer which has zero radial strain. A radial variation in void ratio is expected due to heating from the central thermal PVD. The surcharge is applied in stress-control conditions so settlements in the clay layer can be nonuniform as a function of the radius from the thermal PVD. The settlement values presented in this presentation are for the surface at a radius of 112.5 mm from the center, except in the case that radial settlement profiles are shown.

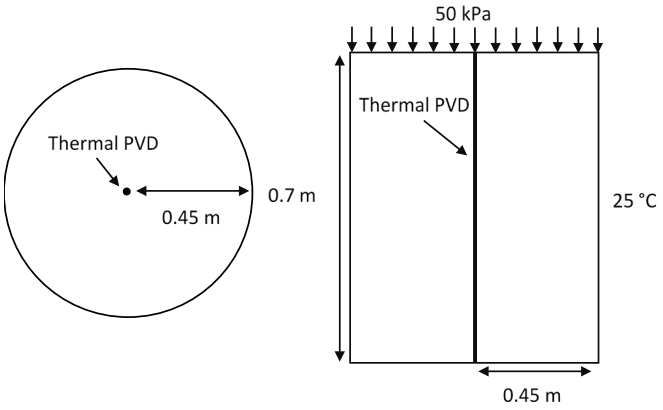

Figure 1. Schematic diagram of the thermal PVD arrangement in a finite soil domain.

Boundary and initial conditions. A constant temperature boundary condition was imposed at the thermal drain whereas a convective temperature boundary condition was maintained at the outer edges of the clay layer. A constant hydrostatic pressure boundary was also applied at the drain location and the far field fluid velocity was taken as zero (i.e., no flow). The initial temperature in the soil domain was 25 °C and the initial pore water pressure was determined based on the hydrostatic conditions and the applied surcharge. The initial porosity of the three clay layers considered (kaolinite, illite, and smectite) was 0.5.

Numerical formulation. For this study, a saturated normally consolidated clay was simulated considering the coupled processes of heat transfer, fluid flow and volume change. The coupled phenomena were simulated using the finite difference method. Both steady state as well as transient variations in temperature, pore water pressure and settlement were solved for using the numerical model. A central difference scheme was used in the spatial domain and a forward difference scheme was used in the time domain. The numerical formulation was implemented and solved using Matlab.

Material properties. This study focuses on the behavior of three clay types surrounding a thermal PVD: kaolinite, illite and smectite. A detailed study on the hydraulic conductivity of these clays as a function of void ratio was conducted by Mesri and Olson (1971). They found that the hydraulic conductivity is sensitive to the clay mineralogy and associated particle size and shape as well as the interaction of the clay particles with the pore fluid. For the void ratio of 0.5 considered in this study, kaolinite will have the highest hydraulic conductivity while smectite will have the lowest as shown in Table 1. The other material parameters used in the numerical simulation including the compressibility indices and the material specific thermal parameter, γ were obtained from literature (Laloui et al. 2008, Ye et al. 2015). The material parameters for each soil type are summarized in Table 1. The thermal conductivity and the specific heat capacity of soil particles were assumed to be 1.9 W/m/°C and 1500 J/kg/°C, respectively, for all three soil types for simplicity. It is acknowledged that the clay mineralogy likely affects the particle thermal conductivity values, but this topic has not been well studied in the literature. The thermal conductivity of pore water was 0.6 W/m/°C. The poromechanics approach used in the analysis permits consideration of changes in thermal conductivity of the bulk soil with changes in volume.

Table 1. Material parameters of clays (Mesri and Olson 1971, Laloui et al. 2008, Ye et al. 2015).

Parameter	Kaolinite	Illite	Smectite
Specific gravity	2.66	2.72	2.69
Hydraulic conductivity at room temperature (m/s)	7.75×10^{-9}	5.50×10^{-11}	1.35×10^{-12}
Initial porosity	0.5	0.5	0.5
Initial total unit weight (kN/m^3)	1830	1860	1845
κ (slope of RCL)	0.01	0.02	0.04
λ (slope of VCL)	0.07	0.11	0.40
γ (soil thermal volume change parameter)	0.53	0.56	1.16

THERMAL PVD RESPONSE IN CLAY

Heat Transfer. A thermal PVD leads to an increase in temperature of the surrounding clay due to radial heat transfer through the soil medium. Spatial as well as temporal variations of temperature within the clays were obtained for each type of clay. The time series of temperature at different radial distances for each clay type is shown in Figure 2. The results in Figure 2 indicate that the soil domain reached thermal equilibrium after about 100 hrs. The locations closer to the drain reached higher temperatures at equilibrium whereas locations farther away reached lower temperatures at equilibrium.

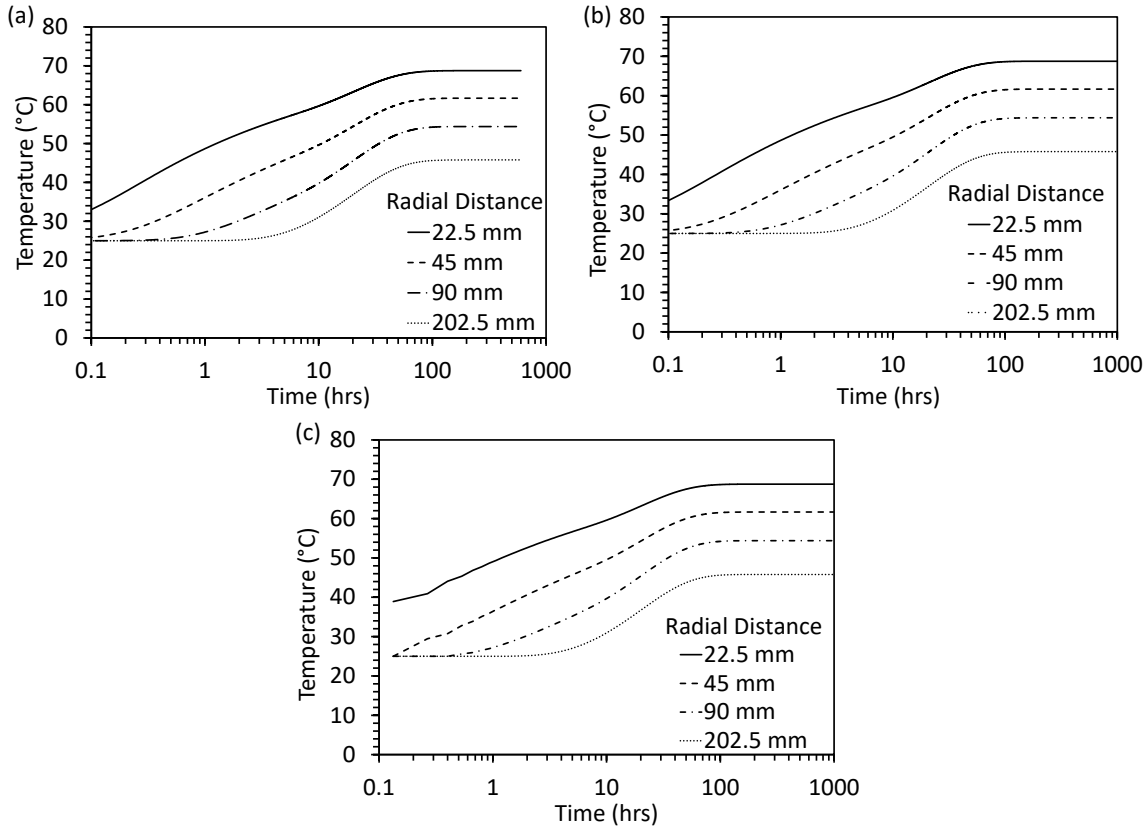

Figure 2. Time series of temperature for (a) kaolinite; (b) illite; (c) smectite.

Excess pore water pressure. The excess pore water pressures generated in each clay layer at a radial location halfway between the thermal PVD and the edge of the container are shown in Figures 3-5. Two cases were compared in which the drain temperature was maintained at 25 °C and 90 °C. The drain temperature of 25 °C is considered to be representative of a conventional PVD where excess pore water pressures are generated only due to the application of the surcharge, whereas the temperature of 90 °C represents a thermal PVD with excess pore water pressures induced by both the surcharge and heating. For kaolinite, the excess pore water pressures generated at both temperatures seem to be almost the same. However, the excess pore water pressures at 90 °C dissipates at a faster rate compared to that at 25 °C. For illite, a higher magnitude of excess pore water pressure is observed at 90 °C. Although the initial excess pore water pressure is higher at 90 °C, it is still observed to dissipate faster compared to a conventional PVD. Thermally induced excess pore water pressures are also observed in the smectite layer and their magnitudes are greater than those observed for illite. The dissipation of excess pore water pressures in smectite with both a conventional as well as a thermal PVD occur over a similar duration of time.

The differences observed in the generation of excess pore water pressures can be attributed to the different hydraulic conductivity values of each clay type. In the relatively fast-draining kaolinite layer, almost no thermally induced excess pore water pressure is generated at this location for the setting considered in this study. The main contribution to excess pore water pressure is from the applied surcharge load. On the other hand, in the slower draining clay layers of illite and smectite, some thermally induced excess pore water pressure is observed as the temperature is increased from 25 to 90 °C. The sudden increase in temperature and the low hydraulic conductivity value in a partially drained condition may have resulted in the observed

increase in excess pore water pressure. On the other hand, the increase in temperature results in a decrease in viscosity of the pore fluid increases the hydraulic conductivity which in turn results in faster rates of dissipation. However, for very slow draining clays, this increase in hydraulic conductivity may still not be sufficient to offset the thermally induced excess pore water pressures during the initial stages of consolidation. However, the additional thermally induced excess pore water pressures generated when using a thermal PVD will contribute towards the thermally induced settlement of the clay layer.

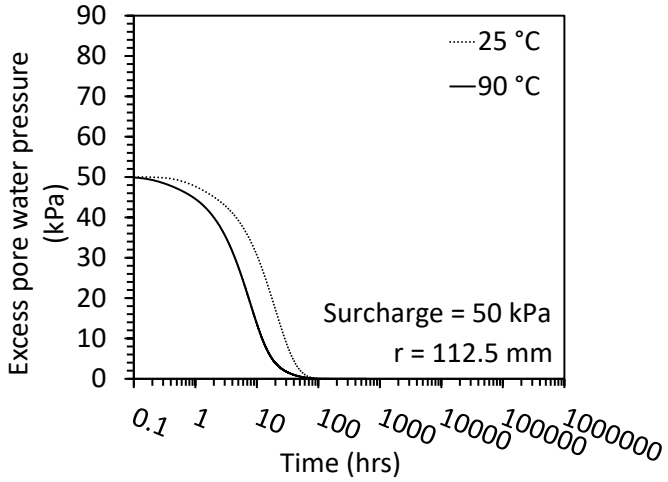

Figure 3. Excess pore water pressure during consolidation in kaolinite.

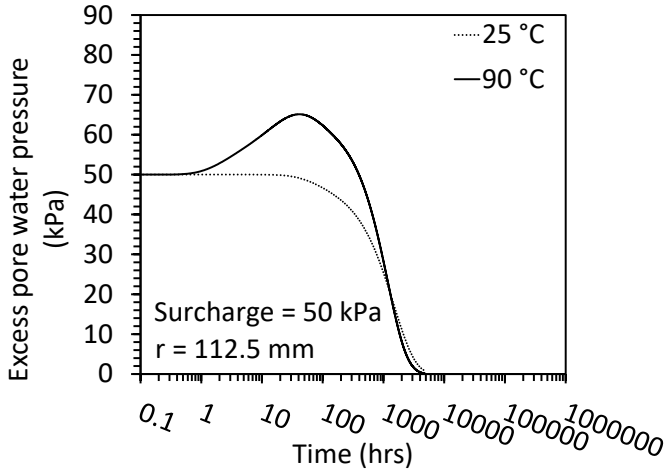

Figure 4. Excess pore water pressure during consolidation in illite.

Volume change. With simultaneous application of a surcharge load and heat, the clay layer will be subjected to mechanically induced as well as thermally induced strains. Mechanically induced contractile strains can be obtained using the one dimensional compressibility relationships for a normally consolidated clay. Thermo-plastic contractile strains were obtained from the relationship proposed by Laloui and Cekerevac (2003) shown in Equation 4, which is only valid for normally consolidated soils.

A comparison of settlements obtained when using a conventional PVD and a thermal PVD for each clay type are shown in Figures 6-8. For all three clay types an increase in the magnitude

as well as the rate of settlement is observed when using a thermal PVD, conforming with the observations made in literature. The differences in the magnitude of thermally induced settlement can be attributed to the differences in the material properties such as hydraulic conductivity, compressibility indices and the thermal parameter, which influences the volume change of each clay type.

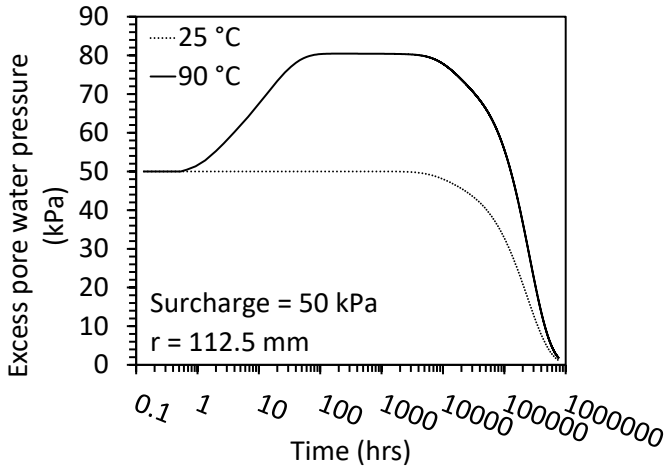

Figure 5. Excess pore water pressure during consolidation in smectite.

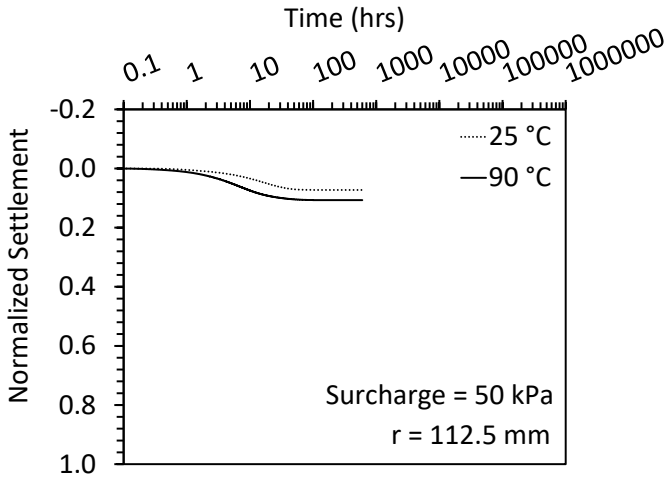

Figure 6. Comparison of settlement curves obtained in kaolinite.

An interesting observation made from the simulation results was the slight initial expansion observed in illite and smectite clay layers at 90 °C. Thermally induced excess pore water pressures were observed in the same two clays. As discussed in the previous section, under partial drainage conditions, some initial expansion can be expected corresponding with the increase in thermally induced excess pore water pressure. Laboratory tests conducted by Campanella and Mitchell (1968) and Ghaaowd et al. (2016) where soil specimens were subjected to an increase in temperature under fully undrained conditions have reported expansion during heating. However, as the clay layer continues to drain, volumetric contraction occurs and the net volume change at the end of consolidation results in contraction. A closer observation of the impact of temperature on the initial expansion and excess pore water pressure in smectite is shown in Figure 9. It can be

observed that the magnitude of initial expansion increases as the temperature is increased. As expected, the amount of excess pore water pressure generated also increases with temperature.

The temperatures at equilibrium varied as a function of radius as shown in Figure 2 and therefore nonuniform settlements can be expected in the clay layer. The equilibrium settlement along a radius for each clay type is shown in Figure 10. The change in settlement along the radius for smectite was more significant where higher settlements were observed closer to the drain. Changes in settlement along a radius for kaolinite and illite were less pronounced.

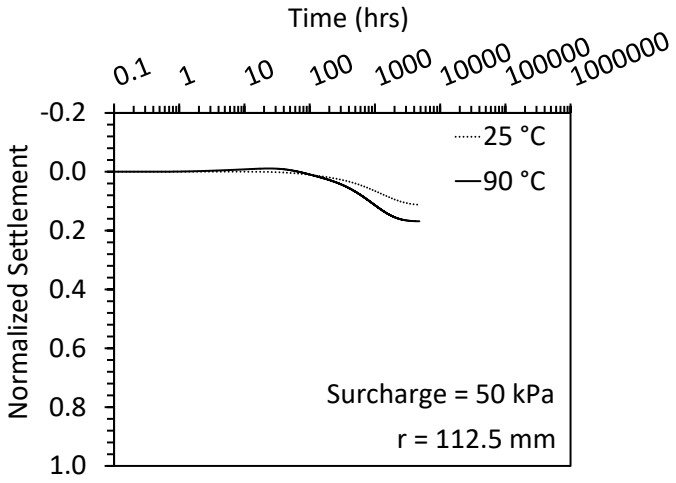

Figure 7. Comparison of settlement curves obtained in illite.

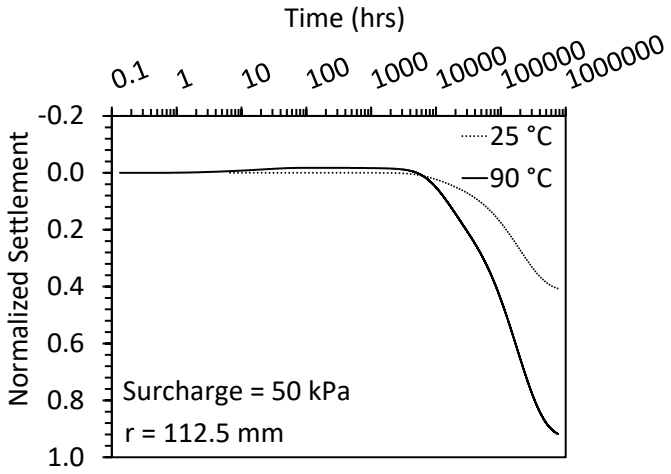

Figure 8. Comparison of settlement curves obtained in smectite.

Hydraulic Conductivity. The hydraulic conductivity of the soil surrounding a thermal PVD will increase as the temperature of the soil domain increases. This increase can be obtained using Equations 1 and 3. For the clay types evaluated in this study, the hydraulic conductivity of the clay when using a thermal PVD was 1.62 times faster than the hydraulic conductivity of the clay when a conventional PVD was being used. Pothiraksanon et al. (2010) estimated the hydraulic conductivity with a thermal PVD to be 1.8 time faster when compared to the hydraulic conductivity with a conventional PVD for a field scale test on Bangkok clay. For, the clay types considered in this study, the decrease in viscosity of the pore fluid for a given temperature increment will be the

same and as a result, the hydraulic conductivity of each clay type increased by a similar amount. However, the compressibility characteristics and the material specific thermal parameter influenced the differences observed in the mechanical and the thermo-plastic volume change of each clay.

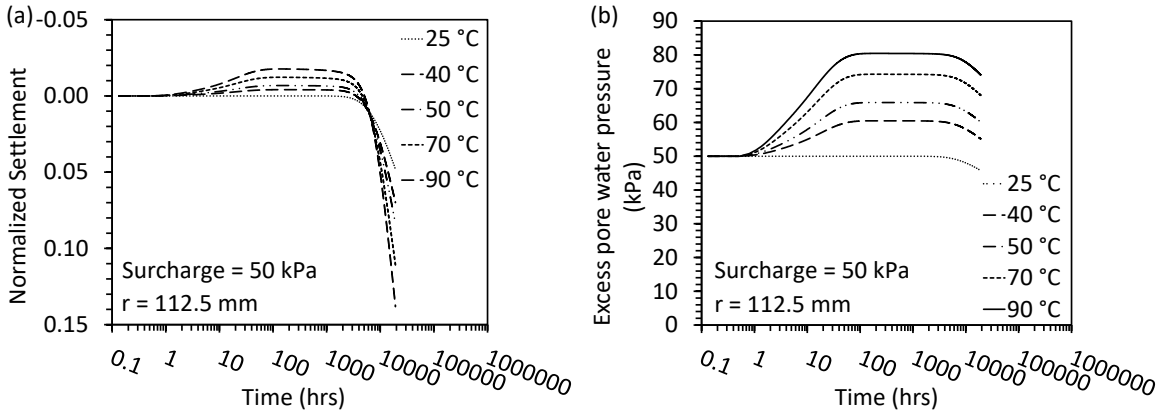

Figure 9. Effect of temperature on the (a) initial expansion and (b) excess pore water pressure in smectite.

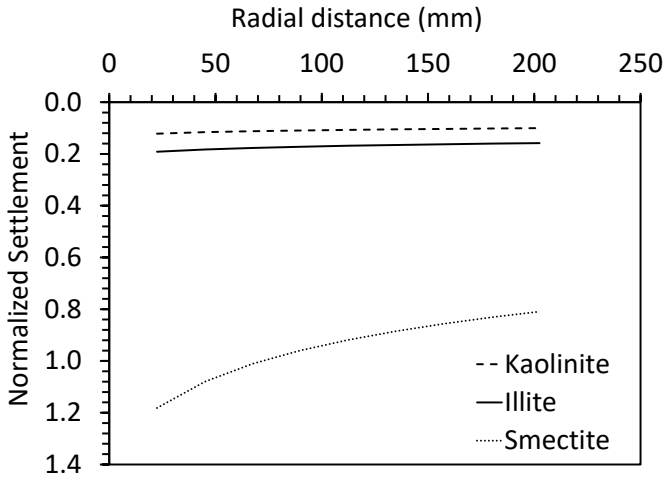

Figure 10. Radial profile of equilibrium settlement obtained from a thermal PVD.

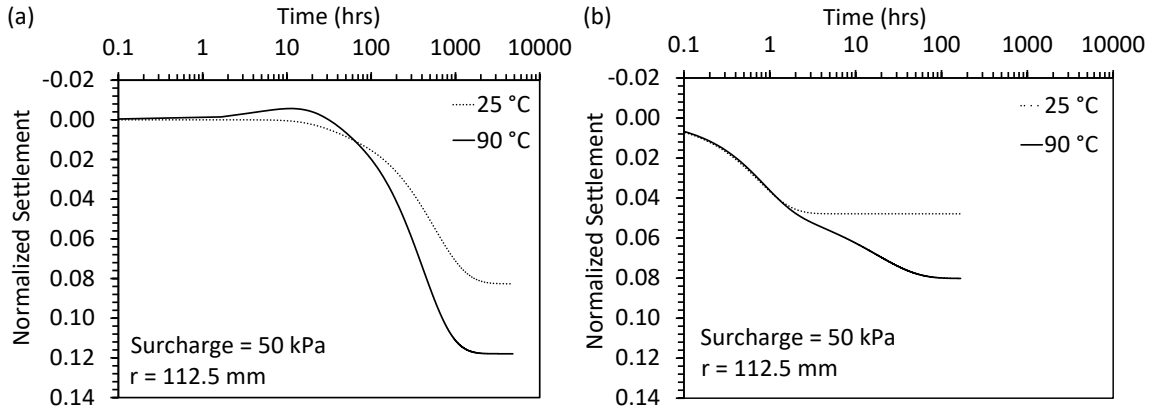

Figure 11. Comparison of settlement curves in kaolinite; (a) n = 0.43 (b) n = 0.67.

To investigate the effect of hydraulic conductivity on the performance of a thermal PVD, kaolinite layers at different initial porosities were considered. The change in hydraulic conductivity with porosity was obtained from Mesri and Olson (1971). Settlement curves obtained for clay layers with initial porosities 0.43 and 0.67 under similar loading conditions as described above are shown in Figure 11. A slight initial expansion was observed in the kaolinite clay layer with the lower initial porosity (i.e., low hydraulic conductivity), similar to the slower draining illite and smectite clay layers. The maximum settlements obtained at different hydraulic conductivity values are summarized in Figure 12.

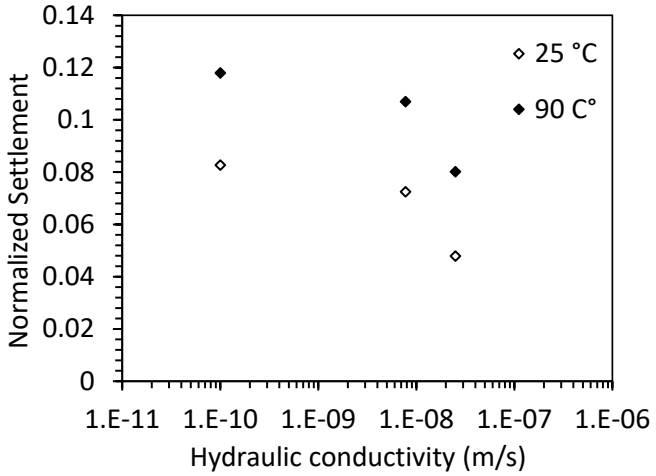

Figure 12. Effect of hydraulic conductivity on equilibrium settlement in kaolinite.

CONCLUSION

A study was conducted on the performance of a thermal PVD on saturated normally consolidated layers of kaolinite, illite and smectite clay. Specifically, a simultaneous application of mechanical and thermal loads was considered and the coupled processes of heat transfer, fluid flow and volume change were simulated using a numerical model. In general, the main conclusion is that the properties of the clay will determine the effectiveness of thermal consolidation as a means of soil improvement. Thermally induced excess pore water pressures were initially observed for the low permeability illite and smectite clay layers, but not in the higher permeability kaolinite clay layer. At the same time, a slight initial expansion was also observed in the illite and smectite clay layers. The observed initial expansion and the thermally induced excess pore water pressure were found to increase with an increase in applied temperature to the thermal PVD. Despite the difference in initial behavior for the illite, smectite, and kaolinite clays, a net contraction was observed for all three clay layers with an increase in the rate as well as magnitude of settlement when a thermal PVD was used. An analysis conducted on the effect of hydraulic conductivity on the performance of a thermal PVD in kaolinite also observed a slight initial expansion for the clay layer with low hydraulic conductivity. Clay layers with different hydraulic conductivity values was observed to have a similar increase in the magnitude of settlement obtained when using a thermal PVD. However, the effect of temperature on the rate of settlement is more significant for clay layers with low hydraulic conductivity. A study on the use of a thermal PVD in different clay types demonstrated that some initial expansion would occur in clays with low hydraulic conductivity values. As this was dependent on the magnitude of temperature at the drain, slower heating using

incremental steps may help reduce the initial expansion observed in these clay layers.

ACKNOWLEDGEMENTS

Funding from NSF grant CMMI 1941571 is appreciated. The opinions are those of the authors.

REFERENCES

Abuel-Naga, H.M., Bergado, D.T. and Suttisak, S. (2006). Innovative thermal technique for enhancing the performance of prefabricated vertical drain system, *Geotextiles and Geomembranes*, 24(6): 359–370.

Artidteang, S., Bergado, D.T., Saowapakpiboon, J., Teerachaikulpanich, N. and Kumar, A. (2011). Enhancement of efficiency of prefabricated vertical drains using surcharge, vacuum and heat preloading, *Geosynthetics International*, 18(1): 35–47.

Baldi, G., Hueckel, T. and Pellegrini, R. (1988). Thermal volume changes of the mineral-water system in low-porosity clay soils, *Canadian Geotechnical Journal*, 25(4): 807–825.

Campanella, R.G. and Mitchell, J.K. (1968). Influence of temperature variations on soil behavior, *Journal of the Soil Mechanics and Foundation Division*, ASCE, 94(3): 709–734.

Cui, Y.J., Sultan, N. and Delage, P. (2000). A thermomechanical model for clays, *Canadian Geotechnical Journal*, 37(3): 607–620.

Ghaaowd, I., Takai, A., Katsumi, T. and McCartney, J.S. (2017). Pore water pressure prediction for undrained heating of soils, *Environmental Geotechnics*, 4(2): 70–78.

Hansbo, S. (1981). Consolidation of fine-grained soils by prefabricated drains, *10th International Conference on Soil Mechanics*, A.A. Balkema, Ed., Stockholm, Sweden: 3: 677-682.

Hillel, D. (1980). *Fundamentals of Soil Physics*, Academic Press, New York, NY, USA.

Hueckel, T. and Borsetto, M. (1990). Thermoplasticity of saturated soils and shales: Constitutive equations, *Journal of Geotechnical Engineering*, 116(12): 1765-1777.

Hueckel, T. and Pellegrini, R. (1992). Effective stress and water pressure in saturated clays during heating-cooling cycles, *Canadian Geotechnical Journal*, 29(6): 1095-1102.

Indraratna, B. and Redana, I.W. (1998). Laboratory determination of smear zone due to vertical drain installation, *Journal of Geotechnical Engineering*, ASCE, 124(2): 180-184.

Laloui, L. and Cekerevac, C. (2003). Thermo-plasticity of clays: an isotropic yield mechanism, *Computers and Geotechnics*, 30(8): 649-660.

Laloui, L., Leroueil, S. and Chalindar, S. (2008). Modelling the combined effect of strain rate and temperature on one-dimensional compression of soils, *Canadian Geotechnical Journal*, 45(12): 1765-1777.

Mesri, G. and Olson, R.E. (1971). Mechanisms controlling the permeability of clays, *Clays and Clay Minerals*, 19(3): 151-158.

Pothiraksanon, C., Bergado, D.T. and Abuel-Naga, H.M. (2010). Full-scale embankment consolidation test using prefabricated vertical thermal drains, *Soils and Foundations*, 50(5): 599-608.

Salager, S., Laloui, L. and Nuth, M. (2012). Efficiency of thermal vertical drains for the consolidation of soils, *2nd International Conference on Transportation Geotechnics*, Hokaido, Japan. 1-10.

Samarakoon, R.A. and McCartney, J.S. (2020). Simulation of prefabricated thermal drains in soft clay, *GeoAmericas 2020: Proc. of the 4th Pan American Conference on Geosynthetics*, 1-9.

Illinois' Second GRS-IBS

David Liu, Ph.D., P.E., S.E.[1]

ABSTRACT

North Central DuPage Regional Trail over County Farm Road (Key Route 0362) is a three-span, Prefabricated Pedestrian Bridge. There are two piers and two Geosynthetic Reinforced Soil abutments. This is Illinois's Second Geosynthetics Abutments. The owner of this bridge is Forest Preserve District of DuPage County. The Geosynthetic Reinforced Soil (GRS) Integrated Bridge System (IBS) provides an economical solution to accelerated bridge construction. During the preliminary design of North Central DuPage Regional Trail over County Farm Road Bridge, different types of abutments such as full height abutments, stub abutments, integral abutments on pile foundation, and Geosynthetic Reinforced Soil abutments are investigated. Geosynthetic Reinforced Soil abutments yields most economical solution at this bridge site, also shortens the construction schedule.

INTRODUCTION

The Geosynthetic Reinforced Soil (GRS) Integrated Bridge System (IBS), FHWA (2018) provides an economical solution to accelerated bridge construction. Employing this technology will help agencies save both time and money in planning and executing projects. GRS-IBS is a fast, cost-effective method of bridge support that blends the roadway into the superstructure to create a jointless interface between the bridge and the approach (FHWA (2018)). With GRS-IBS, shallow foundation is typically used to support the superstructure, which would be cheaper than deep foundation. It consists of three main components: the reinforced soil foundation (RSF), the abutment, and the integrated approach. The RSF is composed of granular fill material that is compacted and encapsulated with a geotextile fabric. It provides embedment and increases the bearing width and capacity of the GRS abutment. It also prevents water from infiltrating underneath and into the GRS mass from a river or stream crossing. This method of using geosynthetic fabrics to reinforce foundations is a proven alternative to deep foundations on loose granular soils, soft fine-grained soils, and soft organic soils. The abutment uses alternating layers of compacted fill and closely spaced geosynthetic reinforcement to provide support for the bridge, which is placed directly on the GRS abutment without a joint and without cast-in-place (CIP) concrete. GRS is also used to construct the integrated approach to transition to the superstructure. This bridge system therefore alleviates the "bump at the bridge" problem caused by differential settlement between bridge abutments and approach roadways.

The North Central DuPage Regional Trail (NCDRT) is a 19-mile trail spanning northern DuPage County. Stretching from Roselle to Wayne, the eastern terminus of the NCDRT connects to trails in Cook County that merge at Busse Woods Forest Preserve in Elk Grove. This Trail has been planning since 2000.

As part of this 19-mile trail, North Central DuPage Regional Trail over County Farm Road (Key Route 0362) is a three-span, Prefabricated Pedestrian Bridge. There are two piers and

two Geosynthetic Reinforced Soil abutments. This is Illinois's Second Geosynthetics Abutments. The owner of this bridge is Forest Preserve District of DuPage County

During the preliminary design of North Central DuPage Regional Trail over County Farm Road Bridge, different types of abutments such as full height abutments, stub abutments, integral abutments on pile foundation, and Geosynthetic Reinforced Soil abutments are investigated. Geosynthetic Reinforced Soil abutments yields most economical solution at this bridge site, also shortens the construction schedule. In this paper, the design procedure for Geosynthetic Reinforced Soil abutments is presented. Construction sequences are also discussed.

In 2018, Forest Preserve District of DuPage County Earns Two Awards for this County Farm Road Bridge Project. The awards were issued by the American Public Works Association and American Council of Engineering Companies of Illinois. Forest Preserve District of DuPage County (2018).

DESIGN PROCEDURE

Pre-fabricated truss is selected to speed up the construction and reduce the traffic impact on County Farm Road. For Spans 1 and 2, constant depth trusses are selected to reduce the cost. For Span 3 over County Farm Road, variable depth truss (top chord has parabolic curve) is selected to have aesthetic appearance.

Before starting the spread footing design, the designer needs to contact the prefabricated truss vendor for reactions under dead load and live load. Then, contact the geotechnical engineer for allowable soil pressure or soil bearing resistance.

The design of spread footing is pretty straight. First, line up the bearing with centerline of spread footing to avoid the eccentric bending. Once footing size can be easily determined with vertical loads and bearing resistance. The footing thickness is designed by bending and shear. The pier was designed by vertical load (dead load from pier self-weight and superstructure and live load) and wind loads.

Hammerhead Pier with architecture treatment (Form Liner) is selected to have aesthetic appearance. The pier is founded on spread footing, which is much cheaper than deep foundation.

CONSTRUCTION

The bridge plans were bided on 03/04/2016. The winning/lowest bid is $2,354,372 (max bid price is $4,392,786), which is much higher than engineer's estimate of $1,264,000 because some unit prices engineer was using were too low because not too many projects using for GRS-IBS. Obviously, the unit price used for GRS-IBS is too low. Martam Construction Incorporated was selected to build the bridge. The construction sequences are:

1. Build embankment
2. Build geosynthetic abutments and piers at the same time.
3. Once substructure construction was completed, erect pre-fabricated truss
4. Cast concrete deck
5. Open to pedestrians and bikers.

The project, which was completed within 95 working days on May 15, 2017, The Geosynthetic Reinforced Soil abutments were completed in about three months. The following is a list of figures took during construction.

1. Fig. 2 Building Geosynthetics Abutments

2. Fig. 3 Bridge Elevation View
3. Fig. 4 Bridge Deck View
4. Fig. 5 Pier View with Architecture Treatment

CONCLUSION

The Geosynthetic Reinforced Soil (GRS) Integrated Bridge System (IBS) provides an economical solution to accelerated bridge construction. Spread footing is typically used at abutments, which is much cheaper than pile foundations. Pedestrian bridges or steel bridges with short spans would be good candidates to use The Geosynthetic Reinforced Soil (GRS) Integrated Bridge System.

REFERENCES

FHWA (2018), Michael Adams and Jennifer Nicks, “Design and Construction Guidelines for Geosynthetic Reinforced Soil Abutments and Integrated Bridge Systems”, PUBLICATION NO. FHWA-HRT-17-080, The FHWA Office of Bridges and Structures, 1200 New Jersey Avenue, SE, Washington DC 20590, June 2018.

Forest Preserve District of DuPage County (2018), “Forest Preserve District of DuPage County Earns Two Awards for County Farm Road Bridge Project”

Fig. 1. Geosynthetics Abutments (Courtesy of FHWA (2018))

Fig. 2 Building Geosynthetics Abutments

Fig. 3 Bridge Elevation View

Fig. 4 Bridge Deck View

Fig. 5 Pier View with Architecture Treatment

Geosynthetics Conference

Load-Bearing Performance of GRS Abutments with Different Facing Alternatives

Kianoosh Hatami, Ph.D., P.Eng.,[1] and Ridvan Doger, Ph.D., P.E.[2]

[1]Professor, School of Civil Engineering and Environmental Science, The University of Oklahoma, Norman, OK, USA; e-mail: kianoosh@ou.edu
[2]Senior Geotechnical Engineer, A&M Engineering and Environmental Services, Inc., Tulsa, OK, USA; e-mail: rdoger@ou.edu

ABSTRACT

The paper describes the construction procedure and load-testing of two instrumented, large-scale model Geosynthetic Reinforced Soil (GRS) abutments in an outdoor test station. The models were built in conformance with the FHWA recommendations relative to the type and quality of materials used, reinforcement length and spacing. The two models were comparable to each other except for their facing configuration. One model was built with cored concrete masonry units (CMU), whereas the other model was built using significantly larger solid concrete blocks. It was observed that using large concrete blocks for the facing helped with the construction quality, construction speed and performance of the GRS abutments, and hence, their use is recommended for field applications where possible.

INTRODUCTION

Geosynthetic Reinforced Soil-Integrated Bridge Systems (GRS-IBS) have gained increased popularity for new or replacement projects in local and county roads across the United States due to several observed advantages over conventional methods, including faster construction at reduced costs, and allowing to eliminate the 'bump at the end of bridge' problem (Adams et al. 2011, 2012; Adams and Nicks 2018). GRS abutments and GRS-IBS as a bridge system have been the subject of several studies in recent years. A review of selected related studies is provided in the papers by Xu et al. (2020) and Doger and Hatami (2020).

In the design of GRS abutments, any possible structural contribution of the facing is not relied upon in the current guidelines (e.g. Adams and Nicks 2018) due to the self-contained structural integrity of the composite fill with tightly spaced reinforcement. Therefore, different facing configurations can be used merely to protect the fill against erosion, sloughing, scour (e.g. in combination with rip rap or other means as necessary) and similar non-structural factors.

At the same time, a large variety of concrete blocks are currently available for use in Mechanically Stabilized Earth (MSE) and other similar applications at affordable costs. Therefore, the focus of this study was to investigate the potential advantages of using large concrete blocks over the more commonly used, cored concrete masonry units (CMU) relative to the construction quality and speed of GRS abutments, and their load-bearing performance.

EXPERIMENTAL

Figures 1 and 2 show schematic cross-sections and elevation-view photographs of the two GRS abutment models examined in this paper, respectively. The two instrumented, large-scale (2.45 m-high) models were constructed in an outdoor test chamber with inside dimensions of 2.75 m (H) ×

2.45 m (W) × 4.75 m (L), made of reinforced concrete (including its floor slab). The loading assembly on the top of the test chamber includes a steel loading frame, two 1,780-kN hydraulic cylinders and two load cells with matching capacity, a 2.4 m (L) × 0.2 m (W) plan-area loading beam, an electric-hydraulic pump, and miscellaneous accessories for uniform and safe application of surcharge loading on different large-scale geotechnical models. Further details on the outdoor test station are provided in the paper by Doger and Hatami (2020).

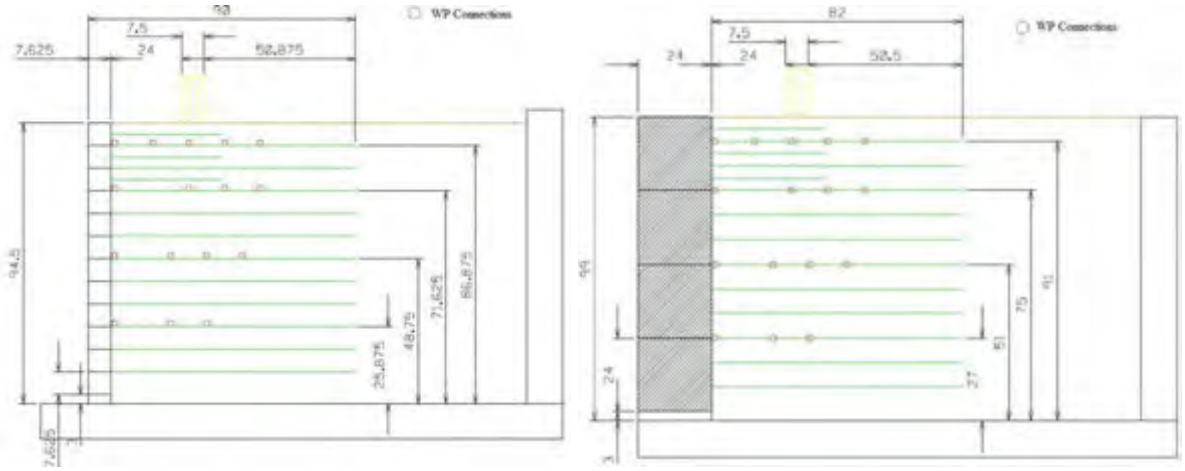

Figure 1. Schematic cross-sections and instrumentation layouts for the GRS model abutments in this study (Doger 2020, Doger and Hatami 2020): (Left) Model #1, (Right) Model #2 (Dimensions shown are in inches; 1 in. = 25.4 mm).

Figure 2. Elevation views of GRS abutment models #1 (left) and #2 (right) at end of construction (Doger 2020, Doger and Hatami 2020).

Materials. The models were built using the same materials and construction procedures except for the size of their facing blocks as shown in Figure 1, and as described below: Model #1 was built using 12 courses of 200 mm × 200 mm × 400 mm cored concrete masonry units (CMU) with reinforcement spacing, S_v = 200 mm, to a full height of H_1 = 2.40 m. Model #2 was built with 4 courses of much larger (i.e. 0.6 m × 0.6 m × 1.2 m) solid blocks for its facing to a full height of H_2 = 2.45 m with the same reinforcement spacing. Both types of blocks were available from a local

supplier. The CMU blocks in Abutment Model #1 were placed and removed manually, whereas the large blocks in Models #2 and #3 were placed and removed (after the test) using forklifts. The reinforcement spacing of 200 mm in both models was smaller than the limiting value of 300 mm in the FHWA guidelines. Similarly, other features of the models as described below were in conformance with the FHWA guidelines (Adams et al. 2011,2012; Adams and Nicks 2018):

The last three courses of CMU blocks in Model #1 were infilled with steel rebar and concrete for added stability. Both models included 2.30 m-long primary reinforcement layers and 1.15 m-long additional layers toward the top to form a reinforced foundation section under the simulated bridge load. All primary reinforcement layers in Model #1 were tucked in between CMU blocks resulting in full-block-thickness (~200 mm) interfaces. The same reinforcement length was also used in Model #2 to keep the size of reinforced mass identical between the two models. Therefore, only 200 mm of the geotextile reinforcement was tucked in between the 600 mm-tall blocks, and only in the three joints that were available over the height of the large-block facing alternative. All other reinforcement layers in Model #2 were merely placed up to, and with no mechanical connection with, the facing.

The loading beam simulating bridge load was placed at a distance of 600 mm behind the facing column, which is greater than a minimum recommended setback of 200 mm. This dimension was also deemed as a practically optimal distance for the 2.45 m-high GRS abutment models in the sense that, it would be close enough to the facing so that it could instigate larger deformations in the models and at the same time, it would not be too close to the facing to cause premature termination of the loading tests due to local failure at the top of the models.

The location of the back of the abutment facing inside the test box was kept the same in both models regardless of the size of their facing blocks to keep the size of their backfill identical between the two models. The middle 1.20 m-wide section of each model was instrumented with a total of sixteen 300 mm-stroke, wire potentiometers (WP) that were connected to select reinforcement layers through the back-wall of the test box during construction. Additional WPs were connected to the facing and the loading beam on the top of the backfill to measure corresponding deformations during the load-testing stage. Lateral deformations of the facing during construction were measured using manual survey of six different points at each block level.

An open-graded aggregate, referred to as the 3/8” #2 Cover (3/8 in. ≈ 10 mm) from a local supplier was used for the GRS fill (Figure 3). The peak friction angle for the abutment aggregate at a lightly packed state (i.e. unit weight of γ = 15.26 kN/m^3) from direct shear tests (DST) in the laboratory was determined as $\phi = 48^o$. This friction angle value is comparable to the results reported by Nicks (2013) and Nicks and Adams (2014) for AASHTO #89 aggregate of comparable gradation in a loose state. The unit weight of the backfill material in dry condition in a Modified Proctor mold (150 mm diameter) in the laboratory was determined as γ_{max} = 16.50 kN/m^3.

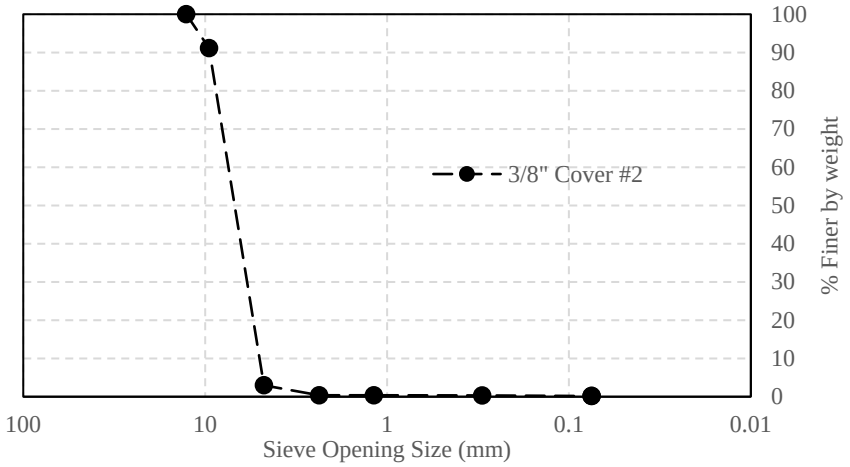

Figure 3. Particle-size distribution of the aggregate used in model GRS abutments.

The reinforcement material used in the abutment models was a polypropylene woven geotextile, with an ultimate strength of 70 kN/m in both machine (MD) and cross-machine directions (XD) as per the ASTM D4595 test protocol. Details of reinforcement instrumentation using WP are given in the paper by Doger and Hatami (2020).

Construction and Load Testing of Models. The GRS abutment models were built in 200 mm lifts using a Jumping Jack compactor in an inward spiral pattern. Backfill compaction using the jumping jack in Model #1 was kept limited to 0.45 m away from the back of the CMU facing - as recommended in FHWA guidelines - to minimize the anticipated block movements during the compaction process. Instead, a 250 mm × 250 mm-plate steel hand tamper was used to compact the fill immediately behind the facing. Additionally, each course of CMU blocks in Model #1 was placed with a 13 mm setback for the same reason, and to counter a negative facing batter at the end of construction. The setback placement of the blocks started with the fifth course when detectable compaction-induced deformation started to occur at that level. In contrast, backfill compaction using the Jumping Jack compactor was done with no problem all the way to the back of the large facing blocks in Model #2, and no setback placement of blocks was necessary to counter block movements during construction.

Construction speed was found to be faster in the case of Model #2 for the above reason, and due to significantly fewer blocks that needed to be placed for comparable lifts of backfill. Model #1 required 74.5 person-hours to complete, which also included time required for steel rod and grouting of the top three courses as per the FHWA guidelines. In comparison, Model #2 took 53.5 person-hours to complete.

Once the construction of each model abutment was complete, the surcharge loading assembly was completed on the top of the abutment fill. A 2.45 m-long × 0.20 m-wide loading beam was placed and leveled, and additional steel blocks were used underneath the hydraulic cylinders as necessary to ensure a uniform application of vertical loading on the beam. The vertical load was applied in 50-100 kN increments followed by a pausing period of several minutes to ensure that readings from the load cells were stabilized before the next loading step was applied. Once the load level on each model reached a magnitude that was considered safe to terminate the loading, the loading assembly was dismantled, and the models were deconstructed in lifts.

RESULTS

Figure 4 shows load-settlement responses of the two model abutments at the top surface under the loading beam. FHWA design values for the bridge abutment service load (190 kPa = 4 ksf) and settlement (i.e. 0.50% of the abutment height = 0.50% × 2.40 m = 12 mm) are also shown in the figure for comparison purposes.

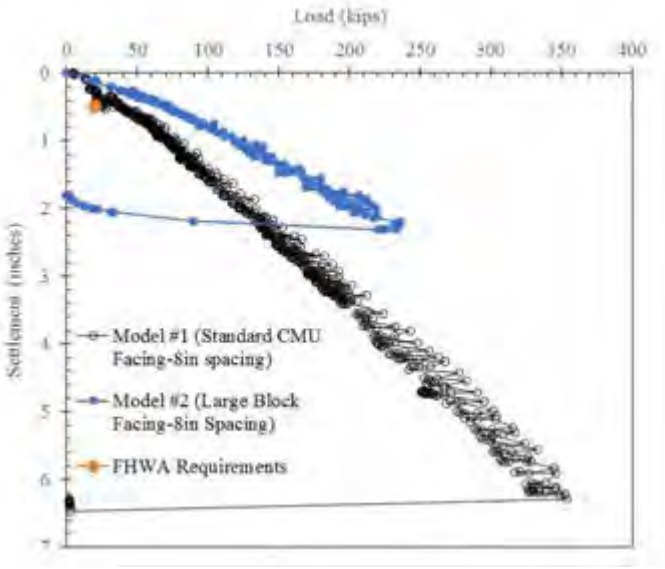

Figure 4. Load-settlement responses of GRS abutment models #1 (CMU facing) and #2 (large-block facing). Note: each 100-kip (445 kN) load shown in this graph is equivalent to 20 ksf (958 kPa) surcharge load on the abutment (Doger 2020, Doger and Hatami 2020) (1 in. = 2.54 mm).

Results in Figure 4 show steady and nearly linear performances for both abutment models throughout their loading stage. Model #1 was subjected to significantly larger loads with the initial objective to determine its load-bearing capacity and observe possible modes of failure. However, apart from a 160 mm of settlement directly underneath the loading beam at 1,572 kN of surcharge load (353.25 kips, equivalent to 3,380 kPa of vertical stress on the abutment), no significant sign of excessive deformation or instability was observed. Therefore, it was decided to abort the load testing procedure for safety reasons, and to prevent the loading frame from overstressing excessively. Load testing of Model #2 was aborted at smaller surcharge load for the same reasons. Nevertheless, results in Figure 4 clearly indicate that Model #2 with large-block facing was significantly stiffer and projected to be much stronger than Model #1. For instance, measured settlement in Model #2 at its maximum load of 1,050 kN was only 56 mm, compared to 95 mm in Model #1 (i.e. 41% less settlement at the same load level). The maximum loads applied on both models were nonetheless an order of magnitude larger than the service load requirement of 190 kPa in the FHWA guidelines.

Maximum lateral movements during construction in both models, measured at the crown of each facing configuration, were equal to 130 mm and 15 mm in Models #1 and #2, respectively (Doger and Hatami 2020). A significant part of these lateral deformations are attributed to a cumulative, compaction-induced movement of the facing blocks over the height of each facing. Since there were significantly more courses of smaller blocks in Model #1, the cumulative effect

of relative movements between the blocks resulted in one order of magnitude larger lateral deformation relative to what was observed in Model #2.

Figure 5 shows a comparison between facing deformations at the top during surcharge loading of the two abutment models. Results indicate that maximum facing deformation in either model was an order of magnitude less than the limiting value of δ_{max} = 1% H = 24 mm (0.95 in.) for their 190 kPa (4 ksf) service load, where H is the abutment height.

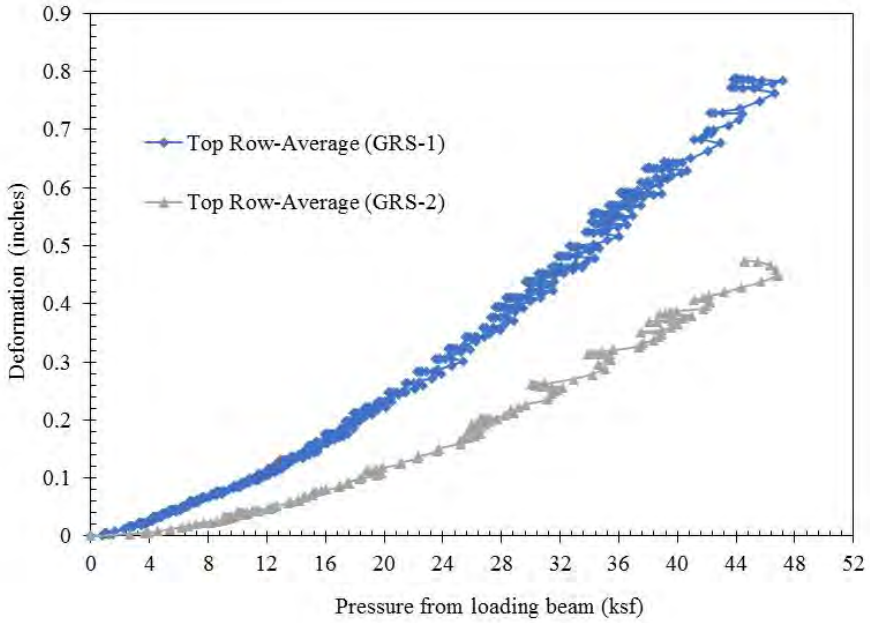

Figure 5. Facing deformations (from mean values of WP readings) at the top for the two abutment models during surcharge loading (Doger 2020, Doger and Hatami 2020) (1 in. = 2.54 mm, 1 ksf = 47.88 kPa).

Figure 6 shows facing deformation profiles for the two abutment models under different magnitudes of surcharge load during the tests. Similar to the results in Figure 5, data in Figure 6 show that facing deformations of both model abutments were significantly smaller than the limiting value recommended in the FHWA guidelines (i.e. 25 mm), and never reached this limit even after they had been subjected to a surcharge load 10 times as large as the design value (i.e. 1,900 kPa = 40 ksf).

Figure 7 shows an example plan view of WP connections to a reinforcement layer in the model abutments in this study. The diagram is shown for the top reinforcement layer at 2.31 m (91 in.) above the foundation slab in GRS Abutment Model #2. Figure 8 shows the corresponding data during surcharge loading and after complete removal of the load. Results in Figure 8 show that WPs closer to the abutment facing consistently measured larger displacements throughout the loading-unloading process. They also indicate that the largest difference in WP displacements occurred between the WPs #2 and #3 (from the facing), consistent with the location of the loading beam on the GRS fill and their proximity to the facing (Figures 1b and 7).

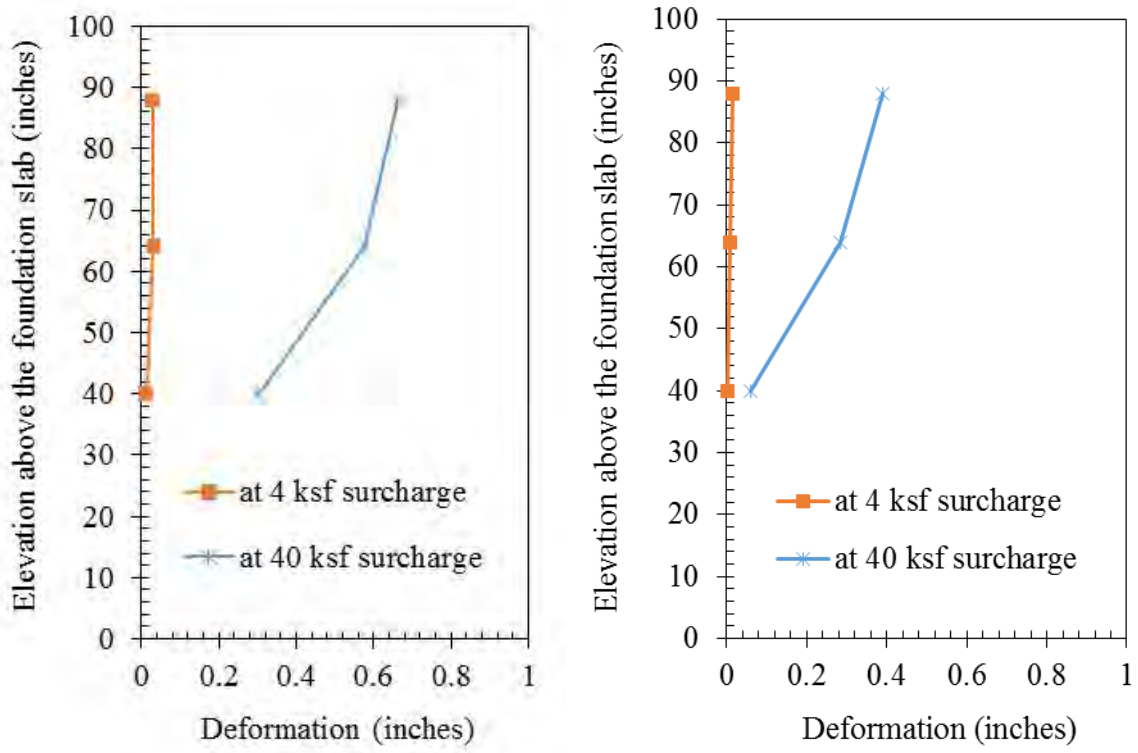

Figure 6. Facing deformation profiles of GRS abutment models #1 (left) and #2 (right) at different loading levels (1 in. = 2.54 mm, 1 ksf = 47.88 kPa).

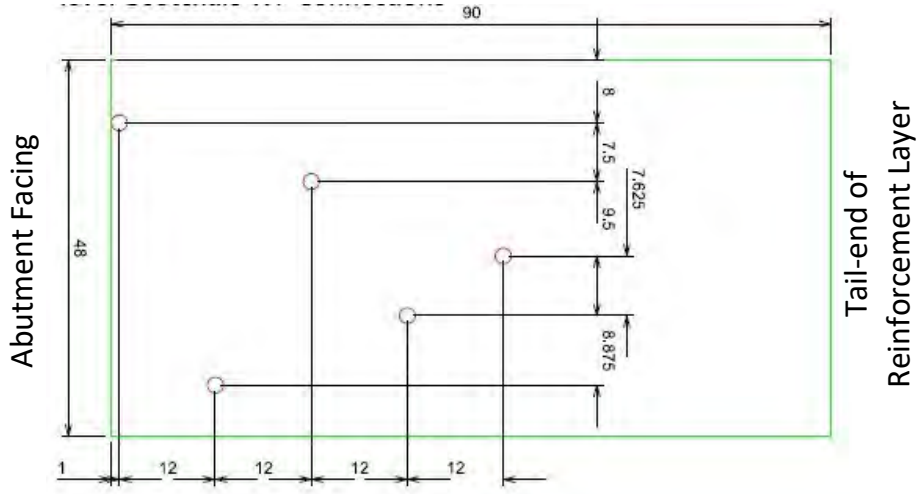

Figure 7. Plan view of WP connections to the top geotextile reinforcement in model #2 (dimensions are in inches; 1 inch = 25.4 mm).

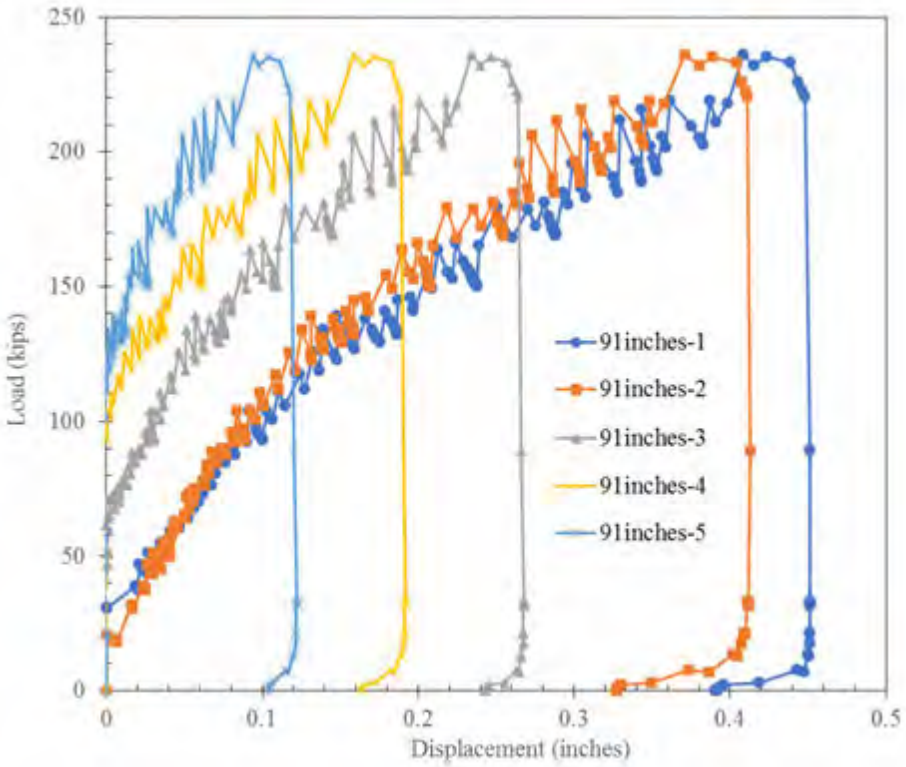

Figure 8. Wire potentiometer readings from the top reinforcement layer in GRS abutment model #2 (large block facing) at the elevation of 2.31 m (91 in.) above the foundation slab during surcharge loading and unloading of the model. WP connections in Figure 7 are numbered sequentially from the facing toward the tail-end of the reinforcement layer. (1 in. = 2.54 mm, 1 kip = 445 kN).

Results of the type shown in Figure 8 were used to calculate global strains at different reinforcement layers in the two models (Doger and Hatami 2020), which indicated that the locations of maximum reinforcement strain in both models, and at different loading magnitudes, remained underneath the surcharge load throughout the testing period. Maximum reinforcement strains underneath the loading beam in Models #1 and #2 at 190 kPa loading level were 0.057% and 0.041%, respectively (Doger and Hatami 2020). These values are significantly smaller than the maximum 2% value recommended in the FHWA guidelines at the service load magnitude of 190 kPa (Adams and Nicks 2018). Maximum reinforcement strains increased only to 1.6% and 1.5% in Models #1 and #2, respectively, after the models were subjected to a 10-fold surcharge load magnitude of 1,900 kPa, which was still below the 2% serviceability level by a safe margin.

CONCLUSIONS

Construction and load-testing of two large-scale (2.45-m tall) model GRS bridge abutments were described in the paper. The models were comparable to each other except for their facing configuration, which varied significantly relative to the size and type of concrete blocks used. The models were instrumented to measure their facing deformations, load-settlement performance at the abutment top surface and reinforcement strains. Results of study showed that:

1. Both abutment models supported a 190 kPa service load at significantly smaller magnitudes of settlement, facing deformation and reinforcement strains relative to the corresponding FHWA limits.
2. Nevertheless, the abutment model with much larger facing blocks showed superior performance relative to its load-settlement response and facing deformation as compared to those of the more common CMU facing alternative.
3. The large-block construction alternative was also faster and allowed for better compaction of the fill behind the facing.

It is therefore concluded that large-block GRS abutments could result in improvements in the load-bearing capacity and performance of GRS abutments, leading to their more widespread use in local and county roadway projects.

ACKNOWLEDGMENTS

Funding for this project was provided by the Oklahoma Department of Transportation (ODOT) through SP&R Item No. 2262-Phase II. The GSI Fellowship granted to the second author by the Geosynthetic Institute in Folsom, PA is gratefully acknowledged. Donations of the fill aggregate by Dolese Bros., Inc. in Oklahoma City, OK and the geotextile reinforcement material by TenCate Geosynthetics, in Cornelia, GA are gratefully acknowledged.

The authors also wish to acknowledge helpful discussions with Mr. Shannon Sheffert, PE (ODOT Local Government Division Engineer at the time of this study), and invaluable assistance from Mike Schmitz, the Fears Structural Laboratory Manager at the University of Oklahoma, and those of graduate students, Jerome Boutin, Kirby Falcon and Matsuura Kazunori, and undergraduate research assistants Stephen Schnabel, Coleman Ross, Uzeir Hodzic, John King, Daniel Farley, Vuth Chea, and Jackie Pham during the construction and testing of the GRS abutment models described in this study.

REFERENCES

Adams M., Nicks J., Stabile T., Wu J., Schlatter W., and Hartmann J. (2011). Geosynthetic Reinforced Soil Integrated Bridge System Synthesis Report, *Report No. FHWA-HRT-11-027*, Federal Highway Administration, Washington, D.C., USA.

Adams M., Nicks J., Stabile T., Wu J., Schlatter W., and Hartmann J. (2012). Geosynthetic Reinforced Soil Integrated Bridge System Interim Implementation Guide, *Report No. FHWA-HRT-11-026*, Federal Highway Administration, Washington, D.C., USA.

Adams M. and Nicks J. (2018). Design and Construction Guidelines for Geosynthetic Reinforced Soil Abutments and Integrated Bridge Systems, *FHWA Publication No: FHWA-HRT-17-080 HRDI-40/06-18(200)E*, Federal Highway Administration, Washington, D.C., USA.

ASTM D4595. Standard Test Method for Tensile Properties of Geotextiles by the Wide-Width Strip Method, *ASTM International*, West Conshohocken, Pennsylvania, USA.

Doger R, (2020). Influence of Facing on the Construction and Structural Performance of GRS Bridge Abutments, *PhD Dissertation*, The University of Oklahoma, Norman, OK, USA.

Doger R and Hatami K, (2020). Influence of Facing on the Performance of GRS Bridge Abutments, *International Journal of Geosynthetics and Ground Engineering*, Springer, 6(4): https://doi.org/10.1007/s40891-020-00225-y.

Nicks J. (2013). Friction Angles of Open-Graded Aggregates From Large-Scale Direct Shear Testing, *FHWA Publication No: FHWA-HRT-13-068 HRDI-40/07-13(200)E*, Federal Highway Administration, Washington, D.C., USA.

Nicks J. and Adams M. (2014). Large-Scale Direct Shear Testing of Common Open Aggregates. *Geo-Congress 2014*, Atlanta, GA, GSP 234, ASCE: 47-53.

Xu P, Li T and Hatami K, 2020. Limit Analysis of Bearing Capacity and Failure Geometry of GRS Bridge Abutments. *Computers and Geotechnics*, 127 (November 2020), https://doi.org/10.1016/j.compgeo.2020.103758

Geosynthetics Conference

Sheffield GRS-IBS: Thermal Interaction between Superstructure and Substructure

Jennifer E. Nicks, Ph.D., P.E.,[1] Michael T. Adams,[2] and Mohammad S. Khan, Ph.D., P.E.[3]

[1] Federal Highway Administration, 6300 Georgetown Pike, McLean, VA 22101; email: jennifer.nicks@dot.gov
[2] Federal Highway Administration, 6300 Georgetown Pike, McLean; VA 22101; email: mike.adams@dot.gov
[3] High Performance Technologies, Inc. (HPTech), 13800 Coppermine Road, Herndon, VA 20171; email: mkhan@hptech-inc.com

ABSTRACT

The Geosynthetic Reinforced Soil Integrated Bridge System (GRS-IBS) technology blends the roadway into the superstructure to create a jointless interface between the bridge and the approach; however, the thermal superstructure movement and induced lateral pressures between the backwall and integrated GRS-IBS substructure are not yet well understood. This paper presents the results of a thermal monitoring program of the State Road (SR) 7A bridge over the Housatonic Railroad in Sheffield, MA after over 2 years of in-service performance. Small, longitudinal movements in the abutment were measured and compared with the theoretical movements of the superstructure and the corresponding lateral pressures behind the backwall. Lateral earth pressures on the reinforced backfill, due to the thermal expansion and contraction of the superstructure, were also measured. It is concluded that in a properly designed and constructed GRS-IBS, the differential thermal movement between the superstructure and substructure, and the resulting pressures, is not an impediment in the adoption and implementation of the technology; rather, the behavior is advantageous. Long-term performance monitoring of the bridge is ongoing to continue evaluating the trends over time.

INTRODUCTION

Geosynthetic reinforced soil (GRS), composed of alternating layers of compacted soil and geosynthetic reinforcement, has emerged as a low-cost, accelerated construction solution to many complex problems. Foundation systems constructed with GRS, such as bridge abutments and integrated bridge systems (IBSs), are increasingly being used. As of December 2016, more than 44 State highway agencies had deployed GRS-IBS technology to construct more than 200 bridges in a variety of environments; 11 States have adopted GRS-IBS technology as a standard practice (Harman, 2017; Alzamora, 2018). A recent manual developed by the Federal Highway Administration (FHWA) provides guidelines for the design and construction of GRS-IBS, materials specifications, performance monitoring, maintenance, and repair, along with quality assurance and quality control procedures (Adams and Nicks, 2018).

When the Massachusetts Department of Transportation (MassDOT) needed to replace the State Road (SR) 7A bridge over the Housatonic Railroad in Sheffield, MA, originally a three-span bridge supported on concrete piers and abutments, with a 105-ft single span, a GRS-IBS was eventually selected. The new bridge consists of steel girders with a cast-in-place (CIP) deck

supported on 14.6- and 18.4-ft-tall GRS abutments. FHWA provided technical support to MassDOT in the adoption and implementation of GRS-IBS; developed an instrumentation program for the GRS-IBS; and performed long-term monitoring to evaluate its long-term performance. The main purpose of the long-term monitoring was to evaluate the thermal interaction between the superstructure and substructure due to diurnal and seasonal temperature fluctuations, particularly since the bridge had a relatively a long span length and because it was skewed. The displacement profile of the GRS-IBS due to the expansion/contraction of the superstructure and the corresponding lateral earth pressures induced/relieved by the movement provide key insights into the interaction of the superstructure and this novel bridge abutment type.

BACKGROUND ON SUPER- SUBSTRUCTURE THERMAL INTERACTION

The role and impact of thermal interaction between the superstructure and substructure of bridges has long been recognized and investigated. Variation in the ambient temperature was cited as the major contributing factor to the movement of bridges in a study conducted by Emanuel and Lewis (1981). Temperature variations in the superstructure generate stresses along the span due to axial elongation or contraction. During expansion of the superstructure, the abutment and approach backfill resists the movement through the development of passive earth pressures. The passive earth pressures imposed on the backfill from an abutment undergoing displacement and rotation can be modeled using Rankine earth pressure theory. As the daily temperature increases from morning through the afternoon, the superstructure will expand, causing the abutment to push against the backfill, generating the highest passive pressure at the maximum displacement. Then, as the daily temperature decreases from late afternoon through the night, the superstructure will contract, causing the abutment to pull away from the backfill, which leads to active earth pressure conditions. The diurnal cycle of temperature variation and corresponding abutment movement continues throughout the life of the bridge (Hassiotis et al., 2006).

The American Association of State Highway and Transportation Officials (AASHTO) LRFD Bridge Design Specifications (2020) includes provisions for addressing stresses in the superstructure components caused by diurnal and seasonal variations in ambient temperature; however, the impact of using a GRS-IBS and its interaction with the superstructure is not provided because it is not yet well understood. The emergence of integral and semi-integral abutment bridges has brought the issue of thermal interaction between the superstructure and substructure back to the forefront. Integral abutment bridges, also known as jointless bridges, are bridges where the deck has no expansion joints and the substructure and superstructure move, expand, and contract as one integral unit. Semi-integral abutments are similar to integral abutments, except that the superstructure moves independently from the substructure, with the bridge traditionally supported on elastomeric bearing pads. Based on the typical design for a GRS-IBS, the technology can be considered a type of semi-integral abutment since the superstructure is not rigidly connected to the GRS abutment.

The concept of integral and semi-integral abutment bridges is more than a century old; however, State DOTs did not embrace the concept until the advent of the Hardy Cross method for the analysis of continuous frames in the 1930s. Integral abutment bridges were further recognized during the construction of the Interstate Highway System in the 1950s, and their acceptance kept growing since they eliminated leaky joints and deteriorated or frozen bearings, which are major contributors to bridge deterioration, and, in some cases, failure of bridges (Kunin and Alampalli, 2000). In 1980, FHWA recommended the use of integral abutment bridges for different types of

bridges, with span length as the controlling factor; for example, up to 500-ft span length for CIP concrete bridges (Hassiotis et al., 2006). Despite their growing acceptance and popularity, integral and semi-integral abutment bridges are still a small proportion of the National Bridge Inventory (NBI). In a 2007 report, integral abutment bridges and semi-integral abutment bridges in the United States were reported to be more than 9,000 and 4,000, respectively, compared to more than 610,000 bridges in the NBI (White, 2007). The lack of understanding of thermal interaction between substructure and superstructure, and limitations on span length and skew, are some of the factors that are limiting the widespread acceptance of integral and semi-integral abutment bridges.

Despite a number of experimental and analytical studies conducted in the past to design integral abutment bridges for thermal loads, in combination with other loads, the current state-of-the-practice for integral abutment bridges is primarily empirical and based on past experience and performance, rather than based on theoretical modeling grounded into realistic assumptions and actual field conditions. The research presented in this paper makes a valuable contribution to the knowledge base on semi-integral abutment bridges designed as a GRS-IBS, particularly in the understanding of thermal interaction between the superstructure and substructure. At the very least, the study will enhance the empirical database on the performance of semi-integral abutment bridges incorporating GRS-IBS.

SR 7A BRIDGE

The SR 7A bridge on Ashley Falls Road over the Housatonic Railroad is in Sheffield, MA. The bridge, with NBI number S10023BDDDOTDES, was originally a three-span structure, including two concrete piers and two concrete abutments (Figure 1a). MassDOT first considered conventional designs for the replacement, including abutments supported by either micropiles or spread footings; however, the construction challenges presented by the existing railway and the excessive estimated cost motivated MassDOT to consider and finally select a GRS-IBS. The new GRS abutments were moved farther from the railway track, supporting a single span length of 105 ft and eliminating the need for piers (Figure 1b). The estimated bearing pressure on each of the abutments due to the weight of the superstructure is 10.2 psi. The new bridge has a wider roadway, wider sidewalk, raised roadway profile, and deeper steel girders, skewed at 30 degrees. The selection of a GRS-IBS for the SR 7A bridge resulted in a cost savings of 49 percent compared to the conventional abutment options considered (Connors, 2016).

(a) **(b)**

Figure 1. (a) Original SR 7A bridge and (b) New SR 7A GRS-IBS. (Source: FHWA.)

The construction of the new SR 7A bridge started in April 2014, and the bridge was opened to traffic in November 2014. The sequence and timeline of construction was as follows: 1) GRS abutments were built during April to June; 2) beams were set and casting of the back walls was completed during July; 3) the CIP deck and GRS integrated approaches were constructed during August to September; 4) the asphalt concrete pavement was placed in October; and 5) construction of ancillary details was completed and the bridge was placed in service in November. At various stages of construction, FHWA installed the instrumentation for the GRS performance monitoring program.

Figure 2 is a cross section of the layout of the west GRS-IBS; the height of the west GRS abutment (H_{abut}) is 14.6 ft. The east GRS-IBS has a similar cross section, but the abutment is taller at 18.4 ft due to the difference in bedrock elevation at its location. In both cases, the height of the GRS integrated approach behind the backwall of the superstructure (H_{rb}) is 6.7 ft. The GRS abutments for the SR 7A bridge were constructed with a crushed, open-graded aggregate; the maximum aggregate size ranged from ⅜ to ½ inch. A 4,800 lb/ft woven, polypropylene geotextile was placed at a nominal spacing of 8 inches. The abutment facing consisted of concrete masonry units (CMUs) measuring 7 ⅝ by 7 ⅝ by 15 ⅝ inches. The geotextile reinforcement extended through each dry stacked course of block, creating a purely frictional connection with the CMUs. Bearing bed reinforcement was constructed directly underneath the beam seat of the superstructure to provide additional strength and reduce lateral deformation; the bearing bed reinforcement in a GRS-IBS serves as an alternative to traditional bearing pads. In the bearing bed zone, the reinforcement layers were placed at a spacing of 4 inches. The abutments were founded on a reinforced soil foundation (RSF) constructed above shallow bedrock, with a depth (D_{RSF}) of 1.0 to 1.5 ft.

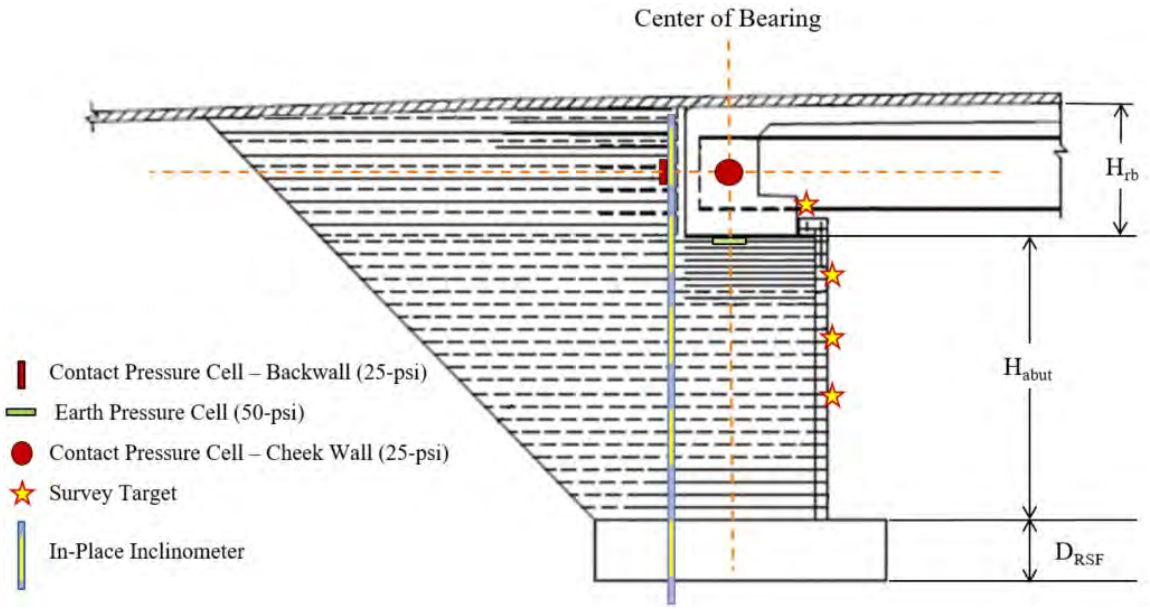

Figure 2. Cross section of the west abutment along with type and location of instrumentation. (Source: FHWA.)

The superstructure was placed on the GRS abutments in five stages (Figure 3a). The first stage included pouring concrete to construct the rectangular footings directly on the bearing bed reinforcement (Figure 3b); the girders were set and leveled on the footings in the second stage; the

third stage entailed a second concrete pour to fill the space between the rectangular footings and the girders; and the fourth and fifth stages were to form the backwall and cast the deck, respectively. The concrete footings had a bearing width of 2.5 ft and the backwall had a height of 6.7 ft. The five-stage design and construction approach results in the GRS abutments behaving similar to a semi-integral type of abutment.

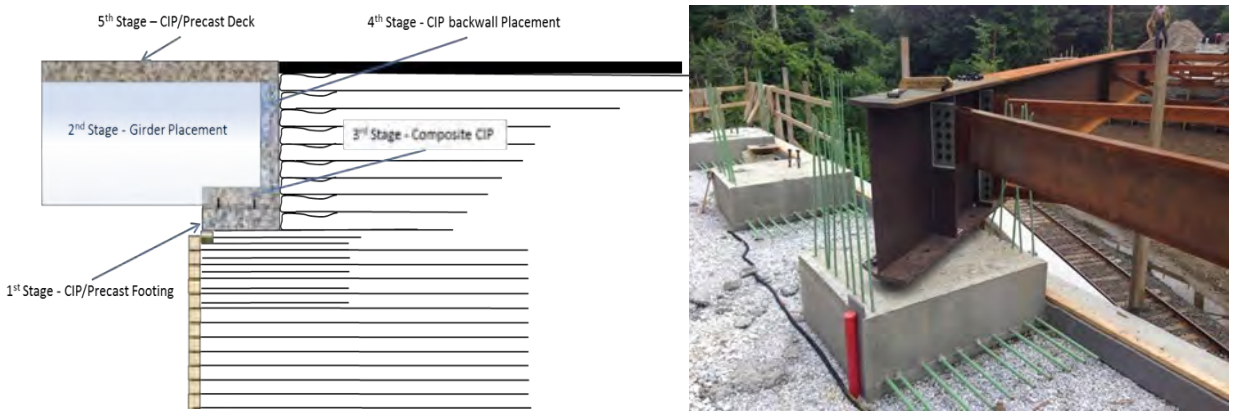

(a) **(b)**

Figure 3. (a) Super-substructure construction stages and (b) construction during stage 2. (Source: FHWA.)

INSTRUMENTATION PLAN

During construction, the SR 7A GRS-IBS was instrumented for long-term performance monitoring. The instrumentation plan used on the SR 7A bridge was adopted from a similar instrumentation plan that was successfully implemented on another GRS-IBS bridge constructed about 18 months before the SR 7A bridge (Nicks et al., 2020). Figure 2 shows a cross section of the instrumentation layout for the SR 7A GRS-IBS. Of particular interest in this paper are the lateral movements within the abutment, measured using in-place inclinometers (IPIs), and the lateral earth pressures behind the back and cheek walls, measured using contact pressure sensors. More information about the sensors used to monitor the responses are described below.

IPIs. IPIs using micro-electro-mechanical systems (MEMS) were installed to monitor the lateral movement at the integrated approach backfill–footing interface for each abutment (Figure 2). The casing that housed the IPIs was installed as the abutment was constructed. Since the bridge was skewed, the grooves of the IPI casing were aligned perpendicularly to the superstructure and along the centerline to capture the movement of the bridge. There were seven sensors located along the depth of the IPI casings for both abutments; for the east abutment, sensors were located at depths of 4.1, 8.2, 12.3, 16.4, 20.5, 24.6, and 28.7 ft below the top of the casing, and for the west abutment, sensors were located at depths of 3.0, 6.1, 9.3, 12.6, 15.9, 19.2, and 22.5 ft.

Contact Pressure Cells (CPCs). Five CPCs, each with a 9-inch diameter and a capacity of 25 psi, were installed for each abutment to measure lateral earth pressures behind the backwall and on the cheek walls and to evaluate thermal interaction and any effect due to the 30-degree skew. A plan view of the CPC instrumentation layout, including the nomenclature used to distinguish the results, is shown in Figure 4. For consistent pressure measurements, the position of each CPC was kept at

the same distance below the top of the bridge deck. Once the forms for the backwall and cheek walls were stripped, each CPC was attached by fastening four mounting tabs with plastic masonry anchors and screws. Prior to attaching the CPCs, a layer of cement grout was applied to each wall to provide a flat bearing area for the CPC. Once the CPCs were attached, it was necessary to protect them from fill placement and compaction during approach construction. A protective sand layer was placed in front of each cell using a plywood sheet as a form and the sheet was removed once fill material was placed.

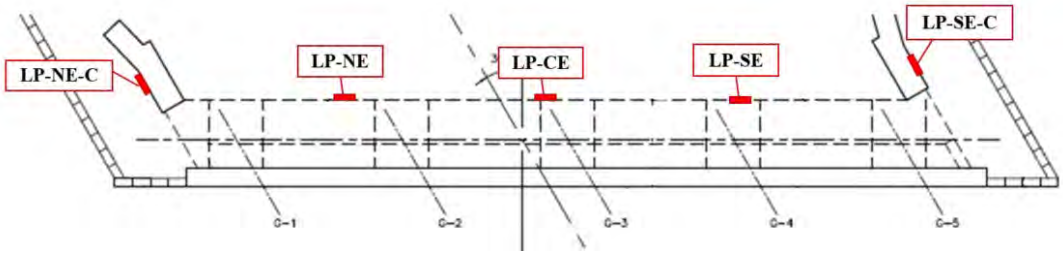

(a) East abutment

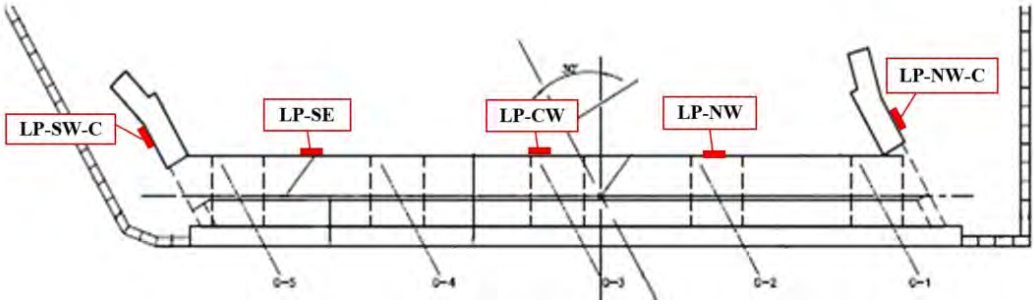

(b) West abutment

Figure 4. CPC instrumentation plan and nomenclature view for the SR 7A GRS-IBS. (Source: FHWA.)

RESULTS

Since the construction of SR 7A, completed in November 2014, a large volume of data has been collected remotely from various sensors installed on and within the two GRS abutments. The data presented and discussed in this paper is focused on the lateral displacement from the IPIs and the lateral earth pressures from the CPCs over a 2-year period to primarily evaluate the response due to the thermal cycles of the bridge, both diurnal and seasonal.

Lateral Displacement. Figure 5 shows the variation of temperature and change in cumulative lateral displacement measured at the top IPI sensor for both the east (IPI-E1) and west (IPI-W1) abutments during a diurnal temperature cycle for winter and summer days during the first year of being in service. The theoretical displacement of the superstructure is also shown, calculated assuming the coefficient of thermal expansion for the steel girders is equal to 7.2E-06 (Roeder, 2002). Note that positive values for the change in displacement indicate movement towards the GRS integrated approach; negative values indicate movement inwards towards the bridge deck or the railway tracks between the abutments.

The cyclic variation in the measured lateral displacement of the abutments corresponds to the daily changes in air temperature (as measured through a reference pressure cell (PC) located next to the remote data acquisition system). In general, a rise and fall in the temperature leads to expansion and contraction of the bridge superstructure, respectively; the measured movement behind the backwall from the top IPI sensors on each abutment indicates the expansion and contraction (Figure 5).

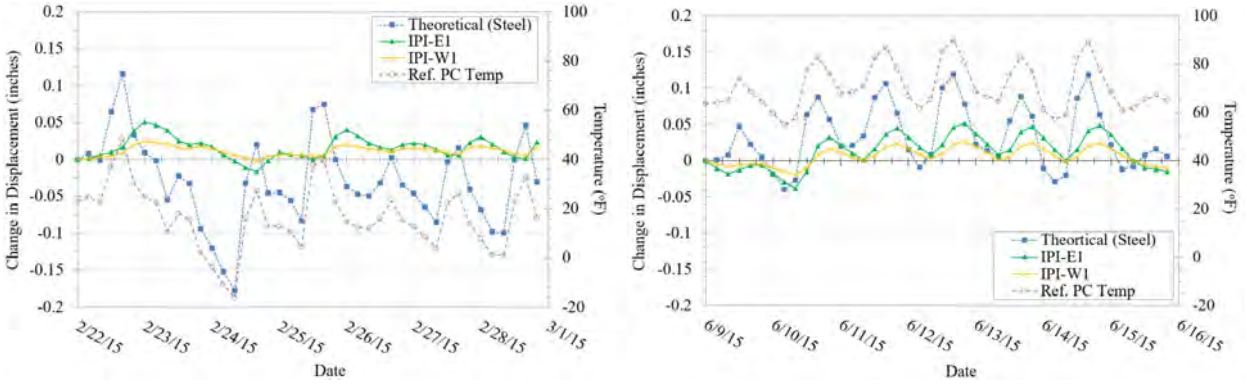

(a) **(b)**

Figure 5. Temperature and displacement during selected (a) winter and (b) summer days. (Source: FHWA.)

Note that there is a lag of about 6 hours between the maximum/minimum recorded air temperatures (and theoretical movement) and the maximum/minimum measured displacement. The 6-hour delay in response is likely due to the temperature differential between the air and the various bridge components (Ooi et al. 2019). Similarly, Lucas (2018) showed that the average measured temperatures of the deck and girders for a traditional semi-integral bridge in Ohio also cycled about 6 hours behind the air temperature. Lucas (2018) also showed that the steel girders had a lower measured temperature compared to the concrete bridge deck. The temperature differential may explain why the changes in measured displacement during diurnal cycles are within a range of about 0.05 inch, whereas the theoretical change in displacement is within a range of about 0.20 inch. The more minimal response measured during the winter as compared to the summer, and as compared to the theoretical movement, may be similarly due to the differences in thermal energy storage and dissipation within the superstructure components.

The changes in measured displacement in the east abutment are slightly more pronounced than the changes in the west abutment, with about a 0.025-inch maximum difference recorded over the 2 weeks capturing summer and winter timeframes (Figure 5). The difference in measured displacement could be due to the slight change in elevation between the top IPI sensors on each abutment; IPI-E1 and IPI-W1 are positioned at a depth of 4.1 ft and 3.0 ft from the top of the roadway, respectively. Another potential factor is the relative location of the abutments with respect to the thermal energy from the sun. Overall, however, the difference in magnitude is very minor, indicating that the bridge is longitudinally expanding and contracting uniformly along its centerline.

Figure 6 shows selected cumulative displacement profiles for the east and west GRS abutments over the first 2 years in service, from September 2014 to September 2016. The profiles show that the movement of the superstructure results in displacements throughout the height of the GRS integrated approach and abutment, stabilizing around the elevation of the RSF. A clear

inflection point in the displacement profile is seen corresponding to the location of the base of the superstructure footing. In addition to diurnal and seasonal variations in the temperature and associated thermal movement of the superstructure transferring to the substructure, changes in the properties of the composite concrete deck–steel girder, particularly the concrete deck, may also be contributing to the thermal movement (Warren et al., 2013). Concrete from the time of its placement and through its entire life undergoes drying shrinkage, particularly at early ages.

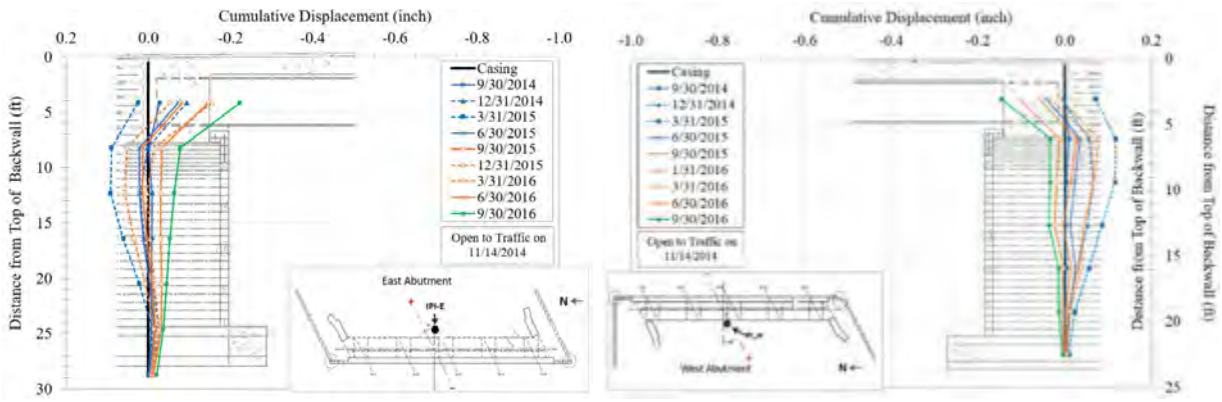

(a) **(b)**

Figure 6. Cumulative displacement of the (a) east and (b) west GRS-IBS. (Source: FHWA.)

The maximum cumulative displacement after 2 years in service is in the integrated approach behind the backwall, about 0.15 to 0.2 inch toward the railway tracks (Figure 6). The inward displacement is counterintuitive, considering during warmer weather, the superstructure should expand toward the integrated approach. One hypothesis is that the seasonal, inward movement is a result of consolidation within the GRS abutment due to the bridge, particularly considering the IPI casing is fixed to the backwall. In any event, the relative movement between the east and west GRS-IBS is similar during seasonal and diurnal temperature variations.

Lateral Earth Pressures. As the bridge expands when it heats up, the longitudinal movement will be resisted by the integrated approach behind the backwall, leading to an increase in the lateral pressure; pressure is then relieved as the bridge contracts. While the movement was only measured along the centerline of the bridge, lateral earth pressures were measured at midheight along the length of the backwall (south, center, and north) and on both the obtuse and acute cheek walls (Figure 4). The lateral pressure measurements will provide some indication into any differential pressures due to movement of the skewed bridge against the integrated approach and associated wing walls.

Figures 7 and 8 show the variation of temperature and lateral earth pressures during a diurnal cycle in winter and during a diurnal cycle in the summer for both abutments, respectively. As expected, the lateral earth pressures increase as the temperature increases (i.e., as the bridge expands) and decreases as the temperature decreases (i.e., as the bridge contracts). Note that the negative lateral earth pressures likely indicate a separation of the back/cheek wall from the integrated approach/wingwalls, although the negative values, instead of zero lateral earth pressure, are artifacts of the instrumentation. Similar to the IPI sensor readings, there is a delayed response between the air temperature and the pressure response.

The variation of lateral earth pressures during winter is more pronounced than that during the summer; similarly, there is more activity on the west abutment than the east abutment. The

larger range of lateral pressures along the backwall in the winter (about 3 psi) may be due to the fact that the bridge was constructed in the summer, so as the bridge returns to its "initial" state, there is less interaction at the integrated approach–bridge interface. Another potential reason may be moisture infiltration and the formation of ice lenses around the pressure cells. The greater pressure fluctuations behind the backwall compared to the pressure fluctuations behind the cheek walls be may be that the superstructure reacts more longitudinally than transversely due to thermal cycles, since the greatest mass is in that direction.

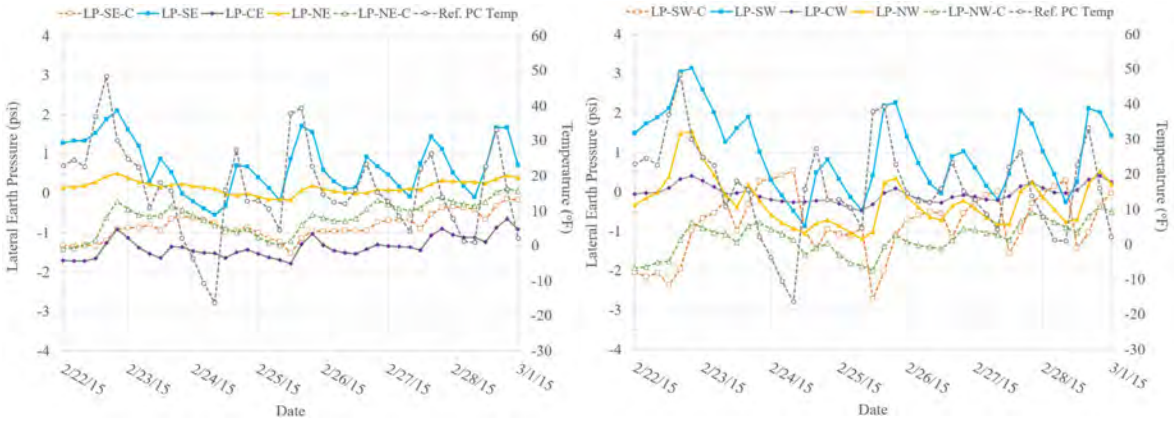

(a) **(b)**

Figure 7. Lateral pressures for the (a) east and (b) west abutment during winter. (Source: FHWA.)

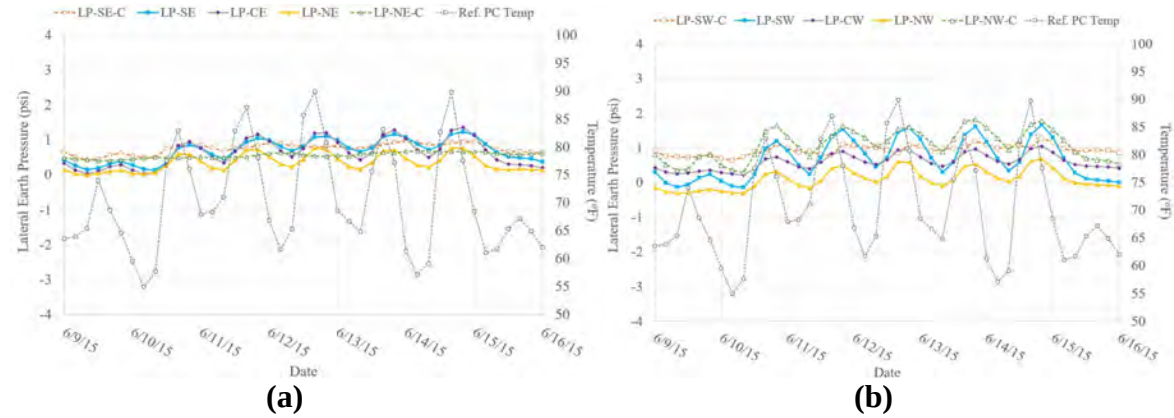

(a) **(b)**

Figure 8. Lateral Pressures for the (a) east and (b) west abutment during summer. (Source: FHWA.)

Figure 9 shows the lateral pressures measured over the first 2-year period. While the pressures change with temperature, there is no appreciable increase in magnitude over the period evaluated. No appreciable increase in magnitude may indicate that the GRS-IBS, particularly the integrated approach and wingwalls, successfully resist the eccentricity in passive pressures caused by the skew of the superstructure. As hypothesized before, the spikes seen in the winter months are possibly due to infiltrated water that froze around the CPCs. In general, however, the measured pressures are within the pressures expected for the backfill during at-rest or active conditions; there is not enough movement to fully mobilize passive pressures.

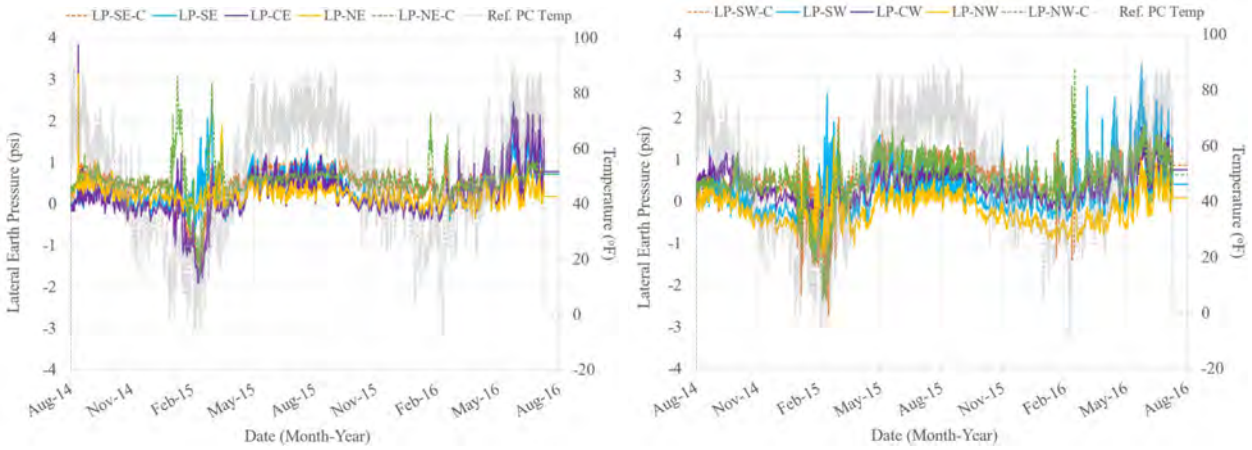

Figure 9. Measured lateral earth pressures behind (a) east and (b) west backwall and cheek walls. (Source: FHWA.)

DISCUSSION

The lateral displacements and lateral earth pressures measured in the two GRS abutments is considered small, with excellent long-term performance of the substructure expected. The lateral displacement profile along the depth of the two abutments is very similar with higher displacement at the top and diminishing to almost zero at the bottom. The east abutment has exhibited a slightly higher negative movement when the abutment pulls away from the soil during falling temperatures, but it is still small. The difference in the lateral displacement of the two abutments may be attributed to the fact that the east abutment is taller than the west abutment.

As small as the lateral displacement and lateral earth pressure in this study are, they are not solely temperature-induced. Rather, they are also a combination of gravity and temperature-induced loads. In the study of New Trammel Creek bridge by Zhihui et al. (2015), it was noted that the contribution of temperature-induced pressure was, on average, 33 percent of the bearing pressure induced by combined gravity and temperature-induced loads. The New Trammel Creek bridge is an example of an integral abutment bridge with traditional design and construction practices. The bridge consists of concrete deck over concrete girders supported by two abutments and three intermediate piers. Based upon finite element modeling, Zhihui et al. (2015) estimated a combined gravity and temperature-induced pressure of 29.2 psi, and temperature-only induced pressure of 9.8 psi.

The lateral displacement data obtained in this study can also be compared with lateral displacement of abutments for traditional integral abutment bridges in studies by others. For example, a detailed parametric and field monitoring study of two Illinois bridges was conducted by LaFave et al. (2017). The bridges studied included the eastbound Kishwaukee River bridge and the eastbound Union Pacific Railroad (UPRR) bridge along I-90. The Kishwaukee River bridge, constructed in 2013, is a four-span and 549-ft-long integral abutment bridge supported on steel piles. The UPRR bridge, constructed in 2014, is a single-span and 184.5-ft-long integral abutment bridge supported on steel piles. From field monitoring of eastbound Kishwaukee River bridge, lateral displacement of the north abutment varied from 0.5 to -2 inches and the lateral displacement of the south abutment varied from 1 to -1.8 inches. Comparatively, the lateral displacements for

SR 7A varied from 0.1 to -0.1 inch for the east abutment and 0.1 to -0.25 inch for the west abutment.

The parametric and field investigation study of the two bridges by LaFave et al. (2017) is preceded by a detailed parametric study on the influence of thermal loading on the performance of integral abutment bridges in general (LaFave et al., 2016). Both studies make a point that, in the past, studies related to the influence of thermal loading in bridges have focused more on substructure and less on superstructure. The primary focus of the two studies is superstructure, including deck, girder, and approach, with limited focus on substructure.

CONCLUSIONS

The deteriorated and structurally deficient three-span SR 7A bridge over the Housatonic Railroad, located in Sheffield, MA, was replaced with a single-span GRS-IBS in 2014. The bridge has two abutments, without any intermediate piers, deck joints, or traditional bearings at the interface of deck and the abutments. The abutments were constructed utilizing the GRS-IBS technology and instrumented with a variety of sensors to measure lateral displacements and pressures due to the thermal movement of the superstructure. The results presented are over a period of 2 years using a remote data acquisition system. Initially, the thermal interaction between the superstructure and substructure was not well understood, although empirically, there have been no concerns when employing GRS-IBS. The results of this study have clearly demonstrated that the SR 7A GRS-IBS has performed better than the traditional integral abutment bridge configuration (i.e., deck–girder–pier–pile configuration). The lateral displacement and lateral earth pressure of the abutments are much smaller compared to traditional integral abutment bridges that have been constructed, instrumented, and monitored within a similar time frame as that of SR 7A bridge.

The monitoring of the SR 7A bridge is ongoing, and a condition survey of the superstructure is planned to have a holistic view of the performance of the bridge. The superstructure of the SR 7A bridge, including the CIP deck and the steel girders, was not instrumented in this study. Also, a parametric study of the bridge is planned to compare the field monitoring data with a theoretical model.

REFERENCES

AASHTO. (2020). *AASHTO LRFD Bridge Design Specifications, 9th Edition*. AASHTO, Washington, DC.

Adams, M. and Nicks, J. (2018). *Design and Construction Guidelines for Geosynthetic Reinforced Soil Abutments and Integrated Bridge Systems*, Report No. FHWA-HRT-17-080. FHWA, Washington D.C.

Alzamora, D. (2018). “Turning Skeptics into Adopters.” *Public Roads, 82*(1). FHWA, Washington, D.C.

Connors, P. (2016). “*Performance of Geosynthetic Reinforced Soil Integrated Bridge Systems (GRS IBS): RT 7A Over Housatonic RR (2014).*” Workshop sponsored by the Transportation Research Board Committees on Geosynthetics and Transportation Earthworks, Transportation Research Board 2016 Annual Meeting, Washington, D.C.

Emanuel, J.H. and Lewis, D.B. (1981). “Abutment-Thermal Interaction of Composite Bridge.” *Journal of Structural Engineering, 107*(11), pp. 2111–2126. American Society of Civil Engineers (ASCE), Reston, VA.

Harman, T. (2017). “What’s New Today is Mainstream Tomorrow.” *Public Roads, 81*(2). FHWA, Washington, D.C.

Hassiotis, S., Khodair, Y., Roman, E., and Dehne, Y. (2006). *Evaluation of Integral Abutments*, Final Report FHWA-NJ-2005-025. Stevens Institute of Technology, Hoboken, NJ.

Kunin, J. and Alampalli, S. (2000). “Integral Abutment Bridges: Current Practice in United States and Canada.” *Journal of Performance of Constructed Facilities, 14*(3), pp. 104–111. ASCE, Reston, VA.

LaFave, J.M., Fahnestock, L.A., Wright, B.A., Riddle, J.K., Jarrett, M.W., Svatora, J.S., An, H., and Brambila, G. (2016). *Integral Abutment Bridges Under Thermal Loading: Numerical Simulations and Parametric Study*, Research Report No. FHWA-ICT-16-014. Illinois Center for Transportation, University of Illinois at Urbana-Champaign, Urbana, IL.

LaFave, J.M., Fahnestock, L.A., Brambila, G., Riddle, J.K., Jarrett, M.W., Svatora, J.S., Wright, B.A., and An, H. (2017). *Integral Abutment Bridges Under Thermal Loading: Field Monitoring and Analysis*, Research Report No. FHWA-ICT-17-017. Illinois Center for Transportation, University of Illinois at Urbana-Champaign, Urbana, IL.

Lucas, J.S. (2018). *Temperature Effects on Skewed Semi-Integral Bridges*. Master’s Thesis, Russ College of Engineering Technology, Ohio University, Athens, OH.

Nicks, J.E., Adams, M.T., Stabile, T., and Li, J. (2020). *Instrumentation and 5-Year Performance Monitoring of A GRS-IBS in St. Lawrence County, NY*, Report No. FHWA-HRT-20-040. FHWA, McLean, VA.

Ooi, P.S.K., Adams, M.T., and Lawrence, J.B. (2019). “Long-Term Behavior of a Geosynthetic Reinforced Soil Integrated Bridge System in Hawaii.” *Transportation Research Record: Journal of the Transportation Research Board*. Sage Journals, Thousand Oaks, CA.

Roeder, C.W. (2002). *Thermal Movement Design Procedure for Steel and Concrete Bridges*, National Cooperative Highway Research Program Report 20-07/106. Transportation Research Board, National Research Council, Washington, D.C.

Warren, K.A., Whelan, M., Adams, M., and Nicks, J. (2013). “*Preliminary Evaluation of Thermally Induced Strains and Pressures Developed in a GRS Integrated Bridge System*.” Geosynthetics Conference 2013, Long Beach, CA.

White, H. (2007). *Integral Abutment Bridges: Comparison of Current Practice Between European Countries and the United States of America*, Special Report 152. Transportation Research and Development Bureau, New York State Department of Transportation, Albany, NY.

Zhihui, Z., Davidson, M.T., Harik, I.E., Sun, L., and Sandefur, K. (2015). “Effect of Superstructure Temperature Changes on Intermediate Pier Foundation Stresses in Integral Abutment Bridges.” *Journal of Bridge Engineering, 20*(1). ASCE, Reston, VA.

Geosynthetics Conference

Geosynthetic Portable Coffer Dams for Civil Construction Applications

Brian Fraser,[1] and Mike Neal[2]

[1]Layfield Geosynthetics, 10038 Marathon Parkway, Lakeside, CA 92040, United States, email: brian.fraser@layfieldgroup.com
[2]Layfield USA, 10038 Marathon Parkway, Lakeside, CA, 92040, United States, email: mike.neal@layfieldgroup.com

ABSTRACT

Geosynthetic cofferdams are increasingly utilized for civil construction applications including dewatering, flood control and sediment control. This paper describes one of the more commonly used geosynthetic dam system which was developed in the early 1990's and has been used extensively in North America as a portable cofferdam. It is a water control structure designed to source water directly from the stream, river or pond to control, contain and divert the flow of water. It is used in applications such as dewatering for bridge foundation work, dam repair, pipeline crossing, canal liner repair and shoreline construction and restoration. Geosynthetic dams provide an economical and modular alternative to conventional construction of earth dikes and mechanical sheet piling in these applications.

This paper highlights a recently installed 1,400 lineal foot (427 m) project to control sediment during the excavation of a new channel during bridge construction in Kilisut Harbor, Washington. The North Olympic Salmon Coalition (NOSC) and the Washington State Department of Transportation (WSDOT) were looking to restore the historic tidal channels and fish runs between southern Kilisut Harbor and Oak Bay in Jefferson County, Washington. This challenging tidal application required the portable geosynthetic dams be installed in various heights up to 12 feet (3.66 m) to isolate the channel for dewatering and sediment removal using excavators and dump trucks.

Figure 1. Installation of 6' Cofferdams – Eagle River, CO

Figure 2. USACE 10' & 8' Cofferdam - Baytown, TX

INTRODUCTION

Cofferdams by definition are an enclosure built within or across a body of water to allow the enclosed area to be dewatered. This creates a dry working environment so that construction can be carried out properly and safely. Typical cofferdams are welded steel structures consisting of sheet piles, wales or cross braces and are normally dismantled after construction. However new portable or temporary geosynthetic cofferdam systems provide an effective alternative. These systems come in a variety of different designs, materials and installation methods and provide a more economical solution for temporary site dewatering versus conventional structural cofferdams. Portable geosynthetic cofferdams are typically lighter weight modular systems produced from geomembrane and geotextile fabrics. They limit the impact of construction generated silt and sedimentation when excavating in submerged or dredging areas, which lessens the environmental impact. Most systems are also modular in design allowing for bends and turns in the project waterway. They can also be installed and removed quicker than standard structural cofferdams which makes them more cost-effective. Properly handled, these dams can also be drained and re-used, eliminating the need to purchase a new dam for different projects in some instances. Common applications for the geosynthetic portable cofferdams include dewatering for bridge foundations, dam repairs, pipeline crossing, irrigation canal repair and shoreline construction and restoration. Smaller diameter geosynthetic dams are also used extensively for flood control barriers. Figure 1 and 2 above show the installation and applications of the geosynthetic cofferdams.

For this paper, the cofferdam system produced by the manufacturer consists of two geomembrane tubes contained by a high strength woven textile outer tube. The two inner tubes are filled with water which creates a stable, non-rolling water-controlled structure. A center baffle curtain is installed for stability, reducing movement or tipping as a result of hydrodynamic loading. The local water source is normally used to fill the inner tubes of the dam. This cofferdam dam system was first introduced in the early 1990’s and is constructed in a range of sizes from 4’ diameter to 16’ diameter in standard 100’ and 200’ lengths. Special connecting collars are used to join the dams during installation. Standard fill and drain ports are installed

into each dam. Installation of the dams requires trained technicians and equipment and can be far more difficult in moving water applications versus slow or still water projects. Special patch kits and repair techniques are used in the event the dams are punctured during the installation or in application. Figure 3 below shows the modular capabilities of the portable cofferdams.

Figure 3. 6' Geosynthetic cofferdams for pipeline repair in Manitoba, Canada

DESIGN & ENGINEERING

This section summarizes the system stability and engineering needs of the water filled manufacturers dams. System stability is critical to the successful use and installation of the portable cofferdams. The basic principle behind the water filled dam system incorporates a dual inner tube system with a center baffle to stabilize the entire structure. This is shown in figure 4 below. The safety factor against sliding depends greatly on the coefficient of friction of the material that the dam is sitting on. In this case where it is sitting on a wet grass surface, the coefficient of friction used is 0.20 (Noon, 1994). The factor of safety against sliding is 1.33 when 24" (0.61 m) of water is being held back.

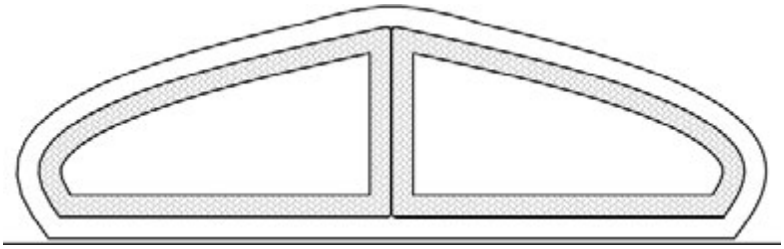

Figure 4. Schematic of water filled dam with inner tubes

As the water builds on one side of the dam, the inner tubes prevent rolling and the dam behaves as a solid barrier as shown in Figure 5.

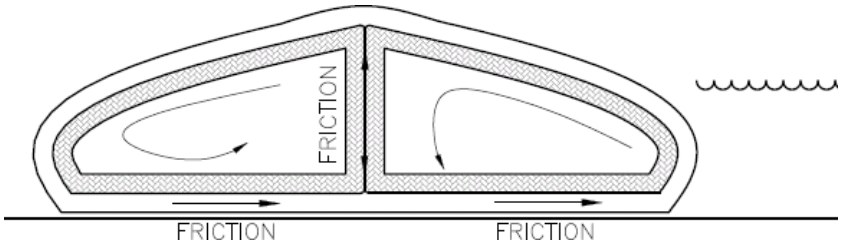

Figure 5. Stability of water filled dam to hydrodynamic loading

Engineering designs with proper calculated safety factors are required based on individual manufactured systems and project specific site conditions. Under hydrodynamic loads the portable dams need to be designed to resist sliding, tipping, and overturning. In order for the manufacturers dam to move as a result of the pressure exerted on one side, it must either be tipped over or slide across the surface on which it rests. In order to tip, the water pressure must lift the first inner tube up and over the second. The following calculation verifies the dam's resistance to tipping:

Assumptions:
The inner tubes are assumed rectangular when filled to facilitate the calculations. The water level on one side will assumed to have reached the top of the Aqua Dam to simulate the worst-case scenario.

P = Pressure
h = water depth
D = width of Aqua Dam
l = length of Aqua Dam
Þ = mass density of water
g = gravitational acceleration
y = specific weight of water
F = Force exerted on the face of the Aqua Dam due to pressure (P)
A = area of the side face of the Aqua Dam
W = weight of water in the inner tube
V = Volume of the inner tube
P = Þgh = yh
Pavg = y(h/2)
A = hl
F = PA = Pavg A
W = yV

The force exerted on the side of the water structure is defined as: $F = \gamma \frac{h}{2} hl$

Having determined the force on the side of the Aqua Dam, the tendency of the Aqua Dam to tip can be evaluated. Point A is assumed the pivot point and moments are calculated about this point. The moment created by each force, is a measure of how much the force contributes to rotating the first column of water around point A. The two formulas are shown below:

$$\sum M_A = W\frac{1}{2}D - F\frac{n}{3} = 0$$

Equation 1. Formula for calculating tipping forces

$$\sum M_A = \rho h\frac{D}{2}l\frac{D}{2} - \rho\frac{h^2}{2}l\frac{h}{3} = 0$$

Equation 2. Optional formula for calculating tipping forces

Simplifying the expression, it is observed that the stability of the dam is dependent on the relationship between its width (D) and the depth of water it must resist. The relationship above indicates the minimum width of the dam to prevent it from tipping when resisting water with a depth (h) equal to the height of the dam itself. The design height for the water structures to prevent tipping would be described as: D> (.82) h

In order to quantify the stability of the dam, the actual dimensions of the standard dam for D and h are substituted into the equation above. The results are expressed in terms of a safety factor. The safety factor indicates how many times greater the water pressure or water depth must be in order to roll the dam.

Based on the current dam designs, the safety factor against tipping when water levels are to the top of the structure as per table 1 below:

Table 1. Design Factor of Safety for Water Level at Top of Manufacturers Dams

B	Inflated Width (in inches)	Safety Factor Against Tipping
36”	68	2.30
48”	120	3.48
72”	186	3.15
84”	282	4.12

Additional site-specific details and risk assessment must also be predetermined for each project. This is done by completing a detailed site assessment prior to installation. Important criteria required for this assessment includes the water body type (lake, river, stream, ocean), anticipated water depth, historical water depths, water flow rates, freeboard level, and ground surface conditions. Site specific project assessment forms are required by the manufacturer for each project estimate.

PROJECT PROFILE – KILISUT HARBOR

In 2019, the North Olympic Salmon Coalition and the Washington State Department of Transportation needed to restore the historic tidal channels and fish runs between southern Kilisut Harbor and Oak Bay in Jefferson, County Washington. This included removing the outdated culverts and installing a new elevated bridge which replaced a causeway as part of creating 2,300 acres of productive fish habitat in the Puget Sound region. The first phase of this project included restoration of the channel on the north side of the highway in a sensitive marine environment. Figure 6 shows the cofferdams being deployed during tide out conditions.

Figure 6. Kilisut Cofferdams being deployed in low tide

PROJECT SCOPE

As part of the new bridge construction, the project scope required the contractor to excavate and dewater a large channel in a very environmentally sensitive region for the protection of salmon stocks and their migration. To address these environmental concerns, silts and sedimentation from construction had to be tightly controlled. Based on the project constraints, the engineer and contractor chose a temporary portable coffer dam. Layfield USA Corporation's modular cofferdam system was chosen for the project. The project scope including the manufacturing and installation support of 1,400 feet (427 m) of multiple sizes dams in sizes of 4', 6', 8', and 12' (1.22, 1.83, 2.44, 3.66 m) in heights. The installation started in September 2019 with a crew of seven field technicians.

Figure 7. Kilisut Harbor Cofferdams

PROJECT CHALLENGES

The project faced a number of unique challenges. One of the main challenges was working in tidal conditions which required the installation of the dams to only take place during low tide cycles. The contractor was also not allowed to operate equipment on the majority of the site in order to protect the pickle grass and wetlands area. This required many of the dams to be unrolled and positioned manually. With the multiple size dams, special fabricated collars were manufactured to connect the different sizes on site.

Figure 8. Aerial view of completed Kilisut Cofferdam installation

Figure 9. 8' Cofferdams being installed - Toppenish, WA

CONCLUSION

The installation of the modular dams took 7 days to complete and were drained and removed in January 2020. The dams performed successfully with the contractor being able to complete solids removal from the channel in dry conditions. This was a significantly faster method versus if they had had to rely on a vacuum dredge. The use of the temporary cofferdams was a key

component in providing an environmentally safe and successful installation. It also provided major cost savings to the contractor and project owner.

Civil engineers and contractors are increasing the use of portable geosynthetic cofferdams to help control water in a variety of excavation and dewatering applications. While there are numerous systems available, each system should be individually reviewed and engineered for each application in order to reduce the risk of failure and ensure safe work conditions. When properly designed and installed, portable geosynthetic cofferdams can provide numerous economic and environmental advantages when used to control water.

REFERENCES

Wikipedia contributors. (August 10, 2020) Cofferdams, In Wikipedia, The Free Encyclopedia, https://en.wikipedia.org/wiki/Cofferdam

Sati, R., (2011) Case Study: Performance of rapid respond flood control system during 2011 flood in Manitoba. 2011 Geo Manitoba, Winnipeg, MB, Canada

Noon, R.k (1994). Engineering Analysis of Vehicular Accidents, CRC Press, Boca Raton

Geosynthetics Conference

High Strength Polymeric Geocell-Reinforced Railway Line Repair in Degraded Permafrost Condition

Sanat Pokharel, Ph.D., P.Eng.[1] and Marc Breault[2]

[1]Principal Engineer, Stratum Logics, AB, Canada; e-mail: sanat.pokharel@stratumlogics.com
[2]President, Paradox Access Solutions, AB, Canada; e-mail: marc@paradoxaccess.com

ABSTRACT

Permafrost degradation by human interventions and climate change has been a serious concern for infrastructure development in the pristine physiographic setting of Northern Canada. Several First Nation settlements spread over that region need permanent year-round access for uninterrupted supply of basic need items. The railway line built a century ago leading to Churchill in Manitoba crosses many stretches of permafrost. The flood in 2017 washed away sections of the railway line rendering the only on-land access to the town unusable. Repair was immediately needed to avoid airlifting the essential commodities for the residents, but it took two years to find an innovative way to do it. There was exposed permafrost at the washout sections, and as it was a linear project, access to the next location was possible only after repairing the damage preceding it. Limited access and construction material and harsh weather conditions were other obstacles. This paper discusses the rehabilitation work using high-strength novel polymeric alloy (NPA) geocell. The findings in this paper are supported by design basis and experience-based construction practice, photographs, and construction records. The two years of track operation has presented a promising technology for the future of transportation infrastructure in the permafrost region.

INTRODUCTION

Churchill is a port city located on Hudson Bay in Northern Manitoba at the mouth of Churchill River. The nearest road head is at the village of Gillam approximately 300km south. The history of the railway discussed in the paper dates back over a century. Hudson Bay Railway (HBR) was initiated in the early 1900s and completed in 1929 to serve as the only mode of land transport to Churchill. This single line railway track has served the northern port of Manitoba uninterrupted since then. It may have lived up to expectation but due to the lack of timely maintenance and upgrades it gets damaged putting extra burden on the maintenance budget and interruption in the services. The railway built on extremely soft ground crosses many stretches of permafrost. In recent years, permafrost deterioration caused by rising temperature and degradation caused by other forms of human intervention has impeded the smoothness of the rail ride and other serviceability features of this rail line. In the spring of 2017, the railway line was severely damaged by the flood in the streams crossing the rail line, some of the damage may have been further aggravated by the degrading permafrost. As the only mode of ground transport feeding the town was rendered unusable everything including the goods of daily need for the local population was air lifted causing further hardships to the remote town, where the daily mean temperature remains subzero for over 8 months in a year.

Even before this 2017 washout, in May 2016 a visit was arranged for the authors by the railway company with the track maintenance personnel to assess the impact of degrading

permafrost on the railway track. Then some measures were also recommended to improve the track condition, especially geocell reinforcement to control the lateral spreading of ballast/sub-ballast material and to reduce the stress transferred to frozen subgrade. That time they were looking to improve the track condition to bring the train speed to 50km/hr throughout the entire length of the track up to Churchill. However, at this time, the intent was a quick and affordable solution to repair the damage caused by recent track washout and re-establish the access at the earliest possible time. Traditional ways of track repair had very high anticipated costs and a longer construction schedule due to the linear nature of the project. Strength requirement at the embankment substructure, erosion control and permafrost protection were other major issues that needed due attention. An innovative design was required to complete the job in 5 weeks duration and total cost was in the range of 20-25% of the over $100million as initially anticipated for the entire rehabilitation work.

For the railway embankment structure, authors had suggested the need for a robust structure to withstand the railway traffic while optimizing the construction costs and utilizing the available resources in that area. The general rule recommended by Pokharel et al. (2017) for other pavement structures applies to the railway tracks too. Hence, high strength Geocell reinforcement is an appropriate solution for the ballast or sub-ballast layer strengthening.

This paper discusses the design and the construction methodology applied using high-strength novel polymeric alloy (NPA) Geocell to complete the work in 5 weeks of Fall 2018 within the anticipated budget. The findings in this paper are supported by design basis and innovative construction practice, photographs, and construction reports. Attempts made to protect the permafrost under the rail line has also been explained. Based on over two years of operation of the railway line, this paper also recommends a viable method for the future of transportation infrastructure development in the permafrost region.

GEOCELLS ON RAILWAY APPLICATION

Geocells was originally developed by the US Army Corps of Engineers to increase the vehicular mobility over loose, sandy subgrade through confinement (Webster and Alford, 1978). Pokharel (2010) and Han et al. (2010) had identified three key mechanisms of geocell reinforcement as lateral and vertical confinement, wider stress distribution and the beam or slab effect. The higher stiffness of the geocell system reduces the stress applied to the subgrade due to bending stiffness of the mattress composite, similar to a slab (Pokharel et al., 2011). Giroud and Han (2016) clearly identified geosynthetics reinforcement to continue to contribute to the structural performance of pavement structures. On road pavement applications Norouzi et al. (2019) had discussed the state of the art of the pavement design method and emphasized the need for a robust structure that experiences repeated loading, recommending Geocell reinforcement as one of the reliable options. Railway embankments also undergo extensive cyclic loading and must be able to withstand the applied repeated load occurrences at the same time be economical to be sustainable in long term. The need for more robust embankment structure poses a huge challenge to the supply of granular material that are of the adequate quality and are affordable (Pokharel et al., 2017). Where a good quality material is not easily available, it requires a strong, high modulus and creep resistant geosynthetic reinforcing material at the substructure. Ability of geocells to use recycled, marginal or poorly graded granular material helps reduce the burden on environment and adds value to the design. In railway applications for the reinforcement of structural layers, Geocells can be used to reinforce the ballast or sub-ballast to improve the reinforced layer’s modulus and reduce the stress

transferred to the soft subgrades (Kief, 2016). NPA Geocell that was used in this project enables the use of inferior quality locally available granular material while improving the modulus ratio over the underlying surface by up to 7.6 times; the higher the strength and stiffness of the reinforcing geocell material the higher will be the improvement factor (Pokharel, 2010). This eliminates the need for hauling high quality granular material that is usually located far from the construction sites resulting in reduced CO_2 emission associated with the construction activities (Pokharel et al., 2016). This cost saving and environmental benefits of geocell reinforcement make them an attractive option from a sustainable development perspective.

Leshchinsky and Ling (2013) had found that the lateral spreading along the railroad substructure was greatly reduced with the ballast confinement with geocells. The prevention of lateral spreading is especially pronounced when the railway substructure overlies softer subgrades and weaker ballast material were used. The use of high strength Geocell confinement resists this spreading above the reinforcement through frictional resistance to the composite mattress and produces uniform stress distribution to the subgrade to a wider area significantly reducing magnitudes of stresses. Leshchinsky and Ling (2013) also reported that the confinement of the ballast using geocell was quite effective in reducing vertical deformations, especially when low-quality material was used. Palese et al. (2017) had conducted performance tests on Amtrak's Northeast corridor near Harve de Grace, MD, USA with NPA Geocell reinforcement in the track substructure. The material was selected due to its strength and creep resistance properties on the FRA (Federal Railway Administration) Class 7 track sees traffic from both highspeed trains (201km/hr) and higher speed regional trains (177km/hr). Palese et al. (2017) reported significant reduction in pressure at the ballast/subgrade interface on the order of 50% as well as a corresponding reduction in the rate of degradation on the order of a factor of 6+. Overall, the test based on the pressure data from load cells placed above the subbase directly beneath the rails and track geometry data had shown significant benefits associated with the installation of the NPA geocell material above and beyond that seen by more traditional rebuild and drainage improvement.

HBR TRACK REHABILITATION AND PERMAFROST CONSIDERATIONS

Designing Sustainable Infrastructure with limited engineering data is always a challenge and more so when it comes to where minimal interference to the environment is expected. Rehabilitation of HBR line had similar challenges as it passes through several stretches of permafrost. The rail line was damaged by flood that was triggered by melting snow and rain, that caused damages to the underlying permafrost as well. This, compounded with the harsh winter, shorter construction season and linear construction sequence, demanded a solution that could address all these issues and complete the work within reasonable time and budget. A design with NPA Geocell reinforcement for the railway embankment addressed issues like:

i) providing necessary structural strength for the railway traffic,
ii) protecting the underlying permafrost from further degradation,
iii) Controlling erosion at the embankment slopes against snow melt and creek flows,
iv) facilitating linear construction schedule to be completed within available time and budget significantly less than that estimated for conventional construction.

The pre-flood condition of the track in May 2016 and post flood condition in Spring of 2017 and 2018 are shown in Figures 1 through 3.

Figure 1. The condition of railway line in May 2016.

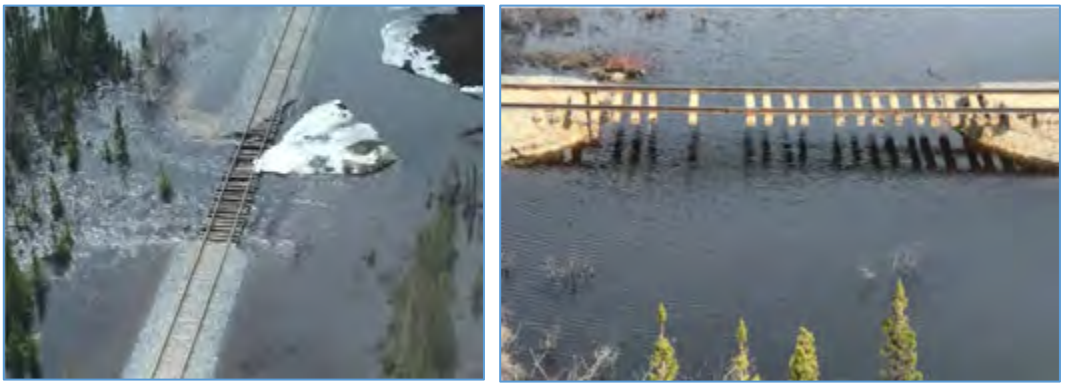

Figure 2. The railway line during the flood in 2017, aerial view. (Global News, 2017)

Figure 3. The condition of railway line after the flood event pictures from 2018.

Very little has been done in dealing with the infrastructure development in permafrost region. Innovative design, construction methods with minimal interference to the surroundings and the protection of the permafrost below the structure is important both for the stability of the structures and to control the degradation of the permafrost. Global warming and other human interventions have led to permafrost degradation as shown by deepening of the active layer, thinning permafrost, rising ground temperatures, expanding taliks and the disappearance of permafrost patches (Jin et al., 2007). Climate change could be the real cause of permafrost degradation but the excessive and unwarranted human intervention to the pristine environment are other important causes that need to be addressed immediately with due diligence. Surface melt due

to warm temperature causes permafrost degradation and at the same time as the subsurface is frozen impermeable medium entire melt becomes surface flow causing floods resulting in damage to the infrastructure and environment. Any design work in this region therefore is needed to avoid creating further problems upstream and downstream location of the creek crossings as well.

Several techniques have been implemented in Tibet (Wu et al., 1998, Wang et al. 2009, and Qi et al., 2012) to construct sustainable transportation infrastructure in Tibetan permafrost region most of them focusing on protecting the permafrost from degradation. One of the major technologies that could protect the underlying permafrost under the railway track is having a cover of geocell mattress that reduces the stress transferred to the subgrade and keeps the cover intact to protect the permafrost. The HBR track in Manitoba was facing severe problems caused by the lateral spreading of the ballast and sub-ballast material. There was erosion of the embankment material too. All these needed a reliable confinement and erosion control mechanism that could only come through a high strength and highly creep resistant geocell under the heavy dynamic loading coming on from the train movement.

Twenty-six locations were identified along the 55km stretch of the track for immediate rehabilitation. The rehabilitation needed different levels of maintenance work and twelve of the major washout locations were designated to be repaired with Geocell reinforcement. All the twelve locations had degraded permafrost and needed culvert pipe installation as there were defined stream flow lines. The length of the washouts ranged from 70m to 210m. The repair work included, but was not limited to, reinforced embankment construction to support the structure from dynamic train loading, installing culverts, and erosion control at the slopes.

THE DESIGN CONCEPTS

The design of transportation infrastructure in the Tibetan permafrost area has brought some light on how they should be sustainably designed. Citing 35 years of experience, Wu et al. (1998) had indicated that the height of embankment over 0.8m maintains a steady state on the permafrost. Based on an overall analysis on the change in permafrost table under the embankment and after considering the fact that the permafrost in the area is degrading and the requirement of the deformation of the road surface is of high quality, it was suggested that 1.6m height of embankment for the gravel road as optimal. Wang et al. (2009) emphasized the need to control the width of embankment as the increase in width was found to increase the gross heat absorption that could lead to permafrost degradation by 1.0m width increase and can bring the permafrost table down by 0.11m. Qi et al. (2012) suggested that in the initial operation years the degree of thaw consolidation of permafrost increases. However, it tends to decrease after the increase in the characteristic drainage length and decrease in the effective consolidation time. But it would take some residual consolidation time to dissipate causing settlement of embankment as an ongoing process. It was important to have minimum cover at the same time avoiding the unnecessary fill to avoid residual consolidation.

The HBR track was not in a good shape especially as it has lost the smoothness of ride because of the undulation in the track. The reason of that rough ride was because of permafrost degradation causing vertical deformations at some locations and at many places the lateral spreading of ballast and the sub-ballast material ultimately unevenly causing the track to settle. The aim this time was to bring it to its running condition as it was before the damaging flood event. The major mode of failure was washout which has exposed the

permafrost and the erosion control at almost all the stream crossings. The pictures in Figures 2 and 3 show the extent of devastation. The design for rehabilitating this railway line needed to address multiple issues that included structural strength, erosion control, protecting the already degraded permafrost from further degradation and most importantly, utilizing the washed-out material deposited at and around the washout locations. If the material was not enough it would have needed to bring virgin aggregate but still it would have been a low quality 75mm minus pit run gravel from Gillam (about 200km to 250km south). It should be noted here that the only access to the site was the railway line itself. Given the timeline of 6 weeks which seemed impossible for any other options thought of at the time because there were more than 26 damage locations along 150km stretch in series.

AREMA and CN railway design principles were checked to confirm the structural requirement of the geocell reinforced structure. The mechanism of load distribution via the slab effect to protect the weaker region within the permafrost was anticipated by transferring the load to a wider and competent area. The design had attempted to make only 5% of the applied stress to be transfered to the subgrade. The lateral and vertical confinement and friction between the geocell wall and infill material were the major factors helping create the stress reduction. Boussinesq's method of stress distribution and stress reduction due to the Geocell reinforcement at different layers were used to calculate the stress transferred to the underlying layers. The geocell reinforcement was designed to increase the modulus of the unreinforced gravel by 3.5 to 4 times. In the design the thickness of geocell plus 25mm was assumed as the reinforced thickness for stress transfer calculations as recommended by Pokharel (2010). The geocell-reinforced typical design cross sections are shown in Figure 4.

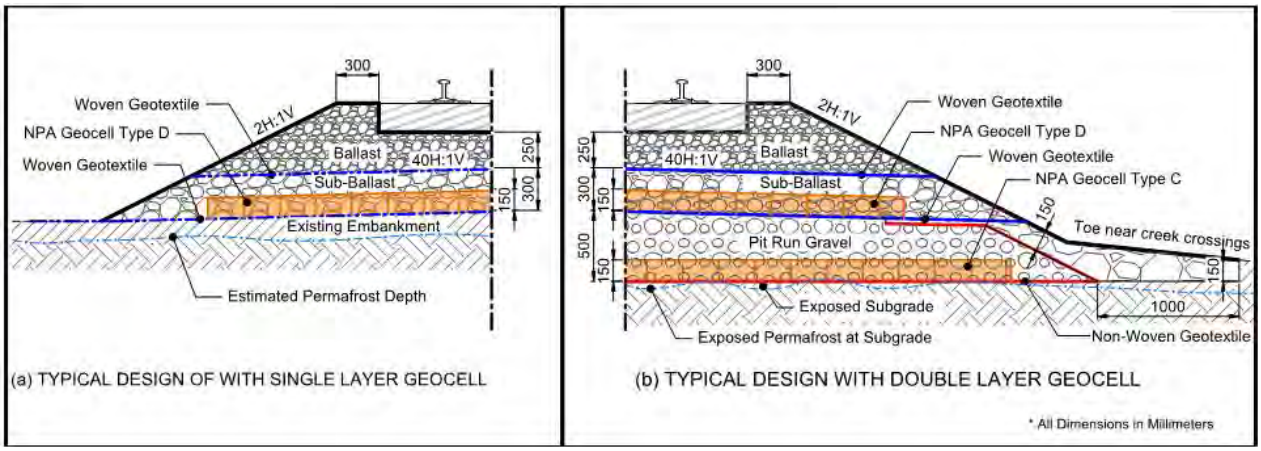

Figure 4. Typical design sections, requiring single and double layers of Geocell

The original plan of the design was to reinforce the ballast section too with perforated NPA geocells to maintain required drainage and provide confinement and control on lateral spreading of the ballast material but, due to the construction constraints and available tamping equipment at the site option to reinforce the ballast was abandoned. The ballast regulators are the common equipment used in railway maintenance which use spikes of about 150mm to 200mm deep to shape and place ballast under the track ties. It turned out that reinforcing the ballast would have increased the ballast thickness by 150mm thus avoiding mechanical damage to

the geocells during tamping operations. To save the costly ballast material this concept was abandoned. Only the sub-ballast layer was reinforced, and a layer of reinforcement required was decided by the fill height. To avoid further damage to the existing surface and protecting permafrost from further degradation nothing was removed from the existing subgrade and construction started right on top of it.

At some locations beaver dams were also found to block the stream flow and at many locations the culvert pipes were found to have settled rendering them useless. The new design raised the culvert beds to the existing stream bed level and provided a semirigid NPA geocell-reinforced mat at the culverts to avoid any such situation in the newly installed culverts. Some of the washout locations needed relocating the culvert location as the stream channel made its own course during the flooding and weaker easily erodible areas were washed away first. For erosion control at the toe of the embankment at and near the stream bank rip rap was provided.

MATERIALS USED

The geosynthetic materials used in this project was woven and non-woven geotextiles and high strength polymeric geocells. Salvaged washed away granular material was used wherever possible. Granular infill material with less than 12% was desired but the site engineer and contractor had to use the washed out granular material deposited at the downstream side to save the construction time and cost in bringing similar material which was available at a gravel deposit near Gillam (200km far). From visual observation and experience-based qualification of the 75mm minus pit run gravel designers approved the material fit for infill in the geocell. The granular fill chosen was the only option available at the site as it had been previously used at the sub-ballast layer, so it was approved. Riprap used was 150mm to 300mm size.

Two different types of NPA Geocell was used for reinforcement. NPA geocell was chosen for the design as it has higher tensile strength, modulus, and creep resistance than other available geocell material. The top layer of sub-ballast just below the ballast was reinforced with Type D geocell and layers below were reinforced with Type C geocell. Both geocells were perforated, 150mm high and had 330mm between seams. Type D, the higher grade geocell of the two was used immediately below the ballast and Type C was used at lower layer where lesser applied stress was expected. The properties Geocells used are given in Table 1.

Table 1. Properties of Geocell used in the design

Properties	Type C Geocell	Type D Geocell
Material	Polymeric nano composite alloy	
Wide-width strength at yield	19 kN/m	22 kN/m
Cell height of geocell	150mm	150mm
Distance between weld seams	330mm	330mm
Coefficient of soil-cell friction efficiency	0.95	0.95
Coefficient of thermal expansion	<135 ppm/°C	<135 ppm/°C
Brittle temperature	<-70°C	<-70°C
Long term plastic deformation at 65°C (load 6.6 kN/m)	3.0%	3.0%
Dynamic (elastic stiffness) modulus at +30°C	>775 MPa	>800 MPa

Both the woven and non-woven geotextiles were used as separation, the non-woven geotextiles used had a grab tensile strength 911N and 1330N with 50% elongation on grab. The woven geotextile had a grab tensile strength of 890N. As the exposed degraded material at the subgrade surface was very soft that could compress further non-woven geotextile was used for the bottom layer.

CONSTRUCTION METHODS

The pictures and videos of damaged area were made available for the design. There was no survey of other engineering data available. The designers conducted aerial survey to assess the extent of damage to determine whether repair work at the washout locations will be good enough to get the rail traffic back. During this it was clear that this project would be a linear construction and ground access to next location would be available only after completing work at the preceding location. The author also reached the first damaged site on highrail and walked to next few location on foot to access the damage and check the suitability of the design plus construction methods. The construction crew also needed to be extra careful as there were protected wild animals including polar bears in the area. As the access was limited the work needed to be completed with limited number of construction equipment or whatever could be transported to the site by available means. Even daily commute for the construction crew from nearest available camp in Gilam on highrail or caboose was not easy. The travel time alone was in the order of 6 hours two way per day.

There was very limited space to work in those locations as the construction team was instructed not to touch/damage any area outside of the railway right of way. Transporting heavy compactor and heavy equipment except for whatever could be accommodated within the width of railway line was out of question. The geosynthetic installation procedures were followed as per the manufacturer's installation guide and experience-based compaction methodology was applied for compacting the granular fill at the sub-ballast and layers below. The lower layer of the gravel fill was compacted to the possible extent only so that the permafrost layer at the subgrade was not damaged. As there was no facility to do compaction testing, ruts developed by the 4-ton compactor were used as an indication of the required degree of compaction. At each location as the construction moved to the upper layers, a maximum rut of 12.5mm under the roller wheel was taken as equivalent to 95% compaction and was used for the entire construction. Twelve passes of the compactor were used as the minimum compaction criteria at the site at every point. The picture in Figures 5 through 8 show the construction sequence of the repair work in order from track cutting and removal, geocell installation, gravel compaction, and reinstalled rail track.

Geocell was stretched and installed at the site with guide stakes. The requirement of more than one layer of the Geocell was decided at the site wherever there was more than 750mm fill required between two layers. The railway track was cut and placed aside to allow the installation of geocell and construct the embankment. When the embankment was ready it was lifted back to the position and connected.

Figure 5. The track removal for the repair works

Figure 6. Geocell installation and compaction

Figure 7. Geocell for sub-ballast reinforcement and section ready for ballast fill

DISCUSSION

Sustainable construction can be achieved by appropriately choosing the technology and using innovative ideas. Reusing the washed-out material can save the environment, cost, and time. As pointed out in the preceding sections the design in this rehabilitation project did not only consider the strength requirement but it also gave due consideration to the environment. The design had to balance among protecting the permafrost, controlling the lateral spreading and

embankment side erosion, or strengthening the sub-ballast structure to bear the railway traffic load. The use of available aggregate from the washed-out locations reduced about 50% of the virgin aggregate extraction and reduced the hauling and stock piling burdens. Geocell provided the required shear strength by confinement of poorly graded granular material. However, a traditional design approach would not have used the washed-out material and achieved the required structural strength. It saved the huge amount of virgin aggregate extraction and carbon emission that would have happened due hauling and mining virgin aggregate from far off location. This was made possible using geocell as reinforcement.

Figure 8. Completed rail re-installation at MP 427 and near switch at MP 414

This project also showed that knowledge and experience of the construction crew to work on the harsh climate and difficult situation plays a very important role especially those who have prior experience working in similar settings and materials. The project was completed in effective 33 working days at a cost about 20% of initially anticipated for conventional rehabilitation work. The saving was primarily because of the reduced construction time, use of the washout material, and working right on top of the existing subgrade without removing the degraded subgrade material. The construction equipment available was limited so a coordinated approach between the geocell installers, culvert pipe installers and earth work crew were of utmost importance to getting the job done in timely fashion.

Unless a ballast tamping method that does not damage the reinforcing geocell at the ballast layer is found out, the ballast layer cannot be reinforced so the loss of ballast material by lateral spreading in this railway line is expected. So, there is a need to find a different technique in the remote area to do the tamping that allows ballast reinforcement as well to control the loss of ballast material by lateral spreading.

All possible precautions were made to cause minimal or no damage to the unspoiled surrounding ground. Better pre planning on construction activities involving all the sub-contractors can improve overall productivity of a project. At times prime contractor and client's engineers understanding of geocell technology, led to some misunderstanding. However, as the work progressed, the work went smoothly.

The damage to this railway infrastructure was contributed in part by the melting permafrost, unmanaged cross drainage structures and erosion prone embankment slopes. The permafrost degradation along the railway track is evident by the uneven settlement along the railway length and subsidence of the existing culvert pipes. Lateral spreading of ballast was

another problem. The railway line is in operation but about 150km stretch of the railway line North of Gillam is still in need of repair. Once those areas are also repaired the rail line can be run at 50km/hr as designed. There are many locations where the ballast and sub-ballast material are seen scattered and spreading laterally. A confinement technique such as high strength geocell reinforcement can control that and reduce the maintenance cost in long run.

This rehabilitation work was completed just when daytime temperature started falling to subzero in that region. The access was reestablished on the last day of October 2018 after the track was inspected and approved for operation by Transportation Safety Board of Canada. The Railway has been in operation for two full seasons after the rehabilitation without any major concerns. This proves the effectiveness of NPA geocell reinforced railway structure. Figure 9 shows the first train arrival in Churchill after the rehabilitation work.

Figure 9. First train arrival October 31st, 2018 in Churchill in almost two years

CONCLUSION

The NPA geocell-reinforced design of the railway embankment proved to be a successful solution for maintaining and strengthening the railway structure. In this project it allowed the railway that was un-operational for almost two years to operate in a short time after the rehabilitation work started. The time required for construction was enough to repair the washout location because about half of the granular infill material was taken from the washout location itself which was made possible by the geocell reinforcement. The geocell reinforcement helped in controlling lateral movement of sub-ballast that was a very poorly graded sandy pit run gravel and controlled the settlement and damage to the permafrost. It also controlled the erosion of the embankment slopes. The design also saved the construction time and budget. Based on over two years of operation of the railway line, this paper also recommends this design as a viable method for the future transportation infrastructure development in the permafrost region and other similar areas.

REFERENCES

Leshchinsky, B. and Ling, H. (2013). Numerical modeling of behavior of railway ballasted structure with geocell confinement, *Geotextiles and Geomembranes,* 36(2013): 33-43.

Giroud, J. P. and Han, J. (2016). Part 1: Mechanisms governing the performance of unpaved road incorporating geosynthetics. *Geosynthetics Magazine*. February 1, 2016.

Global News, (2017). https://globalnews.ca/news/3523871/photos-show-widespread-damage-on-rail-line-to-churchill/ posted on June 13, 2017.

Han, J., Pokharel, S.K., Leshchinsky, D., Parsons, R.L., and Halahmi, I. (2010). Effect of infill material on the performance of geocell-reinforced bases. *9th International Conference on Geosynthetics*, ICG 2010, May 23-27, 2010, Brazil.

Jin, H., Yu, Q., Lu, L., Guo, D., He, R., Yu, S., Sun, G., and Li, Y. (2007). Degradation of permafrost in the Xing'anling mountains, northeastern China; Permafrost and periglacial processes, 18: 245-258.

Qi, J., Yao, X., Yu, F., and Liu, Y. (2012). Study on thaw consolidation of permafrost under roadway embankment. *Cold Regions Science and Technology*, 81(2012): 48–54.

Norouzi, M., Pokharel S. and Breault, M. (2019). Geocell-reinforced pavement structure state of practice in Canada. *Innovation in Geotechnical and material Engineering Session of the 2019 TAC-ITS Canada Joint Conference*, Sept 22-25, 2019, Halifax, NS.

Kief, O. (2016). NPA geocell and geogrid hybrid geosynthetic solution for rail track on expansive clay. *Geo-Americas 2016 conference,* IGS, Miami, USA, April 10-13, 2016.

Palese, J.W., Zarembski, A., Thompson, H., Pagano, W., and Ling, H. (2017). Life cycle benefits of subgrade reinforcement using geocell on a highspeed railway—a case study. *AREMA conference proceedings (American Railway Engineering and Maintenance-of-Way Association)*. Sept 17-20, 2017. Indianapolis, Indiana, USA.

Pokharel, S. K. (2010). Experimental study on geocell-reinforced bases under static and dynamic loading. *CEAE Department*. University of Kansas, Kansas, USA.

Pokharel, S.K., Han, J., Manandhar, C., Yang, X., Leshchinsky, D., Halahmi, I., Parsons, R. (2011). Accelerated pavement testing of geocell-reinforced unpaved roads over weak subgrade. *Journal of Transportation Research Board*, (2204) low volume roads 2: 67-75.

Pokharel S. K., Norouzi M., Martin I., and Breault M. (2016). Sustainable road construction for heavy traffic using high strength polymeric geocells. *Resilient Infrastructure*, CSCE, June 1-4, 2016, London, ON.

Pokharel, S., Norouzi, M., and Breault, M. (2017). New advances in novel polymeric alloy geocell-reinforced base course for paved roads. *2017 Conference of the Transportation Association of Canada, Transportation Association of Canada,* St. John's, NL, Canada.

Wang, S., Chen J.B., and Qi, J.L. (2009). Study on technology for highway construction and engineering practices in permafrost regions. *Sciences in Cold and Arid Regions*, 1(5): 412-422.

Webster, S. L. and Alford, S. J. (1978). Investigation of construction concepts for pavements across soft ground. *Report S-78-6, Geotechnical Laboratory*. U.S. Army Engineer Waterways Experiment Station, Vicksburg, MS.

Wu, Z., Linnan, Z., and Xingmin, G. (1998). Critical height of the embankment in the permafrost regions along the Qinghai-Kangding highway, *Journal of glaciology and geocryology*, 20 (1): 36-41.

Geosynthetics Conference

Monitoring and warning system including a bi-modulus geosynthetic for the reinforcement of cohesive soil on cavities

Mathilde Riot[1], Cyrille Balland[2], Philippe Delmas[3], Pascal Villard[4], Maria Delli Carpini[4], Fabrice Emeriault[4] and Stephan Fourmont[5]

[1]Afitexinov, Rue Louis Blériot, Champhol, FRANCE; mathilde.riot@afitex.com
[2]Ineris, Campus ARTEM, Nancy, FRANCE; cyrille.balland@ineris.fr
[3]Consultant, Paris, FRANCE; philippe.delmas5@wanadoo.fr
[4]3SR, Université de Grenoble, Grenoble, FRANCE; pascal.villard@3sr-grenoble.fr
[5]Afitex-Texel, Parc Industriel Sainte-Marie, Québec, CANADA; sfourmont@afitextexel.com

ABSTRACT

The use of reinforcement geosynthetics to prevent localized collapses such as cavities is common today. Numerous experimental and numerical studies allow a precise understanding of the geosynthetics behavior related to these applications. Within the REGIC (reinforcement by intelligent geosynthetics on natural or anthropic cavities) research project, an innovative solution has been developed and patented by the Afitexinov company. This solution includes a specific reinforcement geosynthetic coupled with an autonomous and remote warning device to detect a localized collapse or sinkhole. This innovative geosynthetic is an inverted bi-modulus reinforcement geosynthetic equipped with optical fibers. The first modulus at lower strength allows detecting possible deformations before transmitting the load to the second modulus with higher strength. This two-stages reinforcement system guarantees a high degree of safety from the start of the failure.

The new geosynthetic solution presented in this article aims to reduce the costs and time related to the installation of a monitoring system on a construction site. This solution's installation and set-up do not require an expert on-site, thanks to a standalone monitoring box. This Preditect® system is able to monitor large critical areas for ground deformations and detect potential underground failures. In case of any unexpected event, it will launch an automatic alert.

INTRODUCTION

Compressible soils are characterized by low shear strength that increases with consolidation, high compressibility, and delayed behavior under loading over time. Any construction on soft soils will face stability and settlement issues. One of the solutions used for the construction of embankments on compressible soils is the use of high modulus geosynthetics. This is a cost-effective solution that permits to save natural resources and reduce the time of work.

Geosynthetics significantly increase the safety factor and the maximum allowed height of the embankment by reducing displacements during construction and uniformizing settlements after construction. In conjunction with other geotechnical ground improvement methods, like rigid inclusions or aggregates piers, high modulus geosynthetics are also used as a distribution mattress to transfer the loads to the pile heads.

Implementing a high modulus geosynthetic makes it possible to secure civil engineering structures built on areas at risk of underground cavities (e.g., karstic zones). It will retain the soil in case of collapse and limit the settlements of the surrounding layer within the acceptable limit for the

stability of the structure and the safety of the users (Figure 1). It also provides the time needed to implement a definitive treatment corresponding to voids filling in areas where collapses have occurred.

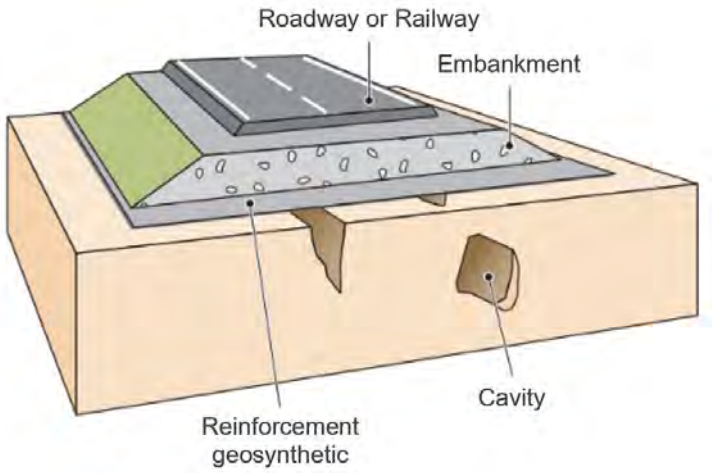

Figure 1. Reinforcement geosynthetic over cavity (credit CFG – Le Moniteur, 2015)

The high modulus geosynthetic material needs to have at least the following characteristics:

- High tensile strength (as per the design considerations),
- High stiffness (immediate tension of the technical yards, raw material used),
- Ability to effectively retain the soil (even if cohesive soil, separation function).

All reinforcement geosynthetic solutions, no matter how well dimensioned they are (Villard et al. 2000), have one main limitation: the monitoring of the reinforced structure over time. This is even more important for Mechanically Stabilized Earth (MSE) walls or reinforced structures on areas at risk of underground cavities. The possibility of having real-time monitoring of the stress-strain distribution in the reinforcement geosynthetics is a real contribution to any of these solutions, especially for the reinforcement of areas at risk of cavities. While the design of high modulus geosynthetics in areas at risk of cavities is currently limited to cavities with a diameter of 5 m, the use of an instrumented geosynthetic in conjunction with the appropriate monitoring system is a solution to detect and monitor the risk of large diameter cavities.

NEW GEOSYNTHETIC DEVELOPMENT

Inverted bi-modulus reinforcement geosynthetic. A new type of reinforcement geosynthetics has been developed to ease the detection of small settlements even for structures that require a product with very high stiffness, like structures with low or no settlement allowed on cavities with large diameters. The strength between the two moduli is well identified. The first modulus with lower strength allows deformation to be measured at low elongations (up to 2%) and prevents the onset of failure; when the second modulus is designed to retain the structure at high deformations (up to 10%), its stiffness will be the same as that of a mono-modulus reinforcing geosynthetic designed for the same reinforcement purpose (Delli Carpini and al. 2021).

The reinforcement geosynthetic is a high-modulus woven-knitted geotextile made with high tenacity yarns, manufactured by a double warp knitting process, GEOTER FPET (Figure 2).

The woven geotextile provides the separation function, whereas the high-tenacity yarns give the high strength capacity to the overall product. It allows tensile strength up to 2,000 kN/m.

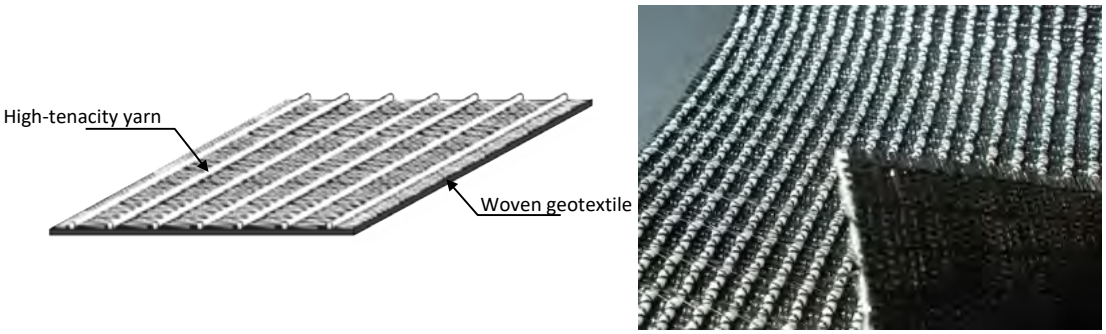

Figure 2. Description of the reinforcement geosynthetic

A numerical model using a Discrete Element Method (DEM) coupled with a Finite Element Method (FEM) has been used to analyze the interaction of the inverted bi-modulus reinforcement geosynthetic with the cohesive soil at the different stages of the collapse. This numerical model has already been tested and validated in the case of mono-modulus reinforcement (Delli Carpini et al., 2020).

Numerical model. The numerical model is based on the Spherical Discrete Element Code (SDEC) calculation code (Donzé, 1997). It uses the DEM to model the soil and the FEM to model the reinforcement geosynthetic. The DEM considers particles interacting at the points of contact, which allows it to describe the soil's behavior under large deformations and the failure in a block as observed for cohesive soils ruptures. The reinforcement geosynthetic is modeled by connected deformable planar elements interacting with the soil at the contact points.

The geometry and main characteristics of the numerical model are shown in Figure 3. The particles are bounded together at their points of contact by a cohesive bound (normal and tangential adhesion) with a Mohr-Coulomb type criterion to simulate the cohesive soil (Delli Carpini, 2021).

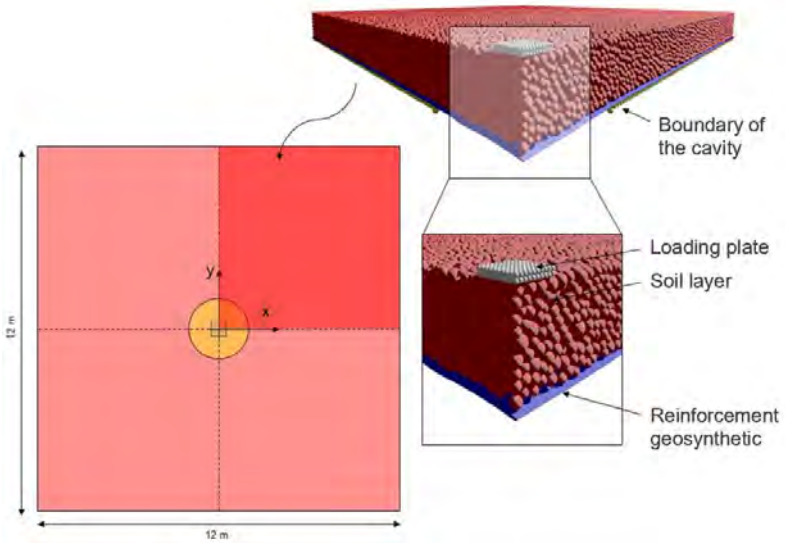

Figure 3. The geometry of the numerical model

The two types of reinforcement geosynthetics (mono-modulus and inverted bi-modulus) are modeled with the products' stiffness from tensile strength laboratory tests. Figure 4 shows the good correlation between the model and the experimental values for the inverted bi-modulus reinforcement geosynthetic. The two stiffness modulus are visible in Figure 4: the lower stiffness modulus for small elongations (inferior to 1.75%), then the high stiffness modulus for larger elongations.

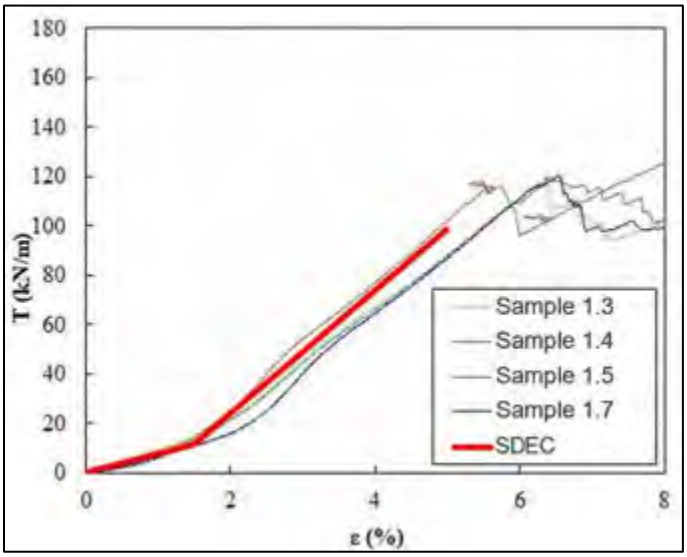

Figure 4. Strength-strain curve from laboratory test and numerical model

Experimental device. An experimental apparatus has been constructed to validate and calibrate the numerical model. Laboratory models have already been implemented (Hassoun et al. 2017), but no in situ model has been carried out. It reproduces a 2 m (80 in) diameter cavity with a trapdoor mechanism to simulate the cavity's opening under the reinforcement geosynthetic. The trapdoor is placed in a concrete sump and allows for draining (when open) the aggregates from the upper chamber to the lower chamber (Figure 5). The trapdoor is divided into several zones to control the opening factor of the cavity and permit to create first a 1 m (40 in) diameter cavity and extend it to 2 m (80 in).

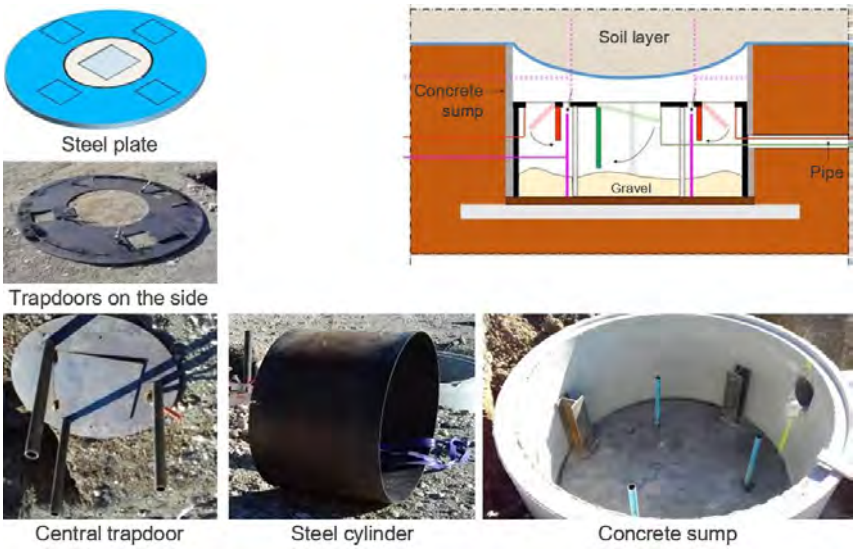

Figure 5. Trapdoor mechanism in the concrete well

The reinforcement geosynthetic is first put in place with the sensors. The Bragg grating sensors used to measure strain within the geosynthetic are placed every 0.5 m (20 in) from the side of the cavity along its diagonal, as shown in Figure 6.

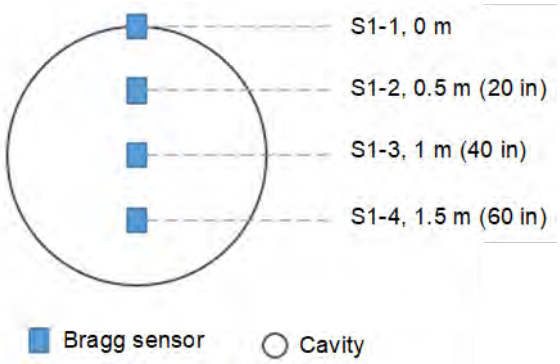

Figure 6. Bragg sensors placement over the cavity

The 0.50 m (20 in) thick layer of cohesive soil is then placed on the reinforcement geosynthetic and compacted. Its main geotechnical characteristics are shown in Table 1.

Table 1. Soil characteristics

	γ_d (kN/m^3)	w (%)	c_{uu} (kPa)	φ_{uu} (°)	σ_t (kPa)
Cohesive soil	15	16-18	18,93	34,9	~15

The experimental device is left in place for 15 days before opening the cavity. It is first opened to 1 m (40 in) diameter; a slight deformation takes place, as shown in Figure 7. Then the cavity is opened to 2 m (80 in) diameter.

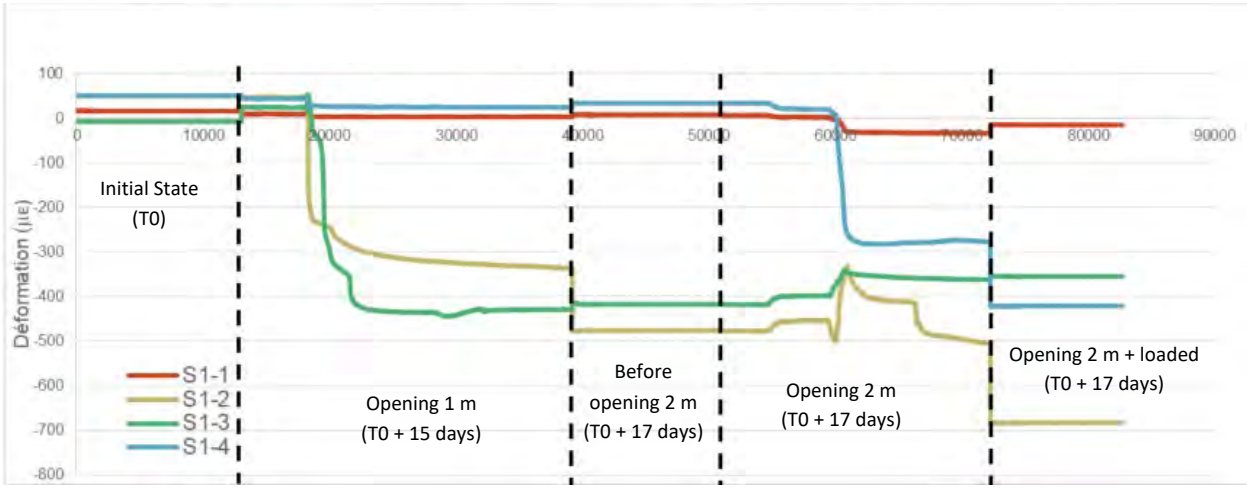

Figure 7. Deformation recorded by the sensors during the test for one iteration

Following the opening of the cavity, the soil layer is loaded with successive steel plates 80 kg (176 lbs), each placed on a steel cube 0.50 m (20 in) wide and 30 kg (66 lbs) in weight (Figure 8). The aim is to produce the collapse of the cavity.

Figure 8. Steel plates on the steel cube

Results. The numerical model has been performed to give the vertical displacement of the two types of reinforcement geosynthetics (mono-modulus and inverted bi-modulus) function of the loading until the failure of the soil layer. Several steps are presented:

- I: Opening of the cavity,
- R: First failure of the cohesive soil layer,
- E: Collapse of the soil bloc on the geosynthetic.

The two products have the same behavior at each step of the loading (Figure 9). The value of 16 kN for the load to reach the soil collapse in the numerical model is higher than the values measured with the experimental device that were not superior to 12 kN. It is explained by the non-homogenous compaction of the soil layer (that has been observed on the experimental device) and its geotechnical characterization.

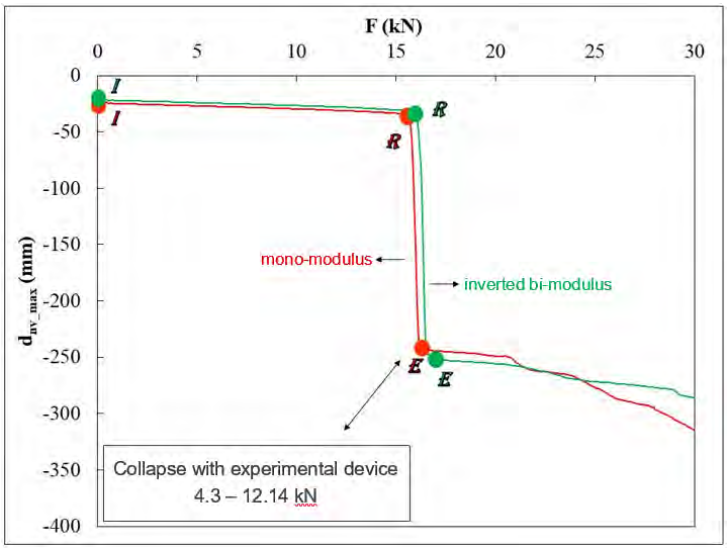

Figure 9. Vertical displacements of the reinforcement geosynthetics function of the loading

The elongation of the reinforcement geosynthetics function of the distance to the center of the cavity has also been modeled for the 3 steps I, R, and E (Figure 9). The total length is 12 m (39 ft), which corresponds to the 2 m (80 in) diameter of the cavity and the anchoring. The maximum elongation in the inverted bi-modulus reinforcement geosynthetic reaches 2.07 % with the numerical model when the experimental value measured is 1.96 %. For the mono-modulus reinforcement geosynthetic, the maximum elongation is 1.5 % with the numerical model compared to 1.46 % with the experimental model.

The numerical model is accurate to characterize the deformations in the geosynthetics. Moreover, it clearly shows the different behavior of the two types of reinforcement geosynthetics, especially in the anchorage zone, which leads to higher deformation values in the center of the cavity for the inverted bi-modulus reinforcement geosynthetic, even though the vertical displacements obtained for both products are the same at 250 mm (Figure 10).

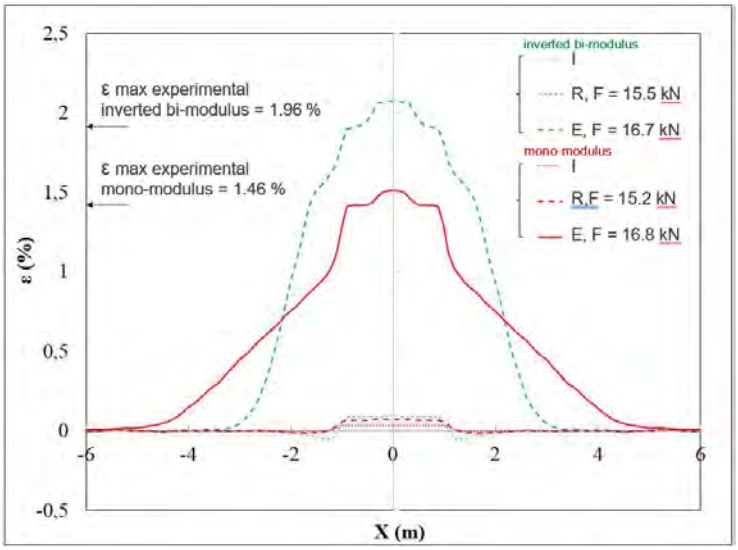

Figure 10. Elongation of the reinforcement geosynthetics at each step (I, R, E)

During the loading step, after the soil collapse on the geosynthetic, the inverted bi-modulus reinforcement geosynthetic leads to lower displacements. This result confirms that the inverted bi-modulus reinforcement geosynthetic fulfills its function: the large initial deformations enable the warning signal transmitted by the optical fibers inserted in the product to be activated at the early stage of the failure. The high stiffness mobilized, later on, ensures surface settlements as it would have been expected with an equivalent in strength mono-modulus reinforcement geosynthetic.

REMOTE MONITORING SOLUTION

Preditect® system. The development of the inverted bi-modulus reinforcement geosynthetic and its specific mechanical behavior allows the use of a monitoring system within the product to detect the soil failure at the early stage. This monitoring system is composed of optical fibers regularly inserted and positioned in the product during the manufacturing process (Figure 11). They are connected on both sides together during the manufacturing process to have a redundancy of the signal. The coverage of the optical fibers is sized according to the required resolution of the system and the sensitivity of the monitored structure.

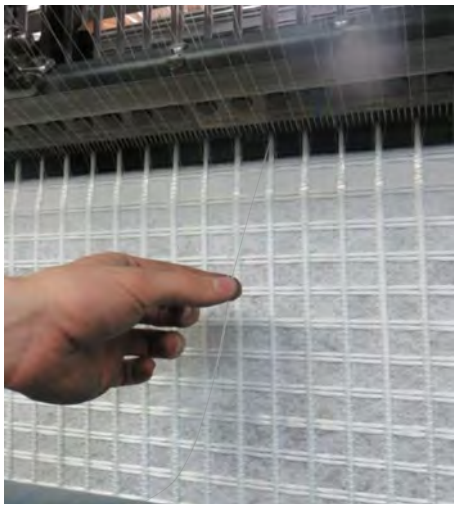

Figure 11. Insertion of the optical fibers in the product

Preditect® system uses the Fiber Bragg Grating (FBG) technology that allows temperature and strain measurements. The optical fibers used in the product can measure deformations up to 6% elongation before breakage and have a range of 50 km. The accuracy is about 1 µdef, the measurement acquisition time is of the order of milliseconds, with a spatial resolution of 8 mm.

The optical fibers are connected on-site to a self-sufficient data logger, powered by a solar panel (Figure 12). The data logger monitors the deformations in the reinforcement geosynthetic on the overall covered area. It generates a detailed report at given intervals through dedicated software and sends an alert to the selected persons in case of an unexpected event (if the deformations exceed the limit values fixed by the user).

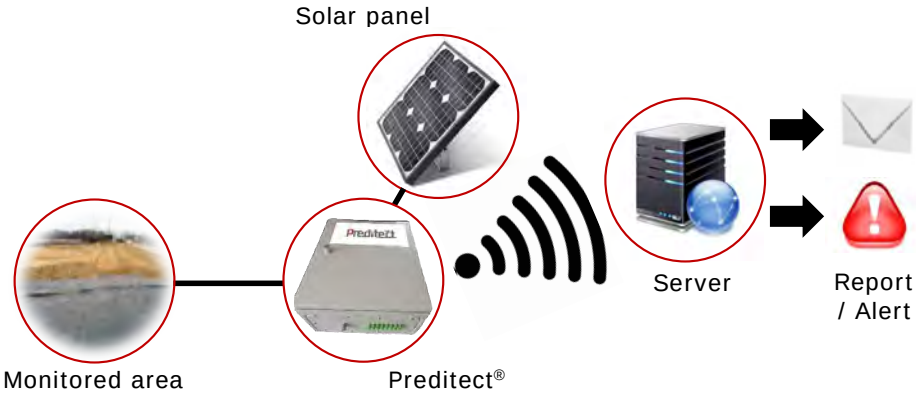

Figure 12. Description of the monitoring system

The Preditect® software allows customizing the acceptable deformations limit in the reinforcement geosynthetic per zones, the generation frequency of the report, the emergency contacts, etc. (Figure 13).

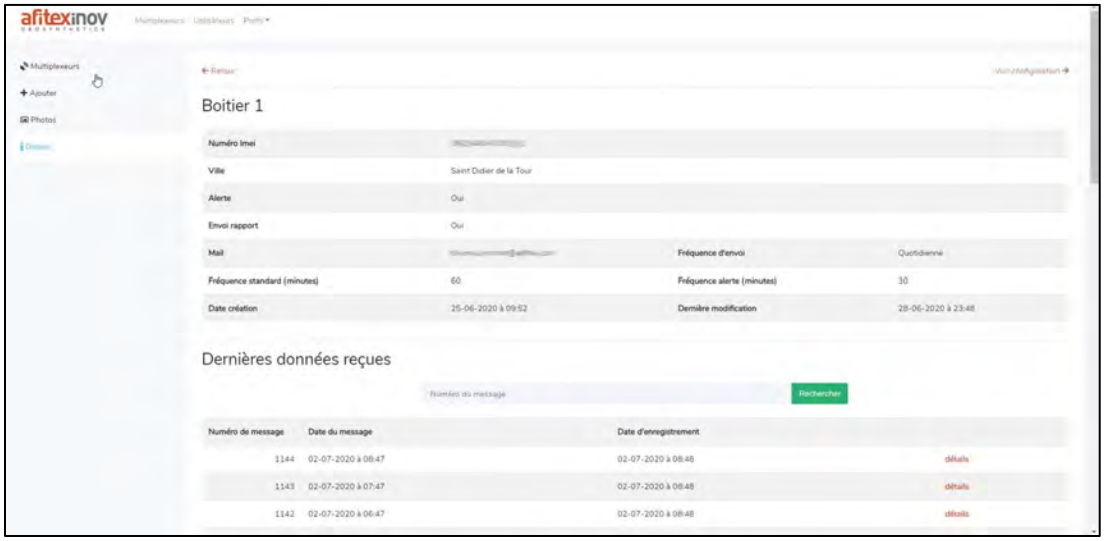

Figure 13. Preditect® software screen view

CONCLUSION

The use of inverted bi-modulus reinforcement geosynthetics increases the elongation in the geosynthetic for small displacements of the surrounding soil compared to a mono-modulus geosynthetic, keeping the same mobilized strength in the geosynthetics and the same behavior of the reinforced structure.

A numerical model has been developed to predict the behavior of the geosynthetic and the failure mechanism of the structure in case of reinforcement of cavities on cohesive soils. This model has been compared to experimental instrumentations, and both confirmed the differences mentioned above between the two types of reinforcement geosynthetics. Therefore, the numerical model seems relevant and could be used for parametric studies (influence of the soil layer's thickness, the geometry, and size of the loading plate or even on the soil model).

The use of the inverted bi-modulus reinforcement geosynthetic equipped with optic fibers and connected on-site to the Preditect® system allows the continuous monitoring of the reinforced structure. It allows, among other things, to monitor the settlements of the structure and send an alert if they exceed a value previously set by the user. This technology, being able to detect a failure at the early stage, gives more time to put in place possible measures to secure the structure and protect people's health.

REFERENCES

Villard P., Gourc J.P., Giraud H. (2000). A geosynthetic reinforcement solution to prevent the formation of localized sinkholes. *Canadian Geotechnical Journal*, Vol. 37, pp 987-999.

Delli Carpini, M., Emeriault, F., Villard P., Riot M., Briançon, L., Delmas P., Al Heib M., (2021). Utilisation d'un géosynthétique à double raideur pour le renforcement des remblais cohésifs, *13èmes Rencontres Géosynthétiques*, Saint-Malo, France.

Delli Carpini, M., Emeriault, F., Briançon, L., Villard, P., Mengue, E., Leguernevel, G. (2020). Etude du comportement des remblais cohesifs renforcés par géosynthétique, *Journées Nationales de Géotechniques de l'Ingénieur*, Lyon, France, pp. 1–8.

Donzé, F. V. (1997). Spherical Discrete Element Code. *Discrete E. Universite du Quebec a Montreal,* Quebec, Canada.

Delli Carpini, M., (2021). Analyse des mécanismes d'effondrement des couches de sol cohésives renforcées par géosynthétique sur cavité, *Ph. D. Grenoble University*, France.

Hassoun, M., Villard, P., Alheib, M., Emeriault, F. (2017). Limitation of the hazard caused by the collapse of roofs of underground cavities using geosynthetic reinforcement, *11èmes Rencontres Géosynthétiques*, Lille, France, pp. 239-248.

Geosynthetics Conference

Prediction Models for Deformation and Punching Shear Resistance of Geogrid-reinforced Working Platforms under Tracked Plant

Arash Khansari,[1] Lars Vollmert,[2] Christopher Quirk,[3] and Jörg Klompmaker[4]

[1]BBG Bauberatung Geokunststoffe GmbH & Co. KG, Espelkamp, Germany; e-mail: akhansari@bbgeo.com

[2]BBG Bauberatung Geokunststoffe GmbH & Co. KG, Espelkamp, Germany; e-mail: lvollmert@bbgeo.com

[3]NAUE Geosynthetics Ltd., Warrington, United Kingdom; e-mail: cquirk@naue.co.uk

[4] BBG Bauberatung Geokunststoffe GmbH & Co. KG, Espelkamp, Germany; e-mail: jklompmaker@bbgeo.com

ABSTRACT

The majority of available models in practice to predict the punching shear resistance of working platforms may result in considerable overestimation of platform thickness due to conservative simplifications in the development process of the design models. With this background, systematic large laboratory tests were conducted to identify and overcome the shortcomings in the available design models with a particular focus on the popular model by BRE470. The focus is laid on achieving an improved understanding of the parameters and processes affecting the behavior of geogrid reinforced working platforms under concentrated loads. In this regard, the working platform is subject to extreme loads representing track loads. The gained improved knowledge from laboratory tests is then used to modify the available bearing capacity equation to account for the effect of a footing punching through a geosynthetic reinforced granular platform material overlying a soft cohesive subgrade. In addition, the data is further analyzed to develop a simplified semi-empirical equation to predict the immediate deformation of working platforms subject to loads from semi-rigid tracks. The developed prediction models are finally applied for the boundary conditions of the laboratory tests and the accuracy of models in terms of bearing capacity and deformation is examined.

INTRODUCTION

Dimensions of piling rigs and cranes as well as their operating loads have grown considerably over the last years as the demand to install larger structural components is increasing (e.g. piled foundations, on-shore wind turbines, etc.). This has resulted in an increasing number of applications using geogrid-reinforced base courses and increased knowledge of understanding the interaction of reinforcement to stabilize granular soils (e.g. Vollmert & Bräu, 2018). Transferring the beneficial behavior to working platforms results in a competitive solution to thicker unreinforced aggregate layers, especially in terms of both costs and response to heavy loads induced by tracked plant. Hardstands for this increasingly heavy equipment demand a reliable, safe and economical ultimate limit state design procedure which enables a complete verification of safety against different failure modes.

Figure 1. Examples of piling rig accidents: a) overturned due to soil low bearing capacity of working platform in Germany 2018; b) at quay in Emsworth, Australia at 30th July 2019

Currently applied design procedures for geogrid reinforced working platforms being exposed to high concentrated loads caused by tracked plant mainly consist of two analyses:

(i) Ultimate Limit State analysis to prove sufficient punching shearing resistance of the reinforced platform subject to the high localised forces;

(ii) Serviceability Limit State analysis to restrict total and differential settlements of working platforms under tracked plant overlying the soft cohesive soil.

For an Ultimate Limit State (ULS) design of working platforms, considerable advances in design and analysis of reinforced working platforms is achieved through the contribution of several research studies and design standards such as the popular methods of load spreading angles, BRE470 etc. Among these models, the model from BRE470 is one of the most popular models due to its simplicity even though that, the limitation of this model is addressed in several research studies (e.g. Dobie et al., 2019; Scotland et al., 2019). In general, the main weakness of the BRE40 method can be summarized as:

- the model does not consider the curved shear planes develop between the edge of the track and the formation and assumes a vertical shear plane which underestimates the working platform shear strength;
- the effect of the geogrid tensile strength in the basic resistance equation proposed by BRE470 has not been considered around the perimeter of the track despite the symmetric shape of track;
- the effect of relative subgrade-working platform stiffness in the reduction of working platform shear strength as suggested by Hanna and Meyerhof (1980) is neglected in BRE model.

For Serviceability Limit State (SLS) designs of working platforms, less attention is paid to the estimation of immediate deformations underneath tracked plant and most of the designs in practice focus solely on the ULS design, which addresses the punching shear resistance of the working platform.

Therefore, new knowledge and modelling techniques need to be generated for both SLS and ULS designs of reinforced working platforms underneath high concentrated loads. Indeed, it is crucial for both, design optimization and safety assessments, to develop an improved

understanding of the process involved in the failure mechanisms and deformation behavior of working platforms against punching loads. Therefore, the objective of this study is to

(i) enhance the available model from BRE470 to determine an optimized thickness of the reinforced working platform and;

(ii) provide a simple equation to account for the effect of reinforcement on the immediate settlement of working platform under tracked plant. This has been conducted on the basis of results from two large scale laboratory tests performed at the Technical Universities in Stuttgart and Aachen, Germany.

LABORATORY TESTS IN STUTTGART

For the laboratory tests in small-scale condition to investigate the bearing capacity of working platforms, several phenomena such as scale effect and the effect of boundary conditions might influence the accuracy of the results. Therefore, large scale experiments were performed on geogrid reinforced working platforms by Stuttgart university in the framework of a DFG (Deutsche Forschungsgemeinschaft) project in Germany (Deutsche Forschungsgemeinschaft). The main objective of these experiments was to investigate the effect of reinforcement on the behavior of the working platform and consequently develop a conceptual model to estimate the working platform thickness and the type of reinforcement under localized high loads from rigid footings.

The model setup of the laboratory tests for the working platform over soft clay subject to loads from footing is shown in Figure 2.

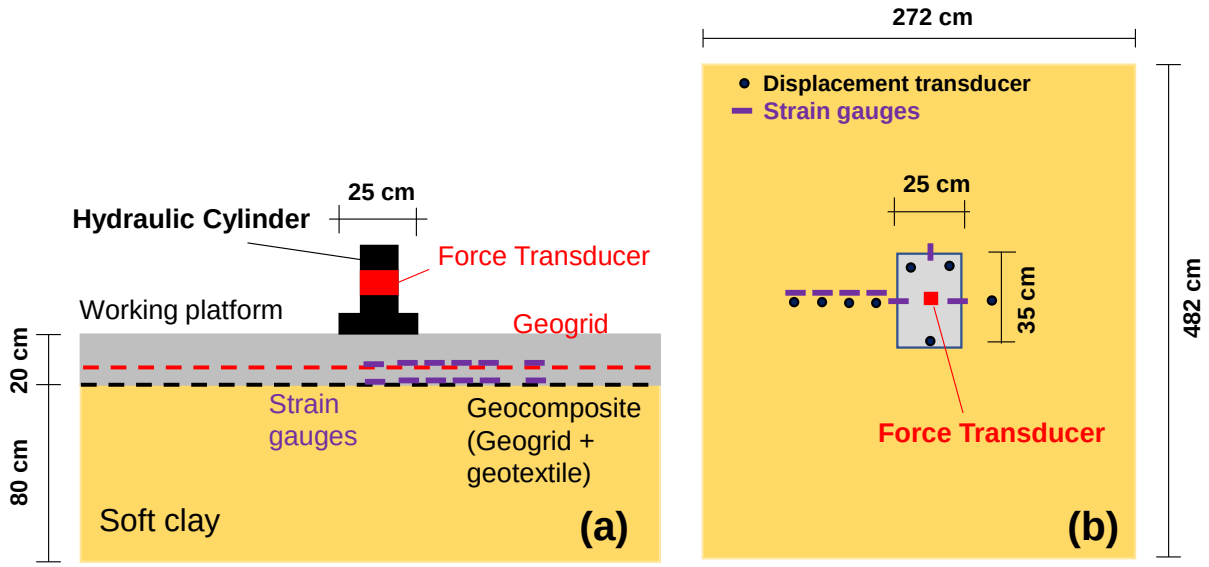

Figure 2. Model setup: a) cross section; b) plan view

Loads of increasing magnitude (P=10, 20, 40, 50 etc.) are applied on the working platform to allow for an incremental comparison of results for reinforced versus non-reinforced platforms and to enable a trackback estimation of maximum allowable bearing capacity. The model is subject to loads from a rectangular shaped plate with the dimension of 25 cm x 35 cm. The geometry of model is considered to represent a prototype problem with a scale of 1/3. The width of the box and the distance between the footing and the wall is chosen large enough to minimize the boundary effects (footing width / box width < 0.1). The settlements in several positions underneath the loaded area corresponding to each load step is measured by the displacement transducers. Different

platforms (including un-reinforced, with one geogrid layer, with two geogrid layers) are set up to investigate the effect of reinforcement. In this paper, the results from the un-reinforced platform versus platform with two geogrid layers are focused. The results show that, the ultimate allowable load to be applied on the model with reinforcement (82.5 kN) is moderately higher (ca. 25%) than the load on the non-reinforced model (67.5 kN), Figure 3. Accordingly, larger deformations were observed in the non-reinforced working platform at the different loading steps, especially before the ultimate bearing capacity of the working platform was achieved (loads smaller than P=25 kN as shown in Figure 8a).

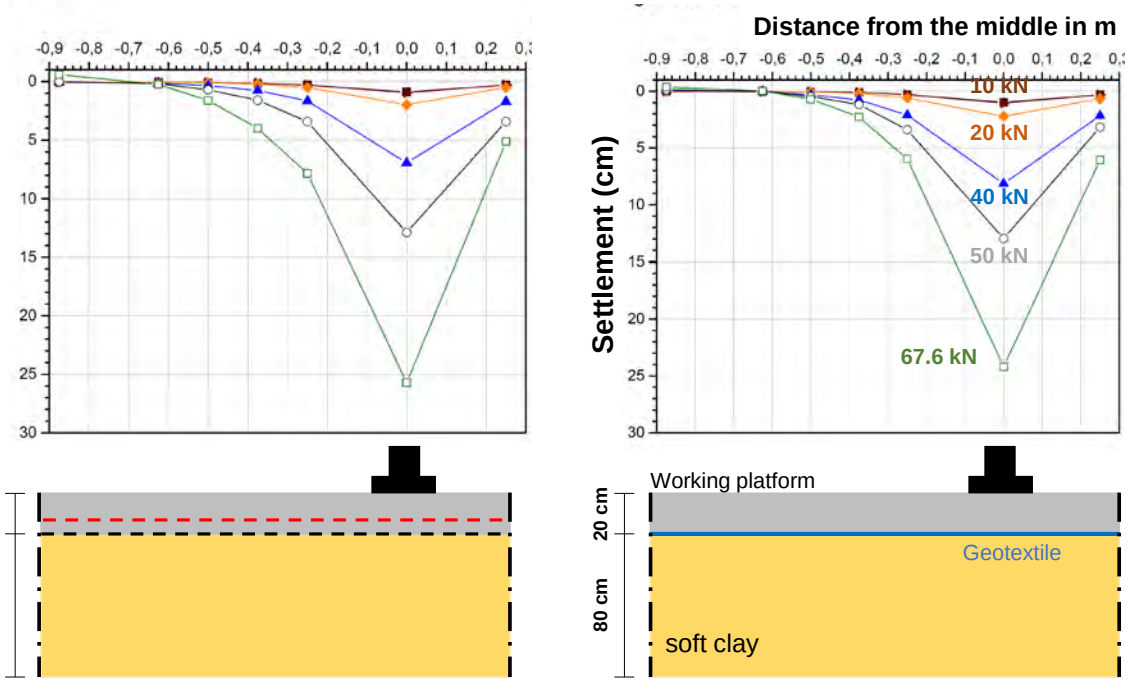

Figure 3. Recorded settlement and ultimate bearing capacity for: a) reinforced working platform and; b) unreinforced working platform

The test results showed that, the extreme loading of the working platform cause large and deep shear failures at the perimeter of plate and further away far from the loaded plate.

LABORATORY TESTS IN RWTH AACHEN

Elastic and immediate settlement will occur directly after the application of loads from the tracks of a heavy machine. The magnitude of the developing settlements is a function of the geotechnical properties of the working platform and subsoil. Among the soil parameters, which affect the immediate settlement, the modulus of elasticity of the working platform is the most decisive parameter to influence the magnitude of the settlement. Several experimental and numerical studies have revealed that, the application of geogrids in working platforms may significantly increase the soil mechanical parameters (e.g. modulus of elasticity). With this background, large triaxial tests of 500 mm diameter and 1.1 m height have been carried out at the Institute of Foundation Engineering, Soil Mechanics and Waterways Construction at RWTH Aachen university for quantification of the effect of geogrid application on the soil characteristics. Figure 4 a) shows the test setup, while the number of geogrid layers has been varied. Strain gauges

have been applied to the welded geogrid. Figure 4 b) shows the development of strains within the reinforcement at a strain of the soil sample of 2 %. The maximum strain required to stabilize the sample is limited to approx. 0.5%. The results from the tests revealed a significant improvement of soil bearing capacity and modulus of elasticity due to the application of geogrid reinforcement. (Figure 4 c and Figure 9)

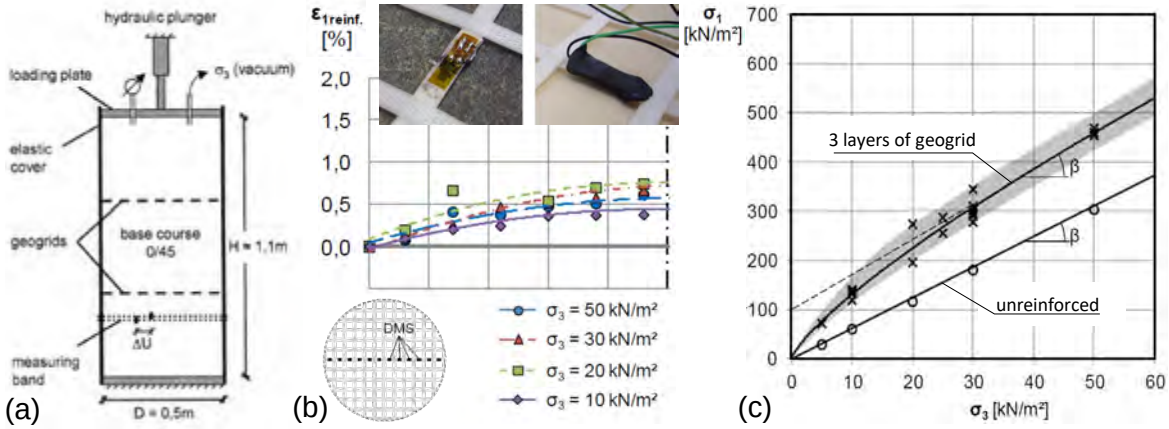

Figure 4. Large scale triaxial tests at RWTH Aachen university (Ruiken, 2013) a) test setup b) strain development of a geogrid placed in the centre of the sample with three layers of Secugrid®30/30 Q6 at a uniaxial strain of the sample of e_1 = 1 % c) increase of appliable stress of a sample with three layers of geogrid Secugrid®30/30 Q1 compared to an unreinforced sample

PREDICTION MODEL FOR PUNCHING RESISTANCE

The ultimate bearing capacity of a single or multi-layered soil is generally determined according to Terzaghi theory (1943) which has been developed by the extension of Prandtl plastic failure theory (1921). Several models have been proposed so far, to refine the solution as provided by the Terzaghi's bearing capacity formula.

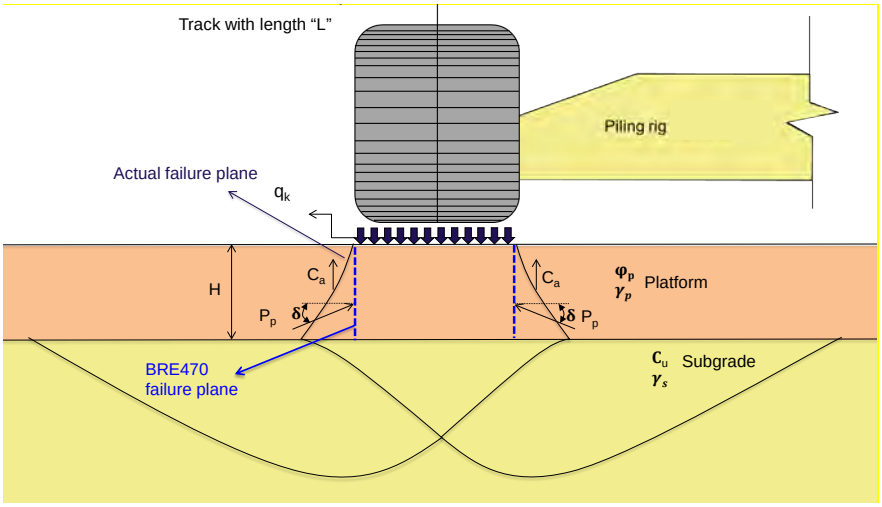

Figure 5. Punching shear failure mechanism of layered soils according to Meyerhof & Hanna (1978)

The bearing capacity of layered soil system for the case of dense working platforms over soft clay has been studied for both strip and circular footings (Meyerhof 1974). Meyerhof (1974) suggested that for the case of loose sand over stiff clay the bearing capacity is limited to the top layer, which means that the failure surface is also limited to the top layer and pressure does not reach down to the bottom layer. For a stiff working platform over a soft clay however, the scenario may be different. The developed theoretical models assume that the failure plane may extend through the soft underlaying soil. Moreover, the laboratory tests and some available conceptual models consider the curved shear planes develop between the edge of the track and the formation (see Figure 5) even though that the majority of simplified models in practice (including BRE470) take a vertical shear plane into account.

The analytical based model by BRE470 is one of the most popular models which covers designs for both reinforced and unreinforced platforms for different uniform subsoil conditions. The main reason for this popularity is probably the wide range of application along with its simplicity. However, the BRE470 model has a high tendency to produce safe (and conservative) results which has been evaluated and addressed in several publications. (e.g. Dobie et al., 2019; Scotland et al., 2019). In fact, the analytical method is based on classical bearing capacity methods for two layered soils (dense soil over weak soil) but uses the concept of punching shear capacity within the platform as suggested by the experimental model developed by Meyerhof and Hanna (1978). For development of model in BRE470 however, several extreme simplifications are made which leads to the conservative estimation of platform thickness.

With this background the methodology as depicted in Figure 6 was planned in this study to improve the BRE equation based on the model from Hanna and Meyerhof (1980) and according to the experience gained from the Stuttgart large scale model tests. For the *punching shear failure*, the BRE method is modified to account for the footing punching through a geosynthetic reinforced granular platform material overlying a soft cohesive subgrade.

In a “First Step”, the large-scale experiments from Stuttgart university were used to investigate the behaviour of the working platform over soft soil in terms of settlements, ultimate resistance of platform, failure mode and type of failure. The test programme is planned to support the development of the model in Step 2.

In the “Second Step”, the model from BRE470 is modified according to the basic Hanna and Meyerhof’s graphs and equation. Generally, the following corrections are undertaken to achieve a safe and optimized model: (i) unlike the model from BRE470 which provides equations in a 2D environment, for the development of the new model the geotechnical problem is investigated in a 3D environment considering the symmetry of the problem. This led to the development of 3D equations to predict the acting and resisting forces; (ii) Geogrid tensile strength has been activated at the perimeter of the track considering the relevant tensile strengths in transverse and longitudinal directions; (iii) A reduction factor (as recommended by Meyerhof) has been implemented in the model to reduce the working platform shear strength as a function of relative bearing capacity of working platform to subgrade. The BRE model neglects the dependency of platform punching strength to the soft soil bearing capacity. The weakness of the main proposed model in the determination of the platform shear strength was covered by implementation of a correction factor based on the study by Burd and Frydman (1997); (iv) unlike BRE470 which considers a vertical shear failure plane, the actual shape of the shear plane (see the inclined failure plane in Figure 5) is taken into account which may reduce the effect of the lateral passive resistance. The angle can be estimated based on laboratory tests considering the condition of subgrade, working platform and type of reinforcement. The main parameters affecting the

platform thickness and reinforcement tensile strength are identified as track dimensions, track loading, platform and subsoil shear strengths, track spacing and stress distribution angle through the reinforced platform.

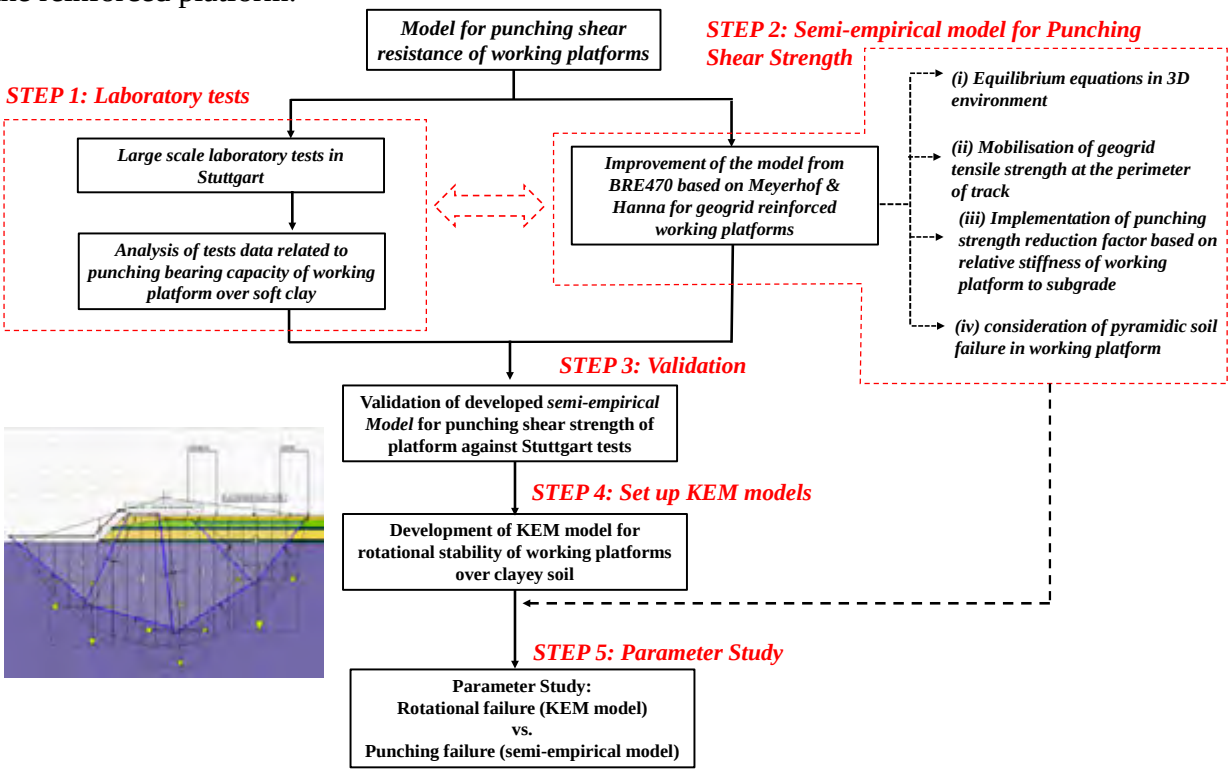

Figure 6. Applied methodology for development of the prediction model for punching shear resistance of reinforced working platform

In the "Third Step" the developed semi-empirical model was applied to estimate the allowable pressure over the working platform to the lab tests in Stuttgart considering the boundary condition of each test. Load settlement curve related to a certain test is shown in Figure 7 (left). As shown in the figure, the ultimate resistance of working platform is obtained with 285.7 kPa (25 kN / B / L) for this particular test. The developed model is this study is then applied for the test condition to predict the maximum allowable load on the working platform. The maximum bearing capacity of the working platform is estimated considering applying load versus settlement. As shown in Figure 7 and 3b, increasing the load from 20 kN to 40 kN has resulted a dramatic settlement of working platform thus the ultimate bearing capacity is expected to be between these values. As shown in Figure 7 (right) the ultimate bearing capacity by the model in this study is estimated with 250 kPa. Afterwards, the original model from BRE470 is implemented to predict the allowable loads on the working platform. As can be seen, the model from BRE470 has dramatically underestimated the allowable loads on working platform (on the safe side). The further results for the prediction model vs. tests are shown in Figure 7 (right). The area below the line is the safe zone where the predicted allowable load is lower than the measured soil bearing capacity. The proposed model in this study and the BRE model are applied to estimate the allowable pressure on the working platform. The result shows that, the developed model in this study tends to predict safe and optimised results (utilisation factor between 0.7 to 0.95). In contrast, even though that the model in BRE has proposed safe results, the allowable load is much smaller

than the platform bearing capacity. Therefore, it can be concluded that, the BRE model has produced very conservative results (utilisation factor between 0.4 to 0.7).

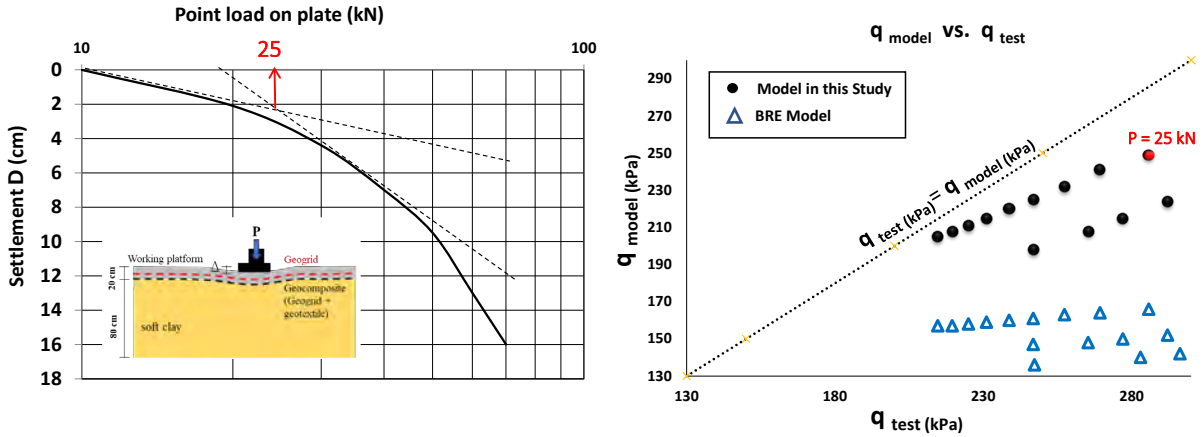

Figure 7. Allowable pressure on working platform: developed model vs. large scale laboratory tests from Stuttgart university

In addition to the semi-empirical model as developed in this study derived from Meyerhof's model, a Kinematic Element Model (KEM) is set up (Step Four) to investigate the rotational and overall stability of the working platform. The KEM model implements the rigid body approach to examine the equilibrium state, thus enabling a full interaction of soil wedges with the intersecting geosynthetic reinforcement. The rotational and overall stability of the working platform might be even more dominant when the construction equipment is positioned close to the edge of working platform.

The KEM and the developed model in this study are applied (Step five) to perform a systematic parametric study by variation of the most influencing parameters affecting the ultimate bearing capacity of the working platform (e.g. soil shear strength, loads, geometry of tracks, etc.). The preliminary results show that, while the stability of working platforms overlying firm to hard cohesive subsoil (approx. c_u > 30 kN/m^2) is commonly governed by the soils punching shear strength, the failure mode of working platforms over very soft to soft cohesive soil may be governed by rotational slip circles. Therefore, it is recommended to investigate the overall and rotational stability of the platform (especially when the heavy machine is positioned close to the platform's edge) during the design phase.

According to the preliminary KEM results in this study, further development of the available models in practice is required to take into account the rotational and overall failure modes of working platforms.

PREDICTION MODEL FOR IMMEDIATE SETTLEMENT

While several design guidelines provide methods and equations for the prediction of the punching shear strength of the working platform, less attention is paid so far to the estimation of deformations underneath the tracked plant. For the design of working platforms under tracked

plant, the relevant settlement is mostly immediate settlement which occurs directly after the application of the load without a change in the moisture content of the soil. In general, foundations are not perfectly flexible and are embedded at a certain depth below the ground surface. It is however recommendable to evaluate the distribution of the contact pressure under a foundation along with the settlement profile under idealized conditions.

For a perfectly flexible foundation resting on an elastic material such as saturated clay, if the foundation is subjected to a uniformly distributed load, the contact pressure will be uniform and the foundation will experience a catenary profile. On the other hand, if a perfectly rigid foundation is resting on the ground surface, the foundation will undergo a uniform settlement and the contact pressure will be redistributed.

Theoretically, for a perfectly flexible foundation the settlement can be expressed by the following equation, as derived from the theory of elasticity:

$$S = D\sigma\,(\alpha B)\,\frac{1-\mu_s^2}{E_s}\,I_s\,I_f \qquad \text{Eq. (1)}$$

Where:
$D\sigma$ = net applied pressure on the foundation
μ_s = Poisson's ratio of soil
E_s = weighted average modulus of elasticity related to reinforced working platform und subsoil under the foundation up to z = 4B
B = the width of track for estimation of maximum deformation
I_s = shape factor
I_f = depth factor
α = factor that depends on the location on the foundation where settlement is being calculated

According to Eq. (1), the influencing parameters can be classified into (i) geometrical parameters; (ii) load parameters and; (iii) soil geotechnical parameters. While less uncertainties in determination of geometrical and load parameters during the design process of working platforms is expected, the correct estimation of soil parameters (especially through application of geogrid reinforcement) is known as the most challenging task for an accurate settlement analysis. Nevertheless, it is crucial to implement the correct value of elasticity modulus as well as Poisson ratio for a reliable deformation estimation of the working platform. Therefore, the focus of this study is on the general equation for immediate deformation of shallow foundation to account for the effect of geogrid stabilization and reinforcement of the working platform material. As a result, a simplified relation is proposed to predict the soil elasticity modulus as a function of geogrid stiffness and the number of reinforcement layers.

For this purpose, the data from the large triaxial tests at RWTH Aachen university is analyzed to investigate the effect of soil stabilization due to application of 1, 3, and 5 geogrid layers. The results from the triaxial tests are depicted in Figure 8 (left). Accordingly, the equivalent elasticity modulus of the soil has been extracted using the classical geotechnical equation according to triaxial tests and are shown in Figure 8 (right). The best fitted exponential function has been determined by statistical analysis of the data and the function is proposed for the particular geogrid as used in this study.

The result from laboratory tests shows that, the application of laid and welded geogrids with a defined initial tensile stiffness may increase the soil elasticity modulus up to ca. 70%.

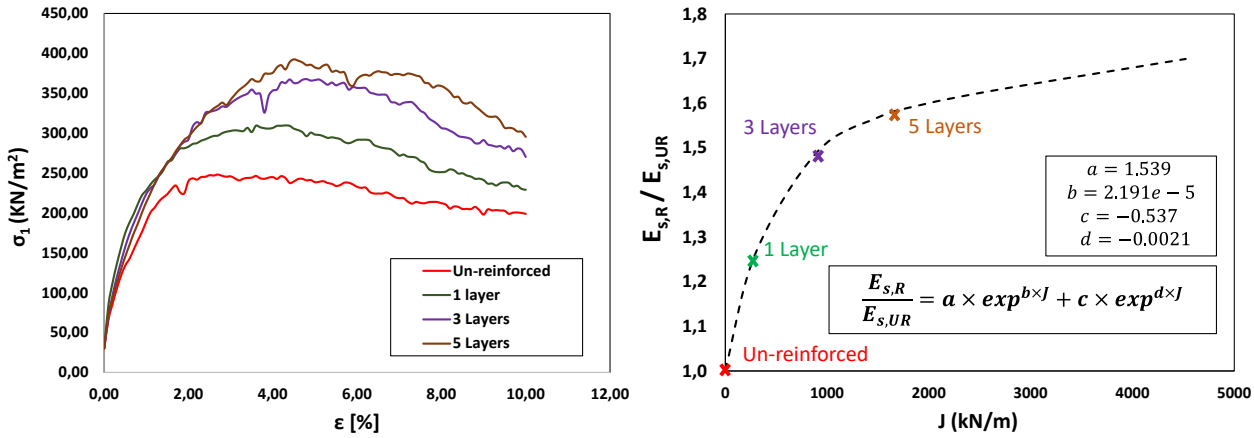

Figure 8. Improvement of soil mechanical behavior due to application of geogrid reinforcement

The modified deformation model is then applied to predict the settlements underneath the footing as measured in laboratory tests from Stuttgart tests taking into account the boundary conditions as defined for the experiments (Dσ = 120 kPa, μ_s = 0.3, $E_{s,UR}$ = 80000 kN/m for sandy material, B=0.25 m, L=0.35 m). For the test with two layers of a laid and welded geogrid reinforcement a total stiffness of 600 kN/m (@ 2% strain) are applied. Therefore, the $E_{s,R}$ can be predicted to 112720 kN/m according to Figure 8 and the proposed equation for estimation of equivalent elasticity. For this particular case study (Stuttgart test), the developed settlement equation estimates an immediate settlement of 21 mm. The comparison of recorded data (see Figure 3a) against the calculated settlement shows an inconsistency of less than 5% for this particular test.

CONCLUSION

The main objective of this study was to (i) generate a knowledge base through performing large scale laboratory tests to improve the understanding of the processes involved in the interaction of laid and welded geogrids and aggregates within working platforms; (ii) develop an optimized and reliable methodological approach for the prediction of the maximum bearing capacity of working platforms by overcoming the weaknesses of the BRE470 design methodology; (iii) quantify the effect of geogrid reinforcement on improvement of soil mechanical behavior and accordingly develop equation for the prediction of total immediate deformation of working platforms. In this regard the key achievement of this study can be summarized as follows:

(i) The large-scale laboratory tests on reinforced and non-reinforced working platforms under a rectangular plate at Stuttgart university along with the large scale triaxial tests at Aachen university were applied to improve the knowledge associated with the ultimate limit state (bearing capacity) and serviceability limit state (deformation) analyses of working platforms. Both tests revealed that the application of a laid and welded geogrid will improve soil mechanical properties and will enhance the working platform behavior in terms of bearing capacity and deformation.

(ii) Given the knowledge and practice gaps in the design of working platform (i.e. aforementioned weaknesses and shortcomings from BRE470) and considering the

results from large scale laboratory tests in Stuttgart a modified model is developed as derived from BRE470 and Hanna and Meyerhof (1980). The verification of model versus the data from large scale model tests showed that, the model is able to produce safe and economic results.

(iii) A new semi-empirical equation has been developed according to large scale triaxial tests at Aachen university to estimate the equivalent soil stiffness taking into account the stabilization function of laid and welded geogrids. The new equation will allow systematical prediction of the soil stiffness as a function of the geogrid axial tensile stiffness. The equivalent stiffness has been adapted into the settlement equation for a perfectly flexible foundation to estimate the immediate deformation of working platforms underlying cohesive soil. The accuracy of the new equation in predicting the platform deformation has been proven by comparing the results versus large-scaled lab tests at Stuttgart university (deviation less than 5%).

(iv) In contrast to currently applied models in practice, which solely focus on the punching resistance of the platform, the analysis in this study using a complex Kinematic Element Method (KEM) revealed that, the overall and rotational stability of the system might be dominant especially when the construction equipment (e.g. crane, piling rig) is positioned at the edge of the working platform. Therefore, it is obligatory to investigate the failure possibility via shear surfaces underneath the track due to rotational and overall failure modes in addition to available models in practice.

Although this study contributed to substantially enhance the BRE470 design model by the development of 3D equations for the prediction of maximum bearing capacity of the working platform over cohesive subgrade, a major limitation and uncertainty still remains which must be overcome in order to achieve a safer design of working platforms. In fact, further research is required to develop a more comprehensive model which can consider overall and rotational failure modes in addition to punching failure criteria.

REFERENCES

Al-Shenawy, A. O., & Al-Karni, A. A. (2005). Derivation of bearing capacity equation for a two layered system of weak clay layer overlaid by dense sand layer. *Pertanika J. Sci. & Technol*, 13(2), 213-235.

Ballard, J.-C., Delvosal, P., Yonatan, P., Holeyman, A. & Kay, S. (2011). Simplified VH equations for foundation punchthrough sand into clay. *Frontiers in Offshore Geotechnics II* (ed. Gourvenec & White), CRC:London, pp. 655-660.

BRE (2004). Working platforms for tracked plant. BR470. Garston, Watford

Burd, H. J., and Frydman, S. (1997). Bearing capacity of plane-strain footings on layered soils. *Canadian Geotechnical Journal*, 34(2), 241-253.

Chen, Q., & Abu-Farsakh, M. (2015). Ultimate bearing capacity analysis of strip footings on reinforced soil foundation. *Soils and Foundations*, 55(1), 74-85.

Das, B. M., & Sobhan, K. (2013). *Principles of geotechnical engineering*. Cengage learning.

Dobie, M., Lees, A., & Khanardnid, J. (2018). Case study: performance of a geogrid stabilised working platform constructed over extremely soft dredged silt. *In Proceedings of the 11th International Conference on Geosynthetics*, Korea.

Dobie, M. J. D., Lees, A. S., Buckley, J., & Bhavsar, R. (2019). Working platforms for tracked plant–BR 470 guideline and a revised approach to stabilisation design with multiaxial

hexagonal geogrids. *13th Australia New Zealand Conference on Geomechanics*, Perth Western Australia

El Samee, W. N. A. (2018). Effect of Shape and Depth of Shallow Foundations on Failure Mechanism and Wedge Angle of Sandy Soil. *In International Congress and Exhibition Sustainable Civil Infrastructures Innovative Infrastructure Geotechnology (pp. 197-216)*. Springer, Cham.

Eshkevari, S. (2019). Bearing capacity of surface strip footings on layered soils, *Doctoral dissertation*, University of Newcastle, Newcastle, England

Hanna, A. M., and Meyerhof, G. G. (1980). Design charts for ultimate bearing capacity of foundations on sand overlying soft clay. *Canadian Geotechnical Journal*, 17(2), 300-303.

Lees, A. 2017b. Bearing capacity of a stabilized granular layer on clay subgrade. *Proceedings of the 10th International Conference on the Bearing Capacity of Roads*, Railways and Airfields (eds. Loizos et al), 28-30th June, pp. 1135-1142.

K S Miller, K. S., (2013). Technical Note on Use of BR470 in Soft Clay

Meyerhof, G. G., & Hanna, A. M. (1978). Ultimate bearing capacity of foundations on layered soils under inclined load. *Canadian Geotechnical Journal*, 15(4), 565-572.

M. J. D. Dobie, A. S. (2019). Working platforms for tracked plant – BR 470 guideline and a revised approach to stabilisation design with multiaxial hexagonal geogrids. *13th Australia New Zealand Conference on Geomechanics*. Perth Western Australia.

Prandtl, L. (1921). über die Eindringungsfestigkeit (Härte) plastischer Baustoffe und die Festigkeit von Schneiden, *Zeitschrift für Angewandte Mathematik und Mechanik*, Basel, Switzerland, Vol. 1, No. 1, 15–20.

Rethaliya, R. P., & Verma, A. K. (2009). Strip footing on sand overlying soft clay with geotextile interface. *Indian Geotech J*, 39(3), 271-287.

Ruiken, A. (2013). Zum Spannungs-Dehnungsverhalten des Verbundbaustoffs "geogitter-bewehrter Boden". Dissertation. Aachen: Fakultät für Bauingenieurwesen, Lehrstuhl für Geotechnik, Rheinisch-Westfälische Technische Hochschule (RWTH).

Salimi Eshkevari, S., Abbo, A. J., & Kouretzis, G. (2019). Bearing capacity of strip footings on sand over clay. *Canadian Geotechnical Journal*, 56(5), 699-709.

Shoaei, M. D., Alkarni, A., Noorzaei, J., Jaafar, M. S., & Huat, B. B. (2012). Review of available approaches for ultimate bearing capacity of two-layered soils. *Journal of Civil Engineering and Management*, 18(4), 469-482.

Scotland, I., Poberezhniy, V., & Tatari, A. (2019). Reinforced soil shear key to mitigate extrusion failure in soft soils under working platforms. *In The XVII European Conference on Soil Mechanics and Geotechnical Engineering Reykjavik Iceland*. International Society for Soil Mechanics and Geotechnical Engineering.

Temporary Works Forum (2019). Design of granular working platforms for construction plant. A guide to good practice, *TWf2019: 02*, Temporary Works Forum, c/o Institution of Civil Engineers, London, England

Vollmert, L. & Bräu, G. (2018). Performance of geogrid reinforced and stabilized base courses. *In Proceedings of the 11th International Conference on Geosynthetics*, Korea.

Geosynthetics Conference

Landfill Closure with Engineered Turf Cover

Ming Zhu, Ph.D., P.E.[1], Bryan Scholl, Ph.D., P.E.[2] and Rutuparna Joshi, P.E.[3]

[1]Watershed Geosynthetics, 11400 Atlantis Place, Suite 200, Alpharetta, GA 30022; e-mail: mzhu@watershedgeo.com
[2]Watershed Geosynthetics, 11400 Atlantis Place, Suite 200, Alpharetta, GA 30022; e-mail: bscholl@watershedgeo.com
[3]Watershed Geosynthetics, 11400 Atlantis Place, Suite 200, Alpharetta, GA 30022; e-mail: rjoshi@watershedgeo.com

ABSTRACT

The final cover system is a critical component of a modern engineered landfill to isolate the waste and protect the environment. Recent years have seen increased use of the engineered turf cover for final closure of municipal and industrial waste landfills and coal combustion residuals (CCR) landfills and impoundments. A typical engineered turf cover consists of, from bottom to top, a structured geomembrane, an engineered turf, and a specified infill. The engineered turf cover overcomes long-standing challenges of soil erosion and veneer-type soil slope instability associated with many traditional soil covers. An overview of the engineered turf cover is provided, followed by a comparison of the engineered turf cover with the traditional soil cover. Technical performance of the engineered turf cover has been documented through extensive laboratory tests and numerous field observations. Major technical aspects of the engineered turf cover are discussed, including ultraviolet (UV) longevity, wind uplift, sand infill mobility, landfill settlement, cover slope stability, and landfill gas management. Beneficial reuse of a closed landfill with a new solar power generation technology is also presented.

INTRODUCTION

The final cover system is critical to achieve the performance standards set forth by regulations to close a landfill with the ultimate goal to manage and mitigate potential long-term risks that the underlying waste may pose to the environment. Traditionally, modern engineered landfills have been closed using soil covers that include both soil and geosynthetic materials (e.g., geomembrane, geosynthetic clay liner [GCL], and geocomposite). The past decade has seen increased use of the engineered turf cover for closure of waste containment facilities, including municipal solid waste (MSW) landfills, coal combustion residual (CCR) landfills and impoundments, and other industrial waste landfills [Abreu and Franklin 2014, Saindon 2019, SWANA 2017].

A typical engineered turf cover (e.g., ClosureTurf) consists of, from bottom to top, a structured geomembrane, an engineered turf, and a specified infill (Figure 1). The structured geomembrane serves as a hydraulic barrier to isolate waste from the environment and minimize infiltration of precipitation into the waste. The engineered turf is manufactured of polyethylene (PE) synthetic turf fibers (synthetic grass blades) tufted into a double-layer geotextile backing, which covers the underlying geomembrane and protects it from ultraviolet (UV) radiation exposure and wind uplift. The specified infill, which is a minimum 0.5-inch (13-millimeter [mm]) thick sand layer buried in the synthetic grass blades, provides additional wind ballast and UV protection and improves trafficability on the cover surface.

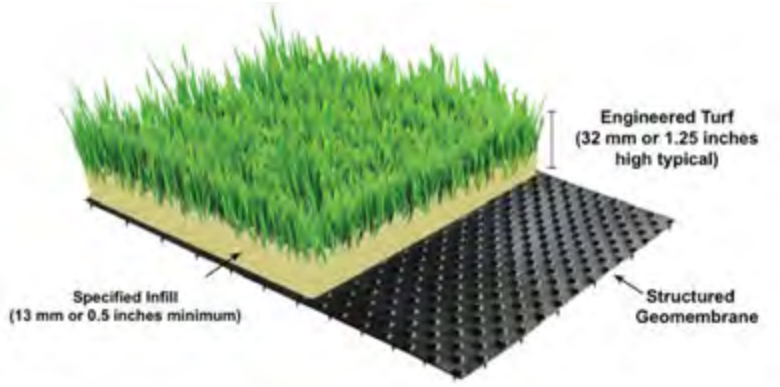

Figure 1. Illustration of the engineered turf cover.

The engineered turf cover meets the performance requirements of a final cover system by the U.S. EPA Subtitle D landfill and local state solid waste management regulations. It has been approved by the regulatory agencies as an alternative to the prescriptive soil cover system for the final closure of landfills. Since the first installation in 2009, more than 2,000 acres (800 hectares) of engineered turf covers have been installed at sites located in a wide range of weather conditions in the U.S. Aerial photos of two landfills installed with the engineered turf covers are shown in Figure 2.

Baldwin County Landfill, Georgia (Green Turf)

Portola Landfill, California (Tan Turf)

Figure 2. Photos of installed engineered turf covers.

COMPARISON BETWEEN ENGINEERED TURF COVER AND SOIL COVER

A traditional landfill soil cover, for example, consists of (from bottom to top) a geomembrane barrier layer, a geocomposite drainage layer, and minimum 24-inch (0.6-meter) thick soil layers (Figure 3). The engineered turf cover uses the engineered turf and specified infill to replace the soil layers in a traditional soil cover, as shown side by side for comparison with the traditional soil cover in Figure 3. Elimination of the soil layers overcomes two long-standing challenges associated with many traditional soil covers, i.e., soil erosion and veneer-type soil slope instability, because the soil layers are the sources of erosion and driving force behind landfill cover downslope movement [Duffy 2016, Zhu et al. 2019].

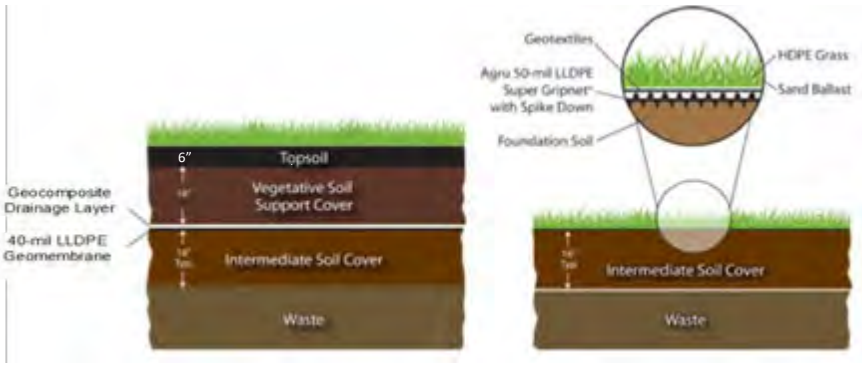

Figure 3. Comparison of a traditional soil cover with the engineered turf cover.

Compared with a traditional soil cover, the engineered turf cover is not dependent on availability and quality of borrow soils. Performance of the engineered turf cover is more predictable and less affected by changing weather conditions. Without the soil layers (except for the thin layer of sand infill), runoff from the engineered turf cover is virtually free of eroded soil particles. Abreu and Franklin [2014] presented a case study where the surface water runoff was sampled and tested to evaluate the quality of runoff from two distinct areas of the Tangipahoa Regional Solid Waste Facility located in Independence, Louisiana. One area was capped with the engineered turf cover and the other area with a clayey intermediate cover. Other than the type of cover installed, both areas were approximately 5 acres (2 hectares) in size and had similar characteristics. The test results indicated a turbidity of 11 Nephelometric Turbidity Units (NTU) for the runoff from the engineered turf cover area, compared to 371 NTU from the soil cover area. The Total Suspended Solids (TSS) concentration was measured to be less than 4 milligram per liter (mg/L) for the runoff from the engineered turf cover area, compared to 349 mg/L from the soil cover area. The runoff samples collected from the site (Figure 4) show the improvement in the runoff quality as a result of the engineered turf cover installation.

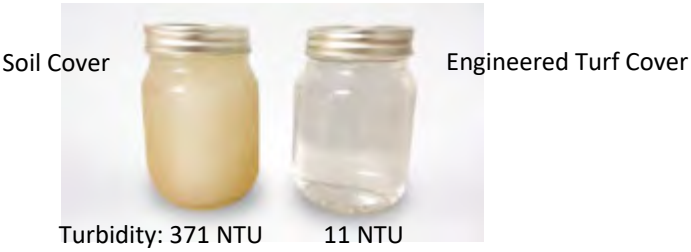

Figure 4. Runoff quality comparison between engineered turf and soil covers.

The engineered turf cover requires much less post-closure maintenance than a traditional soil cover because soil erosion repairs, re-vegetation, fertilization, mowing, and stormwater pond cleaning are not needed. The carbon footprint of the engineered turf cover is estimated to be 5 times less than traditional soil covers due to faster installation, less heavy construction equipment operations, less use of construction materials, and less truck trips, based on the data and calculation procedure by the Geosynthetic Institute (GSI) [Koerner et al. 2019]. Impact on local communities is less as a result of less truck traffic on local roads to transport construction materials. Land disturbance is avoided because borrow soils are not needed for construction of the engineered turf cover.

TECHNICAL ASPECTS OF ENGINEERED TURF COVER

UV Longevity. Advancements in polymer technology have made geosynthetic materials last much longer [Zhu et al. 2019]. The engineered turf cover is projected to last over 100 years, provided it is installed and maintained properly in accordance with design drawings, engineering specifications, and post-closure care requirements. This duration exceeds the current post-closure regulatory period of 30 years in the U.S. by more than 3 times.

The structured geomembrane component of engineered turf cover is protected by the overlying engineered turf and sand infill from UV exposure. Based upon the research by GSI [Koerner et al. 2011 and Koerner et al. 2012], a covered geomembrane has an expected lifetime (i.e., a half-life) of several hundred years. The engineered turf layer is comprised of two distinct parts: (1) a double-layer woven geotextile backing with enhanced UV resistance; and (2) PE turf fibers tufted into the woven geotextiles. The sand infill and turf fibers provide UV shielding of the geotextile backing. With the sand infill in place, the geotextile backing will remain intact and in place covering the structured geomembrane, allowing the geomembrane to realize its full design life.

Outdoor UV longevity testing was performed on the turf fibers at the Atlas Weathering Facility in New River, Arizona, which is among the highest UV radiation places in the U.S. Samples of the turf fibers were collected at approximately 1, 3, 5, and 10 years after being exposed in the field and then tested at an independent geosynthetics laboratory for tensile strength. The remaining tensile strength of the turf fibers was compared to the original tensile strength. Based on the test data, the number of years to reach 50% of the original tensile strength (i.e., the half-life) was projected to be over 100 years [Geosyntec 2015].

The turf fiber tensile strength values over time are compared to the required service value in Figure 5. At Year 100, the turf fibers are projected to have approximately 60% of the original tensile strength. Considering that the average tensile strength of virgin turf fibers is approximately 35 pounds (lbs) (156 Newtons [N]) per fiber, the tensile strength at Year 100 is therefore projected to be approximately 20 lbs (89 N) per fiber, which is still significantly greater than the minimum tensile strength necessary for the turf fibers to perform in the field (i.e., in the order of 3 to 4 lbs [13 to 18 N] per fiber). The minimum required tensile strength of the turf fibers was estimated by comparing a synthetic turf fiber to a real grass stem.

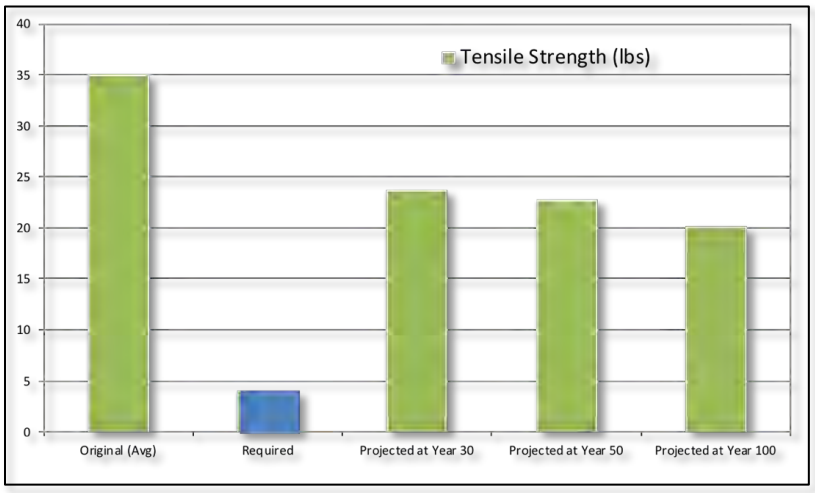

Figure 5. Projected engineered turf fiber tensile strength over time.

Field samples of turf fibers were collected and tested for tensile strength. The samples were collected from two engineered turf cover installations, the LaSalle-Grant Landfill in Louisiana and the Saufley Field Road Landfill in Florida. The exposure times of the field turf samples ranged from 5 to 8 years. The retained tensile strength of the turf field samples was compared with the results of outdoor UV testing in New River, Arizona, as presented in Figure 6. The real-world performance of engineered turf tensile strength matches or exceeds the results from the outdoor testing of UV exposure.

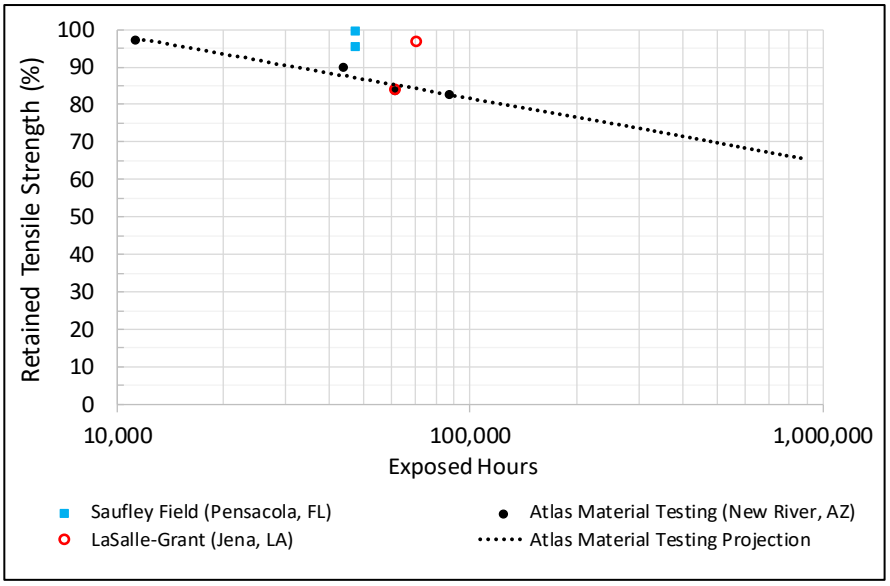

Figure 6. Outdoor testing and field performance of turf fiber tensile strength.

Wind Uplift. Extensive wind tunnel studies have been performed to evaluate the wind performance of the engineered turf cover. It was tested in 2010 for wind speeds up to approximately 120 miles per hour (mph) (190 kilometers per hour [km/h]) at the Georgia Tech Research Institute (GTRI) Aerospace, Transportation & Advanced Systems Laboratory. The test was performed on a flat surface and no uplift of the engineered turf sample was observed due to the wind load. A photo of the test is shown on the left in Figure 7.

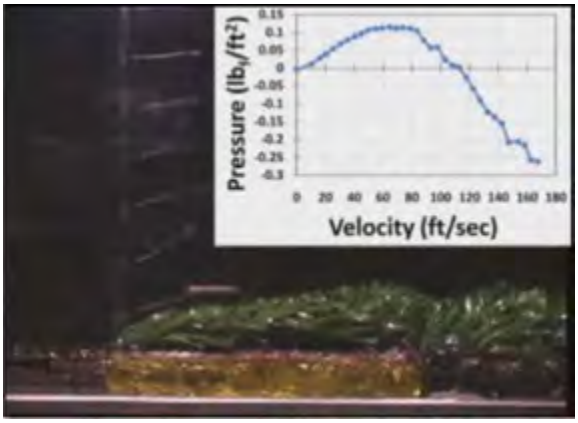

Georgia Tech Test, 2010

Iowa State University Test, 2018 and 2019

Figure 7. Engineered turf cover wind tunnel testing.

More wind tunnel tests of the engineered turf cover were conducted in 2018 and 2019 at the Iowa State University Aerodynamic and Atmospheric Boundary Layer Wind and Gust Tunnel [Zheng et al. 2020]. The tests were conducted on scaled landfill models constructed with a 3 horizontal to 1 vertical (3H:1V) slope on one end, a top deck, and a 4H:1V slope on the other end. A photo of one of the testing models is shown on the right in Figure 7. The pressure distribution along the cover surface was measured using pressure taps. As a comparison to the engineered turf cover, wind tunnel tests were also conducted on an exposed geomembrane cover.

The wind tunnel test results are presented in the format of wind pressure coefficient, C_p. An example of the measured C_p distribution for the case where the 3H:1V slope was facing in the wind direction is presented in Figure 8. Positive C_p corresponds to pressure acting toward the surface (i.e., downward pressure or compression) and negative C_p corresponds to pressure acting away from the surface (i.e., upward pressure or uplift). The horizontal locations of the measurement points, x, were normalized by the length of the model, L, as x/L in the plot. The measured wind uplift pressures for the engineered turf cover are significantly lower than those for the exposed geomembrane cover, as a result of the increased surface roughness of the engineered turf cover.

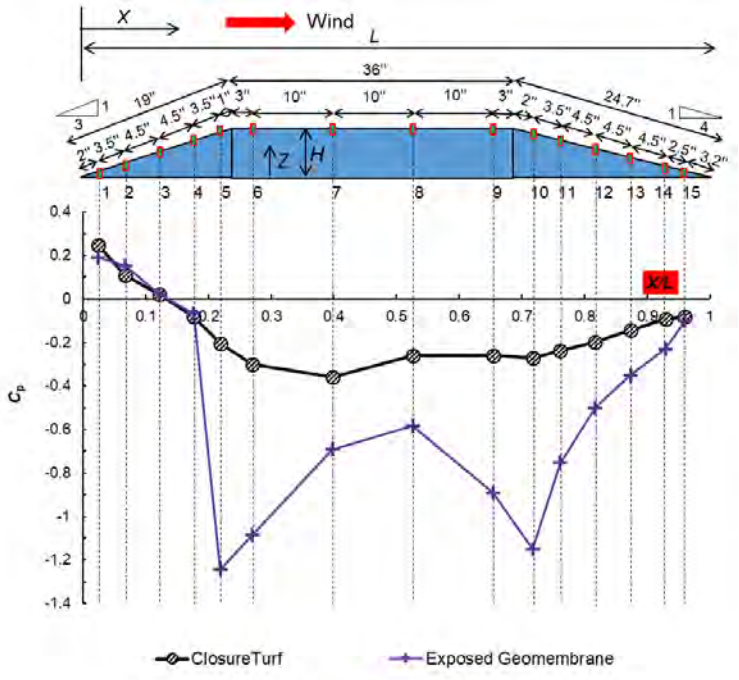

Figure 8. Wind pressure coefficient distributions of engineered turf and exposed geomembrane covers based on wind tunnel testing

The wind pressure coefficient can be used to calculate the wind load using the following equation [Giroud et al. 1995, Wayne and Koerner 1988]:

$$P = \frac{1}{2} \cdot C_p \cdot \rho \cdot U(H)^2$$

where, P (pounds per square foot [psf]) is wind-generated pressure normal to the surface, ρ is the air density (ρ = 0.0024 slug/cubic foot [ft^3] at 59^{o}F and sea level), $U(H)$ (feet/second [ft/s]), is the

upstream mean wind speed at the height of slope H (feet [ft]), and C_p is the wind pressure coefficient (dimensionless).

The results of the wind tunnel tests can be used in engineering practice to evaluate whether the landfill cover system has sufficient ballast to protect it from wind uplift under a design wind speed. Engineered turf covers have been installed in high wind regions along the East, Gulf, and West Coasts in the U.S. To date, there has been no report of damage to the installed engineered turf covers due to wind.

Sand Infill Mobility. Large-scale rainfall erosion testing (ASTM D6459) and channel erosion testing (ASTM D6460) have been conducted to evaluate hydraulic performance of the engineered turf cover, specifically the sand infill mobility. The large-scale rainfall erosion test results show minimal sand loss (i.e., less than 0.1%) at the simulated rainfall intensity up to 6.57 inches per hour (167 mm per hour). The large-scale channel erosion test results show a sand thickness loss of less than 0.05 inches out of the original thickness of 0.5 inches at an estimated hydraulic shear stress of 0.8 psf (38.3 Pascals [Pa]). The sand infill specification has been developed as a result of the extensive hydraulic testing program and is shown in Figure 9. The specification includes requirements of the grain size distribution, angularity, and specific gravity of the sand infill.

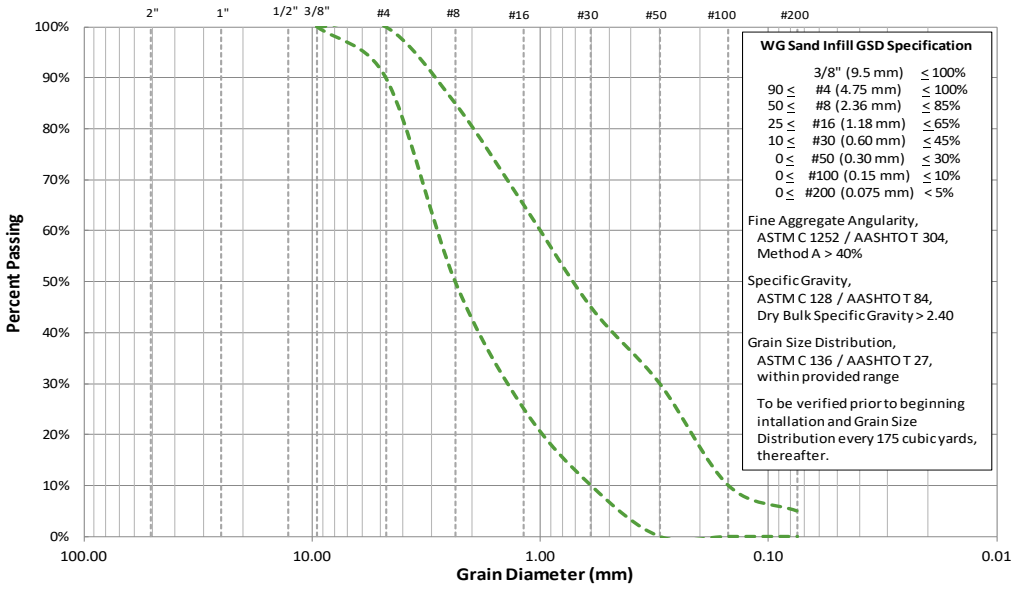

Figure 9. Engineered turf cover sand infill specifications.

Multiple landfill sites along the East Coast installed with engineered turf covers have been hit by significant rainfall events, including hurricanes and tropical storms. Field observations indicate that the engineered turf covers have performed as expected without significant sand infill movement.

Landfill Settlement. Landfill settles due to compression and consolidation of waste and foundation soils. Settlement is expected to continue after the landfill is closed. Differential settlement as a result of inhomogeneous waste properties can create local depression and surface cracks on a traditional soil cover. The engineered turf cover, which consists of flexible geomembrane and engineered turf with high elongation properties, can tolerate much greater

differential settlement than the traditional soil cover. In the technical paper by O'Malley et al. [2017], a case study was presented where the engineered turf cover installed on a 70-acre (28-hectare) industrial ash/sludge impoundment had experienced significant differential settlement two years after closure with no detrimental impact on the overall cover performance.

Repairs of local depression to correct grade reversal of the geomembrane are easier and less costly for the engineered turf cover than a traditional soil cover because no soil layers need to be excavated and backfilled. A local depression on an engineered turf cover, if it occurs, can be repaired by a small crew using light equipment and tools. A flowable backfill (e.g., a mix of fly ash, cement, and water) can be pumped into the void under the engineered turf cover through holes cut into the geomembrane to raise the cover to original grades. After the slurry injection is complete, the holes in the geomembrane are patched and seamed with new pieces of geomembrane. At the end of the repairs, the engineered turf is repaired by a heat-bonded seam, and the sand infill is re-placed to cover the engineered turf.

Cover Slope Stability. As discussed previously, one of the long-standing challenges with traditional soil covers is veneer-type soil slope instability that in some cases could result in failures (i.e., sliding) of the soil covers. Such failures have been documented in literature, a majority of which were attributed to internal drainage clogging and subsequent saturation of soil layers, insufficient internal shear strength of soil materials, and insufficient interface shear strength of the soil layers and underlying geosynthetic materials [Bonaparte et al. 2004, Duffy 2016, Nadukuru et al. 2017, Siebecker 2005, Stark and Newman 2010]. By replacing the overburden soil layers with an engineered turf and a thin layer of sand infill, the engineered turf cover essentially eliminates possibility of veneer-type soil slope instability associated with a traditional soil cover.

Stability of the engineered turf cover is evaluated by investigating the shear strength of the two interfaces, i.e., the turf/geomembrane and geomembrane/subgrade interfaces, to prevent potential movement that could result in wrinkles of the engineered turf cover. Direct shear testing has been performed to evaluate the interface shear strength of the engineered turf layer against the underlying structured geomembrane. For example, Figure 10 shows the direct shear test results of the interface between the engineered turf and Super Gripnet geomembrane. The test results indicate a peak interface friction angle of 36 degrees and a large-displacement interface friction angle of 25 degrees.

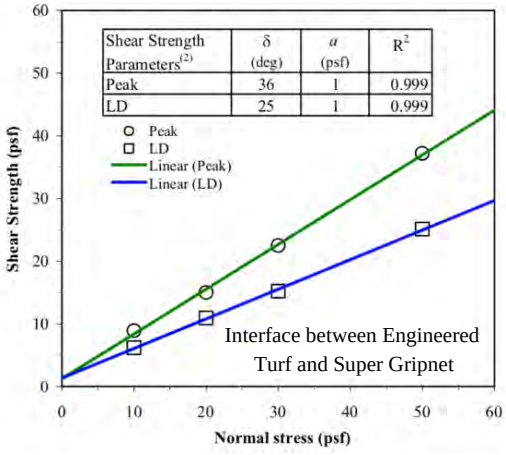

Figure 10. Direct shear results between engineered turf and structured geomembrane

The interface shear strength between the structured geomembrane and the subgrade depends on the subgrade materials at the project site. A site-specific direct shear testing should be performed using subgrade samples collected from the project site to obtain the interface friction angle of the structured geomembrane against the subgrade. The interface shear strength values obtained from the direct shear testing are used by geotechnical engineers to evaluate whether the calculated factor of safety (FS) of the engineered turf cover meets a specified target FS for landfill cover slope stability. Due to the advantage of cover slope stability, the engineered turf cover has been installed on landfills with side slopes as steep as 2.5H:1V to 2H:1V, including sites located in high seismic zones.

Landfill Gas Management. Landfill gas collection and control system (GCCS) is another critical component of modern engineered landfills, especially MSW landfills where significant landfill gas can be generated as the waste degrades over time. The engineered turf cover can be integrated with the conventional landfill GCCS that consists of vertical gas extraction wells, as shown in Figure 11. Geomembrane boots are used to seam the penetration around the gas well to prevent gas migration.

Figure 11. Landfill gas extraction wells integrated with engineered turf cover.

Pressure relief valves have been developed for the engineered turf cover to protect it from potential gas uplift during a shutdown of the landfill gas flare system or due to malfunction of the landfill gas collection system. It is designed as a one-way check valve to relieve the gas pressure below the engineered turf cover, which is only activated when a small positive gas pressure builds up below the geomembrane. A picture of the pressure relief valve installed in the field is shown in Figure 12.

Figure 12. Pressure relief valve for engineered turf cover.

BENEFICIAL REUSE OF LANDFILL COVER

One of the beneficial reuses of the large space after landfill closure is to convert it to a solar farm, a clean source of green energy. The engineered turf cover makes a preferred foundation for a solar farm, because it requires minimal post-closure maintenance. The solar panels are free of potential damage from mowing equipment used for traditional soil covers. The runoff from the drip edge of the solar panels does not create soil erosion that undermines the traditional soil cover foundation. In addition, the landfill closed with the engineered turf cover is a relatively dust free environment promoting more efficient solar collection.

A new solar power generation technology consisting of a patent-pending solar panel system has been custom-designed for direct installation on the engineered turf cover. It is a three-component system that consists of solar panels, mounting rails, and friction strips, as shown in Figure 13.

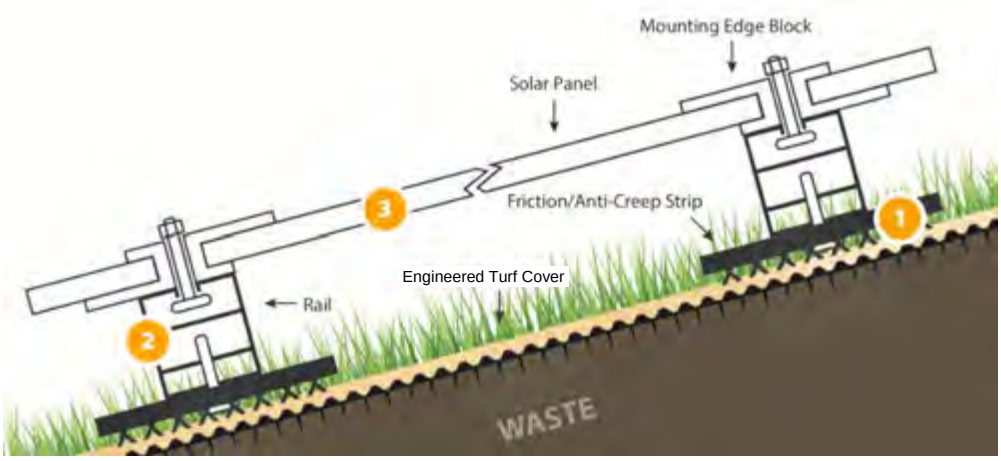

Figure 13. Solar power generation system.
System components: (1) friction strip connected to rail; (2) rail with mounting edge block; and (3) solar panel connected to mounting edge block

The new solar panel system does not require penetrations through or mechanical connections to the engineered turf cover. The friction strips attached to the underside of the mounting rails provide sufficient interface friction between the solar panels and underlying engineered turf cover, which maintains stability of solar panels and keeps them from sliding on slopes with inclinations typical of final cover systems. Because of the non-racking design, this new solar panel system is faster and easier to install than traditional solar systems supported using a ballasted racking system. It can be installed on landfill side slopes in addition to top decks, thereby maximizing the power-generation potential of a closed landfill site. Figure 14 is a photo of the new solar panel system installed on the engineered turf cover at the Chadwick Road Landfill, Georgia, as part of a demonstration project. As can be seen from the photo, the solar panel system is flexible and can accommodate local differential settlement of the landfill cover, allowing for installation of solar panels while the landfill is still going through the settlement stage.

Figure 14. Solar power generation system installed on engineered turf cover.

The new solar panel system has been tested extensively in the wind tunnel facility at the Iowa Stata University using both scaled and full-size solar panel models. The test results have demonstrated satisfactory wind performance due to its low-profile setup and aerodynamic boundary conditions associated with the underlying engineered turf cover. The wind load design guidance has been developed based on the wind tunnel test results and the new solar panel system can be designed properly based on site-specific geometries and the selected design wind speed to keep it from wind uplift.

REMARKS

The engineered turf cover provides an innovative geosynthetic solution to overcome long-standing challenges faced by the traditional soil cover approach. Extensive laboratory testing and over a decade of field installation have demonstrated that the engineered turf cover can meet the performance requirements for landfill closure. The engineered turf cover can be used with the new custom-designed solar power generation technology to provide another innovative solution for beneficial reuse of the closed landfill space and maximize the generation of clean and renewable energy.

REFERENCES

Abreu R.C. and Franklin J. (2014). Design and installation of a geosynthetic final cover utilizing artificial turf in Louisiana, *7th International Congress on Environmental Geotechnics, ICEG 2014*, Barton, ACT, Engineers Australia: 1397-1404.

Bonaparte, R., Gross, B.A., Daniel, D.A., Koerner, R.M., and Dwyer, S.F. (2004). *Technical Guidance for RCRA/CERCLA Final Covers*, United States Environmental Protection Agency, Office of Solid Waste and Emergency Response, Washington DC.

Duffy, D.P. (2016). The worst-case scenario: landfill cover erosion and slope instability, *MSW Management*, Feb. 9th, 2016.

Geosyntec (2015). *Literature Review and Assessment of ClosureTurf® UV Longevity*, Report prepared by Geosyntec Consultants for Watershed Geosynthetics, 15 May 2015.

Giroud, J.P., Pelte, T., and Bathurst, R.J. (1995). Uplift of geomembranes by wind, *Geosynthetics International*, Vol. 2, No. 6, 897-952.

Koerner, R.M., Hsuan, G.Y., and Koerner G.R. (2011). *Geomembrane Lifetime Prediction: Unexposed and Exposed Conditions*, GRI White Paper #6, Original: June 7, 2005 Updated: February 8, 2011.

Koerner, R.M., Koerner G.R., Hsuan, G.Y., and Wong, W.K. (2012). *Lifetime Prediction of Laboratory UV Exposed Geomembranes: Part I - Using a Correlation Factor*, GRI White Paper #42, January 3, 2012.

Koerner, R.M., Koerner, J.R., and Koerner, G.R. (2019). *Relative Sustainability (i.e., Embodied Carbon) Calculations with Respect to Applications Using Traditional Materials Versus Geosynthetics*, GSI White Paper #41, April 10, 2019.

Nadukuru S., Zhu M., Gokmen C., and Bonaparte R. (2017), Combined seepage and slope stability analysis of a landfill cover system, *Geotechnical Frontiers 2017*, ASCE GSP 276.

O'Malley P.C., Urrutia, J.L., and DiGuilio D. (2017), Using a tufted geosynthetic final cover system to effectively close an ash/sludge impoundment, *Geotechnical Frontiers 2017*, ASCE GSP 276.

Saindon, A. (2019), Lessons learned in alternative coal ash pond closure design and construction, *Geosynthetics Magazine*.

SWANA (2017). *Alternative Final Cover Systems and Regulatory Post-Closure Care*, Solid Waste Associate of North America.

Siebecker B. (2005), When final caps fail, *Waste 360*, May 01, 2005.

Stark T.D. and Newman, E.J. (2010), Design of a landfill cover system, *Geosynthetics International 17*, No. 3, 124-131.

Wayne, M.H. and Koerner, R.M. (1988), Effect of wind uplift on liner systems, *Geotechnical Fabrics Report*, July/August.

Zheng, J., Sarkar, P., Jafari, M., Hou, F., Li, Z., Sun, Q., and Zhu, M. (2020), Wind tunnel study of ClosureTurf landfill final cover system, *Geo-Congress 2020*, GSP 316, 650-658.

Zhu, M., Isola M., and Zornberg J. (2019), Advances in geosynthetic solutions for sustainable landfill design - geosynthetics really do last, *GeoStrata*, November/December 2019 Issue: 60-65.

Geosynthetics Conference

Numerical Modeling on the Use of Geotextiles to Reinforce Buried HDPE Pipes Subjected to Localized Ground Subsidence

Min Zhou, Ph.D.,[1] Fei Wang, Ph.D., P.E.,[2] and Yan-Jun Du, Ph.D.[3]

[1]Assitant Professor, School of Science, North University of China, Taiyuan, Shanxi, China, 030051; Formerly, Ph.D. student, Institute of Geotechnical Engineering, Southeast University, Nanjing, Jiangsu 210096, China; e-mail: 20190078@nuc.edu.cn
[2]Assistant Professor, Department of Engineering and Computer Science, Tarleton State University, Box T-0390, Stephenville, TX 76402, USA; e-mail: feiwang@tarleton.edu
[3]Professor and Director, Institute of Geotechnical Engineering, Southeast University, Nanjing, Jiangsu 210096, China; e-mail: duyanjun@seu.edu.cn

ABSTRACT

Failures of buried High-Density Polyethylene (HDPE) pipes caused by localized ground subsidence have been reported all over the world. However, as of today very few studies have been done on the protection of buried pipes subjected to localized ground subsidence. The authors previously conducted 1g physical modeling tests and geotextiles were verified as effective materials to reinforce the buried HDPE pipes subjected to localized ground subsidence. In this study, three-dimensional finite element numerical modeling was adopted to further understand the performance of the geotextile-reinforced buried HDPE pipes subjected to localized ground subsidence. The numerical model was firstly validated using the physical modeling test results. Subsequently, parametric study including five cases was conducted to investigate the influence of installation location and number of geotextile layers on the performance of the reinforced HDPE pipes subjected to localized ground subsidence. Based on the numerical modeling results, single layer of geotextile installed at the pipe bottom was proved as the best mitigation methodology for buried HDPE pipes subjected to localized ground subsidence.

INTRODUCTION

Buried pipelines are increasingly threaten by localized ground subsidence, and the accidents of pipelines caused by localized ground subsidence have been reported all over the world (O'Rourke and Liu, 1999; and Zhou et al., 2019). Localized subsidence is generally defined as a deep and narrow depression with a slope steeper than 1/2000 (Zhou et al., 2019). High Density Polyethylene (HDPE) pipe, widely adopted in municipal projects, could be damaged easily by the localized ground subsidence due to low flexure bending resistance along the pipe (Zhou et al., 2019). Geosynthetics have been widely used in pipeline projects to minimize the effect of external loads on pipes including traffic loads and penetrating loads. Kawabata et al. (2003) used five layers of geogrids to reduce the overburden load on a deeply HDPE buried pipe, which resulted in a reduction of 25% of the overburden load above the pipe. Tafreshi and Khalaj (2008) pointed out that geosynthetic reinforcement was effective to reduce the ground surface settlement and deflection of pipes. Palmeira and Andrade (2010) proposed the use of geogrids to prevent the damages of buried steel pipes from penetrating loading and the wrapped-around reinforcement mode turned out to be the best reinforcing mode. Geocells were used by Mehrjardi et al. (2013) to protect buried PVC pipes, which caused a reduction of 65% and 35% for ground surface

settlement and pipe deflection, respectively. Corey et al. (2014) concluded that the geogrids placed above the pipe could reduce settlement at the backfill surface and the pipe deflection by 11% and 26%, respectively. Zhou et al. (2020) proposed the use of geosynthetics to reinforce pipes subjected to localized subsidence and found out the woven geotextile underneath the pipe had the best performance in terms of the earth pressure on the pipe and the pipe deflection. However, the previous studies are mostly lab-scale model tests, and test cases are limited. In other words, it is impossible to test all cases. Therefore, numerical modeling was adopted in this study to evaluate the performance of geotextile-reinforced buried HDPE pipes subjected to localized ground subsidence considering installation location and layer number of geotextile reinforcement.

NUMERICAL MODELING

Numerical Modeling Cases. Based on the model test results in Zhou et al. (2020), woven geotextile was found to be a better solution for reinforcing flexible pipes subjected to localized ground subsidence compared to geogrids. To further investigate the performance of the proposed mitigation method, the effects of location and layer number of the geotextile on the pipe behaviors were investigated by conducting a series of numerical modeling. Numerical modeling cases are summarized in Table 1.

Table 1. Summary of numerical cases.

Case No.	Reinforcement location	Reinforcement layer number
1*	pipe invert	1
2	0.2 m underneath pipe invert	1
3	0.4 m underneath pipe invert	1
4	pipe invert and 0.2 m from pipe invert	2
5	Pipe invert and 0.2 and 0.4 m from pipe invert	3

** Baseline case*

Baseline Model. A commercial Finite Element Method (FEM) software ABAQUS® was adopted in this study to simulate the performance of HDPE pipe subjected to localized ground subsidence. Considering the symmetry of the numerical model, only half of the baseline model is used as shown in Figure 1. The boundary conditions are shown in Figure 1(a), and a displacement is applied at the bottom of the model to simulate the localized ground subsidence. The side boundaries of the model were restrained against displacements in the horizontal direction, and the top surface was set at free displacement. The height, width, and length of the model were 1,100, 1,000, and 2,000 mm, respectively. The outer diameter of the HDPE pipe was 150 mm, and the wall thickness of the pipe was 9 mm. A layer of geotextile was installed at the bottom of the pipe for the baseline model, which has a width of 1,000 mm and a length of 2,000 mm. The surrounding soil was simulated using C3D20R, and the geotextile was modeled using M3D8R which was the special model for geotextiles provided by the ABAQUS software. Hard contact was used to simulate the interfaces of the pipe and geotextiles with the surrounding soil. Hard contact is a type of contact which the normal force is not limited, and the interfaces would be separated if the normal force is equal to zero. The coefficient of friction at the interface of pipe and soil was 0.7, while the one for geotextile-soil interface was 0.9. Elastic perfect plastic responses of soil were

characterized using the Mohr-Coulomb failure criterion. Elastic model was employed for HDPE pipe and geotextile reinforcement. The parameters used in the numerical model are summarized in Table 2.

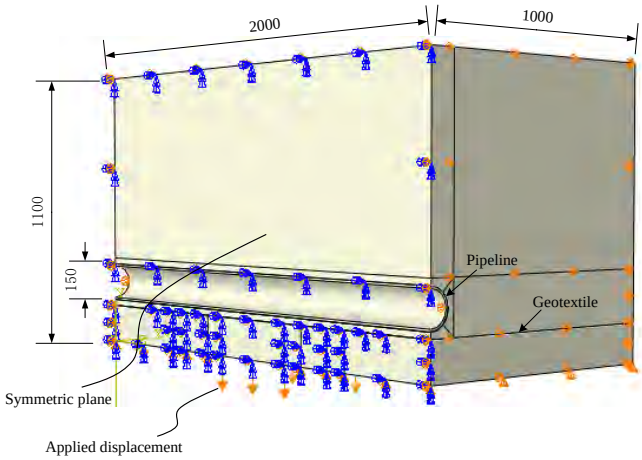

(a)

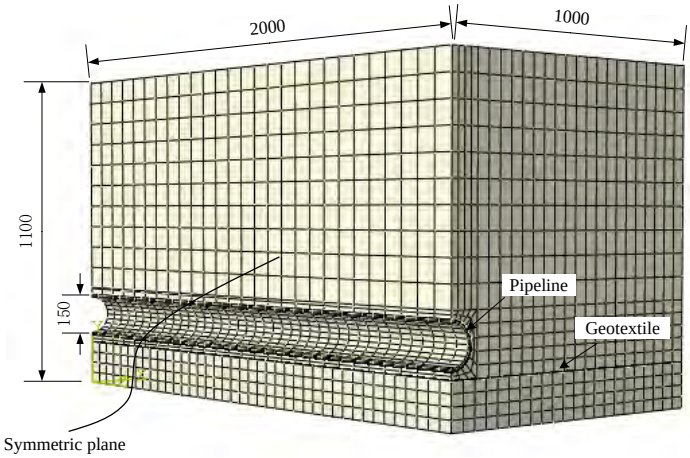

(b)

Figure 1. Numerical baseline model.

Table 2. Summary of parameters used in the numerical modeling.

Parameters	HDPE pipe	Surrounding soil	Geotextiles
Elastic Modulus (MPa)	513	2.6	300
Poisson's Ratio	0.46	0.3	0.45
Density (g/cm^3)	0.95	14.6	0.12
Friction Angle (°)	—	31	—
Cohesion (kPa)	—	1.0	—

The following procedure was adopted in the numerical modeling:

(1) Create the model, mesh, and boundaries.
(2) Apply gravity to the model and run the model to equilibrium.
(3) Reset the displacement to zero and activate the pipe and geotextile elements.
(4) Apply the displacement at the bottom of the model to simulate the localized ground subsidence.

Verification of Numerical Model. To verify the effectiveness of the numerical modeling procedure, physical model test results from Zhou et al. (2020) was adopted to compare with the numerical results. A custom-made model test box with a dimension of 2.0 m in length, 2.0 m in width, and 1.5 m in height was adopted to evaluate the HDPE performance subjected to localized settlement. The bottom of the model test box consists of eight moveable plates with a width of 0.25 m, and the middle four plates (#3, #4, #5, and #6 as shown in Figure 2) were lowered in a designed sequence with different magnitudes to form localized ground subsidence. The numbers (from 1 to 6 in Figure 3) are the lowering sequence, and the lowering magnitudes are 10, 20, and 20 mm for three lowering distances for each plate. Therefore, total lowering distances for each plate are 10, 30, and 50 mm. Three measuring sections were setup to measure pipe displacement with a horizontal distance of 0.5, 0.75 and 1.0 m (i.e., the middle of the box) from the side wall of the box, respectively. More details can be found in Zhou et al. (2020). Measured displacements of the pipe with diameter of 200 mm reinforced by geotextile at pipe invert were used to verify the numerical model used in this study including boundary conditions, constitutive models of HDPE pipe, soil and geotextile.

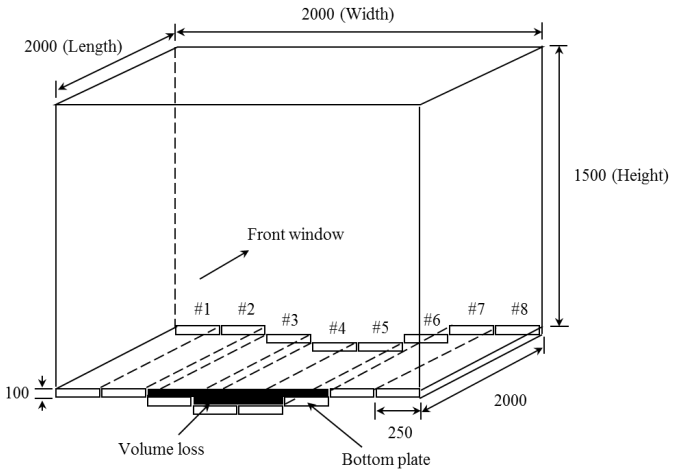

Figure 2. Schematic diagram of physical model box (unit: mm).

Figure 3 shows the comparison of the calculated and measured pipe displacement at different bottom plates lowering sequences. It can be seen from Figure 3 that the error is in a range of 5% to 9%, which demonstrates the numerical modeling procedure used in this study is effective. Table 3 is the comparison of the measured and calculated earth pressures at the pipe top. The relative error of the earth pressures is in a range of 11.2% to 43.8%, which might be caused by the following reasons: (1) the surrounding soil in the numerical model is a continuum media, and the relative displacement of sand particles cannot considered in the numerical modeling, which could not simulate the soil arching effect above the pipe very accurately; and (2) the displacement at the

bottom of the numerical model was directly applied as the target value; however, the displacement at the bottom in the physical model tests was applied gradually to the target value. The soil arching might be different if a different displacement mode is used even with the same target displacement.

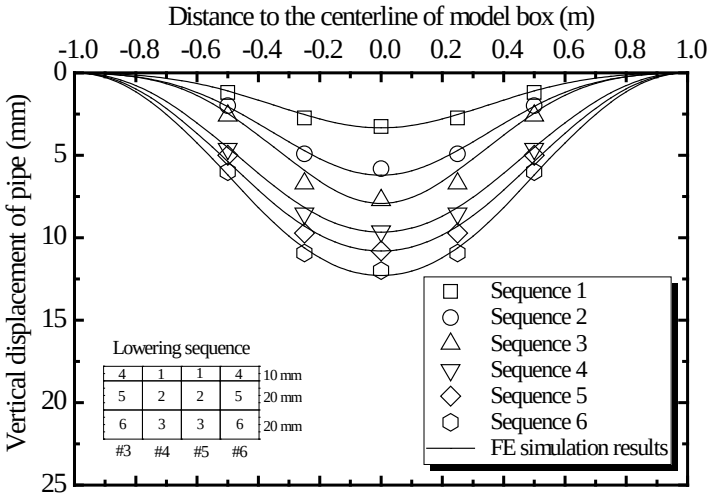

Figure 3. Comparison of measured and calculated vertical displacement of pipe.

Table 3. Comparison of measured and calculated earth pressure at the pipe top.

Lowering sequence	Measuring section 1			Measuring section 2		
	Measured (kPa)	Numerical (kPa)	Error (%)	Measured (kPa)	Numerical (kPa)	Error (%)
1	7.9	6.4	23.4	8	8.9	11.2
2	9	7	28.6	8.3	9.8	18
3	10	7.4	35.1	8.6	10.3	19.8
4	11.5	8	43.8	9.1	11.3	24.2
5	12	8.4	42.9	9.9	11.8	19.2
6	12.5	10.5	19	12	14.7	22.5

NUMERICAL RESULTS ANALYSIS

Vertical Displacement of Pipe. Figure 4 shows variations of vertical displacement of pipe at different applied vertical displacement at the model bottom. It can be seen from Figure 4 that (1) the pipe vertical displacement is much less than the vertical displacement applied at the model bottom, which demonstrates the effectiveness of the geotextile reinforcement; and (2) the vertical displacement of pipe increases with the increase of vertical distance from the location of geotextile to the pipe invert. The possible reason is that the differential settlement in the soil between the geotextile and the pipe could enlarge the deformation of the geotextile which results in a large displacement of the pipe.

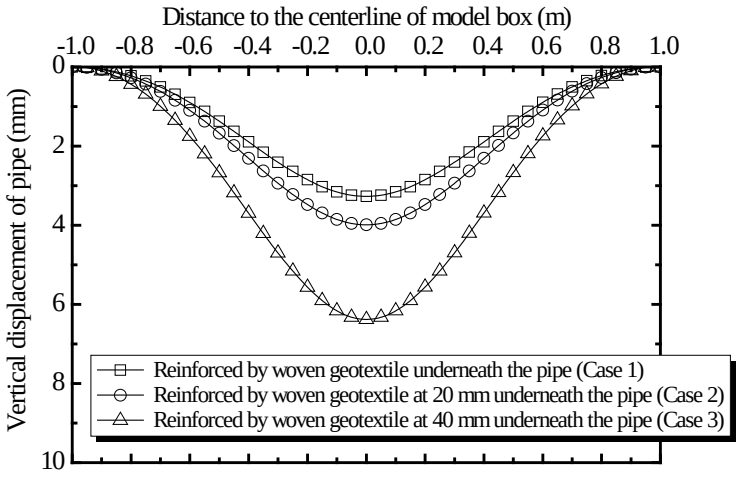

(a) vertical displacement of 10 mm

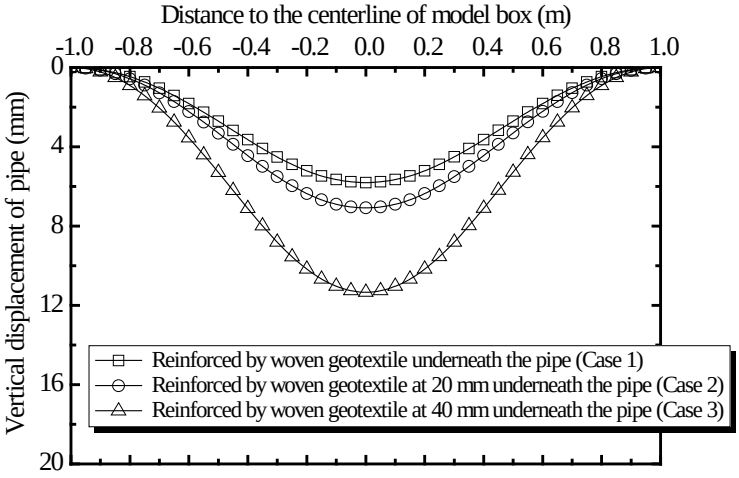

(b) vertical displacement of 30 mm

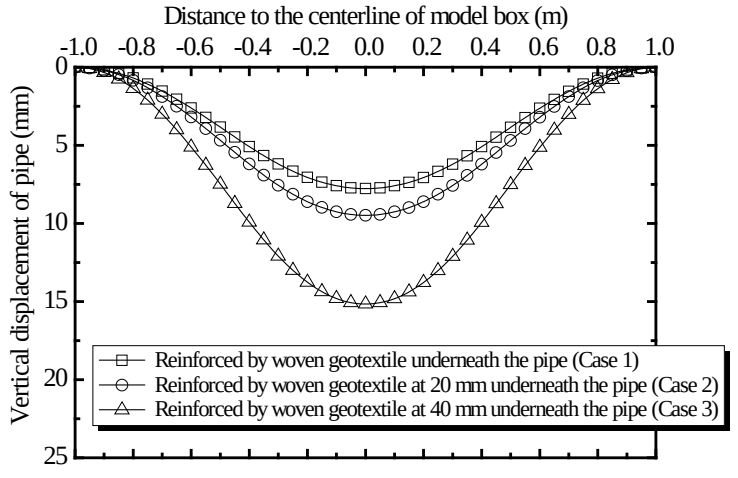

(c) vertical displacement of 50 mm

Figure 4. Variations of vertical displacement of pipe at different vertical displacement at model bottom with a single layer of geotextile reinforcement.

Vertical Displacement of Geotextile Reinforcement. Figure 5 shows variations of vertical displacement of geotextile at different vertical displacement at model bottom with single layer reinforcement. It can be seen from Figure 5 that (1) the vertical displacement of geotextile increases with the increase of the distance from the location of geotextile to the pipe (i.e., decrease of the distance to the model bottom); (2) the vertical displacement of the geotextile is larger than that of the pipe in the same numerical case, which might be caused by the lower bending stiffness of the geotextile compared with the HDPE pipe; and (3) the settlement trough of the geotextile is wider when it is close to the model bottom, and the possible reason is the vertical load above geotextile is carried by the geotextile reinforcement through tensile force in the geotextile, which could cause elongation of the geotextile.

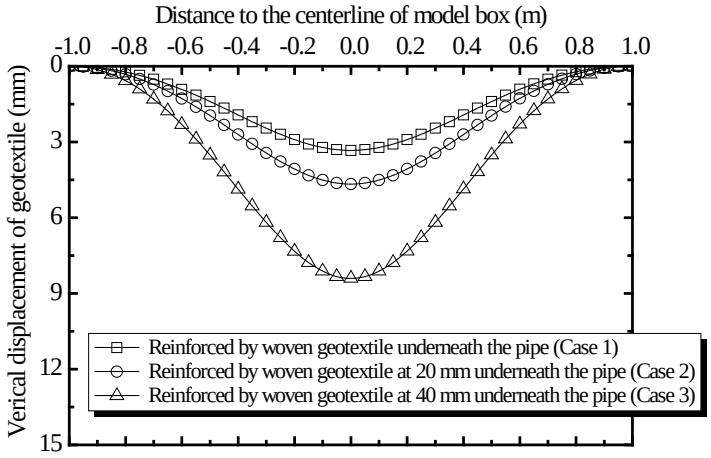

(a) vertical displacement of 10 mm

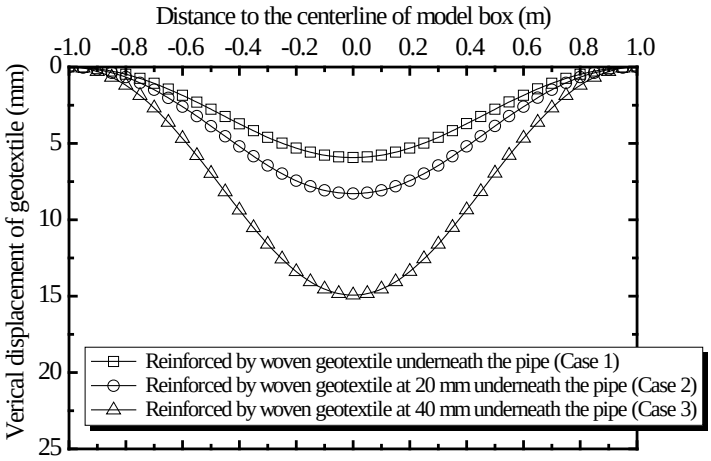

(b) vertical displacement of 30 mm

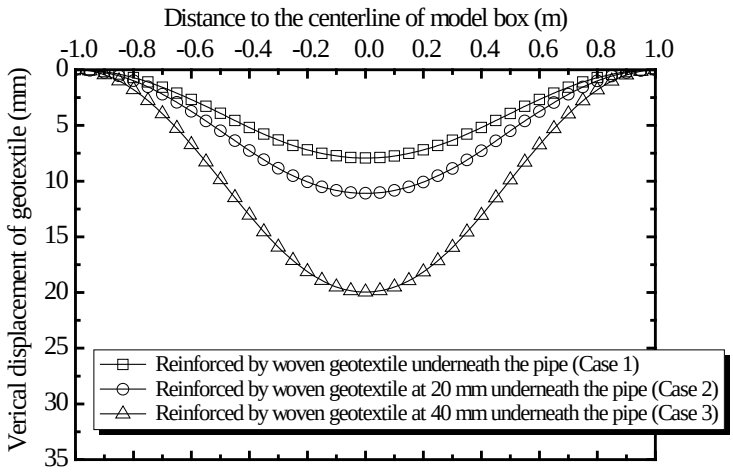

(c) vertical displacement of 50 mm

Figure 5. Variations of vertical displacement of geotextile at different vertical displacement at model bottom with single layer of geotextile reinforcement.

Effect of Geotextile Layer Number. Figure 6 presents variations of vertical displacement of pipe with multiple layers of geotextile reinforcement. It is seen that the vertical displacements of pipes for the cases with single, two, and three layers of geotextile reinforcements are almost the same, and the relative error is less than 5%. The reason is the vertical displacement of the pipe subjected to localized ground subsidence could be controlled mainly by the geotextile installed at the pipe bottom, and the benefits from the other two layers of geotextiles are minimal. It can be concluded that the reinforcement only installed at the pipe bottom should be sufficient to protect the pipe subjected to localized ground subsidence.

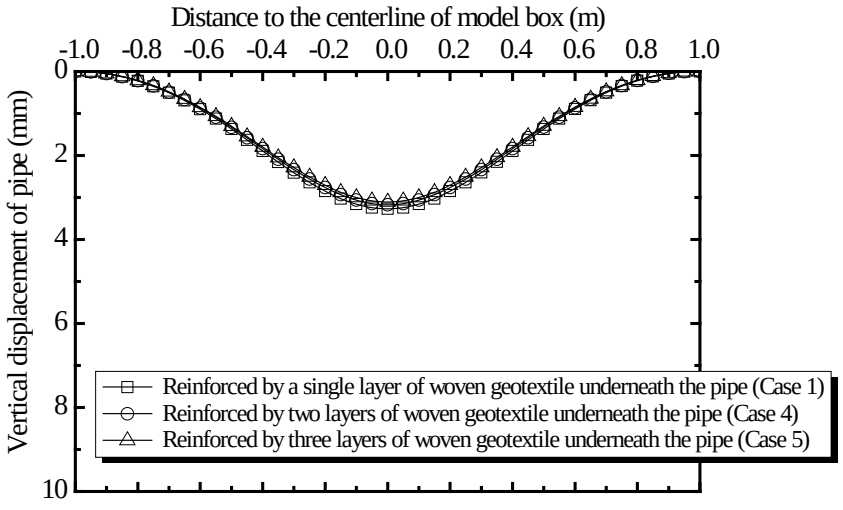

(a) vertical displacement of 10 mm

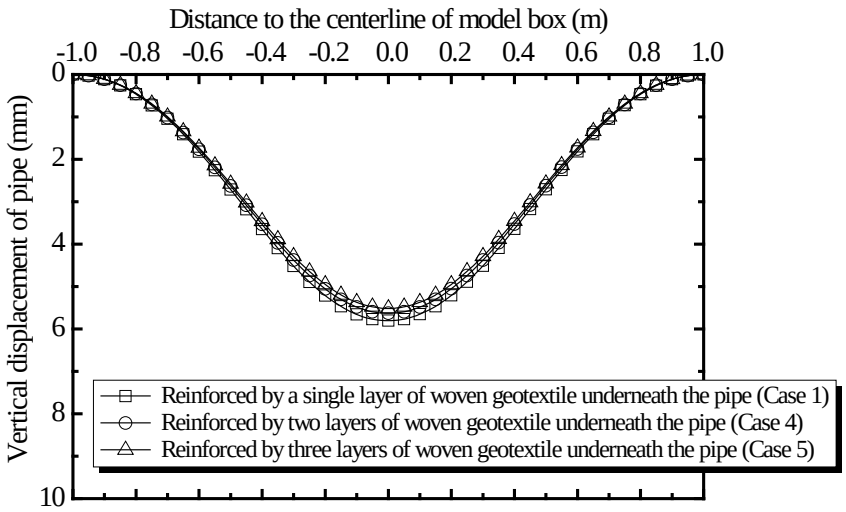

(b) vertical displacement of 30 mm

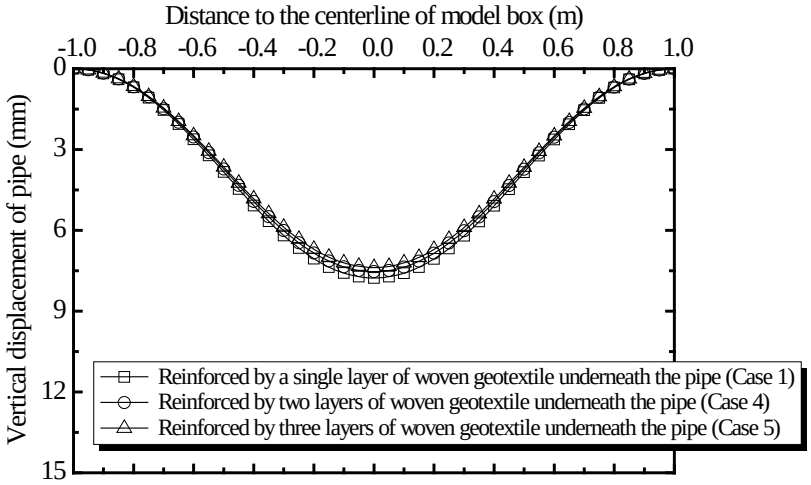

(c) vertical displacement of 50 mm

Figure 6. Variations of vertical displacement of pipe at different vertical displacement at model bottom with different layer number of geotextile reinforcements.

CONCLUSIONS

Buried pipes are threaten by the localized ground subsidence and the accidents have been reported all over the world. Geosynthetics were proposed in Zhou et al. (2020) to reinforce HDPE pipes subjected to localized ground subsidence through physical model tests and the geotextiles was proved as the best reinforcement method. However, the effects of installation location and layer number of the geotextile reinforcement on the performance of the reinforced pipe have not been understood well. In this study, a three-dimensional FEM was employed to investigate the effects of these two factors on the performance of the reinforced pipe subjected to localized ground subsidence. The numerical model was firstly verified by the physical model test results from Zhou et al. (2020), and five numerical cases considering different reinforcing locations and layer number were calculated. The vertical displacements of the pipe and the geotextile were used to evaluate the reinforcement performance. The following conclusions can be drawn:

(1) The vertical displacements of pipe increased with the increase of the distance from the geotextile reinforcement layer to the pipe bottom, which might be caused by the differential settlement of the soil between the pipe and the geotextile. It demonstrates that the geotextile reinforcement located at the pipe bottom has the best performance when single layer of reinforcement is adopted.
(2) The vertical displacements of the geotextile were larger than those of the pipe in the same numerical modeling case.
(3) The vertical displacements of pipe reinforced by single layer of geotextile at the pipe bottom exhibited similar performance with those reinforced by multiple layers of reinforcement. It confirms that single layer of geotextile at the pipe bottom is the best reinforcement method for pipes subjected to localized ground subsidence considering the cost and reinforcing performance.

REFERENCES

Corey, R., Han, J., Khatri, D.K., Parsons, R.L. (2014). Laboratory study on geosynthetic protection of buried steel-reinforced HDPE pipes from static loading. *Journal of Geotechnical and Geoenvironmental Engineering*; 140(6): 04014019.

Kawabata, T., Uchida, K., Hirai, T., Mohri, Y., Ling, H.I., Koyama, N. (2003). Experiments on buried pipe using backfill of cover with geosynthetics. Proc. of the *ASCE International Conference on Pipeline Engineering and Construction*, ASCE, Baltimore, MD: 1271-1278.

Mehrjardi, G.T., Tafreshi, S.N.M., Dawson, A.R. (2013). Pipe response in a geocell-reinforced trench and compaction considerations. *Geosynthetics International*; 20(2): 105-118.

O'Rourke, M.J., Liu, X. (1999). *Response of buried pipelines subject to earthquake effects. Multidisciplinary Center for Earthquake Engineering Research*, Ph.D. Dissertation, University at Buffalo, Buffalo, New York.

Palmeira, E.M., Andrade, H. (2010). Protection of buried pipes against accidental damage using geosynthetics. *Geosynthetics International*; 17(4): 228-241.

Tafreshi, S.N.M., Khalaj, O. (2008). Laboratory tests of small-diameter HDPE pipes buried in reinforced sand under repeated-load. *Geotextiles and Geomembranes*; 26(2): 145-163.

Zhou, M., Wang, F., Du, Y.J., et al. (2019). Laboratory evaluation of buried high-density polyethylene pipes subjected to localized ground subsidence. *Acta Geotechnica*; 14(4): 1081-1099.

Zhou, M., Wang, F., Du, Y.T., Corey, R., and Liu, M.D. (2020). Feasibility study on the use of geosynthetics to reinforce buried HDPE pipe subjected to localized ground subsidence. *Transportation Geotechnics*; 22: 100303-1-11.

IFAI Geosynthetics Conference

The Effectiveness of Geosynthetic Protection of Buried Pipes from Static Loads based on Pipe Stiffness

Ryan A. Corey, Ph.D., P.E.,[1] Deep Khatri, Ph.D.,[2] Jie Han, Ph.D., P.E., F. ASCE,[3] and Robert Parsons Ph.D., P.E., M. ASCE[4]

[1]RTE Technologies, 7924 Floyd Suite 100, Overland Park 66204; e-mail: ryanc@rtetech.com
[2]United Consulting; 625 Holcomb Rd. Norcross, GA 30071;e-mail: dkhatri@unitedconsulting.com
[3] University of Kansas Dept. of Civil Environmental and Architectural Engineering, 2150 Learned Hall, 1530 W. 15th St. Lawrence, KS 66045; e-mail: jiehan@ku.edu
[4] University of Kansas Dept. of Civil Environmental and Architectural Engineering, 2150 Learned Hall, 1530 W. 15th St. Lawrence, KS 66045; e-mail: rparsons@ku.edu

ABSTRACT

A full-scale static load test of a buried pipe with and without a layer of geosynthetic showed that a layer of geosynthetic effectively reduced the load on the pipe. Based on the calibration of a numerical analysis to the full-scale laboratory test of the geosynthetic reinforced pipe, a series of numerical analysis were run with varying pipe stiffness. The behavior and design of buried pipes is controlled by the relative pipe and soil stiffness ratio. Correspondingly the pipe and soil stiffness ratio can be predictive in the effectiveness of attenuating static forces with a geosynthetic layer. By running the same analysis with varying pipe and hoop stiffness an indication of the potential effectiveness of geosynthetic reinforcing for static loads relative to the pipe and soil stiffness ratio is quantified and provided.

INTRODUCTION

There has been an interest in using geosynethics to protect and improve the resiliency of buried pipes. Several researchers have investigated reducing the loads on shallow pipes from static surface loads, dynamic surface loads, and penetrating loads using a variety of geosynthetic and configurations including; Pearson and Milligan (1991), Bathurst and Knight (1998), Kawabata et al. (2003), Bueno et al. (2005), Moghaddas-Tafreshi, and Khalaj (2008, 2011), Palmieri and Andrade (2010), and Pires and Palmieri (2017). This investigation was to determine what pipes will benefit most from the protection and reinforcement from static surface loads. Based on a full-scale test and a calibrated numerical analysis, a parametric study of relative pipe stiffness and hoop stiffnesses, as described by McGrath (1999), was performed to determine the potential benefit of geosynthetic protection of different types of pipes.

FULL-SCALE TESTING

Full scale testing of a geosynthetic protected buried pipe was completed at the University of Kansas in a 3m wide by 2m wide x 2m long box (Fig. 1A). A Fat Clay backfill (Table 1) was placed into the box and compacted in 152 mm lifts, up to 1.6 m deep. The lifts were compacted to a density of 14.5 kN/m^3 resulting in a clay of medium stiffness. With two braced forms, a 1.14 m deep by 1.22 m wide trench was formed in the middle of the 3 m wide box along the entire length of the box. A 152 mm bedding lift of 19 mm clean limestone aggregate (Table 2) was poured

and leveled in the bottom of the trench at a relative density of 45 percent. A 0.610 m diameter steel reinforced HDPE pipe (Table 3) was centered in the middle of the trench and placed on the bedding layer. Six more layers of clean aggregate were dumped on either side of the pipe simultaneously in 152 mm lifts, followed by a final 76mm layer of clean aggregate filling the 1.22 m deep trench. A biaxial polypropylene geogrid, 2.4 meters wide by 2 meters long in the machine direction, was laid down centered over the pipe. Strengths in the cross-machine direction were 9 kN/m at 2% strain and 19.6 kN/m at 5% strain, while the strengths in the machine direction were 6 kN/m at 2% strain and 11.8 kN/m at 5 % strain. The ultimate strengths were 28.8 kN/m in the cross-machine direction, and 19.2 kN/m in the machine direction. Finally, two 114 mm layers of compacted Kansas Department of Transportation AB-3 well graded aggregate (Table 5.) were placed at a relative density of 70%. After construction of the section the pipe had 610 mm of total cover with a geogrid layer 228 mm below the surface.

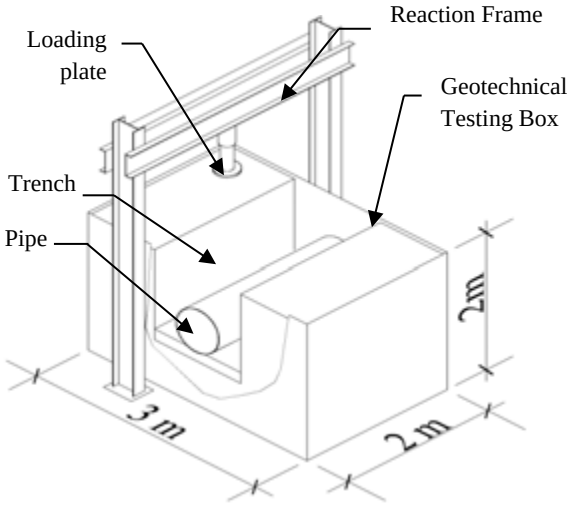

Figure 1A. Big Box Setup.

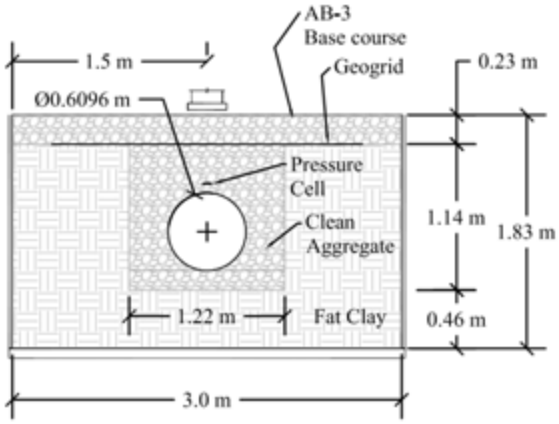

Figure 1B. Big Box Cross-Section

Table 1. Fat Clay Properties.

Property	Subgrade
Liquid/Plastic Limit- LL/PL	54/26
Specific Gravity G_s	2.71
Maximum Dry Unit Weight γ_{dmax} (kN/m^3)	15.4
Optimum Moisture Content w_{opt} (%)	24

Table 2. Clean Aggregate Properties.

Maximum Dry Unit Weight γ_{dmax} (kN/m^3)	16.2
Minimum Dry Unit Weight γ_{dmax} (kN/m^3)	13.5
Coef. of Curvature (Cc)	1.01
Coef. of Uniformity (Cu)	2.3
Mean Particle Size (mm)	11.2
Max Particle size (mm)	19
Friction Angle ϕ at D_r = 45 % (Triaxial Test)	49˚

Table 3. Pipe Properties.

Nominal Pipe Diameter (m)	0.61
Moment of Inertia (Steel Only) (mm^4/mm)	10.5
Modulus of Elasticity Steel E_s (GPa)	200
Steel Yield Strength F_y (MPa)	522
Pipe Wall Area (Steel Only) (mm^2/mm)	0.752
Modulus of Elasticity HDPE E_p (MPa)	441
Pipe Stiffness (parallel plate load test) (kPa)	327

Table 4. Aggregate Base Course.

Liquid/Plastic Limit- LL/PL	20/13
Specific Gravity G_s	2.69
Maximum Dry Unit Weight γ_{dmax} (kN/m^3)	20.6
Optimum Moisture Content w_{opt} (%)	10
Coef. of Curvature (Cc)	1.55
Coef. of Uniformity (Cu)	21
Mean Particle Size (mm)	7.0
Peak/ Residual Friction Angle ϕ_P (Direct Shear)	528/478
Cohesion Peak/Residual (kPa)	7.2/4.7

Two displacement transducers were placed at the center of the pipe directly under the loading plate to measure the relative displacements of the crown, invert, and spring-line. One transducer was placed vertically to measure the vertical displacements of the pipe, while the second transducer was placed in a horizontal position to measure horizontal displacements of the pipe section. A third displacement transducer was placed vertically at the center line of the pipe, 0.30 m longitudinally from the loading plate. The three displacement transducers DT 1, DT 2, and DT 3 can be seen in Figure 2. A tell-tale was attached to the crown of the pipe to measure the movement of the crown of the pipe in relation to a stationary datum.

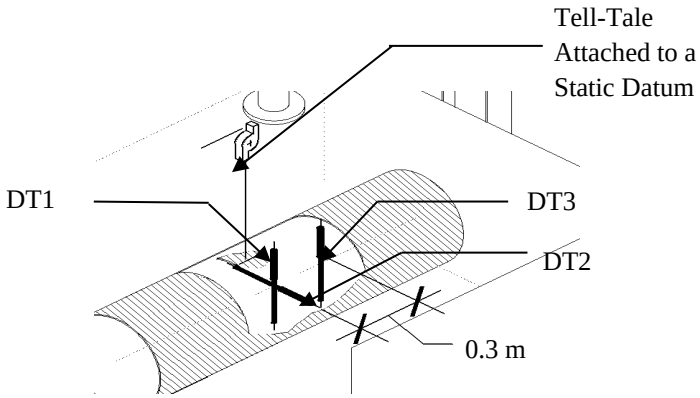

Figure 2. Displacement instrumentation.

An earth pressure cell with a capacity of 500 kPa (KDE-500) was placed 51 mm above the crown of the pipe directly under the loading plate. A 0.30 m diameter loading plate with a rubber base was used to apply a static load in the load increments of 68.9 kPa up to 689 kPa. After the maximum load was reached the load was reduced in four steps.

NUMERICAL ANALYSIS

A calibration numerical analysis of the lab test was performed with FLAC 3D. The geotechnical box was modeled as a fixed boundary. The fat clay fill was modeled as a linearly elastic material with a bulk modulus of 20.8 MPa and a shear modulus of 9.6 MPa. The crushed stone aggregate around the pipe was modeled non-linearly, utilizing the cap-yield soil constitutive model with the parameters shown in Table 5.

The AB-3 aggregate base course was modeled as a linearly elastic perfectly plastic soil. The layer was modeled with a friction angle of 45 degrees and a cohesion of 22 kPA. The elastic properties are shown in Table 6. The stiffness of the unreinforced condition was based on a bulk modulus of 13.7 MPa and a shear modulus of 6.4 MPa. For the reinforced condition, the bulk modulus and shear modulus were estimated at 22.7 and 10.6 MPa, respectively. The orthotropic pipe was modeled as a uniformly thick plate shell. The bending stiffness and membrane stiffness, in the two different directions, were estimated using mechanical properties based in Ugural (1981) and based on the pipe properties (Table 3). The pipe properties are shown in Tables 6 and 7. The geogrid was modeled with a FLAC 3D built in geogrid structural element that resists membrane loads only. Based on the measured strains in the laboratory the geogrid was modeled with a membrane stiffness of 660 kN/m in the machine direction, and a 990 kN/m stiffness in the cross direction. Similarly, to the laboratory tests, vertical pressures under a 0.3 m plate were applied to the model in 68.9 kPa increments up to 689 kPa.

Table 5. Cap-Yield Soil Parameters of Crushed Stone Aggregate.

Parameter	Crushed Stone
G^{e}_{ref} (kPa)	9391
K^{iso}_{ref} (kPa)	135000
R_f	0.95
m	0.77
ϕ_f	48
β	2
n	0.38
y	0

Table 6. FLAC 3D Pipe Shell Bending Stiffness Properties.

D_x (kPa-m^3)	2.7×10^{-4}
D_y (kPa-m^3)	1.24
G_{xy} (kPa-m^3)	6.7×10^{-5}
D_{xy} (kPa-m^3)	1.3×10^{-4}

Table 7. FLAC 3D Pipe Shell Membrane Stiffness Properties.

E_x (kPa)	1.03×10^6
E_y (kPa)	106×10^6
G (kPa)	253×10^3

CALIBRATION RESULTS

A comparison of the plate settlements, vertical deflections, and earth pressures at the crown of the pipe are shown in Figures 4, 5, and 6.

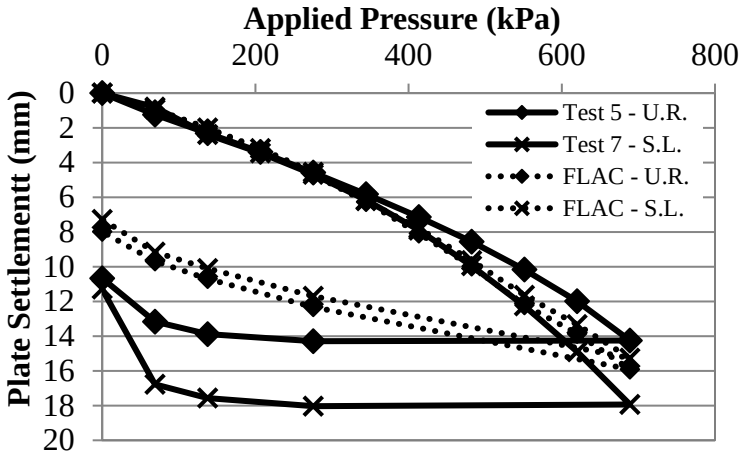

Figure 3. Vertical Plate Settlement.

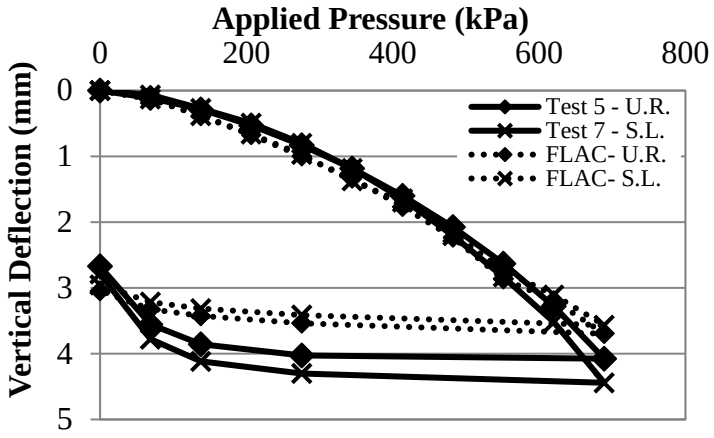

Figure 4. Vertical Pipe Deflection.

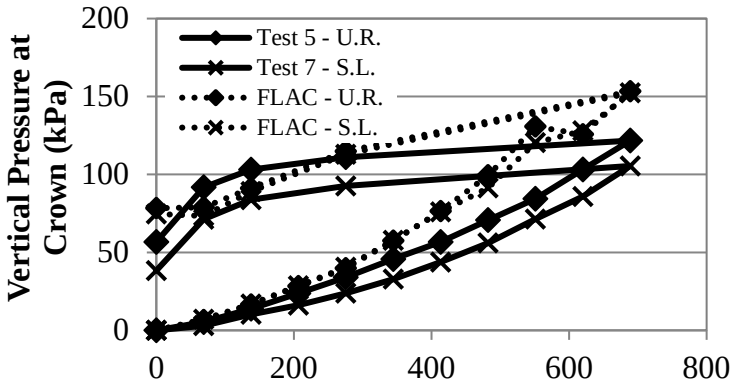

Figure 5. Earth Pressure at Crown.

The results of labs tests 5 and 7, unreinforced and with a single layer respectively as described in the full-scale testing section are shown with a continuous line. The numerical analysis is shown with a dashed line. For this condition, the inclusion of a single layer of geosynthetic protection, slightly increased the vertical plate settlement and vertical deflection of the pipe, while the applied pressure at the crown of the pipe slightly decreased with inclusion of the geosynthetic. Because the steel reinforced HDPE pipe is relatively flexible in bending but stiff axially as compared to a thermoplastic pipe it became important to investigate what pipes would potentially benefit from geosynthetic protection based on these criteria.

PARAMETRIC STUDY

McGrath (1998) introduced the Bending Stiffness Factor (S_b) and the Hoop Stiffness Factor (S_H) based on the parameters for the elastic solution proposed by Burns and Richards (1964). These factors in Equations' 1 and 2, are dimensionless and have been conveniently used to describe and predict pipe behavior:

$$S_B = \frac{M_s R^3}{EI} \quad \textbf{Eq 1.}$$

$$S_H = \frac{M_s}{EA/R} \quad \textbf{Eq 2.}$$

where Ms is the constrained modulus of the soil, E, A, I, and R are the modulus of elasticity, the area, the moment of inertia, and the radius of pipe wall, respectively. The bending stiffness factor describes the ratio of the soil stiffness to the bending stiffness of the pipe wall, similar to the pipe stiffness determined from a parallel plate load test. The Hoop stiffness factor is a ratio of soil stiffness to axial stiffness of pipe wall. A higher number in the bending stiffness and hoop stiffness factors represent a more flexible pipe was as compared to the soil constrained modulus.

The calibrated model was the basis for the parametric study and all parameters of the model were unchanged except for the pipe bending stiffness and pipe hoop stiffness, which were modified individually. The constrained modulus for the aggregate back-fill was estimated as 13.1 MPa based on plate loading tests. Based on the elastic pipe parameters and constrained modulus the bending stiffness factor (SB) was estimated as 282. Since the pipe used for the box test was near the low end of pipe stiffnesses commonly used the pipe stiffness was increased by factors of 1/16, 4, 16, and 256. The hoop stiffness SH of the pipe used on this project was calculated to be 0.026 based on the constrained modulus of 13.1 MPa and the pipe wall area. The hoop stiffnesses selected for the parametric study were selected to range from 0.001 to 10 as shown in Table 10. The bending stiffness was modified by changing Dy in Table 6 and Ey in Table 7. The bending stiffness modifications did not change hoop stiffness for that parametric study and vice versa.

Table 9. Bending Stiffness.

Analysis	S_B	Relative Pipe Stiffness
1	282	1
2	71	4
3	18	16
4	1.1	256
5	4512	1/16

Table 10. Hoop Stiffness Factors.

Analysis	S_H
1	0.001
2	.026
3	0.1
4	0.5
5	1
6	2.5
7	5
8	10

In the following results of the parametric study only the displacements and pressures for maximum applied pressure (689 kPa) is presented. The results of the parametric study were plotted versus the relative pipe stiffness (Figures 6, 7, and 8) and the Hoop Stiffness Factors (S_H) (Figures 8, 9, and 10).

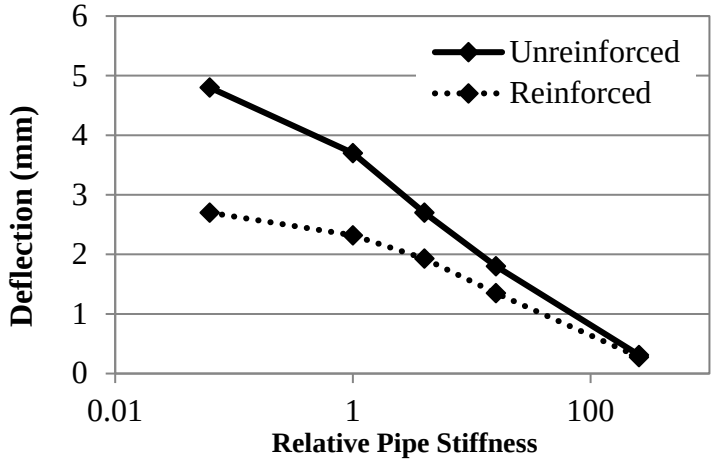

Figure 6. Maximum Vertical Pipe Deflection Vs. Relative Pipe Stiffness.

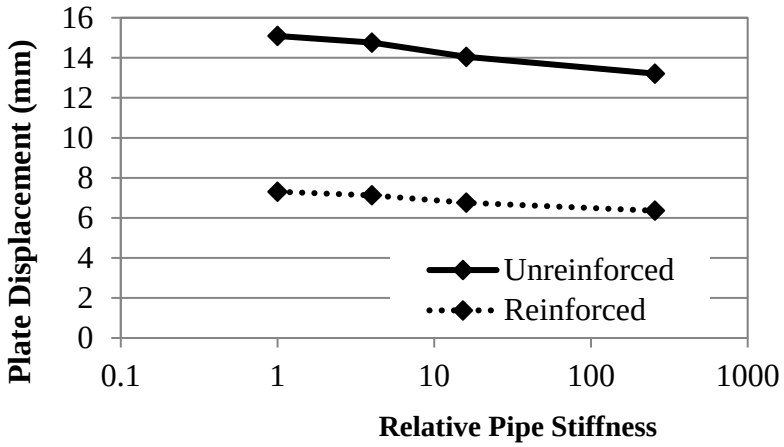

Figure 7. Maximum Plate Settlement vs Relative Pipe Stiffness.

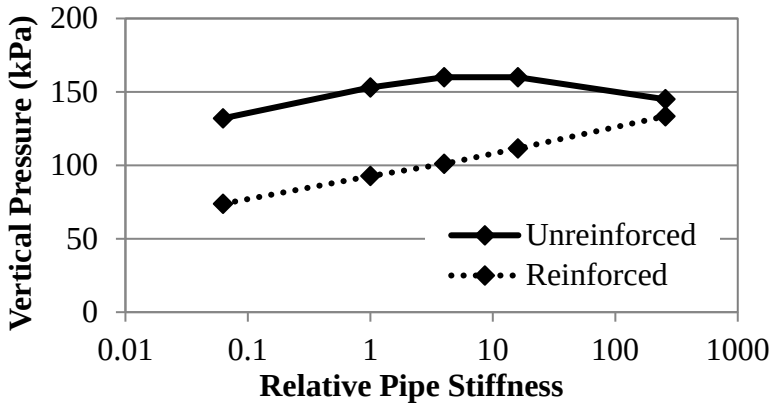

Figure 8. Maximum Vertical Pressure at the Crown vs Relative Pipe Stiffness.

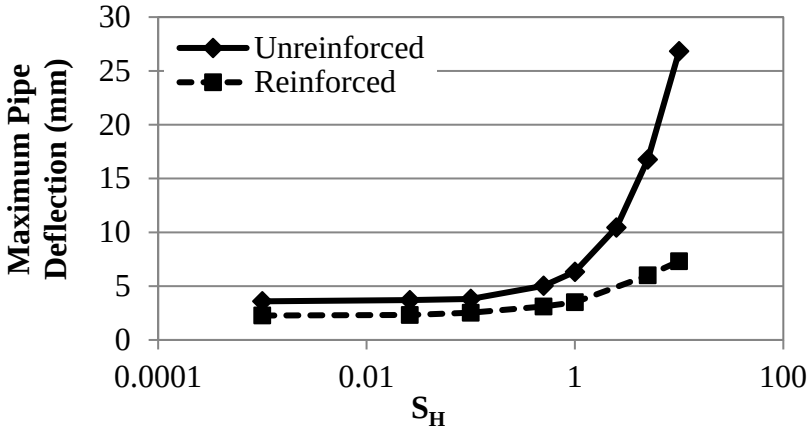

Figure 9. Maximum Pipe Deflection Vs. Hoop Stiffness Factor.

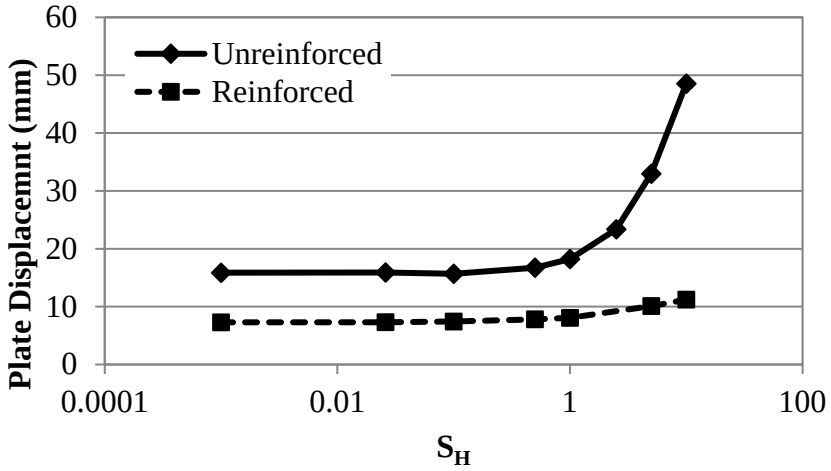

Figure 10. Maximum Plate Settlement Vs. Hoop Stiffness Factor.

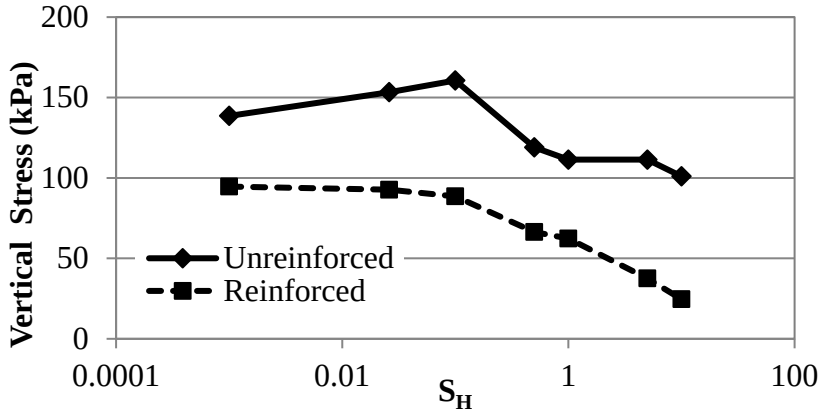

Figure 11. Maximum Earth Pressures Vs. Hoop Stiffness Factor.

Generally, it is desired to reduce pipe deflection and loads transmitted to the pipes by the concentrated load. As can be expected, the stiffer the pipe is in relation to the surrounding soil stiffness, the less effective the geogrid is in reducing soil pressures on the crown of the pipe and vertical pipe deflections. At a bending stiffness ratio of 16 times greater than the pipe stiffness

tested, which is equivalent to a bending stiffness factor of 10 or lower, the benefit of the geogrid is greatly diminished regarding controlling maximum deflections. Likewise, the stress at the crown of the pipe is not reduced for stiffer pipes with a bending stiffness factor less than 10. For a hoop stiffness factor of less than 1 there is little benefit in reducing pipe deflections while for a hoop stiffness factor greater than 1 a benefit can be realized with the inclusion of the geosynthetic.

The benefit of lowered surface displacement was uniform over the range of bending stiffness and hoop stiffnesses, except for pipes with hoop stiffness greater than one, which saw an increasing benefit of including a layer of geosynthetic.

CONCLUSIONS

The benefit of the geosynthetic in respect to loading plate settlements, is generally uniform and independent of this pipe stiffness. The exception being pipes with a low hoop stiffness, or conditions where hoop stiffness factor is greater than 1. For conditions where the hoop stiffness is greater than one the pipe deflection increases significantly, and that displacement is translated to the surface. In these cases there is a distinct benefit from including a geosynthetic. By the finding of this analysis, geosynthetics can be assessed to benefit pipe design when the bending stiffness factor is greater than 10, or the hoop stiffness factor is greater than 1.

REFERENCES

Bathurst, R.J., and Knight, M.A. (1998). “Analysis of geo-cell reinforced-soil covers over large span conduits.” *Computers and Geotechnics*, 3(22), 205-219.

Bueno, B.S., Viana, P.M.F., and Zornberg, J.G. (2005). A novel construction method for buried pipes using geosynthetics. *Proc., Geo-Frontiers 2005*, ASCE, Austin, TX, 4155-4161.

Dave, M. M., Solanki, C. H. (2020). Protection of Buried Pipelines Using Geosynthetics Under Different Loading Conditions—A Review. 249-262.

Kawabata, T., Uchida, K., Hirai, T., Mohri, Y., Ling, H.I., and Koyama, N. (2003). "Experiments on buried pipe using backfill of cover with geosynthetics." *Proc. of the ASCE International Conference on Pipeline Engineering and Construction*, ASCE, Baltimore, MD, 1271-1278.

McGrath, T.J. (1998). *Design method for Flexible Pipe*, A Report prepared for the Polyethylene Pipe Design Task Group of the AASHTO Flexible Culvert Liaison Committee, Simpson Gumpertz, & Heger, Inc., Arlington, MA.

Moghaddas Tafreshi, S.N., and Khalaj, O. (2008). Laboratory tests of small-diameter HDPE pipes buried in reinforced sand under repeated-load. *Geotextiles and Geomembranes*, 26(2), 145-163.

Moghaddas Tafreshi, S.N., and Khalaj, O. (2011). Analysis of repeated-load laboratory tests on buried plastic pipes in sand" *Soil Dynamics and Earthquake Engineering*, 31(1), 1-15.

Palmeira, E.M., and Andrade, H.K.P.A. (2010). Protection of buried pipes against accidental damage using geosynthetics. *Geosynthetics International*, 17(4), 228-241.

Pearson, A.E., and Milligan, G.W.E. (1991). Model tests of reinforced soil in conjunction with flexible culverts. *Proc. of the International Reinforced Soil Conference*, Glasgow, 365-369.

Pires, A.C.G., Palmeira, E.M. (2017). Geosynthetic Protection for Buried Pipes Subjected to Surface Surcharge Loads. *Int. J. of Geosynth. and Ground Eng.*, 3 (4), 1-11.

Geosynthetics Conference

Effects of Geofoam Geometry and Location on Vertical Stresses on Buried Culverts during Construction and under Surface Loading

Mahdi Al-Naddaf, Ph.D., A.M.ASCE[1], Sajjad E. Rasheed[2], S. Mustapha Rahmaninezhad, Ph.D., A.M.ASCE[3] and Jie Han, Ph.D., P.E., F.ASCE[4]

[1]Department of Civil Engineering, Univ. of Kerbala, Kerbala 56001, Iraq; e-mail: mahdi.a@uokerbala.edu.iq
[2]Department of Civil Engineering, the Univ. of Kerbala, Kerbala 56001, Iraq; e-mail: sajjad.e@uokerbala.edu.iq
[3]Terracon consultants Inc., Pharr, Texas 78577, USA; (corresponding author); e-mail: srahmaninezhad@terracon.com
[4]Dept. of Civil, Environmental, and Architectural Engineering, Univ. of Kansas, 1530 W. 15th St., Lawrence, KS 66045-7609, USA; e-mail: jiehan@ku.edu

ABSTRACT

Buried concrete box culverts have commonly been used at shallow depths under roadways for drainage. Higher stiffness of these buried culverts relative to their surrounding soil affects traffic load distribution. For instance, in embankment culverts, the deformation of the soil column above the culvert is less than that of the surrounding soil due to the relative stiffness between the rigid structure and the soil. Therefore, under traffic loads, this stiffness difference increases the traffic-induced stresses on the buried culverts due to the mobilization of negative soil arching. Expanded Polystyrene (EPS) geofoam has been used above the buried culverts as a compressible material to reverse the relative deformation within the embankment and reduce the stresses above the culverts. However, limited studies have been carried out to investigate the effect of the EPS geofoam geometry (such as thickness, width, and location) on the traffic load distribution above the buried structure. In this study, a finite element analysis using Plaxis3D was used to calculate the vertical stress profile on the box culvert due to static traffic loading. The finite element model was built and validated against the reduced-scale physical model tests conducted in the geotechnical lab at the University of Kansas. Then a parametric study was carried out by varying three parameters, i.e., the thickness, the width, and the location of the EPS geofoam, to investigate their effects on the traffic load distribution above a buried box culvert. The numerical results show a reduction in vertical stresses on the box culvert with the use of geofoam due to the mobilization of positive soil arching. Moreover, increasing the thickness of the EPS geofoam reduced the vertical stress on the culvert, while increasing the geofoam width to be larger than the culvert width slightly increased the stress on the culvert. Placing the geofoam farther from the culvert increased the pressure on the culvert.

INTRODUCTION

Buried culverts or pipes within embankments are often subjected to traffic loading. The safety of these infrastructures under surface loadings is important and their behavior depends on their surrounding soil. In addition to the overburden stress, additional stresses from the surface traffic

loading can be crucial to the safety of the buried structure especially under a low embankment height (Acharya et al. 2016; Han et al. 2013). Abdel-Karim et al. (1993) pointed out that the response of a buried structure to a surface (live) load considerably increases as the thickness of a soil cover above the structure decreases.

To obtain a comprehensive understanding, field studies, laboratory tests, and numerical analyses have been performed in the past e.g., (Abu-Farsakh et al. 2017; Alzabeebee 2020; Puppala et al. 2019; Rahmaninezhad et al. 2020; Santos et al. 2020) to provide different insights into the buried structure responses. The stresses on buried structures (e.g., box culverts or pipes) increase or decrease due to the arching phenomenon that is responsible for the stress redistribution within embankment soil. In general, soil arching is caused by a relative movement between a yielding soil zone and a stable soil zone (Terzaghi 1943). Due to the differential stiffness between the buried structure (especially rigid structure) and the surrounding soil, the surrounding soil is more susceptible to large settlement than the soil column above the structure (Chen and Sun 2013). As a result, shear stresses are generated within the embankment soil and cause more stresses to transfer on the structure due to negative soil arching. Higher vertical stresses may cause excessive deformation and even failure of the buried structure (Al-Naddaf 2019).

Having a compressible zone above the buried structure can reverse the differential movement within the embankment soil such that the soil column above the structure would settle more than the surrounding soil zone. This treatment was initially suggested by Marston (1930). Expanded Polystyrene (EPS) geofoam has been increasingly used as a compressible material above a buried structure and investigated by many studies (Al-Naddaf et al. 2019; Al-Naddaf et al. 2019; Kim and Yoo 2005; McGuigan and Valsangkar 2010; McGuigan and Valsangkar 2011; Sun et al. 2011; Sun et al. 2009). Furthermore, the effects of surface loading on the behavior of buried box culverts were studied by several researchers (Al-Naddaf et al. 2019; Meguid et al. 2017; Mosadegh and Nikraz 2017).

Several studies investigated the performance of EPS geofoam above buried structures including the effects of its geometry under embankment self-weight. Kim and Yoo (2005) numerically investigated the effect of geofoam width, thickness, and location on the response of buried box culverts with different fill heights without surface loading. Thus, limited studies have been carried out to investigate the effect of the EPS geofoam geometry on static traffic load distribution above the buried structure. In this study, a numerical model using finite element Plaxis3D software was built and verified based on a small-scale experimental test conducted by Al-Naddaf et al. (2019). Then, a parametric study was conducted to assess the effects of geofoam thickness, width, and location on a buried box culvert response under surface loading.

EXPERIMENTAL TEST

Al-Naddaf et al. (2019) conducted physical model tests under a plane-strain condition at the University of Kansas geotechnical lab to investigate the behavior of buried twin-cell concrete box culverts under static footing loads. The interior dimensions of the test box were 1.76 m long, 0.46 m wide, and 1.50 m high. More details about the test box, conducted tests, and special treatments used to minimize the boundary effects can be found in (Al-Naddaf et al. 2019; Al-Naddaf et al. 2019; Al-Naddaf 2019). Al-Naddaf et al. (2019) simulated two construction methods, the positive projection embankment (PPE) and induced trench installation (ITI) methods. In the PPE test, only a concrete culvert with no geofoam was embedded in the center of the test box, while EPS geofoam was placed atop the concrete culvert in the ITI method test. The numerical models of this study were verified against both the PPE and ITI tests.

The box culvert dimensions were H_c = 0.2 m high, B_c = 0.36 m wide, and L = 0.46 m long and a wall thickness of 0.02 m. On the top of the embankment, a footing load was applied using a hydraulic jack attached to a rigid steel footing. The footing had the same dimensions as the culvert and was centered above the culvert. Figure 1 shows the test box for the ITI method test and the locations and dimensions of the concrete culvert, geofoam, footing, and the instrumentation.

For the embankment material, dry poorly-graded Kansas River sand was used. The maximum and minimum dry unit weights of the sand were 18.85 and 16.02 kN/m^3, respectively. Kansas River sand was compacted to 75% relative density (D_r) in lifts until the embankment height of 0.82 m was reached as shown in Figure 1. At D_r = 75%, the sand had a unit weight of 18.04 kN/m^3 and a peak friction angle of 38º based on triaxial shear tests. The initial elastic modulus of the sand was 25 MPa based on three confining pressures of 35, 70, and 100 kPa in the triaxial shear tests. For the ITI method test simulated in this study, the EPS geofoam had a density of 14.4 kg/m^3 and is designated as EPS 15. The EPS geofoam width was equal to that of the concrete culvert (B_c). Also, the geofoam thickness was 0.2B_c and placed at 0.03 m atop the culvert to accommodate the pressure cells.

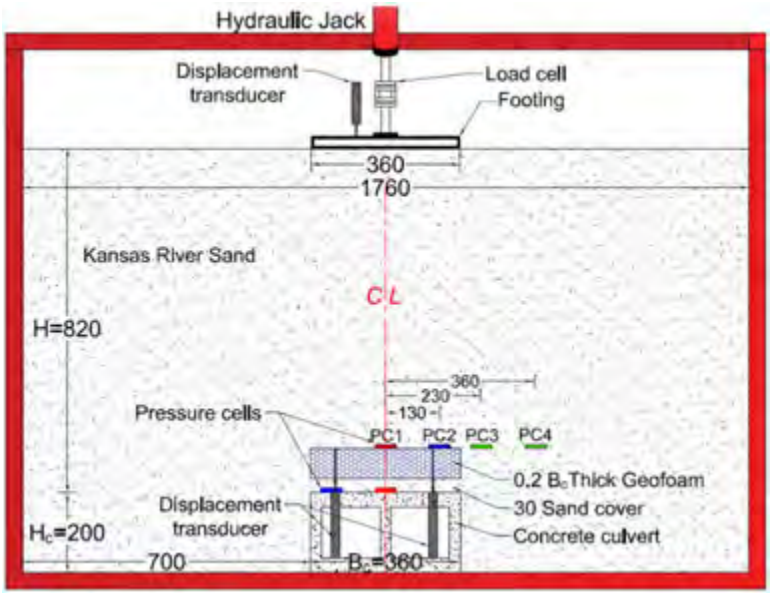

Figure 1. Test box for the ITI method test used for the numerical model showing the locations and dimensions of the culvert, geofoam, footing, and the instrumentation (unit: mm) (Al-Naddaf et al. 2019)

NUMERICAL MODELING

The numerical model was built based on the above-described tests using a finite element mothed (FEM) incorporated in the commercial Plaxis3D software. This paper discusses the FEM analyses that were carried out to investigate the effects of the EPS geofoam geometry including its thickness, width, and location on the responses of buried culverts. Table 1 and Figure 2 present the numerical models used in this study. The hardening soil (HS) model, which is an elastoplastic hyperbolic model to describe the non-linear behavior of the sand, was used to simulate the backfill soil. The HS model includes eight parameters to describe the soil behavior as shown in Table 2. Table 2

provides the soil parameters used in the Plaxis3D analyses. The EPS geofoam was modeled using as a linearly-elastic perfectly-plastic material with the Mohr-Coulomb (MC) failure criterion. Based on the previous studies (Lal et al. 2014; Padade and Mandal 2012; Witthoeft and Kim 2016), the MC model was found to reasonably simulate the EPS geofoam behavior. Padade and Mandal (2012) conducted a physical triaxial test on EPS 15 to obtain the required parameters for the MC model. Subsequently, they used the same parameters in their FE analysis to simulate the triaxial test with the MC model using Plaxis2D as verification of the model. Therefore, the same parameters from Padade and Mandal (2012) were used in this study to simulate EPS 15 as shown in Table 2. The linearly-elastic model was utilized to simulate the concrete culvert and the steel footing. The material parameters for the culvert and the footing used in the FE analyses are shown in Table 2.

Table 1. Details of the numerical models in this study

Model number	Condition	Geofoam geometry			Purpose
		Thickness	Width	Location	
1	PPE (no EPS)	Concrete culvert only			Verification
2	ITI (EPS 15)	$0.2B_c$	$1.0B_c$*	0.030 m	
3	ITI (EPS 15)	$\mathbf{0.2B_c}$	$\mathbf{1.0B_c}$	$\mathbf{0.0B_c}$	Parametric study
4	ITI (EPS 15)	$\mathbf{0.4B_c}$	$1.0B_c$	$0.0B_c$	
5	ITI (EPS 15)	$\mathbf{0.8B_c}$	$1.0B_c$	$0.0B_c$	
6	ITI (EPS 15)	$0.2B_c$	**1.5Bc**	$0.0B_c$	
7	ITI (EPS 15)	$0.2B_c$	**2.0Bc**	$0.0B_c$	
8	ITI (EPS 15)	$0.2B_c$	$1.0B_c$	$\mathbf{0.2B_c}$	
9	ITI (EPS 15)	$0.2B_c$	$1.0B_c$	$\mathbf{0.4B_c}$	

* B_c = 360 mm

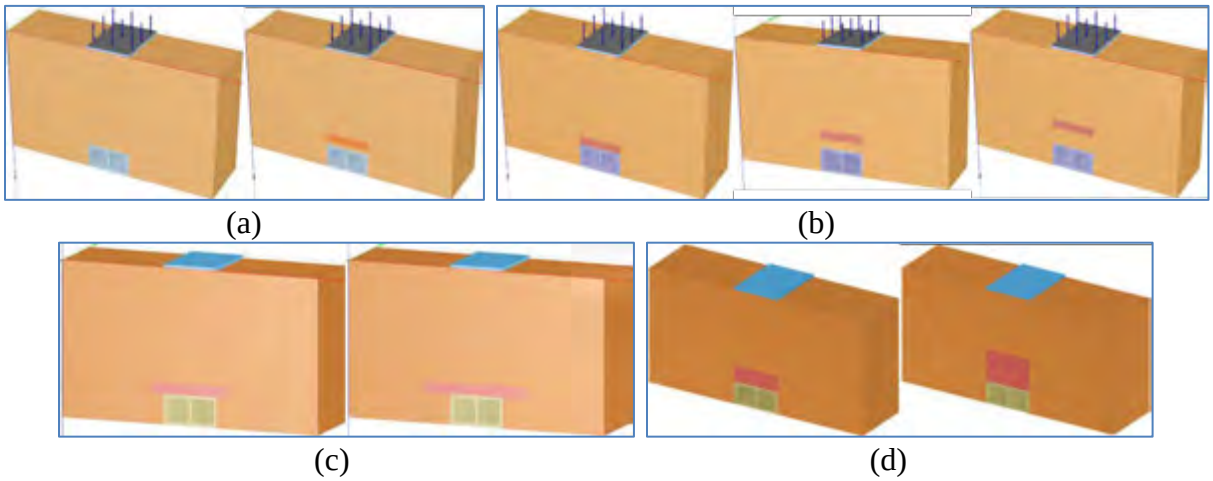

Figure 2. Numerical models for: (a) verification, (b) geofoam location, (c) geofoam width, and (d) geofoam thickness.

Table 2. Material parameters used in the Plaxis3D analyses

Material	Model	Parameters	Unit	Value

Embankment soil (Kansas River sand)	Hardening Soil (HS)	Unit weight, γ	kN/m^3	18.0
		Secant modulus, E_{50}	MPa	20
		Odometer modulus, E_{OED}	MPa	20
		Unloading/reloading modulus, E_{UR}	MPa	70
		Cohesion, c	kPa	0
		Friction angle, φ	Degree	38
		Dilatancy angle, ψ	Degree	0
		Poisson's ratio, v		0.3
		Power for stiffness stress dependency, m		0.5
Geofoam (EPS 15)	Mohr-Coulomb (MC)	Unit weight, γ	kN/m^3	0.15
		Elastic modulus, E	MPa	2.4
		Cohesion, c	kPa	33.75
		Friction angle, φ	Degree	1.5
		Poisson's ratio, v		0.1
Concrete culvert	Linear Elastic	Elastic modulus, E	GPa	20
		Poisson's ratio, v		0.2
Steel footing	Linear Elastic	Elastic modulus, E	GPa	200
		Poisson's ratio, v		0.3

RESULTS AND DISCUSSIONS

This section presents and discusses the numerical results related to the vertical pressure on the box culvert induced by the embankment construction and the static footing load. Nine numerical models were analyzed to better understand the effects of the geofoam geometry on the responses of the buried box culvert.

Model verification. Prior to the parametric study, two numerical models with the parameters in Table 1 were analyzed and verified against the experimental test results of PPE and ITI method tests. Figure 3 shows the vertical pressures on the culvert for the numerical models and those measured in the experimental tests. Figure 3 shows reasonably well agreement between the numerical and experimental results. Figure 3(a) indicates that the hardening soil (HS) model for the embankment soil and the linearly-elastic model for the concrete culvert well simulated the buried culvert-embankment soil interaction. The HS model has been widely used by other researchers to simulate the backfill material above buried structures (Allard and El Naggar 2016; Katona 2017; Kitane and McGrath 2006). Figure 3(b) shows the reasonableness of the numerical model used to simulate the behavior of the buried culvert, EPS geofoam, and embankment soil. Even though a similar trend was obtained for the response of the pressure increase on the culvert, the numerical model (for the ITI condition) slightly over-predicted the average vertical pressure on the culvert. In the following parametric study, the same properties for the concrete culvert, geofoam, and soil were used to investigate the effects of geofoam thickness, width, and location on the behavior of buried culverts.

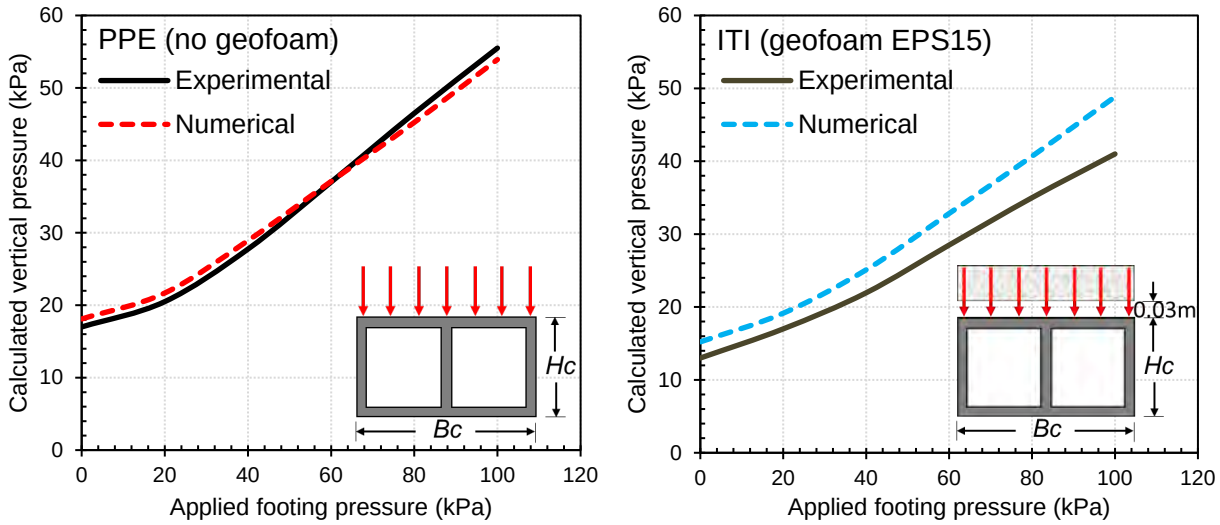

(a) (b)

Figure 3. Numerical model verification by the calculated versus measured vertical pressures on the culvert under footing loading in (a) the PPE test and (b) the ITI method test

Effects of geofoam thickness. Figure 4 shows the calculated vertical pressures on the culvert for different geofoam thicknesses (i.e., $0.2B_c$, $0.4B_c$, and $0.8B_c$) under the embankment overburden load and the monotonic footing load. As the embankment height increased, the geofoam thickness had more effects in reducing the vertical pressure on the culvert as depicted in Figure 4(a). The geofoam with the thickness of $0.8B_c$ resulted in the lowest vertical pressure on the culvert than those with the geofoam thicknesses of $0.2B_c$ and $0.4B_c$, respectively. For instance, at the embankment height of 820 mm, the vertical pressure on the culvert was reduced by approximately 10.2% and 24.2% in the models with the geofoam thicknesses of $0.4B_c$ and $0.8B_c$, respectively, as compared to that in the model with $0.2B_c$. However, as the applied footing pressure increased, the vertical pressure reduction due to a thicker geofoam gradually decreased as shown in Figure 4(b). At an applied footing pressure of 100 kPa, the vertical pressure on the culvert was the same for all three geofoam thicknesses. This result may be attributed to the confining pressure (lateral thrust) on the geofoam sides that restricted the vertical deformation of the geofoam, thus reducing the pressure transfer from the top of the geofoam to the surrounding soil. This is consistent with the reasoning given by Al-Naddaf et al. (2019) for the behavior of the geofoam in their experimental work.

Figure 5 shows the effectiveness of placing the EPS geofoam on the culvert (i.e., the ITI method) in reducing the vertical pressure as compared to that without any geofoam (i.e., PPE). The normalized pressure, shown in Figure 5, was calculated by dividing the pressure on the culvert in the ITI model to that in the PPE model. Figure 5 shows the benefit of the geofoam in reducing the pressure on the culvert by approximately 13%, 22%, and 33% when the geofoam thicknesses were $0.2B_c$, $0.4B_c$, and $0.8B_c$, respectively, as compared with the PPE. This result is attributed to the fact that (1) light-weight material (geofoam) was used instead of heavy soil and (2) positive soil arching mobilized and transferred the pressure away from the culvert to the surrounding soil when the geofoam was used. Furthermore, as the footing pressure increased, the reduction in the vertical pressure decreased to 6% for all three geofoam thicknesses.

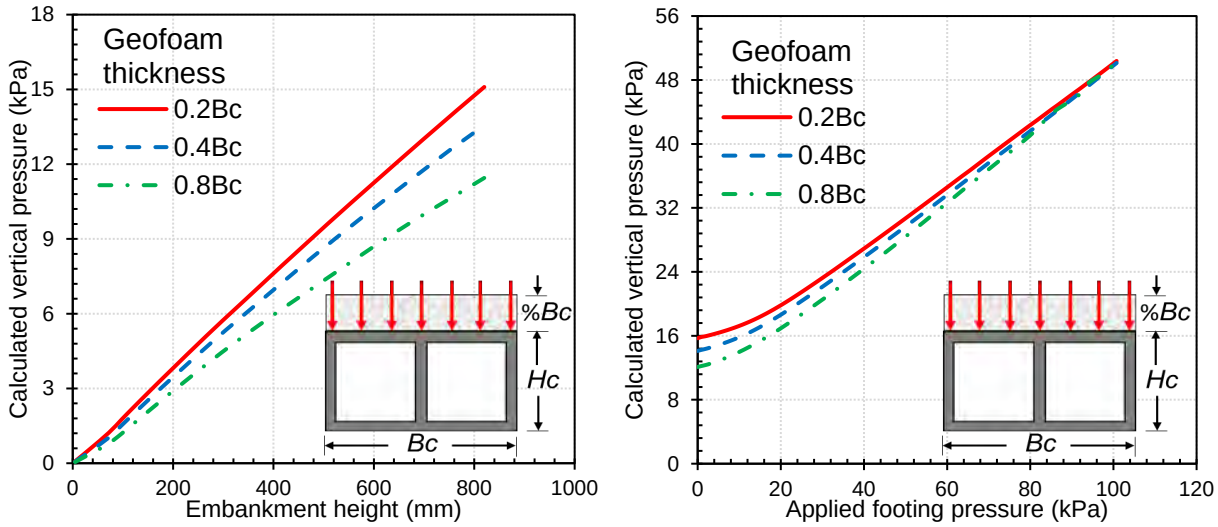

Figure 4. Effects of the geofoam thickness on the vertical pressure on the culvert (a) during embankment construction and (b) under static footing loading

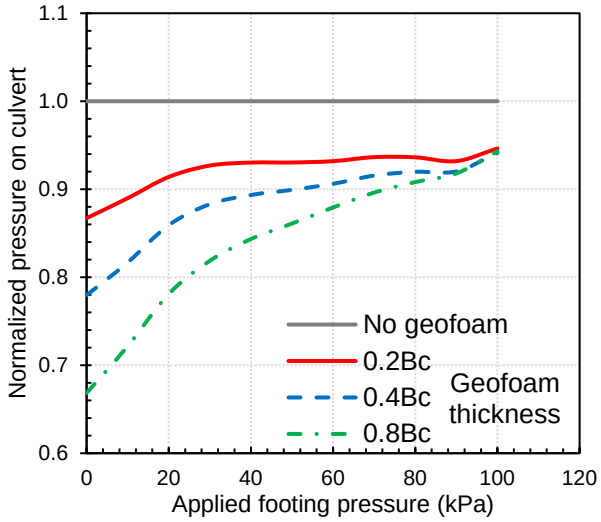

Figure 5. Normalized vertical pressures on the culvert in the ITI models with different geofoam thicknesses and the PPE model under static footing loading

Effects of geofoam width. Figure 6 shows the effect of the geofoam width on the vertical pressure on the culvert during embankment construction and footing loading. Since the geofoam thickness was the same (i.e., $0.2B_c$) for all models, the same average vertical pressure was calculated on the culvert as the geofoam width increased from $1.0B_c$ to $2.0B_c$ during the embankment construction stage. Subsequently, as the footing pressure increased to 100 kPa, the vertical pressure on the culvert slightly increased when the geofoam width increased. Thus, a wider geofoam caused more pressure on the culvert. Increasing the ratio of geofoam to the footing width (for the same culvert width) resulted in a wider zone under the effect of footing load that would transfer the load to the culvert since the geofoam was directly placed on the culvert. This finding is consistent with that reported by (Kang et al. 2008; Kim and Yoo 2005; Meguid et al. 2017). Similarly, Figure 7 shows

that increasing the geofoam width minimized the benefit of the EPS geofoam in reducing the pressure on the culvert as compared to the case without any geofoam (PPE). Thus, the most effective geofoam width is equal to the culvert width.

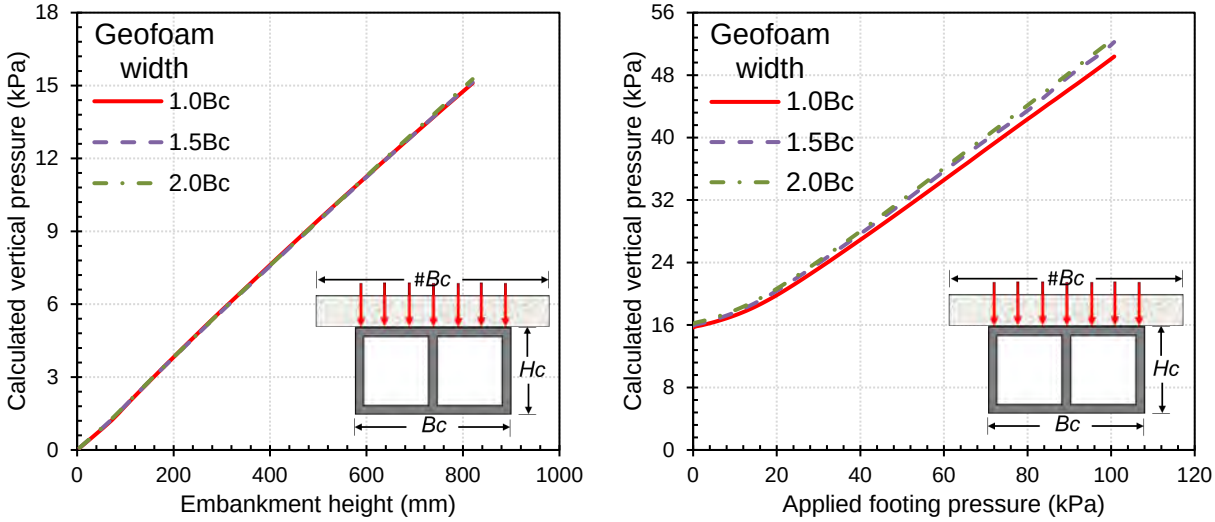

Figure 6. Effects of the geofoam width on the vertical pressure on the culvert (a) during embankment construction and (b) under static footing loading

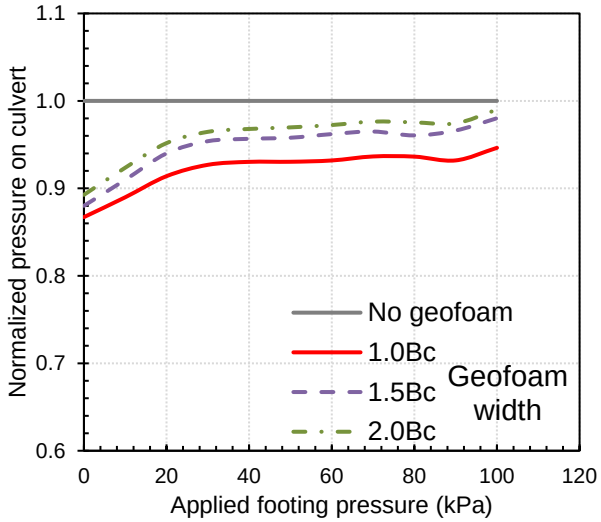

Figure 7. Normalized vertical pressure on the culvert in the ITI models with different geofoam widths and the PPE model under static footing loading

Effects of geofoam location. To evaluate the effects of the geofoam location on the vertical pressure on the culvert, this study evaluated three models with different distances of $0.0B_c$, $0.2B_c$, and $0.4B_c$ from the top of the culvert to the bottom of the geofoam. Figure 8 shows the numerical results of these models during embankment construction and under footing loading. Figure 8 clearly shows that the geofoam placed farther from the culvert increased the pressure transferred to the culvert. Similar findings was reported by Kim and Yoo (2005) in their numerical analysis for a

single-cell box culvert. More interestingly, the vertical pressure on the culvert with the geofoam placed at $0.4B_c$ (144 mm) away from the culvert was higher than that measured without any geofoam (PPE) when the applied footing pressure exceeded 40 kPa as shown in Figure 9. It is expected that the geofoam transferred the stresses on it to the surrounding soil due to positive soil arching, however, since the geofoam was placed at distance from the culvert, these stresses were transferred back to the culvert due to the higher stiffness of culvert as compared to that of the soil. Therefore, geofoam placed at a closer distance to the footing would cause more pressure on the culvert as compared to that when the geofoam is directly above the culvert.

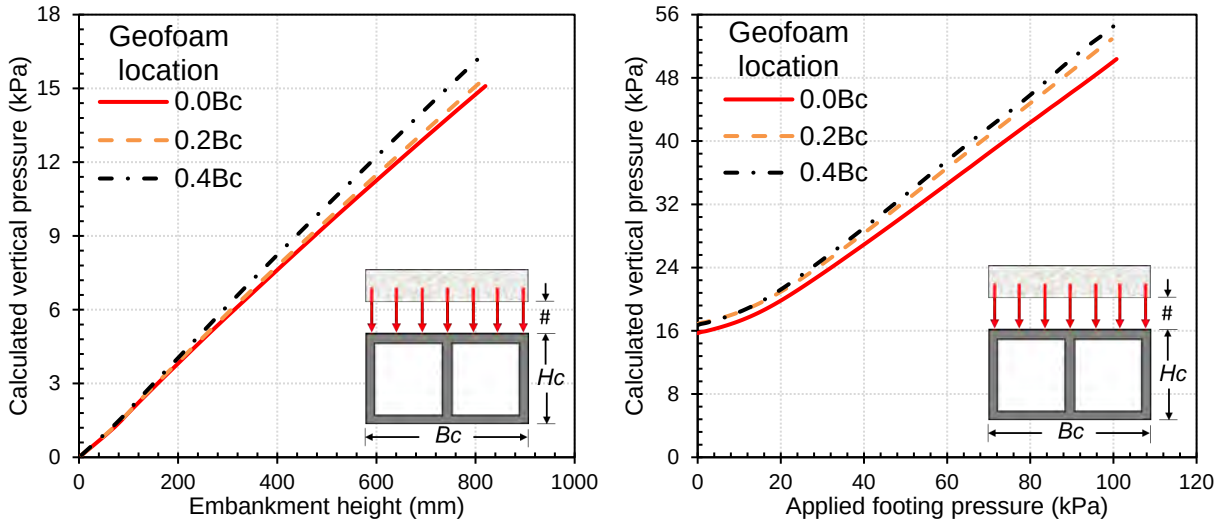

Figure 8. Effects of the geofoam location on the vertical pressure on the culvert (a) during embankment construction and (b) under static footing loading

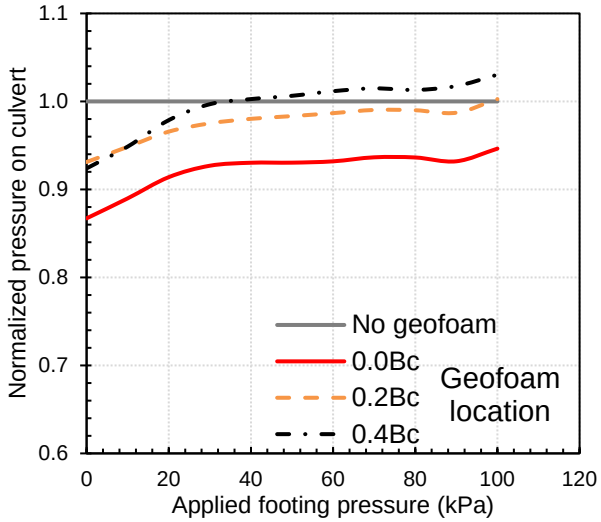

Figure 9. Normalized vertical pressures on the culvert in the ITI models at different geofoam locations and the PPE model under static footing loading

CONCLUSIONS

This study investigated the effects of geofoam geometry on the vertical pressure above the culvert by the finite element method. Two numerical models were first verified against the reduced-scale physical tests before the parametric study. The parametric study considered three geofoam thicknesses ($0.2B_c$, $0.4B_c$, and $0.8B_c$), three geofoam widths ($1.0B_c$, $1.5B_c$, and $2.0B_c$), and three geofoam locations (at distances of $0.0B_c$, $0.2B_c$, and $0.4B_c$ from the culvert top). Based on the numerical results, the following conclusions can be drawn:

1. The use of EPS geofoam reduced the vertical pressure on the culvert due to the mobilization of positive soil arching.
2. Less vertical pressure was applied to the culvert as the geofoam thickness increased from $0.2B_c$ to $0.8B_c$ during the embankment construction stage; however, the vertical pressure on the culvert increased and reached the same value for all geofoam thicknesses under the application of footing pressure.
3. The geofoam width had no effect on the vertical pressure on the culvert during embankment construction. However, it caused a slight increase in the vertical pressure on the culvert under footing loading.
4. The geofoam placed at a farther distance from the culvert transferred the more pressure to the culvert.
5. After the investigation of the geofoam thickness, width, and location, it can be concluded that a thick geofoam with the same width as the culvert and directly placed on the top of the culvert is the most effective geofoam geometry in the vertical pressure reduction.

REFERENCES

Abdel-Karim, A. M., Tadros, M. K., and Benak, J. V. (1993). "Structural response of full-scale concrete box culvert." *Journal of Structural Engineering*, 119(11), 3238–3254.

Abu-Farsakh, M. Y., Haque, M. N., and Tsai, C. (2017). "A full-scale field study for performance evaluation of axially loaded large-diameter cylinder piles with pipe piles and PSC piles." *Acta Geotechnica*, 12(4), 753-772.

Acharya, R., Han, J., Brennan, J. J., Parsons, R. L., and Khatri, D. K. (2016). "Structural response of a low-fill box culvert under static and traffic loading." *Journal of Performance of Constructed Facilities*, 30(1), 04014184.

Al-Naddaf, M., Han, J., and Xu, C. (2019). "Geofoam Stiffness Effect on Surface Load Distribution on Buried Box Culverts Installed with the Induced Trench Method."

Al-Naddaf, M., Han, J., Xu, C., and Rahmaninezhad, S. M. (2019). "Effect of geofoam on vertical stress distribution on buried structures subjected to static and cyclic footing loads." *Journal of Pipeline Systems Engineering and Practice*, 10(1), 04018027.

Al-Naddaf, M. A. M. (2019). "INVESTIGATION OF SOIL ARCHING UNDER DIFFERENT MODES OF SOIL MOVEMENT AND SURFACE LOADING." University of Kansas.

Allard, E., and El Naggar, H. (2016). "Pressure distribution around rigid culverts considering soil–structure interaction effects." *International Journal of Geomechanics*, 16(2), 04015056.

Alzabeebee, S. (2020). "Influence of backfill soil saturation on the structural response of buried pipes." *Transportation Infrastructure Geotechnology*, 7(2), 156-174.

Chen, B., and Sun, L. (2013). "Performance of a reinforced concrete box culvert installed in trapezoidal trenches." *Journal of Bridge Engineering*, 19(1), 120-130.

Han, J., Acharya, R., Parsons, R. L., and Khatri, D. (2013). "Improved load distribution for load rating of low-fill box structures." *Final report submitted to Kansas Department of Transportation, K-TRAN: KU12-3, Lawrence*.

Kang, J., Parker, F., Kang, Y. J., and Yoo, C. H. (2008). "Effects of frictional forces acting on sidewalls of buried box culverts." *International Journal for Numerical and Analytical Methods in Geomechanics*, 32(3), 289-306.

Katona, M. G. (2017). "Influence of soil models on structural performance of buried culverts." *International Journal of Geomechanics*, 17(1), 04016031.

Kim, K., and Yoo, C. H. (2005). "Design loading on deeply buried box culverts." *Journal of Geotechnical and Geoenvironmental Engineering*, 131(1), 20-27.

Kitane, Y., and McGrath, T. J. (2006). "Three-dimensional modeling of live loads on culverts." *Pipelines 2006: Service to the Owner*, 1-8.

Lal, B. R. R., Padade, A., and Mandal, J. (2014). "Numerical simulation of EPS geofoam as compressible inclusions in fly ash backfill retaining walls." *Ground Improvement and Geosynthetics*, 526-535.

Marston, A. "The theory of external loads on closed conduits in the light of the latest experiments." *Proc., Highway Research Board Proceedings*.

McGuigan, B. L., and Valsangkar, A. J. (2010). "Centrifuge testing and numerical analysis of box culverts installed in induced trenches." *Canadian Geotechnical Journal*, 47(2), 147-163.

McGuigan, B. L., and Valsangkar, A. J. (2011). "Earth pressures on twin positive projecting and induced trench box culverts under high embankments." *Canadian Geotechnical Journal*, 48(2), 173-185.

Meguid, M., Hussein, M., Ahmed, M., Omeman, Z., and Whalen, J. (2017). "Investigation of soil-geosynthetic-structure interaction associated with induced trench installation." *Geotextiles and Geomembranes*, 45(4), 320-330.

Mosadegh, A., and Nikraz, H. (2017). "Buried pipe response subjected to traffic load experimental and numerical investigations." *International Journal of GEOMATE*, 13(39), 1-8.

Padade, A. H., and Mandal, J. (2012). "Behavior of expanded polystyrene (EPS) geofoam under triaxial loading conditions." *Electronic Journal of Geotechnical Engineering*, 17, 2542-2553.

Puppala, A. J., Ruttanaporamakul, P., Bheemasetti, T. V., and Shafikhani, A. (2019). "Laboratory and field investigations on geofoam." *Journal of Pipeline Systems Engineering and Practice*, 10(1), 04018036.

Rahmaninezhad, S. M., Han, J., Al-Naddaf, M., Jawad, S., Parsons, R. L., and Lio, H. (2020). "Field evaluation of performance of corroded corrugated steel pipe before and after sliplining rehabilitation." *Tunnelling and Underground Space Technology*, 102, 103442.

Santos, R. R. V., Kang, J., and Park, J. S. (2020). "Effects of embedded trench installations using expanded polystyrene geofoam applied to buried corrugated steel arch structures." *Tunnelling and Underground Space Technology*, 98, 103323.

Sun, L., Hopkins, T., and Beckham, T. (2011). "Long-term monitoring of culvert load reduction using an imperfect ditch backfilled with geofoam." *Transportation Research Record: Journal of the Transportation Research Board*(2212), 56-64.

Sun, L., Hopkins, T. C., and Beckham, T. L. (2009). "Reduction of Stresses on Buried Rigid Highway Structures Using the Imperfect Ditch Method and Expanded Polysterene (Geofoam)."

Terzaghi, K. (1943). "Theoretical Soil Mechanics, John Wiley & Sons, New York."

Witthoeft, A., and Kim, H. (2016). "Numerical investigation of earth pressure reduction on buried pipes using EPS geofoam compressible inclusions." *Geosynthetics International*, 23(4), 287-300.

IFAI Geosynthetics Conference

Reduction of Lateral Earth Pressures behind Retaining Walls Using EPS and Geosynthetic Reinforcement

Hao Liu,[1] Jie Han, Ph.D., F.ASCE,[2] and Robert L. Parsons, Ph.D., F.ASCE[3]

[1]Ph.D. Student, Civil, Environmental, and Architectural Engineering (CEAE) Department, Univ. of Kansas, 1530 W. 15th St., Lawrence, KS 66045-7609; e-mail: h735l988@ku.edu
[2]Glenn L. Parker Professor, CEAE Department, Univ. of Kansas, 1530 W. 15th St., Lawrence, KS66045-7609; e-mail: jiehan@ku.edu
[3]Professor, CEAE Department, Univ. of Kansas, 1530 W. 15th St., Lawrence, KS 66045-7609; e-mail: rparsons@ku.edu

ABSTRACT

To save cost and avoid distresses of retaining walls, Expanded Polystyrene (EPS) foam and geosynthetic reinforcement have been used to reduce lateral earth pressures behind the wall. However, previous studies mostly assumed retaining walls to be non-yielding, but actual retaining walls can deform to some extent. In this study, three model tests were conducted in laboratory with different backfill details (backfill only, EPS placed between the wall facing and the backfill, EPS placed between the wall facing and the geogrid-reinforced backfill) to investigate the effects of EPS and geogrid reinforcement to reduce lateral earth pressures behind the wall facing during construction. Among these three tests, the retaining wall without EPS foam placed behind moved farthest from the backfill, while the retaining wall with EPS and geogrid reinforcement moved the least. Considering the magnitudes of movement and lateral earth pressure of the retaining wall after construction, the geogrid-reinforced backfill with the EPS between the wall facing and the backfill was the best choice to reduce the lateral earth pressures behind the wall.

INTRODUCTION

Magnitude and distribution of lateral earth pressures on the back of a retaining wall are important for wall design. Designers have often assumed lateral earth pressures behind the retaining wall increase with depth linearly (e.g., Jaky, 1944). The lateral earth pressure distribution behind a wall actually depends on many factors, such as height and stiffness of the wall structure, backfill strength, wall movement mode (i.e., rotation about top, rotation about base, translation, and their combination) (Karpurapu and Bathurst, 1992). In addition, the lateral earth pressure distribution behind the retaining wall is often nonlinear due to soil arching between the wall facing and the backfill if the wall facing is flexible and/or wall movement happens (Handy, 1985). Lateral earth pressures near the top surface of the backfill can even reach the Rankine passive state if vibratory compaction (a common method to densify backfill material) is used (Duncan and Seed, 1986; Cheng and Fang, 2008).

Lateral earth pressures on the retaining wall decrease even if the wall has a small lateral movement away from its retained soil. Knowing this concept, several mitigation measures have been proposed to reduce lateral earth pressures behind retaining walls. These measures include a vertical layer of compressible geosynthetic material between the wall facing and its backfill (e.g., Expanded Polystyrene (EPS), Extruded Polystyrene, and tire chips), corrugated cardboard and removable plywood forms, geosynthetic-reinforced backfill, and use of lightweight material to

replace traditional backfill material (e.g., lightweight concrete and recycled tire chips mixed with sand) (Tsukamoto et al., 1999; Ertugrul and Trandafir, 2011; Trandafir et al., 2010; Ertugrul and Trandafir, 2013; Dave and Dasaka, 2014; Azzam and AbdelSalam, 2015; Reddy and Krishna, 2015; Ni et al., 2017; Reddy and Krishna, 2017; Xie et al., 2020). These mitigation measures can be classified into three groups: (1) measures allowing more lateral movement of the backfill by using a vertical compressible inclusion, (2) measures stabilizing the backfill with geosynthetic reinforcement, ground anchoring, or soil nailing, and (3) a combination of the preceding two measures.

In most physical model tests, wall movement was not permitted during backfilling and then allowed in a controlled mode to study the relationship between lateral earth pressures and wall movement (Fang and Ishibashi, 1986; Tsukamoto et al., 1999; Yang and Tang, 2017; Salehi et al., 2020). For an integral abutment that is structurally connected with bridge girders, rotation about the top of the abutment is the most likely wall movement mode; however, bridge decks or girders can be compressed and bent slightly when the lateral earth pressures behind the abutment are large. In other words, the retaining wall can still move even though the support is relatively rigid, and such a small movement away from the backfill will cause reduction in the lateral earth pressures behind the wall. This paper reports three physical model tests conducted to investigate the benefits of EPS and geogrid to reduce lateral earth pressures behind retaining walls. The magnitudes of wall movements and lateral earth pressures were measured during backfilling in each test.

TEST APPARATUS

Figure 1 shows that the retaining wall was 1.05 m high, 0.30 m wide, and 0.12 m thick. The wall was constructed on a firm platform so that it could not move vertically. In addition, the wall was supported laterally both at its base and at the height of 0.99 m. The stiffness of these lateral supports were same in each test; therefore, the movement of the wall was indication of the effect of backfilling on the wall. In other words, if the construction process caused more forces onto the wall, it would move more away from the backfill. The backfill in each model was 1.46 m long, 1.05 m high, and 0.30 m thick and its relative density (D_r=75%) (i.e., a density of 1840 kg/m^3) was controlled by the constant thickness and weight of the air-dried Kansas River sand in each lift. Direct shear tests measured the peak friction angle of this backfill at the relative density of 75% as 42.3°.

Younan and Veletsos (2000) defined wall flexibility using a relative flexibility (d_w) index as shown Eq. (1):

$$d_w = \frac{12GH^3(1-v_w^2)}{E_w t_w^3} \quad (1)$$

where G is the shear modulus of the backfill (i.e., 9.6 MPa derived from Young's modulus (25 MPa) and Poisson's ratio (0.3) of this sand (Al-Naddaf, 2019)), H is the wall height (1.05 m), v_w is the Poisson's ratio of the wall material (0.20), E_w is the Young's modulus of the wall material (25 GPa), and t_w is the thickness of the wall (0.12 m). In this study, the relative flexibility of the wall was 3.0, indicating it was a rigid wall based on the recommendation by Younan and Veletsos (2000).

Each test used two displacement transducers (DTs), five earth pressure cells (EPCs), and a load cell (LC). The bottom DT at the wall height of 0.15 m and the top DT at the wall height of 0.99 m were used to measure lateral movements of the wall during backfilling. Five EPCs were

placed on the back of the wall facing or EPS (if used) at the heights of 0.15, 0.38, 0.59, 0.79 and 0.94 m to monitor the lateral earth pressures during backfilling. In addition, the load cell was used to measure the force to hold the wall in place at the height of 0.99 m.

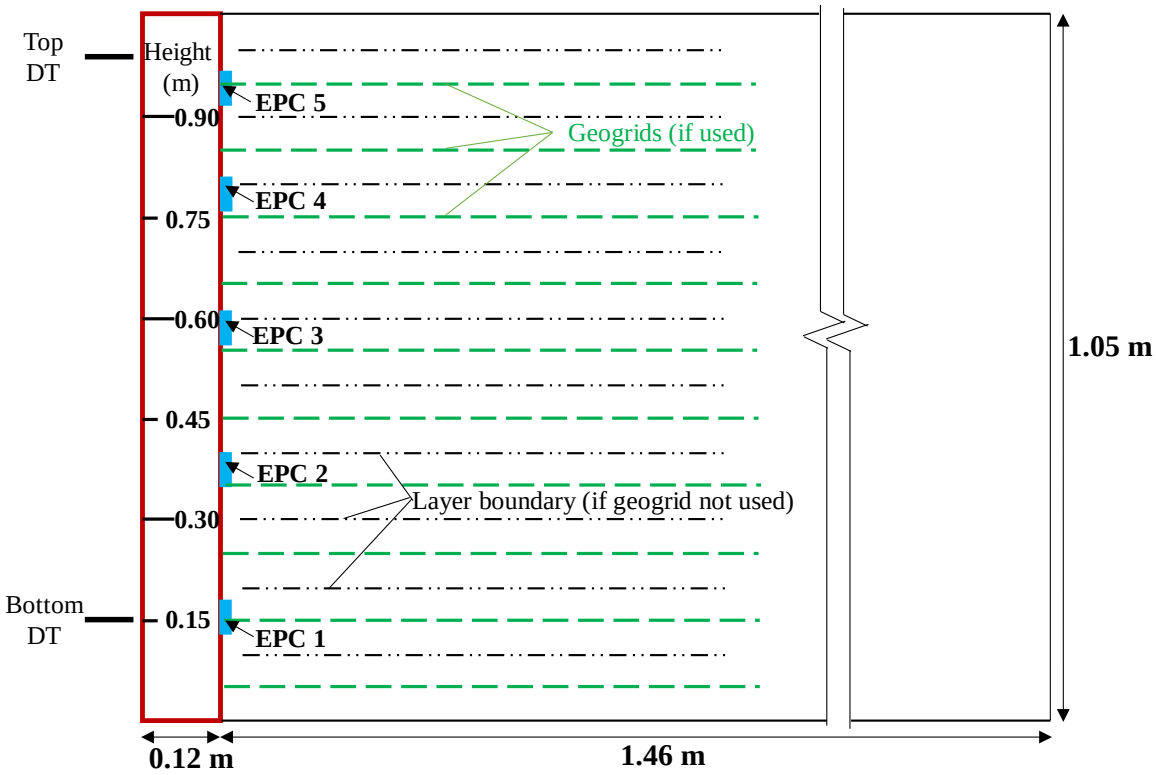

Figure 1. Cross section of the retaining wall with instrumentation.

Table 1 shows the conditions of these three tests whether EPS and/or geogrid were included in the backfill. A piece of EPS with dimensions of 1.05 m high, 0.30 m wide, and 0.025 m thick and a density of 16 kg/m^3 was placed behind the back of the wall facing in T2 and T3. Uniaxial geogrid prepared from a biaxial geogrid by cutting off two ribs of every four ribs in the machine direction was used as backfill reinforcement in this study considering the scale effect. The same uniaxial geogrid was used by Xiao et al. (2016), Kakrasul et al. (2020), and Jawad et al. (2020) in their study. The T1 model included ten lifts of backfill with a lift thickness of 0.10 m without any geogrid. The T2 or T3 model included 10 layers of geogrid with vertical spacing of 0.10 m and length of 0.75 m placed within the backfill (the lowest geogrid layer was placed at the height of 0.05 m).

Table 1. Test conditions.

Test No.	Inclusion in backfill
T1	No EPS and No geogrid
T2	EPS
T3	EPS and geogrid

TEST RESULTS

Movement of wall. Figures 2 and 3 show the lateral displacements of the wall at the heights of 0.15 and 0.99 m, respectively, during backfilling. In general, the wall in T3 moved less away from the backfill than that in T1 and T2, but the walls in T1 and T2 had similar movements. It should be pointed out that the movements in Figures 2 and 3 were the wall movements at the bottom or the top while the backfill was placed up to a certain height. After the backfill was placed up to 0.8 m, the wall in T2 moved less than that in T1, indicating that the EPS in T2 had some benefit in the wall behavior during backfilling. Geogrid reinforcement of the backfill in T3 minimized the movement induced by backfilling. The benefit of the EPS inclusion was not that significant, maybe because of three reasons: (1) the EPS was not compressible enough due to its small thickness (25 mm), (2) the modulus of the EPS was not that low as compared with that of the sand under a low normal stress, and (3) the wall was only 1.05 m tall and the backfill was compacted by a small hand tamper. The EPS was just subjected to low lateral earth pressures induced by self-weight of the backfill and compaction by the tamper; therefore, the deformation of the EPS was small so that it did not fully perform as a stress reliever. However, the geogrid reinforcement limited the stress transfer onto the wall facing during backfilling because the geogrid reinforcement restrained the lateral movement of the sand.

During backfilling, the movement of the wall was a combination of a translation mode (T mode) and a rotation about the base mode (RB mode) when the wall movements at the top and the bottom were not same. However, since their differences were small as compared with the wall height, the portion of the RB mode in the combination did not make an apparent difference. Therefore, the mode of the wall movement could be treated as the T mode only. Horvath (1997) indicated a wall displacement of 0.3%H (H is the wall height) could make a well-compacted sand-gravel backfill reach a fully active state, while Clough and Duncan (1991) suggested a wall displacement of 0.1%H should be enough to reach a fully active state in a dense sand. After backfilling, the movements of the wall in T1, T2, and T3 were 0.06%H, 0.05%H, and 0.04%H, respectively, which are less than those suggested by Horvath (1997) and Clough and Duncan (1991); therefore, the fully active state was not reached in this study.

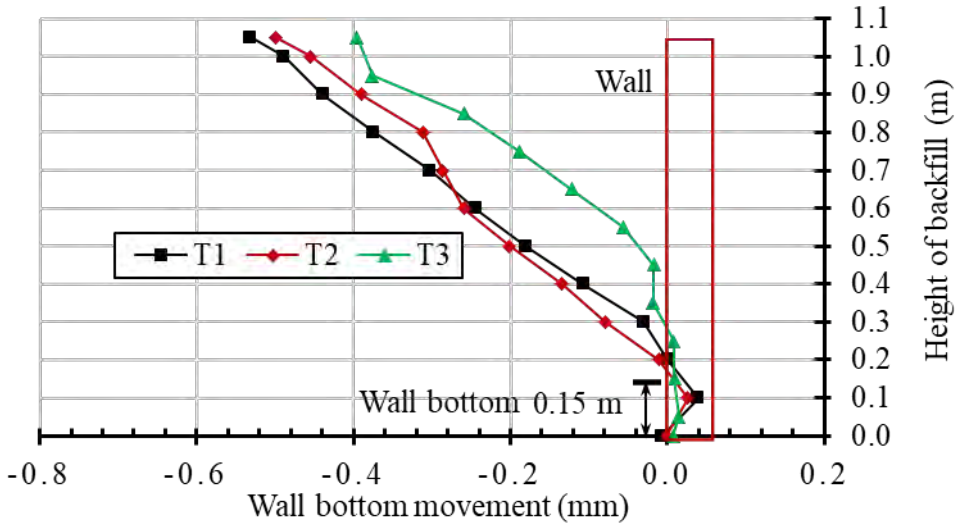

Figure 2. Lateral movement of the wall at the height of 0.15 m during backfilling.

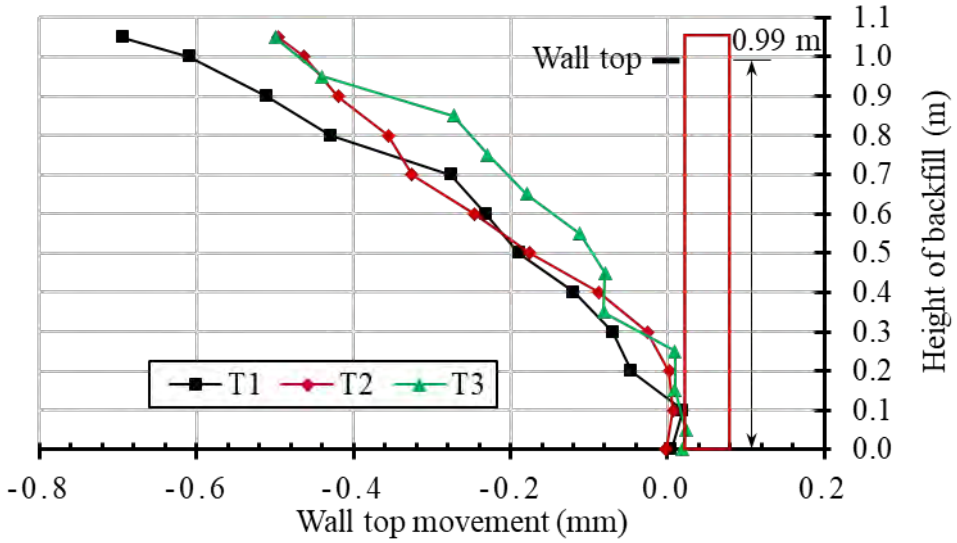

Figure 3. Lateral movement of the wall at the height of 0.99 m during backfill placement.

Earth pressure behind wall. Figures 4 shows the lateral earth pressures behind the wall facing after backfilling. The values of the Rankine active earth pressures (K_a=0.20), the Jaky earth pressures at rest (K_o=0.33), and the Rankine passive earth pressures (K_p=5.10) are also provided for easy comparisons. Chen and Fang (2008) found that vibratory compaction of backfill against a non-yielding wall would induce additional lateral earth pressures within an influence zone, up to the Rankine passive earth pressure near top of the backfill surface as found by Duncan and Seed (1986). However, lateral earth pressures at greater depths might gradually converge back to the at-rest earth pressure due to the increase of wall height and vertical overburden stress. The three tests in this study also showed a similar pattern of lateral earth pressure distribution within the upper soil layers, but the lateral earth pressures in the lower layers decreased significantly to lower than the at-rest pressures. The lower pressures in the bottom layers might be caused by movement of the wall bottom away from the backfill during backfilling. It is expected that the lateral earth pressures near the backfill surface should be higher and closer to the passive earth pressure if the wall was non-yielding.

In general, EPS and geogrid reduced the lateral earth pressures behind the wall facing, considering more movement of the wall from the backfill in T1 (no EPS and geogrids were used). However, the lateral earth pressure at the height of 0.59 m in T3 was higher than that at the same height in T1, while the lateral earth pressure at the height of 0.15 m in T2 was higher than that at the same height in T1. Borms (1971) and US Navy (1982) suggested that the lateral earth pressure behind a retaining wall increased with depth to a value and then kept at this value until the at-rest or Rankine active earth pressure reaching this value. The test results from T1 generally conformed to this lateral earth pressure distribution except for the pressure at the height of 0.15 m, which might be caused by the movement of the wall at the bottom away from the backfill. T2 had a different distribution of the lateral earth pressures behind the wall facing from those in T1 and T3. It appeared that the inclusion of the EPS changed the earth pressure distribution below the middle of the wall.

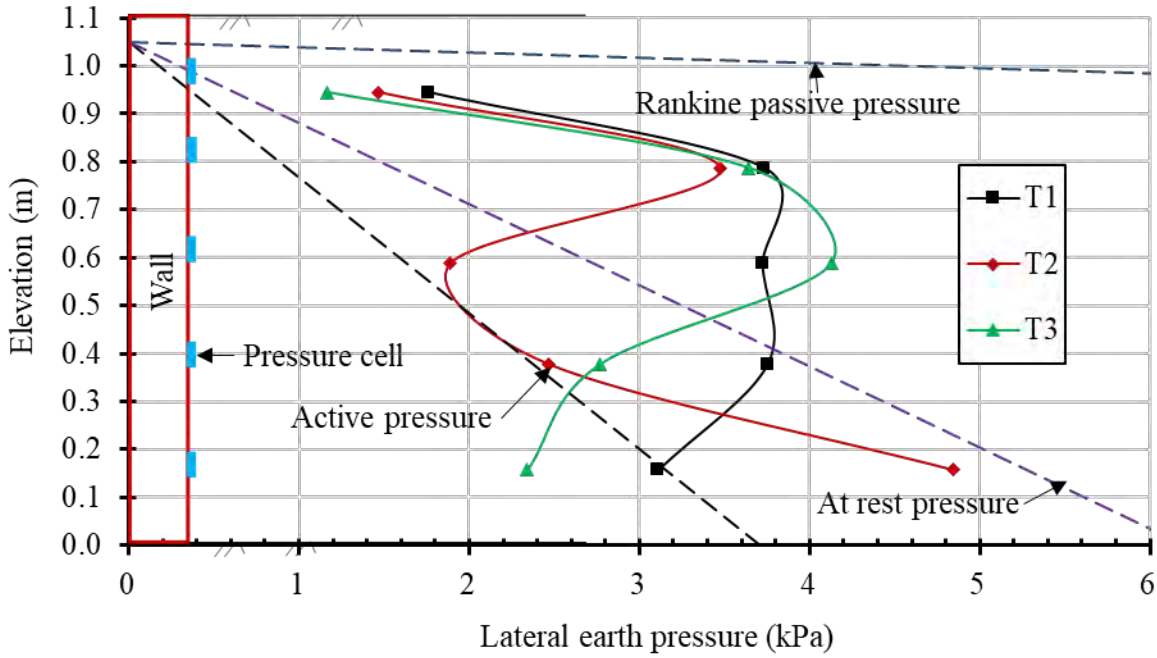

Figure 4. Lateral earth pressure behind the wall after backfilling.

Coefficient of lateral earth pressure. It is a common practice that lateral earth pressures behind wall facing are assumed to increase linearly with vertical overburden stresses at different depths and the slope of this linear relationship is referred to as the coefficient of lateral earth pressure, K. In the test setup in this study, the moment to the wall toe caused by lateral earth pressures should be equal to that provided by the force at the height of 0.99 m to support the wall. Therefore, the coefficient of lateral earth pressure, K, can be estimated using Eq. (2):

$$K = 6F \cdot H/(\gamma h^3 B) \quad (2)$$

where K is the coefficient of lateral earth pressure; F is the force at the height of 0.99 m to support the wall, which was measured by the load cell; H is the height of the load cell (0.99 m); γ is the unit weight of the backfill (18.05 kN/m^3); h is the height of the backfill; and B is the width of the wall facing (0.3 m).

Figure 5 shows the change of the lateral earth pressure coefficient (K) with the height of the backfill placed. It should be pointed out that the lateral earth pressure coefficient calculated using Equation (2) is the overall coefficient and different from the lateral earth pressure coefficient calculated based on the lateral earth pressure divided by the vertical overburden stress at a specific height. This figure indicates that EPS and geogrid reinforcement reduced the coefficient after backfilling. Considering more movements of the wall at the bottom and the top away from the backfill after backfilling in T3 than those in T2, T3 had more reduction in the lateral earth pressures behind the wall facing even though T3 and T2 had almost the same K values at the end of backfilling (i.e., 1.05 m high). During the construction process, the K value for T3 was much smaller than those for the other two tests. At the end of the construction, the K value of the backfill was greater than the coefficient at rest (0.33), due to compaction-induced stresses. The

compaction-induced additional stress zone moved up as the backfill surface increased so that the lateral earth pressures below the zone converged to the at-rest or active earth pressures. This finding explained why the coefficients for T1 and T2 decreased with the increase of the backfill height during backfilling.

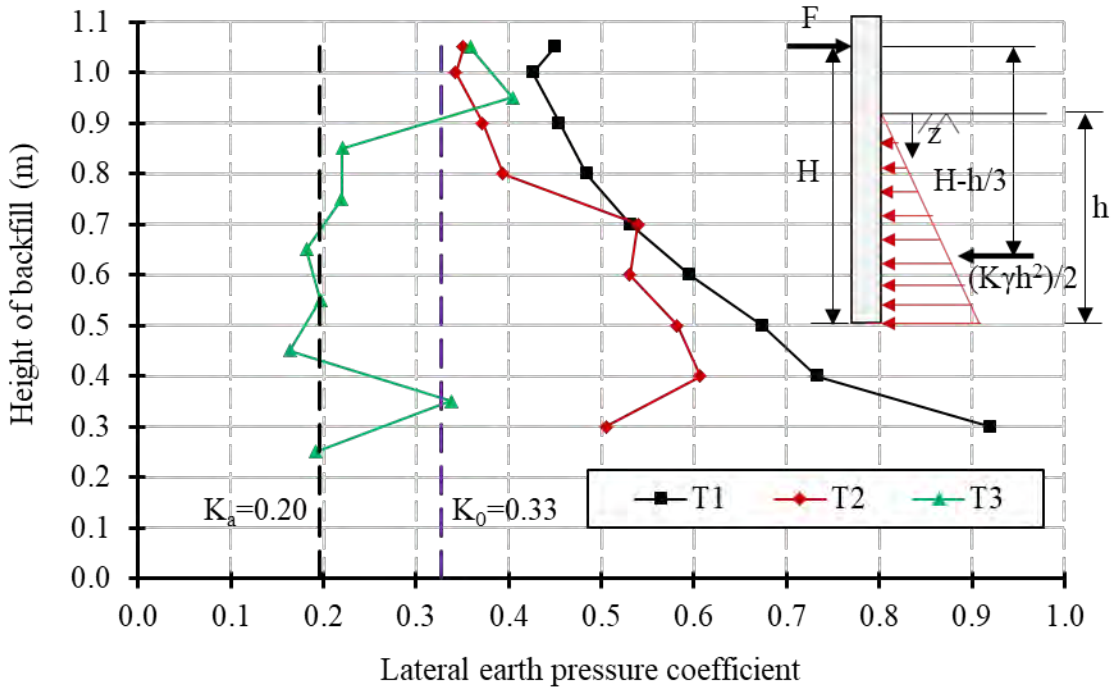

Figure 5. Change of lateral earth pressure coefficient with backfill height during backfilling.

CONCLUSIONS

Lateral earth pressures behind a non-yielding rigid retaining wall often approach the at-rest state after backfilling, but the lateral earth pressures within the upper portion may reach passive earth pressures due to compaction of backfill in lifts. Higher lateral earth pressures require a thicker wall cross section and a higher structural capacity, thus resulting in a higher cost. This study included three physical model tests: (1) T1 without any EPS foam and geogrid, (2) T2 with EPS placed between the wall facing and the backfill, and (3) T3 with EPS placed between the wall facing and the geogrid-reinforced backfill. These tests were used to investigate the effects of EPS and geogrid reinforcement on lateral earth pressures behind the wall facing. Unlike most physical models with non-yielding walls, the magnitude of the wall movement away from the backfill in this study depended on the inclusion of EPS and geogrid reinforcement during the backfilling process. From this study, the following conclusions could be made:

(1) After backfilling, T1 had the largest movement away from the backfill, while T3 had the smallest movement, indicating the combined use of the EPS and the geogrid effectively reduced the backfilling effects on the wall.

(2) All three tests showed additional lateral earth pressures induced by compaction within the upper portion of the wall. Due to the movement of the wall away from the backfill and the

increase of vertical pressure, the lateral earth pressures within the bottom layers dropped to lower than the Jaky at-rest earth pressures.

(3) Considering the change of the lateral earth pressure coefficient with the increase of the height of backfill placed and the magnitude of the movement of the wall from the backfill, the model test with the EPS placed between the wall facing and the geogrid-reinforced backfill was most effective to reduce the lateral earth pressures on the wall.

ACKNOWLEDGEMENTS

This study was financially supported by the Kansas Department of Transportation (KDOT) through the KTRAN program. Mr. Luke Metheny, Chief Geotechnical Engineer at KDOT, was the project monitor. Dr. Saif Jawad at the University of Baghdad, Iraq, and the technician Kent Dye at the University of Kansas provided great help to the test setup. The first author received the GSI fellowship from the Geosynthetic Institute in 2019. The authors gratefully acknowledge all the above support.

REFERENCES

Al-Naddaf, M. A. M. (2019). *Investigation of Soil Arching under Different Modes of Soil and Surface Loading*, Ph.D. thesis, University of Kansas, Lawrence, KS, USA.

Azzam, S. A. and AbdelSalam, S. S. (2015). EPS geofoam to reduce lateral earth pressure on rigid walls. *Proceedings of International Conference on Advances in Structural and Geotechnical Engineering, (ICASGE'15),* Hurghada, Egypt.

Broms, B. (1971). Lateral earth pressures due to compaction of cohesionless soils. *Proceedings of 4th International Conference on Soil Mechanics*, Budapest, Hungary.

Chen, T. J. and Fang, Y. S. (2008). Earth pressure due to vibratory compaction. *Journal of Geotechnical and Geoenvironmental Engineering*, ASCE, 134(4): 437-444.

Clough, G. W. and Duncan, J. M. (1991). Earth Pressures. In *Foundation Engineering Handbook*. Springer, Boston, MA.

Dave, T. N. and Dasaka, S. M. (2014). Surcharge induced earth pressure reduction on rigid retaining wall using EPS geofoam. *Tunneling and Underground Construction*, ASCE: 836-844.

Duncan, J. M. and Seed, R. B. (1986). Compaction-induced earth pressures under K_0-condition. *Journal of Geotechnical Engineering*, ASCE, 122(1): 1-22.

Ertugrul, O. L. and Trandafir, A. C. (2011). Reduction of lateral earth forces acting on rigid nonyielding retaining walls by EPS geofoam inclusions. *Journal of Materials in Civil Engineering*, ASCE, 23(12): 1711-1718.

Ertugrul, O. L. and Trandafir, A. C. (2013). Lateral earth pressures on flexible cantilever retaining walls with deformable geofoam inclusions. *Engineering Geology*, 158: 23-33.

Fang, Y.S. and Ishibashi, I. (1986). Static earth pressures with various wall movements. *Journal of Geotechnical Engineering*, ASCE, 112(3): 317-333.

Handy, R. L. (1985). The arch in soil arching. *Journal of Geotechnical Engineering*, ASCE, 111(3): 302-318.

Horvath, J. S. (1997). The compressible inclusion function of EPS geofoam. *Geotextiles and Geomembranes*, 15(1): 77–120.

Jaky, J. (1944). A nyugalmi nyomas tenyezoje (The coefficient of earth pressure at rest). *Magyar Mernok es Epitesz-Egylet Kozlonye*, Hungary: 355–358 (in Hungarian).

Jawad, S., Han, J., Al-Naddaf, M., and Abdulrasool, G. (2020). Responses of laterally loaded single piles within MSE walls. Journal of Geotechnical and Geoenvironmental Engineering, ASCE, 46(12): 04020128-1 to 11

Kakrasul, J.I., Han, J., and Rahmaninezhad, S.M. (2020). Load-deformation of geosynthetic-reinforced retaining walls with limited fill space under static footing loading. Transportation Infrastructure Geotechnology, 7(3), 309 – 331.

Karpurapu, R. and Bathurst, R. J. (1992). Numerical investigation of controlled yielding of soil-retaining wall structures. *Geotextiles and Geomembranes*, 11(2): 115-131.

Ni, P., Mei, G., and Zhao, Y. (2017). Displacement-dependent earth pressures on rigid retaining walls with compressible geofoam inclusions: physical modeling and analytical solutions. *International Journal of Geomechanics*, ASCE, 17(6): 04016132.

Reddy, S. B. and Krishna, A. M. (2015). Recycled tire chips mixed with sand as lightweight backfill material in retaining wall applications: an experimental investigation. *International Journal of Geosynthetics and Ground Engineering*, 1(4): 1-11.

Reddy, S. B. and Krishna, A. M. (2017). Tyre chips as compressible inclusions in earth-retaining walls. *Proceedings of the Institution of Civil Engineers-Ground Improvement*, 170(3): 137-148.

Salehi, A. N., Khosravi, M. H., and Katebi, H. (2020). Distribution of lateral active earth pressure on a rigid retaining wall under various motion modes. *International Journal of Mining and Geo-Engineering*, 54(1): 15-25

Trandafir, A. C., Moyles, J. F. and Erickson, B. A. (2010). Finite-element analysis of lateral pressures on rigid non-yielding retaining walls with EPS geofoam inclusion. In *Earth Retention Conference*, 3: 756-763.

Tsukamoto, Y., Ishihara, K., Higuchi, T. and Aoki, H. (1999). Influence of geogrid reinforcement on lateral earth pressures against model retaining walls. *Geosynthetics International*, 6(3): 195-218.

US Navy (1982). *Foundations and Earth Structures*, NAVFAC Design Manual DM-7.2, Washington, D.C.

Xiao, C., Han, J. and Zhang, Z. (2016). Experimental study on performance of geosynthetic-reinforced soil model walls on rigid foundations subjected to static footing loading. *Geotextiles and Geomembranes*, 44(1): 81-94.

Xie, M., Zheng, J., Shao, A., Miao, C. and Zhang, J. (2020). Study of lateral earth pressures on nonyielding retaining walls with deformable geofoam inclusions. *Geotextiles and Geomembranes*, in press.

Yang, M. and Tang, X., 2017. Rigid retaining walls with narrow cohesionless backfills under various wall movement modes. *International Journal of Geomechanics*, ASCE, 17(11), 04017098.

Younan, A. H., Veletsos, A. S. (2000). Dynamic response of flexible retaining walls. *Earthquake Engineering and Structural Dynamics*, 29: 1815-1844.

Geosynthetics Conference

Ultra-lightweight Foamed Glass Aggregate as MSE Wall Backfill: Properties and Case Studies

Theresa Andrejack Loux, Ph.D., P.E.[1] and Archie Filshill, Ph.D., ENV SP[2]

[1]Aero Aggregates of North America LLC, Eddystone, PA; e-mail: tloux@aeroaggregates.com
[2]Aero Aggregates of North America LLC, Eddystone, PA; e-mail: archie@aeroaggregates.com

ABSTRACT

Ultra-lightweight foamed glass aggregate (UL-FGA) is a lightweight and insulating fill material used in the construction of retaining structures, embankments, bridge abutments, and foundation slabs. UL-FGA is made from 100% recycled glass and is a sustainable, closed-loop product that has a favorable energy footprint when compared to other lightweight fill options. UL-FGA has in-place densities between 15 and 24 lb/ft^3 and a closed cell structure which minimizes the moisture content of the material. This paper details the physical and engineering properties of the UL-FGA produced via the dry manufacturing process, that are needed for the design of mechanically stabilized earth (MSE) systems with UL-FGA backfill. Internal and external stability considerations when using UL-FGA as MSE backfill are discussed. Finally, two projects where UL-FGA has been used as MSE wall backfill are presented.

INTRODUCTION

Mechanically stabilized earth (MSE) systems are a popular and economic option to construct retaining walls for highways or railways, wingwalls and abutments for bridges, and numerous other applications for public and private development. An MSE wall is comprised of alternating layers of fill and soil reinforcements. The reinforcement materials are generally made of galvanized steel or polymers (e.g., geosynthetics) and take of form of straps or continuous elements. MSE walls have a vertical or near-vertical face typically comprised of concrete panels or blocks, segmental blocks, or is a wrapped-earthen face with or without welded wire forms. Design and construction guidance for MSE walls and backfill specifications for MSE backfill are dependent on the MSE wall application and location. Entities including the Federal Highway Administration (NHI 2009) and the National Concrete Masonry Association (NCMA 2010) have published leading resources.

There are frequent instances where the subsurface conditions warrant the use of a lightweight backfill material such as ultra-lightweight foamed glass aggregate (UL-FGA). The lightweight backfill may be needed because of soft, compressible soils, or because of existing utilities or structures. UL-FGA has been available in Europe since the mid-1990s and is now also manufactured in the U.S. The manufacturing process consists of cleaning and milling post-consumer recycled glass, mixing the glass powder with a dry foaming agent, and then heating the mixture in a kiln to produce a foamed glass cake. Thermal stress breaks the cake into aggregate-sized pieces.

UL-FGA is manufactured from post-consumer recycled glass which has inherent environmental advantages because it is not a material that is mined or petroleum-based. Because of the ultra-lightweight nature, a single truckload delivery of UL-FGA can be upwards of 75 m^3 (100 yd^3) which may greatly eliminate truck traffic on projects which require imported fill.

A more complete discussion of the physical and engineering properties of foamed glass aggregate is available in the literature (e.g., Aaboe et al. 2005, Auvinen et al. 2013, Betti et al. 2014, Frydenlund and Aaboe 2003, Loux et al. 2019a, Loux et al. 2018, Loux et al. 2019b). This paper discusses the physical and engineering properties of the UL-FGA that are needed for the design of mechanically stabilized earth (MSE) systems when using this material as MSE backfill. Internal and external stability considerations of MSE walls with UL-FGA backfill are discussed. The case studies shared in this paper are limited to projects utilizing polymer-based reinforcements with UL-FGA backfill.

UL-FGA - MSE BACKFILL PROPERTIES

Unit Weight and Buoyancy. The typical dry bulk unit weight of closed-cell UL-FGA (Figure 1) as manufactured varies between 192 and 240 kg/m^3 (12 to 15 lb/ft^3). Moist bulk unit weights can vary based on moisture content but are typically between 240 and 300 kg/m^3 (15 and 18.75 lb/ft^3). Placement and compaction processes typically produce a volume reduction of up to 20% from the bulk to compacted state. This equates to a compaction factor of up to 1.25. Therefore, typical minimum and maximum in-place unit weights for UL-FGA are approximately 240 and 375 kg/m^3 (15 and 23.5 lb/ft^3), respectively.

Because of the closed cell nature and slight buoyancy of UL-FGA, a buoyancy check should be completed for projects near waterways. The buoyant unit weight of UL-FGA has been determined through testing to be approximately -240 kg/m^3 (-15 lb/ft^3). Therefore, applying a factor of safety of 1.5, the design buoyant unit weight of UL-FGA is -350 kg/m^3 (-22 lb/ft^3). This buoyancy check will consider the design flood elevation and the thickness and unit weights of the UL-FGA and overlying layers.

Figure 1. Photograph of UL-FGA.

Gradation and Plasticity. The American Association of Highway State Officials (AASHTO) has set forth requirements for MSE backfill material in the Load Resistance Factor Design (LRFD) Bridge Construction Specifications (2017). Table 1 provides the AASHTO requirement for gradation in general accordance with AASHTO T 27 (AASHTO 2014) and the UL-FGA reported values, respectively. Post-compaction analyses on UL-FGA show some breakdown of the

material, but the UL-FGA will still have a grain size distribution within the AASHTO limits shown in Table 1 (Loux et al. 2019b). Additionally, UL-FGA is non-plastic and therefore has a PI of less than 6% in general accordance with AASHTO T 90 (AASHTO 2016).

The relatively uniform gradation of UL-FGA produces a layer with high porosity and therefore, high permeability. To maintain the high porosity and low unit weight of the UL-FGA layer, it is recommended that a separation geotextile is used to encapsulate the UL-FGA layer wherever UL-FGA is in contact with adjacent granular materials (include foundation soil and retained soil) so that intrusion of finer particles into the void space does not occur.

Table 1. Gradation requirements for MSE wall backfill and pre-compacted UL-FGA gradation.

Sieve Size (AASHTO T 27)	***PERCENT PASSING***	
	AASHTO (2017) Gradation Requirements	***UL-FGA Gradation (Pre-compaction)***
100 mm (4.0 inch)	100	100
63 mm (2.5 inch)	-	85-100
9.5 mm (3/8 inch)	-	0-15
425 µm (No. 40)	0-60	-
75 µm (No. 200)	0-15	-

Friction Angle. Shear strength parameters of UL-FGA are affected by the applied normal stress. The apparent friction angle for UL-FGA determined per ASTM D 3080 modified is shown in Table 2. Most UL-FGA applications in MSE walls will fall into the <57.5 kPa (<1200 lb/ft^2) normal stress range, but every wall should be evaluated by the designer.

Table 2. Friction angle requirements for MSE wall backfill and UL-FGA apparent friction angle.

(ASTM D 3080)	***AASHTO (2017) Requirement***	***UL-FGA Apparent Peak Friction Angle***
Up to 57.5 kPa (1,200 psf)	> 34°	54°-55°
Up to 144 kPa (3,000 psf)	> 34°	41°-45°

Soundness. The soundness requirement for MSE backfill material per AASHTO (2017) and UL-FGA results are shown in Table 3. The magnesium sulfate soundness test is a measure of the durability of the aggregate to resist freeze-thaw cycles.

Table 3. Soundness loss requirements for MSE wall backfill and UL-FGA soundness loss.

	AASHTO (2017) Requirement	***UL-FGA Soundness Loss***
Magnesium Sulfate Soundness (loss after 4 cycles)	**≤ 30%**	**4.1%-14%**

Electrochemical Requirements. In the case of MSE walls constructed with steel reinforcements, AASHTO (2017) sets additional electrochemical requirements. These limits and the reported values for the UL-FGA are shown in Table 4.

Table 4. AASHTO electrochemical requirements for MSE wall backfill and FGA reported values.

Parameter	*AASHTO (2017) Requirement*	*UL-FGA Reported Values*
pH	5 to 10	9.2-9.4
Resistivity	≥ 30 Ω · m	>3,366,000 Ω · m (As Received) 52,020 Ω · m (Initial – 100% Saturated) 18,666 Ω · m (24-hr Soak – 100% Saturated) 13,158 Ω · m (48-hr Soak – 100% Saturated)
Chlorides	≤ 100 ppm	<10 -19 ppm
Sulfates	≤ 200 ppm	<10 - 11 ppm

STABILITY CONSIDERATIONS

Internal stability of MSE walls is evaluated during the design process by checking the factor of safety against reinforcement pullout and reinforcement breakage. Internal stability calculations are used to assess or determine the reinforcement spacing, reinforcement lengths, reinforcement strength, and connection strength or overlap distance (for wrapped-face walls). Laboratory scale pullout testing of UL-FGA with several reinforcement materials has been completed to generate a relationship for the coefficient of interaction with normal stress (Loux et al. 2019b). External stability of MSE walls considers overturning, sliding, and global failure of the MSE wall and often requires site-specific knowledge of the existing onsite soils. To complete the internal and external stability evaluations, earth pressures due to retained soil, surcharge loads, and live loads must be considered.

Some projects using UL-FGA backfill may encounter longer than typical reinforcement lengths to satisfy internal and external stability factor of safety requirements. A full-height UL-FGA MSE wall is shown in Figure 2(a). If a MSE wall with UL-FGA backfill has stability concerns, three potential layout adjustments to increase stability are shown in Figure 2(b) through 2(d). In Figure 2(b), while the net surcharge load on the foundation soils will be higher versus a full-height MSE wall with UL-FGA backfill, this layout may still be competitive with other lightweight fill options that are available (i.e. expanded shale or clay or cellular concrete). Figure 2(c) shows extending the reinforcements into typical unit weight reinforced fill. The approach in Figure 2(d) is to cut the existing soils back to a stable angle and fill the triangle formed between the reinforced fill and cut slope with additional UL-FGA. This method, while increasing the quantity of the UL-FGA, will greatly decrease the lateral earth pressures on the wall from the UL-FGA retained backfill.

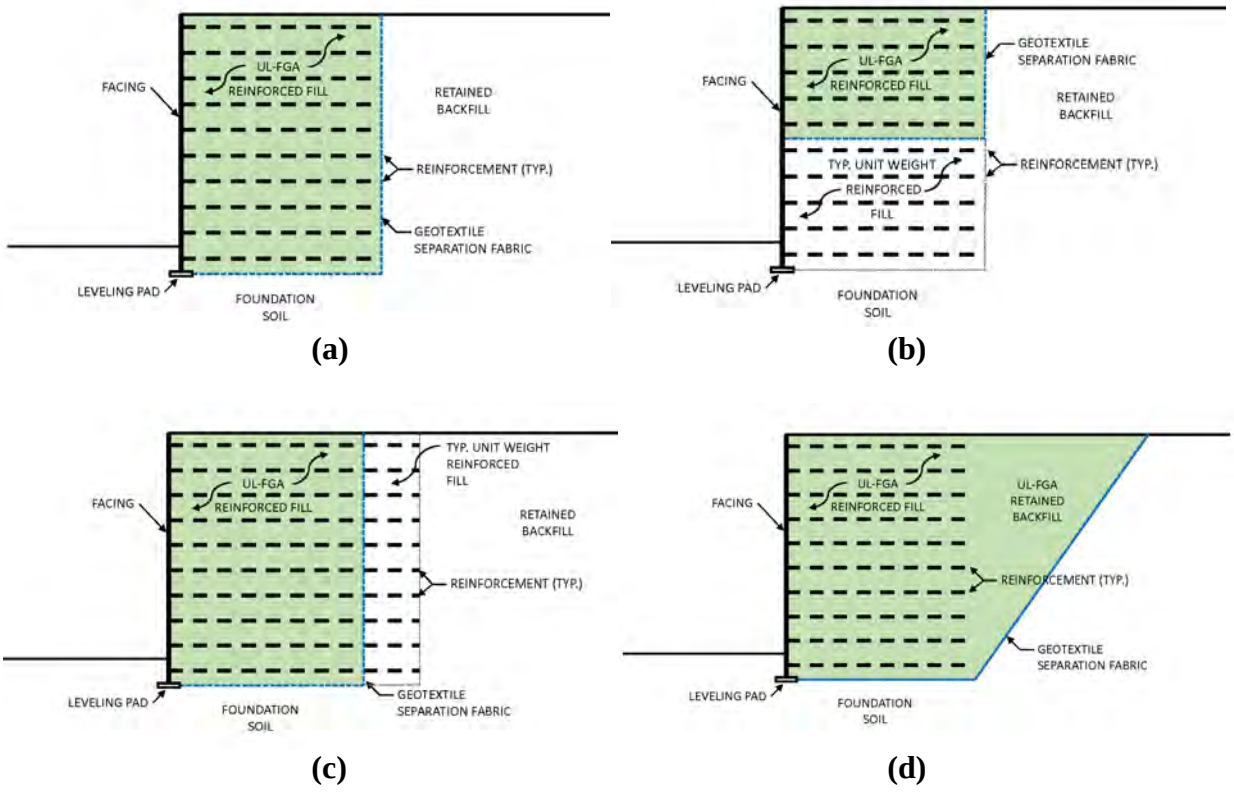

Figure 2. MSE wall (a) with full-height UL-FGA MSE backfill, (b) with ~50% height MSE backfill, (c) with combination UL-FGA and typical unit weight MSE backfill, and (d) with UL-FGA MSE backfill and UL-FGA retained backfill.

ADDITIONAL UL-FGA - MSE CONSIDERATIONS

Other design details that are typically considered for MSE walls include drainage, foundation preparation, and wall facing details. Drainage piping may be included within the UL-FGA to outlet water from the retained soil, but the entire layer will be highly permeable. Piping may be used to outlet low spots within the UL-FGA backfill so that any collected water may be allowed to outlet instead of infiltrate into the foundation soil.

On all walls with UL-FGA backfill that are under roadways, the pavement section should be analyzed to ensure that the distance between the top of pavement and the top of UL-FGA layer is sufficient for the pavement design requirements. It is not unusual for this distance to be 915 to 1220 mm (3 to 4 feet) not only to address a flexible pavement design, but also to accommodate moment slabs for traffic barriers, guide rail, fencing, or buoyancy concerns.

Standard compaction procedures for soils and traditional aggregates should not be applied to UL-FGA. The compaction procedures recommended by European manufacturers are a method-based specification that relies on tracked equipment or vibratory plate compaction only and are based upon over 25 years of experience with UL-FGA. Standard installation procedures from various manufacturers of UL-FGA cite large maximum lift thicknesses (between 0.6 to 1.0 m) [2 to 3.3 ft]. For standard load-bearing applications a compression ratio of between 1.15 and 1.25 is

achieved. A compression ratio of 1.25 corresponds to a volume reduction of 20% from the bulk to compacted state.

The equipment that is typically used to compact UL-FGA is tracked equipment with ground pressures between 30 - 50 kPa (625 - 1,025 psf). This equipment, typically an excavator or dozer, will complete four passes over the UL-FGA layer for a standard installation. Compaction occurs by the static and dynamic forces imparted by the tracked equipment and will produce slight particle breakage but good particle interlock. In areas not accessible to tracked equipment, thinner lifts of 0.3 to 0.6 m (12 to 24 inches) can be compacted using a 50-100 kg (110-220 lbs) plate compactor. This method includes areas of MSE wall backfill close to the wall face. Unless higher degrees of compaction are required, static or vibratory rollers are not recommended to be used for the compaction of UL-FGA.

A lidar study was completed to verify the efficacy of the method-based specification for compaction (McGuire et al. 2021). Because UL-FGA is an open-graded aggregate, typical CQA procedures for soil compaction (i.e., nuclear density gauge testing) are not applicable. Instead, observance and verification of the method based-specification for UL-FGA compaction is necessary.

CASE HISTORIES

I-95 Section GR-4 Staged Construction, Philadelphia, PA. The Pennsylvania Department of Transportation (PennDOT) is actively working on the GIR Section of Interstate 95, a three-mile section from Center City Philadelphia to the north. Both north and southbound viaducts will be fully reconstructed, and the project incorporates improvements to surrounding areas and interchanges, including on- and off- ramps.

Retaining Wall 16 of Section GR4 of I-95 follows a curve in the ramp and has an overall length of approximately 87.7 m (288 feet) and has a maximum height of approximately 9 m (30 feet). The Contractor selected a mechanically-stabilized earth (MSE) system with geosynthetic reinforcement as part of the support of excavation design for the new on-ramp. Because of soft soil concerns, the significant height of the ramp, and the presence of adjacent existing deep foundations, ultra-lightweight foamed glass aggregate (UL-FGA) was used as MSE backfill material on the section of the embankment directly adjacent to the existing ramp. The contract indicated that staged construction be undertaken. First, the Contractor demolished half of the existing on-ramp, constructing half of the new ramp in its place while maintaining traffic on the portion of the existing on-ramp left undemolished. Then, once the partial new on-ramp was completed, traffic transferred onto the new ramp and the remaining portion of the existing ramp demolition was to follow.

The phased construction approach and the switch from an elevated structure to an embankment for the ramp created a concern: there was the possibility that the new on-ramp constructed on fill would exert a high bearing pressure on the underlying foundation soils and possibly compromise the existing ramp's deep foundations which were still carrying traffic on the undemolished elevated portion. Rather than undertake the installation of driven sheet piling next to live traffic then sacrificing the steel sheet material left in the ground which could not be removed once covered by the fill section for the new ramp, the Contractor selected an alternative involving UL-FGA fill within the new on-ramp's embankment to sufficiently lower the load exerted by the new ramp's fill section.

Only a short section of the new ramp (approximately 25m in length) required the use of UL-FGA as backfill because of the proximity of the piers to the existing ramp (see Figure 3). The new ramp was designed as a temporary MSE retaining wall system. The primary reinforcement was coated polyester geogrids and the wall included a polypropylene geotextile facing wrap and steel welded wire mesh facing units. A traffic live load of 17.2 kPa was used. Appropriate applied load factors and applied resistance factors were used based on Load and Resistance Factor Design (LRFD) requirements set forth by AASHTO and PennDOT.

Figure 3. Photograph of the future on-ramp with UL-FGA MSE backfill.

Three geogrid products with long term design strengths of 40.9 kN/m, 64.5 kN/m, 83.3 kN/m were used for the reinforcement in the MSE design. Design reduction factors of 1.25, 1.1, and 1.58 were used for installation damage, durability, and creep, respectively. These values were based on the geogrid manufacturer's information and the proposed fill. Various sections of the Wall were analyzed for internal and external stability. Figure 4 shows the section of SOE 1 with UL-FGA backfill that is closest to the new Abutment D (Earth Engineering Incorporated 2019).

The Contractor was able to stockpile UL-FGA at a staging area adjacent to the new ramp construction. The new abutment wingwall were in place prior to the temporary ramp construction. The geogrid for a portion of the ramp was tied into the new wingwall. There was a geotextile wrap at the steel welded wire mesh temporary facing to prevent any material from falling through the mesh openings. Stormwater piping was brought up in sections concurrently with UL-FGA and geosynthetic placement. Construction of the MSE portion of this project took approximately 4 weeks during May and June of 2019. Photographs of the project during the MSE construction are shown in Figure 5.

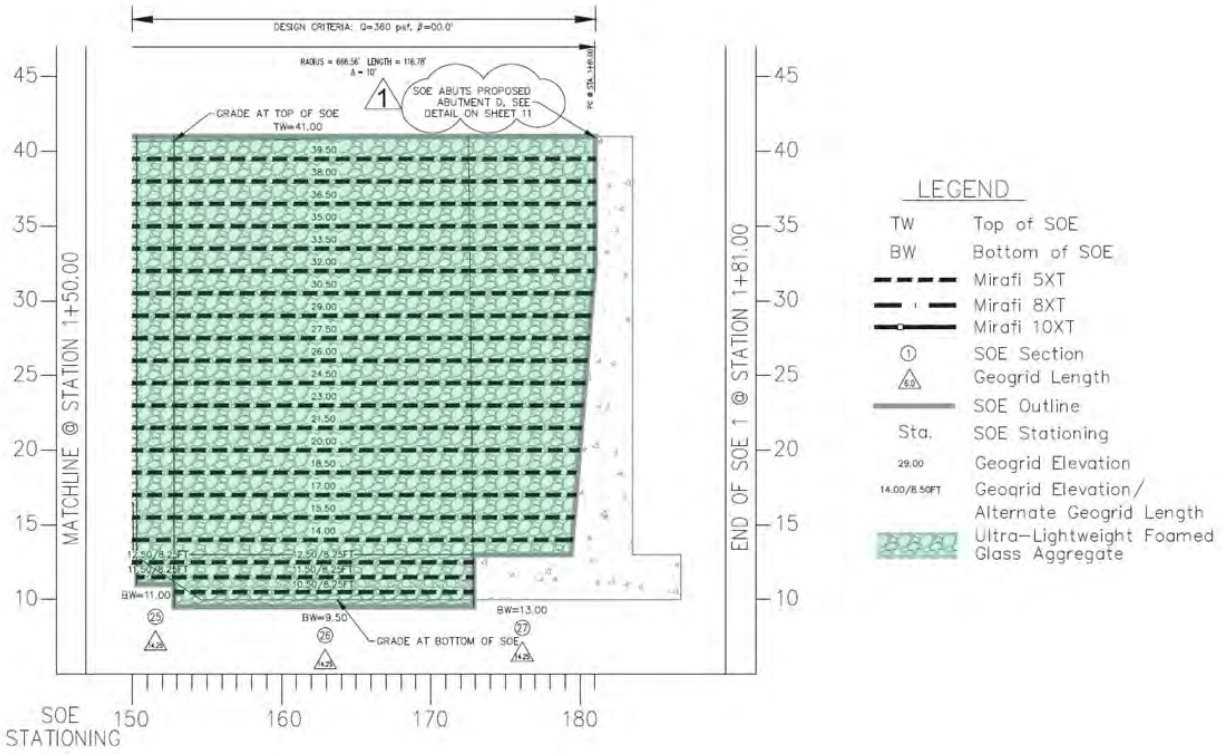

Figure 4. Partial profile showing UL-FGA backfill and geogrid location (modified from Earth Engineering Incorporated 2019).

Figure 5. Photographs of MSE with UL-FGA backfill construction at Section GR4 of I-95 in Philadelphia, PA.

Route 6/10 Reconstruction, Providence, RI. The Route 6/10 Interchange reconstruction project is the largest design-build project to date in the history of the Rhode Island Department of Transportation (RIDOT). The project required embankment construction over buried utilities, including a large 100-year old brick sewer, and challenging subsurface soils. The relocation and/or realignment of the existing utilities was not feasible, and the utility owner required that no additional loads could be imposed by the embankment on the subsurface utilities.

A range of readily available conventional solutions for soft soils and buried utilities was evaluated during the design process including soil-mixed rigid inclusions, expanded polystyrene (geofoam), foamed concrete and expanded shale aggregate. None of these more conventional solutions were found feasible because of uncertainty, time of construction, or technical feasibility and in some cases were cost prohibitive. RIDOT and the design-build team developed the concept of using UL-FGA as MSE backfill to protect the buried utilities against the weight of the embankment and to satisfy the zero settlement constraint of the sewer. This approach has the benefits of reducing the number of trucks on the road required for delivery, saving over $3M versus the next cheapest alternative, and reducing time related to ramp construction on the project schedule.

The MSE walls with UL-FGA backfill on this project are flyover ramp retaining walls FO-1 and FO-2 and Ramp B retaining wall B-1 and B-2 (AECOM 2018). The section of the flyover ramp requiring UL-FGA fill is approximately 137 m (450 feet) long, and the maximum of height of UL-FGA fill in FO-1 and FO-2 is approximately 12.2 m (40 feet). The depth of undercut of the existing soils to maintain a net zero load on the utility varies due to the varying height of the flyover ramp but is maximum at approximately 1.9 m (6.2 feet). At approximately 100 m (330 feet) long and 7.9 m (26 feet) high, maximum, the UL-FGA fill in Ramp B is shorter in length and height than the flyover ramps. The depth of the undercut of the existing soils to maintain a net zero load also varied for Ramp B but maxed out at approximately 1.3 m (4.2 feet).

A cross section of the flyover ramp is shown in Figure 6. The MSE wall system utilized at this project for both the flyover ramp and Ramp B consisted of 1.2 m (4 feet)-tall precast concrete U-shaped panels with alternating layers of geogrid and polymer geostrap reinforcements extending between the retaining wall faces. UL-FGA installation for the flyover ramp construction occurred in July through December of 2019 (Figures 7 and 8).

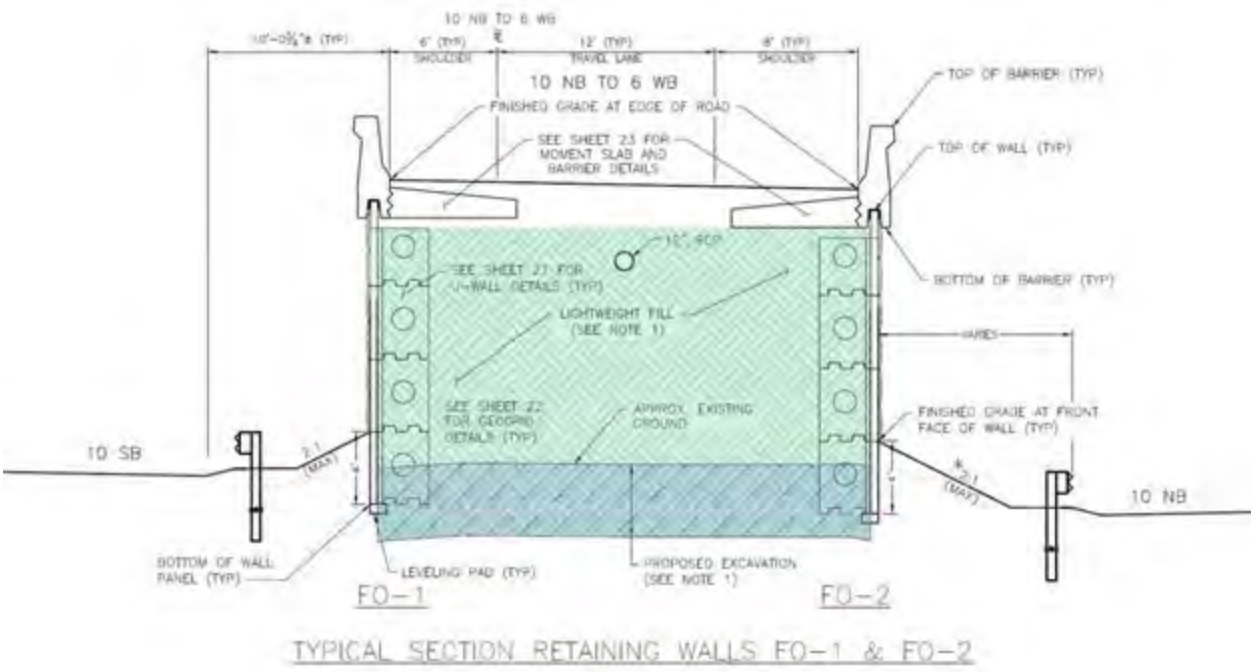

Figure 6. Cross section of flyover ramp at RIDOT Route 6/10 Reconstruction (Modified from AECOM 2018).

(a) **(b)**

Figure 7. Photographs of UL-FGA placement at the RIDOT Route 6/10 Reconstruction project. Geogrid reinforcement can be seen in (b).

(a)

(b)

Figure 8. Aerial photographs of the UL-FGA MSE backfill at the RIDOT Route 6/10 Reconstruction project. Abutment height is approximately ½ of the final height at the time of photography.

CONCLUSION

This paper details the physical and engineering properties of UL-FGA that are needed for the design of MSE systems with UL-FGA backfill. The conformance of UL-FGA with the requirements for MSE backfill per AASHTO's *LRFD Bridge Construction Specifications* was discussed. Considerations when using UL-FGA as MSE backfill are presented, including potential adjustments to UL-FGA layout to increase internal and/or external stability of the wall. There have been numerous projects where UL-FGA has been used as MSE backfill; this paper includes details of two highway projects in the U.S. where UL-FGA has been used in this application.

REFERENCES

Aaboe, R., Oiseth, E., Hagglund, J. (2005). "Granulated foam glass for civil engineering applications." *Recycled materials in road and airfield pavements*, Oslo, Norway.

AASHTO (2017). AASHTO LRFD Bridge Construction Specifications, 4th edition. *American Association of State and Highway Transportation Officials*, 2017, www.transportation.org.

AASHTO (2014). AASHTO Standard T-27, "Standard Method of Test for Sieve Analysis of Fine and Coarse Aggregates". *American Association of State and Highway Transportation Officials*, 2014, www.transportation.org.

AASHTO (2016). AASHTO Standard T-90, "Standard Method of Test for Determining the Plastic Limit and Plasticity Index of Soils". *American Association of State and Highway Transportation Officials*, 2016, www.transportation.org.

AASHTO (2008). AASHTO Standard T-236, "Standard Method of Test For Direct Shear Test of Soils Under Consolidated Drained Conditions". *American Association of State and Highway Transportation Officials*, 2008 (R 2013), www.transportation.org.

AECOM (2018). Retaining Wall Package 1_004_Plans & Profiles, Reconstruction of Route 6 & Route 10 Interchange, Providence, Rhode Island, dated 08/31/18.

American Geotechnical & Environmental Services, Inc. (2017) Structure Foundation Report for Final Design, S.R. 0095, Section GR4, Retaining Wall 16, S.R. 8011 Ramp D, Station 30+33.21 to 33+26.32, Philadelphia County, Pennsylvania. June 2017. Revised August 2017.

ASTM (2011). ASTM Standard D3080/D3080M, 2011, "Standard Test Method for Direct Shear Test of Soils under Consolidated Drained Conditions". *ASTM International*, West Conshohocken, Pennsylvania, 2011, DOI: 10.1520/D3080_D3080M-11, www.astm.org.

ASTM (2013). ASTM Standard D6706, 2013, "Standard Test Method for Measuring Geosynthetic Pullout Resistance in Soil", *ASTM International*, West Conshohocken, Pennsylvania, 2013, DOI: 10.1520/D6706-01R13, www.astm.org.

ASTM (2011). ASTM Standard D3080, 2011, "Standard Test Method for Direct Shear Test of Soils Under Consolidated Drained Conditions", *ASTM International*, West Conshohocken, Pennsylvania, 2011, DOI: 10.1520/D3080_D3080M-11, www.astm.org.

Auvinen, T., Pekkala, J., and Forsman, J. (2013). "Covering the highway E12 in the centre of Hämeenlinna – Innovative use of foamed glass as light weight material of approach embankment." *The XXVIII International Baltic Road Conference*, Vilnius, Lithuania.

Betti, G., Pinori, U., and Marradi, A. (2014). "The use of recycled glassfoam aggregates for lightweight embankment" Sustainability, eco-efficiency and Conservation in Transportation

Infrastructure Asset Management, Losa & Papagiannakis (eds.), Taylor and Francis Group, London, p. 245-254.

Earth Engineering Incorporated. (2019). Construction Drawings for S.R. 0095 Sec GR4, Stage 2/3 Temporary Embankment Support, Philadelphia, Pennsylvania. Rev. 1. March 6, 2019.

Frydenlund, T.E. and Aaboe, R. (2003). "Foamglass – A new vision in road construction." *The XXII PIARC World Road Congress*, Durban, South Africa, 12p.

Loux, T.A., Filshill, A., and Zhang, Z. (2019a). "Foamed Glass Aggregate Lightweight Fill Over Compressible Soils." *Geo St. John's 2019*, 29 Sept – 2 October 2019, St. John's, Newfoundland and Labrador, Canada.

Loux, T.A., Laspee, H.E., and Filshill, A. (2018). "Foamed Glass Aggregate: A Lightweight Fill Alternative Finds the U.S. Market." ASCE Metropolitan Section/ Geo-Institute Chapter Geotechnical Seminar "Practice on the Cutting Edge," 10 May 2018, New York City, New York.

Loux, T.A., Swan, R.H., Yuan, Z., and Filshill, A.F. (2019b). Pullout Testing of Geogrids, Geostraps and Steel Strips Embedded in Foamed Glass Aggregate, *Geosynthetics 2019*, IFAI, Houston, Texas, USA: 728-737.

McGuire, M.P., Loux, T.A., and VandenBerge, D.R. (2021). "Field-scale tests to evaluate foamed glass aggregate compaction." *IFCEE*, 10-14 May 2021, Dallas, Texas, USA.

NCMA (2010). *Design Manual for Segmental Retaining Walls*, 3rd Edition, TR 127B, Herndon, Virginia, USA.

NHI (2009). *Design and Construction of Mechanically Stabilized Earth Walls and Reinforced Soil Slopes – Volume I*, FHWA-NHI-10-024, Washington, District of Columbia, USA.

Geosynthetics Conference

Depth of Influence of a Wicking Geotextile below the Flexible Pavement Constructed over Expansive Subgrade

Nripojyoti Biswas, S.M. ASCE,[1] Anand J. Puppala, Ph.D., P.E., F. ASCE, F. ICE, DGE,[2] Md Ashrafuzzaman Khan, S.M. ASCE,[3] Sayantan Chakraborty, Ph.D., A.M. ASCE,[4] and Surya S. C. Congress, Ph.D., A.M. ASCE[5]

[1]Zachry Department of Civil and Environmental Engineering, Texas A&M University, College Station, TX 77840, U.S.A.; e-mail: nripojyoti.biswas@tamu.edu
[2]Zachry Department of Civil and Environmental Engineering, Texas A&M University, College Station, TX 77840, U.S.A.; e-mail: anandp@tamu.edu
[3]Zachry Department of Civil and Environmental Engineering, Texas A&M University, College Station, TX 77840, U.S.A.; e-mail: mak2019@tamu.edu
[4]Texas A&M Transportation Institute, Bryan, TX 77807, U.S.A.; e-mail: s-chakraborty@tti.tamu.edu
[5]Zachry Department of Civil and Environmental Engineering, Texas A&M University, College Station, TX 77840, U.S.A.; e-mail: congress@tamu.edu

ABSTRACT

The pavements constructed on problematic subgrades suffer from longevity and serviceability issues due to surface cracking, rutting, and differential heaving. The common contributing factors include moisture intrusion from cracks, utility trenches, or subsoil capillary rise, which results in swelling and associated strains in the expansive subgrade. Maintenance and rehabilitation of such distressed pavements result in the delay of traffic operations and account for millions of dollars of annual expenditure. Application of an innovative wicking geotextile in a farm to market road in North Texas was found to improve the lateral moisture drainage capacity of the soil subgrade, creating a suction gradient between the saturated subgrade and the surrounding environment. The moisture draining efficacy was observed to extend to more than 12 in., below the geotextile, into the subgrade layer. Apart from wicking action, this innovative geotextile reduced the normal stresses on the subgrade through reinforcement action, which helped in reducing the permanent deformation on top of the subgrade. Overall, the performance of the reinforced section has shown a remarkable improvement over the traditional unreinforced section.

INTRODUCTION

The subgrade soil of North Texas is primarily characterized by high plasticity indices and substantial swelling and shrinkage potential (Puppala and Musenda 2000, Little and Nair 2009, Hoyos et al. 2011). Construction of pavements and other light-weight structures over such problematic soils results in deterioration of long-term performance and subsequent increase in the maintenance costs during its design period (Texas Department of Transportation 2005, Zornberg and Gupta 2009, Puppala et al. 2017, Das 2018). The Pavement Design Manual of the Texas Department of Transportation (TxDOT) recommends several techniques among which improvement of soil with chemical stabilization techniques, replacement with superior quality

geomaterials, and utilization of geosynthetics are widely adopted to mitigate the problems associated with such expansive soils (Stacks 2019).

The utilization of virgin base aggregates in combination with the geotextile leads to high project expenditures (Khan et al. 2020b). Previous studies indicated that poor-quality materials such as Reclaimed Asphalt Pavement (RAP) aggregates could be reinforced and used as an alternative base course material (George et al. 2019, Khan et al. 2020b). A recent report by the National Asphalt Pavement Association has indicated that increasing RAP stockpiles across the United States could pose a landfill problem in the very near future (Khan et al. 2020a, 2020b). The utilization of RAP in the base layer of pavement can reduce the consumption of the virgin aggregates and simultaneously reduce the project's impact on the environment (Bennert et al. 2000). However, one of the disadvantages of the utilization of 100% RAP aggregates in the base course is its visco-elastic nature contributing to the long-term permanent deformation under repeated loading (Bennert et al. 2000, Garg and Thompson 2007). Therefore, reinforcing a RAP aggregate base course with a geotextile layer could provide the state DOTs with a sustainable construction methodology.

Geotextiles have been extensively used over the last few decades to improve the performance of pavements, retaining walls, slopes, foundations, and marine structures (Giroud 2010, Zornberg et al. 2010, Zornberg 2012, Pokharel et al. 2018, Biswas and Ghosh 2018). The manifold functions performed by a single layer of geotextile provide itself as an ideal candidate to be used in pavement infrastructure (Giroud and Han 2004a). The geotextiles have been extensively used in the pavement for providing separation between layers, reinforcing the weak subgrades or base courses, and providing drainage below the pavement layers (Zornberg et al. 2010). Geotextiles are generally composed of high-density polyethylene fibers, which are capable of providing high elastic modulus, grab strength, and stiffness to the geotextile sheet (Koerner 2012). A single geotextile layer is capable of redistributing the stresses from the repeated axle loads to the lower layers through the membrane effect (Giroud and Han 2004a, 2004b). The stiffer layer of geotextile is also capable of increasing the overall stiffness of the pavement subgrade and consequently reduce the deformation of the pavement layers (Pilarczyk 2000). In addition to the mechanical functions, geotextiles have been extensively used to carry out various other functions, such as improving the hydraulic performance of a pavement system and subsurface drainage (Stormont and Morris 2000, Iryo and Rowe 2005, Lee and Bourdeau 2006, Bhattacherjee and Viswanadham 2015).

Geotextiles and geonets have been traditionally used to improve the drainage of the pavement layers (Pilarczyk 2000, Koerner 2012). However, the ability of the traditional geotextiles to drain out water is limited to the gravity drainage (Iryo and Rowe 2003, Bouazza et al. 2006). A previous study by Iryo and Rowe (2003) reported that the efficiency of traditional geotextiles in draining the subsoil moisture depends on the degree of saturation of the soil-geotextile system. Furthermore, the study also indicated the inability of traditional geotextiles to drain out moisture in the unsaturated soils (Iryo and Rowe 2003). The drainage characteristics of traditional geotextiles were observed to degrade over time due to clogging of the pores and the capillary barrier effect on the interface between the soil and geotextile system (Stormont and Morris 2000, Bouazza et al. 2006). The primary reason was identified as the reduction in the permeability coefficient of the geotextile drainage channels under unsaturated conditions (Iryo and Rowe 2003). As an alternative, an innovative wicking geotextile has been developed by a particular manufacturer to facilitate the drainage of the soil under unsaturated conditions.

This innovative wicking geotextile serves several functions such as drainage, capillary action, separation, and reinforcement in a single layer (Han and Zhang 2014). This geotextile is made of wicking fibers comprising of special hydrophilic and hygroscopic 4DG^{TM} (DG = Deep Grove) fibers with a multichannel cross-section (Han and Zhang 2014). The multichannel cross-section has a high number of wicking channels per fiber and a high shape factor, enabling it to laterally transport water through its channels in an unsaturated environment through capillary action (Guo et al. 2017, Wang et al. 2017, Lin and Zhang 2020). Several small-scale laboratory studies, along with certain numerical analyses, were performed by past researchers to understand the efficacy of this geotextile in removing subsurface moisture (Guo et al. 2017, Wang et al. 2017, Galinmoghadan et al. 2019, Lin et al. 2019). Additionally, a full-scale field study on unpaved roads by Alaska DOT has also indicated the advantages of using this new geotextile for subsurface drainage (Zhang et al. 2014).

The primary objective of this paper is to understand the efficacy of using this newly-available wicking geotextile as a reinforcement for base layer constructed with inferior quality material, such as RAP aggregates, over expansive subgrade of the flexible pavement system. This study discusses moisture removal from subgrade soil using wicking fibers. The results from the moisture sensors were used to predict the possible influence zone of the wicking fibers. Additionally, the ability of wicking fibers to redistribute moisture was observed to influence the permanent deformation of the pavement layers. A comprehensive insight into the utilization of the newly available geotextile on expansive subgrades, where the effect of moisture sensitivity is of primary concern for long-term serviceability, is provided in the following sections.

PROJECT LOCATION

The field test sections were constructed near FM1807 Venus, Texas. The existing pavement layers consisted of a variable 4-5 in. (10-12 cm) thick asphalt layer laid over a 10-11 in. (25-28 cm) base course and an expansive soil subgrade. As part of regular maintenance, the pavement section was overlaid with 2 in. (5 cm) thick asphalt in Fall 2017; however, six months into its service period, the pavement showed signs of rutting and cracking along the wheel paths. Additionally, the presence of moisture in the drainage ditch and utility trenches from nearby agricultural fields compounded the problems associated with the expansive subgrade. Therefore, this road section was used to understand the efficacy of wicking geotextiles. As a result, the eastbound lane was used to construct the Test Section (TS), whereas the westbound lane was used as a Control Section (CS).

DESIGN, CONSTRUCTION, AND INSTRUMENTATION

Section Design and Construction. The design of the TS and CS was performed using TxDOT recommended design software FPS21, which is based on AASHTO-93 design guidelines. The TS was designed as a three-layered system comprising of a subgrade layer, 15 in. (38 cm) base course, and a 2 in. (5 cm) asphalt layer (Figure 1). The materials and stiffness moduli of each layer for both TS and CS are provided in Table 1. The base layer of the TS was reinforced with the wicking geotextile, which was placed above the subgrade layer. The flexible pavement is characterized as a low volume road with an approximate Annual Average Daily Traffic of 1500 vehicles per day. The percentage of the truckload was assumed to be 7%, as suggested by the local TxDOT office.

The estimated design life for TS was considered as 20 years with no overlay required during this period.

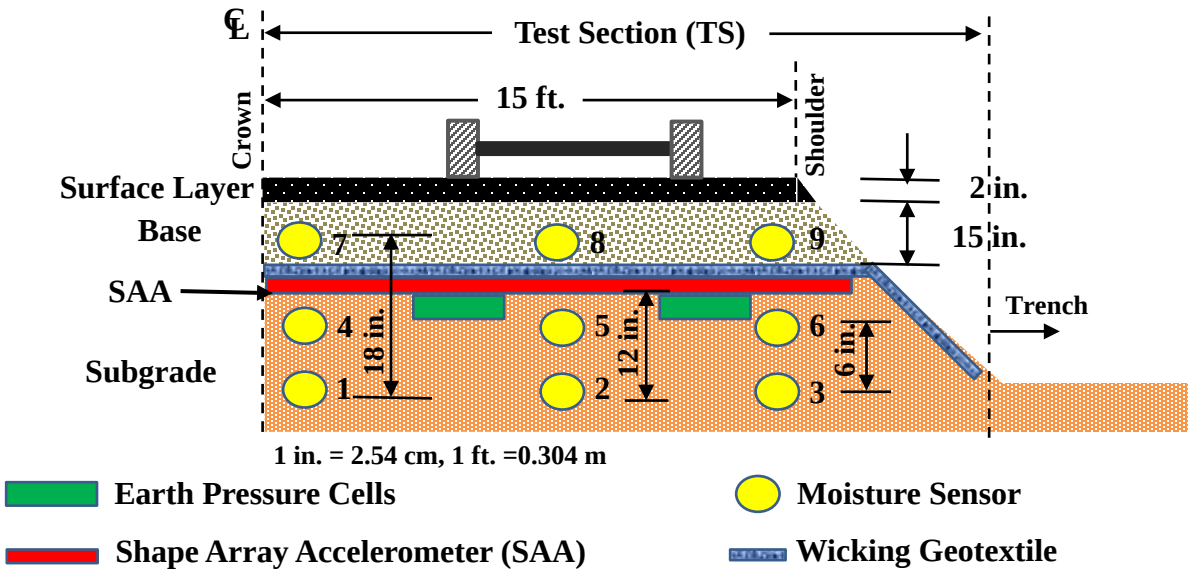

Figure 1. Section design and instrumentation

The efficacy of using the newly available geotextile was also analyzed using a software-based on AASHTO-93 design guidelines (MiraSpec Road Design Software). The material parameters from Table 1, serviceability, and reliability parameters similar to FPS21, were included in this analysis. An additional variable for this analysis was the inclusion of the hydraulic improvement factor (HIF) due to the presence of wicking fibers. The HIF values were obtained based on different CBR values of the subgrade in different regions in the USA. The flexible pavement design software was used to predict the increase in Equivalent Standard Axle Load (ESAL) value, expressed in Figure 2 as $ESAL_{IR}$ (a ratio between ESAL of reinforced section to unreinforced section), due to the inclusion of the wicking fibers. From Figure 2, it can be observed that there is a significant improvement in the ESAL ratio due to the inclusion of the wicking fibers over the unreinforced

sections. The improvement in Structural Number (SN) is also shown in the figure as an improvement ratio (SN_{IR}) between the reinforced and unreinforced sections.

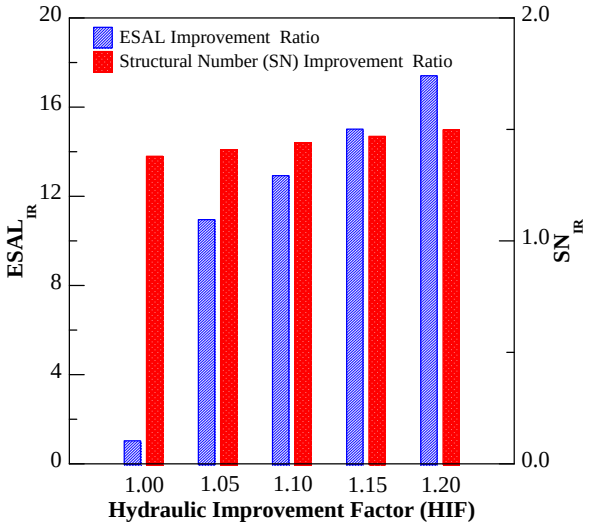

Figure 2. Influence of Hydraulic Improvement Factor (HIF) on pavement performance

Based on the above design guidelines, the test and control sections were constructed in December 2018, and the sections were regularly monitored over the past 15 months using visual and in-situ instrumentation monitoring to understand the pavement performance during this initial service period.

Table 1. Design Parameters for the Test and Control Sections

Description	Parameters	Units	TS	CS# (Unreinforced)
Asphalt Layer	Thickness	in. (cm)	2 (5)	2(5)
	Modulus	ksi (MPa)	500 (3448)	500 (3448)
	Poisson's ratio		0.4	0.4
Base Layer	Thickness	in. (cm)	15 (38)	15(38)
	Modulus	ksi (MPa)	40 (275)	40 (275)
	Poisson's ratio		0.3	0.3
Subgrade	Thickness	in. (cm)	12 (30)	12 (30)
	Equivalent Modulus*	ksi (MPa)	19.8 (137)	9 (62)
	Poisson's ratio		0.3	0.3
Compressive strain at the top of subgrade layer		-	408	657
Rut Life		(million ESAL***)	2.05	0.24

* Equivalent Stiffness = Modification Factor due to reinforcement using wicking geotextile** x Unreinforced Modulus
** Modification Factor = 2.2 (Lin et al. 2019)
*** Equivalent Standard Axle Load
# Overlay required after 12.8 years

Instrumentation. The TS and the CS were instrumented with Shape Array Accelerometers Micro-Electro-Mechanical System (SAA-MEMS) deflection sensors, earth pressure cells, and moisture

sensors (Figure 1). The SAA-MEMS was installed on top of the subgrade layer to understand the improvement in subgrade deformation due to the application of wicking geotextile. The TS was instrumented with nine moisture sensors labeled as MS 1-9. The sensors in the TS were stationed at 6 in. (15 cm), MS 4-6, and 12 in. (30 cm), MS 1-3, below the geotextile layer. Similarly, for the base layers, the MS 7-9 sensors were installed at 6 in. (15 cm) above the geotextile layer.

EFFECT OF WICKING FIBERS ON SUBGRADE MOISTURE

Depth of Influence. The principal objective of the installation of a wicking geotextile is to remove the moisture from the pavement layers. The stiffness of the pavement system depends on the moisture content of the soil. The ability of the soil system to drain out the moisture using the wicking fabrics is inversely proportional to the distance of the layer from the wicking fibers. Lin et al. 2019 conducted a numerical study and reported that the ability to drain out moisture could extend as far as 1 m below the pavement layers. However, they also indicated that the primary efficacy of the fibers was up to a depth of 0.2-0.4 m beneath the wicking fibers. They also indicated that a minor reduction in the moisture content by 0.9% near the wicking fiber could increase the resilient modulus of the subgrade region by 300%. Therefore, in the next section, the current study provided performance monitoring data and discussed the efficacy of the wicking geotextiles in improving the characteristics of the pavement subgrade below the test section.

Subsurface Moisture Analysis. The moisture content below the pavement surface during and after rainfall events in the TS is discussed in this section (Figures 3 and 4). Figure 3 shows the subsurface volumetric moisture (θ_V) after a rainfall event on the 11th of May 2019. The local rainfall station recorded cumulative precipitation of 3.10 in. (7.8 cm) during that period. Figure 3a shows the moisture contours below the pavement section immediately after the rainfall. Figure 3b indicates the percentage change in θ_V over the next six days at different depths below the wicking geotextile. The MS 6 near the edge of the pavement, placed at 6 in. (15 cm) below the geotextile and towards the natural drainage trench, underwent the maximum reduction in volumetric moisture content ($\approx$ 26%). The MS 3, which is located at 12 in. (30 cm) below the geotextile, also underwent a 5% reduction in θ_V value over the same period. The reduction in moisture content near the edges could be attributed to a combination of two factors. First, since the edge soil is near the surface, the soil dries rapidly due to changes in air humidity and an increase in air temperature. Additionally, the presence of wicking fibers enables the rapid migration of moisture through its multichannel cross-section due to the difference in matric suction between the saturated fibers (and surrounding soil) below the pavement and dry fibers exposed to the surface air near the edges.

The sensors MS 4-5 indicated higher θ_V reduction ($\approx$ 4.5 %) as compared to the sensors MS 1-2 ($\approx$ 2 %) located at 12 in. (30 cm) depth in the same sections. The efficacy of the wicking fibers to drain out moisture reduces to more than 50% with an increase in depth from 6 in. (15 cm) to 12 in. (30 cm) below the soil subgrade. However, as indicated by Lin et al. (2019), a reduction in moisture content in soil subgrade as small as 0.9% could increase the matric suction three-fold. Hence, even though the efficacy of wicking fibers decreases with depth, such a small reduction in moisture could increase the overall stiffness of the soil layers, especially with high PI clay subgrade. As a result, this could substantially improve long-term pavement performance. During a similar observation period, the CS recorded a higher average value of $\theta_V \approx 0.40$ m^3/m^3 indicating the efficacy of the wicking fibers in moisture redistribution.

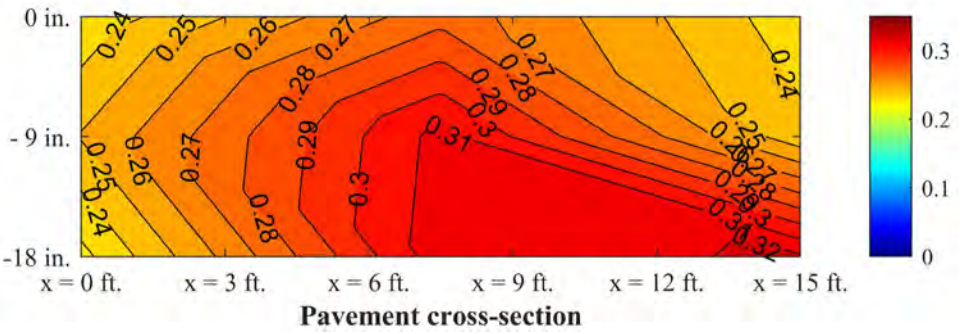

(a)

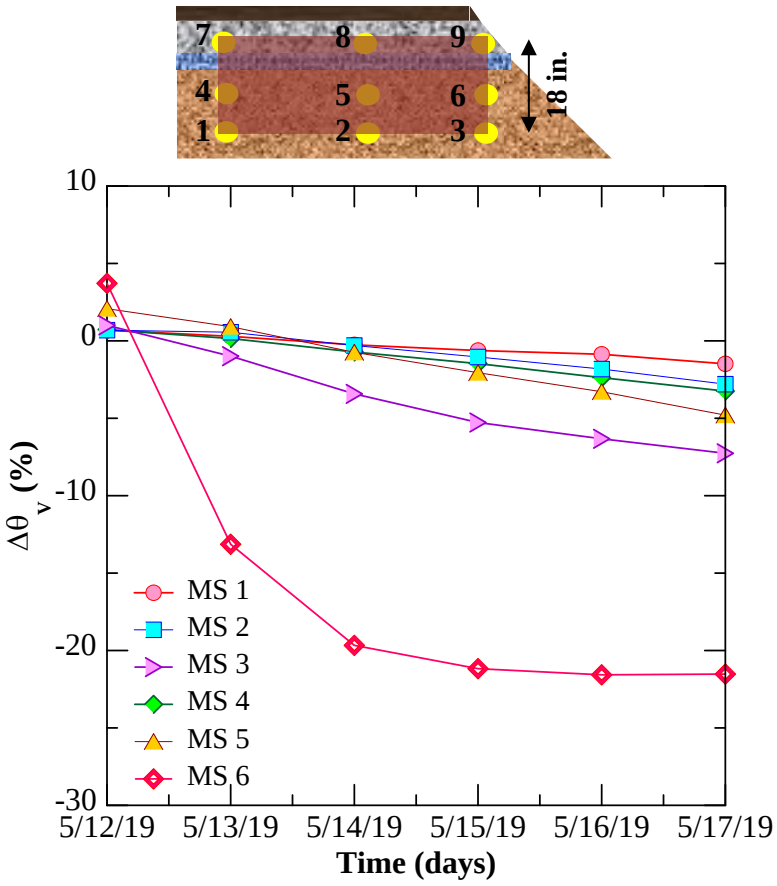

(b)

Figure 3. Subsurface moisture analysis for a rainfall event on 11th of May 2019 (a) Moisture contours immediately after rainfall (b) Percentage reduction in θ_V at different depths below wicking geotextile

Similar results were observed during another rainfall event during the winter month of February 2020 (Figure 4). Figure 4a represents moisture contours for the rainfall event on the 20th of February, having a recorded rainfall of 1.13 in. (2.87 cm). The moisture sensors near the edges underwent a maximum reduction in moisture content as compared to the sensors near the crown over the following five days (Figure 4b).

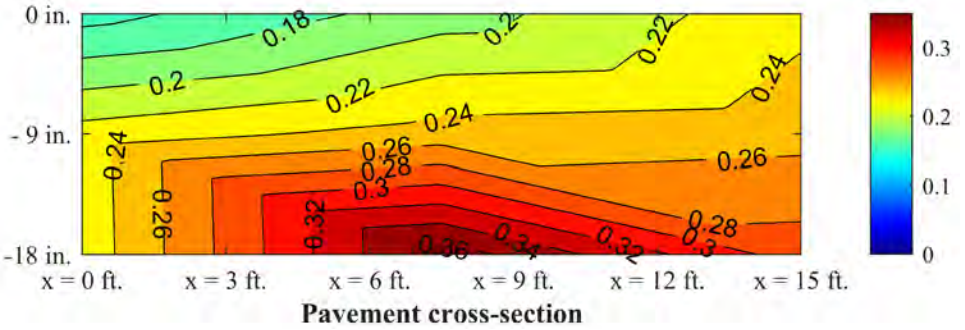

(a)

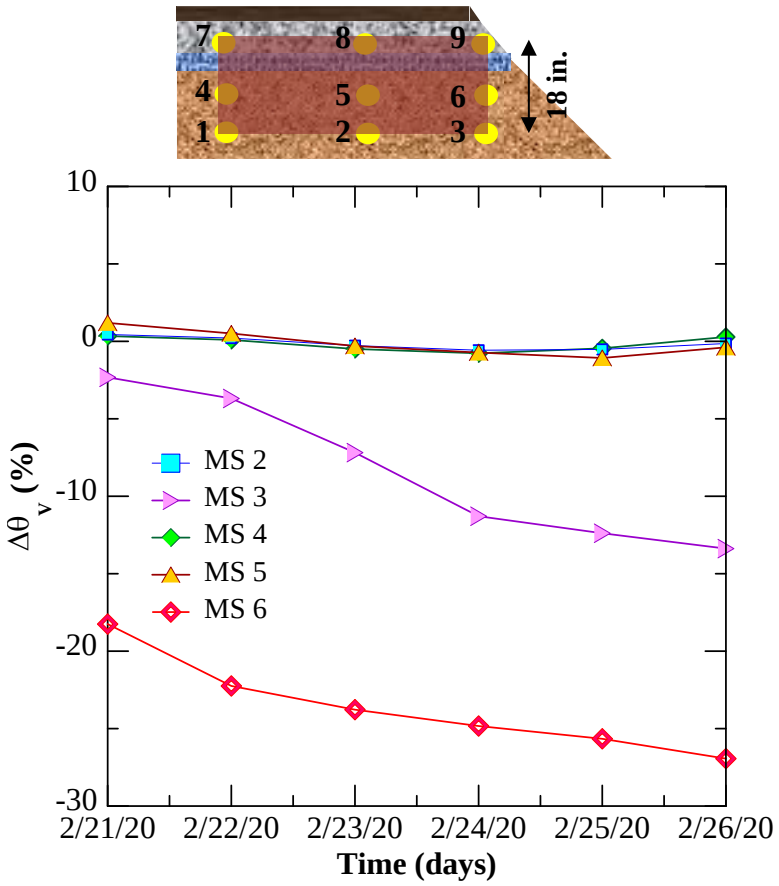

(b)

Figure 4. Subsurface moisture analysis for a rainfall event on 20th of February 2020 (a) Moisture contours immediately after rainfall (b) Percentage reduction in θ_V at different depths below wicking geotextile

The efficacy of geotextile to remove subsoil moisture reduced by 50%, as the depth increased from 6 in. to 12 in. below the geotextile layer (MS 6 and MS 3). Hence, it could be predicted that the wicking fibers have an influence zone of over 12 in. (30 cm) in a pavement subgrade near the center of the pavement (crown), which could extend to much higher depth near the shoulder and edges. Conversely, the moisture sensors in the subgrade of the CS indicated a higher average value of $\theta_V \approx 0.35$ m^3/m^3 consistently during a similar observation period.

The effect of moisture reduction and the associated change in the pavement stiffness has a direct impact on its response to repetitive axle load-induced permanent deformations. The next section discusses the observed permanent deformation on the top of the subgrade layer during this initial monitoring period of 15 months.

EFFECT OF WICKING FIBERS ON PAVEMENT DEFORMATION

Permanent Deformation. In this section, the average permanent deformation (δ_P) of the pavement on the top of the pavement subgrade is analyzed. Figure 5 shows the permanent deformation recorded in both the test and control sections during each month using the SAA-MEMS. The cumulative deformation data due to repetitive traffic loads and the vertical soil movement caused by moisture migration was recorded over time. The unreinforced section showed limited deformation during the initial period after the construction. However, after a significant rainfall period, the unreinforced sections underwent substantial permanent deformation. This could be attributed to the combined effect of moisture intrusion and axle loads. The moisture intrusion decreases the modulus of the subgrade soil. As a result, the weak subgrade underwent large deformation due to repetitive axle loads.

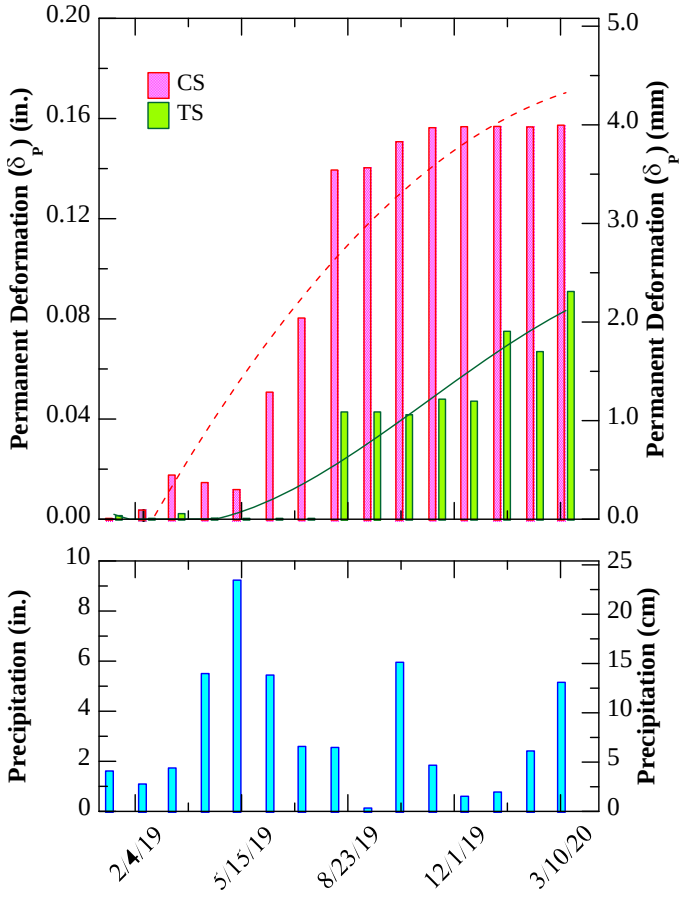

*The red dotted line and solid green line are polynomial fits for the permanent deformation

Figure 5. Permanent deformation in the test and control section

As for the reinforced section, the geosynthetic layer is composed of high-density polyethylene fibers, which increase the overall stiffness of the layer through membrane effect.

Furthermore, the presence of the wicking fiber rapidly removes the moisture within its zone of influence after a rainfall event. This rapid moisture redistribution plays a pivotal role in improving the pavement performance when the subgrade soil is in its weakest state.

The presence of wicking geotextile over the pavement subgrade improved the drainage capacity of the soil subgrade. The rapid reduction in the moisture content was responsible for the improvement in the pavement stiffness and its resilience to permanent deformation. Overall, the application of wicking geotextile improved pavement performance during this initial observation period of 15 months.

CONCLUSION

The paper discusses the efficacy of reinforcement of flexible pavement using a wicking geotextile. The utilization of wicking geotextile provides a two-fold function in a pavement layer through reinforcement as well as moisture redistribution. The ability of the wicking geotextile to remove moisture affects the stiffness of the pavement layer and directly influences the permanent deformation of the subgrade. The primary observations in the present study are listed below:

- The wicking geotextile was observed to reduce the moisture rapidly from the pavement layers after rainfall events.
- The efficacy of wicking fibers to reduce the subgrade moisture was observed to be more significant near the pavement edges (shoulder) as compared to the center (crown) region.
- The efficacy of wicking fibers to remove moisture from the subgrade layer decreased over 50% when the depth increased from 6 in. (15 cm) to 12 in. (30 cm).
- The rapid removal of the moisture has a significant impact on controlling the permanent deformation of the pavement layer when compared with the control section.
- The utilization of RAP aggregate with the wicking geosynthetic reduced the permanent deformation after 15 months of construction.

Overall from the initial monitoring period, the presence of wicking fiber is observed to provide beneficial effects for a pavement constructed over an expansive subgrade. The utilization of inferior quality RAP aggregates with this innovative geotextile could provide a sustainable alternative to existing design guidelines for flexible pavement over expansive subgrades. However, long-term monitoring and analysis are required for developing a comprehensive design guideline for transportation agencies.

ACKNOWLEDGMENT

This research was funded by TenCate, Inc. (Mr. John Lostumbo, P.E.), NSF Industry-University Cooperative Research Center (I/UCRC) program funded ‘Center for Integration of Composites into Infrastructure (CICI)’ site at Texas A&M University (NSF PD: Dr. Andre Marshall; Award # 1464489), and Texas Department of Transportation (TxDOT) - Fort Worth district (Mr. Richard Williammee, P.E. and Mr. Paul Spraggins, P.E.). The authors would like to appreciate their support. The authors would also like to thank Dr. Aritra Banerjee and other members of Geotechnical/Geomechanics Group, TAMU, for their support.

REFERENCES

Bennert, T., Papp, W. J., Maher, A. and Gucunski, N. (2000). Utilization of Construction and Demolition Debris Under Traffic-Type Loading in Base and Subbase Applications. *Transportation Research Record: Journal of the Transportation Research Board*, 1714(1): 33–39.

Bhattacherjee, D. and Viswanadham, B. V. S. (2015). Numerical studies on the performance of hybrid-geosynthetic-reinforced soil slopes subjected to rainfall. *Geosynthetics International*, 22(6): 411–427.

Biswas, N. and Ghosh, P. (2018). Interaction of adjacent strip footings on reinforced soil using upper-bound limit analysis. *Geosynthetics International*, Thomas Telford Ltd , 25(6): 599–611.

Bouazza, A., Zornberg, J. G., McCartney, J. S. and Nahlawi, H. (2006). Significance of unsaturated behaviour of geotextiles in earthen structures. *Australian Geomechanics*, 41(3): 133–142.

Das, J. T. (2018). Assessment of Sustainability and Resilience in Transportation Infrastructure Geotechnics. University of Texas at Arlington.

Galinmoghadan, J., Zhang, X. and Lin, C. (2019). *A Bio-Wicking System to Prevent Frost Heave in Alaskan Pavements: Phase II Implementation*.

Garg, N. and Thompson, M. (2007). Lincoln Avenue Reclaimed Asphalt Pavement Base Project. *Transportation Research Record: Journal of the Transportation Research Board*, 1547: 89–95.

George, A. M., Banerjee, A., Puppala, A. J. and Saladhi, M. (2019). Performance evaluation of geocell-reinforced reclaimed asphalt pavement (RAP) bases in flexible pavements. *International Journal of Pavement Engineering*, Taylor & Francis, 1–11.

Giroud, J. P. (2010). Development of criteria for geotextile and granular filters. *Proceedings of the 9th international conference on geosynthetics*, Guaruja, Brazil.

Giroud, J. P. and Han, J. (2004a). Design Method for Geogrid-Reinforced Unpaved Roads. I. Development of Design Method. *Journal of Geotechnical and Geoenvironmental Engineering*, 130(8): 775–786.

Giroud, J. P. and Han, J. (2004b). Design Method for Geogrid-Reinforced Unpaved Roads. II. Calibration and Applications. *Journal of Geotechnical and Geoenvironmental Engineering*, 130(8): 787–797.

Guo, J., Wang, F., Zhang, X. and Han, J. (2017). Quantifying Water Removal Rate of a Wicking Geotextile under Controlled Temperature and Relative Humidity. *Journal of Materials in Civil Engineering*, 29(1): 04016181.

Han, J. and Zhang, X. (2014). Recent advances in the use of geosynthetics to enhance sustainability of roadways. *20th International Conference on Advances in Civil Engineering for Sustainable Development*, Suranaree University of Technology, Nakhon Ratchasima, Thailand: 29–39.

Hoyos, L. R., Suescun, E. A. and Puppala, A. J. (2011). Small-Strain Stiffness of Unsaturated Soils Using a Suction-Controlled Resonant Column Device with Bender Elements. *Geo-Frontiers 2011*.

Iryo, T. and Rowe, R. K. (2003). On the hydraulic behavior of unsaturated nonwoven geotextiles. *Geotextiles and Geomembranes*, 21(6): 381–404.

Iryo, T. and Rowe, R. K. (2005). Hydraulic behaviour of soil–geocomposite layers in slopes. *Geosynthetics International*, 12(3): 145–155.

Khan, M. A., Biswas, N., Banerjee, A. and Puppala, A. J. (2020a). Performance of Geocell-Reinforced Recycled Asphalt Pavement (RAP) Bases in Flexible Pavements Built on Expansive Soils. *Geo-Congress 2020*, American Society of Civil Engineers, Reston, VA: 488–497.

Khan, M. A., Biswas, N., Banerjee, A. and Puppala, A. J. (2020b). Field Performance of Geocell Reinforced Recycled Asphalt Pavement Base Layer. *Transportation Research Record: Journal of the Transportation Research Board*, 036119812090886.

Koerner, R. M. (2012). *Designing with geosynthetics*. Xlibris Corporation, Indiana, USA.

Lee, S. and Bourdeau, P. L. (2006). Filter performance and design for highway drains. *Joint Transportation Research Program*, 266.

Lin, C. and Zhang, X. (2020). Comparisons of Geotextile-Water Characteristic Curves for Wicking and Non-Wicking Geotextiles. *Geo-Congress 2020*, American Society of Civil Engineers, Reston, VA: 629–636.

Lin, C., Zhang, X. and Han, J. (2019). Comprehensive Material Characterizations of Pavement Structure Installed with Wicking Fabrics. *Journal of Materials in Civil Engineering*, 31(2): 04018372.

Little, D. N. and Nair, S. (2009). *Recommended Practice for Stabilization of Sulfate-Rich Subgrade Soils*. Transportation Research Board, Washington, D.C.

Pilarczyk, K. (2000). *Geosynthetics and geosystems in hydraulic and coastal engineering*. CRC Press, Florida, USA.

Pokharel, S. K., Han, J., Leshchinsky, D. and Parsons, R. L. (2018). Experimental evaluation of geocell-reinforced bases under repeated loading. *International Journal of Pavement Research and Technology*, Chinese Society of Pavement Engineering, 11(2): 114–127.

Puppala, A. J., Pedarla, A., Chittoori, B., Ganne, V. K., Nazarian, S. and Pedarla, A. (2017). Long-Term Durability Studies on Chemically Treated Reclaimed Asphalt Pavement Material as a Base Layer for Pavements. *Transportation Research Record: Journal of the Transportation Research*, 2657: 1–9.

Puppala, A. and Musenda, C. (2000). Effects of Fiber Reinforcement on Strength and Volume Change in Expansive Soils. *Transportation Research Record: Journal of the Transportation Research Board*.

Stacks, D. L. (2019). *Pavement Manual*. *Texas Department of Transportation*, Austin,TX.

Stormont, J. C. and Morris, C. E. (2000). Characterization of unsaturated nonwoven geotextiles. *Advances in Unsaturated Geotechnics*, 153–164.

Texas Department of Transportation. (2005). *Guidelines for Modification and Stabilization of Soils and Base for Use in Pavement Structures*.

Wang, F., Han, J., Zhang, X. and Guo, J. (2017). Laboratory tests to evaluate effectiveness of wicking geotextile in soil moisture reduction. *Geotextiles and Geomembranes*, 45(1): 8–13.

Zhang, X., Presler, W., Li, L., Jones, D. and Odgers, B. (2014). Use of Wicking Fabric to Help Prevent Frost Boils in Alaskan Pavements. *Journal of Materials in Civil Engineering*, 26(4): 728–740.

Zornberg, J. G. (2012). Ingenuity in Geotechnical Design Using Geosynthetics." *Geotechnical Engineering State of the Art and Practice*, American Society of Civil Engineers, Reston, VA: 398–419.

Zornberg, J. G., Bouazza, A. and McCartney, J. S. (2010). Geosynthetic capillary barriers: current state of knowledge. *Geosynthetics International*, 17(5): 273–300.

Zornberg, J. G. and Gupta, R. (2009). Reinforcement of pavements over expansive clay subgrades. *Proceedings of the 17th International Conference on Soil Mechanics and Geotechnical Engineering: The Academia and Practice of Geotechnical Engineering*, 1: 765–768.

Geosynthetics Conference

In Situ Assessment of Geogrid Stabilized Flexible Pavement Using Automated Plate Load Testing

Prajwol Tamrakar, Ph.D.,[1] Mark H. Wayne, Ph.D.,[1] David J. White, Ph.D., [2] and Pavana K. R. Vennapusa, Ph.D.[2]

[1]Tensar International Corporation, 2500 Northwinds Pkwy, Alpharetta, GA 30009, USA
[2]Ingios Geotechnics, P.O. Box 101, Northfield, MN 55057, USA

ABSTRACT

Laboratory-based testing methodologies are usually adopted for the characterization of pavement materials. Most pavement design and analysis approaches rely on such characterization methods for modeling pavement sections and predicting performance. For example, the use of repeated load triaxial testing on a small cylindrical specimen is popular for estimating the resilient modulus of an unbound aggregate layer. This testing utilizes a cylindrical specimen (150 mm in diameter and 300 mm in height) for applying confining pressures and repeated axial stresses. However, laboratory-based triaxial testing cannot truly represent the field conditions. As such, there is a need for in-situ characterization of pavement material on a fully constructed pavement using dynamic loads at different stress levels. An Automated Plate Load Testing (APLT) system can measure in-situ dynamic load-deformation responses using various stress levels and loading cycles and estimate composite as well as layer-specific resilient modulus for pavement layers. This study aims to evaluate such properties for geogrid-stabilized and unstabilized pavements using the APLT system. Field tests were performed on the flexible pavement sections consisting of 190 mm thick hot mix asphalt. The aggregate base course thicknesses for the geogrid stabilized pavement were 150 mm and 200 mm whereas that for the unstabilized pavement was 250 mm. The geogrid stabilized section with a 200 mm aggregate base course had a composite modulus of 424 MPa which is higher than that of the unstabilized section (369 MPa). On the other hand, the total permanent deformations induced in all sections were almost similar (<1.2 mm) despite the difference in thicknesses between the pavement sections.

INTRODUCTION

A composite pavement system is formed by bound and unbound pavement layers consisting of different materials, and a complex interaction of those layers with the existing subgrade. When a geogrid is incorporated in the unbound pavement layer (e.g., aggregate base course, subbase, or subgrade), it enhances the mechanical properties of the pavement system (Abu-Farsakh et al. 2019; Qian et al. 2011; Robinson et al. 2017; Vennapusa et al. 2018). The key features of such a pavement system are stabilized unbound layers and resisting capacity of the pavement layers against degradation or plastic deformation due to traffic and climate.

Laboratory-based testing methodologies are usually adopted for the characterization of pavement materials, and derivation of mechanical properties. Most pavement design and analysis approaches rely on such characterization methods for modeling pavement sections and predicting performance throughout the service life. For example, Pavement Mechanistic Empirical Design (PMED) method considers the resilient modulus (MR) of an unbound aggregate layer as an

important input parameter for pavement performance analysis (AASHTO 2015). Several studies were conducted to understand the factors that affect the MR of an unbound aggregate material (Ba et al. 2013; Tamrakar and Nazarian 2019). Typically, repeated load triaxial testing on a small cylindrical specimen is used for determining MR. This testing utilizes a cylindrical specimen (150 mm in diameter and 300 mm in height) for applying confining pressures and repeated axial stresses, with targeted deviator and confining stresses. However, various challenges with laboratory-based triaxial testing limit a proper understanding of the actual field conditions. These limitations include, but are not limited to, limited sample sizes, lack of accounting for interaction and stress transfer between the different layers, non-representative boundary conditions, and many other inherent experimental limitations with sample preparation (White et al. 2019b). In addition, it is also quite challenging to prepare laboratory specimens consisting of geogrids (i.e., stabilized aggregate base course) because the small specimens cannot capture an effective interaction of geogrids with aggregate particles. As such, there is a need for in-situ characterization of pavement material on a fully constructed pavement using dynamic loads representing real traffic loading. Such characterization methods can identify stress-dependent properties of stabilized and unstabilized unbound material (e.g., aggregate base, subbase and subgrade) and time- and temperature-dependent properties of the bound layer (e.g., hot mix asphalt or HMA).

An Automated Plate Load Testing (APLT) system can measure in-situ dynamic load-deformation responses using various stress levels and loading cycles and estimate composite as well as layer-specific MR of pavement layers (White et al. 2019a). This study aims to evaluate in-situ mechanical properties for geogrid-stabilized and unstabilized pavements such as composite modulus, layer modulus of HMA, aggregate base course (ABC) and subgrade, and permanent deformation responses using the APLT system for the test sections on the Interstate 20 near Atlanta, Georgia.

BASE COURSE STABILIZATION

Base course stabilization is the process of constructing a mechanically stabilized layer (MSL) with the use of geogrid (see Figure 1). The mechanism of “stabilization” is different from “reinforcement” because the former one is referring to “stiffness enhancement” as well as “stiffness retention for a longer period”. In contrast, the term “reinforcement” implies “adding force” (Giroud and Han 2016). This mechanism is only effective if the forces are large which in turn implies that large vertical permanent deformations exist in the aggregate overlying the geogrid.

When a geogrid is incorporated into a granular material, the aggregate particles interlock with the geogrid and are confined within the geogrid apertures. As a result, the particles are restrained from moving laterally. The lateral restraint provided by the geogrid contributes to reducing induced strain due to traffic loading and thereby increases the stiffness of the granular layer (Rakowski and Kawalec 2020; Sun et al. 2020; Wayne et al. 2013, 2019). In addition to the lateral restraint, granular particles immediately adjacent to the interlocked particles are themselves restrained by the particle to particle interlock. Thus the influence of the geogrid inclusion extends beyond the geogrid particle interface. Cook and Horvat (2014) demonstrated the existence of such variation in particle interlocking using a multi-level shear box. The authors found that the influence of the geogrid on the stiffness of a granular layer will decrease in relation to the distance from the geogrid. This can be represented as zones of confinement from fully confined to unconfined as illustrated in Figure 1. Behaviors of confinement due to different geogrid and material types were

also investigated through the use of numerical modeling (Konietzky et al. 2004; McDowell et al. 2006; Stahl et al. 2014; Jas et al. 2015; Lees 2017) as well as bender element shear wave measurement technology (Kang et al. 2020; Kim et al. 2020).

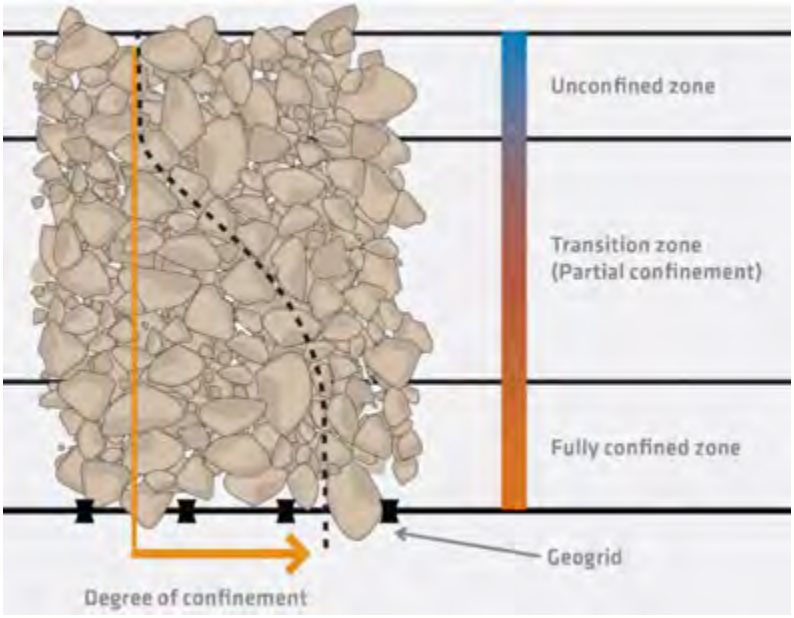

Figure 1. Confinement Zones in an MSL

PROJECT DETAILS

The project site was located in a pavement section of interstate 20 near Atlanta, GA. Field tests were performed on the flexible pavement sections consisting of 190 mm thick HMA. The aggregate base course (ABC) thicknesses for the geogrid stabilized test sections were 150 mm and 200 mm whereas that for the unstabilized test section was 250 mm (see Figure 2). Each test section was approximately 75 m long. Per the Georgia Department of Transportation specifications, the ABC is designated as Class A Graded Aggregate Base (GAB). A punched and drawn triangular aperture geogrid was placed at the interface of ABC and subgrade for constructing stabilized pavements. The properties of the geogrid are summarized in Table 1. Although all three pavement sites were close to each other, there was some variation in the subgrade condition. Based on the Dynamic Cone Penetrometer (DCP) test measurements, the subgrade CBR ranged between 15% and 25% as shown in Figure 2.

Table 1. Summary of Geogrid Properties

Parameters	**Description**
Product	TX160
Rib shape	Rectangular
Aperture shape	Triangular
Rib pitch (mm)	40[l,d]
Mid-rib depth	1.4[l],1.6[d]
Mid-rib width	1.2[l],1.0[d]

[l]Longitudinal/Transverse; [d]Diagonal

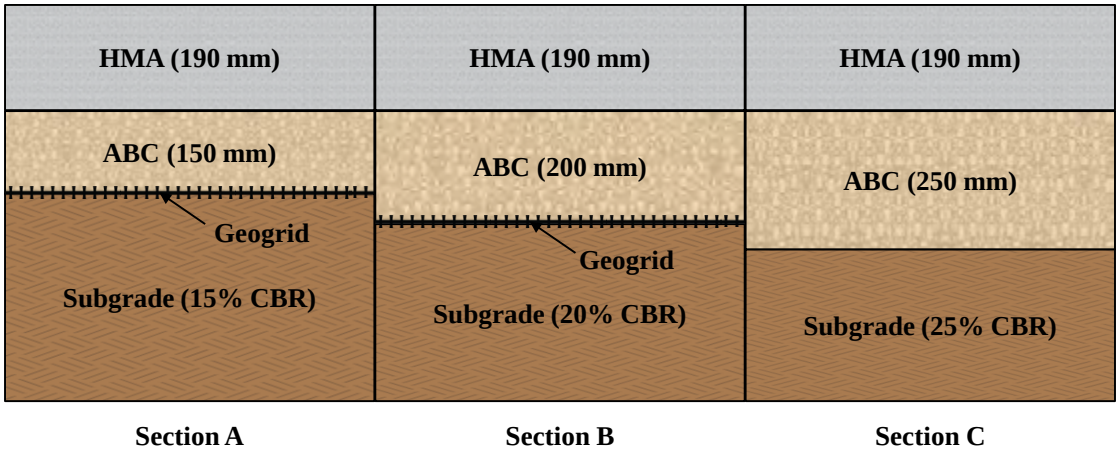

Figure 2. Cross-Section Details for Each Pavement Section

TESTING PROTOCOL

The APLT system (see Figure 3) consists of an advanced electronic-hydraulic control system for applying cyclic and static load pulses through circular steel plates and high-resolution sensors for measuring vertical ground displacements (White and Vennapusa 2017). Compared to Falling Weight Deflectometer (FWD), the APLT has the advantage of applying a conditioning loading prior to testing and measuring peak, resilient and permanent deformations for each loading cycle. In this study, a 304.8 mm diameter plate (see Figure 3c) was used to apply cyclic loads over the HMA layer of geogrid-stabilized and unstabilized pavement sections. A cyclic stress of 482 kPa was applied in five different stages (or loading frequencies) as described in Table 2. The five different loading frequencies were selected to simulate high to low traffic speeds. During Step 1, the accumulated permanent deformation (i.e., rutting) with each loading cycle was recorded to develop a permanent deformation model which can be represented by the power model as shown in Equation 1. Monismith et al. (1975) described a similar power model relationship for relating permanent strain to cyclic loading for repeated triaxial laboratory testing. Such a model can be used for prediction of deformation at higher loading cycles (Vennapusa et al. 2018; Tamrakar et al. 2019).

$$\delta_p = CN^d \qquad (1)$$

where, δ_p is cumulative permanent deformation, C is a regression coefficient representing the initial plastic deformation, and d is the scaling factor.

Table 2. APLT Test Details

Step	Cyclic Stress, kPa	Frequency (Hz)	Numbers of Cycle
Step 1	482	1*	2,000
Step 2		2	150
Step 3		1	50
Step 4		0.1	12
Step 5		0.01	3

**For running permanent deformation test using 0.2 sec loading time and 0.8 sec dwelling time*

The loading steps 2 through 5 were used to determine frequency-dependent composite resilient modulus and back-calculated layer-specific moduli for HMA, ABC and subgrade. For each loading cycle, rebound deflection basin measurements were obtained at 305 mm, 457 mm, and 610 mm away from the center of the plate. Using the deflection basin measurements, 2-Layer back-calculation analysis was performed using the APLT-BACK program, developed by Ingios Geotechnics, assuming a rigid loading plate. Validation results of the APLT-BACK program are provided in (White et al. 2019a).

Surface temperatures were recorded during testing at each test location using an infrared temperature sensor. Mid-layer ("mat") temperatures were calculated using the BELLS2 prediction model, based on the surface temperature measurement, HMA layer thickness, and the previous day mean air temperature. The HMA layer moduli values were temperature corrected to a standard 22^{o}C temperature, following a procedure described in Lukanen et al. (2000).

Figure 3. APLT System

PRESENTATION OF RESULTS

For each pavement section, APLTs were conducted at three test locations. The test locations were marked as 1, 2 and 3, and the separation between the consecutive test locations was about 9 m. Figure 4 shows the permanent deformation responses of stabilized and unstabilized pavement sections for different loading frequencies and loading cycles. The initial loading up to 2000 cycles was for 1 Hz loading frequency that consisted of 0.2 second of loading time and 0.8 second of dwelling time. The permanent deformation increased rapidly for the first 100 cycles (approximately) and then increased gradually afterward. Such deformation behavior can be represented using the power model as described in Equation 1. The coefficients for the power model for stabilized and unstabilized pavement sections are provided in Table 3. Permanent deformations at the end of 2000 loading cycles are shown in Figure 5. Due to the in-situ precise

measurements, the figure shows that there is some variability in deformations with each section. Average permanent deformations at the end of 2,000 cycles for sections A, B and C were 1.16 mm, 0.95 mm and 0.79 mm, respectively. Section A with 150 mm geogrid stabilized ABC showed the highest permanent deformation (1.16 mm) and section C with 250 mm unstabilized ABC showed the lowest permanent deformation (0.79 mm). However, these deformations are considered low, despite the difference in the ABC layer thicknesses between the three sections. The highest deformation in the stabilized section is possibly due to a 40% reduction in the ABC thickness.

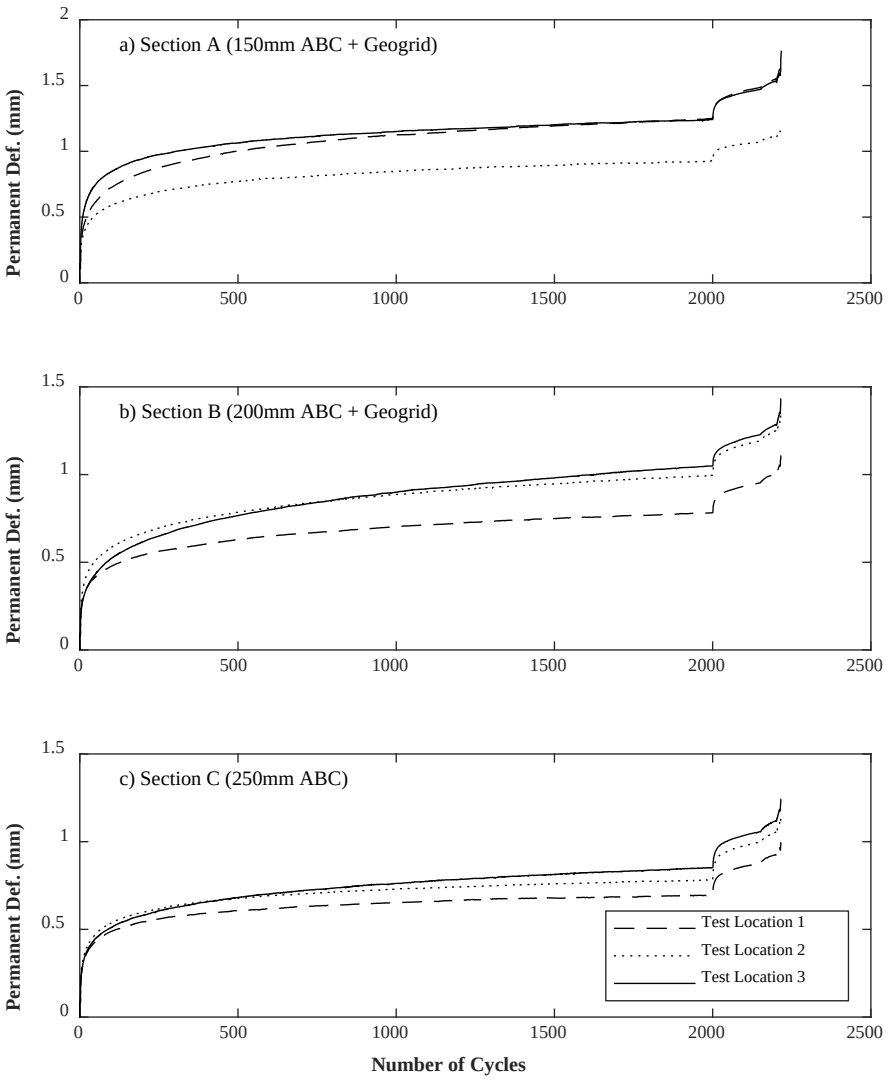

Figure 4. Permanent Deformation Measured at Different Loading Cycles

Table 3. Permanent Deformation Model Coefficients

	Test Locations	C	d
Section A	1	0.012	0.19
	2	0.011	0.16
	3	0.017	0.14
Section B	1	0.009	0.17
	2	0.010	0.18
	3	0.007	0.24
Section C	1	0.010	0.13
	2	0.011	0.14
	3	0.009	0.18

Figure 4 also shows permanent deformations beyond 2000 loading cycles which are for steps 2 through 5 (i.e., for different loading frequencies) as described in Table 2. The permanent deformation increased with the decrease in the loading frequency or increasing loading period. This should be expected because of the visco-elastic nature of the asphalt material, for which lower frequency loadings lead to larger deformations. In addition, stress-dependent behavior unbound pavement materials also contribute to the amplification of the permanent deformation response with the increase in the loading duration (Tamrakar and Nazarian 2017).

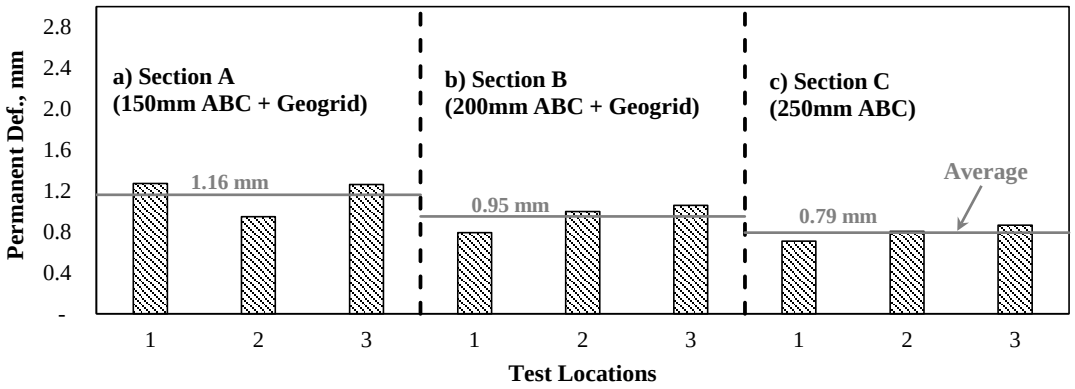

Figure 5. Permanent Deformation at the End of the First Loading Step

Figure 6 shows the composite modulus values for each section. At each test location, the composite modulus decreased with the reduction in the loading frequency. This should be expected for visco-elastic materials, where rebound deformations increase as loading frequency decreases. On average, the stabilized section with 200 mm ABC (Section B) had the highest composite modulus while the remaining two sections had a similar modulus (about 13% to 15% lower than Section B). As the composite modulus represents the overall response of the entire pavement structure to the applied load, it can be considered as an indicative factor for the pavement performance. Further, the moduli at different loading frequencies help to understand the behavior of pavement at different loading rates. Further studies with a wide range of cyclic stresses and loading frequencies including sufficient dwelling periods will be needed to simulate the real traffic scenario.

The back-calculated layer-specific modulus for HMA, ABC and subgrade are provided in Figure 7 through Figure 9. Like the composite modulus, the layer-specific moduli also decreased with the reduction in the loading frequency. The influence of loading frequency on HMA layer modulus is well documented and established in the literature, but it is not well established for the unbound materials.

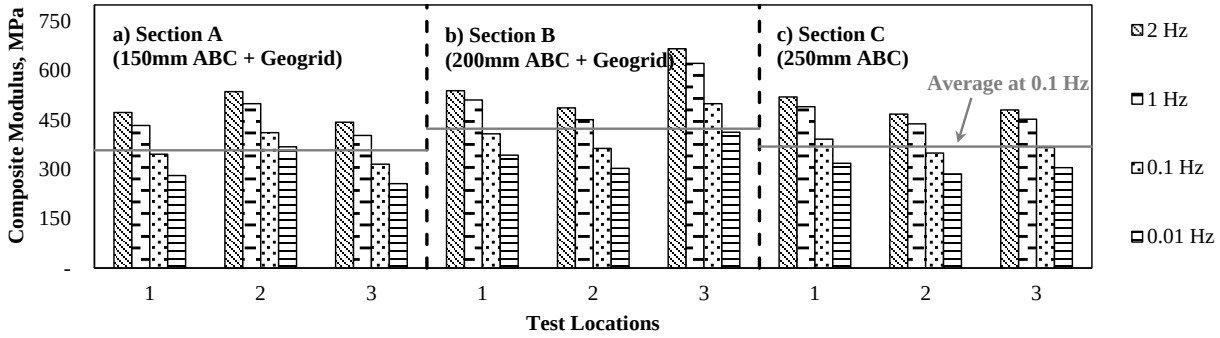

Figure 6. Composite Modulus Measured at Different Loading Frequencies

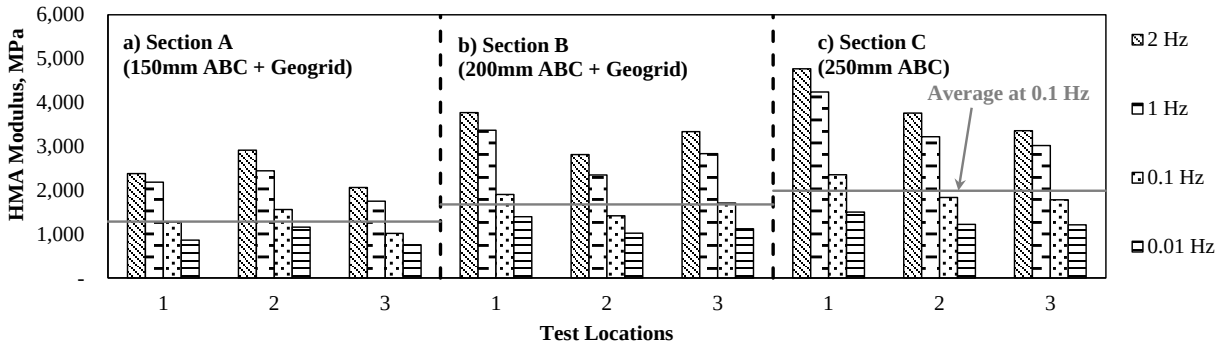

Figure 7. HMA Modulus Measured at Different Loading Frequencies

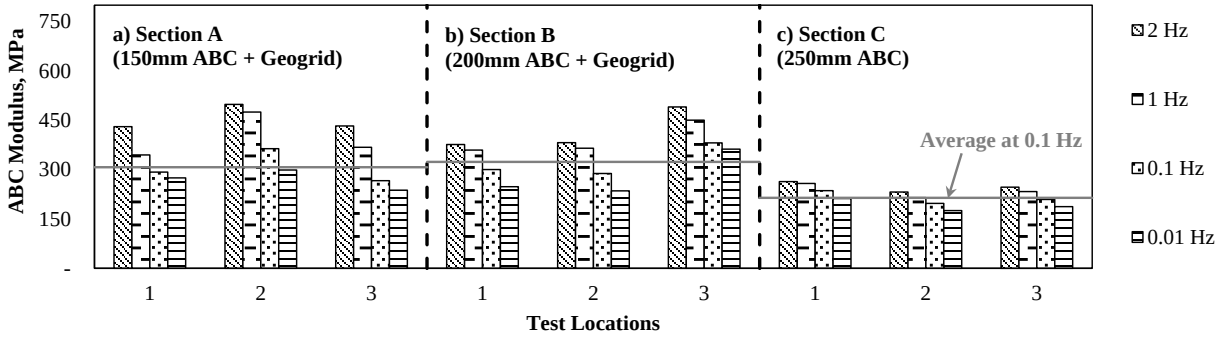

Figure 8. ABC Modulus Measured at Different Loading Frequencies

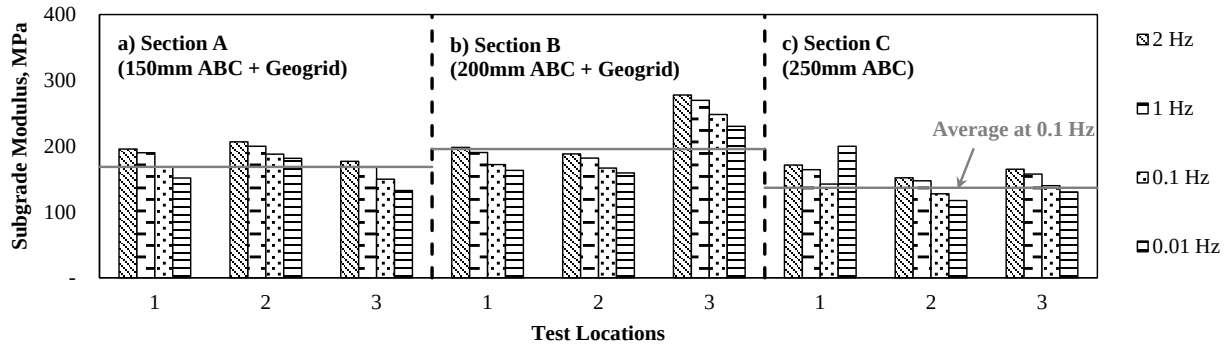

Figure 9. Subgrade Modulus Measured at Different Loading Frequencies

Results indicated that the back-calculated modulus of the ABC layers in the stabilized sections were higher than that of the unstabilized section (see Figure 8). This increase in ABC modulus for stabilized sections is due to base course stabilization. In addition, the rate of change in ABC modulus with the loading frequency was distinctively seen for the stabilized section, more prominent for the stabilized section with 150 mm ABC. These observations suggest that the geogrid stabilized pavements are sensitive to loading frequencies. The back-calculated subgrade layer moduli in the stabilized sections are also higher than that for the unstabilized section (see Figure 9). This can be attributed to lower stresses on the subgrade, because of wider distribution of stresses due to presence of geogrid.

SUMMARY AND CONCLUSION

Field characterization and evaluation of geogrid stabilized and unstabilized pavements were conducted using an APLT system. APLTs were conducted over three flexible pavement test sections consisting of 190 mm thick HMA. The ABC layer thicknesses for two geogrid stabilized pavements were 150 mm and 200 mm whereas that for the unstabilized pavement was 250 mm. A punched and drawn triangular aperture geogrid was used in the stabilized sections.

The key finding from this field testing are:

- The total surface permanent deformation responses of geogrid stabilized and unstabilized pavements were sensitive to the loading frequency and the loading cycles. Such deformation typically increases with the increases in the loading cycles and the decrease in the loading frequency.
- The deformations induced in the stabilized pavement with 200 mm ABC and unstabilized pavements were similar.
- On average, the stabilized pavement with 200 mm ABC had the highest composite modulus while the remaining two pavements had a similar modulus.
- The back-calculated ABC moduli of geogrid stabilized pavements were higher than that of the unstabilized pavement. At the loading frequency of 0.1 Hz, the back-calculated ABC modulus of the stabilized sections A (150 mm ABC + geogrid) and B (200 mm ABC + geogrid) were 44% and 51% higher than that of the control section (250 mm ABC).
- The composite modulus as well as the back-calculated layer-specific modulus for all pavement layers were sensitive to the loading frequency. Those moduli decreased with the reduction in the loading frequency.

- The rate of change in ABC modulus with the loading frequency was distinctively seen for the stabilized pavements, more prominent for the stabilized pavement with 150 mm ABC.

In this study, only one set of cyclic stress (482 kPa) was considered for APLT. Further study with multiple higher cyclic stresses is required for understanding the effects of heavy vehicles. Besides, a random loading pattern with a mixed set of loading frequencies might be needed to represent the actual traffic scenario.

REFERENCES

AASHTO. (2015). *Mechanistic-Empirical Pavement Design Guide, A Manual of Practice*. *AASHTO*, American Association of State Highway and Transportation Officials.

Abu-Farsakh, M. Y., Chen, Q., and Hanandeh, S. (2019). *Accelerated Load Testing of Geosynthetic Base Reinforced/Stabilized Unpaved and Pavement Test Sections*.

Ba, M., Nokkaew, K., Fall, M., and Tinjum, J. M. (2013). "Effect of matric suction on resilient modulus of compacted aggregate base courses." *Geotechnical and Geological Engineering*, Springer, 31(5), 1497–1510.

Cook, J., and Horvat, F. (2014). "Assessment of particle confinement within a mechanically stabilised layer." *10th International Conference on Geosynthetics. Berlin*.

Giroud, J. P., and Han, J. (2016). "Mechanisms governing the performance of unpaved roads incorporating geosynthetics." *Geosynthetics*, 34(1).

Jas, H., Stahl, M., te Kamp, L., Konietzky, H., and Oliver, T. (2015). "Discrete element simulation: Modelling and analysis of a geogrid stabilized sub-base while loaded with a moving wheel." *XVI European Conference on Soil Mechanics and Geotechnical Engineering*.

Kang, M., Kim, J. H., Qamhia, I. I. A., Tutumluer, E., and Wayne, M. H. (2020). "Geogrid Stabilization of Unbound Aggregates Evaluated Through Bender Element Shear Wave Measurement in Repeated Load Triaxial Testing." *Transportation Research Record*, SAGE Publications Sage CA: Los Angeles, CA, 2674(3), 113–125.

Kim, J. H., Kang, M., Byun, Y.-H., Qamhia, I. I. A., Tutumluer, E., and Wayne, M. H. (2020). "Bender Element Shear Wave Measurement Based Local Stiffness Characteristics Related to Permanent Deformation Behavior of Geogrid-Stabilized Aggregate Specimens." *Geo-Congress 2020: Geotechnical Earthquake Engineering and Special Topics*, 517–526.

Konietzky, H., te Kamp, L., Groeger, T., and Jenner, C. (2004). "Use of DEM to model the interlocking effect of geogrids under static and cyclic loading." *Numerical modeling in micromechanics via particle methods*, AA Balkema, Rotterdam, 3–12.

Lees, A. (2017). "Simulation of geogrid stabilization by finite element analysis." *Proceedings of 19th International Conference on Soil Mechanics and Geotechnical Engineering, Seoul*, 1377–1380.

Lukanen, E. O., Stubstad, R., Briggs, R. C., and Intertec, B. (2000). *Temperature predictions and adjustment factors for asphalt pavement*. Publication No. FHWA-RD-98-085, US Department of Transportation, Federal Highway Administration, USA.

McDowell, G. R., Harireche, O., Konietzky, H., Brown, S. F., and Thom, N. H. (2006). "Discrete element modelling of geogrid-reinforced aggregates." *Proceedings of the Institution of Civil Engineers-Geotechnical Engineering*, Thomas Telford Ltd, 159(1), 35–48.

Monismith, C. L., Ogawa, N., and Freeme, C. R. (1975). "Permanent deformation characteristics

of subgrade soils due to repeated loading." *Transportation Research Record*, (537).

Qian, Y., Han, J., Pokharel, S. K., and Parsons, R. L. (2011). "Stress analysis on triangular-aperture geogrid-reinforced bases over weak subgrade under cyclic loading: An experimental study." *Transportation research record*, SAGE Publications Sage CA: Los Angeles, CA, 2204(1), 83–91.

Rakowski, Z., and Kawalec, J. (2020). "The Technology of Mechanically Stabilized Layers for Road Structures in Cold Regions." *Transportation Soil Engineering in Cold Regions, Volume 2*, Springer, 63–70.

Robinson, W. J., Tingle, J. S., and Norwood, G. J. (2017). "Full-Scale Accelerated Testing of Multi-axial Geogrid Stabilized Flexible Pavements." *ERDC-GSL vicksburg United States*.

Stahl, M., Konietzky, H., Te Kamp, L., and Jas, H. (2014). "Discrete element simulation of geogrid-stabilised soil." *Acta Geotechnica*, Springer, 9(6), 1073–1084.

Sun, X., Han, J., Zhao, Y., Guo, J., Huang, L., and Zhang, W. (2020). "Analysis of geosynthetic-stabilized base course over a subgrade considering base modulus degradation in a transversely isotropic layered elastic system." *Computers and Geotechnics*, Elsevier, 125, 103668.

Tamrakar, P., and Nazarian, S. (2017). "Comparison of Laboratory and Field Test Results for Granular Bases." *Geotechnical Frontiers*, 384–392.

Tamrakar, P., and Nazarian, S. (2019). "Moisture effects on moduli of pavement bases." *International Journal of Pavement Engineering*, Taylor & Francis, 1–13.

Tamrakar, P., Wayne, M. H., and White, D. J. (2019). "Permanent and Resilient Deformation Behavior of Geogrid-Stabilized and Unstabilized Pavement Bases." *Geo-Structural Aspects of Pavements, Railways and Airfield*.

Vennapusa, P. K. R., White, D. J., Wayne, M. H., Kwon, J., Galindo, A., and Garcia, L. (2018). "In situ performance verification of geogrid-stabilized aggregate layer: Route-39 El Carbón--Bonito Oriental, Honduras case study." *International Journal of Pavement Engineering*, Taylor & Francis, 1–12.

Wayne, M., Fraser, I., Reall, B., and Kwon, J. (2013). "Performance verification of a geogrid mechanically stabilized layer." *The 18th International Conference on Soil Mechanics and Geotechnical Engineering, Paris*, 1381–1384.

Wayne, M. H., Fountain, G., Kwon, J., and Tamrakar, P. (2019). "Impact of Geogrids on Concrete Highway Pavement Performance." *Geosynthetics Conference*.

White, D. J., and Vennapusa, P. K. R. (2017). "In situ resilient modulus for geogrid-stabilized aggregate layer: A case study using automated plate load testing." *Transportation Geotechnics*, Transportation Geotechnics, 11, 120–132.

White, D. J., Vennapusa, P., Siekmeier, J., and Gieselman, H. (2019a). "Cyclic Plate Load Testing for Assessment of Asphalt Pavements Supported on Geogrid Stabilized Granular Foundation." *Geo-Congress 2019: Geotechnical Materials, Modeling, and Testing*, 296–307.

White, D., Vennapusa, P., and Cackler, T. (2019b). *In Situ Modulus Measurement Using Automated Plate Load Testing for State Wide Mechanistic-Empirical Design Calibration*. ST-003, Iowa Highway Research Board, Iowa Department of Transportation, Ames, IA.

Geosynthetics Conference

Unpaved Access Road Utilizing Polymeric Geocell Reinforcement over High Water Bearing Muskeg

Timothy Yii, P.Eng.,[1] Sanat Pokharel, Ph.D., P.Eng.,[2] Murtaza Ali, P.Eng.,[3] and Marc Breault[4]

[1]Project Engineer, Stratum Logics, AB, Canada; e-mail: timothy.yii@stratumlogics.com
[2]Principal Engineer, Stratum Logics, AB, Canada; e-mail: sanat.pokharel@stratumlogics.com
[3]Project Engineer, Stratum Logics, AB, Canada; e-mail: murtaza.ali@stratumlogics.com
[4]President, Paradox Access Solutions, AB, Canada; e-mail: marc@paradoxaccess.com

ABSTRACT

An 11-kilometer gravel access road was designed and built in MD of Opportunity, Alberta. The surface conditions varied along the road alignment, generally consisting of deposits of muskeg or topsoil over soft to firm clay. Through ground penetrating radar and probing, the thicknesses of the muskeg sections were identified as 1.5-2 m. The project was located in an environmentally sensitive area with a high water table and wetlands. The traditional method requires muskeg removal and replacement with competent soils, which is often costly and disagrees with local regulations. Therefore, a sustainable design option minimizing impacts to the existing ecosystem was desired. A granular road embankment was designed with two layers of novel polymeric alloy (NPA) geocell reinforcement and geotextile for separation. This design did not require the removal of surface materials and maintained water flow using culverts. The road was constructed during the second half of 2019 and withstood a large number of 30 tonne rock truck passes with minimal surface rutting and no failures of the embankment structure. This paper discusses the design, implementation, and performance of the geocell-reinforced granular structure to meet the set design criteria and describes performance after one freeze-thaw cycle and a year of operation.

INTRODUCTION

Muskeg is a marshy, bog-like soil condition present in Canada and covers a large surface area in the country. It has been estimated that Canada has at least 1.2 million square kilometers of muskeg and other peatlands (Terasmae, 2018). Owners of infrastructure projects, especially road owners, often avoid building projects over muskeg if possible. However, there is a need for project development in this region to harness the natural resources which therefore demands innovative techniques to lessen the burden of construction cost while still maintaining the covenants of sustainable development. Design over muskeg conditions is challenging due to its unique engineering properties. Typical characteristics of muskeg include: extremely high moisture content, permanent saturation, high compressibility, immediate settlement under applied stress, high organic content, and weak resistance to shear. Muskeg is also known as “peat bog”.

A basic methodology for constructing road embankments in such conditions is to remove the existing muskeg and to replace it with engineered fill materials, but this typically is only economically feasible for shallower depths (Phukan, 1982). Phukan (1982) summarized construction methodologies for construction of road embankments in muskeg from several publications, and a brief summary of these methodologies follows.

- A thick embankment can be built over peat to displace the muskeg laterally until it is accessible for removal and hauling off site.
- Blasting using explosives can be implemented as an alternative to excavating muskeg.
- The embankment can be floated over muskeg in applications with light loading.
- A “corduroy road” can be constructed using logs to form a working platform.
- The muskeg subgrade can be preloaded prior to construction of the embankment.
- The muskeg can be stabilized by modifying drainage through natural means, sand drains, or chemical grouting.

All of these methods were considered as possible design alternatives for the access road design through muskeg subgrade; however, they were both cost-prohibitive and would have required longer construction time impacting the construction and commissioning of the compressor station that was to be constructed at the end of the 11 km road. An improvement of the floating embankment technique utilizing geotextiles and novel polymeric alloy (NPA) geocell was proposed for this project site in MD of Opportunity, Alberta, Canada. The project was designed based on extensive previous experience with similar projects. A two-layered reinforcement structure consisting of the geocell and woven geotextile reinforcement was chosen as the suitable approach.

The subject of this paper is the design of an 11 km gravel access road over muskeg conditions similar to those described above. A description of the site conditions, design constraints, construction challenges, benefits of the proposed reinforcement solution, and short-term performance results is provided within this paper. The performance of the road after one freeze-thaw cycle and one year of operation has also been discussed. This paper discusses the design, implementation, and performance of the two layered geocell structure and how it met the necessary performance criteria.

GEOSYNTHETIC REINFORCEMENT OVER SOFT SOILS

The use of geocell reinforcement to support embankment structures over soft soils has been found to be an effective technique. Initial experiments on geocells were conducted by Webster and Watkins (1977) who proved geocells were a feasible means of base reinforcement over weak subgrade. Webster (US Army Corps, 1979) performed experiments using beach sand reinforced with geocells. Since then, various research studies have been conducted to further understand the mechanisms of geocell reinforcement (Han et al. 2013). Some of the main reinforcement mechanisms were identified by Pokharel et. al (2010), Thakur et al. (2013), and Kief et al. (2015) to be vertical and lateral confinement, wider stress distribution, and the beam/slab effect. The effectiveness of these mechanisms was also found to be related to higher tensile stiffness, strength, and creep resistance of the geocells. Specifically, Thakur et al. (2013) identified that resistance to creep helped with mitigating the initial deformation and rate of creep in the geocell-reinforced soil composite. Yuu et al. (2008) identified the performance of geocell composites based on various properties of the composite. They found that the quality of infill soil, subgrade strength, loading type, and location of geocell placement were influential factors on the performance of the geocell-reinforced course. Bathurst and Jarett (1989) performed tests to identify that stiffer geocells had better performance. Pokharel et. al (2017) performed experimental studies on single and multiple geocell-reinforced bases under repeated loading and found that the inclusion of geocell could provide a traffic benefit ratio of 12 to road bases.

Design methods for unpaved roads incorporating geosynthetic reinforcement have been developed over the past two decades. Giroud and Han's design method for rut criteria of planar geosynthetics was developed in 2004. Pokharel (2010) conducted research and updated the formula to three dimensional geocells as well. The Han and Pokharel design method (Han, 2015) is now used to design unpaved roads using geocells as reinforcement. Pokharel et al. (2015) showed a number of unpaved road projects where the design methodology was used successfully. Examples of successful geocell implementation includes causeway design (Pokharel et al., 2013), paved road design (Pokharel et al., 2017 and Norouzi et al., 2017), and gravel pads (Pokharel et al., 2019).

THE PROJECT AND EMBANKMENT DESIGN

The project goal was to design and construct an 11 km all-season access road between an existing private industry road and a compressor station. The compressor station was only accessible by helicopter or all-terrain vehicles in the summer, or by ice roads constructed within a power utility cutline every winter. The site was heavily forested and was situated within an environmentally sensitive area with frequent sightings of bears and other wildlife. Therefore, a key goal of the design was to minimize the footprint of the all-season access road in order to protect the environmentally sensitive lands. The road also needed to be designed to be wide enough to allow turning movements of a 56.49 m long compressor unit transport vehicle, and had to cross a small creek and three pipelines without impacting any of these crossings. Construction of the road was limited to linear construction due to the fact that the contractor only had access to the road from one side.

The site was visited twice (once in June 2015 and once in June 2018) during the project's design phase to characterize the site conditions. The purpose of the initial site visit in 2015 was to characterize the site and determine feasibility of road construction. Based on that visit, it was estimated that approximately 8 km of the project site consisted of very soft muskeg deposits and the other 3 km was topsoil over soft to firm clay with approximated undrained shear strength values of 22 kPa. The site condition that was identified in these visits is shown in Figure 1.

The follow up visit in 2018 was conducted to collect information for design and confirmed some of the 2015 findings. The surface strength was determined using dynamic cone penetrometer tests at regular intervals in non-muskeg zones. The surface conditions varied along the alignment of the road, generally consisting of deposits of muskeg or topsoil over soft to firm clay. Ground penetrating radar and muskeg depth probing was used to determine the thickness of the muskeg sections to be 1.5-2 m. The depth of muskeg was not consistent over the entire road alignment and neither was the strength of the surface soils. For most of the road alignment there was a near-surface water table.

The starting point of the road was located in a remote region that was only accessible through several privately-owned unpaved access roads, one of which was a heavily used forestry road. Because of this, any large amounts of material hauling, either away from the site or brought to the site as fill, would increase the project cost not only due to the hauling requirements, but also because the project owner would have to spend money maintaining the roads used to haul the material. The construction schedule was also limited by environmental regulations. A restricted activity period for Caribou migration season limited the road to be constructed outside of a certain time window (February 15 to July 15). No project-related construction activities were permitted.

Due to the constraints of construction schedule, the cost of removing and replacing muskeg, and the project requirement to minimize hauling, the conventional method of removal and replacement of muskeg was not used.

Figure 1. Site conditions at different locations in the 2015 (left) and 2018 (right) site visits.

An alternative solution incorporating geotextile and two layers of novel-polymeric alloy (NPA) geocell placed over the existing native soil was proposed based on the results of basic analytical calculations. The road was designed to have a 7 m road top with steep side slopes at a slant of 2.5 to 1 (horizontal to vertical). The design relied on the presence of the geosynthetic stabilization layers to allow steeper side slopes thereby reducing the total project footprint. The structure design was evaluated to have an appropriate factor of safety against rut criteria as mentioned in Pokharel (2010) and hoop stresses induced by vehicle loading. The road was designed to withstand operational vehicle loads, vehicle loading from new compressor station construction, and loading from construction vehicles for the road itself.

The design thickness of the embankment structure varied along the alignment of the road in response to the varying depth of muskeg and other soft surficial soils as shown in Figure 2. Other factors that were used in considering the design thickness included the location of the ground water table and the California Bearing Ratio (CBR) of the surface soils at locations where it could be measured. Based on these properties the design identified four characteristic sections of varying thickness required for the road embankment structure. This included approximately 500 m of dry, firm clay subgrade; 2500 m of clay subgrade with moderately well-draining surroundings; 4500 m of soft clay and muskeg with a high-water table; and 4000 m of deep muskeg, as identified by the ground penetrating radar and the other aforementioned parameters. Each of the chosen sections incorporated two layers of geocell and geotextile reinforcement.

A layer of non-woven geotextile was chosen as a separation layer to keep the subgrade and granular fill material from mixing. One layer of 19 kN/m NPA geocell filled with sand was designed to be installed over the geotextile. The minimum thickness of this sand layer was either 250 mm, 450 mm, or 600 mm, varying based on the chosen design section. The sand fill thickness was also governed by road geometric requirements for a smooth longitudinal profile. The road was designed for a maximum longitudinal slope of 2.75% with minimum crest and sag k values of 23 and 18, respectively. Above this layer, a woven geotextile was placed. A layer of 22 kN/m NPA Geocell was installed at the top and filled with 325 mm of well-graded crushed gravel with a

maximum particle size of 40 mm. Topsoil and seeding was placed over the side slopes for erosion control. The full structure is shown in the top image of Figure 3.

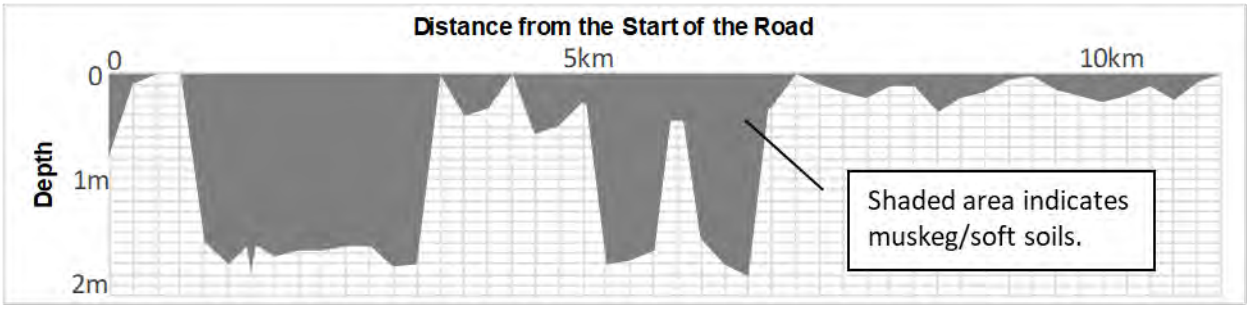

Figure 2. Muskeg and soft soils depth over the length of the road alignment as identified by GPR, DCP, and probing (distorted grid: 0-11.5 km length and 0-2.1 m depth).

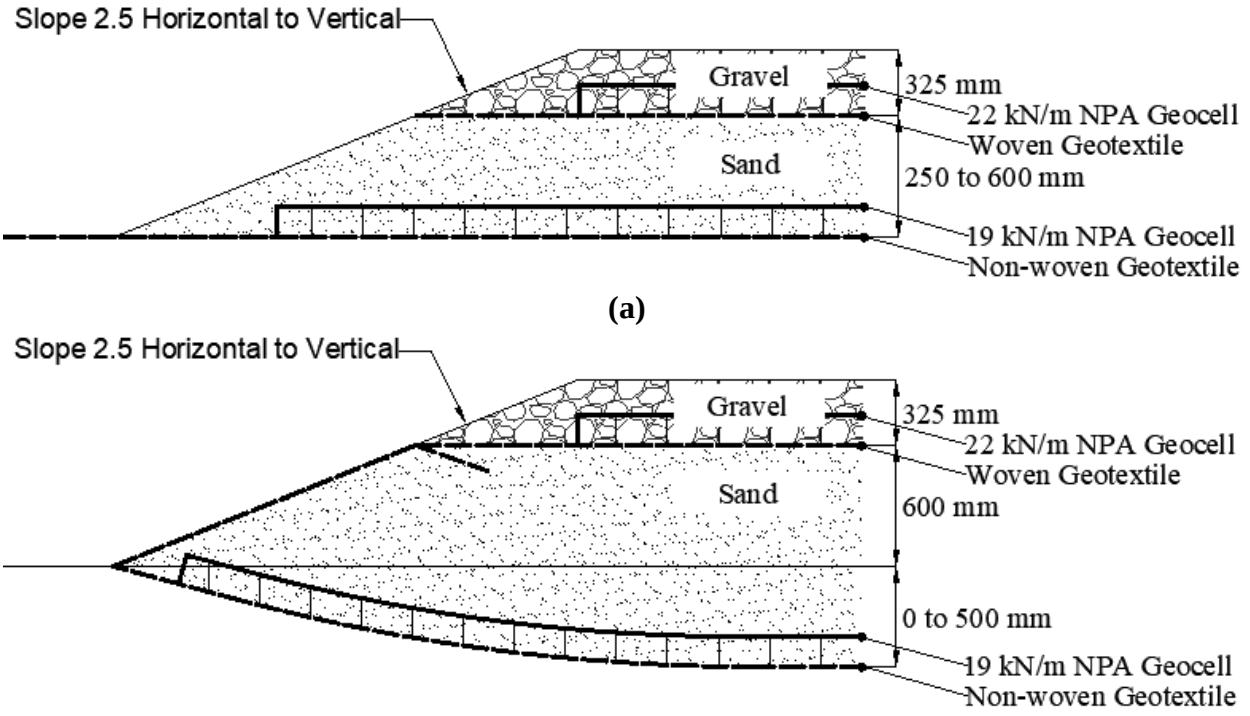

Figure 3. Two-layered NPA Geocell structure in normal condition (a) and a depiction of the settled structure in muskeg condition (b).

The design in muskeg section was similar but also relied on the muskeg gaining strength as it consolidated up to 40% of its initial thickness. In the muskeg section, a higher strength non-woven geotextile was required to provide an appropriate factor of safety against geotextile rupture with settlement. The bottom layer of geotextile in muskeg section was also wrapped around the side slopes of the embankment to protect against soil erosion at the embankment toe, with topsoil and seeding placed on top. The construction methodology was important in assuring successful implementation of the design. The design specified that the all granular fills would be limited to

placement by end-dumping only. The rate of sand fill was to be applied such that an equilibrium point could be reached without shearing the muskeg. A depiction of the final settled surface is shown in the bottom image of Figure 3.

In construction of the new road, the existing drainage patterns had to be maintained. The expected water level for a one in ten-year return period had to be considered on top of the already existing high-water table. In general, the surface topography sloped from the southwest to the north east along the alignment of the road. To prevent flooding on either side of the road a total of 16 culverts were installed at locations of natural drainage in the existing hydrological regime. There was one watercourse crossing at which three culverts pipes were installed.

The key components of the design structure included geocell, woven and non-woven geotextiles, sand, and gravel. Table 1 shows the properties of NPA geocell used in the top and bottom layers as published in material data sheets by the supplier. The non-woven geotextiles had 50% grab elongation. The non-woven geotextile used in muskeg condition had a grab tensile strength of 1330 N whereas the non-woven geotextile used in normal condition had a grab tensile strength of 911 N. The woven geotextile had a grab tensile strength of 890 N. The properties of the granular materials used in embankment construction is shown in Table 2. The specification for both granular materials was less than 12% fines by weight. The gravel had a maximum particle size of 40mm and met the client's gradation specifications.

Table 1. Properties of NPA Geocell

Characteristics	Bottom Layer	Top Layer
Material	Polymeric nano-composite alloy	
Wide-width strength at yield	19 kN/m	22 kN/m
Cell height of geocell	150 mm	150 mm
Distance between weld seams	330 mm	330 mm
Coefficient of soil-cell friction efficiency	0.95	0.95
Coefficient of thermal expansion	<135 ppm/°C	<135 ppm/°C
Brittle temperature	<-70°C	<-70°C
Long term plastic deformation at 65°C (load 6.6 kN/m)	<3.0%	<3.0%
Dynamic (elastic stiffness) modulus at +30°C	>775 MPa	>800 MPa

Table 2. Representative characteristics of sand and gravel

Characteristics	Sand (%)	Gravel (%)
Gravel	2.4	64.2
Sand	96.5	28.2
Fines	1.1	7.6
Moisture content of sampled specimen	4.3	4.8

CONSTRUCTION AND PERFORMANCE OF THE ROAD

Construction of the road embankment began on July 16, 2019 and was substantially completed within the year. The initial construction proceeded at a medium pace as the contractor's workforce mobilized and got familiar with the construction methodology. Rainfall was larger that year than in previous years, contributing to a rise in water table and a less than favorable site condition. Figure 4 shows the partial construction of the bottom layer of the design structure in muskeg

section. Construction over the muskeg had to be completed carefully so as not to shear the muskeg. Installation of the non-woven geotextile was difficult due to the increased weight of the geotextile when it was saturated, while installation of the geocell was relatively easier. Sand fill material was placed slowly into the geocells until equilibrium was achieved. The first lift of sand was placed at least 500 mm thick and was compacted to the greatest achievable extent given the challenging subgrade conditions. Subsequent lifts of sand above the water table were placed carefully in multiple lifts to 95% of standard proctor maximum dry density (SPMDD). To assist the construction schedule, a temporary workspace covered with wooden mats was set up as shown in Figure 5. The construction crew utilized this workspace to transport geotextile rolls and geocell sections, allowing construction of the road to occur without interruptions from material transport and thereby facilitating a quicker schedule. Figure 6 shows the placement of gravel into the top layer geocell. Installation of the top layer of geotextile, geocell, and gravel was comparatively easier than the bottom layer. The top layer geocell was stretched and placed above woven geotextile that was lain over the sand subbase. Gravel fill was end dumped into the geocell and compacted to 98% of the SPMDD. The final road surface was crowned at 3% to shed water off the road surface.

A few construction challenges due to project changes were solved on site. Instead of using lighter construction vehicles in areas where a smaller or the minimum design thickness was required, the construction crew opted to temporarily overbuild the sand embankment to allow for the larger construction equipment already present on site to continue operation. The culverts were installed in local low areas on site within the vicinity of their designed locations. A portion of geocell material had to be cut to fit culverts to the desired elevation. There were also minor surface elevation discrepancies at some locations due to tree removal and the accuracy of LiDAR data used for design compared to that from the field survey during construction.

Figure 4. Stretched NPA geocell and non-woven geotextile separation layer (left) and placement of sand fill (right).


Figure 5. Temporary matted workspace (left) and compaction of fill material (right)


Figure 6. Top layer gravel fill placed in NPA geocell.

DISCUSSION

The geocell stabilized embankment structure was installed successfully and prevented fully shearing the muskeg and soft soils beneath. The composite of non-woven geotextile, geocell, and sand proved to be an effective solution to minimize the distribution of load to the underlying muskeg. Prior to installation of the top layer, the sand composite basal layer was subjected to frequent loading from Volvo A30G rock trucks (29,000 kg capacity). It had been anticipated in design that extreme amounts of loading on this subbase layer could cause structural failures. The contractor was careful to limit travel on these layers whenever possible. Still, with frequent loading of the rock trucks a small amount of lateral spreading occurred near the surface of this basal layer. This was remedied when the embankment slopes were shaped prior to installation of the top layer. Without the contribution of the NPA geocell cellular confinement, these loads would not have been supported and the resulting embankment slope failures would have occurred. The geocell also contributed to reduced stress directed to the muskeg subgrade by distributing loads from traffic during compressor station construction.

Due to the linear nature of the project, the finished portions of the access road were constantly under heavy traffic as materials were brought to construct the road. Even with an

excessive amount of rainfall, frequent traversal by the 30 tonne rock trucks was possible with minimal maintenance of the road (personal communication with contractor's project manager, Eric Ludwig, September 14, 2020).

The predicted distribution of subsurface conditions was mostly accurate. The increased rainfall in the construction year contributed to worse conditions than had been expected. Of the many sources of information gathered to characterize the site, the ground penetration radar was the most accurate in predicting the site conditions. Probing and the dynamic cone penetrometer were good to obtain information about shallow surface soils; however, they could not identify where the larger deposits of muskeg were. The road alignment was also offset from the location of tests due to the presence of trees at the time of testing. The clearing of trees may also have impacted the site conditions prior to road construction.

Measurement of immediate construction settlement was difficult without settlement monitoring tools available. A comparison of the volume of material required versus the actual use of material was conducted instead as a measure to evaluate the settlement predictions. Many variables were involved in the measurement of material volumes, including: the carrying capacity of rock trucks and the consistency of delivery volume, consistency in the volume of stockpiled material placed into the rock trucks, and consistency of the density of the material during the regular stockpiling operations. The evaluation showed that a greater mass of material was required due to a number of reasons including disturbance of the ground from tree clearing activities, differences in estimated versus actual densities of fill materials, losses from material stockpiling, and the presence of more muskeg than anticipated in certain areas.

The costs and quantities for the NPA geocell design was compared to the basic methodology of muskeg removal and replacement with competent soil. The comparison was made using the initial assumed values of muskeg depth and settlement from the design of the 11.5 km road. The geocell design saved approximately 62,600 cubic meters of muskeg removal, and 2,900 cubic meters of gravel. There were also savings of 37,550 cubic meters of embankment fill. The design used sand material sourced from aggregate pits in the surrounding area, which was only possible as an embankment construction material due to geocell stabilization. The conventional design would have required a more expensive material for embankment construction. Compared to removal and replacement, it is estimated there was a 66% savings in cost for aggregate in supply alone. The average haul distance was 140 km from the supply pits to the access road. The geocell-reinforced structure therefore saved at least 14.4 million km-m^3 of hauling, relating to a 77% savings in hauling. Fewer haul trips and less aggregate volume are factors that contribute to reduced CO_2 emissions as previously reported by Norouzi et al. (2017).

As of November 2020, which is one year of operation and one freeze thaw cycle, the road has exhibited no operational concerns and is performing to the desired quality. Confirmation of performance is based on visual observations from regular users of the road, including one of the authors, the contractor's project manager, and client representatives. Videos and recent photographs of the present condition of the road were also observed to identify any issues with the serviceability of the road. Photos of the road at completion and after one freeze-thaw cycle is shown in Figure 7.

Figure 7. Final road structure immediately after construction (left) and after one freeze-thaw cycle (right).

At least additional 10,000 tonnes of granular material had been brought on rock trucks for construction of the compressor station pad site from this road post-thaw period, and in the most recent inspection, the road surface has revealed minimal rutting and there were no instabilities identified in the road embankment (personal communication with the contractor's project manager, Eric Ludwig, September 14, 2020). The project owner was able to use the access road to successfully convey all the construction equipment and materials required to construct a new compressor station without any issues with the road performance. The construction of the compressor station was completed in the summer of 2020.

CONCLUSION

An unpaved access road in northern Alberta was designed and constructed over muskeg subgrade using geotextile separator and NPA geocell. The design relied on predictions of the spatial variability of the subsurface soils and the mechanism of the geocell reinforcement system. The two-layered NPA geocell design was used as an alternative to the conventional method of removing muskeg and replacing with competent fill, which resulted in a reduction in aggregate volume of approximately 66% and reducing CO_2 emissions by approximately 77%. Construction of the road was carried out as per the design intent and successfully provided to access for construction and operational vehicles. Inspection by the authors and the contractor indicate remarkable performance of the road after one year and one freeze-thaw cycle. The road structure as designed was able to effectively satisfy the performance requirements to prevent rutting, embankment failures, and shearing of the muskeg subgrade.

ACKNOWLEDGEMENTS

The authors would like to thank Eric Ludwig from Paradox Access Solutions for feedback on the project performance.

REFERENCES

Bathurst, R.J. and Jarrett, P.M. (1989). Large-scale model tests of geocomposite mattresses over peat subgrades, *Transportation Research Record,* 1188:28-36.

Giroud, J.P. and Han, J. (2004). Design method for geogrid-reinforced unpaved roads. I: Development of design method. *Journal of Geotechnical and Geoenvironmental Engineering,* 130(8): 775–786.

Han, J. (2015). *Principles and Practice of Ground Improvement*, John Wiley & Sons, Inc., Hoboken, NJ, USA.

Han, J., Thakur, J., Parsons, R., Pokharel, S., Leshchinsky, D., and Xiaming, Y. (2013). A Summary of Research on Geocell-Reinforced Base Courses. *Design and Practice of Geosynthetic-Reinforced Soil Structures*. Bologna, Italy.

Kief, O., Schary, Y., and Pokharel, S.K. (2015). High-Modulus Geocells for Sustainable Highway Infrastructure. *Indian Geotechnical Journal,* Springer, 45 (4): 389-400.

Norouzi, M., Pokharel, S.K., Breault, M., & Breault, D. (2017). Innovative Solution for Sustainable Road Construction. Leadership in Sustainable Infrastructure, CSCE, Vancouver, Canada, 085:1-10.

Phukan, A. (1982). Design Methods for Muskeg Area Roads. Civil Engineering Department, University of Alaska, Fairbanks, AK.

Pokharel, S. K. (2010). Experimental Study on Geocell-Reinforced Bases under Static and Dynamic Loading. Civil, Environmental, and Architectural Engineering Department, University of Kansas, Kansas, USA.

Pokharel, S., Martin, I., Norouzi, M., & Breault, M. (2015). Validation of Geocell Design for Unpaved Roads. *Geosynthetics 2015*. IFAI, Portland, Oregon, USA. 711-719.

Pokharel, S., Norouzi, M., & Breault, M. (2017). New Advances in Novel Polymeric Alloy Geocell-Reinforced Base Course for Paved Roads. 2017 *Conference of the Transportation Association of Canada*, Transportation Association of Canada, St. John's, NL, Canada.

Pokharel, S.K., Han, J., Leshchinsky, D., Parsons, R, & Halahmi, I. (2010). Investigation of Factors Influencing Behavior of Single Geocell-Reinforced Bases under Static Loading. *Geotextiles and Geomembranes,* 28:570-578.

Pokharel, S.K., Martin, I., and Breault, M. (2013). Causeway Design with Neoweb Geocells. Proc. of Design and Practice of Geosynthetic-Reinforced Soil Structures, eds. Ling, H., Gottardi, G., Cazzuffi, D, Han, J., and Tatsuoka, F., Bologna, Italy. October 14-16, 2013: 351-358.

Pokharel, S.K., Han, J., Leshchinsky, D., Parsons, R. (2017) Experimental evaluation of geocell-reinforced bases under repeated loading. *International Journal of Pavement Research and Technology*, 11(2): 114-127.

Pokharel, S.K., Yii, T.Y., Breault, M., Norouzi, M. (2019). High Strength Geocell and Geogrid Hybrid Reinforcement for Compressor Station Gravel Pad on Very Soft Subgrade. *Geosynthetics 2019*, IFAI, Houston, TX.

Terasmae, J. (2018). October 5. Muskeg. The Canadian Encyclopedia. Available from https://www.thecanadianencyclopedia.ca/en/article/muskeg [accessed 11 May 2020].

Thakur, J.K., Han, J, and Parsons, R.L. (2013). Creep behavior of geocell-reinforced recycled asphalt pavement bases. *Journal of materials in civil engineering,* ASCE, 25: 1533-1542.

Webster, S.L. (1979). Investigation of beach sand trafficability enhancement using sand-grid confinement and membrane reinforcement concepts. U.S. Army Engineer Waterways Experiment Station, Vicksburg, MS.

Webster, S.L. and Watkins, J.E. (1977). Investigation of Construction Techniques for Tactical Approach Roads Across Soft Ground. Geotechnical Laboratory, U.S. Army Engineer Waterways Experiment System, Vicksburg, MS.

Yuu, J., Han, J., Rosen, A., Parsons, R.L., Leshchinsky, D. (2008). Technical Review of Geocell-Reinforced Base Courses over Weak Subgrade. *The First Pan American Geosynthetics Conference & Exhibition*, IFAI, Cancun, Mexico.

Geosynthetics Conference

A State-of-the-art Large-scale Laboratory Approach to Evaluating the Effectiveness of Geogrid Reinforcement in Flexible Pavements

Hossein Alimohammadi, Ph.D. student,[2] Vernon R. Schaefer, Ph.D., P.E., M. ASCE[2], Junxing Zheng, Ph.D., M. ASCE[3], David J. White, Ph.D., P.E., M. ASCE [4], Guangfan Zheng, M.S.[5]

[1]Civil, Construction and Environmental Engineering, Iowa State University, IA, USA, 50011; email: hosseina@iastate.edu
[2]Civil, Construction and Environmental Engineering, Iowa State University, IA, USA, 50011; email: vern@iastate.edu
[3]Civil, Construction and Environmental Engineering, Iowa State University, IA, USA, 50011; email: junxing@iastate.edu
[4]Ingios Geotechnics, Incorporated, P.O. Box 101, Northfield, MN, USA, 55057; email: david.white@ingios.com
[5]Civil, Construction and Environmental Engineering, Iowa State University, IA, USA, 50011; email: zgf@iastate.edu

ABSTRACT

In this research, an Integrated Mobile Accelerated Test System (IMAS) was used to evaluate geogrids' reinforcement effects. The IMAS system consisted of a 5 ft diameter and 3 ft deep rigid box and an automatic loading frame to apply cyclic loads. A total of eight test configurations were constructed by varying geogrid types, geogrid locations in the base course, and base aggregate thicknesses. The IMAS performs cyclic load tests of pavement foundation sections to a large number of load cycles, which simulates vehicle-loading conditions expected during a pavement system's service life to evaluate the long-term performance of pavement structure. Testing results showed the effectiveness of geogrid reinforcement in the structural performance of pavements. Results show that biaxial and triaxial geogrids can decrease permanent deformation at the end of load cycles with an average value of 47 and 68 percent, respectively. Also, high-strength geogrids provide at least five psi pressure more than low-strength geogrids within the base course, which clarify that the high-strength geogrids can provide more confinement.

INTRODUCTION, BACKGROUND, AND LITERATURE REVIEW

In the United States, 64% of the roads are paved, and 95% of them are flexible pavement. A conventional flexible pavement is constructed using an asphalt layer and granular materials on top of the subgrade layer. Weak subgrade and base course layers are usually the reasons causing the surface rutting under the accumulated load (Alimohammadi et al. 2020b). The pavement's design and construction over the weak and moist subgrade layer, which cannot provide sufficient strength, is always a problem for an engineer. One of the cost-effective methods to reduce the problem and improve flexible pavement behavior is the use of geogrid reinforcement (Alimohammadi et al. 2020). Additionally, geogrids are an environmentally friendly product that has been studied and used as reinforcement for the past two decades. Geogrids provide reinforcement to the pavement structure and offer a number of advantages, including reducing rutting damage, increasing the

resilient modulus, and improving the drainage of the pavement. With the application of using the geogrids, the base course layer's thickness can be reduced, and the service life of the pavement can be extended (Han et al. 2008; Siekmeier and Casanova 2016). These benefits of geosynthetic reinforcement in the pavement are provided by the lateral restraint, separation, and geosynthetics tensioned membrane effect. Due to the load spreading over a wider area on top of subgrade in geosynthetic reinforced sections, vertical stresses transferred through the geosynthetic reinforced base onto subgrade are lower than the unreinforced sections. Geosynthetics can also decrease subgrade stress by absorbing shear stresses. (Zornberg 2017).

To evaluate the effectiveness of the geogrid reinforcement in flexible pavements, several factors should be considered, including geogrid location/depth, geogrid stiffness, geogrid aperture and rib shape, hot mix asphalt thicknesses, base aggregate quality, stiffness thicknesses, and subgrade stiffness (Alimohammadi et al. 2020a). Geogrids are commonly used within or at the bottom of the unbound aggregates to enhance the performance of a flexible base layer or the railroad ballast layer (Cuelho and Perkins 2017; Zornberg and Gupta 2010). Many studies introduced tests performed on large-scale or in-service geogrid-reinforced pavement sections and investigated the effects of the factors as mentioned above in geosynthetic reinforcement applications (Al-Qadi et al. 1994, 2011; Qian et al. 2013; Saghebfar et al. 2016). The results indicate that geogrids are effective in improving the stiffness and stability of the reinforced pavement structures and reducing the accumulated permanent deformation. The results suggest that the effectiveness of geosynthetics reinforcement is more notable on soft subgrade soil. The optimal geosynthetic layer location has been investigated in many investigations and recommended by some researchers to put within the upper one-third of the base layer; however, for the thinner aggregate layer, the reinforcement is recommended to locate the interface of the aggregate and subgrade layer. Also, it was determined that double reinforcement layers led to the better improvement regardless of the geogrid type plus the triangle geogrid provides better improvement compared to the biaxial geogrid with similar tensile moduli (Abu-Farsakh and Chen 2011).

In this research, a large-scale experimental test plan was developed using the Integrated Mobile Accelerated Test System (IMAS) system to evaluate the reinforcement effects of geogrids on pavements' structural benefits. A total of eight test configurations were constructed by varying geogrid types, geogrid locations in the base course, and base aggregate thicknesses, and the effects of these variables were studied on the resilient modulus, deflection, and permanent deformation results of the pavement foundation. The test configurations, the procedure of the tests, some details of the performed tests, and the results are discussed in the following sections.

TEST SECTIONS, CONFIGURATIONS, AND SENSORS

In this section, test sections, configurations, sensors, and procedures of performing the tests are explained.

Test sections. Eight test sections were performed to evaluate the pavement behavior using different geogrid types and under different locations: GE0, GE1, GE2, GE4, GE5, GE7, GE12, and GE15. GE0 was the control section, so no geogrid was installed in this section. Biaxial geogrid was used in GE1, GE2, GE5, and Triaxial geogrid was used in GE4, GE7, GE12, and GE15. For GE1, GE2, GE4, and GE12, the geogrid products were placed at the interface of the base course layer and the subgrade layer; for GE5 and GE7, the geogrid was installed at the middle of the base

course layer. Also, both light-duty and heavy-duty geogrid products were used in the test as well. The details for the test sections are shown in Figure 1 below.

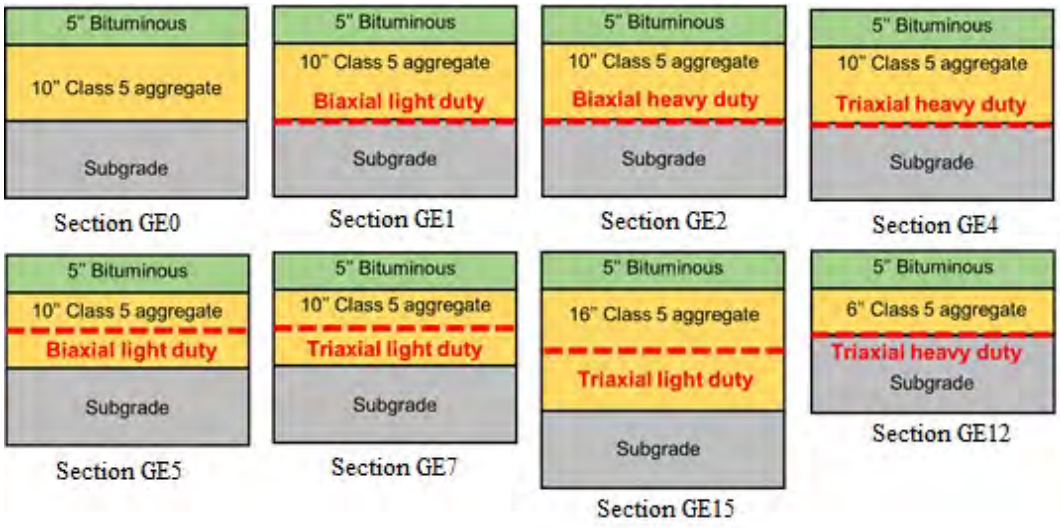

Figure 1. IMAS laboratory test sections

Configurations. The IMAS equipment and section are shown in Figure 2 a and b, and is used to perform the laboratory tests. The IMAS (Ingios Geotechnics 2020) was developed to mimic roadway systems' field loading conditions in a large-scale laboratory system wherein the conditions can be more easily controlled. The IMAS performs a cyclic load test with a large number of load cycles, which simulates vehicle-loading conditions on the pavement foundation. The IMAS can also help determine the resilient modulus, deflection, permanent deformation of the pavement so that the pavement system's service life and the long-term performance of the pavement structure can be evaluated. The IMAS device has a square base container, where the depth is three feet, and the length is five feet. Boundary effects and simulation of the natural soils' stiffness are controlled through the use of rigid walls and a foam layer. The load plate system or the hydraulic actuator is above the device's center to provide the repeated loading during the test. All the sensors are connected to the acquisition system, and the results can be recorded during the test for up to one million cycles. With the use of the IMAS equipment, eight laboratory tests were performed with different parameters. 100,000 cycles of random loading were simulated for each test section, and the test data such as the permanent deformation, strain, and pressure were recorded by the instrumentations like pressure cell and strain gauges.

Sensors. A lot of information can help compare and evaluate the reinforced pavement's behavior with different types of geogrids and determine the optimal placement location of the geogrid. To compare the pavement performance between each test section, it is necessary to record the permanent deformation, the stress at both the subgrade and base layer, as well as the strain behavior on the geogrid rib in different directions. These measurements can help to understand the mechanism for the geogrid and pavement.

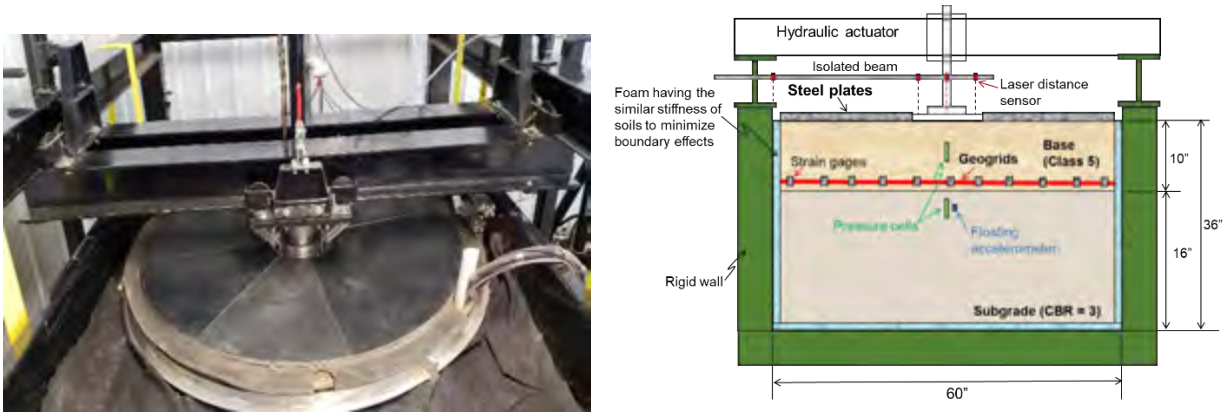

a) **b)**

Figure 2. a) Integrated Mobile Accelerated Test System for laboratory test, b) The test configuration in the IMAS device

Three instrumentations were selected according to the literature review, the data type, and the cost. The laser Linear Variable Differential Transformer (LVDT) was used to measure the deformation occurring on the top plate; two types of strain gauges were used to measure the strain behavior on the biaxial and triaxial geogrid rib, and a pressure cell was used to record the pressure. These instruments are shown in Figure 3.

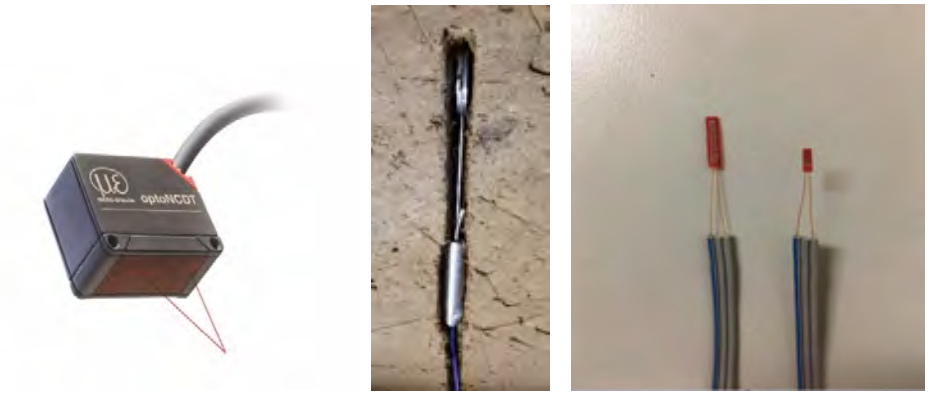

a) **b)** **c)**

Figure 3. The Instrumentations including a) Laser LVDT, b) pressure cells, c) strain gauges

PROCEDURE OF PERFORMING THE TESTS

The following Tensar geogrids were used in the laboratory tests: Light Duty Biaxial – Tensar BX1100, Heavy Duty Biaxial – Tensar BX1200, Light Duty Triaxial – Tensar TX130s, and Heavy Duty Triaxial – Tensar TX7. Class 5 aggregates, which are normally used for driveways and the base of construction projects, were used for the aggregate base layer. A silty clay subgrade soil with CBR = 3, representative of common subgrade soil conditions in Minnesota, was used. To achieve CBR = 3, the subgrade was prepared at a target moisture content of 16.6%.

Subgrade preparation. The subgrade soil was added layer by layer; each layer was less than 15 inches in height to reach a uniform condition. A 50-lb drop hammer, compaction soil hammer, was used to provide compaction after adding each layer. To keep the surface flat, a tamper was used as well after each compaction. Finally, after cleaning the surface, a spirit level tool was used to measure and level the surface. Steps of subgrade preparation are illustrated in Figure 4a.

Base layer preparation. After subgrade preparation, the geogrid was placed at the subgrade surface in some sections, as illustrated in Figure 4b. Then the aggregates were placed above the geogrid layer. A rake was used to level the surface. After leveling the surface, a 6.5 HP plate compactor was used to provide the compaction on the base layer for three minutes. Steps of base preparation are illustrated in Figure 4c. To make sure the geogrids at the interface position will get the maximum involvement and interlocking with the aggregates, a layer of aggregate with a thickness of one inch was placed at the top of the subgrade surface. Then the geogrid was placed at the top of this thin layer, and then base materials were placed and compacted in the tests.

Surface layer preparation. A double layer of steel simulated the asphalt surface, which provides an equivalent weight of the real asphalt surface. The loading plate was set in the middle of the container. Each layer of steel has seven pieces of fan-shaped steel to cover the surface of the base material. Setting the steel surface installation is illustrated in Figure 4d. A thin foam layer was placed between the steel and the base layer to provide friction and protection. The final step was to connect all the sensors to the acquisition system, illustrated in Figures 4e and f.

a) **b)** **c)**

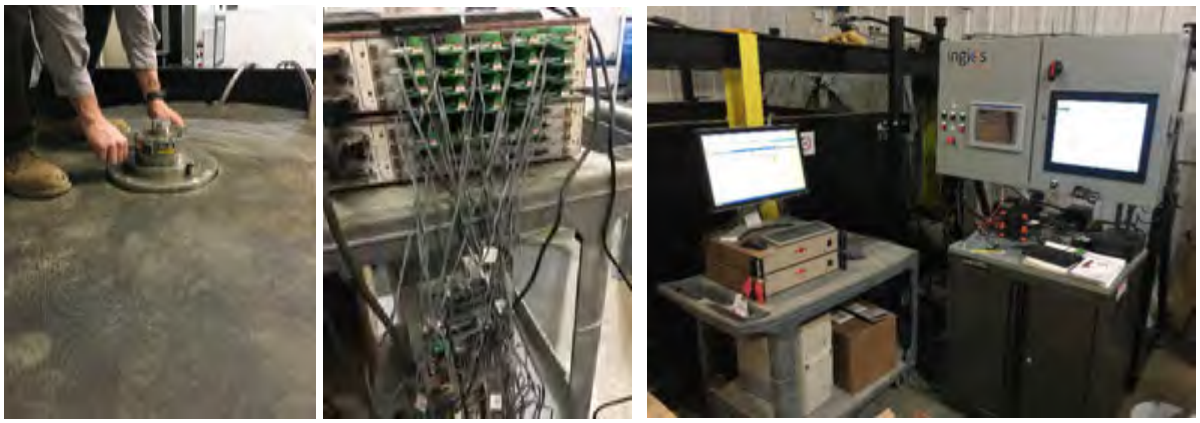

d) **e)** **f)**

Figure 4. Illustration of the a) subgrade preparation, b) setting geogrids, c) base layer preparation and compaction, d) surface layers preparation, e and f) setting the data logger

RESULTS AND ANALYSIS

Figures 5 and 6 illustrate the strain gauge results of biaxial and triaxial geogrids for reinforced sections under the tests' compaction loading steps, respectively. From the results, it can be seen that during the application of compaction loads, the results of strain gauge in biaxial geogrids have fluctuation and reached higher peak values than triaxial geogrids, which gradually increase to get the maximum value of strains. Also, the residual strain in triaxial geogrids is less than biaxial geogrids.

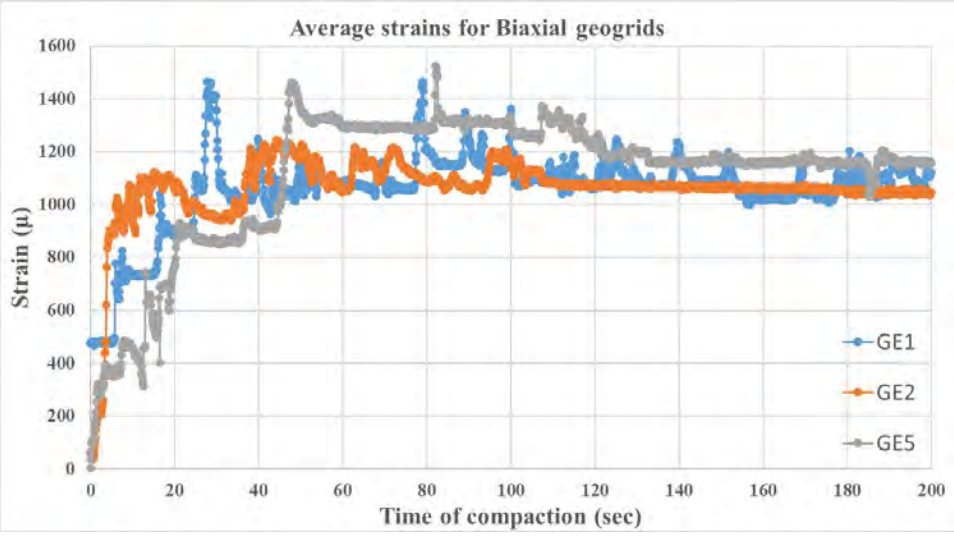

Figure 5. Average strains in the compaction part for Biaxial geogrids

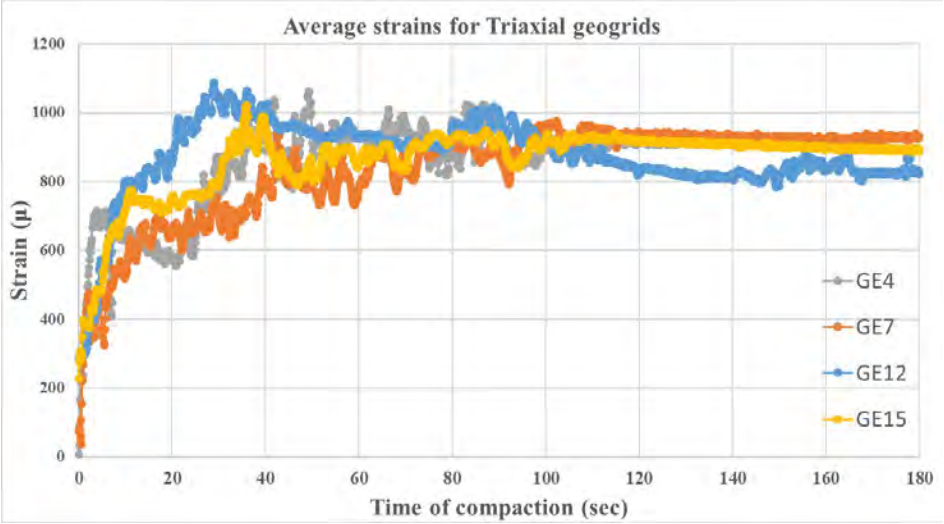

Figure 6. Average strains in the compaction part for Triaxial geogrids

Figure 7 illustrates the permanent deformation results of Triaxial and Biaxial geogrids. The increase in the pavement structure's service life has been commonly defined by the application of the Traffic Benefits Ratio (TBR). The TBR is described as the ratio of the number of load cycles to achieve a particular rutting depth in the reinforced section over an unreinforced section with exactly corresponding thickness, loading characteristics, and material properties. From the results, it can be seen that the triaxial geogrids perform much better than biaxial geogrids in reducing the permanent deformation of the sections for the same cyclic load numbers and increasing Traffic Benefit Ratios (TBR) values of the sections.

Two pressure cells were used for each test, one located on top of the subgrade and the other located on top of geogrid in the base aggregate layer to measure the value of pressure developing in both aggregate and subgrade layers in the tests. Figures 8 a to h show comparisons of both pressure cells in all eight sections performed in this study, and it can be seen from the results that the test sections with the heavy-duty geogrid always have higher pressure cell data reading than the light-duty geogrids. For the overall earth pressure cell results, except for GE4 and GE7 in figure 8 c and e, respectively, the test sections have similar trends: the earth pressure cell data was increasing as the loading occurred, both in the subgrade and base course layer, but the increasing rate and magnitude are higher in base course layer than the subgrade layer. From the results in figure 8 it is obvious that under the same location, the maximum pressure in GE1 with the light-duty geogrid is 10 psi; however, the maximum pressure in GE2 with the heavy-duty can reach 15 psi.

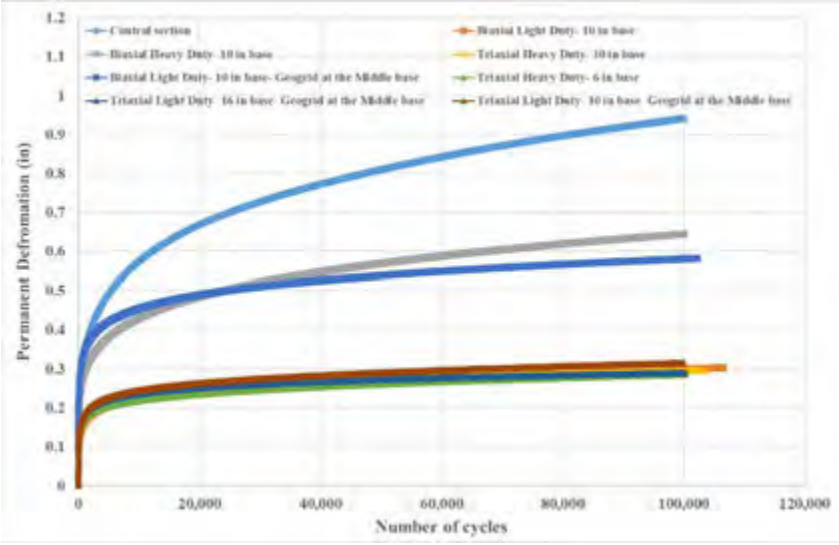

Figure 7. Permanent deformation for Biaxial geogrids and Triaxial geogrids

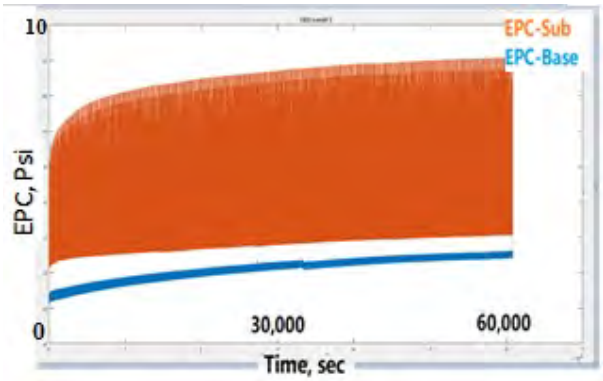

a)

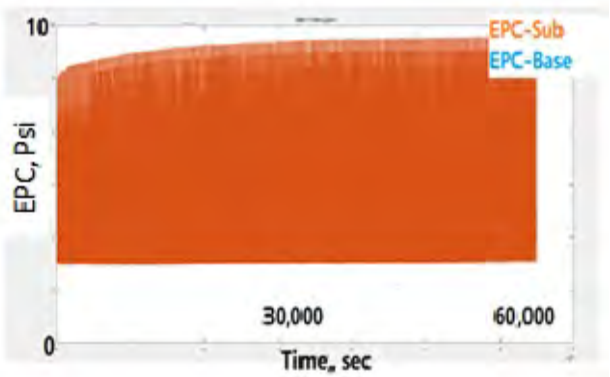

b)

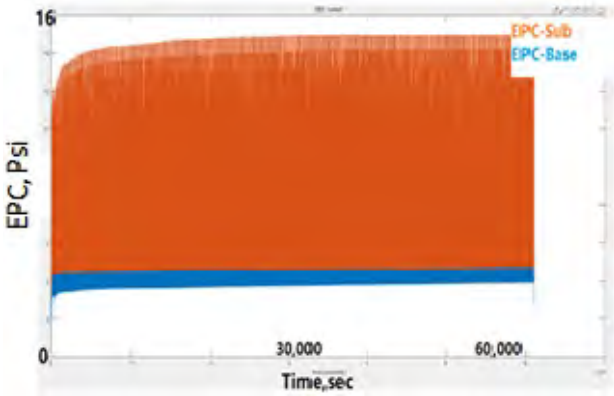

c)

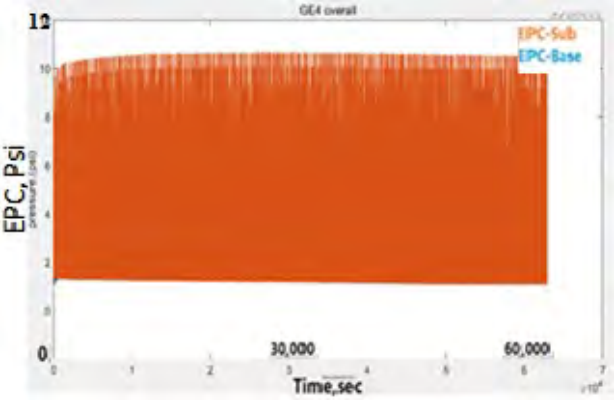

d)

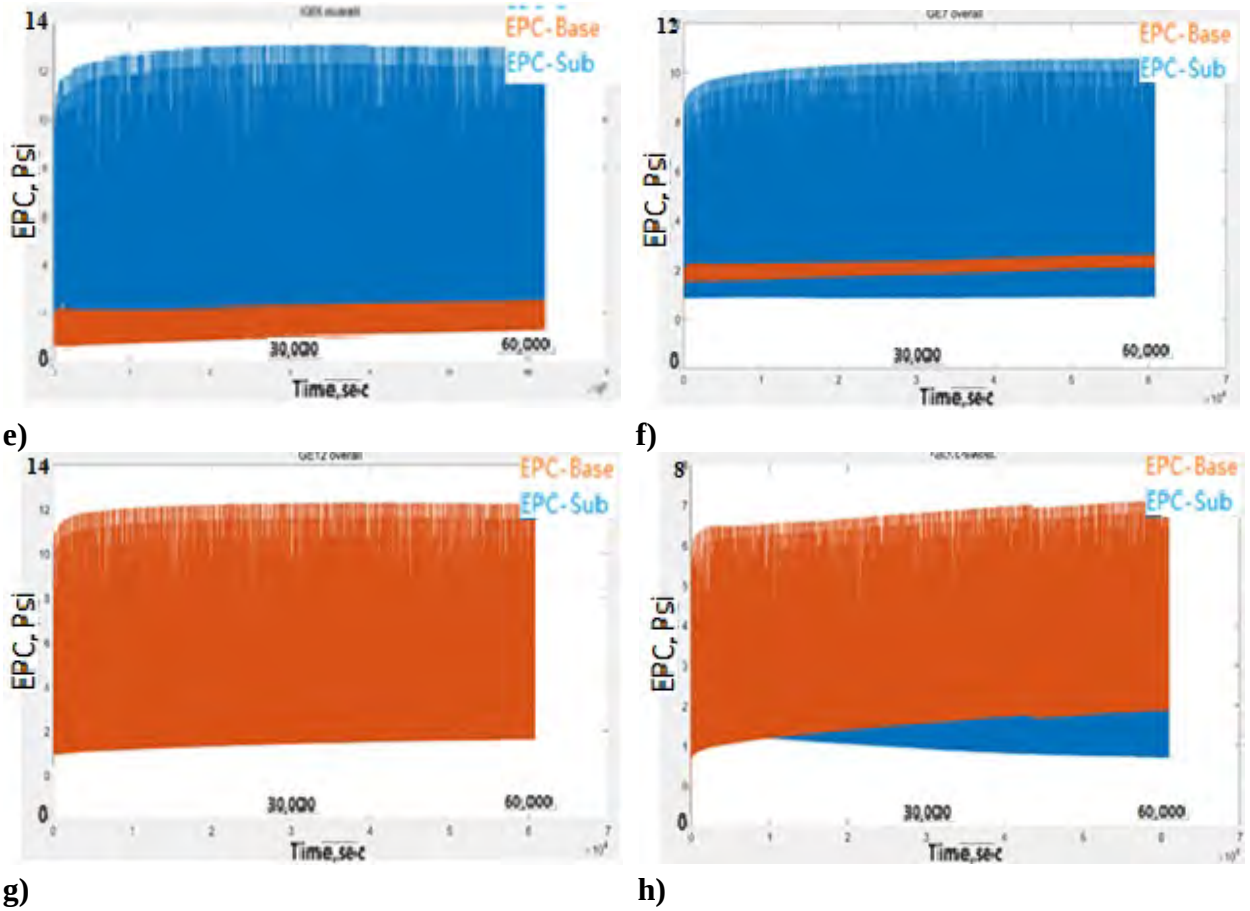

Figure 8. Pressure cells result for sections a) GE0, b) GE1, c) GE2, d) GE4, e) GE5, f) GE7, g) GE12, and h) GE15

CONCLUSIONS

In this study, a series of large-scale laboratory tests were conducted to determine the geogrids' effectiveness under various parameters. These parameters include the types of geogrid, the aperture of the geogrid, the geogrid's stiffness, the location where to install the geogrid, and the thickness of the base course layer. After plotting and comparing the results, the following preliminary observations can be made:

- From the permanent deformation versus the number of loading cycles plot, it can be stated that the deformation of the control section without the geogrid reaches almost one-inch at the end of the test; however, the triaxial and biaxial geogrid reinforced section deformation curves show the maximum deformation around 0.25 and 0.5 inches respectively which is almost one quarter and half of the unreinforced section deformation. Generally, it can be stated that triaxial geogrid perform better than biaxial geogrid in decreasing permanent deformation of the pavement.

- The test sections with the heavy-duty geogrid always have higher-pressure cell readings than the light-duty geogrid. Also, since the heavy-duty geogrid having a higher stiffness

than the light-duty geogrid, the high-strength geogrid can provide more confinement pressure as well.

- For the overall earth pressure cell results, except for GE4 and GE7, the test sections have similar trends: the earth pressure cell data was increasing as the loading occurred, both in the subgrade and base course layer, but the increasing rate and magnitude are higher in base course layer than the subgrade layer. This evidence supports that the geogrids can stabilize both the subgrade and the base course layer, but more in the base course. GE4 and GE7 have a converse result, and the reason could be caused by the geogrid location.

- The average earth pressure cell data in triaxial geogrid tests is higher than the biaxial geogrid tests. The comparison between test section GE1 and GE4 on the earth pressure cell data overall shows that under the same location and same thickness of the base course layer, the pressure in section GE4 in the base course is at least two psi higher than the pressure in the section GE1 on top of subgrade layer. The triaxial geogrid would have more effectiveness than the biaxial.

ACKNOWLEDGEMENTS

This manuscript is based upon work supported by the Minnesota Department of Transportation (MnDOT) under contract number 1034932 entitled "Effectiveness of Geotextile/Geogrids in Roadway Construction; Determine a Granular Equivalent (G.E.) Factor". The authors thank MnDOT for this support. The contents and views in this paper are those of the authors and do not necessarily reflect those of the funding agency.

REFERENCES

Abu-Farsakh, M. Y., and Chen, Q. (2011). “Evaluation of geogrid base reinforcement in flexible pavement using cyclic plate load testing.” *International Journal of Pavement Engineering*, 12(3), 275–288.

Al-Qadi, I. L., Brandon, T. L., Valentine, R. J., Lacina, B. A., and Smith, T. E. (1994). “Labtatory evaluation of geosynthetic-reinforced pavement sections.” *Transportation Research Record*, 1439.

Al-Qadi, I. L., Dessouky, S., Tutumluer, E., and Kwon, J. (2011). “Geogrid mechanism in low-volume flexible pavements: Accelerated testing of full-scale heavily instrumented pavement sections.” *International Journal of Pavement Engineering*, 12(2), 121–135.

Alimohammadi, H., Schaefer, V. R., Zheng, J., and Li, H. (2020a). “Performance evaluation of geosynthetic reinforced flexible pavement: a review of full-scale field studies.” *International Journal of Pavement Research and Technology*.

Alimohammadi, H., Zheng, J., Buss, A., Schaefer, V. R., Williams, C., and Zheng, G. (2020b). “Field and simulated rutting behavior of hot mix and warm mix asphalt overlays.” *Construction and Building Materials*, Elsevier, 265, 120366.

Alimohammadi, H., Zheng, J., Schaefer, V. R., Siekmeier, J., and Velasquez, R. (2020c). “Performance Evaluation of Geogrids in Flexible Pavement: A Review of Large-Scale Laboratory Studies.” *Transportation Geotechnics*.

Cuelho, E. V., and Perkins, S. W. (2017). “Geosynthetic subgrade stabilization – Field testing

and design method calibration.” *Transportation Geotechnics*, Elsevier Ltd, 10, 22–34.
Han, J., Zhang, Y., and Parsons, R. L. (2008). “Development of a Performance-Based Laboratory Test Method for Evaluating Geosynthetic-Soil Confinement.”
Ingios Geotechnics. (2020). “Integrated Mobile Accelerated Test System.” https://www.ingios.com.
Qian, Y., Han, J., Pokharel, S. K., and Parsons, R. L. (2013). “Performance of triangular aperture geogrid-reinforced base courses over weak subgrade under cyclic loading.” *Journal of Materials in Civil Engineering*, 25(8), 1013–1021.
Saghebfar, M., Hossain, M., and Lacina, B. A. (2016). “Performance of geotextile-reinforced bases for paved roads.” *Transportation Research Record*, 2580(2580), 27–33.
Siekmeier, J., and Casanova, J. (2016). “Geogrid Reinforced Aggregate Base Stiffness for Mechanistic Pavement Design.” *Minnesota Department of Transportation*, Report No. MN/RC 2016-24.
Zornberg, J. G. (2017). “Functions and Applications of Geosynthetics in Roadways.” *Procedia Engineering*, Elsevier Ltd, 298–306.
Zornberg, J. G., and Gupta, R. (2010). “Geosynthetics in pavements: North American contributions.” *9th International Conference on Geosynthetics - Geosynthetics: Advanced Solutions for a Challenging World, ICG 2010*, (December 2016), 379–400.

Geosynthetics Conference

Inverse Analysis Method on the Performance Evaluation of Geosynthetic Reinforcements in Highway Pavement on Expansive Soils

Debojit Sarker[1] and Jay X. Wang, Ph.D., P.E.[2]

[1]PhD Candidate, Program of Civil Engineering, Louisiana Tech University, Ruston, LA 71272; e-mail: dsa038@latech.edu
[2]Professor, Programs of Civil Engineering and Construction Engineering Technology, Louisiana Tech University, Ruston, LA 71272; e-mail: xwang@latech.edu

ABSTRACT

Sometimes a pavement deflects only because of seasonal volume change of expansive soils in the pavement subgrade. Engineering practitioners expect an implementable and straightforward analysis method for a geosynthetic-reinforced pavement subjected to the swelling/shrinkage issue of expansive clayey subgrade, in an effort to find the bending moment, shear force and tension force distributions through the reinforced pavement, which are induced from the volumetric changes of subgrade soils. The virtual load method (VLM) was proposed in the past following the Timoshenko beam theory to analyze geosynthetic-reinforced pavement on expansive soils. In the VLM, the unknown virtual distributed load was obtained in the way by applying the inverse theory for the identification of material parameters of the pavement-foundation system. It was seen that the selection of the number of material parameters to obtain virtual load significantly affects the accuracy of the structural properties of the pavement and tensile properties of the geosynthetics if the linear least square method is used. In this paper, a unique numerical scheme was proposed in the hopes of solving the issue. After a forward problem was solved numerically, the Timoshenko beam deflection was taken as a start-up for the inverse problem to back analyze the load applied to the pavement. Solutions from forward/backward examples have explicitly shown the accuracy achieved related to the bending moment in the pavement and tension in the geosynthetic reinforcements. The proposed methodology can be applied for an in-depth understanding of the geosynthetic function for the mitigation of longitudinal cracks on pavements caused by heave/shrinkage of expansive soils.

INTRODUCTION

In the USA, billions of dollars are spent every year to resolve the swelling related distresses on the highways over expansive soils (Al-Qadi et al. 2009). It is typically not feasible to avoid these soils because of the widespread distribution everywhere all over the USA (Snethen 1979). Usually, these soils show volumetric change because of the presence of swelling mineral, e.g., montmorillonite that swells or shrinks with the fluctuation of moisture content (Chen 2012). The highways constructed over these expansive soils are subjected to differential movement with seasonal wetting and drying. They can cause heave or shrinkage, which results in the development of cracks that are found prevalently on the surface of the pavements (Nelson et al. 2015). A few mitigation approaches, including chemical stabilization, compaction, moisture barriers, and pre-wetting, were developed over time to overcome this issue (Khan et al. 2018; Lytton et al. 2005; Sarker et al. 2021; Sebesta 2002). However, these methods sometimes miss the mark because of the unpredictability of the issue and the excessive expense of implementation. Traditional chemical

stabilization is financially reasonable up to a certain depth, while Ca-based stabilizers can lead to the formation of swelling minerals like ettringite within sight of sulfates (Chittoori et al. 2017; Puppala et al. 2018). As a solution to fix this segment of the highway, the authors proposed an adaptable mechanical system using geosynthetics that can moderate the uplift pressures from the expansive soils subgrade and protect the pavement surface.

Pavement structure is good in compression but weak in tension. Engineers added geosynthetics in layer to supplement this limitation of pavement. Significant research has been led to comprehend the effect of traffic loads on the performance of highways by incorporating geosynthetic within pavement layers (Perkins et al. 2005; Zornberg et al. 2017). However, performance measurement is not available to describe the effect of environmental loads (i.e., those resulting from subgrade volumetric changes) on highway performance. Many researchers have used characteristic models to simulate the behavior of reinforced pavement (Ghosh et al. 2017; Maheshwari et al. 2004; Shukla and Chandra 1994; Zhan and Yin 2001; Zhou et al. 2014). However, all these studies concentrated on a common forward problem. The analysis was performed at given external loads on the pavement, considered a reinforced Timoshenko beam, whose subgrade volume does not change significantly with variation in its moisture content. The Timoshenko beam theory cannot directly be applied for the case where deformation of geosynthetic-reinforced pavement is caused by the volume change of the subgrade, rather than a traffic load on the pavement.

Inverse problems in mechanics are formulated as a least-square output error minimization problem. In this research, viable strategies for both the forward and the inverse problems were described and numerically tested. The forward problem was formulated and solved by appropriate use of the boundary conditions combined with specialized algorithms. Effective implementation and parametrization of the structural analysis problem is a key issue for the development and testing of different techniques for the solution of the inverse problem (Stavroulakis 2013). Effective and automatic modeling and solution of geosynthetic-reinforced pavement on expansive soils for static loadings using boundary conditions were made for one-dimensional elastic structures with nonlinear interaction effects. To understand the performance of geosynthetic reinforcements in the pavement on expansive soils, after a forward problem was solved numerically for static loadings, the beam deflection was taken as a start-up for the inverse problem to back analyze the virtual load applied to the pavement. The virtual load, which is to be determined using inverse theory, is expressed as a Fourier series and is the function of the model parameter vector essentially regarded as an array of material parameters of the geosynthetic-reinforced pavement system. Once the model parameter vector is obtained, bending moments and shear forces in the pavement and tension in the geosynthetic layer can be calculated from the standard forward problem.

In this study, extensive computer implementation and parametric investigation of a numerical technique for the solution of the nonlinear least-squares problems which emerge during the investigation of the inverse (here the geosynthetic-reinforced pavement on expansive soils) problems have been performed. The optimization routines are either home-made programs or are taken from matrix analysis software packages (e.g., MATLAB). Numerical results demonstrate the performance of the applied strategies.

RESEARCH METHODOLOGY

In the analytical model, the pavement geometry was considered as symmetric to the centerline, as appeared in Figure 1. The geosynthetic-reinforced pavement was simulated as a reinforced Timoshenko beam on an elastic foundation. Timoshenko beam theory is referred to as the first-order shear deformation theory, which assumes that the transverse shear strain is consistent through the beam thickness. In this study, the Pasternak foundation model was adopted to simulate the subgrade soil because it considers the shear resistance of the reinforced pavement (Fwa et al. 1996). By adopting the Timoshenko beam theory to simulate pavement and the Pasternak model to simulate the foundation soil, we will be able to consider the effect of geosynthetic reinforcement. Finally, the inverse analysis will allow us to understand the mechanism of the initiation and propagation of the pavement cracks caused by heave or shrinkage of expansive soils subgrade.

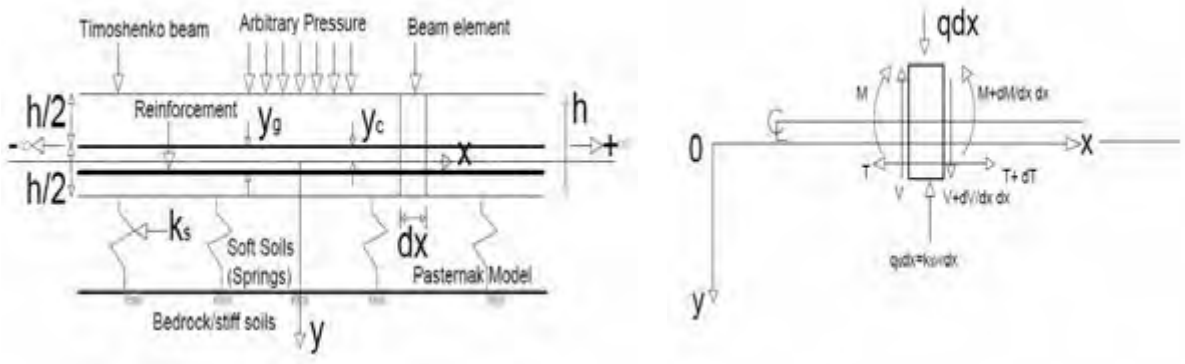

(a) (b)

Figure 1. (a) Schematic diagram of 1-D loaded beam supported on elastic foundation, (b) Relations among loading, shear force, bending moment and tension (Sarker et al. 2019).

Analytical solution. Figure 1(a) shows the reinforcement in a Timoshenko beam resting on an elastic foundation. Two independent variables are settlement *w* and rotation angle Φ. Let us consider a finite beam with a beam length of *L*, bending stiffness *D*, and shear stiffness *C*. The relationship between moment *M* and the rate of rotation angle change can be expressed as (Timoshenko 1921).

$$M = -D\frac{d\Phi}{dx} \tag{1}$$

Where Φ = rotation angle, and *D* is the bending stiffness. The relationship between shear force *Q* and shear deformation can be expressed as (Timoshenko 1921)

$$Q = C\left(\frac{dw}{dx} - \Phi\right) \tag{2}$$

Here, *C* is the shear stiffness of the geosynthetic-reinforced beam.

The vertical force equilibrium of the beam element in Figure 1(b) leads to

$$\frac{dQ}{dx} = k_s w - q \tag{3}$$

Where k_s is the spring constant in kN/m^3, and *q* is the arbitrary pressure on the beam and may be a function of *x*. From the moment equilibrium of the beam element, we get

$$\frac{dM}{dx} = Q \tag{4}$$

We take pressure q as the self-weight, any type of external load, or the virtual load that produces equivalent deflection as the heave or shrinkage-induced vertical deformations on the pavement, acting across the length of the beam. Load q can be expressed as a function of x, that is

$$q = f(x) \text{ for } 0 < x < L \tag{5}$$

Where $f(x)$ can be expressed as a Fourier cosine series.

$$q = \sum_{n=0}^{\infty} A_n \cos\left(\frac{n\pi x}{L}\right) \tag{6}$$

Using (1), (2), (3), (4), and (6), the governing differential equation for a reinforced Timoshenko beam on an elastic foundation can be expressed as (Wang et al. 2018; Yin 2000)

$$D\frac{d^4w}{dx^4} - \frac{k_s D}{C}\frac{d^2w}{dx^2} + k_s w = \sum_{n=0}^{\infty} A_n \left[1 + \frac{n\pi}{L}\frac{D}{C}\right]\cos\frac{n\pi x}{L} \tag{7}$$

The shear stiffness C can be expressed as (Cowper 1966)

$$C = kG_eA \tag{8}$$

Where G_e is the equivalent shear modulus of the reinforced beam, here, k is a reduction faction that depends on Poisson's ratio of the beam. Cross-sectional area A for a unit width can be written as $A = 1 \times h$. The reinforcement sheet, such as geotextile in the pavement, is not considered for shear force but usually is considered to take tension only. When reinforcement is considered taking shear force, the shear modulus G_e for shear stiffness can be expressed as

$$G_e = f(G) + f(G_g)\frac{A_g}{A} \tag{9}$$

Where G, G_g, and A_g are the shear modulus of the beam, shear modulus of the reinforcement, and cross-sectional area of the reinforcement, respectively. Yin showed that reinforcement tensile force T could be expressed as (Yin 2000)

$$T = -E_g(y_g - y_c)\frac{d\Phi}{dx} \tag{10}$$

Here, E_g, y_g, and y_c are Young's modulus of the reinforcement, location of reinforcement, and location of the neutral line.

Eq. 7 is the fourth-order nonhomogeneous linear differential equation. By solving Eq. 7, we can get the beam deflection w in terms of Fourier constant A_n. The solution of the differential equation is the summation of a homogeneous solution of the beam for any type of loading, e.g., a distributed load and a particular solution, which is the function of that load type. After obtaining the general solution for beam deflection w, we can obtain the equation for rotation Φ using Eqs. (1), (2), and (3), (4). Then, the equation of rate of rotation can be obtained to get the equation of bending moment and shear force using Eqs. 1 and 4, respectively.

Applying boundary conditions $M|_{x=0} = 0$, $Q|_{x=0} = 0$, $M|_{x=L} = 0$, and $Q|_{x=L} = 0$ to the equations of bending moment, and shear force, they can be written in the matrix form $[M]\{c\} = [R]$. Where, $\{c\} = [C_1\ C_2\ C_3\ C_4]'$, represents the four integral constants to be determined from the stated boundary conditions. Matrix **M** is a function of basic parameters such as α, β, L, k_s, D, I, and C, while **R** is a function of parameters for load q (e.g., $[a_1\ a_2 \dots a_n]$). Here, α and β are the characteristics of the system, and I is the moment of inertia of the beam. Following the similar mathematical manipulation done by Khan and Wang (2017), the general solution for deflection w

can be reduced into a set of a linear combination of equations. Eq. 11 shows the final matrix solution of the beam deflection. Here, matrix element $\mathbf{H_n}$ is a function of basic parameters such as α, β, L, k_s, D, I, and C.

$$[w(x)] = \left[\frac{1}{k_s}\ H_1\ H_2\ \ldots H_n\right]\begin{bmatrix} A_0 \\ a_1 \\ a_2 \\ \vdots \\ a_n \end{bmatrix} \tag{11}$$

A set of heave or shrinkage-induced vertical displacements caused by expansive soil subgrade indicated by w_P can be predicted based on the unsaturated soil mechanics or directly measured in the field. It is regarded as the observed output for the inverse problem. The calculated pavement (here, beam) deflection can be taken as w_B. The observation data can be related to the model estimated values at the predetermined points can be expressed by the following relationship

$$w_P = w_B(\ X \mid \zeta\ ) + \varepsilon \tag{12}$$

Where $\mathbf{X}$ represents the known input matrix.

$$X = \left(\chi_{ij}\right) \in \mathbb{R}^{m \times (n+1)} \tag{13}$$

Here, matrix element $\boldsymbol{\chi}$ is dependent on parameters such as α, β, L, k_s, D, I, and C.

Model parameter vector, $\zeta = \begin{bmatrix} A_0 \\ a_1 \\ a_2 \\ \vdots \\ a_n \end{bmatrix}$

And, ε is the error vector.

Here, the linear least square method is used, and the algebraic solution of the ordinary equation can be written as (Khan et al. 2020; Sarker et al. 2019)

$$\zeta = (\chi^T \chi)^{-1} \chi^T w_P \tag{14}$$

Once ζ is found, using Eq. 11, we can calculate the beam deflection produced by the virtual load along the cross-section of the pavement. Then, ζ can be used to obtain all the Fourier constants, and by employing Fourier constants in Eq. 6, we can obtain the virtual load imposed on the pavement caused by deflection w_P. After that, using matrix $\{c\} = [M]^{-1}[R]$, all the integral constants can be obtained. Finally, all the parameters will be identified; thus, rotation, moment, and shear force of the pavement and tensile force of the geosynthetic at any cross-section of the beam can be obtained. It was found that the selection of the number of the Fourier terms for the virtual load significantly affects the convergence of the bending moment on the pavement and tension imposed on geosynthetics when the linear least square method is used. The authors propose the following relationship to overcome the convergence issue.

$$m = \frac{L}{\Delta x} \approx n + 1 \tag{15}$$

PARAMETRIC STUDY

In this study, the geosynthetic-reinforced pavement is investigated. It is simplified as a reinforced Timoshenko beam on an elastic foundation. Parametric studies were performed by selecting a group of parameters, as given in Table 1, obtained from previous literature. These parametric studies will allow engineering practitioners to select different parameters of the pavement-

foundation system for evaluation, define the parameter range, specify the design constraints, and analyze the results of each parameter variation.

This study highlights the selection of the number of Fourier terms for the virtual load, which is regarded as an array of material parameters of the geosynthetic-reinforced pavement system. Additionally, the effect of shear stiffness of geosynthetic reinforcements is discussed to evaluate the performance of different types of geosynthetics. Distributions of bending moment and shear force through the reinforced pavement due to variation in geosynthetic shear stiffness are also presented. The structural properties, as defined in Table 1, were obtained from literature to compare the deflection calculated in this study. The Young's modulus E is taken to be 50,000 kPa. Researchers have investigated the applicability and reliability of spring constant k_s, which is known as modulus of subgrade reaction and can be determined using simplified empirical equations (Selvadurai 2013; Terzaghi 1955).

Table 1. Dimensions and properties of the pavement-foundation system.

Properties	Value	Properties	Value
Length of the pavement, L (m)	3	Bending stiffness, D (kN-m)	2,216.2
Thickness of the pavement, h (m)	0.64	Shear stiffness, C (kN/m) (Full G_g)	26,797.4
Load, q_0 (kPa)	1,000	Shear stiffness, C (kN/m) (Zero G_g)	10,457.5
Modulus of subgrade reaction, k_x (kN/m^3)	21,978	Location of the geosynthetic, y_g (m)	0.24

Table source: Yin (2000).

As a validation for the inverse method, the external loads from the forward method and the virtual load computed from the inverse method were plotted and compared. Figure 2 shows the deflection of the geosynthetic-reinforced pavement caused by a predetermined load applied on the pavement and the deflection caused by the virtual load. In the forward analysis, the deflection was caused by external load and plotted as "Wb_FDM". On the other hand, in the inverse analysis, the deflection was caused by the virtual load when deflection data obtained from the forward analysis was taken as input and plotted as "Wb_LLS". The maximum deflection caused by external load was obtained by 3.73 mm while taking this deflection data as input in the inverse model produces a virtual load that causes maximum deflection of 3.50 mm. The percent error between "Wb_FDM" and "Wb_LLS" was 6.2%. However, percent error could be reduced by increasing the number of Fourier terms as the first five terms of Fourier constants were considered in this case for inverse analysis.

Loading, Shear force, and bending moment distribution along the geosynthetic-reinforced pavement cross-section resulted from forward and inverse analysis methods that were plotted in Figures—3, 4, and 5, respectively. It can be observed from Figure 3 that the computed virtual load gets closer to the external load when the number of Fourier terms is increased. In Figures 4 and 5, "FDM" represent the results obtained from the forward analysis or due to applied external load on the pavement. In comparison, "LLS" represent the results obtained from the inverse analysis or due to virtual load. Shear forces and bending moments were calculated for different Fourier terms such as 4, 8, 15, and 100. It can be observed from Figure 5 that the number of Fourier terms for

the virtual load significantly affects the convergence of the bending moments at the beam (here, pavement) boundary when the linear least square method (LLS) is used. Using $\Delta x = 0.03$ in Eq. 15, it can be observed from Figure 5 that, for 100 Fourier terms the bending moment distribution converges well.

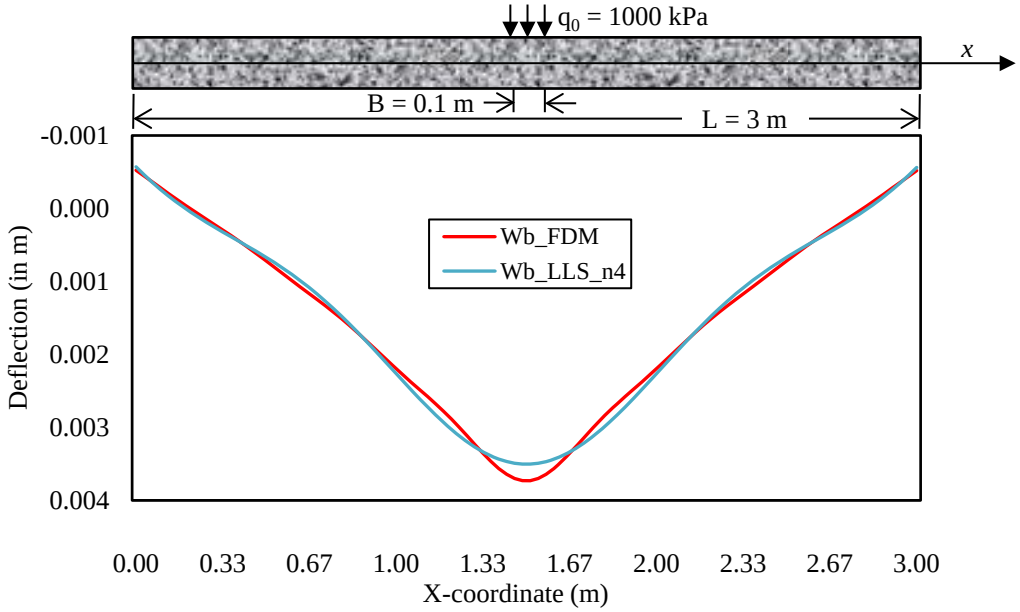

Figure 2. Deflection along the cross-section of the reinforced pavement.

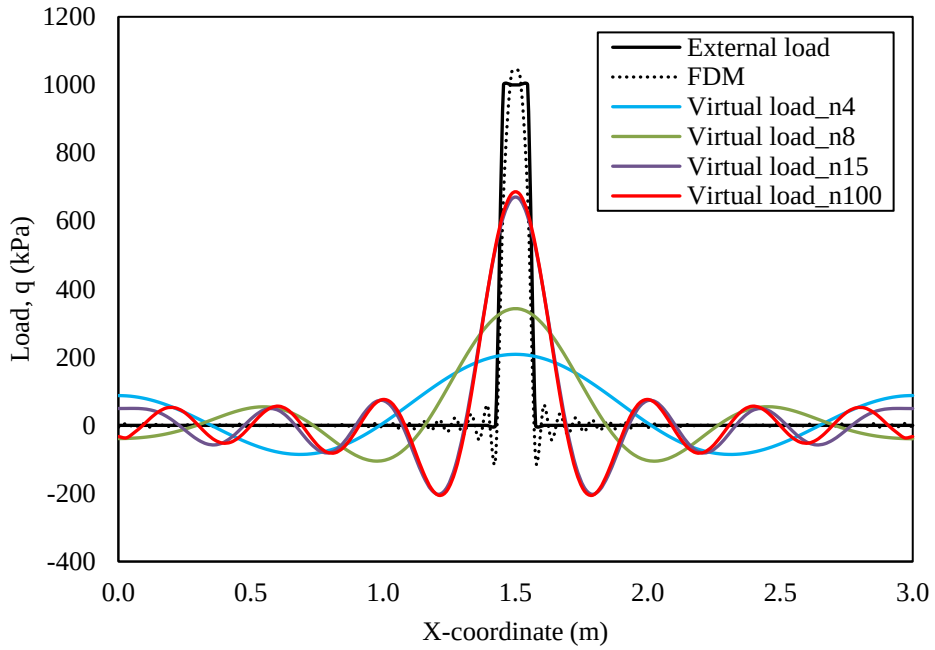

Figure 3. Load distribution along the cross-section of the reinforced pavement.

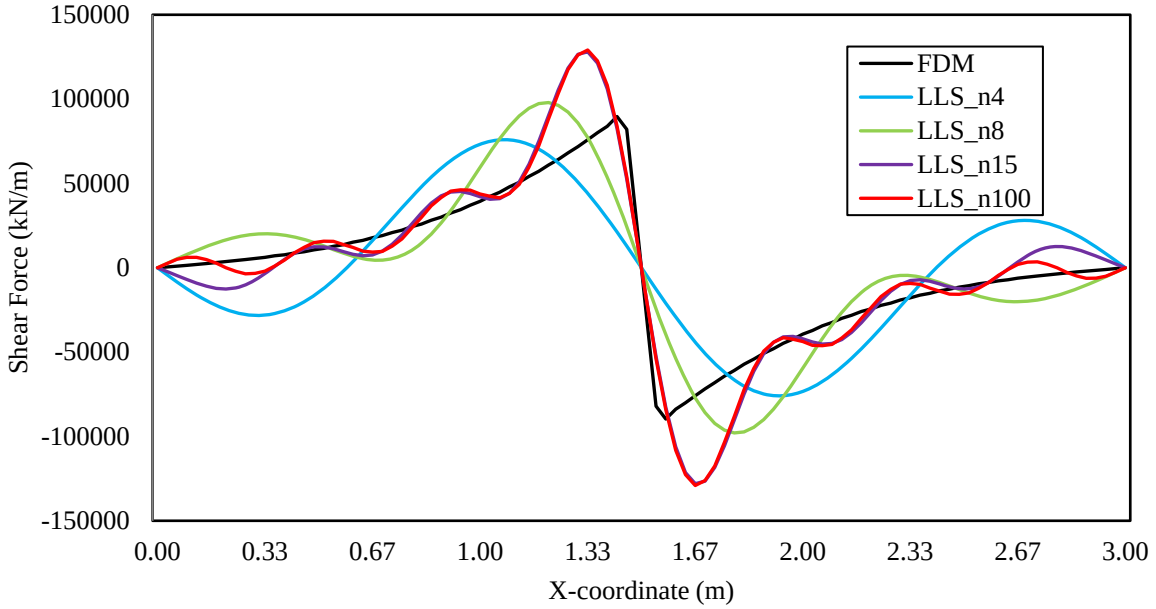

Figure 4. Shear force distribution along the cross-section of the reinforced pavement.

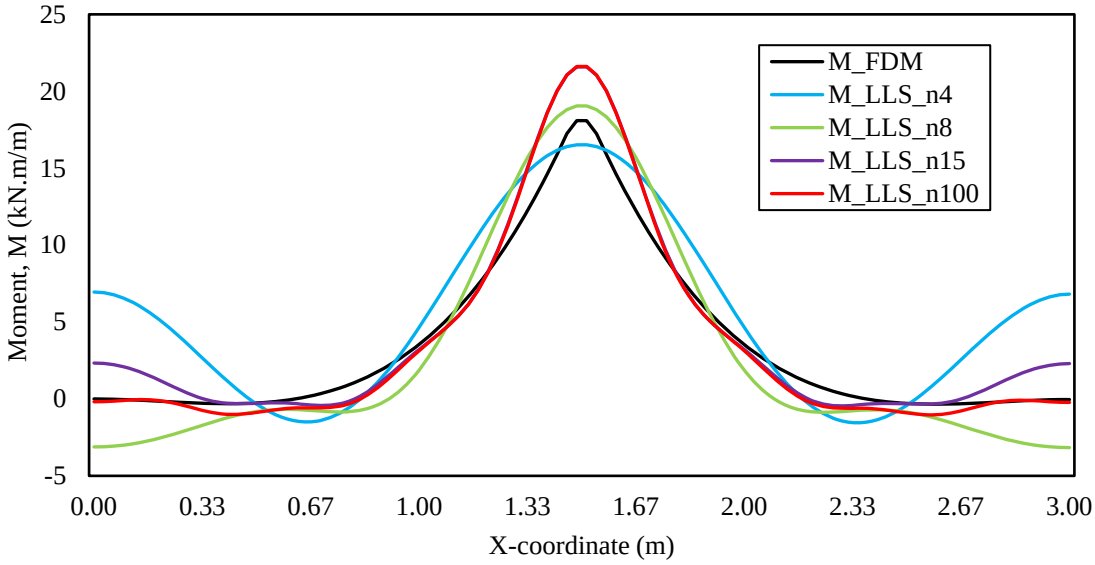

Figure 5. Moment distribution along the cross-section of the reinforced pavement.

The effects of geosynthetic shear stiffness G_g were investigated in this parametric study research, and different outcomes were plotted in Figure 6. Typically, geotextiles are not considered to take shear force but tension only. The geosynthetic shear stiffness G_g was assumed to be zero for this case and plotted as "Zero G_g" (see Figure 6). Then again, geogrid sheets may be considered to take shear force in addition to tensile force. So, for the geogrid case, their shear stiffness was fully considered and plotted as "Full G_g" in Figure 6 as well.

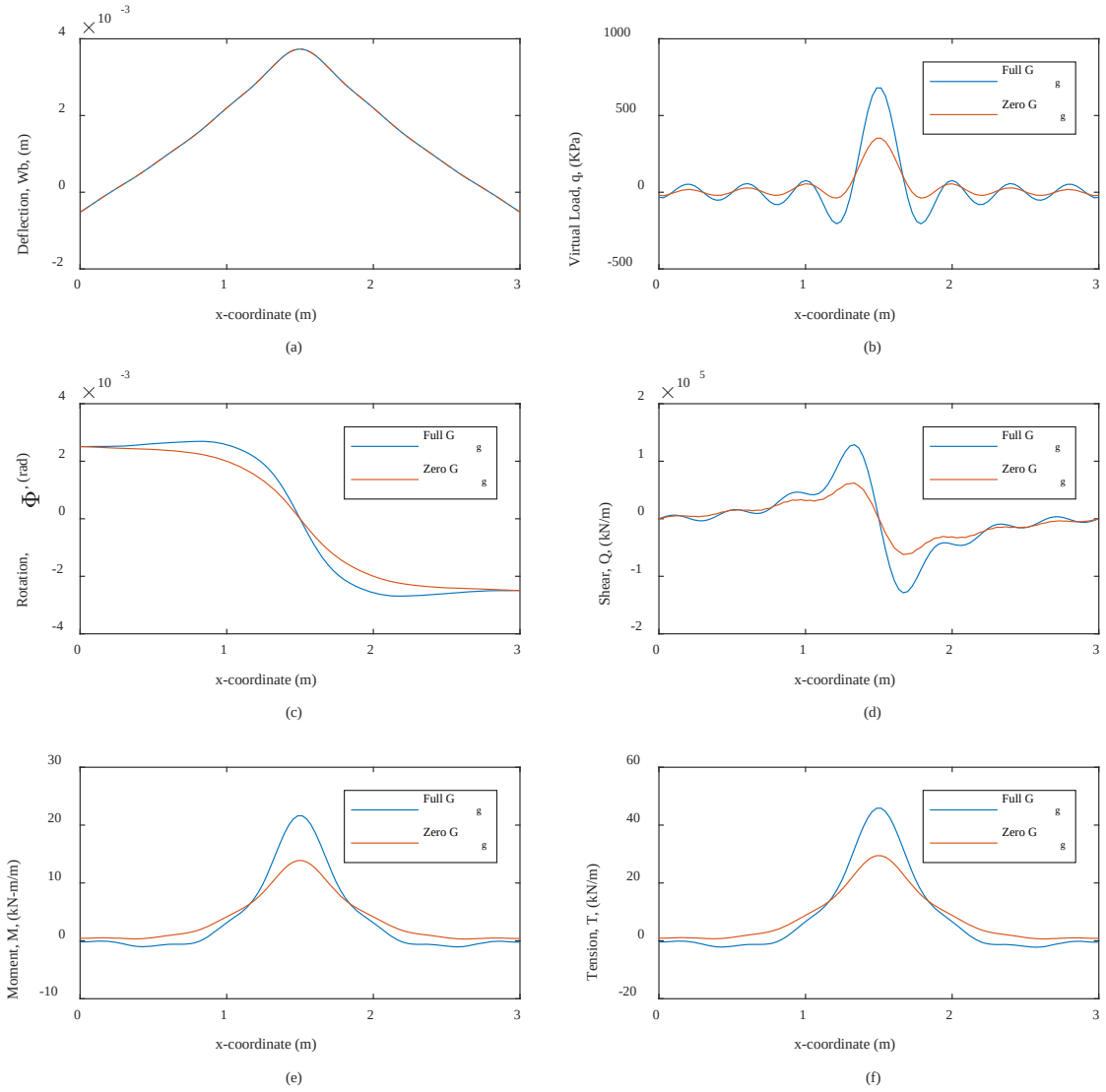

Figure 6. (a) Deflections, (b)Virtual load, (c) Rotation, (d) Shear force, and (e) Bending moment distribution in the pavement, and (f) Tension in the geosynthetic reinforcements.

As indicated above, in the inverse method, performance analyses of a geosynthetic-reinforced pavement on expansive soils requires the input of deformation of the subgrade in the formulations. Researchers investigated field moisture content and soil suction potentials of expansive subgrades and identified the potentials at which soil and pavement cracking occur (Ahmed et al. 2018; Fernandes et al. 2015; Puppala et al. 2012; Sarker and Wang 2021; Zornberg et al. 2010). Numerous methods have been proposed to calculate heave or shrinkage of the expansive soils from moisture content variations. The virtual distributed load causes geosynthetic-reinforced pavement deflection equivalent to heave or shrinkage-induced deformations of the subgrade. As an example of the geosynthetic-reinforced pavement on elastic foundation model, a forward problem was solved numerically for an external load of 1000 kPa. To demonstrate the performance evaluation of geosynthetic reinforcements in pavement on expansive soils, the Timoshenko beam deflection was taken as input for the inverse problem to back-calculate the load

applied to the pavement. Virtual loads, rotations, shear forces and bending moment on the cross-sections, and tensile forces through the geosynthetic reinforcement along the pavement width direction are plotted in Figure 6. The critical values of shear force and bending moment on pavement and tension forces through the geosynthetics can be obtained from Figure 6.

Results with the condition of Zero Gg are for the geotextile condition, and Full Gg is for the geogrid condition. From Figure 6(a), it can be observed that the calculated Timoshenko beam deflections from the virtual loads agreed well with the results obtained from the forward analysis. Figure 6(b) shows the increase in virtual load is about 48% for the geogrid-reinforced pavement section compared to the geotextile-reinforced section. It is interesting to indicate that geogrid-reinforced pavement could take a much greater load than geotextile-reinforced pavement under the same deflection condition caused by the heave/shrinkage of expansive subgrade soils. It is found that, for the geogrid-reinforced pavement, the maximum shear force was 52% higher than that for the geotextile-reinforced pavement, the maximum bending moment 36% higher, and the maximum tension force 37% higher. It can be presumed that the geosynthetic-reinforced pavement deflection initiated from subgrade (e.g. volume change of expansive soils) may resist more shear force or bending moment when the geosynthetic shear stiffness is considered. The tension without considering geosynthetic shear stiffness is smaller than the case where geosynthetic shear stiffness is considered.

CONCLUSION

In this research, an inverse-based analytical model was proposed to evaluate the structural performance of geosynthetic reinforcements in the pavement on expansive soils following the Timoshenko beam theory by incorporating the volume change of subgrade in formulations. A practical, robust, and rapid method for the solution of inverse problems associated with geosynthetic-reinforced pavement on expansive soils was being developed. Numerical results have shown the efficiency of the proposed model to overcome the convergence problem related to bending moment on the pavement and tension on geosynthetic reinforcements. The effects of geogrid and geotextile reinforcement on the performance of pavement on expansive soils were investigated. The study suggests the superior performance of geogrid over geotextile to moderate the uplift pressure from the expansive soils subgrade for protecting the pavement surface. Nevertheless, the method does appear promising and, given data of sufficient precision, will allow for substantial new developments in the geosynthetic industry. This study will allow the geotechnical and pavement engineers to design the geosynthetic-reinforced pavement on expansive soils by integrating volume change-induced deformations of the subgrade in the model.

ACKNOWLEDGEMENT

This work was supported by the Geosynthetic Institute with a 2020-21 GSI Fellowship grant under contract No. 32-4116-65048 at Louisiana Tech University.

REFERENCES

Ahmed, A., Hossain, M. S., Bin Alam, M. J., and Khan, M. S. (2018). “Moisture and Matric Suction Behavior in Unsaturated Subgrade through Field Instrumentation and Numerical Modeling.” *PanAm Unsaturated Soils 2017*, American Society of Civil Engineers, Reston,

VA, 226–235.
Al-Qadi, I. L., Buttlar, W., Baek, J., and Kim, M. (2009). *Cost-effectiveness and performance of overlay systems in Illinois volume 1: effectiveness assessment of HMA overlay interlayer systems used to retard reflective cracking*. Illinois Center for Transportation (ICT).
Chen, F. H. (2012). *Foundations on Expansive Soils*. Elsevier.
Chittoori, B., Tamim, M. M., Gajurel, A., and Mishra, D. (2017). "Evaluating the ability of swell prediction models to predict the swell behavior of excessively high plastic soils." *PanAm Unsaturated Soils 2017*, 177–189.
Cowper, G. R. (1966). "The Shear Coefficient in Timoshenko's Beam Theory." *Journal of Applied Mechanics*, 33(2), 335.
Fernandes, M., Denis, A., Fabre, R., Lataste, J.-F., and Chrétien, M. (2015). "In situ study of the shrinkage-swelling of a clay soil over several cycles of drought-rewetting." *Engineering Geology*, 192, 63–75.
Fwa, T. F., Shi, X. P., and Tan, S. A. (1996). "Use of Pasternak foundation model in concrete pavement analysis." *Journal of transportation engineering*, American Society of Civil Engineers, 122(4), 323–328.
Ghosh, B., Fatahi, B., Khabbaz, H., and Yin, J.-H. (2017). "Analytical study for double-layer geosynthetic reinforced load transfer platform on column improved soft soil." *Geotextiles and Geomembranes*, Elsevier, 45(5), 508–536.
Khan, M. A., and Wang, J. W. (2017). "Application of Euler-Bernoulli Beam on Winkler Foundation for Highway Pavement on Expansive Soils." *Proc., PanAm-UNSAT 2017: Second Pan-American Conference on Unsaturated Soils, ASCE. (Accepted)*.
Khan, M. A., Wang, J. X., and Sarker, D. (2018). "Stabilization of Highly Expansive Moreland Clay Using Class-C Fly Ash Geopolymer (CFAG)." *IFCEE 2018*, American Society of Civil Engineers, Reston, VA, 505–518.
Khan, M. A., Wang, J. X., and Sarker, D. (2020). "Development of Analytic Method for Computing Expansive Soil–Induced Stresses in Highway Pavement." *International Journal of Geomechanics*, 20(2).
Lytton, R., Aubeny, C., and Bulut, R. (2005). *Design procedure for pavements on expansive soils*. Texas Transportation Institute, Texas A & M University System.
Maheshwari, P., Basudhar, P. K., and Chandra, S. (2004). "Analysis of beams on reinforced granular beds." *Geosynthetics International*, 11(6), 470–480.
Nelson, J. D., Chao, K. C., Overton, D. D., and Nelson, E. J. (2015). *Foundation Engineering for Expansive Soils*. Wiley Online Library.
Perkins, S. W., Bowders, J. J., Christopher, B. R., and Berg, R. R. (2005). "Geosynthetic reinforcement for pavement systems: US perspectives." *International Perspectives on Soil Reinforcement Applications*, 1–13.
Puppala, A. J., Manosuthkij, T., Nazarian, S., Hoyos, L. R., and Chittoori, B. (2012). "In situ matric suction and moisture content measurements in expansive clay during seasonal fluctuations." *Geotechnical Testing Journal*, ASTM International, 35(1), 74–82.
Puppala, A. J., Talluri, N., Congress, S. S. C., and Gaily, A. (2018). "Ettringite induced heaving in stabilized high sulfate soils." *Innovative Infrastructure Solutions*, Springer, 3(1), 72.
Sarker, D., Apu, O. S., Kumar, N., Wang, J. X., and Lynam, J. G. (2021). "Application of Sustainable Lignin Stabilized Expansive Soils in Highway Subgrade." *International Foundations Congress & Equipment Expo (IFCEE 2021)*, (Accepted), Dallas, TX.
Sarker, D., and Wang, J. X. (2021). "Experimental Study on Soil Water Retention Properties of

Compacted Expansive Clay." *4th International Conference on Transportation Geotechnics (ICTG 2021)*, (Accepted), Chicago, IL.

Sarker, D., Wang, J. X., and Khan, M. A. (2019). "Development of the Virtual Load Method by Applying the Inverse Theory for the Analysis of Geosynthetic-Reinforced Pavement on Expansive Soils." *Geo-Congress 2019: Geotechnical Materials, Modeling, and Testing*, American Society of Civil Engineers, Reston, VA, 326–339.

Sebesta, S. (2002). *Investigation of maintenance base repairs over expansive soils: Year 1 report*. Texas Transportation Institute, Texas A & M University System.

Selvadurai, A. P. S. (2013). *Elastic analysis of soil-foundation interaction*. Elsevier.

Shukla, S. K., and Chandra, S. (1994). "A generalized mechanical model for geosynthetic-reinforced foundation soil." *Geotextiles and Geomembranes*, 13(12), 813–825.

Snethen, D. R. (1979). *Technical guidelines for expansive soils in highway subgrades*.

Stavroulakis, G. E. (2013). *Inverse and crack identification problems in engineering mechanics*. Springer Science & Business Media.

Terzaghi, K. (1955). "Evaluation of Coefficient of Subgrade Reaction." *Geotechnique, London*, 5(4), 41–50.

Timoshenko, S. P. (1921). "LXVI. On the correction for shear of the differential equation for transverse vibrations of prismatic bars." *The London, Edinburgh, and Dublin Philosophical Magazine and Journal of Science*, Taylor & Francis, 41(245), 744–746.

Wang, J. X., Sarker, D., and Ikra, B. (2018). *Development of a Mechanistic-based Design Method for Geosynthetic-Reinforced Pavement on Expansive Soils and Prediction of Moisture Content Fluctuations in Subgrades*. Southern Plain Transportation Center, Norman, OK.

Yin, J.-H. (2000). "Closed-Form Solution for Reinforced Timoshenko Beam on Elastic Foundation." *Journal of Engineering Mechanics*, 126(8), 868–874.

Zhan, C., and Yin, J. H. (2001). "Elastic Analysis of Soil-Geosynthetic Interaction." *Geosynthetics International*, 8(1), 27–48.

Zhou, W.-H., Zhao, L.-S., and Li, X.-B. (2014). "Analytical study for geosynthetic reinforced embankment on elastic foundation." *Ground Improvement and Geosynthetics*, 444–451.

Zornberg, J. G., Gupta, R., and Ferreira, J. A. Z. (2010). "Field performance of geosynthetic reinforced pavements over expansive clay subgrades." *9th International Conference on Geosynthetics*, Guarujá, Brazil, 1481–1484.

Zornberg, J. G., Roodi, G. H., and Gupta, R. (2017). "Stiffness of Soil–Geosynthetic Composite under Small Displacements: I. Model Development." *Journal of Geotechnical and Geoenvironmental Engineering*, 143(10), 04017075.

Geosynthetics Conference

Life-Cycle Cost Analysis of Geotextile Separator Layer in Low-Volume Secondary Pavement

Chaz Weaver, PE, CPEM[1] and Audrey Moruza[2]

[1]Virginia Department of Transportation, 811 Commerce Road, Staunton, VA 24401; e-mail: Chaz.Weaver@VDOT.Virginia.gov
[2]Virginia Department of Transportation, 530 Edgemont Road, Charlottesville, VA 22903; e-mail: Audrey.Moruza@VDOT.Virginia.gov

ABSTRACT

The goal of ASCE's Grand Challenge is to reduce the life-cycle cost of civil engineered infrastructure by 50% by the year 2025. Currently there are no life-cycle cost analysis models that are designed to evaluate the highway agency budget benefits of geotextile separators in paved roads. To address this gap for the Virginia Department of Transportation (VDOT), life-cycle cost analysis was performed on two common secondary road designs, each with the options of separator geotextile and preventive maintenance, using three plausible rates of subbase contamination. The benefit of geotextile is modeled narrowly as slowing of depth loss of the aggregate layer caused by fines migrating from the subgrade. In each scenario, the 50-year discounted costs of a pavement designed with a geotextile layer are compared with those of an analogous but geotextile-free pavement. The cost analysis required development of conceptual pavement layer deterioration curves that reflect differentiated subbase deterioration due to fines infiltration. The contamination rates used are consistent with established literature on (1) the interaction of traffic loading and aggregate layer contamination and (2) the response of pavement resilient modulus to contamination of the aggregate layer. Under two treatments of the residual value of the pavements at the end of the analysis period, the results indicate that separator geotextile would likely deliver long term cost-effectiveness to asphalt pavements when subgrade fines contamination rates reach 0.1 inch per year and greater.

INTRODUCTION

Although geotextiles are used widely in road design in the U.S., a purely mechanistic life-cycle cost analysis for a geotextile separator layer in a paved road has yet to be published in public literature. A "traffic benefit ratio" resulting from incorporation of geotexile (GTX) separator layers in paved roads was demonstrated 25 years ago (Al Qadi et al. 1994) and consistent findings followed in subsequent research (Perkins 2001, Al-Qadi and Appea 2003). Life-cycle cost analysis (LCCA) was subsequently performed for 25 hypothetical secondary pavements with varying traffic levels, reflecting secondary roads in the Commonwealth of Virginia designed under 1993 AASHTO pavement design guidelines (Yang and Al-Qadi 2007). Yang and Al-Qadi compared agency and user costs for GTX-free AASHTO pavements against the costs of pavements containing GTX designed as earlier proposed by Al Qadi for pavement stabilization and separately by Perkins for pavement reinforcement. The results indicated that the incorporation of GTX could save an agency up to 40%, but might also break even with the agency cost of a GTX-free pavement.

Pennsylvania DOT (PennDOT) recently published laboratory findings that quantified the benefit of GTX separation using one-third scale pavement models under simulated loading (Xiao et al. 2016). In presentations derived from this work, PennDOT showed cost savings of 13% to 15% due to separation GTX in a collector road (Petrasic 2017). The PennDOT model used *AASHTO Guide for Design of Pavement Structures* (AASHTO 1993) for all pavement designs and assumed no reinforcing function from GTX. Unlike the VDOT model described in this study, the PennDOT study compared the costs of GTX with the costs of increasing subbase thicknesses, assuming the absence of GTX allowed a 50% loss of subbase strength and a 20% loss in subgrade strength (i.e., in their model the soil California Bearing Ratio (CBR) declined as contamination proceeded). PennDOT contrasted the costs of alternative strategies at the conclusion of a 20-year period of service by inflating future costs forward to the analysis termination point.

The LCCA model developed in this study, following principles consistent with published guidance (Babashamsi et al 2016), compared two pavement design options for low-volume secondary roads in Virginia, each subject to four alternative scenarios: with or without separation GTX, and with or without preventive maintenance activities. Each scenario was analyzed under three contamination rates. Thus, the analysis covered 24 hypothetical scenarios (2 pavement designs x 4 GTX and/or preventive maintenance options x 3 contamination rates). The pavements were evaluated at 5-year intervals for potential maintenance needs, and the total costs of alternative pavement designs and options were discounted from the end of the analysis period to the present for comparison.

LCCA results depend directly on the 50-year maintenance schedules for each pavement scenario. Each scenario's maintenance schedule responds directly to initial pavement design, pavement layer deterioration curve characteristics, contamination rate of the aggregate layer by subgrade fines, and regular estimates of remaining pavement design life that trigger condition-responsive maintenance services. Unit costs used for the LCCA results are derived from VDOT construction records over the period 2008-2018 and reflect awarded bids.

PAVEMENT DESIGN

The two pavement design options (very low Average Annual Daily Traffic (AADT) and low AADT) are consistent with VDOT's Materials Division Memorandum of Instruction Chapter 6 (VDOT 2018). They were created by means of AASHTO (1993) design method in conjunction with the design input values shown in Table 1. Initial design year is 2020 (end of construction). AADT and truck percent of AADT presented in Table 1 for the two pavement designs correspond to typical low-volume roadways in Virginia. The subgrade resilient modulus value is equivalent to a CBR value of 3.3.

Initial pavement service life of 20 years was considered realistic for both AADT levels with SuperPave surface mix on a secondary road in Virginia, consistent with reduced maintenance on the secondary system. Separation GTX was assumed to provide benefits consistent with the recent findings of Hoppe et al. (Hoppe et al 2019). Specifically, GTX prevents pavement deterioration caused by contamination of the aggregate layer by the migration of subgrade fines.

Table 1. Pavement design input values for two low-volume secondary roads

Inputs	Values	
Average Annual Daily Traffic (2020)	1500[a]	155[a]
Tractor Trailers (%)	5.0[a]	1.0[a]
Single Unit Trucks (%)	1.0[a]	0[a]
Performance Period (years)	20	
AADT Growth Rate (%)	2.0[a]	
Trucks in Design Direction/Lane (%)	50/100	
Equivalent Single Axle Load Factor	Car: 0.0002 Single Unit Truck: 0.46 Tractor Trailer: 1.05	
Initial Serviceability	4.0	
Terminal Serviceability	2.5	
Reliability (%)	75	
Overall Standard Deviation	0.49	
Subgrade Resilient Modulus (psi)	5000[a]	

[a] Values assumed for the initial pavement design; all other values in accordance with VDOT Materials MOI, Chapter 6 for Farm to Market Secondary Route

DETERIORATION CURVES

Empirical pavement layer deterioration curves with and without GTX are not available in public literature. Therefore hypothetical deterioration curves were constructed for this analysis, preserving underlying principles of AASHTO (1993). Structural coefficients for surface, intermediate, and base layer asphalt mixes were based on remaining life factors established in AASHTO *(*1993), recognizing the fundamental tradeoff between Condition Factor and Remaining Life established in the best-fit curve from the AASHO road tests.

It is generally accepted, however, that bound pavement materials do not deteriorate suddenly to the structural coefficient of zero even without the presence of GTX. Furthermore, engineering experience and consensus regarding the function of GTX (Hoppe et al., 2019) suggest that pavement damage resulting from aggregate contamination can be conceptualized in two equivalent ways: (1) aggregate layer thickness remains the same but the structural coefficient of the aggregate layer decreases over time (Figure 1(a)), or (2) the structural coefficient of the aggregate layer remains the same but the thickness of the aggregate layer diminishes with time (Figure 1(b)). The second method was selected for this study because it facilitates simplicity in pavement deterioration calculations.

The accepted mechanisms of pavement layer deterioration when there is no GTX separation layer are summarized in the interaction modeled between the base and surface layers: first, the asphalt base mix undergoes stripping and deterioration due to loss of aggregate subbase thickness; second, asphalt surface mix durability responds differentially to competent versus poor asphalt base mixes. Figure 2 illustrates these interactive layer mechanisms.

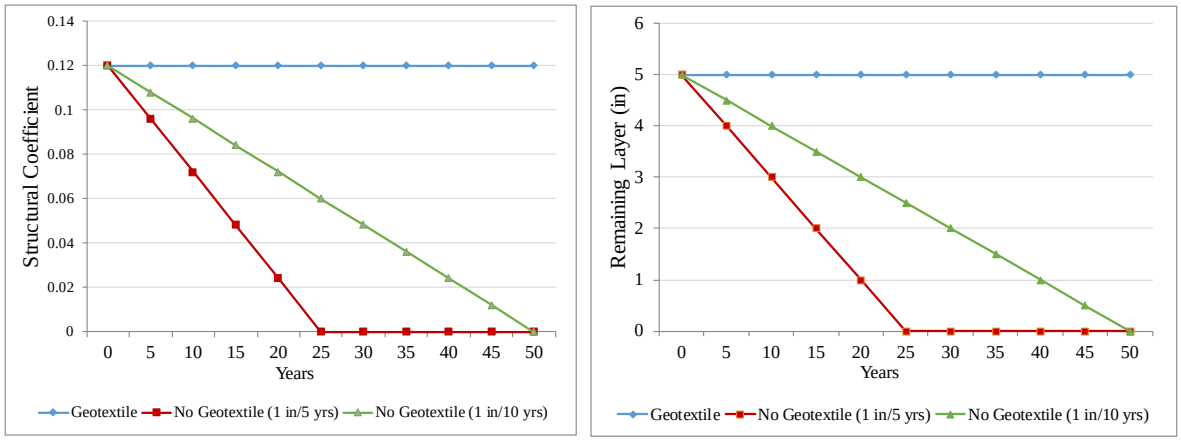

(a) **(b)**

Figure 1. Conceptualizations of pavement damage: (a) structural coefficient response to aggregate contamination; (b) layer thickness response to aggregate contamination.

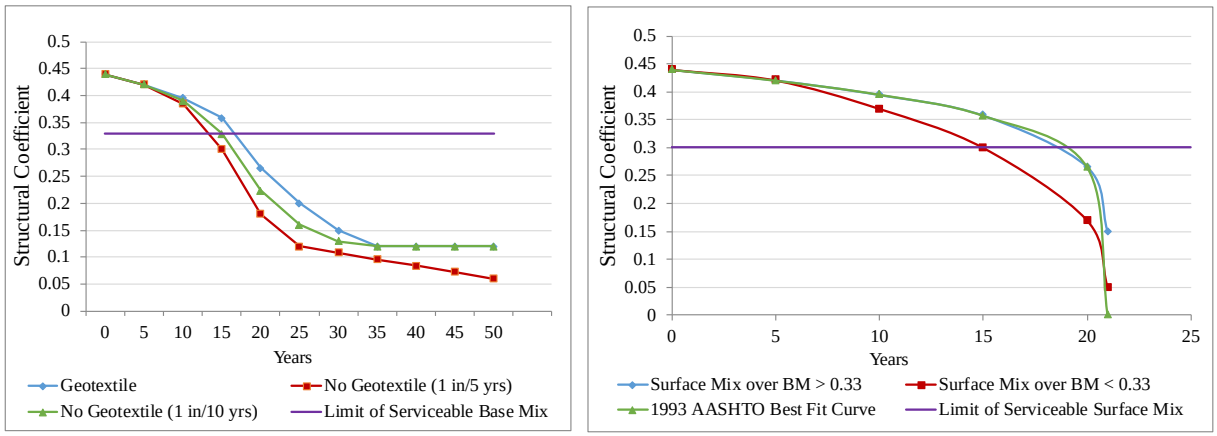

(a) **(b)**

Figure 2. Pavement layer deterioration curves developed for LCCA: (a) base mix deterioration curve; (b) surface mix deterioration curve.

The curves in Figure 2 reflect specific assumptions of the LCCA: all asphalt mixes have an initial structural coefficient of 0.44, consistent with VDOT's Manual of Instruction; base mix deterioration is more rapid for an aggregate layer with infiltrated fines, reflecting pavement damaging mechanisms that depend on pore water increase and potential stripping; surface mix condition over an asphalt base with structural coefficient less than 0.33 deteriorates faster than over an asphalt base with structural coefficient greater than 0.33; surface mix structural coefficient less than 0.30 triggers a higher-level maintenance intervention; surface mixes on low-volume secondary roads degrade over a period of 20 years while base and intermediate mixes degrade over a period of 30 years, as reflected in empirical maintenance practice at VDOT; surface asphalt service life in all scenarios was set at 20 years to reflect typical mix serviceability and reduced maintenance on the secondary roadway system; finally, no structural benefit results from the presence of separation GTX.

CONTAMINATION RATES

VDOT does not currently require the use of GTX in any of its pavement designs and therefore has no benchmark rates of aggregate contamination by subgrade fines. Yet to estimate the potential fiscal benefits of GTXs, the adopted pavement layer deterioration curves require identification of plausible absolute rates of contamination (i.e., inches/year) to trigger the deterioration mechanism of aggregate thickness reduction.

In two recent reports, a comprehensive contract study for PennDOT (Xiao et al. 2016) and a derivative report in Kermani et al. (2019), accelerated pavement testing equipment (MMLS3, model mobile load simulator at 1/3 scale) was used to quantify rates of subgrade fines penetration into aggregate subbase. Selected parameters of the PennDOT study are shown in Table 2 in comparison with typical VDOT values:

Table 2. Comparison of Pennsylvania DOT study parameters to typical Virginia DOT values.

Parameter	PennDOT Study	VDOT
Subgrade Soil		
Soil Type	A-4 (ML)	A-4, A-6, A-7-5, -7-6 ML, CL, MH, CH
Fines Content	55.9%	35 – 100%
Density	AASHTO T 180 Proctor	AASHTO T 99 Proctor
Soaked CBR	5 (initial)	3 to 8
Saturation	Inundated	Variable
Aggregate		
Fines Content	6.5%	4 – 7% (2-9%)[a] (No. 21B) 6 – 12% (4-14%)[a] (No. 21A)
Max Aggregate Size	---	1 inch
Pavement Structure		
Aggregate Subbase	6 inches	8 inches (155 AADT); 5 inches (1500 AADT)
Asphalt	8.5 inches	1.5 inches (155 AADT); 6.0 inches (1500 AADT)

[a] VDOT production tolerance

The results from the PennDOT study indicate that fines contamination of the aggregate subbase layer begins almost immediately and increases with increasing “cycles”, which for the modeled collector road section of the studies was equatable with Equivalent Single Axle Loads (ESALs) (Xiao et al. 2016; Kermani et al. 2019).

An earlier study demonstrated that, starting with aggregate already containing 5.5% fines, the resilient modulus of an aggregate subbase drops precipitously at approximately 13.5% fines content (Jorenby and Hicks 1986). Given VDOT No. 21B production tolerances shown in Table 2, *additional* fines content of 7% was identified as a conservative contamination level sufficient for a potentially abrupt loss of resilient modulus in VDOT aggregate No. 21B. (Note: Table 2 indicates that VDOT No. 21A aggregate can reach 13.5% fines while within its production

tolerances, and thus the level of contamination of No. 21A aggregate that could suddenly impair resilient modulus is lower than the corresponding contamination level for No. 21B).

Based on the best linear fit relationship between pavement loadings in ESALs and full depth laboratory contamination findings in Kermani et al. (2019), Kermani's laboratory findings are (1) extended to higher contamination rates and (2) scaled from the modeled collector facility design of Kermani et al. to the two low-volume pavement designs in the LCCA, as described in Table 2. Figure 3 shows the resulting plots for ESAL-to-percent of full-depth contamination.

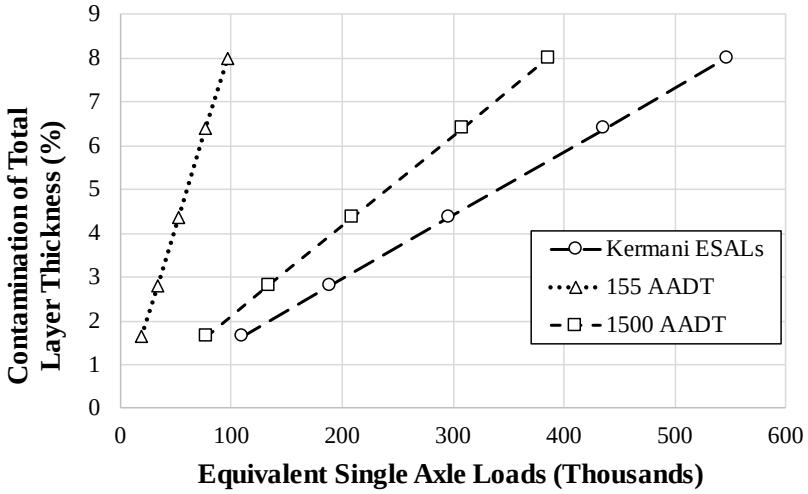

Figure 3. Kermani et al. (2019) collector roadway loadings, LCCA secondary road loadings, and resulting contamination of total layer thickness (%).

Combined, the findings of Kermani and Jorenby and Hicks provide a check on the range of absolute contamination rates used in this study. Back-calculating using AASHTO (1993), the pavements in the present study with initial AADT of 155 and 1500 would reach full-aggregate depth fines contamination of 7% by about 94 years and 18 years after construction, respectively, assuming 2% annual traffic growth. The corresponding absolute annual rates of contamination are calculated at 0.064-in and 0.341-in, respectively. This range nearly overlaps the range of absolute contamination rates used in the present LCCA model, 0.05-0.2-in. per year, and indicates its reasonableness for VDOT aggregate and typical VDOT pavement structures.

Yet it is important that the threshold contamination percentages of fines indicate *the point at which the aggregate layer loses resilient modulus* rather than the time when contamination initiates. In fact, without a GTX separator, the aggregate subbase layer is subjected to contamination practically at initial traffic loading. Below the threshold value of 7%, the aggregate is contaminated to some degree; above the 7% threshold, the aggregate has probably lost nearly *all* of its resilient modulus and exhibits behavior similar to the underlying subgrade soil.

It should be noted that the ESAL loadings shown in Figure 3 are applied while the subgrade soil *is saturated*. Therefore if the subgrade is saturated only half of its life, full-depth contamination will be approximately half of that shown in Fig. 3. Actual saturation over a pavement's service life, however, is typically unquantifiable at the time of construction.

REMAINING DESIGN LIFE

The estimated remaining design life (ERDL) value of each pavement structure in the current year is determined by the maintenance history. In turn, the calculated ERDL determines the choice of pavement maintenance activities in the current year. To calculate ERDL, each pavement scenario in the LCCA is evaluated with the AASHTO (1993) pavement design model at 5-year intervals, starting 10 years after construction (i.e., year 10). Using the pavement design inputs in Table 1 and following AASHTO (1993) pavement design methods (per VDOT Materials Manual of Instructions, Chapter 6), Performance Period is iteratively determined at year *i* by four steps:

1. Increase traffic level by 2% each year up to the current year (year *i*);
2. Reduce the structural coefficients of the asphalt layers per Figures 2(a) and (b) to capture the state of pavement deterioration in the current year;
3. Reduce aggregate layer thickness (if no GTX present) consistent with the scenario contamination rate (in./yr.) to represent the extent of aggregate contamination in the current year;
4. Iteratively change the Performance Period value until the Calculated Design Structural Number (SN) equals the Total Calculated SN of the pavement structure; the Performance Period at which these SN are equal is effectively the ERDL of this pavement structure in the current year.

MAINTENANCE SCHEDULES

Preventive maintenance (PM) was modeled as milling of the existing asphalt surface and replacement with new asphalt mix. “No PM” was modeled as simple overlay with new asphalt surface mix, consistent with observed VDOT practice for rural secondary roads.

Treating PM as an option in this LCCA, all pavement scenarios are evaluated at 5-year intervals for maintenance needs. Surface asphalt patching is considered sufficient when the ERDL falls below 5 years but the surface mix structural coefficient is still above 0.30 (based on 1993 AASHTO pavement design). The first maintenance activity realistically consists of overlay or mill/inlay rather than rehabilitation/rebuild, reflecting typical maintenance procedures.

Other maintenance decisions are triggered as follows: if the structural coefficient of the surface mix is below 0.30, overlay or mill/resurfacing is required; if ERDL is below 5 years (the duration between the current and next *analysis* year), patching is required in direct proportion to the shortfall, unless resurfacing or rebuilding is performed in the same analysis year; if the typical maintenance activity (overlay or mill/inlay) does not result in a recalculated ERDL of *at least* 5 years, pavement rehabilitation or rebuild is necessary. The last calculation includes engineering judgment, although the designs in this analysis minimally meet new design life of 20 years.

Some maintenance activities are determined ad hoc, including the following: 20% of the roadway length (both sides) requires guardrail; guardrail replacement is necessary after overlay exceeds 2 inches; and crack-sealing is considered a routine maintenance activity common to all pavements and therefore is not included in the pavement maintenance histories.

Table 3 shows the maintenance schedule determined for the very low volume secondary road subjected to the maximum contamination rate over the 50-year analysis period under the No GTX-No PM scenario.

Table 3. Example of pavement management without GTX or preventive maintenance.

No GTX - No PM, Initial AADT 155, Contamination Rate 0.2-in./yr.				
Year	ERDL	Maintenance	SSC	AADT
2020	20	Construction	0.44	155
2030	6.2		0.395	189
2035	2.8	*Patch*	0.358	209
2040	0.8	Overlay 1.5" (RRDL = 11.4 yrs)	0.266	230
2045	4.3	*Patch*	0.421	254
2050	1.3	*Patch*	0.395	281
2055	0.31	Overlay 1.5" (RRDL = 5.6 yrs)	0.358	310
2060	2.3	*Patch*	0.421	342
2065	0.51	Rebuild 8.5" 21B, 2" SM (RRDL = 20.0 yrs)	0.395	378
2070	12.3	Remaining service life = 12.3 yrs	0.421	417

Note: ERDL = estimated remaining design life; RRDL = recalculated remaining design life; SSC = surface structural coefficient

COST DATA

Empirical data obtained from VDOT contract awards over the period 2008-2018 were used to determine construction and maintenance costs for each combination of pavement design and scenario over the analysis period. Since documentation of the use of separation GTX is not required by VDOT at the time of this writing, identification of actual costs involved the choice of an item code for the GTX typically used for separation purposes in VDOT roads and selection of a subset of construction projects in which the separator GTX was used on the secondary system. When the tasks were completed, representative quantity-to-unit price relationships were developed for GTX (Figure 4) and for most major items in secondary pavement construction. These unit prices were used to determine the cost of maintenance activities. GTX unit cost in VDOT projects ranged from over $10 per square yard installed for very small quantities to below $2 per square yard installed for high quantities, in inflation-adjusted prices.

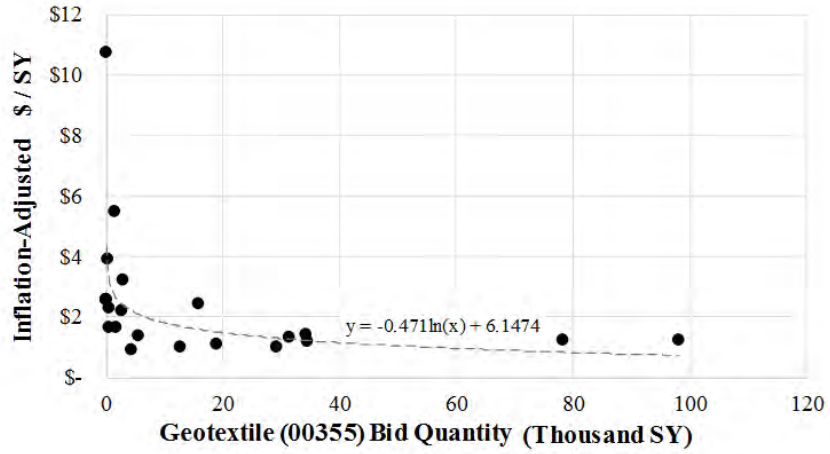

Figure 4. Quantity-to-price relationship for VDOT item 00355 in select roadway projects (2013 Widen Roadway; 2016 Grade/Drain/Pave).

REMAINING VALUE

LCCA results represent the discounted present value of construction and maintenance costs over the 50-year analysis period, plus a factor that considers the "remaining value" of the pavement at 50 years. Accounting for the remaining pavement value at the analysis termination point is an aspect of LCCA on which there is no clear consensus in practice. In this study, two methods are offered for the treatment of remaining value as either (1) an asset ("salvage value") or (2) a "normalized" liability reflecting differing final pavement conditions.

In the first method, salvage value is quantified for each pavement design scenario as the product of ERDL at the beginning of year 50 in ratio to ERDL at original construction (i.e., current ERDL/20) and the cost of a 20-year pavement design (constant for all alternatives) given the AADT in year 50, discounted to the present. Salvage value monetized by this method is a life-cycle cost *offset*, i.e., the salvage value factor is subtracted from the sum of pavement construction and discounted maintenance costs.

In the second method, the modeled condition of each existing pavement structure after 50 years is the basis for the creation of a 20-year "terminal pavement design" for each pavement, reflecting real-world conservation of road inventories. Pavements with low ERDL require more rehabilitation expense to achieve a 20-year design life than pavements with higher ERDL at year 50. The costs of a "terminal" design for each pavement-scenario combination after year 50 are discounted in the same manner as earlier maintenance activity costs. But they are added to the sum of construction and discounted maintenance costs from year 5 through year 50 as a *liability*, of greater or lesser magnitude depending on pavement condition at year 50.

Discount rates of 4% (consistent with VDOT practice) and 1.5% (consistent with FHWA recommendations for long term economic analysis and current rates of return at the time of analysis) were used to determine the life-cycle cost for a scenario, assuming that interest is compounded annually as shown:

$$LCC = \left(\sum_{i=0}^{i=T} \frac{Cost_i}{(1+d)^i}\right) \pm f$$

Where i is years from base year 0, $Cost_i$ is project cost in year i, T is analysis period in years, d is the discount rate, and f is the remaining value factor at 50 years.

RESULTS

The LCCA methodology developed in this study combines empirical VDOT cost data with a quantitative pavement deterioration model to measure the cost-effectiveness per mile of pavements with separator GTX over a 50-year analysis period. Actual VDOT cost data on GTX, aggregate, base material, intermediate layer, milling and guardrail were collected from secondary road projects recorded in VDOT's electronic construction database.

Table 4 shows cost ratios of the GTX pavement (column) to the No GTX pavement (row) for the 50-year period, under each method of analysis termination. Unshaded cells show direct comparisons (the presence or absence of GTX only) and shaded cells show cross-comparisons (i.e., option opposites). For example, at the highest contamination rate modeled here (0.2-in per year), the present value of the 50-year cost of a very low traffic (AADT = 155) secondary pavement with a GTX separation layer and no preventive maintenance (GTX-No PM option) would be 50% of the cost of a pavement with no GTX layer and no PM (No GTX-No PM option), assuming the

"salvage value" analysis termination approach (Table 4(a)). The same cost comparison is even more favorable for the GTX pavement under the lower discount rate. Similar results hold for the 1500-AADT secondary pavement design. Further, incorporating GTX in one pavement and performing preventive maintenance on the other only increases the cost-effectiveness of GTX for very low-AADT pavement designs (45%), regardless of discount rate or analysis termination approach. In summary, the presence of GTX is cost-effective in all scenarios but one when contamination is at least 0.1-in. per year.

The case of the secondary pavement design with initial AADT of 1500, however, results in a unique outcome: if the contamination rate is very low (0.05-in. per year), it is always (i.e., across discount rates and analysis termination approaches) more cost-effective (at least marginally) to incorporate GTX in a pavement design and forego subsequent preventive maintenance *rather than the reverse*.

Table 4. Summary of LCCA results with (a) monetized salvage value and (b) terminal pavement design at end of analysis period.

			Contamination Rate					
			0.2 in./yr		0.1 in./yr		0.05 in./yr	
Discount Rate	Initial AADT	Pavement Design	(a) GTX-No PM	(b) GTX-PM	(c) GTX-No PM	(d) GTX-PM	(e) GTX-No PM	(f) GTX-PM
4.0%	155	No GTX-PM	45%	51%	66%	76%	85%	98%
		No GTX-No PM	50%	57%	85%	98%	103%	118%
	1500	No GTX-PM	71%	75%	90%	95%	94%	99%
		No GTX-No PM	71%	75%	89%	94%	102%	107%
1.5%	155	No GTX-PM	26%	37%	41%	59%	61%	88%
		No GTX-No PM	28%	41%	60%	86%	92%	132%
	1500	No GTX-PM	61%	67%	82%	91%	89%	98%
		No GTX-No PM	61%	67%	82%	91%	100%	110%

(a)

			Contamination Rate					
			0.2 in./yr.		0.1 in./yr		0.05 in./yr.	
Discount Rate	Initial AADT	Pavement Design	(a) GTX-No PM	(b) GTX-PM	(c) GTX-No PM	(d) GTX-PM	(e) GTX-No PM	(f) GTX-PM
4.0%	155	No GTX-PM	51%	55%	74%	80%	95%	102%
		No GTX-No PM	56%	60%	94%	102%	110%	119%
	1500	No GTX-PM	76%	80%	91%	97%	98%	104%
		No GTX-No PM	76%	80%	90%	96%	103%	109%
1.5%	155	No GTX-PM	41%	47%	61%	69%	89%	101%
		No GTX-No PM	43%	49%	85%	97%	114%	130%
	1500	No GTX-PM	71%	78%	85%	95%	99%	110%
		No GTX-No PM	71%	78%	85%	95%	101%	113%

(b)

Note: GTX = geotextile, PM = preventive maintenance.

As expected, in the lowest contamination scenario the GTX-No PM option is typically equal in cost or less cost-effective than doing neither, regardless of initial AADT level, discount rate or analysis termination approach. It should be noted, however, that while some cost savings can be realized by eliminating GTX, these pavements are likely to be rougher and generally in worse condition, consequently requiring more patching, than pavements designed with GTX. Finally, in the lowest contamination scenario the analysis termination method affects whether the

presence or absence of GTX is cost-effective in pavements that will both receive PM. The presence of GTX never results in higher life-cycle costs when both pavements receive PM and remaining value is computed by the monetized salvage value method (column (f) in Table 4 (a)). But the presence of GTX with PM always causes the life-cycle cost to exceed that of pavement with PM when remaining value is computed by the terminal pavement design method.

CONCLUSIONS

Pavements with separator geotextile are expected to be consistently more cost-effective than pavements without separator geotextile at contamination rates above 0.1 inch/year, regardless of whether preventive maintenance is performed or whether initial AADT is set at the lower (155) or higher (1500) level, for discount rates within the range explored in this study (4% and lower).

Separation geotextile in pavement structure can have a significant life-cycle cost advantage over pavement without geotextile for the highest contamination rate tested in this study when both pavements receive preventive maintenance, and the cost advantage of separation geotextile usually increases if neither pavement receives preventive maintenance, regardless of initial AADT.

The life-cycle cost advantage of separator geotextile decreases with decreasing contamination rate, yet separation geotextile is a relatively low-cost item to install as a preventive measure to mitigate potential premature deterioration. PennDOT estimated that a future reconstruction could cost as much as 211% of the present cost of a road with GTX originally incorporated in construction (K. Petrasic 2017). Only surficial maintenance is likely to be required with separation geotextile incorporated into the pavement section.

Although aggregate contamination by fine-grained subgrade soils is a well-documented problem, current pavement design methods do not incorporate this knowledge. Thus, some pavements designed using these methods may deteriorate at a faster rate than anticipated, increasing their life-cycle costs. Aggregate layers protected by means of separator geotextile are more likely to be preserved and reused.

ACKNOWLEDGMENTS

The authors thank Dr. Ed Hoppe and Dr. Shabbir Hossain for their leadership of the research that enabled the analysis presented here.

REFERENCES

American Association of State Highway Transportation Officials (AASHTO). (1993). *AASHTO Guide for Design of Pavement Structures*, Washington, DC.

Al-Qadi, I.L., Brandon, T.L., Valentine, R.J., Lacina, B.A., and Smith, T.E. (1994). “Laboratory Evaluation of Geosynthetic-Reinforced Pavement Sections.” *Transportation Research Record: Journal of the Transportation Research Board*, 1439, 25-31.

Al-Qadi, I. L., and Appea, A. K. (2003). “Eight-Year Field Performance of Secondary Road Incorporating Geosynthetics at Subgrade-Base Interface.” *Transportation Research Record: Journal of the Transportation Research Board*, 1849, 212-220.

Babashamsi, P.,Yusoff, N.I.M., Ceylan, H., Nor, N.G.M., Jenatabadi, H.S. “Evaluation of pavement life cycle cost analysis: Review and analysis.” *International Journal of Pavement Research and Technology*, 9:4, 241-254.

Hoppe, E., Hossain, S., Moruza, A., Weaver, C. (2019). *Use of Geosynthetics for Separation and Stabilization in Low-Volume Roadways.* VTRC 20-R8. Virginia Transportation Research Council, Charlottesville, 2019.

Jorenby, B.N. and Hicks, R.G. (1986). "Base Course Contamination Limits." *Transportation Research Record: Journal of the Transportation Research Board*, 1095, 86-101.

Kermani, B., Xiao, M., Stoffels, S.M., Qiu, T. (2019). "Measuring the migration of subgrade fine particles into subbase using scaled accelerated flexible pavement testing – a laboratory study." *Road Materials and Pavement Design*, 20:1, 36-57. https://www.tandfonline.com/doi/full/10.1080/14680629.2017.1374995. Accessed September 27, 2019.

Perkins, S. W. (2001). "Mechanistic-Empirical Modeling and Design Model Development of Geosynthetic Reinforced Flexible Pavements." Report No. FHWA/MT-01-002/99160-1, Federal Highway Administration, Washington, DC, 170 pp.

Petrasic, K.W. (2017). "Geotextile Separation to Prevent Migration of Subgrade Fines." <http://www.dot.state.pa.us/public/Bureaus/BOPD/2017_QAW/GeoTech_and_Aggregates/Geotextile%20Separation-kwp.pdf> (August 13, 2019).

Virginia Department of Transportation Manual of Instruction for Materials Division. (2018). "Chapter 6 - Pavement Design and Evaluation", Richmond, VA.

Xiao, M., Stoffels, S., Qui, T., and Kermani, B. *Evaluation of Geotextile Separation to Prevent Migration of Subgrade Fines into Subbase*. Pennsylvania State University, State College, PA, 2016.

Yang, S.-H. and Al-Qadi, I. L. (2007). "Cost-Effectiveness of Using Geotextiles in Flexible Pavements." *Geosynthetics International*, 14 (1), 2-12.

Geosynthetics Conference

Load-Carrying Geosynthetic Mechanically Stabilized Earth (GMSE) Bridge Abutments: Lessons Learned from Experimental Evaluations

Amr M. Morsy, Ph.D., P.E. [1,2], Jorge G. Zornberg, Ph.D., P.E.[3], Jie Han, Ph.D., P.E.[4], Burak F. Tanyu, Ph.D.[5], Barry R. Christopher, Ph.D., P.E.[6], and Dov Leshchinsky, Ph.D.[7]

[1] Loughborough University, Loughborough, LE11 3TU, UK. Email: a.morsy@lboro.ac.uk
[2] Cairo University, Giza 12613, Egypt.
[3] The University of Texas at Austin, Austin, TX 78712, USA. Email: zornberg@mail.utexas.edu
[4] University of Kansas, Lawrence, KS 66045, USA. Email: jiehan@ku.edu
[5] George Mason University, Fairfax, VA 22030, USA. Email: btanyu@gmu.edu
[6] Christopher Consultants, Augustine, FL 32080, USA. Email: barryc325@aol.com
[7] ADAMA Engineering, Inc., Clackamas, OR 97015, USA. Email: adama@geoprograms.com

ABSTRACT

This paper presents the findings of an experimental study conducted to define the boundary conditions of composite behavior of Geosynthetic Mechanically Stabilized Earth (GMSE) bridge abutments. The study involved the development of a new soil-geosynthetic interaction device capable of generating data required to assess the mechanical interactions between soils and reinforcing inclusions within a reinforced soil mass. These interactions are key to understanding the effect of reinforcement vertical spacing on the behavior of GMSE bridge abutments. The soil-geosynthetic interaction device was designed to accommodate a reinforced soil mass with three reinforcement layers. One reinforcement layer was subject to increasing tensile loads through an external loading system, while the other two neighboring reinforcement layers were not subject to external loads. An extensive instrumentation program was implemented to monitor the mechanical behavior of the soil and the three reinforcement layers during testing. It was observed that the neighboring reinforcement layers experience increasing passive tension with increasing active tension on the loaded reinforcement layer. The interaction among reinforcement layers was found to increase with decreasing the reinforcement spacing. For the testing program implemented in this study, one actively loaded reinforcement layer can transfer shear loads to a distance up to 0.20 m normal to its plane with a zone of shear influence of 0.15 m. That is, the interaction between two neighboring reinforcement layers could be observed for a reinforcement spacing corresponding to 0.30 m, a spacing capable of forming a composite reinforced soil mass.

INTRODUCTION

Soil-reinforcement interaction is the key property to the mechanical behavior of reinforced soil structures such as retaining walls and bridge abutments. The interactions between soils and reinforcing inclusions are governed by several load transfer mechanisms that have studied extensively over the past few decades (*e.g.*, Palmeria 2009). In design of reinforced soil walls and bridge abutments, soil-reinforcement interaction has always been considered to be of importance in restraining soil mass and has often been ignored in the driving mass. This simplification has been deemed conservative and thus has been acceptable by researchers and practitioners.

Vertical reinforcement spacing in geosynthetic-reinforced soil structures was reported to control the degree of interaction not only between soil and reinforcement layers, but also among

neighboring reinforcement layers. This interaction was found to enhance the overall mechanical behavior of reinforced soil structures (Leshchinsky *et al.* 1994; Leshchinsky and Vulova 2001; Adams *et al.* 2011; Morsy 2017; Zornberg *et al.* 2018, 2019; Shen *et al.* 2019). Reinforcement spacing has been reported to have a greater effect on the stability of a reinforced soil structure than reinforcement tensile strength at ultimate states (Nicks *et al.* 2013), and greater than the reinforcement tensile stiffness under working stresses (Morsy 2017). The interaction mechanisms that result from the confinement of reinforcements were observed to exhibit behaviors not necessarily consistent with results predicted by limit state analyses (Ziegler 2011). However, the need for a greater understanding of the mechanisms and extent of such an effect remains.

This paper presents the findings of an experimental study that involved the development of a new device to comprehensively assess the soil-reinforcement interaction under both working stress and failure conditions considering varying reinforcement vertical spacings. The device was used to conduct a comprehensive testing program that aimed at investigating the effects on the interaction among neighboring reinforcements in relation to: (1) the normal stress at the soil-reinforcement interface; (2) the vertical spacing between reinforcements; (3) the reinforcement properties; and (4) the fill type. Analysis of the experimental results revealed that the existence of the zone of shear influence and its extent can be directly related to the interaction between neighboring reinforcement layers.

EXPERIMENTAL APPROACH

A new experimental device was designed and implemented by Morsy (2017) at the University of Texas at Austin to evaluate soil-reinforcement composite behavior and quantify the thickness of the zone where shear stresses propagate into the soil adjacent to the interface with a reinforcement where shear stresses are imposed. The device was used to conduct soil-geosynthetic interaction tests with various geosynthetic and soil materials under varied testing conditions. This section provides a descriptive summary of the soil-geosynthetic interaction device and its instrumentation. The detailed description of the device is presented in Morsy (2017) and Morsy *et al.* (2019a).

Soil-geosynthetic interaction device. The device consisted of a steel box 1200 mm in depth, 750 mm in width and 1500 mm in length that accommodates geosynthetic-reinforced soil specimens with three reinforcement layers. A general layout of the soil-geosynthetic interaction device is presented in Figure 1. One side of the box was made of transparent acrylic. The normal stress was applied on the geosynthetic-reinforced soil specimens using six pneumatic actuators placed on load distributing wooden pyramids, as shown in Figure 1a. Tensile loading was applied to middle reinforcement layer (active reinforcement) using a hydraulic loading system mounted on smooth liner guides, as shown in Figure 1b. The two other reinforcement layers act as upper and lower boundaries to represent the presence of neighboring reinforcements. These layers are passively loaded (passive reinforcements) through the load transfer from the active reinforcement layer. The soil-geosynthetic interaction device could detect the load transfer amongst neighboring reinforcements that occur when these layers deform differently (Morsy 2017; Zornberg *et al.* 2018; Morsy *et al.* 2019a, 2019b, 2020; Morsy and Zornberg 2020). The active reinforcement was attached to a loading system at its front end and was free at its rear end; whereas, the passive reinforcements were anchored at their rear ends.

Instrumentation and monitoring techniques. The instrumentations used in the soil-geosynthetic interaction device included the following: (1) a load cell measuring the increasing tensile load applied to the active reinforcement; (2) a camera capturing the soil displacement field; (3) artificial gravel particles buried within the soil mass and connected to linear potentiometers via horizontal telltales, which provided a comparison of displacements from internal particles with those obtained from particles adjacent to the transparent wall; and (4) linear potentiometers measuring displacements at numerous locations within the three reinforcement layers. Detailed information about the instrumentation and monitoring techniques is presented in Morsy (2017) and Morsy *et al.* (2019a).

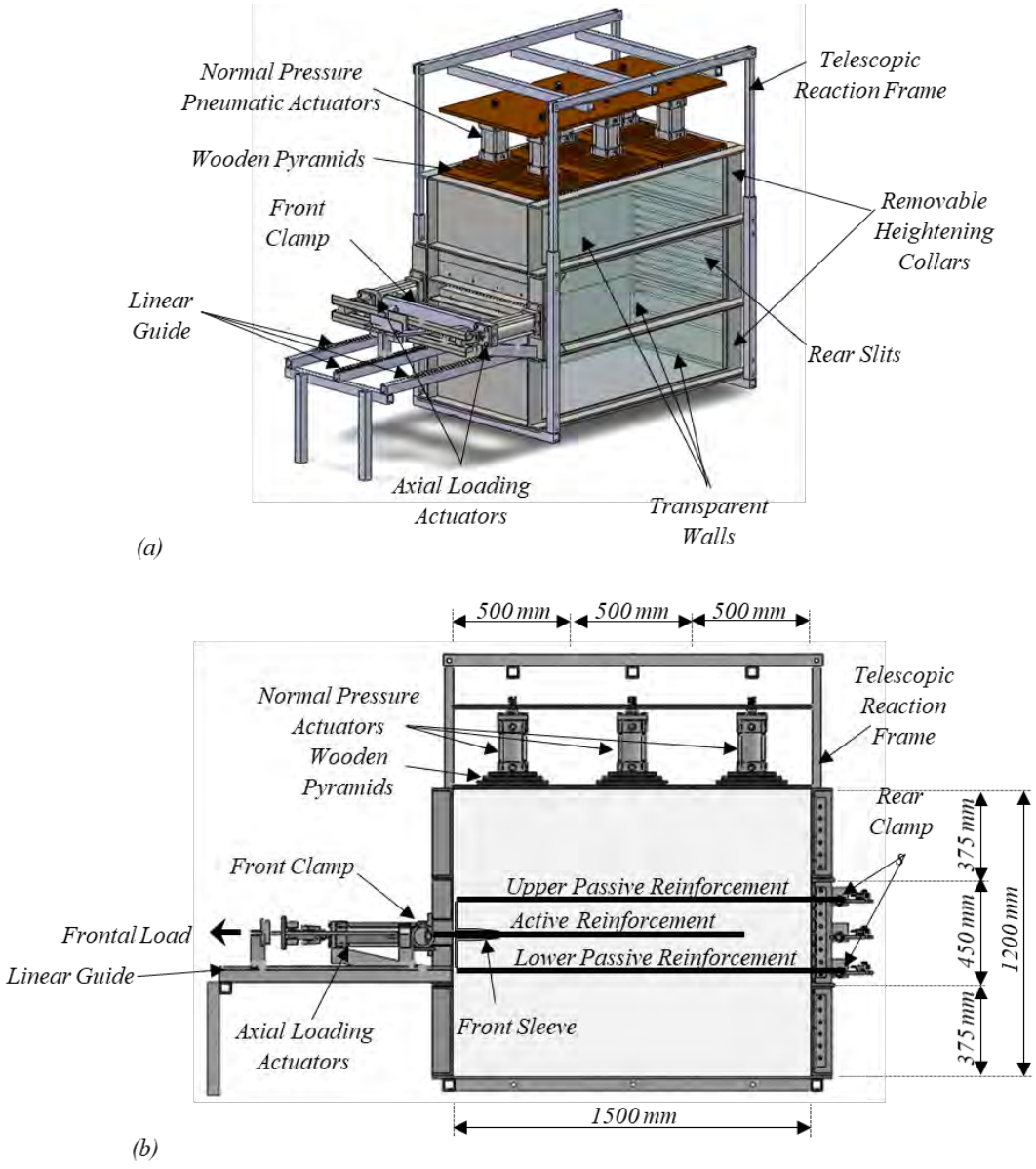

Figure 1. Soil-geosynthetic interaction device: (a) general layout; and (b) schematic cross-sectional side view (Morsy and Zornberg 2020).

EXPERIMENTAL PROGRAM

A comprehensive experimental program was conducted using the new soil-geosynthetic interaction device. Table 1 summarizes the tests conducted as part of this program (Morsy *et al.* 2019b, 2020), which shows several testing series that explored the effects of various parameters on soil-reinforcement interaction. These testing series included repeatability assessment, varying normal stress levels for two reinforcement spacings, varying reinforcement vertical spacings for three normal stress levels, and varying geosynthetic and soil types. The results of the soil-geosynthetic interaction tests are presented in Morsy *et al.* (2019b, 2020).

The baseline soil used in the soil-geosynthetic interaction tests was a pea gravel that conforms to No. 8 gradation. Another soil type that confirms to sand No. 30 gradation was used. Characteristic properties of the two soils used in the testing program are summarized in Table 2. The baseline reinforcement used in the soil-geosynthetic interaction tests was a polypropylene woven geotextile. Other geosynthetic types including geogrids and geotextiles were used in the testing program to cover various geosynthetic characteristics (Morsy *et al.* 2020). Characteristic properties of geosynthetic reinforcements used in the testing program are summarized in Table 3.

Table 1. Summary of soil-geosynthetic interaction tests (after Morsy and Zornberg 2020).

*Testing Scheme **	*Test ID*	*Testing Variables*			
		Soil	*S_v (m)*	*σ_v (kPa)*	*Reinforcements*
Repeat Tests	GP-04-07-G1-G GP-04-07-G1-G(R)	Gravel	0.10	50	W1-GT
Tests with Varying Normal Stress Level	GP-06-02-G1-G	Gravel	0.15	15	W1-GT
	GP-06-03-G1-G			21	
	GP-06-05-G1-G			35	
	GP-06-07-G1-G			50	
	GP-04-03-G1-G	Gravel	0.10	21	W1-GT
	GP-04-07-G1-G			50	
	GP-02-03-G1-G	Gravel	0.05	21	W1-GT
	GP-02-07-G1-G			50	
Tests with Varying Reinforcement Vertical Spacing	GP-02-07-G1-G	Gravel	0.05	50	W1-GT
	GP-04-07-G1-G		0.10		
	GP-06-07-G1-G		0.15		
	GP-08-07-G1-G		0.20		
	GP-12-07-G1-G		0.30		
	GP-16-07-G1-G		0.40		
	GP-02-03-G1-G	Gravel	0.05	21	W1-GT
	GP-04-03-G1-G		0.10		
	GP-06-03-G1-G		0.15		
Tests with Varying Geosynthetic and Soil Types	GP-06-03-G1-G	Gravel	0.15	21	W1-GT
	GP-06-03-G2-G	Gravel			W2-GT
	GP-06-03-G4-G	Gravel			EX-GG
	GP-06-03-G5-G	Gravel			KN-GG
	SP-06-03-G1-G	Sand			W1-GT

* Note: Some tests are mentioned more than once in different testing schemes to show the extent of variation in each scheme.

Table 2. Characteristics of soils used in soil-geosynthetic interaction tests (after Morsy and Zornberg 2020).

Properties	*Gravel*	*Sand*
Particle Size Range, D	1.0-13.0 mm	0.2-2.0 mm
Mean Particle Size, D_{50}	7.0 mm	0.7 mm
Uniformity Coefficient, C_u	1.6	1.9
Curvature Coefficient, C_c	0.9	1.3
Specific Gravity, G_s	2.62	2.65
Range of Void Ratio, e_{min}-e_{max}	0.50-0.73	0.56-0.76
AASHTO Classification	A-1-a	A-3
USCS Classification	GP	SP

TEST RESULTS AND ANALYSIS

Soil displacement profiles. Figure 2 shows the horizontal displacement profiles normal to the reinforcement planes near the location of the frontal load at various loading stages for a representative test (Morsy *et al.* 2019a). The displacements were measured using the artificial gravel particles at the center of the reinforced soil mass, as well as using digital imaging at the side boundary of the reinforced soil mass.

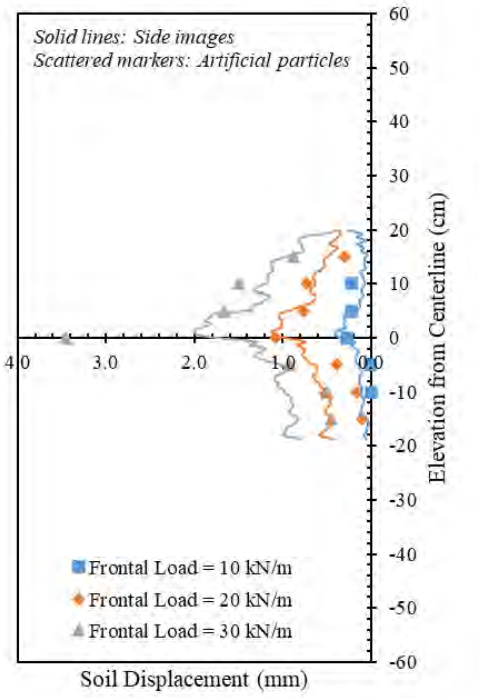

© Morsy *et al.* (2019a)

Figure 2. Horizontal soil displacement.

Reinforcement displacement profiles. Figure 3 shows the displacement profiles of the three reinforcement layers at various loading stages in a representative test (Morsy *et al.* 2019a). Specific

frontal displacements, u1, were used to generate displacement profiles. Figure 3a shows the displacement profiles for the active reinforcement layer at increasing values of the frontal displacement. Figures 3b and 3c show the displacement profiles for the upper and lower passive reinforcement layers, respectively. It should be noted that the stresses generated at the soil-reinforcement interface of the active reinforcement layer shed at an angle. This results in maximum displacement magnitudes towards the middle of the passive reinforcement layers.

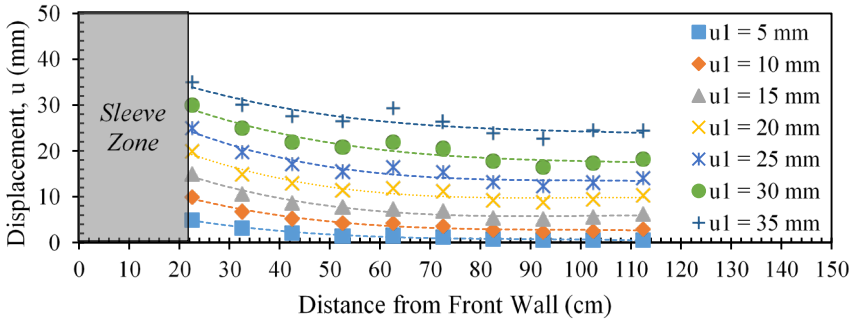

(a)

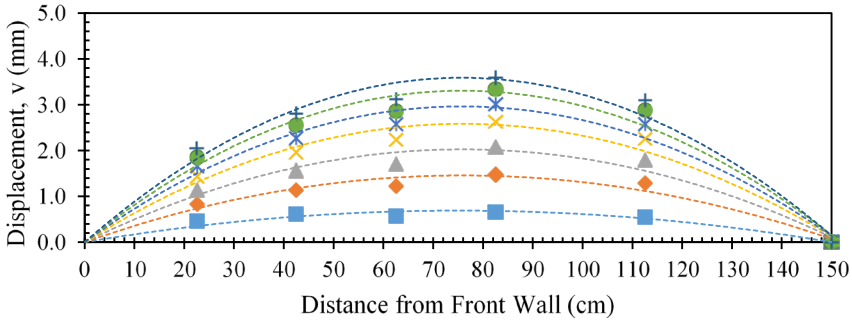

(b)

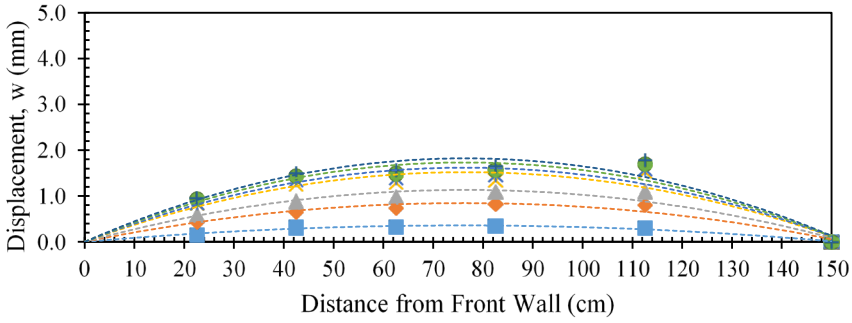

(c)

Figure 3. Reinforcement displacement profiles: (a) active reinforcement; (b) upper passive reinforcement; and (c) lower reinforcement.

Effect of reinforcement spacing. The experimental data generated as part of this study was used to evaluate the vertical reinforcement spacing below which the loading of a geosynthetic reinforcement affects the deformation response and load magnitude of adjacent reinforcement layers (Zornberg *et al.* 2019). Figure 4 shows the experimental data that was used to quantify the effect of reinforcement spacing on the interaction between neighboring reinforcement layers. Specifically, the ratio between the reinforcement displacements measured in a passive reinforcement, v, to the corresponding displacement measured in the active reinforcement, u, was used as an indicator to the degree of interaction between neighboring reinforcement layers. Figures 4a through 4c show the ratio adopted as indicator (v/u) as a function of reinforcement vertical spacing for different stages or loading levels in a test corresponding to u1 of 2, 5, and 10 mm. Two inflexion points can be observed in the relationships shown in the figures: (1) at a vertical spacing $S_{v,c}$ (*i.e.*, composite threshold) below which full interaction occurs between adjacent reinforcements; and (2) vertical spacing $S_{v,nc}$ (*i.e.*, non-composite threshold) beyond which no interaction occurs between adjacent reinforcements. Varying degrees of interaction between adjacent reinforcements can be observed for vertical spacing values ranging from $S_{v,c}$ to $S_{v,nc}$. The results indicate that maximum interaction between neighboring reinforcements occurred below a reinforcement spacing of approximately 0.10 m (*i.e.*, $S_{v,c}$ = 0.10 m) and minimum interaction between adjacent reinforcements occurred beyond a reinforcement vertical spacing value of approximately 0.20 m (*i.e.*, $S_{v,nc}$ = 0.20 m).

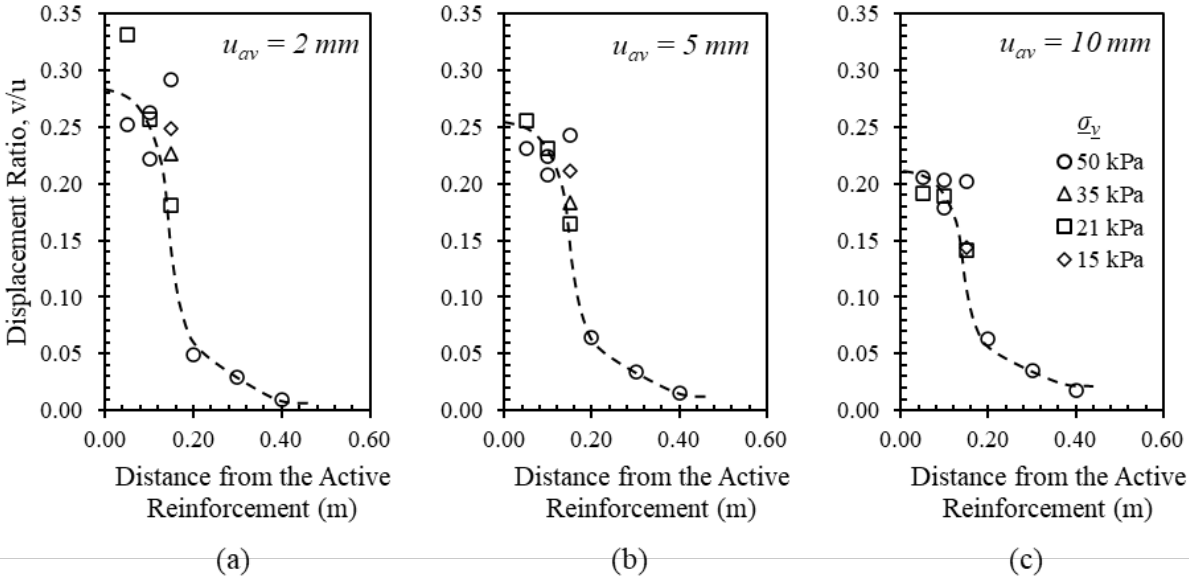

© Morsy *et al.* (2019b)

Figure 4. Average displacement ratio of upper passive reinforcement layers at various average displacements of active reinforcement layers: (a) u_{av} = 2 mm; (b) u_{av} = 5 mm; and (c) u_{av} = 10 mm.

According to these experimental results, interaction between neighboring reinforcements occurred up to an average distance from active reinforcement (*i.e.*, reinforcement vertical spacing) of 0.15 m from the soil-reinforcement interface. In Figure 4, the reinforcement spacing at which a significant change in the interaction between neighboring reinforcements occurred can be used to

define the boundary for the composite behavior of a geosynthetic-reinforced soil mass. It should be recognized that load in the experimental testing setup was mobilized in only one active reinforcement. In the case of multiple active (*i.e.*, loaded) reinforcements, the soil between would be mobilized in shear by the two neighboring reinforcement layers. Consequently, according to these experimental results, composite behavior could be observed for vertical spacing values corresponding to twice the distance from the active reinforcement layer shown in Figure 4. That is, an average of 0.30 m for select soil (AASHTO No. 8 gravel). This value is in good agreement with current limits for reinforcement spacing established by Adams *et al.* (2011) for geosynthetic-reinforced soil structures.

CONCLUSION

An experimental study was conducted to investigate the interactions that take place in geosynthetic-reinforced soils under both working stress and failure conditions considering varying reinforcement vertical spacings. A device was developed to perform this study designed to measure displacement fields of soils and reinforcing inclusions. The newly developed experimental device was used to conduct a comprehensive testing program to study the effects of normal stress, vertical reinforcement spacing, reinforcement type, and fill type on soil-reinforcement interaction. The following conclusions could be made:

- The device was capable of measuring tensile strains developing in both actively tensioned and neighboring geosynthetic reinforcement layers. It allowed direct visualization of the kinematic response of soil particles adjacent to the geosynthetic layers, which facilitated evaluation of the soil displacement field via digital image analysis. Evaluation of the soil displacement field allowed quantification of the extent of the zone of shear influence around a tensioned reinforcement layer. Finally, the device allowed monitoring of dilatancy within the reinforced soil mass, providing additional insight into the effect of reinforcement vertical spacing on the reinforced soil mass.
- Analysis of the experimental results revealed that the existence of the zone of shear influence and its extent can be directly related to the interaction between neighboring reinforcement layers.
- The interaction between adjacent reinforcement layers was found to increase with decreasing reinforcement vertical spacing. A minimum reinforcement vertical spacing threshold was identified below which the interaction between adjacent reinforcements develops fully. In addition, a maximum reinforcement vertical spacing threshold was identified beyond which the interaction between neighboring reinforcements becomes negligible. For the testing program implemented in this study, the minimum and maximum threshold vertical spacings were identified as 0.10 and 0.20 m (4 and 8 in.), respectively.
- According to these experimental results, the zone of shear influence extends an average distance of 0.15 m (6 in.) from the soil-geosynthetic interface. That is, interaction between adjacent reinforcements could be observed for a vertical spacing value corresponding to 0.30 m (12 in.), or twice the average distance from the reinforcement for which interaction occurs.

REFERENCES

Adams, M.T., Nicks, J.E., Stabile, T., Wu, J.T.H., Schlatter, W., and Hartmann, J. (2011). *Geosynthetic Reinforced Soil Integrated Bridge System Interim Implementation Guide*. Report No. FHWA-HRT-11-026, Federal Highway Administration, McLean, VA.

Leshchinsky, D., Kaliakin, V., Bose, P., and Collin, J. (1994). "Failure Mechanism in Geogrid-Reinforced Segmental Walls: Experimental Implications." *Soils and Foundations*, Vol. 34, No. 4, pp. 33-41.

Leshchinsky, D., and Vulova, C. (2001). Numerical investigation of the effects of geosynthetic spacing on failure mechanisms in MSE block walls. *Geosynthetics International*, Vol. 8. No. 4, pp. 343-365.

Morsy, A.M., and Zornberg, J.G. (2020), "Soil-Reinforcement Interaction: Stress Regime Evolution in Geosynthetic-Reinforced Soils," *Geotextiles and Geomembranes*. [In Press]

Morsy, A.M., Zornberg, J.G., Leshchinsky, D., Christopher, B.R., Han, J., and Tanyu, B.F. (2020), "Experimental Evaluation of the Interaction among Neighboring Reinforcements in Geosynthetic-Reinforced Soils," *Journal of Geotechnical and Geoenvironmental Engineering*, Vol. 146, No.10, October 2020, 04020107.

Morsy, A.M., Zornberg, J.G., Leshchinsky, D., and Han, J. (2019), "Soil-Reinforcement Interaction: Effect of Reinforcement Spacing and Normal Stress," *Journal of Geotechnical and Geoenvironmental Engineering*, Vol. 145, No. 12, December 2019, 04019115.

Morsy A.M., Zornberg, J.G., Han, J., and Leshchinsky, D. (2019), "A New Generation of Soil-Geosynthetic Interaction Experimentation," *Geotextiles and Geomembranes*, Vol. 47, No. 4, August 2019, pp. 459-476.

Morsy, A.M. (2017), *Evaluation of Soil-Reinforcement Composite Interaction in Geosynthetic-Reinforced Soil Structures*, Ph.D. Dissertation, Department of Civil, Architectural, and Environmental Engineering, The University of Texas at Austin, Austin, Texas, The United States of America, Advisor: Jorge G. Zornberg, 635p.

Nicks, J.E., Adams, M.T., Ooi, P.S.K., and Stabile, T. (2013). *Geosynthetic reinforced soil performance testing—Axial load deformation relationships*. Report No. FHWA-HRT-13-066, Federal Highway Administration, McLean, VA.

Palmeira, E.M. (2009). "Soil-Geosynthetic Interaction: Modelling and Analysis." *Geotextiles and Geomembranes*, Vol. 27, No. 5, pp. 368–390.

Shen, P., Han, J., Zornberg, J.G., Morsy, A.M., Leshchinsky, D., Tanyu, B.F., and Xu, C. (2019), "Two and Three-Dimensional Numerical Analyses of Geosynthetic-Reinforced Soil (GRS) Piers," *Geotextiles and Geomembranes*, Vol. 47, No. 3, June 2019, pp. 352-368.

Ziegler, M. (2011). "Interaction of soil reinforcement as key issue for ground reinforcement." Invited Lecture, *XV ECSMGE*, Athens, Greece.

Zornberg, J.G., Morsy, A.M., Kouchaki, B.M., Christopher, B.R., Leshchinsky, D., Han, J., Tanyu, B.F., Gebremariam, F.T., Shen, P., and Jiang, Y. (2019), *Proposed Refinements to Design Procedures for Geosynthetic Reinforced Soil (GRS) Structures in AASHTO LRFD Bridge Design Specifications*. NCHRP Web-Only Document 260, National Cooperative Highway Research Program (NCHRP), Transportation Research Board of the National Academies.

Zornberg, J.G., Morsy, A.M., Kouchaki, B.M., Christopher, B.R., Leshchinsky, D., Han, J., Tanyu, B.F., Gebremariam, F.T., Shen, P., and Jiang, Y. (2018), *Defining the Boundary Conditions for Composite Behavior of Geosynthetic Reinforced Soil (GRS) Structures*. Project NCHRP 24-41, National Cooperative Highway Research Program (NCHRP), Transportation Research Board of the National Academies.

Geosynthetics Conference

Load-carrying GMSE Bridge Abutments: Lessons Learned from Field Monitoring Evaluations

Burak Tanyu, Ph.D., P.E.[1], Fitsum Gebremariam, Ph.D.[2], Barry R. Christopher, Ph.D., P.E.[3], Dov Leshchinsky, Ph.D.[4], Jie Han, Ph.D., P.E.[5], Jorge G. Zornberg, Ph.D., P.E.[6]

[1] Department of CEIE, George Mason University, Fairfax, VA 22030, USA. Email: btanyu@gmu.edu
[2] Arup, New York, NY, USA. Email: fitsum.gebremariam@arup.com
[3] Geotechnical Consultant, 1 Linda Mar Drive St. Augustine, FL 32080, USA. Email: barryc325@aol.com
[4] ADAMA Engineering, Inc., Clackamas, OR 97015, USA. Email: adama@geoprograms.com
[5] Department of Civil, Environmental, & Architectural Engineering, the University of Kansas, USA. Email: jiehan@ku.edu
[6] The University of Texas at Austin, Civil Engineering Department, Austin, TX 78712, USA. Email: zornberg@mail.utexas.edu

ABSTRACT

This paper presents summary of findings from a case study in a geosynthetic-reinforced soil (GRS) integrated bridge system (IBS). The GRS-IBS cited in this study was constructed in Virginia by Virginia Department of Transportation (VDOT). The GRS-IBS was 2.2 m high, 9 m wide, and had a 3.6 m bridge span. The facing of the structure was constructed with standard concrete masonry unit (CMU) blocks. AASHTO No. 8 aggregate was reinforced with woven geotextiles that were spaced 0.2 m within the primary reinforcement zone and 0.1 m within the bearing bed zone. The foundation of the GRS-IBS was constructed with VDOT 21B aggregate encapsulated by a woven geotextile which rested on bedrock. This article summarizes the observations related to (1) the vertical stresses within the body of GRS-IBS during and after construction and (2) evaluation of the connection load and stress-strain conditions right behind the facing of the GRS-IBS. Observations presented in this article were based on the data obtained from the instruments installed during construction and monitored over time. The noted vertical stress distributions in this study were used to evaluate the effects of reinforcement spacing, width of the beam seat, and seasonal variations. The results showed the effectiveness of the bearing bed (close spacing) in reducing applied stresses within the abutment and how the width of the beam seat controls the magnitude of the applied stresses on the GRS abutment. The observations from the field also showed that the distributions of both lateral stresses and reinforcement strains with depth were approximately uniform. The connection loads estimated using lateral stresses and reinforcement strains behind the facing were comparable.

INTRODUCTION

Geosynthetic Reinforced Soil - Integrated Bridge System (GRS-IBS) is a technology developed by the Federal Highway Administration (FHWA) to construct bridge abutments to support low volume of traffic (Adams and Nicks, 2018). Similar to other reinforced soil structures, such mechanically stabilized earth (MSE) bridge abutment, GRS-IBS is constructed with layers of compacted granular backfill material reinforced with geosynthetics (i.e., primarily geotextile but occasionally geogrid) where the geosynthetics is frictionally connected to the facing typically constructed using concrete masonry units (CMU) blocks. The vertical reinforcement spacing in GRS-IBS is limited to 0.3 m. Some of the features that distinguishes GRS-IBS from other reinforced soil bridge abutments are the jointless connection between the bridge superstructure and integrated approach to alleviate any potential bump that may occur on the surface of the road and the presence of bearing bed zone with secondary reinforcements underneath the superstructure and reinforced soil foundation (RSF).

The internal stability evaluation in the design of GRS-IBS is based on empirical observations of the large-scale laboratory tests (mini-pier tests) performed by FHWA (Nicks et al., 2013). The vertical stress distribution is estimated using Boussinesq's theory of stress distribution. The connection strength at the facing is not evaluated as part of the internal stability evaluation because GRS is assumed to be internally supported by closely spaced reinforcement and the facing element is not considered as a structural component except providing frictional connection (Adams and Nicks, 2018).

This paper presents the summary of findings from previously developed National Cooperative Highway Research Project (NCHRP) project reports and published articles on a case study in a field monitored GRS-IBS constructed in Virginia (Zornberg et al. 2018 and 2019, Gebremariam et al. 2020a and 2020b;). The field monitoring program was designed and implemented to evaluate: (1) the vertical stresses during and after construction and (2) the connection loads and stress-strain conditions right behind the facing of the GRS-IBS. The stress and strain measurements from the field were quantified based the theoretical methods outlined in the design of GRS-IBS by FHWA and MSE structures by American Association of State Highway and Transportation Officials (AASHTO).

FIELD MONITORED GRS-IBS CONSTRUCTED IN VIRGINIA

The field monitored GRS-IBS project site is located on route 720 in Harrisonburg, Virginia. The construction took place between August 1 and September 15, 2015 and was conducted by collaboration of Virginia Department of Transportation (VDOT) and George Mason University. VDOT's design of the GRS-IBS was conducted following the guidelines specified in the Geosynthetic Reinforced Soil Integrated Bridge System Interim Implementation Guide (Adams et al. 2011).

The GRS-IBS was 2.2 m high, 9 m wide and had a 3.6 m bridge span. The facing of the structure was constructed with standard concrete masonry unit (CMU) blocks. AASHTO No. 8 aggregate and woven geotextile reinforcements were used to construct the abutment. The vertical reinforcement spacing was 0.2 m within the primary reinforcement zone and 0.1 m within the bearing bed zone. The foundation of the structure was constructed with VDOT 21B aggregate

encapsulated by a woven geotextile which rested on bedrock. The bridge slab was constructed using precast reinforced concrete segments and the integrated approach (the roadway behind the bridge slab) was constructed using VDOT 21B aggregate and a woven geotextile. The foundation soil consisted of limestone bedrock with pockets of stiff clay. Figure 1 shows the field monitored GRS-IBS as being constructed in Virginia.

Note: Abutment on the left side is the one being instrumented.

Figure 1. Photo of the GRS-IBS during construction.

The AASHO No.8 aggregate backfill was classified as poorly-graded gravel (GP) with zero fines content in Unified Soil Classification System (USCS). The aggregate had a maximum particle size of 12.5 mm, a dry density of 1.6 g/cm^3, and a friction angle of 47.6 degrees. The VDOT 21B aggregate used to construct the RSF and the integrated approach had a maximum dry density of 2.2 g/cm^3 with optimum moisture content of 8% and a friction angle of 40 degrees. The woven geotextile used for reinforcement in the abutment and the RSF had an ultimate tensile strength of 70 kN/m.

The main purpose of the field monitoring program was to evaluate the vertical stress distribution close and away from the facing and lateral stresses and reinforcement strains immediately behind the facing of the structure. Earth pressure cells that were in circular shape (EPCs) and rectangular (RPCs) were installed at the site to measure vertical and lateral stresses in the abutment respectively. The size of the RPCs were constructed to fit right behind the CMU blocks. Foil type strain gages (SGs) were installed on the geotextile to measure reinforcement strains. The instrumentation program was monitored to record short-term responses of the structure due to self-weight of backfill and placement of bridge slab, in addition to the stage loading that was implemented during construction. Additionally, data from the embedded instruments were

collected to evaluate the long-term responses due to traffic loads and seasonal variations. The characteristics of the field monitored GRS-IBS and detailed layout of the instruments embedded into the structure are presented in detail in Gebremariam et al. (2020a and 2020b).

EVALUATION OF VERTICAL STRESSES

EPCs were installed at five different layers on both abutments ranging from the layer just above the RSF to the aggregate layer just underneath the slab and in between the layers from the bottom to the top. The instrumentation layout was designed to include instruments within both primary reinforcement and bearing bed zones. The following sections describe the evaluation of the vertical stress measurements from the field site.

Effect of Vertical Reinforcement Spacing on Stress Distribution – Stage Loading

During construction, Abutment A was loaded with Jersey barriers to simulate staged loading. Staged loading was conducted to evaluate the effects of differences in vertical spacing between reinforcements on the stresses recorded within the GRS. Four staged loadings were applied on the primary reinforcement zone and three staged loadings were applied on the bearing bed zone. Therefore, a comparison of the vertical stress distribution in each of these zones could be used to evaluate the effects of reinforcement spacing.

The location of each applied staged load was approximately 0.3 m from the facing CMU blocks coinciding within the zones where EPCs were installed at different heights. In total, there were seven staged loadings, four of which involved the use of eight Jersey barriers and three of which involved the use of a single Jersey barrier. Details of Jersey barrier configurations at each layer can be found in Gebremariam et al. (2020a).

The Jersey barrier used in the staged loadings was 0.6 m wide and 3.6 m long and the magnitude of the pressure from one barrier was approximately 11 kPa. In the case of eight Jersey barrier applications, due to the configuration of how the barriers were stacked up on top of each other and the contact to the ground, the total applied load was 89 kPa where the first and third barrier was each approximately applying 39 kPa and the middle barrier was applying 11 kPa.

Figure 2a displays the response of EPCs 1 and 7 when both instruments were loaded with a single Jersey barrier that was located 0.8 m above the EPCs. EPC 1 was loaded as part of stage load 3 and located within the zone where the spacing was 0.2 m. EPC 7 was loaded as part of stage load 7 and located within the zone where the spacing was 0.1 m. Although stage load 7 included eight Jersey barriers, the comparison was made when only the first Jersey barrier was placed on the GRS. The results show that the stress measured by EPC 1 was higher than EPC 7, indicating that the stress values within the primary reinforcement zone (where the spacing between the reinforcements are larger) were higher than the ones in bearing bed zone.

Figure 2b presents the responses of EPCs 1, 2 and 3 to stage load 4 where the spacing was 0.2 m and EPCs 7, 8 and 9 to stage load 7 where the spacing was 0.1 m. In this comparison, both staged loads were conducted with multiple Jersey barriers (39 kPa), but the vertical distance between the location of the applied load and the instruments was 1.2 m and 0.8 m in stage loads 4 and 7,

respectively. The results show that reduced stresses were measured by EPCs 7, 8 and 9, even though these instruments were located a shorter vertical distance from the applied load as compared to EPCs 1, 2 and 3. The stress measured by EPC 3 was less than the stresses recorded by EPCs 1 and 2, and the stress measured by EPC 9 was less than the stresses measured by EPCs 7 and 8 because EPCs 3 and 9 were horizontally farther away from the location of the applied load (Figure 2b). Nonetheless, the stress measured by EPC 3 was higher than that measured by EPC 9. These observations indicate a reduction in the stress distribution in the zone where reinforcements were vertically closer to each other (i.e., within the bearing bed zone).

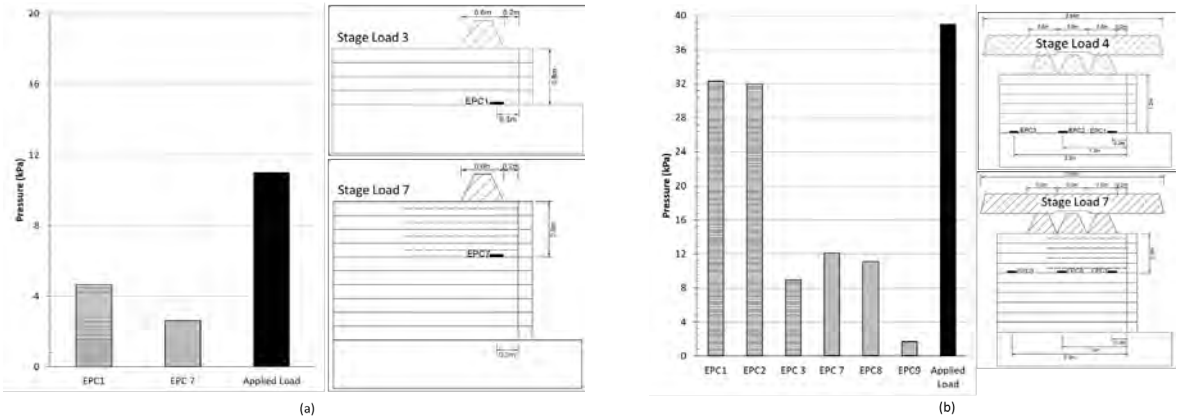

Figure 2. Comparison of vertical stresses measured in the field monitored GRS-IBS during stage loading by means of (a) single Jersey barrier; and (b) from multiple Jersey barriers (figure after Gebremariam et al. 2020a).

The consistent trends observed in Figure 2 (with both single and multiple Jersey barriers) demonstrate that closely spaced reinforcements contribute to reduced vertical stresses in the GRS bearing bed zone. In single Jersey barrier loading, the magnitude of stress was reduced 1.8 times and in multiple Jersey barrier loading, the magnitude of stress was reduced 2.7 to 5.4 times. Moreover, this indicates that the effect of closely spaced reinforcements becomes more prominent with an increase in applied loads. Overall, the results obtained from the staged loadings reveal that a decrease in reinforcement spacing (increased number of reinforcements) leads to reduced vertical stresses in the GRS mass.

Effect of Beam Seat Width on Stress Distribution – Slab Loading

The purpose of this evaluation was to compare the differences in stress distribution within the body of GRS-IBS where both abutments were constructed with the same materials and reinforcement spacing but with two different beam seat widths. One of the abutments had a beam seat width of 0.6 m (Abutment A), which is the minimum width required considering the length of the bridge span, and the other abutment had a beam seat width of 1.2 m (Abutment B, twice the width of Abutment A). Although both abutments were loaded with the same slab, the magnitude of surcharge loads in Abutments A and B were estimated to be 42 and 21 kPa, respectively.

Vertical stress distribution profiles developed in each abutment as determined from the EPCs are shown in Figure 3. The slab at this project site was constructed by multiple segments and it is believed that at the top, between the reinforced aggregate and the slab, in some locations, there

were gaps. Even though the applied slab load for each abutment was the same on all sides (i.e., middle, north, or south sides), in areas where the EPCs coincidentally lined up with these gaps, the data recorded from the instruments showed different values. However, regardless of this condition, at the bottom of the GRS-IBS, in both abutments, the applied load has approximately reduced to one forth. Such observation indicates that the mechanism of vertical stress distribution does not change based on changes in the beam seat width, but that the beam seat dimensions have a significant effect on the applied load. This information could be used to adjust the width of the beam seat to reduce the applied loads on GRS-IBS and consequently, if needed, to adjust the height of the bearing bed (double reinforced zone).

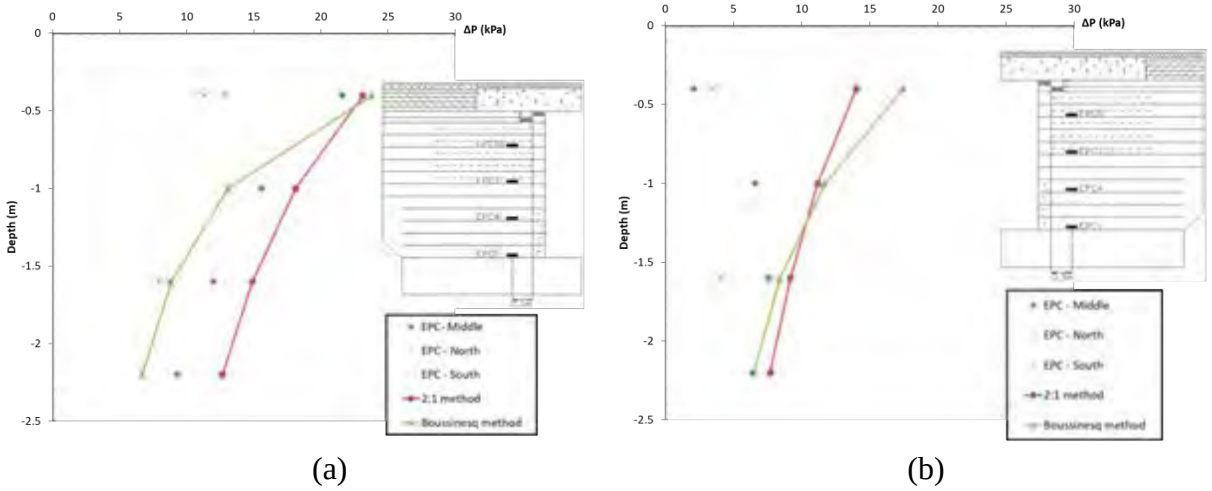

Figure 3. Vertical stress distributions due to bridge slab load at: (a) Abutment A and (b) Abutment B (figure from Gebremariam et al. 2020a).

Figure 3 also shows comparison of the stress distributions calculated based on theoretical Boussinesq and 2:1 methods. Details of how the stresses from these theoretical methods were computed can be found in Gebremariam et al. (2020a). When the difference in stress magnitudes from each of the method were compared with each other, based on the differences in beam seat widths, the difference is in the order of 1.5 to 2 close to the top of the abutment. These differences decrease with depth as the magnitude of applied load also decreases. Although both theoretical stress distribution methods evaluated in this study showed similar trends, Boussinesq method appears to provide slightly better agreement for stress magnitudes when compared with the data obtained from the EPCs and the applied slab loads.

Effect of Seasonal Variations on Vertical Stresses – Truck Loading

The effect of seasonal variations on the vertical stress distribution within the GRS-IBS was monitored by loading the slab with a truck. The goal was to record changes in the measured vertical stress values. To capture the seasonal differences, the truck was parked over the slab at different times of the year: (1) at the beginning of September (response immediately after construction), (2) in December (response during winter season), (3) by March (response during spring season), and (4) by November (response during fall season). The results showed that the vertical stress distribution in the GRS abutment with AASHTO No. 8 aggregate used as backfill material was

not significantly influenced by seasonal variations. The details of the truck loading program and associated results are presented in Gebremariam et al. (2020a).

EVALUATION OF LATERAL STRESSES AND REINFORCEMENT STRAINS

RPCs were installed at Abutment A at locations right behind the facing blocks. Figure 4 present the distribution of lateral stresses within the body of the GRS-IBS as determined from the installed instruments (due to self-weight and after the slab is placed) and based on theoretical calculations. Details of how these theoretical calculations were conducted can be found in Gebremariam et al. (2020b). The field data shows that with the placement of the slab, the lateral stress distribution becomes similar to that defined by the active condition and in general shows a uniform trend with depth. The magnitudes of the lateral stresses measured in the field were slightly lower that the theoretically calculated stresses under the active condition. However, the difference in magnitude of stress is in the order of 0.5 to 1 kPa, which is within the accuracy of the instrument. The results from the field measurements indicate that the theoretical active lateral earth pressure can be used to define the lateral stress distribution in GRS-IBS structures under service loads.

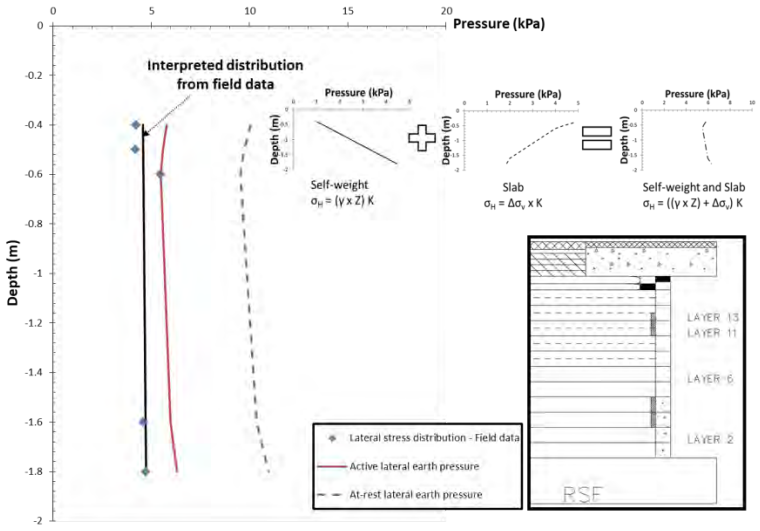

Note: Shaded areas within the insert indicate the location of RPC instruments

Figure 4. Lateral stress distribution within the body of GRS-IBS (figure from Gebremariam et al. 2020b)

Figure 5 presents the minimum, average, and maximum reinforcement strain values obtained from the SGs that were installed on the woven geotextile right behind the facing. Similarly to the lateral stress distribution, the strain distribution with depth also appear to be uniform. The maximum strain recorded in the field was significantly less than the maximum allowable geosynthetic strains (2%) in GRS-IBS design (Adams et al. 2011; Adams and Nicks 2018).

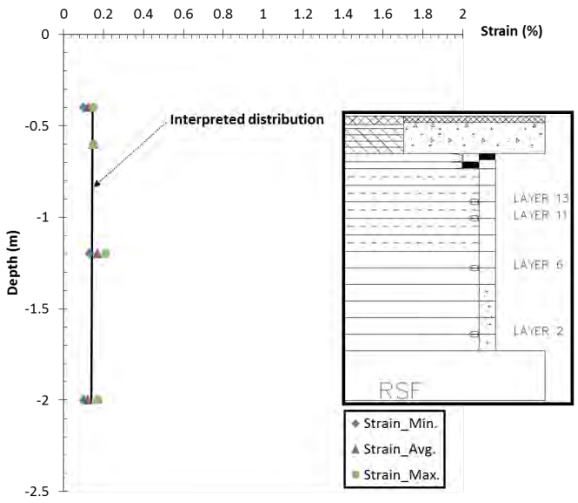

Note: Circles depicted within the insert indicate the location of SG instruments

Figure 5. Reinforcement strain distribution with depth in GRS-IBS after placement of slab load (figure from Gebremariam et al. 2020b).

The lateral stresses and strains measured from the field were then used to estimate the loads at the connection between the geotextiles and the concrete facing blocks. Details of the equations and approaches used for these computations can be found in Gebremariam et al. (2020b). When the connection loads (T_o) calculated from both of these approaches were compared, the magnitudes of the values were very close to one other and ranged between approximately 0.8 and 1.2 kN/m. Distribution of the calculated T_o with depth can be seen in Gebremariam et al. (2020b). Considering the difference in magnitude of the T_o values, the overall distribution is considered uniform.

CONCLUSIONS

This paper presents the summary of findings from a case study in a field monitored GRS-IBS constructed in Virginia. The main objectives of the study were to investigate: (1) the vertical stresses and stress distribution during and after construction (Gebremariam et al. 2020a) and (2) the connection loads and stress-strain conditions right behind the facing of the GRS-IBS (Gebremariam et al. 2020b). The stress and strain measurements from the field were compared with the theoretical calculations outlined in the design of GRS-IBS and MSE structures. The conclusions from this study are summarized as follows:

(1) The results from staged loading revealed that closely spaced reinforcements contribute to a reduction in vertical stresses in the bearing bed zone.
(2) The width of the beam seat affects the stress distribution within the GRS abutment. A wider beam seat effectively reduces the stress distribution in the structure that is caused by the superstructure.
(3) Boussinesq method appears to provide a slightly better estimation of the vertical stress distribution in GRS-IBS than the approximate 2:1 method.

(4) The magnitudes of the lateral stresses from the field after applying the slab load were close to the stresses predicted by the theoretical active condition and the stress distribution was found to be reasonably uniform.
(5) Reinforcement strains obtained from field measurements were significantly below the maximum allowable geosynthetic strains for the GRS-IBS design. The strain distribution with depth in GRS-IBS is interpreted as uniform.
(6) Connection load (T_o) values estimated using reinforcement strains and lateral stresses right behind the facing were in agreement, both in terms of distribution with depth and magnitude. Considering the difference in magnitude of the T_o values, the overall distribution is considered uniform.

REFERENCES

AASHTO (2017). LRFD Bridge Design Specifications, 8th Edition, American Association of State Highway and Transportation Officials, Washington, DC, 1,780p.

Adams, M.T., Nicks, J.E., Stabile, T., Wu, J.T.H., Schlatter, W., and Hartmann, J. (2011). Geosynthetic Reinforced Soil Integrated Bridge System, Synthesis Report. Report No. FHWA-HRT-11-027, Federal Highway Administration, McLean, VA.

Adams, M., Nicks, J. (2018). Design and Construction Guidelines for Geosynthetic Reinforced Soil Abutments and Integrated Bridge Systems. FHWA-HRT-17-080.

Berg, R.R., Christopher, B.R. and Samtani, N.C. (2009). Design and Construction of Mechanically Stabilized Earth Walls and Reinforced Soil Slopes. FHWA NHI-10-024 Vol I and NHI-10-025 Vol II, U.S. DOTFHWA-NHI-09-083 and FHWA GEC-011, Federal Highway Administration, Washington, D.C., 2009, pp 306 (Vol I) and pp. 378 (Vol II).

Gebremariam F, Tanyu B. F., Christopher B., Leschinsky D., Han J., Zornberg J. G. (2020a). Evaluation of Vertical Stress Distribution in Field Monitored GRS-IBS Structure, *Journal of Geosynthetics International*, https://doi.org/10.1680/jgein.20.00004.

Gebremariam F, Tanyu B. F., Christopher B., Leschinsky D., Zornberg J. G., Han J. (2020b). Evaluation of Required Connection Load in GRS-IBS Structures under Service Loads, *Journal of Geosynthetics International*, https://doi.org/10.1680/jgein.20.00022.

Jaky, J. (1948). Pressure in Silos. 2nd ICSMFE, London, 1, 103-107.

Zornberg, J.G., Morsy, A.M., and Mofarraj, B., Christopher, B.R., Leshchinsky, D., Han, J., Tanyu, B.F., Gebremariam, F.T., Shen, P., Jiang, Y. (2018). Defining the Boundary Conditions for Composite Behaviour of Geosynthetic Reinforced Soil (GRS) Structures. National Cooperative Highway Research Program (NCHRP), Project 24-41, Transportation Research Board, Washington D.C., October, 986 p.

Zornberg, J.G., Morsy, A.M., Mofarraj, B., Christopher, B.R., Leshchinsky, D., Han, J., Tanyu, B.F., Gebremariam, F.T., Shen, P., Jiang, Y. (2019). Proposed Refinements to Design Procedures for Geosynthetic Reinforced Soil (GRS) Structures in AASHTO LRFD Bridge Design Specifications. National Cooperative Highway Research Program (NCHRP), Project 24-41, Transportation Research Board, Washington D.C., March, 64 p.

Geosynthetics Conference

Load-Carrying GRS Bridge Abutments: Lessons Learned from Numerical Evaluations

Panpan Shen, Ph.D.[1], Jie Han, Ph.D.[2], Jorge G. Zornberg, Ph.D.[3], Yan Jiang, Ph.D.[4], Dov Leshchinsky, Ph.D.[5], Burak F. Tanyu, Ph.D.[6], and Barry R. Christopher, Ph.D.[7]

[1]Department of Geotechnical Engineering, Tongji University, Shanghai 200092, China; e-mail: hermit_shpp@tongji.edu.cn
[2]The University of Kansas, CEAE Department, Lawrence, KS 66044, USA; e-mail: jiehan@ku.edu
[3]The University of Texas at Austin, Civil Engineering Department, Austin, TX 78712, USA; e-mail: zornberg@mail.utexas.edu
[4]Terracon, Inc., 2201 Rowland Ave, Savannah, GA 31404, USA; e-mail: yan.jiang@terracon.com
[5]ADAMA Engineering, Inc., Clackamas, OR 97015, USA; e-mail: adama@GeoPrograms.com
[6]Department of CEIE, George Mason University, Fairfax, VA 22030, USA; e-mail: btanyu@gmu.edu
[7]Geotechnical Consultant, 210 Boxelder Lane, Roswell, GA 30076, USA; e-mail: barryc325@aol.com

ABSTRACT

This paper presents numerical analyses of load-carrying geosynthetic-reinforced soil (GRS) structures under three different conditions: (1) secondary reinforcement; (2) mini-piers; and (3) bridge abutments. All numerical models were first calibrated and/or verified with test data from the laboratory and/or the field. Most of the numerical analyses were conducted using a two-dimensional (2D) finite difference method, while a three-dimensional (3D) analysis was conducted to examine the 3D effects on GRS mini-piers. Backfill was modeled by a linearly elastic-perfectly plastic model with the Mohr-Coulomb (MC) failure criterion or a stress-dependent Cap-Yield (CY) constitutive model. Geosynthetics were modeled by structural elements. Facing units were modeled as individual elastic solid blocks with interfaces. Numerical results indicated that the use of secondary reinforcement could reduce the facing deflections, and the maximum tensile forces and connection forces in primary reinforcement layers. The use of 2D models to predict the behavior of 3D GRS mini-piers generated conservative results. The MC constitutive model resulted in similar predictions as the stress-dependent CY constitutive model under working stress conditions. When the reinforcement pullout failure mode prevailed in the analysis, the GRS structures with closely-spaced reinforcement layers clearly outperformed those with largely-spaced reinforcement layers, despite both having equal total reinforcement strength or stiffness. When the reinforcement rupture was the controlling failure mode, the GRS structures with closely- and largely-spaced reinforcement layers performed similarly if the total reinforcement strength or stiffness was equal.

INTRODUCTION

Geosynthetics have been successfully used to reinforce earth retaining structures since the early 1970s. More recently, geosynthetic reinforcement has been increasingly used for load-carrying structures, such as bridge abutments. These types of structures are frequently referred to in the

literature as geosynthetic-reinforced soil (GRS) structures. Closely-spaced reinforcement layers have also been used for load-carrying GRS structures, leading to specific design guidelines developed by the US Federal Highway Administration (FHWA) for structures called Geosynthetic-Reinforced Soil-Integrated Bridge Systems (GRS-IBS) (Adams and Nicks, 2018). Large-scale laboratory GRS mini-pier tests conducted by the FHWA (Nicks et al., 2013) clearly demonstrated increased load bearing capacities when closely-spaced reinforcement layers were used. However, a direct comparison of GRS mini-pier test results with the field performance of GRS bridge abutments may be compromised due to different boundary conditions between these two structures. Therefore, the performance of load-carrying GRS structures should be evaluated under different boundary conditions.

This paper presents numerical analyses of load-carrying GRS structures under three different conditions: (1) secondary reinforcement; (2) mini-piers; and (3) bridge abutments. All the numerical models were first calibrated and/or verified with test data from the laboratory and/or the field. Responses of GRS structures under different boundary conditions were then evaluated in terms of applied pressure versus vertical strain curves, lateral facing displacements, and tensile forces in reinforcement layers.

NUMERICAL MODELING OF GEOSYNTHETIC-REINFORCED RETAINING WALLS WITH SECONDARY REINFORCEMENT

Numerical model calibration and validation

Jiang et al. (2019 and 2020) conducted 2D numerical analyses using a finite difference method to evaluate the performance of geosynthetic-reinforced retaining (GRR) walls with secondary reinforcement. Although the GRR walls simulated by Jiang et al. (2019 and 2020) did not carry surface loads, the use of secondary reinforcement in the GRR walls reduced the vertical spacing between primary reinforcement and resembled the use of closely-spaced reinforcement layers in GRS structures. Consequently, as a special case of closely-spaced reinforcement layers, this paper also includes the numerical results of the GRR walls with secondary reinforcement.

Jiang et al. (2019) developed a 2D numerical model to simulate an instrumented GRR wall constructed with secondary reinforcement in Kansas, USA. In addition to a linearly elastic-perfectly plastic model with the Mohr-Coulomb (MC) failure criterion (referred to as the MC model), a stress-dependent Cap-Yield (CY) constitutive model based on the theory of hardening plasticity (referred to as the CY model) was used to simulate the behavior of backfill soil. Calibration and validation details of the 2D numerical model, including the input parameters and modeling procedure, can be found in Jiang et al. (2019). The numerical models with both soil constitutive models were found to adequately predict the behavior of the GRR walls with secondary reinforcement in terms of wall facing displacements, lateral and vertical earth pressures, and reinforcement strains.

Primary conclusions from the numerical analyses of GRR walls with secondary reinforcement

Jiang et al. (2020) performed a parametric study to investigate the effects of secondary reinforcement on the performance of GRR walls. The investigated factors included the length, stiffness, connection, and layout of secondary reinforcement. The following conclusions can be drawn from the parametric study:

(1) The use of secondary reinforcement reduced the maximum tensile forces and connection forces in the primary reinforcement, which is the same as that found by Leshchinsky and Vulova (2001).

(2) The use of secondary reinforcement reduced the deflections of the GRR walls.

NUMERICAL MODELING OF LOAD-CARRYING GRS MINI-PIERS

Numerical model calibration and validation

Shen et al. (2019) and Zornberg et al. (2019) conducted both 2D and 3D numerical analyses using the finite difference method to evaluate the performance of GRS mini-piers. The numerical models were first calibrated and validated against the test results in Nicks et al. (2013), who conducted 19 GRS mini-pier tests to investigate the axial load-deformation relationships of the GRS mini-piers with different reinforcement spacing. In the numerical analyses, the MC model was used for the backfill soil, the geosynthetics were modeled by structural elements, and the facing units were modeled as individual elastic blocks with interfaces. Calibration and validation details of the 2D and 3D numerical models, including the input parameters and modeling procedure, can be found in Shen et al. (2019) and Zornberg et al. (2019). It was concluded that the 3D numerical model reasonably predicted the behavior of 3D GRS mini-piers, while the 2D numerical model predicted larger facing displacements and reinforcement forces than the 3D model due to no consideration of the 3D boundary effects.

Primary conclusions from the numerical analyses of the GRS mini-piers

Parametric studies were conducted under both 2D and 3D conditions to investigate the influences of reinforcement stiffness, reinforcement spacing, and different combinations of reinforcement stiffness and spacing, on the performance of GRS mini-piers under vertical loading (Shen et al., 2019; Zornberg et al., 2019). The following conclusions can be drawn from the parametric studies:

(1) The 2D numerical model conservatively predicted the performance of 3D GRS mini-piers regarding vertical strains under different applied pressures, lateral facing displacements, and maximum reinforcement forces.

(2) GRS mini-piers were mostly controlled by pullout of reinforcement. When the total reinforcement stiffness was equal, the effect of reinforcement spacing was more significant than that of reinforcement stiffness. In other words, under the same ratio of reinforcement stiffness J to spacing S_v, the pier with closely-spaced reinforcement layers showed better performance than the pier with largely-spaced reinforcement layers. Specifically, the pier with closely-spaced reinforcement layers showed smaller vertical strains under the same applied pressure, smaller lateral facing displacements, and lower and more uniformly-distributed reinforcement forces.

NUMERICAL MODELING OF LOAD-CARRYING GRS BRIDGE ABUTMENTS

Numerical model calibration and validation

Zornberg et al. (2019) and Shen et al. (2020) evaluated the responses of load-carrying GRS bridge abutments subjected to slab loading under working stress conditions using the 2D finite difference method. The numerical model was first calibrated and validated using field data from a GRS-IBS constructed in Virginia, USA (Zornberg et al., 2019; Gebremariam et al., 2020a and b). In the numerical analyses, the backfill soil was simulated by the MC model or the stress-dependent CY model. The geosynthetics were modeled by structural elements. The facing units were modeled as

individual elastic blocks with interfaces. The numerical model simulated seven stages of loading conducted in the field during the construction of the Virginia GRS-IBS using rectangular concrete blocks with different densities. Calibration and validation details of the 2D numerical model, including the input parameters and modeling procedure, can be found in Zornberg et al. (2019) and Shen et al. (2020). The numerical results showed that the MC model and the CY model generated similar predictions under working stress conditions, and both models reasonably simulated the field performance of the Virginia GRS-IBS in terms of lateral earth pressures, additional vertical stresses induced by bridge slab loading, and reinforcement strains.

Primary conclusions from the numerical analyses of the GRS bridge abutments

Parametric studies were conducted to investigate the effects of different combinations of reinforcement spacing and reinforcement stiffness, beam seat width, and setback distance, on the responses of the GRS bridge abutments (Zornberg et al., 2019; Shen et al., 2020). The parametric studies also evaluated two layouts with different reinforcement lengths along the height of the abutment (i.e., trapezoidal and uniform reinforcement layouts). The following conclusions can be drawn from the parametric studies:

(1) The GRS abutments with trapezoidal and uniform reinforcement layouts exhibited similar responses under self-weight only and under self-weight with bridge slab loading.

(2) When the total reinforcement stiffness or the ratio of reinforcement stiffness to spacing J/S_v was equal, different combinations of reinforcement stiffness and spacing did not produce significant differences in the GRS abutment responses regarding additional vertical stresses under the beam seat centerline and additional lateral earth pressures behind the abutment facing induced by bridge slab loading.

EFFECTS OF BOUNDARY CONDITIONS ON THE PERFORMANCE OF LOAD-CARRYING GRS STRUCTURES

The numerical results of the GRS mini-pier tests indicated that reducing reinforcement spacing S_v was more beneficial than increasing reinforcement stiffness J to improve the performance of GRS mini-piers in terms of the vertical strain under the applied pressure and the lateral facing displacements. In contrast, the numerical results of the GRS bridge abutments indicated similar behavior for the two structures simulated with the same J/S_v ratio regarding the additional vertical stresses under the beam seat centerline and the additional lateral earth pressures behind the abutment facing induced by bridge slab loading. Zornberg et al. (2019) pointed out that the boundary conditions are the main difference between a GRS mini-pier and a GRS bridge abutment: a GRS mini-pier is similar to a retaining wall with limited fill space, whereas the fill space in a GRS bridge abutment is relatively larger. In addition, the GRS mini-pier included a footing on top, the width of which was approximately equal to the width of the pier, while the GRS bridge abutment included a bridge slab on top, the contact area of which was much smaller than the width of the reinforced zone.

To investigate the effects of boundary conditions, two GRS structures with different geometries were evaluated, as shown in Figure 1. The first structure, labeled Structure 1, is essentially a GRS mini-pier with a height of 2 m and a width of 1 m. The second structure, labeled Structure 2, is a modified GRS mini-pier with longer reinforcement. The ratios of the reinforcement length L to the pier height H were 0.5 and 1.5 for Structures 1 and 2, respectively.

Structure 2 resembles a GRS bridge abutment with adequate fill space behind its facing units and contains a smaller footing on its top.

The constitutive models for the reinforced zone, the footing, the facing units, and the reinforcement were similar to those used in the parametric studies of the GRS mini-pier tests. Detailed input parameters and modeling procedures can be found in Zornberg et al. (2019), and the numerical results are presented below.

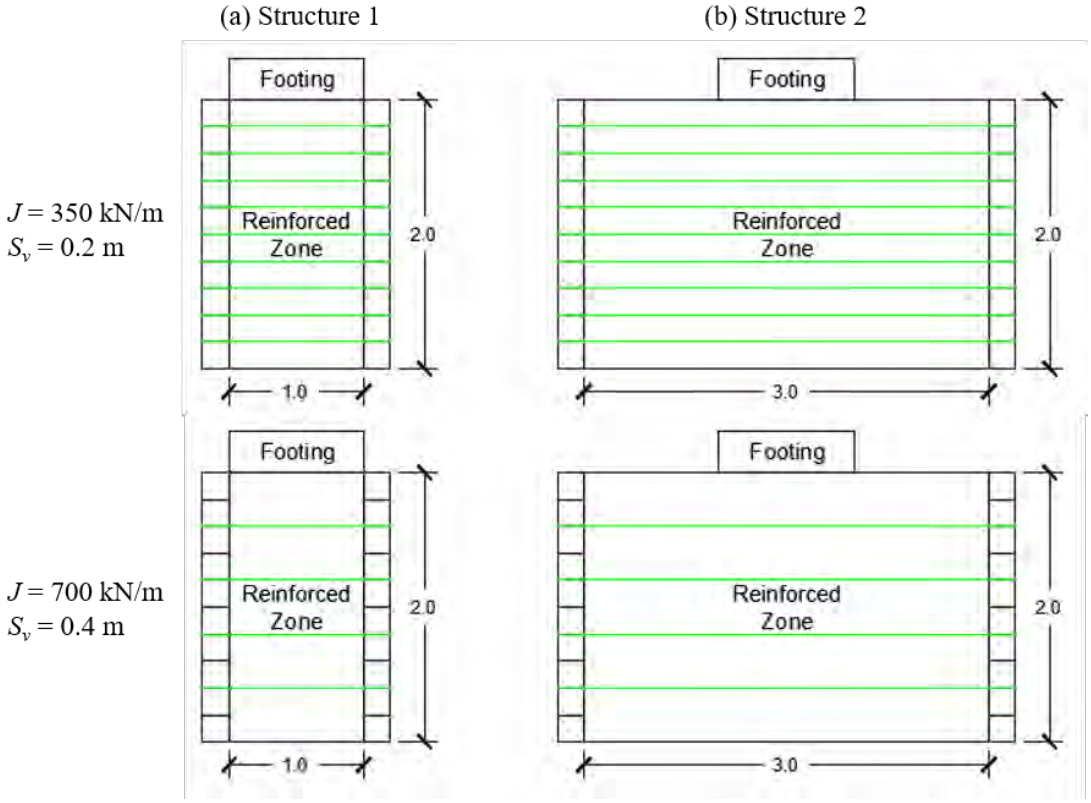

Figure 1. Geometry of numerical models: (a) Structure 1 and (b) Structure 2 (Zornberg et al., 2019).

Applied pressure – vertical strain curves

Figure 2 presents the applied pressure – vertical strain curves for both structures. Figure 2 shows that Structures 1 and 2 had very different results. The numerical results for Structure 1 indicate that the case with closely-spaced reinforcement layers exhibited significantly smaller vertical strains under the same applied pressure than the case with largely-spaced reinforcement layers. The numerical results for Structure 2, however, demonstrated that the reinforcement spacing did not have a significant effect on the applied pressure – vertical strain curves. The change in boundary conditions produced different responses in the GRS structures. The significant differences between the applied pressure – vertical strain curves for Structures 1 and 2 will be clarified subsequently as part of the discussion of the distribution of reinforcement tensile forces.

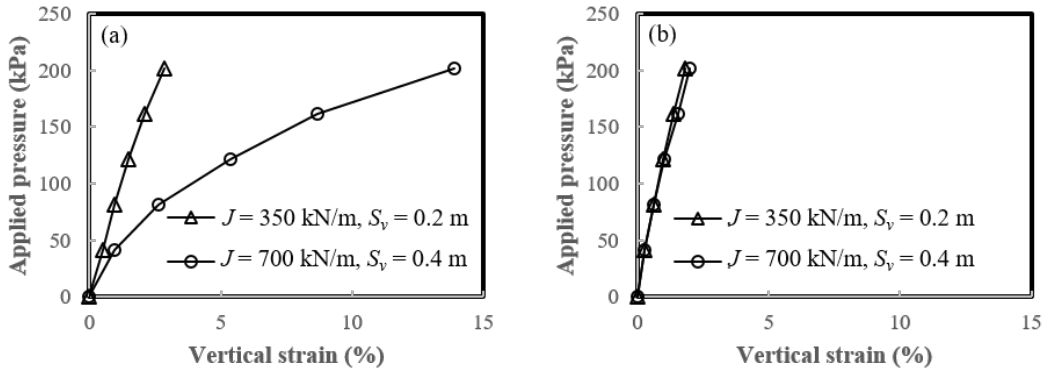

Figure 2. Applied pressure versus vertical strain curves: (a) Structure 1 and (b) Structure 2 (Zornberg et al., 2019).

Lateral facing displacements

Figure 3 shows the lateral facing displacements under an applied pressure of 200 kPa for both structures. Similar to the applied pressure – vertical strain curves, Structures 1 and 2 exhibited significantly different responses under the same applied pressure. Structure 1 exhibited much larger lateral facing displacements for the case with reinforcement spacing S_v = 0.4 m than the case with reinforcement spacing S_v = 0.2 m. Structure 2, however, had approximately the same lateral facing displacements for the two cases with different combinations of reinforcement stiffness and spacing. An explanation of the significant differences in the lateral facing displacements between the two structures will also be provided in the subsequent discussion of the distribution of reinforcement tensile forces.

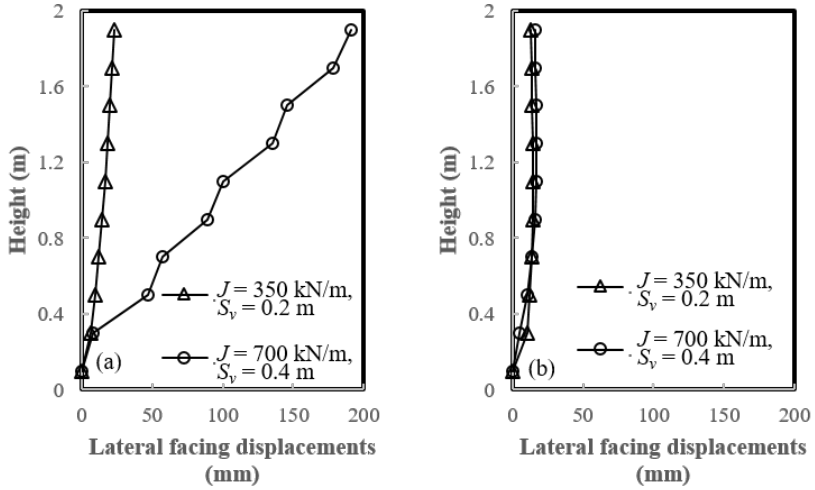

Figure 3. Lateral facing displacements under an applied pressure of 200 kPa: (a) Structure 1 and (b) Structure 2 (Zornberg et al., 2019).

Distributions of reinforcement tensile forces

Figure 4 presents the distributions of tensile forces in the reinforcement at four depths under an applied pressure of 200 kPa for both structures. The envelopes of pullout capacities for reinforcement layers are also plotted in Figure 4. Due to the use of frictional connections between

reinforcement layers and facing units, two pullout capacity envelopes initiated from zero at two opposite ends of the reinforcement layer embedded between two facing units and increased with length toward the center.

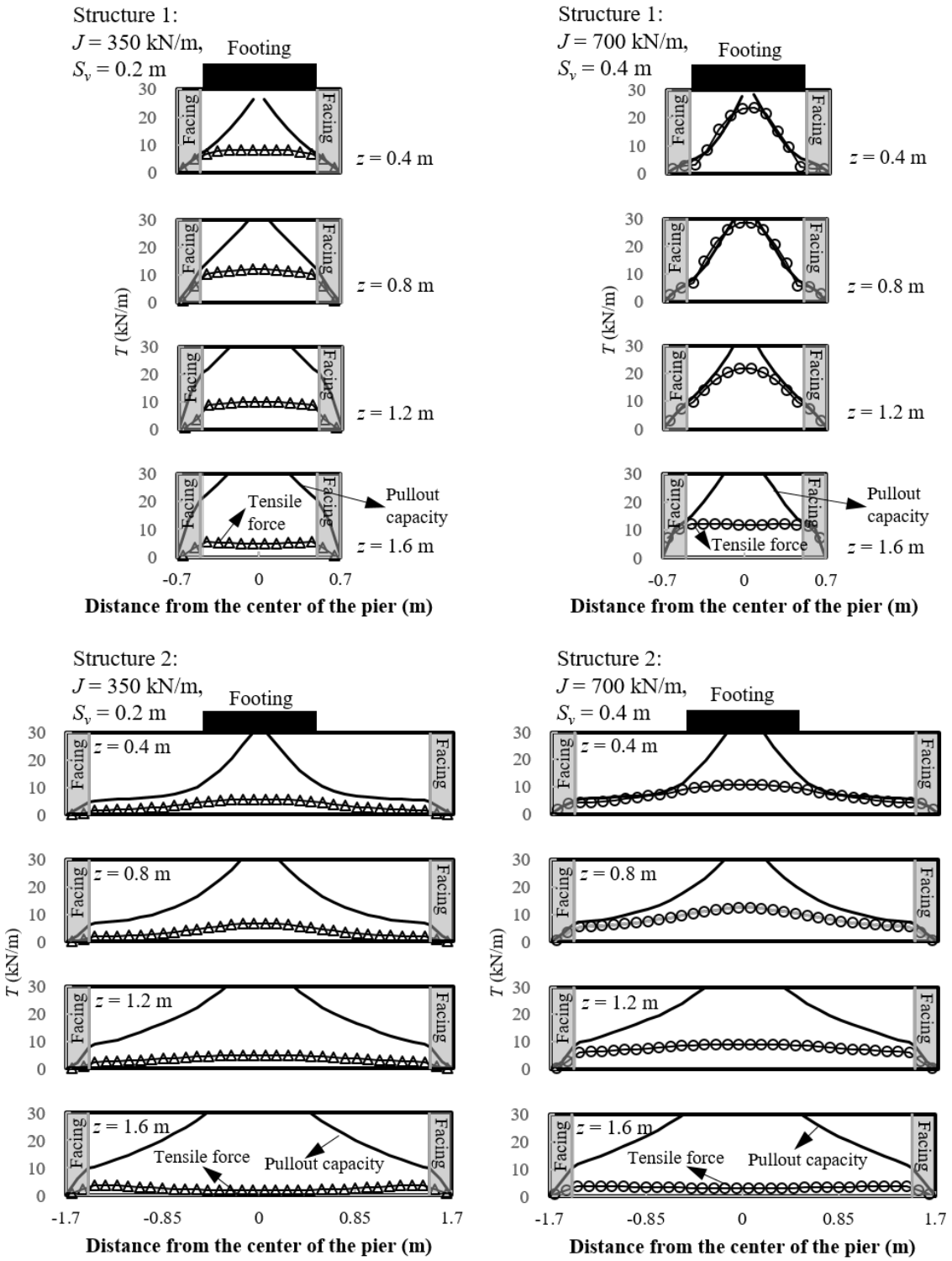

Figure 4. Distributions of tensile forces and pullout capacities of reinforcement layers under an applied pressure of 200 kPa.

The two cases of Structure 1 had different distributions of tensile forces in the reinforcement layers when the reinforcement spacing S_v was changed. When S_v = 0.4 m, the tensile forces in the upper three reinforcement layers were largest under the center of the footing and decreased linearly towards facing units at both left and right ends. Additionally, the tensile forces in the reinforcement layers were approximately the same as the pullout capacities, indicating that pullout failure prevailed at most reinforcement layers. When S_v = 0.2 m, smaller and more uniformly-distributed tensile forces developed in the reinforcement layers. These tensile forces, with the exception of those in the uppermost layer, were smaller than the pullout capacities, indicating that the reinforcement pullout capacities were sufficient and pullout failure did not prevail. The use of largely-spaced reinforcement layers required the mobilization of larger tensile forces in the reinforcement. When the required tensile forces reached the pullout capacities, the rupture strength of the reinforcement could not be mobilized, which resulted in less efficient lateral confinement of the surrounding soil. As a result, the case with largely-spaced reinforcement layers yielded larger vertical strains and lateral facing displacements under the same applied pressure than the case with closely-spaced reinforcement layers. This explains why a reduction in reinforcement spacing S_v led to greater improvement in the performance of the GRS mini-piers than an increase in reinforcement stiffness J under the same J/S_v ratio, as previously discussed.

The two cases of Structure 2, however, had similar distributions of tensile forces in the reinforcement layers despite a change in the reinforcement spacing. For both cases with different combinations of reinforcement stiffness and spacing, the tensile forces in most reinforcement layers were below the envelopes of the pullout capacities, indicating that pullout failure did not prevail in Structure 2. The footing on top of the reinforced zone in Structure 2 served as a load with a limited loading area. The length of the reinforcement beyond the footing provided sufficient anchorage to prevent pullout from occurring. Consequently, the two cases of Structure 2 showed similar responses in terms of the applied pressure versus vertical strain curves and the lateral facing displacements. This explains why two GRS bridge abutments with different combinations of J and S_v, but the same J/S_v ratio, behaved similarly under bridge slab loading as previously discussed.

CONCLUSIONS

This paper presents numerical analyses of load-carrying geosynthetic-reinforced soil (GRS) structures under three different conditions: (1) secondary reinforcement; (2) mini-piers; and (3) bridge abutments. All numerical models were first calibrated and/or verified with test data from the laboratory and/or the field. Most of the numerical analyses were conducted using a two-dimensional (2D) finite difference method, while a three-dimensional (3D) analysis was conducted to examine the 3D effects on GRS mini-piers. Backfill was simulated by a linearly elastic-perfectly plastic model with the Mohr-Coulomb (MC) failure criterion or a stress-dependent Cap-Yield (CY) constitutive model. Geosynthetics were modeled by structural elements and facing units were modeled as individual elastic solid blocks with interfaces. The following conclusions can be drawn from this study:

(1) The use of secondary reinforcement reduced the facing deflections and the maximum tensile forces and connection forces in primary reinforcement.

(2) The 2D numerical model conservatively predicted the behavior of the 3D GRS mini-pier due to no consideration of the 3D boundary effects.

(3) The MC model and the CY model produced similar predictions of the performances of GRS structures under working stress conditions.

(4) When the reinforcement pullout failure mode prevailed, the GRS structures with closely-spaced reinforcement layers clearly outperformed those with largely-spaced reinforcement layers even though the total reinforcement strength or stiffness was equal.

(5) When the reinforcement rupture was the controlling failure mode, the GRS structures with closely- and largely-spaced reinforcement layers performed similarly if the total reinforcement strength or stiffness was equal.

REFERENCES

Adams, M., Nicks, J. (2018). Design and Construction Guidelines for Geosynthetic Reinforced Soil Abutments and Integrated Bridge Systems. FHWA-HRT-17-080.

Gebremariam, F., Tanyu, B. F., Christopher, B., Leshchinsky, D., Han, J., Zornberg, J. G. (2020a). Evaluation of vertical stress distribution in field monitored GRS-IBS structure. *Geosynthetics International*, 27(4): 414-431.

Gebremariam, F., Tanyu, B. F., Christopher, B., Leshchinsky, D., Zornberg, J. G., Han, J. (2020b). Evaluation of required connection load in GRS-IBS structures under service loads. *Geosynthetics International*, in press. doi: 10.1680/jgein.20.00022.

Jiang, Y., Han, J., Parsons, R. L. (2020). Numerical evaluation of secondary reinforcement effect on geosynthetic-reinforced retaining walls. *Geotextiles and Geomembranes*, 48(1): 98-109.

Jiang, Y., Han, J., Zornberg, J. G., Parsons, R. L., Leshchinsky, D., Tanyu, B. (2019). Numerical analysis of field geosynthetic-reinforced retaining walls with secondary reinforcement. *Geotechnique*, 69(2): 122-132.

Leshchinsky, D., Vulova, C. (2001). Numerical Investigation of the Effects of Geosynthetic spacing on failure mechanisms of MSE block walls. *Geosynthetics International*, 8(4): 343-365.

Nicks, J. E., Adams, M., Ooi, P., Stabile, T. (2013). Geosynthetic Reinforced Soil Performance Testing—Axial Load Deformation Relationships. FHWA-HRT-13-066.

Shen, P., Han, J., Zornberg, J. G., Morsy, A. M., Leshchinsky, D., Tanyu, B. F., Xu, C. (2019). Two and three-dimensional numerical analyses of geosynthetic-reinforced soil (GRS) piers. *Geotextiles and Geomembranes*, 47(3): 352-368.

Shen, P., Han, J., Zornberg, J. G., Tanyu, B., Christopher, B., Leshchinksy, D. (2020). Responses of geosynthetic-reinforced soil (GRS) abutments under bridge slab loading: Numerical investigation. *Computers and Geotechnics*, 123: 103566.

Zornberg, J.G., Christopher, B.R., Leshchinsky, D., Han, J., Tanyu, B.F., Morsy, A.M., Shen, P., Gebremariam, F.T., Jiang, Y., Mofarraj, B. (2019). Defining the Boundary Conditions for Composite Behavior of Geosynthetic Reinforced Soil (GRS) Structures. National Cooperative Highway Research Program (NCHRP). Project 24–41. Transportation Research Board, Washington DC: 997p.

Geosynthetics Conference

Case Study: Geosynthetic Wrap-Face Vegetated MSE Walls for Enhancing Public Works Projects

Stanley M. Miller, Ph.D., P.E.,[1] Drew Loizeaux, P.E.[2], Todd Larson[3]

[1]Professor Emeritus, Dept. of Civil Engineering, University of Idaho, and currently Consulting Engineer, Moscow, ID; e-mail: smiller.geosynwall@gmail.com
[2]Engineering Specialist, Propex GeoSolutions, Propex Operating Company LLC, Chattanooga, TN; e-mail: Drew.Loizeaux@propexglobal.com
[3]Territory Business Manager, Propex Operating Company LLC, Chattanooga, TN; e-mail: Todd.Larson@propexglobal.com

ABSTRACT

During the summer of 2019 in the Minneapolis area, two public-school construction projects for facilities expansion required new MSE walls for critical grade-separation areas. A middle school project needed a wall 8-feet (2.4-m) high to provide grade separation between a parking lot and ball fields. The high school project needed walls 6 to 15-feet (1.8 to 4.6-m) high constructed along a steep, natural slope to provide additional flat, usable space at the crest of the slope. Design drawings and architectural plans originally listed these walls as masonry segmental block walls. However, the Contractor and Designers responsible for both projects decided to substitute (with School District approval) an engineered wrap-face vegetated wall system. This geosynthetic alternative provided a more cost-effective solution, as well as an aesthetic green, environmentally friendly option, which was favored by public works officials. This paper presents a case study for the two projects, focused on engineering design, geogrid reinforcement, construction methods, and vegetation establishment.

INTRODUCTION

During the spring and summer of 2019, two public-school facility upgrade and expansion projects in the Minneapolis area (more specifically, in Ramsey County) required the installation of MSE (Mechanically Stabilized Earth) walls to establish grade-separation areas at the sites. Design drawings and architectural plans originally showed these walls as masonry segmental block walls (hardscape). The first project, at Edgewood Middle School (MS) in Mounds View, MN, included a wall approximately 190-feet (58-m) long and 8-feet (2.4-m) high to separate a paved parking lot from grass play fields. The second project, at Mounds View High School (HS) in Arden Hills, MN, was more extensive and included approximately 2,400 square feet (223 square meters) of wall face with some sections 15-feet (4.6-m) high.

The general contractor for both projects, as well as the design engineers, discussed with school district officials the possibility of substituting an engineered vegetated wall system for the planned MSE masonry block walls. As a result, a geosynthetic wrap-face vegetated (GWFV) wall system was selected and approved (known as PYRAWALL), a geosynthetic alternative that provided a cost-effective solution, as well as a green, environmentally friendly option which was favored by public works officials. This reinforced-soil system uses 1-ft (0.3-m) high uniform wrap-lifts and relies on three components (Miller, 2017): 1) a polypropylene high-performance

turf reinforcement mat (HPTRM) to form the wrap-face lifts and secondary soil reinforcement, a product known as PYRAMAT-75 with an estimated design life of 75 years (Propex, 2020); 2) internal fiber-composite braces that hold-up the face and allow filling and compaction of the soil lifts; and 3) geogrid layers extending back into the embankment for primary soil reinforcement.

One of the key geotechnical and construction advantages of this engineered vegetated wall system is that often native, on-site soils can be used within the geosynthetic backfill reinforced zone. Site soils at the school projects were primarily comprised of silty fine sand with some clay and having low to moderate plasticity. Thus, no imported fill materials were required. Another advantage at the Mounds View HS site was the relative ease to transport the light-weight geosynthetic wall components (compared to heavy masonry blocks) to some wall sections with difficult or limited heavy-equipment access.

OVERVIEW OF GWFV WALL SYSTEM

The rolled HPTRM used for the face wraps is 8.5-ft (2.6-m) wide by 120-ft (36.5-m) long. As illustrated in Figure 1, this width provides a typical wrap layer with 4 ft (1.2 m) along the bottom, a 1-ft (0.3-m) near-vertical face, and 3.5 ft (1.1 m) folded back over the soil infill lift. The geosynthetic provides excellent erosion protection as vegetation seeded in the infill soil ("internal seeding") emerges and becomes established. The open-weave of the fabric also is conducive to vegetation being established by hydroseeding ("external seeding") after the wrap-face structure has been completed.

The unique lofted, three-dimensional feature of this HPTRM allows for the insertion (weaving) of bracing-bar components which stand-up the 1-ft (0.3-m) high section of the fabric, forming a face against which infill soil is placed and compacted. These bracing bars are fabricated using a high-strength, fiber-composite material consisting of nylon and fiberglass.

Primary geogrid reinforcement is added to the system by inserting ("sandwiching") the geogrids between successive wrap lifts, applying a thin soil layer to inhibit any fabric-to-fabric contact. Wood stakes or metal pins can be used to stretch both the HPTRM and the geogrid taut and hold them in place while soil backfilling occurs. A schematic drawing presented in the next section (Figure 1) shows the geosynthetic elements of the engineered vegetated wall system, as well as an optional topsoil/organic fill-soil at the wall face.

EDGEWOOD MIDDLE SCHOOL PROJECT

To expand and enhance a parking lot at Edgewood MS, a retaining wall was required to provide grade separation from a lower playfield area. Site preparation and subgrade compaction were generally straightforward at the wall site due to an overall relatively flat construction pad. For the geotechnical design analysis, conservative soil strength values were assumed, and construction monitoring included regular, on-site compaction testing in the wall backfill area (geogrid-reinforced zone). The design approach relied on allowable stress design (ASD) methods to check wall base sliding, wall overturning, and bearing capacity, assuming an estimated traffic load of 250 psf (12 kPa) which could result from heavy truck traffic in the parking lot behind the wall. The design analysis showed geogrid reinforcement for the 8-foot (2.4-m) high wall would need to be 11 feet (3.35 m) long with minimum long-term design strength (LTDS) = 860 lb/ft (12.6 kN/m), and placed at vertical intervals of 2 feet (0.6 m). A generalized schematic of the wall is shown in Figure 1. The contactor placed soil-growth media (organic topsoil material) containing

grass seeds at the wall face during the filling and compaction of each 1-foot (0.3 m) soil lift in the backfill zone.

Once the subgrade was compacted and leveled to the proper grade, the toe-line of the wall was surveyed and marked with paint lines along the ground. A base geogrid layer then was laid out (Figure 2), with the prescribed 11-ft (3.35-m) length. If necessary to keep the geogrid flat, stakes were driven through it after stretching it taut. A thin layer of fill soil then was spread across the geogrid, and the first HPTRM wrap was moved into position with the face braces already installed. The face of the lift was positioned along the painted toe-line, then staked in position along the front and back of the base layer, using a stake about every 6-8 ft (1.8-2.4 m) along the fabric length. The local area around braces was backfilled first to hold them down and keep them vertical, followed by filling across the entire width of the wrap. Compaction of each 6-in (0.15-m) soil lift was accomplished using plate or roller compactors, with two compaction lifts per each face wrap, and thus repeating for subsequent wraps to build the wall (Figure 3).

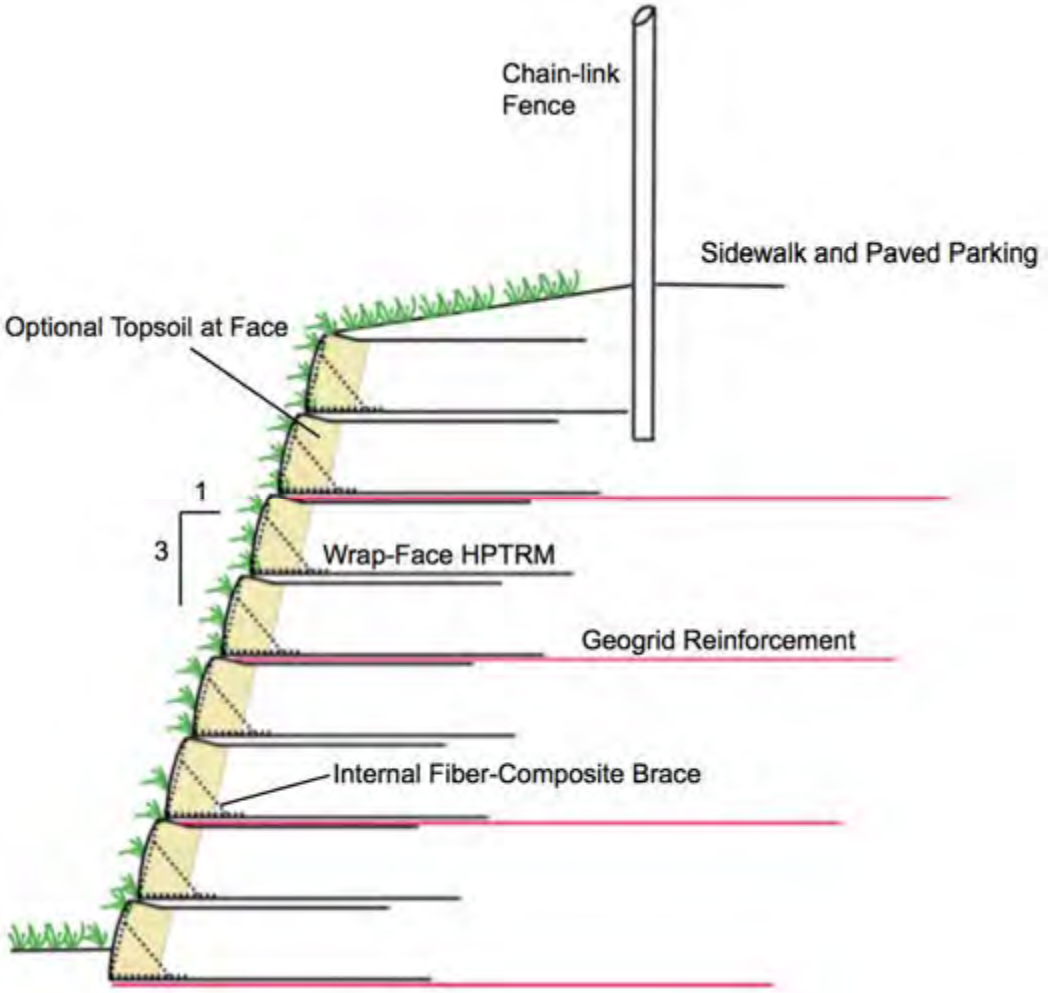

Figure 1. Generalized schematic of 8-foot high GWFV wall at Edgewood MS (design geogrid length is 11 feet).

Figure 2. Subgrade pad and first layer of geogrid at Edgewood MS wall project.

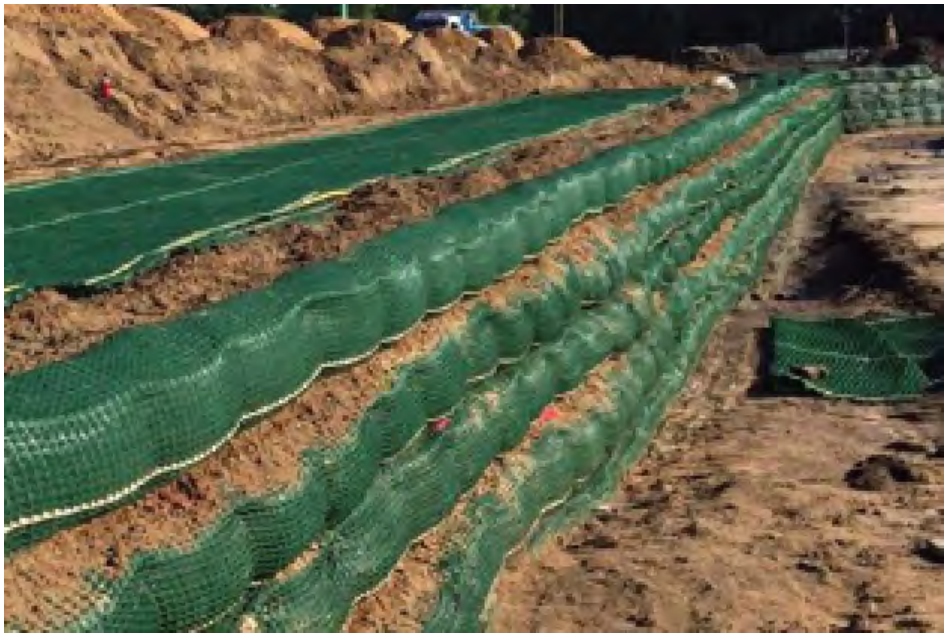

Figure 3. Partially completed GWFV wall at Edgewood MS.

After the wall was completed, the face was hydroseeded using a slurry mulch with a selected seed mix. The contractor elected to use combined internal and external seeding to enhance new growth and provide extensive vegetation coverage, per the request of school officials. Vegetation filled in quickly during the early fall, exceeding stakeholder expectations. The completed wall and parking lot are shown in Figure 4, an aerial view from October 2019. The entire wall was nearly completely covered in vegetation by June 2020, providing a green sustainable success story (Figure 5).

Figure 4. Edgewood MS construction site, showing completed engineered vegetated wall system in October of 2019 (looking west); courtesy of Google Earth.

Figure 5. Edgewood MS vegetated wall in June 2020.

MOUNDS VIEW HIGH SCHOOL PROJECT

Due to extended building footprints near a steep natural slope at Mounds View HS, the wall system was needed along the western edge of the site (Figure 6) to provide more flat area at the slope crest for traffic flow, especially for emergency vehicles including fire trucks. Subgrade preparation here was extensive due to topographic variations causing final wall heights to range from 6 to 15 feet (1.8 to 4.6-m). It is important to note that wall construction was facilitated by beginning at the lowest elevation portions of the wall base, then progressing upward as grade changes dictated. This means that "foundation steps" were required along the base of the wall. Care was taken to make sure these step heights corresponded directly to the height of wrap lifts; that is, 1 ft (0.3 m).

For the geotechnical design analysis, conservative soil strength values were assumed, and construction monitoring included regular, on-site compaction testing in the geogrid-reinforced zone. The design approach relied on allowable stress design (ASD) methods to check wall base sliding, wall overturning, and bearing capacity, assuming an estimated traffic load of 250 psf (12 kPa) in the travel way behind the wall. In addition, global stability analysis for large-scale rotational failure paths (Abramson et al., 2002) was conducted to assess whether stronger geogrid layers would be needed in the lower portion of the backfill zone to provide adequate resistance to potential "compound" failure paths that could pass through the reinforced zone. The ASD and Slope/W analysis (GEO-SLOPE, 2018) showed that geogrids 13-feet (4-m) long with minimum LTDS = 1320 lb/ft (19.3 kN/m) would be needed for the higher wall sections.

Figure 6. Mounds View HS construction site in 2019 (looking north), showing approximate location of planned MSE wall; courtesy of Google Earth.

At the north end of the proposed wall alignment, site conditions did not require the finished face to be any steeper than 1H:1.25V (horizontal to vertical), or approximately 51 degrees, so this portion of the grade separation structure was designed as a steep, reinforced soil slope, rather than an MSE wall. Bracing and backfilling this section of the geosynthetic structure are illustrated in Figure 7. The fiber-composite braces were spaced at regular 2-ft (0.6-m) intervals along the face, with backfill soil placed by hand in and around the braces prior to mechanical compaction of the soil lifts. This figure also shows the primary geogrid reinforcement placed within the embankment prior to installing this geosynthetic lift. Such geogrid layers were used every other lift; that is, at a regular vertical spacing of 2 feet (0.6 meters). No specialized granular drainage system was needed for this flexible wall system due to the silty sand used in the embankment and the lofted character of the HPTRM used near the face, both of which provide for the free movement of any potential groundwater that may occur within the slope.

To achieve the flatter face angles of a reinforced soil slope (i.e., less than 70 degrees), the GWFV wall wrap-lifts were installed with set-back “ledges” of several inches to match the desired overall face angle, allowing the engineered vegetated wall system to be simply modified to a stepped and steep, reinforced soil slope system (Figure 8). Also, note that a curved slope face was readily constructed using this flexible wall system, meaning that such flexibility allows for a wide variety of geotechnical projects focused on terrain forming or contour shaping for landscape design and construction.

Figure 7. Backfilling a geosynthetic lift for a reinforced soil slope section at the Mounds View HS project.

Figure 8. Partially completed reinforced soil slope at Mounds View HS project.

The overall completed wall system at Mounds View HS comprised approximately 2,400 square feet (223 square meters) of wall face with some sections 15-feet (4.6-m) high. The contractor chose to rely solely on post-construction hydroseeding for vegetation establishment, so no top soil was added to the backfill soil lifts near the face, and no grass seed was placed internally within each wrap face. A few weeks after hydroseeding, newly germinated grass was growing nicely and becoming well-established along the face of the engineered vegetated wall system (Figure 9).

A few intense thunder storms with heavy rainfall occurred during the first month after the wall system was completed; however, the HPTRM wrap face provided complete erosion protection as the grass seed germinated and began to grow. This erosion protection continued throughout the winter and into the next growing season to support vegetation establishment. Another characteristic of this particular woven HPTRM is its ability to retain and hold soil even when subjected to high-water flow events and flooding (Miller and Loizeaux, 2019). The HPTRM has a manufacturer's estimated design life of 75 years, so long-term erosion protection and flood protection is another advantage of this engineered wall system. By the summer of 2020, most of the wall face was grass covered, and the overall engineered structure comprised of wall and steep reinforced soil slope was blending well into the green surroundings of the natural slope west of the high school (Figure 10).

Figure 9. Portion of GWFV wall at Mounds View HS a few weeks after hydroseeding.

CONCLUSION

A GWFV wall system was selected as a means to provide cost-effective and environmentally friendly MSE structures at two Minneapolis-area public school construction projects in 2019. On-site soil comprised of silty fine sand with some clay was suitable for use as structural fill soil in the backfill zone, (i.e., the geogrid-reinforced zone). Compaction control was monitored regularly throughout wall construction using a nuclear moisture-density gage per project recommendations.

At the Edgewood Middle School project, a growth media (organic topsoil) with grass seed was used in the wrap-lifts near the wall face, and hydroseeding was used post-construction to apply additional seed at the wrap face. This resulted in excellent vegetation establishment, with the wall effectively disappearing into the green landscape within 8 months. At the Mounds View High School project site where the wall faced toward a natural wooded area, no topsoil was placed in the wrap lifts, and grass seed was supplied solely by post-construction hydroseeding. This resulted in a reasonably good vegetation cover that is expected to further fill-in and become more dense over the next several years.

Figure 10. Vegetation coverage on face of the GWFV wall at Mounds View HS as of June 2020.

These projects demonstrated that this engineered vegetated wall system can provide a cost-effective green alternative to masonry hardscape structures for public works projects where sustainable, environmentally friendly options are preferred by the designer or by the public at large. Advantages include: 1) this vegetated wall system not only provides a reinforced soil mass to resist lateral earth pressures, but also provides immediate and long-term erosion protection; 2) on-site soil can be used for backfill in the reinforced zone, eliminating the cost and carbon footprint of importing soil to the site; 3) lightweight geosynthetic components are easily transported and handled in areas with steep or difficult access; 4) the geosynthetic HPTRM at the face has superior UV resistance for up to 75 years of design life; 5) the system has flexibility to easily install curves along the wall or reinforced-slope alignment.

For many possible MSE wall applications, owners and designers now have an engineered vegetated wall option (i.e., a green option) that may be advantageous over hardscape to meet aesthetic or environmental goals for given projects in some public areas. In some cases, a living green wall may be preferred over hardscape as a means to blend into natural features and thus eliminate graffiti and its associated maintenance/cleanup costs. In general, the future demand for such green alternatives likely will increase, providing an expanded market for these types of

geosynthetic solutions for MSE walls and steep reinforced soil slopes in private, commercial, and public applications.

ACKNOWLEDGEMENTS

Many thanks to the following stakeholders and project team members:
Mounds View Public School District
Arden Hills Public School District
Braun Intertec
Wold Architects and Engineers
Anderson-Johnson Associates, Inc.
Belair Site Services
Minnesota Utilities and Excavating

REFERENCES

Abramson, L. E., Lee, T. S., Sharma, S., and Boyce, G. M. (2002). *Slope Stability and Stabilization Methods, 2nd Ed.*; John Wiley & Sons, Inc., New York, 712 p.

GEO-SLOPE International, Ltd. (2018). Slope stability software for personal computers, *Slope/W*.

Miller, S.M. (2017). Internally Braced Geosynthetic Wrap-Face Vegetated Walls and Reinforced Soil Slopes, *Geosynthetics*, 35(5): 24-33.

Miller, S.M. and Loizeaux, D. (2019). Highway Embankment Construction Using a Geosynthetic Wrap-Face Vegetated Wall System; in Proc. of *Geosynthetics 2019*, IFAI, Houston, TX, USA: 793-803.

Propex Operating Co. LLC (2020). Website: http://propexglobal.com/Pyramat

Geosynthetics Conference

Limit Equilibrium Analysis of Geosynthetic-Reinforced Retaining Wall-Supported Footings

S. Mustapha Rahmaninezhad, Ph.D., A.M.ASCE,[1] Jie Han, Ph.D., PE, F.ASCE,[2] and Mahdi Al-Naddaf, Ph.D., A.M.ASCE,[3] Jaber Mamaghanian, Ph.D.[4]

[1]Geotechnical Department, Terracon Consulting Inc., 1506 Mid Cities Dr, Pharr, TX 78577, USA e-mail: srahmaninezhad@terracon.com
[2]Department of Civil, Environmental, and Architectural Engineering, the University of Kansas, 1530 W. 15th St., Lawrence, KS 66045-7609, USA; e-mail: jiehan@ku.edu
[3]Department of Civil Engineering, University of Kerbala, Kerbala, 56001, Iraq; e-mail: mahdi.a@uokerbala.edu.iq
[4]School of Civil Engineering, Iran University of Science and Technology, Tehran, Iran; e-mail: mamaghani@iust.ac.ir

ABSTRACT

Geosynthetic-reinforced retaining (GRR) walls have been used as bridge abutments to support bridge beams on spread footings instead of traditional deep foundations (such as piles and shafts). However, so far limited studies have been carried out to investigate the performance of the GRR wall subjected to footing loads considering possible failure surfaces and bearing capacities of the footings. This study evaluated the effect of footing loads on the global stability of GRR walls with modular blocks. The limit equilibrium (i.e., the Bishop simplified method) in a software was used to determine the possible failure surfaces and the bearing capacities of the footings which were defined at the factor of safety (FS) equal to one (FS = 1.0). A parametric study was carried out to investigate the effect of the embedment depth and the offset distance of the footing from the wall facing on the possible failure surfaces and the bearing capacities of footings. The numerical results indicated that the possible failure surfaces began from the center of the footing and developed into the reinforced zone towards the wall facing. When the embedment depth of the footing was increased to 0.4H (H is the height of the wall), the bearing capacity increased by approximately 26%. However, when the offset distance of the footing from the wall facing was increased to about 0.4H, the bearing capacity increased by approximately 138%.

Keywords: Abutment; Embedded Footing; Geosynthetic; Limit Equilibrium; Retaining Wall; Stability

INTRODUCTION

Geosynthetic-reinforced soil (GRS) has been successfully used for construction of many earth structures, such as retaining walls, slopes, and embankments. Among these structures, the geosynthetic-reinforced retaining (GRR) walls have been commonly utilized for many applications in transportation systems (Zhu et al., 2008; Yang et al., 2012; Han, 2015; Tatsuoka et al., 2014; Jiang et al., 2016; Kakrasul et al., 2018; Jawad, 2019; Jawad et al., 2020). In recent years, GRR walls have been increasing used as bridge abutments instead of pile foundations (Lee and Wu, 2004; Skinner and Rowe, 2005; Adams et al., 2011; Adams and Nicks, 2018; Kakrasul et al., 2020). In this technology, GRR abutment walls support bridge beams on spread footings constructed directly on the reinforced fill for bridge approach embankments, roadways, and railways, which are subjected to traffic loads. To reduce bridge span, footings are often placed close to the wall facing. The major advantages of this technology are to eliminate pile foundations thus reducing the overall cost of construction and to minimize bumps at the end of bridges (Abu-Hejleh et al., 2001; Helwany et al., 2003; Skinner and Rowe, 2005; Rahmaninezhad, 2019; Liu et al., 2020). Bumps at the end of bridges usually happen due to the differential settlement between approaching embankments and pile-supported abutments.

According to the FHWA design guideline, design of GRR abutment walls is considered as a complex geometry and a special condition (Berg et al., 2009). Figure 1 shows a bi-linear potential failure surface for the abutment wall, which starts from the far edge (i.e., right edge) of the footing (Berg et al., 2009). In this paper, the “FHWA potential failure surface” is referred to as the present analysis following the FHWA design guideline. Figure 1 shows that *h* is the height of the wall as measured from bottom of the footing to the finished roadway surface and/or the approaching slab and *D* is the offset distance between the back face of the wall and the close edge (i.e., left edge) of the footing. In this study, *h* and *D* are considered as the embedment depth of the footing and the offset distance of the footing from the wall facing, respectively.

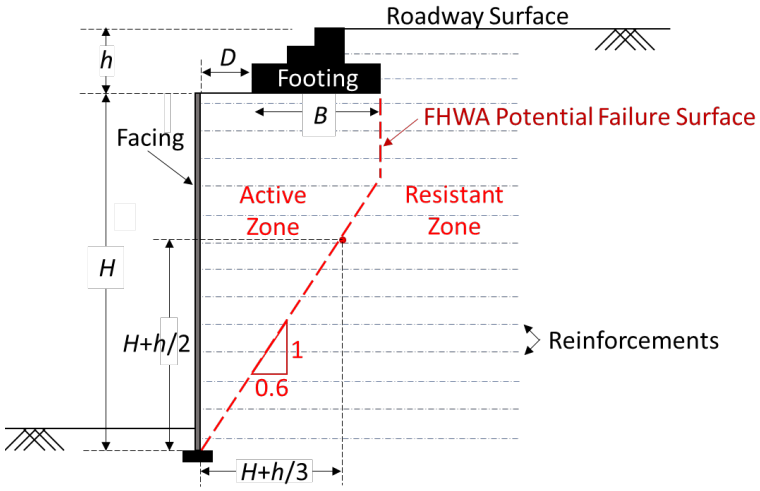

Figure 1. FHWA potential failure surface proposed for the GRR abutment walls (after Berg et al. 2009)

The limit equilibrium (LE) method has been successfully used to evaluate the global stability of GRR walls (Han and Leshchinsky, 2010; Xiao et al., 2016; Song et al., 2017; Gaudio et al., 2018; Hung et al., 2020). Xiao et al. (2016) studied the failure surfaces of the GRR walls subjected to strip footing loads under a plane strain condition. Xiao et al. (2016) found that the LE analysis well predicted the observed failure surfaces in the GRR walls under footing loads. Kakrasul (2018) studied the effect of the dimension of the GRR walls with modular block facing on their global stability using the LE analysis. Rahmaninezhad (2019) proposed a relationship between the global stability and the lateral and vertical deformations of the GRR abutment walls. Xie et al. (2019) developed an LE approach to predict the bearing capacity of strip footings on the GRR abutment walls. Rahmaninezhad et al. (2020) used the LE analysis to investigate the effects of the width and offset distance of the footing from the wall facing on the global stability of GRR abutment walls with modular block facing.

Although several studies have been conducted to evaluate the effect of the embedment depth of the footing on the GRS backfill (Yetimoglu 1994; Patra et al., 2005; Yasrobi et al., 2009; rahmaninezhad et al., 2009; Sharma at al., 2009;Chen and Abu-Farsakh, 2015), limited studies have been carried out to investigate the effect of the embedment depth of the footing on the behavior of GRR abutment walls. The objective of this study is to evaluate the effect of the embedment depth and the offset distance of the footing from the wall facing on the possible failure surfaces and the bearing capacities of footings of the GRR abutment walls with modular block facing.

The LE method incorporated in the ReSSA software Version 3.0, developed by the ADAMA Engineering, Inc. (2008), was employed to determine the potential failure surfaces and calculate the factors of safety of GRR walls subjected to footing loading using Bishop's simplified method (Bishop, 1955). However, this paper does not evaluate other aspects of GRR wall stability (such as internal stability, sliding, and overturning).

LIMIT EQUILIBRIUM ANALYSIS

Mobilization of reinforcement tension at the intersection between reinforcement and a failure surface depends on soil strength, rear pullout resistance of reinforcement, and long-term strength of reinforcement (Han and Leshchinsky, 2010; Han, 2015; Rahmaninezhad et al., 2018). The failure surface corresponding to the largest mobilized soil strength (i.e., the lowest factor of safety) at LE is considered as the potential failure surface (Han and Leshchinsky, 2010). Bishop's simplified method can be modified to include a horizontal tensile force of reinforcement intersecting the failure surface. This method has been commonly used in the practice to analyze global stability of geosynthetic reinforced slopes and GRR walls (Han and Leshchinsky, 2010).

MODELING

Figure 2 shows the geometry and material properties of the baseline model used in this study. To prevent any possible failure in the foundation soil below the GRR wall, the foundation soil was assumed to have high strength values. The model walls had a height of 6 m from the top of the foundation level to the finished approaching slab (*H*+*h*). In the model walls, the reinforcement length increased linearly from 8 m at the bottom with a 1:1 slope toward the approaching slab and road pavement. The vertical spacing of reinforcement layers was 0.4 m. The embedment depth of the footing (*h*) and the offset distance between the back of the wall facing and the close edge of the footing (*D*) were varied. In this parametric study, one parameter was changed from the baseline model while all others were unchanged.

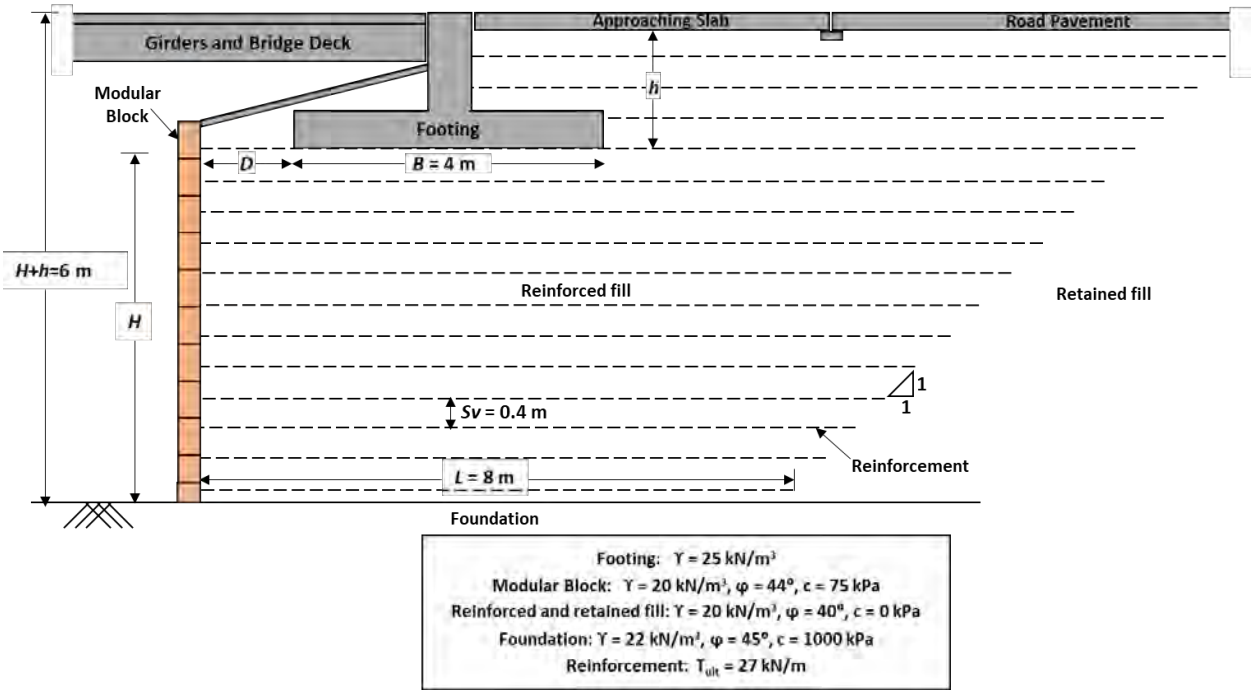

Figure 2. Dimensions and material properties of the baseline model

RESULTS

The possible failure surface and the ultimate bearing capacity of the footing on the GRR abutment wall were examined in this study. In this paper, the ultimate bearing capacity is defined as the pressure at which the corresponding factor of safety using Bishop's simplified method is equal to one. However, this approach does not consider the footing load-induced confining stress effect on the soil and reinforcement resistance.

Effect of Embedment Depth of Footing: Figure 3 shows the calculated ultimate bearing capacity of the footing on the GRR abutment wall versus the embedment depth of the footing at a constant

footing offset (D=1.5m) using Bishop's simplified method. The results indicate that the walls with a deeper h had higher ultimate bearing capacities than the walls with a shallower footing. The ultimate bearing capacities of the footing with an embedment depth ratio, $h/(H+h)$, of 0, 0.2, and 0.4 were 455, 493, and 572 kPa, respectively. In other words, the increase of the embedment depth ratio from 0 to 0.2 and 0.4 resulted in 8.4% and 25.7% higher footing ultimate bearing capacities, respectively.

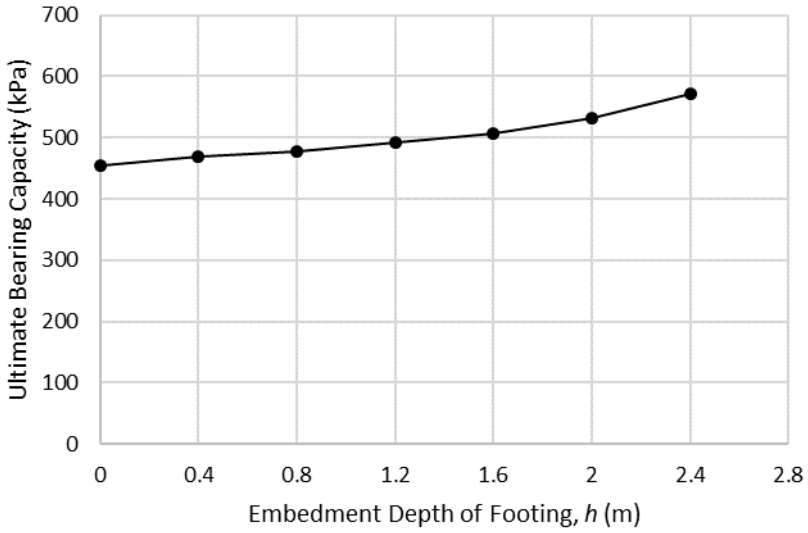

Figure 3. Calculated ultimate bearing capacity versus embedment depth of footing (h)

Figure 4 presents the locations and shapes of potential failure surfaces within the walls at different embedment depths of the footing and the constant footing offset (D=1.5m) determined using Bishop's simplified method. Figure 4 shows that the potential failure surfaces began or passed from the center of the footing and developed into the reinforced zone towards the wall facing. The footing with a deeper embedment resulted in a slightly deeper failure zone than that with a shallower embedment as shown in Figure 4.

The comparison between Bishop's simplified and the FHWA method indicates that the potential failure surface in the wall with a shallow footing determined by Bishop's simplified method was close to the surface identified by the FHWA method. However, an increase of the embedment depth of the footing, the potential failure surface identified by Bishop's simplified method became deeper than that proposed by the FHWA method.

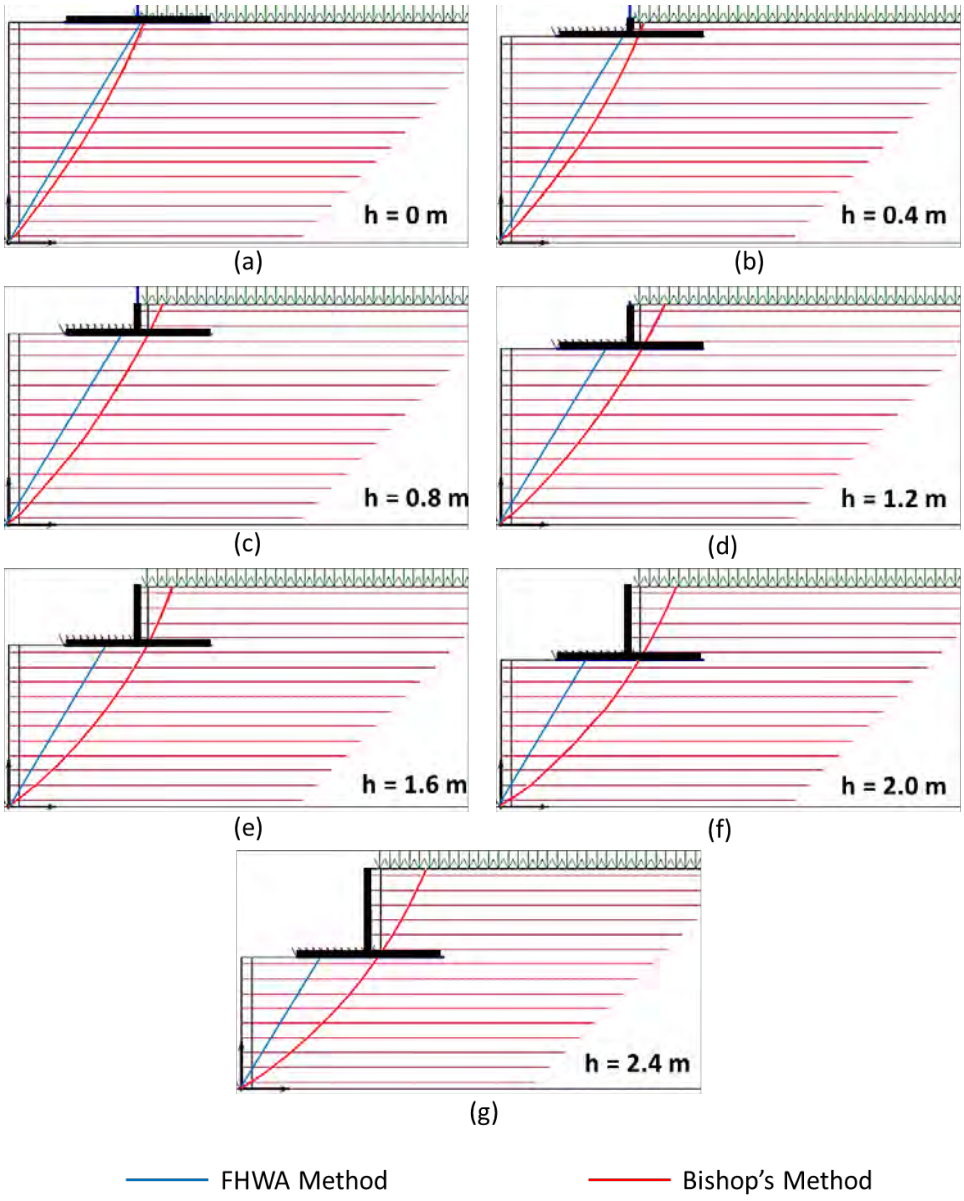

Figure 4. Locations and shapes of potential failure surfaces within the walls with different embedment depths of the footing (*h*)

Effect of Offset Distance of Footing: Figure 5 presents the calculated ultimate bearing capacity of the footing versus the offset distance of the footing with a constant embedment depth (h=1.2 m) using Bishop's simplified method. The results show that the wall with a larger offset distance had a higher ultimate bearing capacity for the footing than the wall with a smaller offset distance. When the footing was located next to the wall facing (D=0), the calculated ultimate bearing capacity was 73.1% and 138.5% lower than that with an offset ratio, $D/(H+h)$, of 0.25 and 0.42, respectively.

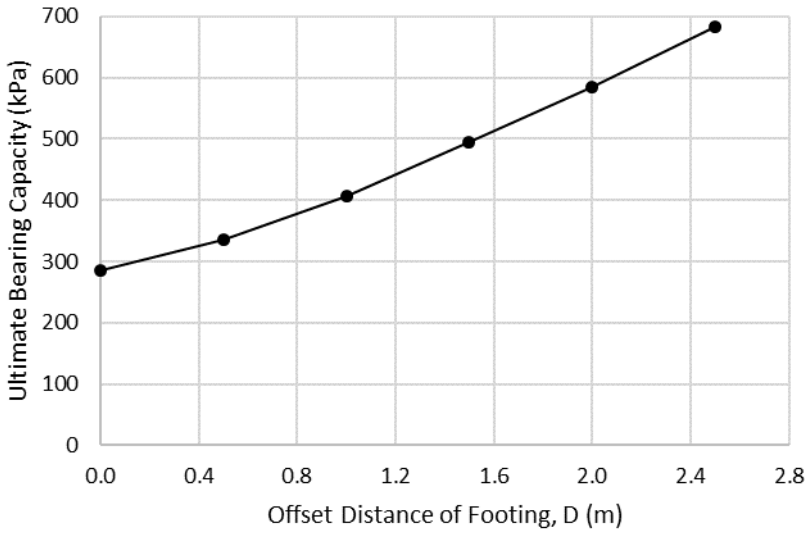

Figure 5. Calculated ultimate bearing capacity versus offset distance of the footing (D)

Figure 6 presents the locations and shapes of the potential failure surfaces within the walls at different offset distances that were determined using Bishop's simplified and the FHWA method. The potential failure surface, using Bishop's simplified method, began from the center of the footing and developed into the reinforced zone towards the wall facing. Therefore, the wall with a larger footing offset distance had a deeper potential failure surface as compared with that with a smaller offset distance, using Bishop's simplified method. When the wall had an offset distance smaller than 0.5 m ($D/(H+h)$=0.1), the potential failure surfaces proposed by Bishop's simplified and the FHWA method were similar. However, as the offset distance of the footing increased, the potential failure surface identified by Bishop's simplified method was deeper than that proposed by the FHWA method.

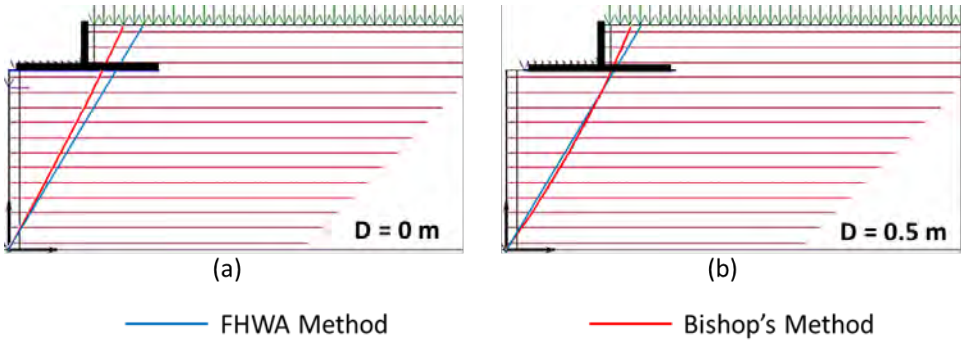

Figure 6. Locations and shapes of potential failure surfaces with the walls with different offset distances of the footing (D)

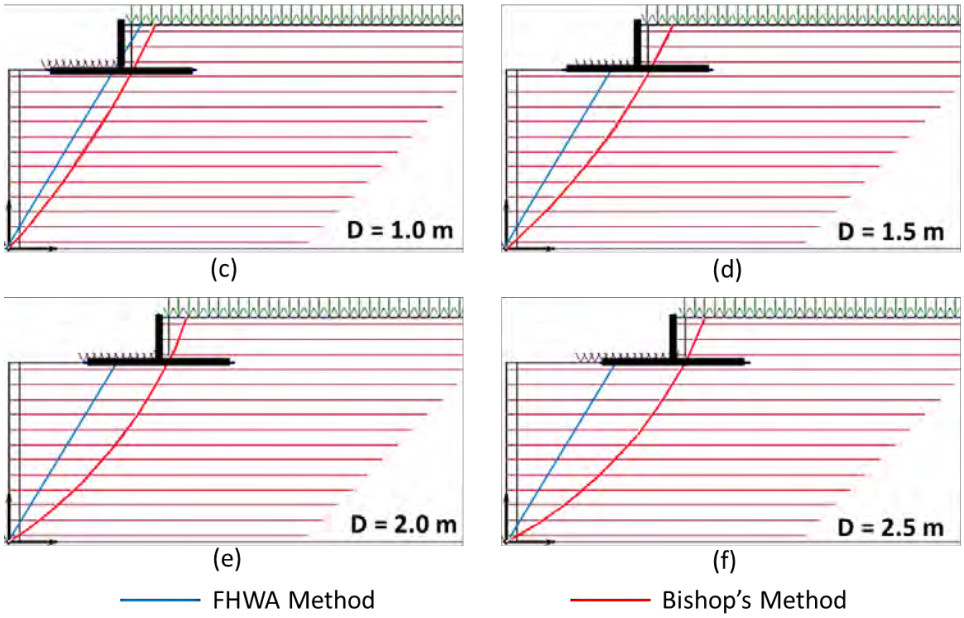

Figure 6. Locations and shapes of potential failure surfaces with the walls with different offset distances of the footing (D) (continued)

CONCLUSIONS

This study investigated the effect of a footing (i.e., the embedment depth of the footing and the offset distance of the footing from the wall facing) on global stability of geosynthetic-reinforced retaining (GRR) abutment walls with modular block facing. The limit equilibrium (LE) program was used to determine the potential failure surfaces and calculate the ultimate bearing capacity of the footings using Bishop's simplified method. From this study, the following conclusions can be made:

1. The increase in the embedment depth slightly increased the ultimate bearing capacity of the footings.
2. The potential failure surfaces, identified by Bishop's simplified method, began from the center of the footing and developed into the reinforced zone towards the abutment walls facing toe.
3. The potential failure surfaces, determined using Bishop's simplified method, of the abutment walls with a larger embedment depth of the footing were slightly deeper than those of the walls with a shallower footing.
4. The abutment wall with a longer offset distance had a higher ultimate bearing capacity for footings than the walls with shorter offset distance.

5. The abutment wall with a larger footing offset distance had a deeper potential failure surface as determined by Bishop's simplified method, as compared with the wall with a smaller offset distance.
6. It is worth mentioning that the LE approach employed in this study is only considering force and moment equilibrium. However, this approach does not consider the footing load-induced stress level effect on the soil and reinforcement behavior. Future studies using numerical methods should be conducted to take into account the stress-deformation behavior of the geosynthetic reinforcement-soil system under footing loading and verify the results obtained in this study.

REFERENCES

Abu-Hejleh, N., Zornberg, J. G., Wang, T., and McMullen, M. (2001). Performance of geosynthetic-reinforced walls supporting the Founders/Meadows Bridge and approaching roadway structures. *Report 2: Assessment of the performance and design of the front GRS walls and recommendations for future GRS abutments*.

ADAMA Engineering, Inc, (2008). ReSSA Software Version 3.0 Newark, Delaware, USA.

Adams, M., and Nicks, J. (2018). Design and construction guidelines for geosynthetic reinforced soil abutments and integrated bridge systems. United States. Federal Highway Administration.

Adams, M., Nicks, J., Stabile, T., Wu, J. T., Schlatter, W., and Hartmann, J. (2011). Geosynthetic reinforced soil integrated bridge system, synthesis report. United States. Federal Highway Administration.

Berg, R., Christopher, B., and Samtani, N. (2009). Design and construction of mechanically stabilized earth walls and reinforced soil slopes, vols. 1 & 2. Report No: FHWA-NHI-10–024. FHWA, U.S. Department of Transportation.

Bishop, A.W. (1955). The use of the slip circle in the stability analysis of slopes. *Geotechnique 5*, 7–17.

Chen, Q. and Abu-Farsakh, M., (2015). Ultimate bearing capacity analysis of strip footings on reinforced soil foundation. *Soils and Foundations, 55*(1), pp.74-85.

Gaudio, D., Masini, L. and Rampello, S., (2018). A performance-based approach to design reinforced-earth retaining walls. *Geotextiles and Geomembranes, 46*(4), pp.470-485.

Han, J., 2015. *Principles and practice of ground improvement*. John Wiley & Sons.

Han, J. and Leshchinsky, D. (2010). Analysis of back-to-back mechanically stabilized earth walls. *Geotextiles and Geomembranes, 28*(3), pp.262-267.

Helwany, S.M., Wu, J.T. and Froessl, B. (2003). "GRS bridge abutments—an effective means to alleviate bridge approach settlement." *Geotextiles and Geomembranes, 21*(3), pp.177-196.

Hung, W.Y., Yang, K.H., Nguyen, T.S. and Pham, T.N.P. (2020). Performance of geosynthetic-reinforced soil walls at failure. *Journal of GeoEngineering, 15*(1), pp.13-29.

Jawad, S., 2019. Evaluating behavior of laterally loaded piles within mse walls under static and

cyclic loading (Doctoral dissertation, University of Kansas).

Jawad, S., Han, J., Al-Naddaf, M. and Abdulrasool, G., (2020). Responses of laterally loaded single piles within mechanically stabilized earth walls. *Journal of Geotechnical and Geoenvironmental Engineering*, *146*(12), p.04020128.

Jiang, Y., Han, J., Parsons, R.L. and Brennan, J.J. (2016). "Field instrumentation and evaluation of modular-block MSE walls with secondary geogrid layers." *Journal of Geotechnical and Geoenvironmental Engineering*, *142*(12), p.05016002.

Kakrasul, J.I., Han, J. and Rahmaninezhad, S.M. (2020). Load-deformation behavior of geosynthetic-reinforced retaining walls with limited fill space under static footing loading. *Transportation Infrastructure Geotechnology 7*, pp.309–331

Kakrasul, J.I., Han, J., and Rahmaninezhad, S.M. (2018). Laboratory evaluation of deformations of geosynthetic-reinforced retaining walls subjected to footing loading. *11th International Conference on Geosynthetics*, Seoul, Korea.

Kakrasul, J.I., Han, J., Rahmaninezhad, S.M. and Weldu, M. (2016). Model tests of geosynthetic-reinforced earth walls with limited-space retained fill. *Vol. 2 of Proc., 3rd Pan-American Conf. on Geosynthetics (GeoAmericas)*, pp. 1279-1286.

Lee, K.Z., Wu, J.T. (2004). A synthesis of case histories on GRS bridge-supporting structures with flexible facing. *Geotextiles and Geomembranes 22* (4), pp.181-204.

Liu, H., Han, J., Jawad, S. and Parsons, R.L., (2020). Literature Review of Causes and Mitigation Techniques for Bumps at Ends of Bridges. *In Geo-Congress 2020: Geotechnical Earthquake Engineering and Special Topics*, pp. 862-871.

Patra, C.R., Das, B.M. and Atalar, C., (2005). Bearing capacity of embedded strip foundation on geogrid-reinforced sand. *Geotextiles and Geomembranes*, *23*(5), pp.454-462.

Rahmaninezhad, S.M., 2019. *Geosynthetic reinforced retaining walls with flexible facing under footing loading* (Doctoral dissertation, University of Kansas).

Rahmaninezhad, S.M., Han, J. and Al-Naddaf, M., (2020). Limit equilibrium analysis of geosynthetic-reinforced retaining walls subjected to footing loading. *In Geo-Congress 2020: Engineering, Monitoring, and Management of Geotechnical Infrastructure*, pp. 464-471.

Rahmaninezhad, S.M., Han, J., Kakrasul, J.I., and Weldu, M. (2018). Stress Distributions and Pullout Responses of Extensible and Inextensible Reinforcement in Soil Using Different Normal Loading Methods. *Geotechnical Testing Journal*, *42*(6).

Sharma, R., Chen, Q., Abu-Farsakh, M. and Yoon, S., (2009). Analytical modeling of geogrid reinforced soil foundation. *Geotextiles and Geomembranes, 27*(1), pp.63-72.

Skinner, G.D., Rowe, R.K. (2005). Design and behaviour of a geosynthetic reinforced retaining wall and bridge abutment on a yielding foundation. *Geotextiles and Geomembranes*, *23*(3), pp. 234-260.

Song, F., Liu, H., Chai, H. and Chen, J. (2017). Stability analysis of geocell-reinforced retaining walls. *Geosynthetics International*, *24*(5), pp.442-450.

Tatsuoka, F., Tateyama, M., Koseki, J., Yonezawa, T. (2014). "Geosynthetic-reinforced soil

structures for railways in japan." *Transportation Infrastructure Geotechnology, 1* (1), pp. 3-53.

Yang, G., Liu, H., Lv, P., and Zhang, B. (2012). Geogrid-reinforced lime-treated cohesive soil retaining wall: Case study and implications. *Geotextiles and Geomembranes 35*, pp. 112-118.

Yasrobi, S.S., Rahmaninezhad, S.M., and Eftekharzadeh, S. F., (2009). Large physical modeling to optimize the geometrical conditions of geotextile in reinforced loose sand. *In Characterization, Modeling, and Performance of Geomaterials: Selected Papers From the 2009 GeoHunan International Conference*, pp. 53-59.

Yetimoglu, T., Wu, J.T. and Saglamer, A., (1994). Bearing capacity of rectangular footings on geogrid-reinforced sand. *Journal of Geotechnical Engineering*, *120*(12), pp.2083-2099.

Xiao, C., Han, J. and Zhang, Z. (2016). Experimental study on performance of geosynthetic-reinforced soil model walls on rigid foundations subjected to static footing loading. *Geotextiles and Geomembranes*, *44*(1), pp.81-94.

Xie, Y., Leshchinsky, B. and Han, J. (2019). Evaluation of Bearing Capacity on Geosynthetic-Reinforced Soil Structures Considering Multiple Failure Mechanisms. *Journal of Geotechnical and Geoenvironmental Engineering*, *145*(9), p.04019040.

Zhu, H., Ma, Y., Liu, Y.X., Wang, J. (2008). Application of the geogrid reinforced soil retaining walls for a high slope supporting project. *Geosynthetics in Civil and Environmental Engineering*, pp. 266-270.

Geosynthetics Conference

Simplified Method for Calculating Vertical Stresses in Limited-Space Geosynthetic-Reinforced Soil Walls

Yu-qiu Ye,[1] Jamal Ismael Kakrasul, Ph.D.,[2] Jie Han, Ph.D., PE, F.ASCE,[3] and Rui Rui, Ph.D.[4]

[1]Civil, Environmental and Architectural Engineering Department, the University of Kansas, USA; e-mail: yuqiu@ku.edu
[2]Department of Civil Engineering, Soran University, Iraq; e-mail: jamal.kakrasul@soran.edu.iq
[3]Dept. of Civil, Environmental, and Architectural Engineering, the University of Kansas, 1530 West 15th St., Lawrence, KS 66045-760; e-mail: jiehan@ku.edu
[4]Department of Geotechnical Engineering, Wuhan University of Technology, Wuhan, China; e-mail: r.rui@whut.edu.cn

ABSTRACT

Geosynthetic-reinforced Soil (GRS) walls have been widely used in geotechnical engineering practice, such as highways, bridge abutments, and service roads. In some areas, space for GRS wall construction is limited. Past research has shown that the magnitude and distribution of earth pressures in limited-space GRS walls are different from those with large space. This paper briefly reviewed two model tests carried out to study the vertical stress distribution of limited-space GRS walls subjected to footing loading. Test results indicated that the measured vertical stresses decreased with depth, but increased with footing loading. This paper also proposed a simplified method by modifying the 2:1 stress distribution method to calculate the vertical stress distribution in limited-space GRS walls under static footing loading. The simplified method adopted a horizontal slice concept and considered the wall-soil friction effect. Accuracy of this proposed method and improvement from the 2:1 stress distribution method were assessed with the test results.

INTRODUCTION

Geosynthetic Reinforced Soil (GRS) walls have been widely used for highways, railways, and bridge abutments (Abu-Hejleh et al., 2000, 2001; Wu et al., 2006; Han, 2015; Shen et al. 2020). Static and dynamic footing or traffic loads are applied on the top of GRS walls as part of bridge abutments and important for their design. There have been a number of studies on GRS walls in recent years through full-scale tests (e.g., Jiang et al. 2016), physical model tests (e.g., Xiao et al., 2015; Kakrasul et al. 2016, 2020; and Kakrasul 2018), analytical solutions (e.g., Han and Leshchinsky 2006), and numerical analysis (e.g., Leshchinsky and Vulova 2001: Ling and Leshchinsky 2003; Han and Leshchinsky 2010). Mojtahedi and Fakharian (2002) conducted a parametric study for GRS abutments under static and seismic loading, and proposed their design methods. These studies were based on GRS walls with large space behind wall facing. Wu et al. (2006) investigated the bearing capacity of GRS walls with different soil stiffness and foundation stiffness. Bourgeois et al. (2011) analyzed the influence of a local load on the interaction between the reinforcement and the backfill material in GRS walls using full-scale tests and finite element analyses. Xiao et al. (2015) conducted a series of model tests to evaluate the effects of geogrid

reinforcement length, connection type between geogrids and facing on bearing capacities of GRS walls. Zheng and Fox (2016) conducted a numerical study to investigate the displacements, lateral and vertical stresses, tensile strains and forces of reinforcement behind the GRS abutments under static loading. These studies were based on large-space backfill conditions.

Generally, horizontal earth pressures behind retaining walls can be calculated using Rankine's theory or Coulomb's theory. Due to site constraints, some GRS walls have limited space behind wall facing. In 1895, Janssen developed an equation to estimate horizontal earth pressures in a silo considering a wall-soil friction effect. Handy (1985) showed that wall-soil friction could reduce magnitudes of horizontal earth pressures applied on retaining walls and this phenomenon is often referred to as soil arching (Khosravi et al. 2013 and Rui et al. 2020). Frydman and Keissar (1987) conducted physical model tests showing the reduced horizontal earth pressures due to limited space. Leshchinsky et al. (2004) developed design charts for reduced horizontal earth pressures in limited GRS walls. Model tests (Rui et al. 2020) also showed that wall-soil friction could reduce horizontal earth pressures behind limited-space retaining walls. Morrison et al. (2006) proposed a 2:1 stress distribution method to calculate vertical stresses behind the GRS wall facing subjected to footing loading. Kakrasul (2018) and Kakrasul et al. (2016; 2020) showed that the performance of GRS walls was affected by backfill width, reinforcement rear anchorage, and applied footing load and its offset distance. Vertical stress distribution in limited-space GRS walls subjected to footing loading is not well investigated. Kakrasul (2018) conducted physical model tests to measure the vertical stresses using earth pressure cells and showed the 2:1 stress distribution method did not predict the measured stresses well. This study aimed to improve this prediction using a horizontal slice concept and considering the wall-soil friction effect as compared with the same measured data. As a result, a simplified method was proposed for calculating the vertical stresses in limited space GRS walls under footing loading. The calculated results using the proposed method better match the model test data than the 2:1 stress distribution method.

MODEL TESTS

Test Setup. Before the presentation of the proposed simplified method, selected model tests conducted by Kakrasul (2018) are briefly described herein. Details of these tests can be found in Kakrasul (2018). Kakrasul (2018) adopted a model box for his experimental study on the performance of limited-space GRS walls subjected to footing loading. The test setup was composed of a model box, sand, geogrid layers, a loading plate, a hydraulic jack, and a reaction frame, dial gauges, earth pressure cells, and a load cell. Figure 1 shows the inner dimensions of the test box as 1100 mm high, 450 mm wide, and 2400 mm long. The front side was made of transparent glass plates with the thickness of 10 mm each. The glass wall allowed visual observation and photogrammetry of displacements of wall facing and backfill. The strip footing was composed of a steel plate of 200 mm wide, 450 mm long, and 25 mm thick. To ensure a plane strain condition, the length of the footing was approximately equal to the inner width of the box. Kansas River sand was used as the backfill material. The sand was compacted to a relative density R_d =70%, which corresponds to a dry unit weight 17.8 kN/m^3 in the model tests. The peak internal friction angle at this density was measured to be 37° using triaxial compression tests.

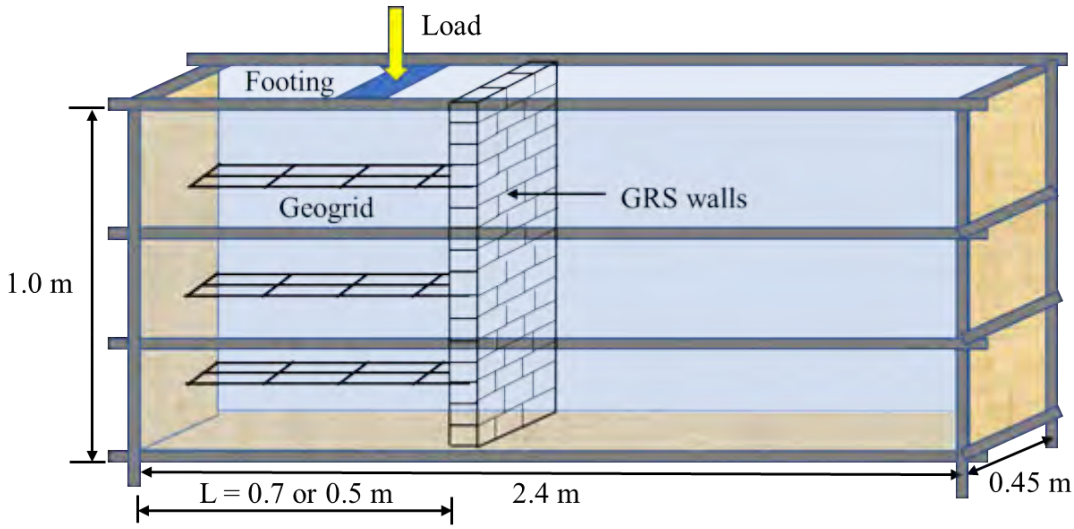

Figure 1. Test setup and dimensions.

Geosynthetic reinforcement. Punched-drawn biaxial geogrid (BX) made of polypropylene material was used in the model tests. Calibration tests showed that the ultimate tensile strengths of the geogrid was 12.4 kN/m in the machine direction and 19 kN/m in the cross-machine direction. To create a configuration of uniaxial geogrid, three ribs of a biaxial geogrid in the machine direction (transverse ribs) were removed every four ribs. This modification was first used by Xiao et al. (2016) and then by Kakrasul et al. (2016).

Test program. Two model tests were selected in this study, which had two different backfill lengths L = 0.7 m (Test 1, labeled as T1) and 0.5 m (Test 2, labeled as T2) as shown in Figure 2. The offset d of the footing was 0.2 m, the reinforcement spacing was 0.2 m, and the backfill height H was 1 m, respectively. Earth pressure cells were placed along the centerline of the loading plate to measure the vertical stresses in the reinforced backfill.

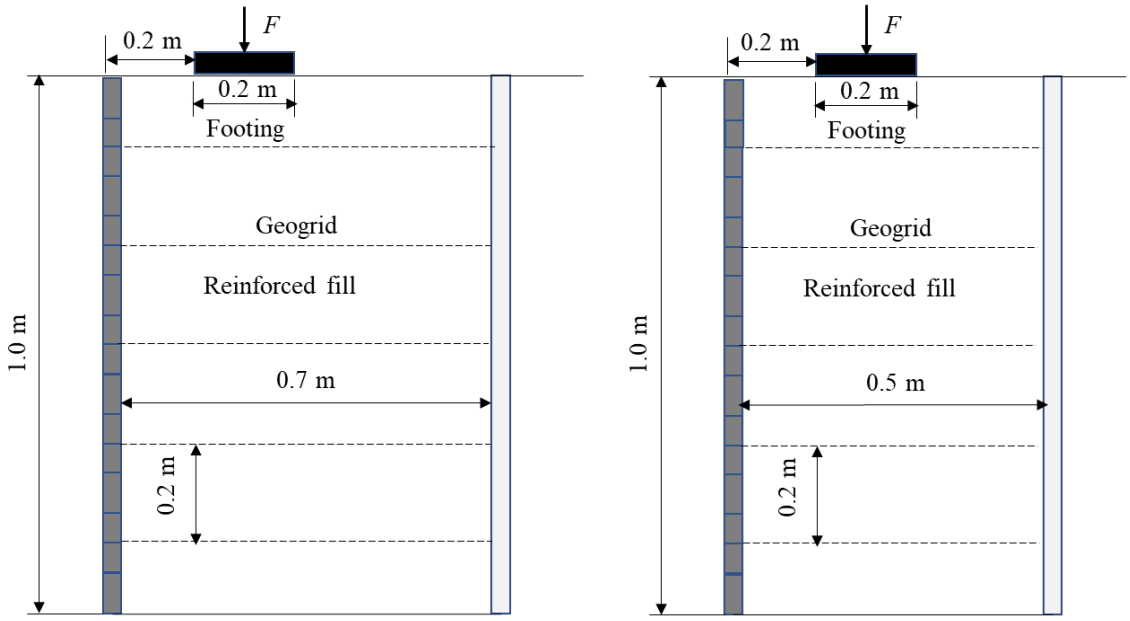

(a) T1 (L = 0.7 m) (b) T2 (L = 0.5 m)

Figure 2. Test layouts.

TEST RESULTS

Figure 3 shows the distributions of the measured vertical stress versus depth under three different footing applied pressures (50, 100, and 150 kPa) for T1 and T2. The symbols, Test_50, Test_100, and Test_150 in these tests, represent the applied pressures of 50, 100, and 150 kPa. These two tests had similar distribution trends of the measured vertical stresses under all the applied footing pressures. The measured vertical stresses decreased with the depth and increased with the increase of the applied footing pressure. The increase of the stresses became smaller with the increase of the depth. Clearly, the footing had a limited influence depth, which was approximately five times the footing width, which is consistent with the theoretical solution (i.e., the Boussinesq solution).

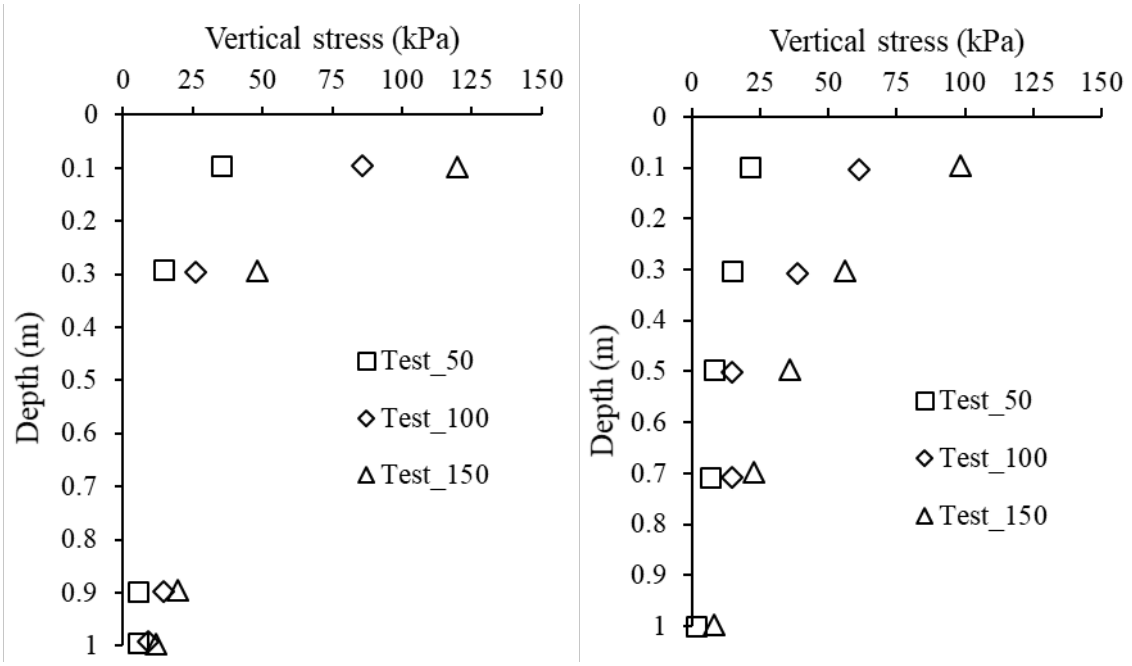

(a) T1 (b) T2

Figure 3. Vertical stress versus depth distributions in the GRS walls induced by footing loading.

SIMPLIFIED METHOD

The 2:1 stress distribution method has been commonly used to calculate vertical stresses in GRS walls under footing loading. However, for limited-space conditions, wall-soil friction has a great influence on the distribution of vertical stresses. In this study, a simplified method was proposed considering the wall-soil friction effect. The horizontal slice concept was adopted in the derivation as shown in Figure 4. The symbols used in the derivation are provided in Figure 4 and other symbols are described as they appear in equations.

The backfill is divided into n horizontal slices of equal thickness h_i.

$$h_i = \frac{H}{n} \tag{1}$$

where H is the height of backfill. The effective length D_i of the ith slice can be expressed as follows:

$$D_i = \begin{cases} B_f & if\ Z_i = 0 \\ B_f + Z_i & if\ 0 < Z_i \le Z_1 \\ B_f + d + Z_i/2 & if\ Z_1 < Z_i \le Z_2 \\ L & if\ Z_2 < Z_i \end{cases} \tag{2}$$

where $Z_1 = 2d$, $Z_2 = 2(L\text{-}d\text{-}B_f)$ and $Z_i = \sum_{m=1}^{i} h_m$.

For the *i*th slice layer, the applied vertical stress can be expressed as follows:

$$\Delta\sigma_i = \frac{F\left(B_f W\right) - \sum_{m=1}^{i-1} f_m}{D_i W} \tag{3}$$

When $Z_1 < Z_2$, the wall-soil friction applied on the *i*th slice can be expressed as follows:

$$f_i = \begin{cases} \Delta\sigma_i K_0 \tan(\delta) h_i (2D_i) & if\ 0 \le Z_i \le Z_1 \\ \Delta\sigma_i K_a \tan(\delta) h_i W + \Delta\sigma_i K_0 \tan(\delta) h_i (2D_i) & if\ Z_1 < Z_i \le Z_2 \\ \Delta\sigma_i K_a \tan(\delta) h_i W + \Delta\sigma_i K_0 \tan(\delta) h_i (2D_i + W) & if\ Z_2 < Z_i \end{cases} \tag{4}$$

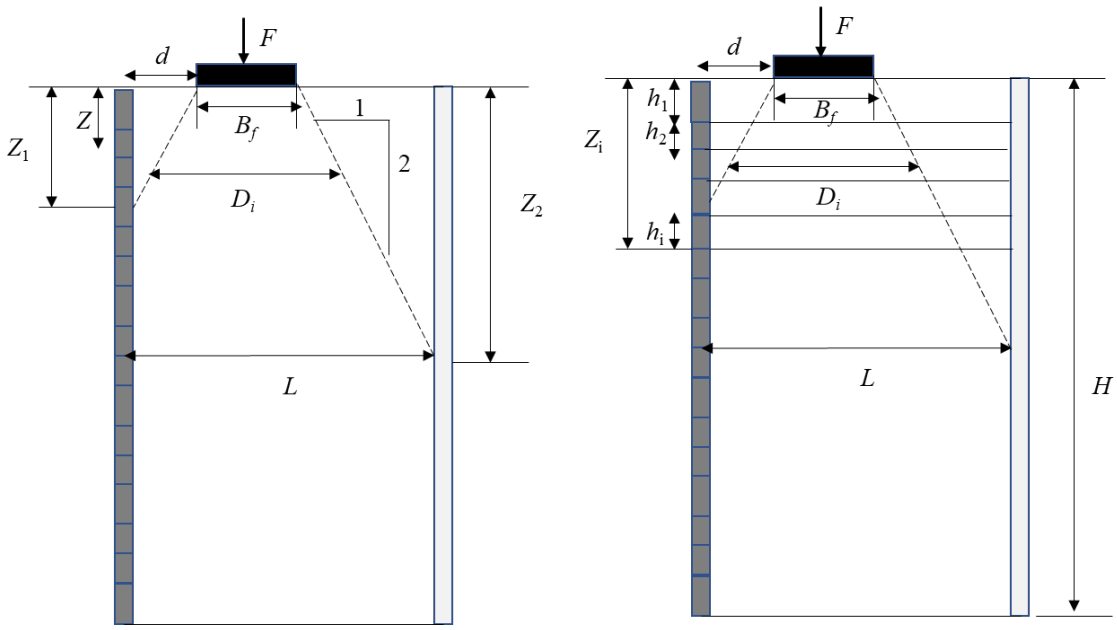

Figure 4. Analytical model.

When $Z_1 > Z_2$, the wall-soil friction applied on the *i*th slice can be expressed as follows:

$$f_i = \begin{cases} \Delta\sigma_i K_0 \tan(\delta) h_i (2D_i) & if\ 0 \le Z_i \le Z_1 \\ \Delta\sigma_i K_0 \tan(\delta) h_i (2D_i + W) & if\ Z_1 < Z_i \le Z_2 \\ \Delta\sigma_i K_a \tan(\delta) h_i W + \Delta\sigma_i K_0 \tan(\delta) h_i (2D_i + W) & if\ Z_2 < Z_i \end{cases} \tag{5}$$

where K_0 is the earth pressure coefficient at rest, K_a is Rankine's active earth pressure coefficient, δ is the wall-soil friction angle (assume $\delta = 2/3\varphi$) and φ is the soil internal friction

angle, *W* is the backfill width, and *F* is the applied footing load. In this derivation, the lateral earth pressure on the back of wall facing is assumed to be active while the lateral earth pressure between the reinforced backfill and the retained soil is assumed to be at rest.

Figure 5 compares the calculated vertical stresses with depth using the proposed simplified method with the measured ones in this study. The calculated results from the 2:1 distribution method are presented in this figure as well for comparisons. It is shown that the calculated vertical stresses by the 2:1 method were close to the measured ones within the depth ranging from 0 to 0.3 m before the distribution lines hit the wall facing and/or the interface between the reinforced backfill and the retained soil; however, there were obvious differences between the calculated and measured values and their differences became more significant when the depth increased from 0.3 to 1 m. The calculated vertical stresses from the proposed simplified method were smaller than those from the 2:1 method due to the wall-soil friction effect in the simplified method. Clearly the simplified method better matched the measured vertical stresses than the 2:1 distribution method. This comparison verifies that the proposed simplified method considering the wall-soil friction is reasonable and effective to calculate the vertical stresses for the limited space GRS walls.

CONCLUSIONS

Two model tests were selected to investigate the distribution of vertical stresses measured by earth pressure cells along the centerline of the footing in limited space GRS walls under static footing loading. The 2:1 stress distribution method was modified by adopting the horizontal slice concept and considering the wall-soil friction effect as a simplified method proposed in this paper.

The model tests showed the measured vertical stresses decreased from the bottom of the footing with the increase of the depth to the minimum value at the depth of five times the footing width.

The calculated vertical stresses using the proposed simplified method were compared well with the measured ones in the model tests and better than those calculated by the 2:1 stress distribution method.

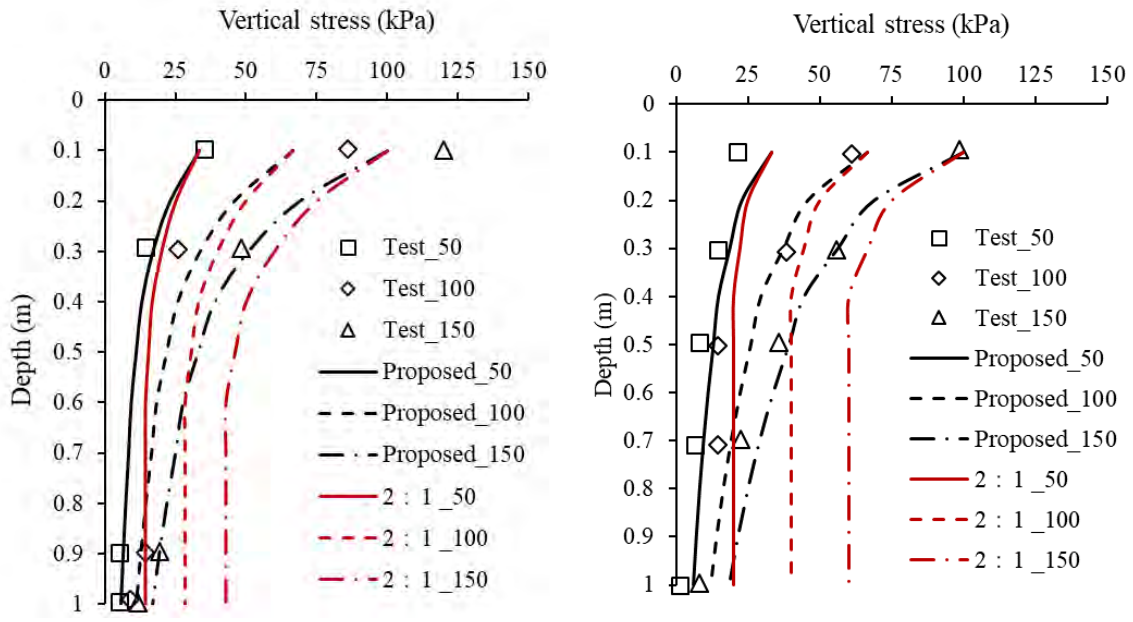

(a) T1 (b) T2

Figure 5. Measured versus calculated vertical stresses using the proposed method and the 2:1 stress distribution method.

REFERENCES

Abu-Hejleh, N., Wang, T. and Zornberg, J.G. (2000). Performance of geosynthetic reinforced walls supporting bridge and approaching roadway structures. *In: ASCE Geotechnical Special Publication No. 103. ASCE*, Reston, VA, United States, 218-243.

Abu-Hejleh, Zornberg, J.G. and Wang, T. (2001). Performance of Geosynthetic-reinforced Walls Supporting the Founders/Meadows Bridge and Approaching Roadway Structures. Colorado Department of Transportation Research Branch, Report No. CDOT-DTD-R-2001-12.

Bourgeois, E., Soyez, L. and Le Kouby, A. (2011). Experimental and numerical study of the behavior of a reinforced-earth wall subjected to a local load, *Computers and Geotechnics*, 38(4): 515-525.

Frydman, S., and Keissar, I. (1987). Earth pressure on retaining walls near rock faces, *Journal of Geotechnical Engineering*, 113(6): 586-599.

Handy, R. L. (1985). The arch in soil arching, *Journal of Geotechnical Engineering*, 111(3): 302-318.

Han, J. (2015). *Principles and Practice of Ground Improvement*, John Wiley & Sons, Hoboken, New Jersey, USA, ISBN: 978-1-118-25991-7, June, 432p.

Han, J. and Leshchinsky, D. (2010). Analysis of back-to-back mechanically stabilized earth walls, *Geotextiles and Geomembranes*, 28(3): 262-267.

Han, J. and Leshchinsky, D. (2006). General Analytical Framework for Design of Flexible Reinforced Earth Structures, *Journal of Geotechnical and Geoenvironmental Engineering*, 132(11): 1427-1435.

Jiang, Y., Han, J., Parsons, R.L., and Brennan, J.J. (2016). Field instrumentation and evaluation of modular-block MSE walls with secondary geogrid layers. ASCE *Journal of Geotechnical and*

Geoenvironmental Engineering, 142(12), 05016002.

Kakrasul, J. I. (2018). Geosynthetic reinforced retaining walls with limited fill space under static footing loading, Ph.D. dissertation, Department of Civil, Environmental, and Architectural Engineering, the University of Kansas.

Kakrasul, J.I., Han, J., Rahmaninezhad, S.M., and Weldu, M. (2016). Model tests of geosynthetic-reinforced earth walls with limited-space retained fill, 3rd Pan-American Conference on Geosynthetics, Miami Beach, FL, USA: 1279-1286.

Kakrasul, J.I., Han, J., and Rahmaninezhad, S.M. (2020). Load-deformation of geosynthetic-reinforced retaining walls with limited fill space under static footing loading. *Transportation Infrastructure Geotechnology*, 7(3), 309 – 331.

Khosravi, M. H., Pipatpongsa, T., and Takemura, J. (2013). Experimental analysis of earth pressure against rigid retaining walls under translation mode, *Géotechnique*, 63(12): 1020-1028.

Leshchinsky, D., Hu, Y.H., and Han, J. (2004). Limited reinforced space in segmental retaining walls. *Geotextiles and Geomembranes*, 22(6): 543-553

Leshchinsky, D. and Vulova, C. (2001). Numerical Investigation of the Effects of Geosynthetic Spacing on Failure Mechanisms of MSE Block Walls. *Geosynthetics International*, 8(4): 343-365.

Ling, H. and Leshchinsky, D. (2003). Finite element parametric study of the behavior of segmental block reinforced-soil retaining walls, *Geosynthetics International*, 10(3): 77-94.

Morrison, K. F., Harrison, F. E., Collin J. G., Dodds A., and Arndt B. (2006). Shored Mechanically Stabilized Earth (SMSE) Wall Systems Design Guidelines. Report No. FHWA-CFL/TD-06-001, Federal Highway Administration.

Mojtahedi M., and Fakharian, K. (2002). Behavior of bridge abutments reinforced with geogrid I: Parameters affecting deformations, *Proceedings of the 3rd Iranian International Conference on Geotechnical Engineering and Soil Mechanics*, Tehran, Iran, Vol. II: 299–307.

Rui, R., Ye, Y. Q., Han, J., Zhang, L., and Zhai, Y. X. (2020). Experimental and Theoretical Investigations on Active Earth Pressure Distributions behind Rigid Retaining Walls with Narrow Backfill under a Translational Mode, *International Journal of Geomechanics*, 20(10), 04020178.

Shen, P., Han, J., Zornberg, J. G., Tanyu, B. F., Christopher, B. R., and Leshchinsky, D. (2020). Responses of geosynthetic-reinforced Soil (GRS) abutments under bridge slab loading: Numerical investigation. *Computers and Geotechnics*, 123, 103566-1 to 17.

Wu, J. T., Lee, K. Z., and Pham, T. (2006). Allowable bearing pressures of bridge sills on GRS abutments with flexible facing, *Journal of Geotechnical and Geoenvironmental Engineering*, 132(7), 830-841.

Xiao, C., Han, J. and Zhang, Z. (2016). Experimental study on performance of geosynthetic-reinforced soil model walls on rigid foundations subjected to static footing loading, *Geotextiles and Geomembranes*, 44(1): 81-94.

Zheng, Y. and Fox, P. J. (2016). Numerical investigation of geosynthetic-reinforced soil bridge abutments under static loading, *Journal of Geotechnical and Geoenvironmental Engineering*, 142(5): 04016004.

ISBN: 978-0-935803-23-5